LEVEL II

AGARD-CP-291

AGARD-CP-291

AGARD

ADVISORY GROUP FOR AEROSPACE RESEARCH & DEVELOPMENT

7 RUE ANCELLE 92200 NEUILLY SUR SEINE FRANCE

AD A098428

AGARD CONFERENCE PROCEEDINGS No. 291

Computation of Viscous-Inviscid Interactions

DTIC
ELECTE
S MAY 4 1981 D
D

NORTH ATLANTIC TREATY ORGANIZATION



DTIC FILE COPY

DISTRIBUTION AND AVAILABILITY
ON BACK COVER

DISTRIBUTION STATEMENT A
Approved for public release;
Distribution Unlimited

81 4 30 224

(14) AGARD-CP-291

NORTH ATLANTIC TREATY ORGANIZATION

ADVISORY GROUP FOR AEROSPACE RESEARCH AND DEVELOPMENT

(ORGANISATION DU TRAITE DE L'ATLANTIQUE NORD)

(9) AGARD Conference Proceedings No.291

(6) COMPUTATION OF VISCOUS-INVISCID INTERACTIONS

(11) Feb 81

(12) 437

Accession For
NTIS GRA&I [X]
DTIC TAB [ ]
Unannounced [ ]
Justification
By
Distribution/
Availability Codes
Dist | Avail and/or Special
A

DTIC ELECTE MAY 4 1981 S D
D

DISTRIBUTION STATEMENT A
Approved for public release;
Distribution Unlimited

Papers presented and discussions held at the Fluid Dynamics Panel Symposium held at the United States Air Force Academy, Colorado Springs, Colorado, USA – 29 September – 1 October 1980

400 043

THE MISSION OF AGARD

The mission of AGARD is to bring together the leading personalities of the NATO nations in the fields of science and technology relating to aerospace for the following purposes:

- Exchanging of scientific and technical information;
- Continuously stimulating advances in the aerospace sciences relevant to strengthening the common defence posture;
- Improving the co-operation among member nations in aerospace research and development;
- Providing scientific and technical advice and assistance to the North Atlantic Military Committee in the field of aerospace research and development;
- Rendering scientific and technical assistance, as requested, to other NATO bodies and to member nations in connection with research and development problems in the aerospace field;
- Providing assistance to member nations for the purpose of increasing their scientific and technical potential;
- Recommending effective ways for the member nations to use their research and development capabilities for the common benefit of the NATO community.

The highest authority within AGARD is the National Delegates Board consisting of officially appointed senior representatives from each member nation. The mission of AGARD is carried out through the Panels which are composed of experts appointed by the National Delegates, the Consultant and Exchange Programme and the Aerospace Applications Studies Programme. The results of AGARD work are reported to the member nations and the NATO Authorities through the AGARD series of publications of which this is one.

Participation in AGARD activities is by invitation only and is normally limited to citizens of the NATO nations.

The content of this publication has been reproduced
directly from material supplied by AGARD or the authors.

Published February 1981

Copyright © AGARD 1981
All Rights Reserved

ISBN 92-835-0286-8



Printed by Technical Editing and Reproduction Ltd
Harford House, 7–9 Charlotte St, London, W1P 1HD

EXECUTIVE SUMMARY

Computational aircraft performance prediction is with no doubt the final goal of all the fundamental research in Aerodynamics because computational methods are indispensable to define and above all to optimize the aircraft we have to build.

Today, even more than in the past, one wants to define as quickly as possible with minimum recourse to experiments, economically optimized configurations having good performance up to the limits of the flight envelope and to know in advance their absolute level of performance.

Obviously, to accomplish this, one needs to take all the features of the flow into account, especially its viscous character.

Apart from the Navier-Stokes approach in the whole flow field, which will not be useable on three-dimensional practical shapes for several years, the only way to do this now is to take advantage of the huge amount of work done on the parts of the flow where viscosity plays a major role – the boundary and the shear layers – as well as on those where the perfect fluid assumption can be made and to find adequate methods and algorithms to link the viscous and the inviscid parts of the flow.

This symposium was consequently organized to review the search for coupling procedures. It appears that the situation is quite satisfactory for 2D flows. Very good correlations can be found between the computational results and the experiments provided that the methods include the wake displacement and curvature effects, and adequate treatment of the trailing edge region and of the shock boundary layer interactions. If so, useful and reliable tools are available for engineering purposes.

However, the agreement generally deteriorates with the extension of separated regions or when the shock intensity increases and further improvements are still needed, for example, for single or multielement airfoils near maximum lift or at high Mach numbers. In addition it must be stressed that the quality and the accuracy of the experimental data become questionable as the capability of the computational methods to adequately describe more and more complex situations increases. Therefore precise and reliable code validation requires more and more well documented benchmark data.

For 3D configurations, the work is much less advanced; only a few studies have been made and a lot of work has still to be done, especially in the transonic regime. However, the first results obtained using the ideas which have proven to be efficient in 2D are encouraging. The problem of separation with formation and rolling-up of vortex sheets which is specific to 3D flows is of primary importance and the studies already made on this subject will have to be pursued and extended in the compressible and transonic regime. Finally, it has been recorded that the need for detailed benchmark experiments is even greater in 3D than in 2D.

B.MONNERIE
B.QUINN

AGARD FLUID DYNAMICS PANEL

Chairman: Dr K.J.Orlik-Rückemann
National Aeronautical Establishment
National Research Council
Montreal Road
Ottawa, Ontario K1A 0R6, Canada

Deputy Chairman: M. l'Ing. en Chef B.Monnerie
Chef de la Division d'Aérodynamique Appliquée
ONERA
29 Avenue de la Division Leclerc
92320 Châtillon, France

PROGRAM COMMITTEE MEMBERS

M. l'Ing. en Chef B.Monnerie (Co-Chairman)
Chef de la Division d'Aérodynamique Appliquée
ONERA
29 Avenue de la Division Leclerc
92320 Châtillon, France

Dr J.E.Green
Head of Aerodynamics Department
Royal Aircraft Establishment
Farnborough, Hants GU14 6TD, UK

Prof. Dr F.J.Hindelang
Fachbereich Luft-und-Raumfahrttechnik
Hochschule der Bundeswehr Munchen
8014 Neubiberg, FRG

Prof. Dr Ir. J.L. van Ingen
Department of Aerospace Engineering
Delft University of Technology
Kluyverweg 1
2629 HS Delft, The Netherlands

Prof. S.J.Kline
Mechanical Engineering Department
Thermosciences Division
Stanford University
Stanford CA 94305, USA

Dr B.Quinn (Co-Chairman)
President
Aeronautical Research Associates
Princeton
50 Washington Road
Princeton NJ 08540, USA

Prof. E.Mattioli
Director Istituto Meccanica Applicata
University di Ancona
Via della Montagnola No. 30
60100 Ancona, Italy

Dr A.G.Panaras
Captain, Hellenic Air Force
Kabbatha 14
Athens (624), Greece

M.M.Sirieix
Directeur Adjoint de l'Aérodynamique
ONERA
29 Avenue de la Division Leclerc
92320 Châtillon, France

PANEL EXECUTIVE

Robert H. Rollins II

CONTENTS

	Page
EXECUTIVE SUMMARY	iii
PANEL AND PROGRAM COMMITTEE MEMBERS	iv
	Reference
SESSION I – UNSEPARATED FLOWS, THIN LAYER CONCEPT	
CALCUL DES ECOULEMENTS A FORTE INTERACTION VISQUEUSE AU MOYEN DE METHODES DE COUPLAGE par J.C. Le Balleur	1
A REVIEW OF METHODS FOR PREDICTING VISCOUS EFFECTS ON AEROFOILS AND WINGS AT TRANSONIC SPEEDS by R.C.Lock	2
INVISCID-VISCOUS INTERACTIONS IN THE NEARLY DIRECT DESIGN OF SHOCK-FREE SUPERCRITICAL AIRFOILS by H.E.Nebeck, A.R.Seebass and H.Sobieczky	3
THE COUPLING OF A SHOCK BOUNDARY LAYER INTERACTION MODULE WITH A VISCOUS-INVISCID COMPUTATION METHOD by E.Stanewsky, M.Nandanan and G.R.Inger	4
COUPLAGE FLUIDE PARFAIT-FLUIDE VISQUEUX EN ECOULEMENT INSTATIONNAIRE BIDIMENSIONNEL INCOMPRESSIBLE ET TRANSSONIQUE par A.Desopper et R.Grenon	5
VISCOUS FLOW SIMULATION OF HIGH LIFT DEVICES AT SUBSONIC AND TRANSONIC SPEED by S.Leicher	6
FLOW COMPUTATION AROUND MULTI-ELEMENT AIRFOILS IN VISCOUS TRANSONIC FLOW by H.Rosch and K.D.Klevenhusen	7
CALCULATIONS OF TRANSONIC FLOW OVER WING/BODY COMBINATIONS WITH AN ALLOWANCE FOR VISCOUS EFFECTS by M.C.P.Firmin	8
PLANAR TRANSONIC AIRFOIL COMPUTATIONS WITH VISCOUS INTERACTIONS by J.C.Wai and H.Yoshihara	9
SESSION II – TURBULENT STRONG INTERACTION WITHOUT EXTENSIVE SEPARATED FLOW REGIONS	
TURBULENT INTERACTIONS ON AIRFOILS AT TRANSONIC SPEEDS – RECENT DEVELOPMENTS by R.E.Melnik	10
CALCUL D'ECOULEMENTS VISQUEUX DECOLLES SUR PROFILS D'AILES PAR UNE APPROCHE DE COUPLAGE par J.C. Le Balleur et M.Néron	11
THE CALCULATION OF INCOMPRESSIBLE BOUNDARY LAYERS WITH STRONG VISCOUS-INVISCID INTERACTION by A.E.P.Veldman	12
A VISCOUS-INVISCID INTERACTION MODEL OF JET ENTRAINMENT by R.G.Wilmoth and S.M.Dash	13

Reference

ANALOGIE DES SINGULARITES DANS LES METHODES DIRECTES DE CALCUL DES COUCHES LIMITES TRIDIMENSIONNELLE STATIONNAIRE ET BIDIMENSIONNELLE INSTATIONNAIRE – ANALYSE DES MODES INVERSES
par J.Cousteix et R.Houdeville 14

A PHENOMENOLOGICAL MODEL FOR DISPLACEMENT THICKNESS EFFECTS OF TRANSONIC SHOCK WAVE-BOUNDARY LAYER INTERACTIONS
by W.-H.Jou and E.M.Murman 15

SIMPLE APPROXIMATIONS FOR THE ASYMPTOTIC DESCRIPTION OF THE INTERACTION BETWEEN A NORMAL SHOCK WAVE AND A TURBULENT BOUNDARY LAYER AT TRANSONIC SPEEDS
by T.C.Adamson, Jr and A.F.Messiter 16

NORMAL SHOCK-TURBULENT BOUNDARY LAYER INTERACTION AT A CURVED WALL
by R.Bohning and J.Zierep 17

SOME FEATURES OF A SHOCK-TURBULENT BOUNDARY LAYER INTERACTION THEORY IN TRANSONIC FLOW FIELDS
by G.R.Inger 18

COMPUTATIONAL ASPECTS AND RESULTS OF LOW SPEED VISCOUS FLOW ABOUT MULTICOMPONENT AIRFOILS
by B.Oskam 19

SEPARATION AND REATTACHMENT NEAR THE LEADING EDGE OF A THIN AIRFOIL AT INCIDENCE
by T.Cebeci, K.Stewartson and P.G.Williams 20

BULBE DE DECOLLEMENT LAMINAIRE AVEC TRANSITION – ESSAI DE PREVISION AVEC COUPLAGE LOCAL
par C.Gleyzes, J.Cousteix et J.L.Bonnet 21

SESSION III – SEPARATED FLOWS

THE 1980-81 AFOSR-HTTM-STANFORD CONFERENCE ON COMPLEX TURBULENT FLOWS: COMPARISON OF COMPUTATION AND EXPERIMENT
by S.J.Kline 22

THEORETICAL AND EXPERIMENTAL INVESTIGATIONS OF TWO-DIMENSIONAL FLOWS WITH SEPARATED REGIONS OF FINITE LENGTH
by K.Gersten, H.Herwig and P.Wauschkuhn 23

TWO-DIMENSIONAL SEPARATED FLOW: EXPERIMENT AND DISCRETE VORTEX DYNAMICS SIMULATION
by W.T.Ashurst, F.Durst and C.Tropea 24

THE DEVELOPMENT AND APPLICATION OF A METHOD FOR CALCULATING THE VISCOUS FLOW ABOUT HIGH LOFT AEROFOILS
by D.J.Butter and B.R.Williams 25

A DIRECT-INVERSE TECHNIQUE FOR LOW SPEED HIGH LIFT AIRFOIL FLOWFIELD ANALYSIS
by L.A.Carlson 26

A SECOND ORDER ACCURATE NUMERICAL METHOD FOR SUPERSONIC INTERACTING BOUNDARY LAYER FLOW PAST A COMPRESSION CORNER
by B.Fortunato 27

CALCUL DE L'INTERACTION ONDE DE CHOC/COUCHE LIMITE AVEC DECOLLEMENT
par P.Ardonceau, Th.Alziary and D.Aymer 28

	Reference
TOWARD A SPLINE TECHNIQUE FOR THE HIGH REYNOLDS NUMBER INTERACTION (TRIPLE DECK) PROBLEM by M.Napolitano and G.Vacca	29
A THEORY OF THE SEPARATED FLOW PAST A SLENDER ELLIPTIC CONE AT INCIDENCE by S.P.Fiddes	30
PREDICTION OF AERODYNAMIC CHARACTERISTICS FOR WINGS WITH EXTENSIVE SEPARATIONS by B.Maskew, B.M.Rao and F.A.Dvorak	31
OPEN DISCUSSION SESSION	
AN EXPERIMENTAL STUDY OF THE FLOW ON A SWEPT WING IN FLIGHT by A.Bertelrud	OD
ROUND TABLE DISCUSSION	RTD

CALCUL DES ECOULEMENTS A FORTE INTERACTION VISQUEUSE AU MOYEN DE METHODES DE COUPLAGE

J.C. LE BALLEUR

Office National d'Etudes et de Recherches Aérospatiales (ONERA)
29, avenue de la Division Leclerc - 92320 Châtillon - FRANCE

RESUME

Les méthodes de calcul du fluide visqueux par des approches de couplage sont analysées globalement On dégage d'abord les niveaux d'approximations et les concepts mis en jeu, ainsi que les formulations généralisées de l'effet de déplacement visqueux sur le fluide parfait. On analyse ensuite les méthodes de couplage fort qui s'appuient sur des approximations de couches visqueuses minces.

Dans ce cadre, on propose une formulation déficitaire du calcul de l'écoulement visqueux, évaluant l'écart à un écoulement de fluide parfait superposé. Cette approche permet de traiter approximativement les gradients de pression normaux et d'éliminer les comportements supercritiques au sens de Crocco-Lees. Elle maintient des équations intégrales simples. On passe ensuite en revue les principales techniques numériques de couplage actuelles. Les possibilités globales et les espoirs des méthodes sont examinés au vu des calculs de profils d'ailes. Des résultats nouveaux sur le décollement de bord de fuite sont présentés, ainsi qu'une méthode approchée originale pour traiter numériquement l'interaction au pied des ondes de choc.

COMPUTATION OF FLOWS INCLUDING STRONG VISCOUS INTERACTIONS WITH COUPLING METHODS

SUMMARY

The calculation of viscous flows with coupling methods is surveyed. The approximation levels and concepts are firstly outlined, as well as the generalized formulations of the viscous displacement for the inviscid flow. Then, the strongly interacting methods that are based on thin viscous layers approximations are discussed.

On this way, a matching formulation of the viscous flow, calculated as a difference with the inviscid overlaying flow, is suggested, in order to restitute approximately the normal pressure gradient inside of the layers, as well as to remove the supercritical behaviours, in the Crocco-Lees sense. This analysis maintains simple viscous integral equations. A review is then given of the main numerical techniques presently available for the coupling problem. The global state of the art and possible extensions are looked at through the viscous methods for airfoils. New results are presented for trailing-edge separation, and an approximate method is suggested to capture numerically the viscous interaction under the shock-waves.

1. INTRODUCTION

Les écoulements à grand nombre de Reynolds se caractérisent par l'existence de phénomènes localisés à évolution très rapide, associant étroitement d'une part les effets de la viscosité et de la turbulence, généralement confinés dans des couches minces, d'autre part leur répercussion sur la structure de l'écoulement non dissipatif. L'exemple typique d'une telle situation est celui de l'interaction choc-couche limite.

Ces phénomènes concentrés et à petite échelle peuvent conditionner l'écoulement macroscopique dans sa totalité en raison du caractère non linéaire des équations qui le régissent et donner naissance à des régimes complexes, dits de forte interaction visqueuse, par opposition aux régimes de faible interaction fondamentalement différents et conduisant à des solutions proches de l'approximation classique du fluide parfait.

Malgré les progrès importants de méthodes numériques adaptées à la résolution des équations de Navier-Stokes complètes, en principe capables de traiter ces régimes de forte interaction, une approche purement mathématique du problème aérodynamique reste difficile dans la mesure où elle demeure largement tributaire de la précision des techniques numériques, de l'élaboration de modèles de turbulence suffisamment généraux, du recours nécessaire à des maillages très fins supposant l'emploi de moyens de calcul très puissants et pas encore disponibles.

Une approche plus physique est de ce fait présente dans toute l'aérodynamique numérique pratique. Elle apparaît entre autres dans l'introduction d'équations, de conditions aux limites ou de "modèles" locaux simplifiés, dans l'élaboration de méthodes de résolution composites fondées sur le couplage de plusieurs méthodes numériques distinctes, dans le recours nécessaire à des maillages adaptés aux circonstances locales de l'écoulement. Il est clair que l'origine de telles méthodes est étroitement associée à la structure en échelle multiples de l'écoulement ainsi qu'à l'existence d'équations approchées et de méthodes numériques appropriées à chaque échelle. L'adaptation de ces méthodes à la physique des phénomènes s'est bien souvent révélée comme une source d'efficacité, notamment pour des niveaux d'approximation visqueuse relativement modestes. Un exemple typique est fourni par le calcul difficile des profils transsoniques pour lesquels les méthodes fondées sur des analyses de fluide parfait et de couche limite en interaction possèdent encore des performances meilleures que les analyses de type Navier-Stokes, à la fois quant au coût des calculs et quant à leur précision.

A plus long terme, on peut penser que l'adaptation des méthodes de couplage aux aspects physiques spécifiques des grands nombres de Reynolds devrait conduire, parallèlement au développement des méthodes de résolution directes, soit à une économie pour des performances égales, soit au traitement de problèmes plus complexes

pour un coût de calcul donné, en tridimensionnel par exemple, soit enfin au développement indirect de techniques numériques nouvelles pour résoudre les équations de Navier-Stokes.

Nous allons examiner ici succinctement, dans les parties 2 et 3, les niveaux d'approximations et les concepts généraux qui paraissent se dégager des méthodes de calcul actuelles, en régime de forte interaction visqueuse. Les parties 4, 5 et 6 seront consacrées aux méthodes s'appuyant sur des approximations visqueuses simples, obtenues à partir d'hypothèses de Prandtl ou de couche mince. Après discussion de leurs répercussions sur un modèle de calcul par couplage avec le fluide parfait, nous passerons brièvement en revue les méthodes numériques actuellement capables de résoudre un couplage de ce type, problème de base dont l'étude est encore cependant récente et limitée. Nous examinerons enfin, sur l'exemple de synthèse des profils transsoniques où divers phénomènes d'interaction visqueuse interfèrent, quelles sont les possibilités et espoirs des méthodes de couplage de cette catégorie.

2. APPROXIMATION NUMERIQUE DU FLUIDE VISQUEUX : NIVEAUX GENERAUX D'ANALYSE ET METHODES DE COUPLAGE

Il est hors du propos de cette brève analyse de passer en revue les diverses méthodes en usage pour le calcul du fluide visqueux, l'objectif étant ici seulement de dégager qualitativement les grandes voies d'approche, les niveaux d'approximation possibles, ainsi que les limites d'utilisation.

Comme l'indique la figure 1,une classification en quatre niveaux paraît concevable, le niveau I regroupant des approches variées, mais fondées sur une résolution directe, tandis que les niveaux II, III, IV correspondent aux principales approches indirectes ou méthodes de couplage. Bien que, pour chaque niveau, des approximations plus ou moins fortes puissent intervenir, ce qui exclut de ce classement une hiérarchie stricte, la généralité des méthodes les plus complètes de chaque catégorie est croissante dans le sens allant de IV vers I.

2.1. Méthodes de résolution directes

Le niveau I correspond aux méthodes de résolution directes et inclut en particulier la résolution complète des équations de Navier-Stokes, ainsi que les résolutions limitées aux structures turbulentes à grande échelle, avec modélisation des structures fines. D'un point de vue plus orienté vers les méthodes actuellement utilisables dans les applications, le niveau I correspond à une approche qui peut être qualifiée de globale [1 à 4] dans la mesure où elle adopte une même méthode numérique et un même système d'équations, uniformément valables dans tout le champ d'écoulement. Il s'agit soit des équations de Navier-Stokes moyennées, associées à un modèle de turbulence,soit des équations de Navier-Stokes tronquées par des approximations de couche mince [5, 6].

2.2. Méthodes directes avec commutation d'équations

Une première extension de l'approche globale consiste à conserver une méthode numérique unique, mais à commuter les équations résolues, en fonction des zones de calcul, sur des systèmes complets ou simplifiés [7], figure 2. Cette approche, voisine dans ses motivations des méthodes de couplage par zones, ne peut être considérée comme identique. Il est clair en effet que les frontières de commutation d'équations ainsi mises en jeu ne matérialisent nullement des domaines de calcul numérique disjoints, raccordés par leurs seules conditions aux limites, mais qu'au contraire une continuité numérique des dérivées normales aux frontières de commutation est implicitement postulée. L'approche de commutation d'équations par zones correspond donc essentiellement à un allègement des calculs,obtenu en supposant a priori l'annulation d'une partie des termes des équations dans certaines régions, à la précision de la technique de résolution numérique. Cet allègement peut être complété par une optimisation de la géométrie des frontières de commutation.

2.3. Méthodes de couplage fort avec dissociation par domaines

L'approche par commutation d'équations peut conduire à l'apparition de problèmes mathématiques ou numériques nouveaux par rapport à une approche globale avec équations de Navier-Stokes complètes, en cas de troncature importante de ces dernières. Ils seront par exemple associés aux changements d'ordre des équations aux dérivées partielles, aux changements de domaine de dépendance ainsi que desconditions aux limites nécessaires.

Ainsi est-on conduit au niveau II et à l'approche de couplage par dissociation de domaines de calcul, figure 3, dans laquelle les problèmes mathématiques et numériques sont traités indépendamment, tandis que le problème global est reconstitué par le biais d'un couplage rigoureux, dit couplage fort, entre les conditions aux limites des divers sous-domaines, le long de leurs frontières communes. Les équations utilisées dans les divers sous-domaines sont en général, soit les équations de Navier-Stokes complètes, soit des équations tronquées dans des approximations de couche mince, de Prandtl ou d'Euler [8, 9, 10 , 11].

Les changements d'ordre et de nature des équations aux dérivées partielles avec les sous-domaines de calcul contraignent à moduler en conséquence le nombre des conditions de couplage le long des frontières de raccordement, et à opérer des choix guidés par la physique des phénomènes ainsi que la nature des équations locales. Le couplage des paramètres aérodynamiques sur une frontière de raccordement ne conduit plus ici, en particulier au raccordement de leurs dérivées normales à cette frontière, le défaut de raccordement résiduel étant représentatif de la précision du modèle de couplage, pour un découpage de zones et d'équations déterminé.

Il est à noter que le passage du niveau I au niveau II fait surgir un problème numérique nouveau. Il s'agit de réaliser, par des méthodes itératives ou implicites, en stationnaire comme en instationnaire, le couplage fort des conditions aux limites associées aux divers sous-problèmes. Il est clair que cette difficulté majeure, qui ne saurait se résumer à l'établissement d'un organigramme de calcul, n'a fait l'objet au

au niveau de l'aérodynamique que d'un nombre encore restreint d'études, motivées essentiellement par le raccordement des équations d'Euler et de Prandtl,(cf paragraphe 5).

2.4. Méthodes de couplage fort avec dissociation par équations

La technique précédente de dissociation par domaines suppose que dans chacun d'entre eux les équations résolues décrivent à elles seules le comportement local de l'écoulement. En cas de niveaux d'approximation assez modestes, comme par exemple celui des équations de Prandtl, une telle situation peut conduire à des limitations importantes. On doit remarquer par ailleurs qu'une telle technique de raccordement est évitée dans les méthodes analytiques de développements asymptotiques raccordés, dans lesquelles les domaines de calcul associés aux diverses échelles se trouvent superposés dans un même domaine physique.

Nous avons trouvé [3, 12 à 15] que l'introduction de domaines de calcul en recouvrement, figure 4, dans la formulation de méthodes composites couplées pour le calcul du fluide visqueux à nombre de Reynolds élevé, pouvait conduire à un progrès important, relié physiquement à la possibilité de traiter l'écoulement de fluide visqueux en termes d'écarts à l'écoulement de fluide parfait fictif dont il est le plus voisin. Cette analyse constitue une généralisation des méthodes de couche limite, classiques ou bien avec fort gradient normal de l'écoulement externe. Si nous considérons par exemple un repère curviligne xOy le long d'une paroi, que nous supposerons plane pour simplifier l'exposé , si $\bar{u}$ et $\bar{v}$ sont les composantes de la vitesse, $\bar{\rho}$ la masse volumique et $\bar{p}$ la pression, si u , v , ρ , p sont leurs homologues pour l'écoulement de fluide parfait superposé, les équations du fluide visqueux, notées (1) + (2) , seront dissociées en un système d'équations de fluide parfait, notées (1) , et en un système d'équations déficitaires visqueuses notées (2) . Les équations dynamiques stationnaires deviennent ainsi :

$$(1)\quad \begin{cases} \dfrac{\partial \rho u}{\partial x} + \dfrac{\partial \rho v}{\partial y} = 0 \\ \dfrac{\partial \rho u^2}{\partial x} + \dfrac{\partial \rho uv}{\partial y} = -\dfrac{\partial p}{\partial x} \\ \dfrac{\partial \rho uv}{\partial x} + \dfrac{\partial \rho v^2}{\partial y} = -\dfrac{\partial p}{\partial y} \end{cases} \qquad (2.1)$$

$$(2)\quad \begin{cases} \dfrac{\partial \rho u - \bar{\rho}\bar{u}}{\partial x} + \dfrac{\partial \rho v - \bar{\rho}\bar{v}}{\partial y} = 0 \\ \dfrac{\partial \rho u^2 - \bar{\rho}\bar{u}^2}{\partial x} + \dfrac{\partial \rho uv - \bar{\rho}\bar{u}\bar{v}}{\partial y} = -\dfrac{\partial p - \bar{p}}{\partial x} - \dfrac{\partial \sigma_x}{\partial x} - \dfrac{\partial \tau_{xy}}{\partial y} \\ \dfrac{\partial \rho uv - \bar{\rho}\bar{u}\bar{v}}{\partial x} + \dfrac{\partial \rho v^2 - \bar{\rho}\bar{v}}{\partial y} = -\dfrac{\partial p - \bar{p}}{\partial y} - \dfrac{\partial \sigma_y}{\partial y} - \dfrac{\partial \tau_{xy}}{\partial x} \end{cases} \qquad (2.2)$$

σ_x , σ_y , τ_{xy} représentant les composantes du tenseur des contraintes. Cette formulation déficitaire du problème visqueux conduit à une résolution sensiblement du même type que dans l'approche de couplage par domaines, en raison du couplage fort qui doit être réalisé entre (2) et les conditions aux limites (1) pour que :

$$0 = \lim_{y \to \infty} [f - \bar{f}] \qquad \text{avec } f = \{u, v, p, \rho\} \qquad (2.3)$$

On note toutefois que l'importance du choix, relativement arbitraire dans l'approche de couplage par raccordement de domaines, de la frontière externe des couches visqueuses $y = \delta(x)$, est éliminée.

Un avantage de la formulation déficitaire (2.2) apparaît clairement en cas d'approximation par des hypothèses intermédiaires entre celles de Prandtl et celles des équations de Navier-Stokes en couches minces. Il vient alors :

$$\begin{cases} \dfrac{\partial \rho u - \bar{\rho}\bar{u}}{\partial x} + \dfrac{\partial \rho v - \bar{\rho}\bar{v}}{\partial y} = 0 \\ \dfrac{\partial \rho u^2 - \bar{\rho}\bar{u}^2}{\partial x} + \dfrac{\partial \rho uv - \bar{\rho}\bar{u}\bar{v}}{\partial y} = -\dfrac{\partial \tau_{xy}}{\partial y} \\ \dfrac{\partial p - \bar{p}}{\partial y} = 0 \end{cases} \qquad (2.4)$$

Ce qui, d'après (2.3), fournit $\bar{p}(x,y) = p(x,y)$. Cette approximation sur la pression est beaucoup moins

restrictive que celle qui serait déduite des équations de Prandtl dans un couplage par raccordement de domaines :

$$\frac{\partial \bar{p}}{\partial y} = 0 \qquad \bar{p}(x,y) = \bar{p}(x) = p(x,\delta) \qquad (2.5)$$

alors que la résolution du système parabolique (2.4) avec u , v , p , ρ donnés par (2.1) est d'une complexité équivalente à la résolution des simples équations de Prandtl.

En cas de simplifications moins importantes que (2.4), ou d'application des équations de Navier-Stokes (2.2), le choix de la formulation déficitaire (2.1) (2.2) devient intimement lié au choix et au conditionnement des techniques numériques appliquées à (2.1) et (2.2), ainsi qu'à leur couplage. Nous noterons enfin qu'au niveau d'approximation II de la figure 1, la dissociation effectuée en système d'équations visqueuses et non-visqueuses suppose une analyse de couplage en forte interaction, qui correspond à la résolution stricte de (2.1) (2.2) (2.3), et qui prend en compte l'influence exercée par l'aval de l'écoulement sur l'amont. Des approches de ce type, bien que plus ou moins simplifiées, ont été récemment expérimentées [16, 17, 18]. D'autres approches maintiennent en revanche des approximations de systèmes d'équations paraboliques, résolus directement d'amont en aval, ce qui les rapproche des méthodes de couche limite en faible interaction du niveau IV [19, 20].

2.5. Méthodes de couplage faible

Les niveaux d'approximations I et II correspondent à une modélisation du fluide visqueux capable de décrire au moins qualitativement les régimes de forte interaction visqueuse, soit en raison des équations visqueuses résolues, soit grâce à un effet de couplage fort au fluide parfait, dans le cas des équations visqueuses les plus simples. Il est toutefois important de considérer que cette capacité de traiter les zones de forte interaction suppose l'utilisation de maillages fins appropriés pour être effective, quelles que soient les équations résolues. En régime turbulent, même pour les systèmes d'équations les plus simples, les échelles de résolution ne sauraient en particulier être plus grossières que l'épaisseur locale des couches visqueuses mises en jeu.

Les niveaux III et IV correspondent à des analyses simplifiées dont la généralité d'application est moins grande, mais qui restent le support de la plupart des applications actuelles. Les plus répandues sont les méthodes de couches limites du niveau IV, en utilisation conjointe avec des calculs en fluide parfait traditionnels, résolus de manière découplée. L'absence de résolution couplée provient du concept d'interaction ou de couplage faible, qui s'associe à la théorie asymptotique du second ordre de la couche limite dans le cas laminaire [21], et à des théories de même nature dans le cas turbulent [22, 23].

La figure 5 schématise la simplification apportée au niveau du couplage. En première approximation, le champ de fluide parfait est obtenue indépendamment de toute couche limite. Il détermine pour celle-ci un champ de pression simplifié qui permet le calcul d'une première approximation de la couche limite et de son épaisseur de déplacement. Celle-ci suffit à déterminer l'approximation finale du fluide parfait, ainsi que celle du champ de pression de la couche limite. Une approximation de second ordre peut alors être calculée pour la couche limite, qui alors possède toujours un gradient de pression normal prédéterminé mais non nul en cas de courbure de la paroi. Le couplage est "faible" dans la mesure où la couche visqueuse est entièrement conditionnée, à un ordre d'approximation donné, par un écoulement de fluide parfait sur lequel ne s'exerce aucune influence réciproque.

Dans cette analyse, l'idée d'itération sur l'épaisseur de déplacement visqueuse est absente et se trouve remplacée par une correction directe et unique. L'insuffisance éventuelle d'une telle correction unique marque précisément l'apparition de phénomènes de forte interaction visqueuse, liés aux décollements, ondes de choc, bord de fuite, ainsi que la nécessité de modèles à couches multiples si l'on veut maintenir l'emploi de théories asymptotiques [23 à 31], sans toutefois pouvoir éliminer l'apparition d'un problème de couplage fort.

Une propriété caractéristique du couplage faible asymptotique est de conduire, pour le problème visqueux, à la résolution d'un système parabolique dans lequel on ignore l'influence que peut exercer l'aval de l'écoulement sur l'amont. Une telle influence ne peut donc être retrouvée que par les conditions aux limites imposées par le fluide parfait, et se trouve de ce fait totalement supprimée pour un écoulement externe supersonique, ou encore dans l'approximation d'un écoulement de fluide parfait subsonique monodimensionnel.

La simplification correspondante apportée à la résolution, qui peut alors procéder en marchant de l'amont vers l'aval, a fait l'objet de transpositions dans des méthodes abandonnant les équations simples de Prandtl au profit d'équations moins restrictives, qualifiées au niveau IV de la figure 1 d'approximations paraboliques des équations de Navier-Stokes. Dans ce cas, les équations de Navier-Stokes sont d'abord assujetties à des approximations de couches minces, qui consistent à éliminer les termes visqueux de diffusion suivant Ox , si Ox représente la direction de l'écoulement principal. Cette simplification des niveaux I ou II ne suffit pas cependant à elle seule, dans le cas général, pour paraboliser totalement le système d'équations dans la direction des x positifs, notamment en présence de régions d'écoulement subsonique [32, 33]. On peut alors parler de systèmes d'équations elliptiques à cause du champ de pression, dans la mesure où les systèmes redeviennent paraboliques soit lorsque la pression est figée, soit lorsque son évolution longitudinale moyenne selon x est figée mais que sa variation secondaire dans le plan yOz est calculée [34], soit enfin lorsque l'évolution longitudinale de la pression est elle aussi calculée d'amont en aval mais au prix d'une approximation quasi-monodimensionnelle et d'une altération de la pression dans l'équation de quantité de mouvement selon Ox [35].

Dans tous les cas, le passage d'un tel problème parabolisé de couplage faible à un problème elliptique de couplage fort du niveau I ou II suppose l'addition d'une itération sur la pression, capable d'éliminer à convergence les diverses approximations mises en jeu à chaque itération parabolisée [16, 17, 34, 36].

2.6. Méthodes intermédiaires entre couplage faible et fort

La figure 1, au niveau III, fournit des exemples de ce type d'analyse. Le premier peut être fourni par l'extension progressive des méthodes de calcul de profils d'ailes. Partant de l'insuffisance évidente d'une approche de couplage faible, une extension allant dans le sens de la recherche d'un couplage fort a été progressivement développée, par le biais d'itérations sur l'effet de déplacement visqueux. Bien que les niveaux d'approximation obtenus diffèrent sensiblement entre les différentes méthodes, par exemple [15, 29, 37 à 40], soit en raison du recours à des lissages ou à des modélisations relativement arbitraires de l'épaisseur de déplacement, soit en raison de techniques de couplage incomplètes, numériquement ou analytiquement, au niveau des décollements, des bords de fuite, des interactions couches limites - ondes de choc ou des maillages de calcul, il est clair que l'évolution d'ensemble devrait déboucher à terme sur des méthodes de couplage fort du niveau II.

Une seconde catégorie de méthodes intermédiaires entre couplage faible et fort est fournie par la modélisation des décollements en fluide parfait. Un premier exemple est donné ici par le calcul d'écoulements de fluide parfait comportant des nappes tourbillonnaires issues de lignes de décollement prédéterminées [41]. Un second exemple est celui des modélisations de grands décollements par calcul de frontières libres isobares dans un écoulement de fluide parfait, utilisées notamment dans les problèmes de décrochage [42].

3. CONDITIONS AUX LIMITES DU FLUIDE PARFAIT - DEPLACEMENT

Les méthodes de calcul en fluide parfait s'appuient d'une part sur la condition de glissement, qui traduit l'imperméabilité à la paroi, et d'autre part sur la condition de Joukowski qui, lorsqu'elle est mise en jeu, paraît seule rappeler que l'objectif est la modélisation d'un fluide visqueux. Le calcul fait en outre apparaître, au titre des solutions faibles, des nappes de glissement au travers desquelles la vitesse normale et la pression sont continues.

Si le problème physique est abordé par l'analyse d'un fluide visqueux, à l'échelle d'un milieu continu, de telles conditions de glissement deviennent impossibles quel que soit le nombre de Reynolds, et c'est la théorie asymptotique de la couche limite qui nous indique que l'écoulement externe non-visqueux à considérer est affecté, en première approximation, aux conditions de glissement précédentes. Celles-ci acquièrent de ce fait une origine liée à la viscosité. Au second ordre d'approximation, une vitesse normale non nulle à la paroi, ainsi qu'une discontinuité de vitesse normale et de pression sur les nappes de glissement, traduisent l'effet du déplacement visqueux sur le domaine de fluide parfait résiduel. Si les indices 1 et 2 désignent les ordres d'approximation successifs, on a par exemple :

$$
\left.
\begin{aligned}
& y = \mathcal{R}^{-\frac{1}{2}}\,\bar{y} \qquad\qquad \mathcal{R} = \text{Reynolds} \\
& \delta_1^*(x)\,\left[\rho_1 u_1\right]_{(x,0)} = \mathcal{R}^{-\frac{1}{2}} \int_0^{\infty} \left\{ \left[\rho_1 u_1\right]_{(x,0)} - \left[\bar{\rho}_1 \bar{u}_1\right]_{(x,\bar{y})} \right\} d\bar{y} \\
& \left[\rho_2 v_2\right]_{(x,0)} = \frac{d}{dx}\left[\rho_1 u_1 \delta_1^*\right]_{(x,0)}
\end{aligned}
\right\} \qquad (3.1)
$$

3.1. Couplage fort par domaines raccordés

La transposition de ces conditions aux problèmes de couplage à nombre de Reynolds fini a été initiée par Crocco et Lees [43] pour le calcul des décollements supersoniques, dans une approche de couplage fort par raccordement de domaines, figure 6, utilisant des équations de Prandtl pour $0 < y < \delta(x)$, δ étant une épaisseur physique de la couche limite. Dans le cas le plus habituel où une seule condition aux limites d'origine visqueuse en $y = \delta(x)$ suffit à déterminer le fluide parfait, la relation appliquée par Crocco et Lees est générale, puisqu'elle s'appuie seulement sur l'intégration en y de la seule équation de continuité. Si $K(x)$ est la courbure de la paroi :

$$
\left.
\begin{aligned}
& \left[\frac{v}{u}\right]_{(x,\delta)} = \frac{1}{1+K\delta}\left\{ \frac{d\delta^*}{dx} - (\delta - \delta^*)\left[\frac{1}{\rho u}\,\frac{d\rho u}{dx}\right]_{(x,\delta)} \right\} \\
& \delta^*(x)\left[\rho u\right]_{(x,\delta)} = \int_0^{\delta} \left\{ \left[\rho u\right]_{(x,\delta)} - \left[\bar{\rho}\bar{u}\right]_{(x,y)} \right\} dy
\end{aligned}
\right\} \qquad (3.2)
$$

Cette formulation du déplacement $\delta^*(x)$ est exempte d'approximation autre que celle attachée au calcul de $\left[\bar{\rho}\bar{u}\right]_{(x,y)}$.

D'autres façons d'introduire la condition de couplage (3.2) dans le calcul du fluide parfait sont fréquemment utilisées. Il peut par exemple paraître plus commode de considérer, soit qu'il n'y ait aucun débit à travers la frontière du fluide parfait, et l'on parle alors de concept de déplacement, soit que cette frontière s'appuie simplement sur la paroi. Dans les deux cas une certaine équivalence avec (3.2) peut être obtenue en considérant un report analytique approché de (3.2) de $y = \delta(x)$ en $y = Y(x)$. L'équation de continuité non visqueuse donne :

$$
\left[\frac{v}{u}\right]_{(x,Y)} = \left[\frac{v}{u}\right]_{(x,\delta)} - (Y-\delta)\left[\frac{1}{\rho u}\,\frac{d\rho u}{dx}\right]_{(x,Y)} + \ldots \qquad (3.3)
$$

ce qui conduit à une condition de glissement si $Y > \delta^*$, d'injection si $Y < 0$, et à des expressions correspondantes pour $\delta^*(x)$:

$$\left[\frac{v}{u}\right]_{(x,\delta^*)} = \frac{d\delta^*}{dx} + \cdots\cdots \qquad (3.4)$$

$$[\rho v]_{(x,0)} = \frac{d}{dx}\left[\rho u \delta^*\right]_{(x,0)} + \cdots\cdots \qquad (3.5)$$

$$\delta^*(x)\,[\rho u]_{(x,Y)} = \int_0^{\delta} \left\{ [\rho u]_{(x,Y)} - [\bar{\rho}\bar{u}]_{(x,y)} \right\} dy \qquad (3.6)$$

Les formulations du déplacement (3.4) (3.5) (3.6) sont toutefois approchées, de même que l'équivalence avec (3.2). La validité asymptotique de cette équivalence lorsque $\mathcal{R} \to \infty$ n'est pas automatique dans la mesure où l'ordre du développement (3.3) dépend par exemple de l'ordre de $d\rho u/dx$, quantité souvent non bornée lorsque $\mathcal{R} \to \infty$ dans les théories asymptotiques à couches multiples. Les formulations (3.4) (3.5) peuvent toutefois être dégagées de toute approximation par le choix de nouvelles définitions pour $\delta^*(x)$.

3.2. Couplage fort avec domaines en recouvrement

Un tel changement de définition de $\delta^*(x)$ apparaît aisément par introduction, figure 7, de domaines de calcul en recouvrement, sur lesquels sont dissociés les équations visqueuses comme indiqué au paragraphe 2.4. Dans ce cas, la simple intégration en y de l'équation de continuité (2.2) fournit, puisque $0 = \lim_{y \to \infty} [\rho v - \bar{\rho}\bar{v}]$:

$$\left.\begin{aligned} [\rho v]_{(x,0)} &= \frac{d}{dx}\left[\rho u \delta^*\right]_{(x,0)} \\ \delta^*(x)\,[\rho u]_{(x,0)} &= \int_0^{\infty} \left\{ [\rho u]_{(x,y)} - [\bar{\rho}\bar{u}]_{(x,y)} \right\} dy \end{aligned}\right\} \qquad (3.7)$$

Cette généralisation de la définition de $\delta^*(x)$ tient compte en particulier des gradients de pression normaux internes à la couche visqueuse, à travers les variations en y du terme visqueux $\bar{\rho}\bar{u}$ et du terme non visqueux ρu, celles-ci pouvant éventuellement être rapides, voire discontinues, à la différence des analyses de couche limite. Une illustration schématique en est donnée figure 8, dans le cas où $(\bar{u}/u) = \varphi(x,y)$ est supposée être une fonction continue.

Une formulation de $\delta^*(x)$ adaptée au concept de déplacement peut de même être définie :

$$\left.\begin{aligned} \left[\frac{v}{u}\right]_{(x,\delta^*)} &= \frac{1}{1+K\delta^*}\,\frac{d\delta^*}{dx} \\ \int_{\delta^*}^{\infty} [\rho u]_{(x,y)}\, dy &= \int_0^{\infty} [\bar{\rho}\bar{u}]_{(x,y)}\, dy \end{aligned}\right\} \qquad (3.8)$$

Au total il importe de considérer que l'utilisation d'une épaisseur de déplacement pour formuler un problème de couplage n'est nullement synonyme du recours à des approximations de couche limite.

4. APPROXIMATIONS SIMPLES DU FLUIDE VISQUEUX - INFLUENCE DU COUPLAGE FORT

Tant pour des raisons historiques que pratiques, les méthodes de couplage actuelles ont surtout été développées en s'appuyant sur des hypothèses de type couche limite. Nous nous limiterons dans la suite à cette classe de méthodes, utilisant soit les équations de Prandtl, soit l'extension voisine des équations de couche mince, indiquée au paragraphe 2.4, dans laquelle la pression $\bar{p}(x,y)$ est identifiée à celle du calcul non visqueux $p(x,y)$.

4.1. Décollement et zones à courants de retour

Le problème de couche limite, assujetti aux équations de Prandtl et découplé du fluide parfait, doit être fermé par une condition aux limites externe, pour laquelle on a longtemps utilisé la pression $p(x,\delta)$ de la même façon que dans les théories asymptotiques de faible interaction. On connaît alors le comportement singulier de Goldstein [44], en "racine carrée", que présentent les solutions au voisinage du point de frottement nul en écoulement bidimensionnel stationnaire, comportement reproduit également par les méthodes intégrales de couche limite [12]. En écoulement instationnaire [45] ou tridimensionnel [46], les méthodes intégrales font apparaître des singularités d'un type différent, constituées des discontinuités d'épaisseurs intégrales associées aux solutions faibles des systèmes d'équations, dont la localisation ne s'attache plus à l'origine des zones à courant de retour, et qui pourraient expliquer certaines anomalies numériques, rencontrées dans la résolution des équations de Prandtl instationnaires avec courants de retour et champ de pression imposé.

Distribution Unlimited

On a pu montrer cependant que ces comportements singuliers irréalistes ne doivent pas être confondus avec une limite de validité des équations de Prandtl, ou encore avec une séparation brutale de la couche visqueuse et de la paroi, mais qu'ils résultent du choix de la pression pour condition aux limites externe . Lorsque la pression devient une inconnue du calcul, soit en formulant un problème inverse assujetti à une autre condition externe, soit par couplage au fluide parfait, des solutions régulières et réalistes vis à vis des petits décollements ont été obtenues [12, 47 à 55]. Le même comportement est observé en instationnaire [45]. Il est clair toutefois que le problème de Prandtl en couplage fort avec le fluide parfait externe ne constitue plus un système parabolique exempt d'influence de l'aval, même en l'absence de courants de retour, en raison de la condition aux limites inconnue a priori que constitue la distribution de pression extern. avec effet de couplage, figure 6.

4.2. Influence de l'aval sur l'amont en supersonique et en transsonique

Une question essentielle soulevée par le calcul raccordé d'équations de Prandtl et d'Euler est toutefois la suivante : la nature elliptique des équations de Navier-Stokes stationnaires est-elle aussi retrouvée par le modèle de couplage lorsque l'écoulement de fluide parfait est localement supersonique et que l'influence de l'aval sur l'amont ne peut plus avoir une origine exclusivement non visqueuse? Depuis le travail initial de Crocco-Lees, une longue investigation a été menée [12, 14, 56 à 59] la réponse étant positive pour une couche visqueuse dite "subcritique", négative pour une "couche supercritique".

Dans le cas subcritique, le couplage d'équations non-visqueuses hyperboliques avec des équations visqueuses paraboliques conduit à un problème de conditions initiales qui est mal posé, dans la mesure où une amplification exponentielle des perturbations initiales éventuelles se produit sur une échelle courte, de l'ordre de l'épaisseur de la couche limite, selon un processus de solutions de branchement . Le caractère de problème mal posé est éliminé si l'une des conditions aux limites est transférée de l'amont vers l'aval, ce qui révèle la nature elliptique du modèle. En plus, le processus de branchement permet en général d'introduire une telle condition aux limites à l'aval comme une contrainte purement excédentaire qui est le reliquat dans le modèle de couplage des conditions aux limites couramment imposées à l'aval des calculs de type Navier-Stokes. L'apparition d'une influence de l'aval sur l'amont par effet de couplage trouve en outre un support théorique dans les théories asymptotiques de forte interaction, telle que par exemple le modèle laminaire en triple couche. On a pu d'ailleurs vérifier numériquement que les solutions supersoniques des équations de triple couche sont également solutions asymptotiques du modèle de couplage, lorsque le nombre de Reynolds tend vers l'infini [27], figure 9.

Dans le cas supercritique, la nature elliptique des équations visqueuses n'est que partiellement retrouvée dans le modèle de couplage de Crocco-Lees, par le biais de solutions faibles dont les sauts de pression transforment soudainement les couches supercritiques en couches subcritiques, toutes les fois qu'une influence de l'aval sur l'amont est localement indispensable. Le comportement supercritique est alors retrouvé vers l'aval après franchissement d'un "point critique", où la régularité nécessaire de la solution joue le rôle de condition aval excédentaire pour la zone subcritique [59]. Une interprétation simple des comportements du modèle au voisinage des sauts et des points critiques peut être directement déduite des comportements locaux des solutions de branchement, ainsi que des conditions aux limites stabilisatrices nécessaires, voir figures 10, 11.

Les lacunes précédentes du modèle de Crocco-Lees ne sont pas liées, comme il a parfois été imaginé, aux approximations utilisées pour résoudre les équations de Prandtl par une méthode intégrale, mais en fait au champ de pression simplifié $\bar{p}(x) = p(x,\delta)$ de la couche visqueuse. Dans une méthode intégrale, la relation (3.2) conduit à une relation quasi-linéaire entre la déflexion visqueuse $\theta = (v/u)$ et le gradient de pression en $y = \delta(x)$:

$$D_1\,\theta = D_2\,\delta^*\frac{dp}{dx} + D_3 \qquad (4.1)$$

D_1 s'annule aux décollements ou recollements, où le gradient de pression ne peut être quelconque, mais tel que $\delta^*(dp/dx) = -(D_3/D_2)$, pour assurer la régularité des solutions. D_2 s'annule aux points critiques, où la régularité impose $\theta = (D_3/D_1)$. On peut noter, pour le modèle de couplage par raccordement, la symétrie des singularités de Goldstein et de Crocco-Lees. La relation (4.1) ou simplement :

$$\theta = B\frac{dp}{dx} + C \qquad B = \frac{D_2}{D_1}\,\delta^* \qquad (4.2)$$

est déterminante pour les solutions de branchement, stables selon x si $B<0$, instables si $B>0$. Pour une couche attachée, le cas instable correspond au comportement subcritique et à un problème de type elliptique. Notons cependant qu'en cas de décollement, D_1 change de signe, donc B , ce qui conduit à des solutions de branchement stables dans la zone décollée, l'influence de l'aval sur l'amont résultant alors de la seule sélection des solutions régulières au point de recollement, figure 12. En cas de résolution locale des équations de Prandtl, une relation analogue à (4.2) subsiste [57], démontrant l'importance du nombre de Mach local $\bar{M}$ dans les comportements supercritiques :

$$B = \lim_{\varepsilon\to 0}\int_{\varepsilon}^{\delta}\frac{1-\bar{M}^2}{\gamma\,\bar{p}\,\bar{M}^2}\,dy \qquad (4.3)$$

La limite $\varepsilon \to 0$ étant souvent singulière, le comportement des solutions de branchement ne se déduit généralement pas de façon directe de (4.3), voir [3, 12, 15]. Il ressort toutefois de (4.3) que les comportements supercritiques ($B<0$) ne peuvent résulter que de la présence de régions visqueuses supersoniques, et qu'elles dépendent fortement du choix de la frontière δ dans le modèle de raccordement. Tout couplage subcritique peut ainsi être transformé en un couplage supercritique, par sélection d'une frontière $y = \delta(x)$ plus éloignée de la paroi [3].

Le caractère subcritique ou supercritique de Crocco-Lees ne constitue pas de ce fait une propriété intrinsèque de la couche visqueuse, mais plutôt du modèle de couplage par raccordement [3, 15]. Son

interprétation physique doit donc faire appel au fluide parfait externe. On peut ainsi noter que le comportement supercritique d'un décollement supersonique à nombre de Mach croissant n'apparaît que lorsque l'onde de choc de focalisation s'est rapprochée jusqu'à l'atteindre de la frontière externe de la couche visqueuse, toute pénétration à l'intérieur de la couche visqueuse étant exclue par le modèle de calcul, et devant être simulée par un saut de pression, figure 13.

4.3. Traitement approché du gradient de pression normal. Formulation déficitaire

Les insuffisances précédentes du modèle simple de Crocco-Lees pour le traitement des écoulements à forte interaction visqueuse en supersonique, ainsi qu'en transsonique ($M \simeq 1,20$), provient du champ de pression exagérément simplifié $\bar{p}(x) = p(x,\delta)$. Nous avons toutefois trouvé [3, 12, 13, 15] que ces insuffisances sont éliminées de manière relativement simple, si l'on établit une formulation déficitaire du calcul visqueux, correspondant à des domaines de calcul visqueux et non visqueux en recouvrement, figure 7, comme indiqué au paragraphe 2.4, et si l'approximation sur la pression devient $\bar{p}(x,y) = p(x,y)$

Ne gardant dans le système (2.2) que le terme visqueux de Prandtl, on obtient par intégration en y de l'équation de mouvement selon x et de son premier moment par rapport à u :

$$\frac{\partial}{\partial x}\left\{\int_0^\infty \left[\rho u^2 - \bar{\rho}\bar{u}^2\right]_{(x,y)}\, dy\right\} - \left[\rho u v\right]_{(x,0)} = \tau_{(x,0)} - \frac{\partial}{\partial x}\int_0^\infty \left[p - \bar{p}\right]_{(x,y)}\, dy \qquad (4.4)$$

$$\frac{\partial}{\partial x}\left\{\int_0^\infty \left[\rho u^3 - \bar{\rho}\bar{u}^3\right]_{(x,y)}\, dy\right\} - \left[\rho u^2 v\right]_{(x,0)} = \rho u^3 \Phi - 2\int_0^\infty \frac{\partial p}{\partial x}\left[u - \bar{u}\right] dy + 2\int_0^\infty \bar{u}\,\frac{\partial p - \bar{p}}{\partial x}\, dy \qquad (4.5)$$

tandis que l'équation de mouvement en $\left[x\,,\,\delta(x)\right]$ fournit l'équation d'entraînement :

$$\frac{d\delta}{dx} - \left[\frac{\rho v}{\rho u}\right]_{(x,\delta)} = E \qquad (4.6)$$

avec :

$$\Phi = \frac{2}{\left[\rho u^3\right]_{(x,0)}}\int_0^\infty \tau\,\frac{\partial \bar{u}}{\partial y}\, dy \qquad E = \left\{\frac{\partial \tau/\partial y}{\rho u\left[\partial(u-\bar{u})/\partial y\right]}\right\}_{(x,\delta)}$$

L'approximation $\bar{p}(x,y) = p(x,y)$ élimine en outre le dernier terme dans (4.4) et dans (4.5). Si l'on définit des épaisseurs intégrales de mouvement et d'énergie cinétique généralisées, d'une manière analogue à celle adoptée pour l'épaisseur de déplacement dans (3.7) :

$$\left.\begin{aligned}
\left[\delta^*(x) + \theta(x)\right]\left[\rho u^2\right]_{(x,0)} &= \int_0^\infty \left[\rho u^2 - \bar{\rho}\bar{u}^2\right]_{(x,y)}\, dy \\
\left[\delta^*(x) + \theta^*(x)\right]\left[\rho u^3\right]_{(x,0)} &= \int_0^\infty \left[\rho u^3 - \bar{\rho}\bar{u}^3\right]_{(x,y)}\, dy \\
\delta_i^*(x)\, u_{(x,0)} &= \int_0^\infty \left[u - \bar{u}\right]_{(x,y)}\, dy
\end{aligned}\right\} \qquad (4.7)$$

On obtient des équations intégrales très voisines de celles issues des équations de Prandtl :

$$\left[\frac{d\theta}{dx} + \frac{\delta^* + 2\theta}{u}\,\frac{\partial u}{\partial x} + \frac{\theta}{\rho}\,\frac{\partial \rho}{\partial x}\right]_{(x,0)} = \frac{Cf}{2} \qquad (4.8)$$

$$\left[\frac{d\theta^*}{dx} + \frac{\theta^*}{\rho u^3}\,\frac{\partial \rho u^3}{\partial x} + 2\,\frac{\delta^* - \delta_i^*}{u}\,\frac{\partial u}{\partial x}\right]_{(x,0)} = \Phi + \Phi_p \qquad (4.9)$$

On note cependant que l'équation d'énergie cinétique (4.9) demande la modélisation d'un terme de gradient de pression normal Φ_p , lié dans (4.5) à la variation en y de $\partial p/\partial x$, tandis que l'équation d'entraînement (4.6) permet de s'en dispenser. Une certaine approximation est toutefois présente si l'équation d'entraînement (4.6) est transformée pour ne faire intervenir que $\rho(x,0)$, $u(x,0)$, $\tau(x,0)$:

$$\left[\frac{d\delta}{dx} - \frac{d\delta^*}{dx} + \frac{\delta - \delta^*}{\rho u}\,\frac{\partial \rho u}{\partial x}\right]_{(x,0)} = E \qquad (4.10)$$

Outre l'avantage de prendre en compte un gradient de pression normal approché, la formulation déficitaire (3.7) (4.7 à 4.10) nous a conduit, pour l'analyse des comportements supercritiques à substituer à l'intégrale B de (4.3) une intégrale B' [12] :

$$B' = \lim_{\varepsilon \to 0}\int_\varepsilon^\infty \frac{M^2 - \bar{M}^2}{\gamma\, p\, M^2\, \bar{M}^2}\, dy \qquad \begin{aligned} M(y) &= \text{non-visqueux} \\ \bar{M}(y) &= \text{visqueux} \end{aligned} \qquad (4.11)$$

Un premier progrès, commun à (3.7) (4.7 à 4.11) est d'éliminer totalement le rôle relativement arbitraire de la frontière de raccordement $y = \delta(x)$. En second lieu, le terme $(1 - \bar{M}^2)$ de (4.3), générateur des

comportements supercritiques lorsque $\bar{M} > 1$, est remplacé par ($M^2 - \bar{M}^2$), terme vraisemblablement toujours positif. Nous avons ainsi pu conclure [12] que le couplage par recouvrement de domaine conduit toujours à des comportements subcritiques, où l'influence de l'aval sur l'amont est pleinement respectée, et où les distributions de pression sur les parois $p(x,0)$ sont toujours continues. En conséquence, les ondes de choc éventuelles prennent toujours naissance par focalisation interne au domaine de calcul non visqueux celle-ci pouvant toutefois se produire à l'intérieur même des couches visqueuses, figure 14. Dans ces cas de gradient de pression normaux intenses, une correction de second ordre peut être appliquée a posteriori à l'approximation $\bar{p}(x,y) = p(x,y)$, sous la forme :

$$\frac{\partial p - \bar{p}}{\partial y} = K(x) \left[\rho u^2 - \bar{\rho} \bar{u}^2 \right](x,y) \qquad (4.12)$$

$K(x)$ est une courbure moyenne des lignes de courant, qui ne peut être confondue avec celle des parois ou des lignes moyennes des sillages que dans les zones de faible interaction. A la paroi ou au centre d'un sillage, on obtient :

$$p(x,0) - \bar{p}(x,0) = K(x) \left[\delta^*(x) + \theta(x) \right] \qquad (4.13)$$

On doit enfin remarquer que les comportements supercritiques, éliminés dans le couplage par recouvrement Précédent, seraient encore possibles dans le couplage par addition d'une épaisseur de déplacement, la relation (4.11) devenant :

$$B^* = \int_0^{\varepsilon} \left[\frac{1 - \bar{M}^2}{\gamma p M^2} - dy \right] + \int_{\delta^*}^{\infty} \frac{M^2 - \bar{M}^2}{\gamma p M^2 \bar{M}^2} \, dy \qquad (4.14)$$

intégrale dans laquelle le premier terme peut toujours être négatif, le seuil de passage au comportement supercritique étant alors sensiblement M = 2 pour une couche turbulente de plaque plane.

5. METHODES NUMERIQUES DE COUPLAGE FORT

Les simplifications apportées à la résolution du fluide visqueux, au niveau II de la figure 1, au moyen d'une dissociation appliquée soit aux domaines de calcul, soit aux équations mises en jeu, ont pour contrepartie la génération artificielle d'un problème numérique de couplage fort. Dans le cas du couplage par raccordement de domaines, il s'agit d'assurer la compatibilité rigoureuse des conditions aux limites des divers sous-problèmes sur leurs frontières communes. On peut admettre, puisqu'en pratique la non-linéarité des équations visqueuses rend inéluctable une résolution itérative, que le problème reste sensiblement de même nature dans le couplage par dissociation d'équations, avec domaines de calcul en recouvrement.

5.1. Nature du problème

Ce couplage fort des conditions aux limites sur les interfaces des divers calculs constitutifs exige une rigueur de résolution numérique au moins comparable à celle utilisée dans chaque sous-problème, sous peine de faire dégénérer le traitement du couplage fort en une approximation de couplage faible. Cet impératif se trouve renforcé par la grande sensibilité des calculs en fluide parfait à la précision du traitement numérique des conditions aux limites. Il l'est encore davantage si l'on considère que, dans les problèmes visqueux de couches minces, l'effet de couplage peut à lui seul changer la nature mathématique du comportement des divers sous-problèmes, par l'intermédiaire des solutions de branchement rappelées au paragraphe 4.2 et conduire à des différences d'ordre unité entre les solutions assujetties à un couplage rigoureux et celles issues d'un couplage approché.

En cas d'emploi de méthodes aux différences finies, par exemple, le couplage doit être réalisé en chaque noeud de discrétisation de l'interface avec des schémas numériques consistants, comparables à ceux utilisés dans chaque domaine. L'interpolation sur l'interface est concevable en cas de maillages discontinus, à condition qu'elle soit cohérente avec l'ordre des schémas numériques, ainsi qu'avec les domaines d'influence mathématique . L'application de lissages ou filtrages est en revanche à rejeter, excepté si la technique peut se réduire à l'implantation d'une dissipation numérique, évanescente lorsque le pas de discrétisation tend vers zéro.

Si l'on envisage la résolution de problèmes d'évolutions, la même difficulté du couplage fort doit être surmontée à chaque pas de temps sous peine de procéder à une résolution visqueuse inconsistante en temps ou bien à une approche de faible interaction. Dans le cas de méthodes itératives de relaxation ou pseudo-instationnaires, dans lesquelles seule la solution finale importe, la consistance en temps peut être négligée. En revanche, les erreurs de couplage à chaque itération ne doivent pas s'amplifier et une étude de stabilité particulière doit être envisagée. La spécificité et la difficulté de celle-ci provient du fait que, bien qu'il faille analyser des grandeurs confinées sur l'interface de couplage, l'amplification des erreurs est gérée par un opérateur faisant appel à la résolution des sous-problèmes adjacents à cette interface, ce qui définit un problème mathématique sur un espace ayant une dimension de plus que celui de l'interface où les erreurs de couplage sont étudiées.

Il est clair toutefois que, sauf circonstances exceptionnelles, la définition d'une méthode de couplage itérative ne peut se réduire, en cas de couplage fort, à la simple définition d'un organigramme de calcul. En premier lieu, il est nécessaire pour le couplage de choisir des schémas numériques consistants, au moins en espace, respectant non seulement les domaines de dépendances des équations de chaque sous-domaine prises isolément, mais encore le domaine de dépendance réel du problème mathématique couplé, compte tenu notamment d'éventuelles solutions de branchement. A titre d'exemple, la consistance ne sera pas obtenue pour le couplage des équations d'Euler et de Prandtl le long d'une frontière localement supersonique, avec une couche limite attachée subcritique, si des schémas aux différences totalement décentrés vers l'amont sont utilisés et si, au moins pour discrétiser les relations de couplage, l'un d'entre eux n'échappe pas à ce choix. Nous avons montré au contraire, dans ce cas, l'intérêt d'un

décentrement vers l'aval [13].

En second lieu, la généralité d'une méthode de couplage itérative suppose la maîtrise du problème complexe de stabilité, dans le but d'adapter des techniques de relaxations, c'est-à-dire de moduler les coefficients de relaxation stabilisateurs en fonction des pas de temps et d'espaces locaux, ainsi que des grandeurs aérodynamiques. Cette contrainte est voisine, par exemple, de la nécessité de calculer, dans une méthode numérique instationnaire explicite, le pas de temps local maximum compatible avec la stabilité du calcul, en fonction du pas d'espace local.

Le rejet de cette contrainte a longtemps conduit à des itérations instables pour les calculs de couches limites sur profils d'ailes et au recours relativement arbitraire à des techniques de lissage. Ces instabilités, purement numériques, sont influencées par le caractère de faible ou de forte interaction du couplage visqueux local, mais elles ne sont jamais absentes si le pas de discrétisation est suffisamment petit. Elles apparaissent en particulier pour des couches limites de plaque plane [60]. La figure 15 en donne une illustration relative au couplage fluide parfait - couche limite en instationnaire [61] au voisinage d'un écoulement uniforme sur plaque plane ; elle montre que, toutes choses égales par ailleurs, une légère réduction du pas d'espace ou augmentation du pas de temps suffit à passer d'une itération de couplage stable à une itération instable.

Bien évidemment enfin la réduction des instabilités numériques des techniques itératives simples de couplage, à caractère explicite, peut être recherchée dans le développement de méthodes traitant à chaque itération le couplage de manière plus implicite, ou bien s'appuyant sur des techniques numériques non-linéaires plus générales.

5.2. Loi de comportement de la couche limite stationnaire -

La plupart des méthodes numériques de couplage visqueux - non visqueux développées ont un caractère faiblement implicite, pour des raisons évidentes de simplicité, de généralité d'application et d'interchangeabilité de modules visqueux et non visqueux. Le recours à des modules visqueux utilisant des équations de Navier-Stokes, complètes ou dans l'approximation de couche mince, reste rare dans les méthodes de couplage [8 à 11, 32 à 34], les techniques numériques correspondantes semblant être encore relativement heuristiques pour la partie propre au couplage. Des méthodes plus précises se dégagent au contraire dans le cas des approximations visqueuses simples du paragraphe 4.

Dans le cas des méthodes intégrales de couche limite, le problème à résoudre est essentiellement celui d'un écoulement de fluide parfait dont les conditions aux limites ne sont plus connues à l'avance. Celles-ci deviennent au contraire les solutions d'un système d'équations différentielles ordinaires sur la frontière, comme par exemple (3.7) (4.8) (4.9), liant la pression $p(x,0)$, la direction angulaire de l'écoulement $\Theta(x,0)$, ainsi que les épaisseurs visqueuses. Après quelque élimination, on peut en extraire la relation entre $\Theta(x,0)$ et $p(x,0)$ effectivement appliquée au fluide parfait :

$$A_1 \Theta = A_2 \delta^* \frac{dp}{dx} + A_3 \qquad (5.1)$$

x est mesuré le long de la frontière du fluide parfait - A_1, A_2, A_3, δ^* dépendent des autres équations différentielles, des valeurs initiales des épaisseurs visqueuses ainsi que des évolutions non visqueuses $\Theta(x)$ et $p(x)$. L'équation (5.1) conduit à des comportement fortement non-linéaires ; A_1 s'annule aux décollements ou recollements, A_2 s'annule aux points critiques lorsque ceux-ci n'ont pas été éliminés. Le terme de petite échelle δ^* conduit aux phénomènes de solutions de branchement, dont l'importance a été rappelée et qui conduisent à l'addition de conditions aux limites excédentaires à l'aval.

Dans le cas où les méthodes intégrales de couche limite sont remplacées par les équations visqueuses locales de Prandtl, le comportement de la couche visqueuse, en tant que condition aux limites du fluide parfait, reste sensiblement de même nature que (5.1), au moins si l'on se limite à une analyse de perturbation autour d'une solution $[\Theta_0(x,0), p_0(x,0)]$:

$$A_1 \left[\Theta - \Theta_0\right] = A_2 \delta^* \left[\frac{dp}{dx} - \frac{dp_0}{dx}\right] \qquad (5.1')$$

relation à rapprocher de (4.2) (4.3) (4.11) (4.14). L'utilisation de la relation fondamentale (5.1) comme condition aux limites de fermeture d'un calcul en fluide parfait représente donc sous forme schématique le problème de couplage à résoudre, dans le cas de couches visqueuses minces. On note que la relation visqueuse (5.1) n'accorde pas un rôle symétrique aux variables $\Theta(x,0)$ et $p(x,0)$, la pression seule y intervenant sous forme de dérivée, cette différence majeure avec le problème non visqueux résultant sans doute plus du caractère de couche mince que des approximations visqueuses utilisées.

5.3. Méthodes de conditions initiales en supersonique

Le caractère local de la relation (5.1) avait initialement conduit à la recherche de solutions supersoniques au problème de couplage fort. Dans ce cas, la simplification apparente des méthodes de conditions initiales, procédant de l'amont vers l'aval avec résolution simultanée de (5.1) a été largement utilisée par Crocco-Lees et de nombreuses successeurs [32, 33, 43, 59, 62 à 66] notamment en cas d'onde simple. On sait cependant que les solutions de branchement instables donnent naissance à un problème mal posé, qui exige une technique de résolution par tâtonnements successifs sur une perturbation initiale, de façon à séiectionner à convergence une solution ayant un comportement ou une régularité appropriée à l'aval. Comme le schématise la figure 16, la perturbation initiale ϵ était classiquement apportée à la pression dans les cas subcritiques, tandis qu'elle portait sur la position initiale du saut de pression permettant à la solution, dans les cas supercritiques, de franchir sans singularité un point critique situé plus en aval.

En pratique, une telle résolution est extrêmement difficile et manque de généralité. Elle est à peu près

irréalisable dès que la zone de début d'interaction forte, c'est-à-dire de la zone de perturbation, n'est pas connues à l'avance, ou dès que des interactions fortes successives sont présentes, a fortiori si elles interfèrent entre elles.

5.4. Méthodes pseudo-instationnaires

Une première amélioration importante a été suggérée par Werle-Vatsa [67 à 69] pour les écoulements externes supersoniques du type onde simple, dans lesquels le calcul non-visqueux se réduit à une simple relation algébrique locale entre pression et direction de l'écoulement. Moyennant un couplage par glissement sur la surface de déplacement, on obtient :

$$p_x = -\beta\, \delta^*_{xx} \qquad (5.2)$$

L'idée de base de Werle-Vatsa consiste simplement à substituer au problème de couplage un problème d'évolution fictif, obtenu en remplaçant le terme δ^*_{xx} par $\left[\delta^{**}_{xx} - \delta^*_t\right]$, et à calculer l'état asymptotique lorsque $t \to \infty$ au moyen d'une méthode numérique de directions alternées à deux pas, le premier étant implicite en (y,t), le second en (x,t). Si nous considérons par exemple l'équation de mouvement en x qui contient le seul terme instationnaire :

$$\rho u\, u_x + \rho v\, u_y = \beta\left[\delta^{**}_{xx} - \delta^*_t\right] + \left[\varepsilon\, u_y\right]_y \qquad (5.3)$$

on obtient schématiquement pour passer du temps n au temps $(n+1)$:

$$\left.\begin{aligned}\left[\rho u\, u_x + \rho v\, u_y\right]^{n+\frac{1}{2}} &= \beta\left[\left(\delta^{**}_{xx}\right)^n - \frac{2}{\Delta t}\left(\delta^{*\,n+\frac{1}{2}} - \delta^{*n}\right)\right] + \left[\varepsilon\, u_y\right]_y^{n+\frac{1}{2}}\\ \left[\rho u\, u_x + \rho v\, u_y\right]^{n+\frac{1}{2}} &= \beta\left[\left(\delta^{**}_{xx}\right)^{n+1} - \frac{2}{\Delta t}\left(\delta^{*\,n+1} - \delta^{*\,n+\frac{1}{2}}\right)\right] + \left[\varepsilon\, u_y\right]_y^{n+\frac{1}{2}}\end{aligned}\right\} \qquad (5.4)$$

Le premier demi-pas de temps se réduit à un calcul classique de couche limite où δ^{**}_{xx}, donc p_x, est imposé. Il est résolu d'amont en aval, une linéarisation des équations faisant appel au pas de temps précédent étant introduite pour éviter les comportements singuliers aux décollements. Le second demi-pas de temps se réduit à :

$$\beta\left(\delta^*_{xx}\right)^{n+1} - \beta\left(\delta^*_{xx}\right)^n = \frac{2}{\Delta t}\left[\delta^{*\,n+1} - 2\,\delta^{*\,n+\frac{1}{2}} + \delta^{*n}\right] \qquad (5.5)$$

ce qui conduit, après discrétisation, à la simple résolution de matrices tridiagonales pour $\delta^{*\,n+1}$
La méthode a été étendue aux écoulements externes incompressibles semi-illimités par Napolitano, Werle, Davis [69] dans le cadre des équations de triple couche laminaire. Dans ce cas, la relation algébrique (5.2) doit être remplacée par une intégrale de Cauchy (5.6) qui rend plus complexe le second demi-pas de temps (5.7) :

$$\delta^*_{xx} = \frac{1}{\pi}\oint_{-\infty}^{+\infty} \frac{p_\xi}{x-\xi}\, d\xi \qquad (5.6)$$

$$\left(\delta^*_{xx}\right)^{n+1} = \frac{1}{\pi}\oint_{-\infty}^{+\infty} \frac{p_\xi^n + 2/\Delta t\left[\delta^{*\,n+1} - 2\,\delta^{*\,n+\frac{1}{2}} + \delta^{*n}\right]}{x-\xi}\, d\xi \qquad (5.7)$$

Après discrétisation (5.7) conduit pour $\delta^{*\,n+1}$ à un système algébrique présentant une matrice pleine, mais à dominance diagonale. Une itération de relaxation est donc nécessaire, en incompressible, pour résoudre le second demi-pas de temps par inversions successives de simples matrices tridiagonales.

Une méthode pseudo-instationnaire toute différente a été proposée par Briley, Mc Donald [70] et utilisée par Gleyzes, Cousteix, Bonnet [71] pour calculer les bulbes courts de décollement transitionnels des bords d'attaque, en incompressible, par une approche simplifiée de couplage fort local. L'idée de base est d'utiliser les équations instationnaires véritables de la couche limite, tout en conservant des équations de fluide parfait stationnaires. La résolution est elle aussi pseudo-instationnaire, dans la mesure où la couche limite est calculée à partir du champ de pression non visqueux de l'instant antérieur, le fluide parfait étant ajusté a posteriori comme un écoulement stationnaire subissant l'effet de déplacement le plus récemment calculé. Cette technique simple n'a été encore justifiée que par l'obtention effective de solutions stationnaires asymptotiques lorsque $t \to \infty$.

5.5. Méthodes de relaxation directes ou inverses

Le principe de cette classe de méthodes repose sur une formulation plus rigoureuse et une extension des méthodes itératives traditionnelles, utilisées pour améliorer les techniques de couplage faible au prix de quelques approximations successives sur l'épaisseur de déplacement.

Le couplage fort est ici obtenu à convergence rigoureuse de résolutions successives découplées des problèmes de fluide parfait et de couches limites stationnaires, toute technique de lissage arbitraire étant exclue. La stabilité de l'itération est gérée par sous-relaxation [3, 13, 15, 39, 72, 73]. L'enchaînement de calculs visqueux et non visqueux dissociés conduit à une grande commodité et une grande généralité d'emploi, en subsonique, transsonique ou supersonique. L'influence de l'aval sur

l'amont en supersonique peut être obtenue de façon automatique [3, 13, 15], comme dans les techniques pseudo-instationnaires, par imposition directe des conditions aux limites appropriées à l'aval, que soient mis en jeu des interactions fortes successives interférant entre elles, ou des écoulements ne se réduisant pas à une onde simple. La contrepartie de cette généralité apparaît, pour certains cas, dans la lourdeur des calculs a priori nécessaires à l'itération de couplage. Néanmoins, l'expérience a montré [3, 13, 15 39, 77] que cette itération de couplage pouvait être aisément menée de front avec celles nécessaires au calcul du fluide parfait, dans le cas des méthodes de relaxation subsoniques ou transsoniques. Dans ce cas, l'itération de couplage apparaît comme une technique de relaxation explicite de la condition aux limites visqueuse (5.1) appliquée au fluide parfait, et l'augmentation du coût des calculs liée à la viscosité est limitée.

Considérant que la relation (5.1) s'identifie à une résolution de la couche limite, l'itération de couplage est dite directe ou inverse selon que l'on résout au cycle $(n+1)$ un problème non visqueux de type direct ou inverse :

Direct : $$\Theta^{n+1} = \frac{A_2}{A_1}\,\delta^* \left[\frac{dp}{dx}\right]^n + \frac{A_3}{A_1} \qquad (5.8)$$

Inverse : $$\left[\frac{dp}{dx}\right]^{n+1} = \frac{A_1}{\delta^* A_2}\,\Theta^n - \frac{A_3}{\delta^* A_2} \qquad (5.9)$$

Pour la méthode directe, si l'on admet que le fluide parfait est un opérateur qui associe une pression $p^n(x)$ à une distribution angulaire $\Theta^n(x)$ donnée, l'addition de (5.8) conduit à l'opérateur F associé à l'itération de point fixe globale :

$$\Theta^{n+1}(x) = F\left[\Theta^n(x)\right] \qquad (5.10)$$

De même, lorsque A_1 peut s'annuler en raison d'un décollement, la résolution (5.8) doit être évitée et, admettant qu'un opérateur de fluide parfait inverse associe $\Theta^n(x)$ à la donnée de $p^n(x)$, on obtient en ajoutant la relation (5.9), intégrée en x, une itération de point fixe dite inverse :

$$p^{n+1}(x) = G\left[p^n(x)\right] \qquad (5.11)$$

L'adoption de l'une des deux techniques (5.10) (5.11), ou même leur emploi conjoint dans une méthode mixte alternant (5.10) ou (5.11) en fonction de domaines prédéfinis sur la frontière Ox, ont été utilisés par Lock [39], Klineberg, Steger [74], Le Balleur [61, 72], Carter [73], Melnik, Chow, Mead [26, 29], parmi de nombreux autres auteurs. Dans tous ces cas, la méthode était stabilisée par une sous-relaxation importante ω, indépendante de x, déterminée sans critère autre que l'expérience numérique préalable :

$$\Theta^{n+1}(x) = \Theta^n(x) + \omega\left\{F\left[\Theta^n(x)\right] - \Theta^n(x)\right\} \qquad (5.12)$$

Le manque de généralité de l'approche précédente a toutefois pu être éliminée par le présent auteur grâce à une étude de stabilité approchée [13] permettant un calcul local de $\omega(x)$. L'étude montre que l'opérateur F de (5.10), linéarisé autour de $\Theta^m(x)$, admet sensiblement des distributions harmoniques de perturbation $\left[\Theta(x) - \Theta^m(x)\right]$ comme fonctions propres et que l'approximation correspondante des valeurs propres complexes de F est μ_D, celle de G étant μ_I, avec :

$$\mu_D \cdot \mu_I = 1 \qquad \mu_D = \frac{\alpha\,\tilde{B}\,\delta^*}{\sqrt{1-M^2}} \qquad (5.13)$$

M désigne le nombre de Mach local de l'écoulement non visqueux, α la fréquence de l'harmonique, $\tilde{B}$ est un paramètre de forme visqueux en relation avec B' dans (4.11), ou encore (A_2/A_1) dans (5.1). La plus grande valeur propre $\mu_D(x)$ ou $\mu_I(x)$ permet de déterminer $\omega(x)$, fortement dépendant de x comme μ_D ou μ_I (voir [13]), une surrelaxation locale n'étant pas à exclure.

Si $R(\alpha)$ et $I(\alpha)$ désignent les parties réelles et imaginaires de μ_D par exemple, la stabilité de (5.12) sera obtenue si :

$$\omega(x) \leq 2\,\omega_{opt}\,(\alpha_{max}) \qquad \omega_{opt} = \frac{1-R}{(1-R)^2 + I^2} \qquad \alpha_{max} = \frac{\pi}{\Delta x} \qquad (5.14)$$

Dans le cas direct (5.10), un pas de discrétisation Δx petit accroît la plus grande fréquence α des perturbations possibles et réduit la valeur de $\omega(x)$, l'échelle de référence étant $\delta^*(x)$. Les régions transsoniques et celles de décollement conduisent aussi à réduire $\omega(x)$ dans le problème direct (5.10), ω devant être nul aux points de décollement ou de recollement où $A_1 = 0$, $\tilde{B} \longrightarrow \infty$, $\mu_D \longrightarrow \infty$. Dans le mode inverse (5.11) au contraire, l'annulation de μ_I conduit en ces points à $\omega = 1$.

Numériquement le calcul local de $\omega(x)$ montre que la relaxation en mode direct (5.10) est bien conditionnée pour les couches limites attachées, la relaxation inverse sur la pression (5.11) l'étant à son tour au voisinage des couches décollées ou proche de l'être.

5.6. Méthode linéarisée implicite

Outre la dualité de comportement précédente, reliée physiquement à une influence dominante du fluide parfait ou de la couche limite sur la détermination de la pression, selon que la couche limite est plutôt attachée ou plutôt décollée, le recours à une sous-relaxation (5.12) d'autant plus forte que Δx est plus petit traduit le caractère explicite de la méthode (5.10) ainsi que l'intérêt probable d'une méthode plus implicite. L'idée d'une méthode de Newton pour résoudre l'équation (5.10) discrétisée a été suggérée par Brune, Rubbert, Nark [60]. On doit alors à chaque itération déterminer les matrices d'influence du fluide parfait P_{ij}^* et de la couche limite B_{ij}^*. Elles s'écrivent, si l'on choisit pour variables $p(x)$ et $\delta^*(x)$, discrétisées en p_i et δ_i^* dans le fluide parfait, en $\bar{p}_i$ et $\bar{\delta}_i^*$ dans la

couche limite :

$$\left.\begin{aligned} p_i - p_i^n &= P_{ij}^n \left(\delta_j^* - \delta_j^{*n} \right) \\ \bar{\delta}_i^* - \bar{\delta}_i^{*n} &= B_{ij}^n \left(\bar{p}_j - \bar{p}_j^n \right) \end{aligned}\right\} \qquad (5.15)$$

On peut alors adopter, à l'itération $(n+1)$ la solution du problème couplé linéarisé qui s'écrit, sous forme matricielle :

$$\left.\begin{aligned} p^{n+1} = \bar{p}^{n+1} &= p^n + (I - P^n B^n)^{-1} \left[P^n \left(\bar{\delta}^{*n} - \delta^{*n} \right) + P^n B^n \left(p^n - \bar{p}^n \right) \right] \\ \delta^{*n+1} = \bar{\delta}^{*n+1} &= \bar{\delta}^{*n} + B^n \left[\left(p^n - \bar{p}^n \right) + \left(p^{n+1} - p^n \right) \right] \end{aligned}\right\} \qquad (5.16)$$

Si les effets non linéaires sur P_{ij}^n et B_{ij}^n sont faibles, la convergence doit être rapide. Chaque itération est cependant complexe, demandant l'inversion d'une matrice pleine $[I - P^n B^n]$ et surtout l'estimation des matrices d'influence P^n et B^n, évaluation a priori coûteuse dans le cadre des méthodes de différences finies, notamment en transsonique. Peu d'informations sur cette approche, dont l'utilisation est cependant indiquée par Thiede [54], sont actuellement disponibles. Une technique assez proche est indiquée par Arieli, Murphy [76] pour des calculs pseudo-directs de la couche limite.

5.7. Méthodes de relaxation semi-inverses

La complexité, d'un point de vue pratique, de l'approche précédente ainsi que des méthodes itératives de relaxation de type mixte, directes ou inverses par régions, nous a conduit à proposer [3, 13 à 15, 75] une itération de relaxation nouvelle pour les régions de couche limite décollée ou proche de l'être. Cette méthode peut être qualifiée de semi-inverse dans la mesure où seul le problème de couche limite est traité de manière inverse, la donnée étant soit la direction de l'écoulement externe $\Theta^n(x)$, soit l'épaisseur de déplacement $\delta^{*n}(x)$. Comme l'indique la figure 17, $\Theta^n(x)$ fournit à chaque itération un double prédicteur de la pression, l'un donné par le fluide parfait $p^n(x)$, l'autre fourni par la couche limite $\tilde{p}(x)$ le problème étant de corriger itérativement $\Theta^n(x)$ de façon à ce que $p^n(x)$ converge vers $\tilde{p}(x)$.

L'analyse de stabilité approchée des itérations de couplage directes ou inverses que nous avons évoquée au paragraphe 5.4 nous a permis de fournir une solution à ce problème. On peut en effet remarquer que, si la correction choisie $[\Theta^{n+1}(x) - \Theta^n(x)]$ est telle que la perturbation $[p^{n+1}(x) - p^n(x)]$ dans le fluide parfait soit précisément $[\tilde{p}(x) - p^n(x)]$, la nouvelle distribution $\Theta^{n+1}(x)$ s'identifie au résultat d'un calcul inverse de fluide parfait assujetti à $\tilde{p}(x)$. L'enchaînement d'un tel calcul inverse simulé pour le fluide parfait, et d'un calcul inverse véritable pour la couche limite, reproduit donc l'itération (5.11) et peut être stabilisée comme celle-ci, par le calcul local d'un coefficient de relaxation $\omega(x)$, d'après (5.13) (5.14). L'analyse doit toutefois être complétée par une technique appropriée pour résoudre le problème de petites perturbations inverses, de type Prandtl-Glauert, permettant de calculer $[\tilde{\Theta}^{n+1}(x) - \Theta^n(x)]$ à partir de $[\tilde{p}(x) - p^n(x)]$. Nous avons montré [13] qu'une analyse harmonique permet de se ramener, pour chaque mode de fréquence α, à une relation algébrique locale dont la combinaison avec la relaxation (5.13) (5.14) conduit, si $U^n(x)$ et $\tilde{U}(x)$ désignent les vitesses associées aux pressions $p^n(x)$ et $\tilde{p}(x)$, aux corrections :

$$\left.\begin{aligned} &\text{Points subsoniques :} && \Theta^{n+1} - \Theta^n = \frac{\delta^* B \sqrt{1-M^2}}{\alpha\, \delta^{*n} \tilde{B} - \sqrt{1-M^2}} \left[\frac{1}{\tilde{U}} \frac{d\tilde{U}}{dx} - \frac{1}{U^n} \frac{dU^n}{dx} \right] \\ &\text{Points supersoniques :} && \Theta^{n+1} - \Theta^n = \frac{\delta^{*2} \tilde{B}^2 \sqrt{M^2-1}}{\alpha^2 \delta^{*2} \tilde{B}^2 + (M^2-1)} \left[\frac{1}{\tilde{U}} \frac{d^2\tilde{U}}{dx^2} - \frac{1}{U^n} \frac{d^2U^n}{dx^2} \right] \end{aligned}\right\} \qquad (5.17)$$

la dépendance par rapport à α des corrections locales précédentes sur Θ^n étant enfin éliminée, sans altérer leur stabilité, en adoptant $\alpha = \alpha_{max.} = (\pi/\Delta x)$. On remarque qu'entre autres avantages, l'itération semi-inverse (5.17) exige seulement la détection des erreurs de couplage sur le gradient de pression. Elle permet de ce fait d'alterner aisément son utilisation avec celle de l'itération directe (5.12), en fonction du paramètre de forme local de la couche visqueuse, sans jamais conduire à des distributions de pression discontinues au cours de la convergence, quel que soit le nombre des zones résolues au mode inverse, ou leur modification au cours des itérations.

Cette méthode mixte a par exemple été utilisée pour calculer le décollement supersonique sur une rampe de compression, en laminaire ou turbulent, dans l'hypothèse d'onde simple, en résolvant directement un problème bien posé avec un gradient de pression nul au dernier point de calcul, figures 18 et 19. Elle a été également appliquée au calcul de profils transsoniques symétriques en théories des petites perturbations avec décollement de choc ou de bord de fuite, et capture numérique sur maillage fin de l'interaction forte au pied du choc, figures 20 à 22.

Une méthode de correction semi-inverse légèrement différente a été plus récemment proposée par Carter [78]. A chaque itération, la correction porte sur l'épaisseur de déplacement $\delta^*(x)$ et non sur la direction angulaire de l'écoulement $\Theta^n(x)$. Dans le cas incompressible, par exemple, la correction est écrite sous la forme algébrique locale :

$$\delta^{*n+1} = \Omega\, \delta^{*n} \left[\frac{\tilde{U}}{U^n} \right] \qquad (5.18)$$

dans laquelle Ω est un coefficient de relaxation, voire de surrelaxation ($1 < \Omega < 2$). Cette méthode a été récemment utilisée par Kwon, Pletcher [79], Whitfield et al. [80].

Il est intéressant de remarquer qu'une analogie existe entre (5.18) et (5.17) dans le cas subsonique. Si nous supposons par exemple que le couplage est obtenu par addition de l'épaisseur de déplacement, soit $\Theta = (d\delta^*/dx)$, la dérivation de (5.18) donne directement :

$$\Theta^{n+1} - \Theta^n = \frac{d\delta^{*n+1}}{dx} - \frac{d\delta^{*n}}{dx} = \Omega\, \delta^* \left[\frac{1}{\tilde{U}} \frac{d\tilde{U}}{dx} - \frac{1}{U^n} \frac{dU^n}{dx} \right] \qquad (5.19)$$

L'identité rigoureuse des formulations (5.17 (5.18) serait donc obtenue, en incompressible, dans le cas où $\Omega = [\tilde{B}\Delta x/(\pi\delta^*\tilde{B}\cdot\Delta x)]$. L'analogie (5.17) (5.19) montre également l'ambiguité de la notion de surrelaxation ou de sous relaxation dans (5.17) (5.18), la sous relaxation indiquée figure 17 intervenant dans (5.17) seulement au niveau des concepts, la surrelaxation Ω de (5.18) étant pondérée par le facteur multiplicatif δ^* .

Rappelons enfin que l'emploi de techniques non-automatisées du type semi-inverse a été mentionné initialement par Kuhn [81, 82].

5.0. Méthodes semi-implicites

Des tentatives récentes ont enfin été effectuées pour développer des méthodes partiellement affranchies du caractère explicite des techniques de relaxation des paragraphes 5.5 et 5.7, mais conduisant à des résolutions plus simples que la méthode de Newton au paragraphe 5.6.

Une première analyse a été suggérée par Veldman [83] dans le cas des écoulements incompressibles illimités pour lesquels, si le couplage est obtenu par distribution de sources à la paroi, la vitesse de perturbation induite par la couche visqueuse est donnée par une intégrale de Caughy homologue de (5.6) :

$$u - u_0 = \oint_{-\infty}^{+\infty} \frac{v}{x-\xi}\, d\xi \qquad\qquad v = \frac{d}{d\xi}(u\delta^*) \qquad (5.20)$$

Après discrétisation, la distribution de vitesse u_i ou de pression p_i se trouve reliée en vertu de (5.20) à la distribution d'épaisseur de déplacement δ_i^* par une forme linéaire dont les coefficients A_{ij} , à dominance diagonale, sont directement calculables. On peut écrire :

fluide parfait :
$$p_i^{n+1} - A_{ii}\,\delta_i^{*n+1} = \sum_{j<i} A_{ij}\,\delta_j^{*n+1} + \sum_{j>i} A_{ij}\,\delta_j^{*n} \qquad (5.21)$$

Schématiquement, la couche limite apparaît sous forme discrète comme un opérateur de matrice B_{ij} , sensiblement triangulaire inférieure :

couche limite :
$$\delta_i^{*n+1} - B_{ii}^{n+1}\, p_i^{n+1} = \sum_{j<i} B_{ij}^{n+1}\, p_j^{n+1} + \sum_{j>i} B_{ij}^{n}\, p_j^{n} \qquad (5.22)$$

Il est clair que les indices d'itérations n et $(n+1)$ ont été choisis dans (5.21) (5.22) de façon telle qu'une résolution procédant de l'amont vers l'aval puisse résoudre implicitement les premiers membres à la station i , les seconds membres étant connus, selon une technique de type Gauss-Seidel. Comme cette dernière, la méthode (5.21) (5.22) peut en outre être surrelaxée.

Une seconde analyse semi-implicite a été développée par Wai, Yoshihara [84] pour le calcul des profils transsoniques dans l'approximation des petites perturbations. Le problème potentiel :

$$(1 - M_0^2 - \lambda\varphi_x)\,\varphi_{xx} + \varphi_{yy} = 0 \qquad (5.23)$$

$$\varphi_y(x,0) = f(x) + \Theta(x) \qquad (5.24)$$

est résolu, en fluide parfait où $\Theta(x) = 0$, par la méthode de relaxation de Murman-Cole, implicite par colonnes selon y , semi implicite ou implicite en x selon le décentrement appliqué à φ_x et φ_{xx} . En fluide visqueux, la relation de comportement de la couche limite (5.1) fournit :

$$\varphi_y(x,0) = f(x) + b(x)\,\varphi_{xx} + c(x) \qquad (5.25)$$

relation dans laquelle $b(x)$ et $c(x)$ doivent être calculés par les autres équations de couche limite. Si ce calcul est effectué d'amont en aval en même temps que le balayage par colonnes pour φ , il est clair que (5.25) (5.23) peuvent être résolus simultanément de manière semi-implicite, exactement comme en fluide parfait, avec la même discrétisation pour φ_y et φ_{xx} . Le principal avantage est que le traitement interactif (5.25), même discrétisé de manière semi-implicite pour φ_{xx} en subsonique, élimine toute singularité au décollement. La convergence du couplage visqueux (5.25) en subsonique reste apparentée à celle d'une technique de relaxation en raison des schémas centrés appliqués à φ_{xx} , le progrès étant celui d'une technique de Gauss-Seidel, en analogie avec (5.21) (5.22).

La relaxation simultanée des équations intégrales de couche limite et de la fonction de courant, au cours de balayages successifs implicites par colonnes, avait été également indiquée par Moses, Jones, O'Brien [85] dans le cas d'écoulements subsoniques décollés. Elle est utilisée par Ghose, Kline [86] dans le calcul des diffuseurs.

6. EXEMPLE DE SYNTHESE - CALCUL DES PROFILS D'AILES

Parmi les méthodes de calcul des écoulements compressibles de fluide visqueux autour de profils d'ailes, au moyen d'approches de couplage correspondant aux approximations des paragraphes 4 et 5, on peut citer celles de Bavitz [37], Bauer, Korn [38], Lock, Collyer, Firmin, Jones [39], Melnik, Chow, Mead [29], Wai,

Yoshihara [84], Nandanam, Stanewsky, Inger [40], Le Balleur [15], une telle liste n'étant toutefois pas limitative. Nous ne nous intéressons pas ici aux performances comparées des méthodes d'un point de vue pratique, la plupart faisant encore l'objet de développements en cours et fournissant en général des résultats plus précis que les solveurs Navier-Stokes actuellement utilisables [87]. Nous recherchons ici seulement un exemple de calcul de synthèse, directement utilisable dans les applications, réunissant diverses interactions visqueuses s'influençant mutuellement (bord de fuite, interaction choc-couche limite décollement), et révélant l'évolution des méthodes d'une part vers un traitement effectif des couplages forts, et d'autre part vers une méthodologie suffisamment complète pour décrire en totalité le fluide visqueux à grand nombre de Reynolds, en extension directe des techniques numériques développées pour le fluide parfait.

6.1. Méthodes de Bavitz, de Bauer, Korn et al.

Dans ces premières méthodes de calcul des profils en fluide visqueux, les approximations utilisées pour le couplage sont encore proches des méthodes de couplage faible. Le sillage n'est pas pris en compte. L'effet de déplacement des couches limites est obtenu par modification de la géométrie du profil, après addition de l'épaisseur de déplacement. La stabilisation et la convergence des itérations de couplage sont relativement incertaines et incorporent des lissages ou extrapolations de $\delta^*(x)$, un traitement empirique de la région de bord de fuite étant utilisé en compensation dans la méthode de Bavitz. Le fluide parfait est calculé par la méthode potentielle de Garabedian, Korn. La forme non conservative est le plus souvent préférée en raison d'une certaine compensation d'erreur avec l'absence de prise en compte des effets visqueux au pied du choc, le maillage étant précisément sélectionné de façon à étaler suffisamment la compression sous le choc pour éviter tout décollement dans le calcul de couche limite [37].

6.2. Méthodes de Collyer, Lock et al.

Indépendamment des performances pratiques de ces analyses, la recherche de méthodes plus complètes vis à vis des phénomènes de forte interaction a été initiée par Lock et ses collaborateurs en résolvant le fluide parfait d'abord par des techniques de petites perturbations transsoniques, figure 23, puis par la méthode potentielle de Garabedian et Korn. La figure 23 rappelle que les effets de sillage ont été introduits, sous forme d'un saut de vitesse normale, correspondant à l'effet de déplacement (3.5) et d'un saut de vitesse tangentielle ou de pression, associé à un effet de courbure du sillage du type (4.13). La courbure des lignes de courant considérée est toutefois une courbure moyenne. De plus, dans le cas de l'équation du potentiel complète, les conditions de sillage sont appliquées sur une ligne de maillage et non sur le sillage visqueux lui-même. Les décollements ne sont pas traités.

Par rapport aux méthodes précédentes, outre le traitement du sillage, les progrès essentiels sont le recours à une vitesse normale sur la paroi du profil pour traduire l'effet de déplacement sans modification de géométrie, l'itération simultanée sur les effets visqueux et sur le calcul potentiel, l'abandon des techniques de lissage sur δ^* au profit d'une sous-relaxation visqueuse uniforme, déterminée empiriquement mais n'altérant pas la solution à convergence. Le dernier progrès a consisté à simuler au mieux les sauts de pression des ondes de choc délivrés par le calcul potentiel, au moyen d'une pondération des techniques numériques conservatives et non conservatives . Aucun traitement visqueux spécial n'est toutefois introduit pour l'interaction choc-couche limite.

6.3. Méthode de Melnik, Chow, Mead.

Comme la méthode précédente, cette analyse s'applique aux profils exempts de décollements, s'appuie sur la méthode intégrale de Green pour les calculs de couche limite et de sillage, et n'introduit aucun traitement particulier pour l'interaction forte au pied des ondes de choc. La figure 24 rappelle que, hormis la région de bord de fuite, les conditions aux limites visqueuses appliquées au fluide parfait sont semblables à la méthode de Lock et al., les conditions sur le sillage étant toujours appliquées sur une ligne légèrement différente du sillage réel.

Les progrès apportés par la méthode consistent d'une part en l'utilisation du calcul potentiel de Jameson sous forme conservative, et d'autre part d'un traitement élaboré de l'interaction forte turbulente au bord de fuite : celle-ci s'appuie sur une analyse asymptotique multi-couche, figure 25, et garantit un comportement rationnel du modèle à la limite infinie du nombre de Reynolds. D'un point de vue pratique, on doit remarquer sur la figure 25 que le modèle de calcul visqueux incorpore, dans la couche externe, la prise en compte d'un gradient de pression normal non-irrotationnel. Celui-ci est traduit dans le calcul potentiel par une modulation locale au bord de fuite des conditions aux limites de couplage traditionnelles, figure 24. Il conduit en général à des sauts de pression majorés sur le sillage au voisinage immédiat du bord de fuite.

6.4. Méthode de Nandaman, Stanewsky, Inger.

Cette méthode est plus simple que les deux précédentes, à l'exception du traitement de l'interaction choc-couche limite. Elle utilise la méthode potentielle de Jameson, sous forme conservative ou non conservative, ainsi qu'une méthode intégrale pour la couche limite. Le sillage n'est pas calculé. Les décollements ne sont pas traités. Le couplage est obtenu en modifiant la géométrie du profil par addition d'une épaisseur déplacement assujettie à un lissage important, notamment dans la région du choc.

La méthode serait donc à rapprocher de celles du paragraphe 6.1. Si un traitement plus élaboré de l'interaction choc-couche limite n'était incorporé. Celui-ci apparaît comme un module séparé, qui a pour rôle d'une part de déterminer avec une meilleure précision l'état de la couche limite après choc, et d'autre part de fournir une estimation plus réaliste de la pression à la paroi dans la région du choc. Ce module s'appuie sur l'analyse non-asymptotique multi-couche de Inger [88]. Les résultats sont améliorés si la compression

appliquée au module de Inger, théoriquement celle d'un choc droit, est celle du choc oblique de déflection maximale.

6.5. Méthode de Wai, Yoshihara.

La méthode, d'un développement récent, utilise pour l'écoulement potentiel un simple calcul de petites perturbations transsoniques. La couche limite et le sillage sont calculés par une méthode intégrale, décollements inclus. La première particularité consiste en une résolution simultanée des équations de petites perturbations potentielles et de la condition aux limites visqueuses (5.1), au cours de la relaxation par colonne associée à la technique de Murman-Cole. Ce procédé, évoqué au paragraphe 5.8, est semi-implicite dans la mesure où les balayages par colonnes doivent être répétés pour assurer la convergence. En revanche, le traitement interactif du calcul visqueux élimine les problèmes de singularité au décollement.

La seconde particularité de la méthode, est de substituer une modélisation, dite de rampe visqueuse, au calcul intégral de couche limite dans la région de choc, en cas de décollement, faute de résoudre le couplage fort avec un maillage suffisamment fin. La modélisation consiste schématiquement à imposer pour surface de déplacement une rampe, dont l'angle correspond sur la polaire de choc à un niveau de recompression prédéterminé, l'empirisme conduisant à sélectionner une valeur intermédiaire entre la déviation sonique et la déviation maximale [89]. Cette modélisation de δ^* est nécessaire non seulement pour améliorer la comparaison à l'expérience, mais encore pour assurer la convergence du calcul.

6.6. Méthode de Le Balleur.

La méthode utilise pour le fluide parfait le calcul potentiel de Chattot, Coulombeix, Tomé [90] qui résout l'équation sous une forme conservative, avec la viscosité artificielle de Jameson. La couche limite, laminaire ou turbulente, ainsi que le sillage sont calculés par une méthode intégrale incluant les écoulements de retour, le sillage pouvant être calculé avec ou sans l'effet de dissymétrie. La formulation déficitaire du paragraphe 4.3 conduit pour le fluide parfait à des conditions aux limites sur la paroi et sur le sillage analogues à celles de Lock et al. ou de Melnik et al.. Toutefois la géométrie de la ligne de sillage est ici adaptée périodiquement au cours du calcul pour coïncider avec la ligne moyenne du sillage visqueux. La méthode ne comporte pas de traitement spécial au bord de fuite, mais y respecte strictement le couplage fort associé à la formulation déficitaire ; l'effet de courbure appliqué (4.13) incorpore enfin des estimations moyennées de $K(x)$, distinctes pour les demi-sillages supérieur et inférieur.

Le couplage est réalisé par une itération de relaxation, directe ou semi-inverse, en fonction du paramètre de forme local instantané de la couche visqueuse. Cette itération, exposée aux paragraphes 5.5 et 5.7, est menée de front avec celle utilisée pour le calcul du fluide parfait, figure 26. Le gradient de pression le long de la paroi est estimé dans le fluide parfait par des schémas centrés en subsonique, décentrés vers l'aval en supersonique. Le passage de la couche limite au sillage est assimilé à un processus continu pour le fluide parfait ainsi que pour $\delta^*(x)$, mais discontinu pour le calcul visqueux. La méthode capture automatiquement la modification apportée aux distributions de pression par la viscosité dans le voisinage immédiat du bord de fuite, pourvu que les mailles soient de l'ordre de l'épaisseur locale de la couche visqueuse, qu'il y ait décollement ou non.

Les figures 27 à 32 montrent l'utilisation de la méthode aux basses vitesses et aux grandes incidences, pour le profil NACA 0012. Sur ce profil, le calcul approche l'incidence de décrochage, avec un décollement d'extrados à 70 % de la corde et un recollement dans le sillage. Dans l'état actuel de développement de la méthode, ce calcul à l'incidence de 16° n'est possible qu'en respectant la dissymétrie du sillage, les figures 27 et 31 montrant le changement d'aspect associé de sa ligne moyenne. Les figures 39 à 41 montrent enfin, par le tracé de lignes de courant et de lignes iso-Mach que la méthode de calcul restitue non seulement l'écoulement de fluide parfait lointain, mais encore l'écoulement moyen de fluide visqueux dans son détail.

Les figures 33 et 34 montrent l'utilisation de la méthode dans les cas transsoniques subcritiques sur le profil RAE 2822, expérimenté par Cook, Mc Donald, Firmin [91]. Dans les cas transsoniques supercritiques, contrairement aux calculs effectués dans l'approximation des petites perturbations, figures 20-21, il demeure actuellement impossible de capturer numériquement l'interaction forte au pied des ondes de choc sur un maillage fin approprié aux épaisseurs locales des couches limites, en raison de difficultés numériques dans la résolution de l'équation du potentiel sur de tels maillages. Faute de cette résolution complète du couplage visqueux local, la compression sous le choc est surestimée par la méthode conservative appliquée au fluide parfait.

Pour pallier cette difficulté, une méthode approchée a été définie pour l'interaction choc-couche limite. Comme le schématise la figure 36, cette méthode consiste simplement à résoudre une interaction locale fictive à l'échelle agrandie $\mathcal{E}_2$, compatible avec le maillage. Celle-ci est une image homothétique de l'interaction réelle d'échelle $\mathcal{E}_1$, obtenue par simple dilatation de l'épaisseur locale δ de la couche visqueuse dans le rapport ($\mathcal{E}_2 / \mathcal{E}_1$) sans toutefois altérer le nombre de Reynolds $\mathcal{R}_\delta$. Le couplage fort réalisé sur la région d'interaction fictive $\mathcal{E}_2$ conduit d'une part à une estimation interactive plus réaliste de l'épaississement de la couche limite, et d'autre part à la réduction attendue du niveau de recompression, comme le montre la figure 37. En revanche, le traitement est essentiellement une approximation dans la mesure où l'altération subie par le fluide parfait dans le domaine $\mathcal{E}_2$ est incohérente avec l'échelle C du calcul global. Pour celui-ci, une résolution numérique de qualité ne sera donc maintenue que si $\mathcal{E}_2 \ll C$, et même $\mathcal{E}_2 \ll L$, L désignant l'étendue de la poche supersonique. On peut observer sur la figure 38 que le calcul prévoit, grâce au seul effet de couplage visqueux un nombre de Mach après choc faiblement inférieur à l'unité, plus proche de l'expérience. On constate en outre que la structure numérique du choc du calcul potentiel est remplacée par une compression visqueuse continue, relativement étalée en raison du maillage utilisé, figure 37. Les figures 42 à 44 montrent enfin l'aspect des lignes iso-Mach et des lignes de courant dans l'écoulement de fluide visqueux calculé.

7. CONCLUSIONS

Un effort spectaculaire a été consenti ces dernières années dans le domaine du fluide parfait en vue de renforcer l'efficacité et la généralité des techniques de calcul. Il est important de souligner en premier lieu la valorisation majeure que peut en pratique apporter le couplage de ces techniques à des calculs visqueux complémentaires, à condition toutefois de se dégager des approximations trop restrictives du couplage faible. L'évolution des méthodes de prévision des caractéristiques locales et globales des profils et des ailes est révélatrice le cette tendance.

Dans cette optique, on doit noter la conjugaison de progrès d'ordre analytique effectués sur le calcul visqueux interactif des phénomènes fondamentaux tels que écoulements de bords de fuite, décollement en couche mince, interaction couche limite - onde de choc, et de progrès d'ordre numérique, ayant consisté essentiellement à développer des techniques nouvelles originales de couplage fort. Ces progrès ont permis de dépasser le stade du traitement des phénomènes ponctuels ou locaux, et de synthétiser des moyens de de calculs appropriés aux écoulements complexes rencontrés dans les applications industrielles, en compétition avec les méthodes globales de résolution directe du fluide visqueux.

Il est clair cependant que les deux approches des phénomènes d'interaction visqueuse, l'approche globale et l'approche par couplage fort, sont en fait plus complémentaires que compétitives. Le choix actuel d'approximations visqueuses relativement simples dans les méthodes de couplage n'est en effet guidé que par le souci d'utiliser des maillages de discrétisation moins fins que ceux indispensables dans l'approche globale pour résoudre numériquement les couches et sous-couches visqueuses. Les méthodes de couplage à équations visqueuses simples, et notamment celles mettant en jeu des équations intégrales de type couche limite, matérialisent en pratique les densités de maillage minimales compatibles avec la résolution numérique des phénomènes de couplage fort. De telles densités, intermédiaires entre celles utilisées en fluide parfait et celles des calculs de type Navier-Stokes, conduisent à une économie qui peut être mise à profit pour calculer des écoulements plus complexes, incorporant par exemple des interactions visqueuses multiples ou des phénomènes tridimensionnels.

Sur des maillages moins restrictifs, les progrès effectués dans l'approche globale possèdent des répercussions évidentes sur le calcul des régions visqueuses dans l'approche de couplage par domaines. Il est enfin concevable également d'utiliser des solveurs Navier-Stokes dans des méthodes de couplage en substitution des calculs de fluide parfait actuels et sur des maillages analogues. Une telle technique permettrait, en tridimensionnel par exemple, de capturer les phénomènes visqueux macroscopiques par une résolution locale des équations de Navier-Stoles avec modèle de turbulence, tandis que les phénomènes concentrés de couche mince près des parois, leur interaction avec l'écoulement externe ainsi que leur impact sur la génération de nappes tourbillonnaires continueraient à bénéficier de traitements moins coûteux, en extensions des méthodes intégrales de couche limite interactives actuellement développées pour les profils d'aile et les voilures de grand allongement.

D'un point de vue plus ponctuel enfin, quelques idées marquantes ou besoins nous paraissent se dégager des méthodes de couplage actuelles :

(i) la réalisation de calculs couplés de forte interaction présente deux voies relativement différenciées. La première utilise un concept de domaines raccordés par leurs conditions aux limites, avec la possibilité d'incorporer directement des modules existants de type Navier-Stokes. La seconde s'appuie sur l'idée d'un recouvrement des domaines de calcul visqueux et non-visqueux, avec la possibilité de développer des méthodes numériques originales pour résoudre les équations de Navier-Stokes par une technique d'éclatement d'équations.

(ii) L'abandon nécessaire des approximations de couplage faible au profit d'un couplage fort rigoureux conduit au besoin impératif de développer des méthodes numériques spécialisées, soulevant des problèmes au moins aussi complexes que ceux associés aux techniques numériques constitutives de fluide parfait et de fluide visqueux. Ce besoin est apparu clairement pour les problèmes de bord de fuite, de décollement et d'interaction choc-couche limite. L'analyse est particulièrement peu développée pour le couplage entre équations d'Euler et de Navier-Stokes.

(iii) Le traitement des interactions couches limites - ondes de choc apparaît comme l'un des problèmes les plus délicats des techniques de calcul, non seulement en raison de l'incertitude attachée aux modélisations de la turbulence, mais encore à cause des échelles réduites qui devraient être mises en jeu localement, même pour le calcul du fluide parfait dans le cas d'une méthode de couplage à maillage minimal. Des difficultés analogues d'échelles multiples de résolution sont présentes dans les décollements de couches visqueuses au voisinage des bords d'attaque.

(iv) Parmi les améliorations relatives au calcul des profils d'ailes, la substitution des équations d'Euler à l'équation du potentiel devra être examinée, notamment aux régimes transsoniques supérieurs, en cas de décollement naissant sous le choc, avec le bénéfice ultérieur d'une application directe aux écoulements internes. La réalisation de comparaisons calcul-expérience dégagées des incertitudes de corrections parois des souffleries, serait également fort souhaitable pour l'affinement des méthodes de calcul existantes.

(v) Les calculs de profils dans les régimes extrêmes, proches du décrochage ou du décollement sous le choc par exemple, révèlent la très grande sensibilité de l'écoulement global à la précision du calcul des couches visqueuses depuis l'origine de celle-ci. Le développement de modèles de turbulence est donc important, même sous les formes simplifiées rencontrées dans les méthodes intégrales.

REFERENCES

[1] PEYRET R., VIVIAND H. - Computation of viscous compressible flows based on the Navier-Stokes equations AGARD AG-212 (Sept. 1975)

[2] VIVIAND H. - Traitement des problèmes d'interaction fluide parfait - fluide visqueux en écoulement bidimensionnel compressible à partir des équations de Navier-Stokes. VKI/AGARD LS 94, ou "Three dimensional and unsteady separation at high Reynolds numbers" (Feb. 1978).

[3] LE BALLEUR J.C., PEYRET R., VIVIAND H. - Numerical studies in high Reynolds number aerodynamics. Symposium on Computers in Aerodynamics, Farmingdale (June 1979, Computers and Fluids, vol. 8, n° 1, p. 1-30 (March 1978)

[4] HOLLANDERS H., VIVIAND H. - The numerical treatment of compressible high Reynolds numbers flows. VKI Lecture Serie sur le "Traitement numérique des équations de la dynamique des fluides" (19-23 Mars 1979), T.P. ONERA 1979-22.

[5] MURPHY J.D., PRESLEY L.L., ROSE W.C. - On the calculation of supersonic separating and reattaching flows. AGARD CP-168 (1975).

[6] STEGER J.L. - Implicit finite difference simulation of flow about arbitrary geometrics with application to airfoils. AIAA Paper n° 77-665 (1977).

[7] JONCHERAY P. - Modèle bidimensionnel pour la formation des nappes tourbillonnaires s'échappant du bord latéral d'une aile. Thèse de 3e cycle, Université P. et M. Curie, Paris 6 (1977).

[8] BRUNE G.W., RUBBERT P.E., FORESTER C.K. - The analysis of flow fields with separation by numerical matching. AGARD CP-168, (1975).

[9] SEGINER A., ROSE W.C. - A numerical solution of the flow field over a transonic airfoil including strong shock-induced flow separation. AIAA Paper n° 76-330, San Diego (July 14-16, 1976).

[10] SEGINER A., ROSE W.C. - An approximate calculation of strong interaction on a transonic airfoil. AIAA Paper N° 77-210, Los Angeles (January 24-26, 1977).

[11] ROSE W.C., SEGINER A. - Calculation of transonic flow over supercritical airfoils sections. J. of Aircraft, vol 15, n° 8, p. 514-519 (1978).

[12] LE BALLEUR J.C. - Couplage visqueux - non visqueux : analyse du problème incluant décollements et ondes de choc. La Recherche Aérospatiale, n° 1977-6, p. 349-358 (Nov.1977) - ESA TT. 476 (1978).

[13] LE BALLEUR J.C. - Couplage visqueux - non visqueux : méthode numérique et applications aux écoulements bidimensionnels transsoniques et supersoniques. La Recherche Aérospatiale, N° 1978-2, p. 67-76 (Mars 1978) -

[14] LE BALLEUR J.C. - Calculs couplés visqueux - non visqueux incluant décollements et ondes de choc en écoulement bidimensionnel - VKI/AGARD LS-94 on "Three dimensional and unsteady separation at high Reynolds numbers" (Feb. 1978).

[15] LE BALLEUR J.C. - VIVIAND H. - Méthodes de calcul des écoulements décollés bidimensionnels aux grands nombres de Reynolds - 16e Colloque AAAF, Lille (Nov. 1979), T.P. ONERA n° 1979-145.

[16] DODGE P.R. - Numerical method for 2D and 3D viscous flows - AIAA Journal, vol. 15, n° 7, p. 961-965, (July 1977).

[17] DWOYER D.L. - Application of a velocity-split Navier-Stokes solution technique to external flow problems. 4th Computational fluid Dyanmics conf., AIAA Paper n° 79)1449 (July 1979).

[18] JOHNSTON W., SOCKOL P. - A viscous-inviscid interactive compressor calculation. AIAA Paper n° 78-1140 (July 1978).

[19] BRILEY W.R., Mc DONALD H. - Analysis and computation of viscous subsonic primary and secondary flows. 4th Computational fluid dynamics conf. AIAA Paper n° 79-1453 (July 1979).

[20] DASH S.M., WILMOTH R.G., PERGAMENT H.S. - Overlaid viscous/inviscid model for the prediction of near-field jet entrainment. AIAA Journal vol. 17, n° 9, p. 950-958 (Sept. 1979).

[21] VAN DYKE M. - Perturbation methods in fluid mechanics. The parabolic Press (1975).

[22] MELLOR G.L. - The large Reynolds number asymptotic theory of turbulent boundary layers. Intern. J. of Engineering Sci., Vol. 10, pp. 851-873 (1972).

[23] MELNIK R.E., GROSSMAN B. - Analysis of the interaction of a weak normal shock wave with a turbulent boundary layer. AIAA Paper n° 74-598, Palo-Alto (June 17-19, 1974).

[24] STEWARTSON K. - Multistructured boundary layers on flat plates and related bodies. Advances in Appl. Mech., vol. 14, pp. 145-239 (1974).

[25] MELNIK R.E., CHOW R. - Asymptotic theory of two-dimensional trailing-edge flows. NASA SP 347, Part 1, Langley (March 4-6, 1975).

[26] CHOW R., MELNIK R.E. - Numerical solutions of the triple deck equations for laminar trailing edge stall. Grumman Rept. RE-526J (October 1976).

[27] BURGGRAF O.R., RIZETTA D., WERLE M.J., VATSA V.N. - Effect of Reynolds number on laminar separation of a supersonic stream. AIAA Journal vol. 17, n° 4, p. 336-343 (Apr. 1979).

[28] MELNIK R.E., GROSSMAN B. - Interaction of normal shock waves with turbulent boundary layers at transonic speeds. Grumman Rept. RE-517J (March 1976).

[29] MELNIK R.E., CHOW R., MEAD H.R. - Theory of viscous transonic flow over airfoils at high Reynolds number. AIAA Paper 77-680, Albuquerque (June 27-29, 1977).

[30] MESSITER A.F. - Interaction between a normal shock-wave and a turbulent boundary layer at high transonic speeds. Part I : pressure distribution ; J. of Applied Math. and Physics (ZAMP), vol. 31, p. 204-226 (1980).

[31] LIOU M.S., ADAMSON T.C. - Interaction between a normal shock-wave and a turbulent boundary layer at high transonic speeds. Part II : Wall shear stress. J. of Applied Math. and Physics (ZAMP), vol. 31, p. 227-246 (1980).

[32] OHRENBERGER J.T., BAUM E. - A theoretical model of the near wake of a slender body in supersonic flow. AIAA J., vol.10, n° 9, pp. 1165 (sept. 1972).

[33] BAUM E., DENISON M.R. - Interacting supersonic laminar wake calculations by a finite difference method. AIAA J., Vol. 5, N° 7, p. 1224 (July 1967).

[34] MAHGOUB H.E.H., BRADSHAW P. - Calculation of turbulent inviscid flow interactions with large normal pressure gradients. AIAA Journal, Vol. 17, n° 10, pp. 1025-1029 (Oct. 1979).

[35] PATANKAR S.V., SPALDING D.B. - A calculation procedure for heat, mass and momentum transfer in three-dimensional parabolic flows. Int. J. Heat Mass Transfer. Vol. 15, pp. 1787-1806 (1972).

[36] SPALDING D.B. - Numerical computation of steady boundary layers - A survey. Computational methods and problems in aeronautical fluid dynamics. London and New York Academic Press (1976).

[37] BAVITZ P.C. - An analysis method for two-dimensional transonic viscous flow. NASA TN D.7718 (January 1975).

[38] BAUER F., KORN D. - Computer simulation of transonic flow past airfoils with boundary layer correction. 2nd AIAA Compt. Fluid. Dyn. Conf., Hartford (June 1975).

[39] COLLYER M.R., LOCK R.C. - Prediction of viscous effects in steady transonic flow past and airfoil. Aero. Quart., Vol. 30, part 3 (aug. 1979).

[40] NANDANAN M., STANEWSKY E., INGER G.R. - A computational procedure for transonic airfoil flow including a special solution for shock boundary layer interaction. AIAA Paper n° 80-1389 (July 1980).

[41] REHBACH C. - Calcul numérique d'écoulements tridimensionnels instationnaires avec nappes tourbillonnaires - La Recherche Aérospatiale n° 1977-5, pp. 289-298 (Sept. 1977).

[42] HENDERSON M.L. - A solution to the 2-D separated wake modeling problem and its use to predict CL_{max} of arbitrary airfoil section. - AIAA Paper n° 78-156 (Jan. 1978).

[43] CROCCO L. , LEES L. - A mixing theory for the interaction between dissipative flows and nearly isentropic streams. J. Aero. Sci., vol. 19, n° 10 (October 1952).

[44] GOLDSTEIN S. - On laminar boundary layer flow near a position of separation. Quart. J. Mech. Appl. Math. 1, 43-69 (1948).

[45] COUSTEIX J., LE BALLEUR J.C., HOUDEVILLE R. - Calcul des couches limites turbulentes instationnaires en mode direct ou inverse, écoulements de retour inclus. Analyse des singularités. La Recherche Aérospatiale n° 1980-3, pp. 147-157 (Mai 1980).

[46] COUSTEIX J., HOUDEVILLE R. - Analogie des singularités dans les méthodes directes de calcul des couches limites tridimensionnelles stationnaires et bidimensionnelles instationnaires. Analyse des modes inverses. Proceed. AGARD Symp. on Computation of viscous-inviscid interactions, Colorado Springs (29 Sept. - 1 Oct. 1980).

[47] CATHERALL D., MANGLER K.W. - The integration of two-dimensional laminar boundary layer equations past the point of vanishing skin friction. J.F.M., Vol. 26, part 1 (Sept. 1966).

48 KLINEBERG J.M., STEGER J.L. - On laminar boundary layer separation. AIAA Paper n° 74-94, Washington (Jan. Febr. 1974).

49 CARTER J.E. - Inverse solutions for laminar boundary layer flows with separation and reattachment. NASA TR-R-447 (Nov. 1975).

50 CEBECI T., KELLER H.B., WILLIAMS P.G. - Separating boundary layer flow calculations. J. of Comput. Physics 31, 363-378 (1979).

51 PLETCHER R.H. - Prediction of incompressible turbulent separating flow. J. of Fluids Engineering Vol. 100, p. 427-432 (Déc. 1978).

52 EAST L.F., SMITH P.D., MERRYMAN P.J. - Prediction of the development of separated turbulent boundary layers by the lag-entrainment method. RAE-TR-77046 (March 1977).

53 KUHN G.D., NIELSEN J.N. - Prediction of turbulent separated boundary layers. AIAA Paper n° 73-663 (1973).

54 THIEDE P.G. - Prediction method for steady aerodynamic loading on airfoils with separated transonic flow. AGARD-CP -204 (1976).

55 DELERY J., CHATTOT J.J., LE BALLEUR J.C. - Interaction visqueuse avec décollement en écoulement transsonique. AGARD-CP-168 on "Flow separation", Göttingen (May 1975).

56 GARVINE R.W. - Upstream influence in viscous interaction problems. The Physics of Fluids, vol. 11, p. 1413 (July 1968).

57 WEINBAUM S., GARVINE R.W. - On the two-dimensional viscous counterpart of the one-dimensional sonic throat. J.F.M. vol 39, pp 57-85 (1969).

58 KING MON TU, WEINBAUM G. - A non-asymptotic triple-deck model for supersonic boundary layer interaction. AIAA J. vol. 14, n° 6, pp. 767-775 (June 1976).

59 KLINEBERG J.M. - Theory of laminar viscous-inviscid interactions in supersonic flow. Cal. Inst. Tech., Ph. D. Thesis (May 1968).

60 BRUNE G.W., RUBBERT P.E., NARK T.C. - A new approach to inviscid flow-boundary layer matching. AIAA Paper n° 74-601, Palo Alto (June 17-19, 1974).

61 COUSTON M., ANGELINI J.J., LE BALLEUR J.C., GIRODROUX-LAVIGNE P. - Prise en compte d'effets de couche limite instationnaire dans un calcul bidimensionnel transsonique. Proceed. AGARD meeting on Boundary layer effects on unsteady airloads, Aix-en-Provence (17-18 Sept. 1980).

62 LEES L., REEVES B.L. - Supersonic separated and reattaching laminar flows. Pt I : General theory and application to adiabatic boundary layer-shock wave interaction. AIAA J., Vol. 2, N° 10 (1964).

63 HOLT M. - Numerical methods in fluid dynamics. Springer-Verlag, Series in Computational Physics (1977).

64 HANKEY W.L., HOLDEN M.S. - Two-dimensional shock wave-boundary layer interactions in high speed flows. AGARDograph AG-203 (June 1975).

65 REYHNER T.A., FLUGGE-LOTZ - The interaction of a shock-wave with a laminar boundary layer. Stanford Univ. Dir. of Eng. Mech. (November 1966).

66 NIELSEN J.N., LYNES L.L., GOODWIN F.K. - Calculation of laminar separation with free interaction by the method of integral relations. AFFDL TR-65-107 (June 1965).

67 WERLE M.J., VATSA V.N. - New method for supersonic boundary layer separations. AIAA J., vol. 12, n° 11 (November 1974).

68 VATSA V.N., WERLE M.J. - Quasi three-dimensional supersonic viscid-inviscid interactions including separation effects. Univer. Cincinnati, Ohio, Tech. Rep. AFFDL-TR-75-138 (Sept. 1975).

69 NAPOLITANO M., WERLE M.J., DAVIS R.T. - Numerical technique for the Triple-Deck problem. AIAA J. vol. 17, n° 7, pp. 699-705 (July 1979).

70 BRILEY W.R., McDONALD H. - Numerical prediction of incompressible separation bubbles. J.F.M., vol. 69, pt 4, pp. 631-656 (1975).

71 GLEYZES C., COUSTEIX J., BONNET J.L. - Bulbe de décollement laminaire avec transition : théorie et expérience. L'Aéronautique et l'Astronautique n° 1980-1 (Jan. 1980).

72 LE BALLEUR J.C., MIRANDE J. - Etude expérimentale et théorique du recollement bidimensionnel turbulent incompressible. AGARD-CP-168 on "Flow separation", Göttingen (May 1975).

73 CARTER J.E., WORNOM S.F. - Solutions for incompressible separated boundary layers including viscous-inviscid interaction. NASA SP-347, pp. 125-150 (1975).

74 KLINEBERG J.M., STEGER J.L. - Calculation of separated flows at subsonic and transonic speeds. Proceed. of Intern. Conf. on Numerical Methods in Fluid Mech., Springer Verlag, vol. 11, pp. 161-168 (1973).

75 LE BALLEUR J.C. - Viscous interaction including turbulent boundary layer separation in two-dimensional flows. Communication au workshop on "Viscous interaction and boundary layer separation", Colombus, Ohio (July 1976).

76 ARIELI R., MURPHY J.D. - Pseudo-direct solutions to the boundary layer equations for separated flow. AIAA Paper n° 79-0139 (Jan. 1979).

77 LOCK R.C. - Calculation of viscous effects on aerofoils in compressible flows. RAE Tech. Memo. Aero. 1646 (Sept. 1975).

78 CARTER J.E. - A new boundary layer inviscid iteration technique for separated flow. 4th Computational fluid dynamics conf., AIAA Paper 79-1450 (July 1979).

79 KWON O.K., PLETCHER R.H. - Prediction of incompressible separated boundary layers including viscous-inviscid interaction. J. of Fluids engineering vol. 101, p. 466-472 (Déc. 1979).

80 WHITFIELD D.L., SWAFFORD T.W., JACOCKS J.L. - Calculation of turbulent boundary layers with separation, reattachment and viscous-inviscid interaction. AIAA Paper n° 80-1439 (July 1980).

81 KUHN G.D., NIELSEN J.N. - Prediction of turbulent separated boundary layers. AIAA J., vol. 12, N° 7 (July 1974).

82 KUHN G.D. - Calculation of separated turbulent flows on asixymmetric afterbodies including exhaust plume effects. AIAA J., vol. 18, n° 3, pp. 235-242 (March 1980).

83 VELDMAN A.E.P., DIJKSTRA D. - A fast method to solve incompressible boundary layer interaction problems. Proceed. of 7th Int. Conf. on numerical methods in fluid Dynamics, Stanford and NASA Ames (23-27 June 1980).

84 WAI J.C., YOSHIHARA H. - Viscous transonic flow over airfoils. Boeing Rep. D180-29934-1, and Proceed. of 7th int. Conf. on numerical methods in fluid dynamics, Stanford and NASA Ames (23-27 June 1980).

85 MOSES H.L., JONES R.R., O'BRIEN W.F. - Simultaneous solution of the boundary layer and freestream with separated flow. AIAA J., vol. 16, n° 1, pp. 61-66 (Jan. 1978).

86 GHOSE S., KLINE S.J.- The computation of optimum pressure recovery in two-dimensional diffusers. J. of Fluid engineering, vol. 100, pp. 419-426 (Dec. 1978).

87 SWAFFORD T.W. - Calculation of skin friction in two-dimensional, transonic, turbulent flows. ARO Inc., Sverdrup, AEDC-TR-79-12, Arnold Air Force Station (April 1979).

88 INGER G.R. - Upstream influence and skin friction in non-separating shock-turbulent boundary layer interactions. AIAA Paper n° 80-1411 (July 1980).

89 MAGNUS R.J., YOSHIHARA H. - Calculation of the transonic oscillating flap with "viscous" displacement effects. AIAA Paper n° 76-327 (1976).

90 CHATTOT J.J., COULOMBEIX C., TOME C. - Calculs d'écoulements transsoniques autour d'ailes. La Recherche Aérospatiale n° 1978-4, pp. 143-159 (Juillet 1978).

91 COOK P.H., Mc DONALD M.A., FIRMIN M.C.P. - Aerofoil RAE 2822 : pressure distributions, and boundary layer and wake measurements. AGARD-AR-138, Experimental data base for computer program assesment (1979).

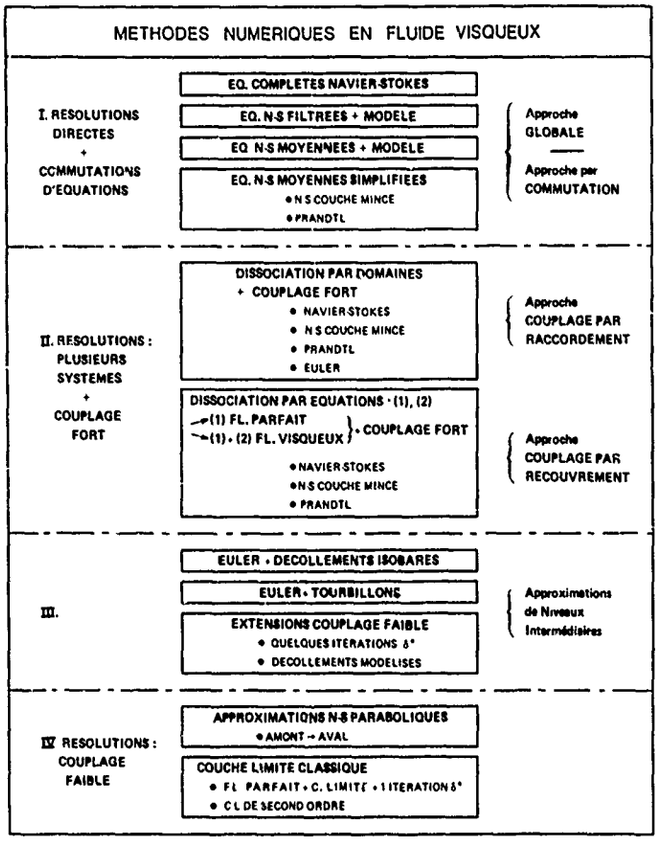


Fig. 1 – Méthodes de calcul en fluide visqueux.

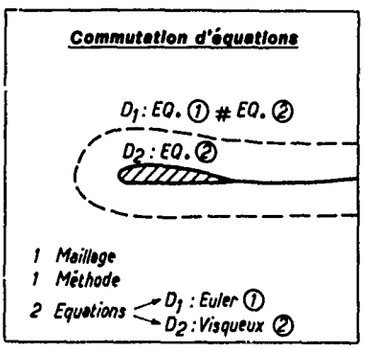


Fig. 2 – Approche par commutation d'équations.

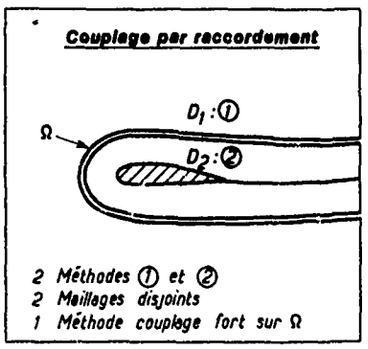


Fig. 3 – Approche de couplage par raccordement.

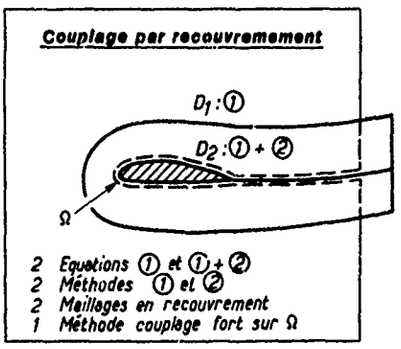


Fig. 4 – Approche de couplage par recouvrement.

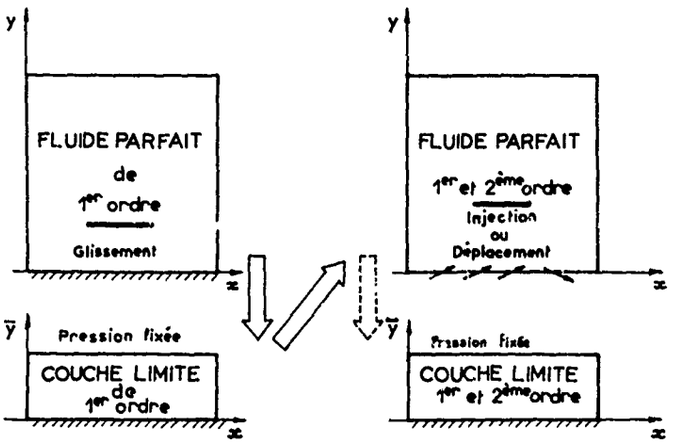


Fig. 5 — Couplage faible asymptotique.

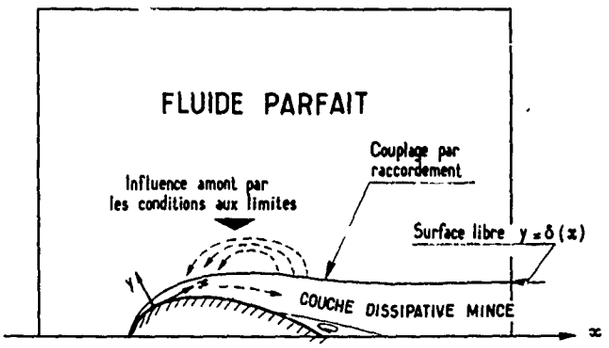


Fig. 6 — Couche de Prandtl en forte interaction: Couplage par raccordement.

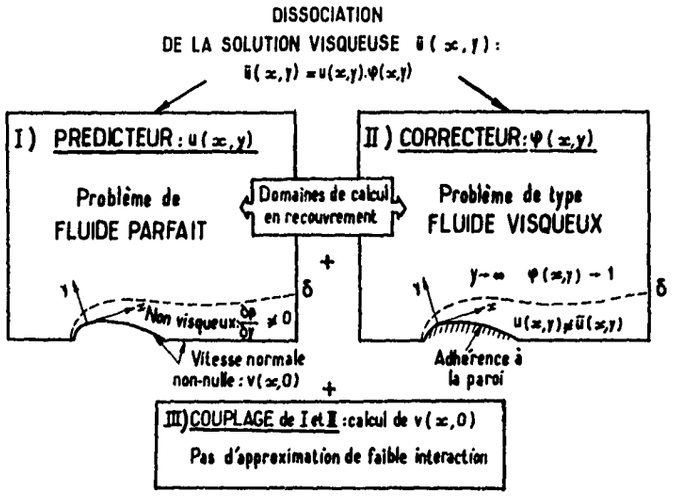


Fig. 7 — Couplage fort par recouvrement: Formulation déficitaire du calcul visqueux:

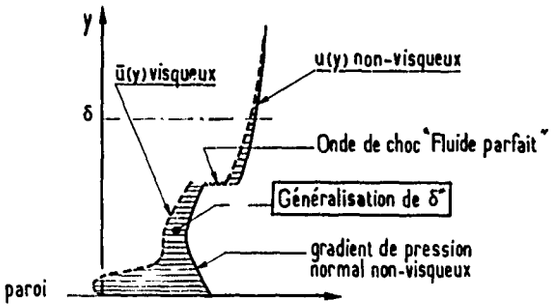


Fig. 8 — Formulation déficitaire : schéma des solutions visqueuses et non-visqueuses, à une abscisse x donnée.

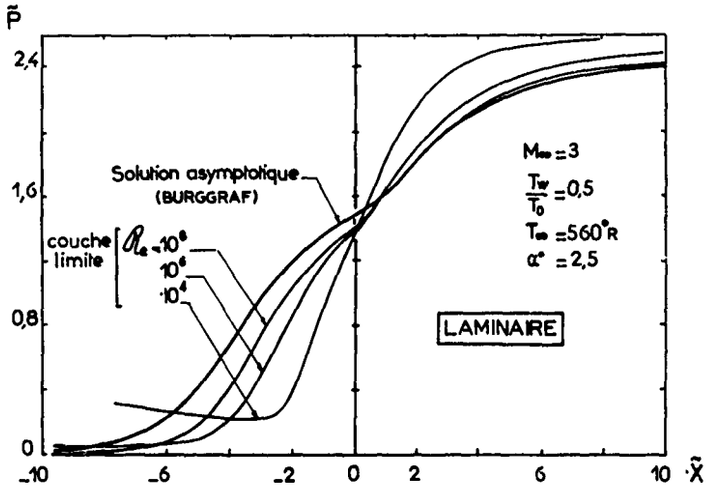


Fig. 9 — Rampe supersonique laminaire - Comportement asymptotique des équations de Prandtl en interaction, d'après Burggraf, Rizetta, Werle, Vatsa, réf. [27].

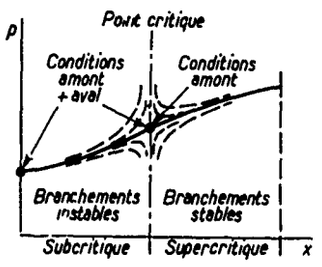


Fig. 10 — Points critiques au sens de Crocco-Lees.

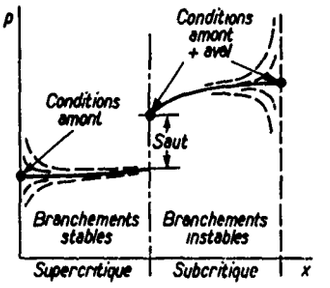


Fig. 11 — Sauts supercritiques-subcritiques.

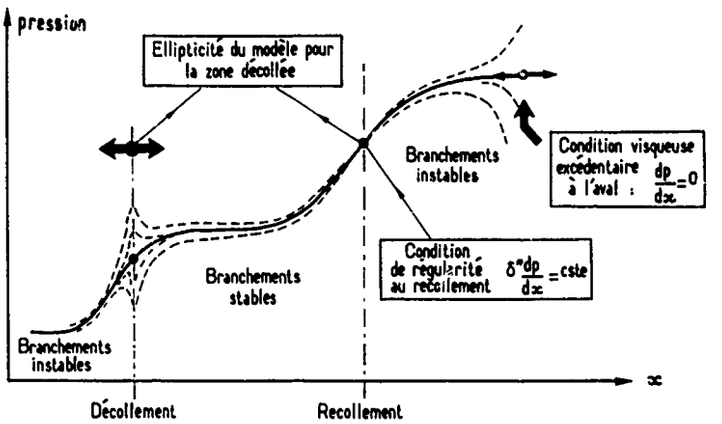


Fig. 12 – Décollement supersonique sur une rampe - Schéma des solutions de branchement pour une couche initialement subcritique.

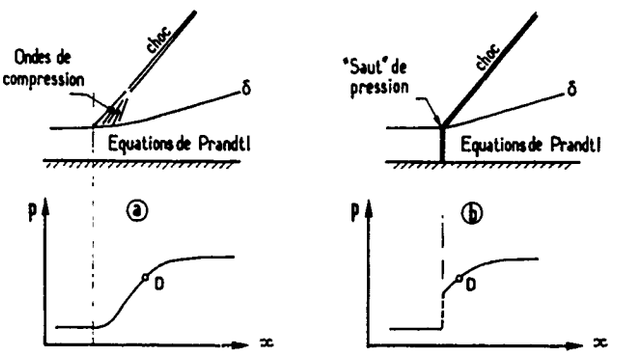


Fig. 13 – Décollement supersonique avec le modèle de couplage par raccordement : a) subcritique b) supercritique

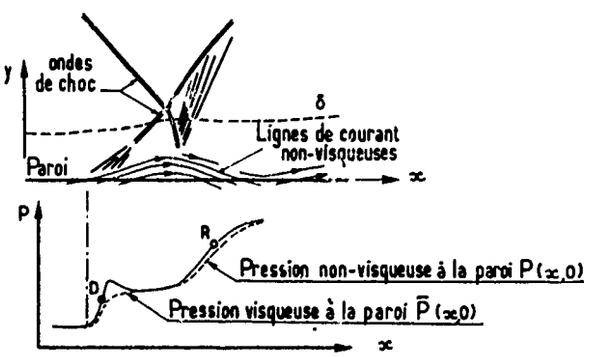


Fig. 14 – Couplage par recouvrement : schématisation non-visqueuse d'un décollement turbulent supersonique - Distributio. s de pression à la paroi.

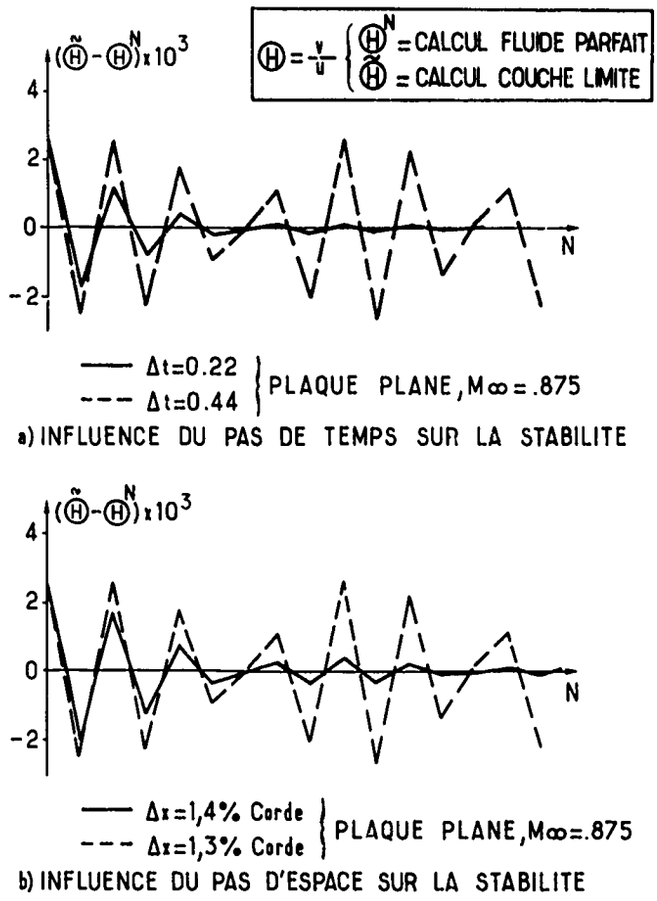


Fig. 15 – Instabilités numériques des itérations de couplage classiques sur une plaque plane en instationnaire en fonction de Δx et Δt.

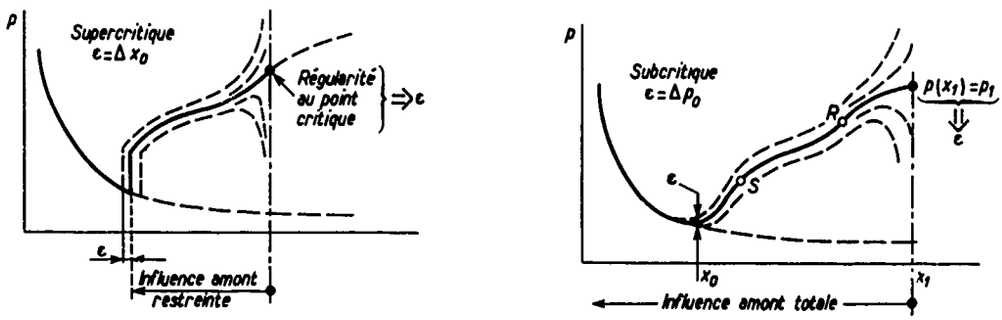


Fig. 16 – Méthodes de conditions initiales en supersonique.

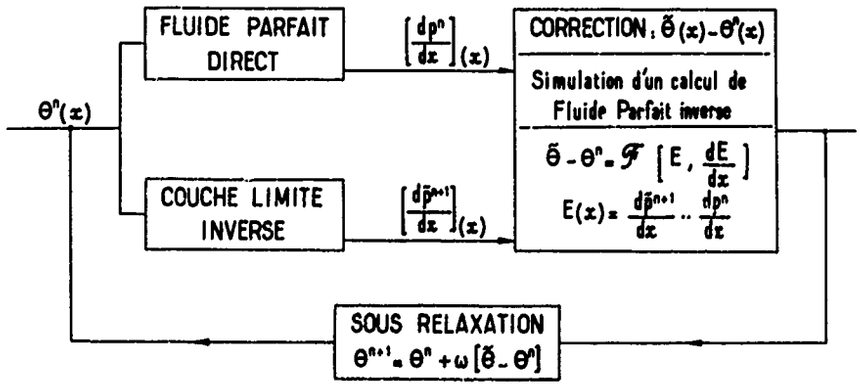


Fig. 17 – Méthode numérique de couplage semi-inverse.

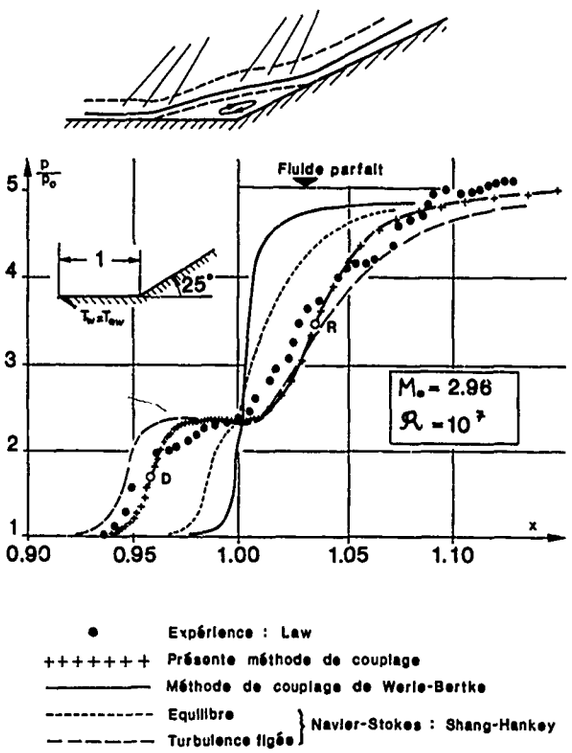


Fig. 18 – Décollement supersonique turbulent sur une rampe.

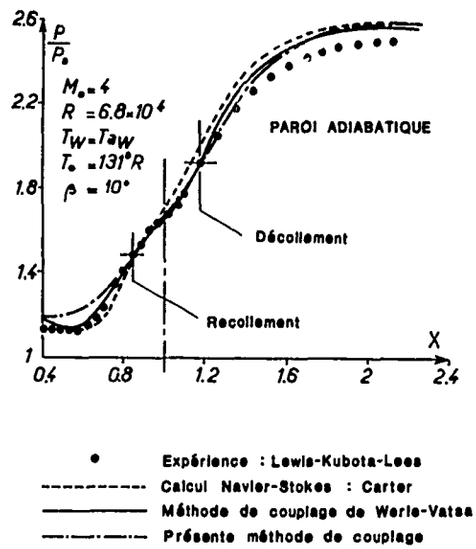


Fig. 19 – Décollement supersonique laminaire sur une rampe.

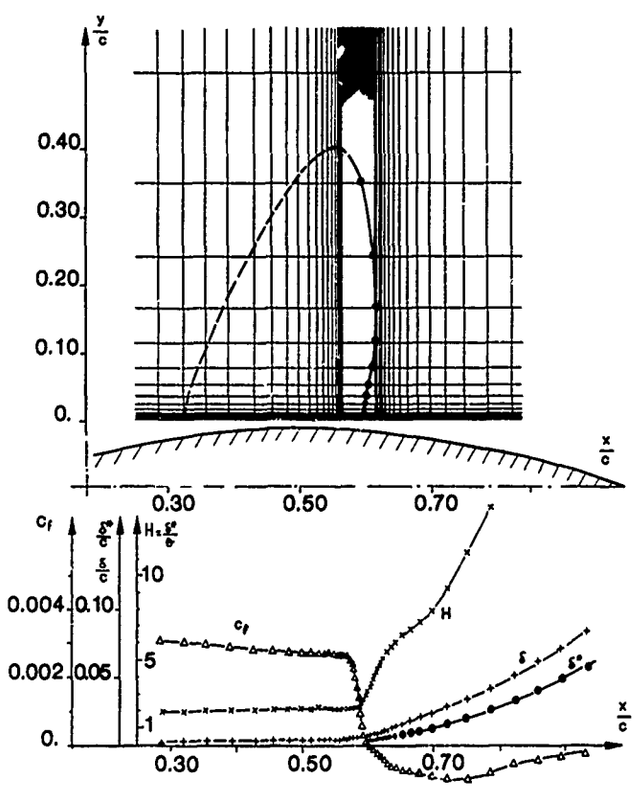


Fig. 20 – Calcul par couplage fort d'un décollement transsonique turbulent sous le choc d'un profil symétrique circulaire de 18%. $M = 0{,}788$ - $R = 4 \times 10^6$.

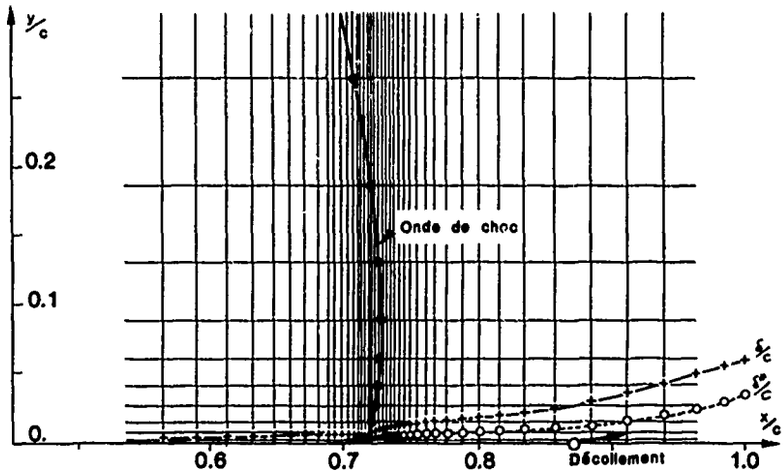


Fig. 21 — Région d'interaction choc-couche limite dans un calcul par couplage fort en petites perturbations transsoniques. Epaisseurs visqueuses.

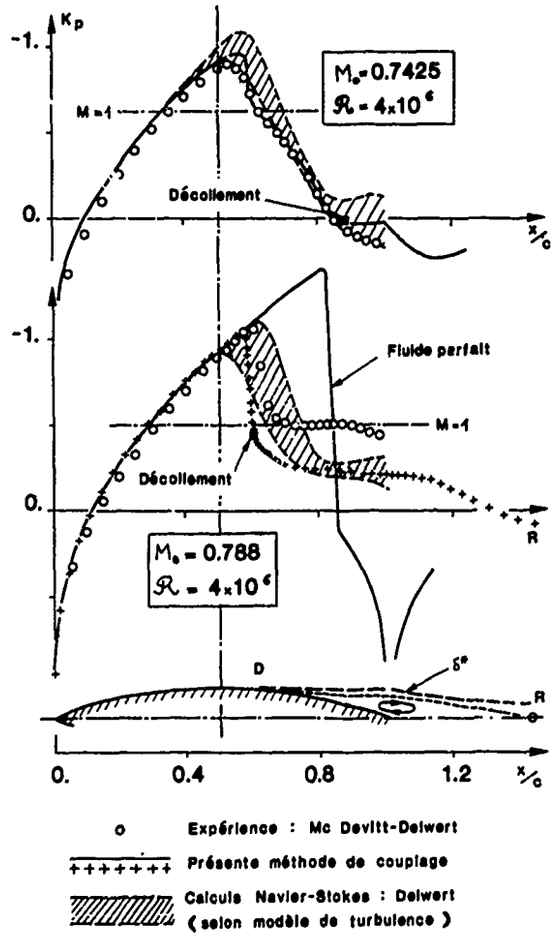


Fig. 22 — Profil circulaire symétrique de 18% en théorie des petites perturbations.

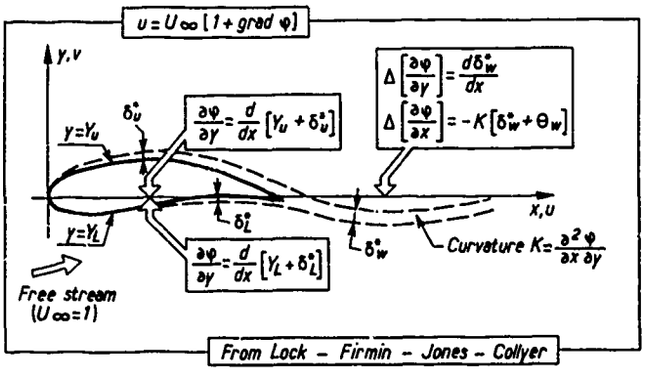


Fig. 23 — Calcul des profils en fluide visqueux par couplage : conditions aux limites du fluide parfait, en petites perturbations, d'après réf. [77].

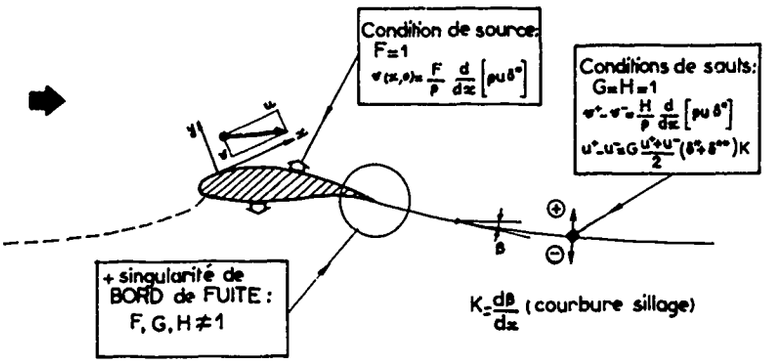


Fig. 24 — Calcul des profils en fluide visqueux par couplage : conditions aux limites du fluide parfait d'après Melnik, Chow, Mead, réf. [29].

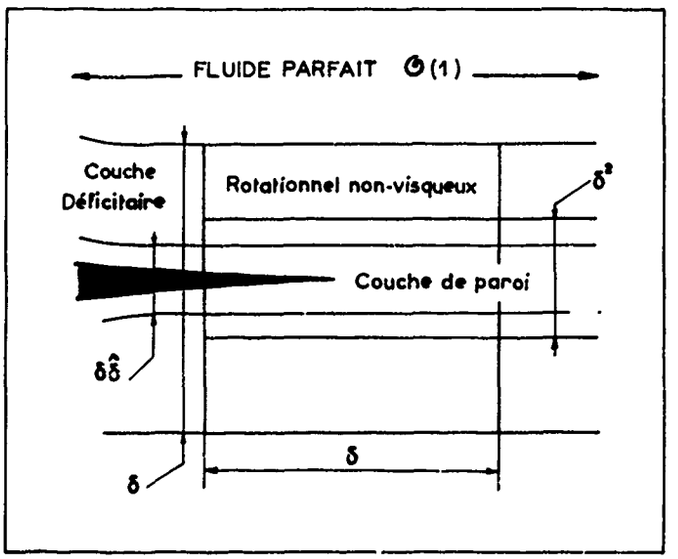


Fig. 25 — Bord de fuite turbulent non-décollé : modèle asymptotique de Melnik, Chow, d'après réf. [29].

M : nombre de Mach
Θ : angle paroi-vitesse

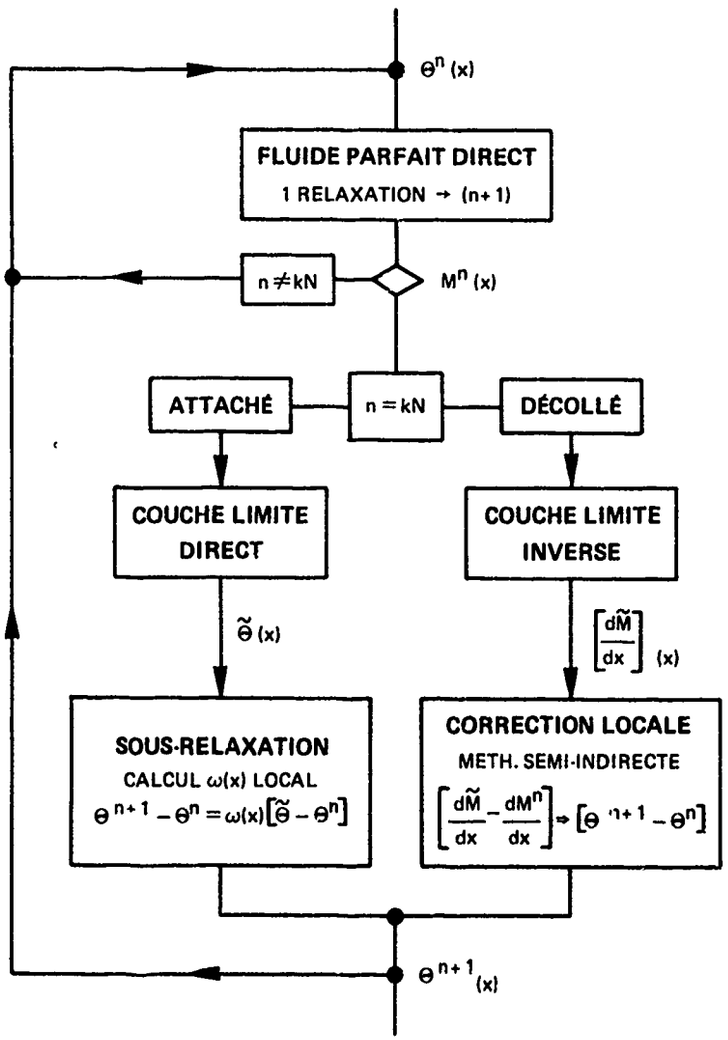


Fig. 26 – Méthode de relaxation mixte, directe ou semi-inverse.

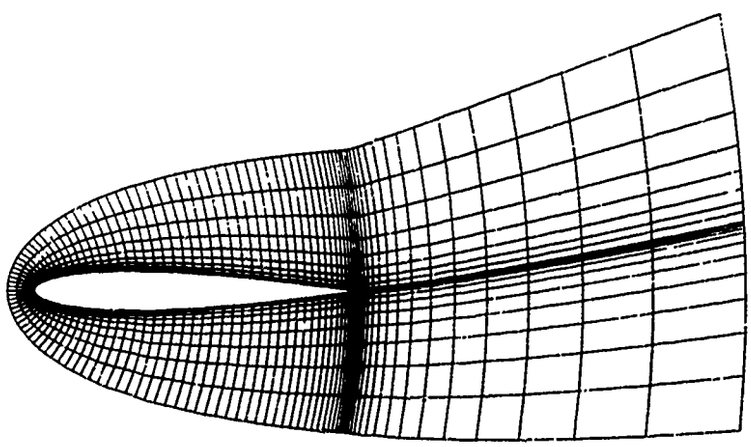


Fig. 27 – Maillage avec positionnement du sillage dans l'approximation symétrique ($M = 0{,}116$, $\alpha = 15°$, $R = 2 \times 10^6$).

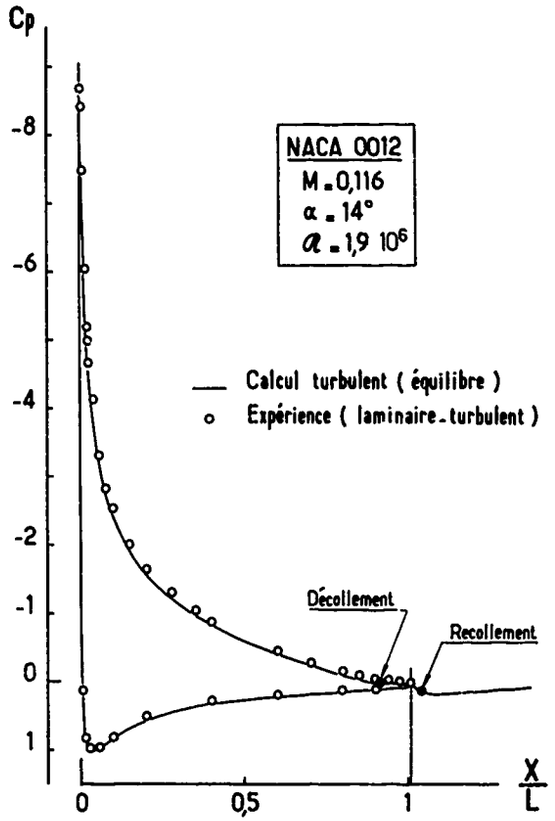


Fig. 28 – Profil NACA 0012 (V_o = 40 m/s). Calcul couplé turbulent, sillage symétrique.

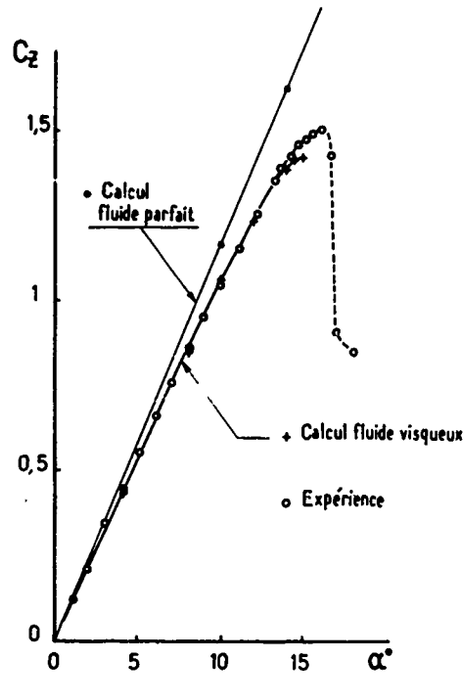


Fig. 29 – Portance du profil NACA 0012 - V_o = 40 m/s, R = 1,9 x 10^6. Calcul par couplage fort (turbulent, sillage symétrique).

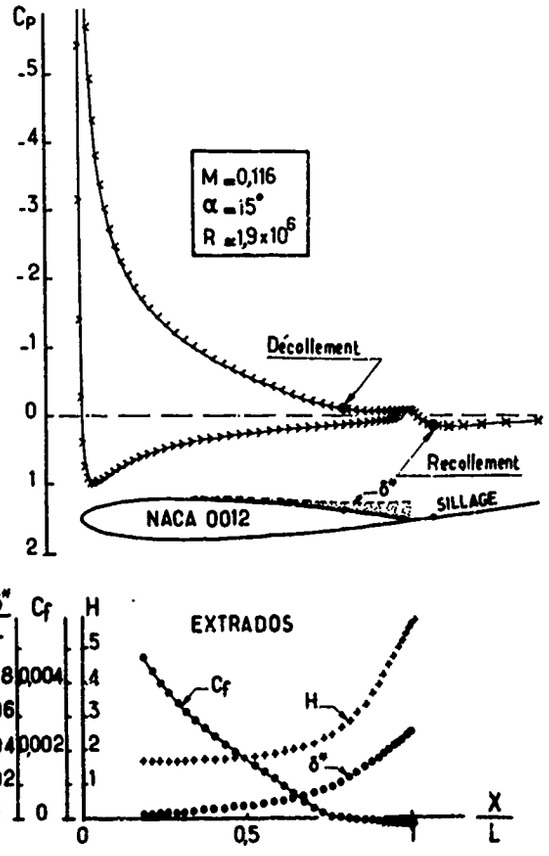


Fig. 30 – Effets visqueux au bord de fuite et plateau de pression. Calcul couplé turbulent, sillage symétrique.

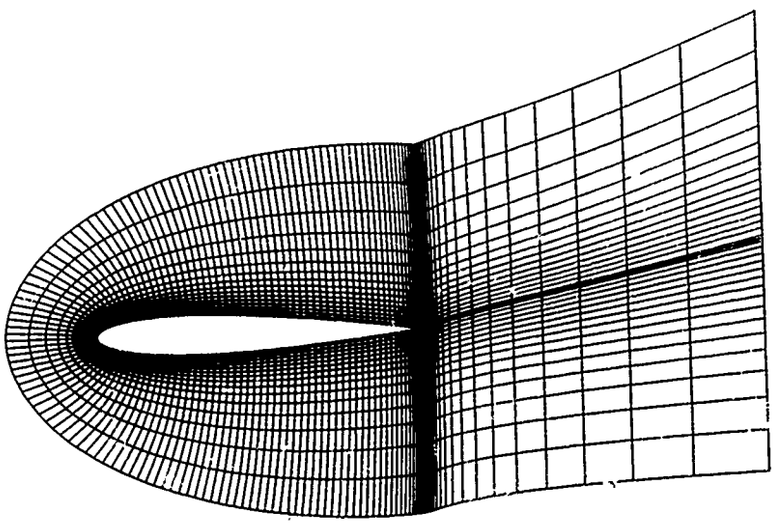


Fig. 31 – Maillage avec positionnement du sillage dans l'approximation dissymétrique ($M = 0.116$, $\alpha = 16°$, $R = 2 \times 10^6$).

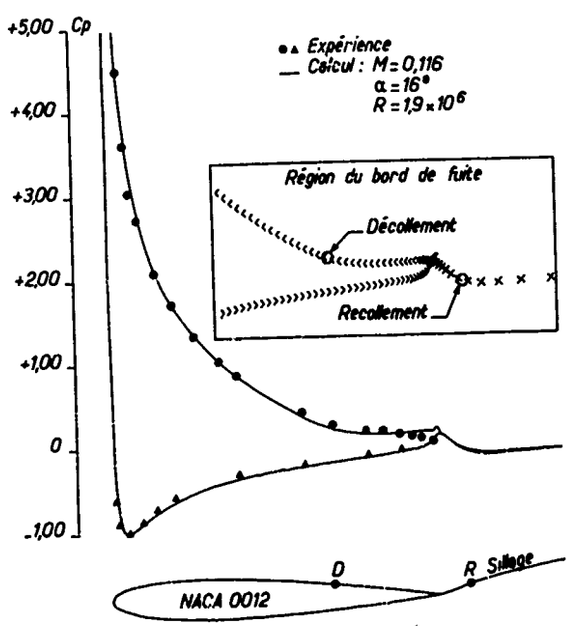


Fig. 32 – Calcul du profil NACA 0012 à grande incidence avec sillage dissymétrique.

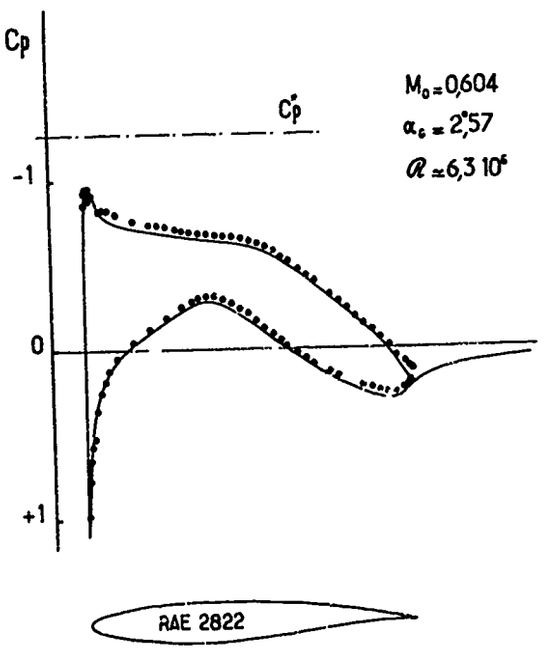


Fig. 33 – Calcul du profil RAE 2822 en régime subcritique.

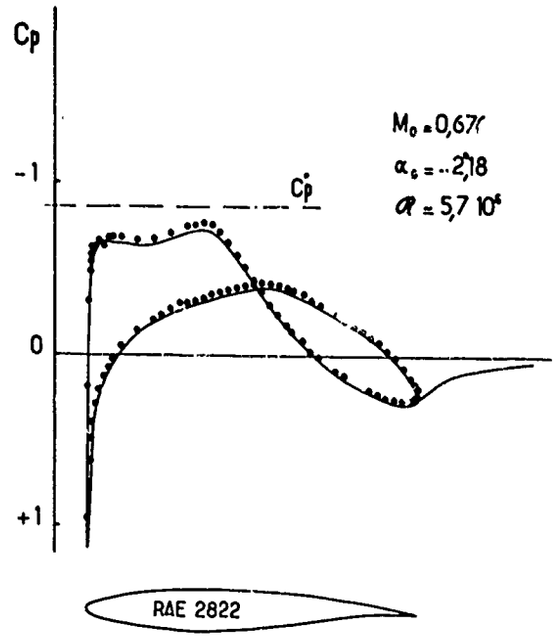
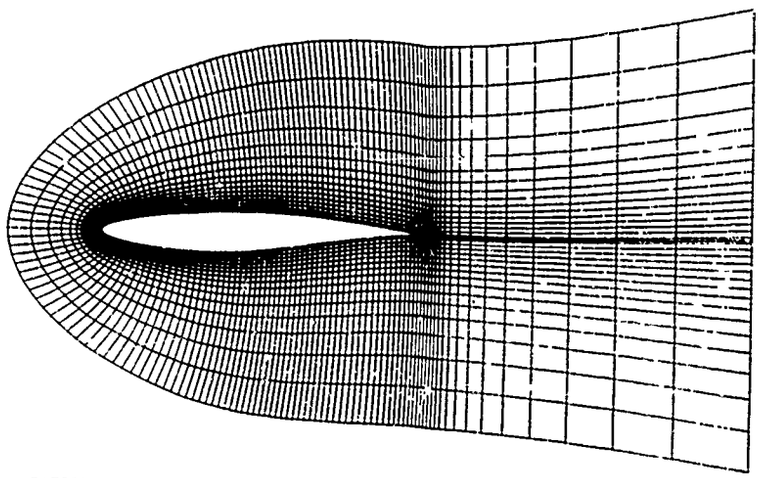


Fig. 34 – Calcul du profil RAE 2822 en régime subcritique.



RAE2822 CAS08 - ICFOILR - 181X27

Fig. 35 – Maillage en régime transsonique supercritique avec sillage symétrique.

Interaction choc - couche limite = CAS $\epsilon_2 \ll L < C$

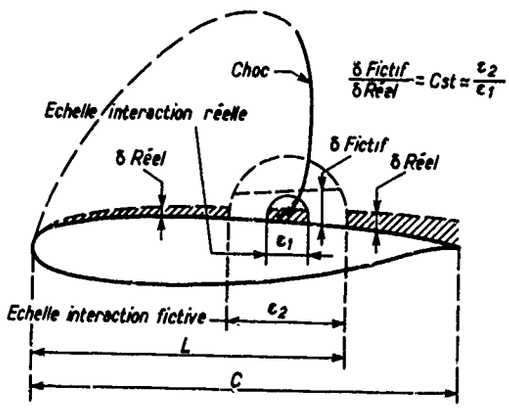


Fig. 36 – Calcul approché de l'interaction choc - couche limite si $\epsilon_2 \ll L < C$.

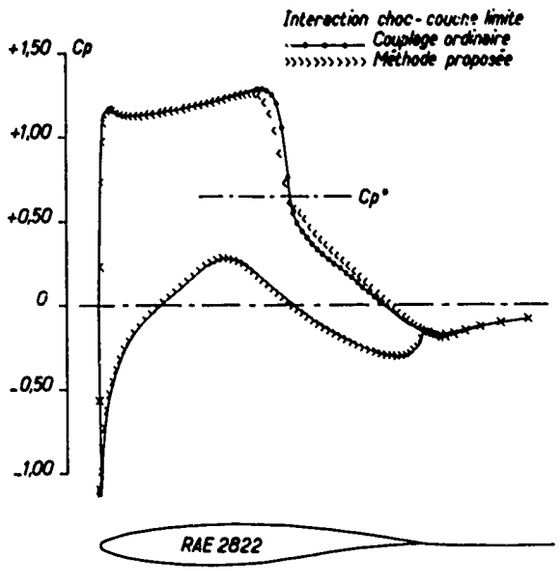


Fig. 37 – Effet du calcul approché de l'interaction choc - couche limite.

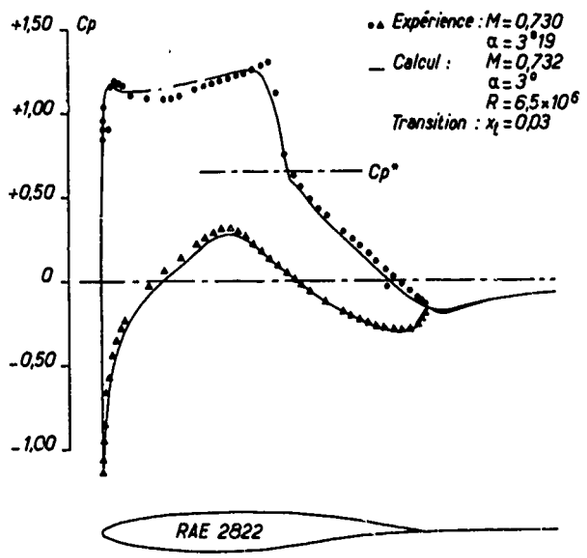


Fig. 38 – Calcul du profil RAE 2822 en régime supercritique.

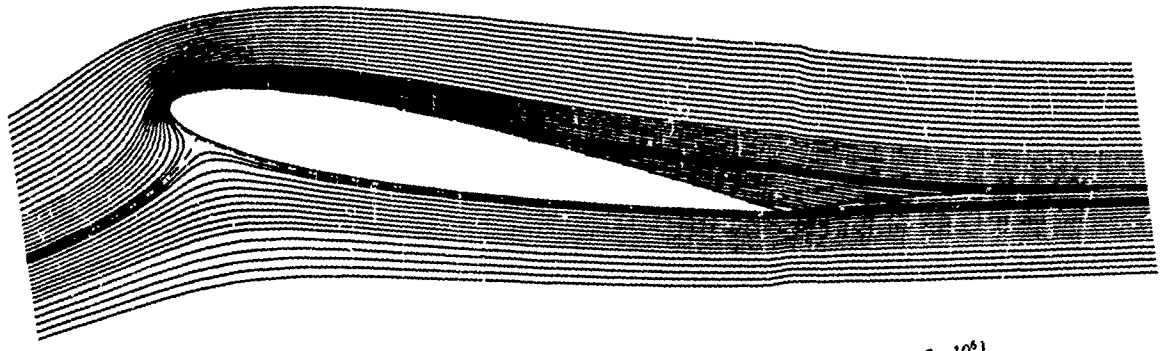


Fig. 39 – Lignes de courant dans le fluide parfait. Profil NACA 0012 ($M = 0{,}116$, $\alpha = 16°$, $R = 2 \times 10^6$).

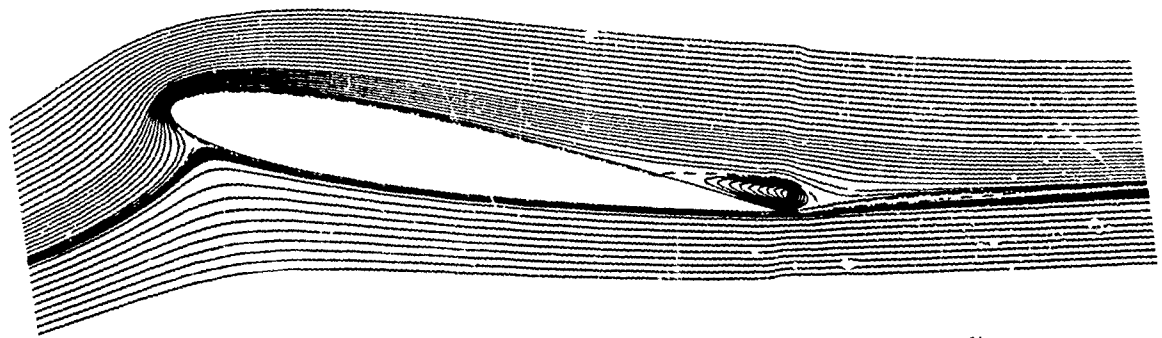


Fig. 40 – Lignes de courant dans le fluide visqueux. Profil NACA 0012 ($M = 0{,}116$, $\alpha = 16°$, $R = 2 \times 10^6$).

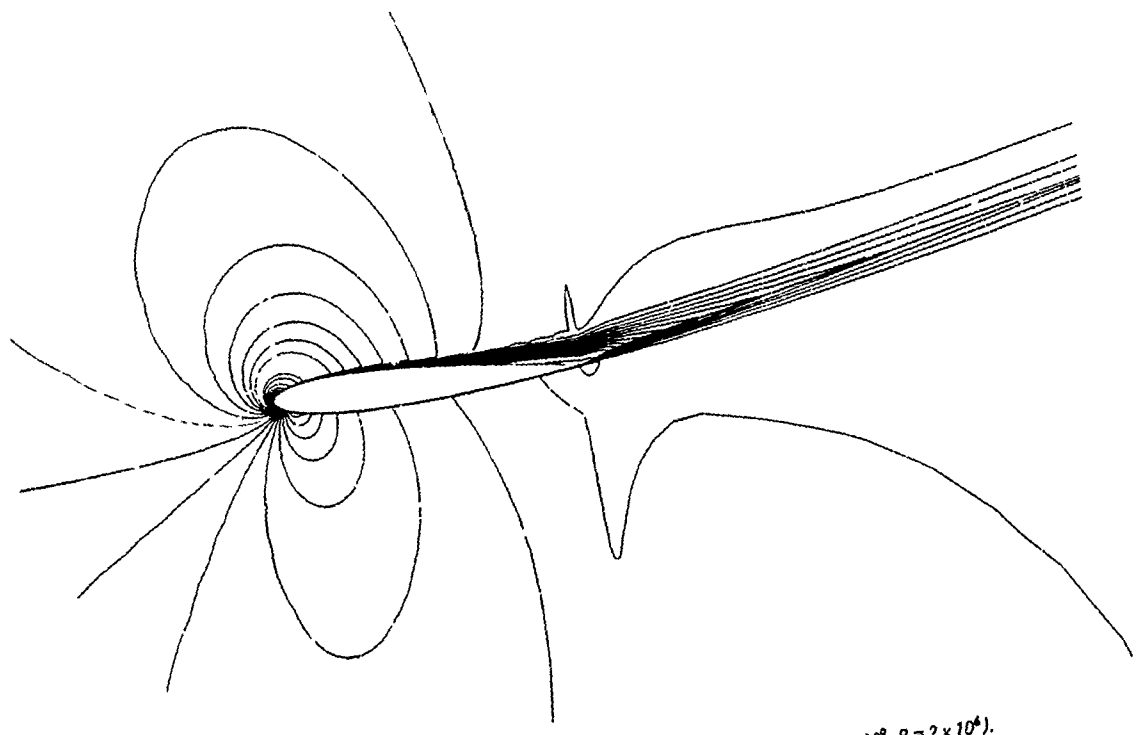


Fig. 41 – Lignes iso-Mach dans le fluide visqueux. Profil NACA 0012 ($M = 0{,}116$, $\alpha = 16°$, $R = 2 \times 10^6$).

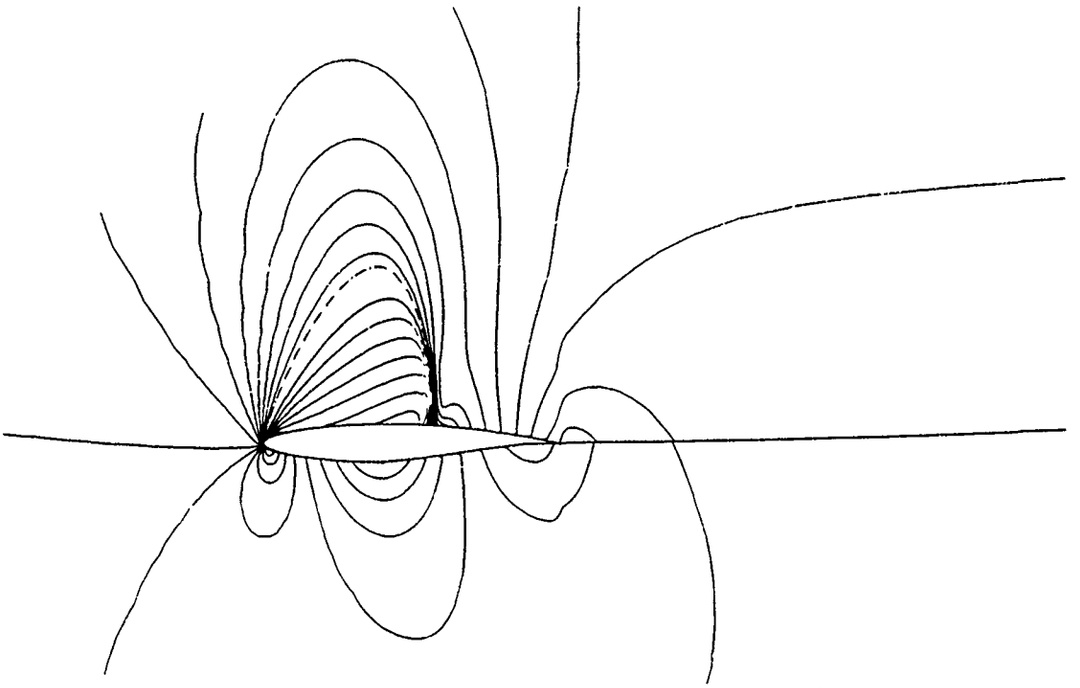


Fig. 42 – Lignes iso-Mach dans le fluide parfait. Profil RAE 2822 supercritique ($M = 0,732$, $\alpha = 3°$, $R = 6,5 \times 10^6$).

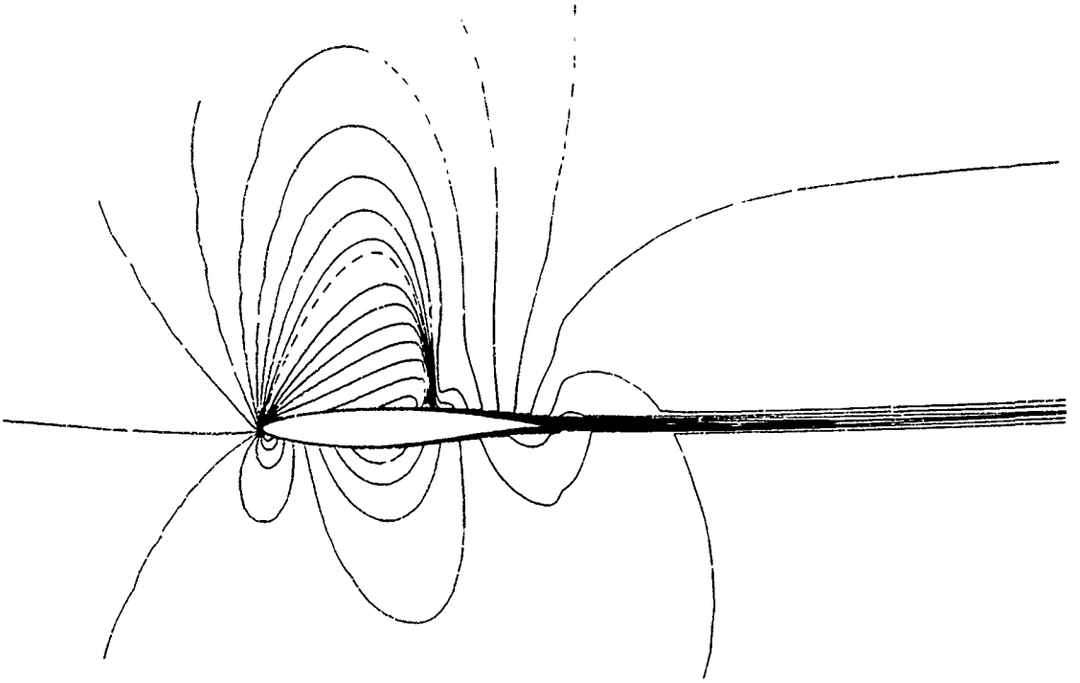


Fig. 43 – Lignes iso-Mach dans le fluide visqueux. Profil RAE 2822 supercritique ($M = 0,732$, $\alpha = 3°$, $R = 6,5 \times 10^6$).

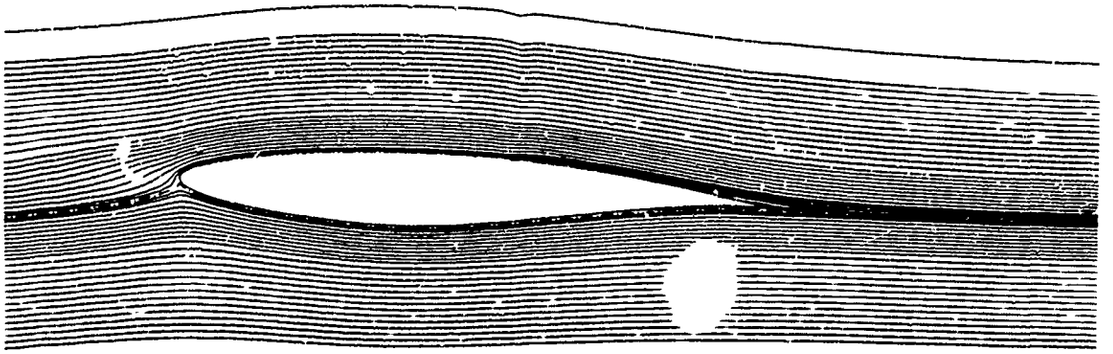


Fig. 44 – Lignes de courant dans le fluide parfait. Profil RAE 2822 ($M = 0,732$, $\alpha = 3°$, $R = 6,5 \times 10^6$).

A REVIEW OF METHODS FOR PREDICTING VISCOUS EFFECTS ON AEROFOILS AND WINGS AT TRANSONIC SPEEDS

R. C. Lock
Aerodynamics Department
Royal Aircraft Establishment
Farnborough, Hampshire, UK

SUMMARY

Methods are reviewed in which the problem of viscous-inviscid interaction is treated by assuming that the effects of viscosity are confined to thin boundary layers and wakes. With this assumption, an iterative procedure may be set up in which the inviscid flow is calculated first and the result used to specify the pressure distribution from which the development of the viscous layers can be determined. The inner boundary condition for the equivalent inviscid flow is then modified to allow for the displacement effect of the viscous layers; and the procedure is repeated until convergence is obtained.

In the first section of the paper two alternative mathematical models for the displacement effect are derived, valid to second-order accuracy. After a brief historical review of the subject, an account is then given of the principal methods that are currently available for the two-dimensional problem (single aerofoils) at transonic speeds. Next, some of the corresponding methods for three-dimensional wings or wing-body combinations are briefly reviewed; and finally some general conclusions are drawn, with suggestions for future needs and possibilities.

LIST OF SYMBOLS

a	speed of sound
c	chord length
C_D	drag coefficient
C_L	lift coefficient
C_f	skin friction coefficient
C_p	pressure coefficient
H	boundary layer shape parameter (see Ref 40)
M_∞	free stream Mach number
M_1	Mach number upstream of shock wave
p	static pressure
Re	Reynolds number
(s, n)	curvilinear coordinates
t	thickness of wing or aerofoil
(u, v, w)	velocity components
(x, y, z)	Cartesian coordinates
X_T (or X_{tr})	value of x/c at transition
α	angle of incidence (α_T: theory, α_G: experiment)
δ	thickness of boundary layer
δ^*	displacement thickness
γ	ratio of specific heats
κ	surface curvature
κ^*	curvature of displacement surface
λ	parameter in VGK method
θ	momentum thickness
ϕ	velocity potential
ρ	density
Suffices	
e	value at edge of boundary layer
i	inviscid
0	value on surface
W	wake

1 INTRODUCTION

At a Conference having the present title, there is no need to stress the importance of viscous effects on the flow about aerofoils and wings, or the necessity of being able to predict these effects theoretically if results of practical usefulness are to be achieved. The aspect of the subject reviewed here is the development of methods which involve separate calculations of the viscous shear layers - laminar or turbulent - over the wing and in its wake, and of the inviscid flow external to these layers, together with a matching process which enables the mutual interaction of these flows to be determined. This approach has proved extremely successful for a wide variety of cases, provided that the boundary layers remain attached until close to the trailing edge and that any shock waves that are present are not so strong as to cause separation. We shall concentrate on methods applicable to problems of transonic (high subsonic) flow, since these are in many ways the most difficult to solve and involve viscous effects which are frequently large and hence of major practical importance.

The considerable effort that is currently being devoted to the alternative approach of solving the full Navier-Stokes equations, with appropriate turbulence modelling, is of course of great importance; but nevertheless it seems certain that methods of the present type will continue to hold a practical advantage, in both speed and accuracy of computation, for solving the problems to which they are best suited. These could also include cases with restricted regions of separated flow, provided that suitable modifications are made to the viscous matching technique. Thus it is only when gross flow separations are present that it will become essential to make use of numerical solutions to the Navier-Stokes equations.

In the present paper, we derive in section 2 the basic concepts required for the matching process referred to above. A brief historical survey of the subject is given in section 3, and section 4 then describes the principal methods that are currently in use for calculations on two-dimensional aerofoils in transonic flow. The application of similar principles to general three-dimensional wings and wing-body combinations is reviewed in section 5. Finally, in section 6, some remarks are made about the future prospects for methods of the present type - involving the 'thin shear-layer' assumptions - about various aspects in which they are currently deficient and ways in which it might be possible to improve them.

2 BASIC PRINCIPLES

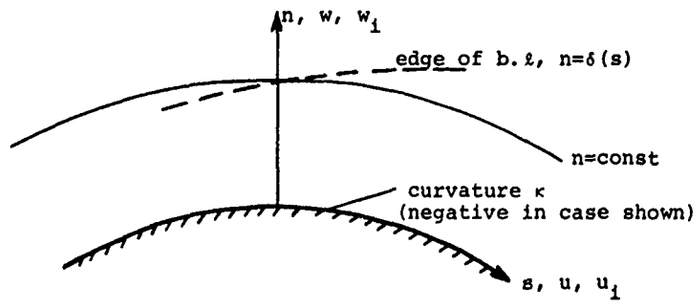
Before describing any of the particular methods that have been developed for solving problems of this class, we shall first show how two alternative mathematical models of the 'displacement effect', that are needed in the process of solution, may be derived.

We suppose that methods are available for calculating (a) the development of the viscous layers - the boundary layers over the wing and the wake behind it - for given external boundary conditions: and (b) the inviscid flow external to these viscous layers, for given internal boundary conditions. Of course, it would be possible in principle (and is being tried in practice by Bradshaw and his colleagues[4]) to determine the direction of flow at the edge of the boundary layer from (a), and to use this information as the required inner boundary condition for (b). But it is much more convenient - because it leads to boundary conditions of a simpler type - to consider an analytic continuation of the inviscid flow into the regions where viscous effects are important; we shall call this (where it differs from the real viscous flow) the 'equivalent inviscid flow'.

2.1 Conditions on the wing

These simple boundary conditions can be derived by integrating the equation of continuity across the boundary layer for both the real flow and the equivalent inviscid flow, and matching the two flows at the edge of the boundary layer. In doing this there is no need to make the usual assumption of first-order boundary layer theory, that the pressure is constant along a normal to the surface.

In the following higher-order treatment, it is necessary to use curvilinear coordinates as defined in the sketch below.



Sketch (a)

The coordinates (s, n), parallel and normal to the surface respectively, have metric coefficients $(1 - \kappa n, 1)$, where κ is the curvature of the surface (positive when this is concave). The equation of continuity for the real viscous flow is then

$$\frac{\partial}{\partial s}(\rho u) + \frac{\partial}{\partial n}\{(1 - \kappa n)\rho w\} = 0 \qquad (1),$$

where ρ is the density. Integrating Eq.(1) across the boundary layer, we obtain

$$(1 - \kappa\delta)\rho_e w_e = -\int_0^\delta \frac{\partial}{\partial s}(\rho u)dn \qquad (2)$$

where suffix e denotes values at the edge of the boundary layer, defined by $n = \delta(s)$. Denoting by (u_i, w_i) and ρ_i the corresponding values for the equivalent inviscid flow, and integrating the equation of continuity from n to δ, we obtain

$$(1 - \kappa n)\rho_i w_i = (1 - \kappa\delta)\rho_{ie} w_{ie} + \int_n^\delta \frac{\partial}{\partial s}(\rho_i u_i)dn \qquad (3)$$

($\rho_i u_i$ need not be assumed to be constant across the region occupied by the boundary layer). Now the matching condition gives $\rho_{ie} w_{ie} = \rho_e w_e$, so that from Eq.(2) we obtain

$$(1 - \kappa n)\rho_i w_i = \int_n^\delta \frac{\partial}{\partial s}(\rho_i u_i)dn - \int_0^\delta \frac{\partial}{\partial s}(\rho u)dn \qquad (4).$$

We are now in a position to derive the two types of boundary condition that we require for the equivalent inviscid flow.

(A) 'Surface transpiration' model

Putting $n = 0$ into Eq.(4), we get (since $\rho_i u_i = \rho u$ when $n = \delta$)

$$\rho_{i0} w_{i0} = \frac{d}{ds}\int_0^\delta (\rho_i u_i - \rho u)dn \qquad (5)$$

where suffix 0 denotes values on the wall.

If we now *define* a displacement thickness δ_A^* by

$$\delta_A^* = \frac{1}{\rho_{i0} u_{i0}}\int_0^\delta (\rho_i u_i - \rho u)dn \qquad (6),$$

then Eq.(5) can be written

$$w_{i0} = \frac{1}{\rho_{i0}}\frac{d}{ds}(\rho_{i0} u_{i0} \delta_A^*) \qquad (7).$$

This fundamental result, analogous to one due to Lighthill[1], was first obtained by Gersten[2]. It states that the mass flow normal to the wall in the equivalent inviscid flow is equal to the streamwise rate of change of the 'mass flow deficit' in the boundary layer.

(B) 'Solid displacement surface' model

We want to find a surface, $n = \delta_B^*(s)$, which is a streamline of the equivalent inviscid flow. For this we need

$$\left.\frac{w_i}{u_i}\right|_{n=\delta_B^*} = \frac{1}{1 - \kappa\delta_B^*}\frac{d\delta_B^*}{ds} .$$

Using Eq.(4), we obtain

$$(\rho_i u_i)_{n=\delta_B^*}\frac{d\delta_B^*}{ds} = \int_{\delta_B^*}^\delta \frac{\partial}{\partial s}(\rho_i u_i)dn - \int_0^\delta \frac{\partial}{\partial s}(\rho u)dn \ ;$$

or

$$(\rho_i u_i)_{n=\delta_B^*} \frac{d\delta_B^*}{ds} = \frac{d}{ds}\left[\int_{\delta_B^*}^{\delta} \rho_i u_i dn - \int_0^{\delta} \rho u dn\right] + (\rho_i u_i)_{n=\delta_B^*} \frac{d\delta_B^*}{ds} .$$

This is satisfied if

$$\int_{\delta_B^*}^{\delta} \rho_i u_i dn = \int_0^{\delta} \rho u dn \qquad (8),$$

which provides the required definition of δ_B^* (*cf* Myring[3]). It is simply an expression of the fact that the mass flow between the displacement surface and the edge of the boundary layer in the equivalent inviscid flow must equal the total mass flow in the real boundary layer.

In cases where the assumptions of first-order boundary layer theory are valid, we have $\rho_i u_i$ = constant = $\rho_e u_e$, and both Eq.(6) and Eq.(8) reduce to

$$\delta^* = \int_0^{\delta} \left(1 - \frac{\rho u}{\rho_e u_e}\right) dn \qquad (9),$$

the standard expression for displacement thickness.

In the general case, when the variation of $(\rho_i u_i)$ across the boundary layer should be taken into account, the three alternative definitions of the displacement thickness (Eqs. (6), (8), (9)) will normally give different values. A first approximation to the relationship between them can be obtained by expanding $(\rho_i u_i)$ as a Taylor series with respect to n :

$$\rho_i u_i \triangleq \rho_{i0} u_{i0} + n \frac{\partial}{\partial n} (\rho_i u_i)\Big|_{n=0} + 0(n^2) \qquad (10).$$

Now

$$\frac{\partial}{\partial n} (\rho_i u_i)\Big|_{n=0} = \rho_{i0}(1 - M_0^2) \frac{\partial u_i}{\partial n}\Big|_{n=0} ,$$

where M_0 is the Mach number at the surface for the equivalent inviscid flow; and since this flow is irrotational,

$$\frac{\partial w_i}{\partial s} = \frac{\partial}{\partial n} [u_i(1 - \kappa n)] ,$$

so that

$$\frac{\partial u_i}{\partial n}\Big|_{n=0} = \frac{dw_{i0}}{ds} + \kappa u_{i0} ,$$

where w_{i0} is given by Eq.(7).

Hence

$$\frac{\partial}{\partial n} (\rho_i u_i)\Big|_{n=0} = k\rho_{i0} u_{i0}(1 - M_0^2) \qquad (11)$$

where

$$k = \kappa + \frac{1}{u_{i0}} \frac{dw_{i0}}{ds} \qquad (12).$$

Thus Eq.(10) becomes

$$\rho_i u_i \triangleq \rho_{i0} u_{i0}\{1 + k(1 - M_0^2)n\} \qquad (13).$$

Substituting this relation into the equations (6) and (8) which respectively define δ_A^* and δ_B^* , we obtain the following expressions, correct to second order (in δ):

surface transpiration

$$\delta_A^* = \delta^* - \tfrac{1}{2}k(1 - M_0^2)\delta(\delta - 2\delta^*) \tag{14}$$

solid displacement surface

$$\delta_B^* = \delta^* - \tfrac{1}{2}k(1 - M_0^2)(\delta - \delta^*)^2 \tag{15}.$$

Here δ^* has the standard first-order definition, Eq.(9), while from Eqs.(7) and (12),

$$k = \kappa + \frac{1}{u_{i0}}\frac{d}{ds}\left\{\frac{1}{\rho_{i0}}\frac{d}{ds}(\rho_{i0}u_{i0}\delta^*)\right\} \tag{16}.$$

If ρ_{i0}, u_{i0} can be considered as 'slowly varying' functions of s, then

$$k \triangleq \kappa^* = \kappa + \frac{d^2\delta^*}{ds^2} \tag{16a},$$

which is the curvature of the displacement surface.

For a typical aerofcil at high Reynolds number, the parameter k will be small except in two regions: near the leading edge (where κ is large); and towards the trailing edge $\left(\text{where } \frac{d^2\delta^*}{ds^2} \text{ may become relatively large}\right)$. In the leading-edge region, however, the boundary layer is so thin that the second-order terms in the expressions (14) and (15) for δ_A^* and δ_B^* may nevertheless be neglected; but they may become just appreciable near the trailing edge where the boundary layer is thickest and increasing most rapidly. Note that the difference between the two second-order displacement thicknesses is

$$\delta_A^* - \delta_B^* = \tfrac{1}{2}k(1 - M_0^2)\delta^{*2} \tag{17},$$

and since δ^{*2}/δ^2 is numerically small (less than about 0.1, say), even for boundary layers approaching separation, this means that the alternative second-order definitions differ less from each other than they do from the first-order definition δ^*.

The arguments given above provide two alternative inner boundary conditions which can be used in the calculation of the equivalent inviscid flow over the aerofoil surface: (A) a 'transpiration' condition for non-zero normal velocity, specified by Eq.(7); or (B) the condition that the displacement surface is a streamline. Which of these mathematical models is chosen in any particular application depends on the convenience or preference of the user; either of them is an equally valid representation of the displacement effect of the boundary layers on the external flow. Normally, only the first-order forms of the boundary conditions will be used, namely

$$w_{i0} = \frac{1}{\rho_{i0}}\frac{d}{ds}(\rho_{i0}u_{i0}\delta^*) \tag{7}$$

and

$$\delta^* = \int_0^\delta \left(1 - \frac{\rho u}{\rho_e u_e}\right) dn \tag{9}$$

2.2 Conditions on the wake

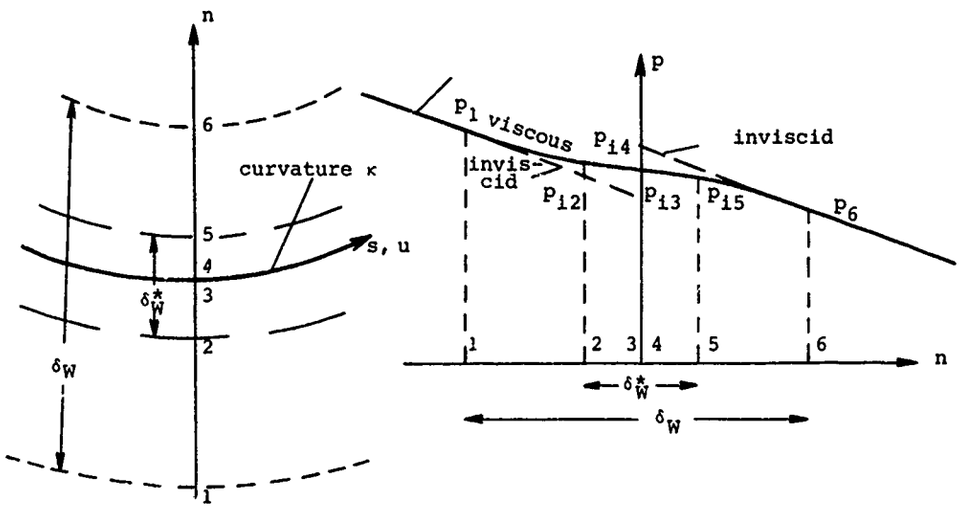
The displacement effect of the wake is precisely analogous to that of the boundary layer over the solid surface of the wing. Thus it can be represented either (A) by a source distribution over an infinitesimally thin surface, leading to a discontinuity in velocity normal to this surface given by

$$\Delta w_{iW} = \frac{1}{\rho_{iW}}\frac{d}{ds}(\rho_{iW}u_{iW}\delta_W^*) \tag{18},$$

where the suffix W refers to conditions on the wake surface; or alternatively (B) as a streamtube of thickness δ_W^*. In either case the normal first-order definition of δ_W^* will suffice, since the effect of the wake on the pressure distribution of the wing is small (though by no means negligible).

A further condition is required to fix the position of the wake; this can be considered at two levels of approximation. As a first approximation, in which the curvature of the wake is neglected, we have simply the condition that the pressure change across the wake is zero - whether it is considered as a thick flexible streamtube or a thin source sheet. But because the curvature of the wake close behind the trailing edge

tends to be relatively large, it is desirable to use a higher approximation which takes into account the pressure change across the wake in the real flow, and matches this change in the equivalent inviscid flow.



Sketch (b) Sketch (c)

We make use of the fact that in inviscid flow, and approximately in viscous flow (neglecting normal stress terms)

$$\frac{\partial p}{\partial n} = -\kappa\rho u^2 \tag{19}$$

where κ is the streamline curvature.

Integrating this across the wake (see sketch (b)), we have in the real viscous flow

$$\begin{aligned} p_6 - p_1 &= -\int \kappa\rho u^2 dn \\ &\triangleq -\kappa\rho_W u_W^2[\delta_W - (\theta_W + \delta^*_W)] \end{aligned} \tag{20}$$

where θ_W is the momentum thickness, $\int \frac{\rho u}{\rho_W u_W}\left(1 - \frac{u}{u_W}\right) dn$, and we may take ρ_W, u_W to be the means of the values of ρ and u on either side of the wake (or the mean values of ρ_i, u_i for the equivalent inviscid flow).

The corresponding variation of pressure across the wake is shown in sketch (c). In the inviscid flow models we find that for
Model (A): a jump in pressure across the surface representing the wake must be introduced, given by

$$\Delta p (= p_{i4} - p_{i3}) = (p_6 - p_1) + \kappa\rho_W u_W^2 \delta_W ,$$

and using Eq.(20) this becomes

$$\Delta p = \kappa\rho_W u_W^2(\delta^*_W + \theta_W) \tag{21}.$$

Since Δp is small, this is equivalent to a jump in tangential velocity

$$\Delta u = (u_{i4} - u_{i3}) \approx -\kappa u_W(\delta^*_W + \theta_W) \tag{22}.$$

For Model (B), the corresponding pressure difference is

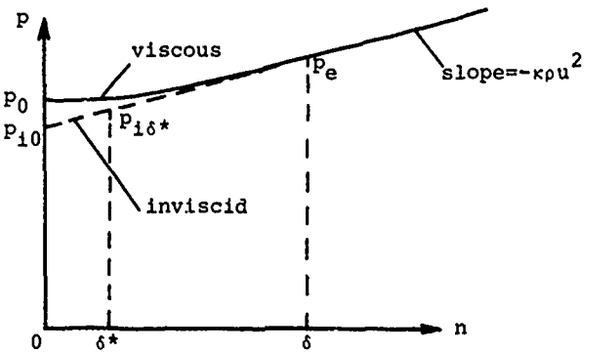
$$\Delta p = p_{i5} - p_{i2} = \kappa\rho_W u_W^2 \theta_W \tag{23}.$$

The effect described abc is similar to that of a 'jet flap', but of opposite sign, with the jet momentum coefficient replaced by $(\delta^*_W + \theta_W)$. Now the curvature of the wake of a lifting wing in inviscid flow has in general an inverse square root singularity at

the trailing edge. The viscous interaction will remove this singularity and reduce the curvature to a finite value, but in the near wake this may remain large; so that although $(\delta_W^* + \theta_W)$ is generally small, the overall effect of the wake curvature on the lift and pressure distribution is often appreciable, and should if possible be taken into account when calculating the interaction.

2.3 Calculation of surface pressure

When the equivalent inviscid flow has been calculated, using boundary conditions given by either Model (A) or Model (B) described above, the pressure will then be known (for this flow) either (a) on the wing surface or (b) on the displacement surface. We now need to consider how to adjust these calculated pressures in order to obtain the pressure on the wing in the real viscous flow (see sketch (d)).



Sketch (d)

The effect of the curvature of the wall on the normal pressure gradient is precisely analogous to that of the wake, discussed in section 2.2. The same argument leads to the following expressions for the wall pressure p_0 :

Model (A):
$$p_0 = p_{i0} - \kappa\rho_{i0}u_{i0}^2(\theta + \delta^*) \qquad (24),$$

Model (B):
$$p_0 = p_{i\delta^*} - \kappa\rho_{i\delta^*}u_{i\delta^*}^2\theta \qquad (25).$$

[For a convex wing surface, κ is negative - this is the situation shown in the sketch.] Now for a typical wing κ will be large only near the leading edge, where the boundary layer is extremely thin; so that the corrections to the pressure given above can usually be neglected ($\Delta C_p < 0.01$, say).

However, Eqs.(24) and (25) are correct only to first order in δ^*, and potentially important second-order effects are present because (a) the full equation for $\partial p/\partial n$ contains terms, other than $\kappa\rho u^2$, of order (δ^*), (b) the curvature of the equivalent inviscid flow near the wall differs from that of the real flow by an amount of order $\left(\frac{d^2\delta^*}{dx^2}\right)$.

The magnitude of these effects may become appreciable towards the trailing edge on the upper surface (or on the lower surface of a rear-loaded aerofoil), where the boundary layer is relatively thick and highly curved. A full second-order theory for turbulent flow has been derived recently by East[5]. His full expression for the pressure correction is complicated but by making simplifying approximations likely to be valid for boundary layers approaching separation, it can be shown that Eq.(24) may be replaced, to a reasonable approximation, by

$$p_0 = p_{i0} - \kappa^*\rho_{i0}u_{i0}^2(\delta^* + \theta) \qquad (26)$$

where $\kappa^* = \kappa + \frac{d^2\delta^*}{dx^2}$ is the curvature of the displacement surface - as might perhaps have been expected intuitively. There is an obvious analogy here with the corresponding treatment of the second-order displacement effect, given in section 2.1 (*cf* Eqs.(16) and (16a)); neither effect is appreciable unless κ^* is relatively large.

2.4 The Kutta condition

The condition that has to be applied at the trailing edge, to fix the circulation and hence the lift, depends on the degree of approximation used to calculate the surface presence. If only a first-order theory is used, so that pressure variations across the boundary layer are neglected, then the pressures on the upper and lower surfaces must

approach the same value at the trailing edge for the equivalent inviscid flow, just as they do for the real viscous flow. Thus the form of the Kutta condition is unaltered. But if second-order effects are taken into account, as described in the previous section, then the pressure correction at the surface will be different for the upper and lower parts of the boundary layer at the trailing edge, because of the differences in the thickness parameters θ and δ^* and in the effective curvature of the flow. This implies that the equivalent inviscid flow should have a non-zero pressure difference at the trailing edges, which must be chosen so that the *corrected* pressures in the real viscous flow are in fact equal.

Because the standard first-order theory - both for the viscous-inviscid matching process and for the calculation of the turbulent boundary layers and wake - may no longer be sufficiently accurate in the trailing-edge region, an alternative approach has been proposed recently by Melnik *et al*[6,7]. In this an asymptotic solution of the Navier-Stokes equation for high Reynolds number, with appropriate turbulence modelling, is obtained for the immediate vicinity of the trailing edge, and is then matched with a standard first-order treatment upstream on the wing and downstream in the wake; a suitable form of the Kutta condition is included. An account of this method will be given in section 4.

3 HISTORICAL SURVEY: METHODS FOR SUBCRITICAL FLOW

The general principles by which the displacement effect of the boundary layers on an aerofoil affects the pressure near the trailing edge and reduces the lift, compared with their values for inviscid flow, were first established by Preston[8] in the 1940s (see Ref 9, Ch. V). His mathematical treatment involved the use of a conformal mapping of the aerofoil shape onto a flat plate to solve the inviscid part of the problem (for incompressible flow), together with a matching process based on the transpiration Model (A) described in section 2. Measured boundary layer thicknesses were used to provide the necessary information about the viscous part.

Preston's work was simplified and extended by Spence[10] in the early 1950s, who incorporated a method for calculating the development of the turbulent boundary layers. He was able to determine theoretically the scale effect on the reduction in lift due to viscosity for a typical symmetrical aerofoil (12% thick Joukowski), showing that this varied from about 15% at a Reynolds number of 5×10^6 to 5% at 50×10^6.

None of the work mentioned above made it possible to calculate the effect of viscosity on the complete pressure distribution of an arbitrary cambered aerofoil, even for incompressible flow; this would have been impracticable in the era of hand calculating machines. Further progress had to wait for the advent of the modern electronic computer. An advance in this direction was made in about 1965 by Powell[11]. His method put into practice for the first time the idea of organising the computation as an iterative process, involving successive calculations of

(a) the inviscid pressure distribution over the displacement surface of the aerofoil (and wake) and

(b) the boundary layer development for a given external pressure distribution.

For stage (a), the small-perturbation method of Weber[12], with empirical compressibility corrections suggested by Wilby[13], was used, and for stage (b) a simple integral method for turbulent boundary layers due to Nash[14]. Since the latter method did not permit the calculation of the wake, an empirical extrapolation procedure had to be used to estimate its displacement effect; the wake curvature effect was neglected. In spite of these crudities, good agreement with experiment was generally obtained up to the critical Mach number, as can be seen from the example shown in Fig 1 (taken from Ref 15). The 14% thick cambered aerofoil NPL 3111 combines a 'roof-top' type of upper-surface distribution with some rear loading; it was tested at a Reynolds number of 15×10^6 in the 8 ft × 8 ft wind tunnel at RAE Bedford. Note particularly the standard of agreement on both surfaces as the trailing edge is approached, which rivals that achieved by even the best modern methods (*cf* section 4). It should however be pointed out that these calculations have been made for the same values of the lift coefficient as in the experiment; there is a small discrepancy in the angles of incidence which suggests that the method slightly underestimates the magnitude of the viscous effects.

Further progress was made a few years later by Firmin[16]. He used a similar method for the inviscid part of the calculations, but incorporated the entrainment method of Green[17] for compressible turbulent boundary layers and wakes; it was therefore possible to calculate properly the displacement effect of the wake, thus removing the empiricism present in Powell's method. He also introduced an allowance for the curvature of the wake, approximating it by a vortex sheet lying on the continuation of the chord line of the aerofoil. This was found to produce a further contribution to the reduction of lift due to viscous effects, which could be appreciable particularly in the case of rear loaded aerofoils. A typical example is shown in Fig 2; the aerofoil, RAE 2822, is 12% thick and the calculations were made at $M_\infty = 0.67$, $Re = 6 \times 10^6$. The reduction in lift coefficient, compared with the value for inviscid flow, is 20% if wake curvature effects are neglected, and 23% if they are included. A comparison with experimental results from the RAE 8 ft × 6 ft wind tunnel for a similar, but just supercritical, example is given in Fig 3. The standard of agreement is very good; the only appreciable discrepancy, on the upper surface near mid-chord, is probably due to approximations made in the inviscid part of the method. In this case the comparison has been made at an effective angle of incidence, α_{eff}, obtained from the nominal value set up in the wind tunnel by applying a

correction for wall interference based on measurements on models of different sizes. A critical assessment of the method, made recently by Engineering Sciences Data Unit[18], concluded that it could predict lift and lift-curve slope (for subcritical flow) with an accuracy better than 5% in most cases, though there were some exceptions probably caused by anomalies in the wind-tunnel measurements.

An illustration of the use of the method in the prediction of scale and compressibility effects on the lift of a standard symmetrical aerofoil, NACA 0012, is given in Fig 4. This shows the variation with Reynolds number and Mach number of the ratio of the $\frac{dC_L}{d\alpha}$ for viscous flow to the corresponding inviscid value; transition is assumed to be fixed at 5% chord in all cases. It can be seen that the reduction in lift due to viscous effects, though small (about 5%) at low speeds and full-scale Reynolds number (40×10^6), can increase to 15-20% at a Mach number of 0.7 and Reynolds numbers typical of many wind tunnels (1 to 5×10^6).

In drawing an arbitrary line between historical and contemporary matters, we can also make the more fundamental distinction between the field of subcritical flow - to which all the methods considered so far have been restricted - and that of supercritical, transonic flow, which is the main subject of this review.

4 METHODS FOR TRANSONIC FLOW OVER AEROFOILS

The restriction to subcritical flow of the methods mentioned in the previous section was almost entirely due to limitations on the methods that were then available for calculating the inviscid part of the flow. It was the development of modern finite difference methods for computing the complete compressible flow field past an aerofoil, inspired in particular by the solution of the transonic problem by Murman and Cole[19], just over 10 years ago, that provided the tools necessary for extending our techniques for the prediction of viscous effects into the true transonic regime. In 1972 Jones and Firmin[21] made use of certain improvements to Murman and Cole's basic transonic small perturbation (TSP) method suggested by Krupp[20] and Albone *et al*[23], and incorporated an approximate allowance for the displacement effect of the viscous layers and the curvature of the wake. Two examples of the application of their method (with some improvements described in Ref 22) to the RAE 2822 aerofoil are given in Fig 5; the Reynolds number of the experiments is 6×10^6. For subcritical flow (Fig 5a) the standard of agreement between theory and experiment is slightly poorer than for the earlier method of Ref 16 (*cf* Fig 3); but the important point is that for a supercritical case (Fig 5b) the position and strength of a marked shock wave are predicted with reasonable accuracy.

The approximations, both to the flow equation and to the boundary conditions, that are inherent in the TSP methods make them unreliable for applications to general aerofoil shapes at arbitrary free stream Mach numbers. Fortunately, efficient methods for solving the full potential (FP) flow equations with exact boundary conditions are now readily available. The earliest (1971) of these, probably still the best and certainly the most widely used, is that of Garabedian *et al*, described with various developments in Refs 24 to 26; it will be referred to hereafter by the initials 'G & K'. The G & K method is too well known to need detailed description here. It will suffice to mention that the coordinate system is derived from a conformal mapping of the region exterior to the aerofoil onto the interior of a circle, in which a uniform grid in r and θ is set up; and that the full equation for the velocity potential ϕ is then solved by a relaxation technique analogous to that used by Murman and others for the TSP equation; the novel feature of which is the replacement of a standard central difference scheme for subsonic flow by 'retarded' (upstream) differencing when the flow is supersonic. Because the mapping is singular at a sharp trailing edge, the only condition required to fix the circulation is that the transformed velocity in the circle plane shall be zero at the image of the trailing-edge point, leading to a finite velocity there in the physical plane. This condition is usually carried over without alteration when viscous effects are included.

The G & K method is nominally exact for subcritical flows, or for shock-free supercritical flows. When shock waves are present, however, there are two potential sources of error and uncertainty:

(a) the assumption is made, in using the potential flow equations, that the flow is everywhere irrotational and isentropic. As a result, the correct jump conditions across a shock wave cannot be satisfied; mass and total energy can be conserved, but not momentum. The effect of this on the pressure ratio (p_2/p_1) across a normal shock wave is shown in Fig 6. We see that the pressure rise for an 'isentropic shock' is always greater than that for a true (Rankine-Hugoniot) shock, by an amount which becomes appreciable when the upstream Mach number M_1 exceeds about 1.2 - a value well below that at which shock-induced boundary-layer separation would be expected ($M_1 \approx 1.3$ to 1.4):

(b) the numerical solution of the equations will depend on the finite difference scheme used to solve them, in particular on the way in which the switch, from retarded differencing in the supersonic flow upstream of the shock to central differencing in the subsonic flow downstream, is introduced.

In the original version of the G & K method[24,25] no attempt was made to conserve mass across shock waves, and this so-called 'non-conservative' (N-C) scheme leads to solutions in which the shock pressure rises are much less than the 'correct' values (for isentropic

flow). Subsequently Jameson[26,27], developing an idea of Murman[28], introduced a special form of the difference scheme at the 'shock point' (the first subsonic point downstream of the shock), which gives 'quasi-conservative' (Q-C) solutions in which mass is conserved with adequate accuracy and a good approximation to the 'correct' pressure rise is predicted.

It is found that these two alternative options, N-C and Q-C, lead to results in which the position, as well as the strength, of the shock waves can differ appreciably. Very recently, accurate solutions of the full Euler equations have been obtained[29], which suggest that the truth lies somewhere between these two extremes, generally closer to the first (N-C) than to the second. The implications of this situation on the calculation of viscous effects will be discussed further when the individual methods are described below.

Before we proceed to do this, one further point should be mentioned. The interaction between a normal shock wave in transonic flow over the surface of an aerofoil and the boundary layer at its foot is a complicated subject which has received considerable theoretical attention (see Ref 30 for a critical review). In the methods which are the subject of the present review, however, no attempt has been made to treat this interaction in any special way, but merely to regard it as a region in which an ordinary turbulent boundary layer is subject to a local rapid pressure rise, followed by a milder (but usually still adverse) pressure gradient. This approach is due originally to Green[31], who suggested that, provided that the pressure jump through the shock wave is spread (if necessary artificially) over a few boundary-layer thicknesses, then any reliable method for calculating turbulent boundary layers (particularly one which takes the 'lag' effect into account) might be expected to predict the main effects of the interaction on the subsequent development of the boundary layer downstream, at least when the flow remains attached. The relative success of this procedure can be judged from the examples which follow.

We have selected four methods for description in some detail, all of which are currently in use for the solution of practical aerofoil problems in transonic flow.

4.1 Bauer, Garabedian, Korn and Jameson (BGKJ)

Appropriately enough, the originators of the inviscid G & K method were the first[32] to incorporate into it an allowance for viscous effects. The resulting computer program has been published in Ref 26, and we shall therefore refer to it by the initials of the authors of that book, BGKJ. The procedure adopted is basically very simple, and makes use of the solid displacement surface model of the viscous-inviscid interaction; the effects of the wake are neglected completely. The development of the turbulent boundary layer is calculated by the integral method of Nash and Macdonald[14]; this is based on the assumption of local equilibrium conditions, and may therefore lose accuracy if departures from equilibrium are large, as is likely to occur at the foot of a shock wave or in the adverse pressure gradient on the lower surface of a strongly rear-loaded aerofoil.

The calculations start with a few iterations of the basic inviscid method, sufficient to establish a reasonable approximation to the pressure distribution. This is used to calculate the displacement thickness, δ^*, of the turbulent boundary layer, starting from specified transition positions. A suitable proportion of δ^* is then added to the aerofoil ordinates to define a new effective shape, which will now have a trailing edge of non-zero thickness. At this stage it is necessary to perform a new mapping onto the inside of the circle - a feature which sounds inefficient but can in fact be done very rapidly with the aid of fast Fourier transforms. Next, a few further iterations of the inviscid flow calculations are performed; and the whole procedure is repeated until convergence is obtained.

As in most methods of this type, difficulties are generally encountered at an early stage in the iterative process near the trailing edge, where the adverse velocity gradient $\left(-\frac{du_i}{ds}\right)$ predicted by the inviscid part of the program is much higher than it will be in the final converged state - theoretically infinite in fact for the purely inviscid flow, as has been pointed out by Melnik[6]. As a result the boundary-layer method will predict the onset of separation before the trailing edge is reached and it may be impossible to continue the calculations. It is therefore necessary to incorporate some artificial 'safety valve' which will inhibit the breakdown of the method past separation. In the BGKJ method this is done by examining the parameter $\left(-\frac{\theta}{u_i}\frac{du_i}{ds}\right)$ and restricting its value to the maximum 0.004 that indicates separation; thus if $-du_i/dx$ becomes too great the growth of the boundary layer is automatically reduced. This device is also advantageous in passing through a shock wave. In addition, some smoothing of the displacement thickness δ^* is introduced, and an extrapolation procedure is used to determine the variation of C_p very close to the trailing edge.

Some applications of the method to examples where experimental results are available for comparison are shown in Figs 7 to 9. The two 'supercritical' aerofoils were designed by the hodograph method of Garabedian and Korn[25,26] to give shock-free flow at a Mach number of 0.75 and lift coefficients of 0.6 and 0.7; they were respectively 11.5% and 14.5% thick and are designated by the codes 75-06-12 and 75-07-15. Models of 12 inch chord were tested[33,34] in the 60 inch × 15 inch wind tunnel at NAE Ottawa, which has perforated top and bottom walls with open area ratio 20%. The Reynolds number of the tests was 20×10^6; transition was not fixed but probably occurred close to the leading

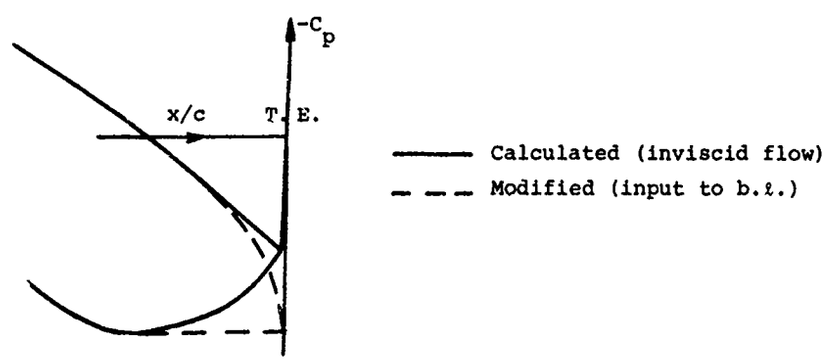
edge. For the first aerofoil we have chosen an off-design case, $M_\infty = 0.727$, $C_L = 0.787$, where there is a shock wave of moderate strength ($M_1 = 1.25$) on the upper surface at about 50% chord. The calculations have been made in this and other cases for the same value of C_L as in the experiment; the discrepancies in α may be ascribed partly to the effects of wall interference (for which no correction has been made), partly to shortcomings in the viscous modelling. In Fig 7a the experimental pressure distribution is compared with the result of a calculation by the N-C version of the method. The agreement is fair over most of the aerofoil, and the position of the shock wave is estimated quite well; but the pressure level behind it is much too low and a slightly supersonic plateau is indicated where in fact the flow is well subsonic. The Q-C version (Fig 7b) does better in this respect, but the pressure distribution ahead of the shock is now in poor agreement; this may explain the considerable underestimation of the drag, which was predicted well - possibly coincidentally - by the N-C version. The variation of C_D with M_∞ at a lower value, 0.6, of C_L is shown in Fig 8. In this case the method (N-C) predicts the drag creep quite well, but underestimates the Mach number at which the rapid drag rise occurs by about 0.02; part of this discrepancy could be due to a negative blockage effect in the wind tunnel.

Results for the thicker aerofoil, 75-07-15, are compared in Fig 9. Fig 9a shows a subcritical case; here the agreement is excellent everywhere except near the trailing edge where the pressure is considerably overestimated, no doubt mainly because of the omission of wake effects in the BGKJ method - though a similar, but less marked, trend has been found with methods which do take the wake into account, for thick heavily rear-loaded aerofoils like the present one - see section 4.3. We have chosen an interesting (though difficult) supercritical example (Fig9b&c) in which the experiment shows a shock wave at about 60% chord followed by a marked expansion before the final compression to the trailing edge. This feature is predicted qualitatively by the N-C version (Fig 9b), although the suction level is slightly too low ahead of the shock and too high behind it. With the Q-C version (Fig 9c) it was found necessary to reduce M_∞ by 0.008 - a plausible blockage correction for this wind tunnel - in order to get reasonable agreement on shock position; but then the shock upstream Mach number is underestimated and a spurious adverse pressure gradient is predicted over the forward part of the upper surface. In view of this the good agreement found with regard to drag may be misleading.

4.2 Bavitz

A method that is in many ways analogous to the previous one is due to Bavitz; this is described in Ref 35 which contains a listing of the computer program. The main point of difference concerns the calculation of the boundary layers; here the method is that of Bradshaw *et al*[36]. The turbulent energy equation is turned into a partial differential equation for the turbulent shear stress using empirical relations derived from measurements in incompressible flow, and this is solved along with the mean continuity and momentum equations by the method of characteristics. The additional assumption is made that the turbulent structure is essentially unaltered by compressibility, and for the moderate Mach numbers encountered in transonic flow calculations this should be entirely adequate. The method should be accurate for all types of pressure distribution, provided only that separation is not approached too closely. However, a calculation of the wake development is not included, and this omission will limit the overall accuracy of Bavitz's method.

As with the BGKJ method, the solid displacement surface model is used to provide the matching between the inviscid and viscous parts of the calculation. Inevitably, some empirical features have to be introduced to deal with the trailing edge region. In this case they include (a) strong smoothing of the shape of the displacement surface before the inviscid flow calculations are performed; (b) modifications to the predicted inviscid pressure distribution (for rear-loaded aerofoils) when calculating the boundary layers, as shown in the sketch below; (c) linear extrapolation of the shape of the displacement surface from a predicted separation point, rearward to the trailing edge.



Sketch (e)

Although (b) could be held to provide an empirical allowance for likely pressure changes across the boundary layer on the upper surface, it does appear to some extent incompatible with (c), since the latter removes the curvature of the displacement surface that is the cause of these pressure changes; while (b) will also surely exaggerate the tendency of the boundary layer to separate before the trailing edge is reached and hence bring (c) into operation earlier than would otherwise have been the case.

To illustrate the use of the method we have chosen the second (thinner) of the two supercritical aerofoils described in section 4.1, designated 75-06-12. Comparisons with the same experiments, made at NAE Ottawa, are shown in Fig 10. In the first example (Fig 10a), for well subcritical flow, the agreement is excellent everywhere except just ahead of the trailing edge on the upper surface - probably a symptom of the neglect of the wake effects in the calculation. In the second example (Fig 10b) there is a shock wave at 35% chord on the upper surface, behind which the suction level is overestimated - no doubt because the N-C version of the inviscid flow program has been used. The next case (Fig 10c) shows a double-shock pattern on the upper surface; this type of flow is always difficult to predict, but the agreement between theory and experiment is good. Finally, Fig 10d shows that when the shock wave is further aft (about 60% chord) both its position and the pressure level behind it are reasonably well predicted. This indicates a trend which is consistent with experience with the BGKJ program: that a N-C version gives satisfactory results for shocks aft of (say) 50% chord but a conservative version may be preferable for shocks on the forward part of the aerofoil.

Comparisons of Fig 10a-d show inconsistencies in the shape of the predicted pressure distribution just ahead of the trailing edge on the upper surface; sometimes there is a 'flat' (Fig 10a&d), sometimes a nearly uniform gradient (Fig 10b&c). In all four cases the real flow would be expected to be well clear of trailing edge separation, so that the prediction of a pressure plateau is doubtless a vagary of the empiricism involved in treating the trailing-edge region.

The general standard reached by this method appears to be similar to that of the previous one. In view of this it scarcely seems justified to have introduced a much more sophisticated method for the viscous part of the calculations; but on the other hand the typical computation times quoted remain satisfactorily short - about 5 to 10 minutes on a CDC 6600 computer.

4.3 Collyer and Lock (VGK)

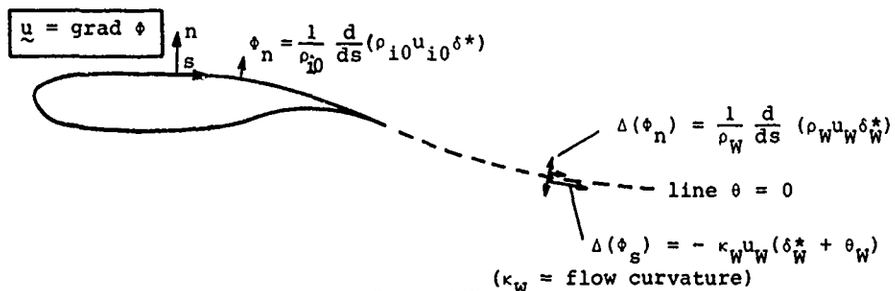
As a natural extension of previous work on the subject at NPL and RAE (*cf* section 3) it was decided to develop a new version of the G & K method in which viscous effects were taken into account. The resulting method, known as 'VGK', of which a full account is given in Refs 37 to 39, differs from its predecessors in sections 4.1 and 4.2 in a number of ways, the most important of which are briefly described below.

(i) The turbulent boundary layers and wake are calculated by a development of the entrainment technique, the 'lag' entrainment method of Green *et al*[40]. In this an empirical relation for the entrainment is replaced by a further ordinary differential equation, derived from the turbulence energy equation, along the locus of maximum shear stress in the boundary layer. As a result, improvements in accuracy are achieved for 'relaxing' pressure gradients, typical examples of which are the flow through a shock wave or on the lower surface of a rear-loaded aerofoil.

(ii) The surface transpiration model ((B) of section 2.1) is used to represent the displacement effect of the boundary layers and wake on the equivalent inviscid flow. This was chosen in preference to the solid displacement surface model normally employed because the boundary condition is applied on the actual surface of the aerofoil; so the numerical mapping of the contour onto the circle need be performed only once and does not have to be repeated after each new calculation of the boundary layer.

(iii) Both the thickness and curvature effects of the wake are taken into account, as specified in section 2.2. Here the simplification is made of applying the appropriate boundary conditions, not on the true line of the wake but on the transform in the physical plane of the line $\theta = 0$ in the circle plane; this should not introduce significant errors since the wake effects are in any case relatively small.

The boundary conditions implied by (ii) and (iii) are summarised in the sketch below.



Sketch (f)

(iv) An empirical modification is introduced into the G & K method with the aim of improving the prediction of shock waves in the inviscid flow. The need for this stems from the discrepancy between results obtained respectively by the N-C and Q-C (or fully conservative) versions, in cases where the shock wave is relatively strong ($M_1 > 1.2$, say) - as remarked at the beginning of section 4. When the VGK method was being developed similar (though less marked) discrepancies were observed in predictions of viscous flows: that is, with the N-C version the pressure level downstream of the shock is too low while with the Q-C version it is too high. A similar trend has been found with the BGKJ method (*cf* section 4.1). Clearly an intermediate scheme would be desirable. Such a scheme can be produced very simply by modifying the difference operator used at the shock point to represent the leading term in the partial differential equation for the velocity potential. In the N-C version a central difference expression is used, while in the Q-C version this is replaced by the sum of central and upwind expressions. The modification consists of taking instead the sum 'central' + λ × 'upwind', where λ is an arbitrary parameter between 0 and 1; thus $\lambda = 0$ gives the N-C version and $\lambda = 1$ the Q-C version, while values of λ between 0 and 1 naturally give intermediate solutions, as required. This scheme has been called 'partially conservative' (P-C); full details are given in Refs 38 and 39. It has been found that, for a number of cases in inviscid flow, values of λ between 0.25 and 0.5 give a reasonable approximation to the true (Rankine-Hugoniot) shock pressure rise. A typical example is shown in Fig 11 for the RAE 2822 aerofoil; this illustrates both the large difference between the N-C and Q-C solutions, and also the apparently satisfactory result obtained with $\lambda = 0.5$. Further confirmation of the efficacy of this device has been obtained recently by comparison with numerical solutions of the full Euler equations due to Sells[41]. Fig 12 gives results for the NACA 0012 aerofoil at $M_\infty = 0.85$, $\alpha = 0$. In this case the value $\lambda = 0.3$ has been found to simulate the true solution as regards both the position and strength of the shock, while the drag is also well predicted; on the other hand both the N-C and conservative solutions of the potential flow equations (particularly the latter) have significant errors in all respects. Both these examples are admittedly somewhat extreme (M_1 is between 1.3 and 1.35), and in any case one would not always expect such good results from the P-C scheme; but nevertheless it does seem likely to provide a sounder basis for calculations of viscous flow than either of the extremes used previously.

Applications of the VGK method to the calculation of transonic flows with shock waves are given here for two aerofoils, both tested in the RAE 8 ft × 6 ft wind tunnel at a Reynolds number of 6×10^6. The first of these, the 12% thick RAE 2822, has been referred to previously in section 3 (*cf* Figs 2, 3, 5); a selection of experimental results has been published in Ref 42. Theoretical and experimental pressure distributions are compared in Fig 13 for Cases 7 and 8 of Ref 42; a small positive blockage correction ($\Delta M_\infty = 0.004$) has been applied to the experimental results to match the calculated pressure at $x/c = 0.4$ on the lower surface. In the first case (Fig 13a) the agreement is good in most respects, particularly as regards the position of the shock wave and the pressure at its foot; the wiggle near the leading edge is probably the effect of the roughness band used to fix transition (at $x/c = 0.03$). In the second case (Fig 13b) the shock is stronger ($M_1 \triangleq 1.30$) and the pressure is slightly overestimated at its foot, possibly because the boundary layer is close to separation. There is also a similar discrepancy, in both cases, just ahead of the trailing edge ($x/c > 0.95$) on the upper surface; this feature will be further discussed below. The predicted variation of C_D with C_L at $M_\infty = 0.73$ is in good agreement with the experimental measurements (Fig 14).

For the second aerofoil, the 14% thick RAE 5217, a selection of pressure distributions is presented in Fig 15. The general standard of agreement between theory and experiment is good, particularly as regards the position and strength of the shock waves. There is however a tendency to overestimate the pressure towards the end of a long adverse pressure gradient; this is most marked on the lower surface near 80% chord. Discrepancies of this type are usually found with the present method, whenever the boundary layer shape parameter $\bar{H}$ exceeds about 1.8; predicted values of $\bar{H}$ are marked at appropriate points on Fig 15 and it can be seen that the same conclusion is valid here. This is now believed to be due to underestimation of the displacement thickness under such circumstances by the form of the lag entrainment method that has been used in the calculations. Possible modifications which should improve the situation in this respect (see for example Ref 43) are currently being investigated. No doubt for similar reasons, the drag of this aerofoil is somewhat underestimated (see Fig 16). However, the general nature of the drag 'creep' is well predicted, and so is the Mach number for rapid drag rise, particularly if a plausible blockage correction ($\Delta M_\infty = 0.005$) is applied. The figure also shows the calculated variation of drag coefficient with Mach number for a typical full-scale Reynolds number (50×10^6); an appreciable reduction in drag creep is predicted.

4.4 Melnik

The most recent, and certainly the most sophisticated, published method for the solution of the viscous transonic problem for aerofoils has been developed over the past few years by Melnik and his colleagues (see Refs 6, 7, 44, amongst others). A full account of this work will be given by Melnik later in the Conference, so that we shall concentrate here on pointing out the principal features in which the method differs from and improves on its predecessors.

In many respects there is a close resemblance to the VGK method (section 4.3). The same method (lag-entrainment) is used to calculate the boundary layers and wake, while the basic matching between the viscous and inviscid parts is again effected by the transpiration model (A) on both the aerofoil surface and the wake (the position of the latter is

approximated in an identical way). Two options are available for solving the inviscid flow equations: a N-C scheme equivalent to that of Garabedian *et al*[25,26], and a fully conservative scheme following the suggestions of Jameson[27], in which the equation of continuity is written explicitly in conservation form (for Cartesian coordinates)

$$\frac{\partial}{\partial x}(\rho u) + \frac{\partial}{\partial z}(\rho w) = 0 \qquad (27)$$

where $u = \phi_x$, $w = \phi_z$ and

$$\rho = \left[1 - \frac{\gamma - 1}{2} M_\infty^2 (u^2 + w^2)\right]^{\frac{1}{\gamma - 1}} \qquad (28).$$

This differs from the Q-C scheme given in Ref 26 (and used in the VGK method), where the corresponding equations take the so-called 'quasi-linear' form

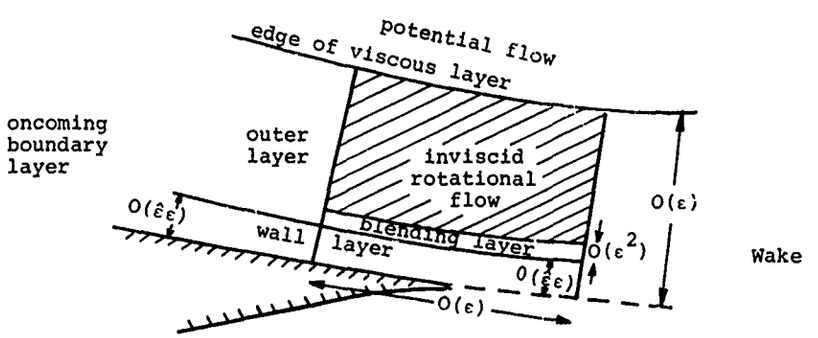
$$(a^2 - u^2)\phi_{xx} + (a^2 - w^2)\phi_{zz} - 2uv\phi_{xz} = 0 \qquad (29)$$

with

$$a^2 = M_\infty^{-2} + \tfrac{1}{2}(\gamma - 1)(1 - u^2 - w^2) \qquad (30).$$

In both cases the switching from central to retarded differencing in going from subsonic to supersonic points is achieved by using Jameson's concept of adding artificial viscosity in conservation form; and it has been found that in most examples almost identical numerical results are obtained. Although the fully conservative approach is perhaps more satisfactory from a mathematical point of view, there is a time penalty due to the recurrent need to evaluate a non-integer exponent (compare the auxiliary equations (28) and (30)); and it would also be difficult to modify it to obtain a 'partially-conservative' scheme along the lines adopted in the VGK method, if that were thought desirable.

The most fundamental point of difference lies in the way in which the neighbourhood of the trailing edge is treated. In the VGK method there is no special treatment, apart from a rough allowance for the change in pressure across the boundary layer (*cf* section 2, Eq.(26)); and as a result it has been found necessary to incorporate some smoothing of the inviscid pressure distribution before the viscous layers are calculated. The particular feature of Melnik's method is a new solution for the trailing edge region, based on asymptotic theory of turbulent shear flows in the limit $Re \to \infty$. The normal assumptions of first-order boundary-layer theory no longer apply in this region, and in particular the transverse variation of the pressure must be properly taken into account. A full derivation of the theory is given in Refs 6 and 7; it turns out that a 'multi-deck' model is required, as indicated in Sketch (g) below.



Sketch (g)

Two length scales are involved, the thickness of the approaching boundary layer, δ , which is $O(\varepsilon)$ with $\varepsilon = \sqrt{\tfrac{1}{2}C_f} = O\left(\frac{1}{\log Re}\right)$, and the thickness of the wall layer, which is a fraction $\hat{\varepsilon}$ of δ with $\hat{\varepsilon} = \frac{1}{\varepsilon^2 Re} = O\left(\frac{\log Re}{Re}\right)$. The length of the special trailing-edge region is also taken to be $O(\varepsilon)$, so that it is assumed to extend about one boundary-layer thickness upstream and downstream of the trailing edge. The particular feature of the solution, which makes it feasible to use in practice, is that the flow in the outer layer is governed to a consistent approximation by a linearised Poisson equation for inviscid, but rotational, flow whose vorticity is identical to that in the outer part of the oncoming boundary layer. It is this outer layer which determines the displacement effect of the viscous flow on the outer inviscid flow, and in which most of the transverse variation of pressure takes place; so that it is unnecessary to obtain a solution for the inner layers (which would involve the assumption of some particular turbulence model)

unless the local variation of skin friction is required. By using complex variable theory for a transformed incompressible flow, Melnik *et al*[7] were able to obtain an explicit analytical solution to the Poisson equation, and to derive from it matching conditions for the equivalent inviscid flow precisely analagous to those used over the rest of the aerofoil and wake. The solution ensures that the corrected pressure reaches identical values as the trailing edge is approached either from upstream on the upper or lower surfaces, or from downstream in the wake; thus the Kutta condition is automatically satisfied.

This analysis represents an entirely self-consistent model of the flow, without the need to introduce any arbitrary treatment near the trailing edge. The only feature that might be questioned is the accuracy to which the basic assumption, that the vorticity in the outer part of the viscous layers may be regarded as 'frozen' as the flow traverses the trailing-edge region, is actually satisfied at the moderate Reynolds numbers encountered in practice. Unfortunately, it would be extremely difficult to verify this directly by experimental means. Thus, as with other methods, the main justification must be by comparison of results with measured pressure distributions and overall forces.

The aerofoil for which the most extensive calculations have been published is again the G & K 75-06-12 referred to previously in sections 2.1 and 2.2. Comparisons for a selection of typical pressure distributions are given in Fig 17; the calculations were all made at the same values of C_L as in the experiments, using the conservative version of the method. In the first example (Fig 17a) the flow is subcritical, and as expected the agreement is very good except for a slight tendency to underestimate the pressure over the central part of the upper surface. In the second case (Fig 17b), for $M_\infty = 0.75$ at a low value (0.1) of C_L, there is a shock wave at about 30% chord on the lower surface, which is well predicted provided that a small negative blockage correction ($\Delta M_\infty = 0.004$) is applied; the overall agreement is then excellent. In the final example (Fig 17c), with $M_\infty \triangleq 0.7$, $C_L = 0.82$, there is a fairly strong shock wave ($M_1 \triangleq 1.28$) on the upper surface at about 35% chord. The position of this is well predicted (with the same blockage correction), but the pressure level behind it is slightly underestimated - somewhat surprising in view of the fact that a conservative difference scheme is being used.

The estimation of the influence of wind-tunnel interference on the effective angle of incidence is a notoriously difficult and controversial subject, particularly for ventilated walls under supercritical conditions. Nevertheless, Melnik *et al*[7], have made a thorough investigation of the subject for the NAE transonic facility in which the 75-06-12 aerofoil was tested, and deduced a correction to the angle of incidence which is extremely plausible. A comparison between the measured and calculated lift curves, for $M_\infty \triangleq 0.75$, is shown in Fig 18. The agreement between theory and experiment is remarkably good, even as regards the fall-off in lift which occurs for $C_L > 0.8$ (due no doubt to the rapid growth of the boundary layer near the trailing edge under conditions approaching separation).

The variation of drag with lift for the same Mach number is illustrated in Fig 19. The general shape of the drag polar is well predicted (by the conservative version of the method), particularly as regards the increase in wave drag which occurs for $C_L > 0.6$ of < 0.1. The drag is however appreciably underestimated (by nearly 15%) for intermediate values of C_L, and this is difficult to explain since the flow is only just supercritical, the pressure gradients are relatively mild and the Reynolds number is high - conditions under which all aspects of the method would be expected to be reliable. There could perhaps be an undetected source of error in the drag measurements, but if so it must be a consistent one since there is little scatter in a large number of experimental points.

The last two figures also show the results of calculations by a numerical solution of the Navier-Stokes equations, due to Deiwert[45]. The agreement with both the corrected wind-tunnel data and the present theory is generally poor; this may be due to the use of an insufficiently refined computational grid, but it is a point which should be checked before much reliance can be placed on such methods for practical purposes.

Returning finally to the present method, the evidence that has been presented for its verification (here and elsewhere) is generally satisfactory. There is however a dearth of published results for cases in which the shock wave lies well back along the chord ($x/c \geq 0.6$, say), where the use of a fully conservative difference scheme might be expected to cause appreciable errors in the inviscid part of the calculation (*cf* Figs 11 and 12, also Ref 29). It is in such cases that the VGK method, with its option of using a 'partially conservative' scheme, would be expected to have an advantage. It is also probable that the accuracy will deteriorate (for the same reason as with the VGK method - *cf* Fig 16) for aerofoils with long adverse pressure gradients under which the boundary layer is approaching separation; to remedy this deficiency improvements in the boundary-layer method will be needed.

5 PREDICTION OF VISCOUS TRANSONIC FLOWS OVER WINGS

Strictly speaking, all the work on two-dimensional problems reviewed in the previous sections should be regarded as a preparation for an attack on the most important practical aspect of our subject, namely the prediction of viscous effects in transonic flow on three-dimensional wings, and eventually on wing-body combinations and complete aircraft configurations. Fortunately, most of the concepts that have been established from two-dimensional considerations can be carried over into three dimensions without

much alteration, though some new ideas are of course required. In particular, it is obvious that any satisfactory overall method must continue to depend on the availability of methods of adequate accuracy for predicting separately:

(a) the inviscid flow about the configuration in question;
(b) the development of the boundary layer, and preferably also the wake, on at least the wings; together with
(c) a matching condition whereby appropriate boundary conditions for (a) and (b) can be supplied, and
(d) a global iterative procedure in which the linked viscous and inviscid calculations are successively repeated so that their mutual interaction can be gradually built up.

With regard to (a), we are limited at present to the assumptions of potential flow, so that the experience that has been gained in two dimensions about the relative merits of non-conservative and conservative formulations of the difference equations (when shock waves of appreciable strength are present) should be taken into account; although this will not be of much help for some of the complex shock patterns (*eg* a triple shock system) that can occur on swept wings. It may also be convenient, at least as an interim measure, to make the additional assumptions involved in transonic small perturbations (TSP) theory, since this will enable complicated configurations to be treated more easily and without excessive increases in requirements for computer storage and run time, while still retaining reasonable accuracy for a variety of wing or body shapes.

Turning now to (b), the calculation of the viscous layers, an even greater variety of choice is available than in two dimensions, ranging from the use of a quasi two-dimensional 'strip theory' approach, through the so-called 'integral' methods to the more sophisticated (and time-consuming) 'differential' methods - which still of course involve the assumption of a suitable turbulence model. Additional problems, that are not present in two dimensions, will occur in corner regions (such as wing fuselage junction) and near the wing tips, where the normal assumptions of boundary-layer theory are no longer valid, while the cross flow in the wake and its eventual rolling up also present extra complications. Up to the present, such problems have either been ignored or overcome by arbitrary means.

With regard to (c), the matching between the viscous and inviscid parts of the flow can be effected by means of the same two alternative mathematical models that have been described in section 2. For three-dimensional problems there is even more justification for preferring the 'surface transpiration' model (A), since it is the one which derives most directly and naturally from the equation of continuity. This can be seen as follows:

Neglecting surface curvature and using for simplicity rectangular coordinates (x, y, n), with n normal to the surface, the equation of continuity is

$$\frac{\partial}{\partial n}(\rho w) = -\frac{\partial}{\partial x}(\rho u) - \frac{\partial}{\partial y}(\rho v) \qquad (31).$$

Integrating with respect to n from 0 to δ, and subtracting the corresponding equations for the viscous and equivalent inviscid flows, we obtain (with the suffix notation of section 2)

$$\rho_{i0} w_{i0} = \frac{\partial}{\partial x}\int_0^{\delta} (\rho_i u_i - \rho u)\,dn + \frac{\partial}{\partial y}\int_0^{\delta} (\rho_i v_i - \rho v)\,dn \quad ,$$

which may be written

$$w_{i0} = \frac{1}{\rho_{i0}}\left[\frac{\partial}{\partial x}(\rho_{i0} q_{i0} \delta_1^*) + \frac{\partial}{\partial y}(\rho_{i0} q_{i0} \delta_2^*)\right] \qquad (32)$$

where

$$q_{i0} = \sqrt{u_{i0}^2 + v_{i0}^2}$$

is the surface speed (in the inviscid flow) and

$$\delta_1^* = \frac{1}{\rho_{i0} q_{i0}}\int_0^{\delta} (\rho_i u_i - \rho u)\,dn \quad ,$$

$$\delta_2^* = \frac{1}{\rho_{i0} q_{i0}}\int_0^{\delta} (\rho_i v_i - \rho v)\,dn \quad ,$$

and the components of the mass-deficit integral.

In order to obtain the displacement thickness, δ^*, however, it can be shown[57] that it is necessary to solve the partial differential equation

$$\frac{\partial}{\partial x}\left(\rho_{i0}u_{i0}\delta^*\right) + \frac{\partial}{\partial y}\left(\rho_{i0}v_{i0}\delta^*\right) = \rho_{i0}w_{i0} \qquad (33).$$

There are additional advantages in being able to use a boundary condition on the body shape itself; this applies particularly if the method of solution of the inviscid flow problem involves a mapping process (or if a 'panel' method is used). Nevertheless, the solid displacement surface model seems to remain the favourite!

After this preamble, we can now proceed to review what appears to be the most important of the (relatively few) published methods for the three-dimensional wing problem. Three of these will be described in a little detail, while others will be mentioned briefly at the end of the section. Unlike the two-dimensional case, there does not seem to be a natural order of presentation - on either chronological or technological grounds - so that our choice in this respect has been largely arbitrary.

5.1 Mason *et al*[46]

The inviscid part of this well-integrated computational procedure is provided by a development of TSP theory due to Ballhaus *et al*[47] Special features include the addition of extra nonlinear terms to the basic partial differential equation to improve its accuracy for swept wings, coupled with a coordinate system which is 'tailored' to the wing planform over most of the span. The boundary condition for the wing are applied on the wing reference plane $z = 0$, using a standard linearised approximation. The normal first-order expression is also used for the pressure coefficient. In order to take into account the important effects of the fuselage on the flow field over the wing, approximate boundary conditions (based on the ideas of slender-body theory) are satisfied on a rectangular box of streamwise-constant cross section over which the appropriate flow inclination can be specified.

The characteristics of the turbulent boundary layer (on the wing only) are calculated by means of a 'strip-theory' technique using the two-dimensional turbulent energy method of Bradshaw[36], modified to simulate the flow on an infinite swept wing with the appropriate local chordwise pressure distribution and sweep angle. Such an approximation may be reasonably satisfactory (at least in the present context of modelling the gross effects of the viscous-inviscid iteration), provided that the flow in the boundary layer is not dominated by strongly three-dimensional effects emanating from the regions near the root, the tip or a crank in the planform. With this simplification there is no difficulty in calculating δ^*, and the boundary condition on the plane $z = 0$ can then be modified by adding the streamwise slope of the displacement surface to that of the wing.

In any practical method for calculating viscous effects on wings there is an urgent need - even greater than in the two-dimensional problem - to incorporate some suitable device for inhibiting any catastrophic effects on the overall computational process that may be caused by the predicted onset of boundary-layer separation, whether this is a spurious symptom occurring only in the early stages of the iterations or a genuine feature of the converged solution. In the present method, a scheme similar to that suggested by Bavitz[35] (*cf* section 4.2) is adopted, in which the shape of the displacement surface is extrapolated linearly from a predicted point of separation to the trailing edge. This device has proved extremely effective and could be quite acceptable provided that only small traces of it remain in the final converged solution.

As an example of the application of the method to a practical configuration, a comparison is given in Fig 20 with pressure distributions measured on a model of an 'advanced technology' fighter. This has a wing of aspect ratio 5.5, with 42.5° basic leading-edge sweep and extensions to both the leading and trailing edges at the root; the design involves the use of 'supercritical' aerofoil sections. The Reynolds number of the tests is not stated. A reasonably good prediction is achieved (over the outer part of the wing) of the general shape of the pressure distribution on the upper surface and of the position of the shock wave, except at the innermost station. Over the lower surface the agreement is poor; this could be partly due to a failure to model properly the shape of the bottom part of the fuselage. It is naturally impossible to tell whether the deficiencies revealed by this example (and by others in the same paper) are mainly due to the approximations involved in the inviscid part of the program or to faults in the modelling of viscous effects.

5.2 Kordulla[48,49]

For the inviscid part of the calculations, the modified TSP formulation of Bailey and Ballhaus, referred to in the previous section, is again used. In this case an allowance for the effects of a fuselage is not included; when one is present a vertical reflection plane through the wing-fuselage junction is assumed. The principal feature of the method is the use of a new finite-difference scheme for solving the fully three-dimensional boundary layer equations, for either laminar or turbulent flow. For the latter case, the scalar eddy viscosity model of Cebeci[50] for the Reynolds stresses is used to provide the necessary turbulence closure conditions. As in all numerical methods for solving the three-dimensional boundary-layer equation, care has to be taken to satisfy the domain of dependence principle; if this is not done instability will usually result. In the present case an implicit scheme due to Krause[51] is used, which provides the ability to march outwards along the span, even when the cross-flow is in the negative (inwards) direction, and yet retain (conditional) stability. The Krause scheme is second-order accurate for constant step lengths, although a variable computational grid, growing with the boundary layer, is normally used for increased efficiency.

It is consistent with the approximations made in the TSP method to assume that the boundary layer develops on a plane coincident with the wing planform ($z = 0$). In this plane, the natural (non-orthogonal) coordinate system is formed by lines of constant y and constant $\xi = \dfrac{x - x_{LE}(y)}{c(y)}$ (where c is the local chord and x_{LE} the coordinate of the leading edge). With any three-dimensional boundary-layer method it is necessary to provide input from the inviscid flow solution of both the magnitude and direction of the velocity vector over the whole wing plane. Special starting solutions are also required along the wing root, $y = 0$, where symmetry conditions are assumed to apply, and along the leading edge, $\xi = 0$, which is taken to be the attachment line; along both these lines quasi-two-dimensional forms of the equations result.

The matching between the viscous and inviscid parts of the program is achieved by first calculating the displacement thickness, δ^*, of the boundary layer (by integrating a partial differential equation analagous to Eq.(33)), and then adding its streamwise derivative, $\dfrac{\partial \delta^*}{\partial \xi}$, to the slope of the wing surface to form a new input for a further inviscid solution. A fully iterative procedure has been set up, the convergence of which is judged by examining the variation in C_p between successive iterations. In order to avoid breakdown of the method in cases where boundary-layer separation is predicted - either in the early stages of the iterations or as a feature of the final solution - drastic measures have to be taken. As soon as the chordwise wall shear stress becomes negative, the velocity at the edge of the boundary layer is gradually increased until the separation is suppressed and the solution can continue. In addition to this, it is sometimes necessary to make further modifications to the shape of the displacement thickness towards the trailing edge in order to avoid unrealistic predictions of the pressure distribution in that region. As remarked in section 5.1, the plausibility of such devices has to be judged according to the degree to which their effects still remain in the final solution.

Two examples have been chosen to illustrate the use of the method. The first of these (Fig 21, taken from Ref 48) concerns the ONERA M6 wing, a half-model of which was tested in the S2 wind tunnel at Modane at a Reynolds number (based on root chord) of about 3×10^6 (see Ref 42, Paper B1). The wing has a leading-edge sweep angle of 30^o, aspect ratio 3.8 and taper ratio 0.56; the streamwise section (ONERA 'D') is uncambered and about 10% thick. This particular example ($M_\infty = 0.92$, $\alpha = 3^o$) presents a difficult problem, since relatively strong, almost unswept shock waves are observed towards the rear on both surfaces, while there is also a highly swept forward shock on the upper surface. Preliminary inviscid calculations using the two options, non-conservative (NCR) and fully conservative (FCR), available in the program, showed that the latter produced a shock wave very close to the trailing edge on the upper surface, and so strong as to render any boundary-layer calculations impossible. Even with the N-C option it was found necessary to bring into play the inhibiting devices mentioned in the previous paragraph. As can be seen from Fig 21, the inclusion of viscous effects does improve the prediction of the position of the main shock wave on the upper surface. On the lower surface there is little difference between the viscous and inviscid solutions, and both of them indicate a shock that is too far forward towards the wing tip. The pressure is considerably overestimated towards the trailing edge on both surfaces; this may be due partly to the 'damping' of the viscous effects mentioned previously, partly to the omission of the effects of the wake.

The second example (Fig 22) refers to a transport aircraft wing, of fairly conventional design, tested by the Lockheed Georgia Company at a Reynolds number (based on root chord) of 11×10^6 and a Mach number of 0.8. The wing has a net aspect ratio of about 7, 27.5^o leading-edge sweep, a taper ratio of 0.34 and is 11% thick. It was mounted in high position on a fuselage and had nacelles suspended from the lower surface. Neither the fuselage nor the nacelles could be allowed for in the calculations, and this may be partly responsible for the poor agreement between theory and experiment for the pressure distribution on the lower surface of the wing. On the upper surface, there is a considerable difference between the inviscid solutions obtained with the two alternative options (NCR and FCR). In this case, it was found possible to obtain a converged viscous solution with the FCR option, in which the position of the shock wave is well predicted; but to achieve this it was again necessary to introduce an artificial modification to the predicted shape of the displacement surface, in this case over about the last 20% chord.

5.3 Lynch[52]

This method, developed at the Douglas Aircraft Company, appears to have been the first to incorporate a solution of the full equations of potential flow, with exact boundary conditions, in preference to the more approximate TSP approach. The program selected was that of Jameson and Caughey[52], known as 'FLO-22'. A non-orthogonal coordinate system is used, combining a sheared grid in plan view having a coordinate line following the leading edge, with a parabolic 'unwrapping' transformation applied to the wing sections in chordwise planes $y = \text{constant}$. In this particular system spanwise coordinate lines are parallel to the leading edge, so that for a tapered wing the trailing edge is not a coordinate line; and as a result the number of chordwise points on a wing section diminishes towards the wing tips, leading in some cases to poor flow definition in the tip region. Because of the parabolic transformation, the grid spacing in the chordwise direction becomes progressively coarser as the trailing edge is approached; thus shock waves lying on the aft part of the wing tend to be severely 'smeared', while the flow in the trailing-edge region is poorly defined leading to

uncertainties in the representation of the Kutta condition. However, all these features - though inherently unsatisfactory in themselves - do combine to alleviate the problems (mentioned in the previous section) that beset three-dimensional boundary-layer methods behind strong shock waves and in the neighbourhood of the trailing edge and the wing tips. For a similar reason, a 'non-conservative' formulation of the finite-difference scheme was adopted; and this certainly seems preferable to a 'fully-conservative' system if no other option is available.

At the time when the paper was written, it was not possible to take account explicitly of the effects of the fuselage on the flow. Instead, a vertical reflection plane is assumed at the side of the fuselage - particularly suitable for a low-wing configuration; while a correction to the mean Mach number, based on calculations by a panel method of the flow field due to the isolated fuselage, is applied to the oncoming flow over the wing to allow approximately for the gross effects of the fuselage.

For the calculations of the three-dimensional boundary layers on the wings, a development of the 'differential' method of Cebeci *et al*[54] is used. The basic equations are essentially the same as those considered by Kordulla (section 5.2). They are solved numerically by the well-known Keller 'box' finite-difference technique, incorporating a modification suggested by Stewartson to take into account the domain of dependence principle, which is essential to avoid the instability that would otherwise occur when marching spanwise in a region where the cross flow is in the opposing direction. As in the similar method of Kordulla, edge conditions are required along the leading edge (strictly, the attachment line) and the root, but not at the tip. The displacement thickness is again calculated by solving the appropriate partial differential equation, and is then added to the wing surface ordinates to provide the equivalent shape for a new inviscid calculation.

All the ingredients are thus available for the development of a fully-integrated method for solving the viscous interaction problem. However, at the time of writing (1978) it appears that this had not actually been implemented. Instead, the calculations shown in the following example (Fig 23) were made with only a single iteration of the overall process. The wing is of high aspect ratio (10.8), with a 30° sweep of the quarter-chord line, and the average thickness/chord ratio is 12%; wind-tunnel tests were made at a Reynolds number (based on mean aerodynamic chord) of 2×10^6. There is considerable rear loading, and the experiments also show a reasonably satisfactory supercritical flow development over the forward part of the wing, with a shock wave lying between 30% and 40% chord over the central portion of the semi-span, strongest in the neighbourhood of the trailing edge crank. The calculations (unlike some of those shown previously) show good agreement with experiment over most of the lower surface. On the upper surface, the suction levels near the leading edge are well predicted except close to the tip; but the shock wave is so severely 'smeared' that it bears little resemblance to what is actually observed. Towards the trailing edge the agreement is remarkably good, considering - or more likely because of - the crudity of the treatment of that region. It is claimed that the boundary-layer method provided a satisfactory guide to the onset of separation, and it was in fact used in developing this wing to give an improvement in performance over an inferior predecessor.

5.4 Other methods

Other work in this area, no less worthy of mention than that described above, includes the following:

(a) A collaborative research programme between FFA (Stockholm) and Dorniers, described by Hedman[55]. This involves a coupling between a version of the TSP technique due to Schmidt[56] with the entrainment 'integral' method for three-dimensional turbulent boundary layers of P.D. Smith[57].

(b) A method developed at the Boeing Company, described briefly in Ref 58, whose principal components are: the Jameson-Caughey 'FLO 27' program[59] for the full potential flow equations, using a finite-volume technique; and the differential method of McLean[60] for three-dimensional turbulent boundary layers.

(c) Research at RAE led by Firmin, combining a recent TSP method for wing-body combinations[61] with Smith's integral boundary-layer method[57], modified to include 'lag' effects. This work, which includes for the first time an allowance for the thickness effects of the wake, has not been reported previously but will be described in a later paper at this Conference.

6 CONCLUDING REMARKS

In this final section, we conclude with some remarks on the 'state of the art' of the subject, and make some suggestions about the needs and potentialities of future work along the same lines.

(i) The general principles are now well established of determining viscous effects (at least for basically 'attached' flows) by a procedure involving separate calculations for (a) an equivalent inviscid flow and (b) the viscous flow in thin shear layers over the wetted surfaces and in the wake, and combining them through a matching process, derived from the equation of continuity, which can be extended (if necessary) to include higher-order effects. There is reason to expect that many of the inadequacies that still exist in current methods could be remedied by further attention to the component parts ((a) and (b)).

(ii) Therefore, much of the need for the future is for improvements - both in accuracy and efficiency - to methods for calculating inviscid transonic flows about increasingly complicated configurations, and viscous flows - laminar and turbulent - both of the relatively simple 'boundary sheet' type and of the more complicated variety occurring in corners, near edges (trailing and tip) and in wakes. For the inviscid methods, provision should be built in to the program for a specified, non-zero value of the velocity normal to the surface, so as to allow the 'transpiration' boundary condition (Eq.(32)) for the viscous matching to be implemented.

(iii) Special treatment may be needed of the shock-wave/boundary-layer interaction phenomenon; this must involve both the inviscid flow calculations (so that a 'realistic' shock wave is produced at the correct position in the external flow) and the local interaction region. However, it has been shown in two dimensions that reasonably satisfactory results can often be obtained without such special treatment; and this is fortunate since to provide it in three dimensions would cause considerable complications. The same also applies to the trailing-edge region, though here a 'quasi-two-dimensional' extension of Melnik's ideas to three dimensions might be both feasible and adequate.

(iv) In two dimensions, the standard of achievement for the best methods currently available is generally satisfactory. The chief shortcomings appear to be in the prediction of pressures and drag in cases where the adverse pressure gradients bring the boundary layer close to separation. The causes probably lie mainly in inadequacies in the boundary-layer methods, which should be possible to rectify provided that some second-order effects are taken into account.

(v) The situation in three dimensions is at present less satisfactory, largely due to the sheer complexity of organising the operations involved in the full iterative process, relatively simple though the basic concepts may be. There are additional difficulties, peculiar to three-dimensional boundary layers, associated with high cross-flow angles occurring near the wing tips (particularly if no attempt is made to model the tip vortices) or towards a swept trailing edge. Future work should also consider the effects of the boundary layer on the fuselage and its interaction with that on the wing.

(vi) Although the prediction of flows with gross boundary-layer separations may eventually require the solution of the Navier-Stokes equations, there is some potentiality in extending the 'classical' methods of the present paper to deal with mildly separated flows, and thus usefully increase their range of applicability. In order to do this some modifications will be needed to the viscous part of the calculations, so as to operate in an inverse mode (*cf* Ref 43) - and hence also to the inviscid part; while second-order effects in the matching process should be taken into account.

(vii) In order to provide adequate means of verification of this (or any other) theoretical approach to the problem of predicting viscous-inviscid interactions, it is important that additional careful experiments should be made, involving at the least measurements of the mean flow in the viscous shear layers as well as the surface static pressures; this applies particularly to three-dimensional configurations[62], although any such experiment is of course bound to be both time-consuming and expensive.

REFERENCES

No.	Author	Title, etc
1	M.J. Lighthill	On displacement thickness. *J. Fl. Mech.* 4, p 383 (1958)
2	K. Gersten	Displacement thickness in higher order boundary layers. *Z.A.M.M.*, 54, p 165 (1974)
3	D.F. Myring	The effect of normal pressure gradients on the boundary layer momentum integral equation. RAE Technical Report 68214 (1968)
4	H.E.H. Mahgoub P. Bradshaw	Calculation of turbulent-inviscid flow interactions with large normal pressure gradients. *AIAA Journal*, 17, p 1025 (October 1979)
5	L.F. East	Private communication
6	R.E. Melnik R. Chow	Asymptotic theory of two-dimensional trailing edge flows. NASA SP 317 (1975)
7	R.E. Melnik R. Chow H.R. Mead	Theory of viscous transonic flow over airfoils at high Reynolds number. AIAA Paper 77-680 (1977)
8	J.H. Preston	The calculation of lift taking account of the boundary layer. ARC R & M No.2725 (1949)
9	Ed B. Thwaites	*Incompressible Aerodynamics.* Oxford University Press (1960)

REFERENCES (continued)

No.	Author	Title, etc
10	D.A. Spence	Prediction of the characteristics of two-dimensional aerofoils. *J. Aero. Sci.*, 21, p 577 (1954)
11	B.J. Powell	The calculation of the pressure distribution of a thick cambered aerofoil at subsonic speeds including the effect of the boundary layer. NPL Aero. Report 1238 (1967)
12	J. Weber	The calculation of the pressure distribution on the surface of thick cambered wings. ARC R & M No.3026 (1957)
13	P.G. Wilby	The calculation of subcritical pressure distributions on symmetric aerofoils at zero incidence. NPL Aero. Report 1208 (1967)
14	J.F. Nash A.G.J. Macdonald	The calculation of momentum thickness in a turbulent boundary layer at Mach numbers up to unity. NPL Aero. Report 1207. ARC Current Paper 963 (1966)
15	R.C. Lock P.G. Wilby B.J. Powell	The prediction of aerofoil pressure distributions for sub-critical viscous flows. *Aero. Qu.*, 21, p 291 (1970)
16	M.C.P. Firmin	The calculation of pressure distribution, lift and drag, on single aerofoils at subcritical speeds. Part I Interim method. RAE Technical Report 72235 (1973)
17	J.E. Green	Application of Head's entrainment method to the prediction of turbulent boundary layers and wakes in compressible flow. RAE Technical Report 72079 (1972)
18	R.H. Blockley M.D. Hodges	Comparisons between selected experimental data and current first-order viscous theory for subcritical flow over two-dimensional aerofoils. UK Ministry of Defence S & T Memo-2-78 (1978)
19	E.M. Murman J.D. Cole	Calculation of plane steady transonic flows. *AIAA Journal*, 9, p 114 (1971)
20	J.A. Krupp	The numerical calculation of plane steady transonic flows past lifting airfoils. Boeing Sci. Res. Lab. Paper D180-12958-1 (1971)
21	A.F. Jones M.C.P. Firmin	On the calculation of viscous effects on the supercritical flow past an aerofoil. RAE Technical Report 72233 (1973)
22	M.G. Hall M.C.P. Firmin	Recent developments in methods for calculating transonic flows over wings. ICAS Paper 74-18 (1974)
23	C.M. Albone D. Catherall M.G. Hall Gaynor Joyce	An improved numerical method for solving the transonic small-perturbation equation for the flow past a lifting aerofoil. RAE Technical Report 74056 (1974)
24	P.R. Garabedian D.G. Korn	Analysis of transonic airfoils. *Comm. Pure Appl. Math.*, 24, p 841 (1971)
25	F. Bauer P.R. Garabedian D.G. Korn	Supercritcal wing sections. (Lecture notes in economics and mathematical systems, No.66). Springer-Verlag, Berlin (1972)
26	F. Bauer P.R. Garabedian D.G. Korn A. Jameson	Supercritical wing sections II. (Lecture notes in economics and mathematical systems, No.108). Springer-Verlag, Berlin (1975)
27	A. Jameson	Numerical computation of transonic flow with shock waves. Symposium Transsonicum II, p 385. Springer-Verlag, Berlin (1976)
28	E.M. Murman	Analysis of embedded shock waves calculated by relaxation methods. *AIAA Journal*, 12, p 626 (1974)

REFERENCES (continued)

No.	Author	Title, etc
29	Ed. A. Rizzi H. Viviand	GAMM workshop on numerical methods for the computation of inviscid transonic flow with shock waves; held at FAA, Stockholm (to be issued) (1980)
30	T.C. Adamson A.F. Messiter	Analysis of two-dimensional interactions between shock waves and boundary layers. *Ann. Rev. Fluid Mech.*, 12, p 103 (1980)
31	J.E. Green	A discussion of viscous/inviscid interactions at transonic speeds. RAE Technical Report 72050 (1972)
32	F. Bauer P.R. Garabedian	Computer simulation of shock wave boundary layer interaction. *Comm. Pure Appl. Math.*, 26, p 659 (1973)
33	J.J. Kacprzynski	A second series of wind tunnel tests of the shockless lifting aerofoil No.1. Project Report 5 × 5/0062, NRC of Canada, Ottawa (1972)
34	J.J. Kacprzynski	Wind tunnel tests of a shockless lifting aerofoil No.2. Lab. Tech. Report LTR-HA-5×5/0067, NRC of Canada, Ottawa (1973)
35	P.C. Bavitz	An analysis method for two-dimensional transonic viscous flow. NASA TN D-7718 (1975)
36	P. Bradshaw D.H. Ferriss	Calculation of boundary-layer development using the turbulent energy equation: compressible flow on adiabatic walls. *J. Fluid Mech.*, 46, Pt.1 (1971)
37	M.R. Collyer	An extension to the method of Garabedian and Korn for the calculation of transonic flow past an aerofoil to include the effects of a boundary layer and wake. RAE Technical Report 77104 (1977)
38	M.R. Collyer R.C. Lock	Improvements to the viscous Garabedian and Korn (VGK) method for calculating transonic flow past an aerofoil. RAE Technical Report 78039 (1978)
39	M.R. Collyer R.C. Lock	Prediction of viscous effects in steady transonic flow past an aerofoil. *Aero. Qu.*, 30, p 485 (1979)
40	J.E. Green D.G. Weeks J.W.F. Brooman	Prediction of turbulent boundary layers and wakes in compressible flow by a lag-entrainment method. ARC R & M No.3791 (1973)
41	C.C.L. Sells	Numerical solutions of the Euler equations for transonic flow past a lifting aerofoil. RAE Technical Report 80065 (1980)
42	P.H. Cook M.A. McDonald M.C.P. Firmin	Aerofoil RAE 2822 - pressure distributions, and boundary layer and wake measurements. AGARD AR 138, Paper A6 (1979)
43	L.F. East P.D. Smith P.J. Merryman	Prediction of separated flow by the lag-entrainment method. RAE Technical Report 77046 (1977)
44	R.E. Melnik	Recent developments in a boundary layer theory for computing viscous flows over airfoils. Paper presented at USAF/FRG Data Exchange Meeting, Meersberg, April 1979
45	G.S. Deiwert	Computation of separated transonic turbulent flow. *AIAA Journal*, 14, p 735 (1976)
46	W. Mason D.A. Mackenzie M.A. Stern J.K. Johnson	A numerical three-dimensional viscous transonic wing-body analysis and design tool. AIAA 78-101 (1978)
47	W.F. Ballhaus F.R. Bailey J. Frick	Improved computational treatment of transonic flow about swept wings. NASA CP-2001 (1976)
48	W. Kordulla	Investigations related to the inviscid-viscous interaction in transonic flows about finite 3-D wings. *AIAA Journal*, 16, p 369 (1978)

REFERENCES (concluded)

No.	Author	Title, etc
49	W. Kordulla	Viscous transonic flows about 3-D wings. *Z. Flugwis. Weltraumforsch.*, 2, p 306 (1978)
50	T. Cebeci	Calculation of three-dimensional boundary layers. II Three-dimensional flows in Cartesian coordinates. *AIAA Journal*, 13, p 1056 (1975)
51	E. Krause	Numerical solutions of boundary layer equations. *AIAA Journal*, 5, p 1231 (1967)
52	F.T. Lynch	Recent applications of advanced computational methods in the aerodynamic design of transport aircraft configurations. *Aero. J., R.Ae.S.*, 82, p 495 (1978)
53	A. Jameson D.A. Caughey	Numerical calculation of the transonic flow past a swept wing. New York University ERDA Rep. C00-3017-140 (1977)
54	T. Cebeci K. Kaups J.A. Ramsey	A general method for calculating three-dimensional compressible laminar and turbulent boundary layers on arbitrary wings. NASA CR-2777 (1977)
55	S.G. Hedman	Pressure distributions for a swept wing body configuration obtained from coupling transonic flow calculations and boundary layer calculations. AGARD CP 204, Paper 18 (1977)
56	W. Schmidt S.G. Hedman	Recent explorations in relaxation methods for three-dimensional transonic potential flow. ICAS Proceedings (1976)
57	P.D. Smith	An integral prediction method for three-dimensional compressible turbulent boundary layers. ARC R & M No.34452 (1973)
58	A.L. da Costa	Application of computational aerodynamics methods to the design and analysis of transport aircraft. ICAS Paper B2-01 (1978)
59	A. Jameson D.A. Caughey	A finite volume method for transonic potential flow calculations. AIAA Paper 77-635 (1977)
60	J.D. McLean	Three-dimensional turbulent boundary layer calculations for swept wings. AIAA Paper 77-3 (1977)
61	C.M. Albone M.G. Hall G. Joyce	Numerical solutions for transonic flows past wing-body combinations. Symposium Transsonicum II, p 541, Springer Verlag (1976)
62	K.G. Winter L.H. Ohman	Recommendations for future testing: from 'Experimental data base for computer program assessment'. AGARD AR 138 (1979)

Copyright ©, Controller HMSO, London 1980

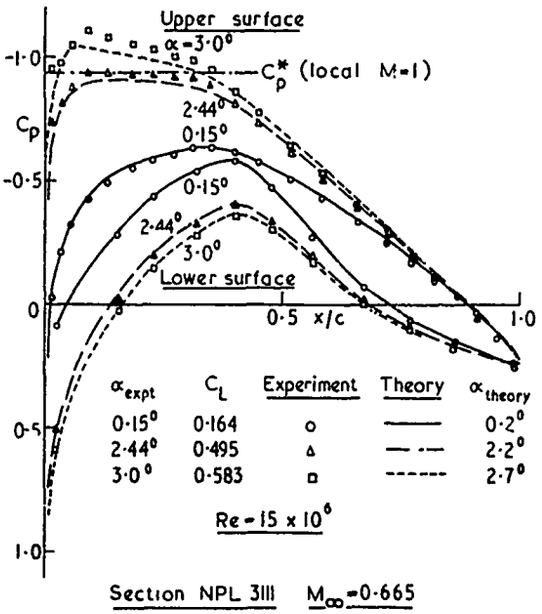


Fig 1 Pressure distributions in viscous flow: Powell's method[15]

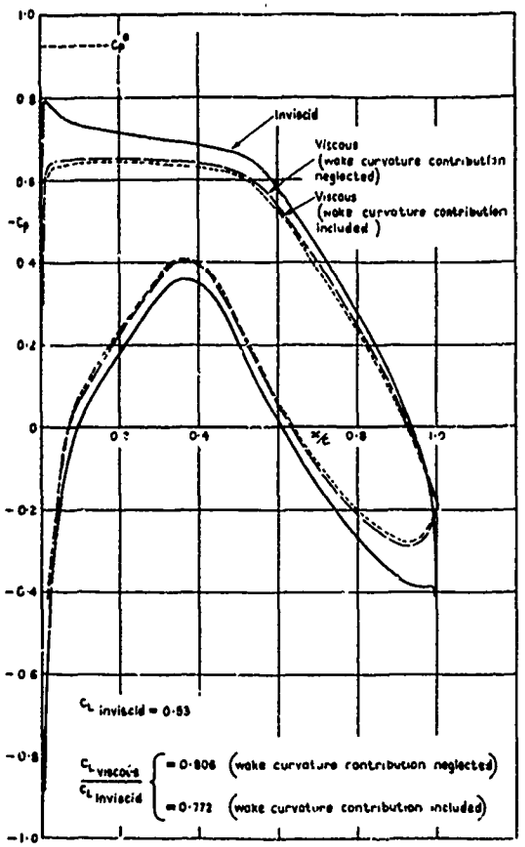


Fig 2 Calculated pressure distributions: Firmin's method[16]. RAE 2822, M_∞ = 0.667, α = 1.06°. Re = 6 × 10^6

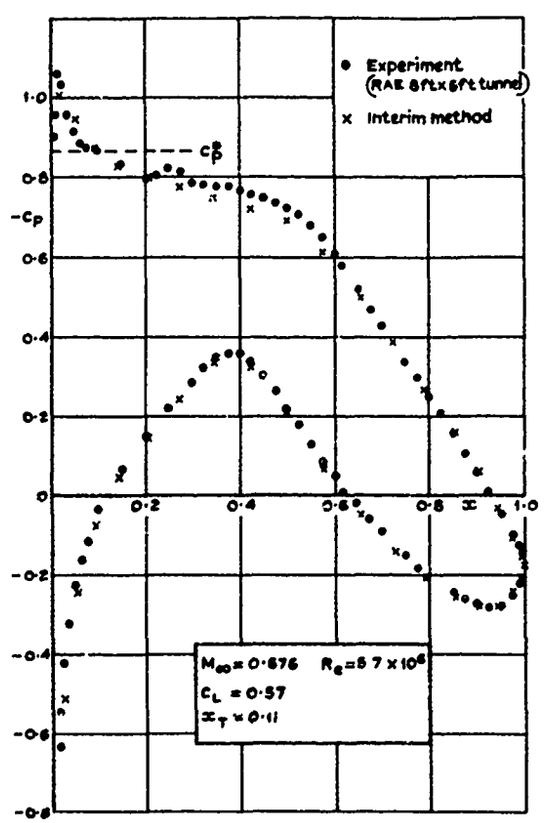


Fig 3 Measured and theoretical pressure distributions: Firmin's method[16]. RAE 2822, α_{eff} = 2.03°

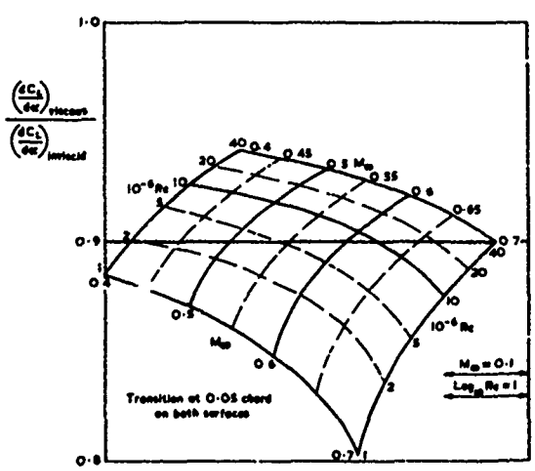


Fig 4 Viscous effects on $\frac{dC_L}{d\alpha}$: NACA 0012

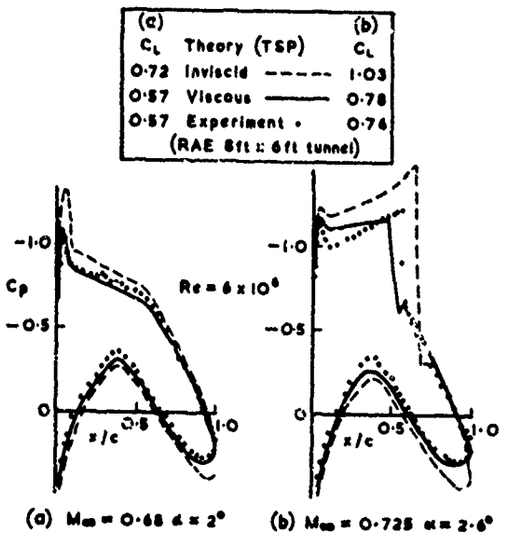


Fig 5 Viscous effects on RAE 2822 aerofoil: Jones and Firmin[21]

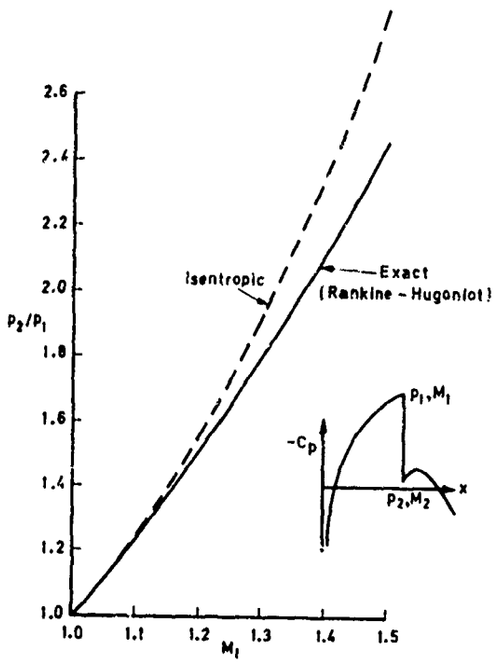
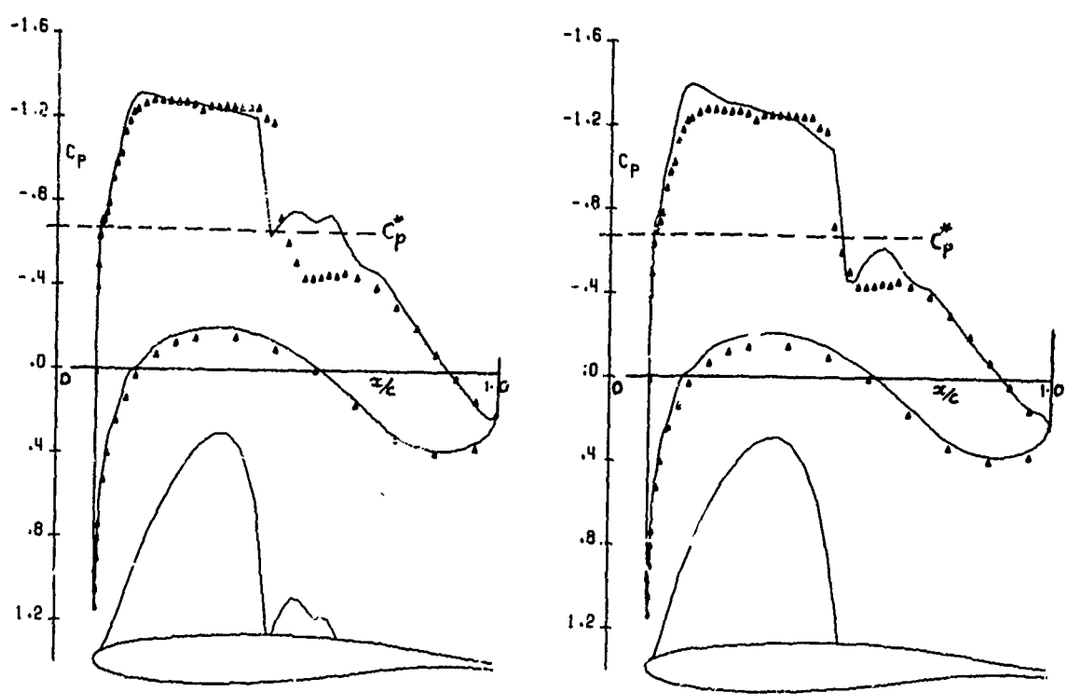


Fig 6 Pressure ratios for normal shocks



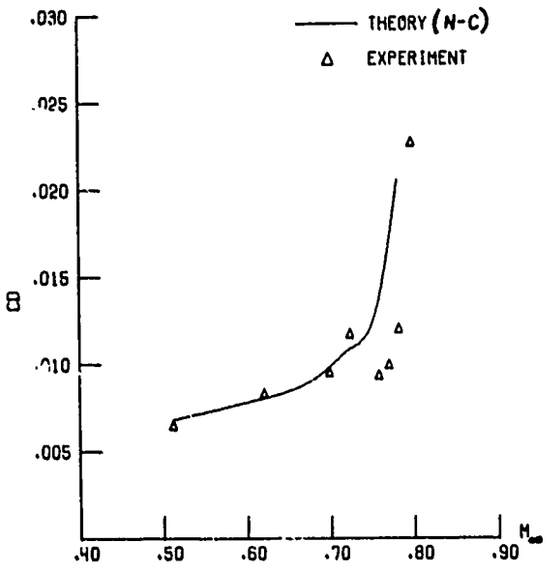
AIRFOIL 75-06-12 M=N=160=30 NCY= 400 R=20 MILLION
— THEORY M=.727 ALP= 2.16 CL= .787 CD=.0193
Δ EXPERIMENT M=.727 ALP= 3.49 CL= .787 CD=.0185

(a) N-C version

AIRFOIL 75-06-12 M=N=160=30 NCY= 400 R=20 MILLION
— THEORY M=.727 ALP= 1.97 CL= .787 CD=.0124
Δ EXPERIMENT M=.727 ALP= 3.49 CL= .787 CD=.0185

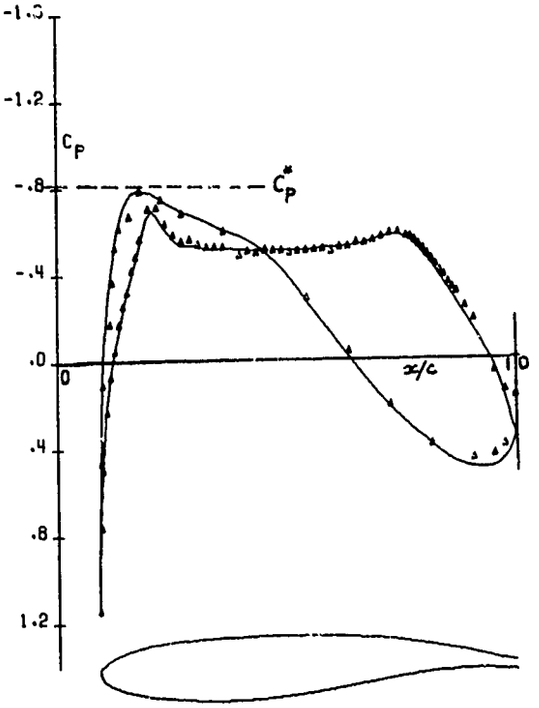
(b) Q-C version

Fig 7 G & K 75-06-12. M_∞ = 0.73, C_L = 0.79. BGKJ method[26]



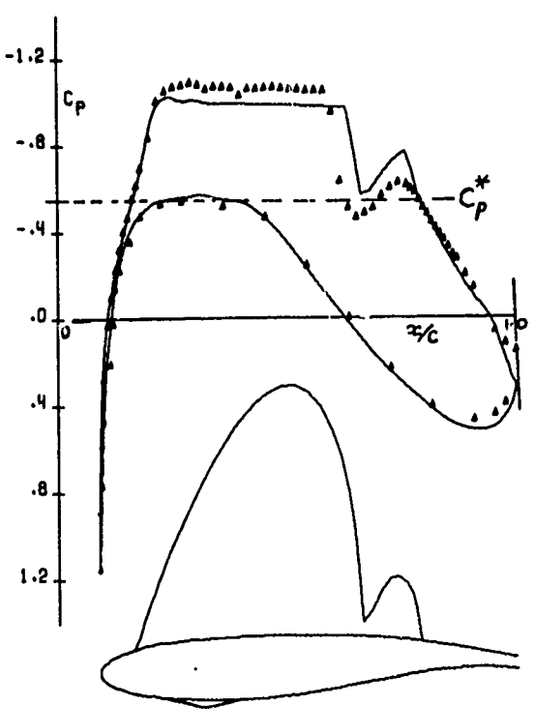
DRAG POLAR FOR AIRFOIL 75-06-12 COMPARING OTTAWA EXPERIMENTAL DATA WITH THEORETICAL ANALYSIS FOR CL = 0.6 AND R = 20 MILLION

Fig 8 G & K 75-06-12. Variation of C_D with M_∞, BGKJ method (N-C)



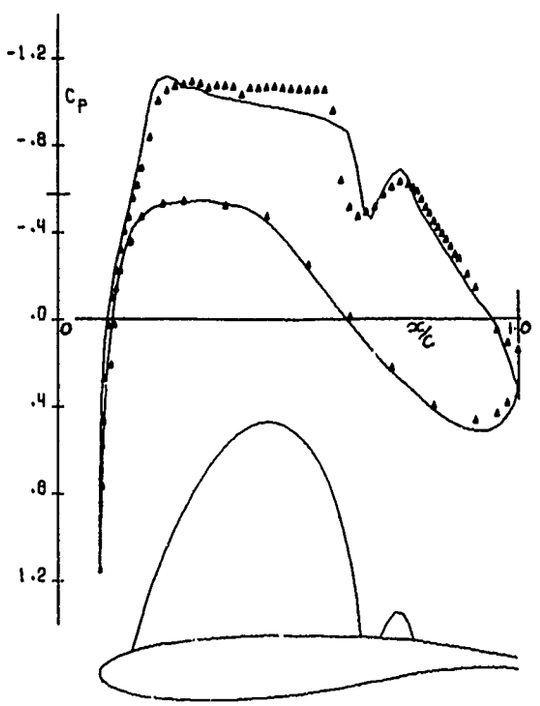
AIRFOIL 75-07-15 M=N=160=30 NCY= 400 R=20 MILLION
— THEORY M=.691 ALP= -.66 CL= .237 CD=.0095
Δ EXPERIMENT M=.691 ALP= -.02 CL= .237 CD=.0102

Fig 9(a) $M_\infty = 0.69$, $C_L = 0.24$



AIRFOIL 75-07-15 M=N=160=30 NCY= 400 R=20 MILLION
— THEORY M=.763 ALP= 1.03 CL= .584 CD=.019?
Δ EXPERIMENT M=.763 ALP= 2.01 CL= .584 CD=.0?

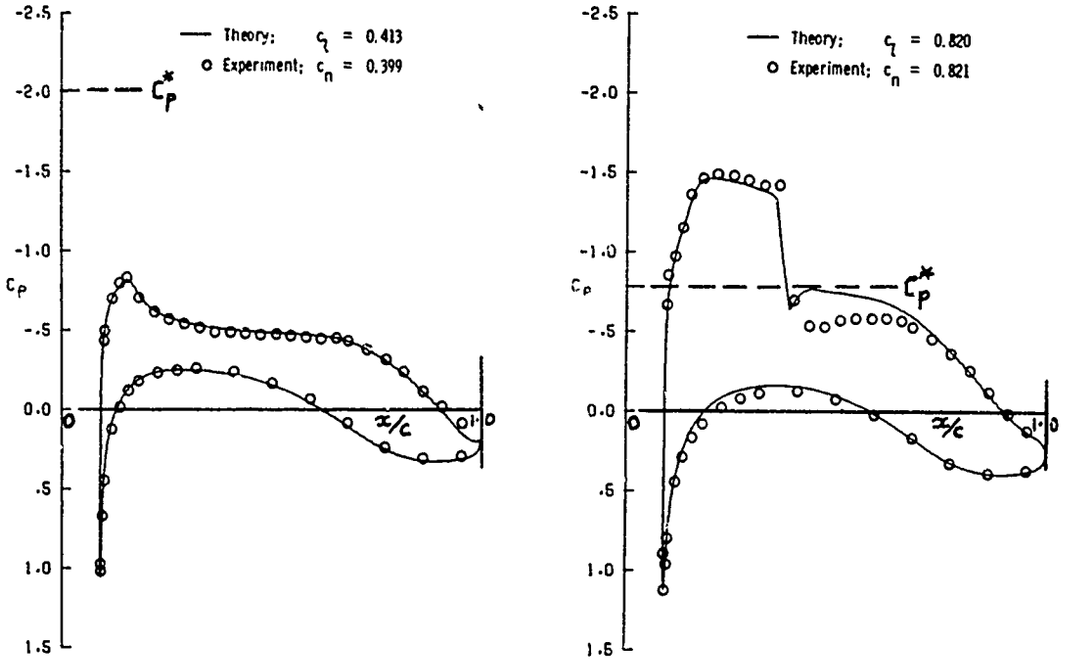
(b) $M_\infty = 0.76$, $C_L = 0.58$ (N-C)



AIRFOIL 75-07-15 M=N=160=30 NCY= 400 R=20 MILLION
— THEORY M=.755 ALP= .92 CL= .584 CD=.0123
Δ EXPERIMENT M=.763 ALP= 2.01 CL= .584 CD=.0128

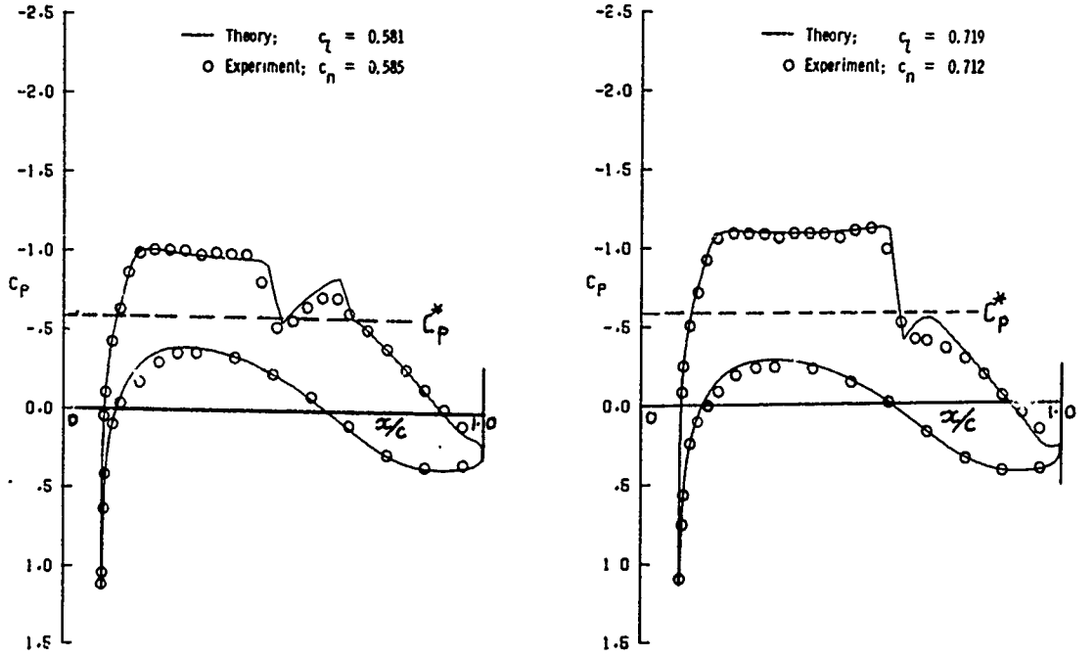
(c) $M_\infty = 0.76$, $C_L = 0.58$ (Q-C)

Fig 9 G & K 75-07-15. BGKJ method



(a) $M_\infty = 0.5=$, $\alpha = 0.75^0$

(b) $M_\infty = 0.70$, $\alpha = 2.25^0$



(c) $M_\infty = 0.75$, $\alpha = 0.45^0$

(d) $M_\infty = 0.75$, $\alpha = 1.25^0$

Fig 10 G & K 75-06-12. Bavitz' method.[35]
Re = 21 × 10^6

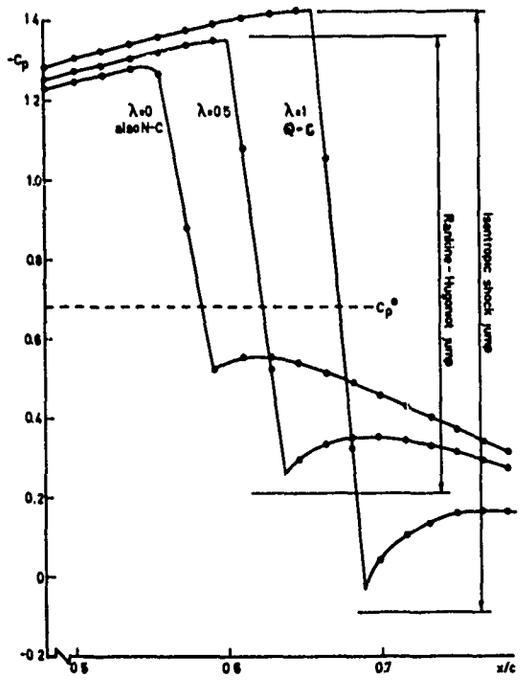


Fig 11 RAE 2822: A comparison of inviscid solutions. $M_\infty = 0.725$, $\alpha = 2^0$

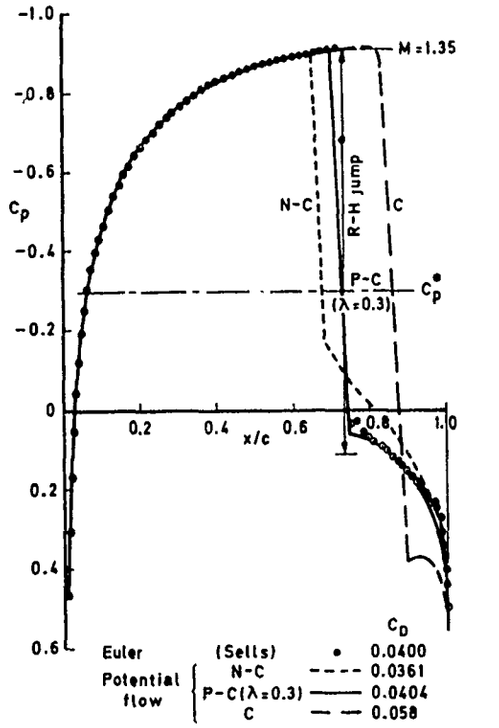
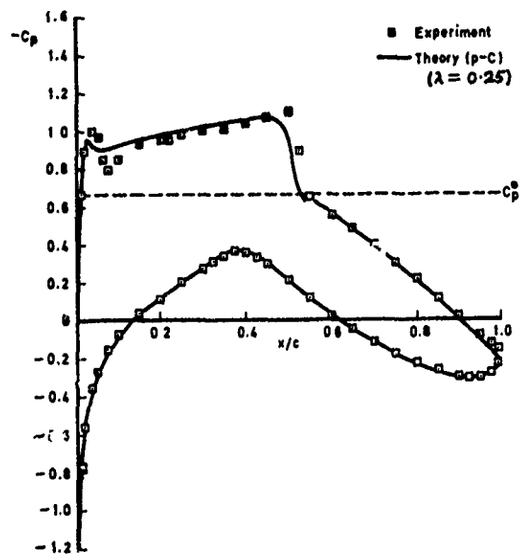
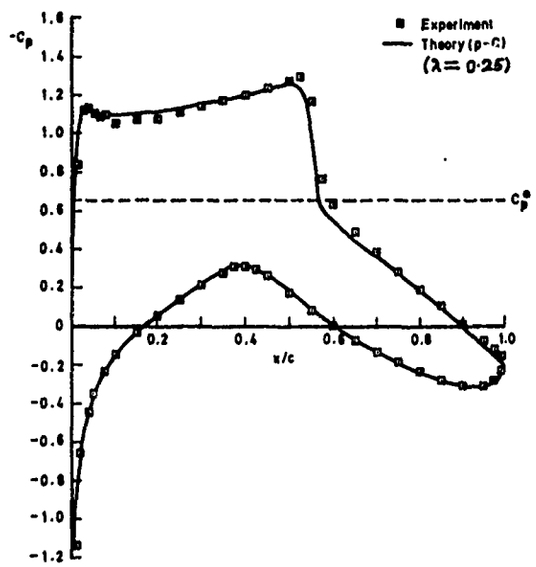


Fig 12 NACA 0012, $M_\infty = 0.85$, $\alpha = 0$. A comparison of solutions of Euler and potential flow equations



(a) $M_\infty = 0.73$, $C_L = 0.66$



(b) $M_\infty = 0.732$, $C_L = 0.79$

Fig 13 RAE 2822: Re = 6.5×10^6, VGK method[39]

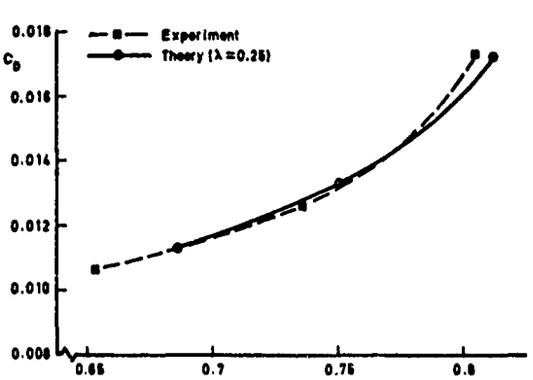


Fig 14 RAE 2822: Variation of C_D with C_L. VGK method

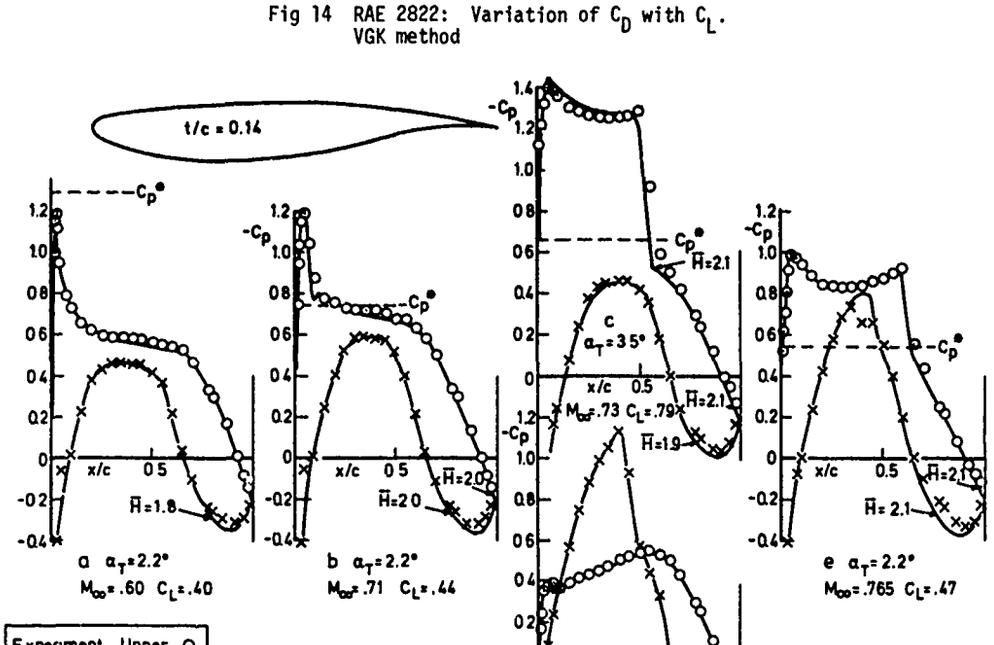


Fig 15 RAE 5217: General comparison between theory (VGK) and experiment

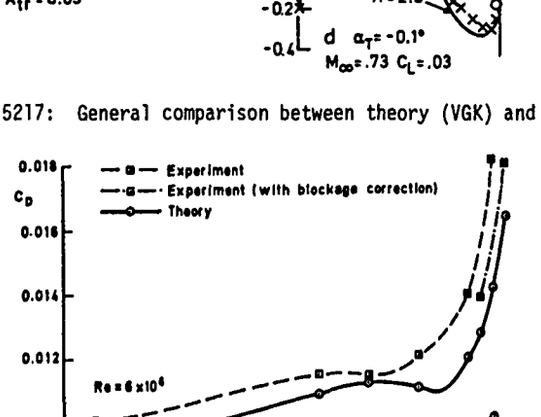
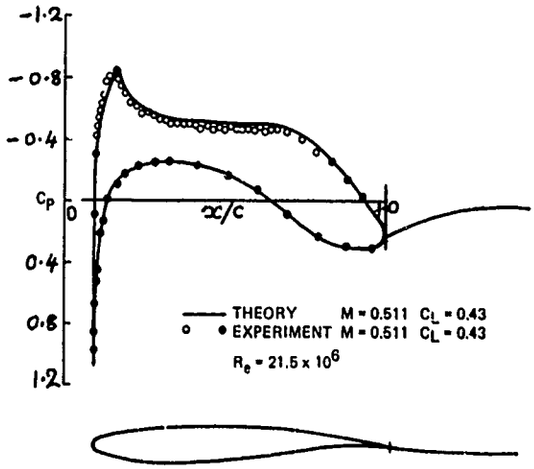
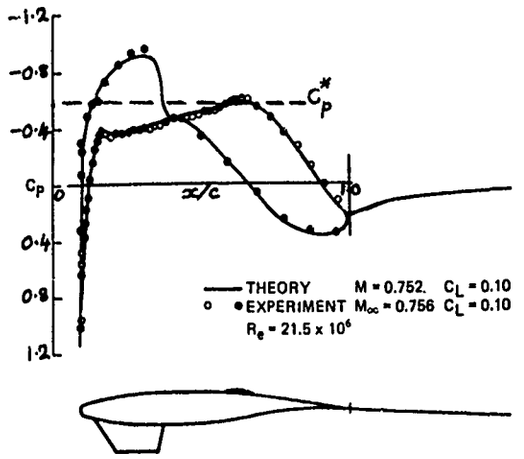


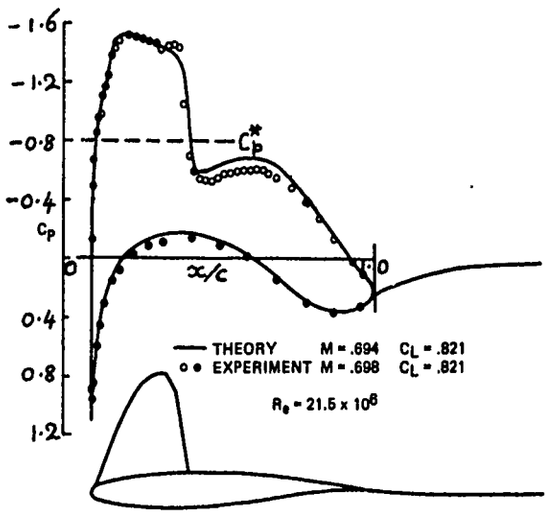
Fig 16 RAE 5217: Variation of C_D with M_∞, C_L = 0.6. VGK method



(a) M_∞ = 0.51, C_L = 0.43



(b) M_∞ = 0.75, C_L = 0.10



(c) M_∞ = 0.69, C_L = 0.82

Fig 17 Pressure distribution on G & K 75-06-12. Melnik's method[44]

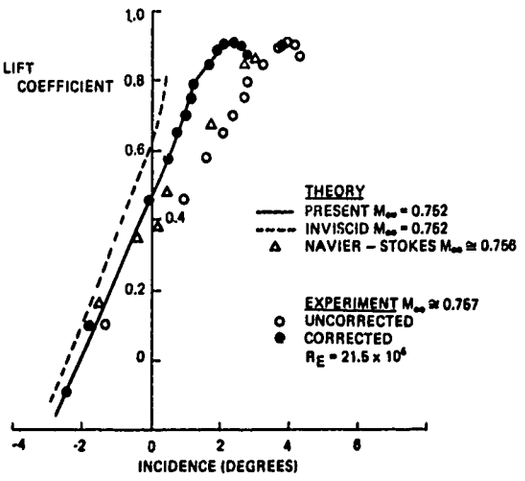


Fig 18 Lift coefficient for G & K 75-06-12. Melnik's method

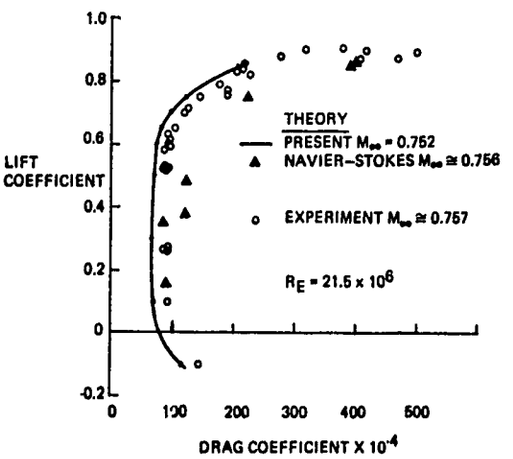


Fig 19 Drag polar for G & K 75-06-12. Melnik's method

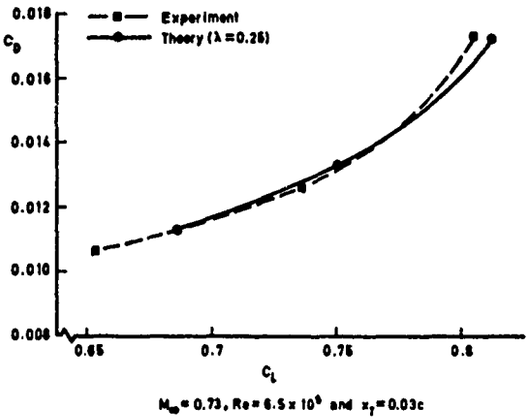


Fig 14 RAE 2822: Variation of C_D with C_L. VGK method

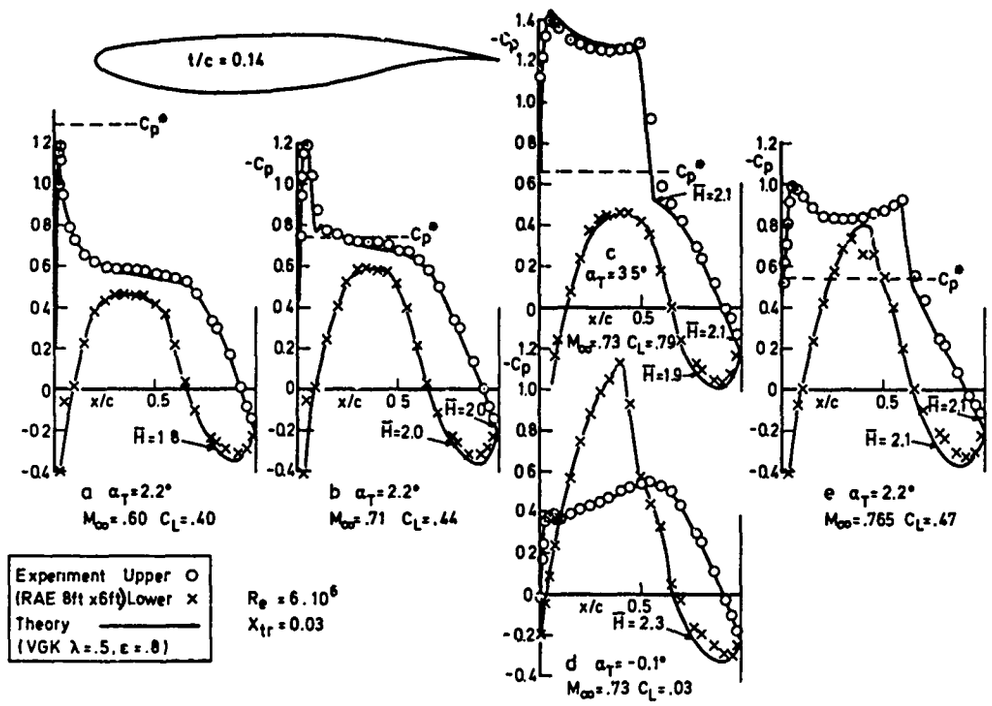


Fig 15 RAE 5217: General comparison between theory (VGK) and experiment

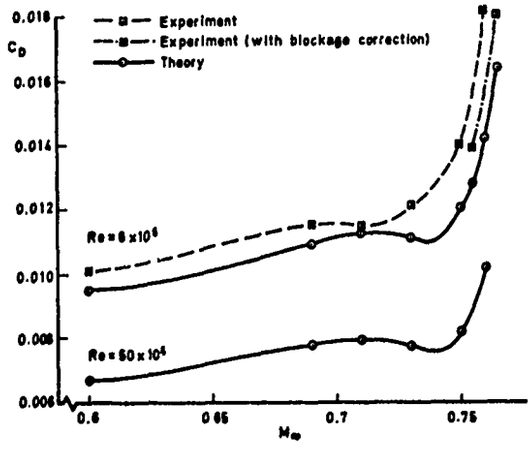
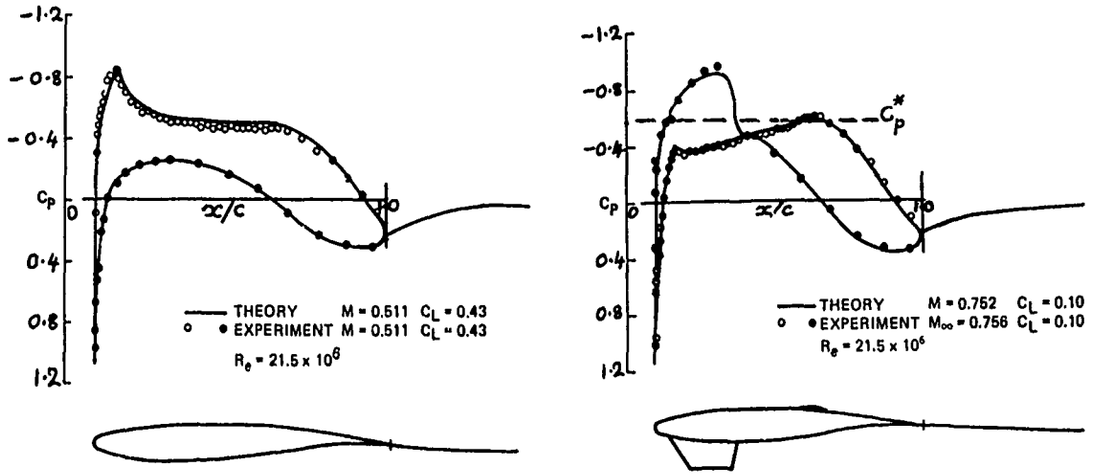
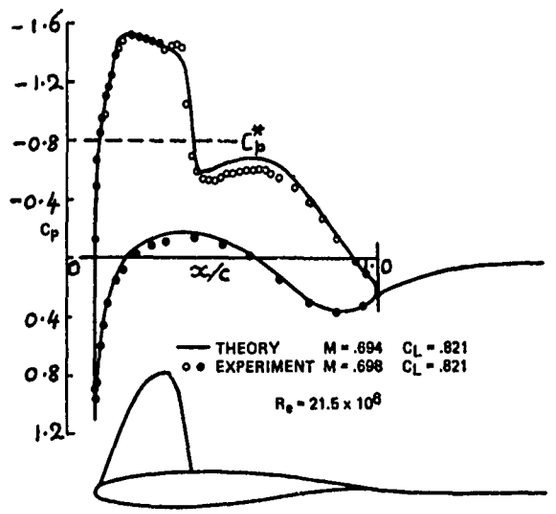


Fig 16 RAE 5217: Variation of C_D with M_∞, C_L = 0.6. VGK method



(a) M_∞ = 0.51, C_L = 0.43

(b) M_∞ = 0.75, C_L = 0.10



(c) M_∞ = 0.69, C_L = 0.82

Fig 17 Pressure distribution on G & K 75-06-12. Melnik's method[44]

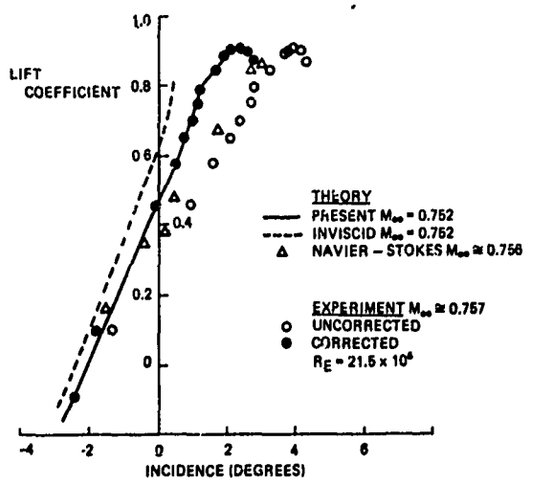


Fig 18 Lift ccefficient for G & K 75-06-12. Melnik's method

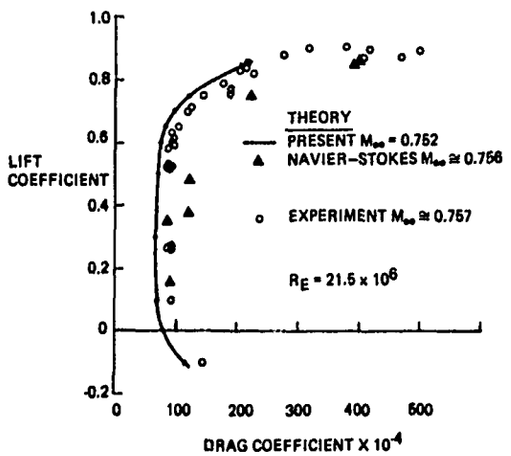


Fig 19 Drag polar for G & K 75-06-12. Melnik's method

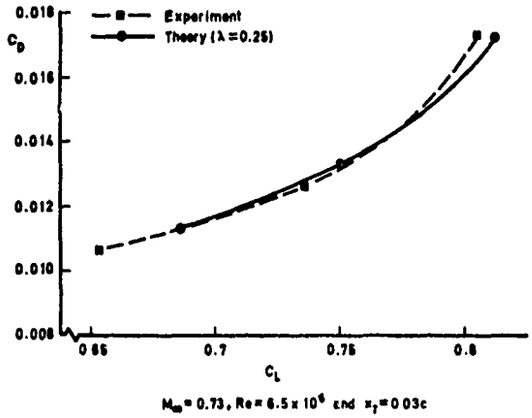


Fig 14 RAE 2822: Variation of C_D with C_L. VGK method

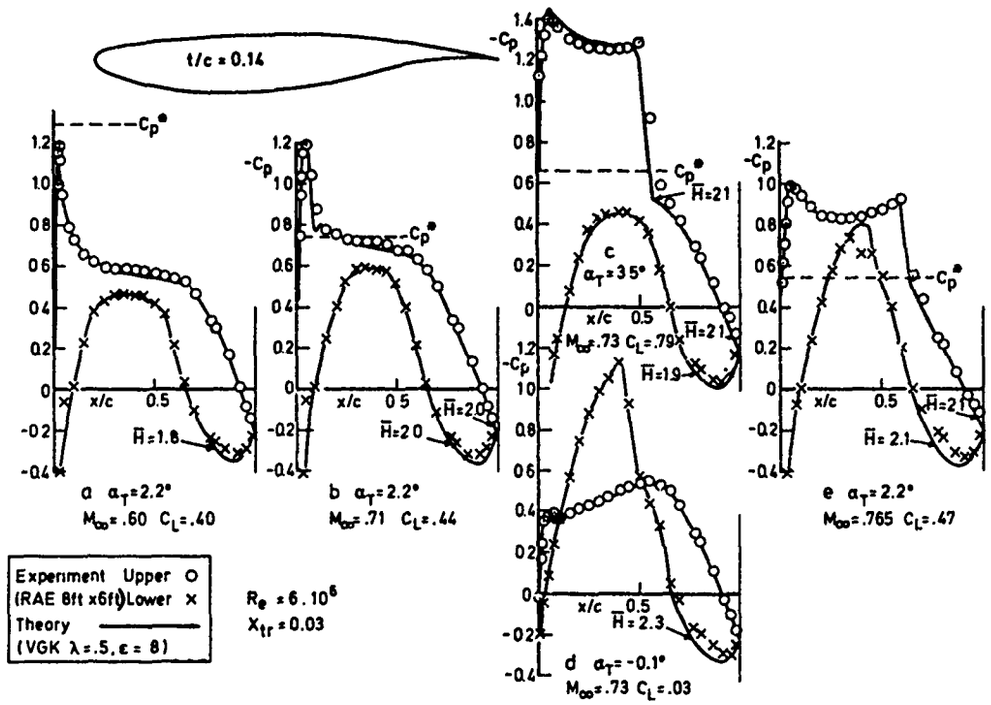


Fig 15 RAE 5217: General comparison between theory (VGK) and experiment

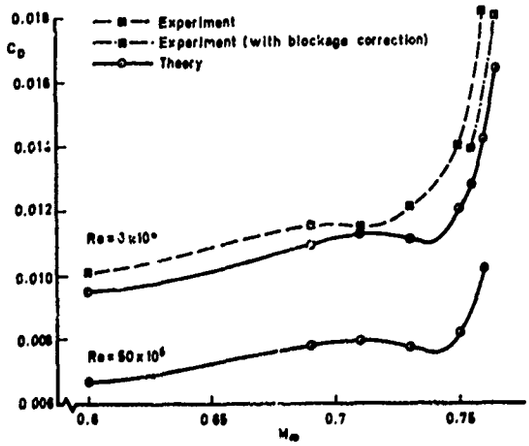
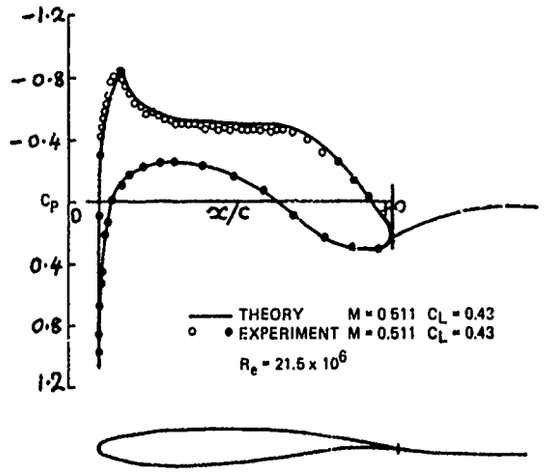
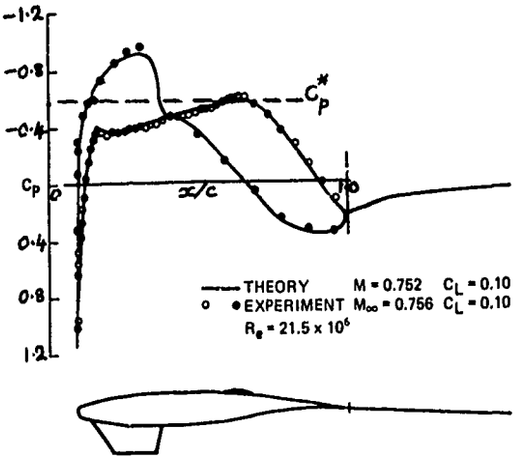


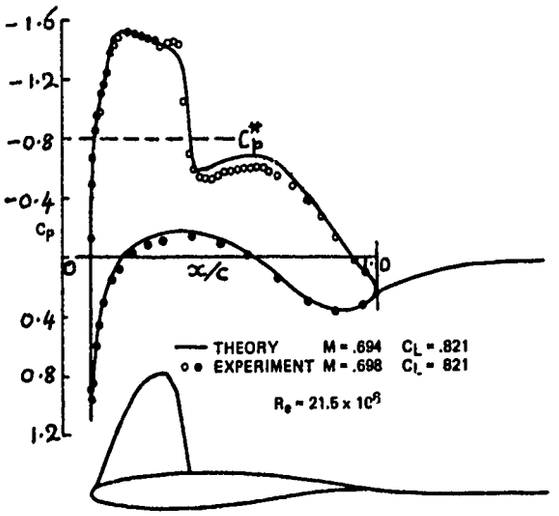
Fig 16 RAE 5217: Variation of C_D with M_∞, $C_L = 0.6$. VGK method



(a) M_∞ = 0.51, C_L = 0.43



(b) M_∞ = 0.75, C_L = 0.10



(c) M_∞ = 0.69, C_L = 0.82

Fig 17 Pressure distribution on G & K 75-06-12. Melnik's method[44]

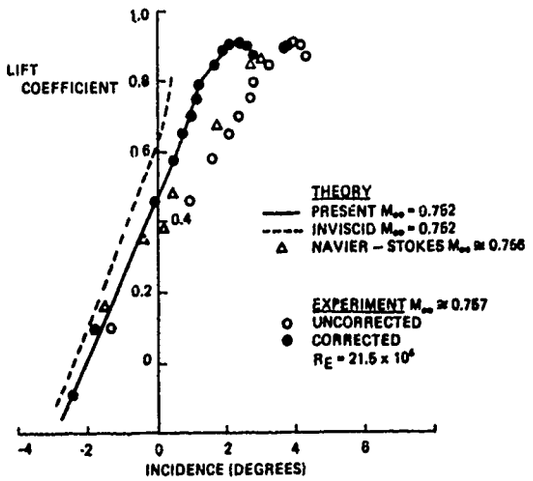


Fig 18 Lift coefficient for G & K 75-06-12. Melnik's method

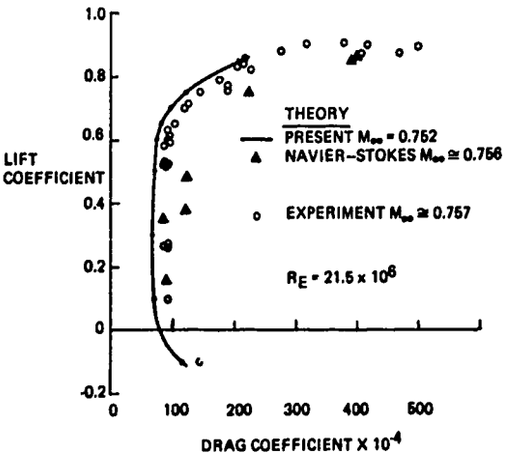
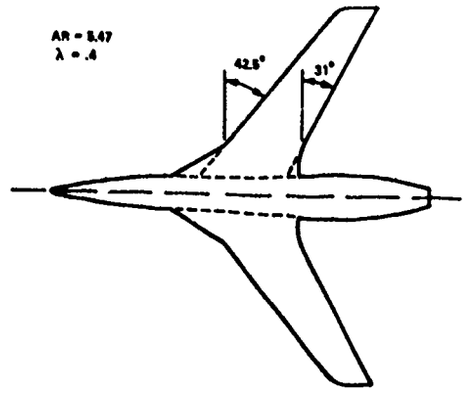
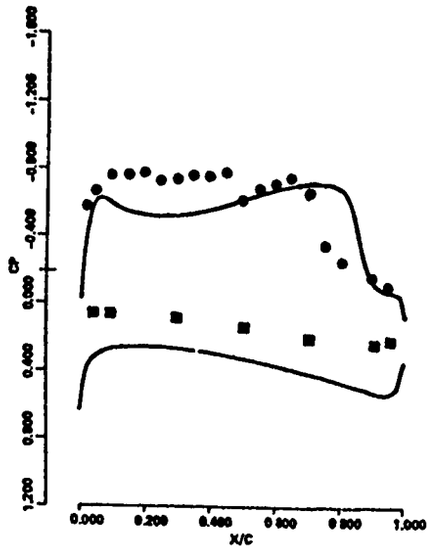


Fig 19 Drag polar for G & K 75-06-12. Melnik's method



(a) Advanced Technology Fighter



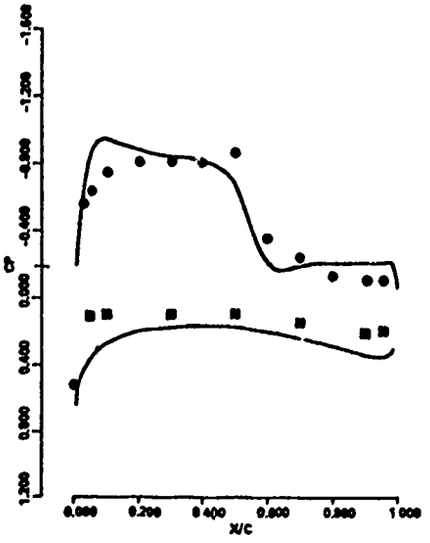
(b) y/s = 0.44



(c) y/s = 0.62



(d) y/s = 0.75



(e) y/s = 0.91

Fig 20 Pressure distributions for an 'advanced technology' fighter, $M_\infty = 0.90$, $C_L \triangleq 0.9$. Method of Mason *et al*[46]

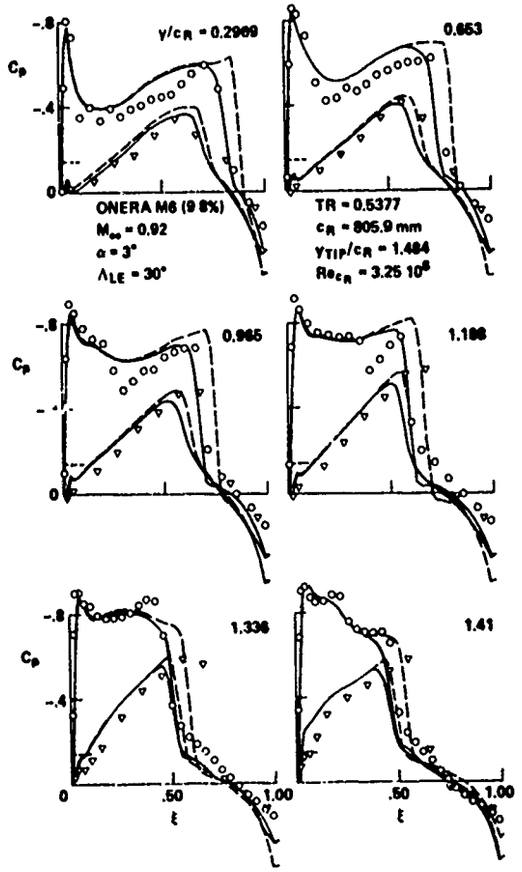


Fig 21 Comparisons of pressure distributions for the ONERA M6 wing. Kordulla's method[48]

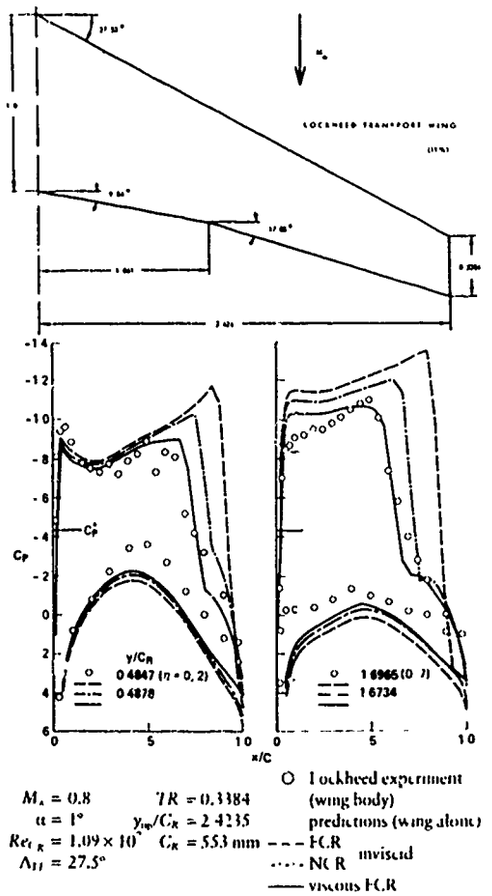


Fig 22 Comparisons of pressure distributions for a Lockheed transport wing (11% thick). Kordulla's method[49]

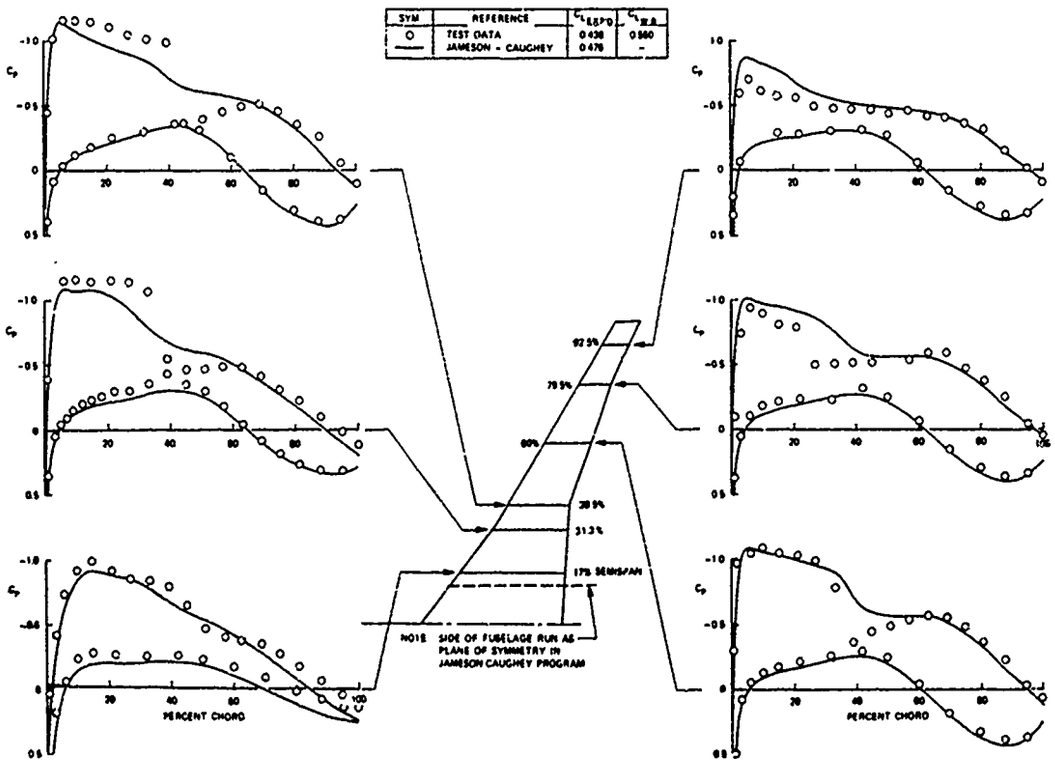


Fig 23 Comparison of pressure distributions for a Douglas transport wing, M_∞ = 0.80. Lynch's method[52]

INVISCID-VISCOUS INTERACTIONS IN THE NEARLY DIRECT DESIGN OF SHOCK-FREE SUPERCRITICAL AIRFOILS

by
H. E. Nebeck and A. R. Seebass
University of Arizona
Tucson, Arizona 85721
and
H. Sobieczky
DFVLR
Göttingen, West Germany

SUMMARY

An especially simple procedure for finding airfoil shapes that have desirable aerodynamic characteristics and that will be shock free at Mach numbers close to the highest values possible is described. The procedure accounts for overall inviscid-viscous interactions that are weak and includes the locally strong interaction at the trailing edge as incorporated in the Grumfoil algorithm.

INTRODUCTION

In the last decade substantial progress has been made in the computation of aerodynamic flow fields in which the global inviscid-viscous interaction is weak. For two-dimensional transonic flows the fundamental interactions, carefully delineated nearly a decade ago by Green (1), are now adequately modeled by computational analysis, provided that the global interaction is weak and that the boundary layer suffers at most mild separations. This is accomplished by coupling a numerical analysis of the inviscid flow, which assumes the main body of the flow is irrotational, hence derivable from a single scalar potential, with a numerical solution of an integral formulation of the boundary layer equations. Much more sophisticated computational tools, such as large eddy simulation, are becoming available but they are not yet efficient enough for their application to design problems.

The application of these analysis tools in design can take many forms. Perhaps the most basic is that of prescribing a pressure distribution and determining the airfoil that will generate this pressure field. This inverse problem is not well-posed and extensive computations are usually required in order to obtain useful results. A variant of this procedure is to prescribe desired changes to an already existing pressure field that is generated by a given airfoil. Here the inverse problem may be linearized about an existing flow and the resulting problem is more amenable to analysis. Another procedure is to use numerical optimization to find which of a family of possible airfoils will provide the best airfoil performance. Here the main limitations are the family of airfoils considered and the computational expense of exploring incremental changes for improvements in performance that are only marginally larger than the errors in the computed performance parameters. A third, but more limited, possibility also exists, namely, determining the changes required in a baseline airfoil to make the flow past it shock free at a prescribed lift coefficient and Mach number. This presumes that an airfoil baseline which meets performance goals for subcritical Mach numbers is known. One then invokes the "fictitious gas" procedure of Sobieczky (2) to find a new shape for the upper surface of the airfoil that will produce shock-free flow at the prescribed conditions. This shape is not unique, nor is it possible to find such shapes for all flow conditions. For a prescribed lift coefficient and airfoil thickness, there is a freestream Mach number above which a shock-free shape is not possible. While the feasibility of this procedure has been amply demonstrated for inviscid flows, indeed, even for three-dimensional flows (3,4), its success for flows with inviscid-viscous interaction has not previously been documented.

The goal of this paper is to demonstrate the ability of the fictitious gas procedure to design advanced shock-free airfoils at little computational expense even when inviscid-viscous interactions are taken into account.

ANALYSIS ALGORITHMS

A number of numerical algorithms have been developed to calculate the transonic flow past an airfoil in the presence of weak inviscid-viscous interactions. One of the early successes was the algorithm of Bauer et al, (5), which we will call BGKJ. It employs a nonconservative formulation of the potential equation, coupled with the integral boundary layer code of Nash and MacDonald (6) and a constant thickness wake model. The nonconservative difference scheme fails to conserve mass and underpredicts the irrotational shock strength. As a consequence, the inviscid version of this algorithm gave results that agreed well with experimental results for the pressure coefficient when compared at the same Mach number and lift coefficient. Collyer and Lock (7) modified the inviscid analysis portion of this program to include a combination of conservative and nonconservative differencing in order to better capture the correct shock pressure rise, and coupled it with Green's lag-entrainment method (8) for computing the turbulent boundary layer. They included the modification of the inviscid flow due to wake curvature but did not model the strong interaction that occurs at the trailing edge. Nandanan, Stanewsky, and Inger (9) have used Jameson's conservative version (10) of the BGKJ algorithm together with Rotta's integral dissipation method (11) and Inger's model of shock-boundary layer interaction (12) to compute flows with weak embedded shock waves. Perhaps the most

advanced algorithm of this type in the U.S. is that due to Melnik, Chow, and Mead (13). They coupled Jameson's inviscid algorithm with Green's lag-entrainment method for the boundary layer. The effects of the strong interaction near the trailing edge are also included in the algorithm. This is accomplished by incorporating the results of Melnik and Chow (14) for the multi-layered turbulent boundary layer at a cusped trailing edge. This coupled calculation provides a self-consistent result for the inviscid flow, the boundary layer, and the wake. It also removes the singularity in the inviscid pressure associated with the trailing edge of the airfoil. Wake curvature effects are included and are found to have a significant effect on the results. This algorithm has been called "Grumfoil" by its authors, and we will use the same appellation here. While no shock-boundary layer interaction model is included, the algorithm seems to be accurate for shock strengths for which the irrotational approximation is itself satisfactory.

SHOCK-FREE DESIGN

Inviscid analysis algorithms such as those discussed above have amply demonstrated the generality of Morawetz's (15) result of the mid-1950s, namely, that shock-free flows are mathematically isolated one from another. Despite this isolation they have played an important role in providing moderate increments in aircraft performance. Wind tunnel research by Pearcey at the National Physical Laboratory (16) and Whitcomb (17) at NASA Langley Research Center first demonstrated that such flows could be realized and would have important applications. Subsequently, Garabedian and Korn (18), Nieuwland (19), Boerstoel (20), and Sobieczky (21) developed analytical tools for the prescription of shock-free airfoil shapes. These tools relied on the hodograph transformation, and viscous effects could only be accounted for to the extent that the boundary layer could be computed independently of the inviscid flow. The extension of this capability to the physical plane by the introduction of a fictitious gas for a preliminary calculation of the supersonic portion of the flow field makes it possible to design shock-free airfoils with a proper accounting of the coupled nature of the inviscid and viscous flow fields. This capability requires one crucial approximation that has now been justified by numerical experiment, namely, that the boundary layer displacement thickness is not altered in any consequential way by the difference between the pressure field of the fictitious gas and that of the real gas. Given no essential differences in the boundary layer displacement thickness in the supersonic domain due to the difference between the real and fictitious pressures there, nor any due to the minor change in airfoil thickness, then the inviscid and viscous flow fields must be correct and correctly coupled.

We begin the design process with the selection of a baseline airfoil. Normally, this would be an airfoil that meets subcritical design goals and that has a reasonable amount of upper surface curvature. Here we have used a supercritical section, both for convenience and to see if we can improve its performance somewhat. Our goal here, however, is not advanced airfoil design, but rather, to show that the fictitious gas design procedure is feasible in the presence of coupled inviscid-viscous interactions. We then modify the Grumfoil algorithm to incorporate a fictitious density-flow speed relation when the Mach number exceeds one. Both the baseline airfoil and the fictitious density relationship are at the investigator's disposal and they interact in a way that allows the generation of a limited family of candidate airfoils. Because our concern is with demonstrating the feasibility of the proposed procedure we limit our attention to the simple relation

$$\rho/\rho^* = (a^*/q)^P, \tag{1}$$

where ρ and q are the fictitious density and real flow speed and ρ^* and q^* are their real sonic values. The exponent P is a parameter that varies the gas law (1). For values of P less than one relation (1) insures that the governing equation, namely,

$$\mathrm{div}(\rho q) = 0, \tag{2}$$

where $q = \nabla\phi$, and ϕ is the velocity potential, remains elliptic. For such relations the fictitious mass flow in the supersonic domain is greater than it would be for a real gas. The solution to this fictitious flow problem is used to provide values for the flow deflection on the embedded sonic line. To insure the accuracy of this data we generally insist on convergence to a maximum residual of 10^{-6} on a 160 by 32 grid. This data on the sonic line is used to compute the velocity potential and stream function there. A simple characteristics routine is then used to march down from the sonic line to find the streamline consistent with stream function values at the sonic line airfoil juncture. (This must be done in a way that is consistent with the mass flow added to the flow by the boundary layer displacement effect.) This defines the new body streamline if the characteristics calculation succeeds. It may not, but may rather signal the intervention of a limit line and indicate the failure of the sonic line data to be consistent with shock-free flow. In this event the baseline airfoil and fictitious density law can be modified in an attempt to circumvent the failure. The new airfoil surface will be thinner than the baseline airfoil because the real density is less than the fictitious density and, hence, for the fixed mass flow entering the sonic line, the real gas requires more area. The amount that the airfoil's vertical coordinate is thereby reduced can be added to the baseline airfoil and the process repeated until the baseline airfoil thickness is retained in the shock-free design. Changes in the choice of the gas law, here simply limited to changes in P, also have an effect on airfoil thickness, albeit a small one. Further progress in airfoil design requires an understanding of the relationship between the baseline airfoil and the fictitious gas law chosen. We do not explore that question further here.

The designed airfoil must now be analyzed by the original algorithm to see how well it performs. The boundary layer calculation used in the design process was based upon the pressure gradient of the fictitious gas calculation. The designed airfoil will have a somewhat different pressure gradient. If the displacement thickness were correct, then only the pressure field in the supersonic domain is altered. However, this change in the pressure field alters the boundary layer displacement thickness and, to some degree, the extent of the supersonic domain. We find in practice, however, that the error in the displacement thickness is so small that we need not correct for it.

RESULTS

We selected the VFW airfoil Va2 for our baseline as characteristic of the wing sections that will be used on future commercial transport aircraft. This airfoil, which is 12.5% thick, has a design Mach number, M_∞, of 0.73 and a design lift coefficient, C_ℓ of 0.525. Our coordinates are slightly different from those for the Va2 and we have used our own designation, 47070M, for this baseline airfoil. As this airfoil is already an advanced design we only examined a modest increment in design conditions, namely, M_∞ = 0.75 and C_ℓ = 0.550 at a flight Reynolds number of 35 million. Figure 1 depicts the pressure distribution and sonic line - shock wave shape for the baseline airfoil at the new flight conditions. It has a drag of 67 counts. When we repeat this calculation using the fictitious density law (1) with P = 0.9, we find results like those depicted in Figure 2. Because we are solving an elliptic equation we obtain a smooth pressure distribution and well behaved sonic line. Although it has no physical meaning we note the drag is now 61 counts. None of this can be wave drag because we solved an elliptic equation and we must attribute it to viscous effects. The undulations in the upper surface pressure near the leading edge are due to irregularities in the airfoil shape and the boundary layer's transition to turbulent flow.

We now use the flow speed and deflection angle on the sonic line to calculate the flow in the supersonic domain in the manner described above. This defines the new body surface. Since it is thinner than the original body, we choose to repeat the process with a baseline airfoil shape that is the original airfoil plus a multiple of the difference between the original and the shape calculated using the design procedure outlined above. The pressure distribution and sonic line for the fictitious flow past this airfoil are depicted in Figure 2. Performing the design process on this new baseline results in an airfoil that has essentially the same thickness as the original baseline airfoil. We now compute the flow past this new airfoil (47073) to see if we have indeed found improved performance.

The results of this final calculation are shown in Figure 3. Shock-free flow has been achieved. The calculation was done with the lift coefficient set to 0.550. The drag coefficient, not too surprisingly, is the same as that calculated using the fictitious gas. Figure 4 compares the redesigned airfoil and the original baseline airfoil with the vertical scale magnified five times so that the small differences between the two airfoils can be observed. The improvement in lift to drag ratio over the baseline at M_∞ = 0.75 is 10%. The entire design process required about 500 CPU seconds on a CDC 7600. It could be repeated to recover the very small loss in airfoil thickness.

The success of the design procedure depends on the boundary layer displacement thickness for the fictitious gas analysis being essentially the same as that for the real gas analysis of the new airfoil. Figure 5 compares the displacement thickness for the original airfoil, 47070M, that for the fictitious gas flow past a thickened airfoil 47070B, and that of the final design, 47073. There are very minor differences between the displacement thickness for the 47070B and the 47073 airfoils at about 62% of the chord. This is more readily noticed in Figure 6, which compares the skin friction coefficients for the three airfoils. This small difference in the displacement thickness manifests itself in a small difference in the subsonic portion of the pressure distributions of Figures 2 and 3 just downstream of the sonic line airfoil juncture. The difference is so small that it can really only be discerned when the two pressure distributions are overlayed. The supersonic pressure is, of course, always different.

If we compare the off-design performance of the two airfoils we discover that the improvement in the drag divergence Mach number is not even 0.01. Figures 7 and 8 compare the pressure distributions and the sonic line shapes for the two airfoils at M_∞ = 0.74 and 0.76. From these results it is easy to see how the new design achieves the modest improvement in drag at M_∞ = 0.75. The variation in the drag coefficient with Mach number at the design lift coefficient and with the lift coefficient at the design Mach number for the two airfoils is depicted in Figures 9 and 10. If we repeat the design process at a higher Mach number, and with a somewhat thicker baseline airfoil, we find another new airfoil, 47081, which achieves a 0.015 increment in the drag rise Mach number. The drag coefficient as a function of Mach number for the 47081 is also shown in Figure 9. Figure 11 depicts the pressure distribution and sonic line shape for the 47081 airfoil and Figure 12 compares this airfoil with the 47070M baseline airfoil. While the improvement in drag rise Mach number is very small, there can be no doubt that, other things being equal, such small improvements are of major importance in the design of a commercial transport. There is a limit to the Mach number at which shock-free designs can be found for a fixed lift and airfoil thickness. With the 47070M as a baseline this would seem to be about M_∞ = 0.77 for C_ℓ = 0.550 and 12.5% thickness.

CONCLUSION

We have described a computationally efficient method for finding airfoil shapes with desirable aerodynamic properties that are also shock-free at supercritical Mach

numbers. The process of making them shock free can be successfully carried out even in the presence of coupled inviscid-viscous interactions. The shock-free design process is as reliable as the analysis algorithm used to compute the flow field. A wide range of airfoil shapes can be found, depending on modifications to a selected baseline and on the choice of the gas law. There is a limit to the maximum drag divergence Mach number that can be achieved for a prescribed airfoil thickness and lift coefficient. Our experience with this process in inviscid flow gives us confidence that these limits can be achieved with an artful selection of baseline airfoils and fictitious gas laws.

ACKNOWLEDGEMENTS

This research was supported by Grant Number AFOSR-76-2954I from the Air Force Office of Scientific Research and by Grant Number N00014-76-C-0182 from the Office of Naval Research.

REFERENCES

1. Green, J. E. "Some Aspects of Viscous-Inviscid Interactions at Transonic Speed, and Their Dependence on Reynolds Number," AGARD CP-83-71, 1971, pp. 2-1, 2-12.

2. Sobieczky, H. "Die Berechnung lokaler Räumlicher Überschallfelder," ZAMM, 58T, 1978, pp. 215-216.

3. Sobieczky, H., Yu, N. J., Fung, K-Y., and Seebass, A. R. "New Method for Designing Shock-free Transonic Configurations," AIAA J., Vol. 17, No. 7, July 1979, pp. 722-729.

4. Fung, K-Y., Sobieczky, H., and Seebass, R. "Shock-Free Wing Design," AIAA J., (to appear). Also AIAA Paper 79-1557.

5. Bauer, F., Garabedian, P. R., and Korn, D. G. "Supercritical Wing Sections," Lecture Notes in Economics and Mathematical Systems, No. 66, Springer-Verlag, 1972

6. Nash, J. F. and MacDonald, A. G. J. "The Calculation of Momentum Thickness in a Turbulent Boundary Layer at Mach Numbers up to Unity," ARC CP-93, London, 1967.

7. Collyer, M. R. and Lock, R. C. "Prediction of Viscous Effects in Steady Transonic Flow Past an Airfoil," Aero. Quart., August 1979, pp. 485-505.

8. Green, J. E., Weeks, D. J., and Broomen, J. W. F. "Prediction of Turbulent Boundary Layers and Wakes in Compressible Flow by a Lag Entrainment Method," RAE Tech. Report, 72231, 1973.

9. Nandanan, M., Stanewsky, E., and Inger, G. R. "A Computational Procedure for Transonic Airfoil Flow Including a Special Solution for Shock Boundary Layer Interaction," AIAA Paper 80-1389, 1980.

10. Jameson, A. "Numerical Computation of Transonic Flow with Shock Waves," Symposium Transsonicum II, Springer-Verlag, New York, 1975.

11. Rotta, J. C. "Turbulent Boundary Layer Calculation with the Integral Dissipation Method," Computation of Turbulent Boundary Layers, 1968 AFOSR-IFP Stanford Conference, Vol. 1, pp. 177-181.

12. Inger, G. R. and Cantrell, J. C. "Application of Shock-Turbulent Boundary Lay Interaction Theory to Transonic Aerodynamics," 4th U. S.-F. R. G. Meeting on Viscous and Interacting Flow Field Effects, BMVG-FBWT 1979, pp. 100-115.

13. Melnik, R. E., Chow, R., and Mead, H. R. "Theory of Viscous Transonic Flow Over Airfoils at High Reynolds Number," AIAA Paper 77-680, 1977.

14. Melnik, R. E. and Chow, R. "Asymptotic Theory of Two-dimensional Trailing Edge Flows," NASA Conference on Aerodynamic Analysis Requiring Advanced Computers, NASA SP-347, 1975, pp. 177-249.

15. Morawetz, C. S. "On the Non-Existence of Continuous Transonic Flows Past Profiles, I, II, and III," Communications on Pure and Applied Mathematics, 1956, 1957, and 1958, p. 45-68, 107-131, and 139-144.

16. Pearcey, H. H. "The Aerodynamic Design of Section Shapes for Swept Wings," Advances in Aeronautical Sciences, Vol. 3, 1962, pp. 277-322.

17. Whitcomb, R. T. and Clark, L. R. "An Airfoil Shape for Efficient Flight at Supercritical Mach Numbers," NASA TM X-1109, July 1965.

18. Garabedian, P. R. and Korn, D. G. "Numerical Design of Transonic Airfoils," Numerical Solutions to Partial Differential Equations, Vol. II, Academic Press, New York, 1978, pp. 253-271.

19. Nieuwland, G. Y. "Transonic Potential Flow Around a Family of Quasi-Elliptical Airfoil Sections," NLR Report TR-T 172, 1967.

20. Boerstoel, J. W. "Design and Analysis of a Hodograph Method for the Calculation of Supercritical Shock-free Airfoils," NLR Report TR-77046 U, 1977.

21. Sobieczky, H. "Entwurf überkritischer Profile mit Hilfe der rheoelektrischen Analogie," DFVLR Report DLR-FB 75-43, 1975.

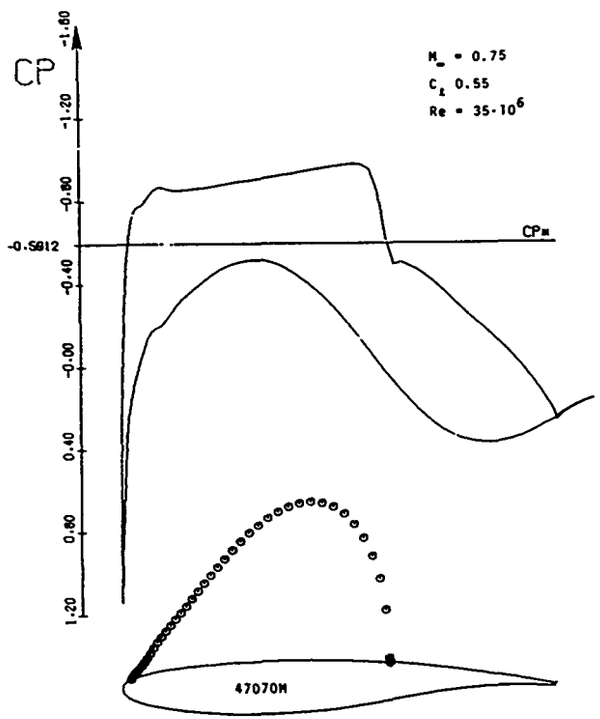


Figure 1. Grumfoil analysis of the baseline airfoil 47070M.

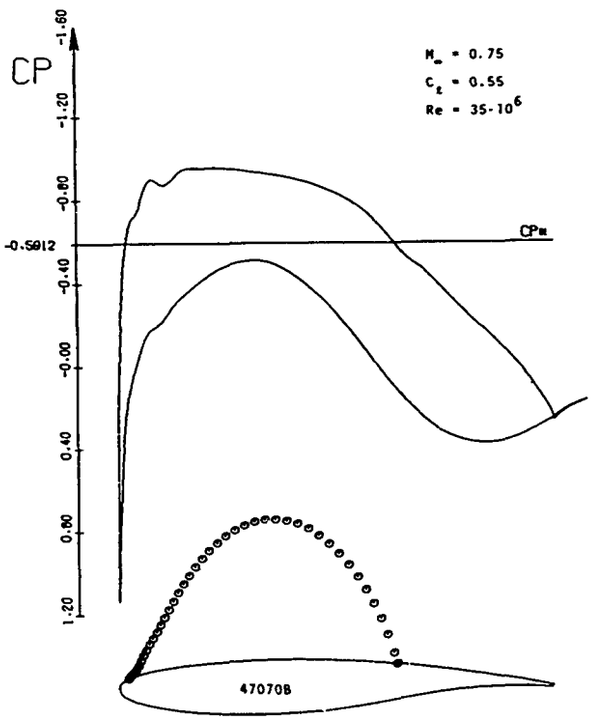


Figure 2. Grumfoil fictitious gas (P = 0.9) analysis of the baseline airfoil plus a bump (47070B).

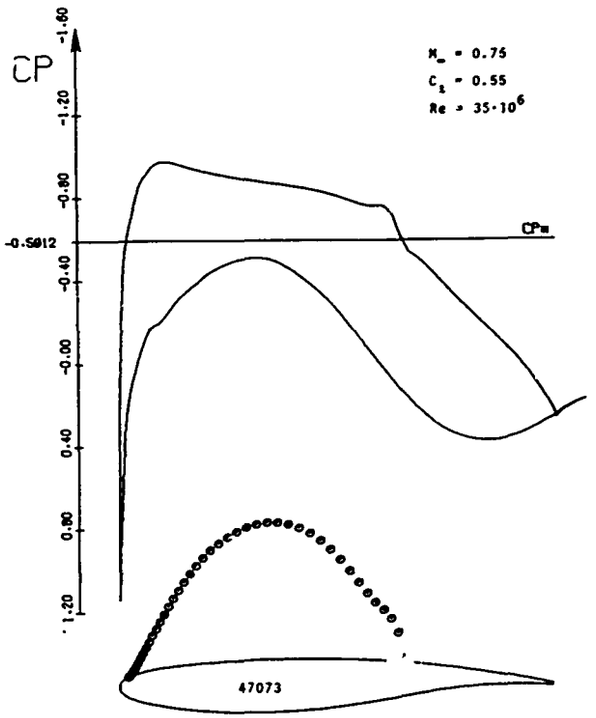


Figure 3. Grumfoil analysis of the shock-free design airfoil (47073).

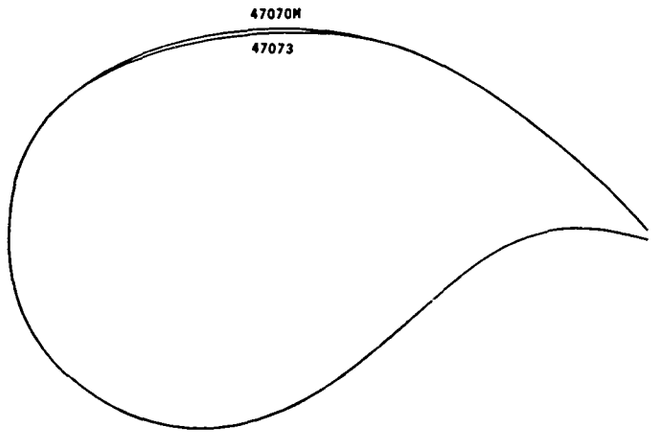


Figure 4. Comparison of the baseline and shock-free design airfoils. The vertical scale is magnified five times.

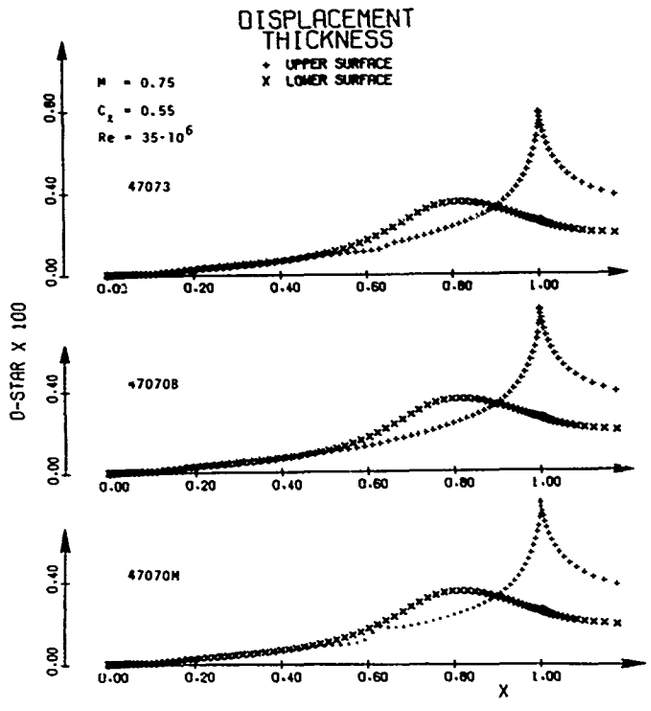


Figure 5. Displacement thickness for the three airfoils of Figures 1-3.

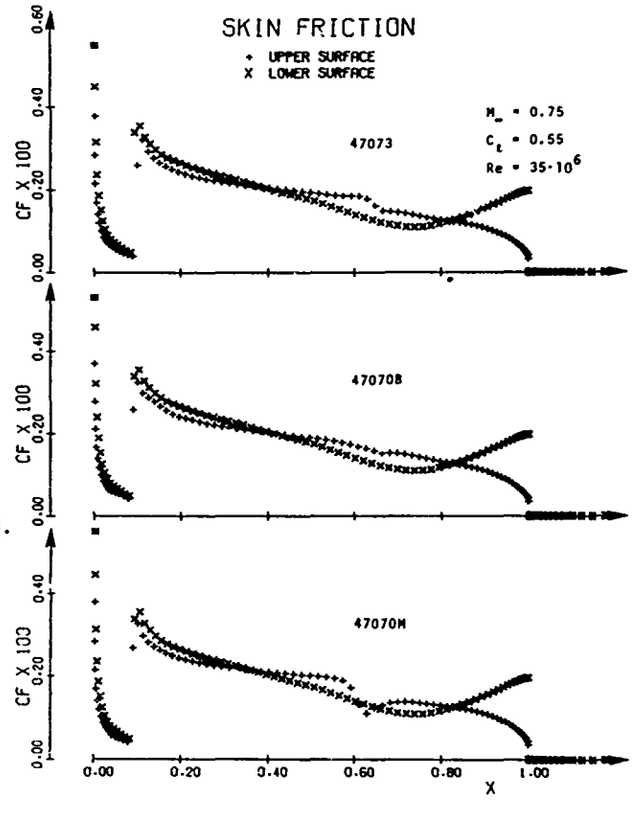


Figure 6. Skin friction coefficients for the three airfoils of Figures 1-3.

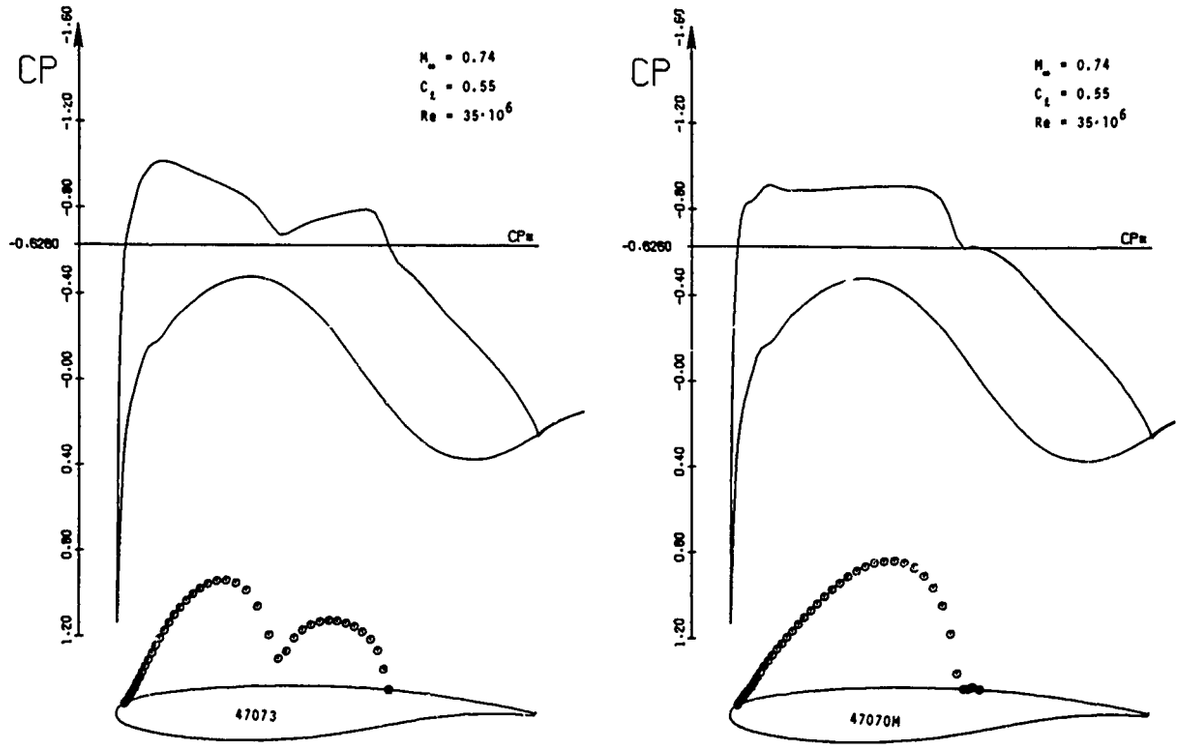


Figure 7. Pressure distributions and sonic line - shock wave shapes for the baseline and shock-free airfoils at M_∞ = 0.74.

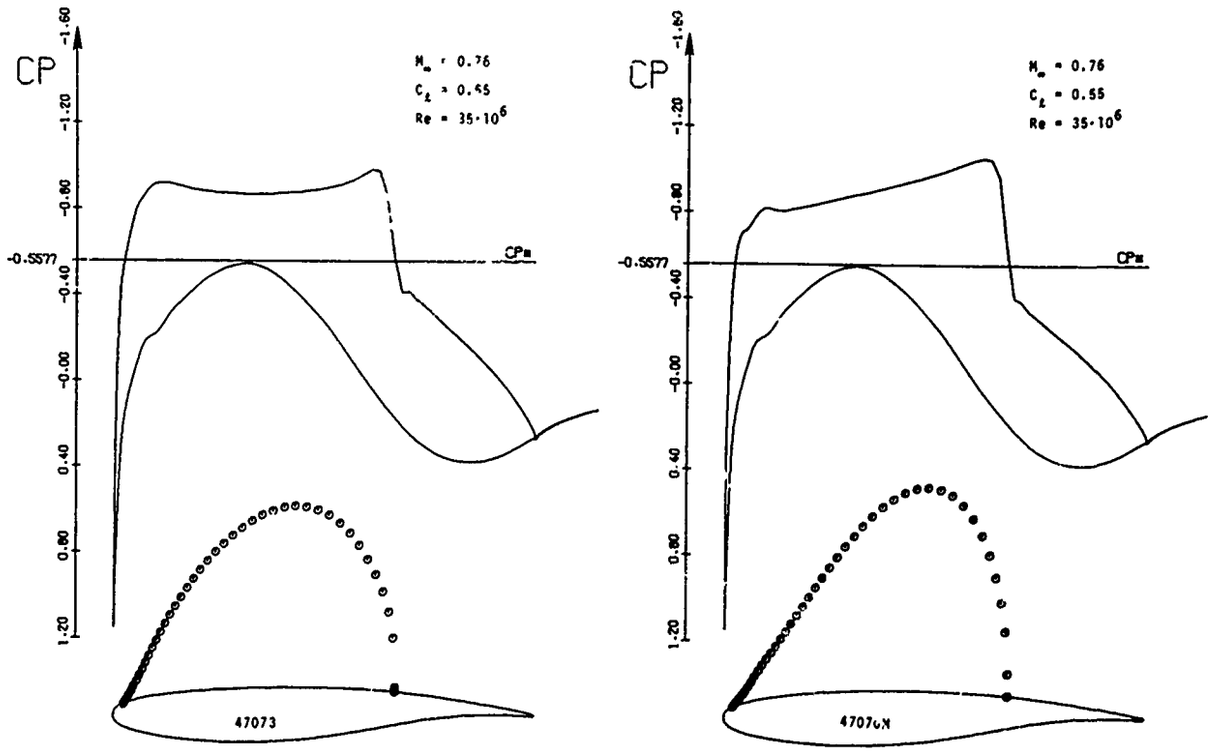


Figure 8. Pressure distributions and sonic line - shock wave shapes for the baseline and shock-free airfoils at M_∞ = 0.76.

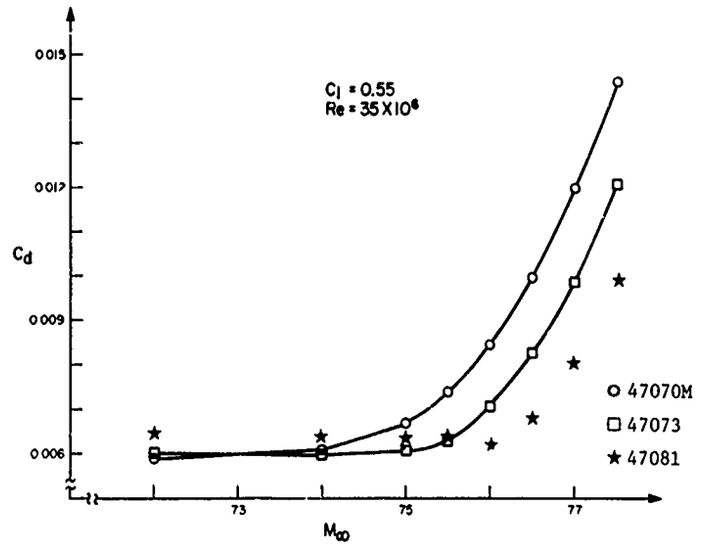


Figure 9. Drag coefficient as a function of Mach number for the 47070M, 47073, and 47081 airfoils at C_ℓ = 0.55, Re = $35 \cdot 10^6$.

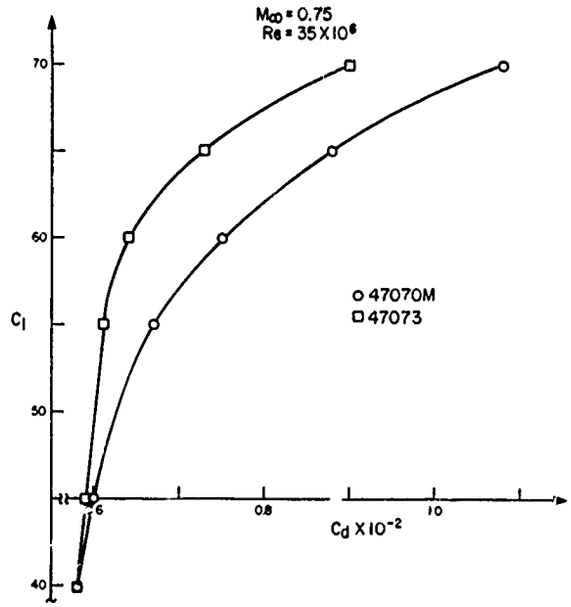


Figure 10. Lift coefficient as a function of drag coefficient of the 47070M, 47073, 47081 airfoils at M_∞ = 0.75, Re = $35 \cdot 10^6$.

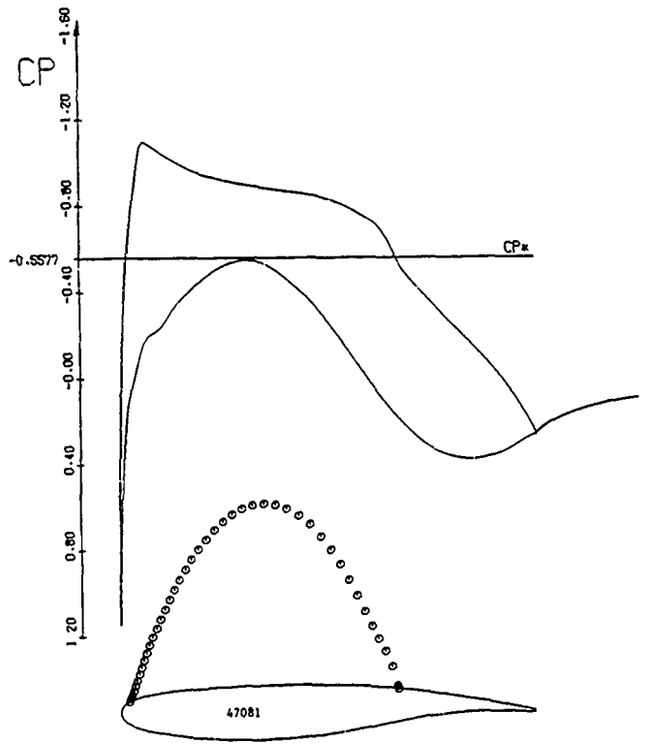


Figure 11. Pressure distribution and sonic line shape for the 47081 airfoil at $M_\infty = 0.76$, $C_\ell = 0.55$, $Re = 35 \cdot 10^6$.

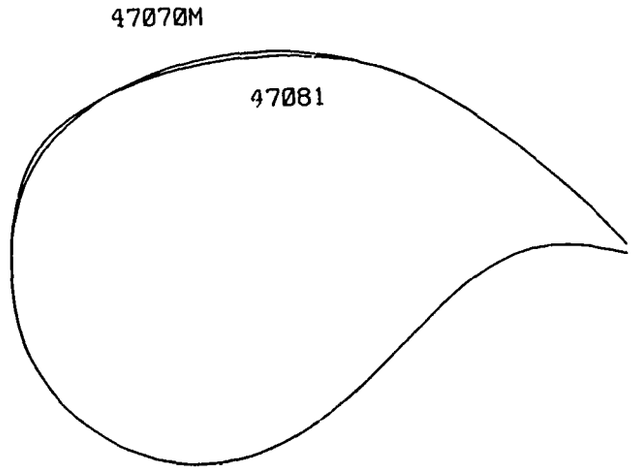


Figure 12. Comparison of the 47070M and 47081 airfoils. The vertical scale is magnified five times.

THE COUPLING OF A SHOCK BOUNDARY LAYER INTERACTION MODULE WITH A VISCOUS-INVISCID COMPUTATION METHOD

by

E. Stanewsky* and M. Nandanan**
Deutsche Forschungs- und Versuchsanstalt für Luft- und Raumfahrt e.V.
Aerodynamische Versuchsanstalt Göttingen
ttingen, FRG
and
G.R. Inger+
Virginia Polytechnic Institute and State University
Blacksburg, Virginia 24061, USA

SUMMARY

In the present approach to transonic airfoil flow analysis, limited to non-separating turbulent flow, an analytical solution for near-normal shock boundary layer interaction is coupled with a state-of-the-art viscous-inviscid computation code. This paper gives a brief description of the present method and its components and compares results obtained with (1) the combined boundary layer/shock boundary layer interaction code and (2) the complete viscous-inviscid method with corresponding data from boundary layer and surface pressure distribution measurements, with emphasis, however, placed on (2). Present results are, in addition, compared with data obtained by other methods. From the results discussed in this paper one may conclude that in transonic airfoil flow analysis it is generally necessary to incorporate a physically correct treatment of the interaction of a shock with the boundary layer.

LIST OF SYMBOLS

c	airfoil chord
c_D	dissipation coefficient
c_f	skin friction coefficient
C_L	lift coefficient
C_m	pitching moment coefficient
c_p	pressure coefficient, $(p-p_\infty)/q_\infty$
H	shape factor, δ^*/θ
$\bar{H}$	δ^*/θ
M_∞	free stream Mach number
M_{∞_c}	corrected free stream Mach number
M	local Mach number
p	static pressure
q	dynamic pressure
Re	Reynolds number based on free stream conditions and chord
Re_{δ^*1}	local Reynolds number based on δ_1^*
U_e	velocity at the edge of the boundary layer
x, y	rectangular coordinates
x/c	non-dimensional chord
α, α_g	corrected and geometric angle of attack, respectively
δ	boundary layer thickness
δ^*	displacement thickness
θ	momentum thickness
θ^*	energy thickness
ρ	density

Subscripts

B	boundary layer
e	edge of boundary layer
1	immediately upstream of the shock
∞	free stream conditions

---

* Research Scientist ** Research Scientist, National Aeronautical Laboratory, Bangalore, India, on deputation to DFVLR

+ Professor of Aerospace and Ocean Engineering

I. INTRODUCTION

Computational Fluid Dynamics (CFD) plays an ever increasing role in the design and analysis of aerodynamic shapes for transonic application. Appreciable progress has been made in this field; however, one major obstacle to complete CFD success remains: Viscous effects. Unfortunately, transonic airfoil (or wing) flow is largely influenced by these effects and here two of the more crucial flow phenomena are the interaction of the shock wave and the interaction of the sustained rear adverse pressure gradients with the boundary layer on the upper surface of an airfoil.

To demonstrate this, the experimentally determined displacement thickness δ^* (the experiments will be discussed in Section III) is plotted in Figure 1 for various prominent positions on the airfoil, i.e., upstream and downstream of the shock and at the trailing edge, as a function of the shock upstream Mach number, M_1, for two different initial boundary layer (displacement) thicknesses. The initial difference in δ^* was obtained by placing transition strips at 7% and 30% of the chord, respectively. The initial difference - lower left hand side diagram of Fig. 1 - is relatively small, amounting to 0.05% of the airfoil chord. Considering a shock upstream Mach number of $M_1 = 1.30$, for instance, this difference is amplified by the shock - upper left hand side diagram - to about 0.25%c and subsequently by the sustained rear adverse pressure gradients - diagram on the right hand side - to 1.4%c. The amplification factors for the shock and the rear adverse pressure gradients are here 5 and 5.6, respectively, resulting in a total amplification of an initially small difference by a factor of 28. (Note that the amplification factor is one - but not the only - indicator for the sensitivity of an airfoil to viscous effects.)

These results have a strong bearing on CFD. They suggest that because of the amplification of small errors the boundary layer properties upstream of the shock and the change in boundary layer properties across the shock must be predicted with a high degree of accuracy. The former can certainly be accomplished by a state-of-the-art boundary layer method; however, considering shock boundary layer interaction, the physics of the flow are not well represented by boundary layer theory and it is doubtful whether such a theory can predict the change in boundary layer properties due to the shock with the accuracy required for transonic airfoil flow analysis, even if artificial means such as smearing of the pressure rise due to the shock are introduced.

In the present approach to transonic airfoil flow analysis, limited to non-separating turbulent flow, we have adopted a special solution for normal shock wave boundary layer interaction and incorporated it as a module within a state-of-the-art viscous-inviscid computation code. In this paper the present method will be briefly described - more details having been given in Ref.1 - and theoretical results will be compared with corresponding data from boundary layer and surface pressure distribution measurements on three transonic airfoils with emphasis, however, placed on the latter. Present results will, in addition, be compared to results from two other computational methods. It will be shown that in transonic airfoil flow analysis it seems generally necessary to incorporate a physically correct treatment of the interaction of a shock with the boundary layer.

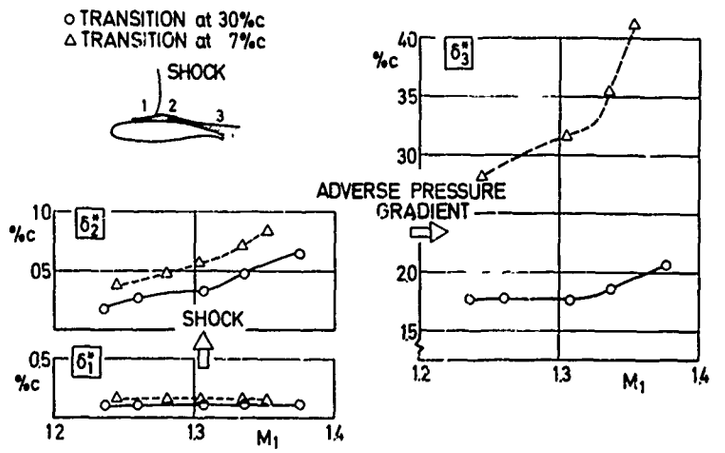


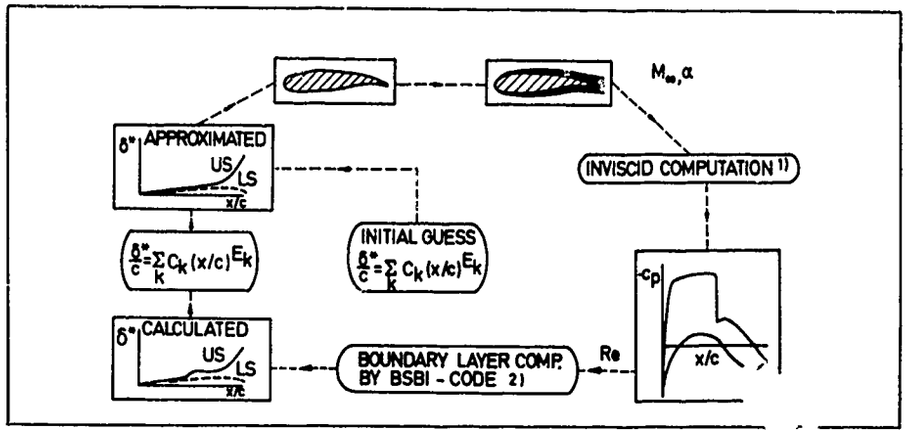
Figure 1. Amplification of an Initial Difference in Displacement Thickness. Airfoil CAST 10-2/DOA2. $M_\infty = 0.765$, $Re = 1.95 \times 10^6$

II. THEORY

In discussing the present method, we would like to start out with a short description of the computational procedure, identifying the individual components of the method as we go along and give, subsequently, a brief account of these components and their coupling.

Computational Procedure

The viscous flow analysis is based on the displacement surface concept. The computational procedure starts, Figure 2, with an initial guess for the displacement thickness



1) Inviscid theory: Jameson's fully conservative or non-conservative scheme [2]

2) BSBI-code: Rotta's integral dissipation method [4] plus Inger's triple deck solution for shock boundary layer interaction [5]

Figure 2. Components and Computational Procedure of Present Viscous-Inviscid Method

distribution generally represented by the analytical relation

$$\frac{\delta^*}{c} = \sum_k C_k \, (x/c)^{E_k} \tag{1}$$

with the proper choice of C_k and E_k. The displacement surface is added to the geometric airfoil contour and the effective airfoil shape submitted to the inviscid computation code. Here, we utilize Jameson's version[2] of the relaxation method of Bauer et al. (BGKJ-method[3]) either in fully conservative or non-conservative form. The non-conservative scheme is usually employed in low-lift cases thus eliminating the need for a more careful modelling of the "bump" in the displacement thickness distribution due to the interaction of the boundary layer with the shock.

The pressure distribution calculated after a certain prescribed number of iterations by the inviscid code is used as input to the Boundary Layer/Shock Boundary Layer Interaction code (BSBI-code) which determines a new displacement surface. The BSBI-code consists of Rotta's integral dissipation method[4] and Inger's triple deck solution for transonic shock wave boundary layer interaction[5]. The displacement surface thus obtained will be approximated analytically by Eq. (1), smoothing over the more rapid change in displacement thickness due to the shock (see Fig. 2), then added to the geometric contour of the airfoil and the inviscid computation repeated. This procedure continues until the required convergence is achieved.

Components and Coupling

Inviscid code: There is no need to give here details of the well known relaxation method of Jameson[2] employed for the computation of the outer inviscid flow field. The code provides solutions to the quasi-linear equation for the velocity potential (non-conservative scheme) and the equation for the conservation of mass (fully conservative scheme). The inviscid calculations are carried out in a computational plane obtained by conformally mapping the effective airfoil contour into a unit-circle. The solution is established by employing a sequence of meshes using Jameson's accelerated iterative scheme[2] to speed up convergence. The viscous wake is represented, although very crudely, by a semi-infinite parallel displacement body extending downstream of the trailing edge[3].

Boundary layer code: Here Rotta's integral dissipation method[4] is employed. This method determines the boundary layer properties by simultaneously integrating the von Kármán momentum equation

$$\frac{d\theta}{dx} + \theta\left[\frac{H+2}{U_e}\frac{dU_e}{dx} + \frac{1}{\rho_e}\frac{d\rho_e}{dx}\right] = \frac{c_f}{2} \tag{2}$$

and the energy equation

$$\frac{d\theta^*}{dx} + \theta^*\left[\frac{3}{U_e}\frac{dU_e}{dx} + (2-\gamma)\frac{1}{\rho_e}\frac{d\rho_e}{dx}\right] = c_D \tag{3}$$

These equations are solved by utilizing additional relations for ① the shape factor H, ② the skin friction coefficient, c_f, and ③ the dissipation coefficient c_D. These

are obtained from ① a certain group of power law profiles, ② the Ludwieg-Tillmann formulation[6] and ③ an extended form of the dissipation law based on Nash's equilibrium boundary layer relation which accounts for upstream history effects[7].

Interaction code: To handle the transonic shock boundary layer interaction problem, Inger's analytical triple deck solution for non-separating turbulent boundary layers is used. The method and some of its applications have been thoroughly described in the literature[5,8,9], so here only a brief look at the flow model on which the solution is based shall suffice.

The model, Figure 3, consists of a mixed flow layer outside the boundary layer comprised of an incoming uniform supersonic flow in Region ① and a subsonic potential flow in Region ③ separated by a shock discontinuity whose strength is given by the shock upstream Mach number, M_1. Situated below Regions ① and ③ is the non-uniform boundary layer (Region ②) that contains a highly rotational mixed transonic disturbance flow. Near the wall exists a viscous disturbance sublayer that contains the upstream influence and the skin friction perturbation.

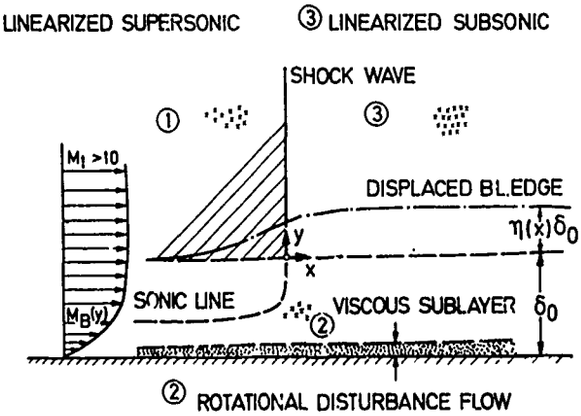
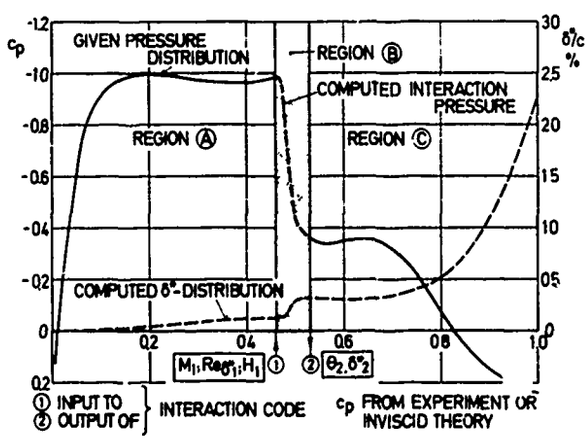


Figure 3. Model of Shock Boundary Layer Interaction

A solution is obtained by assuming linearized disturbances ahead of and behind the shock with the shock being considered as a simple discontinuity across which the Hugoniot shock jump relations are satisfied. To simplify the problem the shock jump conditions are only imposed at the boundary layer edge neglecting the details of the shock penetration into the underlying non-uniform flow region. The resulting equations are solved by operational methods. Note that in the present version of the code, we have replaced the normal shock jump relation by the jump condition for maximum stream deflection which gives, as is shown in Ref. 1, better agreement with experiment. The input necessary to initiate the interaction code and the quantities computed by the code are given below.

Coupling of boundary layer and shock boundary layer interaction codes: The domains of application of the BSBI-code (boundary layer/shock boundary layer interaction code) are sketched in Figure 4. For a given pressure distribution, obtained either by experiment or by inviscid theory, the boundary layer code computes the boundary layer properties in



Region Ⓐ Ⓑ: Boundary layer theory

Region Ⓒ: Shock boundary layer interaction theory

Figure 4. Domains of Application of BSBI-code

Region Ⓐ, providing at the upstream interface of the interaction region (on Ⓑ) the input necessary to start the interaction module, viz., the local Reynolds number based on

the displacement thickness, $Re_{\delta^*_1}$, and the shape factor H_1. The required shock upstream Mach number, M_1, and the shock location are obtained from the given pressure distribution. Within Region (B) the interaction code determines the displacement thickness growth, the shape factor (hence the momentum thickness θ) and the skin friction together with the interacting surface pressure distribution. To reinitiate the boundary layer code in Region (C), the momentum thickness, θ, and the energy thickness, θ^*, are required. With θ and δ^* given by the interaction code, the energy thickness is determined[1] by a semi-empirical relation for the shape factors $H = \delta^*/\theta$ and $\bar{H} = \theta^*/\theta$, viz.,

$$\bar{H} = 1.26\ H\ /\ (H - 0.39) + 0.26/H \qquad (4)$$

which is based on a relation for a certain group of power law profiles[10] and results from the boundary layer measurements described below. The boundary layer computation in Region (C) is carried out down to the trailing edge with no special trailing edge solution being included.

III. EXPERIMENT

The theoretical results to be discussed are compared to experimental data from boundary layer and surface pressure measurements on three "supercritical" airfoils conducted in the DFVLR wind tunnels 1 x 1 Meter Transonic Wind Tunnel Göttingen (TKG) and Transonic Wind Tunnel Braunschweig (TWB) and for DFVLR in the Lockheed-Georgia Comp. Compressible Flow Wind Tunnel (CFWT). In the following we will briefly outline characteristic features of the experimental investigation, beginning with the airfoils tested.

Airfoils and Test Program

Airfoils: The transonic airfoil sections considered here, Figure 5, are the DORNIER designs CAST 7/DOA1 and CAST 10-2/DOA2[11] and the VFW design VA2[12]. The thickness ratios of these airfoils are 11.8, 12.1 and 13 percent, respectively. Other distinguishing features are the large trailing edge angle of CAST 10-2/DOA2, the latter being about 14°, and the increased upper surface curvature over the last 30% of the chord of this airfoil. Both features are likely to make the airfoil more sensitive to errors in the viscous computation. The airfoil VA2 is characterised by a relatively large rear loading.

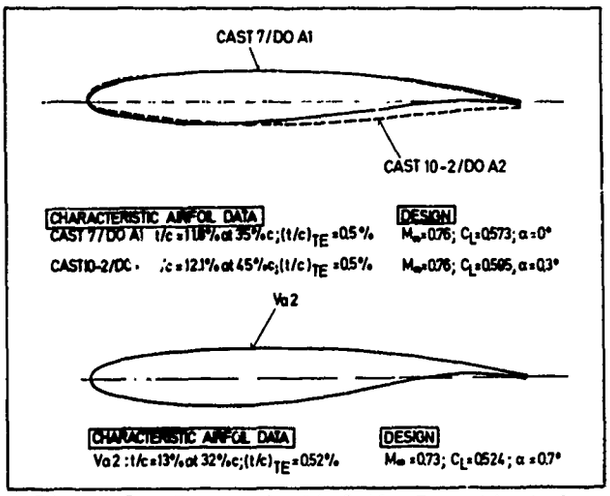


Figure 5 . Transonic Airfoils Investigated

Test program: Extensive boundary layer and flow field measurements were carried out on the upper surface of the airfoils CAST 7/DOA1 and CAST 10-2/DOA2. Here, the free stream conditions were such that the shock upstream Mach number, representative of the shock strength, varied between $M_1 = 1.23$ and $M_1 = 1.40$ centered about the vaguely known Mach number for the onset of shock induced separation, i.e., $M_1 = 1.30$. Boundary layer and wake measurements were also conducted on the airfoil Va2 starting, however, with the boundary layer surveys only at x/c = 0.60, i.e., downstream of the shock. Surface pressure and wake rake measurements were carried out on all three airfoils testing one, viz., CAST 10-2/DOA2, at Reynolds numbers up to $Re = 31 \times 10^6$. The complete test program is given in Table 1.

Airfoil	M_∞	$\alpha_g°$	Re x 10^{-6}	Transition	M_1	Type of Measurement	Wind Tunnel	$(x/c)_{Probe}$ [3]
CAST 10-2/DOA2	0.765	2.0 to 3.9	2.0; 3.5, 2.0	107 BA at 7% c [1] 124 at 30% c	1.23 to 1.40	Boundary layer	TKG	0.25 - 1.1
	0.78	2.0	2.4	Free 220 K at 15% c [2]	1.24	Boundary layer	TKG	0.25 - 1.1
	0.5 to 0.82	-2 to 10	1.3 to 4.0	Free Loc: 5% to 45% c Type. 220 K	1.5 (max.)	Surface pressure and wake	TKG	
	0.6 to 0.82	-2 to 10	4.0 to 31.0	Free Loc: 7% c Type. 60 BA/548A	1.5 (max.)	Surface pressure and wake	Lockheed CFWT	
CAST 7/DOA1	0.765	2.0 to 3.9	2.0	107 BA at 7% c 124 BA at 30% c	1.23 to 1.40	Boundary layer	TKG	0.25 - 1.1
	0.5 to 0.82	-2 to 10	1.3 to 4.0	Loc: 7% c to 30%c Type: 150 to 220K	1.5 (max.)	Surface pressure and wake	TKG	
	0.6 to 0.80	-2 to 6	4.0 to 14.0	60 BA at 7% c	1.45 (max)	Surface pressure and wake	TWB	
Va 2	0.6 to 0.75	2.5 to 6.25	2.4	220 K at 30% c on upper and 25% on lower surface	1.19 to 1.40	Boundary layer	TKG	0.60 - 1.5
	0.5 to 0.82	-2.0 to 10	2.4, 4.0	Free 220 K at 30% c 220 K at 8% c	1.5 (max.)	Surface pressure and wake	TKG, TWB	

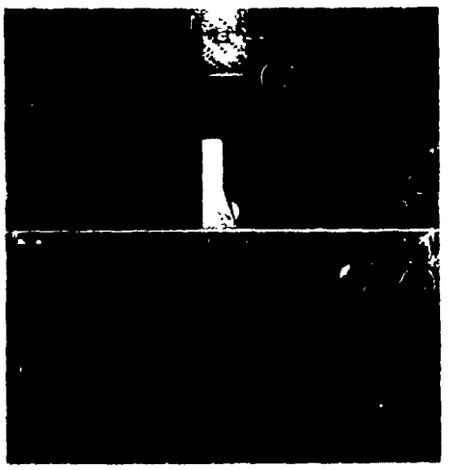
1) 107 BA, 124 BA: Glass spheres of 0.107 and 0.124 mm diameter, respectively. 2) 220 K: No. 220 Carborundum grit (average height 0.073 mm).

3) $(x/c)_{Probe}$: Range of chord where boundary layer measurements were carried out.

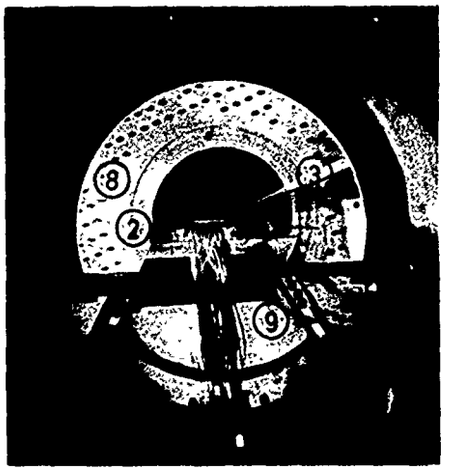
Table 1. Test Program

Wind Tunnels, Test Set-up and Data Reduction

Wind tunnels and test set-up: The boundary layer measurements on CAST 7/DOA1 and CAST 10-2/DOA2 and the boundary layer and surface pressure measurements on the Va2 quoted in this paper were made in the 1 x 1 Meter Transonic Wind Tunnel (TKG). This tunnel[13] is equipped with a fixed porosity, 6%-open perforated test section with a cross section of 1 meter x 1 meter. The holes of the perforation are slanted 30° to the flow direction. The models generally have a chord of 200 to 250 mm and span the entire width of the test section, Figure 6. The boundary layer probe plus drive mechanism, Fig. 6, was mounted for these tests on a sting usually employed to hold complete aircraft models. This allowed to change the inclination of the probe so that it could always be set tangential to the model surface and traversed normal to it. The probe itself consisted of a 0.15 mm flattened pitot probe, a cone-cylinder static probe and a directional probe made of two tubes cut-off under 45°. More details concerning the boundary layer measurements are given in Ref. 14.



Front view. Probe positioned for measurements on the lower surface



Side view. Probe positioned for measurements on the upper surface

1 Drive unit encasement; 2 Airfoil model; 3 Probe support; 4 Probe; 5 Strut; 6 Sting; 7 Turn-table; 8 Schlieren window; 9 Steel insert to carry model loads; 10 Perforated test section walls; 11 Pressure leads

Figure 6. Model and Boundary Layer Probe Installation (1 x 1 Meter Transonic Wind Tunnel Göttingen)

The experimental surface pressure distributions for CAST 7/DOA1 to be presented for comparison were obtained in the Transonic Wind Tunnel Braunschweig (TWB). This tunnel[15] has a slotted, 2.35%-open test section (slots are only in the top and bottom walls) optimized for zero blockage effects at $C_L = 0$. Tests with different size models of the same transonic airfoil have also indicated that at the Mach numbers of interest here ($M_\infty \approx 0.76$) only minor corrections to the angle of attack seem to be required. The cross section area of the tunnel is 0.34 meter x 0.60 meter. The model chord in the present tests was c = 200 mm.

The high Reynolds number measurements on CAST 10-2/DOA2 were conducted in the Lockheed Compressible Flow Wind Tunnel (CFWT). The tunnel[16] is equipped with a variable porosity perforated test section with a cross section area of 0.51 meter x 0.71 meter. The holes of the perforation are, as in the case of the TKG, slanted 30° to the flow direction. In the present investigation, the model chord was c = 177 mm and the wall open area ratio 4%. The model installations in the TWB and the CFWT were similar to the one shown in Fig. 6, however, with the boundary layer probe and probe support replaced by a wake rake.

Data reduction procedure: Here only two remarks concerning the boundary layer measurements are deemed necessary: ① To obtain velocity and density distributions in the boundary layer from the measured pitot and static pressures it was assumed that the total temperature is constant across the viscous layer. ② The boundary layer integral parameters were determined by integration after having added to the measured data points, where applicable, i.e., generally in the thin boundary layer upstream of the shock, the laminar sublayer. Details of the data reduction procedure are given in Ref. 14.

IV. RESULTS

In the following discussion we will mainly concentrate on results obtained with the complete viscous-inviscid method. However, we will begin with considering two representative test cases computed with the boundary layer/shock boundary layer interaction code (BSBI-code) using the experimental pressure distribution as input. A more extensive coverage of test cases concerning the theoretical and experimental boundary layer development was given in Ref. 1.

Comparison of the Boundary Layer Development

It was shown in the Introduction that the boundary layer development can be severely affected by the upper surface shock and the subsequent sustained adverse pressure gradients. The question of main concern here is whether conventional boundary layer theory can predict this development.

Shown in Figure 7 is the displacement thickness distribution over the upper surface of the airfoil CAST 7/DOA1 for a relatively thick initial boundary layer, the displacement

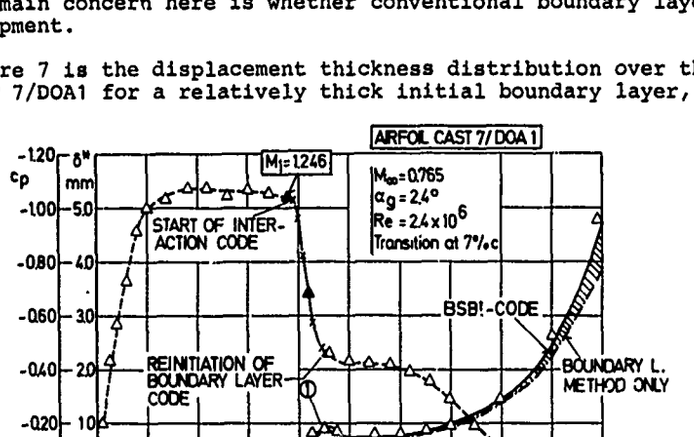


Figure 7. Comparison of δ^*-distributions Obtained by Boundary Layer Code, BSBI-code and Experiment. Airfoil CAST 7/DOA1

thickness upstream of the shock being about 0.1% of the chord. Applying the boundary layer code, with the experimental pressure distribution as input, throughout, i.e., also in the interaction region, results in an overprediction of the experimentally determined jump in displacement thickness due to the shock, a subsequent underprediction of the decrease in δ^* in the area of the relaxed pressure gradient downstream of the shock and a considerable underestimation of the experimental value at the trailing edge. Refering back to the first figure with its experimental demonstration of the amplification phenomenon, one may conclude that the large discrepancy at the trailing edge is a direct consequence of the small difference in δ^* at the beginning of the plateau region downstream of the shock.

Applying the BSBI-code results in a considerable improvement in the agreement between the experimental and the theoretical δ^*-distribution.

A closer look at details in the interaction region, Figure 8, shows that the interaction code, initiated at x/c = 0.38, quite accurately predicts the jump in displacement thickness due to shock impingement with good agreement between experiment and theory occuring not only in the magnitude of the δ^*-jump but also in the gradient. The same holds for the interacting surface pressure distribution. The overprediction of δ^* in the interaction region and the underestimation in the plateau region when applying the boundary layer code are clearly indicated.

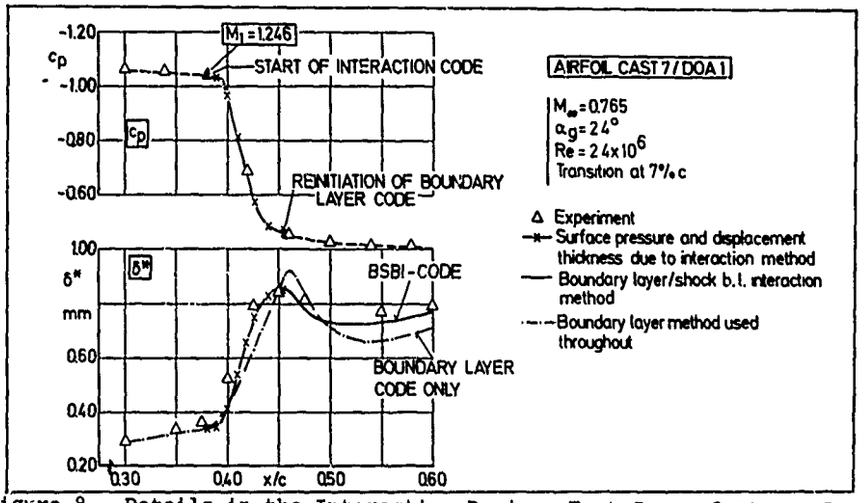


Figure 8. Details in the Interaction Region. Test Case of Figure 7

Figure 9 presents the experimental and theoretical displacement thickness distributions for the airfoil CAST 10-2/DOA2, which exhibits more severe rear adverse pressure gradients than CAST 7/DOA1, under conditions similar to the preceding test case. Using the boundary layer code throughout again results in an underprediction of the experimental displacement thickness distribution downstream of the shock. Note that the discrepancy in the trailing edge region is here much more pronounced than in the CAST 7/DOA1 case, Fig. 7, which can mainly be attributed to the afore-mentioned more severe rear adverse pressure gradients. (For the two test cases considered, the factors by which the errors downstream of the shock are amplified are 11 and 20, respectively.) Treating the interaction in a physically correct way by applying the interaction code leads to excellent agreement with experiment in the interaction region and, reinitiating the boundary layer computation with the correct values, down to the trailing edge.

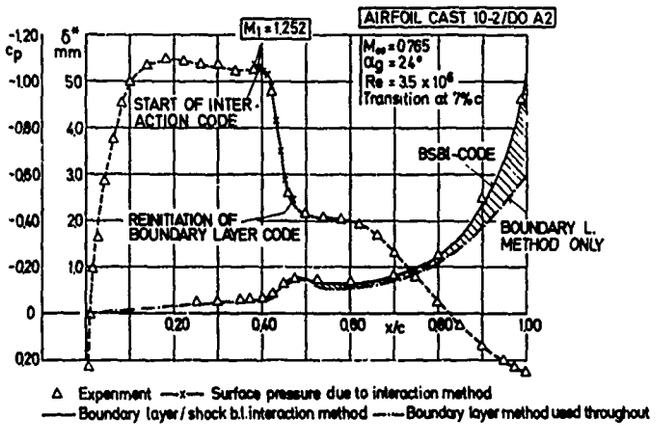
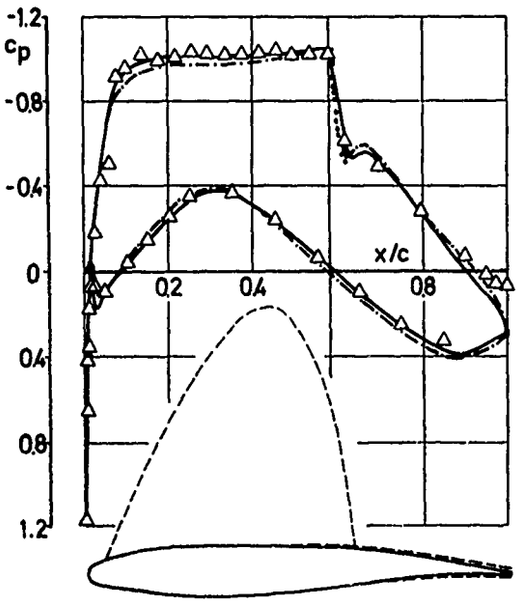


Figure 9. Comparison of δ^*-distributions Obtained by Boundary Layer Code, BSBI-code and Experiment. Airfoil CAST 10-2/DOA2

Comparison of Surface Pressure Distributions

It was shown in the preceding subsection that treating shock boundary layer interaction by conventional boundary layer theory results in an underprediction of the experimental displacement thickness development between shock and trailing edge. In this section we will compare experimental and theoretical pressure distributions, the latter obtained by ① the present method, treating the interaction by the interaction code and by the boundary layer code, respectively, and ② the methods of Bousquet[17], and Collyer and Lock[18].

As in the case of the boundary layer comparisons, we start out with the generally less demanding airfoil CAST 7/DOA1. In Figure 10 surface pressure distributions computed by the present method and by the method of Bousquet[17,19] are compared with experimental results[20] at a free stream Mach number of $M_\infty = 0.760$ and a lift coefficient of $C_L \approx 0.650$. The Reynolds number is $Re = 5.9 \times 10^6$ and transition fixed at 7% chord. The agreement between the present method (non-conservative version) and experiment is very good, including the agreement in shock location, and minor differences occur only near the trailing edge. Bousquet also predicts the shock location accurately; however, there is a noticeable overprediction of the pressure over the forward part of the upper surface and the rear part of the lower surface. The discrepancy in pressure near the trailing edge on the



AIRFOIL CAST7/DOA1

	EXP. △	PRESENT METHOD ———	BOUSQUET [19] -·-·-
M_∞	0.760	0.760	0.760
$\alpha°$	1.00	0.50	0.15
C_L	0.63	0.650	0.645
C_m	-0.131	-0.137	-0.145

$Re = 5.9 \times 10^6$
TRANSITION at 7%c
WIND TUNNEL: DFVLR-TWB

- Surface pressure due to interaction code

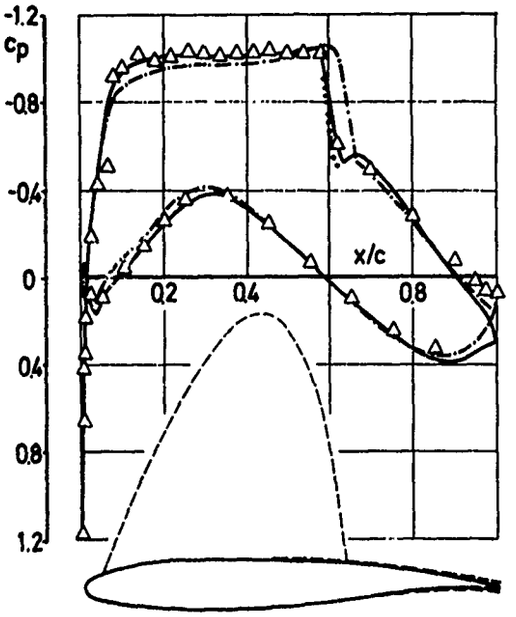
Figure 10. Comparison of Present Method with Experiment and the Method of Bousquet. Airfoil CAST 7/DOA1

upper surface is, in comparison with the present method, confined to an area closer to the trailing edge. Both methods give approximately the same lift; however, there is a marked difference in angle of attack, the latter being 0.5° for the present and 0.15° for Bousquet's method. The experimental value is $\alpha = 1.0°$.

It should be remembered (see Section III) that the wind tunnel TWB[15] utilized for the present experiments has a slotted wall test section optimized for zero blockage at $c_L = 0$ and that tests with different size models of the same airfoil have indicated that at the present Mach number only minor corrections to the angle of attack seem to be required (also see Ref. 20).

Bousquet's method[17] is similar to the present approach in its use of the displacement surface concept. It employs for the inviscid computation the method of Garabedian and Korn (non-conservative) and for the boundary layer computation the integral method of Michel et al.[21].

In Figure 11 the test case of Fig. 10 is compared to results obtained by the method of Collyer and Lock (VGK-method)[18,19]. The most pronounced disagreement with experiment



AIRFOIL CAST7/DOA1

	EXP. △	THEORY PRESENT METHOD ———	VGK [19] -·-·-
M_∞	0.760	0.760	0.760
$\alpha°$	1.00	0.50	0.05
C_L	0.630	0.650	0.630
C_m	-0.131	-0.137	-0.145

$Re = 5.9 \times 10^6$
TRANSITION at 7%c
WIND TUNNEL: DFVLR-TWB

- Surface pressure due to interaction code

Figure 11. Comparison of Present Method with Experiment and VGK-method. Airfoil CAST 7/DOA1

- and as a matter of fact with the present method - occurs on both the upper and the lower surface over the forward part of the airfoil and in the shock location. The angle of attack used for the computation is even lower than the one used by Bousquet's method, viz., 0.05°, probably causing the discrepancies over the first 30 % of the chord. Note, however, that here the experimental lift coefficient is matched. The VGK-method shows better agreement than the other two methods considered in the trailing edge region, which may be due to the wake treatment incorporated in the former.

Basic ingredients of the VGK-method[18] are: The Garabedian and Korn method for the inviscid and the lag-entrainment method of Green et al.[22] for the boundary layer and wake computation. Unique to this method is the treatment of the shock in the inviscid computation involving an arbitrary parameter λ which allows one to proceed smoothly from a non-conservative version ($\lambda = 0$) to a quasi-conservative version ($\lambda = 1.0$). The method applies the transpiration concept.

Staying at the same Mach number of $M_\infty = 0.76$ but going to a lower lift coefficient, we reach in the case of CAST 7/DOA1 conditions where a double shock appears on the upper surface of the airfoil. Figure 12 shows that the experimentally observed double shock system is well predicted by the present method (non-conservative form). Both, Bousquet's method and the VGK-method, only predict a single shock. The discrepances between these methods

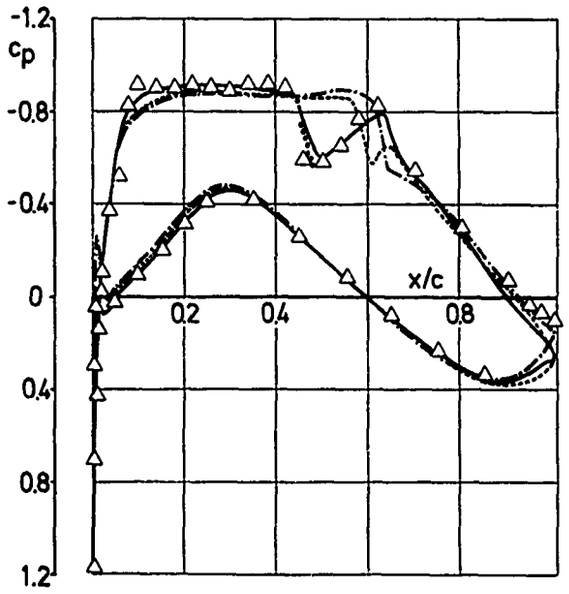


Figure 12. Comparison of Present Method with Experiment and Other Methods Under Double Shock Conditions. Airfoil CAST 7/DOA1

and experiment in the pressure distribution over the forward part of the airfoil are similar to the ones in the preceding test case (Fig. 10 and 11), an overprediction of the pressure on the upper and an underprediction of the pressure on the lower surface. The angles of attack also differ similarly: $\alpha = 0.1°$ for the present and $\alpha = -0.4°$ for the other two methods considered; the experimental value is $\alpha = 0.5°$.

The test case of Fig. 12 was rerun at the same free stream conditions, however, with the boundary layer code used throughout, i.e., also in the shock boundary layer interaction region. As a consequence, Figure 13, the double shock system merged into a single shock and the lift increased from $C_L = 0.521$ to $C_L = 0.573$.

It was shown earlier that treating the interaction by boundary layer theory leads to an underprediction of the displacement thickness between shock and trailing edge. The present analysis has indicated that the same occurred here causing the changes in pressure distribution as a result of a combination of local and global effects, the latter due to changes in the flow conditions at the trailing edge. Reducing the angle of attack to reduce the lift coefficient to the experimental value did not restore the double shock pattern.

Reconsidering now the previous comparisons between experiment and the method of Bousquet and the VGK-method, it seems that the discrepancies observed - and the low angles of attack used in the computations - were mainly due to an underprediction of the displacement thickness between the shock and the trailing edge.

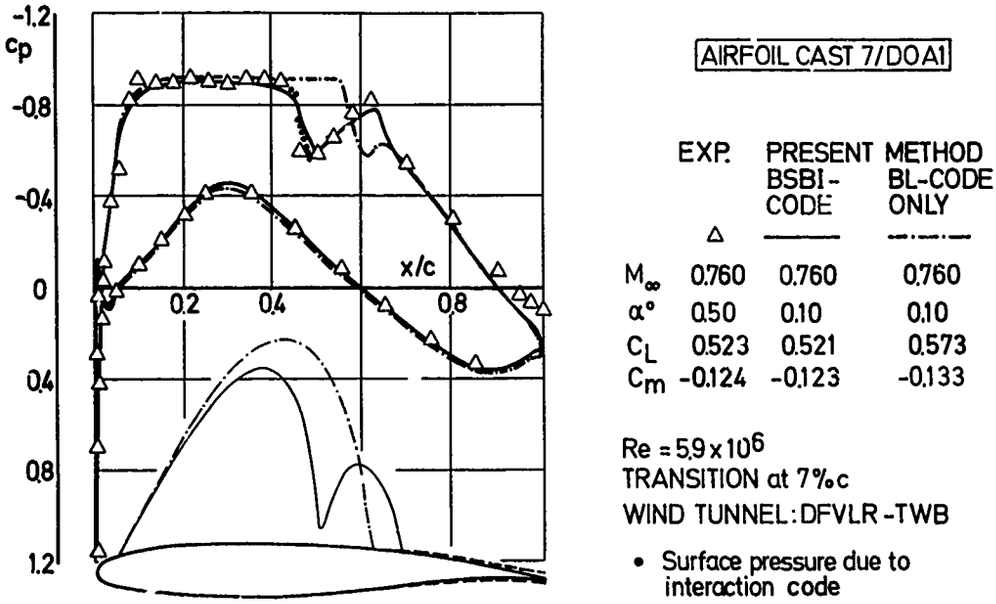


Figure 13. Comparison of Results Obtained by Applying BSBI-code and BL-code Under Double Shock Conditions. Airfoil CAST 7/DOA1

The pitching moment is one of the more sensitive aerodynamic parameters one may use when comparing results from experiment and/or theory. To conclude the CAST 7/DOA1 comparisons, we have plotted this parameter in Figure 14 for the preceding test cases as function of the lift coefficient. The trend in the experimentally determined pitching moment coefficient (C_m) with increasing lift coefficient is, in the range investigated, well predicted

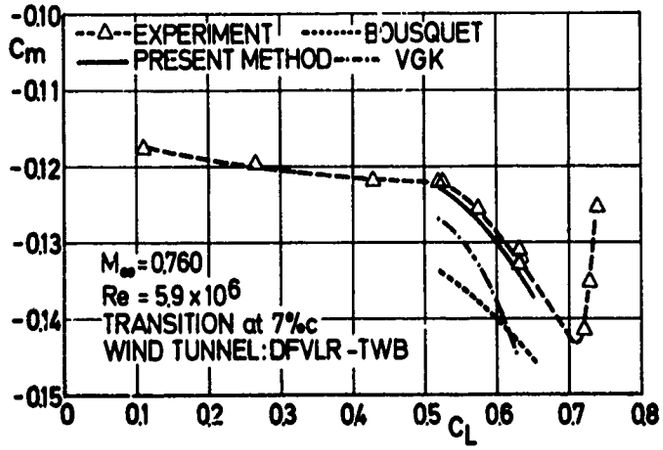


Figure 14. Comparison of Pitching Moments from Experiment and Various Theoretical Methods. Airfoil CAST 7/DOA1

by the three methods considered; however, quantitative agreement is only obtained by the present method reflecting, of course, the good agreement in the pressure distributions.

It was already demonstrated in comparing the experimental and theoretical boundary layer developments that CAST 10-2/DOA2 is more sensitive to small errors in the displacement thickness immediately downstream of the shock than is CAST 7/DOA1. To demonstrate the effect of the underprediction of δ^* on the overall pressure distribution for this airfoil, we are comparing in Figure 15 the experimental c_p-distribution at a Mach number of $M_\infty = 0.765$ and moderate lift ($C_L = 0.574$) with theoretical distributions obtained by ① applying the BSBI-code and ② utilizing the boundary layer code throughout. (For the inviscid computation the non-conservative scheme is used.) Here, the Reynolds number is $Re = 10 \times 10^6$ and transition fixed at 7% chord. As before, there is quite good agreement when properly accounting for shock boundary layer interaction; however, just using the boundary layer code, keeping the free stream conditions the same, completely fails to predict the experimental pressure distribution, the difference clearly reflecting the underprediction of the displacement thickness over the rear of the airfoil. The resulting increase in lift is here almost 20%. The increase in the CAST 7/DOA1-case of Fig. 13, although under slightly different conditions, is about 10%.

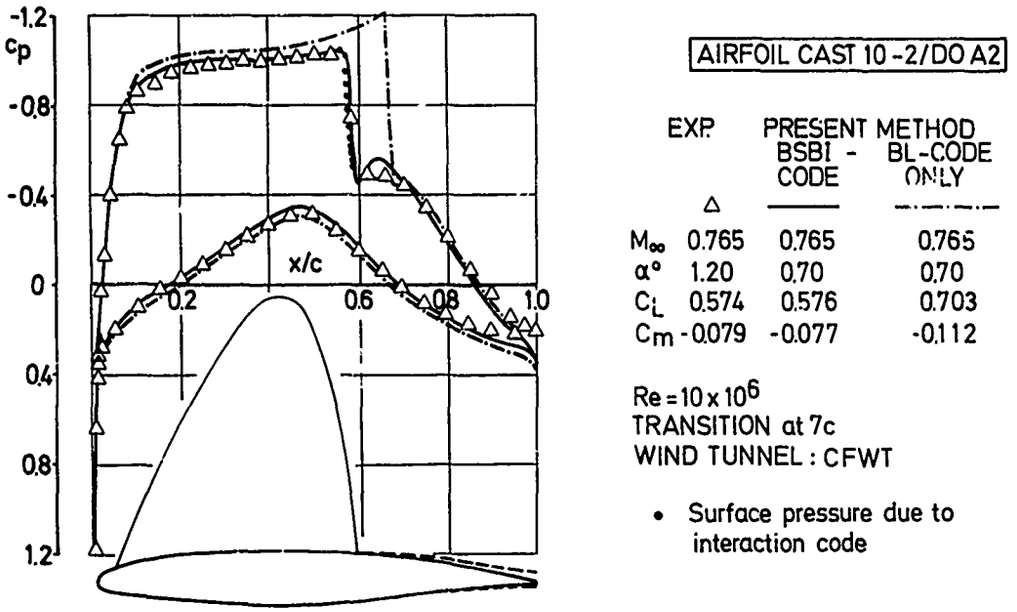


Figure 15. Comparison of Results Obtained by Applying BSBI-code and BL-code Throughout, Respectively. Airfoil CAST 10-2/DOA2

The last test case we will consider, Figure 16, concerns the transonic VFW design Va 2 at a Mach number of $M_{\infty C}$ = 0.734 under high lift conditions (C_L = 0.780)[14]. The Reynolds number here is rather low, viz., Re = 2.4 x 10^6; however, transition was fixed at 40% c on the upper and 25% c on the lower surface resulting in a relatively thin initial boundary layer, at least on the upper surface. The theoretical pressure distribution was computed using the fully conservative version of the inviscid code. The agreement between experiment

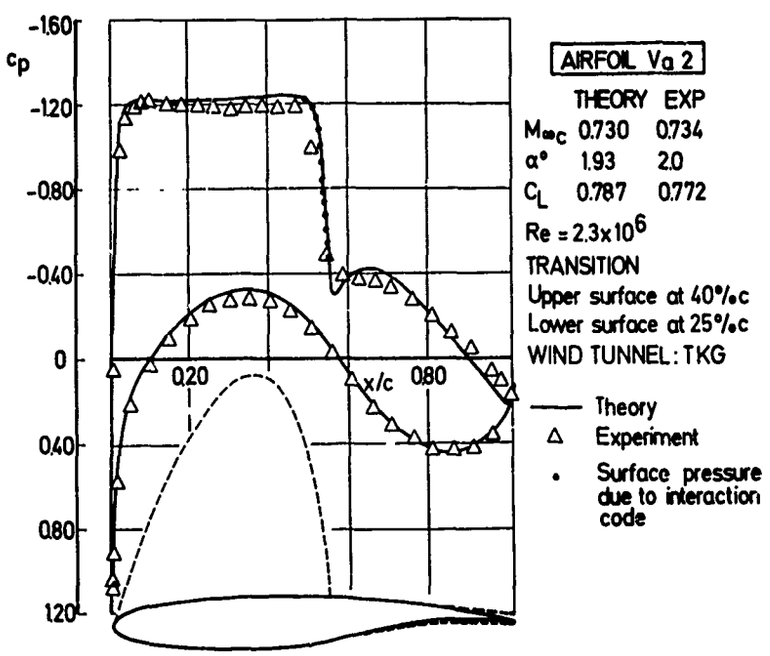


Figure 16. Theoretical and Experimental Pressure Distributions for the Airfoil Va2

and theory in this high lift case is quite satisfactory. The slight overprediction of the jump in pressure due to the shock by the fully conservative scheme is a consequence of the smoothing of the displacement bump in the interaction region. This overpredi tion can, as shown in Ref. 1, be avoided by properly modelling the displacement thickness in this region.

In Figure 17 the experimental displacement thickness distribution corresp. ing to the test case of Fig. 16 is compared to the δ^*-distribution ① added to the geometric airfoil contour for the computation of the final pressure distribution and ② computed by the BSBI-code with the final distribution as input. The agreement on the lower surface is excellent reflecting the good agreement in the corresponding pressure distribution.

This also holds for the upper surface except in the region very close to the trailing edge where the computed δ^*-distribution shows a slight decrease which is, of course, due to the "hook" in the corresponding input pressure distribution, Fig. 16. This type of

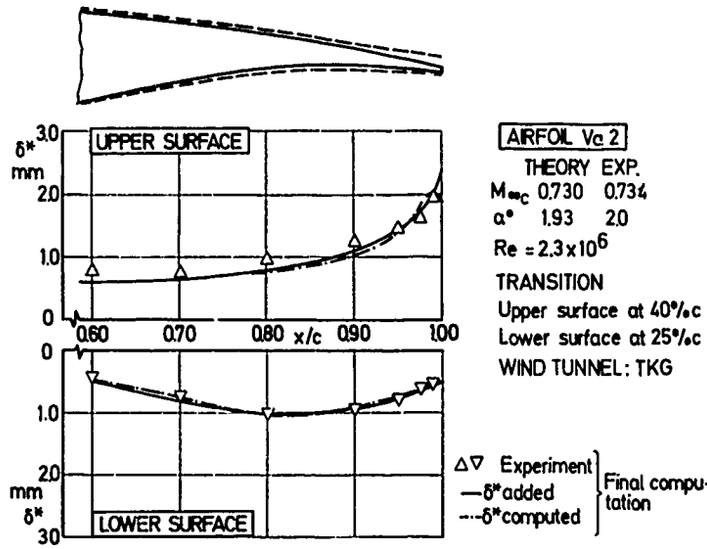


Figure 17. Theoretical and Experimental Displacement Thickness Distribution for the Airfoil Va2

behaviour may be attributed to not correctly treating the trailing edge interaction. Note, that the displacement thickness added generally ignores such irregularities and is of the form shown in Fig. 17 by the solid line.

V. CONCLUDING REMARKS

In this paper a brief description of a computational method for transonic airfoil flow analysis which incorporates an analytical solution for near-normal shock boundary layer interaction into a state-of-the-art viscous-inviscid computation code was given. Theoretical results obtained with the present method were compared to representative data from boundary layer and surface pressure measurements on three transonic airfoils. The agreement between theory and experiment in both, the boundary layer properties and the surface pressure distributions, was, for all test cases considered, quite good.

Treating the shock boundary layer interaction by conventional boundary layer theory generally lead to a slight underprediction of the displacement thickness immediately downstream of the shock and, due to the amplifying effect of the sustained rear adverse pressure gradients, to an appreciable underestimation of the displacement thickness at the trailing edge. The latter was also clearly reflected in the pressure distributions and aerodynamic coefficients compared.

Considering these results, one may conclude that it is generally necessary to include a physically correct treatment of shock wave boundary layer interaction in the analysis of transonic airfoil flow.

VI. REFERENCES

1. Nandanan, M., Stanewsky, E. and Inger, G.R., "A Computational Procedure for Transonic Airfoil Flow Including a Special Solution for Shock Boundary Layer Interaction," AIAA 13th Fluid and Plasma Dynamics Conference, July 14-16, 1980, Snowmass, Colorado, Paper No. 80-1389

2. Jameson, A., "Numerical Computation of Transonic Flow with Shock Waves," Symposium Transsonicum II, Springer-Verlag, Berlin, Heidelberg, New York, 1975

3. Bauer, F., Garabedian, P., Korn, D. and Jameson, A., "Supercritical Wing Sections," Springer-Verlag, Berlin, Heidelberg, New York, 1975

4. Rotta, J.-C. "Turbulent Boundary Layer Calculations with the Integral Dissipation Method," Computation of Turbulent Boundary Layers - 1968 AFOSR-IFP Stanford Conference, Vol. I, p. 177 (also Ing.-Archiv 38 (1969), pp. 212-222)

5. Inger, G.R. and Mason, W.H., "Analytical Theory of Transonic Normal Shock-Turbulent Boundary-Layer Interactions," AIAA Journal, Vol. 14, No. 9, Sept. 1976, pp. 1266-1272

6. Ludwieg, H. and Tillmann W., "Untersuchungen über die Wandschubspannung in turbulenten Reibungsschichten," Ing.-Archiv 17 (1949), pp. 288-299

7. Nash, J.F., "Turbulent-Boundary-Layer Behaviour and the Auxiliary Equation," NPL Aero Rep. 1137, 1965 (also AGARDograph 97 (1965), p.245)

8. Panaras, A.G. and Inger, G.R., "Transonic Normal Shock-Turbulent Boundary Layer Interaction in Pressure Gradient Flows," ASME Paper No. 77-GT-34, 1977

9. Inger, G.R. and Cantrell, J.C., "Application of Shock-Turbulent Boundary Layer Interaction Theory to Transonic Aerodynamics," BMVg-FBWT 79-31, pp. 100-115 (4th US-FRG-Meeting on Viscous and Interacting Flow Field Effects)

10. Schlichting, H., "Boundary Layer Theory," McGraw-Hill Book Comp., Inc., New York, Toronto, London, 5th Edition, 1979

11. Kühl, P. and Zimmer, H., "Design of Airfoils for Transport Aircraft with Improved High Speed Characteristics," DORNIER GmbH, Report 74/16B, 1974 (also: Stanewsky, E. and Zimmer, H., "Development and Wind Tunnel Test of Three Supercritical Airfoils for Transport Aircraft," Zeitschrift für Flugwissenschaften 23 (1975), Heft 7/8)

12. Hilbig, R., "Design of the Transonic Airfoil Va 2", Ziviles Komponentenprogramm (ZKP), LFK 7511 Flügelsektion, Report No. 7

13. Hottner, Th., and Lorenz-Meyer, W., "The Transonic Wind Tunnel of the Aerodynamische Versuchsanstalt Göttingen," DGLR-Jahrbuch 1968, pp. 235-244

14. Stanewsky, E. and Thiede, P., "Boundary Layer and Wake Measurements in the Trailing Edge Region of a Rear-Loaded Transonic Airfoil," BMVg-FBWT 79-31, pp.31-53 (4th US-FRG-Meeting on Viscous and Interacting Flow Field Effects)

15. Stanewsky, E., Puffert, W. and Müller, R., "The DFVLR Transonic Wind Tunnel Braunschweig: Calibration Results for the Modified Test Section and Results for the Airfoil CAST 7/DOA1," DFVLR-Report IB 151-77/10, 1977 (also: DGLR-Symposium Transonic Configurations, Bad Harzburg, 13-15 June, 1978)

16. Pounds, G.A. and Stanewsky, E., "The Research Compressible Flow Facility," Lockheed-Georgia Comp. Report ER-9219, 1967 (On wall interference corrections see: Blackwell, J.A., "Wind Tunnel Blockage Correction for Two-Dimensional Transonic Flow," J. Aircraft, Vol. 16, No. 4, 1979)

17. Bousquet, J., "Calculs bidimensionnels transsonique avec couche limite," AAAF 11th Colloque d'Aerodynamique Applicée, Nov. 1974

18. Collyer, M.R. and Lock, R.C., "Improvements to the Viscous Garabedian and Korn (VKG) Method for Calculating Transonic Flow Past an Airfoil," RAE Technical Report 78039,1978

19. Lock, R.C., "Report on a Combined Experimental and Theoretical Investigation of the Airfoil CAST 7/DOA1," RAE Technical Report 79073 (GARTEur/TP-1), June 1979

20. Stanewsky, E., Puffert, W., Müller, R. and Bateman, T.E.B., "Supercritical Airfoil CAST 7 - Surface pressure, wake and boundary layer measurements," AGARD-AR-138, Experimental Data Base for Computer Program Assessment, May 1979, pp.A3-1 to A3-35

21. Michel, R., Quemard, C. and Cousteix, J., "Méthode practique de prévision des couches limites turbulents bi et tri-dimensionnels," La Recherche Aerospatiale,No.1, pp.1-4,1972

22. Green, J.E., Weeks, D.J. and Brooman, J.W.F., "Prediction of Turbulent Boundary Layers and Wakes in Compressible Flow by a Lag-entrainment Method," ARC R&M 3791, 1973

COUPLAGE FLUIDE PARFAIT-FLUIDE VISQUEUX[*] EN ECOULEMENT INSTATIONNAIRE BIDIMENSIONNEL INCOMPRESSIBLE ET TRANSSONIQUE

par A. DESOPPER et R. GRENON

Office National d'Etudes et de Recherches Aérospatiales
29, avenue de la Division Leclerc
92320 Châtillon - FRANCE

RESUME

Parallèlement aux études expérimentales entreprises par l'ONERA dans le cadre des recherches sur les écoulements instationnaires, une méthode de calculs couplés fluide visqueux - fluide non visqueux en écoulement bidimensionnel instationnaire a été développée.

On décrit tout d'abord la méthode de calcul qui comprend :
- pour le calcul en fluide parfait, soit une méthode de singularités en régime incompressible, soit une méthode résolvant l'équation des petites perturbations en régime transsonique ;
- une méthode intégrale pour la détermination des caractéristiques de la couche limite instationnaire ;
- une technique de couplage du type couplage à la paroi ne prenant pas en compte les régions décollées.

On présente ensuite des résultats obtenus par cette méthode. En écoulement incompressible, les forces aérodynamiques sont calculées pour un profil supercritique muni d'une gouverne de bord de fuite oscillante ; des résultats concernant un profil oscillant en tangage sont également présentés. En écoulement transsonique on détermine les caractéristiques aérodynamiques d'un profil NACA 64 A 006 muni d'une gouverne oscillante ; de plus, quelques cas correspondant à un profil oscillant en tangage et à une section de pale d'hélicoptère en configuration non portante sont traités.

Les résultats obtenus mettent en évidence l'influence des effets visqueux sur les répartitions de pression locale, sur les coefficients aérodynamiques, sur l'intensité et sur la position des chocs. Les résultats de calcul sont comparés à divers résultats expérimentaux disponibles.

VISCOUS-INVISCID COUPLED CALCULATIONS IN UNSTEADY TWO-DIMENSIONAL INCOMPRESSIBLE AND TRANSONIC FLOW

SUMMARY

At ONERA, both experimental and theoretical works are performed on unsteady aerodynamics. A calculation method in which viscous effects have been taken into account has been developped.

We first describe this method ; it uses :
- for the inviscid flow calculation, a singularity method in incompressible flow or a small disturbances method in transonic flow ;
- an integral method for the calculation of the unsteady boundary layer ;
- a coupling technique called "coupling at the wall" not taking into account the problem of separation.

Then, some results obtained by this method are presented :
- in incompressible flow for a supercritical profile with an oscillating flap and for a profile oscillating in pitch ;
- in transonic flow for a NACA 64 A 006 profile with an oscillating flap and some results for a profile oscillating in pitch and for a helicopter blade section in a nonlifting case.

These results show the influence of the viscous effects on the unsteady pressures, on the total force coefficients, on the strength and on the location of the shock waves. When it is possible the results are compared with the experimental ones.

NOTATIONS

a	: vitesse du son (m/s)	α	: incidence du profil (°)
ρ	: masse volumique (kg/m^3)	δ_m	: braquage moyen du volet (°)
V	: vitesse de l'écoulement (m/s)	δ_i	: amplitude des oscillations du volet (°)
M_∞	: nombre de Mach à l'infini amont	t	: temps (s)
c	: corde (m)		

[*] Etude effectuée avec la participation financière du Service Technique des Programmes Aéronautiques du Ministère de la Défense.

ω : pulsation du mouvement harmonique (rad/s)

$f = \frac{\omega}{2\pi}$: fréquence des oscillations (Hz)

$K = \frac{\omega c}{2V_\infty} = \frac{\pi f c}{V_\infty}$: fréquence réduite

p : pression instantanée (Pa)

p_m : pression moyenne (Pa)

Δp : fluctuation de pression (Pa)

$K_p = \frac{p - p_\infty}{1/2 \rho_\infty V_\infty^2}$: coefficient de pression instantanée (ou stationnaire)

$C_p = \frac{\Delta p}{1/2 \rho_\infty V_\infty^2 \delta_i}$: coefficient de pression instationnaire

C_{p_1} : module du premier harmonique du coefficient de pression

K_p^* : valeur de Kp lorsque $M_\ell = 1$

c_z : coefficient de portance instantanée

c_m : coefficient de moment de tangage instantané

c_{z_δ} : coefficient de portance instationnaire

c_{m_δ} : coefficient de moment de tangage instationnaire

$c_{m_{c\delta}}$: coefficient de moment de charnière instationnaire

φ : angle de phase (°)

φ_1 : angle de phase du premier harmonique (°)

R_e : nombre de Reynolds

δ : épaisseur de la couche limite (m)

U : composante longitudinale de la vitesse dans la couche limite (en m)

$\theta = \int_0^\delta \frac{\rho U}{\rho_e U_e}\left(1 - \frac{U}{U_e}\right) dy$: épaisseur de quantité de mouvement de la couche limite (en m)

$\delta_1 = \int_0^\delta \left(1 - \frac{\rho U}{\rho_e U_e}\right) dy$: épaisseur de déplacement de la couche limite (en m)

H : facteur de forme de la couche limite

C_f : coefficient de frottement local.

INDICES :

ℓ : valeurs locales (a, V, M)

∞ : valeurs à l'infini amont (a, V, M)

1 - INTRODUCTION -

Au cours des dernières années deux motivations principales ont conduit à un développement rapide des recherches concernant les écoulements instationnaires, tant du point de vue expérimental que théorique, il s'agit :

- du développement des techniques de contrôle actif généralisé qui nécessite l'emploi de gouvernes à court temps de réponse.

- de l'optimisation des performances des rotors d'hélicoptère qui demande une meilleure connaissance de l'écoulement instationnaire autour des pales.

Dans le cadre de ces recherches, l'ONERA a entrepris l'étude expérimentale détaillée d'un profil supercritique muni d'une gouverne de bord de fuite oscillante et l'étude de l'écoulement autour d'une pale de rotor d'hélicoptère.

Parallèlement à ces études expérimentales, des méthodes de calculs instationnaires permettant de rendre compte des phénomènes observés ont été étudiées. Une première méthode de calculs couplés fluide visqueux-fluide non visqueux en écoulement bidimensionnel instationnaire a été développée.

On décrit tout d'abord la méthode de calcul qui comprend :

. pour le calcul en fluide parfait, soit une méthode de singularités en régime incompressible, soit une méthode résolvant l'équation des petites perturbations en régime transsonique ;

. une méthode intégrale pour la détermination des caractéristiques de la couche limite instationnaire.

. une technique de couplage du type couplage à la paroi ne prenant pas en compte les régions décollées.

On présente ensuite des résultats obtenus par cette méthode :

- en écoulement incompressible pour le profil supercritique avec gouverne et pour un profil NACA 0012 oscillant en tangage.

- En écoulement transsonique pour les expériences du NLR sur un profil NACA 64A006 muni d'une gouverne oscillante, pour un profil NACA 64 A 010 oscillant en tangage et pour une section de pale d'hélicoptère en configuration non portante.

Les résultats obtenus mettent en évidence l'influence des effets visqueux sur les répartitions de pression locale, sur les coefficients intégrés, sur l'intensité et sur la position des chocs. Les résultats de calcul sont comparés aux résultats expérimentaux disponibles.

2 - METHODE DE CALCUL -

Comme indiqué précédemment on s'intéresse aux écoulements bidimensionnels instationnaires.

2.1 - Méthodes de calcul en fluide parfait -

Chacune des méthodes de calcul utilisées sera brièvement présentée. Pour plus de détails, on se reportera aux ouvrages cités en référence.

Pour traiter les écoulements instationnaires on peut utiliser la théorie linéarisée de la plaque plane. Une méthode couramment employée pour les calculs de structures à l'ONERA utilise une technique de répartition de doublets [1]. Le profil est en fait assimilé à une ligne sans épaisseur ni cambrure, seule la réponse instationnaire est obtenue et l'influence de l'écoulement moyen (effet d'incidence moyenne, de braquage moyen du volet) sur l'instationnaire n'est pas prise en compte.

Cette méthode est donc insuffisante pour tenir compte des phénomènes d'épaisseur ou d'interaction avec l'écoulement moyen en incompressible et bien évidemment ne fait pas apparaître d'onde de choc en subsonique élevé ; on s'est donc plutôt intéressé à des méthodes non-linéaires.

- écoulement incompressible

Pour représenter l'influence de l'écoulement moyen sur la réponse instationnaire aux basses vitesses on utilise un programme de calcul en écoulement instationnaire incompressible développé par la Société BERTIN [2] et basé sur la méthode de GIESING [3]. Le profil est représenté par des sources et des puits sur son contour et des tourbillons sur la ligne moyenne. Le sillage est constitué de tourbillons libres émis à chaque pas de temps pour conserver la circulation totale de l'écoulement. Cette méthode tient compte de la forme et du mouvement exacts du profil, ainsi que de la déformation du sillage tourbillonnaire.

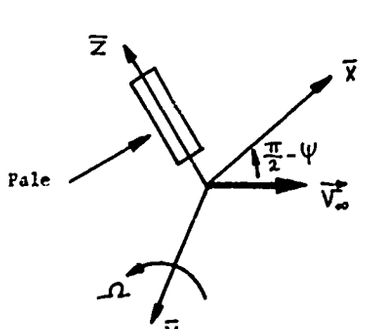
- écoulement transsonique

Les méthodes de calcul non linéaires actuellement utilisées en régime supercritique instationnaire sont basées soit sur la résolution des équations d'EULER [4] à [8], soit sur l'hypothèse d'écoulement potentiel : résolution de l'équation du potentiel instationnaire complète [9] ou résolution de l'équation dans l'approximation des petites perturbations transsoniques [10], [11].

Jusqu'à maintenant, seules les méthodes basées sur la résolution de l'équation du potentiel des vitesses avec l'approximation des petites perturbations transsoniques sont d'un coût relativement raisonnable. On s'est donc servi d'un programme initialement développé pour l'étude des écoulements sur pales d'hélicoptère par F.X. CARADONNA [11] et qui a été adapté au cas du profil ou du volet oscillant par J.J.THIBERT de l'ONERA. Ce programme résout l'équation du potentiel instationnaire des vitesses dans les hypothèses de petites perturbations transsoniques et de faible fréquence réduite.

Les équations finalement adoptées pour la configuration hélicoptère [11] et pour la configuration profil ainsi que les conditions limites sont précisées ci-dessous.

FORMULATION HELICOPTERE :

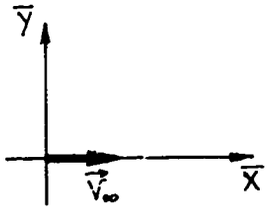


$$\frac{2M_n^2}{\lambda' \tau^{2/3}}(1+\nu'\sin\psi)\,\bar{\Phi}_{x\psi} = \bar{\Phi}_{xx}\left\{\frac{1-M_n^2(1+\nu'\sin\psi)^2}{\tau^{2/3}} - (1+\gamma)M_n^2(1+\nu'\sin\psi)\bar{\Phi}_x\right\} + \bar{\Phi}_{yy}$$

Avec τ épaisseur relative ;

$$\lambda' = \frac{n}{c} \; ; \; \nu' = \frac{V_\infty}{\omega R} \; ; \; M_n = \frac{\omega n}{a_\infty} \; ; \; X = \frac{\bar{X}}{c} \; ; \; Y = \tau^{1/3}\frac{\bar{Y}}{c} \; ; \; \Phi = \bar{\Phi} \times \frac{1}{\omega n c\, \tau^{2/3}}$$

FORMULATION PROFIL :



$$4M_\infty^2 \frac{K}{\tau^{2/3}}\bar{\Phi}_{XT} = \bar{\Phi}_{XX}\left\{\frac{1-M_\infty^2}{\tau^{2/3}} - (\gamma+1)M_\infty^2\bar{\Phi}_X\right\} + \bar{\Phi}_{YY}$$

Avec τ épaisseur relative ; $K = \frac{\omega c}{2V_\infty}$; $X = \frac{\bar{X}}{c}$;

$$Y = \frac{\bar{Y}}{c}\tau^{-1/3} \; ; \; T = 2KV_\infty\frac{\bar{t}}{c} \; ; \; \Phi = \frac{\bar{\Phi}}{\tau^{2/3}V_\infty c}$$

CONDITIONS AUX LIMITES :

. Sur le profil la condition de glissement :

$$\bar{\Phi}_Y(X, 0^\pm) = T'(X) \pm \frac{\alpha}{\tau} \pm \beta\left(\frac{\partial\alpha}{\partial T}\right)$$

($T'(X)$: pente du profil au point X)

. Sur le sillage :

$$2K\frac{\partial[\bar{\Phi}]}{\partial T} + \frac{\partial[\bar{\Phi}]}{\partial X} = 0$$

($[\bar{\Phi}]$: saut de potentiel à la traversée du sillage)

. A l'infini amont : $\bar{\Phi} = 0$

. A l'infini aval : $\bar{\Phi}_X = 0$

. Sur les frontières latérales : $\bar{\Phi}_Y = 0$

Le coefficient de pression étant déterminé par $K_p = -\frac{2\tau^{2/3}}{(1+\nu'\sin\psi)^2}\left[\lambda'\bar{\Phi}_\psi + (1+\nu'\sin\psi)\bar{\Phi}_X\right]$ pour la formulation hélicoptère et par $K_p = -2\tau^{2/3}(2K\bar{\Phi}_T + \bar{\Phi}_X)$ pour la formulation profil.

Cette méthode a les limitations liées à la théorie des petites perturbations : profil peu épais, faible incidence, chocs de faible intensité. Sur la figure 1 les résultats obtenus pour un profil NACA 0012 muni d'un volet oscillant sont comparés à ceux fournis par la résolution des équations d'EULER [6]. L'amplitude de la variation du coefficient de portance et celle du déplacement de l'onde de choc obtenues par la méthode des petites perturbations sont plus faibles mais il faut remarquer que les deux calculs font apparaître un important déphasage entre le mouvement du choc et celui du volet (de l'ordre de 90°). Pour un cas hélicoptère la comparaison entre les deux méthodes de calcul est présentée sur la figure 2 ; l'évolution de la pression dans la région d'écoulements transsoniques en pale avançante obtenue par l'une ou l'autre des méthodes est tout à fait comparable.

Compte tenu de ces résultats et du temps de calcul nécessaire à la résolution des équations d'EULER la méthode petites perturbations est utilisée tout en ayant conscience de ses limitations.

2.2 - <u>Méthode de calcul de la couche limite</u> :

Les premières comparaisons calcul-expérience en écoulement incompressible (fig. 5 et 6) ont montré que les résultats obtenus par la méthode de GIESING étaient plus éloignés des résultats expérimentaux que ceux obtenus par la théorie de la plaque plane. Cette dernière bénéficie d'une heureuse compensation

entre les effets d'épaisseur et de cambrure d'une part et ceux de la viscosité d'autre part, effets qui jouent en sens contraire déjà en quasi-stationnaire [12]. La prise en compte des effets visqueux est alors apparue nécessaire.

Depuis 1974 le Centre d'Etudes et de Recherches de Toulouse poursuit des études détaillées sur les couches limites turbulentes instationnaires : couche limite de plaque plane [13], [14] ou en présence de gradient de pression défavorable [15]. Les études expérimentales entreprises portent sur la structure de la turbulence et les résultats obtenus ont permis de tester différentes méthodes de calcul. Des méthodes basées sur la résolution des équations locales et une méthode intégrale ont ainsi été mises au point [13 à 16].

- Calcul de la couche limite turbulente :

Pour le couplage on a utilisé la méthode intégrale de calcul des couches limites turbulentes en écoulement compressible instationnaire. Il s'agit d'une méthode intégrale basée sur la résolution de l'équation globale de quantité de mouvement ou équation de VON KARMAN (1) et de l'équation globale de continuité ou équation d'entraînement (2) :

$$(1)\qquad \frac{C_f}{2} = \frac{\partial \theta}{\partial x} + \theta\left[(2+H)\frac{1}{U_e}\frac{\partial U_e}{\partial x} + \frac{1}{\rho_e}\frac{\partial \rho_e}{\partial x}\right] + \frac{\delta}{\rho_e U_e^2}\frac{\partial(\rho_e U_e \delta_1)}{\partial t}$$

$$(2)\qquad \frac{1}{\rho_e U_e}\frac{\partial}{\partial x}\left[\rho_e U_e(\delta - \delta_1)\right] + \frac{1}{U_e}\frac{\partial \delta}{\partial t} = P\sqrt{\frac{C_f}{2}}$$

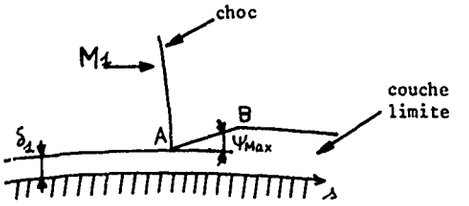
Les relations de fermeture nécessaires à la résolution de ce système d'équations sont identiques à celles utilisées en stationnaire [17]. Par rapport à la formulation stationnaire on remarquera la présence d'un terme instationnaire dans chacune des équations.

$U_e(x,t)$ et $\rho_e(x,t)$ étant fournis par un calcul de fluide parfait, les équations (1) et (2) sont résolues par une méthode différences finies de type explicite. Les conditions initiales sont les valeurs de H et de θ en fonction de s sur la ligne $x = x_0$ (abscisse initiale du calcul fixée arbitrairement à 7% du bord d'attaque) et en fonction de x sur la ligne $t = t_0$ (instant initial). Les valeurs de H et θ en $x = x_0$ sont calculées à chaque instant à partir des relations de plaque plane en utilisant les conditions locales de vitesse et de Reynolds. A l'instant initial les équations (1) et (2) sont résolues de façon quasi-stationnaire.

Les résultats présentés sur la figure 3 concernent l'évolution du point de décollement de la couche limite turbulente ($C_f = 0$) pour un profil oscillant en tangage à basse vitesse. Ils montrent l'importance des effets instationnaires pour le calcul en fluide parfait et pour celui de la couche limite. On remarquera en particulier que par rapport à l'utilisation d'une méthode de calcul stationnaire de la couche limite celle d'une méthode de calcul instationnaire donne une région décollée moins importante lorsque l'incidence augmente, un retard de phase du point de décollement maximum et un décollement plus important lorsque l'incidence décroît. Ces phénomènes sont à rapprocher de ceux observés dans les configurations de décrochage dynamique.

- Traitement de la région du choc

Lorsque le choc est de faible intensité la recompression à la traversée du choc est prise en compte dans le calcul de la couche limite comme un gradient de vitesse. Un traitement spécial est employé pour les chocs d'intensité plus forte ($M \geq 1{,}2$) afin d'éviter les difficultés liées à l'apparition d'un décollement en pied de choc.



En amont du choc (point A) on fait un calcul classique de couche limite ; dans la région du choc (région AB) on suppose que l'épaississement de la couche limite est égal à l'angle de la déviation qui pour un Mach devant choc M_1 donnerait un écoulement sonique immédiatement en aval du choc. En aval du choc (point B) le calcul de couche limite reprend avec des valeurs H_B et θ_B déduites des valeurs H_A et θ_A par les relations de RESHOTKO et TUCKER [18].

..3 - Technique de couplage

La méthode utilisée est une méthode de couplage faible, les effets visqueux sont supposés ne concerner qu'une région très limitée autour du profil, seul l'effet des couches limites qui se développent sur le profil est pris en compte en supposant ces couches limites non décollées et d'épaisseur δ faible devant la dimension du profil.

Le domaine de calcul est ainsi divisé en deux : la région des couches limites entourant le profil et la région extérieure où l'on fait l'hypothèse de fluide parfait. Les conditions à imposer à la frontière $y = \delta$ entre les deux domaines sont : $(\rho_e)_\delta = (\rho)_\delta$, $(U_e)_\delta = U_\delta$ et $(V_e)_\delta = V_\delta$ (les grandeurs indicées e provenant du domaine fluide parfait et celles non indicées correspondant à la couche limite). Les deux premières relations sont vérifiées puisque les répartitions $U_e(x,t)$ et $\rho_e(x,t)$ obtenues par le calcul en fluide parfait servent de conditions aux limites dans le calcul de la couche limite. Il reste donc à imposer la condition sur la vitesse verticale $(V_e)_\delta = V_\delta$ ou $\left(\frac{V_e}{U_e}\right)_\delta = \left(\frac{V}{U}\right)_\delta$.

Par intégration de l'équation de continuité

$$\frac{\partial \rho}{\partial t} + \frac{\partial \rho U}{\partial x} + \frac{\partial \rho V}{\partial y} = 0 \qquad \text{on obtient :} \quad \left(\frac{\rho V}{\rho U}\right)_\delta = \frac{\partial \delta_1}{\partial x} + (\delta - \delta_1)\frac{1}{(\rho U)_\delta}\frac{\partial (\rho U)_\delta}{\partial x} - \frac{1}{(\rho U)_\delta}\int_0^\delta \frac{\partial \rho}{\partial t}\, dt$$

où δ_1 est l'épaisseur de déplacement.

La relation de couplage stricte en y = δ : $\left(\frac{V_e}{U_e}\right)_\delta = \left(\frac{V}{U}\right)_\delta$
s'écrit donc :

$$\left(\frac{V_e}{U_e}\right)_\delta = \frac{\partial \delta_1}{\partial x} - (\delta - \delta_1)\frac{1}{(\rho_e U_e)_\delta}\frac{\partial (\rho_e U_e)_\delta}{\partial x} - \frac{1}{(\rho_e U_e)_\delta}\int_0^\delta \frac{\partial \rho}{\partial t}\, dy$$

En fait on n'utilise pas cette relation de couplage stricte mais on procède comme en stationnaire [19] à un couplage dit couplage à la paroi en utilisant une relation écrite à la paroi (y=o) :

$$\left(\frac{V_e}{U_e}\right)_0 = \frac{\partial \delta_1}{\partial x} + \frac{\delta_1}{(\rho_e U_e)_0}\frac{\partial (\rho_e U_e)_0}{\partial x} + \frac{1}{(\rho_e U_e)_0}\int_0^\delta \left[\left(\frac{\partial \rho_e}{\partial t}\right)_\delta - \left(\frac{\partial \rho}{\partial t}\right)\right] dy$$

Le calcul en fluide parfait est donc effectué jusqu'à la paroi du profil (y = 0) et la condition de glissement fait intervenir les pentes géométriques locales du profil modifiées de la quantité $(V_e/U_e)_0$ pour tenir compte du développement de la couche limite. Concrètement, cela se traduit par un débit de fluide à travers la paroi caractérisé par une vitesse normale V_e dans le programme de singularités et par une modification des pentes locales du profil de la quantité $(V/U)_p$ dans le programme de petites perturbations transsoniques V_e et $\left(\frac{V}{U}\right)_p$ sont donnés par :

$$\frac{V_e}{U_e} = \left(\frac{V}{U}\right)_p = \frac{1}{\rho_e U_e}\frac{\partial}{\partial x}(\rho_e U_e \delta_1) \qquad (3)$$

Pour l'ensemble des résultats présentés le terme instationnaire $\frac{1}{\rho_e U_e}\int_0^\delta \left[\left(\frac{\partial \rho_e}{\partial t}\right)_\delta - \left(\frac{\partial \rho}{\partial t}\right)\right] dy$ a été négligé, même en compressible. Il faut remarquer que les cas traités correspondent à des valeurs faibles de la fréquence réduite et que des premiers calculs effectués en tenant compte de ce terme n'ont pas montré de différence notable.

A chaque pas de temps on effectue deux ou trois itérations fluide parfait-couche limite avec éventuellement l'utilisation d'une méthode de relaxation. Concrètement, à l'instant $t+dt$, le calcul s'effectue de la façon suivante :

1) Calcul du fluide parfait avec comme paramètre intervenant dans la condition aux limites sur le profil : la pente géométrique locale du profil corrigée de la couche limite calculée à l'instant t s'il s'agit de la première itération ou de celle calculée à l'itération précédente (cf. équation 3).

2) Calcul de la couche limite à partir des caractéristiques de la couche limite à l'instant précédent et des distributions de vitesse et de masse volumique déterminées par le calcul du fluide parfait en 1 ; puis retour en 1 pour une nouvelle itération.

Les principaux problèmes rencontrés dans les calculs sont essentiellement liés à l'apparition de décollements au bord de fuite et à la présence de chocs d'intensité non négligeable. Dans certaines configurations un léger décollement apparaît vers le bord de fuite pendant une partie du mouvement et dans ce cas les grandeurs de couche limite sont simplement extrapolées afin de poursuivre le calcul. On voit donc apparaître deux limitations majeures de ces calculs : le traitement de façon simplifiée de l'interaction onde de choc-couche limite et celui des régions décollées.

3 - RESULTATS OBTENUS - INFLUENCE DES EFFETS VISQUEUX -

3.1 - Ecoulement incompressible -

a) Profil supercritique RA 16 SC 1 :

Des études expérimentales détaillées ont été menées par l'ONERA sur un profil supercritique de 16 % d'épaisseur relative développé par la Société Aérospatiale (profil RA 16 SC 1). Le profil est muni d'une gouverne de bord de fuite de 25% de profondeur pouvant osciller; un schéma du montage est présenté sur la figure 4.

Sur la figure 5, tirée de la réf.[21] les pressions instationnaires obtenues expérimentalement (module et phase) pour une configuration faiblement chargée ($\delta_m = 0$) sont comparés aux résultats fournis par la théorie linéarisée. On remarquera que cette théorie linéaire donne des pressions instationnaires infinies au bord d'attaque et à la charnière.

- Influence de la viscosité sur les répartitions de pression instationnaire :

Sur la figure 6, les résultats expérimentaux présentés sur la figure 5 sont comparés aux résultats du programme de calcul par singularités en fluide parfait incompressible avec et sans couplage. Le calcul en fluide parfait prévoit des modules de pression instationnaire plus forts que la théorie linéarisée (voir figure 5) mais il différencie bien l'extrados de l'intrados et donne une meilleure représentation qualitative des phénomènes instationnaires notamment au voisinage du bord d'attaque et de la charnière.

La prise en compte de la couche limite se traduit par une diminution des modules de pression instationnaire, les phases sont pratiquement inchangées sauf au voisinage du bord de fuite où apparaît un très léger décollement durant une partie de la période.

L'influence du couplage apparaît encore davantage sur la figure 7 qui représente un cas de forte interaction visqueuse, avec un braquage moyen du volet de 5° : en effet, lorsque le volet est braqué de 5° en stationnaire, un décollement apparait au bord de fuite extrados , vers $x/c = 0,95$. Le calcul en fluide parfait donne des niveaux de pression instationnaire entre le bord d'attaque et la charnière nettement supérieurs à ceux observés expérimentalement. Le couplage avec prise en compte de la couche limite réduit de près de 70% l'écart sur les modules des pressions instationnaires et fait évoluer les phases dans le sens d'une légère avance. Le calcul couplé représente assez bien l'évolution des pressions instationnaires le long de la corde jusqu'à $x/c = 0,9$ environ : on observe à l'extrados une très forte avance de phase derrière la charnière et une augmentation des modules des pressions instationnaires vers le bord de fuite. Cependant les dix derniers pour cent de la corde ne peuvent pas être calculés de façon réaliste en raison du traitement simplifié de la zone décollée et cela entraîne une imprécision des valeurs des modules et des phases des pressions instationnaires sur l'ensemble du profil. Le programme couplé fonctionne donc ici à la limite de ses possibilités.

- Influence de la viscosité sur les coefficients intégrés :

Si l'on considère l'intensité des pressions instationnaires entre le bord d'attaque et la charnière par exemple (fig. 5 et 6) le calcul non linéaire couplé peut paraître décevant en regard de la théorie linéarisée. Cependant, en supprimant les infinis du bord d'attaque et de la charnière, en donnant des résultats bien meilleurs que ceux de la théorie linéarisée sur le volet et en rendant compte de l'influence des paramètres de l'écoulement moyen, le calcul non linéaire couplé donne des résultats nettement plus intéressants du point de vue des coefficients globaux. C'est ce que montrent les figures 8 à 10 où sont présentés des résultats obtenus par le programme BERTIN avec et sans couche limite, par la théorie linéarisée et des résultats expérimentaux.

L'évolution des trois coefficients instationnaires (portance, moment de tangage à 25% et moment de charnière) en fonction de la fréquence réduite dans des configurations où le braquage moyen de la gouverne est nul est présentée sur la figure 8. L'influence de la viscosité se traduit par une diminution de l'amplitude de ces coefficients, les phases étant pratiquement inchangées. A l'exception de la phase du moment de charnière le programme couplé donne de meilleurs résultats que la théorie linéarisée, le gain étant particulièrement important sur l'amplitude du moment de tangage et sur celle du moment de charnière. Ce résultat n'est pas surprenant dans la mesure où les couches limites sont les plus épaisses au niveau du bord de fuite et interviennent donc directement sur l'efficacité instationnaire de la gouverne.

La figure 9 montre l'évolution des trois mêmes coefficients globaux instationnaires en fonction du braquage moyen de la gouverne pour une fréquence réduite $k = 0,167$. Les coefficients donnés par la théorie linéarisée sont constants puisque par hypothèse l'écoulement instationnaire ne dépend pas de l'écoulement moyen. Les coefficients donnés par le programme de singularités en fluide parfait varient très faiblement lorsque le braquage moyen de la gouverne varie de -10° à + 10°. Les résultats obtenus par le calcul couplé indiquent à nouveau une nette diminution de l'amplitude des coefficients par l'effet des couches limites et les coefficients de portance et de moment de tangage instationnaires sont assez proches des résultats des coefficients expérimentaux et évoluent de la même façon avec le braquage moyen : le module décroît de plus en plus vite lorsque la charge moyenne de l'aile augmente et la phase évolue dans le sens d'une avance lorsqu'on approche des configurations où apparaissent des décollements. Le calcul couplé n'a pas été poursuivi au-delà de $\delta_m = 5°$ en raison de l'importance des zones décollées. On peut donc conclure que le phénomène non linéaire de dépendance au braquage moyen qui affecte les performances instationnaires des gouvernes aux basses vitesses est essentiellement d'origine visqueuse. La méthode non-linéaire permet de prévoir également les valeurs moyennes des coefficients intégrés comme le montre la figure 10 où l'on a tracé les valeurs moyennes du coefficient de portance en fonction du braquage moyen de la gouverne.

En ce qui concerne le moment de charnière, le calcul couplé montre une évolution en fonction du braquage moyen plus importante que le calcul en fluide parfait mais les valeurs théoriques s'éloignent de plus en plus des valeurs expérimentales pour les grands braquages. Il faut toutefois remarquer que la détermination expérimentale du moment de charnière instationnaire manque de précision du fait du nombre limité de capteurs de pression sur le volet (10 au total).

La méthode de calculs couplés non-linéaires permet donc de déterminer à la fois les caractéristiques aérodynamiques moyennes et instationnaires de façon correcte et de prendre en compte l'interaction du stationnaire sur l'instationnaire. Les calculs effectués pour des configurations faiblement chargées ont en outre fait ressortir que les effets d'épaisseur et de cambrure d'une part et les effets visqueux d'autre part jouent en sens contraire et qu'il est donc indispensable de tenir compte des effets de couche limite lorsqu'on utilise une méthode non linéaire.

Des résultats expérimentaux et théoriques plus détaillés encore concernant ce profil supercritique peuvent être trouvés dans les références [20] et [21].

b) Profil NACA 012 oscillant en tangage :

Sur la figure 11 on présente les cycles de portance et de moment de tangage à 25% pour un profil NACA 0012 oscillant en tangage à une fréquence réduite $k = 0,1$. L'évolution de la portance montre que les effets visqueux diminuent la valeur moyenne de la portance et son amplitude de variation.

Pour cette valeur relativement basse de la fréquence réduite (k = 0,1) le calcul en fluide parfait ne fait apparaître aucun déphasage entre l'évolution du Cz et la variation d'incidence, la courbe d'évolution Cz (α) est donc parfaitement linéaire ; la prise en compte de la couche limite introduit un léger déphasage qui se traduit par la présence de deux lobes sur la courbe d'évolution Cz (α). Cette caractéristique encore plus marquée pour une fréquence réduite plus élevée (figure 12) correspond qualitativement à ce qui est observé expérimentalement [22]. L'influence de la viscosité est particulièrement sensible sur la boucle d'évolution du coefficient de moment de tangage.

Pour la configuration présentée sur la figure 12, il apparaît un décollement de la couche limite au bord de fuite et les résultats obtenus par le calcul couplé ne convergent pas vers une solution parfaitement périodique. Ces résultats sont donc à prendre comme une tendance qui indique que, pour le cas considéré, le déphasage introduit par la couche limite est la principale cause de la largeur de la boucle du coefficient de portance. Une méthode de calcul incluant des décollements limités devrait permettre de traiter les cas à la limite du décrochage dynamique dans lesquels le point de décollement oscille entre x/c $\simeq$ 0,7 et le bord de fuite.

3.2 - Ecoulement transsonique -

a) Profil NACA 64 A 006 avec volet oscillant -

Des études expérimentales détaillées ont été menées au NLR sur un profil NACA 64 A 006 muni d'un volet de bord de fuite oscillant autour d'un axe situé à 75% de la corde [23]. Les configurations étudiées et les résultats obtenus ont servi de base de comparaison pour les calculs effectués avec la méthode de résolution de l'équation des petites perturbations du potentiel instationnaire des vitesses avec et sans couche limite dans le domaine transsonique.

Pour une incidence et un braquage moyen du volet nuls, un nombre de Mach à l'infini M_∞ = 0,875 un écoulement supersonique se développe sur le profil entre le bord d'attaque et une onde de choc située à $x/c \simeq 0,6$. Les pressions instationnaires sous la forme du module et de la phase du premier harmonique du ΔC_p (Cp extrados - Cp intrados) sont présentées sur la figure 13 pour une oscillation du volet de 1° d'amplitude et de fréquence réduite K = 0,234 (f = 120 Hz). Les résultats expérimentaux font apparaître un pic sur la courbe des modules correspondant à l'oscillation du choc ; la hauteur de ce pic caractérise l'intensité du choc et sa largeur l'amplitude de l'oscillation de l'onde de choc. Pour atteindre la région supersonique les perturbations créées par le mouvement du volet doivent contourner l'onde de choc ; ceci se traduit par un retard de phase très important et un niveau de pression instationnaire faible en amont du choc et un saut brutal de la phase à sa traversée.

Les résultats obtenus par la théorie linéarisée ne permettent pas de rendre compte des phénomènes locaux observés, en particulier du caractère de singularité très marquée caractérisant l'onde de choc et son déplacement . Malgré cette incapacité de prévoir l'existence des chocs les coefficients intégrés obtenus par la méthode linéaire ne sont pourtant pas totalement irréalistes .

Influence de la viscosité sur les répartitions de pression instationnaire

Sur la figure 14, les résultats expérimentaux présentés sur la figure 13 sont comparés avec les résultats du programme petites perturbations avec et sans couplage. Le calcul en fluide parfait permet de retrouver la singularité du choc : un pic sur la courbe des modules, un déphasage important dans la région supersonique et un saut de phase à la traversée du choc. On observe que le choc est d'intensité plus forte et positionné plus en aval que dans l'expérience et que le retard de phase dans la région supersonique est plus important. L'effet de la couche limite est de diminuer le module des pressions instationnaires en aval du choc, de diminuer l'intensité du choc et de le positionner plus en amont. La couche limite, en diminuant la taille de la zone supersonique, source de retard, diminue légèrement le retard de phase devant le choc.

Dans l'ensemble, la prise en compte des couches limites donne donc des résultats plus proches des résultats expérimentaux, particulièrement en aval du choc, bien que l'on observe un déphasage trop important dans la région supersonique, un choc un peu trop fort et situé plus aval que dans l'expérience.

En régime supercritique la position des chocs est un point crucial et elle est fortement influencée par les conditions expérimentales et par les effets de paroi de la soufflerie. L'écart théorie-expérience est certainement en partie dû à ces phénomènes, aucune correction n'ayant été apportée au nombre de Mach ni à l'incidence pour tenir compte des effets de paroi.

Influence de la viscosité sur les coefficients intégrés

L'évolution des coefficients de portance, moment de tangage à 25% et moment de charnière est présentée sur la figure 15 pour la configuration M_∞ = 0,875 ; α_m = 0°, k = 0,234. On peut observer notamment un retard de phase de la portance de l'ordre de 35° par rapport à une évolution quasi-stationnaire.

Les effets visqueux se traduisent par une diminution de l'amplitude de variation de coefficients, les phases étant pratiquement inchangées. Le calcul couplé donne des amplitudes de variation des coefficients globaux de portance et de moment de tangage inférieures aux résultats expérimentaux. Ceci est certainement dû aux effets de paroi et à la sensibilité au nombre de Mach car pour cette valeur du nombre de Mach (M_∞ = 0,875) les coefficients varient très rapidement (fig.19). Les déphasages des trois coefficients et l'amplitude du moment de charnière sont bien rendus par le calcul.

L'évolution des trois coefficients instationnaires en fonction de la fréquence réduite à $M_\infty = 0,8$; $\alpha_m = -2°$; $\delta_m = 0°$ portée sur la figure 16 confirme que la couche limite joue peu sur les phases et entraîne une diminution de leur amplitude de variation. Les très basses fréquences ($K < 0.05$) sont difficiles à calculer car il faut augmenter fortement le nombre de pas en temps par période pour avoir un pas suffisamment petit pour bien faire converger le calcul.

Le programme instationnaire permet de calculer également des configurations transitoires et à convergence une configuration stationnaire. La répartition de pression moyenne (fig.17) sur le profil ainsi obtenue indique comme en stationnaire une diminution de l'intensité du choc et une avancée du choc vers le bord d'attaque avec la prise en compte de la couche limite.

Effet du nombre de Mach

La position du choc est très sensible au nombre de Mach comme le montre les pressions instationnaires (fig.18). Pour une variation de 1 point sur le nombre de Mach entre $M_\infty = 0,875$ et $M_\infty = 0,865$ les résultats de calcul indique que le choc avance de 8 à 10%, que les pressions instationnaires voient leur amplitude augmentée et leur phase diminuée de 35° dans la région supersonique.

L'évolution expérimentale des coefficients instationnaires de portance et de moment de tangage (fig.19) en fonction du nombre de Mach montre un caractère fortement non linéaire avec une diminution brutale de ces coefficients à partir de $M_\infty = 0,85$. Les résultats obtenus par la méthode des petites perturbations permettent de retrouver ce phénomène même si le calcul couplé anticipe quelque peu le point de cassure. La théorie linéarisée bénéficie de compensation d'erreurs jusqu'à un Mach élevé mais elle ne peut absolument pas apparaître de phénomènes non-linéaires, en particulier le coefficient de moment de tangage continue à augmenter au-delà de $M_\infty = 0,85$.

Les calculs n'ont pas été effectués pour un nombre de Mach $> 0,9$ car ils donnent un choc positionné sur la gouverne et d'intensité très forte.

Effet du braquage moyen

L'évolution du coefficient de portance en fonction du temps de t = 0 jusqu'à convergence pour les valeurs du braquage moyen 0°et 3° (fig.20) montre que l'influence de la couche limite est comme en stationnaire de diminuer la valeur moyenne de la portance. La variation des coefficients instationnaires globaux avec le braquage moyen (fig.21) met en évidence l'influence de l'écoulement moyen sur la réponse instationnaire. La théorie linéarisée donne évidemment des valeurs constantes ; les résultats obtenus par la théorie des petites perturbations avec prise en compte de la couche limite indiquent une évolution comparable à celle obtenue expérimentalement. Les calculs n'ont pas été poursuivis pour des braquages moyens inférieurs à - 1° car le choc recule alors jusque sur la gouverne et son intensité devient très forte.

b) Profil NACA 64 A 010 oscillant en tangage

Les résultats de calcul concernant un profil NACA 64 A 010 oscillant en tangage à $M_\infty = 0,8$ sont présentés sur les figures 22 et 23. La répartition de pressions instationnaires (fig.22) obtenue par le calcul en fluide parfait fait apparaître un choc situé vers le milieu du profil qui se caractérise par un pic sur la courbe des modules et par un saut brusque de la phase. Comme dans le cas du profil avec volet oscillant, la prise en compte de la couche limite a pour effet de diminuer l'intensité du choc et de le positionner plus près du bord d'attaque. L'influence des effets visqueux est également de diminuer l'amplitude des coefficients intégrés (fig.23) ; la couche limite fait de plus apparaître un déphasage du coefficient de moment de tangage par rapport à la solution en fluide parfait.

Dans les expériences disponibles réalisées à AMES [24] correspondant à ce cas la transition est libre et des comparaisons systématiques calculs- expérience seront entreprises avec une méthode de calcul prenant en compte la partie laminaire de la couche limite.

c) Section de pale d'hélicoptère en configuration non portante

La méthode a été appliquée également au calcul de l'écoulement autour d'une pale d'hélicoptère dans une configuration non-portante. Les résultats expérimentaux présentés proviennent d'expériences réalisées à l'ONERA à l'aide d'un rotor bipale dont les extrémités de pales sont équipées de capteurs de pression absolue. La configuration étudiée correspond à une vitesse d'avancement de 100 m/s, la vitesse de rotation en bout de pale est de 200 m/s. Les calculs effectués correspondent à la section $r/R = 0,89$ dans la région pale avançante où apparaissent les phénomènes transsoniques. Pour cette section , le profil de la pale est un NACA 00 12.

La figure 24 montre l'évolution du coefficient de pression en fonction de l'azimut pour 3 positions en corde. Le passage d'un choc à une position donnée se traduit par une brusque évolution de la pression, correspondant au passage d'un écoulement supersonique à subsonique ou inversement. De $\Psi = 0°$ à $\Psi = 90°$ le nombre de Mach incident augmente et le choc lorsqu'il existe, recule, alors que, de $\Psi = 90°$ à $\Psi = 180°$, le nombre de Mach incident diminue et le choc avance ; ceci est tout à fait net sur les courbes d'évolution du coefficient de pression à $X = 0,32$ et $X = 0,4$. Les résultats expérimentaux indiquent en particulier que le choc ne recule pas jusqu'à $X = 0,48$. Le calcul fluide parfait donne un choc plus fort que les résultats expérimentaux et un recul du choc plus prononcé ; le calcul couplé corrige en partie ces écarts, en particulier il indique que le choc ne recule pas jusqu'à $X = 0,48$.

Les répartitions de pressions instantanées autour du profil à trois azimuts différents (fig. 25) mettent en évidence l'effet principal de la couche limite en écoulement transsonique qui est de diminuer

l'intensité des chocs et d'en avancer la position. Si l'on fait l'hypothèse que les conditions d'attaque en flèche positive avant $\Psi = 90°$ et négative après 90° ne jouent pas un rôle fondamental pour cette section $x/R = 0,89$, la dissymétrie de réponse ($\Psi = 60°$ et $\Psi = 120°$) ne peut être attribuée qu'à l'effet d'une vitesse d'attaque croissante avant 90° et décroissante après 90°. En effet à $\Psi = 60°$ et $\Psi = 120°$ le nombre de Mach incident est le même, le caractère instationnaire de l'écoulement se traduit par la présence d'un choc à $\Psi = 120°$ alors qu'à $\Psi = 60°$ il y a une recompression quasi-isentropique. Les calculs effectués, en particulier avec couplage, rendent bien compte de ces phénomènes présentés plus en détail dans la référence [25].

Le calcul d'écoulements transsoniques instationnaires nécessite l'emploi de méthodes non-linéaires. La méthode des petites perturbations utilisée, malgré les limitations liées à une telle technique, permet de rendre compte des principaux phénomènes observés expérimentalement. La prise en compte de la couche limite apparaît indispensable pour positionner correctement les chocs.

4 - CONCLUSION -

Cette étude montre que la prévision détaillée des phénomènes en aérodynamique instationnaire nécessite l'emploi de théories non linéaires afin de rendre compte notamment de l'effet de l'écoulement moyen sur la réponse purement instationnaire. Cependant ces méthodes non linéaires qui permettent de faire apparaître les singularités dûes au choc en écoulement transsonique doivent également tenir compte des phénomènes visqueux afin de mieux positionner les chocs ou de rendre compte correctement de l'interaction écoulement moyen- réponse instationnaire en incompressible.

Les résultats obtenus par cette méthode de calculs couplés fluide parfait-fluide visqueux mettent en évidence que l'influence des effets visqueux est de diminuer l'amplitude de variation des pressions instationnaires et de celle des coefficients globaux en écoulement incompressible, de donner des chocs d'intensité plus faible positionnés plus en amont et également de diminuer l'amplitude de variation des coefficients globaux en écoulement transsonique. Il reste cependant des progrès à faire dans la technique de couplage, notamment en ce qui concerne la prise en compte de la partie laminaire de la couche limite, le traitement des zones décollées et des interactions onde de choc couche limite. Enfin pour affiner les comparaisons théorie expérience il faudra s'efforcer de tenir compte soit expérimentalement soit par le calcul des effets de paroi en instationnaire.

REFERENCES

[1] E.ALBANO, W.P. RODDEN -
A doublet lattice method for calculating lift distributions on oscillating surfaces in subsonic flow.
AIAA Journal vol.7 n° 2 (1969).

[2] N.BAUDU, TH.LE -
Etude du comportement aérodynamique d'un profil avec gouverne oscillante
R.S.F. BERTIN Note 75 CC 06 (1975).

[3] J.P.GIESING -
Non linear two dimensional unsteady potential flow with lift
Journal of Aircraft, vol.5 n° 2 (1968).

[4] R.MAGNUS, and H.YOSHIHARA -
The Transonic Oscillating Flap
AIAA Paper 76-327 (1976).

[5] P.LAVAL -
Calcul de l'écoulement instationnaire autour d'un profil oscillant par une méthode à pas fractionnaires.
Archives of Mechanics, 28, 5-6, p. 855-880 (1976).

[6] A.LERAT, J.SIDES -
Numerical Simulation of Unsteady Transonic Flows using the Euler Equations in Integral Form.
21 st Israël Annual Conference on Aviation and Astronautics, Fev.1979 ;
T.P. ONERA n° 1979-10.

[7] A.M.BEAM, R.F. WARMING -
An Implicit Finite- Difference Algorithm for Hyperbolic Systems in Conservation-Law Form.J'Comput. Phys.22 p.87-110 (1976).

[8] W.J.CHYU, S.S.DAVIS -
Calculation of Unsteady Transonic Flow Over an Arbitrary Airfoil.
AIAA 12 th. Fluid and Plasma Dynamics Conference (July 1979).

[9] K.I.SOCAI -
Calculation of Unsteady Transonic Flow over Oscillating Airfoils Using the Full Potential Equation.
AIAA Paper 77-448,1977.

[10] M.COUSTON, J.J.ANGELINI.
Solution of Non-steady two-dimensional Transonic Small Disturbance Potential Flow Equation.
ASME Symposium on Unsteady Fluid Dynamics. San Francisco, Déc.1978.

[11] F.X. CARADONNA, J.J. PHILIPPE -
The flow over a hélicopter blade tip in the transonic regime.
ONERA T.P 1976-115 - Vertica.

[12] H.TIJDEMAN, R.DESTUYNDER -
Comments on Transonic and Wing Store Unsteady Aerodynamics : High subsonic and transonic effects in Unsteady Aerodynamics, by H.TIJDEMAN AGARD Report 636.

[13] A.DESOPPER -
Etude expérimentale des couches limites turbulentes et transitionnelles en écoulement pulsé. Essais de prévision théorique. Thèse présentée à l'ENSAE, Juin 1977.

[14] J.COUSTEIX, R.HOUDEVILLE, A.DESOPPER -
Résultats expérimentaux et méthodes de calcul relatifs aux couches limites turbulentes en écoulement instationnaire.
AGARD CP 227 (1977).

[15] R.HOUDEVILLE, J.COUSTEIX -
Premiers résultats d'une étude sur les couches limites turbulentes en écoulement pulsé avec gradient de pression moyen défavorable.
Présenté au "15ème Colloque d'Aérodynamique Appliquée" Marseille 7-9 Novembre 1978. NT AAAF.

[16] J.COUSTEIX, R.HOUDEVILLE -
Turbulent boundary layer calculations in unsteady flow. Presented at "Numerical Methods in Applied Fluid Dynamics".
University of Reading 4-6 January 1978.

[17] R.MICHEL, C.QUEMARD, J.COUSTEIX -
Methode pratique de prévision des couches limites turbulentes bi et tri-dimensionnelles.
La Recherche Aérospatiale n° 1972-1 (TP ONERA 1972-1062)

[18] E.RESHOTKO, M.TUCKER -
Effect of a discontinuity on turbulent boundary-layer-thickness parameters with application to shock-induced separation.
NACA TN 3454 November 1955.

[19] J.C LE BALLEUR -
Couplage visqueux-non visqueux : analyse du problème incluant décollements et ondes de choc
La Recherche Aérospatiale 1977 n°6 (Novembre Décembre).

[20] R.GRENON, J.THERS -
Etude d'un profil supercritique avec gouverne oscillante en écoulement subsonique et transsonique
AGARD CP 227 - 1977.

[21] R.GRENON, A.DESOPPER, J.SIDES -
Effets instationnaires d'une gouverne en écoulement bidimensionnel subsonique et transsonique.
AGARD CP 262 - 1979.

[22] W.J. Mc CROSKEY, K.W.Mc ALISTER, L.W.CARR, S.L.PUCCI, O.LAMBERT, R.F.INDERGRAND -
Dynamic Stall on Advanced Airfoil Sections
36 th Annual Forum of AHS. Washington May 1980.

[23] H.TIJDEMAN -
Investigations of the Transonic Flow around Oscillating Airfoils.
NLR TR 77090 U.

[24] S.S.DAVIS, G.N.MALCOLM -
Experiments in Unsteady Transonic Flow
AIAA/ASME/ASCE/AHS 20 th Structures, Structural Dynamics and Materials Conference April 4-6, 1979
St LOUIS, Missouri.

[25] J.J.PHILIPPE, P.LAFON, J.C BOHL -
Etudes experimentales d'aérodynamique instationnaire sur des maquettes de rotors d'hélicoptère en soufflerie.
15ème Colloque d'Aérodynamique Appliquée AAAF Marseille, 7/9 Novembre 1978 - NT AAAF.

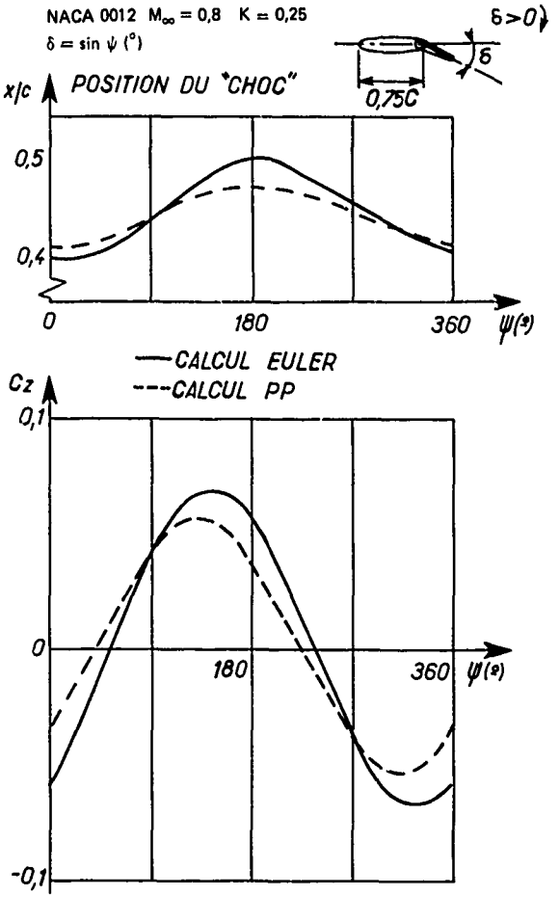


Fig. 1 – Profil NACA 0012 avec volet oscillant. Comparaison calcul Euler - calcul petites perturbations.

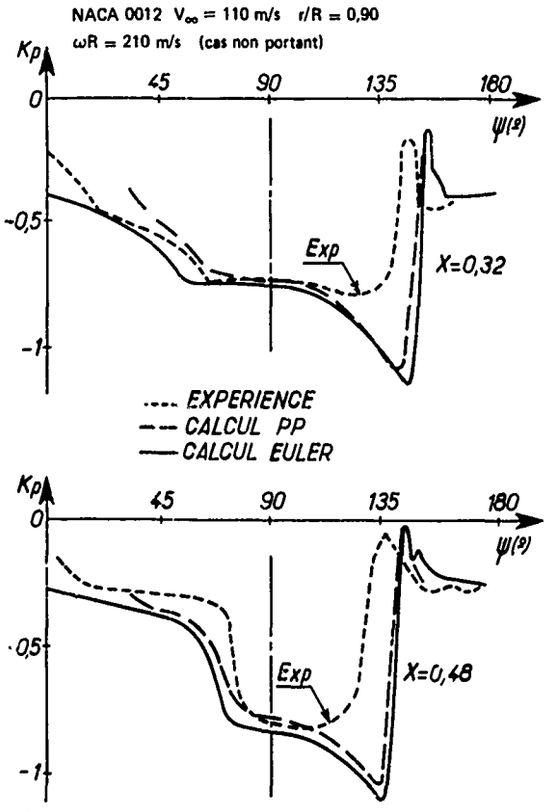


Fig. 2 – Configuration hélicoptère. Comparaison calcul Euler - calcul petites perturbations.

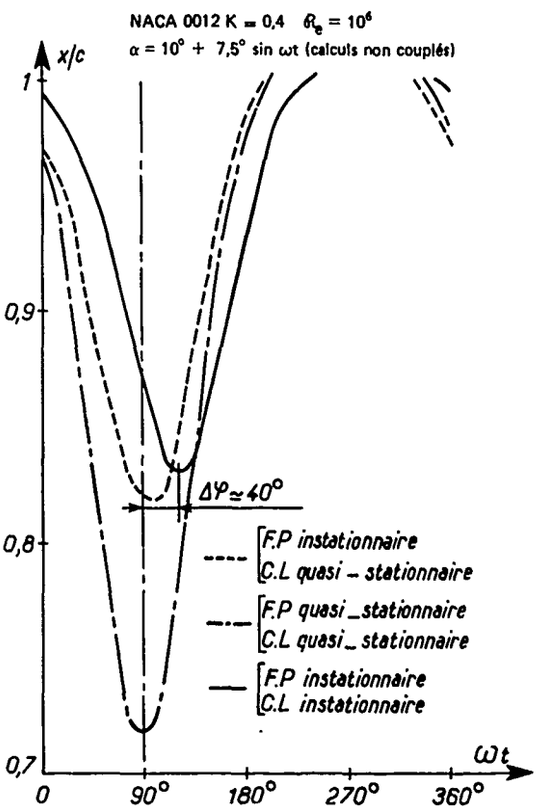


Fig.3 – Comparaison calcul quasi-stationnaire calcul instationnaire de l'évolution du point de décollement.

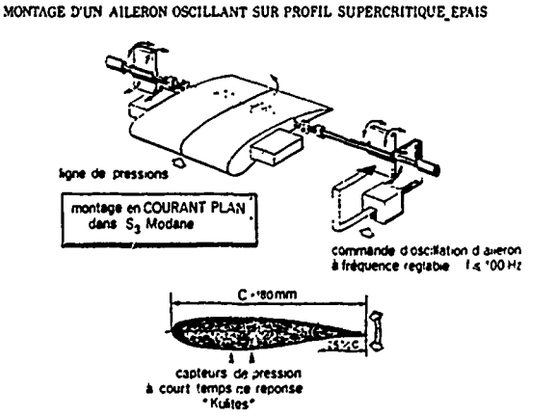


Fig. 4 – Montage d'un aileron oscillant sur profil supercritique épais.

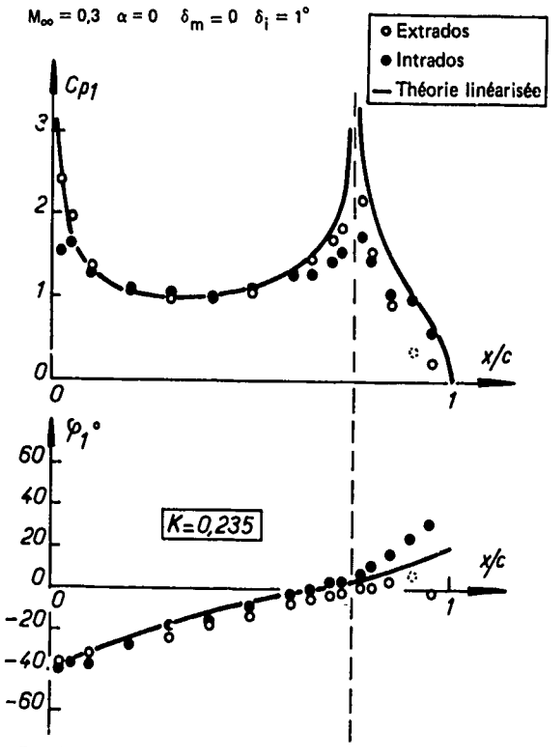


Fig. 5 – Profil RA 16 SC 1 avec volet oscillant. Comparaison résultats expérimentaux - théorie linéarisée.

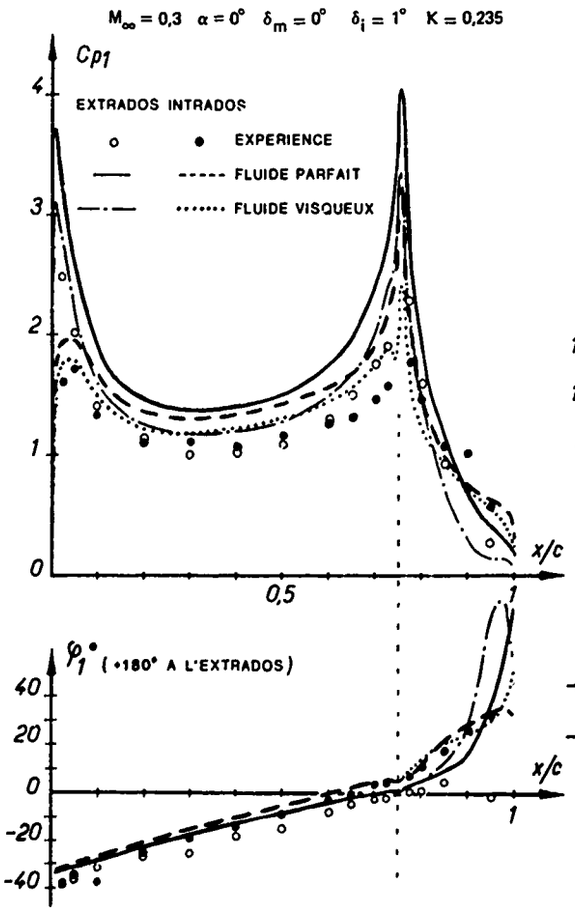


Fig. 6 – Profil RA 16 SC 1 avec volet oscillant ($\delta_m = 0°$).

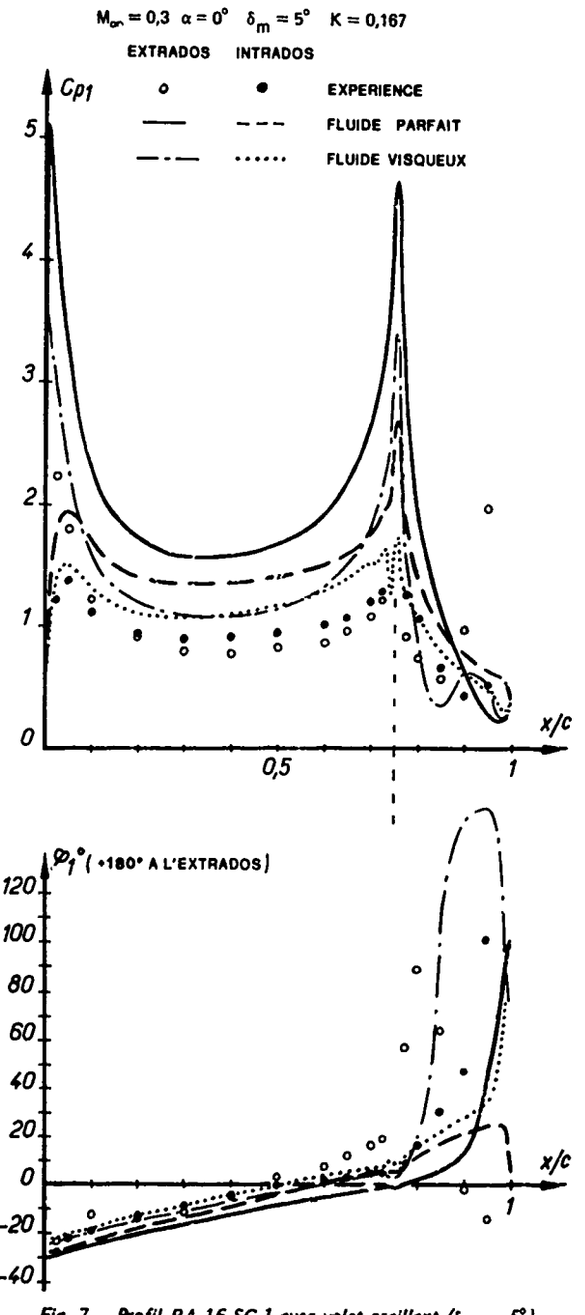


Fig. 7 – Profil RA 16 SC 1 avec volet oscillant ($\delta_m = 5°$).

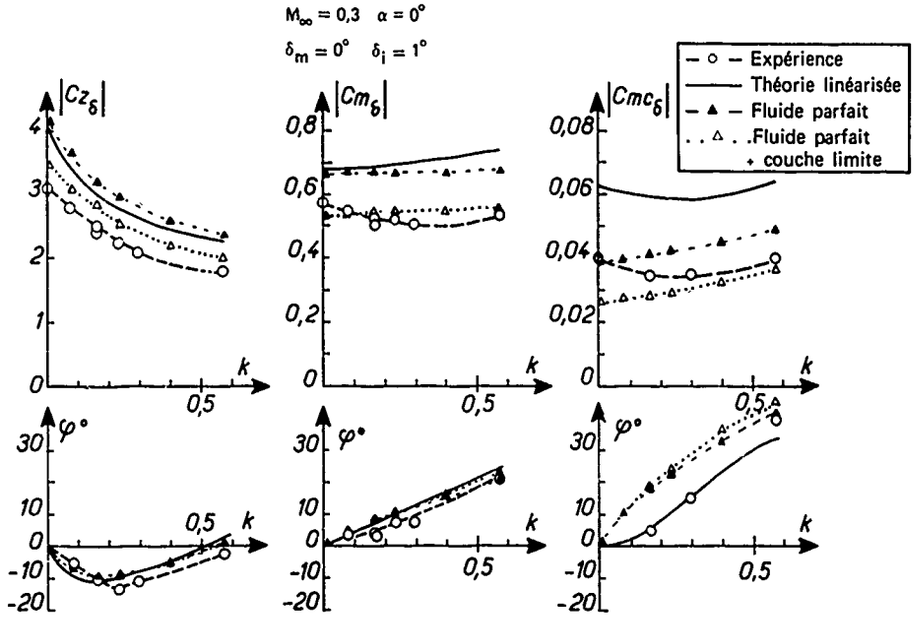


Fig. 8 – Profil RA 16 SC 1. Influence de la fréquence réduite sur les coefficients instationnaires globaux.

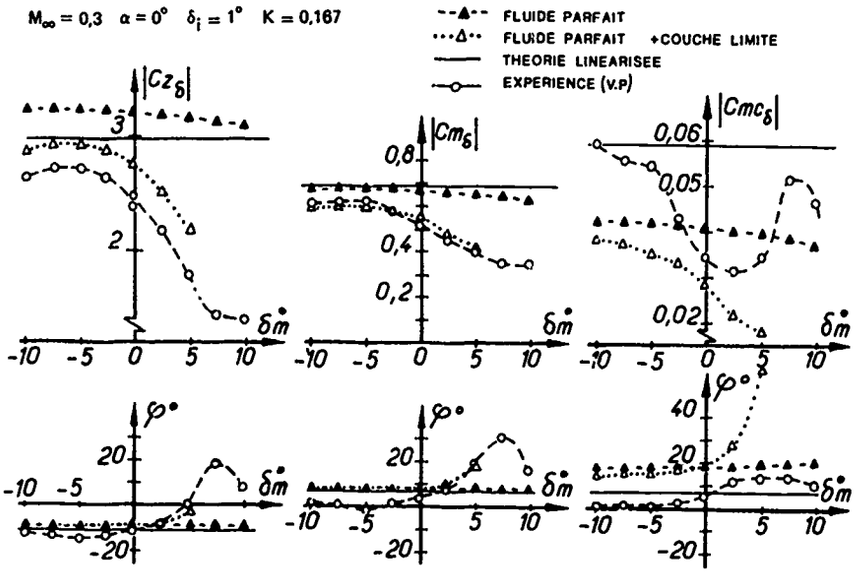


Fig. 9 – Profil RA 16 SC 1. Influence du braquage moyen sur les coefficients instationnaires globaux.

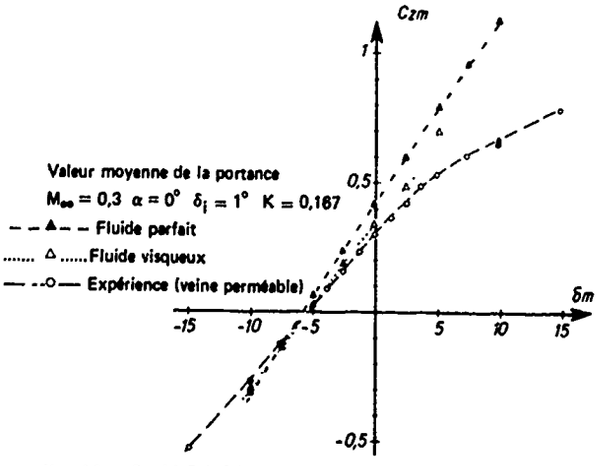


Fig. 10 – Profil RA 16 SC 1. Influence du braquage moyen sur la valeur moyenne de la portance.

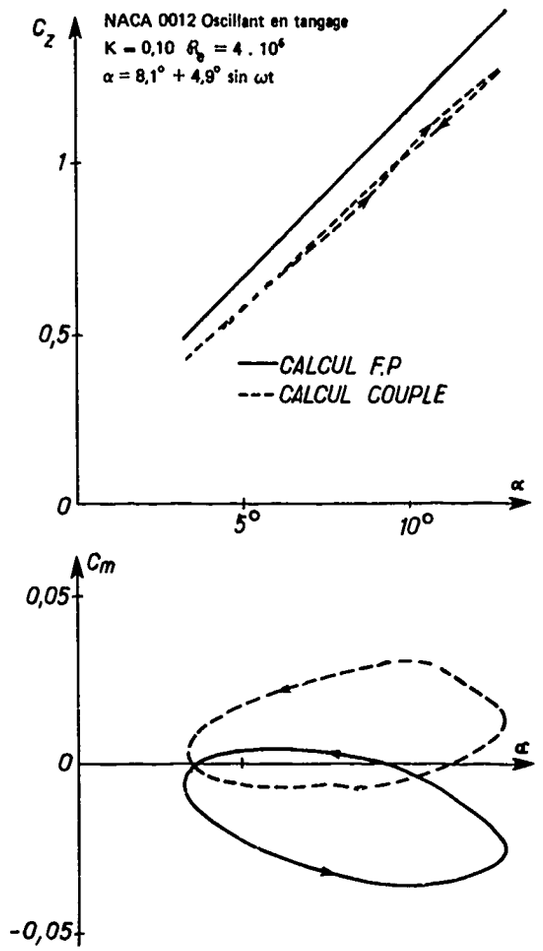


Fig. 11 – Profil NACA 0012 oscillant en tangage (K = 0,1).

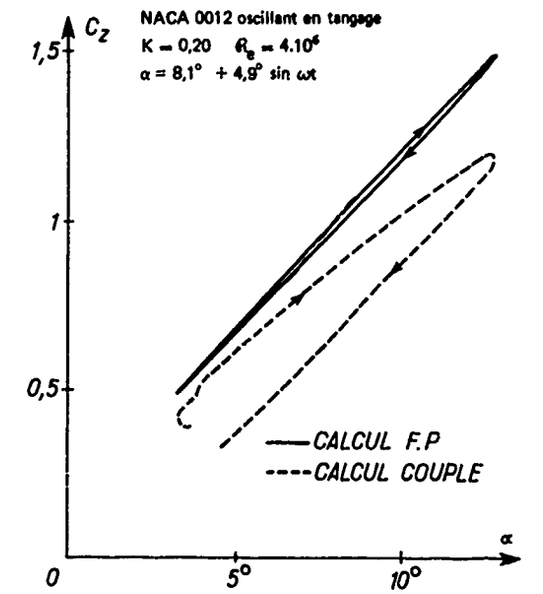


Fig. 12 – Profil NACA 0012 oscillant en tangage (K = 0,2).

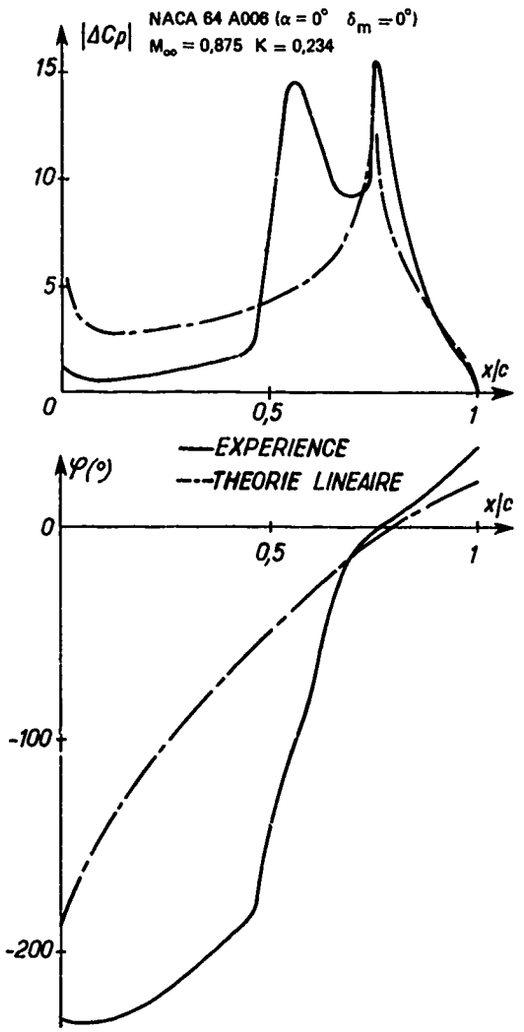


Fig. 13 – Profil NACA 64 A006 avec volet oscillant.

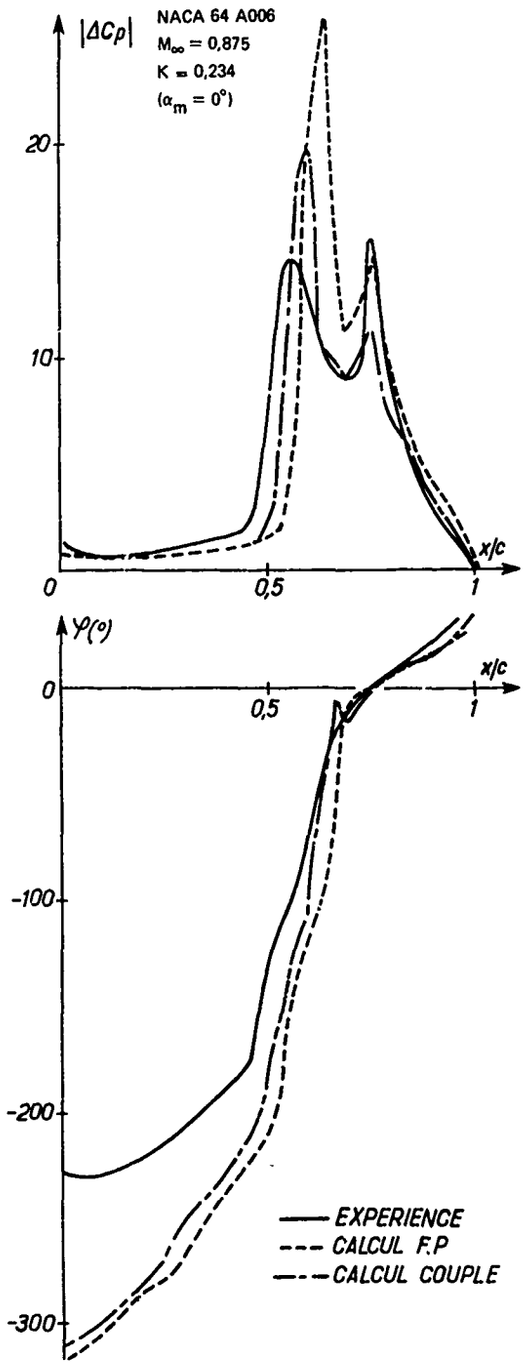


Fig. 14 – Profil NACA 64 A006 avec volet oscillant. Pressions instationnaires.

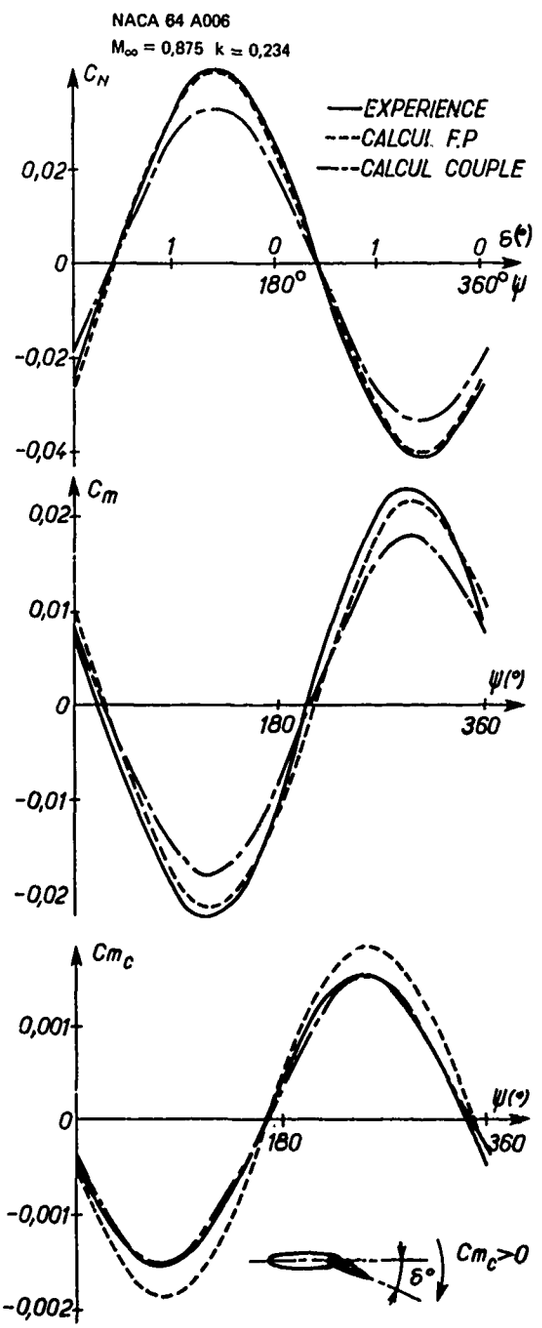


Fig. 15 – Profil NACA 64 A006 avec volet oscillant. Coefficients globaux.

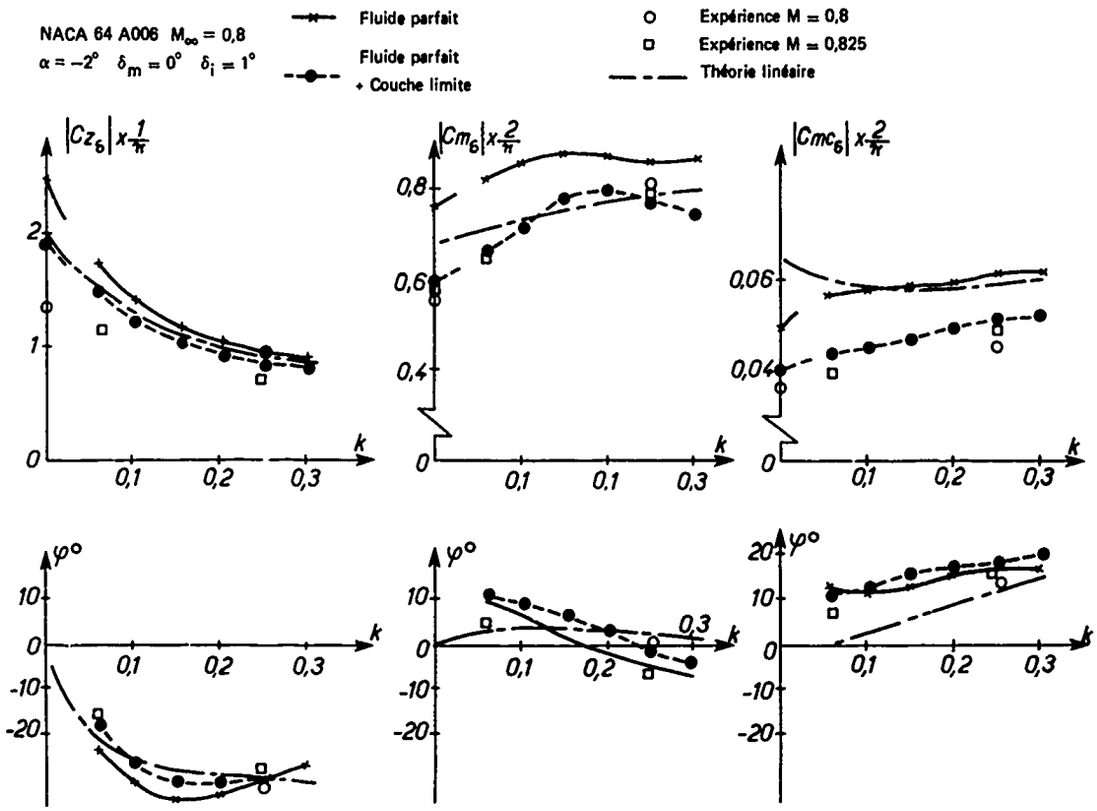


Fig. 16 – Profil NACA 64 A006. Influence de la frequence réduite sur les coefficients instationnaires globaux.

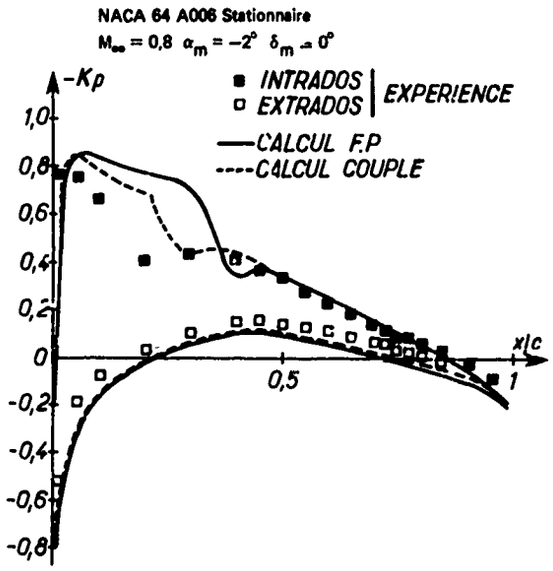


Fig. 17 – Profil NACA A006 avec volet oscillant. Répartition de pression moyenne.

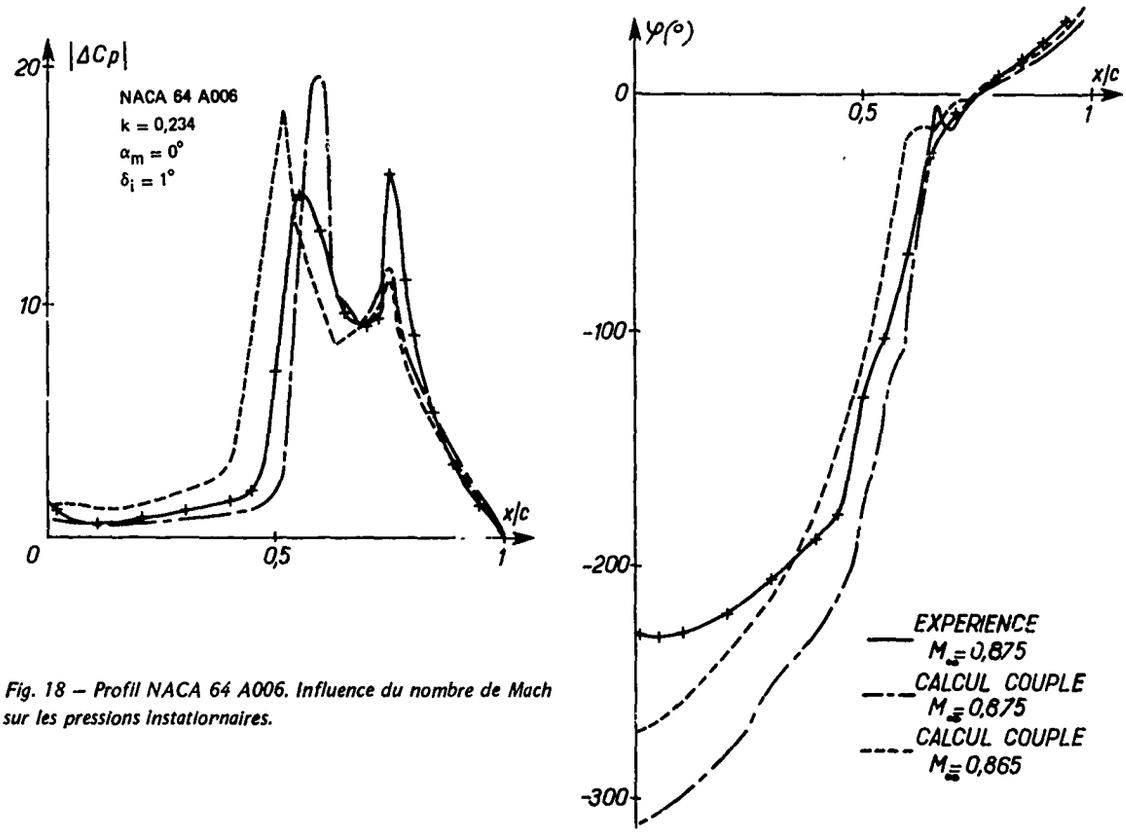


Fig. 18 – Profil NACA 64 A006. Influence du nombre de Mach sur les pressions instationnaires.

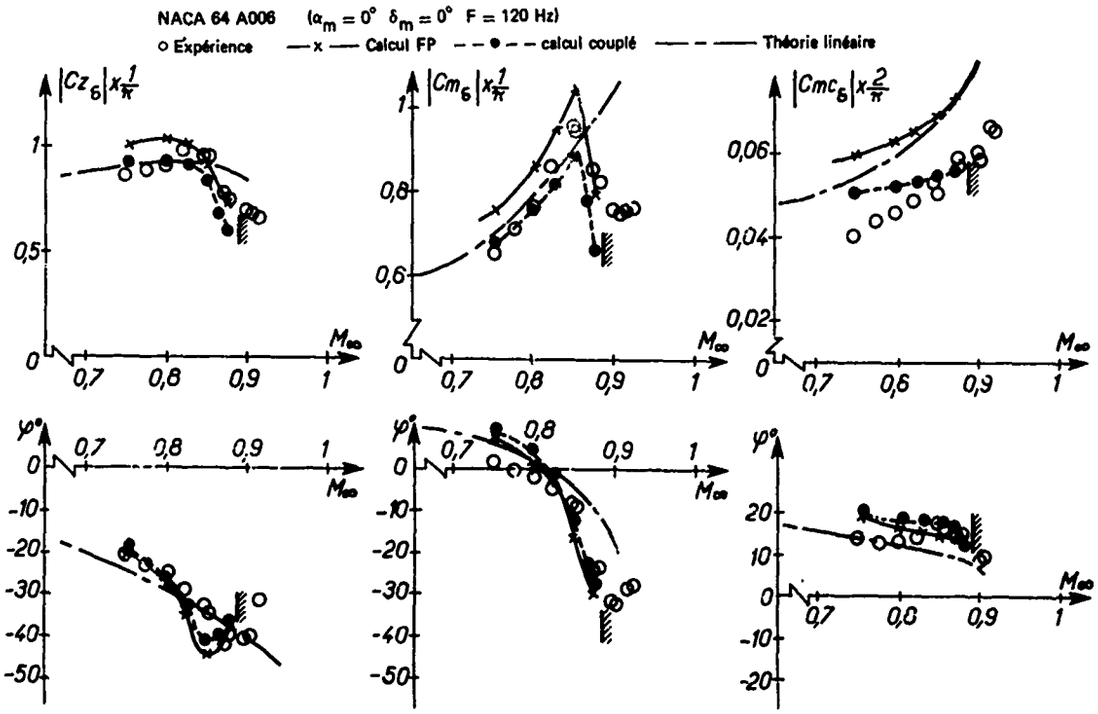


Fig. 19 – Profil NACA 64A006. Influence du nombre de Mach sur les coefficients instationnaires globaux.

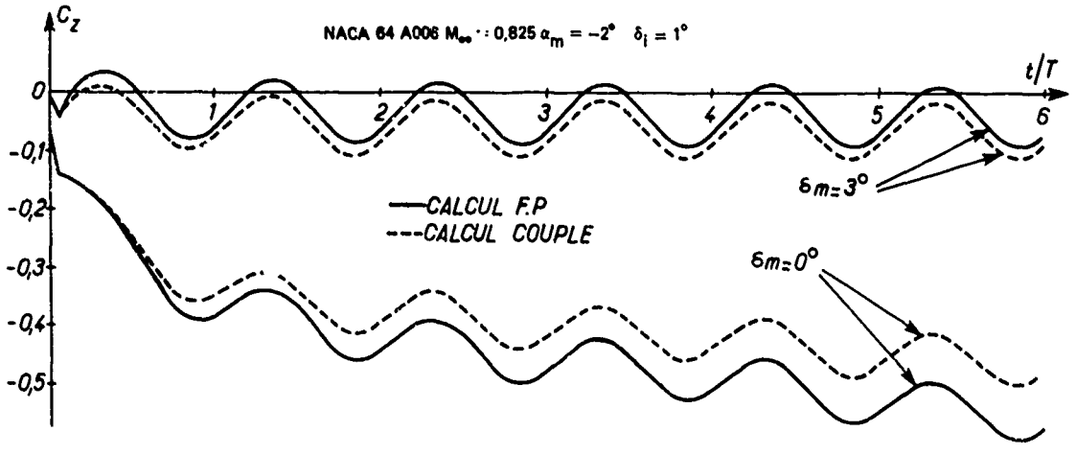


Fig. 20 – Profil NACA 64 A006. Influence du braquage moyen du volet sur la portance.

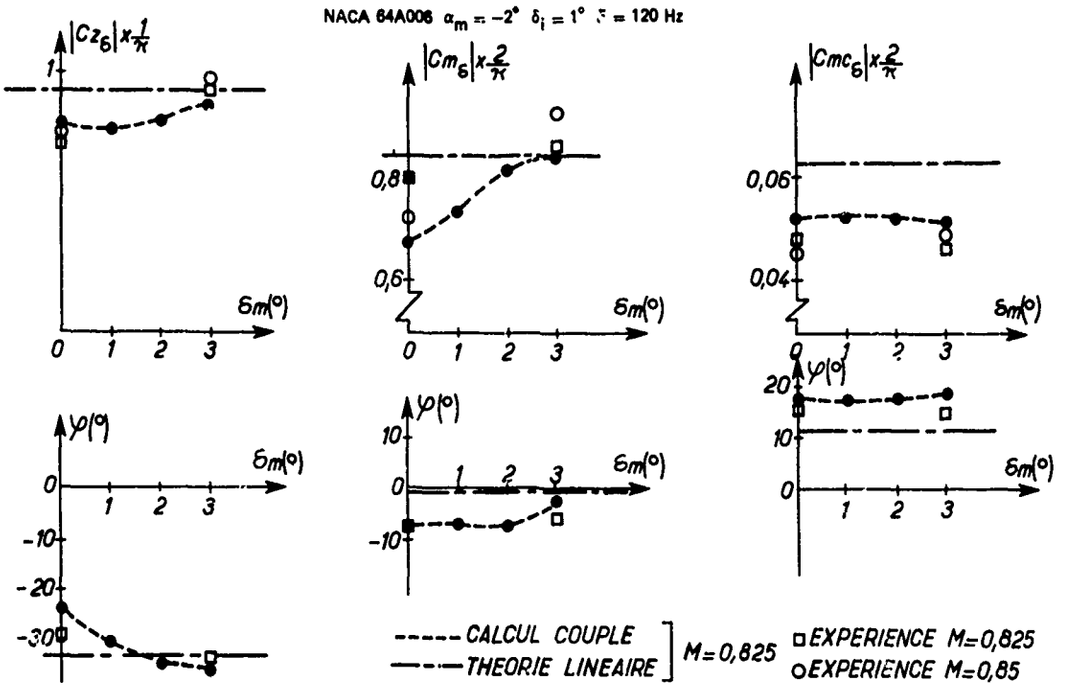


Fig. 21 – Profil NACA 64 A006. Influence du braquage moyen sur les coefficients instationnaires globaux.

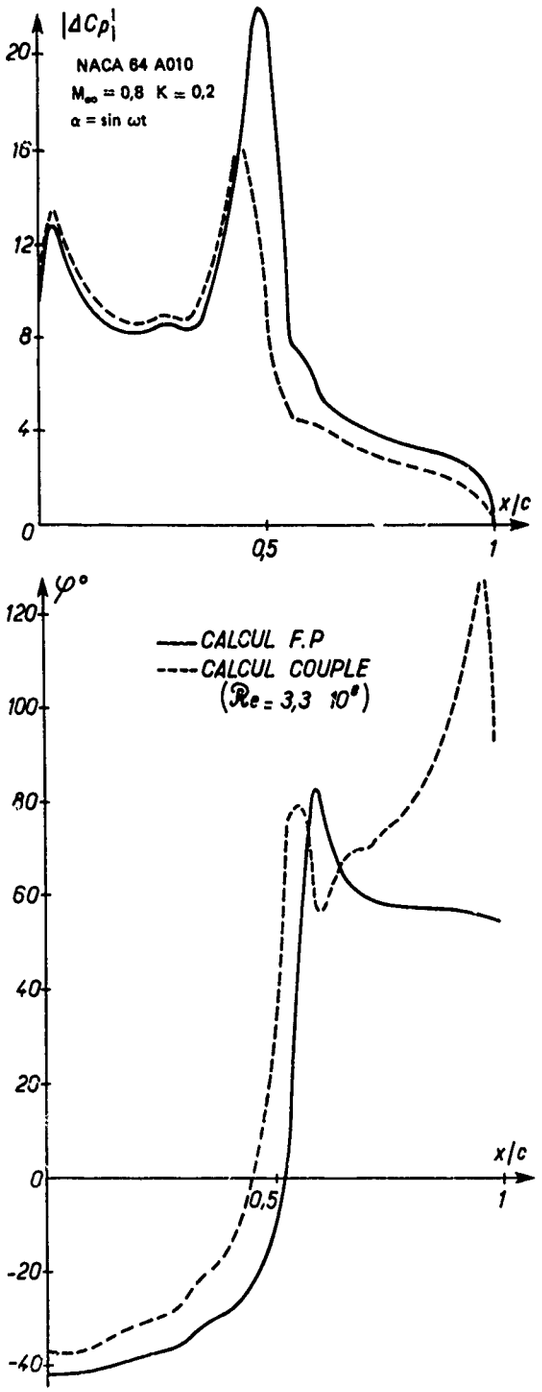


Fig. 22 – Profil NACA 64 A010 oscillant en tangage.
Pressions instationnaires.

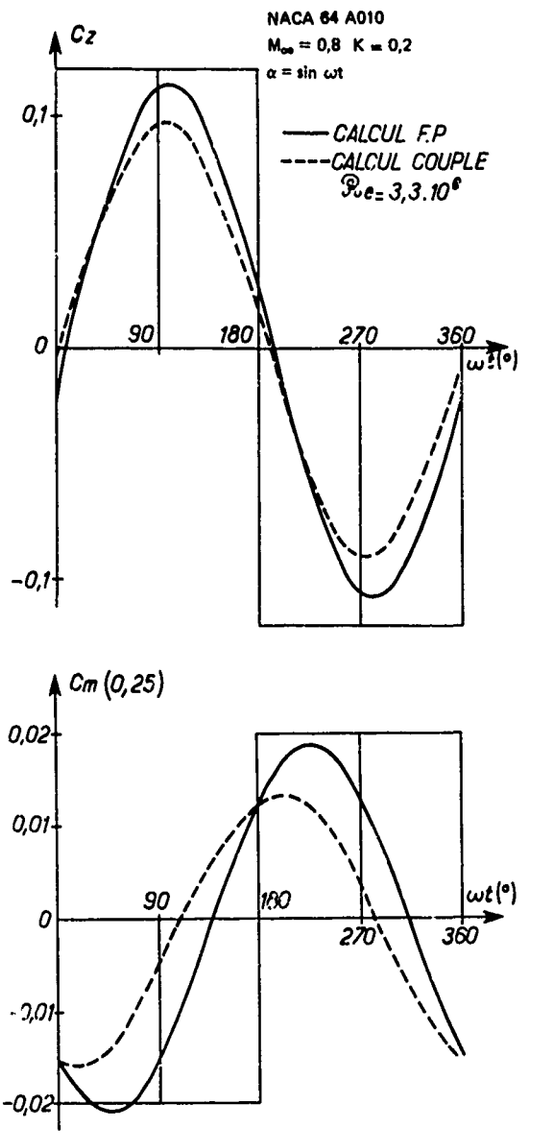


Fig. 23 – Profil NACA 64 A010 oscillant en tangage.
Coefficients globaux.

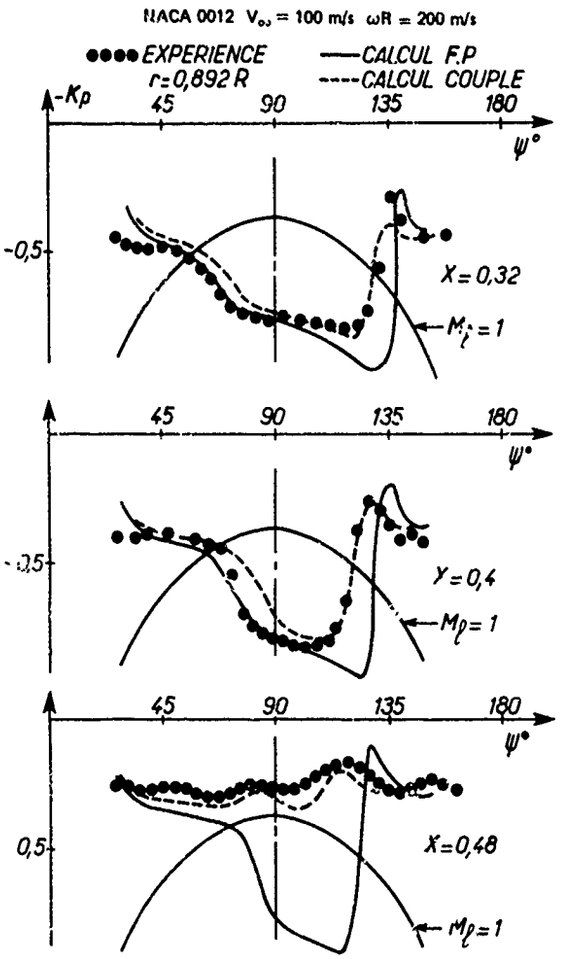


Fig. 24 – Configuration hélicoptère. Evolution de la pression en fonction de l'azimut.

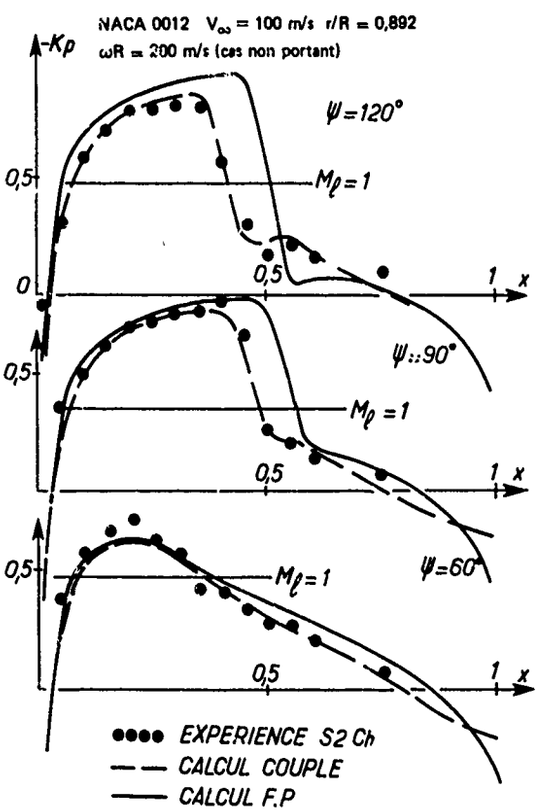


Fig. 25 – Configuration hélicoptère. Répartition de pression à $\psi = 60°$; 90° et 120°.

VISCOUS FLOW SIMULATION OF HIGH LIFT DEVICES AT SUBSONIC AND TRANSONIC SPEED

Dipl.Ing. Stefan Leicher
Postfach 1420
D-7990 Friedrichshafen
Germany

SUMMARY

A numerical method for the calculation of viscous flow over multicomponent airfoils is presented. The report deals with some theoretical features in a short description and presents many of computed results and comparisons with other methods and experimental data.

The part of the code containing the viscous methods is decoupled from the inviscid one in order to be easily combined with any suitable inviscid method. The iterative use of both parts leads finally to a converged solution.

The viscous part consists of a one parameter integral method for laminar boundary layers, a modified Nash integral method or the lag-entrainment method of Horton for turbulent boundary layers and a special integral procedure (optional) for confluent boundary layers. Laminar short and long separation bubbles as well as bubble burst are calculated. Transition can be either fixed or calculated using the Reynolds number criterion of Michel. Turbulent separation of bubble-type as well as common trailing-edge separation are simulated within the standard boundary layer methods by means of semi-empirical correlations. The numerical simulation of the viscous effects is made using either the displacement-thickness-concept (transonic, subsonic) or the equivalent source approach (subsonic only).

For transonic speed the inviscid flow field is calculated by a method, which solves the full potential equation by means of a relaxation method and Jameson's rotated difference scheme. An orthogonal computer grid is derived by conformally mapping the components onto two concentric circles. An initial mapping step takes care of thick trailing edges, modelling a wake with zero pressure jump smoothly leaving the airfoils and extending to infinity.

For subcritical cases a two dimensional panel method is used because of its generality and ease of use. In this case the viscous effects can be simulated by either thickening the original airfoil contour by the calculated displacement thickness or by using the equivalent source concept. The latter has some advantages in treating thick trailing edges.

At subsonic and transonic speed the important influence of viscous effects on high lift maneuver-devices is shown by comparison with wind tunnel data and other methods. Different case studies are shown to illustrate the practical use of such a method for flap/slat analyses.

NOTATIONS

c	chord length
c_A	axial force coefficient
c_D	drag coefficient
c_D	dissipation coefficient
C_E	entrainment coefficient
c_L	lift coefficient
c_N	normal force coefficient
$c_f = 2\,\tau_w/\rho U_e^2)$	skin friction coefficient
c_p	pressure coefficient
$H = \delta^*/\theta$	shape parameter
$H^* = \delta^*/\theta^*$	shape parameter
$H_i = \frac{1}{\theta}\int_0^\delta \rho/\rho_e\,(1-\frac{U}{U_e})\,dy$	shape parameter
$H_i^* = \delta_i^*/\theta^*$	shape parameter
l_{sep}	separation length
M	Mach number
n	normal direction
Re	Reynolds number
s, ds	arc-length
U	velocity
α	angle of attack
$\delta^* = \int_0^\delta (1-\frac{\rho U}{\rho_e U_e})\,dy$	displacement thickness
$\delta_1^* = \int_0^\delta (1-\frac{U}{U_e})\,dy$	
$\delta_4 = \int_0^\delta \frac{\rho U}{\rho_e U_e}\,(\frac{\rho_e}{\rho}-1)$	enthalpy thickness
$\theta = \int_0^\delta \frac{\rho U}{\rho_e U_e}\,(1-\frac{U}{U_e})\,dy$	momentum thickness
$\theta^* = \int_0^\delta \frac{\rho U}{\rho_e U_e}\,(1-\frac{U^2}{U_e^2})\,dy$	energy thickness
ω_1	relaxation factor
μ	dynamic viscosity
$\Omega = \frac{1}{\rho_e U_e}\int_0^\delta \mu\,(\frac{\partial \frac{U}{U_e}}{\partial y})^2\,dy$	dissipation integral
Φ	potential
ρ	density

Subscripts		Superscripts	
e	value at edge of boundary layer	ν	iteration counter
R	reattachment		
sep	separation		
ts	transition		
∞	free stream condition		

1. INTRODUCTION

The performance of mechanical high-lift devices is of increasing importance for the overall economy and operational efficiency of all types of aircraft. The use of such devices for combat aircraft at transonic speed offers the chance of greatly enhancing maneuvering capabilities without effecting cruise performance. Modern fighters like F4, F16, F17, F1E Mirage and F14 have proven this. Their climb and turn rates at transonic speed are remarkably improved by the use of slats, although these configurations have not been completely optimized.

At low speed such devices can be efficiently designed by means of numerical methods [1], [2] and the extensive available experimental data. At transonic speed, however we are lacking experimental data for airfoils with slats and flaps to establish a data base. Extensive wind tunnel testing on such airfoil systems is highly costly due to the large number of parameters and at transonic speed no simple interpolation in a data base is possible. Fig. 1 gives an impression of the complex viscous flowfield around two element high-lift systems. Only in the very last years a few computational methods for the analysis and design of inviscid and viscous transonic high lift device flow fields have been published [3] - [7]. All those methods solve the full potential equation using more or less advanced relaxation methods, but different contour conformal grid systems. The viscous parts consists of quite different methods only partly allowing for separated regions.

Such computational methods are useful tools for designers looking for efficient high lift and maneuver devices. The design time as well as cost can be quite reduced by using numerical results.

The present paper shows results for subsonic and transonic flow conditions as well as for airfoils and for multicomponent profile systems. Included are examples with weak and strong boundary layer influence, with separation bubbles and trailing edge separation.

2. VISCOUS EFFECTS

The viscous effects in the present approach are computed by boundary layer integral methods and semi-empirical procedures for separated flows. The following chapters will sketch the basic ideas of the different components.

2.1 LAMINAR BOUNDARY LAYER

A two dimensional version of Stock's compressible laminar boundary layer method [8] is used. This integral method uses for the one-parameter velocity profiles similar solutions according to Falkner and Skan [9], the momentum and the moment of momentum integral equations, and the Stewartson transformation to account for compressibility.

With the

momentum equation

$$\frac{d\theta}{ds} + \theta \frac{1}{U_e} \frac{dU_e}{ds} \{2 - M_e^2 + H\} = \frac{C_f}{2} \qquad (2.1)$$

and the

moment of momentum equation

$$\frac{d\theta^*}{ds} + \theta^* \frac{1}{U_e} \frac{dU_e}{ds} \{3 - M_e^2 + 2 (H^*-H_i^*)\} = 2\,\Omega \qquad (2.2)$$

we get the following system of equations

$$\frac{d\theta}{ds} = \frac{C_f}{2} - \frac{\theta}{U_e} \frac{dU_e}{ds} (2-M_e^2+H) \qquad (2.3)$$

$$\theta_\theta^* \frac{d\theta}{ds} + \theta_a^* \frac{da}{ds} = 2\,\Omega - \frac{\theta^*}{U_e}\frac{dU_e}{ds}\{3 - M_e^2 + 2\,(H^*-H_i^*)\}$$

With (2.3) we finally get

$$\frac{d\theta}{ds} = \frac{C_f}{2} - \frac{\theta}{U_e}\frac{dU_e}{ds}(2-M_e^2+H) \qquad (2.4)$$

$$\frac{da}{ds} = \frac{1}{\theta_a^*}\left[2\,\Omega - \theta_\theta^*\frac{C_f}{2} - \frac{1}{U_e}\frac{dU_e}{ds}\{\theta^*\,[3-M_e^2+2(H^*-H_i^*)] - \theta_\theta^*\;\theta\,(2-M_e^2+H)\}\right]$$

and with

$$\theta_a^* = \frac{d\theta^*}{da} \quad ; \quad \theta_\theta^* = \frac{d\theta^*}{d\theta}$$

where a is the single parameter describing the velocity profiles

2.2 TRANSITION, LAMINAR SEPARATION AND REATTACHMENT CRITERIONS

The transition from laminar to turbulent boundary-layer is a very complex phenomenon depending on pressure gradient, wall roughness, free steam turbulence, local Mach number, Reynolds number, heat transfer, body forces etc. The present method will only take care of pressure gradient, local Mach number and Reynolds number.

Since Granville's transition curve [10] seems to be somewhat questionable at large negative pressure gradients, Michel's empirical correlation [11] modified by Smith-Gamberoni [12] and Cebeci-Smith [13] is used. Alternatively, transition can be specified by input.

$$Re_{\theta,ts} = 1{,}174 \cdot Re_{s,ts}^{.46} \quad , \quad 2 \cdot 10^5 < Re_{s,ts} < 2 \cdot 10^7 \qquad (2.5)$$

Using Michel's method transition occurs somewhat further downstream compared with Granville's instability curve [14].

Laminar separation is assumed if $c_f = 0$ during the laminar boundary layer computation. The criterion of Goradia and Lyman [15] is then used to determine if either laminar stall or a short bubble type separation is apparent.

$$-0.002 \cdot Re_\theta - 1. < \frac{dM_e}{ds/\delta} \qquad (2.6)$$

For short and long bubbles Horton's [16] correlation is used for the separation bubble length l_{sep}.

$$l_{sep} = \frac{5 \cdot 10^4 \cdot \theta_{sep}}{Re_{\theta_{sep}}} \qquad (2.7)$$

Inside the bubble $U_e^3\theta$ is assumed to be constant leading to the reattachment momentum thickness

$$\theta_R = \theta_{sep}\frac{U_e^3{}_{sep}}{U_e^3{}_R} \qquad (2.8)$$

No model is available if bubble burst is indicated.

After reattachment the computation starts with the calculation of the turbulent boundary layer setting the shape parameter H to a value of 1.55.

2.3 TURBULENT BOUNDARY LAYER

There are two turbulent boundary layer methods available. One is the energy integral method of Nash [19], the other is the lag-entrainment integral method of Horton [18].

2.3.1 Energy Method

In the Nash method the momentum and energy equations are solved simultaneously, the energy equation being used to provide an auxiliary equation to calculate the local value of H_i used in the momentum equation.

Momentum: $$\frac{d}{ds}(\rho_e U_e^2 \theta) = \rho_e U_e^2 \left[c_f/2 - \frac{\delta^*}{U_e}\frac{dU_e}{ds}\right]$$

Energy: $$\frac{d}{ds}(\rho_e U_e^3 \theta^*) = \rho_e U_e^3 \left[c_D - \frac{2\delta_4}{U_e}\frac{dU_e}{ds}\right] \qquad (2.9)$$

In order to prevent the failure of the code due to the inability of standard boundary layer methods to compute boundary layer parameters beyond the predicted separation point, the following procedure is incorporated.

For separated flow the shape parameter H_i is frozen at a constant value indicative of separation.

For $H_i = 2.5$ Nash's friction law gives zero skin friction. The momentum equation then reduces to

$$\frac{d\theta}{ds} + (H_{i,sep} + 2)\frac{\theta}{U_e}\frac{dU_e}{ds} \simeq 0 \qquad (2.10)$$

for incompressible flow. This equation integrates to give

$$\frac{\theta}{\theta_{sep}} = \left(\frac{U_{e,sep}}{U_e}\right)^{H_{i,sep}+2} = \left(\frac{U_{e,sep}}{U_e}\right)^{4.5} \qquad (2.11)$$

This relation is similar in form to an empirical relation obtained by Ross and Robertson [17] based on experimental data in decelerated, attached boundary layers:

$$\frac{\theta}{\theta_{sep}} = \left(\frac{U_{e,sep}}{U_e}\right)^{4.8} \qquad (2.12)$$

The exponent in (2.12) implies a value of $H_{i,sep} = 2.8$ in equation (2.10). We take an intermediate value of 2.6 for $H_{i,sep}$.

2.3.2 Lag-entrainment Method

For attached flow the entrainment method is essentially that of Horton [18], with suitable modifications for compressibility. The energy equation from (2.9) is replaced by the following entrainment equation

Entrainment: $$\frac{d}{ds}\left[\rho_e U_e (\delta - \delta^*)\right] = \rho_e U_e C_E \qquad (2.13)$$

This equation is solved simultaneously with the momentum equation using the empirical history equation for the entrainment rate

$$\frac{dC_E}{ds} = \frac{0.014}{\theta}\left[C_{E_{eq}} - C_E\right] \qquad (2.14)$$

The empirical shape parameter and entrainment relations used are based on those of Horton [18] and are

$$H_i = 0.88 + \left(\frac{0.591}{H_1 - 3.607}\right)^{0.4} \quad \text{for } H_i \geq 1.68$$

and $$\qquad (2.15)$$

$$H_i = 0.88 + \left(\frac{0.92326}{H_1 - 3.244}\right)^{1/1.85} \quad \text{for } H_i < 1.68,$$

where $H_1 = (\delta - \delta^*)/\theta$ is Head's shape paraemter.

(These correspond to Horton's relations for $Re_\theta = 10^4$).

$$C_{E_{eq}} = \frac{0.057}{H_1 - 3.0}(c_f/c_{fi}) \qquad (2.16)$$

In the case of separation a constant values of the entrainment coefficient $C_{E_{eq}}$ that corresponds to a shape parameter $H_{i,sep} = 4$ is used. From equations (2.15) and (2.16) we then get

$$C_{E_{eq}} = 0.16\ (c_f/c_{fi})$$

which is in fair agreement with experiment at least in incompressible flow.

The length scale θ in Equation (2.14) is set equal to the value of θ at separation, since this is characteristic of the separated shear layer thickness. The momentum equation is discarded, and θ and δ^* are calculated from the computed values of $(\delta-\delta^*)$.

2.3.3 Skin friction and re-attachment

In both methods c_f is calculated from a compressible form of the Ludwieg-Tillmann relation:

$$c_f = \frac{0.246}{(1+0.13\ M_e^2)\ Re_\theta^{0.268}\ 10^{-0.678H_i}} = (c_f/c_{fi})\ c_{fi} \qquad (2.17)$$

where

$$Re_\theta = \frac{\rho_e U_e \theta}{\mu_e} \quad , \quad c_f/c_{fi} = (1+0.130\ M_e^2)^{-1}$$

Turbulent "re-attachment" is simulated by evaluating dH_i/ds at each step in the separated flow from the shape parameter equation, and allowing H_i to become less than $H_{i,sep}$ once the derivative becomes negative.

2.4 CONFLUENT BOUNDARY LAYER

Only a few confluent boundary layer methods are available. We use Goradia's method [1], [20] except for minor changes. It represents the mixing of the wake with the boundary layer and is followed by an ordinary turbulent boundary layer up to the trailing edge or point of separation. In most of our cases the confluent boundary layer extended up to the trailing edge of the profile, however. Since the method has no suitable separation criterion and the need for confluent boundary layer modelling is configuration dependent the computation is optional in the present method.

2.5 COMBINATION WITH POTENTIAL FLOW SOLUTIONS

The part of the method containing the viscous methods contains special input- and output routines, so that it can be easily combined with any potential flow method. The code can be applied not only to single profiles but also to multicomponent-systems up to four components.

3. ITERATIVE SIMULATION PROCEDURE

A cyclic iterative procedure between the potential flow methods and the boundary layer parts is used to finally provide the converged viscous solution (figure 2).

- an inviscid potential flow solution is provided for the physical airfoil shape
- by means of the viscous method described in the preceding pages the displacement thickness δ^*-distribution is computed for the given pressure distribution
- the relaxed displacement thickness

  $$\delta^* = \omega_1 \cdot \delta^*_{new} + (1-\omega_1)\ \delta^*_{old}$$

  is either added to the physical shape and for this shape the inviscid flow field is computed by means of the potential flow method or the equivalent source concept as described in chapter 5.1 is used.
- again, the viscous quantities are computed and the whole cycle between viscous and inviscid computations is continued until either convergence criterions are reached or the cycle is stopped by the user.

4. FORCE AND MOMENT COMPUTATION

Lift, drag and moment coefficients are computed by integration of surface pressure and skin friction. Alternatively, drag can be computed using the approach of Squire and Young [21] which is only valid if no shock-losses are apparent.

5. HIGHT LIFT METHODS AND RESULTS

As mentioned before the special structure of the viscous part makes it possible to combine it with any suitable potential flow method. We obtained until now four different combinations differing in the poten-

tial flow solution (for different Mach number ranges) or in the way they take into account the viscous effects.

5.1 SUBSONIC FLOW PROCEDURE

DOPAN1 DOPAN2

Both methods are identical except in the treatment of viscous effects. In DOPAN1 the original contour is thickened by the calculated δ^*-distribution. The program DOPAN2 uses the equivalent source concept allways fullfilling boundary condition on the original airfoil surface. The standard solid wall condition

$$\frac{\partial \Phi}{\partial n}_{n=0} = 0$$

is then replaced by the equation

$$\frac{\partial \Phi}{\partial n}_{n=0} = \frac{d}{ds}(U_e \delta^*) \qquad \text{inc.}$$

$$\frac{\partial \Phi}{\partial n}_{n=0} = \frac{1}{\rho_\infty}\frac{d}{ds}(\rho U_e \delta^*) \qquad \text{compr.}$$

It can be shown that either the displacement or the equivalent source concept leads to similar results [24]. However, at high angle of attack or large boundary layer thicknesses the equivalent source concept seems to be superior since it avoids the additional modelling of thick trailing edges.

The basic potential flow program is a singularity method according to A.M.O. Smith. It is useable either for single profiles or for multicomponent systems. Each component is approximated by a closed polygon where corner points are situated on the original surface. Control points are placed at the mid-point of each panel and here the boundary conditions are introduced.

Experiments indicate, that in separated regions the pressure coefficient is nearly constant. This phenomenon is implemented as an additional condition.

Results

Fig. 3 and Fig. 4 show results for the NACA 4412 airfoil at $M_\infty = 0$ and $\alpha = 6.4^0$ and 10.0^0. The agreement with experiments [22], plotted too, and an other theory [23] is good. The pressure in the separated flow region is a little bit too small, while the separation point seems to be predicted quite well. Fig. 5 shows c_L versus α and again good agreement is obtained. The theory of Grashof [23], which is taken as a reference, simulates the near wake by a finite afterbody, whose location is determined iteratively by the condition of being forceless (mixed free-boundary value problem).

Fig. 6 is a comparison between the present method DOPAN1 and the Goradia method [1] both using the displacement thickness concept. Fig. 7 a,b,c shows pressure distributions at higher angles of attack, which demonstrates the upstream movement of the separation point on the suction surface of the flap. In this case the cp = const. condition is only applied to the flap. Fig. 8 compares the c_L/α curves.

5.2 TRANSONIC AIRFOIL PROCEDURE

DOFOIL

This program is a combination of the viscous part with Jamesons FLO6 [25]. As well known, this code solves the full potential equation in nonconservative form by means of a finite difference method using the Murman difference scheme and circle plane mapping. It can be applied to single profiles and is mainly used for transonic flow conditions only. The viscous effects are incorporated by adding the δ^* distribution to the original airfoil shape. The thick trailing edge is simulated by a constant thickness uncurved wake.

A second version of DOFOIL uses a fully conservative scheme.

Results

Fig. 9 shows a subsonic result on the NACA 4412 airfoil compared with results of the program DOPAN2. Although both methods use different concepts for the implementation of the viscous effects they give nearly the same answer.

The following figures show comparisons for transonic flow conditions around the DO-A1 (CAST-7) airfoil. DO-A1 is a 12 % thick transonic airfoil designed at Dornier in the past. As reference there are taken results from Lock's report [26], in which he compares several theoretical codes with two different experiments. The theories taken as a reference are two variants of the well known inviscid method of Garabedian and Korn [27]. BGKI is the code of Bauer [28] and uses the conventional displacement thickness approach for introducing the viscous effects. No account is taken of the wake. VGK is the method of Collyer and Lock [29] and simulates the viscid flow by using a "transpiration" model with a wake model included.

Fig. 10 to Fig. 12 show the comparison for M_∞ - .76 at different angles of attack. In all cases the angle of attack and the Mach number are exactly the same as in the experiment, while the results of the reference theories are derived at lift coefficients equal to the experimental once. Since the results in Fig. 11a for $\alpha = -1^0$ showed substantial deviations from the experiment, a second computation was made to match lift. Fig. 11b now shows a good agreement with the experiment as well as the VGK results at this angle of attack. For an angle of attack of .5 degrees the double shock system is represented quite well, as depicted on Fig. 12.

Fig. 13 shows a comparison for the higher $M_\infty = .78$ and $\alpha = .5^0$. Again the result is quite satisfactory.

The variation of drag increase ($c_D - c_{D_{c_L=.1}}$) drag increase versus lift for $M_\infty = .76$ is plotted in Fig. 14.

For a constant angle of attack of $.5^0$ Fig. 15 shows the drag rise ($c_D - c_{D_{M_\infty=.6}}$) versus Mach number. Again the predicted drag rise curves are quite good.

Fig. 14 shows that drag rise is mainly contributed by the pressure losses due to shocks rather than by the viscous effects as represented by the Squire and Young formula.

A comparison of the moment coefficient at different c_L's at $M_\infty = .76$ is given in Fig. 16. Our result is just between that of the VGK method and the experiments.

5.3 TRANSONICS MANEUVER DEVICE PROCEDURE

This program has been developed as a joint venture between SAAB and Dornier. It is used to calculate the flow around two element airfoil systems and to design maneuver devices at transonic speed.

The inviscid transonic potential flow is computed using Arlinger's [4], [7] finite difference method. This method can treat arbitrarily shaped airfoil sections by means of a series of conformal mappings. As shown on figure 17 the physical domain outside the two sections is mapped into the ring domain between two concentric circles, the interior of the outer circle being the exterior of the main airfoil and the exterior of the inner circle being the exterior of the secondary airfoil. A special transformation takes care of thick trailing edges as shown on figure 18. The Kutta-Condition is fullfilled by prescribing equal pressure on the upper and lower surface trailing edge. The discrepancies between the pressure distributions for artifically closed and blunt profiles are shown on Fig. 19 and 20. Within the ring domain the flow field is computed solving the nonconservative transformed full potential equation by means of Jameson's rotated difference scheme [30] and successiveline over-relaxation (SLOR) in combination with nonlinear extrapolation similar to [31] and [32] or Brandt's multigrid technique. Details on the inviscid method can be found in [4], [7] and [33].

Results

Fig. 21 shows pressure on a slat profile system at transonic speed with extensive separation on the lower surface of the slat. Although the angle of attack was diminished about 1 degree the agreement on the slat is not satisfactory. Also to be seen is the result of an inverse calculation, where the pressure in the separated region on the lower surface of the slat was prescribed by the test data, and the good agreement is achieved by changing the angle of attack to a value of 3.3 degrees.

Fig. 22 compares the calculated displacement surface with the result of the inverse solution. Although the difference in the contour of both computations is small, the pressure distribution differs a lot. The comparison indicates that the separation is determined too far downstream.

Fig. 23 and Fig. 24 show results for the same main airfoil, but now connected with a flap. The first case (Fig. 23) was a rather tough example with an trailing edge shock (inviscid result) and leads to such a great separated region that the iteration diverged. Nevertheless it is an example for the great influence of viscous effects at transonic speed. Fig. 24 shows a result of the same configuration at a lower Mach number and angle of attack. The comparison with experiment is quite satisfying.

6. CONCLUSION

The present method for viscous flow simulation has proven to be useful for evaluating the efficiency of high lift devices. For subsonic flow conditions multicomponent airfoil sections up to four elements can be studied. The present state of application at subsonic flow conditions is shown in Fig. 25. It is a result for a four component high lift system with considerable trailing edge separation. At transonic conditions the flow around two-element airfoil systems can be calculated. Even for large separation bubbles and strong trailing edge separation fair agreement is reached.

For transonic cases with large turbulent separation the method sometimes fails due to an inadequate shock induced separation and thick wake modelling. For large separated regions even at subsonic speeds the convergence rate can become very poor. However, such cases can be seen as beyond the design limits of efficient devices and in general lead to unsteady flow fields for which other numerical methods are appropriate.

Further studies will show if it is possible to correlate windtunnel results at fairly low Reynolds numbers to free flight conditions by means of the method presented here.

REFERENCES

[1] W.A. Stevens, S.H. Goradia, I.A. Braden
Mathematical Model for Two-Dimensional Multi-Component Airfoils in Viscous Flow
NASA CR-1943, 1971

[2] G.W. Brune, J.W. Manke
Upgraded Viscous Flow Analysis of Multi-Element Airfoils
AIAA Paper 78-1224, Seattle July 1978

[3] G. Grossmann, R.E. Melnik
The Numerical Computation of the Transonic Flow Over Two-Element Airfoil Systems
Lecture Notes in Physics,
Vol. 59, pp. 220-227, 1976

[4] B. Arlinger
Analysis of Two-Element High Lift Systems in Transonic Flow
ICAS Paper No. 76-13, 10th ICAS Congress, Ottawa

[5] G. Grossmann, G. Volpe
The Viscous Transonic Flow Over Two-Element Airfoil Systems
AIAA-Paper 77-688, 1977

[6] K.-D. Klevenhusen
Hochwirksame Manöverklappen im Transschall
Berechnung für Mehrfachklappensysteme
ZTL-Bericht FAG 4 VFW-FOKKER 4.33.-1, 1977

[7] B. Arlinger, W. Schmidt
Design and Analysis of Slat Systems in Transonic Flow
ICAS-Paper B2-06, Proceedings Vol. 2 of the XI ICAS Congress,
Lissabon, Sept. 10-16, 1978

[8] H.W. Stock
Integralverfahren zur Berechnung dreidimensionaler, laminarer und turbulenter Grenzschichten
Dornier FB 77/51 B 1977

[9] V.M. Faulkner, S.W. Skan
Some Approximate Solutions of the Boundary Layer Equations
ARC R & M 1314, 1930

[10] Granville, P.S.
The Calculation of Viscous Drag of Bodies of Revolution
Rep. 849, David Taylor Model Basis, July 1953

[11] R. Michel
Etudes de la transition sur les profiles d'aile, établissement d'un critère de determination du point de transition et calcul de la trainée de profil en incompressible
ONERA Rapport 1/1578-A (1951)

[12] Smith, A.M.O.
Transition, Pressure Gradient, and Stability Theory
International de Mēcanique Appliquēe
1957, pp. 234-244

[13] Cebeci, T., Smith, A.M.O.
Analysis or Turbulent Boundary Layers
Academic Press, 1974

[14] Stein I. Erikson
Calculations of two dimensional boundary layer parameters in subsonic flow around leading edge slats and wing noses
FFA AX-1272:1, Sweden 1975

[15] Goradia, S.H., Lyman, V.
Laminar Stall Prediction and Estimation of $C_{L_{max}}$
"Journal of Aircraft, Vol. 11, No. 9,
Sept. 1974

[16] H.P. Horton
Laminar separation bubbles in two- and three-dimensional incompressible flow.
PhD Thesis, Queen Mary College, University of London

[17] D. Ross, J.H. Robertson
An Empirical Method for Calculation of the Turbulent Boundary Layer
JAS, Vol. 21, No. 5, pp. 355-358, May 1954

[18] H.P. Horton
Entrainment in Equilibrium and Non-Equilibrium Turbulent Boundary Layers
Hawker Siddeley Aviation Ltd., Hatfield, Rep. Nr. Research/1094/HPH (1969)

[19] J.F. Nash, S.G. Hicks
An Integral Method Including the Effects of Upstream History on the Turbulent Shear Stress.
Comoutation of Turbulent Boundary-Layers - 1968, AFOSR-IFP-Stanford Conference, August 1968.

[20] S.H. Goradia
Confluent Boundary Layer Flow Development with Arbitrary Pressure Distribution
Ph.D. Thesis, Georgia Institute of Technology, August 1971

[21] H.B. Squire, B.A. Young
The Calculation of Profile Drag of Airfoils
ARC-Report R.&M. No. 1838, November 1937

[22] R.M. Pinkerton
The variation with Reynolds number of pressure distribution over an airfoil section
NACA Rep. No. 613 (1937)

[23] H. Grashof
Berechnung der Druck- und Schubspannungsverteilung auf Körpern mit Totwasser in ebener inkompressibler Parallelströmung
Dissertation Karlsruhe 1973

[24] W.J. Piers and J.W. Slooff
Calculation of the displacement effect in two dimensional subsonic attached flow around aerofoils; Examples of calculations using measured displacement thickness
NLR TR 72116 U 1972

[25] F. Bauer, P.R. Garabedian, D.G. Korn and A. Jameson
Supercritical wing sections II
Lecture notes in economics and mathematical systems
No. 108, Springer Verlag (1975)

[26] R.C. Lock
Report on a combined experimental and theoretical investigation of the aerofoil CAST 7
RAE Technical Report 79073 (1979)

[27] F. Bauer, P.R. Garabedian, D.G. Korn
Supercritical wing sections.
Lecture notes in economics and mathematical systems
No. 66, Springer Verlag (1972)

[28] F. Bauer, D.G. Korn
Computer simulation of transonic flow past aerofoils with boundary layer correction.
Proc AIAA 2nd Computational Fluid Dynamics Conference, June 1975

[29] M.R. Collyer, R.C. Lock
Improvements to the Viscous Garabedian and Korn (VGK) method for calculating transonic flow past an aerofoil.
RAE Technical Report 78039 (1978)

[30] A. Jameson
Iterative Solution of Transonic Flow Over Airfoils and Wings Including Flow at Mach 1
Comm. Pure and Appl. Math., Vol. 27, 1974

[31] M.M. Hafez, H.K. Cheng
Convergence Acceleration of Relaxation Solution for Transonic Flow Computations
AIAA J., Vol. 15, No. 3, pp. 329-336 (1977)

[32] D.A. Caughey, Jameson, A.
Accelerated Iterative Calculation of Transonic Nacelle Flow Fields
AIAA Paper 76-100, 1976

[33] S. Leicher
A method for the calculation of viscous flow over airfoils with slats or flaps at transonic speed
Paper DEA-Meeting, Meersburg 1979

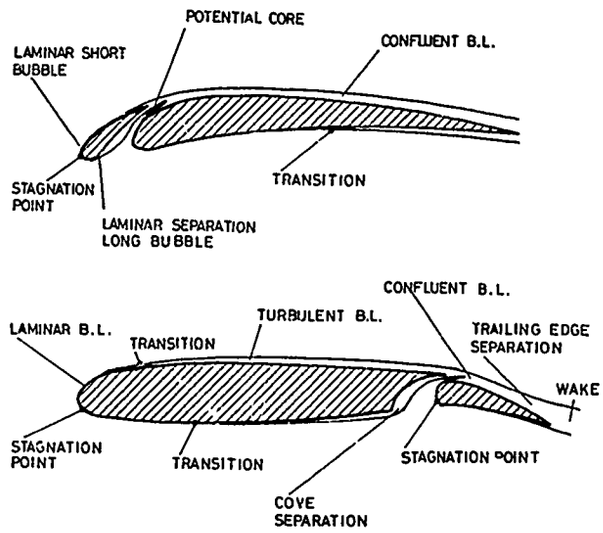


FIG. 1: FLOW AROUND TWO-ELEMENT AIRFOILS

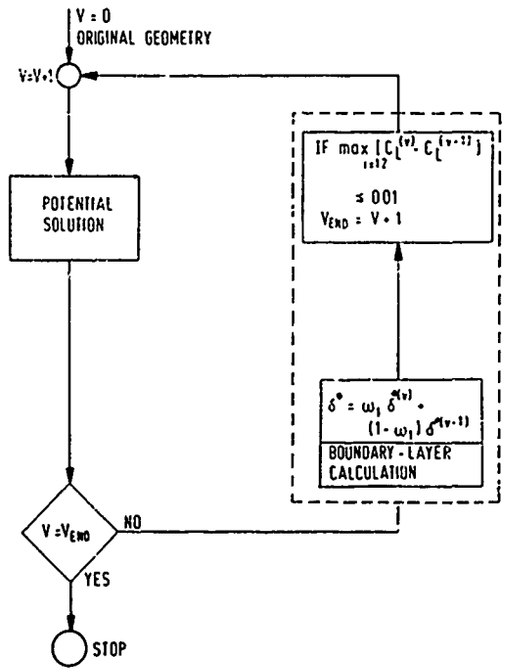


FIG. 2: ITERATION SCHEME

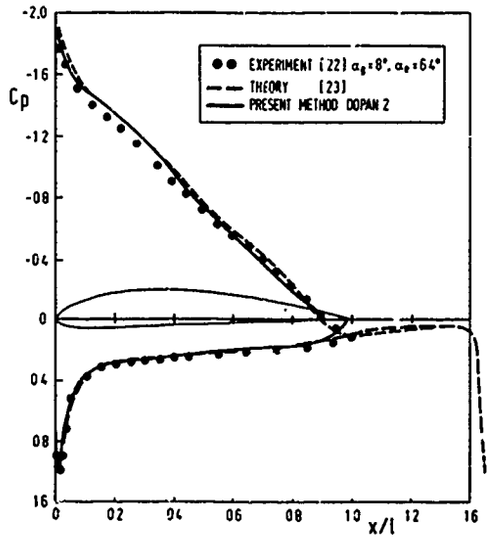


FIG. 3: NACA 4412 $Re = 1.8 \cdot 10^6$, $M_\infty = 0.0$ $\alpha = 6.4^0$

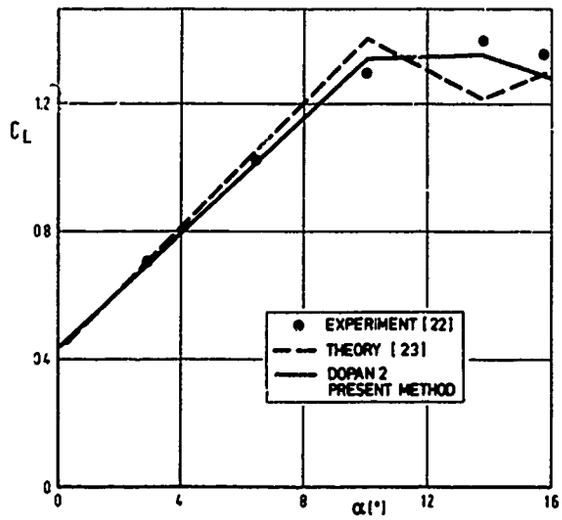


FIG. 5: NACA 4412 $Re = 1.8 \cdot 10^6$, $M_\infty = 0.0$

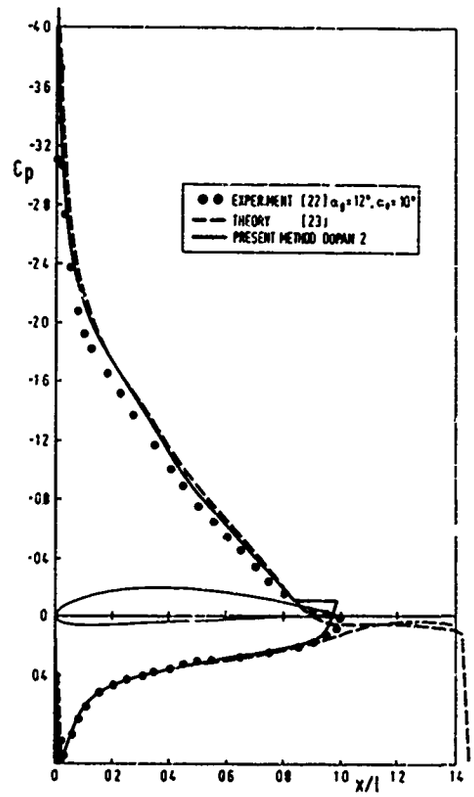


FIG. 4:

NACA 4412 $Re = 1.8 \cdot 10^6$, $M_\infty = 0.0$ $\alpha = 10.0^0$

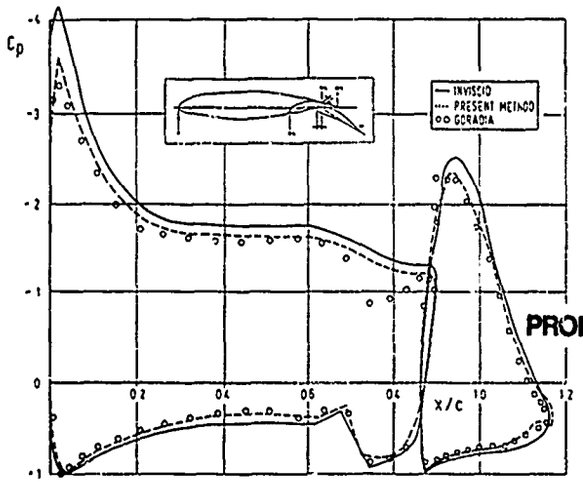


FIG. 6: EFFECTS OF VISCOUS CORRECTIONS IN A LOW SPEED CASE

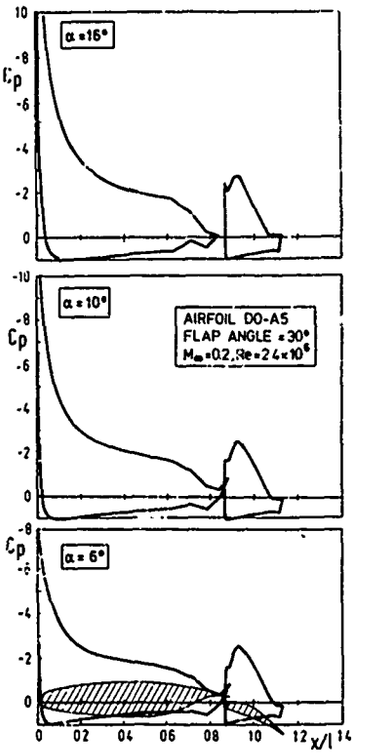


FIG. 7:
PRESSURE DISTRIBUTION AND TRAILING EDGE SEPARATION FOR DIFFERENT ANGLES OF ATTACK

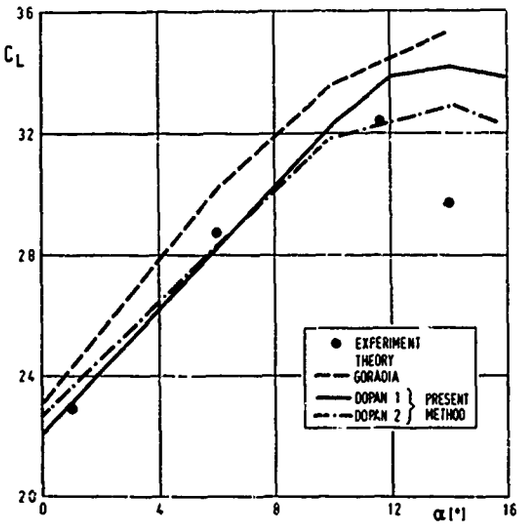


FIG. 8:
AIRFOIL DO-A5 WITH FLAP $\eta_F = 30^0$, $M_\infty = .2$, Re = $2.4 \cdot 10^6$

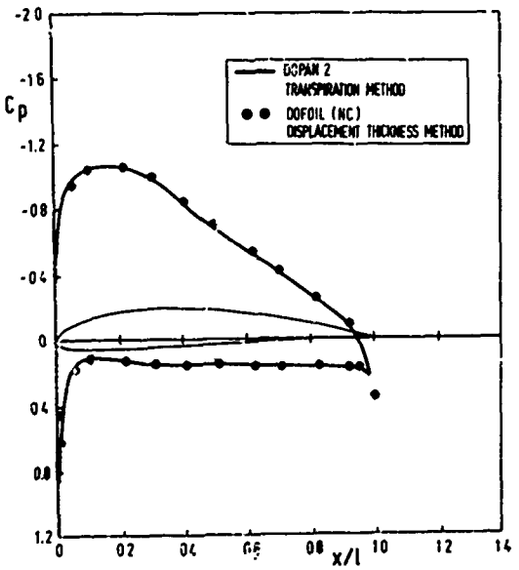
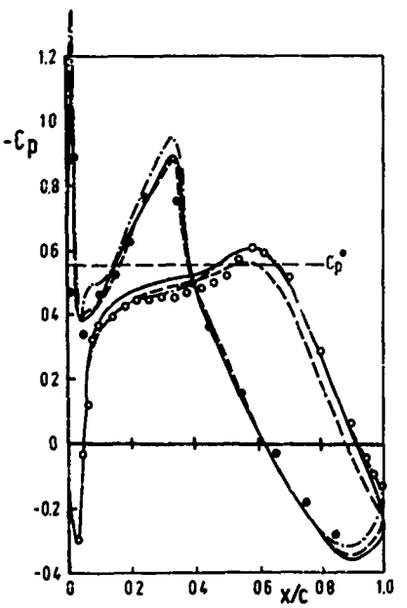


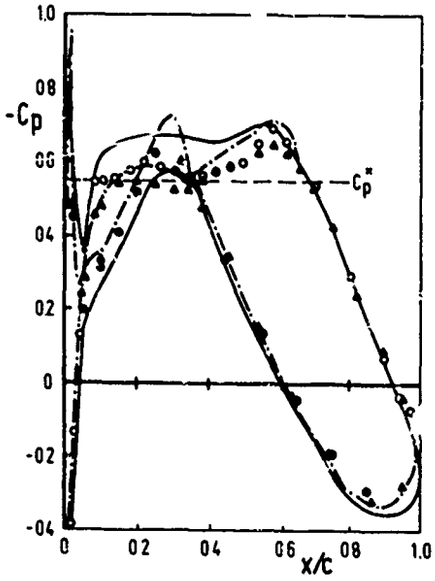
FIG. 9: NACA 4412 Re = $1.8 \cdot 10^6$, $M_\infty = 0.0$ $\alpha = 2.9^0$



EXPERIMENT:	C_L	α	C_D	C_M
● ○ DFVLR	0.107	-2°	0.0102	-0.117
THEORY:				
—·—VGK	0.107	-2.25°	0.0104	-0.127
- - - BKGJ (NC)	0.108	-1.77°	0.0138	-0.110
—— DOFOIL (NC)	0.149	-2°	0.0076	-0.124

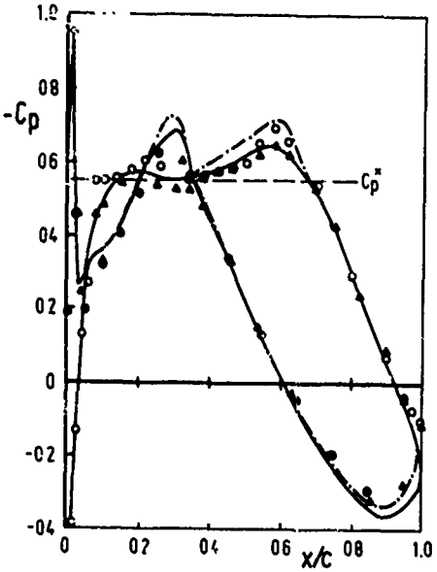
FIG. 10:

CAST 7 AIRFOIL Re = $6 \cdot 10^6$, $M_\infty = .76$ $\alpha = -2^0$



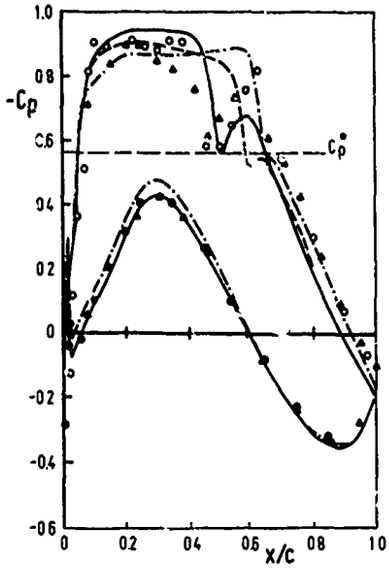
EXPERIMENT:	C_L	α	C_D	C_M
● ○ DFVLR	0 263	-1°	0 0101	-0.120
▲ ▲ ARA	0 240	-1°	0 0104	-0.122
THEORY:				
—·—VGK	0 263	-1.5°	0.0094	-0 131
—— DOFOIL (NC)	0 367	-1°	0 0076	-0 131

FIG. 11a: CAST 7 AIRFOIL $Re = 6 \cdot 10^6$, $M_\infty = .76$ $\alpha = -1^0$



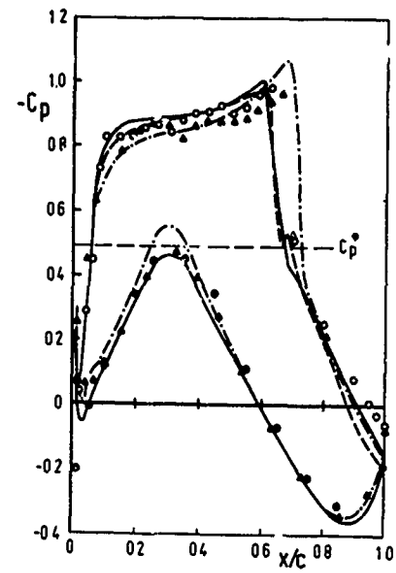
EXPERIMENT:	C_L	α	C_D	C_M
● ○ DFVLR	0 263	- 1°	0 0101	- 0.120
▲ ▲ ARA	0.240	- 1°	0 0104	- 0.122
THEORY :				
—·—VGK	0 263	-1.5°	0 0094	- 0 131
—— DOFOIL (NC)	0 248	-1.5°	0 00758	-01255

FIG. 11b: CAST 7 AIRFOIL $Re = 6 \cdot 10^6$, $M_\infty = .76$ $c_L \sim .25$



EXPERIMENT:	C_L	α	C_D
● ○ DFVLR	0 52	0 5°	0 0107
▲ ▲ ARA	0 50	0 5°	0 0107
THEORY:			
—·—VGK	0 52	-0 4°	0 0099
– – –BGKJ	0 52	0 1°	0 0119
—— DOFOIL (NC)	0 52	0 5°	0 01263

FIG. 12: CAST 7 AIRFOIL $Re = 6 \cdot 10^6$, $M_\infty = -.76$ $\alpha = .5^0$



EXPERIMENT:	C_L	α	C_D	C_M
● ○ DFVLR	0 534	0.5°	0 0164	-0137
▲ ▲ ARA	0 52	0 5°	0 0139	-0137
THEORY·				
—·—VGK	0 534	-0 4°	0 016:	-0.155
– – –BGKJ (NC)	0 533	0.23°	0 0198	-0129
—— DOFOIL (NC)	0 550	0 5°	0 0216	-0131

FIG. 13: CAST 7 AIRFOIL $Re = 6 \cdot 10^6$, $M_\infty = .78$ $\alpha = .5^0$

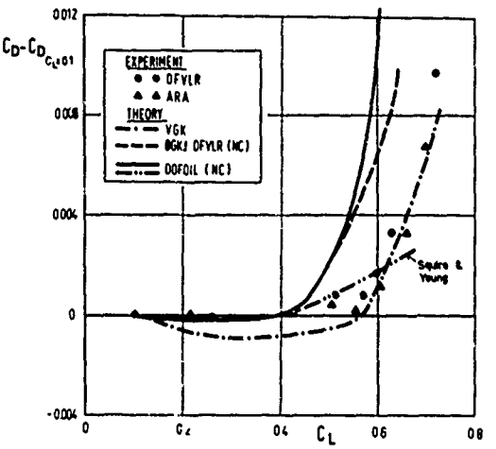
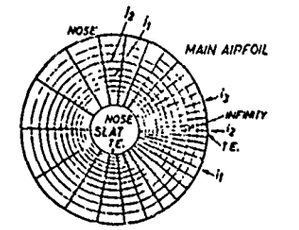
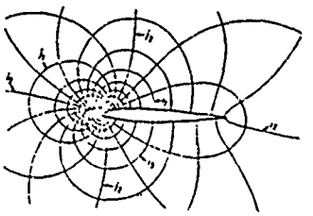
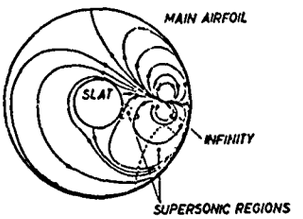


FIG. 14: CAST 7 AIRFOIL
VARIATION OF DRAG INCREMENTS
$M_\infty = .76$, $Re = 6 \cdot 10^6$



CONNECTION BETWEEN COMPUTATIONAL AND PHYSICAL PLANE





STREAMLINES IN COMPUTATIONAL PLANE

FIG. 17:
CORRESPONDING GRIDS IN THE COMPUTATIONAL AND PHYSICAL PLANES

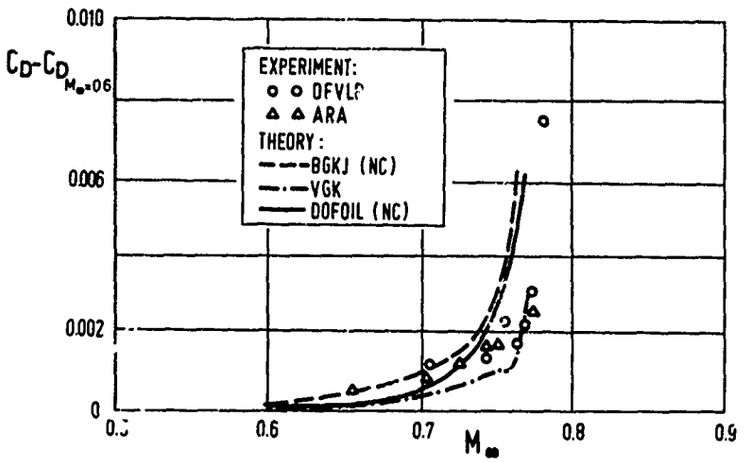


FIG. 15: CAST 7 AIRFOIL
VARIATION OF DRAG INCREMENTS
$Re = 6 \cdot 10^6$, $\alpha = .5^0$

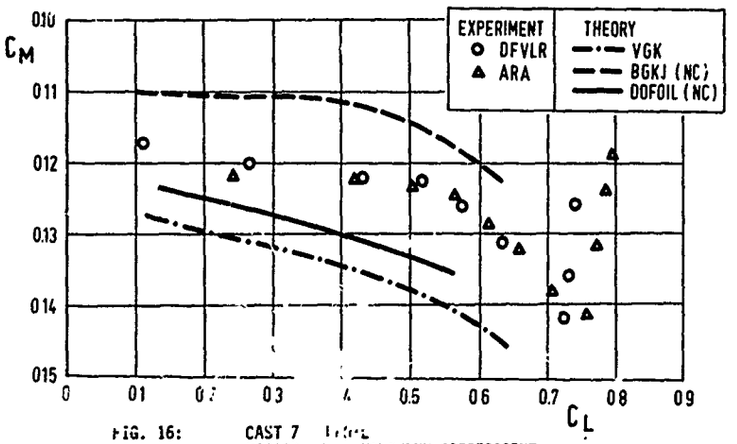


FIG. 16: CAST 7 [illegible]
VARIATION OF MOMENTUM COEFFICIENT
$M_\infty = .7$[illegible] $Re = 6 \cdot 10^6$

MAPPING OF THICK TRAILING EDGES

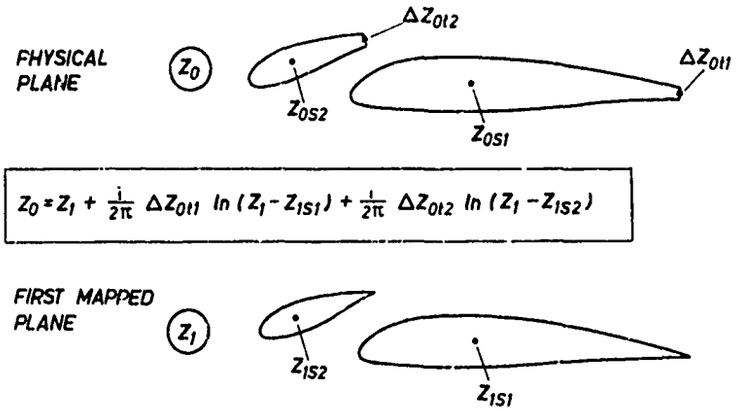


FIG. 18: NOTATIONS FOR INITIAL MAPPING STEP

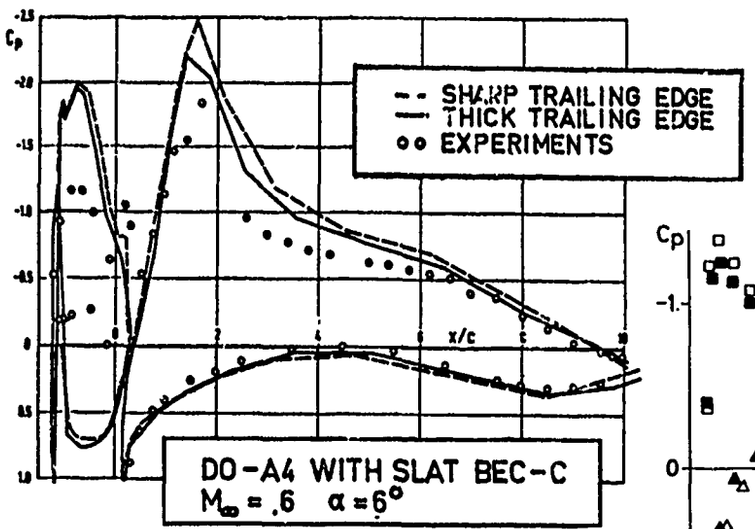


FIG. 20: EFFECT ON PRESSURE OF REMOVING THICKNESS OF TRAILING EDGES BY LENGTHENING THE PROFILES

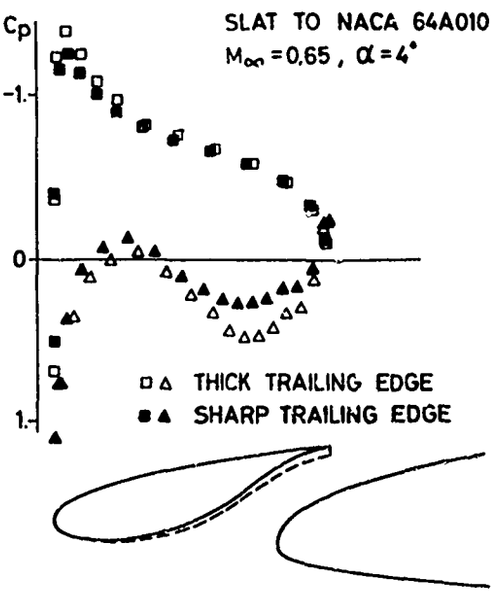


FIG. 19:

EFFECT ON SLAT PRESSURE OF REMOVING THICKNESS OF TRAILING EDGE BY MODIFYING LOWER SURFACE

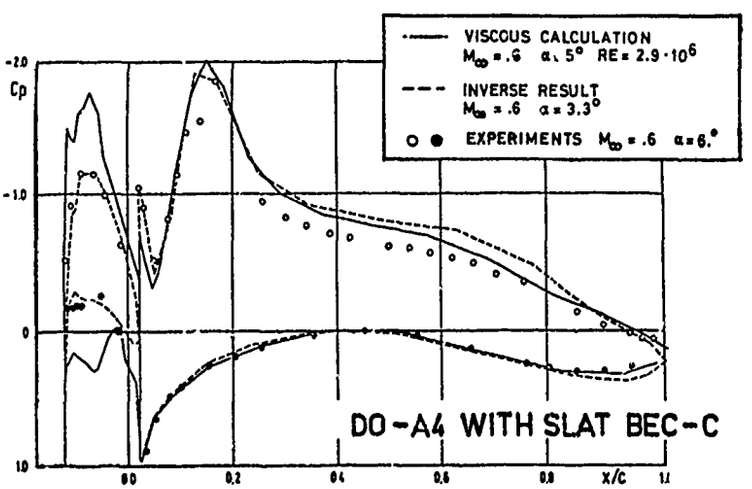
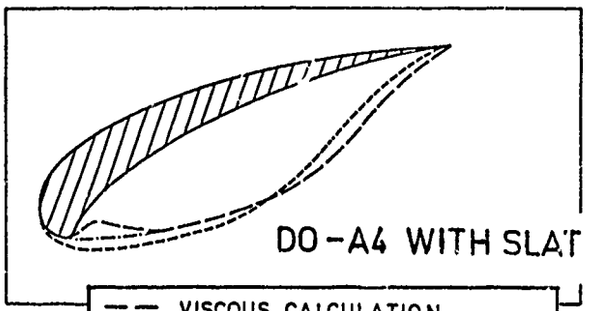


FIG. 21: SLAT PROFILE SYSTEM WITH SEPARATION ON THE LOWER SURFACE OF THE SLAT

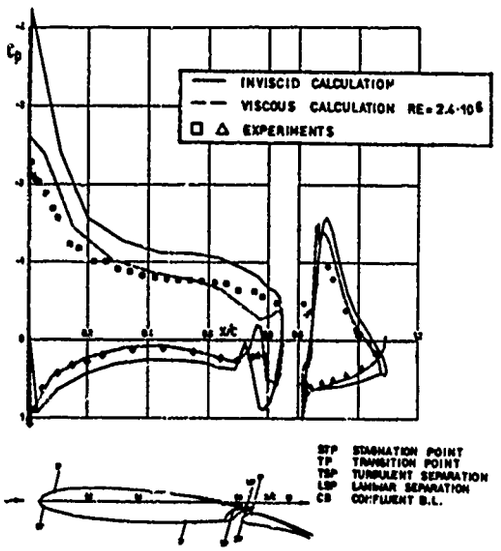


— — VISCOUS CALCULATION
$M_\infty = .6 \quad \alpha = 5° \quad RE = 2.9 \cdot 10^6$

– – – INVERSE RESULT
$M_\infty = .6 \quad \alpha = 3.3°$

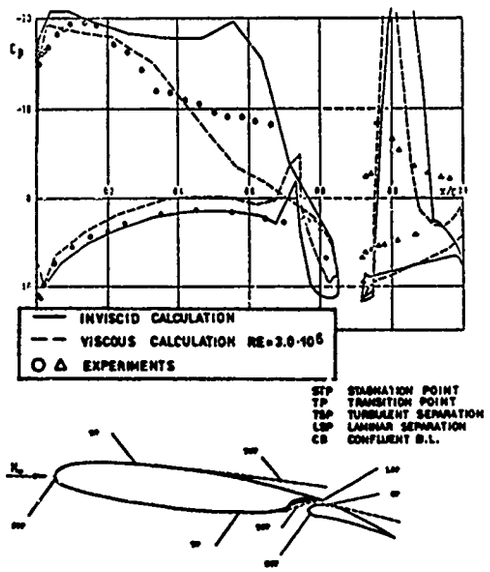
—•— VISCOUS CALCULATION
SMOOTHED FOR INVISCID PART

FIG. 22: CALCULATED SEPARATED FLOW REGION



DO-A4 WITH FLAP POS.1
$M_\infty = .5 \quad \alpha = 4°$

FIG. 24: FLAP PROFILE SYSTEM WITH WEAK TRAILING EDGE SEPARATION



DO-A4 WITH FLAP POS.1
$M_\infty = .7 \quad \alpha = 8°$

FIG. 23:
FLAP PROFILE SYSTEM WITH LARGE TRAILING EDGE SEPARATION
(NO CONVERGED SOLUTION)

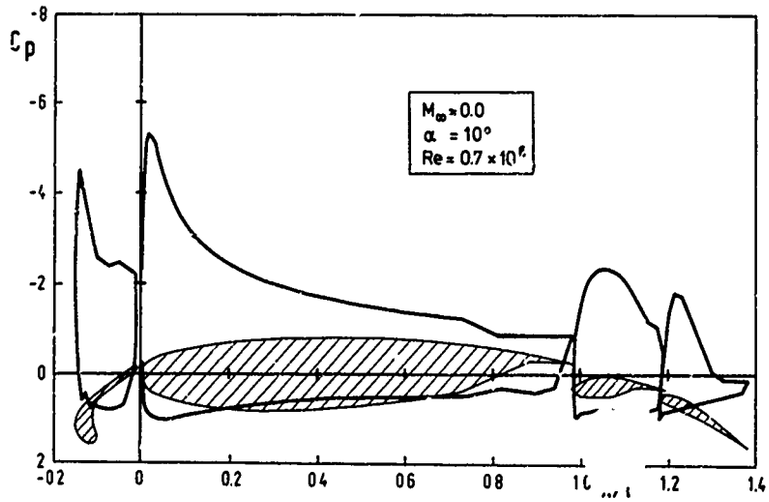


FIG. 25: FOUR COMPONENT HIGH LIFT SYSTEM IN INCOMPRESSIBLE FLOW

FLOW COMPUTATION AROUND MULTI-ELEMENT AIRFOILS IN VISCOUS TRANSONIC FLOW

H. Rosch and K.D. Klevenhusen

Vereinigte Flugtechnische Werke GmbH
D 2800 Bremen, Hünefeldstraße 1-5, FRG

ABSTRACT

A new singularity method is applied to multi-element airfoils in the physical plane for calculating both, the incompressible velocities and the incompressible potential- and streamfunction along the contur of each element. The values of the preceding computation are used to build an orthogonal grid in which the airfoil is mapped to a line in the streamline plane. The computational domain is this streamline plane wherein the full transonic potential equation is solved using a finite difference method. The great influence of viscous effects has been incorporated using the so-called surface transpiration concept. The representation of the displacement effect of the boundary layer and wakes is based on the well-known integral method and a trailing edge flow concept which includes normal pressure gradients and wake curvature effects. Comparisons of the theory with high Reynolds number experiments show the good agreement for pressure distribution and lift.

NOMENCLATURE

a	Local Speed of Sound
B	Square of the compressible velocities
C	Chord length
C_p	Pressure coefficient
M_∞	Mach number at infinity
n	Normal direction
Q	Square of the incompressible velocities
q	Flow speed
s	Arc length along airfoil and wake streamline
t	Tangential direction
u,v	Velocity components
x,y	Cartesian coordinates
x',y'	"disturbance" coordinates
α	Angle of attack
β	Prandtl-factor $\sqrt{1-M_\infty^2}$
γ	Specific heats
δ^*	Displacement thickness
Θ	Momentum thickness
κ	Curvature $\left(\frac{1}{u}\frac{\partial u}{\partial n}\right)$
ρ	Density
Φ	Compressible potentialfunction
φ	Incompressible potentialfunction
ψ	Incompressible streamfunction
$\Delta\varphi$	Potential jump at the trailing edge

SUBSCRIPTS

A	Airfoil
n	Direction normal to airfoil and wake
SEP	Separation point
TE	Trailing edge
t	Direction tangent to wake
w	Wake
x	Derivative in x-direction
y	Derivative in y-direction
δ	Denotes boundary layer edge

φ Derivative in φ -direction
ψ Derivative in ψ -direction
v Iteration count
∞ Free Stream

I. INTRODUCTION

Several published methods are known for the solution of two-dimensional viscous, steady transonic flow problems. These methods can generally be divided into two types. The first uses the small disturbance transonic potential equation (1) and adds a boundary layer code to include viscous effects.

The second method, and the one on which the work presented here is based, uses the full transonic potential equation in connection with various boundary layer codes (2, 3, 4, 5, 6, 7). With the exception of (2), which uses a Cartesian system, they all solve the equation in a curvilinear coordinate system provided by conformal mapping based on an early work of Sells (8).

The present work solves the transonic potential equation by a finite difference method using an orthogonal bodyfitted streamline coordinate system. This provides a transonic computational plane where one set of mesh lines is approximately aligned with the flow and the other is normal to the boundaries of the flow. The transformed coordinates used are the incompressible stream function and potential function, which are obtained from an incompressible solution of the flow field in question.

An early paper of Colehour [9] uses a similar approach but unlike the present paper he solves the incompressible stream function equation $\nabla^2\psi = 0$ using a finite difference method to get the desired stream function and potential funktion. The present method uses a new singularity distribution which is applied to bodies or even multi-element airfoils in the physical plane calculating both the incompressible velocities and the stream function and potential function along the surface of each element.

In calculating the boundary layer development, a laminar boundary layer is assumed to commence from the stagnation point and to continue to some specified transition position is reached where a turbulent boundary layer is initiated. The representation of the displacement effect of boundary layer and wake is developed by Thiede et al [10] and is based on an integral method expanded to handle the wake displacement effects too. The integral method to determine the boundary layer is described in detail by Walz [11].

An iterative procedure is employed to obtain consitent solutions for the inviscid flow and the boundary layer. In the interaction procedure the concept of the surface transpiration model presented by Lock [12] is used to represent the effect of the various viscous layers on the outer potential flow. In this manner the repetition of the airfoil transformation after every boundary layer calculations is avoided. An allowance for curvature effects of the boundary layer and the wake is included in these boundary conditions.

The subsequent paper is devided into four parts. The first describes the formulation of the compressible flow equations with viscous effects, the second the representation of the boundary layer and wake the third the inviscid-viscous interaction scheme while in the fourth part some of the results are presented.

II. THE BASIC INVISCID METHOD

The governing equation chosen for this analysis is the full inviscid equation for compressible flow. The usual from of this equation for two-dimensional flow is:

$$\left(a^2 - \phi_x^2\right)\phi_{xx} - 2\phi_x\phi_y\phi_{xy} + \left(a^2 - \phi_y^2\right)\phi_{yy} = 0 \qquad (1)$$

The local speed of sound can be determind from the energy equation

$$a^2 + \frac{\gamma-1}{2}q^2 = \left(\frac{1}{M_\infty^2} + \frac{\gamma-1}{2}\right)q_\infty^2 \qquad (2)$$

and on the profile the solution should satisfy the Neumann boundary condition

$$\frac{\partial\phi}{\partial n} = 0 \qquad (3)$$

Before the transonic solution is started, these equations are transformed to the incompressible φ - ψ - plane.

Consider for example a two-element airfoil given in cartesian coordinates, see for example Fig. 1.

The incompressible flow around this airfoil can be determined by solving a Dirichlet-problem

$$\nabla^2 \psi = 0 \qquad (4)$$

with

$$\psi = \text{const} \qquad (5)$$

at the boundaries of the airfoil and

$$\psi = \psi_\infty \qquad (6)$$

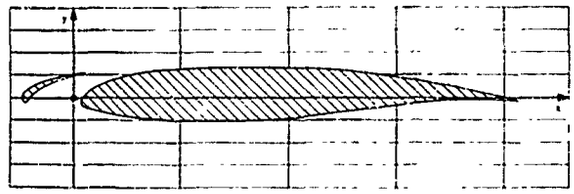


Fig. 1 Airfoil with slat in cartesian coordinates

at infintity. Differing from the well-known panel methods, see for example [13,14] and only for numerical reasons a doublet distribution with tangential doublet axes along the contour is used. With this distribution arbitrary thick and infinite thin elements can be used without any difficulty.

The singularity model leads to a well behaved system of linear equations and is very appropriate for calculating the incompressible flow around multi-element airfoils. Some details of the singularity model is presented by Klevenhusen in Ref. [15].

The streamline coordinate system necessitates the velocity potential distribution along the contours which is obtained by taking the same doublet strength as for the streamfunction but positioning the doublet axes normal to the contour. The behavior of the velocity potential of doublets is in such a way that the unavoidable numerical errors decreases with increasing distance from the locus of the doublet. Therefor a doublet model is more suitable than a source or vortex model for determining the potential function and stream function.

Only open contours and non-constant streamfunction on the boundary require additional singularity distributions - a constant soure distribution for the velocity potential and a constant vortex distribution for the stream function. Furthermore it is possible to seperate the part of the potential function due to the circulation. The velocities along the contours are obtained by differentiating the potential function. Both, the velocities and the seperated potential function are needed for the finite difference calculation.

The transformed transonic potential equation requires the knowledge of the squares of the incompressible velocities at every node point (φ, ψ) in the streamline plane. The velocities are considered as functions of φ and ψ. Furthermore we can define disturbance velocities

$$u' = u - U_\infty \cos\alpha \qquad (7)$$

$$v' = v - U_\infty \sin\alpha \qquad (8)$$

The velocities u' and v' are potential functions in the φ-ψ-plane and bounded at infinity. To get the required velocities at the node points a Laplace equation in the flow field

$$u_{\varphi\varphi} + u_{\psi\psi} = 0 \qquad (9)$$

is to be solved. The necessary boundary conditions are known from the calculation in the physical plane. A similar Laplace equation can be formulated for v' in the same way.

These two boundary value problems can be solved by doublet distributions along the slit with oblique doublet axes in the streamline plane using the above mentioned panel method. After solving the boundary value problems the doublet distributions are known and the velocities u and v can be calculated at every given point in the streamline plane.

Finially the physical coordinates are also conjugate functions in the streamline plane. Defining "disturbance coordinates"

$$x' = x - \varphi\cos\alpha + \psi\sin\alpha \qquad (10)$$

$$y' = y - \varphi\sin\alpha - \psi\cos\alpha \qquad (11)$$

the x' and y' are bounded at infinity so we can handle x' and y' in the same way as u' and v'. An example of this procedure is given in Fig. 2.

The computational domain is the streamline plane, Fig. 3 wherein the full transonic potential equation is solved using a finite difference method. The transonic potential equation (1) in the incompressible streamline coordinate system is given by

$$2a^2\left(\Phi_{\varphi\varphi}+\Phi_{\psi\psi}\right)-\left(\Phi_{\varphi}B_{\varphi}+\Phi_{\psi}B_{\psi}\right)=0 \qquad (12)$$

with

$$B=\left(\Phi_{\varphi}^2+\Phi_{\psi}^2\right)\cdot Q \qquad (13)$$

which denotes the square of the local compressible velocity and

$$Q=\varphi_x^2+\varphi_y^2 \qquad (14)$$

which denotes the square of the local incompressible velocity. The equation of the speed of sound (2) is transformed to

$$a^2=a_\infty^2-\frac{\gamma-1}{2}\left(B-U_\infty^2\right) \qquad (15)$$

A good approximation for the compressible streamlines is achieved using the same angle of attack for the determination of the grid and for calculating the transonic flow. Since the mesh lines are approximately aligned with the flow the use of a rotated difference scheme is eliminated and the transonic potential equation (12) can be simplified considerably, as all first derivatives normal to the streamline are incremental and terms of second order can be neglected:

$$2a^2\left(\Phi_{\varphi\varphi}+\Phi_{\psi\psi}\right)=2Q\Phi_{\varphi}^2\Phi_{\psi\psi}+\Phi_{\varphi}^2\left(Q_{\varphi}\Phi_{\varphi}+\Phi_{\psi}Q_{\psi}\right) \qquad (16)$$

All transonic calculations using the present method are based upon this equation. The boundary condition is given by

$$\Phi_{\psi}=0 \qquad (17)$$

at the contour of each element.

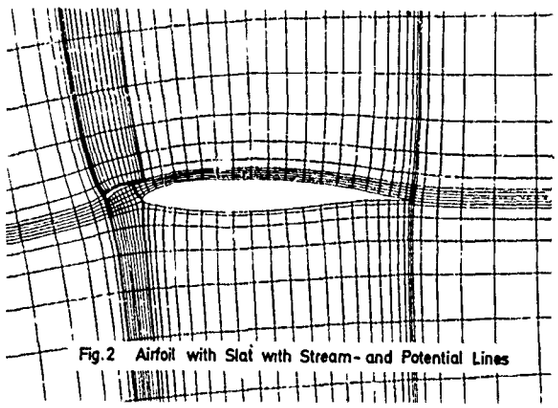


Fig.2 Airfoil with Slat with Stream- and Potential Lines

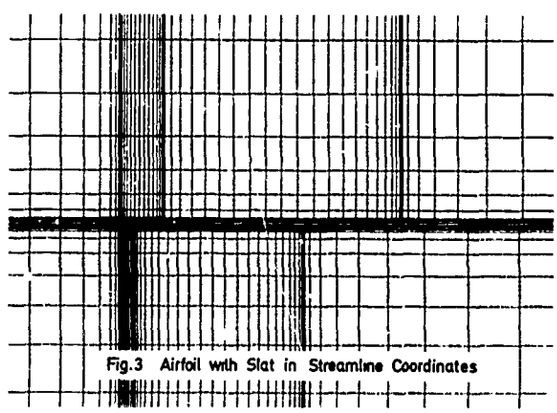


Fig.3 Airfoil with Slat in Streamline Coordinates

Lifting airfoils requires a technique for the determination of airfoil circulation as part of the solution. The transonic solution plane presents a cut in this plane. Part of this cut represents the airfoil surface and part represents the trailing streamline. Along the trailing streamline, Φ values above and below are discontinuous but static pressure must match. The jump in Φ across the trailing streamline is the circulation for the flow field and is controlled by satisfying the Kutta condition at the trailing edge, i.e. same velocities on the upper and lower surface, resp.

Some considerations must be mentioned about the the stagnation point. Equation (16) usually implies a singular behaviour at the stagnation point of the coordinates. This point is treated without any artifice since numerical methods are used and therefor the velocity at the stagnation point will be only close to zero. But it is not possible to determine the correct position of the compressible stagnation point. While some movement of the stagnation point would be expected, this restriction does not appear to cause numerical problems. It is believed that this inaccuracy has only a local effect and in most cases it is not restricting the practical use of the present method as can be seen later.

III. REPRESENTATION OF THE BOUNDARY LAYER

In the interaction procedure the concept of displacement thickness is used to represent the effect of the various viscous layers on the outer potential flow. Instead of adding the displacement thickness to the airfoil geometry a distribution of sources along the airfoil surfaces and along the wake center lines is utilized for the simulation of the viscous flow displacement effects. In this case we may rewrite the boundary condition, eq (17), for the inviscid flow as follows:

$$\Phi_{\psi}=v_n/\sqrt{Q} \qquad (18)$$

where v_n is the normal outflow the airfoil due to the boundary layer. The viscous boundary conditions are as follows:

- on the airfoil

$$v_{n_A} = \frac{1}{\rho_\delta} \frac{d}{ds} \left(\rho_\delta q_\delta \delta^* \right) \tag{19}$$

- in the wake

$$\Delta v_{n_W} = \frac{1}{\rho_\delta} \frac{d}{ds} \left(\rho_\delta q_\delta \delta^* \right) \tag{20}$$

$$\Delta v_{t_W} = -\varkappa q_\delta \left(\delta^* + \Theta \right) \tag{21}$$

The boundary layer values δ^* and Θ are obtained by an integral method described by Walz [11] and expanded by Thiede [10] to handle wake effects.

A further change to the inviscid scheme is introduced in order to allow for the effect of the curvature of the airfoil and wake on the pressure change across the viscous layer and is given by

$$\Delta p_{A,W} = -\varkappa \rho_\delta q_\delta^2 \left(\delta^* + \Theta \right) \tag{22}$$

which must be added to the inviscid pressure distribution. The required curvature used in equations (21) and (22) is given by

$$\varkappa = \frac{1}{q} \frac{\partial q}{\partial n} \tag{23}$$

which is positive in the wake. It is shown in Ref. [7] that equation (22) is approximately equivalent to adjust the calculated inviscid velocity q to q', where

$$q' = q \left[1 + \varkappa \left(\delta^* + \Theta \right) \right] \tag{24}$$

with a similar correction for the velocity in the wake. The velocity q' is used to calculate the boundary layer.

IV. THE NUMERICAL PROCEDURE

The mathematical formulations of the inviscid and viscous flow problems are coupled through their respective boundary conditions. The objective of the solution. procedure is to find those particular distributions of surface velocity and boundary layer thickness which simultaneously satisfy both the potential flow problem an the boundary layer problems.

A basic feature of the numerical scheme is that the repetition of the airfoil transformation after every boundary layer calculation is avoided. The numerical solution of the transonic boundary value problem proceeds in a manner similar to that of Murman and Cole [16] . A successive line overrelaxation method is used where the flow field is swept in the downstream direction only, and difference formulas are switched depending on whether the flow is subsonic or supersonic.

A sulution is sought for the same angle of attack in both calculations, i.e. calculations to get the desired streamline plane and to get the desired transonic results. This assures the proper alignment of the incompressible streamlines with the compressible ones in the converged transonic solution.

During the iterative procedure, Fig. 4, a prescribed Number, NS1, of inviscid interations are performed with the current boundary conditions. The velocity is then calculated on the airfoil surface and along the wake, and is used to calculate the currenct boundary layer. The boundary layer on each surface is calculated seperately and is extended beyond the trailing edge to obtain the part of the wake on either side of the trailing edge streamline. The pressure distribution is specified at node points along the dividing streamline in the streamline plane, but is specified for the boundary layer analysis as values at the corresponding x and y coordinate points, starting at the stagnation point rather than the leading edge and proceding downstream towards infinity an each surface.

As results the boundary layer calculations produces the displacement thickness, δ^*, and the momentum thickness, Θ , at the various meshpoints. Unterrelaxation is employed in order to determine the actual values of the displacement thickness

$$\delta_\nu^* = \delta_{\nu-1}^* + \mathrm{RDEL} \left(\delta_\nu^* - \delta_{\nu-1}^* \right) \tag{25}$$

and the momentum thickness

$$\Theta_\nu = \Theta_{\nu-1} + \mathrm{RDEL} \left(\Theta_\nu - \Theta_{\nu-1} \right) \tag{26}$$

where RDEL is an underrelaxation parameter. With these relaxed values equations (19), (20), (21) and (24) are used to calculate the new boundary conditions and further flow field calculations are performed with the new boundary conditions.

After every NS1 inviscid iterations have been performed the whole cyle is repeated. This process continues until either a certain convergence criteria is satisfied or until a specified number of iterations have been completed. After the completation of the iterative procedure the lift coefficients on the airfoil are calculated.

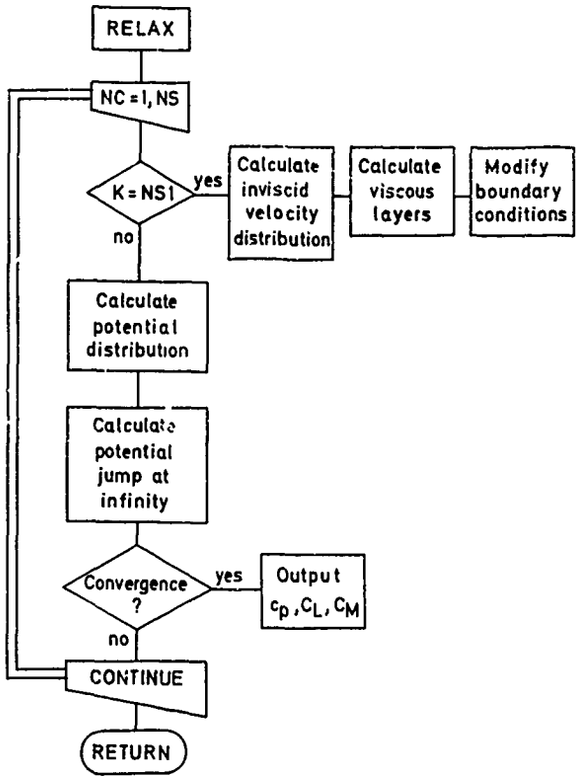


Fig. 4: Flow Chart for Iterative Methods

V. RESULTS

Several test cases have been selected to demonstrate the flexibility of the method. The first example compares pressure distributions a two-dimensional airfoil section, the same as in Fig. 2. The calculations, Fig. 5, have been done for

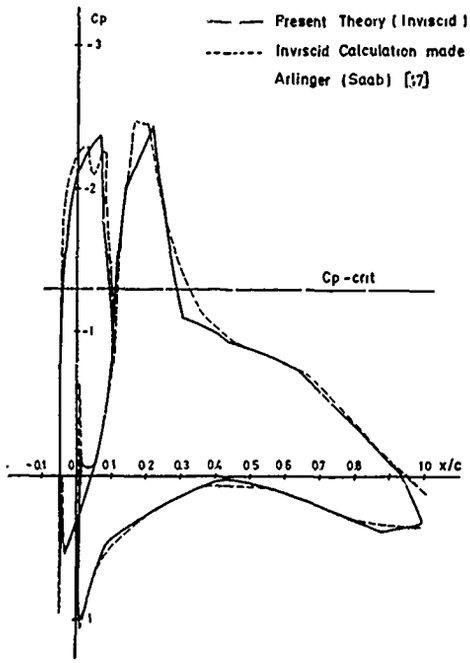


Fig. 5: Two-Element Airfoil, $M_\infty = 0.6$, $\alpha = 6°$

the inviscid case. The agreement between the present result and the result obtained by Arlinger [17] is excellent, however Arlinger used a conformal mapping [18] to get the desired computational mesh. It demonstrates clearly that the pressure distribution obtained by the two methods are almost the same but the present method has the advantage to use a simpler mapping.

The next two figures demstrate the effect of the pressure variation across the viscous layer. Fig. 6 shows for an NACA 65_1-213 airfoil a calculation with a correction for viscous effects only on the profile and without the described normal pressure correction. Comparison is made with measurements obtained by Burdges at al [19]. The next figure, Fig. 7, shows the including of the normal pressure correction. It clearly demonstrates the influence of the pressure correction on the last 10% of the airfoil chord. With this correction the agreement between theory and measurement for this simple airfoil shape is excellent.

Some typical results of a comparison of the pressure distributions for the supercritical airfoil VFW-VA2 are presented in the next two figures. Fig. 8 shows a calculation with the pressure correction but without the displacement effects. The experiment is taken from Ref. [20] . In the next calculation the effects of the wake are included and Fig. 9 shows the good agreement between the present method and the measurement.

The next few figures will show some results from calculations of the flow field around multielement airfoils. Since the effective angle of attack of the model in the tests was uncertain, a suggested increment in Ref. [21] of $\Delta\alpha = -1.0°$ due to the wind tunnel wall correction is chosen. The effective angle of attack quoted in the figures includes this increment.

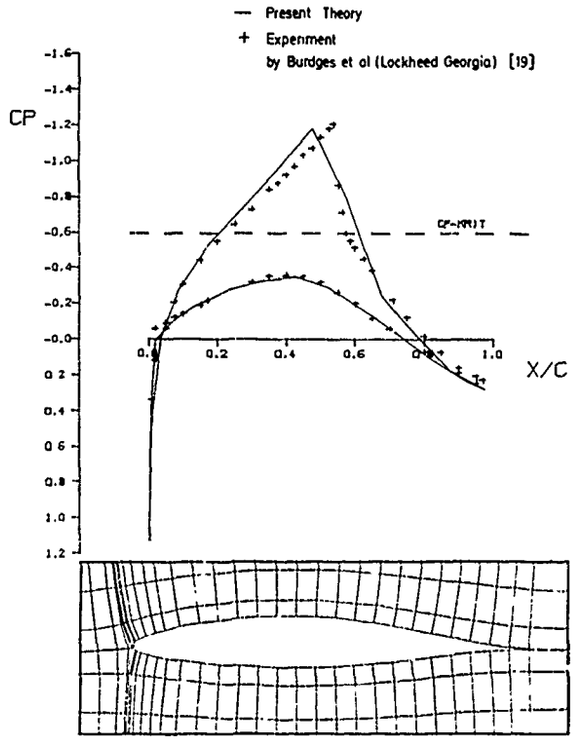


Fig.6: NACA 65_1 -213, α = 0 5 Airfoil
Calculation without Curvature Effects

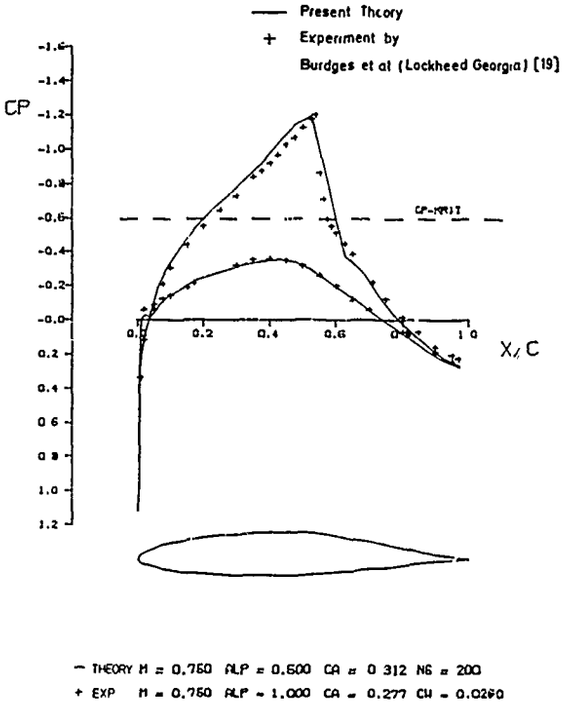


Fig. 7: NACA 65_1 - 213, α = 05 Airfoil
Calculation with Curvature Effects

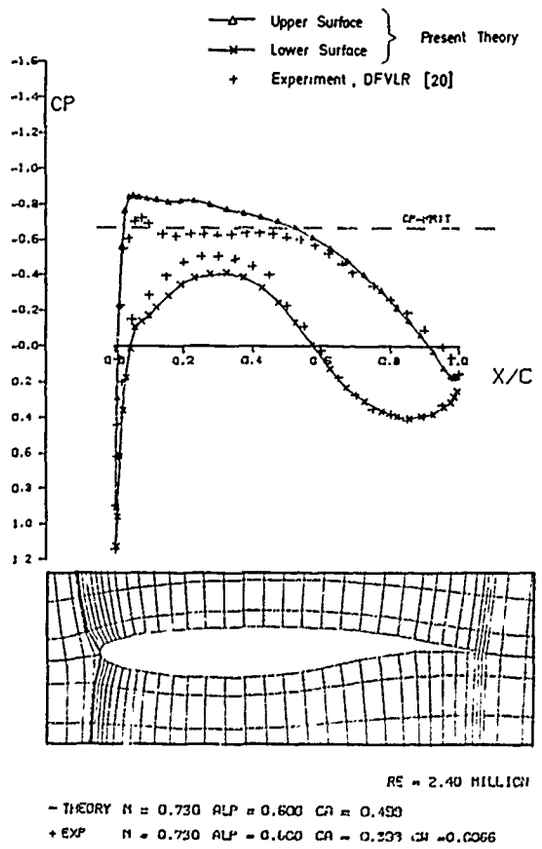


Fig.8: VFW VA-2 Airfoil
Calculation without Wake Effects

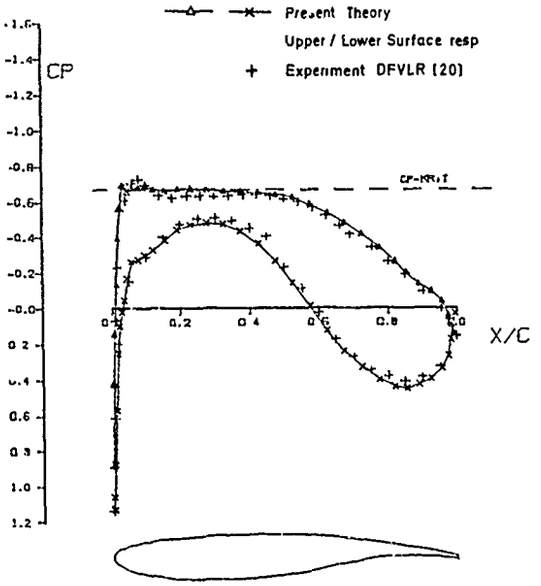
The first results are for the SKF 1.1 airfoil with extended flap. The solution shown includes the effect of the wake. Fig. 10 shows the pressure distribution at a free stream Mach number of .6 together with the airfoil in the streamline plane. The agreement between the present method and the measurement [21] is good. However, the airfoil contour is not smoothed at the cutout on the main airfoil at the trailing edge.

The same calculation is done but with a free stream Mach number of .7 which produce a greater supersonic region on the airfoil. Fig. 11 shows the result of the present theory together with measurements of Ref. [21]. The overall agreement is good but the local discrepancies in the shock strength and at the leading edge are probably due to the fact that the pressure distribution in the cutout region of the main airfoil is not well predicted.

A last example is depicted in Fig. 12. It shows the three-element airfoil with slat and flap. Comparison are made with unpublished material of VFW [22] . The agreement between the present theory and the measurement is satisfactory. Note that this prediction is made without wake effects.

The main reason is as follows:

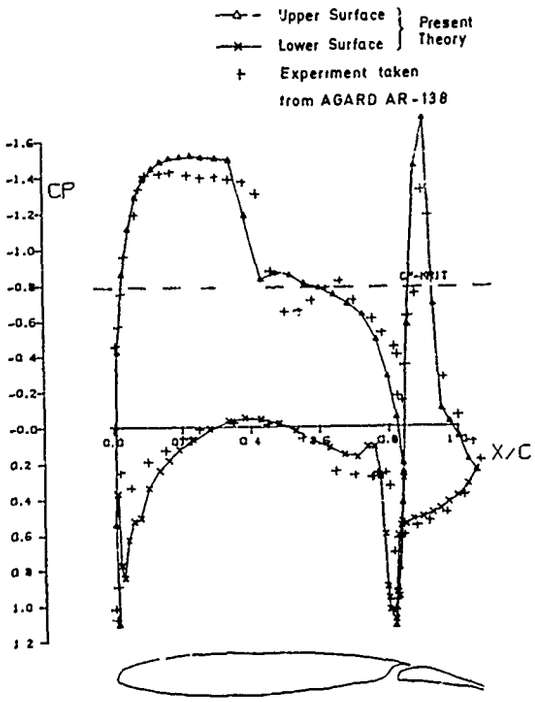
In the interaction region of the gap between main airfoil and flap the boundary layer flow will seperate at the beginning of the cutout. The boundary layer theory are only valid just prior to the seperation point. This leads to a somewhat heuristic seperation streamline based on emperism and experience. This might be an acceptable way to calculate the boundary layer if only a small seperation



RE = 2.40 MILLION

- THEORY M = 0.730 ALP = 0.600 CA = 0.330
+ EXP M = 0.730 ALP = 0.600 CA = 0.393 CM =-0.0066

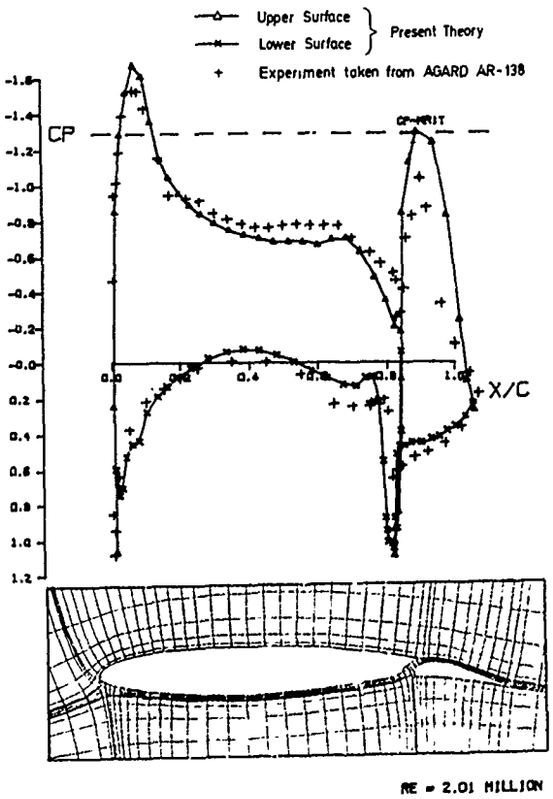
Fig.9: VFW VA-2 Airfoil
Calculation with Curvature and Wake Effects



RE = 2.22 MILLION

- THEORY M = 0.700 ALP = 2.000 CA = 1.281
+ EXP M = 0.701 ALP = 3.000 CA = 1.181

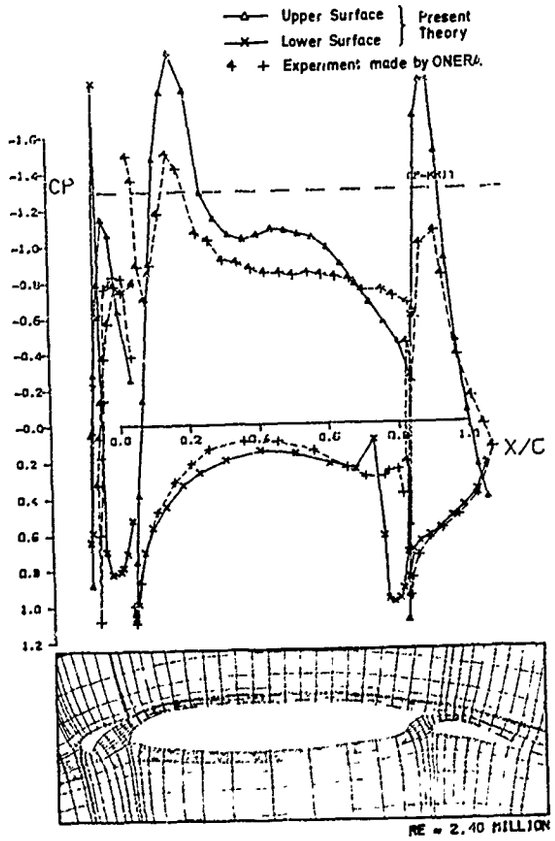
Fig.11: SKF 1.1 Airfoil with Flap
Calculation with Curvature and Wake Effects



RE = 2.01 MILLION

- THEORY M = 0.600 ALP = 2.000 CA = 1.053
+ EXP M = 0.600 ALP = 3.000 CA = 1.054 CM =-0.0199

Fig.10: SKF 1.1 Airfoil with Flap
Calculation with Curvature and Wake Effects



RE = 2.40 MILLION

THEORY M = 0.600 ALP = 1.000 CA = 1.668
EXP M = 0.600 ALP = 2.000 CA = 1.258

Fig.12: SKF-Conf. C Airfoil with Slat and Flap
Comparison with Viscous Calculation and Measurement

region exists. But if massive separation will appear which is assumed due to the strong adverse pressure gradient like the one shown in the foregoing figures one of the following is recommended:

The full Navier-Stokes-Equations have to be solved or

to develop a more sophisticated viscous/inviscid interaction model in the separation region or

to avoid these pressure gradients the airfoil has to be smoothed like a separation streamline or

to take the results as they are.

If the results are taken as they are no one expects that use of the Kutta-condition, i.e. same velocities on the upper and lower surface at the trailing edge, will give the right circulation. These conditions will lead to the pressure distributions shown here.

However, the overall agreement between the present theory and the experiments for single airfoils or even multi-element airfoils are quite satisfactory. For the three-element airfoil the agreement is not as good due to the reason stated above. But for engineering application the results are quite encouraging, since there is little known about the interaction of inviscid/viscous flow around multi-element airfoils in the transonic speed regime.

VI. CONCLUSIONS

The method presented here represents a great improvement on those that have been available previously for single or two-element airfoils and has the extension to handle more than two-element airfoil sections. Thus it is of considerable practical value in airfoil design. However, there are deficiencies in the method notably in the region where the boundary layer assumptions are strictly invalid, i.e. when the flow is approaching, or beyond, separation.

The use of a streamline coordinate transformation procedure in transonic flow analysis allows a general method to be developed that is not confined to a special class of geometry. The method gives results which are in reasonable agreement with experiments. The resulting computer program which has been developed enables a converged solution over a typical two-element airfoil section to be obtained in about 2-3 minutes on an IBM 3033 computer.

VII. REFERENCES

[1] C.M.Albone, D. Catherall, M.G. Hall, G. Joyce:

An improved numerical method for solving the transonic small pertubation equations for flow past a lifting aerofoil.
RAE Technical Report 74056 (1974)

[2] L.A. Carlson:

Transonic Airfoil Analysis and Design Using Cartesian Coordinates.
J.Aircraft, Vol 13, No.5, May 1976, pp 349-356

[3] P.C. Bavitz:

An Analysis Method for Two-Dimensional Transonic Viscous Flow.
NASA TN D-7718, 1975

[4] F. Bauer, P. Garabedian, D. Korn, A. Jameson:

Supercritical Wing Section II.
Lecture Notes in Economics and Mathematical Systems, Vol. 108,
Spinger-Verlag, Berlin, Heidelberg, New York, 1975

[5] K.D. Klevenhusen, R. Hilbig:

Beitrag zur Untersuchung der überkritischen Profilströmung.
DGLR-Vortrag Nr. 74-99 (1974)

[6] R.E. Melnik, R. Chow, H.R. Mead:

Theory of Viscous Transonic Flow over Airfoils at High Reynolds Number.
AIAA-paper 77-680. 15.th Aerospace Science Meeting Jan., 24-26. 1977,
Los Angeles, Calif., USA

[7] M.R. Collyer, R.C. Lock:

Prediction of Viscous Effects in Steady Transonic Flow Past an Aerofoil.
Aeronautic. Quart., Aug. 1979, p. 485

[8] C.C.L. Sells:

Plane Subcritical Flow Past a Lifting Aerofoil.
Proc. Roy. Soc. (London), Vol 308A, 1968, pp 377-401

[9] J.L. Colehour:

Transonic Flow Analysis Using a Streamline Coordinate Transformation Procedure.
AIAA-paper 73-657, 6th Fluid and Plasma Dyn. Conf., July 16-18, 1973,
Palm Springs, Calif., USA

[10] P. Thiede, J. Dargel:

Hinterkantenströmungen
Verbesserte Erfassung der Reibungseffekte im Hinterkantenbereich von
überkritischen Profilen.
RüFo Endbericht T/RF41/70022/71421 VFW-Fokker, 1979

[11] A. Walz:

Boundary Layer of Flow and Temperature.
MIT Pres, Cambridge, Massachussetts, (1969)

[12] R.C. Lock:

Calculations of viscous effects on aerofoils in compressible flow.
5th Australian Conference on Hydraulics and Fluid Mechanics,
University of Canterbury, N.Z., Dez. 1974

[13] J.L. Hess, A.M.O. Smith:

Calculation of Potential Flow About Arbitrary Bodies.
Progress in Aeron. Science, Vol 8, New York, Pergamon Press, 1966

[14] H.J. Oellers:

Die kompressible Potentialströmung in der Gitterstufe.
WGLR-Jahrbuch, 1962, Braunschweig 1963, p 349

[15] K.D. Klevenhusen:

A Calculation Method for Multielement Airfoils in Subsonic and Transonic
Potential Flow.
AIAA-paper 80-0340, 18th Aerospace Science Meeting, Jan. 14-16. 1980,
Pasadena, Calif. USA

[16] E.M. Murman, J.D. Cole:

Calculation of Plane Steady Transonic Flows
AIAA-paper 70-188, 1970

[17] B.C. Arlinger:

Private Communication, 1978

[18] B.C. Arlinger:

Analysis of Two-element High Lift Systems in Transonic Flow.
ICAS-paper 76-13, Oct. 1976

[19] K.P. Burdges, J.A. Blackwell, G.A. Pounds:

High Reynolds Number Test of a NACA 65-215, a = 0.5 Airfoil at Transonic Speeds.
NASA CR-2499, March 1975

[20] R.D. Boehe:

Transonik-Messungen am VFW-F Profil.
ZKP-Bericht, LFK 7511 Flügelsektion, 1976

[21] -

Experimental Data Base for Computer Program Assessment.
AGARD-AR-138, 1979

[22] Windkanalmessungen mit dem 2D-Modell SKF bei der ONERA.
Unpublished Paper, VFW

CALCULATIONS OF TRANSONIC FLOW OVER WING/BODY COMBINATIONS WITH AN ALLOWANCE FOR VISCOUS EFFECTS

M.C.P. Firmin
Aerodynamics Department
Royal Aircraft Establishment
Farnborough, Hampshire, England

SUMMARY

The paper shows how a viscous-inviscid interaction scheme developed for aerofoils can be successfully generalised to account for the three-dimensional effects of the boundary layers and wake over the wing of a wing/body combination.

Two main elements make up the method:

(a) the RAE Mk 4 transonic small perturbation method which has been modified to allow changes to be made to the boundary conditions over the wing and in the wake;

(b) a three-dimensional integral boundary-layer method, using the scheme of solution devised by P.D. Smith, to extend the two-dimensional 'lag' entrainment method of Green, Weeks and Brooman.

The paper discusses the coupling of the two main elements of the method and the difficulties encountered in providing an adequate iterative scheme. Computing times are discussed in relation to the time required for the basic calculation for inviscid flow. Several examples are given of results obtained and comparisons are shown between experimental measurements and results from the scheme.

LIST OF PRINCIPAL SYMBOLS

c	local chord
$\bar{c}$	mean chord of wing
C_E	entrainment coefficient (Eq.(13))
$C_{L_{(local)}}$	local lift coefficient based on local chord
C_{L_W}	lift coefficient for wing based on wing area
C_p	pressure coefficient
ΔC_p	change in pressure coefficient due to wake curvature (Eq.(10))
$\bar{H}$	transformed shape factor (Eq.(16))
H_{11}	streamwise boundary-layer shape factor
H_1	$(\delta - \delta_1)/\theta_{11}$
M_∞	stream Mach number
$Re_{\bar{c}}$	Reynolds number based on mean chord
s, n	streamwise coordinates
x, y, z	rectangular coordinates in physical space
y_B, z_B	coordinates of body
X, Y, Z	transformed coordinates in computing space
Y_B, Z_B	sides of rectangular box representing body
α	flow direction on the wing surface
α_B	body incidence
α_W	wing incidence
β	angle between the external streamline and the direction of limiting streamline on the wing surface
γ	ratio of specific heats (Eq.(1))
$\gamma( )$	change in boundary conditions due to boundary layers (Eq.(5))
δ^*	displacement thickness
ξ	non-dimensional position on chord of wing
ω	relaxation factor for viscous effects (Eq.(21))
η_{gross}	non-dimensional position on the gross semi-span of wing
θ_{11}	streamwise momentum thickness
ρ	density
Suffix	
e	edge of boundary layer or wake

1 INTRODUCTION

One of the major challenges facing aerodynamicists has been to provide practical methods which may be used in the design of aircraft. This necessitates being able to determine the pressure distribution and loads on the component parts in flight. This challenge has always posed a most difficult problem, and particularly so when shock waves exist in the flow; and at present no ideal method exists. Unfortunately as aircraft designs have advanced the flows have become more complicated and often more sensitive to scale effects, and therefore less amenable to calculation. For some of the more complex shapes, and where flow separations exist, it is still essential to rely mainly on wind-tunnel tests; but these are expensive, time-consuming and involve wall interference and scale effects of uncertain magnitude. Recently advances in computational fluid dynamics have allowed the prospect of making good estimates, even for examples with transonic flow and shock waves, of the loading of aircraft for conditions of attached flow. This is done by considering the problem as one where the flow is predominantly inviscid but also one where corrections can be made for the viscous effects. Thus for this restricted range of conditions there is a prospect of reducing the number of wind-tunnel tests necessary in any design development and so reduce the timescale and cost.

An invited paper by Lock[2], for this Symposium, reviews the subject in detail, but as the scheme to be described here for wing/body combinations relies heavily on the previous work on aerofoils, the main points are also summarised here. Several methods have been developed for taking into account the interaction between the boundary layers and wake with the external inviscid flow, and some of these have been extended to deal with transonic flows, for cases where the shock waves are not too strong and the boundary layers remain attached[3-6]. The methods in most common use, so far, are based on solutions for the inviscid potential flow and an allowance is made for the effects of the boundary layers and viscous wake by modifying the internal boundary conditions in the region of the aerofoil surface and the wake. Two possible concepts have been used; either a new boundary is considered as envisaged by Preston[1], or the boundary conditions at the aerofoil surface and on a line representing the wake are modified, to account for the displacement effects of the boundary layer and wake[7]. The overall solution then depends on an iterative scheme in which the boundary conditions are modified in steps as the calculation proceeds using an under-relaxation scheme[3]. These methods have given such good results that it seems reasonable to attempt an extension of the ideas to the wings of wing/body combinations, although for aerofoils there are still some doubts about the detailed representation of the flow in a shock-wave boundary-layer interaction[5] and in the neighbourhood of a trailing edge[6]. In spite of these inherent deficiencies the methods still appear to be more accurate and economical than the numerical solutions that have appeared so far from the Reynolds averaged Navier-Stokes codes, even for attached flow over aerofoils[8].

In this paper a method is described in which the main inviscid element is the RAE Mk 4 Transonic Small Perturbation (TSP) method[10] for the flow over wing/body combinations, and the boundary layers and wakes are calculated using an integral method which is an extension of the 'lag' entrainment method of Green, Weeks and Brooman[12] to three-dimensional flow, and uses the scheme of solution devised by Smith[13]. For regions of the wing near the attachment line and where laminar boundary layers exist a yawed wing assumption is made.

The paper discusses the coupling of the two main elements of the method and the difficulties encountered in providing an adequate scheme. Several examples are given of results obtained.

2 STATEMENT OF PROBLEM

The method requires, as for aerofoils, two basic elements to be linked together: (a) a method for calculating the inviscid flow over a wing/body combination, where boundary conditions are applied either at the displacement surface or alternatively on the original surface, but with a non-zero normal velocity at the surface and with a modified jump condition downstream in the wake; and (b) a method for calculating the boundary layer and wake flow generated by a wing. It will be assumed that the boundary layers may be either laminar or turbulent in the region of the leading edge but that in any case transition to turbulent flow will occur at some prescribed location on the forward part of the wing.

The linking of the two methods is essential, since the boundary conditions which are applied to the method for inviscid flow are obtained from boundary-layer and wake calculations, while the boundary-layer calculations are dependent on the pressure distribution which is obtained from the inviscid flow method. An interactive sequence has to be built up and this will take the form of a doubly iterative scheme as first suggested by Jones and Firmin[9] for aerofoils. They found that by modifying the boundary conditions, at intervals, during the iterative sequence for the inviscid flow method, it was possible to obtain solutions for an aerofoil with a correction for the effects of the attached boundary layers provided a low relaxation factor was used in modifying the aerofoil's boundary conditions. The total computing times were increased by the order of 50% due to the necessity to regularly calculate the boundary-layer characteristics for the gradually changing pressure distribution and the need for an increased total number of interactions to obtain a converged solution of the inviscid method. Similar results might be expected for the work on wing/body combinations as the methods being used are derivatives of those used in the original work.

3 CHOICE OF METHODS

3.1 Inviscid flow

For the calculation of the inviscid flow over wing/body combinations in compressible flow where shock waves may occur, the only method available within the UK at the time this work was started was the RAE TSP method being developed by Albone, Hall and Joyce[7,10]. This method is based on the assumption that the flow is irrotational so that a velocity potential exists, and also that the perturbations in velocity potential are small. The method has been well tested for two-dimensional flow against solutions of the full potential method for a wide range of aerofoils and over Mach number ranges likely to be of interest in the design of aircraft, and has been found to give surprisingly accurate results[11].

In the derivation given by Albone *et al* the method for wings and wing/body combinations reduces to the two-dimensional form for an infinite sheared wing. For three-dimensional flow the differential equation is:

$$\left[1 - M_\infty^2 - (\gamma + 1)M_\infty^2\phi_x\right]\phi_{xx} + \left[1 - (\gamma - 1)M_\infty^2\phi_x\right]\phi_{yy} + \phi_{\bar{z}\bar{z}} - 2M_\infty^2\phi_y\phi_{xy} = 0 \qquad (1)$$

where the scaled perturbation potential ϕ is related to the velocity potential Φ by

$$\phi = M_n^{r-4/3}(\Phi - x) \qquad (2)$$

with $\bar{z} = M_n^{(2/3-r/2)}z$ and $M_n = M_\infty \cos\Lambda$. Λ is an angle which is zero at the centre line of the body and tends to the local angle of sweep-back of the mid-chord of the wing outside the body. M_∞ is the free stream Mach number and r is an empirically defined parameter. The boundary conditions used in the method are modified slightly to allow viscous corrections to be applied. Over the body no modification is required as, at this stage, corrections are not included for the influence of the body boundary layer; so the boundary conditions, applied on the sides of the rectangular box $y = y_0$, $z = z_0$, are:

$$(\phi_y)_{y=y_0} = M_n^{r-4/3}\left(\frac{\partial y_B}{\partial x}\right) + \left[M_n^{r-4/3}\alpha_B + (\phi_{\bar{z}})_{y=y_0}\right]\cdot\left(\frac{\partial y_B}{\partial z}\right) \qquad (3)$$

and

$$(\phi_{\bar{z}})_{\bar{z}=\bar{z}_0} = M_n^{r-4/3}\left[\left(\frac{\partial z_B}{\partial x}\right) - \alpha_B\right] + (\phi_y)_{\bar{z}=\bar{z}_0}\left(\frac{\partial z_B}{\partial y}\right) \qquad (4)$$

where $\bar{z} = \bar{z}_0(x,y)$ and $y = y_B(x,z)$ defines the body surface and α_B is the body incidence. In the method the boundary conditions are not applied on the body itself but equivalent conditions are applied on the side of the rectangular box, which acts as a porous boundary.

Over the wing and in the wake corrections are included for the wing boundary layers and the viscous wake. The boundary condition applied on $z = 0^+$ and on $z = 0^-$ becomes

$$(\phi_{\bar{z}})_{\bar{z}=0} = M_n^{3r/2-2}\left[\left(\frac{\partial z_s}{\partial x}\right) - \alpha_W + \gamma(x,y)\right] \qquad (5)$$

where $z = z_s(x,y)$ is the equation of the actual wing surface, α_W is the angle of incidence of the wing and $\gamma(x,y)$ is the additional term due to the displacement effect of the boundary layers on the wing. $\gamma(x,y)$ is derived from a knowledge of the boundary-layer parameters and depends on the applied pressure distribution, so it is different for the upper and lower surfaces of the wing.

The conditions to be satisfied on the trailing vortex sheet are modified, but the sheet is still represented by a jump in velocity potential across $z = 0$. The modified conditions to be satisfied on the trailing vortex sheet are:

$$\left[\phi(x,y,\bar{z}=0^+) - \phi(x,y,\bar{z}=0^-)\right]_{x>x_{te}} = \Gamma(x,y) \qquad (6)$$

$$\phi_z(x,y,\bar{z}=0^+) - \phi_z(x,y,\bar{z}=0^-) = \Delta\phi_z(x,y) \qquad (7)$$

where

$$\Gamma(x,y) = \Gamma(x = +\infty, y) + \Delta\Gamma(x,y)\,. \qquad (8)$$

$\Delta\Gamma$ and $\Delta\phi_z$ are dependent on the wake curvature and thickness, and the trailing edge of the wing is defined by $x = x_{te}$.

At $x = +\infty$ the perturbation potential ϕ satisfies the reduced equation

$$\phi_{yy} + \phi_{\bar{z}\bar{z}} = 0 \qquad (9)$$

subject to the conditions

$$\phi(y,\bar{z}=0^+) - \phi(y,\bar{z}=0^-) = \begin{cases} \Gamma(x=+\infty,y) \\ 0 \end{cases}$$

for $y \begin{cases} \leq \\ > \end{cases}$ y semi-span, and $\phi \to 0$ as $y \to \infty$ and $\bar{z} \to \pm\infty$. For other values of x, $\phi \to 0$ with increasing distance from the wing/body combination.

The pressure coefficient is given by an approximate relationship

$$C_p = -2M_n^{3/2-r}\phi_x - M_n^{3-2r}(\phi_x)^2(1 - M_\infty^2) - M_n^{3-2r}(\phi_y)^2 + \Delta C_p \qquad (10)$$

where ΔC_p is a correction to the pressure coefficient due to the difference in pressure between the value on the actual surface obtained from the inviscid-flow model and the value in the real flow. ΔC_p is obtained from the difference in the change in pressure across the boundary layer and that across an equivalent layer of inviscid flow.

3.2 Boundary layer and wake flow - turbulent

With the success of the 'lag' entrainment turbulent boundary-layer method[12] used in connection with the development of schemes for calculating viscous effects on aerofoils, it is natural to use a similar method for three-dimensional flows. The 'lag' entrainment method is an integral method in that the governing partial differential equations in the three independent variables (x,y,z) are reduced, by an integration in the direction normal to the surface (z), to another set of partial differential equations, but with two independent variables. The method, which is an extension of the entrainment method of Smith[13], is based on four such equations, the two momentum integral equations, the continuity integral equation, and the 'lag' equation. For the use made here the main advantage of the integral method over differential method is one of speed for a given accuracy, which is important when the viscous layers have to be determined repeatedly during the course of the calculations.

The momentum integral equations written in streamline coordinates are[14]:

$$\frac{\partial\theta_{11}}{\partial s} + \frac{\partial\theta_{12}}{\partial n} = \frac{1}{2}C_{f_1} - \theta_{11}(H + 2 - M_e^2)\frac{1}{u_e}\frac{\partial u_e}{\partial s} + \theta_{12}M_e^2\frac{1}{u_e}\frac{\partial u_e}{\partial n} - (\theta_{11} - \theta_{22})\frac{1}{r}\frac{\partial r}{\partial s} \qquad (11)$$

and

$$\frac{\partial\theta_{21}}{\partial s} + \frac{\partial\theta_{22}}{\partial n} = \frac{1}{2}C_{f_2} - \theta_{21}\left\{(2 - M_e^2)\frac{1}{u_e}\frac{\partial u_e}{\partial s} + \frac{2}{r}\frac{\partial r}{\partial s}\right\} - \left\{\theta_{11}(H + 1) + \theta_{22}(1 - M_e^2)\right\}\frac{1}{u_e}\frac{\partial u_e}{\partial n}$$

.....(12)

where s represents a distance along an external streamline, n a distance parallel to the wing surface and normal to an external streamline and $\frac{1}{r}\frac{\partial r}{\partial s}$ is associated with the divergence of the streamlines.

The continuity integral equation is:

$$\frac{\partial(H_1\theta_{11})}{\partial s} - \frac{\partial\delta_2}{\partial n} = C_E - H_1\theta_{11}\left[\frac{1}{r}\frac{\partial r}{\partial s} + (1 - M_e^2)\frac{1}{u_e}\frac{\partial u_e}{\partial s}\right] - \delta_2 M_e^2\frac{1}{u_e}\frac{\partial u_e}{\partial n} \qquad (13)$$

The various displacement and momentum thicknesses are defined as:

$$\left.\begin{aligned}
\delta_1 &= \int_0^\delta \left(1 - \frac{\rho u}{\rho_e u_e}\right) dz , & \delta_2 &= -\int_0^\delta \frac{\rho v}{\rho_e u_e}\, dz , \\
\theta_{11} &= \int_0^\delta \left(1 - \frac{u}{u_e}\right)\frac{\rho u}{\rho_e u_e}\, dz , & \theta_{12} &= \int_0^\delta \left(1 - \frac{u}{u_e}\right)\frac{\rho v}{\rho_e u_e}\, dz , \\
\theta_{21} &= -\int_0^\delta \frac{\rho u v}{\rho_e u_e^2}\, dz , & \theta_{22} &= -\int_0^\delta \frac{\rho v^2}{\rho_e u_e^2}\, dz ,
\end{aligned}\right\} \qquad (14)$$

with the shape factors $H = \delta_1/\theta_{11}$ and $H_1 = (\delta - \delta_1)/\theta_{11}$. u , v , C_{f_1} and C_{f_2} are the components of the velocity and skin friction vectors in the s and n directions respectively. The subscript e refers to conditions at the outer edge of the boundary layer, and ρ is the density.

The two-dimensional 'lag' equation[12] is assumed to hold along an external streamline, so

$$\theta_{11}\frac{\partial C_E}{\partial s} = F\left[\frac{2.8}{H + H_1}\left\{(C_\tau)^{\frac{1}{2}}_{EQ_0} - \lambda (C_\tau)^{\frac{1}{2}}\right\} + \frac{\theta_{11}}{u_e}\left(\frac{\partial u_s}{\partial s}\right)_{EQ} - \frac{\theta_{11}}{u_e}\frac{\partial u_e}{\partial s}\left\{1 + 0.075M_e^2\,\frac{1 + 0.2M_e^2}{1 + 0.1M_e^2}\right\}\right] \qquad (15)$$

where C_τ is the shear stress coefficient and λ is a factor which is set to unity for boundary layers unless secondary influences are included. The suffices EQ_0 and EQ refer to equilibrium conditions, the quantities being calculated as suggested by Green *et al*[12]. Following Green, $\bar{H}$ is introduced as:

$$\bar{H} = \frac{1}{\theta_{11}}\int_0^\delta \left(1 - \frac{u}{u_e}\right)\frac{\rho}{\rho_e}\, dz \qquad (16)$$

and it is assumed by Smith, as in the entrainment method[13], that all crossflow thicknesses may be related to the streamwise momentum thickness θ_{11} by the relationships

$$\left.\begin{aligned}
\theta_{21} &= f_1(\bar{H})\theta_{11}\tan\beta \\
\theta_{12} &= f_2(\bar{H})\theta_{11}\tan\beta \\
\delta_2 &= f_3(\bar{H})\theta_{11}\tan\beta \\
\theta_{22} &= f_4(\bar{H})\theta_{11}\tan\beta
\end{aligned}\right\} \qquad (17)$$

where β is the angle between the external streamline and the direction of the limiting streamline on the wing surface. The streamwise skin friction coefficient is assumed to be given by the relationship due to Green *et al*[12] for two-dimensional flow. The crossflow skin-friction coefficient is assumed to be given by

$$C_{f_2} = C_{f_1}\tan\beta . \qquad (18)$$

The above equations are transformed to a non-orthogonal system and are solved numerically by a simple explicit finite difference method in which the forward step size is controlled by the requirement that the downstream point remains within the domain of influence of the upstream point and its immediate neighbours. The input velocity distribution and geometry are all interpolated by using bicubic spline interpolation.

The boundary-layer method is extended into the wake by making basically the same assumptions as made by Green for two-dimensional aerofoils. The computation of the

boundary-layer growth over one surface of the wing is taken beyond the trailing edge to treat the development of the part of the wake on one side of the stream surface originating at the trailing edge, by continuing the solution of the governing differential equations. Downstream of the trailing edge, the only changes to the method are:

(1) C_{f_1} (including the related value for a flat plate) is set to zero in all the equations in which it occurs;

(2) the dissipation length scale is doubled (*ie* $\lambda = 0.5$).

The first change implies no contribution from skin friction in the momentum integral equations (11) and (12), as C_{f_2} is related to C_{f_1} through Eq.(18). Green justifies the change for aerofoils in terms of physical considerations and by comparing with experimental evidence; no further justification is given here. In practice it is found that the crossflow angle β decays as the pressure gradients are reduced in the wake. β now becomes the angle between the external streamline and the corresponding streamline at the stream surface dividing the upper and lower surface wakes. No account has been taken of the viscous interaction between the wakes leaving the upper and lower surfaces of the wing.

3.3 Boundary layers near a leading edge

In this work the aim has been to make allowance for viscous effects when the boundary layers are predominantly turbulent over the wings, but it is still essential to make some allowance for the layers ahead of transition and to have a method available for determining the starting conditions for the turbulent layers. Although methods exist for the calculation of three-dimensional compressible laminar boundary layers they did not fit easily into the scheme proposed here. Difficulties occurred because the flow direction can change rapidly in the region of the attachment line and the grid system may not match the requirements of the laminar boundary-layer methods.

These practical difficulties were avoided in the current method by assuming that, in the region of the leading edges of the wing, variation in the spanwise direction (*ie* along wing generators) can be neglected and so a 'yawed-wing' version of Smith's boundary-layer program[15], which has been prepared for laminar or turbulent boundary layers, can be used from the leading edge of the wing back to a convenient point at each spanwise station. For flow which is laminar at the attachment line and up to some transition location, the momentum thickness is evaluated using an approximation suggested by Cooke[16], and then the turbulent boundary layer is started assuming that the momentum thickness is continuous at transition, and that the twist through the boundary layer β is initially zero. The shape factor at the start of the turbulent boundary layer is determined by assuming equilibrium flow.

When the direction of the transition front does not coincide with that of a grid line used in the combined method, the 'yawed wing' method for turbulent boundary layers is used to bridge the gap. The obvious anomaly in the region of the wing/body junction needs further investigation, but the results obtained so far do not appear to be highly sensitive to the conditions applied in this region.

4 COUPLING

The grid system used for the inviscid element of the program was devised to obtain computing efficiency with reasonable simplicity, but it took no special account of the need to calculate boundary layers over the wings and the wake. The basic grid used in the computing space is regular within the rectangular box $|X| \leqslant 1$, $|Y| \leqslant 1$, $|Z| \leqslant 1$ and is divided into L*M*N elements, L, M and N being the number of subdivisions in the X, Y and Z directions respectively. This box corresponds to the infinite domain in the physical space (x, y, z) with the wing plane $z = 0$ transformed to $Z = 0$, and the plane of symmetry $y = 0$ transformed to $Y = 0$. The lines $x = g_1(y)$ and $y = g_2(y)$, as shown in Fig 1 and defined in the plane $z = 0$, coincide with the leading and trailing edges respectively of the wing, except within the body and near and outboard of the tip where they are curved to become parallel with the y-axis. The lines $x = g_1(y)$ and $x = g_2(y)$ become lines $X = \text{const.}$ in the computing space. Ahead of the leading edge and behind the trailing edge, the lines $X = \text{const.}$ become progressively less 'swept' as $x \to \pm\infty$.

The main boundary-layer program requires a grid of surface points which can be transformed into a rectangular grid, with the trailing edge a coordinate line, and with the starting values for the boundary-layer parameters (θ_{11}, H_{11} and β) prescribed on the upstream edge and for any side along which the flow is directed into the computational region. As mentioned above, the starting values at the upstream edge are obtained by making 'yawed wing' assumptions. For most of the remaining region over which it is necessary to compute the boundary layers and the wake the grids used in the two methods are fully compatible, but near the tip of the wing some interpolation of the pressure distribution may be necessary to form a suitable grid. The results from the boundary-layer method will then need to be reinterpolated to obtain the modified boundary conditions for the inviscid flow element of the program.

In coupling the methods together difficulties exist at the edges of the region over which the boundary layers and wake are to be computed, because no attempt is made to calculate the viscous layers outside the region covered by the wing and wake (*ie* for wing; $y_{body} < y < y_{semi\text{-}span}$). The boundary conditions at the sides of the region are not readily available, since the flow in the wing/body junction is difficult to model; while the conditions near the tip of the wing in the inviscid flow method may lead to a physically unrealistic solution which could cause the boundary-layer method to break down artificially. In consequence, at the present time the following conditions are applied:

(a) at the wing/body junction

$$\frac{\partial \theta_{11}}{\partial y} = \frac{\partial \bar{H}}{\partial y} = \frac{\partial \delta^*}{\partial y} = \frac{\partial C_E}{\partial y} = 0 \ ;$$

$\frac{\partial \beta}{\partial y}$ is taken as antisymmetric about the junction. This condition is strictly only correct for a junction where the main stream flow is along $y = y_{body}$;

(b) At the 'tip' (*ie* last station on the span),

$$\frac{\partial \theta_{11}}{\partial Y} \ , \ \frac{\partial \bar{H}}{\partial Y} \ , \ \frac{\partial \delta^*}{\partial Y} \ , \ \frac{\partial \beta}{\partial Y} \ , \ \frac{\partial C_E}{\partial Y}$$

are all obtained using the backward difference equation so that the derivatives are obtained from quantities defined within the computational region. Here Y is defined in the transformed computing space.

In coupling the inviscid element to the boundary-layer method the input needed by the boundary-layer element is the velocity distribution over the surface. In using the TSP method the main output is the pressure coefficient which is obtained from the perturbation velocities using only an approximate formula (Eq.(10)), and so the direction of the velocity vector is not known. In developing the TSP method it is the pressure coefficient which has been compared with more exact methods and consequently the magnitude of the velocity vector is well established, but its direction has not been specially considered. In the present method the direction of the velocity vector is nevertheless taken directly from the TSP solution, while its magnitude is deduced from the pressure coefficient by means of Bernoulli's equation. The required velocity gradients are then derived by bicubic spline fits to the velocity vectors.

In solving the boundary-layer equations Smith relies upon difference equations to obtain the derivatives in the Y direction, using backward, forward, or central differences depending upon the flow directions within the boundary layer. It was found that this method did not work well where the grid spacing was sparse or where the spanwise derivatives were changing rapidly. In this work it is not realistic to increase the number of grid points used in the boundary-layer calculation, and so increase the required storage and the time taken to compute the boundary-layer characteristics. Instead a modified definition is used for determining the derivatives,

$$\left(\frac{\partial \theta_{11}}{\partial Y}\right)_{I,J} \ , \ \left(\frac{\partial \bar{H}}{\partial Y}\right)_{I,J} \ , \ \left(\frac{\partial \beta}{\partial Y}\right)_{I,J} \quad \text{and} \quad \left(\frac{\partial C_E}{\partial Y}\right)_{I,J}$$

which is of the form

$$\left(\frac{\partial \theta_{11}}{\partial Y}\right)_{I,J} = \frac{(1-k)(\theta_{11})_{I,J+1} + 2k(\theta_{11})_{I,J} - (1+k)(\theta_{11})_{I,J-1}}{2\Delta Y} \qquad (19)$$

(where $k = \sin(\alpha + 0.5\beta)/\sin\lambda$ and λ is the angle between grid lines in physical space), so that the derivatives change smoothly in the spanwise direction. If $k = 0$, the equation is the same as for a central difference and $k = 1$ and $k = -1$ are the same as the backward and forward difference schemes respectively, as used by Smith. As k is varied it is equivalent to determining the derivative at a point $I, J + \frac{1}{2}k$ instead of the point I, J by the central difference scheme.

When using a boundary-layer method in an iterative scheme, such as the one described here, it is essential that the boundary-layer calculation does not fail when computing the boundary layer or wake, even for some rather unrealistic pressure distribution which may occur during an intermediate stage in the iterative calculation. In the boundary layer and wake calculation arbitrary limits have been set to avoid this and in addition increments to the boundary-layer parameters are reduced below the changes required by the method if $\bar{H}$ exceeds 3.0. The absolute limit set on $\bar{H}$ is at present 3.5. The values for the limits on $\bar{H}$ are well above the value at which boundary-layer

separation would normally be expected, so if either of these values are reached in the converged solution then significant boundary-layer separation would be expected and the solutions would be unlikely to compare well with measured parameters.

The solution of the boundary-layer equations is, as mentioned before, obtained numerically by a simple explicit finite difference method with the forward step increment in the positive X direction, thus requiring the flow external to the boundary layer to be in the positive X direction. In addition a limit has been placed on the maximum twist within the boundary layer which is permitted, thus making sure that the surface flow is also in the positive X direction, *i.e*

$$\lambda - 180 - \alpha < \beta < \lambda - \alpha$$

where λ is the angle between the grid lines in the physical space and α is the direction of the flow at the edge of the boundary layer with respect to the y-axis.

Another aid to convergence, which appears to work well, is to repeat the boundary-layer and wake calculations, if $\bar{H} = 3.5$ is reached on the wing, with the Reynolds number for the calculation increased to 1.5 times the Reynolds number for the previous attempt. This is done automatically in the program but a limit is set at present of 4.0 times the required Reynolds number. In this way unrealistically large changes to the boundary-layer parameters can usually be avoided in obtaining a converged result at the required Reynolds number.

The main coupling from the boundary-layer calculations back to the inviscid method involves a knowledge of the normal velocity imparted to the flow outside the boundary layer by the presence of the boundary layers. The change required to the boundary conditions is to apply a non-zero normal velocity (w) at the surface (or on the dividing stream surface in the wake) given by

$$w = \frac{1}{r\rho_e}\frac{\partial}{\partial s}(r\rho_e u_e \delta^*) = \frac{1}{r\rho_e}\frac{\partial}{\partial s}(r\rho_e u_e \delta_1) + \frac{u_e}{\rho_e}\frac{\partial}{\partial n}(\rho_e \delta_2) \quad . \tag{20}$$

δ^* is the displacement thickness, which is not usually identical to δ_1 for three-dimensional flow as pointed out by Lighthill[17].

For the work on aerofoils it was found inadequate just to modify the boundary conditions as suggested; it was necessary to apply some under-relaxation to the coupling in order to obtain a scheme which would converge. The degree of under-relaxation required depends on the example considered. In the work on three-dimensional wings we take

$$\gamma(x,y) = \gamma_{old}(x,y) + \omega\{w - \gamma_{old}(x,y)\} \tag{21}$$

where $\gamma(x,y)$ is the change required to the boundary conditions in Eq.(5), γ_{old} is the value of γ used for the previous iteration for the viscous layers and ω is a relaxation factor. γ_{old} is initially set to zero. In the wake

$$\Delta\phi_z(x,y) = \Delta\phi_{z,old}(x,y) + \omega\{w_u + w_\ell - \Delta\phi_{z,old}(x,y)\} \tag{22}$$

where $\Delta\phi_z(x,y)$ is the change in ϕ_z required in the wake according to Eq.(7). w_u and w_ℓ are the values w from Eq.(20) for the wake from the upper (u) and lower (ℓ) surfaces. The relaxation factor ω is usually taken as 0.1 or 0.2 but examples have been found where successful results can be obtained with ω as high as 0.5. When convergence is obtained

$$\gamma(x,y) = w$$

and

$$\Delta\phi_z(x,y) = w_u + w_\ell \tag{23}$$

which is the required result to within the approximations used in the TSP method. For the results given in this paper the corrections to Γ in Eq.(8) and the correction to C_p in Eq.(10), have been neglected.

The overall viscous-inviscid interaction scheme described here is given in diagrammatic form in Fig 2. For a calculation without corrections for viscous or aeroelastic effects the procedure is exactly as given by Albone *et al* and may be summarized as follows:

(i) the geometry of the wing/body combination and the form of the coordinate transformations are specified and the appropriate boundary conditions are derived. These transformations are of shearing and stretching types which map the infinite physical shape into a finite computing space. They are chosen so that a uniform mesh in the computing space provides a low mesh density in the far-field of physical space and especially high mesh densities near the leading edge of the wing, the wing/body junction and the wing tip;

(ii) finite difference approximations of the Murman-Cole type are substituted for the derivatives in the transformed equations and boundary conditions, thus replacing the differential equations by algebraic equations;

(iii) the resulting nonlinear system of algebraic equations is solved by successive line relaxation together with a scheme for accelerating convergence.

The calculation proceeds round the 'INVISCID LOOP' until the required number of iterations have been completed (unless convergence or divergence is recorded). If the calculation is complete or convergence has been obtained, then the pressure distribution is calculated, and the flowfield potentials and boundary conditions are stored for subsequent calculations, as a continuation run.

For aeroelastic or viscous corrections to the calculations the boundary conditions are modified periodically, but otherwise the calculation proceeds in the same way as for inviscid flow. Although it is possible to include aeroelastic effects in the Mk 4 TSP method this facility has not been used for the results presented. When a correction is applied for viscous effects the inviscid calculation is interrupted every M iterations (usually M = 10) in order to calculate the boundary layers as described in sections 3.1 and 3.2. The calculation then proceeds round the 'VISCOUS LOOP', and as mentioned previously, the changes to the boundary conditions are made using under-relaxation (Eqs.(21) and (22)).

Convergence of the overall scheme is judged on the changes in pressure distribution and lift that occurs over the wing and the maximum difference between $\gamma(x,y)$ and w in Eq.(21) which is extended into the wake for this purpose. Separate values are recorded for the upper and lower surfaces.

5 CONVERGENCE AND RUN TIMES

The normal method adopted for running the program, where viscous corrections are applied, has been to calculate 100 'coarse' grid iterations of the inviscid element of the program, and then a further 200 'coarse' grid iterations with intersperced boundary-layer calculations, changing the boundary conditions every ten iterations of the inviscid method. After completion of the coarse grid calculations a minimum of 300 'fine' grid iterations will be needed, again changing the boundary conditions every ten iterations. In addition, at least 200 additional 'fine' grid iterations are needed after 'satisfactory' boundary-layer calculations have been performed. (Satisfactory boundary-layer calculations are those where $\bar{H}$, β etc have not reached the specified limits.)

An example of the convergence of the method is given in Fig 3. For this wing/body combination the inviscid calculation converged smoothly and the lift decreased gradually after changing to the fine grid calculation. After about 300 iterations the lift was within 1% of the value calculated for about 1000 iterations. For the viscous calculation the boundary-layer method reached limits of $\bar{H}$ and β at points on the wing during the first 200 iterations so at least a total of 400 fine grid iterations was necessary. At this stage it appears that the lift is within about 1% of a converged result.

By using a method where corrections for the boundary layers and wake are made in the way suggested in this paper, it is possible to obtain a solution in a total computing time which is usually less than twice the time taken for the equivalent inviscid-flow calculation. The computing time for a calculation depends on several factors, such as the number of grid points on the wing, the total mesh size, and the nearness of the boundary layers to failure through possible boundary-layer separation, so it is difficult to be more precise. If a correction for viscous effects is made every ten iterations of the inviscid flow calculation, then the additional time required to calculate the boundary layers and wake is between 20% and 35% of the time taken. The lower figure is for 17 spanwise stations on the wing and the upper value for 26. The comparable times for aerofoils were broadly similar although the total time to obtain a solution as a percentage of the time for the inviscid calculation is slightly less. These results are generally what might be expected as both the inviscid and boundary-layer methods are similar to their two-dimensional counterparts, and the spanwise derivatives in the three-dimensional boundary-layer method are obtained by finite differences. The times quoted for the boundary-layer calculations include all the additional calculations required in preparing input data for them. Only about 33% of the time is taken up in actually calculating the boundary-layer integral parameters from the boundary-layer equations.

6 METHOD EVALUATION

The examples used in the evaluation cover two classes of configuration, the moderate to high aspect ratio transport type and the low aspect ratio combat type of aircraft.

6.1 Wing/body (1)

In the first example, use is made of a wing/body combination designed by British Aerospace in the early 1970s. The wing is mounted on a circular body in a low position, with a fillet to fair the wing to the body over the rear part of the wing. The configuration, W/B(1), has a planform as shown in Fig 4 with a trailing-edge crank, leading edge sweep of about 28 degrees, an aspect ratio of 7.7 and a taper ratio of 0.23. In the calculations which are presented no account will be taken of the fillet.

In calculating the pressure distribution the grid used has 60 points in the X direction with 38 points on each surface of the wing and 40 points in the spanwise direction of which 17 were on the wing. The spacing of points in the region of the trailing edge are rather sparse with intervals of about 4% chord in the X direction, the trailing edge being approximately between grid points. Ideally a finer grid would be desirable to simulate the rapid changes in the boundary layers in the region of the trailing edge. There is also some rounding of the pressure distribution in the region of the shock wave (see Fig 6), which is similar to that found for calculations on aerofoils, but again this is likely to be influenced by grid spacing.

Results obtained using the method described are given in Figs 5 to 10, but as mentioned previously no account is taken of the pressure changes due to the curvature of the viscous layers. In all other respects the 'viscous' results are obtained with the full method unless otherwise stated. In Fig 5 the local lift coefficient ($C_{L_{(local)}}$) is given across the span of the wing as a function of gross semi-span (η_{gross}) for three different calculations. One 'viscous' calculation is given together with 'inviscid' calculations at the same wing lift, and at the same incidence. For this condition ($M_\infty = 0.78$, $\alpha = 1.11$ degrees) the spanwise lift distribution is modified only slightly if an inviscid calculation is made at the same lift, but the other calculated result suggests that viscous effects account for a loss in lift of about 11% for this condition even at the moderately high Reynolds numbers chosen for these calculations. Previous work on aerofoils[21] suggest that curvature effects might reduce the lift by a further 2 to 3%, but with a wing of finite aspect ratio the magnitude of the curvature effects to be applied near the tip has not yet been studied in any detail. From the results of the spanwise lift distribution it might be thought that it is adequate to use inviscid calculations at the same lift coefficient since the spanwise lift distributions are very similar; but as shown in Fig 6, the influence of viscous effects is to reduce the rear loading, and to compensate for this appreciable changes are required in the pressure distribution over the forward part of the upper surface. With these discrepancies in shock position and aft pressure gradient it would be impossible to judge a design adequately from an inviscid calculation, and in particular any judgement which could be made on the separation boundaries would be quite misleading. It appears that the use of inviscid flow calculations would lead to very conservative designs as the effect of the viscous correction has been to reduce the pressure gradient significantly over both the upper and lower surfaces of the wing.

Fig 7 compares the spanwise lift distribution for experimental results with three calculations all for the same conditions, but at a lower incidence than for the results in Fig 5. The experimental results were obtained in tests on a half model in the RAE 8 ft × 8 ft wind tunnel at a Mach number of 0.78 and Reynolds number of 12×10^6 with boundary-layer transition fixed at 5% chord. They suggest that the method (*ie* the 'viscous' calculation) gives an exceptionally good representation of the spanwise lift distribution at a given lift coefficient, but that the overall lift at a given geometric incidence is overestimated (when wake thickness effects are included). The reason for this is not fully understood; part of it is accounted for by the neglect of curvature effects as already mentioned, but in addition secondary influences (such as the effect of curvature on turbulence structure[12] and the revised $\bar{H}$ *vs* H_1 relationship suggested by East *et al*[18]) would tend to reduce the calculated lift and so improve agreement at a given incidence. In the calculations for this wing no account has been taken of the small aeroelastic twist; this would tend to reduce the local incidence near the tip. Near the root of the wing, the inclusion of the effect of the fillet would also be likely to reduce the estimated lift slightly judging by the results for W/B(3) given by Boone[20]. The overall method also relies heavily on the accuracy of the inviscid element, which is limited by the use of the TSP equations using a non-conservative scheme at the shock waves. Published results for aerofoils suggest that the method is surprisingly accurate[11] but very few comparisons have so far been published between full potential methods and the RAE TSP method for wings or wing/body configurations.

The change in lift produced if the effect of the finite thickness of the wake is neglected (see Fig 7) is slightly larger than expected, although similar in form to the results published previously for aerofoils at Reynolds numbers about half the value used for the present calculations. Fig 8 gives details of the calculated pressure distributions for the three spanwise stations marked on Fig 4; including the effect of wake thickness reduces the pressure coefficient over most of the upper surface, increases the rear loading by a significant amount and also reduces the pressure level near the trailing edge. Very little effect is felt on the lower surface.

Fig 9 gives details of comparisons between the full version of the method and experimental results at the same incidence ($\alpha_W = 0.29$ degrees) and the same spanwise stations as used in the previous figure. The results confirm the need to make the comparisons at a given lift coefficient rather than at the same incidence, but otherwise the results suggest quite good agreement. It is interesting to note that the trailing-

edge pressure and the level of rear loading are reasonably well predicted, especially in the light of the small additional loss of rear loading which will occur if curvature effects are included. Fig 10 gives a further comparison of pressure distributions for a higher incidence where the shock waves are stronger especially on the outboard part of the wing. The calculations were made at 0.85 degrees, which is below the geometric incidence (1.11 degrees) set in the experimental tests, but not low enough to match the overall lift coefficient. The comparisons show that the same conclusions are valid as for the results at the lower incidence, but over the rear of the outboard part of the wing the measured pressure level on the lower surface is very slightly higher than the predicted values. This may be caused by the finite body correction which is necessary in calculations, such as these, where the grid does not adequately represent the nose and tail of the body, being slightly overestimated over the outboard part of the wing. The same effect is present to a lesser extent at the lower incidence.

6.2 Wing/body (2)

In the second example presented (W/B(2)), the wing is mounted on a square body with circular corners, in a high position, as occurs for some combat aircraft. The wing has a planform with a rounded tip, as shown in Fig 11, a leading-edge sweep of 40 degrees, a taper ratio of 0.25, and aspect ratio of 4.0. This is an interesting example because in the tests made in the ARA 9 ft × 8 ft transonic wind tunnel, boundary-layer transition was fixed well aft of the leading edge on the upper surface over the outer part of the span and at a forward position on the lower surface; as a result the thickness of the boundary layers on the upper and lower surfaces near the trailing edge are similar over the outer part of the span. For this example the boundary layers are well away from incipient separation. The tests were made at a Reynolds number of 3.7×10^6 based on a mean chord and transition fixed as indicated in the table, with a linear variation in chordwise position between the given points.

Table 1
Transition positions on W/B(2)

Upper surface		Lower surface	
η_{gross}	ξ	η_{gross}	ξ
body side	0.05	body side	0.05
0.4	0.05	1.00	0.05
0.74	0.35		
0.89	0.30		
1.00	0.30		

With the above arrangement for transition fixing the calculations suggest that for this wing, only quite small viscous effects occur (Fig 12), the main change being in the rear loading with almost no effect of viscosity over the front half of the wing. This conclusion allows the experimental results to be used in effect as a check on the RAE TSP method for inviscid flow over the wing. Some results (using the 'viscous' version) are given in Fig 13. It appears that the method gives a fair representation of the form of supercritical flow development, but that the rear shock wave appears to be too far aft over the inner part of the wing; in addition, the rapid recompression near 20% chord over the inboard part of the wing (which may be a highly swept shock wave) is not well represented. For this wing there is also evidence that the pressure increase through the shock wave is insufficient in the theory, a feature noticed previously for two-dimensional flow using the TSP method. Comparisons over the rear of this wing suggest that the trailing-edge pressure is not so well represented, but the rear loading is adequately predicted away from regions influenced by the incorrect shock location.

The inability to estimate the trailing-edge pressure for this example is partly caused by not including a contribution for the influence of a blunt base; the wing has a blunt base of about 0.5% of $\bar{c}$. An example of the errors likely to occur if the effect of the blunt base is not included is given in Fig 14; the experimental results are from measurements made on an aerofoil with a blunt base thickness of 1.1% of $\bar{c}$. For this example boundary-layer and wake measurements were made in the region of the trailing edge of the aerofoil at a Reynolds number of 5.4×10^6 and with forward transition and modelled by changing the normal velocity so that a more correct displacement effect is achieved. The results (obtained by the VGK method[5]) suggest that a change in pressure coefficient of the order of 0.1 occurs when modelling a blunt base of about 1% in thickness; but the lift coefficient was also increased by about 10%, with the suction level increased over most of the upper surface of the aerofoil. This evidence suggests that the inclusion of blunt base effects in the current method would be worthwhile and probably improve the predicted trailing-edge pressure coefficient for W/B(2), except over the inner part of the wing where the results are already good. The small increase to be expected in the suction over the upper surface of the wing would tend to increase the strength of the rear shock wave and therefore make the agreement worse in this respect. It is possible to include blunt base effects in the current method by modifying $\Delta\phi_z$ in Eq.(7); this technique has already been successfully included by the author in the viscous TSP method for aerofoils.

In the development of the inviscid element of the method, the aim has been to match with the two-dimensional form of solution by applying standard sweep relationships for an infinite swept wing. It is therefore for a low aspect ratio wing such as W/B(2) that the results are likely to be least reliable. Thus in order to obtain more reliable results for wings with lower aspect ratios it appears to be necessary to link the boundary-layer element of a method such as the one described here to one of the full potential methods that are now becoming available, provided that they can simulate the complicated body geometries used with combat wings. Alternatively, further work would be necessary to improve the inviscid flow part of this method by making comparisons with the full potential methods for low aspect ratio wings and the simpler bodies which they can represent.

Haines[19] has presented a result for W/B(2) using the ARA full potential (inviscid) method but representing the body by a circular cylinder, which indicates that the shock waves will be better represented by using a full potential method. It is not clear if this is due to the much larger number of chordwise grid stations used over each wing surface (about 80), or to the use of the full potential equation and boundary conditions.

6.3 Wing/body (3)

A further example with a wing of high aspect ratio, designated W/B(3), has been chosen because it has a complicated spanwise variation of the flow. It was designed at ARA in the early 1970s and proved to have an unsatisfactory inner wing design, thus showing up inadequacies in the methods being developed at that time[19]. The wing has a planform as shown in Fig 15 with a cranked leading and trailing edge. The leading-edge sweep inboard of the crank is 40 degrees and 34.4 degrees outboard, the taper ratio is 0.22 and the aspect ratio is 9.0. The wing/body combination W/B(3) was tested in the ARA 9 ft × 8 ft transonic wind tunnel at a Reynolds number of 3.7×10^6 with a rear transition band on the upper surface and a forward band on the lower, located as shown in the figure.

At the time the wing was designed only an early version of the RAE TSP method was available, without an adequate way of allowing for the influence of a body or for correcting for viscous effects. Haines[19] gives a result from the early calculations which suggests that the estimated level of surface pressure coefficient over the forward part of the wing on the upper surface in the region of the crank was about 0.2 too high, the shock wave was about 15% chord too far aft and the shock upstream Mach number (M_s) was estimated at 1.19 instead of the 1.30 measured. This was clearly a most unsatisfactory state of affairs. The results shown in Fig 15 give the answers from the latest calculations for the example cited by Haines; the pressure distributions are given for all the stations at which the pressures were measured, since the form of pressure distribution varies considerably over the span. The calculations were made at the same Mach number and incidence as in the experiment, but a small allowance is made for aeroelastic twist, which is taken to be -0.3 degrees at the tip, tapering off to zero by the crank. The wing is mounted in a low position on a body of circular cross section and the junction of the wing to the body is faired in. A correction is included, as mentioned for WB(1), to account for the finite length of the body. Albone[20] has presented a calculation showing the influence of the fairing on the pressure distribution for this wing, using the inviscid element of the present method. His results indicate that the pressure coefficient on the upper surface at the innermost station is increased by about 0.1 and that the shock wave is moved forward by about 6% chord by including the influence of the fairing. The results from the latest method appear to predict the main features of the pressure distribution exceptionally well considering the approximate nature of the method. On the upper surface the method predicts the strength of the shock wave in the region of the crank well, but indicates a more rapid weakening of the shock wave which occurs inboard of the crank; however, good comparisons are obtained for the two stations nearest to the wing root. Outboard of the crank the changing chordwise pressure distributions are well predicted but the magnitude of the pressure rise behind any shock wave tends to be underestimated and the shock waves appear smeared. As mentioned for W/B(2), the combat wing, this feature is a common fault with the non-conservative scheme used in the region of a shock wave. Near the tip of the wing the flow over the upper surface is close to sonic, and appears to contain weak shock waves in the experimental results rather than the predicted smooth recompression. On the lower surface except near the leading edge the pressure distribution is well predicted. The reason for the mismatch in the leading-edge region is not understood, as Haines[19] has quoted an almost identical result, for the lower surface, from the full potential method, where the boundary layer was taken into account using a fixed displacement surface.

6.4 Boundary-layer characteristics

In all these calculations the boundary-layer characteristics are obtained automatically, thus giving the user details which are essential for the design of wings. Provided that the flow is not dominated by conditions at the root or tip of the wing, where the conditions applied in the present method are not fully satisfactory, it should be possible to determine the separation boundary and judge the type of flow breakdown which will occur, in a similar way to what can be done already for aerofoils. In addition the results should also enable the user to obtain some information about the drag of the wing.

The boundary-layer method used has been checked against experimental evidence of a general nature but at the present time very little experimental evidence exists for wings or wing/body combinations in conditions similar to those given here for the comparisons

of pressure distributions, so no results are presented. It is however interesting to compare the calculated results for the three wings; these are presented in Fig 16. Three values are given: $\bar{H}_{0.98}$, $\bar{H}_{max}$ and $\bar{H}_{max_{(lower)}}$. $\bar{H}_{0.98}$ is the value of $\bar{H}$ near the trailing edge on the upper surface (*ie* $\xi = 0.98$),, $\bar{H}_{max}$ is the maximum value of $\bar{H}$, which is reached in the region of a shock wave on the upper surface, and $\bar{H}_{max_{(lower)}}$ is the maximum value of $\bar{H}$ reached at the end of the adverse pressure gradient on the lower surface of the wing. Only values which exceed about 1.6 have been given. For W/B(1), $\alpha_w = 0.85$ degree, the transformed shape factor $\bar{H}$ is always below 1.51 on the lower surface and reaches about 1.99 at 98% chord on the upper surface over the middle of the span, well below the value of $\bar{H}$ usually associated with boundary-layer separation on aerofoils. The twist through the boundary layer (β) is also moderate reaching 17 degrees in the outboard direction in this region. There is some indication that the shock wave on the outer part of the wing is likely to separate the boundary layer at a slightly higher incidence. In the present example $\bar{H}$ has already reached 2.3 with β reaching 10 degrees; both $\bar{H}$ and β fall rapidly behind the shock wave. The magnitude of $\bar{H}$ in the region of a shock wave can be a guide to possible separation but the actual value calculated by a method such as this is likely to depend on the grid spacing.

For W/B(2) boundary-layer transition was fixed at about 30% chord on the outer part of the wing, and the distribution of $\bar{H}$ reflects this, with only moderate values of $\bar{H}$ being predicted for the upper surface of the wing near the trailing edge. The value of $\bar{H}$ reaches a high point of 2.09 in the region where the forward highly swept shock wave meets the rear shock wave. The value of $\bar{H}$ on the lower surface never exceeds 1.65. It was shown in Fig 12 that viscous effects for this wing are quite small and this would be expected from these boundary-layer calculations.

The results for W/B(3) are also presented; they suggest that the shock wave in the region of the crank on the upper surface is close to causing separation of the boundary layer ($\bar{H}_{max} = 2.10$, $\eta_{gross} = 0.39$). Over the outer part of the span the boundary layers are closer to separation near the trailing edge than on the other two wings. A peak value of $\bar{H} = 2.09$ is reached with a twist through the boundary layers of about 30 degrees near the trailing edge ($\xi = 0.98$) at about 60% gross semi-span. On the lower surface the maximum values of $\bar{H}$ are higher than on the other two wings because more rear loading is being carried on the outer part of the span.

7 CONCLUSIONS

It has been shown how the scheme previously developed for two-dimensional aerofoils to account for the effects of the boundary layers and wake can be extended with equal success to the wings of wing/body combinations. There is a suggestion that the transonic small perturbation method is not wholly adequate for low aspect ratio combat type wings, but it still appears to predict satisfactorily the main features of the flow.

The method provides adequate estimates of the pressure near the trailing edge, provided that the effects of the variation in wake thickness are taken into account, but for wings with thick trailing edges the method needs further modification. Further work is also needed to investigate the use of the method for the prediction of drag.

REFERENCES

No.	Author	Title, etc
1	J.H. Preston	The calculation of lift taking account of the boundary layer. ARC R & M No.2725 (1949)
2	R.C. Lock	A review of methods for predicting viscous effects on aerofoils and wings at transonic speeds. Paper No. 1 AGARD FDP Symposium on viscous-inviscid interaction - Colorado Springs - 29 September to 1 October 1980
3	M.G. Hall M.C.P. Firmin	Recent developments in methods for calculating transonic flows over wings. 9th Congress of ICAS, Haifa, Paper 74-18, August 1974
4	M.R. Collyer R.C. Lock	Prediction of viscous effects in steady transonic flow past an aerofoil. *The Aeronautical Quarterly*, Vol.XXX, pp 485-505, August 1979
5	M.R. Collyer R.C. Lock	Improvements to the viscous Garabedian and Korn (VGK) method for calculating transonic flow past an aerofoil. RAE Technical Report 78039 (1978)
6	R.E. Melnik R. Chow H.R. Mead	Theory of viscous transonic flow over aerofoils of high Reynolds number. AIAA Paper 70-680 (1977)

REFERENCES (concluded)

No.	Author	Title etc
7	R.C. Lock	Research in the UK on finite difference methods for computing steady transonic flows. IUTAM Symposium Transonicum II, Göttingen, September 1975
8	G.S. Deiwert H.E. Bailey	Prospects for computing airfoil aerodynamics with Reynolds averaged Navier-Stokes codes. Paper 8, NASA Conference Pub 2045, Langley Research Center, March 1978
9	A.F. Jones M.C.P. Firmin	On the calculation of viscous effects on the supercritical flow over an aerofoil. RAE Technical Report 72233 (1973)
10	C.M. Albone M.G. Hall Gaynor Joyce	Numerical solutions for transonic flows past wing-body combinations. IUTAM Symposium Transonicum II, Göttingen, September 1975
11	R.H. Blockley	A comparison of various numerical methods for calculating supercritical inviscid isentropic flow over two-dimensional aerofoils. S & T Memorandum 4/75, BR 47382 (1975)
12	J.E. Green D.G. Weeks J.W.F. Brooman	Prediction of turbulent boundary layers and wakes in compressible flows by a lag-entrainment method. ARC R & M No.3791 (1973)
13	P.D. Smith	An integral prediction method for three-dimensional compressible turbulent boundary layers. ARC R & M No.3739 (1974)
14	P.D. Smith	Calculation with the three-dimensional lag-entrainment method. Unpublished note (1980)
15	P.D. Smith	A calculation method for the turbulent boundary layer on an infinite yawed wing in compressible, adiabatic flow. RAE Technical Report 72193 (1972)
16	J.C. Cooke	Boundary layers over infinite yawed wings. *The Aeronautical Quarterly*, Vol.XI, p 333 (1960)
17	M.J. Lighthill	On displacement thickness. *Journal of Fluid Mechanics*, 4, pp 383-392 (1958)
18	L.F. East P.D. Smith P.J. Merryman	Prediction of the development of separated turbulent boundary layer by the lag-entrainment method. RAE Technical Report 77046 (1977)
19	A.B. Haines	Recent progress in advanced wing design for civil and military aircraft. Royal Aero. Society Symposium, London, 11 December 1979
20	C.M. Albone	Some examples of the use of the RAE TSP method for calculating flow past configurations consisting of a wing-fuselage upon which a variety of interfering bodies may be mounted. RAE Technical Memorandum Aero 1845 (1980) (Contribution to AGARD report on computational method - to be published)
21	M.R. Collyer	An extension of the method of Garabedian and Korn for the calculation of transonic flow past an aerofoil to include the effects of a boundary layer and wake. RAE Technical Report 77104 (1977)

Copyright ©, Controller HMSO London 1980

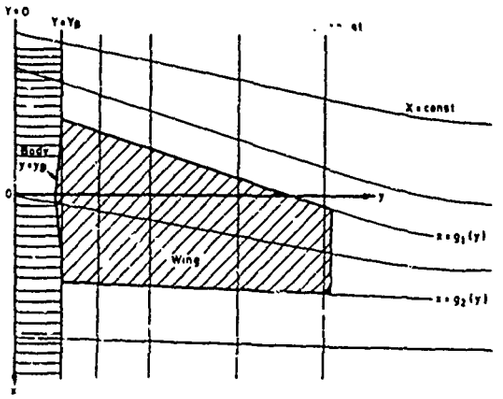


Fig 1 Grid lines X = const, Y = const, in plane Z = 0

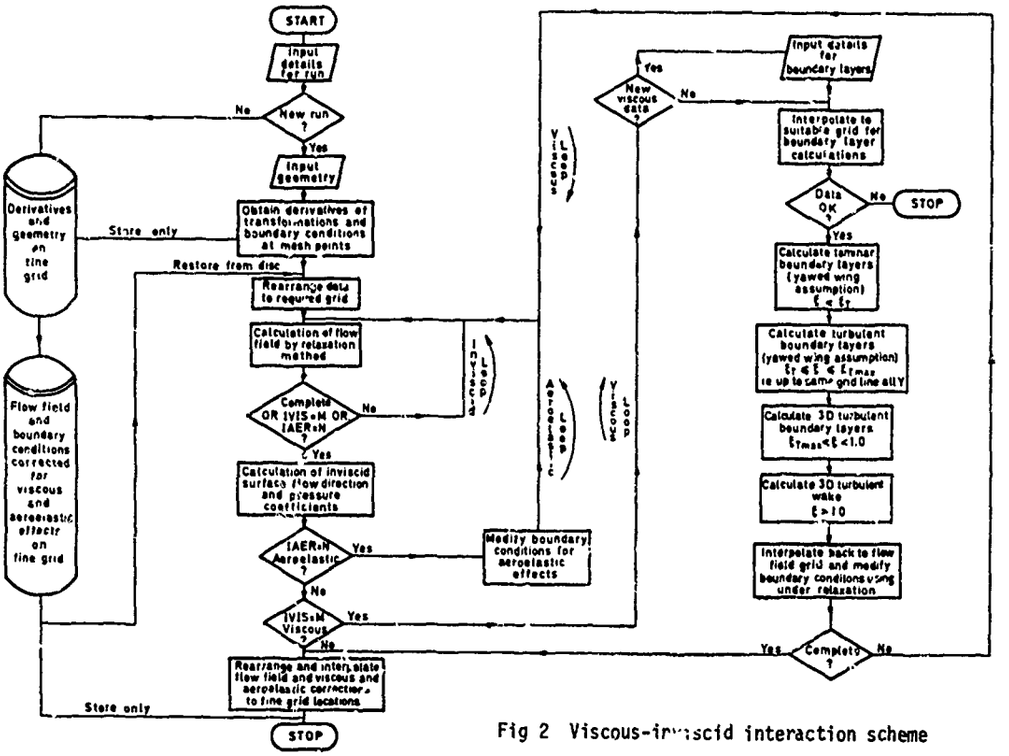


Fig 2 Viscous-inviscid interaction scheme

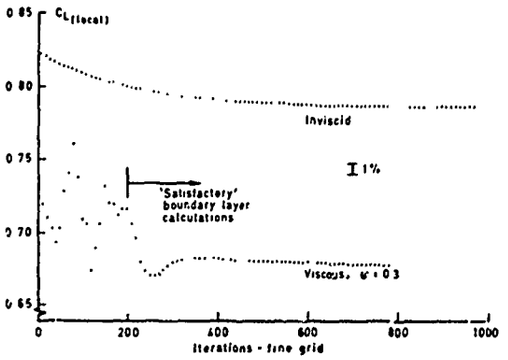


Fig 3 Convergence $M_\infty = 0.78$, $\alpha_W = 0.29$ degree, wing/body (1), $\eta_{gross} = 0.545$

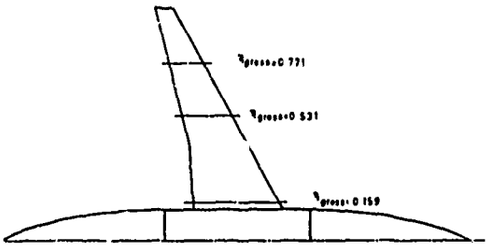


Fig 4 Wing/body (1) as tested in RAE 8ft x 8ft tunnel

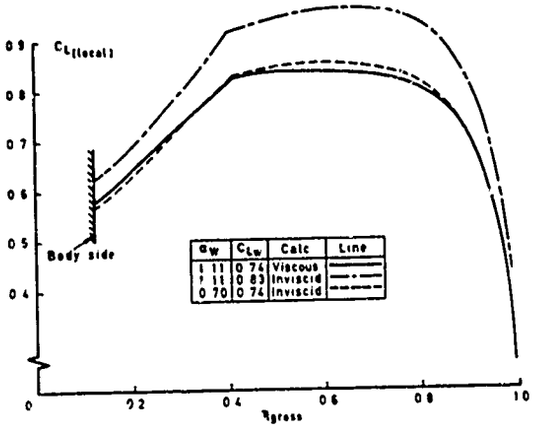


Fig 5 Comparison of distribution of $C_{L(local)}$, $Re_{\bar{c}} = 12 \times 10^6$, wing/body (1), $M_\infty = 0.78$

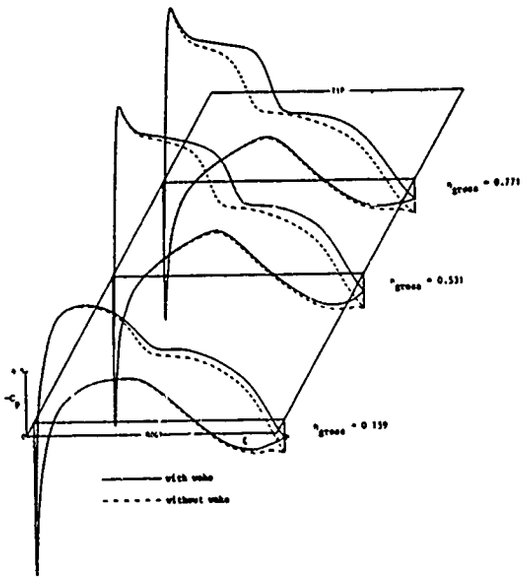


Fig 8 Distribution of pressure coefficient, wing/body (1), $M_\infty = 0.78$, $Re_{\bar{c}} = 12 \times 10^6$, $\alpha_W = 0.29$ degree

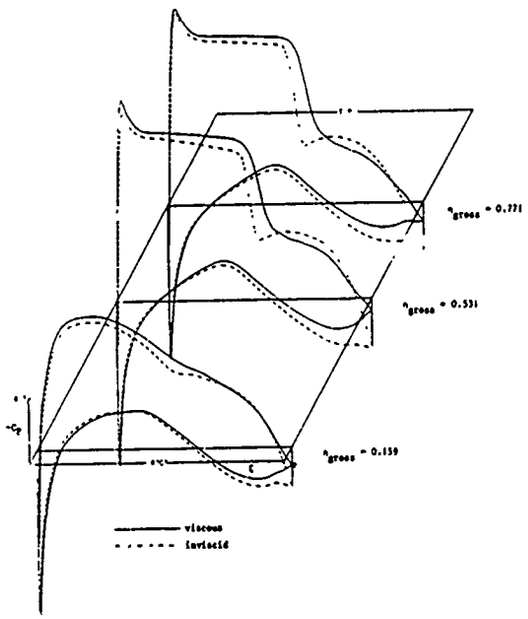


Fig 6 Distribution of pressure coefficient, wing/body (1), $M_\infty = 0.78$, $Re_{\bar{c}} = 12 \times 10^6$, $C_{L_W} = 0.74$

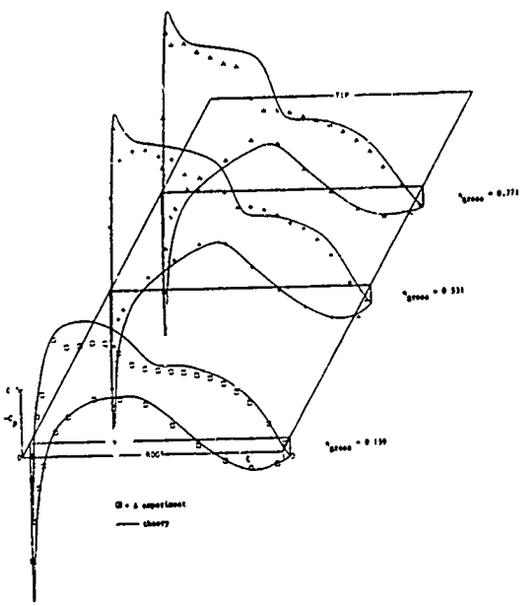


Fig 9 Distribution of pressure coefficient, wing/body (1), $M_\infty = 0.78$, $Re_{\bar{c}} = 12 \times 10^6$, $\alpha_W = 0.29$ degree

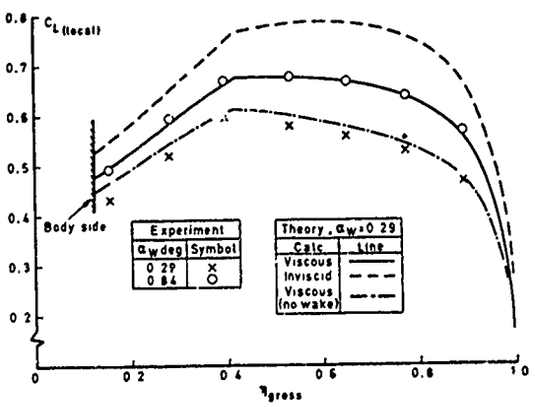


Fig 7 Spanwise distribution of local lift coefficient $M_\infty = 0.78$, $Re_{\bar{c}} = 12 \times$, $\xi_{T_u} = \xi_{T_\ell} = 0.05$, wing/body (1)

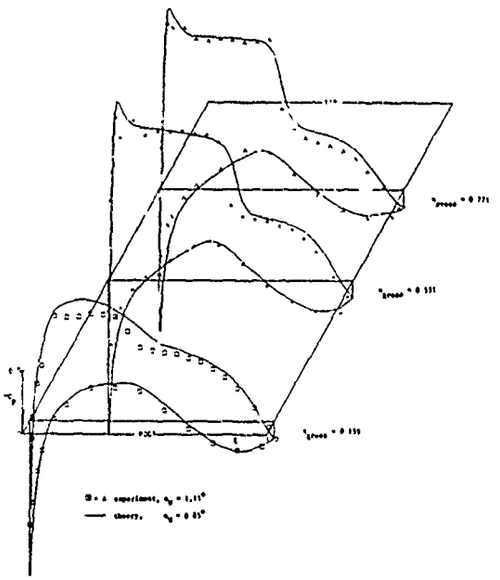


Fig 10 Distribution of pressure coefficient, wing/body (1), $M_\infty = 0.78$, $Re_{\bar{c}} = 12 \times 10^6$

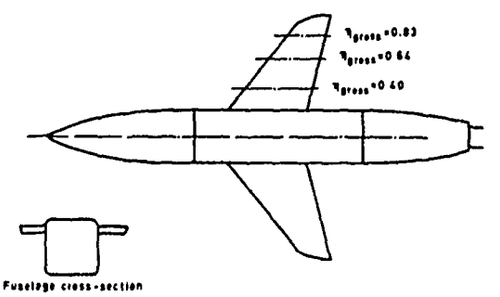


Fig 11 Wing/body (2) as tested in ARA 9ft x 8ft tunnel

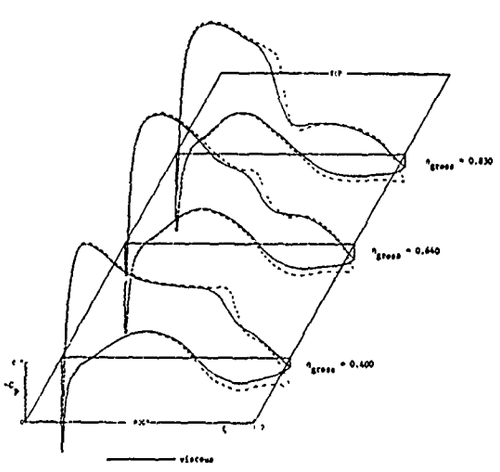


Fig 12 Distribution of pressure coefficient, wing/body (2), $M_\infty = 0.87$, $Re_{\bar{c}} = 3.7 \times 10^6$, $\alpha_W = 2.87$ degrees

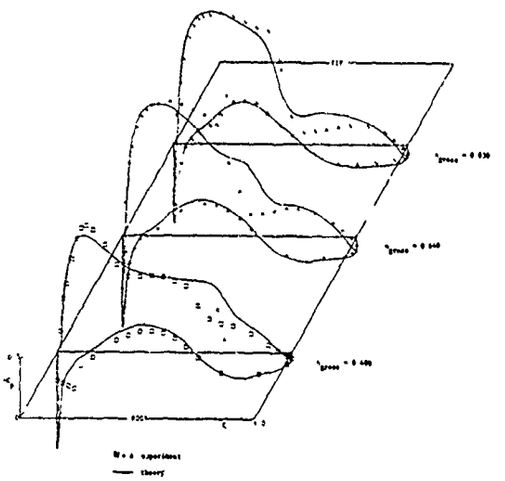


Fig 13 Distribution of pressure coefficient, wing/body (2), $M_\infty = 0.87$, $Re_{\bar{c}} = 3.7 \times 10^6$, $\alpha_W = 2.87$ degrees

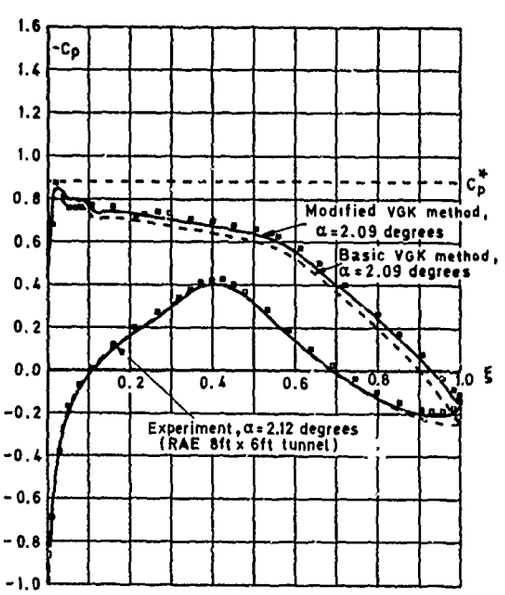


Fig 14 Effect of a blunt base: RAE 2822 (blunt) section, $M_\infty = 0.676$, $Re_{\bar{c}} = 5.4 \times 10^6$, $\xi_T = 0.11$

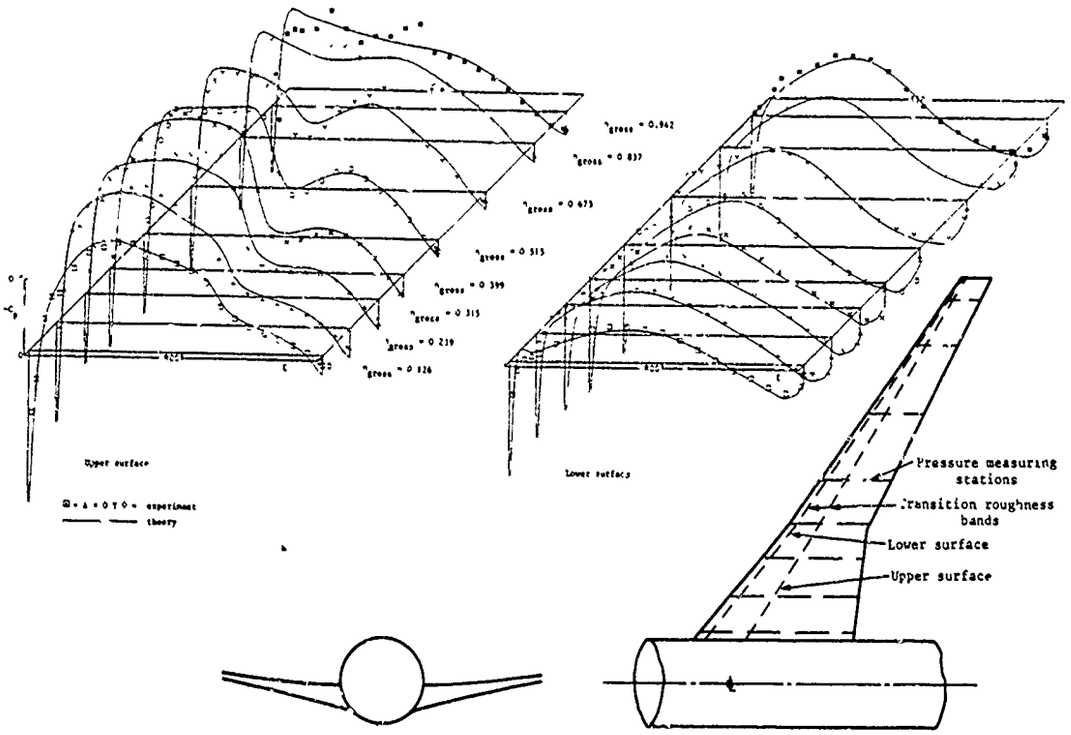


Fig 15 Distribution of pressure coefficient, wing/body (3), $M_\infty = 0.85$, $Re_{\bar{c}} = 3.7 \times 10^6$, $\alpha_W = 0.18$ degree;
Pressure distributions, $\alpha = 0.18$ degree, $Re = 3.7 \times 10^6$.

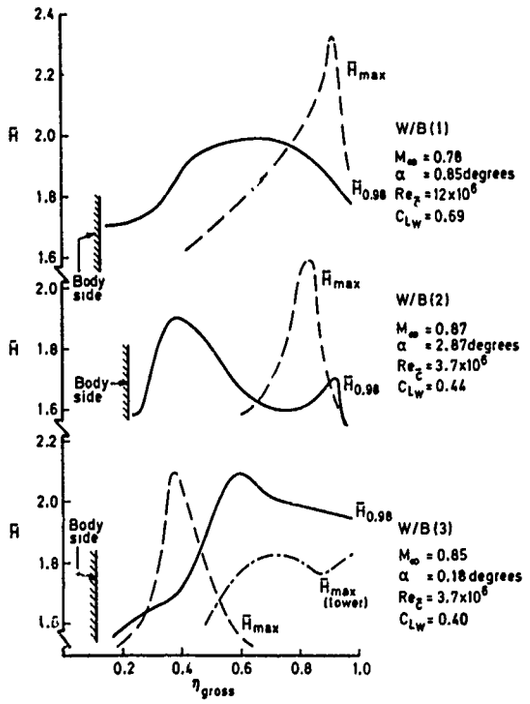


Fig 16 Transformed shape factor ($\bar{H}$) for wing/body combinations, wing/body (1), wing/body (2), and wing/body (3)

PLANAR TRANSONIC AIRFOIL COMPUTATIONS WITH VISCOUS INTERACTIONS

J. C. Wai, Senior Engineer, and
H. Yoshihara, Engineering Manager
Boeing Military Airplane Company
PO Box 3707, M/S 3N-29
Seattle, WA 98124 USA

SUMMARY

Green's lag-entrainment integral boundary layer and wake equations (Ref. 1) are coupled to the transonic small disturbance potential equation (TSFOIL code, Ref. 2) to calculate flows with shock-induced and aft separations. The shock-boundary layer interaction is treated phenomenologically by incorporating a wedge ramp at the base of the shock to achieve an empirically defined post-shock pressure. The remainder of the boundary layer and wake are treated by a coupled scheme used earlier in Ref. 3 where the boundary layer equations are used as boundary conditions along the airfoil and wake for the inviscid flow calculation. The procedure is first illustrated for the case of the NASA Supercritical Airfoil 12 without separation and then to the case of the RAE 2822 with shock-induced separation.

1. INTRODUCTION

The objective is to calculate the planar steady transonic flow over airfoils with shock-induced and aft separations. Such flows are very complex in structure. The primary viscous effects are the shock-boundary layer interaction, which affects the shock strength and location, and the effective camber modification due to the difference in viscous displacements on the two sides of the airfoil. Finally of lesser importance is the displacement effects of the near-wake. These viscous interactions usually have a significant effect on the forces and moment on the airfoil.

Unquestionably the most complex aspect of the viscous interaction is that at the shock. In the present method a simplified phenomenological model is used where a wedge-nosed ramp is inserted at the base of the shock in the inviscid calculations. The wedge ramp simulates the post-shock boundary layer displacement and is fashioned to yield an empirically defined post-shock pressure. The bridging across the shock is then completed by inputting the resulting pressure gradient or the ramp displacement slopes into the boundary layer equations to obtain the post-shock values of the boundary layer variables. Here the boundary layer equations are posed in the appropriate stiff form (See Ref. 4) that tolerates input inaccuracies. The post-shock values are then used as starting conditions for the remainder of the boundary layer and the wake which are calculated by a coupled procedure.

In the sections to follow we shall first give a brief review of the Green's lag-entrainment boundary-layer and wake equations, the phenomenological treatment of the shock-boundary layer interaction, and then describe the coupled procedure. Finally the results for the illustrative examples of the NASA Supercritical Airfoil 12 and the RAE 2822 airfoil are given and compared to experimental results.

2. GREEN'S LAG-ENTRAINMENT INTEGRAL METHOD

Green's equations (Ref. 1) are based on the boundary layer approximations and comprise three first order ordinary differential equations . Two of the equations are

obtained by integrating the continuity and streamwise momentum equations across the layer. The third is derived from the Bradshaw-Ferriss turbulent energy equation (Ref. 5), yielding a rate equation for the entrainment function measuring the rate at which the outer inviscid flow enters the boundary layer.

For separated flows, this integral method has several advantages over partial differential equation methods. First, the partial differential boundary layer equations are usually of the hyperbolic type and must be marched in the downwind direction. With reversed flow present, such a marching would pose a difficult problem. On the other hand, the integral equations can be marched without difficulty into the reversed flow when the problem is properly posed. Finally, significantly less computer time is required to integrate the system of ordinary differential equations, this being an important consideration in our objective.

Physically, one must rationalize the downwind marching into the reversed flow. East, Smith, and Merryman (Ref. 4) suggest that the separated flow assumes a near-equilibrium state whereby the velocity and shear stress profiles of the boundary layer tend to be a streamwise invariance. Existence of this invariance then provides the a priori accounting of the upstream effect of the reversed flow to permit the downstream marching. Here a suitable definition of the equilibrium flow must be furnished such as provided by the "equilibrium locus" in Green's method.

Green's equations are also applicable for the wake when the skin friction coefficient is set equal to zero, and the dissipation length scale is halved. The latter is used to recover the correct asymptotic far-field wake.

Green's equations have the important stiffness properties which are essential to the treatment of separated flows. These properties can be described using the form of Green's equations derived by East, Smith, and Merryman (Ref. 4); that is,

$$\delta_x^* = F_1 + F_2\phi_{xx} \qquad \text{(Direct)} \qquad (1)$$

or alternatively rearranging the terms,

$$\phi_{xx} = F_2^{-1}(\delta_x^* - F_1) \qquad \text{(Indirect)} \qquad (2)$$

where δ^* is the displacement thickness, ϕ is the perturbation potential, F_1 and F_2 are functions of the boundary layer variables, and the subscripts denote differentiations with x being the streamwise coordinate. Equation (1) or (2) is supplemented by additional boundary layer equations.

For unseparated flows East, et al point out that $|F_2\phi_{xx}| \ll |F_1|$, so that the direct equation (1) represents a stiff equation for δ_x^*. That is, the displacement slopes are relatively insensitive to the input pressure gradient ϕ_{xx}.

On the other hand, for fully separated flows $|F_2| \gg |F_1|$ so that the indirect equation (2) represents the desired stiff equation for the pressure gradient. In this case the proper input is the displacement slope.

3. SHOCK-BOUNDARY LAYER INTERACTION

As sketched in Figure 1 the shock-boundary layer interaction is complex. The flow is unsteady as the result of the large scale coherent turbulence on both sides of the shock interacting with the shock. The shock wave weakens as it penetrates into the

boundary layer and terminates at the sonic line. There is further a subsonic region beneath the shock through which the shock pressure-rise is attenuated. As a result, the pressure distribution of the shock as measured conventionally in the wind tunnel assumes a profile due to the time averaging and the subsonic cushion beneath the shock.

It is clear that in the resulting interaction flow, the boundary layer approximations are violated. Here the pressure is not invariant across the layer, and the normal derivatives do not overwhelm the streamwise derivatives.

In the computation of the inviscid flow, the shock waves are captured with a profile generated by truncation error viscosity. It acquires a thickness that is unphysical, and the resulting interaction becomes mesh dependent.

With such difficulties on hand, it is therefore not unreasonable to turn to a simplified phenomenological model for the interaction. For this purpose we shall use the viscous ramp model used previously. (More recently in Refs. 6 and 7) Here a wedge-nosed ramp is placed at the base of the shock to convert the normal shock to an oblique shock in an inviscid flow yielding an empirically defined post-shock pressure. Following Ref. 3, this pressure is taken as $P_2/H = 0.54$ (H being the total pressure). The nose angle of the shock ramp is then given by the oblique shock conditions as a function of M_1, the Mach number upstream of the shock. The shock ramp slopes used in the present calculations are shown in Figure 2.

The use of the post-shock pressure is appropriate since it plays an important role in the positioning of the shock. In general, the functional relation between the pressures across the shock is a local phenomenon which is independent of the airfoil, and most importantly, of the wall interference. Furthermore, reasonable values of the shock pressure-rise and shock positioning can be obtained without an excessive refinement of the mesh near the shock.

To complete the modeling of the interaction, the post-shock values of the boundary layer variables must be determined for the further marching of the boundary layer. This is accomplished by inputting the calculated pressure gradient or the ramp displacement slopes into the appropriate mode of the boundary layer equations. When the post-shock boundary layer is unseparated, the equations in the direct mode are used with the calculated shock pressure rise profile as an approximate input. If the boundary layer becomes separated within the shock profile, the equations are switched to the indirect mode. In the present calculations, for convenience, the direct mode is used until the displacement slope attains the shock wedge angle. Thereafter to the post-shock mesh point (the first subsonic point), the indirect mode is used with the wedge angle inputted for the displacement slope. In this way the proper stiffness form of the boundary layer equations is used enabling the determination of the post-shock boundary layer variables with approximate input data.

4. VISCOUS-INVISCID FLOW COUPLING

The viscous-inviscid flow coupling procedure of Ref. 3 is used to compute the remainder of the boundary layer downstream of the shock, on the lower surface of the airfoil and the wake region. Green's lag-entrainment boundary layer equations are used to form a viscous tangency condition for the inviscid flow. In the small disturbance formulation of the inviscid flow, the boundary condition at the airfoil is imposed in a quasi-planar fashion as

$$\phi_y(x,0) = f_x(x) + \delta^*_x(x) \qquad (3)$$

where $y = f(x)$ defines the airfoil. The viscous tangency boundary condition for the inviscid flow is obtained by inserting (1) into (3); that is,

$$\phi_{xx} = F_2^{-1}(\phi_y - f_x - F_1) \tag{4}$$

Downstream of the trailing edge, the viscous wake generates a displacement afterbody across which a slope discontinuity in the flow occurs. The equivalent condition to Eq. (4) is applied as

$$[\phi_y] = [\delta_x^*] = [F_1 + F_2\phi_{xx}] \tag{5}$$

where the square brackets denote the jump in the bracketed quantity across the wake which has been shrunk to the x-axis. The wake displacement is treated as two separate layers patching onto the boundary layers on the two sides of the airfoil. In addition, the pressure is assumed to be constant across the wake as in the inviscid calculation, that is,

$$[\phi] = \text{constant.} \tag{6}$$

In the present approach, the outer inviscid and the boundary layer flows are integrated simultaneously with the viscous conditions (4), (5) and (6).

5. NUMERICAL FORMULATION

The outer inviscid flow calculation is carried out with transonic TSFOIL code (Ref. 2). This algorithm solves the transonic small disturbance potential equation with an iterative successive line overrelaxation method.

The boundary layer method as described above is coupled to the TSFOIL code. In the viscous calculations, for convenience, it is assumed that upstream of the shock on the upper surface and upstream of the adverse pressure gradient on the lower surface, the boundary layer displacement effects on the inviscid flow are negligible. This permits the coupled treatment of the boundary layer and the inviscid flow to be initiated downstream of the above points with the necessary initial values for the boundary layer furnished by a simple flat-plate type theory.

The shock-boundary layer interaction model described in Section 3 is used to define the shock location and the boundary layer growth across this discontinuity. Downstream of the shock, the viscous tangency condition in Eq. (4) is used. The ϕ_{xx} and ϕ_y are differenced as in the inviscid flow. F_1 and F_2 are initially approximated by using the values from the prior iteration and then upgraded using the boundary layer variables at the new point obtained by the integration of the auxiliary boundary layer equations in the proper mode.

The wake is treated essentially the same as in the inviscid procedure. A jump in ϕ_y as given by Eq. (5) is additionally imposed across the wake slit. This is accomplished by introducing an analytical continuation across the slit, both from above and from below, and relating the potentials on the two sheets by the wake contact jump conditions.

6. RESULTS AND DISCUSSION

The first case calculated is the NASA Supercritical Airfoil 12, at $M = 0.78$, angle of attack 2 degrees, and the chord Reynolds number of 7.7×10^6 (63.5 cm chord).

This case was selected because of its significant viscous effects. Furthermore, this airfoil is an extreme case for the small disturbance code because of the large blunt nose and the pronounced aft camber. In Figure 3, the inviscid and the experimental results (Ref. 8) are compared with the calculated pressure distribution with the viscous-inviscid coupling. The boundary layer is not separated. As discussed in Ref. 8, the experimental data are not corrected for the slotted wind tunnel wall effect. In assessing this test-theory comparison, this effect of the unknown wall interference must be kept in mind. In Figure 4, the resulting boundary layer quantities are plotted. Corresponding experimental results were not measured.

The second case considered is the RAE 2822 airfoil at M = 0.75, angle of attack 3.19 degrees, and the chord Reynolds number of 6.2×10^6 (61 cm chord). In Figure 5, the pressure distributions are compared with the experiment (Ref. 9). Reasonable agreement is obtained in this shock-induced separation case. The boundary layer quantities are compared in Figure 6. The present method overpredicts the displacement thickness, and reattachment of the boundary layer is not achieved.

In both of these examples, the standard TSFOIL mesh is used, which in the region of the shock is 3% chord. The addition of the viscous equations required little additional computing time, amounting to 20% relative to the inviscid flow computation time of approximately 50 seconds CPU time on the CYBER 175 computer.

7. CONCLUDING REMARKS

In the present study the transonic small disturbance potential code (TSFOIL) is coupled directly with Green's lag entrainment boundary layer and wake equations. The boundary layer equations served as a viscous tangency condition at the airfoil and the wake afterbody. With this direct coupling, the inviscid flow and the boundary layer equation are integrated simultaneously, leading to a well-behaved numerical procedure.

The shock-boundary layer interaction is treated phenomenologically with a wedge ramp model attached to the base of the shock. The boundary layer equations are integrated with the correct stiff form to yield the post-shock state. With this procedure, a reasonable shock-boundary layer interaction is achieved.

Comparison has been made with the experiments on the NASA Supercritical 12 airfoil and the RAE 2822 airfoil. The former case involved an unseparated flow field, and the latter has a shock-induced separation. Reasonable agreements with the trend of the viscous effects are predicted, suggesting the present approach to be a viable base upon which to develop a transonic separated flow method. Further refinement of the lag-entrainment integral method is needed to improve the shock-boundary layer modeling.

REFERENCES

1. Green, J., Weeks, D., and Brooman, J., "Prediction of Turbulent Boundary Layers and Wakes in Incompressible Flow by a Lag-Entrainment Method," RAE Reports and Memoranda 3791, 1973

2. Murman, E., Bailey, R., and Johnson, M., "TSFOIL-A Computer Code for Two-Dimensional Transonic Calculations, Including Wind Tunnel Wall Effects and Wave-Drag Evaluation," NASA Report SP 347, 1975.

3. Wai, J. C. and Yoshihara, H., "Viscous Transonic Flow Over Airfoils," Proceedings of the Seventh International Conference on Numerical Methods in Fluid Dynamics, 1980.

4. East, L., Smith, P., and Merryman, P., "Prediction of the Development of Separated Turbulent Boundary Layers by the Lag-Entrainment Method," RAE Report 77046, 1977.

5. Bradshaw, P., and Ferriss, D., "Calculation of Boundary Layer Development Using Turbulent Energy Equations; Compressible Flow on Adiabatic Walls," J. Fluid Mech., Vol 46, 1971.

6. Rizzetta, D. and Yoshihara, H., "Oscillating Supercritical Airfoils in the Transonic Regime with Viscous Interactions," AGARD Specialist Meeting on Boundary Layer Effects on Unsteady Airloads, Sept. 1980.

7. Jou, Wen-Huei and Murman, E. M., "A Phenomenological Model for Displacement Thickness Effects of Transonic Shockwave Boundary Layer Interactions, " AGARD Symposium on Computation of Viscous-Inviscid Interactions, 1980.

8. Harris, C. D., "Aerodynamic Characteristic of an Improved 10% Thick NASA Supercritical Airfoil," NASA TM X-2978.

9. Cook, P. H., McDonald, M. A., and Firmin, M. C. P., "Aerofoil RAE 2822 - Pressure Distributions, and Boundary Layer and Wake Measurements," AGARD - AR - 138.

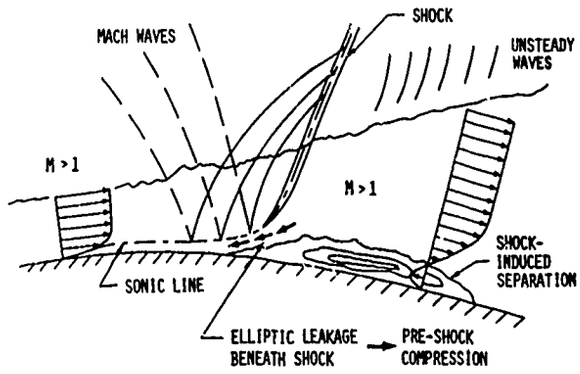
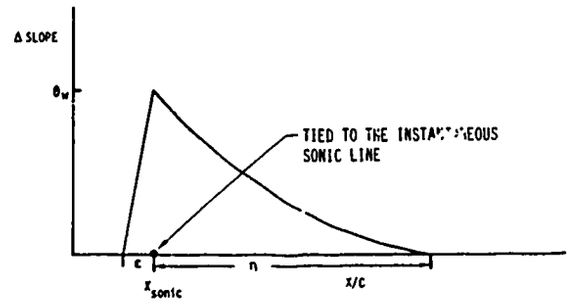


Figure 1. Schematic of Shock-Boundary Layer Interaction



$$\Delta \text{SLOPE} = \begin{cases} \theta_w = 1/2\left[\theta_{max} + \theta_{sonic}\right] \\ \theta_w \dfrac{X + \varepsilon - X_{sonic}}{\varepsilon} & X_{sonic} - \varepsilon \le X \le X_{sonic} \\ \theta_w \left(1 - 2\xi + \xi^2\right) & X_{sonic} \le X \le X_{sonic} + \eta \\ \quad \xi = \dfrac{X - X_{sonic}}{\eta} \\ 0 & X \ge X_{sonic} + \eta \end{cases}$$

IN GENERAL $\varepsilon = 2\%$

$\eta \sim 10$ TO 20%

Figure 2. Viscous Wedge Ramp Model

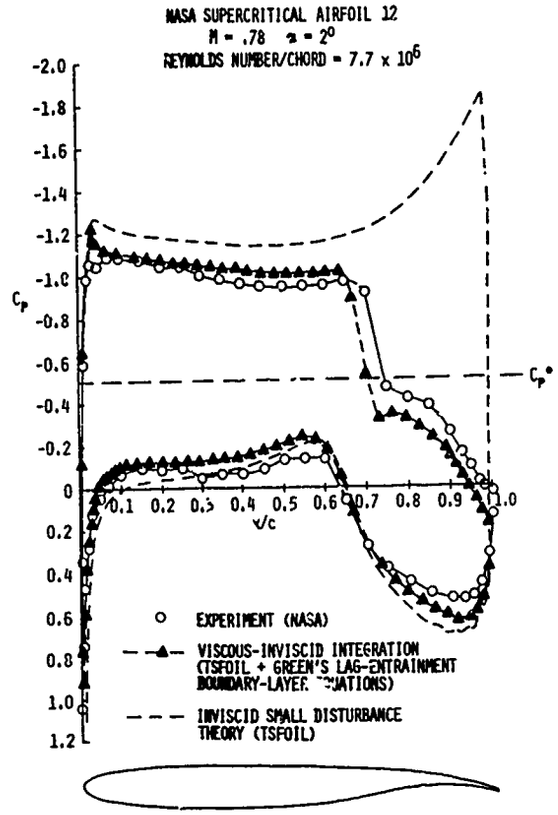


Figure 3. Theory/Experiment Comparison - Pressure Distribution

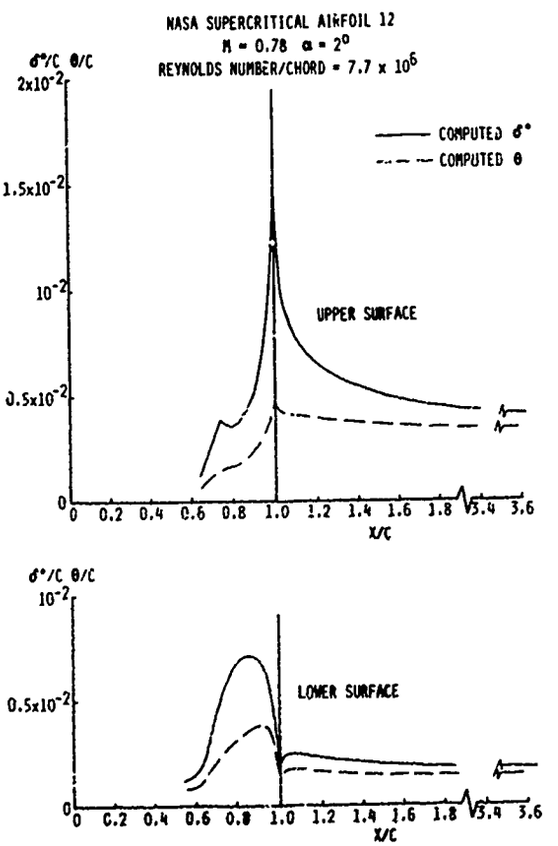


Figure 4. Boundary Layer and Wake Characteristics

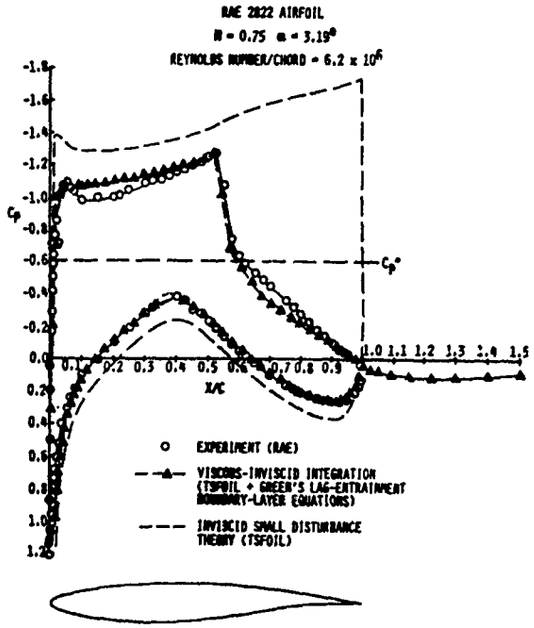


Figure 5. Theory/Experiment Comparison - Pressure Distribution

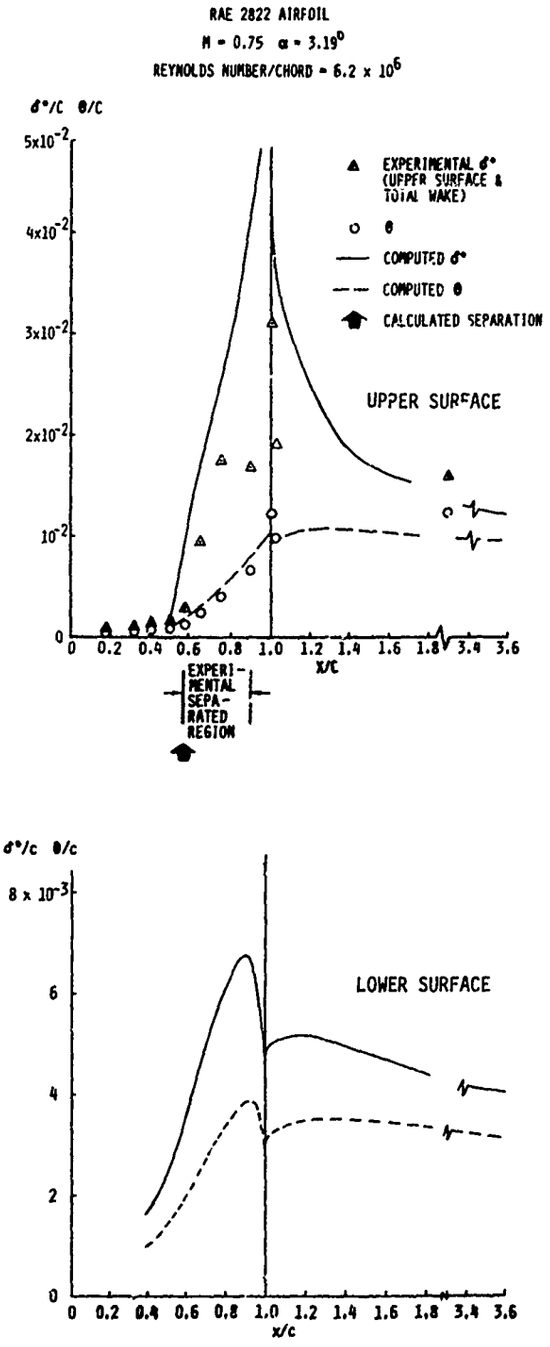


Figure 6. Boundary Layer and Wake Characteristics

TURBULENT INTERACTIONS ON AIRFOILS AT TRANSONIC SPEEDS - RECENT DEVELOPMENTS

by
R.E. Melnik
Research Department
Grumman Aerospace Corporation
Bethpage, New York 11714
U.S.A.

SUMMARY

In this lecture I review recent developments in theoretical concepts for the analysis of viscid-inviscid interations on airfoils at transonic speeds under conditions where the boundary layer is unseparated and is turbulent over most of the airfoil. Included is a discussion of the overall weak interation between the boundary layer, wake and "outer" inviscid flow; and the strong local interaction at shock waves and trailing edges. The paper discusses recent efforts to incorporate important wake displacement and wake curvature effects into an interacting boundary layer formulation. Recent progress in the development of local, large Reynolds number, asymptotic solutions for turbulent shock-wave boundary-layer and trailing edge interaction are described and related to Lighthill's earlier two-layer model of strong interactions. Reasons for the difference between laminar and turbulent strong interaction theories are discussed. Techniques are described for incorporating the local trailing edge solution into an interacting boundary layer formulation which includes a complete treatment of the wake. Theoretical predictions, obtained with this formulation, are compared with wind tunnel data to illustrate the accuracy that can be achieved with an interacting boundary layer formulation when the wake and trailing edge interaction effects are included in the theoretical model.

1. INTRODUCTION

The theoretical prediction of airfoil section characteristics is one of the classical problems in aerodynamic theory. Recent advances in numerical techniques for solving the full nonlinear potential flow equation have led to practical methods for determining the inviscid, supercritical flow over airfoils at transonic speeds. Although this is an important development it is generally recognized that inviscid solutions by themselves do not lead to useful predictions of airfoil section characteristics. I am sure that everyone in this audience is aware of the importance of viscous effects on airfoils and of the need to incorporate them into the theoretical formulation, especially at transonic speeds. At the high Reynolds numbers of practical interest the shear layers are thin and the viscous effect can be attributed to an overall viscid-inviscid interaction between the boundary layer, wake and external inviscid flow. The principal interaction arises from the displacement thickness effect leading to a thickened semi-infinite equivalent body causing significant changes to the surface pressures and forces. The appearance of shock waves in the flow field tends to significantly enhance the viscous effect at transonic speeds. In this regime the boundary layer effect can reduce the lift by as much as 50% and move the shock wave by 20-30% chord even when the Reynolds number is very high ($Re > 10^6$) and the boundary layers are fully attached.

In this paper the terminology "viscid-inviscid interaction" refers to all flow situations in which the boundary layer has a significant influence on the pressure distribution. Weak interactions are defined as interactions for which the viscous effect on pressure is small, or more specifically, is the order of the (nondimensional) displacement thickness, δ^*/c - for laminar flow this is $O(Re^{-1/2})$ while for turbulent flow it is $O(\ln Re)^{-1}$ If the order of magnitude of the pressure disturbance is larger than this, the interaction is classified as a strong viscid-inviscid interaction. The flow over an airfoil (Fig. 1) involves both a weak overall interaction and strong interaction regions at shock waves and at the trailing edge. Transition to turbulence occurs near the leading edge with the result that the important interactions on an airfoil are turbulent in practice. The weak interaction arises both from standard displacement effects and also from the less familiar wake curvature effect. The displacement effect leads to an equivalent thickening of the airfoil and wake that is most pronounced on the upper surface near the trailing edge. The rapid buildup of the upper surface boundary layer is the most important part of the weak interaction. It is equivalent to a significant decambering of the airfoil that acts to reduce the lift. There is also a thinning effect of the shear layer in the initial stages of the wake that contributes significantly to the profile drag of the airfoil through a small, but important, reduction in the pressures near the trailing edge. The wake curvature effect also acts to reduce the lift. It arises from the turning of low momentum fluid along the curved streamlines of the wake and acts much like a jet flap with a negative momentum coefficient.[1] The magnitude of the wake curvature effect is formally the same order as the displacement effect but in practice is usually somewhat smaller.

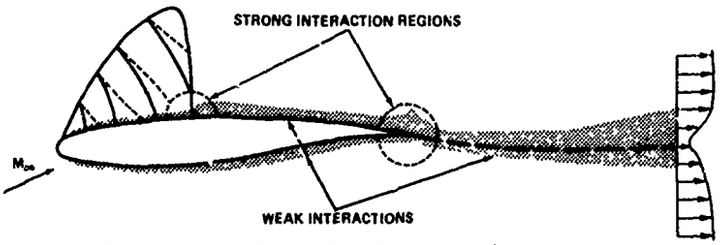


Fig. 1 Viscid/inviscid interactions on airfoils.

The strong interaction between a shock wave and a turbulent boundary layer involves the penetration of the shock wave into the boundary layer. The diffraction of the shock wave by the nonuniform flow in the boundary layer leads to significant normal pressure gradients and to a complete breakdown of the usual boundary layer approximation. The interaction produces both local and global effects. The principal local effect of the interaction is to smear the otherwise discontinuous pressure rise across the shock wave over several boundary layer thicknesses. If this were the only effect of the interaction it would have a small influence on the section characteristics of the airfoil. However, an important global effect arises from the substantial thickening of the boundary layer by the shock wave which significantly increases the thickness of the boundary layer approaching the trailing edge. This greatly increases the decambering effect of the boundary layer leading to much larger losses in lift when shock waves are present.

The flow near the trailing edge also involves a strong interaction problem. The highly curved streamlines in the near wake generate large pressure variations across the boundary layer and wake that are an order of magnitude larger than the pressures induced by standard displacement effects. As in the shock wave boundary layer interaction, these large normal pressure gradients lead to a failure of the standard boundary layer approximations in the trailing edge region. Since the pressure variations across the boundary layer must be accounted for in the "Kutta" condition at the trailing edge they can be expected to have a strong global effect and be important in the determination of airfoil section characteristics.

It is the very rapid buildup of the boundary layer at the upper surface trailing edge as amplified by shock waves, that is most responsible for the very large viscous effects observed at transonic speeds. The boundary layer acts much like a trailing edge flap that opposes the geometric aft camber of the airfoil leading to significant viscous effects on lift. The boundary layer thickening across the shock wave magnifies this effect and induces a much larger loss of lift. The "extra" thickening of the boundary layer across the shock wave acts as an equivalent reduction in Reynolds number at the trailing edge. Conversely, the shock position and strength are strongly influenced by the value of the lift coefficient and hence by the trailing edge flow. It is this coupling between the strong interaction regions at the shock wave and trailing edge that is most responsible for the significant Reynolds number sensitivity and scale effect observed at transonic speeds even when the Reynolds number is large and the boundary layers are fully attached. For further discussions of the physical aspects of viscous effects on airfoils at transonic speeds the reader is referred to the papers by Pearcey, Osborne and Haines[2] and Green[3].

From this discussion it is apparent that to arrive at a completely satisfactory description of viscous flow over airfoils at transonic speeds with a boundary layer type method we must account for:

- Displacement effects on the airfoil
- Displacement effects in the wake
- Wake curvature effects
- Strong interaction at shock waves
- Strong interaction at the trailing edge.

Although complete solutions of the airfoil problem including all these effects have not yet been obtained significant progress has been achieved in each of the areas. Numerical methods for solving the interacting boundary layer equations for transonic flows over airfoils have been developed by a number of groups. These methods are based on the iterative solution of the coupled inviscid and boundary layer equations. The Bauer, Garabedian, Korn, Jameson[4,5] (BGKJ), Collyer, Lock[6,7] (CL), and Melnik, Chow, Mead, Jameson[8-11] (MCMJ) methods are based on numerical solutions of the full potential equation by mixed flow relaxation techniques in the "circle plane". Integral methods are employed for the solution of the boundary layer equations in all three approaches. The BGKJ approach employs a very simple model of the viscous flow that accounts only for displacement thickness effects with the wake modeled as a constant thickness extension of the airfoil. Techniques for taking full account of both wake thickness and wake curvature effects in a circle plane formulation were developed independently in the CL and MCMJ studies. The MCMJ group also developed a rational asymptotic solution for the strong turbulent interaction at a trailing edge when the airfoil is cusped. Simple procedures using the local solution were also presented[10,11] for correcting the interacting boundary layer approach for strong interaction and normal pressure gradient effects at trailing edges of cusped airfoils. It should be stressed that none of these methods properly treat the shock-wave boundary-layer interaction. Although it has not reached the stage where it can be incorporated into a full airfoil solution, there has been significant theoretical progress in the analysis of the strong interaction at shock waves. Recent efforts[12-18] have focused on the use of large Reynolds number asymptotic expansions to develop local solutions for weak shock waves interacting with turbulent boundary layers. These methods have their roots in the important work of Lighthill[19] on upstream influence in boundary layers.

This paper reviews recent developments in the theoretical analysis of viscous effects on airfoils. As is appropriate for this meeting, the concern is exclusively with boundary layer type methods that take advantage of the fact that the Reynolds number is large and the flow is nearly inviscid everywhere except in thin shear layers and strong interaction zones on the airfoil and in the wake. The paper discusses recent developments (mainly over the preceding five years) in interacting boundary layer theory, and in methods for analyzing strong interactions at shock waves and trailing edges. Some early work is also covered in order to provide an historical prospective and to trace the origins of the key ideas. Significant progress has, of course, also been achieved in the development of methods for the direct numerical solution of the full Reynolds equations of turbulent flow. Although these methods hold the promise of offering the most complete and accurate solution for viscous flow over airfoils they have been somewhat limited in practice because of their large computing requirements. Since time does not permit justice to be done to these developments they are not covered in these lectures. Instead I will restrict myself to boundary layer type methods, a subject that I can speak of with some confidence.

The paper is organized as follows. The next section describes recent developments in Interacting Boundary Layer Theory (IBLT). A review of the displacement surface concept and a discussion of new insights into free interactions in turbulent flow, following from recent work of LeBalleur[20-22] is presented. In this section the wake curvature condition is discussed and the main features of recently developed computer codes for calculating the viscous transonic flow over airfoils using IBLT are described. In Section 3 I review developments in analytical theories of shock wave boundary layer interactions in turbulent flow. Attention is focused primarily on interaction with weak normal shock waves at transonic speeds. The progress that has been achieved on this very difficult interaction problem is described starting from Lighthill's landmark 1953 paper[19] down to the recent developments of rational asymptotic theories[12-18]. Then, in Section 4, I describe the asymptotic theory of Melnik and Chow[8,11] for the strong turbulent interaction at cusped trailing edges. Section 5 describes how the local trailing edge solution can be used to correct a standard interacting boundary layer method for strong interaction effects at the trailing edge of a cusped airfoil. Included is a description of the recently developed MCMJ computer code[8-11] which is based on an interacting boundary layer formulation that includes a complete treatment of wake thickness, wake curvature and strong interaction effects at cusped trailing edges. Results are presented that illustrate the importance of the individual viscous effects that appear in the theoretical model. Some comparisons with experimental data are also provided to give an indication of the accuracy that can be achieved. The paper concludes with Section 6 which summarizes the current state-of-the-art and identifies major remaining problem areas offering interesting opportunities for further research.

2. INTERACTING BOUNDARY LAYER THEORY (IBLT)

As discussed in the previous section, interacting boundary layer theory is based on the solution of the coupled inviscid and boundary layer equations with the coupling being through the conventional viscous matching conditions. The solution of these equations by an overall global iteration has been a standard approach to viscid/inviscid interactions on airfoils. The formal basis for IBLT is derived from the large Reynolds number expansion of the full viscous equations. Before proceeding I should clarify some terminology. When referring to the "outer inviscid flow" or "outer inviscid solution" I mean the outer region or solution of a coupled interacting boundary layer approach. Alternatively, reference to the "inviscid solution", without any modifying adjective, will denote a solution of the inviscid equations in the absence of all viscous effects.

For laminar flow the formal asymptotic theory leads to the standard two layer description in terms of an outer inviscid flow and an inner boundary layer with the solution in each region being expanded in powers of $Re^{-1/2}$. This formulation is commonly referred to as "2nd-order boundary-layer theory". It is valid for weak interactions where the inviscid solution provides the proper leading approximation for the surface pressure distribution. It is well known that this simple approach fails in strong interaction problems because of the appearance of nonuniformities at shock waves or in the surface boundary conditions. The premises of IBLT are that the boundary layer approximations remain valid in strong interaction regions and that the failure of 2nd-order boundary-layer theory is caused by the fact that the inviscid solution does not provide the correct leading approximation for the surface pressure distribution. It is then assumed that the proper pressure distributions can be determined and the nonuniformities eliminated by obtaining a self-consistent solution of the coupled inviscid and boundary layer equations. For laminar flow this is known to be true. The more detailed "Triple Deck" theories of Stewartson and Messiter (e.g., Ref 23) provide the formal justification for IBLT in strong interaction problems. Interacting boundary layer theory can be viewed as a composite equation approach which contains all the leading terms of "Triple Deck" theory. Unfortunately, this does not hold true for turbulent flow where IBLT does not provide the correct leading order description of the flow.

The difference between laminar and turbulent strong interactions is related to the structure of the respective boundary layers near the wall. It is well known that the turbulent boundary layer develops a two layer, law of the wall-law of the wake, structure at high Reynolds number. The momentum balance in the wall layer is dominated by the turbulent shear stresses and is largely unaffected by pressure gradients, which are exponentially small in comparison. Consequently, an interacting sublayer like that arising in laminar "Triple Deck" theory does not occur in turbulent interactions. This changed character of turbulent flows near the wall leads to minor technical differences in the solution for noninteracting and weakly interacting boundary layers but to profound differences in the analytic structure of strong interactions. Before preceding with the discussion of IBLT I review some general features of turbulent boundary layers.

2.1 The Turbulent Boundary Layer and the Large Re Limit

It is well known (eg. Ref 24) on both physical and theoretical grounds, that the turbulent boundary layer at high Reynolds numbers develops the two layer structure sketched in Fig. 2. In the outer region the velocity profile is well represented by the small defect form of the law of wake

$$U = U_e - u_* f(y/\delta,\ x/L) \tag{1}$$

where U_e is the boundary layer edge velocity, u_* is the friction velocity, δ is the boundary layer thickness and L is a measure of the running length of the turbulent part of the boundary layer. Near the wall the velocity profile takes on a law of the wall form

$$U = u_* F(y/\delta^+,\ x/L) \tag{2}$$

where δ^+ is the thickness of the wall layer and is related to the friction velocity and viscosity by

$$\delta^+ = \nu/u_* \tag{3}$$

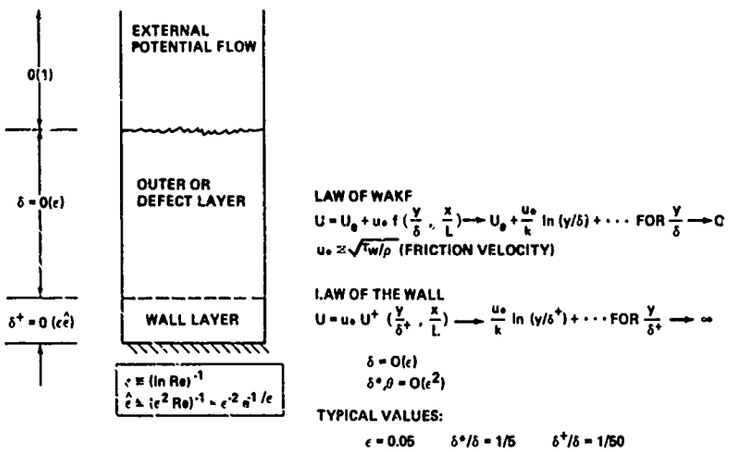


Fig. 2 Two-layer structure of a turbulent boundary layer.

The outer layer is essentially independent of the laminar viscosity, except through its indirect influence on the values of u_* and δ, and the wall layer is independent of the outer parameters U_e, δ. The momentum balance in the wall layer is dominated by the shear stresses with the result that the total shear stress, laminar plus turbulent, is constant across the wall layer.

Matching the inner and outer velocity profile leads to the logarithmic skin friction law and to the estimate

$$\epsilon \equiv u_*/U_e = 0(\ln \mathrm{Re})^{-1} \tag{4}$$

where ϵ can be taken as the basic parameter to characterize the large Reynolds number limit. From the matching of the velocity profiles it is also established that the profile has a logarithmic form in the overlap region defined by $y/\delta \to 0$, $y/\delta^+ \to \infty$, i.e.,

$$U \to u_*[A \ln(y/\delta^+) + B], \qquad 30 \le y/\delta^+ \le 300 \tag{5}$$

with $B \cong 5.0$ and $A \equiv k^{-1} = 2.44$ ($k = 0.41$, von Karman constant). The thicknesses of the main part of the boundary layer and of the wall layer are given by

$$\delta/L = 0(\epsilon) \quad \text{and} \quad \delta^+/L = 0(\epsilon\hat{\epsilon}),$$

where $\hat{\epsilon}$ is a second small parameter defined by

$$\hat{\epsilon} \equiv (\epsilon^2 \mathrm{Re})^{-1} = \epsilon^{-2} e^{-1/\epsilon}. \tag{6}$$

The parameter $\hat{\epsilon}$ is the ratio of the thicknesses of the inner and outer layers. The second expression indicates that the wall layer is exponentially thin compared to the boundary layer thickness. The small defect form of the outer velocity profile ($U\text{-}U_e \ll 1$) implies that the displacement and momentum thicknesses are small compared to the boundary layer thickness, and in particular

$$\delta^* = 0(\epsilon\,\delta) = 0(\epsilon^2) \text{ and } \theta = 0(\epsilon\,\delta) = 0(\epsilon^2) \tag{7}$$

Typical values for ϵ and the length scales in a large wind tunnel are

$$\epsilon \simeq 0.05, \quad \delta^+/\delta \simeq 0.02, \quad \delta^*/\delta \simeq 0.2. \tag{8}$$

Thus, the basic small parameter for wall turbulence is not impressively small at Reynolds numbers of interest in aeronautics but it is small enough to expect an asymptotic analysis to make sense.

These ideas, which were first developed by Millikan [25] and von Karman [26] on physical grounds, have been developed into a fairly complete asymptotic theory of turbulent boundary layers in incompressible flow by Mellor, [27] Bush and Fendall, [28], Yajnik [29] and others. The extension of the theory to compressible flow by Afzal [30] is in error and needs to be modified to account for density variations in the wall layer solution. In Ref (12) it is indicated how this can be accomplished simply by the use of van Driest's compressibility transformation. The asymptotic theory differs from the corresponding theory for the laminar boundary layer mainly in the two layer structure of the turbulent boundary layer and in the fact that the inertia terms in the momentum equation are linearized to lowest order in the turbulent theory. The formal asymptotics are rarely used in practical computations of turbulent boundary layers. Instead, solutions are usually based on the standard boundary layer equations with the full nonlinear inertia terms. The conventional boundary layer equations can be viewed as a composite equation valid in both the outer and inner layers of the boundary layer. The matching conditions to the outer inviscid flow are then exactly the same as for the laminar problems. It should be noted that formal asymptotic theory adds little to what is already known about noninteracting turbulent boundary layers. Its main contribution is to suggest a systematic approach to strong interaction problems. This has been accomplished for both shock wave boundary layer and trailing edge interactions as discussed in Sections 4 and 5, respectively.

The most important general results to emerge from the formal theory are:

- The wall layer is exponentially thin compared to the overall thickness of the boundary layer
- Pressure gradient effects do not influence the lowest order description of the wall layer solution unless the flow is separated or the pressure gradient is very large, that is unless

$$0(p_x) \geq 0(\epsilon/\hat{\epsilon}) \tag{9}$$

- The velocity profile in the outer part of a turbulent boundary layer does not satisfy the nonslip condition at the wall but instead possesses a logarithmic behavior for $y \longrightarrow 0$.

These conclusions are crucial for a proper understanding of strong interactions in turbulent flow as will become apparent from our discussion of these problems in Sections 3 and 4.

2.2 Displacement Effects and Application to Free Interaction in Turbulent Flow

The displacement effect arises from the failure of the inviscid solution for the normal velocity component to match the boundary layer solution. Physically it arises from the need to displace the outer inviscid flow away from the surface in order to allow for the deceleration of the mainstream in the boundary layer. The requirement that the inviscid and boundary layer solutions for the normal velocity component match, leads to corrections to the outer inviscid solution forced by modifications to the impermeable wall boundary condition. As discussed in Lighthill, [31] there are a number of equivalent formulations to the matching conditions that couple the inviscid and boundary layer solutions. Integration of the continuity equation provides the far field behavior of the boundary layer solution for the normal component of velocity, V namely

$$V_{bl}(S, N) \sim -\left(\frac{d\rho_e U_e}{\rho_e dS}\right) N + \frac{d\rho_e U_e \delta^*}{\rho_e dS} \qquad \text{for } N/\epsilon \to \infty \tag{10}$$

when S, N are coordinates along and normal to the surface and δ^* is the displacement thickness. The solution, as determined from Eq. 10, must match the inviscid solution for $N \longrightarrow 0$. The first term in Eq. 10 is common to both the inviscid and boundary layer solutions so that the requirement that the inviscid solution match Eq. 10 leads to the following equivalent forms of the matching condition

$$V_{inv}\Big|_{N=0} = \frac{d\rho_e U_e \delta^*}{\rho_e dS} \equiv v_o \quad \text{Transpiration Velocity (Matching at } N=0) \tag{11}$$

$$V_{inv}\Big|_{N=\delta^*} = U_e \frac{d\delta^*}{dS} \quad \text{Equivalent Displacement Body (Patching at } N=\delta^*) \tag{12}$$

$$V_{inv}\Big|_{N=\delta} = U_e \frac{d\delta^*}{dS} + (\delta^* - \delta) \frac{d\rho_e U_e}{\rho_e dS} \quad \text{(Patching at } N=\delta) \tag{13}$$

All of the above forms are asymptotically equivalent to lowest order in Re, differing only by higher order terms in the Taylor series expansion of the inviscid solution. Although the forms (and other discussed in Ref. 31) are asymptotically equivalent and have all been used in viscid-inviscid interaction studies it is important to note that they can lead to radically different solutions in strong interaction problems where the streamwise pressure gradients are large (see LeBalleur [20-22]).

An interesting application of IBLT, involving just the displacement effect, is LeBalleur's [22] computation of the flow over a symmetric, 18% thick circular-arc airfoil. The calculations shown in Fig. 3 were carried out at zero incidence so that the overall flow was symmetric, and therefore did not involve the wake curvature effects (to be discussed in the next subsection). The computation was based on the transpiration velocity form of the matching condition given by Eq. 11. Solutions of the coupled inviscid and boundary layer equations were obtained by a semi-inverse global iteration method well suited for dealing with separated flows. The inviscid flow was determined from solutions of the transonic small disturbance equation using the conservative version of the Murman-Cole relaxation method. The turbulent boundary layer was solved using an integral entrainment method. Solutions at two high subsonic Mach numbers are compared with experimental data and with Deiwerts' [32] Navier-Stokes solution. The results of the IBLT theory show very good agreement with experiment in the lower Mach number case which involves only a small separation zone. Only qualitative agreement is obtained at the higher Mach number, involving large shock-induced separation. It is not clear whether the discrepancy in the pressure levels behind the shock wave is due to some failings in the theoretical model or to problems in the wind tunnel simulation (e.g., side wall boundary layer effects). The IBLT and Navier-Stokes solutions for this problem are comparable, with the IBLT showing slightly better agreement with experiment. The spread in the Navier-Stokes results is due to differences in the levels of convergence of the plotted results.

Next we consider the question of "free interaction" in turbulent flow from the viewpoint of IBLT. Free interaction effects arise in problems of boundary layers interacting with supersonic external flows. Oswatitsch and Wieghardt [33] showed that upstream propagation can arise in a supersonic viscid-inviscid interaction from the displacement effect of the boundary layer even though the flow is governed by a coupled hyperbolic and parabolic system of equations. The mathematical explanation for this effect was given by Garvine [34] along with a discussion of the significance of the coupling in these problems.

It is known from the early work of Crocco-Lees[35] that two types of behavior are possible in supersonic viscous interaction depending on the nature of the response of a boundary layer to imposed pressure gradients. Subcritical behavior occurs in situations where the boundary layer thickens in response to adverse pressure gradient and thins in favorable pressure gradient. For turbulent flow this occurs for free stream Mach numbers below $M_\infty \approx 1.5$, depending on the theoretical model used for the turbulent boundary layer. In subcritical flow the displacement effect of the boundary layer generates self-induced pressure disturbances which propagate upstream. The resulting "free interaction" pressure distribution is independent of the provoking mechanism. It is this subcritical behavior of the flow that is responsible for the presence of the so-called departure or branching solutions in many viscid-inviscid interaction problems and necessitates the specification of a downstream boundary condition to fix the solution. Werle and Vatsa[36] have shown that it is best to approach these problems with a global iteration scheme. For supercritical flow the boundary layer will thin in an adverse pressure gradient and thicken in a favorable one with the result that will be no upstream influence and no free interaction unless a supercritical-subcritical jump is inserted into the solution. There has been much controversy since the initial work of Crocco-Lees[35] regarding when and under what conditions the boundary layer will exhibit subcritical behavior and on the physical meaning of the supercritical-subcritical jumps.

It was clearly demonstrated in recent studies by LeBalleur[20-22] that the issue of subcritical and supercritical behavior has no physical significance and is controlled solely by the choice of the matching condition coupling the inviscid and boundary layer equations. In these studies LeBalleur shows that supercritical behavior in turbulent flow is associated with the use of coupling conditions based on patching at $y = \delta^*$ or $y = \delta$ (Eq 12 and 13) and that the transpiration boundary condition always leads to subcritical behavior. These observations are illustrated in results presented in Fig. 4, taken directly from LeBalleur's[22] paper. They are for supersonic flow in a compression corner with an upstream Mach number of 2.96, a corner angle of 26° and a Reynolds number at the wedge of 10^7. The wall is adiabatic and the boundary layer is assumed to be turbulent starting from the leading edge. Interacting boundary layer solutions obtained by LeBalleur,[22] using a simple wave solution (Prandtl-Meyer Flow) for the inviscid flow, a transpiration boundary condition for the coupling, and by Werle and Berkte,[37] using the displacement thickness patching approach, are compared with the experimental data of Law[38] and with the Navier-Stokes solutions of Shang and Hankey[39]. At this high Mach number most boundary layer approaches based on patching, at either $y = \delta^*$ or at $y = \delta$, would lead to supercritical behavior with either no upstream influence or with supercritical-subcritical jumps in the solutions. The Werle and Berkte results, which were obtained with a finite difference solution of the turbulent boundary layer equations, clearly indicate a supercritical behavior with no upstream influence The results of LeBalleur, obtained with a simple integral entrainment method, show a smooth subcritical behavior with significant upstream influence. LeBalleur's interacting boundary layer solution is seen to be in reasonably good agreement with the experimental data and an improvement over the existing Navier-Stokes solutions. This study indicates that the matching condition based the transpiration velocity, Eq. 11, is the best choice for turbulent interaction problems since it eliminates supercritical behavior and supercritical-subcritical jumps.

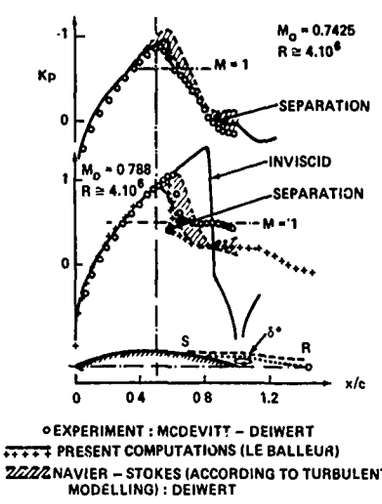


Fig. 3 Pressure over an 18% circular arc symmetrical airfoil.
(REPRINTED FROM REF 22)

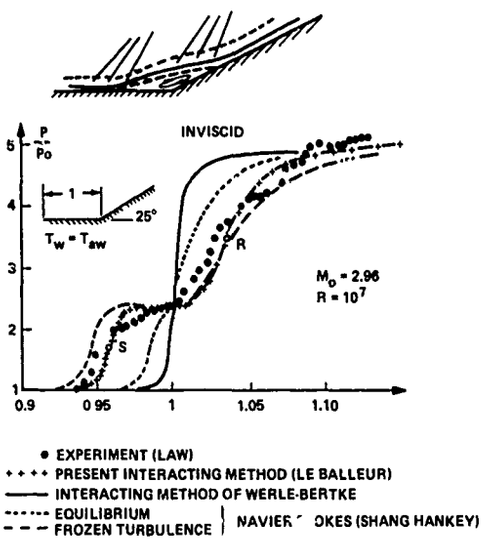


Fig. 4 Pressure along a supersonic ramp (turbulent)
(REPRINTED FROM REF 22)

2.3 Application to Airfoils Including Wake Effects

In application of IBLT to airfoil flows the displacement conditions on the airfoil are supplemented by viscous matching condtions in the wake. Two types of terms arise in the wake matching conditions, one due to the displacement thickening effect of the wake and the other due to the wake curvature effect. The wake thickness effect originates from the matching of the inviscid and boundary layer solutions for the velocity component normal to wake. (The wake conditions can be referenced to any arbitrary curve emanating from the trailing edge and lying within the wake.) A formal matching analysis leads to the requirement that the inviscid solution for the normal component of velocity, V_{inv}, be discontinuous across the wake with a jump given by

$$[\![V]\!] = \frac{d\rho_e U_e \delta_w^*}{\rho_e dS} \tag{14}$$

where δ_w^* is the displacement thickness of the complete wake. This result follows from an integration of the continuity equation across the viscous wake. The wake curvature effect arises from the turning of the low momentum flow along the curved wake streamlines. This turning generates a pressure difference across the wake. The requirement that the outer inviscid flow match this pressure rise across the wake leads to the following jump condition on the inviscid solution for the pressure, p_{inv}.

$$[\![p_{inv}]\!] = -C_w \kappa(S) \tag{15a}$$

where κ is the curvature of the wake and C_w is a coefficient given in terms of the displacement and momentum thicknesses of the wake, i.e.,

$$C_w = -\rho_e U_e^2 (\delta_w^* + \theta_w). \tag{15b}$$

Equation 15 is derived from integration of the boundary layer approximation to the normal momentum equation. Because of the form of Eq 15, the wake curvature condition produces effects similar to a jet flap with a negative blowing coefficient ($C_w < 0$). The importance of the wake curvature effect and its relationship to the jet flap was first noted by Preston[1] in 1954 (see also Spence and Beasley[40]). However, serious attempts to include wake curvature effects in calculations based on IBLT were not undertaken until the mid 1970's in a series of studies at the RAE[6,7,41-43] and at the Grumman Aerospace Corp. (GAC)[8-11]. For a detailed asymptotic derivation of both wake conditions the reader is referred to the paper by Viviand[44].

IBLT has recently been applied to the computation of transonic flow over airfoils by three research groups, BGKJ[4,5], CL[6,7] and MCMJ[8-11]. These methods all employ a finite difference solution of the full potential equation for the inviscid flow and integral methods for the boundary layers. Each make different recommendations for the type of differencing to use in the inviscid solution: BGKJ recommends nonconservative (NC) differencing, CL partially conservative (PC) differencing and MCMJ fully conservative (FC) differencing. The partially conservative scheme is a method developed by CL[7] for improving the performance of potential flow methods at shock waves. The BGKJ methods employs the Nash-McDonald[45] integral method while the CL and MCMJ methods use Green's lag entrainment method[46] for the turbulent boundary layer. The following table summarizes the main features of the theoretical formulation employed in each of the methods.

Table 1 Description of recent IBLT formulations.

METHOD			WEAK INTERACTION			STRONG INTERACTION	
			Displacement Effect		Wake		
			Airfoil	Wake	Curvature	Shock	Trailing Edge
	Inviscid Flow	Boundary Laye.	1	2	3	4	5
BGKJ[4, 5]	NC	N M[45]	δ^*	No	No	No	No
CL[6, 7]	PC	G[46]	V_σ	$\|V_\sigma\|$	Yes	No	No
MCMJ[8-11]	FC	G[46]	V_σ	$\|V_\sigma\|$	Yes	No	Yes

Since all three weak interaction effects are of the same order of magnitude (i.e., $O(\epsilon^2)$) they must all be retained to achieve a completely consistent formulation of IBLT. Note that only the CL and MCMJ methods do so and, furthermore that only the MCMJ method accounts for strong interaction effects at the trailing edge (discussed in Section 4).

The fact that the shock wave penetrates into the boundary layer and generates large normal pressure gradients is not properly accounted for in any of the above formulations. Nevertheless, experience gained with the use of these codes indicates that they all provide a reasonable overall description of the pressure rise and boundary layer growth across the shock wave. It should also be noted that both the CL and MCMJ methods employ a transpiration boundary condition for the displacement effect which, from LeBalleur's work, is known to produce a subcritical description of the shock-wave boundary-layer interaction. Therefore a shock-wave boundary-layer interaction is modeled in these formulations as a steep but continuous increase in the boundary layer thickness. The rapid build-up of the boundary layer thickness generates compression waves that annul the shock wave and prevent discontinuities from impinging on the boundary layer (see in Fig. 5). With this formulation the "free interaction" mechanism always leads to a nonsingular description at shock waves.

The results for the RAE 2822 airfoil in Fig. 6 attest to the level of accuracy that can be achieved by IBLT in airfoil flows, even under supercritical conditions involving a shock wave. The results were obtained with the CL method [7] and hence fully account for all weak interaction effects. The results show that the pressure rises to about sonic pressure behind the shock, resulting in about half the jump required by the normal shock wave relations. This behavior, which is typical for airfoils, is seen to be well predicted by IBLT. Additional information on the CL method is given by Lock in the paper at this meeting. Results from the MCMJ method, which also accounts for strong interactions at the trailing edge, are presented in Section 5.

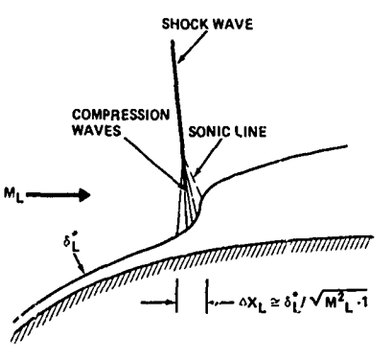


Fig. 5 Shock-wave boundary-layer interaction – IBLT.

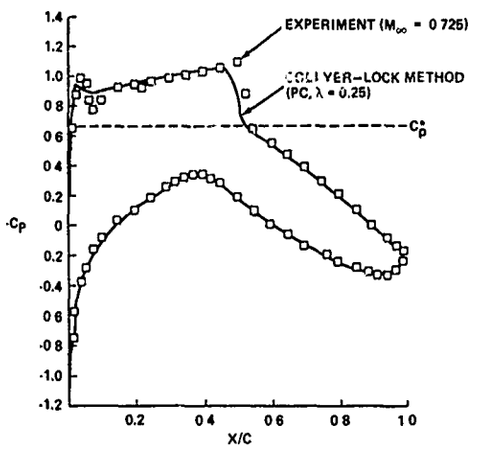


Fig. 6 RAE 2822 $M_\infty = 0.730$, $\alpha_g = 2.55°$, $\alpha = 2.00°$, Re = 6.5 x 10^6, $X_T = 0.03$, $C_L = 0.66$. (REPRINTED FROM REF 7)

3. STRONG TURBULENT INTERACTIONS AT SHOCK WAVES

The shock-wave boundary-layer interaction on an airfoil at transonic speed is an important feature of the flow. Here, its most noticeable effect is a significant reduction in the pressure rise across the shock wave. Both experimental data and theoretical computations over airfoils indicate that the magnitude of the reduction is about one half of the jump condition for normal shock waves. Although this effect seems to be well represented by IBLT, the details of the interaction are not adequately described. As discussed previously, IBLT, with the transpiration boundary condition always leads to a subcritical response with the shock wave terminated outside the boundary layer. In an actual shock-wave boundary-layer interaction the shock wave penetrates well into the boundary layer when the flow is turbulent and generates large normal pressure gradients that are not accounted for in IBLT.

In the early 1950's Lighthill [19] developed an approximate linearized theory for shock-wave boundary-layer interaction that recognized the importance of shock penetration and normal pressure gradient effects. In this remarkable paper Lighthill clearly identified the dominant physical mechanisms in strong inter-

actions. He also developed the key theoretical concepts that have formed the basis for nearly all subsequent models of strong viscid-inviscid interaction. It was in this paper, following earlier more approximate attempts, that Lighthill established the inviscid rotational flow model of strong interactions. The theory was not much used over the following 16 years until, in 1969, Stewartson and Williams[47], Stewartson [48] and Messiter[49] showed how the theory could be developed into a rational asymptotic theory for laminar interactions. This work led to the development of the laminar "Triple Deck" theory. At about the same time, Rose, Murphy and Watson[50], for oblique shock waves, and Roshko and Thomke,[51] for compression corners, showed how the inviscid rotational flow model could be used in a semi-empirical fashion for turbulent interactions at supersonic speeds. In the mid 1970's Melnik and Grossman[12-14] and Adamson, Messiter and their students[15-18] developed the inviscid rotational flow concept into a rational asymptotic theory for interactions of weak normal shock waves with turbulent boundary layers. Subsequently Melnik and Chow[8] developed a similar theory for strong turbulent interactions at the trailing edge of cusped airfoils.

In this section I review the main features of the Lighthill 1953 theory and discuss the reasons why the original form of the theory is not directly applicable to turbulent interactions. Next, I discuss Roshko and Thomke's semi-empirical theory for supersonic, turbulent interactions in a compression corner and then the section is concluded with a review of the asymptotic theories for weak normal shock waves. These topics are also discussed in a recent, comprehensive survey of the shock-wave boundary-layer interaction literature by Adamson and Messiter[52].

3.1 Lighthill's Two Layer Theory[19]

In his 1953 paper, Lighthill examined the question of upstream propagation in a supersonic shock-wave boundary-layer interaction. He developed a simple linear theory that described the interaction of weak external disturbances with a boundary layer that could be either laminar or turbulent. Following earlier unsuccessful attempts by himself[53] and Robinson [54] to treat the problem with a single layer model, Lighthill proposed the two layer model of the boundary layer sketched in Fig. 7. The two layer model consists of a thick outer region covering most of the boundary layer and a thin sublayer near the wall. Lighthill recognized that the interaction region was narrow, and consequently that the shear stresses could be neglected in the outer layer. Considering only weak disturbances he linearized the solution about the unperturbed flow upstream of the interaction. Thus, he assumed expansions for the streamwise and normal velocity components, u, v and pressure p in the form

$$u = U_o(y) + \bar{u}(x,y) + \cdots$$

$$v = \qquad \bar{v}(x,y) + \cdots$$

$$p = P_o + \bar{p}(x,y) + \cdots$$

where $U_o(y)$ is the streamwise velocity profile and P_o is the constant pressure in the unperturbed flow upstream of the interaction (barred variables denote perturbed quantities). The equations governing the inviscid rotational flow in the main part of the boundary layer were developed into a single equation for the disturbance pressure, viz.

$$[1 - M_o^2(y)]\bar{p}_{xx} - \frac{2M_o'(y)}{M_o(y)}\bar{p}_y + \bar{p}_{yy} = 0 \tag{16}$$

where $M_o(y)$, $M_o'(y)$ are the upstream Mach number profile and its derivative. This equation governs the propagation of small disturbances in the nonuniform flow in the boundary layer. Within this model, disturbances propagate upstream by simple wave propagation up the subsonic streamtubes in the inner part of the boundary layer. To complete the formulation of the outer problem this equation must be supplemented by appropriate boundary conditions. At the outer edge of the boundary layer, $y = \delta$, solutions must match the incoming and reflected disturbances, which are governed by the linearized supersonic flow equations. The outer problem is closed by specifying boundary conditions at wall. In the early one layer model, Lighthill [53] and Robinson[54] imposed the condition that $v \to 0$ as $y \to 0$ (equivalent to $\bar{p}_y = 0$). Unfortunately, this simple condition leads to a trivial solution for the pressure and to a failure of the model. This can be seen by considering the expression governing the perturbation pressure gradient obtained from the streamwise momentum equation, i.e.

$$\bar{p}_x = -\rho_o(y)\,[U_o(y)\,\bar{u}_x + \bar{v}\,U_o'(y)] \tag{17}$$

If the initial profile is of boundary layer type, $U_o(y)$ vanishes at the wall as does $\bar{v}$, if the inviscid wall condition is imposed. Consequently, both terms on the right side of Eq 17 vanish at the wall where the pressure must then approach a constant. This problem arises because the zero velocity streamline at the wall cannot overcome a pressure rise by inviscid mechanisms alone.

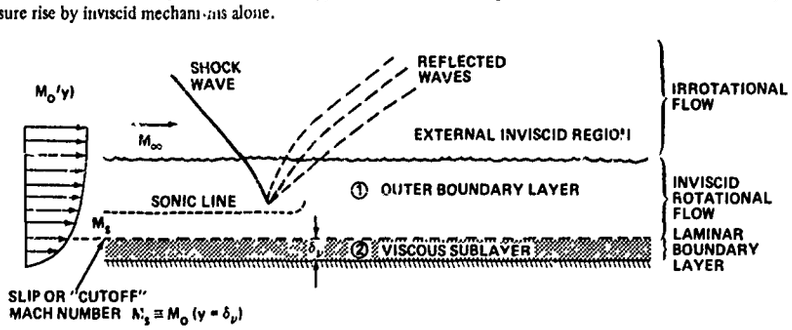


Fig 7 Lighthill (1953) two-layer model of a strong interaction.

In his 1953 paper, Lighthill recognized the need to account for shear stresses near the wall and proposed his two layer model. In this model the shear stresses are fully accounted for in a thin sublayer near the wall. Because the sublayer is thin, the pressure is constant across the layer and can be evaluated from the outer solution. In addition, the solution in the sublayer is linearized about the upstream profile, which is assumed to have a linear, laminar-like behavior near the wall. Hence, the flow in the sublayer is governed by linearized boundary layer equations and the pressure is determined from the outer solution. Matching of the outer and sublayer solutions leads to a displacement type coupling condition connecting the two regions. Lighthill has shown that the matching of the inner and outer solutions can be accomplished using a suitably chosen cutoff in the initial velocity or Mach number profile. Thus, the sublayer can be accounted for by simply solving the outer inviscid problem with this truncated initial Mach number profile. The fact that the value of the cutoff, $M_2 \equiv M_o(y_{crit})$ depends on both the Reynolds number and the position along the surface complicates the problem but solutions can be readily determined with Fourier transform methods.

It is now recognized that, for laminar flow, Lighthill's two layer theory is generally correct in all the important details. It predicts the structure of the flow, the scale of upstream influence, $\Delta x/\delta = Re^{1/8}$ and the thickness of the sublayer, $\Delta y/\delta = Re^{-1/8}$ that follow from a more rational asymptotic analysis. Lighthill's theory was developed into a systematic theory for laminar interactions by Stewartson[47,48] and Messiter[49]. The "triple deck" theory that followed from these studies is consistent with Lighthill's formulation except that the full nonlinear boundary layer equations are generally required for the sublayer solution. The "triple deck" theory also indicates that the pressure and flow deflection can be taken as constant across the outer boundary layer, leading to a description of laminar interaction in terms of a displacement type coupling between the external inviscid flow and the sublayer. The flow deflection generated by the sublayer in response to imposed pressures (from the external flow) is transported unchanged across the main deck producing a deflection of the mainstream. The deflection of the mainstream then generates pressures that affect the solution in the sublayer. Consequently, the solutions in the mainstream and sublayer are coupled and must be determined in a self-consistent manner. The "Triple Deck" theory is closely related to IBLT. The latter can be considered as a "composite equation" approach that includes all the leading order terms of the "Triple Deck" equations. In this way, "triple deck" theory provides a rational basis for the use of IBLT for laminar interaction problems.

Lighthill also applied the theory to turbulent interactions by simply accounting for differences in the initial profile and skin friction when the flow is turbulent. The interacting sublayer was retained as an important feature of the turbulent flow and the laminar solution for the cutoff M_2 was employed in the solution of the inviscid equations in the outer boundary layer. Detailed analysis indicates that this procedure is inconsistent with the law of the wall structure of the inner part of a turbulent boundary layer. The pressure gradient cannot affect the flow in the wall layer unless its order of magnitude is larger than $0(\epsilon/\hat{\epsilon})$ or

$$0(p_x) \geq 0(\epsilon/\hat{\epsilon}) \approx 0(\epsilon^3 e^{1/\epsilon}) \approx 0\left[\frac{Re}{(\ln Re)^3}\right] \tag{18}$$

If the shock wave does not penetrate the wall layer it can be shown that the limiting pressure gradient in Eq. (18) is exponentially large compared to the gradients that arise in a strong interaction region. In this case the effect of pressure gradients on the wall layer flow must be small so that deflections of the wall layer cannot have a primary role in turbulent interactions. This conclusion can also be extracted from physical arguments related to the nature of a typical turbulent velocity profile. In a turbulent flow the streamwise velocity remains high, of 0(1), except in the exponentially thin wall layer. Because of their much higher velocities, the streamlines near the wall of a turbulent boundary layer are not nearly as responsive to imposed pressure gradients as those of a laminar flow. Thus, for weak shock waves, with a sonic line outside the wall layer, it should be possible to formulate a consistent turbulent interaction theory without consideration of an interacting sublayer.

It follows from formal asymptotic theories, discussed later in this section, that the difficulties at the wall in Lighthill's theory can be avoided by careful specification and use of the initial profile. The importance of the initial velocity profile in turbulent interaction was clearly recognized in the asymptotic theories of Melnik and Grossman[12-14] and Adamson and Messiter[15-18]. The velocity profile in the undisturbed flow upstream of the interaction develops a small defect form at large Reynolds number so that $U_o(y)$ in Lighthill's analysis should take the form

$$U_o(y) = U_e[1 + \epsilon u_o(y/\delta)] \tag{19a}$$

Note that $U_o(y)$ does not satisfy the no-slip condition and is not linear near the wall, but in fact is logarithmic in behavior, $U_o \to k^{-1} \ln(y/\delta)$ for $(y/\delta) \to 0$. If Eq. (19a) is used for $U_o(y)$ in Lighthill's equation and the results are expanded for $\epsilon \to 0$ then the difficulty of the theory at the wall is eliminated. Following this procedure, $U_o(y)$ is replaced by U_e in the first term of the expression for the pressure gradient in Eq. 17 thus avoiding the trivial solution when $y \to 0$. The resulting solution can be viewed as a perturbation to the wave system outside the boundary layer by small nonuniformities in the boundary layer. This approach has been developed into a complete, rational theory for interaction of weak normal shock waves at transonic speeds in the asymptotic theories mentioned above.

Ventres[55] has shown that the trivial solution can also be avoided in an ad hoc approach based on the use of a power law profile

$$U_o(y) = U_e(y/\delta)^{1/n} \tag{19b}$$

Where n is a constant chosen to give a best fit to the initial profile (Ventres used n = 7). Ventres has shown that nontrivial solutions of Lighthill's outer equations are obtained for $n > 2$. In this case the pressure gradient is balanced by the second term in Eq. 17 where the zero in v is multiplied by a corresponding singular term in $U_o(y)$ for $y \to 0$. The Princeton University group has used the power law profile to develop the Lighthill theory into a useful engineering approach to a variety of unsteady and three dimensional shock flow problems. The asymptotic studies[12-18] and Ventres'[55] ad hoc approach have clearly demonstrated that the difficulties in Lighthill's one layer interaction theory can be eliminated by a proper treatment of the initial velocity profile. These difficulties are caused by the use of an initial profile that has the velocity vanish linearly at the wall. The use of the law of the wake profile in the rational theories or a power law profile as in Ventres' method completely eliminates the trivial solution without the unjustified use of an interacting sublayer.

Recent application of Lighthill's theory to interactions of normal shock waves with turbulent boundary layers at transonic speeds have been carried out by Inger and Mason[56] and Bohning and Zierep[57, 58]. However, these applications are subject to the same criticisms as the original Lighthill theory. The use of a laminar interacting sublayer in these problems is an arbitrary procedure that is not consistent with the known structure of a turbulent flow near a wall. Moreover, such a procedure is unnecessary since the problems at the wall can be completely avoided, either by use of the asymptotic theory based on the law of wake initial profile and the limit $\epsilon \to 0$, or by use of power law profile as in Ventres' approach. Bohning and Zierep[57] do, in fact, employ a power law profile in their theory, although still retaining Lighthill's laminar sublayer to justify a cutoff, M_2, of the initial Mach number profile. Ventres'[55] results indicate that the inclusion of a laminar sublayer in Bohning and Zierip's[57] theory is unnecessary since a nontrival solution for the pressure distribution can be obtained by ignoring the sublayer and letting M_2 approach zero. Unfortunately, Inger and Mason[56] employ an initial Mach number profile with a linear zero at the wall so that the procedure of letting $M_2 \to 0$ in their formulation would lead to the trival solution of constant pressure. The use of power law profiles in the Bohning-Zierep theory[57], although not consistent with the flow near the wall, does provide a simple and direct procedure for applying Lighthill's theory to the determination of the pressure distribution in turbulent interactions. However, the application of the laminar sublayer theory to the determination of the skin friction in the Inger-Mason[56] and Bohning-Zierep theories[58] is unjustified, and is not consistent with the known structure of the flow near the wall of a turbulent boundary layer. Consequently, it should not be unexpected that the solution for the incipient separation Mach number in the Bohning-Zierep theory[58] shows a much greater dependence on Reynolds numbers than indicated by either the rational asymptotic theory of Liou and Adamson[18] or the experimental data of Roshko and Thomke[51]. For further discussion of these points see the recent review article by Adamson and Messiter[52].

3.2 Nonlinear Inviscid Flow Theories

The concept of treating the local interaction as an inviscid rotational flow has been applied to a variety of turbulent viscid-inviscid interaction problems. In supersonic flow, Rose, Watson and Murphy[50] use it for the analysis of the interaction of an oblique shock wave with a turbulent boundary layer while Roshko and Thomke[51] apply it to interactions in a compression corner. In order to treat problems with strong shock waves their studies are based on the full nonlinear inviscid equations. The problem is completely specified by the initial Mach number profile $M_o(y)$ and by either the surface geometry or the incident shock configuration. Difficulties at the wall are avoided by the use of an empirical slip Mach number M_s as a cut-off in the initial Mach number profile, which

then is given by

$$M = \begin{cases} M_o(y) & y \geq y_s \\ M_s & 0 \leq y < y_s \end{cases} \qquad (20)$$

The slip Mach number is considered to be an empirical parameter to be determined from experiment. This is equivalent to assuming that there is a thin sublayer beneath the outer inviscid flow that is of constant thickness and unaffected by imposed pressure gradients. In problems where the appropriate slip velocity is high enough, the local Mach number remains supersonic in the entire outer region and the inviscid equations can be solved by a hyperbolic marching scheme. Calculations of this type have been carried out for supersonic interactions in compression corners by Roshko and Thomke[51], Elfstrom[59] and Carriere, et al.[60]

The theoretical model assumed for the Roshko-Thomke computations is sketched in Fig 8. The pressure rise occurs in two stages, a very rapid, nearly discontinuous rise, followed by a more gradual approach to the level required by the oblique shock relations. The initial pressure rise is assumed to occur discontinuously through an oblique shock wave at the corner. The initial pressure and shock angle are completely fixed by the value of the slip Mach number and the wedge angle. In Roshko and Thomke's calculations M_s is chosen to match the initial value of the experimental pressure on the wedge and the solution is continued downstream by the method of characteristics. Many calculations have been carried out for various free stream Mach numbers, wedge angles and Reynolds numbers. A typical result for a $M_\infty = 3.93$ free stream into a 15° corner at Re = 5.5 million is given in Fig 9. The excellent agreement observed here is typical of other results presented in Roshko and Thomke's paper. Similar agreement has also been obtained for the impinging oblique shock problem by Rose, Murphy and Watson[50]. The generally favorable agreement of these computations with experiment strongly supports the concept of treating turbulent interaction by inviscid techniques. This excellent agreement, attained by virtually ignoring the sublayer, gives strong indication that sublayer interaction is not important in turbulent interactions.

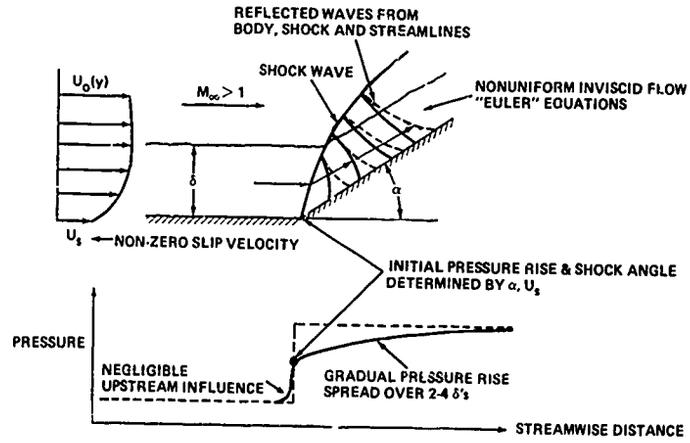


Fig. 8 Roshko-Thomke inviscid rotational flow Model.

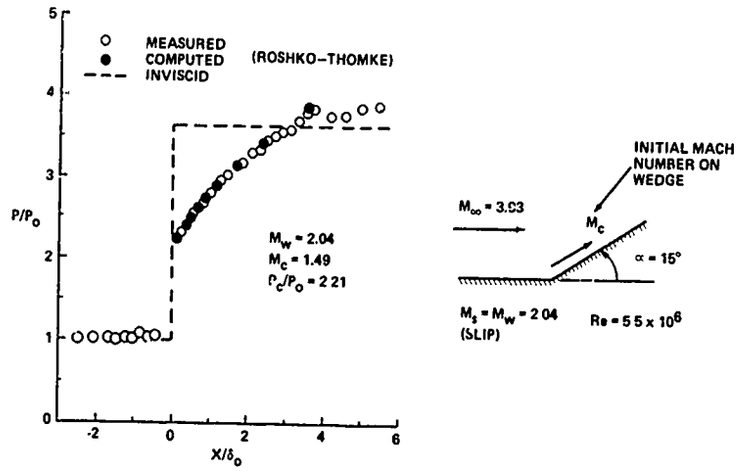


Fig. 9 Supersonic interaction in a compression corner – typical result from Roshko-Thomke method (reprinted from ref 51).

Although these theories are quite accurate when the proper value of slip is assigned, they are incomplete since no theoretical means for the specification of the slip Mach number is offered. The question of how to determine the slip velocity had remained open for about ten years until, in a noteworthy paper presented earlier this year, Rosen, Roshko and Pavish[61] developed an approximate answer Their approach recognizes that the shock wave forms near the tip of the wedge, deep within the wall layer, and interacts strongly with the flow in this region. Thus, the flow field structure sketched in Fig. 10 is assumed, and in the computation of the flow in the inner wall layer, near the tip of the wedge, all terms of the full Navier-Stokes equation are retained. The solution of the full Navier-Stokes equations on the scale of the sublayer thickness in both directions, is of course, a very difficult numerical problem which they do not attempt. Instead, they carry out a simple control volume balance of mass and momentum, including both momentum equations and employing the compressible law of the wall for the streamwise velocity profiles. The analysis yields relatively simple expressions for the initial pressure on the wedge and for the width of the inner wall region which is found to be $O(\delta^+)$. This result is consistent with the observation that the full Navier-Stokes equations are required in the tip region.

A typical result obtained by using the predicted initial pressure in a method of characteristics calculation is given in Fig. 11. The good agreement observed in this example is typical of other results presented in the paper[61]. The success of these calculations clearly indicates that the overall flow model for the slip

velocity is correct and that the full Navier-Stokes equations are required to describe the initial rapid pressure rise at the tip of the wedge. It should be noted that the streamwise length scale for the initial region is very small, on the order of the wall layer thickness, δ^+. The small length scales of this region greatly complicate the problem of solving the full Navier-Stokes equations by direct numerical solution. The further development of the Rosen, Roshko and Pavish theory into a complete rational theory is a worthy research objective.

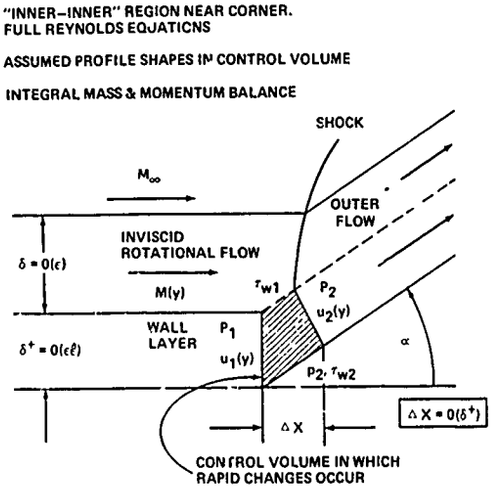


Fig. 10 Rosen-Roshko-Pavish flow model for the "Slip" velocity determination.

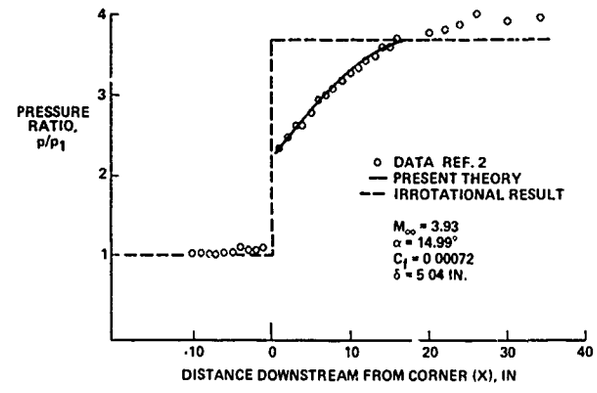


Fig. 11 Supersonic interaction in compression corner – typical result of Rosen-Roshko- Pavish (1980) method for slip velocity (REPRINTED FROM REF 61)

3.3 Asymptotic Methods for Normal Shock Waves

Formal asymptotic methods have been applied to interactions of shock waves with turbulent boundary layers at transonic speeds. Efforts have focused on interactions involving normal shock waves because of their importance in airfoil and channel flows. For simplicity, attention has been mainly restricted to interactions on flat plates where the pressure is observed to rise monotonically across the shock wave to a level determined by the normal shock relations. It should be mentioned, at the outset, that such studies do not address a significant aspect of shock-wave boundary-layer interactions on airfoils, namely, the pressure jump across the shock wave is observed in both experiments and IBLT calculations to be only about half the value given by the normal shock wave relations. Thus, the significance of flat plate solutions to the airfoil problem remains to be clarified. In this section I briefly review recent progress in the development of such formal asymptotic theories for the interaction of weak normal shock waves with turbulent boundary layers. For a more comprehensive review of this subject the reader is referred to the recent survey by Adamson and Messiter[52].

The flow field sketched in Fig. 12 is typical of the flows considered in the analysis of Melnik and Grossman [12-14]. They address interactions in the transonic regime for which the shock waves can be characterized as weak and nearly normal to the flat plate. They also assume that the Reynolds number is high so that the velocity profile is "full" and can be accurately represented by a conventional form of the law of the wake/law of the wall. In particular, the velocity profile in the outer part of the boundary layer is represented by a small defect form with a logarithmic behavior at the wall. Furthermore, they hypothesize and verify a posteriori, that the boundary layer remains fully attached for the range of weak shock strength under consideration. Under these conditions, it is demonstrated that the overall flow structure is as sketched in Fig. 12 with the sonic line lying in the outer part of the boundary layer.

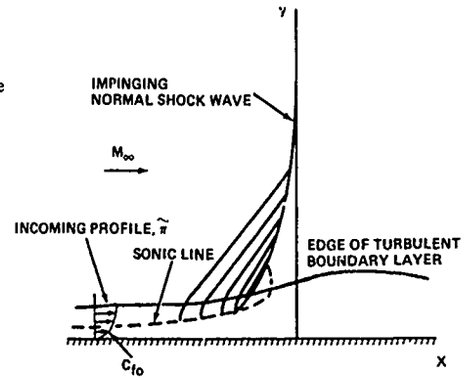


Fig. 12 Schematic of shock wave – turbulent boundary laye. interaction (ref 12-14).

Two basic parameters appear in the problem, the free stream Mach number, M_∞, and the Reynolds number, Re. The analysis of Melnik and Grossman [12-14] is based on a formal asymptotic expansion of the full Reynolds averaged Navier-Stokes equations in the double limit $M_\infty \to 1$ and $Re \to \infty$. The large Reynolds number limit is expressed in terms of the dimensionless friction velocity, $\epsilon \equiv u_\tau/U_\infty$, associated with the initial velocity profile upstream of the interaction.

Thus, the solution is characterized by the double limit

$$\begin{matrix} M_\infty \to 1 \\ \epsilon \to 0 \end{matrix} \qquad (21)$$

Since the shock strength is proportional to $(M_\infty^2 - 1)$ the first limit implies a weak shock wave and since $\epsilon = 0\,(\ln Re)^{-1}$ the second limit implies a large Reynolds number limit $Re \to \infty$. The structure of the flow field and the form of the solution depend on the magnitude of a parameter χ_t defined by

$$\chi_t \equiv (M_\infty^2 - 1)/\epsilon \qquad (22)$$

This parameter can be interpreted as a normalized shock strength parameter that controls the relative rates at which the two basic parameters M_∞ and ϵ approach their respective limits. Two distinguished limits and two subcases appear depending on the relative magnitudes of $(M_\infty^2 - 1)$ and ϵ. The two distinguished limits are the weak shock limit and the strong shock limit defined by

$$\left.\begin{matrix} M_\infty \to 1 \\ \epsilon \to 1 \end{matrix}\right\} \chi_t = O(1) \qquad \text{weak shock limit} \qquad (23)$$

$$\left.\begin{matrix} \epsilon \to 0 \\ M_\infty \neq 1 \end{matrix}\right\} \chi_t \to \infty \qquad \text{strong shock limit} \qquad (24)$$

The two other limit cases that appear are subcases of the weak shock limit Eq. (23), namely

$$\left.\begin{matrix} M_\infty \to 1 \\ \epsilon \to 0 \end{matrix}\right\} \quad \chi_t \to 0 \qquad \text{very weak shock limit} \tag{25}$$

$$\left.\begin{matrix} M_\infty \to 1 \\ \epsilon \to 0 \end{matrix}\right\} \quad \chi_t \to \infty \qquad \text{moderate shock limit} \tag{26}$$

The weak limit, Eq. (23) and the two subcases Eq. (25) and (26) are appropriate for transonic flows while the strong shock limit defined by Eq. (24) applies to supersonic flows with strong shock waves.

The overall structure of the flow field associated with each of the limits is sketched in Fig. 13. The weak shock distinguished limit $\chi_t = 0(1)$ (Eq. 23) has been analyzed by Melnik and Grossman[12-14]. This limit is characterized by the fact that the velocity change across the boundary layer is of the same order as the velocity change across the shock wave. Consequently, since the velocity profile is "full", the sonic line is in the main part of the boundary layer as sketched in Fig. 13. The shock wave penetrates the boundary layer and terminates someplace in the supersonic zone in the outer part of the boundary layer. Because the profile is "full", nonlinear transonic effects are important in the entire outer part of the boundary layer. Since the wall layer is thin it does not influence the flow in the outer part of the boundary layer.

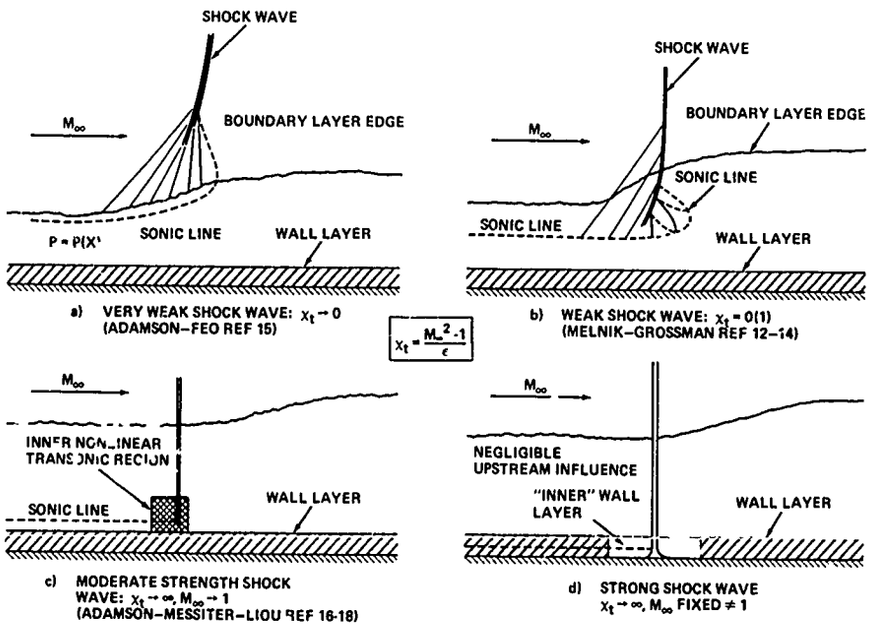


Fig. 13 Flow field structure variation with shock strength.

In the strong shock distinguished limit (Eq. 24) the free stream is supersonic and the shock strength is 0(1). The sonic line lies within the wall layer and the shock wave penetrates deep into the boundary layer terminating in the wall layer. Since the nonuniformities in the approaching boundary layer are small, as a consequence of the large Reynolds limit $\epsilon \to 0$, the shock wave is nearly straight down to the wall and there is negligible upstream influence. The major interaction occurs in the wall layer where an embedded inner region arises at the foot of the shock. The structure at the foot of the shock wave is similar to that arising near the tip of the wedge in Rosen, Roshko and Pavish's[61] analysis of the supersonic viscid-inviscid interaction in a compression corner. The embedded inner region is expected to have a width of $\Delta x = 0(\delta^+) = 0(\epsilon\hat{\epsilon})$, the same order as the wall layer thickness, and to require an analysis based on the full Navier-Stokes equations. It should be mentioned that there have been no rational studies of this case and that much of the above description remains conjecture based on consideration of the behavior of the weak shock limit for $\chi_t \to \infty$ and on reflection of Rosen, Roshko and Pavish's theory.

The subcase $\chi_t \to 0$, corresponding to the very weak shock limit Eq. (25), was analyzed by Adamson and Feo[15]. In this case the sonic line lies near the edge of the boundary layer and the shock wave is weakened by compression waves generated by the boundary layer thickening so that it does not penetrate into the boundary layer. Detailed analysis shows that the interaction spreads the pressure rise over a distance large compared to the boundary layer thickness. It follows that pressure variations across the boundary layer are negligible and that the flow in the outer part of the boundary layer is governed by the inviscid boundary layer equations. Boundary layer approximations remain valid and IBLT is applicable in this limit.

Adamson, Messiter and Liou[16-18] analyzed the moderate shock strength limit $\chi_t \to \infty$. In this limit the sonic line approaches the wall as $\chi_t \to \infty$ but remains outside the wall layer (since $M_\infty \to 1$). The shock wave is nearly straight and penetrates deep into the boundary layer but terminates outside the wall layer. There is negligible upstream influence, and the flow on the downstream side of the shock wave can be described as a linear perturbation to the constant state behind the straight unperturbed shock wave. The outer linear solution develops a nonuniformity at the wall which is resolved by an embedded inviscid region at the shock foot dominated by nonlinear transonic flow effects. The turbulent wall layer does not influence either the outer or the embedded inviscid regions.

The weak and moderate shock strength limits cover the parameter range of most interest for transonic flows and therefore are reviewed in some detail. Although the analysis of the various limiting cases have been carried out independently, it is of interest to note that both the very weak and the moderate shock strength limits are contained in the weak shock formulation of Melnik and Grossman[12] and can be extracted from that theory in the limit $\chi_t \to 0$ and $\chi_t \to \infty$, respectively.

3.3.1 Weak Shock Limit $\chi_t = 0(1)$

On the basis of the formal asymptotic analysis, Melnik and Grossman[12-14] have demonstrated that this limit corresponds to a distinguished limit with the asymptotic flow structure sketched in Fig. 14. Upstream of the interaction the boundary layer has a conventional two layer, law of the wall/law of the wake, form. In the interaction region the boundary layer develops a three layer structure consisting of 1) an outer inviscid rotational flow, extending over most

of the boundary layer, which, following "triple deck" terminology we call the main deck, 2) a conventional wall layer, which is a continuation of the upstream wall layer, and 3) a blending layer between the outer and wall layers. This structure proves typical of other turbulent strong interaction problems.

The flow can be considered inviscid in the outer region because the streamwise length scale is small so that the pressure gradient and inertia terms are large in comparison to the shear stress terms. The displacement effect of the wall layer is negligibly small in this problem and, consequently, the wall layer cannot significantly influence the solution in the outer inviscid region. This conclusion follows from the observation that the pressure gradient, though large, is negligbly small compared to the magnitude, $(\epsilon/\hat{\epsilon})$, needed to influence the momentum balance at the wall. The requirement for a blending layer can be understood from a consideration of the Reynolds stress variations along streamlines of the outer and wall layers. Because of the small horizontal scale of the interaction zone, the Reynolds stresses can be considered "frozen" on the streamlines of the outer solution. In the inner wall layer, however, the Reynolds stresses are in equilibrium with the local value of skin friction which varies significantly in the streamwise direction. The difference in the streamwise development of the Reynolds stresses in the outer and wall layers produces a mismatch in both the Reynolds stress and streamwise velocity between the outer and wall layer solution. The mismatch is resolved by the blending layer solution which is governed by a linear boundary layer type equation that allows for a balance of inertia, streamwise pressure gradient and turbulent shear stress transport across streamlines. Melnik and Grossman's analysis [12] demonstrates that the vertical component of velocity in the blending layer is two orders of magnitude less than that in the outer layer so that the blending layer also does not influence the solution in the outer inviscid region.

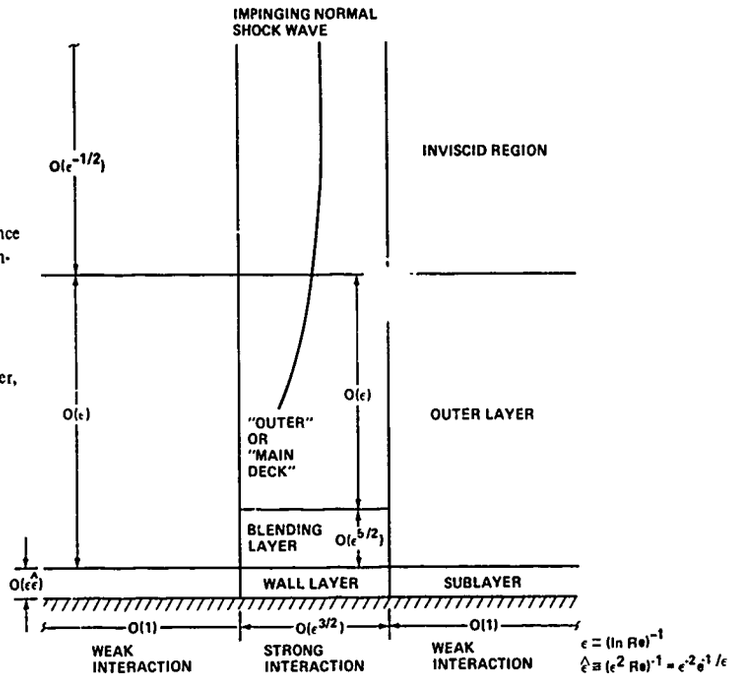


Fig. 14 Asymptotic flow field structure for a weak normal shock-wave boundary layer interaction (ref 12-14).

The solution in the outer layer is represented by the expansion,

$$U = 1 + \epsilon u_1(\bar{x}, \bar{y}) + \cdots \tag{27}$$

$$V = \epsilon^{3/2} v_1(\bar{x}, \bar{y}) + \cdots \tag{28}$$

where the stretched variables $\bar{x}, \bar{y}$ are defined by

$$x = \epsilon^{3/2}\bar{x}, \quad y = \epsilon\bar{y} \tag{29}$$

and U, V, x, y are horizontal and vertical velocity components and coordinates, respectively. All velocities are normalized by the free stream velocity upstream of the shock wave and all lengths are scaled by the distance to the shock impingement point. The scales of the vertical coordinate and the streamwise disturbance velocity are determined by matching to the initial velocity profile, $U_o(y)$, which is assumed to be in the form

$$U_o(y) = 1 + \epsilon u_o(y/\delta) \tag{30a}$$

where u_o is given by the law of wake/law of wall,

$$u_o(y) = \begin{cases} k^{-1}\left[\ln(y/\delta) + \tilde{\pi} W(y/\delta)\right] & 0 \le y/\delta \le 1 \\ 0 & y/\delta > 1 \end{cases} \tag{30b}$$

and $\tilde{\pi}$ and $W(y/\delta)$ are Coles' wake parameter and wake function.

The scales for x, V are determined to be $O(\epsilon^{3/2})$, by balancing the dominant terms in the continuity and vorticity equations under the assumption that a nontrivial equation results in the transonic limit $M_\infty \longrightarrow 1$. The latter requirement yields a distinguished limit with $\chi_t = (M_\infty^2 - 1)/\epsilon = O(1)$.

A disturbance velocity potential, ϕ_1, is defined by

$$u_1 = u_o(\bar{y}) + \phi_{1\bar{x}} \tag{31a}$$

$$v_1 = \phi_{1\bar{y}}. \tag{31b}$$

Substitution of the above expansions into the full Navier-Stokes equations produces the following nonlinear partial differential equation for the disturbance potential.

$$\left[\chi_t + (\gamma+1) M_\infty^2 \left(u_o(\bar{y}) + \phi_{\bar{x}}\right)\right] \phi_{\bar{x}\bar{x}} - \phi_{\bar{y}\bar{y}} = 0 \tag{32}$$

where γ is the ratio of specific hearts. Equation (32) differs from the standard nonlinear-transonic small disturbance equation only in the appearance of the extra term $u_o(\bar{y})$ which arises from the vorticity in the upstream boundary layer. The pressure is determined from the standard small disturbance relationship

$$p_1 = -\phi_{1\bar{x}} \tag{33}$$

The differential equation is supplemented by boundary conditions requiring the disturbance velocity, $\phi_{1\bar{x}}$, to vanish far upstream (i.e. $\bar{x} \longrightarrow -\infty$) and to

match the prescribed normal shock conditions for $\bar{y} \to \infty$. The formulation is completed by constraining the vertical component of velocity to vanish at the wall, i.e.,

$$\phi_{\bar{y}}(\bar{x}, \bar{y}) = 0 \qquad \bar{y} = 0 \tag{34}$$

The latter condition is deduced from the observation that the blending layer and wall layer are thin and cannot affect the solution in the outer inviscid region.

Equation (32) is a nonlinear mixed elliptic-hyperbolic partial differential equation and must be solved by numerical techniques. Solutions are obtained in Melnik and Grossman's[12] study by use of a Murman-Cole nonconservative finite difference method. The solution is facilitated by a scale transformation that removes all but two parameters, χ_t and $\tilde{\pi}$, from the formulation and leads to the following similarity property of the pressure coefficient

$$C_p = C_p(x,\ y;\ \mathrm{Re},\ M_\infty,\ \gamma,\ \tilde{\pi},\ \delta) = \epsilon C_p(\bar{x},\ \bar{y};\ K_t,\ \tilde{\pi}) \tag{35a}$$

where

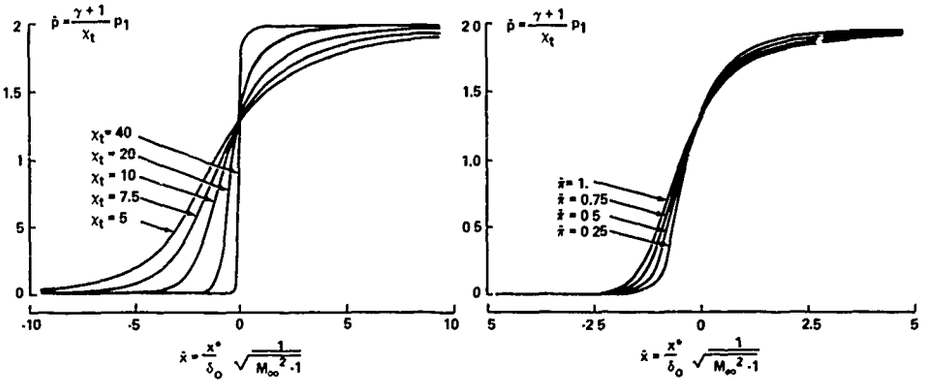
$$\bar{x} = \frac{x}{(\gamma+1)^{1/2} M_\infty \delta \epsilon^{1/2}} \tag{35b}$$

$$\bar{y} = \frac{y}{\delta} \tag{35c}$$

and K_t is a viscous transonic similarity parameter defined by

$$K_t \equiv \frac{\chi_t}{(\gamma+1) M_\infty^2} = \frac{M_\infty^2 - 1}{(\gamma+1) M_\infty^2 \epsilon}, \qquad \epsilon \equiv \sqrt{C_{f_0}(\mathrm{Re})/2} \tag{35d}$$

Thus, flows with the same values of the viscous transonic similarity parameter K_t and Cole's wake parameter, $\tilde{\pi}$, are similar. Results, taken directly from the Melnik and Grossman[12] paper, which illustrate the effect of χ_t, (or K_t), and $\tilde{\pi}$ on the pressures are given in Fig. 15. Recall that χ_t is a measure of the shock strength and $\tilde{\pi}$ is a measure the shape of the initial profile ($\tilde{\pi} \approx \frac{1}{2}$ for a constant pressure turbulent boundary layer). From Fig. 15 it is seen that the effect of increasing shock strength is to reduce upstream influence and to significantly steepen the pressure rise. The overall behavior of the solution in the weak ($\chi_t \to 0$) and moderate shock strength ($\chi_t \to \infty$) limit is evident in the result. The effect of the velocity profile is much less significant. Reduction of $\tilde{\pi}$, corresponding to an increase in the "fullness" of the velocity profile, leads to a reduction of upstream influence and an increase in steepness of the pressure rise as expected.



a) EFFECT OF SHOCK STRENGTH (χ_t) ON SURFACE PRESSURE DISTRIBUTION FOR $\tilde{\pi}$ = 0.5

b) EFFECT OF PROFILE SHAPE ($\tilde{\pi}$) ON SURFACE PRESSURE DISTRIBUTION FOR χ_t = 20.

Fig. 15 Surface pressure distributions from the Melnik-Grossman theory[12] for weak normal shock-waves.

It has not been possible to make an unambiguous comparison of these two-dimensional results with experiment due to the lack of suitable data. Existing channel flow experiments tend to be three dimensional because of the significant effect of the side wall boundary layers. Therefore, in order to compare with the circular pipe flow experiments of Gadd[62] the formulation is generalized to include the extra axisymmetric term arising from the continuity equation. Results of the axisymmetric calculations for one of Gadd's cases are shown in Fig. 16, 17. The results include a plot of the shock shape, sonic line and wave structure upstream of the shock wave. Note that the compression waves generated by the thickening of the upstream boundary layer show no evidence of focusing to form a lambda shock pattern. The theoretical solution for the surface pressure shows reasonably good agreement with Gadd's data, particularly with regard to the extent of upstream influence. Also shown in the result are the downstream limiting values of the pressure as determined from both the axisymmetric and two-dimensional results. The comparison of these limits clearly indicates the significance of the axisymmetric effects in this flow.

Melnik and Grossman[12] have also carried out the formulation and matching analysis of the solutions in the wall and blending layers. The analysis is fairly complicated and is not discussed in this paper except to indicate the form of the solution for the skin friction. The matching of the inner, blending and wall layers leads to the following expression for the skin friction

$$C_f/C_{f_0} = (2 - R)\left[1 + (A_1 + A_2 \epsilon \ln\epsilon)\, \epsilon\, p_{1_W}(x) + O(\epsilon^2)\right] \tag{36a}$$

where

$$R^{-1} = \frac{\rho_w(x)}{\rho_w(0)} = \left\{1 + \epsilon\gamma M_\infty^2 [\epsilon\, p_{1_W}(x) + O(\epsilon^2)]\right\} \tag{36b}$$

$$A_1 = 2/q \tag{36c}$$

$$A_2 = 3\left[\frac{1 + (1 + m_e)\, q}{q^2/2}\right] \tag{36d}$$

$$q = m_e^{-1/2} \sin^{-1}\left(\frac{m_e}{1+m_e}\right)^{1/2} \tag{36e}$$

$$m_e = \left(\frac{\gamma-1}{2}\right) M_e^2 \tag{36f}$$

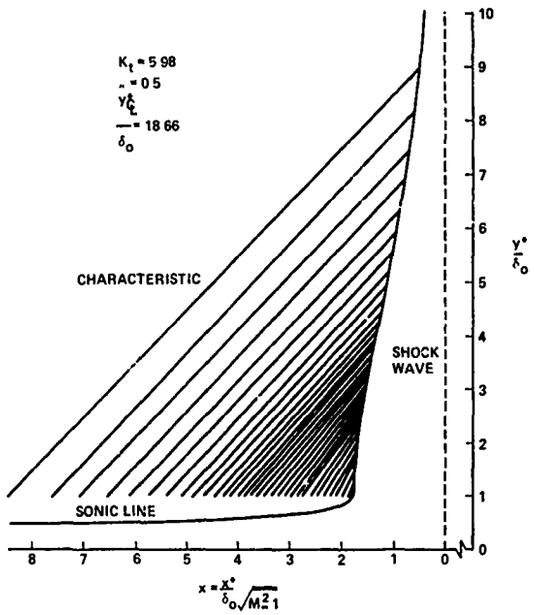


Fig. 16 Computed shock shape, sonic line and characteristics (from Melnik-Grossman theory[13, 14] for weak normal shock-waves – GADD case).

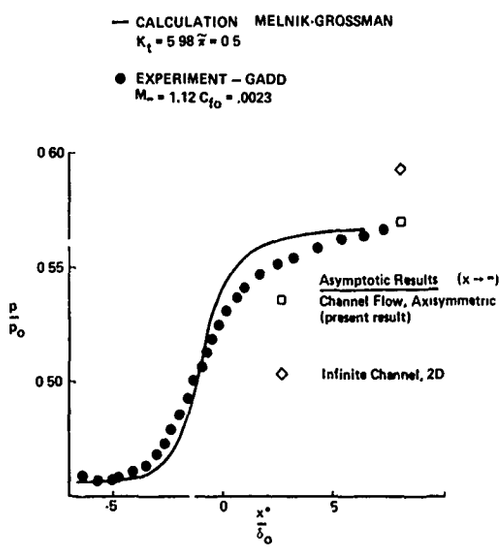


Fig. 17 Comparison of surface pressure distribution from Melnik-Grossman theory[13, 14] with GADD's data for circular pipe.

Equation (36) amounts to a sight rearrangement of the result given in Ref (12) and is intended to improve its accuracy. The particular form of the solution given above results from the compressible version of the law of wall. The factor R^{-1} is equal to the ratio of the density at the wall to its initial value upstream of the interaction. The solution follows directly from a simple matching of the solutions in the various regions and does not, to the order indicated, require solution of the partial differential equations governing the flow in the blending layer. However, the solution of the blending layer equations is required to determine the skin friction to $0(\epsilon^2)$.

The above solution indicates that the skin friction variation throughout the interaction is $0(\epsilon)$, so that separation does not occur in the weak shock limit. The solution suggests that separation first occurs when $\epsilon p_1 = 0(1)$, which implies that the pressure rise for incipient separation, Δp_s, is given by

$$\Delta p_s = 0(1) \qquad \mathrm{Re} \to \infty \tag{37}$$

which corresponds to the str shock limit $\epsilon \to 0, M_\infty^2 - 1 = O(1)$.

3.3.2 Moderate Shock Strengtl. Limit $\chi_t \to \infty$

As this limit is approached the sonic line approaches the wall. The shock wave becomes nearly vertical and approaches the wall, but remains outside the wall layer since $\chi_t < 0(\epsilon^{-1})$ as sketched in Fig. 13c. The mathematical structure of the solution in this limit is sketched in Fig. 18. The structure is similar to that arising in the weak shock limit is shown in Fig. 14 with the exception that extra embedded inviscid region is required at the foot of the shock wave. The solution in this limit can be obtained either from a formal asymptotic analysis of the weak shock formulation (Eq. 32-34) or directly from the full Navier-Stokes equations in the limit $\epsilon \to 0, M_\infty \to 1$ such that $\chi_t \to \infty$. This latter approach has been pursued by Adamson and Messiter[16] in an extensive study and complete solutions of the outer inviscid problem for the pressure distribution have been presented by Messiter[17]. Solutions of the blending layer equations for the skin friction have been obtained by Liou and Adamson[18].

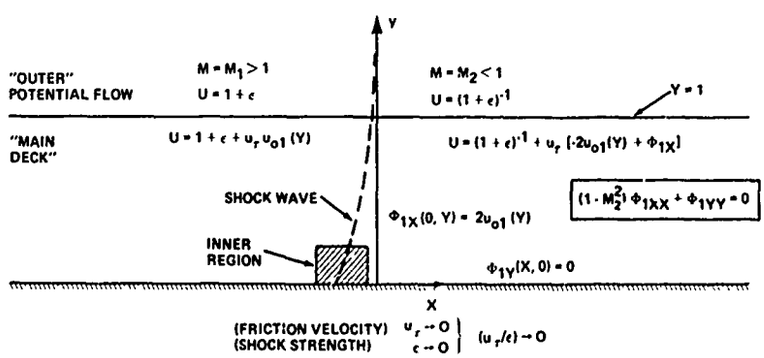


Fig. 18 Adamson-Messiter interaction theory[16, 17] for moderate strength normal shock-waves.

Messiter's [17] solution of the outer problem for the pressure distribution is summarized here. The interested reader is referred to the extensive analysis in Liou and Adamson[18] for a discussion of the solution of the blending and wall layer equations and the determination of the skin friction. Messiter employs a notation different from that used earlier in this paper. In Messiter's study all velocities are referenced to sonic speed, the friction velocity is denoted by u_τ and the parameter ϵ denotes a nondimensional shock strength parameter defined by the condition $\epsilon = 1 - U_\infty$ where U_∞ is the nondimensional free stream speed upstream of the shock wave. In the following discussion the notation of Messiter's original papers is employed.

In the moderate shock strength limit the flow upstream of the shock wave is undisturbed with the streamwise velocity given by

$$U = 1 - \epsilon + u_\tau u_0(y) \tag{38}$$

The solution on the downstream side of the shock wave is expanded in the form

$$U = 1 - \epsilon + u_\tau [u_0(y) + \phi_{1x}(x, y) + \cdots] \tag{39a}$$

$$V = \epsilon^{1/2} u_\tau (\gamma + 1) [\phi_{1y}(x_1 y) + \cdots] \tag{39b}$$

where the stretched variables x, y are defined in terms of the unstretched coordinates X, Y by

$$X = (\gamma + 1) \epsilon^{1/2} u_\tau x, \quad Y = \delta y. \tag{40}$$

Substitution of the expansions into the full Navier-Stokes equations indicates that the flow on the downstream side of the shock wave can be treated as a simple linear perturbation to the state downstream of the normal shock wave. With the chosen normalization, the disturbance potential is governed by Laplace's equation

$$\phi_{1xx} + \phi_{1yy} = 0. \tag{41a}$$

The effect of the blending and wall layers on the outer inviscid flow is also negligible in this case so that the boundary condition, $\phi_{1y}(x,0) = 0$ on the plate surface is appropriate. The remaining boundary conditions are also the same as in the weak shock limit, except that the asymptotic upstream condition is replaced by normal shock conditions on the x axis. Thus,

$$\phi_{1x}(x, y) = -2u_0(y) \quad x \to 0_+ \tag{41b}$$

The solution of the linear boundary value problem can be found by inspection. The solution for the pressure distribution on the wall is given in terms of a simple line integral along the shock wave, i.e.

$$p_w(x) = -u_\tau \gamma \phi_{1x}(x, y) = (4\gamma u_\tau/\pi) \int_0^\infty \frac{u_0(\eta)}{x^2 + \eta^2} \, d\eta \tag{42}$$

The solution for the pressure develops a logarithmic singularity at the foot of the shock wave given by

$$p_w(x) \to (2\gamma u_\tau^2/k) \ln(x) \quad \text{for } x \to 0_+ \tag{43}$$

A typical result taken from Adamson and Messiter[16] is given in Fig. 19. Comparison of the theory with experiment have been hindered by lack of suitable two-dimensional data. Nevertheless, Messiter[17] carried out a comparison of the two-dimensional theory with Ackeret, Feldmann and Rott's experiment [63] for transonic flow over a "bump" on a wind tunnel wall. The comparisons showed only qualitative agreement probably because the assumptions of the theory ($\chi_t \gg 1$) were not well satisfied in this experiment, in which the sonic line was not near the wall. For further discussion of this comparison the reader is referred to Messiter[17].

An axisymmetric version of the theory has also been developed by Messiter[17] for comparison with Gadd's[62] circular pipe data. The axisymmetric solution is given in form of an infinite series. Figure 20 compares the axisymmetric solution with Gadd's[62] measurements of the surface pressure for the same case as discussed earlier in this paper. For comparison, the figure also includes Melnik and Grossman's [13,14] axisymmetric solution for the same case. These results clearly show a significant axisymmetric effect in the same manner as is evident in the weak shock solution. It should be noted that Messiter's solution is a large χ_t approximation to the more exact Melnik, Grossman theory. The significant differences between the two solutions, evident in Fig. 20, is probably because the underlying assumptions of the moderate shock limit, $\chi_t \to \infty$ are also not well met in this case. In particular, in this experiment, the sonic line is positioned in about the middle of the boundary layer (i.e., $\delta_{sonic}/\delta \simeq 0.45$) while the Messiter theory assumes it to lie near the wall!

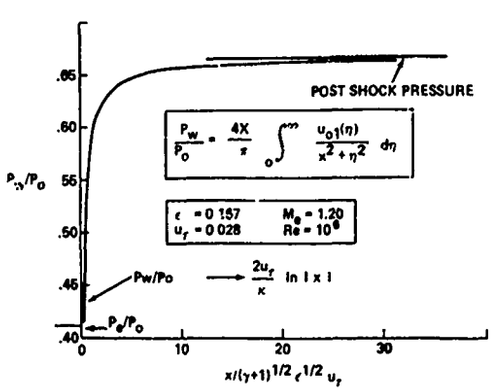


Fig. 19 Calculated wall pressure distribution from Adamson-Messiter theory for normal shock-wave interacting with a turbulent flat plate boundary layer. (REPRINTED FROM REF 16)

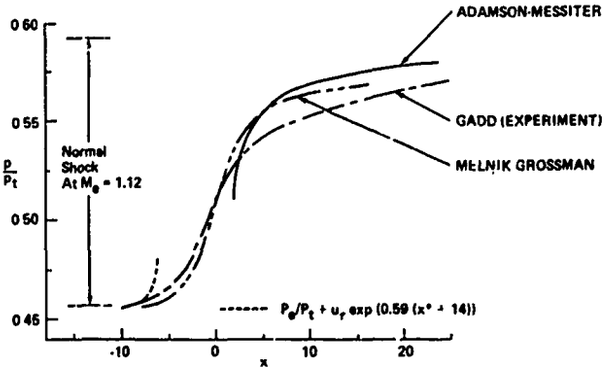


Fig. 20 Surface pressure distribution in a circular pipe. (REPRINTED FROM REF 17)

3.3.3 Current Status of the Asymptotic Theories

The asymptotic methods described here provided a nearly complete local description of the interaction of a shock wave with a turbulent boundary layer under the conditions of most interest for airfoils in the transonic regime. The principal conclusion of these studies is that the local interactions in the main part of a turbulent boundary layer are dominated by inviscid mechanisms and are independent of the direct influence of turbulent structure. Both the asymptotic theories[12-18] and the numerical studies of Roshko and Thomke[51] and others provide convincing evidence that the pressure distribution and the flow in the main part of the boundary layer are well represented by solutions of the inviscid rotational flow equations. Turbulence structure and closure assumptions have only an indirect influence on the overall solution through their effect on the establishment of the initial velocity profile upstream of the interaction. These studies also clearly indicate that the solution in the outer region of a turbulent interaction is little affected by sublayer displacement effects of the type arising in laminar interactions. Lighthill's 1953 proposal to treat turbulent interactions using an interacting sublayer formulation (followed up in the recent work of Inger-Mason [56] and Bohneng-Zierep [57,58]), is not supported either by rational asymptotic analyses or by the numerical studies of Roshko, Thomke[51] and Rose, Murphy and Watson[50].

The local asymptotic solutions discussed in this section have not yet been integrated into an overall airfoil computation. The main issue that must be resolved before this can be accomplished is to determine how the differences between theory and observations for the pressure rise across the shock wave can be accommodated in an overall airfoil calculation. Both experiments and interacting boundary layer solutions on airfoils display shock pressure rises that are only about half those required by the normal shock wave relations while the local strong interaction theories for flat plates indicate a full pressure rise to normal shock wave levels.

4. STRONG TURBULENT INTERACTIONS AT A TRAILING EDGE

It is well known that both laminar and turbulent flows near the trailing edge of an airfoil involve a strong viscid-inviscid interaction between the boundary layer, wake and external inviscid flow. Although the analysis of the local flow near the trailing edge involves a multi-layer description in both the laminar and turbulent case the analytical structure of the solutions are vastly different. For laminar flows, the displacement effect of the sublayer on the outer inviscid flow is the dominant physical mechanism in the interaction, while in turbulent flow it is entirely negligible. Detailed analytical studies by Stewartson[48], Messiter[49] and Brown and Stewartson[64] have established that the boundary layer approximations remain valid, to lowest order, at the trailing edge when the boundary layer is laminar. In this case, the "triple deck" theory (see Stewartson[23] for a comprehensive review of laminar interaction theory), which follows from a rational asymptotic analysis of the Navier-Stokes equations for $Re \to \infty$, provides a complete description of the local flow near the trailing edge of a cusped airfoil. This analysis indicates that the singularities that arise in the weak interaction solution at the trailing edge are caused by the use of the inviscid solution for the leading approximation to the pressure distribution. The "Triple Deck" theory shows that the singularities are removed if the pressure distribution is determined from a self-consistent solution of the coupled inviscid and (sublayer) boundary layer equations. Thus, the theory establishes a formal justification for the use of IBLT at the trailing edge when the boundary layer is laminar.

When the boundary layer is turbulent at the trailing edge, the resolution of the nonuniformity in the weak interaction solution occurs through a completely different mechanism. In a turbulent flow the interaction region is narrow (the order of a boundary layer thickness) and consequently, the streamline curvatures and normal pressure gradients are moderately large in the vicinity of the trailing edge. Melnik et al. [8, 11] have shown that the pressure variations across the boundary layer are an order of magnitude larger than the pressure variations induced by the boundary layer displacement effect. Quantitatively, the normal pressure gradient effect is $0(\epsilon^{3/2})$ in comparison to the $0(\epsilon^2)$ effect of the displacement thickness (ϵ is equal to the friction velocity as in the early sections of this paper). Experimental evidence of significant normal pressure gradients in the trailing edge region appears in the early works of Preston and Sweeting[65] and Mendelson[66]. The occurrence of significant normal pressure gradients near the trailing edge in a turbulent flow raises the possibility of a failure of the boundary layer approximation in this region. The asymptotic estimates in Melnik et al.[8, 11] demonstrate that this is indeed the case for airfoils with cusped trailing edges and is also certainly true for airfoils with wedge-shaped trailing edges.

Of course IBLT, which is based on the boundary layer approximation and ignores normal pressure gradient effects, has for many years been routinely applied to airfoil problems involving turbulent boundary layers. Numerical experience with IBLT suggests that the coupling of the inviscid and boundary layer equations to obtain self-consistent solutions for the pressure and boundary layer development eliminates the singularities that would otherwise arise in a weak interaction solution. Detailed analysis indicates that the streamwise extent of the trailing edge interaction region implied by IBLT is $0(\epsilon^2)$ which is much too small and clearly incompatible with the normal momentum equation. These studies indicate that, although IBLT seems to produce reasonable behavior at the trailing edge, these solutions are not entirely satisfactory and should be corrected to account for pressure variations across the boundary layer and wake in the trailing edge region.

Melnik et al.[8-11] have developed a local analytical solution for strong turbulent interaction at a trailing edge under the assumptions that the Reynolds number is large, and that the boundary layer upstream of the trailing edge is fully developed with a velocity profile described by Coles' law of the wake/law of wall. It is also assumed that the boundary layer is unseparated, that the airfoil has a cusped trailing edge and that the local flow near the trailing edge is completely subsonic. Under the above conditions they develop a local solution from a formal asymptotic expansion of the full (averaged) Navier-Stokes equations in the limit of large Reynolds numbers ($Re \to \infty$). The analysis yields a three layer structure of the boundary layer that is similar to that arising in Melnik and Grossman's[12] weak shock theory. The principal results of the study are the establishment of a closed form analytical solution for the inviscid outer region of the boundary layer and the development of procedures for incorporating the local trailing edge solution into a complete airfoil method. In this section a review of the Melnik et al.[8-11] development of the local trailing edge solution is given and in the following section its application to the solution of a complete airfoil problem is discussed.

The asymptotic structure deduced by Melnik et al.[8-11] for $Re \to \infty$ is sketched in Figure 21 along with a specification of the length scales of the various regimes. The overall structure is similar to that which appears in the asymptotic analysis of a shock-wave boundary-layer interaction. Upstream of the interaction the turbulent boundary layer develops a conventional two layer structure with a law of the wake/law of the wall velocity profile. In the interaction region the solution develops a three layer structure to accommodate the mismatch between the inner and outer layer Reynolds stresses. The length scales in the trailing edge and shock wave interaction problems differ only because of the differences in the assumed value of the local free stream Mach number. A new feature appearing in the trailing edge structure is the additional embedded region in the wall layer at the trailing edge. The width of this "inner wall" layer is the same order of magnitude as the thickness of the wall layer, $\epsilon\delta$. This extra region is required to properly describe the extinction of the wall layer as it crosses the trailing edge into the wake. It can be shown that the solution in this region requires a description based on the full Navier-Stokes equations. The need for this "extra" region has not been discussed in previous publications[8-11] by the author.

The overall structure of the trailing edge solution follows from the general observations that, 1) pressure gradients do not influence the solution in the wall layer, 2) both inner sublayers can be neglected in the solution of the outer region, 3) the small streamwise length scale of the interaction justifies the neglect of Reynolds stresses in the outer region, and 4) the flow is subsonic in the entire interaction region. These observations again lead to the conclusion that the flow in the outer region can be approximated as an inviscid rotational flow that can be determined without the need to consider the flow in the two inner sublayers.

Only the solution in the outer inviscid rotational flow is addressed in the study of Melnik et al.[8]. The asymptotic analysis reduced the outer problem to the solution of the subsonic rotational flow equations with the vorticity completely defined by the upstream velocity profile. Since sublayer displacement ef-

fects are negligible the formulation leads to standard impermeable wall conditions at the airfoil surface. Because of the law of the wall/law of the wake form assumed in the initial profile, the nonuniformity in the upstream boundary layer can be assumed to be small in the limit $\epsilon \to 0$. It follows that the external potential flow solution provides the leading approximation to the inviscid rotational flow solution in the outer part of the boundary layer. For cupsed airfoils, the surface geometry can be represented locally as a flat p'ate and the streamlines of the external potential flow can be assumed to be nearly parallel in the vicinity of the trailing edge. These observations suggest that the effect of the boundary layer can be found from a superposition of weak, rotational, disturbances on an irrotational, nearly parallel main stream. Following this suggestion, Melnik et al.[8] are led to assume the following asymptotic expansion for the stream function and the horizontal and vertical components of velocity in the outer, trailing edge region,

$$\psi = \Psi_{inv}(x,y) + \epsilon^2 \psi_o(y) + \epsilon^{5/2}\psi_1(x,y) \tag{44a}$$

$$u = U_{inv}(x,y) + \epsilon u_o(y) + \epsilon^{3/2} u_1(x,y) + \cdots \tag{44b}$$

$$v = V_{inv}(x,y) + \epsilon^{3/2} v_1(x,y) + \cdots \tag{44c}$$

where x, y are stretched cartesian coordinates parallel and normal to the flat plate approximating the airfoil Ψ_{inv}, U_{inv}, V_{inv} are the stream function and the horizontal and vertical velocity components from the external potential flow solution, U_{te} is the value of U_{inv} at the trailing edge, ψ_o (y) and u_o (y) are the defect parts of the initial stream function and velocity profiles. The velocity defect is assumed to have the form given in Eq (30),

$$u_o(y) = u_* k^{-1}[\ln(y/\delta) + \tilde{\pi} W(y/\delta)] \tag{45}$$

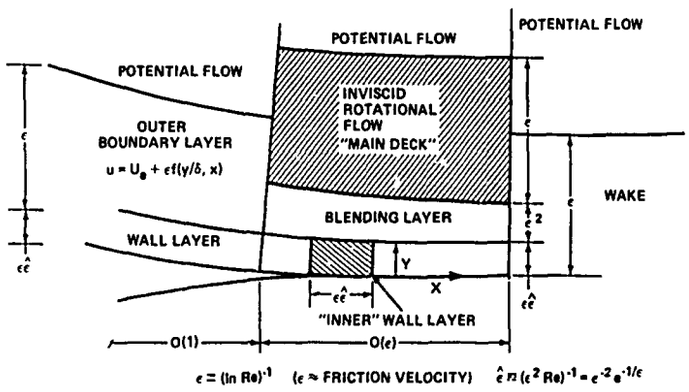


Fig. 21 Asymptotic flow field structure near trailing edge in Melnik et al theory[8-11].

The quantities u_1, v_1 are the disturbance velocities induced by the interaction of the boundary layer with the external potential flow. The stretched coordinates are defined in terms of the physical cartesian coordinates x*, y* and the thickness of the boundary layer $\delta(\epsilon)$ upstream of the trailing edge by

$$x \equiv x^*/\delta(\epsilon), \quad y = y^*/\delta(\epsilon) \tag{46}$$

where we recall $\delta(\epsilon) = 0(\epsilon)$. The local analysis requires only the expansion of the potential flow solution near the trailing edge, which is written in the (complex) form

$$U_{inv} - \frac{i}{B} V_{inv} = U_{te}\left[1 - i\epsilon \frac{C_\alpha}{B} (x + iBy)^{1/2} + \cdots\right]$$
$$B = \sqrt{1 - M_{te}^2}, \quad i \equiv \sqrt{-1} \tag{47}$$

where M_{te} is the Mach number at the trailing edge and C_α is a constant, both determined from the potential flow solution. Substitution of the above expansions into the full Navier-Stokes equations produces a set of linearized shear layer equations for compressible flow. A straightforward generalization of the Prandtl-Glauert transformation to rotational flow eliminates most of the parameters appearing in the formulation and reduces the boundary value problem to an equivalent incompressible flow. The transformed disturbance stream function and velocities $\bar{\psi}_1, \bar{u}_1, \bar{v}_1$ are determined from solutions of the Poisson equation,

$$\nabla^2 \bar{\psi}_1 = -\bar{\zeta}_1(\bar{x}, y) \equiv \bar{u}_0''(y)\, \Psi_1(\bar{x}, y) \tag{48a}$$

and

$$\bar{u}_1 = \bar{\psi}_{1y}, \quad \bar{v}_1 = -\bar{\psi}_{1\bar{x}} \tag{48b}$$

where $\bar{\zeta}_1(\bar{x}, y)$ is the disturbance vorticity and $\Psi_1(\bar{x}, y)$ is the (scaled) perturbation stream function of the external potential flow, given by

$$\Psi_1(\bar{x}, y) \equiv -\tfrac{2}{3} C_\alpha \rho_{te} U_{te} \mathrm{Real}\{\bar{x} + iy\}^{3/2} \tag{49}$$

and $\bar{x}$ is a transformed coordinate defined by

$$\bar{x} \equiv x/B \tag{50}$$

The transformed pressure is determined from

$$\bar{p}_1 = -\bar{u}_1(\bar{x}, y) - \bar{u}_o(y)\, U_1(\bar{x}, y) + \bar{u}_o'(y)\, \Psi_1(\bar{x}, y) \tag{51}$$

The form of the perturbation vorticity, $\bar{\zeta}_1(\bar{x}, y)$, appearing in Eq. 48 can be understood from the following Taylor series expansion of the "exact" vorticity

$$\bar{\zeta}(\psi) = \bar{\zeta}\{\epsilon y + \epsilon^{3/2}\Psi_1(\bar{x}, y) + \cdots\} \tag{52}$$

$$= \underbrace{-\bar{u}_o'(y)}_{\substack{\text{vorticity in the} \\ \text{initial profile}}} \underbrace{-\epsilon^{1/2}\bar{u}_o''(y)\Psi_1(\bar{x}, y) + \cdots}_{\substack{\text{disturbance} \\ \text{vorticity, } \bar{\zeta}_1}}$$

From Eq. 52, $\bar{\zeta}_1$, can be interpreted as a vorticity disturbance generated by convection of the known upstream vorticity along the streamlines of the inviscid potential flow as indicated schematically in Fig. 22.

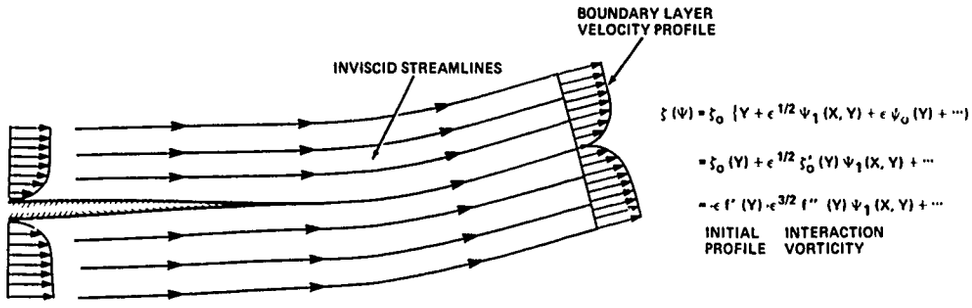


Fig. 22 Vorticity distribution in trailing edge region.

Equation (48) is to be solved subject to the boundary conditions

$$\bar{v}_1(\bar{x},0) = -\bar{\psi}_{1\bar{x}}(\bar{x},0) = 0 \qquad \bar{x} < 0 \tag{53}$$

$$\bar{p}_1(\bar{x},y) \text{ and } \bar{\omega}_1(x,y) \text{ is continuous at } y = \begin{pmatrix} 0 \\ \delta_t \\ \delta_b \end{pmatrix} \tag{54}$$

where $\bar{\omega}_1$ is the perturbation flow angle, defined by,

$$\bar{\omega}_1(\bar{x},y) \equiv \bar{v}_1(\bar{x},y) - \bar{u}_o(y)\,V_1(\bar{x},y) \tag{55}$$

and δ_t, δ_b denotes the edge of the upper and lower boundary layer. In addition, a far field boundary condition

$$\bar{u}_1 - i\bar{v}_1 \to \frac{D_\alpha \ln(\bar{x}+iy)+K}{(\bar{x}+iy)^{1/2}} \text{ for } |\bar{x}+iy| \to \infty \tag{56}$$

is required where the above form is determined by matching to the weak interaction solution upstream of the trailing edge, D_α is a known constant and K is a constant to be determined as part of the inner trailing edge solution. The solution of this boundary value problem is not unique, as it contains a one parameter family of solutions, each having a different singular behavior at the trailing edge. Uniqueness is obtained by imposing a "Kutta" condition requiring the pressure to bounded at the trailing edge. Thus

$$\bar{p}_1(\bar{x},y) \quad \text{bounded for } (\bar{x}+iy) \to 0 \tag{57}$$

This condition amounts to a correction to the usual "Kutta" condition in the inviscid flow, to account for the variation of pressure across the boundary layer.

The above problem is a standard linear elliptic boundary value problem similiar in type to that arising in thin airfoil theory. The solution is represented as a sum of particular and homogeneous solution.

$$\bar{\psi}_1 = \bar{\psi}_{1p} + \bar{\psi}_{1h} \tag{58}$$

Closed form analytical expression for the particular integral is given in the original work[8]. Solutions for the homogeneous contributions are not presented but can easily be obtained by standard thin airfoil techniques. The solutions for the particular integral result in the following expressions for the downwash and pressure on the airfoil and wake centerline (y = 0)

$$\bar{v}_{1p}(\bar{x},y) = \frac{C_\alpha u_e \delta^{1/2}}{k}\{\sigma_1(\bar{x}/\delta) + \tilde{\pi}\sigma_2(\bar{x}/\delta)\} \tag{59a}$$

$$\bar{p}_{1p}(\bar{x},0) = \frac{C_\alpha u_e \delta^{1/2}}{k}\{\beta_1(\bar{x}/\delta) + \tilde{\pi}\beta_2(\bar{x}/\delta)\} \tag{59b}$$

where $\sigma_{1,2}$ and $\beta_{1,2}$ are explicit algebraic expressions given in the original papers. The σ_1, β_1 terms arise from the law of the wake and the σ_2, β_2 terms arise from the law of the wall components of the initial velocity profile. The functions are graphed for negative values of $\bar{x}/\delta$ in Fig. 23. Values for positive $\bar{x}/\delta$ follow from the skew symmetric property

$$\beta_{1,2}(-\bar{x}/\delta) = \sigma_{1,2}(\bar{x}/\delta) \tag{60}$$

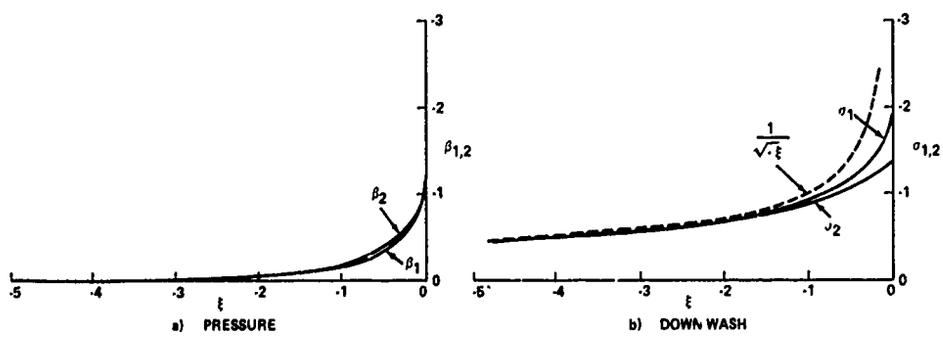


Fig. 23 Particular solutions for local trailing edge problem.

Contributions from the boundary layers on the upper and lower surfaces are treated separately resulting in expressions of the form given in Eq. (59) which are then superposed to complete the particular solution.

The analysis in this section shows that strong interaction effects at the trailing edge can be represented by simple (inviscid) vorticity concepts. The particular integral provides expressions for the direct effect of the vorticity in the boundary layer and wake on the local flow near the trailing edge. The solution shows that there are two effects, one a downwash on the airfoil and the other, a pressure drop across the boundary layer/wake, each induced by the spatial distribution of vorticity along the curved streamlines near the trailing edge. Homogeneous solutions are added to the particular integrals in order to cancel the downwash on the airfoil and the pressure jump in the wake generated by the particular solution at $y = 0$.

Although only the particular integrals have been determined in the study, they are all that is required to correct IBLT for strong interactions at the trailing edge. Melnik et al.[10,11] have shown how the particular integrals for the downwash and pressure Eq. (59) can be used to make local corrections to the transpiration velocity and wake curvature boundary condition of IBLT in the vicinity of the trailing edge of cusped airfoils. These procedures are reviewed in the next section.

The studies of Melnik et al.[8-11] leave unfinished the solution of the inner sublayers which are required to complete the solution for the skin friction. They also do not address the solution of the "inner wall" layer which is required for the detailed description of the transition from boundary layer type velocity profiles on the airfoil to wake-like profiles downstream of the trailing edge. In a related matter it should be noted that the local trailing edge solution develops a strong "pole" singularity on the wake axis $y = 0, x > 0$. The singularity is related to an improper shift of the logarithmic term in the velocity profile from the wake streamline ($y = y_0(x)$ to the wake axis ($y = 0$). This singularity, which was not noted in previous studies of the problem, is easily removed either by a simple "PLK" type coordinate straining or by the use of von Mises' streamline coordinates (x, Ψ) in place of the cartesian coordinates (x, y). With the elimination of the pole singularity, the velocity profile in the wake is given to lowest order by the initial profiles shifted from the y axis to the wake streamline $y = y_0(x)$. Thus, the outer solution in the wake is given by

$$U = \begin{cases} U_{te} + \dfrac{\epsilon u_{*t}}{k}\left[\ln\left(\dfrac{y - y_0(x)}{\delta_t}\right) + \tilde{\pi}_t W\left(\dfrac{y - y_0(x)}{\delta_t}\right)\right] + \cdots & \text{for } y - y_0(x) > 0 \qquad (61a) \\ U_{te} + \dfrac{\epsilon u_{*b}}{k}\left[\ln\left(\dfrac{y_0(*) - y}{\delta_b}\right) + \tilde{\pi}_b W\left(\dfrac{y_0(x) - y}{\delta_b}\right)\right] + \cdots & \text{for } y - y_0(x) < 0 \qquad (61b) \end{cases}$$

It is clear from Eq. (61) that the outer solution is not uniformly valid in the wake because of the logarithmic behavior at the wake axis. The transition from the logarithmic behavior in the outer solutions on either side of the wake to a wake-like profile at the wake axis is effected by a separate "inner" wake solution centered on the wake axis. The details of the solution in this region have not yet been addressed. Although these matters are of some theoretical interest and should be pursued in the interest of completing the theoretical description of the trailing edge region, they do not affect the determination of the particular integral or their use in correcting IBLT.

5. AIRFOIL COMPUTATIONS

Melnik et al. (MCMJ[10,11]) have developed systematic procedures for incorporating the local trailing edge solution into a complete airfoil computation. Referring to the earlier general discussion of viscous effects on airfoils, (in connection with Fig. 1) the MCMJ method accounts for four of the five important viscid-inviscid interaction effects occurring in transonic flows over airfoils, namely, displacement effects on the airfoil, wake thickness, wake curvature and trailing edge interaction effects. The local solution employed for the trailing edge interaction is strictly applicable only for airfoils with cusped or nearly cusped trailing edges. Nevertheless, the method seems to produce reasonably good predictions of the pressures and forces on practical airfoil shapes, although there is a tendency to overpredict the pressure levels at the trailing edge and to underpredict the drag when the trailing edge included angle is greater than about 15°.

The method does not provide for a satisfactory treatment of the shock-wave boundary-layer interaction. In this region the MCMJ formulation reduces to a standard version of IBLT employing a transpiration boundary condition for the displacement effect. Recall, from Section 2, that this form of the matching condition always leads to subcritical behavior at a shock-wave boundary-layer interaction. The shock wave is weakened by boundary layer generated compressions so that it does not impinge on the boundary layer, and the pressure discontinuity at the shock wave is replaced by a steep but smooth pressure rise across the interaction zone (see Fig 5). Although this flow model certainly does not lead to a correct detailed description of the interaction, (it does not account for shock penetration or normal pressure gradients) it does seem to produce a very good prediction of the pressure level behind the shock wave.

In this section I briefly review the overall features of the MCMJ method and present some comparisons with experimental data that are indicative of the accuracy that can be achieved with the method. Also discussed are the results of some theoretical experiments that illustrate the sensitivity of solutions to selected components of the viscous matching conditions. The discussion is based on results obtained with the latest version[10,11] of code. The new version of the code eliminates certain numerical smoothing procedures that had been employed at the shock wave and trailing edge and simplifies the method for incorporating the local trailing edge solution into the formulation. Numerical smoothing was employed in the early stages of the study because of anticipated numerical problems in the strong interaction regions. It was subsequently discovered that such smoothings are not only unnecessary but, in fact, are the source of the objectionable "wiggles" sometimes evident in such calculations[8]. It should be stressed that the latest version of MCMJ[10,11] employs no numerical smoothings and contains no adjustable parameters (aside from those appearing in the turbulence model).

Recently, other boundary layer type methods have also been developed for computing viscous flows over airfoils at transonic speed. The CL[7] method of the RAE is similar in many respects to the MCMJ method, but does not account for strong interaction effects at the trailing edge. It also differs in its use of a partially conservative (PC) method for the solution of the inviscid equations (MCMJ employs a fully conservative (FC) method.) The RAE method is described in the paper given by Lock at this meeting.

Two other methods of interest were recently developed by Whitfield, Swafford and Jacocks[67] and by Nandanan, Stanewsky and Inger[68]. Since these methods are very new there has not been sufficient time to properly study them for inclusion in the present paper, hence only the following brief remarks are made. Both methods, in common with the MCMJ[10,11] and CL[6,7] procedures, employ an integral method for the trubulent boundary layer. The Whitfield et al,[67] method is based on conventional IBLT with a transpiration velocity form of the viscous matching condition. The method basically accounts only for displacement effects on the airfoil and does not incorporate any of the wake or strong interaction effects discussed in this paper. It does, however, provide for a more accurate description of the inviscid flow based on solutions of the full Euler equations and it does allow for three dimensional effects in the inviscid solution. Results are not presented for lifting airfoils at transonic speed but applications in this direction are in progress. The Euler solutions obtained with this code can be expected to be very useful for assessing the adequacy of the potential flow approximation in flows involving boundary layer effects.

The Nandeman et al.[68] method is also an IBLT approach; it is basically a modification of the BGKJ[5] method aimed at improving the solution at shock waves. It employs the displacement thickness form of the matching condition and does not fully account for wake effects and trailing edge interaction effects

(the wake is modeled by a semi-infinite parallel displacement body as in the original BGKJ formulation) The method employs the Inger and Mason[56] strong interaction solution to correct the pressure and displacement thickness near shock waves but then arbitrarily smooths the "corrected" displacement thickness across the shock wave. They also employ an arbitrary procedure to reduce the pressure rise in the Inger and Mason solution to match the smaller jump observed in experiments. Because of the arbitrariness of these steps it is difficult to evaluate the effectiveness of these correction procedures, particularly since IBLT by itself already gives very good results for the pressure rise across shock waves without using any empirical information or numerical smoothings.

5.1 Trailing Edge Corrections

The procedures developed by Melnik et al.[10,11] use the local trailing edge solution (Section 4) to correct IBLT for strong interactions at the trailing edge. In their approach the complete viscous solution is represented by composite expressions formed by adding contributions from the inviscid, boundary layer and trailing edge solutions and subtracting their "common parts". The result is a standard sum-type composite solution of the method of matched asymptotic expansions. For example, the representation for the velocity components and pressure are written in the form

$$U = U_{inv}(N, S, V_\sigma; [\![V_\sigma]\!]; \Gamma) + [U_{bl}(\eta, S) - \bar{U}_{bl}(\eta, S)] + [U_{te}(\eta, \xi) - \bar{U}_{te}(\eta, \xi)] \tag{62a}$$

$$V = V_{inv}(\quad\quad\quad\quad\quad\quad) + [V_{bl}(\eta, S) - \bar{V}_{bl}(\eta, S)] + [V_{te}(\eta, \xi) - \bar{V}_{te}(\eta, \xi)] \tag{62b}$$

$$P = P_{inv}(\quad\quad\quad\quad\quad\quad) + [P_{bl}(\eta, S) - \bar{P}_{bl}(\eta, S)] + [P_{te}(\eta, \xi) - \bar{P}_{te}(\eta, \xi)] \tag{62c}$$

where N, S are curvilinear coordinates normal and tangent to the airfoil surface and wake streamline, U and V are the streamwise and normal components of velocity along the N, S coordinates lines and η, ξ are stretched coordinates defined by

$$\eta \equiv N/\epsilon \qquad \xi = (S - S_{te})/\epsilon \tag{63}$$

The leading terms in Eq. (62) are solutions of the outer inviscid equations with viscous matching condition, the terms of the second group are from solutions to boundary layer equations minus their "common parts" (denoted by a bar) and the terms of the third group are from the local solutions in the trailing edge region minus their "common parts". The function, V_σ, is the transpiration velocity appearing in the boundary condition on the airfoil surface (N = 0); $[\![V_\sigma]\!]$ is the jump in transpiration velocity along the wake streamline arising from the wake thickness effect and Γ is the "circulation" along the wake streamline arising from the wake curvature effect. The circulation is equal to the jump in potential across the wake $\Gamma = [\![\phi]\!]$. Expressions for these quantities can be found by imposing boundary and continuity conditions on the composite solutions U, V, P. For example, when the trailing contributions to the solution in Eq (62) are neglected, the usual matching conditions in IBLT are recovered by requiring the composite expression for V to vanish on the airfoil surface and also requiring the composite solution to be continuous in the wake. Thus, in this case, we obtain

$$V_\sigma = \epsilon^2 \left[\frac{d\rho_e U_e \delta^*}{\rho_e dS} \right] \tag{64a}$$

$$[\![V_\sigma]\!] = \epsilon^2 \left[\frac{d\rho_e U_e \delta^*_w}{\rho_e dS} \right] \tag{64b}$$

$$\frac{d\Gamma}{dS} = -\epsilon^2 [U_e(\delta^*_w + \theta_w)\, \kappa(S)] \tag{64c}$$

where the subscript, e, denotes surface values of the composite solution and where δ^*_w and θ_w are the "total" displacement and momentum thicknesses of the wake. Equation (64c) is equivalent to the wake curvature given in Eq. (15).

The key to Melnik et al.[10,11] approach is the use of corrected or "composite" matching conditions in the solution to the outer inviscid problem. Corrected matching conditions are found by repeating the above procedure but this time retaining the contributions of the local trailing edge solution to the composite expressions, Eq. (62). Only the contributions from the particular integral are included in the trailing edge term in Eq. (62). It can be shown that this is equivalent to incorporating the homogeneous parts of the trailing edge solution in the first (inviscid) terms of Eq. (62).

The composite matching conditions derived in this manner are in the form of a sum-type composite expansion. Away from the trailing edge, the expressions reduce to the conventional matching conditions given in Eq. (64) while in the vicinity of the trailing edge they include extra terms that "correct" for strong effects at the trailing edge. In addition to providing corrections to the matching conditions, the composite expressions for the surface pressure, Eq. (62c). with N = 0, also includes terms that account for the pressure change across the boundary layer and wake.

For convenience in numerical applications the sum-type composite matching conditions for V_σ and Γ are replaced by equivalent multiplication type expressions of the form

$$V_\sigma = \epsilon^2 \left[\frac{d\rho_e U_e \delta^*}{\rho_e dS} \right] G_n \tag{65a}$$

$$\frac{d\Gamma}{dS} = -\epsilon^2 [U_e(\delta^*_w + \theta_w)\, \kappa(S)]\; G_w \tag{65b}$$

where the functions G_n, and G_w are analytic expressions determined from the local trailing edge solution. Equations (65) provide corrected matching conditions that are uniformly valid in the trailing edge region. The functions G_n and G_w approach zero at the trailing edge with a square root behavior that just cancels the singularities that arise in the conventional matching conditions. Both functions approach one for $|\xi| \to \infty$ and Eq. (65) reduce to the standard matching conditions in this limit. Near the trailing edge ($\xi \equiv O(1)$), equations (65) reduce to a form that recovers the local trailing edge solution

The correction for the wake thickness term is stated in the form

$$[\![V_\sigma]\!] = \epsilon^{3/2} G_t + \epsilon^2 \frac{d\rho_e U_e \delta^*_w}{\rho_e dS} \tag{66}$$

where G_t is also an analytic expression determined from the local trailing edge solution. A sum type composite expression is employed for this term because, here, the common part vanishes to the order considered and expressions like Eq. (65) cannot be formed. The correction functions completely eliminate the singularities arising in the conventional matching conditions and lead to solutions that are uniformly valid in the trailing edge region.

The composite solution for the pressure on the airfoil surface can be written in the form

$$P_b = P(N = 0, S) = P_{inv}(0, S) - \epsilon^{3/2} \Delta P \tag{67}$$

where the first term is determined from the outer inviscid solution (subject to the composite matching conditions) and the second term is a correction to

account for the pressure change across the boundary layer in the trailing edge region. The matching conditions lead to the discontinuities in the pressure across the wake in the outer inviscid solution given by the first term in Eq. (62c). Compensating discontinuities also arise in the other terms of Eq. (62c) which exactly cancel the jump in the first term leading to a composite solution that is continuous across the wake, as it should be.

Typical results illustrating the effect of the trailing edge corrections on the transpiration boundary condition and the wake curvature condition are given in Fig. 24. The quantity V_A is the difference between the transpiration velocity on the upper and lower surfaces of the airfoil (equivalent camber effect) and ΔC_p is the equal to the jump in pressure coefficient across the wake appearing in the outer inviscid solution.

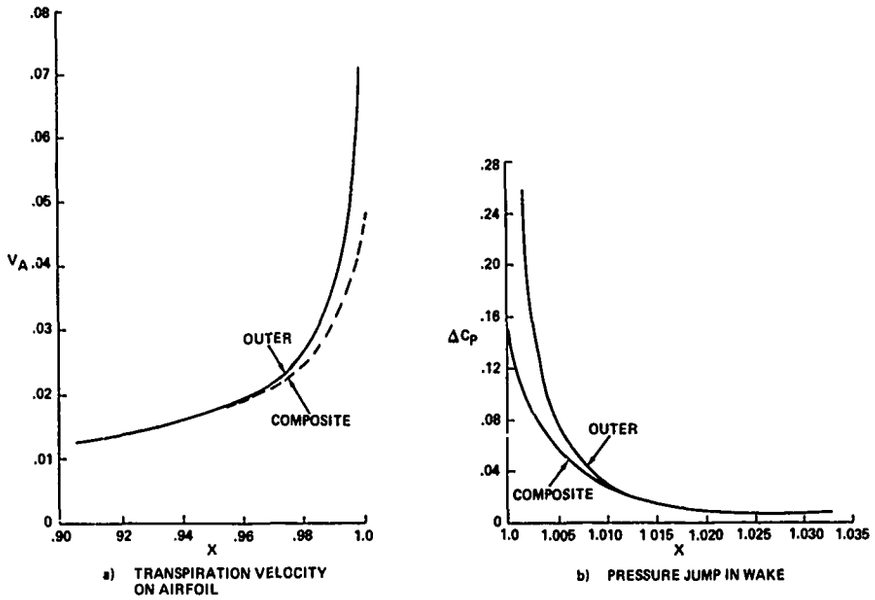


Fig. 24 Typical composite solutions for viscous matching conditions[8].

5.2 Solution Procedure

With the modified matching conditions discussed above the determination of the viscous flow over airfoils is reduced to the familiar problem of solving the coupled inviscid and boundary layer equations. The only changes from conventional IBLT involve the corrections to the matching conditions in Eq. (65) and (66) and the correction to the surface pressure to account for the pressure change across the boundary layer. A similar correction of the pressure also occurs in the wake. Solutions to the inviscid equations are obtained with Jameson's[69] fully conservative, rotated difference scheme for the full potential equation. An option for a nonconservative formulation is also provided.

The integral parameters appearing in the matching conditions are determined from the solution of the boundary layer equations. The equations are solved with simple integral methods consisting of a compressible version of Thwaites method for the laminar boundary layer near the leading edge and Green's lag-entrainment method[46] for the turbulent flow downstream of transition. The transition point locations can either be assigned or predicted by one of three standard semi-empirical methods programmed into the code. The wake is modeled in Green's method as independent symmetric half-wakes which seems to provide a reasonable engineering description of the integral parameters in the wake. Although the theory is strictly rational only for airfoils with cusped trailing edges the program can be applied with good results to airfoils with trailing edge included angles as large as 15°.

5.3 Typical Results

References 10 and 11 present extensive comparisons of the MCMJ method with wind tunnel data. Typical results (taken from Ref. 11), which are indicative of the level of accuracy that can be achieved with the method, are given in Fig. 25-27. The results are for the RAE 2822 airfoil which is a 12% thick supercritical airfoil with a moderate degree of rear loading and a trailing edge angle equal to 8.67°. The airfoil was tested[70] in the RAE 8 x 6 foot transonic tunnel; measurements included both surface pressure and boundary layer development. The results in Fig. 25 and 26 are for Case 6 (RAE designation) which corresponds to a nominal free stream Mach number $M_\infty = 0.725$, Reynolds number $Re = 6.5 \times 10^6$ and a (geometric) incidence angle $\alpha = 2.92°$. Transition was fixed at 3% chord on both the upper and lower surfaces of the airfoil. These conditions result in a large supersonic zone with a relatively strong shock wave.

The theoretical and experimental pressure distributions are compared in Fig. 25. The comparisons are carried out at the same (measured) lift coefficient in order to avoid the uncertainty in the effective incidence due to wall interference. In addition, a small blockage correction of $\Delta M_\infty = 0.003$ is applied to the comparison in that the "corrected" free stream Mach number is taken equal to $M_\infty = 0.728$. Solutions obtained with both fully conservative (FC) and nonconservative (NC) methods are shown in the figure for comparison. The FC solution clearly shows the best agreement with experiment. The agreement between theory and experiment is excellent on the lower surface and shock wave position and strength on the upper surface are well predicted in the FC solutions. This set of results also shows very good agreement with experiment for the pressure rise across the shock wave. Both the theoretical and experimental results indicate that the pressure rise across the shock wave is only about one-half of that required by the normal shock wave relations. The overall levels of the pressure distribution on the upper surface of the airfoil are also reasonably well predicted. The small discrepancies between theory and experiment over the forward part of the upper surface is probably due to the roughness strip used to fix transition. The slight overprediction of the pressure on the upper surface near the trailing edge is likely due to effects associated with the finite trailing edge angle not accounted for in the current trailing edge solution. The comparison of the pressure distribution shown in Fig. 25 is typical of many other comparisons given in Ref. 10 and 11 and is indicative of the good results that can be achieved with a "complete" IBLT.

The theoretical solution (FC) for the boundary layer development on the upper surface of the airfoil is compared with experimental measurements in Fig. 26. Included in the figures are the solutions for displacement and momentum thicknesses, δ^*, θ, shape factor, H, skin friction coefficient, C_f and the transpiration velocity, V_0, appearing in the viscous matching conditions. The overall agreement is seen to be relatively good, with a tendency to slightly underpredict δ^*, θ and H over the rear of the airfoil. The very rapid nearly discontinuous rise in displacement thickness at the shock wave is typical of these flows.

These solutions show a large and highly localized increase in transpiration velocity at the shock wave followed by a more gradual growth toward the trailing edge. These results clearly show the highly localized nature of the shock-wave boundary-layer interaction in the present theoretical model. The interacting boundary layer description basically truncates the delta function behavior that would otherwise arise at the shock impingement point were interaction not included in the formulation. The resulting transpiration velocity displays a highly peaked, but finite, distribution which increases in amplitude with increasing shock strength, as indicated in other cases presented in Ref 11.

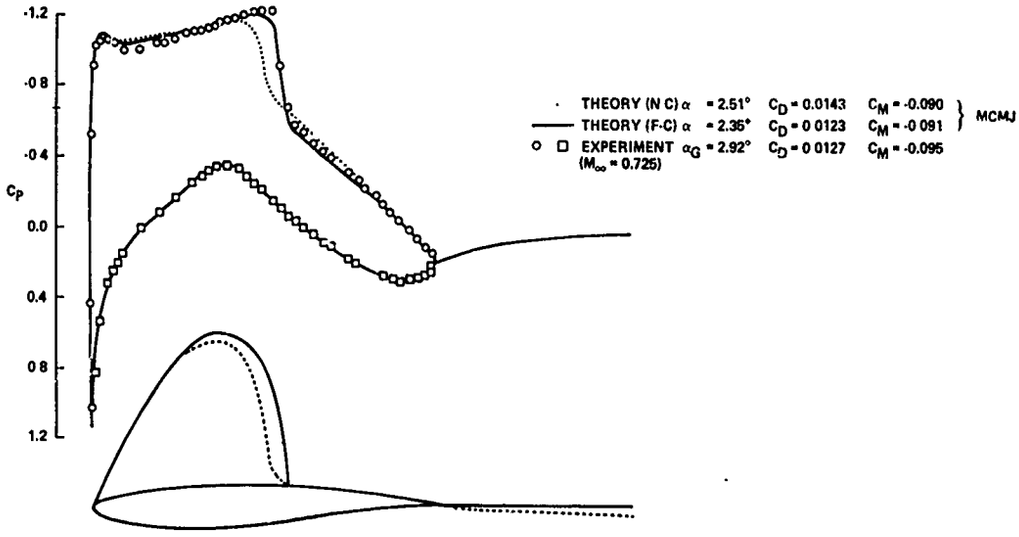


Fig. 25 RAE 2822 – pressure distribution at $M_\infty = 0.728$, $C_L = 0.743$, $Re = 6.5 \times 10^6$ ($X_T = 0.03$). (REPRINTED FROM REF 11)

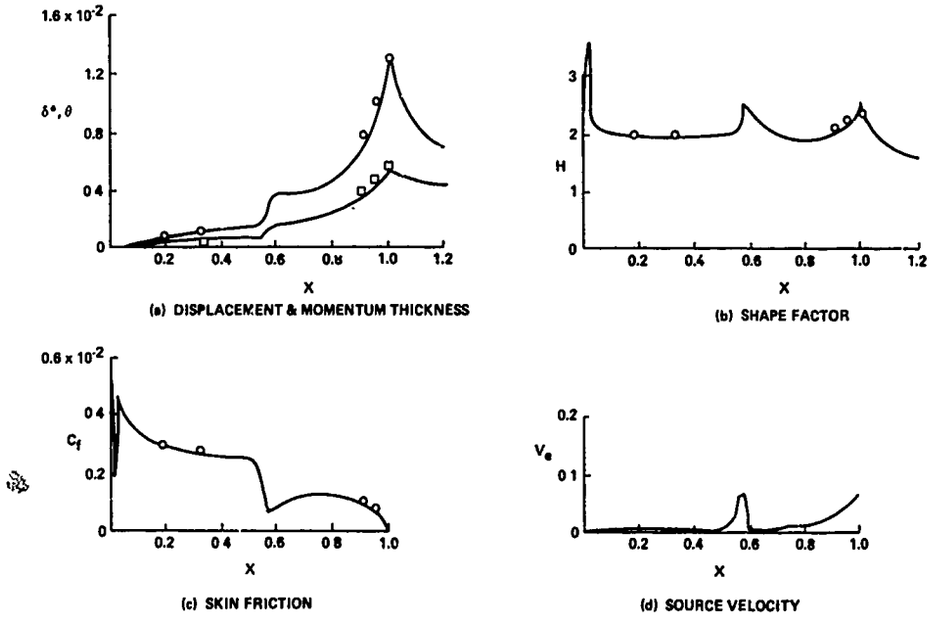


Fig. 26 RAE 2822 – boundary layer development at $M_\infty = 0.728$, $C_L = 0.743$, $Re = 6.5 \times 10^6$ ($X_T = 0.11$). (REPRINTED FROM REF 11)

The theoretical predictions of the drag polar are compared with experimental data in Fig. 27 for a nominal free stream Mach number of $M_\infty = 0.730$. The theoretical drags are computed from an integration of the surface pressure and skin friction. We note the FC solution is again in best agreement with the measured values of drag. The small underprediction of the FC solution evident in the figure amounts to no more than five counts of drag. About half of this difference is due to numerical error caused by use of first-order accurate differencing in the inviscid solution. Use of a second-order accurate formula has been demonstrated[11] to increase the drag by two counts. The remaining discrepancy can be associated with the slight overprediction of pressures on the upper surface near the trailing edge. These and other results presented in Ref 11 clearly show that the NC scheme produces inferior predictions of both shock wave location and drag.

A theoretical study is carried out in Ref 11 using the MCMJ method to determine the relative importance of the various viscous effects arising in the airfoil problem. This is accomplished by comparing results of a series of calculations carried out with individual terms in the matching conditions selectively dropped from the formulation. The results include two cases for the RAE 2822 airfoil, one subcritical and one supercritical case and one supercritical case for a heavily rear loaded NASA (Langley Research Center) supercritical airfoil. For each case, a series of solutions are obtained with each of the terms appearing in the matching conditions selectively dropped. Solutions for the drag, lift and trailing edge pressure are summarized in Tables 2 through 4. In these Tables C_D is the total drag, determined from integration of the pressure and skin friction over the airfoil surface, C_{DB} (Table 4) is the total drag that includes a base drag contribution when the airfoil has a nonzero base thickness, and C_{D_∞} is the profile drag determined from the wake momentum thickness far downstream (i.e., $C_{D_\infty} = 2\theta_\infty$). Profile drag is equal to the total drag less the wave drag and is due solely to momentum losses in the boundary layer. For subcritical flow C_{D_∞} is equal to the total drag of the airfoil and should be equal to C_{DB} as determined by surface integration. In general, however, these two evaluations of the drag

will not be equal with the differences due to numerical errors in the solution of the governing equations and to approximations in the formulation of the viscous effects. The momentum drag (i.e., $2\theta_\infty$) seems to be relatively insensitive to the details of the numerical method and the formulation of the viscous theory and is thought to be the more accurate prediction of drag in subcritical flows. In these cases the difference between profile and integrated drag is a useful measure of the overall accuracy of the theoretical model.

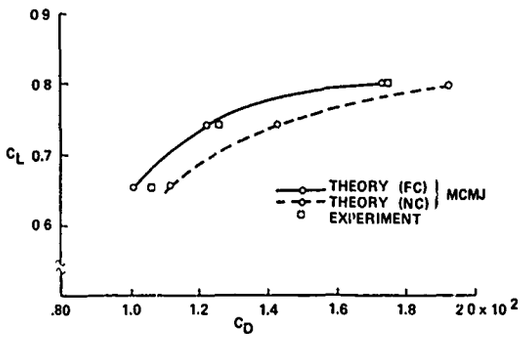


Fig. 27 RAE 2822 – drag polar at $M_\infty \cong 0.73$, Re = 6.5 x 10^6, (X_T = 0.03) (REPRINTED FROM REF 11)

Table 2 RAE 2822 – effect of wake and trailing edge corrections, $M_\infty = 0.676$, $\alpha = 1.06°$, Re = 5.7 x 10^6, (X_T = 0.11)

Mode	Theoretical Model	C_D	C_{D_∞}	C_L	C_{PTE}
(A)	Inviscid	0	0	0 571	0.438
(B)	Full Viscous (MCMJ)	0.0084	0.0083	0 431	0 234
(C)	(B) Less TE Corrections	0 0080	0 0083	0.416	0.234
(D)	(B) Less Wake Curvature	0.0081	0 0083	0 454	0.234
(E)	(B) Less Wake Thickness	0.0069	0.0082	0 398	0.289
(F)	(B) Less TE Corrections, Wake Curvature & Thickness	0.0064	0.0082	0 399	0.278
(C')	RAE (NC) [6]	0 0081	0 0083	0.430 (0 420)	0.226

The results in the tables include solutions for (A) the inviscid theory, (B) the full viscous theory, (C) the full viscous theory less the trailing-edge corrections, (D) less the wake-curvature term, and (E) less the wake thickness terms. In the latter solution the wake is modeled as a constant thickness extension of the displacement surface on the airfoil surface. We have also carried out solutions neglecting the trailing edge corrections and both the wake-curvature and thickness terms. This version of the theory (F), includes only the displacement effect on the airfoil surface and is therefore equivalent to the formulation employed in the BGKJ[4, 5] method and its derivatives [71, 72]. For the two supercritical cases studied using this latter formulation solutions were also obtained with the NC version of the method (labeled (G) in the tables). In addition, the two RAE 2822 cases considered in Tables 2 and 3 also include available results from the RAE (NC)[6]. The RAE method accounted for both wake-thickness and wake-curvature but not trailing-edge interaction effects.

The results for the subcritical RAE 2822 case are listed in Table 2. Comparisons of the inviscid (A) and full viscous (B) solutions illustrate the large effect of the boundary layer on lift. Even for this subcritical case the presence of the boundary layer caused a nearly 1/3 decrease in lift. The results given in lines (C), (D) and (E) illustrate the effect of the individual terms in the matching conditions. Comparisons of the results in lines (A)–(E) indicate that the largest effect is caused by the displacement effect on the airfoil surface with the other terms also producing significant effects. The effect of wake thickness on lift was unanticipated since predominately symmetric effects were expected from this source. However, on reflection, this behavior is not surprising. The neglect of the wake thickness term leads to an increase in pressure at the trailing edge, which induces a significant increase in boundary layer thickness near the trailing edge. The increase is largest on the upper surface because of the larger initial boundary layer thickness on this surface. It is this differential increase in boundary layer thickness caused by the neglect of the wake thickness term that leads to the observed lift reduction. We also call attention to the insensitivity of the momentum drag, C_{D_∞}, to differences in the theoretical model, and to the good agreement between the two evaluations of drag in the full viscous solution (B). The good agreement evident in this case is an encouraging indication of the overall accuracy of the MCMJ method. The underprediction of the integrated drag and the poor agreement with C_{D_∞} when the wake-thickness terms are suppressed (E), are indications of the importance of these terms. The comparisons in Table 2 indicate that the formulation based on airfoil displacement thickness only, underpredicts the drag by 25% and the lift by 7% in this case.

The results of the (NC) RAE method [6] (C') which is equivalent to the formulation employed in case (C) of the present method, are in good agreement. Two values of the lift coefficient are given for the RAE method. The higher value results from a version of their method that employs considerable numerical smoothing of the wake curvature terms near the trailing edge. The smaller value, obtained with less smoothing is in better agreement with the results of case (C) of the present method. It has been reported [6] that convergence difficulties are experienced in this latter version and its use is not recommended.

The results of a similar series of calculations carried out for the same airfoil at a higher free-stream Mach number, resulting in a supercritical flow, are listed in Table 3. In this case the integrated drag includes wave drag and so is no longer equal to the momentum drag, C_{D_∞}. The difference between C_D and C_{D_∞} is a relatively accurate measure of the wave drag in the full viscous solution (case B) but not in the other cases because of the inadequacies of the viscous formulation clearly evident in the subcritical results. The neglect of wake and trailing edge interaction effects in this supercritical case leads to a 35% underprediction of the drag coefficient (case F) compared to the full viscous solution. Case (F) was also repeated with the NC formulation (line G in Table 3). The NC scheme produces a weaker, more forward shock wave but gives a higher drag. This extra drag arises from a spurious mass generation at the shock wave caused by NC differencing. This spurious drag increase is also evident in the comparison of the RAE results (case C') with the present, equivalent formulation using FC differencing (case C).

The solutions for the pressure distribution on the airfoil surface are given in Fig. 28. Included are the inviscid solution (A), the full viscous solution, (B), and the viscous solution less the trailing correction and both wake terms, (F). Both FC and NC calculations of the latter case are included. These results illustrate the very large effect of the boundary layer on the flow field in supercritical conditions even at the relatively large Reynolds number of the computations. The boundary layer drives the shock wave forward from $x \simeq 0.80$ to $x \simeq 0.55$, and significantly increases the pressure level on the upper surface and reduces it on the lower surface of the airfoil, resulting in a reduction of the lift coefficient by nearly a factor of two. The neglect of the wake and trailing edge contributions to the matching conditions is seen to drive the shock wave forward by about 5% and to reduce the lift by 10% and drag by 35% below the full viscous solution (Table 3). The switch to a NC scheme is seen to drive the shock wave even further forward.

The details of the pressure distribution near the trailing edge for the full viscous solution at the higher Mach number, $M_\infty = 0.725$ is plotted on an expanded scale in Fig. 29. Included here are the "composite" and "outer" solutions computed from the full viscous theory. The composite solution contains contributions from the "outer" and "inner" solution as given in Eq. (62c) which account for the pressure variations across the boundary layer and wake. The outer solution clearly exhibits the wake pressure jump imposed as part of the viscous matching conditions. The pressure jump is largest at the trailing edge and rapidly decays away from the trailing edge both in the wake and on the airfoil surface. The relatively large jump in pressure at the trailing edge ($\Delta C_p \simeq 0.2$) is indicative of the importance of normal pressure gradients near trailing edges. The crossing of the outer solution on the airfoil is a typical property of the viscous wake solution which clearly distinguishes it from jet flap solutions with positive blowing coefficient.

Table 3 RAE 2822 – effect of wake and trailing edge corrections, $M_\infty = 0.725$, $\alpha = 2.3°$, $Re = 6.5 \times 10^6$, ($X_T = 0.03$)

Mode	Theoretical Model	C_D	C_{D_∞}	C_L	$C_{P_{TE}}$
(A)	Inviscid	·	·	1.300	0 5265
(B)	Full Viscous (MCMJ)	0 0110	0 0098	0 726	0 222
(C)	(B) Less TE Corrections	0 0101	0 0096	0.700	0 227
(D)	(B) Less Wake Curvature	0 0112	0 0100	0.758	0 224
(E)	(B) Less Wake Thickness	0 0080	0 0093	0 661	0 276
(F)	(B) Less TE Corrections, Wake Curvature & Thickness	0 0072	0.0093	0 658	0 271
(G)	(F) With Nonconservative Differencing	0.0091	0 0092	0.648	0.269
(C)	RAE (NC)[6]	0 0119	·	0 699	0 219

Table 4 NASA supercritical airfoil – effect of wake and trailing edge corrections, $M_\infty = 0.768$, $\alpha = 0.15°$, $Re = 7.7 \times 10^6$, ($X_T = 0.28$)

Mode	Theoretical Model	C_{DB}	C_{D_∞}	C_L	C_{PTE}
(A)	Inviscid	NOT AVAILABLE			
(B)	Full Viscous (MCMJ)	0.0122	0 0082	0 852	0.137
(C)	(B) Less TE Corrections	0 0097	0 0078	0 808	0.156
(D)	(B) Less wake Curvature	0 0131	0.0091	0 871	0.120
(E)	(B) Less wake Thickness	0.0105	0 0079	0.835	0.155
(F)	(B) Less TE Corrections, Wake Curvature & Thickness	0 0088	0.0079	0 821	0.168
(G)	(F) With Nonconservative Differencing	0.0098	0 0074	0 768	0.155

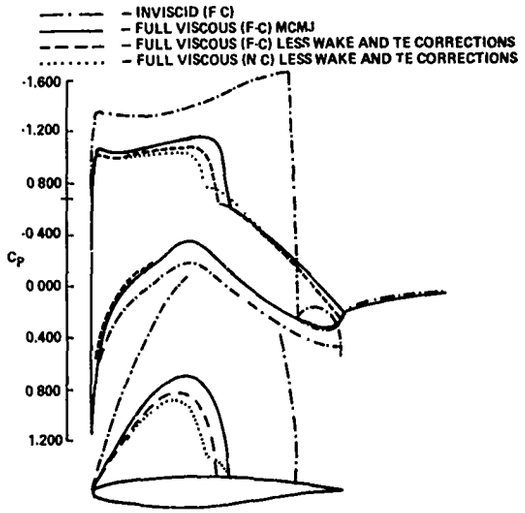


Fig. 28 RAE 2822 – effect of wake & trailing edge corrections in MCMJ theory at $M_\infty = 0.725$, $\alpha = 2.3°$, $Re = 6.5 \times 10^6$ ($X_T = 0.03$). (REPRINTED FROM REF 11)

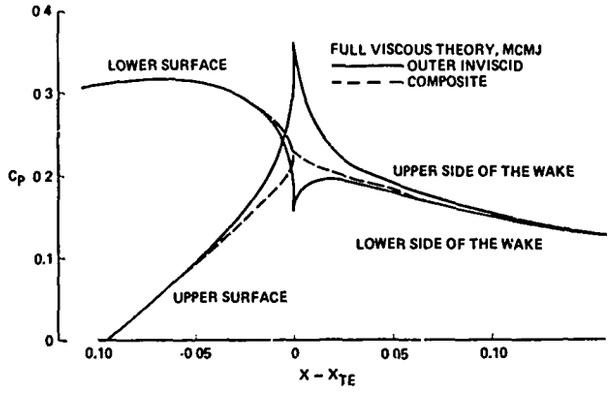


Fig. 29 RAE 2822 – Details of pressure distribution near trailing edge M_∞ = 0.725, $\alpha = 2.3°$, $Re = 6.5 \times 10^6$ ($X_T = 0.03$). (REPRINTED FROM REF 11)

The RAE 2822 is an airfoil with moderate rear loading. The calculations of the highly rear loaded supercritical airfoil developed by the NASA Langley Research Center (LRC) are summarized in Table 4. The calculations for this case have been carried out for a free stream Mach number $M_\infty = 0.768$ and an angle of attack of $\alpha = -0.151°$ resulting in a lift coefficient in the full viscous solution of $C_L = 0.852$. The airfoil has a nonzero trailing edge thickness which requires an estimate for the base-drag contribution to C_{DB}. This contribution amounts to 7 counts of drag for all cases considered in Table 4. The shock position in the inviscid solution at this incidence and Mach number appears to be downstream of the trailing edge and, because of this, the inviscid solution cannot be computed with the circle plane code. The viscous solution, however, can be determined without difficulty. The inclusion of the boundary layer in the viscous solution drives the shock wave forward to 73% chord, again demonstrating the very large effect of the boundary layer on the flow field at transonic speeds. The results in Table 4 indicate that the trailing edge correction and the variation of profile drag with the theoretical model are much larger than in previous cases. Also, note that the neglect of the trailing edge correction and the wake terms (F) leads to a 30% underprediction of drag and that the use of a NC formulation leads to a partially compensating increase in drag of about 10%. As a point of reference, in Fig. 30 we provide a comparison of the full viscous solution with wind tunnel data for conditions that are close to those employed in the computations in Table 4.

Table 5 compares the drag prediction of the MCMJ method with experimental measurements of the NACA 0012 airfoil carried out at Ohio State University [73] and with theoretical predictions of the BGKJ [5] and Carlson [72] methods carried out in Ref. 73. The MCMJ results include solutions obtained with the full viscous method and also with the parallel wake assumption. Included in the table are the solutions for the total drag C_{DB}, the total drag less the base drag, C_D, both determined from an integration of pressure and skin friction, and the momentum drag, C_{D_∞}.

The momentum drag C_{D_∞}, which is thought to be the most accurate result, is in excellent agreement with the experimental value. The integrated drag, C_{DB}, in the full viscous MCMJ solution however, is seen to underpredict both the experimental and momentum drag by 12%. The theoretical pressure distribution is compared with experimental data in Fig. 31. The agreement is good, except near the trailing edge where theory indicates a more positive pressure which is consistent with the error in integrated drag. The error in integrated drag is thought to be due to the neglect of strong interaction effects associated with the large trailing edge angle of this airfoil ($\theta_{tc} = 16°$). The wedge-shaped trailing edge is expected to induce significant pressure reduction across the boundary layer which will have a tendency to increase the drag.

Neglect of the wake-thickness term is seen to lead to a substantial increase in the error in integrated drag but does not affect the solution for momentum drag. A significant part of the discrepancy between the two evaluations of drag is due to the contribution of the base, which in this case amounts to seven counts of thrust. Note the very large underprediction of the drag by both the BGKJ and Carlson methods. With the base drag included these methods are seen to underpredict the drag by a factor of two. The base drag contribution is not included in the original solutions presented in Ref 73. In order to provide a uniform basis of comparison the BKGJ and Carlson results in Table 5 have been corrected for base drag by subtracting 9 counts from the results given in Ref 73.

The results discussed here, and others presented in Ref 10 and 11, indicate that the MCMJ method can give very good prediction of the pressure distribution, shock location, and forces when the boundary layer is attached and in the prediction of drag, when the trailing edge angle is not large. However, in

recent calculations carried out by the author for the NACA 0012 airfoil, there has been some tendency for the MCMJ theory (FC) to predict shock positions that are about 10% aft of experimental locations. The discrepancies can be eliminated by employing a blockage-type correction to justify a reduction of free stream Mach number. Because of the general uncertainty of blockage effects in wind tunnels, it has yet to be determined whether these discrepancies are due to real blockage effects or to shortcomings in the theoretical formulation, perhaps due to the use of the potential flow approximation.

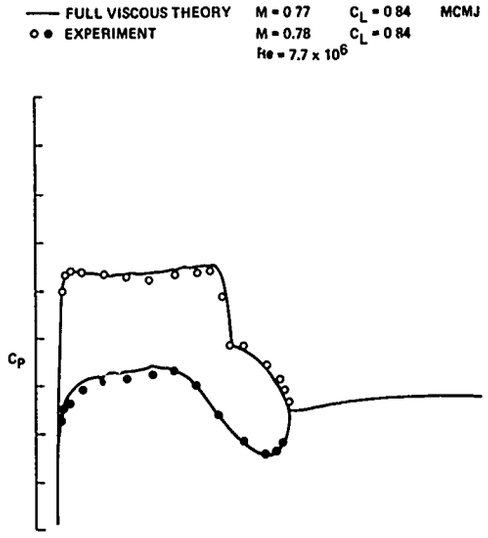


Fig. 30 Pressure distribution on a NASA supercritical airfoil.

Table 5 NACA 0012 – profile drag study at zero lift.

Theory	C_D	C_{D_B}	C_{D_∞}
Present - Full viscous (MCMJ)	0 0079	0 0072	0.0082
Present Parallel wake (MCMJ)	0.0063	0.0054	0 0081
BGKJ [73]	0 0047	0 0036*	-
Carlson [73]	0.0051	0 0042*	-
Experiment [73]	0 0081		

* Obtained by subtracting ΔC_{P_B} = 0 0009 from C_D

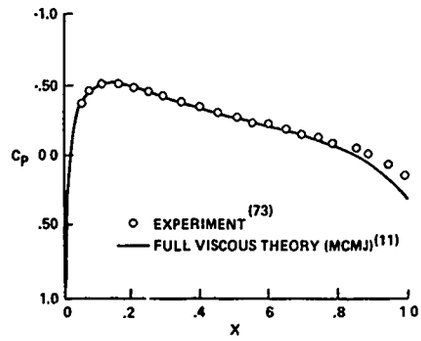


Fig. 31 NACA 0012 – pressure distribution at zero lift $M_\infty = 0.575$, $Re = 4.68 \times 10^6$ ($X_T = 0.10$).

6. CONCLUDING REMARKS

Significant progress has been achieved by boundary layer type methods in the computation of viscous flow, without extensive separation, over airfoils. Efficient numerical methods have been developed for the computation of the outer inviscid flow, practical methods have been developed for incorporating both wake thickness and wake curvature effects in the viscous flow formulation, and local asymptotic solutions have been developed for the strong turbulent interactions at shock waves and trailing edges. In addition, using the local trailing edge solution, simple procedures have been developed to correct IBLT for strong interaction effects at the trailing edge. Two computer codes have been written that implement a "complete" IBLT formulation including both wake effects viz., CL[6,7] and MCMJ [10,11]. Furthermore, the MCMJ [10,11] method also incorporates trailing edge interaction effects into the formulation. The MCMJ method thus accounts for every important viscid-inviscid interaction effect on the airfoil except the strong interaction at shock waves. Nevertheless, extensive experience with the MCMJ method (and apparently also with the CL method) indicate that it gives good predictions of the pressure rise across shock waves. The theory seems to accurately predict the partial pressure rise across shock waves, observed in experiments on airfoils, to levels about half those required by the normal shock wave relations.

The combination of efficient mixed flow relaxation techniques for the inviscid flow, with Green's lag entrainment method for the turbulent boundary layer, has proven to be an effective method for the prediction of airfoil section characteristics. The method requires little computing time, and employs a turbulent closure that is well suited to airfoil flows. Calculation of difficult supercritical cases with shock waves by the MCMJ method generally requires less than ten minutes for a 160 x 32 grid on an IBM 376–168 computer.

Theoretical solutions obtained with the MCMJ presented in Ref 10, 11 have shown generally favorable agreement with wind tunnel data. These comparisons indicate that good predictions of airfoil section characteristics can be obtained with an interacting boundary layer method provided the formulation includes both wake and trailing edge interaction effects and provided a fully conservative difference method is employed in the outer inviscid solution. It must be stressed, however, that because of uncertainties in the experimental data, due primarily to wall interference, these conclusions must be regarded as tentative and in need of further substantiation. The main cause of uncertainty is due to the blockage effect on the equivalent free stream Mach number. There has been some tendency for the fully conservative theory to predict shocks that are too far aft when the calculations are carried out at the experimentally quoted free stream Mach number. The discrepancy in shock position can usually be eliminated by applying a small blockage "correction" to the free stream Mach number. Whether these differences are due to a "real" blockage effect or are caused by deficiencies in the theoretical method remains to be determined. The question of code validation remains a major concern for the future. There is a continuing need for wind tunnel data with small and well documented wall interference corrections.

Because of their possible effect on the section characteristics, the principal aspects of the MCMJ method that warrant further study are the strong interaction at wedge-shaped trailing edges and the computation of the outer inviscid flow. The trailing edge corrections employed in the MCMJ method are strictly applicable to cusped airfoils. Fortunately, the method seems to yield reasonably good predictions when applied to more general trailing edges provided that the edge angles are small. However, solutions for the NACA 0012 airfoil ($\theta_{te} = 16^\circ$) show pressures that are somewhat high near the trailing edge and drags that are underpredicted by about 10%. These observations are likely a general indication of a failing of the correction procedure at the trailing edge when the trailing edge angle is appreciable. These discrepancies are undoubtedly caused by pressure variations across the boundary layer that are not accounted for by the local trailing edge solution. These extra pressure variations across the boundary layer are generated by the curved streamlines associated with the local wedge flow near the trailing edge. These effects can be incorporated into the MCMJ method through generalization of the local trailing edge solution to account for effects due to wedge-shaped trailing edges. Kuchmann [74] carried out semi-empirical calculations for a wedge-shaped trailing edge using the inviscid rotational flow model with an empirical "cutoff" of the initial velocity profile.

It is generally recognized that the potential flow approximation used in the outer inviscid solution breaks down as the shock strength increases. Evidence from comparison with solutions for the Euler equations for "purely" inviscid flow indicates that the potential flow approximation breaks down under con-

ditions of practical interest and that the potential flow shock waves are significantly aft of the "exact" (i.e., Euler solution) shock positions. The significance of this behavior for full viscous solutions is not clear since shock waves are considerably weakened by displacement effects. Evidence from the RAE 2822 comparisons indicates that the potential flow approximation remains useful up to the point that the shock strength is large enough to separate the boundary layer. However, some comparisons with experimental data from other wind tunnels have shown a tendency for the MCMJ method to predict shock waves that are aft of the experimental shock position. In these cases a small reduction in free stream Mach number (blockage correction?) eliminates the discrepancy. The question of whether this is a "real" blockage effect associated with the particular wind tunnel or a sign of the breakdown of the potential flow approximation remains to be answered. Because of the uncertainty in the range of usefulness of the potential flow approximation, it is desirable to develop an interaction boundary layer method using the Euler equations for the outer inviscid flow. Steps in this direction have been taken by Whitfield et al. [67] but their method has not yet been developed to the point where complete airfoil calculations can be carried out with both wake and trailing edge interaction effects included in the formulation.

Other problem areas of a theoretical nature that could benefit from further study are:

- The solution of the inner layers and the determination of the skin friction in the trailing edge region. The nature of the solution in the "inner" wall layer, which describes the transition of the boundary layer to the wake across the trailing edge, is poorly understood.
- The integration of the weak shock asymptotic solutions into a complete airfoil calculation. It remains to be explained how the asymptotic solutions can be made compatible with the partial shock jumps observed in both IBLT and in experiment.
- The development of local asymptotic solutions for shock-wave boundary-layer interactions when the shock strength is O(1). This is the range of shock strength that is important for shock induced boundary layer separation.
- The development of asymptotic methods for small separation zones at shock waves and trailing edges. The studies discussed in this paper are all restricted to attached boundary layers. Progress in the understanding of flows with small separation regions, which can carry significant pressure variations, has been limited.

In concluding this discussion I should also mention the importance of extending these ideas to three-dimensional flows over wings.

Editorial Note: At the request of Symposium participants, slides used in the presentation by the author are reproduced as an appendix to the paper.

ACKNOWLEDGEMENTS

The author is grateful to A. Rubel of the Grumman Research Department for his detailed critique of a preliminary draft of this paper.

REFERENCES

1. Preston, J. H., "Note on the Circulation in Circuits Which Cut the Wake of an Airfoil at Right Angles," British ARC, R&M 2957, 1954.
2. Pearcey, H. H., Osborne, J. and Haines, A.B., "The Interaction Between Local Effects at the Shock and Rear Separation – a Source of Significant Scale Effects in Wind-tunnel Tests on Aerofoils and Wings," AGARD CP No. 35, 1968.
3. Green, J.E., "Some Aspects of Viscid-Inviscid Interactions at Transonic Speeds and their Dependence on Reynolds Number" in Facilities and Techniques for Aerodynamic Testing at Transonic Speeds and High Reynolds Number, AGARD Conference Proceedings CP 83, 1971.
4. Bauer, F., Garabedian, P. and Korn, D., Supercritical Wing Sections, Lecture Notes in Economics and Mathematical Systems, No. 66, Springer-Verlag, New York, 1972.
5. Bauer, F., Garabedian, P., Korn, D., and Jameson, A., Supercritical Wing Sections II, Springer-Verlag, New York, 1975.
6. Collyer, M.R., "An Extension to the Method of Garabedian and Korn for the Calculation of Transonic Flow Past an Aerofoil to Include the Effect of a Boundary Layer and Wake," British ARC, R&M No. 3328, 1978.
7. Collyer, M.R. and Lock, R.C., "Prediction of Viscous Effects in Steady Transonic Flow Past an Aerofoil," Aeronautical Quarterly Vol XXX, August 1979.
8. Melnik, R.E., Chow, R., and Mead, H.R., "Theory of Viscous Transonic Flow Over Airfoils at High Reynolds Number," Paper No. 77-680, AIAA 10th Fluid and Plasma Dynamics Conference, Albuquerque, N.M., June 1977.
9. Melnik, R.E., "Wake Curvature and Trailing Edge Interaction Effects in Viscous Flow Over Airfoils," Advanced Technology Airfoil Research Conference, CP 2045, Part 1, 1978.
10. Melnik, R.E., "Recent Developments in a Boundary Layer Theory for Computing Viscous Flows Over Airfoils," paper presented at 4th" USAF/FRG Data Exchange Meeting, BMVg-FBWT 70-31 Meersberg, Germany, 1979.
11. Melnik, R.E., Chow, R.R., Mead, H.R. and Jameson, A., "An Improved Viscid/Inviscid Interaction Procedure for Transonic Flow Over Airfoils," NASA CR - (to be released) 1980.
12. Melnik, R.E. and Grossman, B., "Analysis of the Interaction of a Weak Normal Shock Wave with a Turbulent Boundary Layer," AIAA Fluid and Plasma Dynamics Conference, Paper No. 74-598, June 1974.
13. Melnik, R.E. and Grossman, B., "Further Developments in an Analysis of the Interaction of a Weak Normal Shock Wave with a Turbulent Boundary Layer," Symposium Transsonicum II, Springer-Verlag, New York, 1975, pp. 262–272.
14. Melnik, R.E. and Grossman, B., "Interactions of Normal Shock Waves with Turbulent Boundary Layers at Transonic Speeds," in Transonic Flow Problems in Turbomachinery, Hemisphere Publ. Co., 1977, pp. 415–433.

15. Adamson, T.C. Jr. and Feo, A., "Interaction Between a Shock Wave and a Turbulent Boundary Layer in Transonic Flow," SIAM J. Appl. Math., Vol. 29, 1975

16. Adamson, T.C Jr. and Messiter, A.F., "Normal Shock Wave Turbulent Boundary Layer Interactions in Transonic Flow near Separation," in Transonic Flow Problems in Turbomachinery, Hemisphere Publ. Co., 1977, pp. 392–414.

17. Messiter, A.F., "Interaction Between a Normal Shock Wave and a Turbulent Boundary Layer at High Transonic Speeds, Part I: Pressure Distribution," ZAMP, Vol. 31, 1980.

18. Liou, M.S. and Adamson, T.C., Jr., "Interaction Between a Normal Shock Wave and a Turbulent Boundary Layer at High Transonic Speeds, Part II: Wall Shear Stress," ZAMP, Vol. 31, 1980.

19. Lighthill, M.J., "On Boundary Layers and Upstream Influence, II Supersonic Flows Without Separation," "Proc. Royal Soc. A, Vol. 217, 1953.

20. LeBalleur, J.C., "Couplage Visqueux-Non Visqueux: Analyse du Probleme Incluant Décollements et Ondes de Choc," Rech. Aerosp. No. 6 1977

21. LeBalleur, J.C., "Couplage Visqueux-Non Visqueux: Methode Numerique et Applications aux Ecoulements Bidimensionnels Transsoniques et Supersoniques," Rech. Aerosp. No. 2, 1978

22. LeBalleur, J.C., Peyret, R. and Viviand H., "Numerical Studies in High Reynolds Aerodynamics," Computers and Fluids, Vol. 8, 1980.

23. Stewartson, K , "Multistructured Boundary Layers on Flat Plates and Related Bodies" in Advances in Applied Mechanics Vol 14, Academic Press, 1974, pp. 145–239.

24. Bradshaw, P. (Ed.) Turbulence (Topics in Applied Physics – Vol. 12), Springer-Verlag 1978, pp. 34–39.

25. Millikan, C.B., "A Critical Discussion of Turbulent Flow in Channels and Circular Tubes," Proceedings of the Fifth International Congress on Applied Mechanics (Cambridge, Mass. 1938) J. Wiley, New York, 1939.

26. Karman, Th., von "Mechanische Ahnlichkeit und Turbulenz," Nachrichten der Akademie der Wissenshaften Gottingen Math Phys. Klass, 58, 1930.

27. Mellor, G.L., "The Large Reynolds Number Asymptotic Theory of Theory of Turbulent Boundary Layers," Int. J. Engr. Sci., Vol. 10, 1972.

28. Bush, W.B. and Fendell, F., "Asymptotic Analysis of Turbulent Boundary Channel and Boundary Layer Flow," J. Fluid Mech., Vol. 56, 1972.

29 Yajnik, K., "Asymptotic Theory of Turbulent Shear Flows," J. Fluid Mech., Vol. 42, 1970.

30. Afzal, N., "A Higher Order Theory for Compressible Turbulent Boundary Layers at Moderately Large Reynolds Numbers," J. Fluid Mech., Vol. 57, 1973.

31. Lighthill, M.J., "On Displacement Thickness," J. Fluid Mech., Vol. 4, 1958.

32. Deiwert, G.S., "Computation of Separated Transonic Turbulent Flow," AIAA J., Vol. 14, 1976.

33. Oswatitsch, K., Wieghardt, K., 1942, Lilienthal-Gesellschaft für Luftfahrtforschung Bericht S 13/1 Teil, pp. 7–24. Engl. Transl. Theoretical analysis of stationary potential flows and boundary layers at high speed. NACA TM 1189 1948.

34. Garvine, R.W., "Upstream Influence in Viscous Interaction Problems," The Physics of the fluids, Vol. 11, 1968.

35. Crocco, L. and Lees, L., "A Mixing Theory for the Interaction Between Dissipative Flows and Nearly Isentropic Streams," J. Aero Sci., Vol. 19, 1952.

36. Werle, M.J. and Vatsa, V.N., "New Method for Supersonic Boundary Layer Separations, "AIAA J. Vol. 12, 1974.

37. Werle, M.J. and Bertke, S.D., "Application of an Interacting Boundary Layer Model to the Supersonic Turbulent Separation Problem," Rep. AFL 76-4-21, Univers. Cincinnati, Ohio, 1976.

38. Law, C.H., "Supersonic Turbulent Boundary Layer Separation," AIAA J., Vol. 12, 1974.

39. Shang, J.S. and Hankey, W.L., "Numerical Solution for Supersonic Turbulent Flow over a Compression Ramp," AIAA J., Vol. 13, 1975.

40. Spence, D.A. and Beasley, J.A., "The Calculation of Lift Curve Slopes, Allowing for Boundary Layer, with Application to the RAE 101 and 104 Aerofoils," British ARC, R&M 3137, 1960.

41. Firmin, M.C.P., "The Calculation of Pressure Distribution, Lift and Drag, on Single Aerofoils at Subcritical Speeds Part I Interim Method," British RAE TR 72235, 1973

42. Hall, M.G. and Firmin, M.C.P., "Recent Developments in Methods for Calculating Transonic Flows over Wings," ICAS Paper 74-18, 1974.

43. Lock, R C., "Calculation of Viscous Effects on Aerofoils in Compressible Flow," paper presented at Fifth Australian Conference on Hydraulics and Fluid Mechanics, Dec., 1974.

44. Viviand, H., "Application des Méthodes Asymptotiques à L'étude des Couches Visqueuses Libres " Rech. Aerosp. No. 431, July–Aug. 1969

45. Nash, J.F. and McDonald, H.G.J., "The Calculation of Momentum Thickness in a Turbulent Boundary Layer at Mach Numbers up to Unity," British Arc CP 963, London 1967.

46. Green, J.E., Weeks, D.J., and Broomen, J.W.F., "Prediction of Turbulent Boundary Layers and Wakes in Compressible Flow by a Lag Entrainment Method," British RAE Tech. Report, 72231, 1973.

47. Stewartson, K., Williams, P.G., "Self Induced Separation," Proc. R. Soc. Ser. A Vol. 312, 1969.

48. Stewartson, K. "On the Flow Near the Trailing Edge of a Flat Plate II," Mathematika, Vol. 16, 1969.

49. Messiter, A.F., "Boundary Layer Flow Near the Trailing Edge of a Flat Plate," SIAM J. Appl. Math. Vol. 18, 1970.

50. Rose, W.C., Murphy, J.D. and Watson, E.C., Interaction of an Oblique Shock Wave with a Turbulent Boundary Layer," AIAA J. Vol. 6, 1968.

51. Roshko, A. and Thomke, G.J., "Supersonic Turbulent Boundary Layer Interaction with a Compression Corner at Very High Reynolds Number," Proc. of the Symposium on Viscous Interaction Phenomena in Supersonic Hypersonic Flow, USAF Aerospace Research Laboratories, Wright-Patterson AFB, Ohio, University of Dayton Press, May 1969.

52. Adamson, T.C. and Messiter, A.F. "Analysis of Two-Dimensional Interactions Between Shock Waves and Boundary Layer," Ann. Rev. Fluid Mech., Vol. 12 Annual Reviews Inc. Palo Alto, CA, 1980, pp. 103–138.

53. Lighthill, M.J., "Reflection at a Laminar Boundary Layer of a Weak Steady Disturbance to a Supersonic Stream, Neglecting Viscosity and Heat Conduction," Quart J. Mech. and Appl. Math. Vol. III, 1950.

54. Robinson, A., Wave Reflections Near a Wall," Proc. Camb. Philos. Soc., Vol. 47, 1959.

55. Watson, C.N., "Shear Flow Aerodynamics: Lifting Surface Theory," AIAA J., Vol. 13, 1975.

56. Inger, G.R. and Mason, W.H., "Analytical Theory of Transonic Normal Shock Turbulent Boundary Layer Interaction," AIAA J., Vol. 14, Sept. 1976.

57. Bohning, R. and Zierep, J., "Der ebene Verdichtungsstoss an der gekrümmten Wand unter Berucksichtigung der Reibung," ZAMP, Vol 27, 1976.

58. Bohning R. and Zierep, J., "Berechnung für das Einsetzen der Ablösung der turbulenten Grenzschicht an der Gekrümmten Wand mit senkrechtem Verdichtungsstoss, ZAMP, Vol 29, 1978.

59 Elfstrom, G.M., "Turbulent Hypersonic Flow at a Wedge Compression Corner," J. Fluid Mech., Vol. 53, 1972.

60 Carriere, P., Sirieix, M., and Delery, J., "Méthodes de calcul des écoulements turbulents décollés en supersonique," Prog. Aerosp. Sci., Vol. 16, 1975, pp. 385–429.

61. Rosen, R., Roshko, A. and Pavish, D.L., "A Two Layer Calculation for the Initial Interaction Region of the Unseparated Supersonic Turbulent Boundary Layer with a Ramp," AIAA Paper 80 0135, 1980.

62. Gadd, G.E., "Interactions Between Normal Shock Waves and Turbulent Boundary Layers," British ARC R&M 3262, 1961.

63. Ackeret, J., Feldmann, F., and Rott, N., 1946. Mitteil Inst. für Aerodyn, ETH Zurich, No. 10 Engl. transl. "Investigations of Compression Shocks and Boundary Layers in Gases Moving at High Speed," NACA TM 1113, 1947.

64. Brown, S.N. and Stewartson, K., "Trailing Edge Stall," J. Fluid Mech., Vol. 42, 1970.

65. Preston, J.H., and Sweeting, N.E., "The Experimental Determination of the Boundary Layer and Wake Characteristics of a Simple Joukowski Aerofoil with Particular Reference to the Trailing Edge Region," British ARC, R&M 1998, 1943.

66. Mendelson, R.A., "Wind Tunnel Investigation of the Boundary Layer and Wake and Their Relation to Airfoil Characteristics NACA 65, -012 Airfoil with a True Contour Flap and a Beveled Trailing Edge Flap," NACA TN 1304, 1947.

67 Whitfield, D.L., Swafford, T.M. and Jacocks, J.L., "Calculation of Turbulent Boundary Layers with Separation, Reattachment and Viscous-Inviscid Interaction," AIAA Paper No. 80-1439 AIAA 13th Fluid and Plasma Dynamics Conference, Snowmass Col. July 1980.

68. Nandanan, M., Stanewsky, E. and Inger, G.R., "A Computational Procedure for Transonic Flow Including a Special Solution for Shock Boundary Layer Interaction," AIAA Paper No. 80-1389 AIAA 13th Fluid and Plasma Dynamics Conference, Snowmass, Col. July 1980.

69. Jameson, A. "Transonic Potential Flow Calculations Using Conservation Form," Proc. AIAA 2nd Computational Fluid Dynamics Conference, June 1975, pp. 148-161.

70. Cook, P.H., McDonald, M.A. and Firmin, M.C.P., "Airfoil RAE 2822 Pressure Distributions and Boundary Layer Measurements," in Experimental Data Base for Computer Program Assessment, AGARD AR-138, 1979.

71. Bavitz, P.C., "An Analysis Method for Two-Dimensional Transonic Viscous Flow," NASA TN D-7718, 1975.

72. Carlson, L.A., "Inverse Transonic Airfoil Design Including Viscous Interaction," Advanced in Engineering Sciences NASA CP 2001, 1976.

73. Freuler, R.J. and Gregorek, G.M., "An Evaluation of Four Single Element Airfoil Methods," in Advanced Technology Airfoil Research, NASA CP 2045, Part I, 1978.

74. Kuchemann, D. "Inviscid Shear Flow Near the Trailing Edge of an Aerofoil," British RAE TR 67068, 1968.

APPENDIX

TURBULENT INTERACTIONS ON AIRFOILS AT TRANSONIC SPEEDS - RECENT INTERACTIONS

R.E. MELNIK
Research Department
Grumman Aerospace Corporation
Bethpage, New York 11714
U.S.A.

At the request of symposium participants, material used by the author in his talk which is not included in the text are reproduced hereinafter. A correspondence between the presentation and the printed paper indicating the order of visual material presented and references to figures and tables included in the text and additional slides included in the Appendix follows:

Order of Presentation	Location: Text or Appendix				
Slide 1	Text	Figure	1	page	10-1
Slide 2	Appendix	Slide	2	page	10-30
Slide 3	Appendix	Slide	3	page	10-30
Slide 4	Text	Figure	4	page	10-5
Slide 5	Text	Figure	3	page	10-5
Slide 6	Text	Figure	5	page	10-6
Slide 7	Appendix	Slide	7	page	10-30
Slide 8	Text	Table	1	page	10-6
Slide 9	Text	Figure	6	page	10-6
Slide 10	Appendix	Slide	10	page	10-31
Slide 11	Text	Figure	7	page	10-7
Slide 12	Text	Figure	2	page	10-3
Slide 13	Appendix	Slide	13	page	10-31
Slide 14	Appendix	Slide	14	page	10-31
Slide 15	Text	Figure	11	page	10-10
Slide 16	Text	Figure	12	page	10-10
Slide 17	Appendix	Slide	17	page	10-32
Slide 18	Text	Figure	13	page	10-11
Slide 19	Text	Figure	14	page	10-12
Slide 20	Appendix	Slide	20	page	10-32
Slide 21	Text	Figure	16	page	10-14
Slide 22	Text	Figure	20	page	10-15
Slide 23	Appendix	Slide	23	page	10-32
Slide 24	Appendix	Slide	24	page	10-33
Slide 25	Text	Figure	21	page	10-17
Slide 26	Appendix	Slide	26	page	10-33
Slide 27	Appendix	Slide	27	page	10-33
Slide 28	Text	Figure	24	page	10-21
Slide 29	Text	Figure	25	page	10-22
Slide 30	Text	Figure	26	page	10-22
Slide 31	Text	Figure	27	page	10-23
Slide 32	Text	Figure	28	page	10-24
Slide 33	Text	Figure	29	page	10-24
Slide 34	Text	Figure	30	page	10-25
Slide 35	Text	Table	4	page	10-24
Slide 36	Text	Figure	31	page	10-25
Slide 37	Text	Table	5	page	10-25
Slide 38	Appendix	Slide	38	page	10-34

OUTLINE

I INTERACTING BOUNDARY LAYER THEORY (IBLT)

II SHOCK WAVE BOUNDARY LAYER INTERACTIONS

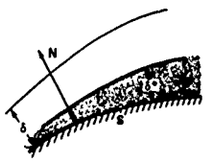
III TRAILING EDGE INTERACTIONS

IV COMPLETE AIRFOIL COMPUTATIONS

Slide 2

INTERACTING BOUNDARY LAYER THEORY

DISPLACEMENT EFFECT



$$V_{bl} = U_e \frac{d\delta^*}{ds} + (\delta - N)\frac{d\rho_e U_e}{\rho_e ds} + \cdots \text{ FOR } N \to \infty$$

MATCHING CONDITION

(1) $V_{inv}(s, N=0) = \frac{d\rho_e U_e \delta^*}{\rho_e ds} \equiv v_o$ — MATCHING AT N = 0 (EQUIVALENT TRANSPIRATION VELOCITY)

(2) $V_{inv}(s, N=\delta^*) = U_e \frac{d\delta^*}{ds}$ — PATCHING AT $N = \delta^*$ (EQUIVALENT DISPLACEMENT BODY)

(3) $V_{inv}(s, N=\delta) = U_e \frac{d\delta^*}{ds} + (\delta^* - \delta)\frac{d\rho_e U_e}{\rho_e ds}$ — PATCHING AT $N = \delta$

FREE INTERACTION

$B = \frac{\delta\theta}{\delta p_s}$ (INFLUENCE FUNCTION) $\quad (\tan\theta \equiv V_{inv}/U_{inv})$

SUPERCRITICAL BEHAVIOR $B < 0$
SUBCRITICAL BEHAVIOR $B > 0$ } MATCHING AT N = 0 → ALWAYS SUBCRITICAL (LE BALLEUR)

Slide 3

INTERACTING BOUNDARY LAYER THEORY

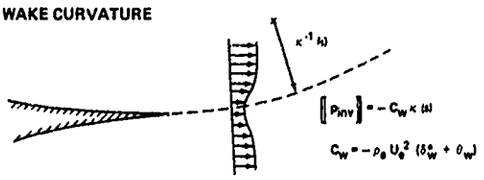
WAKE EFFECTS

WAKE THICKNESS



$$[\![V_{inv}]\!] = \frac{d\rho_e U_e \delta_w^*}{\rho_e ds}$$

WAKE CURVATURE



$$[\![p_{inv}]\!] = -C_w \kappa(s)$$

$$C_w = -\rho_e U_e^2 (\delta_w^* + \theta_w)$$

Slide 7

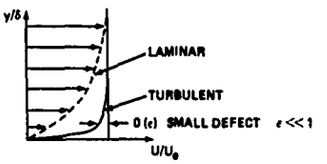
KEY CONCEPTS IN STRONG TURBULENT INTERACTIONS

1940	OSWATITSCH & WIEGHARDT		FREE INTERACTION UPSTREAM INFLUENCE
1950	HOWARTH TSIEN & FINSTON LIGHTHILL (1950) ROBINSON		INVISCID ROTATIONAL FLOW APPROXIMATION
1953	LIGHTHILL (1953)		VISCOUS SUBLAYER
	LAMINAR FLOW	TURBULENT FLOW	
1970	STEWARTSON & WILLIAMS STEWARTSON & MESSITER	ROSE, MURPHY & WATSON ROSHKO & THOMKE	EMPIRICAL SLIP VELOCITY
	(TRIPLE DECK THEORY)		
		MELNIK & GROSSMAN ADAMSON, MESSITER, FEO, LIOU	ASYMPTOTIC THEORY FOR WEAK NORMAL SHOCK WAVES
		INGER & MASON BOHNING & ZIEREP	LIGHTHILL TWO-LAYER THEORY FOR WEAK NORMAL SHOCK WAVES
		VENTRES	POWER LAW PROFILES
		MELNIK, CHOW & MEAD	ASYMPTOTIC THEORY FOR TRAILING EDGE INTERACTIONS
1980		ROSEN, ROSHKO & PAVISH	THEORY FOR THE "SLIP" VELOCITY

Slide 10

CONTRAST BETWEEN LAMINAR & TURBULENT STRONG INTERACTIONS

VELOCITY PROFILE



TWO-LAYER STRUCTURE OF TURBULENT FLOW

- VELOCITIES HIGHER NEAR THE WALL
- PRESSURE GRADIENTS NEGLIGIBLE IN WALL LAYERS UNLESS:

$$O(p_x) > O(u_e^3/\nu)$$

$$O(p_x) > (\epsilon/\hat{\epsilon}) \approx 0 \quad \left\{\epsilon^3 \exp(\epsilon^{-1})\right\}$$

STREAMWISE LENGTH SCALE

LAMINAR: $\Delta x > O(\delta)$

TURBULENT: $\Delta x < O(\delta)$

Slide 13

APPROACHES TO SLIP VELOCITY PROBLEM

LAMINAR SUBLAYER	$M_s = M_e\,(y = \delta_v)$
LIGHTHILL INGER & MASON BOHNING & ZIEREP (POWER LAW PROFILE)	
POWER LAW PROFILES	$U/U_e = (y/\delta)^{1/n}$
VENTRES	$p_x \cong -\rho_e(y)\,[v\,U_e'(y)] \neq 0$ FOR $y \to 0$
ASYMPTOTIC METHODS	
MELNIK & GROSSMAN ADAMSON, FEO, LIOU, MESSITER	$U/U_e = 1 + \frac{\epsilon}{k}\,[\ln(y/\delta) + \frac{1}{2}\,W(y/\delta)]$ $(\epsilon \to 0)$ $p_x = -\rho_e(y)\,[U_e u_x] \neq 0$ FOR $y \to 0$
SEMI-EMPIRICAL METHODS	
ROSE, MURPHY & WATSON ROSHKO & THOMKE ELFSTROM CARRIERE, SIRIEIX, DELERY	M_s FROM EXPERIMENT
CONTROL VOLUME METHOD	
ROSEN, ROSHKO, PAVISH	FULL NAVIER STOKES EQUATIONS

Slide 14

ASYMPTOTIC THEORY FOR NORMAL SHOCK WAVES

BASIC ASSUMPTIONS

- WEAK SHOCK WAVES $M_\infty \to 1$
- FULLY DEVELOPED TURBULENT BOUNDARY LAYER $Re \to \infty$
- LOG LAW INITIAL PROFILE (C_{f_0}, ℓ) $U - U_e = \epsilon f(y/\delta) \ll 1$
- ATTACHED BOUNDARY LAYERS

KEY PARAMETERS

- SHOCK STRENGTH $M_\infty - 1$
- FRICTION VELOCITY $\epsilon = \sqrt{C_{f_0}/2}$ $\epsilon = (\ln Re)^{-1}$

LIMITS

$$\left.\begin{matrix} M_\infty \to 1 \\ \epsilon \to 0 \end{matrix}\right\} \quad \chi_t = \frac{M_\infty^2 - 1}{\epsilon}$$

$\chi_t \to 0$	VERY WEAK
$\chi_t = 0(1)$	WEAK
$\chi_t \to \infty$	MODERATE
$\epsilon \to 0$, $M_\infty \neq 1$	STRONG

Slide 17

BASIC EQUATIONS – MAIN DECK

EXPANSIONS

$U = 1 + \epsilon\,(u_0(y) + \phi_x) + \cdots$ $\quad x = \epsilon^{3/2}\, x^*/L$

$V = \epsilon^{3/2}\, \phi_y + \cdots$ $\quad y = \epsilon\, y^*/L$

DIFFERENTIAL EQUATION

$$[\chi_t + (\gamma+1)\,(u_0(y) + \phi_x)]\,\phi_{xx} - \phi_{yy} = 0$$

$\phi_x(x, 0) = 0$ NO SUBLAYER DISPLACEMENT EFFECT

INITIAL PROFILE. $u_0(y) = k^{-1}\,[\ln(y/\delta) - \ell\, W(y/\delta)]$

SIMILARITY

$C_p(x^*, y^*; \delta; \ell; Re; M_\infty; \gamma) = \epsilon\, \bar{C}_p(\bar{x}, \bar{y}; k_t; \ell)$

$$\bar{x} = \frac{x^*/\delta}{(\gamma+1)^{1/2}\, M_\infty\, \epsilon^{1/2}} \qquad \bar{y} = y^*/\delta$$

$$\boxed{\chi_t = \frac{M_\infty^2 - 1}{(\gamma+1)\, M_\infty^2\, \epsilon}}$$ BASIC SIMILARITY PARAMETER

Slide 20

OTHER DEVELOPMENTS

- SOLUTION IN THE INNER LAYERS

  $C_f/C_{f_0} = 1 + (A_2 + A_2\, \epsilon \ln \epsilon)\, \epsilon\, p_1(x) + \cdots$

- PRESSURE RISE TO SEPARATION

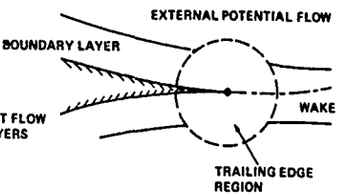
  $\Delta P_s = 0(1)$ FOR $Re \to \infty$

MAJOR REMAINING PROBLEM AREAS

- INTEGRATION INTO "COMPLETE" AIRFOIL PROBLEM
- STRONG SHOCK LIMIT

Slide 23

TRAILING–EDGE FLOW



SCOPE
- LARGE REYNOLDS NUMBER
- FULLY DEVELOPED TURBULENT FLOW
- UNSEPARATED BOUNDARY LAYERS
- CUSPED TRAILING EDGES
- SUBSONIC LOCAL FLOW

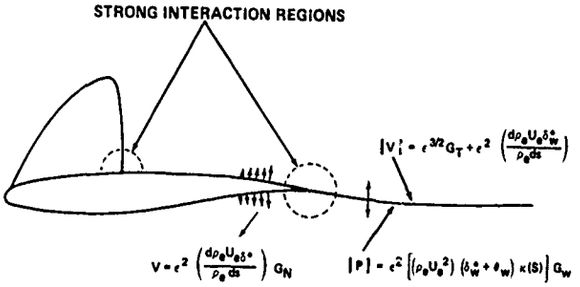
APPROACH
- MATCHED ASYMPTOTIC EXPANSIONS $Re \to \infty$
- LOCAL SOLUTION NEAR TRAILING EDGE
- INVISCID ROTATIONAL FLOW

RESULTS
- ANALYTIC LOCAL SOLUTION
- DOWNWASH CORRECTIONS FOR TRANSPIRATION VELOCITY
- CORRECTIONS TO WAKE CURVATURE CONDITIONS

Slide 24

VISCOUS MATCHING CONDITIONS

STRONG INTERACTION REGIONS



SURFACE PRESSURE:

$$P(0,s) = P_{inv}(0,s) + \epsilon^{3/2} |p|$$

Slide 26

SUMMARY OF THE METHOD

OUTER INVISCID SOLUTION
- FULL POTENTIAL EQUATION
- CONFORMAL MAPPING TO CIRCLE
- JAMESON'S FULLY CONSERVATIVE ROTATED DIFFERENCE SCHEME
- FAST SOLVER

BOUNDARY LAYER METHOD
- GREEN'S LAG ENTRAINMENT METHOD
- TURBULENT ENERGY EQUATION
- SIMPLE WAKE SOLUTION
- LAMINAR STARTING SOLUTION

Slide 27

CONCLUSIONS

- "COMPLETE" IBLT YIELDS ACCURATE PREDICTIONS OF SECTION CHARACTERISTICS
- WAKE & TRAILING EDGE INTERACTIONS ARE IMPORTANT
- DETAILS OF SHOCK-WAVE BOUNDARY-LAYER INTERACTIONS NOT IMPORTANT FOR PREDICTION OF SECTION CHARACTERISTICS
- FULLY CONSERVATIVE METHODS APPEAR TO GIVE BEST RESULTS

RESEARCH OPPORTUNITIES

- STRONG INTERACTIONS AT WEDGE SHAPED TRAILING EDGES
- SUBLAYER SOLUTIONS IN TRAILING EDGE THEORY – BOUNDARY LAYER/WAKE TRANSITION
- SLENDER SEPARATION REGIONS
- IMPROVED INVISCID FORMULATION (EULER EQUATIONS)
- WAKE & TRAILING EDGE INTERACTIONS IN 3D
- THEORY VALIDATION { 1981 STANFORD CONFERENCE; IMPROVED WIND TUNNEL EXPERIMENTS

Slide 38

CALCUL D'ECOULEMENTS VISQUEUX DECOLLES SUR PROFILS D'AILES PAR UNE APPROCHE DE COUPLAGE (*)

par

J.C. LE BALLEUR et M. NÉRON

Office National d'Etudes et de Recherches Aérospatiales (ONERA)

92320 Châtillon - FRANCE

RESUME

Le calcul en fluide visqueux des écoulements incompressibles autour de profils d'ailes monocorps ou multicorps, avec ou sans décollements, est réalisé, en s'appuyant d'une part sur un calcul en fluide parfait, modifié dans ses conditions aux limites, et d'autre part sur une méthode réalisant le calcul et le couplage des couches limites et sillages, en régime de forte interaction visqueuse (**).

Le fluide parfait est traité par une méthode de singularités, où le conditionnement numérique est amélioré en répartissant sur les profils une double distribution sources-tourbillons et en imposant des conditions de régularité aux écoulements fictifs intérieurs aux profils. Le calcul visqueux évalue par une méthode intégrale directe ou inverse l'écart à la solution de fluide parfait couplée, en laminaire ou turbulent, avec ou sans écoulements de retour. La méthode numérique de couplage détermine itérativement les conditions aux limites du fluide parfait. Dans les régions à couches visqueuses attachées, elle calcule la sous-relaxation nécessaire à la stabilité. Dans les régions décollées ou proches de l'être, elle applique un algorithme spécial "semi-inverse". Des comparaisons à l'expérience sont présentées.

COMPUTATION OF VISCOUS FLOWS OVER AIRFOILS, INCLUDING SEPARATION, WITH A COUPLING APPROACH (*)

SUMMARY

The computation of viscous incompressible flows over single or multiple airfoils, with or without separation, is achieved using on one hand an inviscid flow calculation, with modified boundary conditions, on the other hand a method providing calculation and coupling for boundary layers and wakes, within conditions of strong viscous interaction (**).

The inviscid flow is calculated with a method of singularities, the numerics of which has been improved by using both source and vortex distributions over profiles, associated with regularity conditions for the fictitious flows inside of the airfoils. The viscous calculation estimates the difference between viscous flow and inviscid interacting flow, with a direct or inverse integral method, laminar or turbulent, with or without reverse flow. The numerical method for coupling determines iteratively the boundary conditions for the inviscid flow. For attached viscous layers regions, an underrelaxation is locally calculated to insure stability. For separated or separating regions, a special "semi-inverse" algorithm is used. Comparisons with experiments are presented.

INTRODUCTION.

Le calcul des écoulements aux basses vitesses autour de profils monocorps ou multicorps ne peut être obtenu, dans le domaine des grands coefficients de portance, par une simple analyse de fluide parfait. L'addition de calculs classiques de couche limite sous forme d'un couplage "faible", obtenu au prix de quelques itérations, se trouve souvent en échec soit en raison d'effets de décollement ou de bord de fuite, pour lesquels l'aspect interactif du calcul des couches visqueuses redevient dominant, soit en raison d'instabilités numériques suscitées par les itérations de couplage [1, 2, 3, 4], notamment au voisinage du bord de fuite.

En l'absence de décollements, de nombreux progrès ont été apportés aux méthodes de calcul des profils d'ailes [5, 6], l'évolution tendant à introduire de façon plus ou moins complète les phénomènes de forte interaction visqueuse [7, 8, 9]. Une première amélioration, en cas de décollement et de zone de recirculation de grande dimension, peut être obtenue en ajoutant aux méthodes de faible interaction des modélisations simples pour les zones décollées. Il est possible, par exemple, de définir les positions géométriques approchées des

---

(*)Etude effectuée avec le soutien financier de la DRET.

(**) Le calcul du fluide parfait est un travail original de M. Néron, le calcul visqueux et la méthode de couplage représentant la contribution de J.C. Le Balleur.

points de séparation au moyen de techniques classiques de couche limite, et de modéliser le décollement par de simples frontières libres isobares, déterminées par le fluide parfait [10]. La principale limitation des analyses de ce type provient de la modélisation excessive du calcul visqueux, notamment au voisinage des points de décollement, des points de recollement éventuels, et de sa relative inaptitude au calcul des décollements du type bulbe. La prévision des points de séparation par des méthodes de couche limite faiblement interactive reste par ailleurs incertaine.

Pour traiter de façon plus satisfaisante les cas de forte interaction visqueuse on peut utiliser deux types d'approche [4]. La première consiste en une approche globale, résolvant un système d'équations unique valable dans tout le champ d'écoulement (équations de Navier-Stokes complètes ou tronquées). La seconde possibilité utilisée ici est l'approche par couplage fort, dans laquelle un calcul en fluide parfait peut être maintenu, grâce à la résolution séparée, mais couplée, d'un système visqueux complémentaire. Celui-ci détermine en pratique les conditions aux limites d'un problème de fluide parfait modifié, tant par la présence des couches limites que des sillages. Les décollements éventuels sont pris en compte sans traitement supplémentaire par le calcul visqueux interactif, pourvu que soit surmonté le problème numérique du couplage fort avec le fluide parfait. Ceci suppose en particulier l'emploi d'une discrétisation du calcul avec un pas de l'ordre de l'épaisseur locale des couches limites et sillages dans toutes les zones de forte interaction visqueuse.

Les cas considérés ici sont ceux pour lesquels des approximations visqueuses de type couche mince peuvent être valablement invoquées. A ce niveau d'approximation il a été montré sur des problèmes transsoniques ou supersoniques [2, 4, 9, 11], qu'une "formulation déficitaire" pour recomposer la solution visqueuse réelle à partir des deux calculs couplés visqueux et non visqueux constitutifs conduit, pour un niveau de complexité comparable, à des avantages majeurs par rapport aux méthodes qui opèrent traditionnellement un simple raccord entre solutions d'équations d'Euler et de Prandtl.

Cette formulation déficitaire suppose en pratique le recouvrement des domaines de calculs visqueux et non visqueux, le rôle du calcul visqueux se ramenant à évaluer, dans les régions de couche visqueuse, l'écart qui existe entre la solution de fluide parfait effectivement calculée et la solution visqueuse réelle. En transsonique ou supersonique, cette formulation élimine de façon simple [12] les comportements supercritiques des couches limites, au sens de Crocco-Lees. Dans le cas présent des basses vitesses cette analyse [4, 9, 11] apporte d'une part la commodité numérique d'un domaine de calcul du fluide parfait s'appuyant sur les parois, et surtout d'autre part la prise en compte, au moins approximative, des gradients de pression normaux internes aux couches visqueuses.

Pour des raisons pratiques de généralité, notamment en ce qui concerne les possibilités de calcul des profils multiples, une méthode de singularités surfaciques distribuées sur les profils et les sillages a été développée pour le fluide parfait. Le calcul visqueux déficitaire et la technique numérique de couplage ont été obtenus à partir de méthodes développées pour les profils transsoniques [2, 9, 11] . Celles-ci comportent une méthode intégrale traitant les couches limites laminaires et turbulentes, ainsi que les sillages, avec ou sans décollements. Toutefois, la possibilité de calculer les décollements laminaires n'a pas encore été utilisée sur les profils, en raison de la petitesse des échelles de calcul exigées. Présentement, enfin, les problèmes liés au mélange éventuel de plusieurs sillages ou d'un sillage et d'une couche limite n'ont encore fait l'objet d'aucun traitement particulier.

2. MODELISATION DU FLUIDE VISQUEUX.

2.1. Formulation.

Nous désignerons ici par xOy un repère cartésien curviligne, tangent à la paroi ou à la ligne moyenne du sillage, constituée du lieu des points à vitesse minimale. Soient dans ce repère u , v les composantes de la vitesse, p , ρ la pression et la masse volumique pour l'écoulement non visqueux. Soient $\bar{u}$, $\bar{v}$, $\bar{p}$, $\bar{\rho}$, leurs homologues pour la solution de fluide visqueux.

Les analyses de couplage fort supposent souvent que les équations du fluide parfait sont résolues pour $y > \bar{\delta}(x)$, $\bar{\delta}$ étant l'épaisseur physique de la couche limite, et que les équations de Prandtl sont résolues pour $y < \bar{\delta}(x)$, de sorte que l'approximation sur la pression s'écrit $\bar{p}(x,y) \simeq \bar{p}(x) = p(x,\bar{\delta})$ Cette formulation ignore totalement les gradients de pression internes aux couches visqueuses, ce qui peut représenter une source d'erreur importante en cas de couches épaisses, fortement comprimées ou détendues, près des bords de fuite notamment.

La formulation déficitaire adoptée ici met à profit le prolongement du calcul en fluide parfait à l'intérieur de la couche visqueuse pour, entre autres avantages, éliminer la limitation précédente ainsi que supprimer toute influence au choix, quelque peu arbitraire, de la frontière externe des couches visqueuses $y = \bar{\delta}(x)$. Cette formulation conduit à des équations intégrales relativement simples et classiques, *Figure 1*.

2.2. Equations intégrales de couche limite.

La différence entre les équations des solutions visqueuses et non visqueuses est intégrée selon y , avec l'hypothèse d'un raccordement des solutions lorsque $y \to \infty$. Les approximations de couche mince effectuées portent d'une part sur l'élimination des termes visqueux autres que celui des équations de Prandtl, et d'autre part sur l'hypothèse que le champ de pression visqueux $\bar{p}(x,y)$, bidimensionnel, s'identifie en première approximation au champ de pression non visqueux $p(x,y)$. On obtient alors [4, 9, 11] :

$$\frac{d\delta_1}{dx} + \frac{\delta_1}{\rho u}\frac{\partial \rho u}{\partial x} = \frac{v}{u} = \mathcal{H}(x,0) \qquad \text{continuité}$$

$$\frac{d\delta_2}{dx} + \frac{\delta_1 + 2\delta_2}{u}\frac{\partial u}{\partial x} + \frac{\delta_2}{\rho}\frac{\partial \rho}{\partial x} = \lambda \frac{C_f}{2} \qquad \text{Eq. Mouvement selon } x$$

$$\frac{d\bar{\delta}}{dx} - \frac{d\delta_1}{dx} + \frac{\bar{\delta} - \delta_1}{\rho u}\frac{\partial \rho u}{\partial x} = \lambda E \qquad \text{Eq. Entraînement si turbulent, } \lambda = \lambda(x)$$

$$\frac{d\delta_3}{dx} + \frac{\delta_3}{\rho u^3}\frac{\partial \rho u^3}{\partial x} + 2\frac{\delta_1 - \delta_{1i}}{u}\frac{\partial u}{\partial x} = \lambda \phi + \phi_p \qquad \text{Eq. Energie Cinétique si laminaire, } \lambda = 1, \phi_p = 0$$

$$\begin{aligned}
\delta_1(x)\,[\rho u]_{(x,0)} &= \int_0^\infty [\rho u - \bar{\rho}\bar{u}]_{(x,y)}\, dy \\
[\delta_1(x) + \delta_2(x)]\,[\rho u^2]_{(x,0)} &= \int_0^\infty [\rho u^2 - \bar{\rho}\bar{u}^2]_{(x,y)}\, dy \\
[\delta_1(x) + \delta_3(x)]\,[\rho u^3]_{(x,0)} &= \int_0^\infty [\rho u^3 - \bar{\rho}\bar{u}^3]_{(x,y)}\, dy \\
\delta_{1i}(x)\,[u]_{(x,0)} &= \int_0^\infty [u - \bar{u}]_{(x,y)}\, dy
\end{aligned}$$

$\lambda(x)\, E_{(x)}$: taux d'entraînement $\qquad \lambda E = \frac{1}{\rho u}\left[\frac{\partial \tau / \partial y}{\partial (u - \bar{u})/\partial y}\right]_{(x,\bar{\delta})}$

$\lambda(x)\,\phi_{(x)}$: intégrale de dissipation $\qquad \lambda\phi = \frac{2}{\rho u^3}\int_0^\infty \tau \frac{\partial u}{\partial y}\, dy$

$\phi_p(x)$: terme supplémentaire, négligeable si $\frac{\partial^2 p}{\partial x \partial y}$ est petit.

Dans ces équations intégrales, les grandeurs non visqueuses ρ, u, v et leurs dérivées partielles sont relevées en (x,o). La formulation déficitaire apparaît dans la définition des épaisseurs intégrales, qui prend en compte les variations selon y de $\rho(x,y)$ et $u(x,y)$ dans la solution de fluide parfait, et par voie de conséquence de $p(x,y)$. Les approximations de calcul autres que $\bar{p}(x,y) \simeq p(x,y)$ sont ainsi éliminées des équations de continuité et de mouvement (à l'exception du terme C_f).

Ces approximations consistent en une modélisation de relations de fermeture liant les épaisseurs autres que δ_1 et δ_2, ainsi que les termes visqueux C_f, E, λ en turbulent, C_f et ϕ en régime laminaire ou transitionnel. Dans le cas laminaire, elles sont demandées à des solutions de similitude, avec ou sans courants de retour [13]. Dans le cas turbulent, les profils de vitesse sont modélisés par une loi composite rappelant celle de Coles [14],

$$\frac{\bar{u}}{u} = 1 + C_1 \log \eta - C_2 \bar{F}(\eta) \qquad \eta = y/\bar{\delta}(x)$$

C_1 étant lié à C_2 de façon à respecter la loi logarithmique universelle de paroi. La loi de sillage $\bar{F}(\eta)$ ne saurait toutefois se réduire à une approximation sinusoïdale, comme l'indique l'analyse expérimentale [15]. Présentement on adopte l'approximation plus générale :

$$\bar{F}(\eta) = 1 \qquad \text{si} \qquad 0 < \eta < h$$

$$\bar{F}(\eta) = F\left[\frac{\eta - h}{1 - h}\right] \qquad \text{si} \qquad h < \eta < 1$$

dans laquelle une loi simple telle que $F(\eta) = [\eta^{3/2} - 1]^2$ est utilisée avec $h = 0$ pour les couches limites attachées ou faiblement décollées, tandis qu'une loi linéaire $h[\delta_{1i}/\bar{\delta}]$ est adoptée pour les grands paramètres de forme. On suppose enfin, dans le cas turbulent adiabatique, que s'identifient les enthalpies totales visqueuses et non visqueuses $\bar{h}_i(x,y) \simeq h_i(x,y)$. La modélisation des grandeurs visqueuses λC_f, λE, $\lambda\phi$ est effectuée à partir de lois d'équilibre C_f, E, ϕ, associées aux profils de vitesse précédents et à un modèle de turbulence algébrique [16, 17], et d'une loi d'écart à l'équilibre $\lambda(x)$ calculée grâce à une modélisation très simple de l'équation d'énergie cinétique turbulente. Enfin, présentement, les zones de couche limite transitionnelles sont modélisées en pondérant les relations de fermeture laminaires et turbulentes par une fonction d'intermittence, relativement heuristique.

Si on suppose par exemple que $\rho(x,o)$ et $u(x,o)$ sont donnés par le calcul de fluide parfait, la condition aux limites $v(x,o)$, ainsi que deux épaisseurs visqueuses indépendantes $\delta_1(x)$ et $\delta_2(x)$ sont calculées au moyen des équations intégrales de continuité, de mouvement, et d'une équation de moment (entraînement ou énergie cinétique). L'équation de l'énergie cinétique est retenue dans les régions laminaires et transitionnelles où $\partial p/\partial y \simeq 0$, l'équation de l'entraînement étant préférée dans les régions turbulentes où il pourrait être nécessaire de modéliser un terme $\phi_p(x)$, lorsque $\frac{\partial^2 p}{\partial x \partial y}$ est important [4, 9, 11].

2.3. Equations de sillage.

En première approximation, l'identité des pressions visqueuses et non visqueuses $\bar{p}(x,y) \simeq p(x,y)$ conduit, en raison de la continuité du champ de pression visqueux $\bar{p}(x,y)$, à une discontinuité de pression nulle dans le fluide parfait, le long de la ligne moyenne du sillage :

$$< p(x,0) > = 0$$

Une correction de seconde approximation, dite d'effet de courbure, présentement négligée, pourrait être introduite dans la condition de couplage précédente. Elle peut cependant toujours être négligée dans le calcul visqueux.

Dès lors, pour un écoulement de fluide parfait potentiel stationnaire, la continuité de la pression $p(x,0)$ entraîne la continuité de la vitesse $u(x,0)$ et de la masse volumique $\rho(x,0)$. Dans ces conditions, on peut montrer que les équations intégrales du sillage sont formellement identiques aux équations de couche limite, à condition de remplacer $v(x,0)$ par $<v(x,0)>$, la discontinuité de vitesse normale qui traduit dans le fluide parfait l'effet de déplacement visqueux.

Les épaisseurs visqueuses mises en jeu sont alors celles définies pour un sillage, par intégration selon y entre $-\infty$ et $+\infty$. Le terme de frottement C_f disparaît. L'entraînement d'équilibre $E(x)$ est environ quadruplé par rapport à une couche limite, un premier doublement résultant de l'existence de deux frontières $y=\bar{\delta}^+(x)$ et $y=\bar{\delta}^-(x)$, le second doublement étant la conséquence de l'augmentation de la viscosité tourbillonnaire dans une couche turbulente libre. Les relations de fermeture sont issues de profils de sillages, obtenus par annulation de $C_f(x)$, mais elles sont, dans le cadre présent, identiques pour un sillage symétrique ou dissymétrique. Au bord de fuite, le passage couches limites-sillage est traité de manière discontinue pour les profils de vitesse, mais de manière continue pour le fluide parfait, ainsi que pour les épaisseurs $\delta_1(x)$, $\delta_2(x)$.

2.4. Résolution des équations visqueuses.

Le système différentiel visqueux est résolu d'amont en aval par une méthode d'intégration qui, selon l'importance relative du pas Δx et de l'épaisseur $\bar{\delta}(x)$, choisit des schémas numériques du premier ou du second ordre, explicites ou implicites, avec itération sur les termes non linéaires.

L'influence exercée par l'aval sur l'amont en cas de décollement résulte du fluide parfait et du couplage. Les grandeurs $\frac{\partial u}{\partial x}(x,0)$ et $\frac{\partial \rho}{\partial x}(x,0)$ sont évaluées dans le fluide parfait par des schémas centrés. La résolution visqueuse découplée, où $\frac{\partial u}{\partial x}$, $\frac{\partial \rho}{\partial x}$ sont fixés tandis que $\mathcal{H}(x,0)$ est calculé , présente une singularité qui se manifeste dans le cas turbulent vers $H_i = \frac{\delta_{1i}}{\delta_{2i}} = 2,6$, ce qui correspond pour le système d'équations intégrales à une transposition de la singularité de Goldstein des équations de Prandtl voir [12]. Cette singularité est éliminée par effet de couplage. Toutefois, le couplage étant réalisé par une technique itérative, la singularité doit en pratique être éliminée aussi du calcul visqueux découplé, en cas de décollement. Classiquement ce résultat est ici obtenu en adoptant, pour les grandes valeurs de H_i ($H_i \geqslant 1,3$), une méthode de résolution visqueuse inverse où $\mathcal{H}(x,0)$ est fixé, $u(x,0)$ étant calculé et $\rho(x,0)$ déduit de la condition d'isentropie de l'écoulement externe. La difficulté est ainsi rejetée sur la méthode itérative de couplage.

3. METHODE NUMERIQUE DE SINGULARITES POUR LE FLUIDE PARFAIT.

3.1. Introduction.

L'écoulement de fluide parfait bidimensionnel irrotationnel incompressible stationnaire autour de profils monocorps ou multicorps est calculé par une méthode de singularités. Comme il est bien connu, le principal avantage de ces méthodes réside dans leur faible coût, lié à la présence d'inconnues sur la seule surface des profils, à l'exclusion de toute discrétisation au sein de l'écoulement.

Les méthodes de singularités permettent notamment de traiter simplement les configurations multicorps. Lorsque les conditions limites du problème de fluide parfait sont appliquées à la paroi, elles présentent un intérêt supplémentaire lié à la fixité de la géométrie et, par suite, des coefficients des systèmes linéaires. Il devient possible de calculer une fois pour toutes l'inverse de la matrice du système, et ce pour toutes les itérations de couplage et pour toutes les incidences. Dès lors, après cette inversion initiale dont le coût, pour une matrice de dimension N est de N^3 , le nombre d'opérations effectuées à chaque itération de couplage est de l'ordre de $(N+P)^2$, si N et P sont respectivement les nombres de singularités évaluées implicitement et explicitement.

On s'est attaché tout particulièrement dans cette étude à la qualité de la représentation de l'écoulement de fluide parfait dans la région voisine du bord de fuite. En effet, l'écoulement dans cette zone détermine, comme on le sait, l'intensité de la circulation et, par suite, le niveau général de la portance. Il a donc une influence majeure sur tout l'écoulement. Par ailleurs, l'évolution des phénomènes dans cette région est rapide, déjà aux incidences usuelles, et plus encore aux incidences élevées. De plus, les études passées, tout en donnant des résultats appréciables sur la quasi-totalité du profil, ont mis en évidence l'existence de difficultés au bord de fuite pouvant conduire à l'apparition d'oscillations, en y rendant délicate l'application d'une condition de Joukovsky. A fortiori ici, où le calcul visqueux doit être prolongé au-delà du bord de fuite, la qualité du traitement de l'écoulement de fluide parfait en son voisinage, est tout particulièrement importante.

3.2. Pose du probleme.

Considérons l'écoulement extérieur stationnaire irrotationnel et incompressible de fluide parfait autour d'un profil multicorps à m éléments (fig. 2). Ces hypothèses permettent de considérer la vitesse comme le gradient d'un scalaire Φ qui satisfait l'équation de Laplace :

$$\nabla^2 \Phi = 0$$

dans le domaine $(\mathcal{D})$ du plan privé des domaines $(d_1),\ldots,(d_m)$ représentant les éléments du profil, respectivement délimités par les courbes $(C_1),\ldots,(C_m)$. Le domaine $(\mathcal{D})$ est muni de coupures $(S_1),\ldots,(S_m)$ issues de leurs bords de fuite respectifs, et permettant de modéliser les sillages. Les conditions limites aux parois des profils, et au travers des sillages sont :

$$\frac{\partial \Phi}{\partial n} = \vec{n} \cdot \vec{\nabla} \Phi = V_n \quad , \text{ sur } (C_1),\ldots,(C_m).$$

$$\left(\frac{\partial \Phi}{\partial n}\right)_{ext} - \left(\frac{\partial \Phi}{\partial n}\right)_{int} = \vec{n} \cdot \left(\vec{\nabla} \Phi_{ext} - \vec{\nabla} \Phi_{int} \right) = \Delta V_n \text{ , sur } (S_1),\ldots,(S_m)$$

où $\vec{n}$ est la normale extérieure à l'élément considéré, et où V_n et ΔV_n sont respectivement les vitesses normales et les sauts de vitesse normale imposés.

De façon classique, la solution d'un tel problème s'obtient par superposition de champs de vitesse élémentaires induits par des singularités placées aux parois et dans les sillages. Dans le cas présent, chaque sillage est modélisé par une répartition de densités de sources, nulles à la première itération de couplage, et déterminées explicitement à partir des sauts de vitesse normale calculés après chaque itération. La donnée sur les profils de la vitesse normale imposée conduit alors au calcul implicite des singularités aux parois, par résolution d'un système linéaire.

3.3 Sources et tourbillons ; écoulements intérieur et extérieur.

Les méthodes de singularités employées couramment utilisent des densités de sources, des densités de tourbillons ou des doublets perpendiculaires aux parois, l'utilisation de doublets pouvant se ramener à une méthode de densités tourbillonnaires. Notons que les deux premiers types de singularités cités ont un sens physique direct : une densité de sources sur une coupure (C) du plan figure un saut de vitesse normale, une densité de tourbillons figure un saut de vitesse tangentielle. Ces effets élémentaires, où les écoulements de part et d'autre jouent des rôles symétriques nous rappellent que les méthodes de singularités définissent conjointement, en plus de l'écoulement extérieur recherché, un écoulement dit intérieur dans l'espace délimité par les lignes de coupure fermées modélisant les profils[*]. Notons que l'on peut définir une méthode de singularités en choisissant des sources ou des tourbillons ou n'importe quelle combinaison de singularités élémentaires, pourvu que le modèle comporte au moins par profil un terme agissant sur la circulation en problème portant, et un terme agissant su le débit en présence de couche limite. Mathématiquement, les différents modèles, pourvu qu'ils soient soumis à des conditions extérieures identiques, consistant par exemple, en méthode directe, à imposer la vitesse normale extérieure, fourniront des solutions extérieures identiques, mais par contre les écoulements intérieurs seront différents. Dans beaucoup de cas, toutes ces méthodes donnent des résultats acceptables, sauf éventuellement dans la région des bords de fuite. Pour aller au-delà, et notamment pour traiter plus correctement les cas délicats, l'analyse des problèmes présents, tant physiques que numériques, fait apparaître trois types de préoccupations.

3.4. Régularité de l'écoulement intérieur et choix du modèle de singularités

Il n'est pas nécessaire, au niveau du modèle mathématique, de se soucier de l'écoulement intérieur, qui peut être quelconque. Au niveau du modèle discrétisé, par contre, les conditions imposées sur les profils le sont en des points particuliers et non tout le long des frontières. Il en résulte que les solutions intérieures et extérieures ne sont plus strictement indépendantes. La solution dépend du modèle choisi. Or les singularités prises comme inconnues aux parois représentent des sauts de Φ ou de ses dérivées à travers ces parois. Par suite, l'erreur résultant de la discrétisation affecte les écarts de valeur d'une même grandeur entre les écoulements extérieur et intérieur. En d'autres termes, les erreurs portant sur les écoulements intérieur et extérieur sont liées.

Par suite (préoccupation 1), il nous est apparu nécessaire de rechercher un modèle où l'écoulement intérieur soit régulier, et, dans les cas difficiles, de lui imposer des conditions de régularité.

Corrélativement (préoccupation 2), il paraît souhaitable d'adapter la nature des singularités employées aux écoulements à modéliser. Ainsi, des singularités de type source, représentant des sauts de vitesse normale, semblent bien adaptées au cas d'un profil symétrique sans incidence. Inversement, des singularités de type tourbillon, modélisant des sauts de vitesse tangentielle semblent préférables dans le cas d'un profil mince en cas portant. D'une manière générale, un modèle de singularités fixé arbitrairement peut conduire à des écoulements intérieurs irréguliers, associés à une erreur de discrétisation importante. Soulignons que cette adaptation du modèle doit se faire par rapport au problème traité, et non pas seulement par rapport aux seules conditions imposées en données.

Puis (préoccupation 3), afin notamment de limiter les termes d'erreur, on recherchera une méthode où la matrice du système linéaire soit bien conditionnée. C'est en particulier le cas des matrices de coefficients d'influence de singularités de type source sur les vitesses normales, ou de singularités de type tourbillon

---

[*] Cet écoulement intérieur n'est pas, en général, tangent au profil.

sur les vitesses tangentielles. Ceci incite à rechercher une adaptation réciproque des inconnues déterminées implicitement et des conditions imposées à celles-ci. On notera que cette recherche d'un bon conditionnement suppose en outre un mode de discrétisation adéquat, et en particulier un choix convenable de la géométrie des répartitions élémentaires de singularités et de leur position respective par rapport aux points de contrôle où sont imposées les conditions aux limites.

Soulignons la distinction à effectuer entre l'adaptation du modèle de singularités à l'écoulement à modéliser (préoccupation n° 2), qui n'est pas liée au choix des conditions prises comme données du problème, mais présente un caractère intrinsèque, et l'adaptation citée ici (préoccupation n° 3) des seules inconnues implicites aux conditions imposées à celles-ci, qui ne concerne que le mode de détermination numérique. Remarquons que la première conduit aux mêmes conclusions que le problème soit direct ou inverse, ce qui n'est pas le cas pour la seconde .

3.5. Méthode développée, de type sources, à caractère mixte au(x) bord(s) de fuite.

L'analyse des difficultés rencontrées antérieurement en méthode de densités tourbillonnaires a conduit à développer un modèle de type sources, sauf dans des régions spécifiées (en pratique dans les zones minces au voisinage des bords de fuite). Chaque élément de profil, indicé ℓ ($1 \leq \ell \leq m$), comme chaque sillage, est figuré par une répartition de densités élémentaires de source σ_j^ℓ variant linéairement sur chaque segment joignant deux des n_ℓ points de définition consécutifs de cet élément ($1 \leq j \leq n_\ell+1$) (fig. 3). Chaque σ_j^ℓ est d'intensité maximale au point de contrôle courant, et nulle aux autres points. Les densités σ_1^ℓ et $\sigma_{n_\ell+1}$ présentent leur intensité maximale au bord de fuite. Le choix des singularités de type source associées à des conditions de vitesse normale extérieure imposées permet de bénéficier du bon conditionnement de la matrice d'influence correspondante.

Compte tenu des discontinuités de pente existant aux points de définition des lignes brisées qui figurent les profils et les sillages, les informations échangées entre la couche limite et le fluide parfait ne sont pas évaluées en ces points, mais en des points de contrôle situés au milieu de chaque segment élémentaire.

En l'absence de point de contrôle au bord de fuite, la densité de source locale $\sigma_{n_\ell+1}^\ell$ dans le sillage y est évaluée implicitement par interpolation du saut de vitesse normal au sillage ($V_{n\,ext} - V_{n\,int}$) entre les deux derniers points de contrôle aval situés sur le profil et le premier point de contrôle situé sur le sillage. Le traitement de problèmes portants exige la présence d'au moins un terme tourbillonnaire implicite par élément de profil. Ce terme correspond ici à une densité tourbillonnaire répartie sur tout l'élément, d'intensité variant linéairement avec l'abscisse x , maximale au bord d'attaque, et nulle au bord de fuite. La condition de Joukovsky lui est associée, de façon à déterminer la circulation. La forme retenue pour cette condition a consisté à imposer au bord de fuite l'égalité des pressions intrados et extrados. Comme il est bien connu, cette condition n'est pas linéaire et ne peut être imposée, dans le calcul couplé, qu'à convergence. A l'extrados comme à l'intrados, la pression est obtenue par extrapolation sur le dernier demi-segment à partir des valeurs de la vitesse aux deux derniers points de contrôle voisins du bord de fuite. Les densités de singularités se raccordent au bord de fuite de façon à satisfaire la relation vectorielle implicite de régularité :

$$(\bar{V}_{ext} - \bar{V}_{int})_{profil} = (\bar{V}_{ext} - \bar{V}_{int})_{sillage}$$

Par suite, la forme choisie pour la condition de Joukovsky a imposé l'introduction sous forme implicite d'une densité tourbillonnaire $\gamma_{n_\ell+1}^\ell$ au bord de fuite, dans le sillage, sur le premier demi-segment. Le modèle ainsi construit répond au problème extérieur posé. Toutefois, afin d'améliorer le traitement au bord de fuite, un second terme tourbillonnaire a été introduit sur chaque élément de profil. Il correspond à une double densité tourbillonnaire, intrados et extrados, linéaire en fonction de l'abscisse, et d'intensité maximale au bord de fuite. Il est évalué implicitement de façon à assumer seul le saut de vitesse tangentielle à travers l'élément, sans intervention des densités de sources σ_1^ℓ et $\sigma_{n_\ell+1}^\ell$. Ces dernières, responsables du seul saut de vitesse normale gardent alors des intensités modérées.

La méthode ainsi définie s'est avérée satisfaisante dans le cas classique du profil NACA 0012, mais elle est apparue insuffisante dans le cas du profil multicorps RA 16 SC1, profil supercritique de 16 % d'épaisseur relative développé par la SNIAS, dont le bord de fuite du corps principal est à la fois mince et cambré. L'analyse des difficultés rencontrées a fait apparaître, d'une manière générale, la nécessité d'une méthode localement mixte dans les zones de faible épaisseur, nécessité liée à la préoccupation n° 2. La présence conjointe, sous forme implicite, de densités de sources et de densités de tourbillons semble exigée pour modéliser convenablement les sauts de vitesse normale et tangentielle à travers le profil dans le cas limite où celui-ci est infiniment mince. Par suite, le modèle a été développé en utilisant pour chaque élément de profil, en plus des densités de source, un profil de densité tourbillonnaire à k_ℓ paramètres, leur nombre et la position des densités associées à ceux-ci pouvant être choisis au gré de l'utilisateur (fig. 4). A chacun des termes tourbillonnaires correspondent deux distributions de densité tourbillonnaire, l'une à l'intrados, l'autre à l'extrados, chacune présentant une valeur maximale en un point de contrôle choisi. Ces distributions sont construites à partir de densités tourbillonnaires élémentaires de même géométrie que les densités de source élémentaires et de profils $\beta_{k_\ell}(x)$ linéaires par morceaux en fonction de l'abscisse x (fig. 4). Les $(k_\ell-2)$ profils courants présentent une valeur maximale égale à 1 au point de contrôle considéré, et une valeur nulle aux points de contrôle choisis pour les densités voisines. Les profils correspondant au premier et au dernier terme présentent leur maximum respectivement au bord d'attaque et au bord de fuite. Chaque distribution de densité tourbillonnaire, indicée k_ℓ , s'obtient en affectant chaque densité tourbillonnaire élémentaire évaluée au point courant d'abscisse x_j , du coefficient $\beta_{k_\ell}(x_j)$. Dans la méthode ainsi définie, les $(k_\ell-2)$ termes tourbillonnaires rajoutés, comme celui introduit précédemment au bord de fuite, ne sont pas déterminés par les conditions imposées à l'écoulement extérieur, mais constituent autant de degrés de liberté supplémentaires dont est muni le modèle de singularité et qui sont disponibles de façon à l'adopter à chaque cas traité.

Les conditions supplémentaires associées à ces degrés de liberté ont été définies après mise en évidence des préoccupations 1 et 3. Le souci de régularité de l'écoulement intérieur a fait rechercher une condition liée aux dérivées des composantes de la vitesse intérieure, et donc à son gradient. L'attention portée à cet

écoulement intérieur dans les zones de faible épaisseur incitait à rechercher une condition impliquant les composantes transversales du gradient. L'adaptation locale des densités tourbillonnaires, liée à la recherche d'un bon conditionnement conduisait à s'intéresser aux composantes tangentielles de la vitesse. Aussi, la condition choisie a-t-elle consisté à imposer à l'écoulement intérieur l'égalité des vitesses tangentielles à la paroi en chacun des $(k_\ell - 2)$ couples de points de contrôle de même abscisse où les densités extrados et intrados correspondent à un même terme tourbillonnaire (fig. 5). La condition discrétisée $(V_{t\,ext})_i = (V_{t\,int})_i$ revient dans le cas limite de deux parois infiniment proches à annuler la composante $\frac{\partial V_t}{\partial y}$ du gradient de la vitesse tangentielle intérieure. Les calculs ont fait apparaître la nécessité, dans les régions de faible épaisseur, de placer les densités tourbillonnaires en chacun des points de contrôle, un profil grossier étant localement insuffisant. La méthode a donc été utilisée en situant ces densités exclusivement dans les régions de bords de fuite mince, mais, dans celles-ci, en les plaçant en chacun des couples de points de contrôle correspondants. Notons que le procédé présente l'inconvénient d'exiger des maillages analogues à l'extrados et à l'intrados, les deux points de contrôle où sont évaluées les densités correspondant à un même terme tourbillonnaire devant être situées en regard.

La méthode ainsi définie s'est avérée satisfaisante dans les cas traités. Elle fait partie de la classe de méthodes de singularités dans lesquelles le nombre N des inconnues est supérieur à celui M des conditions extérieures imposées implicitement. Les (N-M) degrés de liberté supplémentaires permettent de satisfaire à autant d'autres conditions, dans le but d'améliorer le modèle discrétisé de singularités, au prix d'un effort de calcul accru. Nous avons vu que ces conditions supplémentaires portent sur l'écoulement intérieur.

A ce titre, elle pourra être comparée à la méthode de singularités proposée par D.R. BRISTOW dans [18]. Cette dernière est totalement mixte, chaque profil étant figuré par une double répartition de sources et de tourbillons. Les conditions supplémentaires nécessaires sont obtenues par une minimisation au sens des moindres carrés. Cette méthode a donné d'excellents résultats notamment dans le calcul de l'écoulement autour d'une plaque plane modélisée par un profil très mince à section losangique.

La méthode proposée dans cet article entend s'insérer entre celle de D.R. BRISTOW, et les méthodes usuelles, pour lesquelles M = N. On notera en particulier qu'ici l'accroissement (N-M) = $\sum_\ell (k_\ell - 1)$ de la dimension du système linéaire reste modéré devant le nombre $M = \sum_\ell n_\ell$ des paramètres implicites de l'écoulement extérieur, dans la mesure où l'introduction des paramètres supplémentaires, à raison d'un par couple de points intrados et extrados, est limitée aux seules régions de bord de fuite mince.

4. METHODE NUMERIQUE DE COUPLAGE FORT.

Le couplage est réalisé par itérations successives sur des résolutions découplées du fluide parfait et des couches visqueuses. La méthode, utilisable également en régime transsonique ou supersonique, a été détaillée par ailleurs [2, 4, 9]. Nous en rappellerons seulement les grandes lignes, figure 5 .

Selon le paramètre de forme local de la couche visqueuse $H = \delta_1/\delta_2$, le calcul visqueux est résolu soit comme un problème direct ($H_i < 1{,}8$), soit comme un problème inverse ($H_i > 1{,}8$). Le calcul de fluide parfait est, quant à lui, toujours résolu comme un problème direct. Il associe à une distribution de vitesse normale sur le profil, et de discontinuité de vitesse normale sur le sillage, repérées par $\frac{\gamma}{U} = \Theta^n_{(x,0)}$, une distribution de module de la vitesse $U^n_{(x,0)}$.

Après quelques éliminations dans le système d'équations intégrales visqueuses, il est possible d'extraire une équation différentielle entre $U_{(x,0)}$ et $\Theta_{(x,0)}$, qui représente la condition aux limites appliquée au fluide parfait. Elle peut s'écrire schématiquement :

$$A_1(x)\,\Theta_{(x,0)} = \delta_1(x)\,A_2(x)\left[\frac{dU}{dx}\right]_{(x,0)} + A_3(x)$$

x est mesuré le long de la frontière du fluide parfait, paroi ou sillage. A_1, A_2, A_3, δ_1 dépendent des autres équations visqueuses, des conditions initiales visqueuses $\delta_1(x_0)$ et $\delta_2(x_0)$, ainsi que des évolutions non visqueuses $\Theta_{(x,0)}$ et $U_{(x,0)}$. A_1 s'annule aux points de décollement et de recollement, où les solutions ne sont régulières que si : $\delta_1[dU/dx] = -[A_3/A_2]$. Cette condition est vérifiée à convergence du couplage par adaptation de $[dU/dx]$; elle n'est vérifiée au cours des itérations que dans le calcul visqueux de type inverse, où $[dU/dx]$ est un résultat de calcul.

4.1. Itération directe ($\delta_1/\delta_2 < 1{,}8$).

Comme le rappelle la figure 6 , on associe dans ce cas au calcul direct de fluide parfait un calcul visqueux de type direct qui, d'après la relation ci-dessus, fournit un prédicteur $\tilde{\Theta}_{(x,0)}$ pour la vitesse normale du fluide parfait à l'itération suivante :

$$\tilde{\Theta}_{(x,0)} = \delta_1\,B(x)\left[\frac{dU}{dx}\right]^n_{(x,0)} + C(x) \qquad B = \frac{A_2}{A_1} \qquad C = \frac{A_3}{A_1}$$

Il est connu [1, 2] que l'adoption d'une itération simple où $\Theta^{n+1}_{(x,0)} = \tilde{\Theta}_{(x,0)}$ conduit fréquemment à une méthode instable, comme on peut intuitivement s'y attendre, en remarquant que $B \to \infty$, lorsque $A_1 \to 0$ au voisinage des décollements. Il a été montré lors d'une étude spéciale et approchée de stabilité [2] que l'itération directe peut être stabilisée par une sous-relaxation locale $\omega(x)$:

$$\Theta^{n+1}_{(x,0)} = \Theta^n_{(x,0)} + \omega(x)\left[\tilde{\Theta}_{(x,0)} - \Theta^n_{(x,0)}\right]$$

avec :

$$\omega = \frac{1}{1-\mu_D} \qquad \mu_D = \frac{\pi B \delta_1}{\Delta x \sqrt{1-M^2}}$$

dans laquelle Δx est le pas d'espace local avec lequel est discrétisé $U^n_{(x,0)}$, le gradient $[dU/dx]^n_{(x,0)}$ étant estimé dans le fluide parfait par des schémas aux différences centrés. Il est clair que $\omega(x)$ est d'autant plus petit que l'est lui-même le pas Δx des noeuds de couplage, relativement à l'épaisseur locale

$\delta_1(x)$ de la couche visqueuse, ceci même dans le cas d'une couche limite classique de plaque plane. De même, $\omega(x)$ est d'autant plus petit, pour un pas $\Delta x/\delta_1$ fixé, que la constante visqueuse B est plus grande, c'est-à-dire que la couche visqueuse est plus proche du décollement, où l'on aurait $\omega = 0$.

4.2. Itération semi-inverse ($\delta_1/\delta_2 \geq 1{,}8$).

Pour une distribution $\Theta^n_{(x,0)}$ donnée, figure 7 , on associe dans ce cas d'une part un calcul de fluide parfait, qui fournit un premier prédicteur de $\frac{dU}{dx}$, soit $\left[\frac{dU}{dx}\right]^n_{(x,0)}$, et d'autre part un calcul visqueux inverse qui fournit un second prédicteur $\left[\frac{d\tilde{U}}{dx}\right]_{(x,0)}$. Il a été montré par ailleurs [2] qu'il est possible de corriger itérativement $\Theta^n_{(x,0)}$ en chaque noeud de couplage , indépendamment des autres noeuds. Qualitativement, l'algorithme répond à la question : comment faut-il perturber $\Theta^n_{(x,0)}$ pour que la perturbation induite sur $\left[\frac{dU}{dx}\right]^n_{(x,0)}$ par un calcul de fluide parfait ajuste celui-ci sur $\left[\frac{d\tilde{U}}{dx}\right]_{(x,0)}$ Il est clair que la réunion du calcul de fluide parfait direct et de la perturbation précédente simule un calcul de fluide parfait inverse. Finalement, une méthode stable de correction de $\Theta^n_{(x,0)}$, est obtenue, voir [2], en appliquant aux noeuds de couplage subsoniques la relation suivante :

$$\left[\Theta^{n+1}_{(x,0)} - \Theta^n_{(x,0)}\right] = \frac{\delta_1 B \Delta x \sqrt{1-M^2}}{\pi \delta_1 B - \Delta x \sqrt{1-M^2}} \left[\frac{1}{\tilde{U}}\frac{d\tilde{U}}{dx} - \frac{1}{U^n}\frac{dU^n}{dx}\right]_{(x,0)}$$

Dans cette expression, le gradient $\left[\frac{dU^n}{dx}\right]_{(x,0)}$ est estimé à partir de la solution de fluide parfait au moyen de schémas aux différences centrés identiques à ceux utilisés pour l'itération en mode direct. Il en résulte à convergence une continuité absolue de la solution numérique aux noeuds de commutation entre itération directe et itération semi-inverse.

5. RESULTATS DE CALCUL - COMPARAISON A L'EXPERIENCE.

5.1. Introduction .

Dans ce paragraphe sont présentées des comparaisons entre les résultats obtenus avec la méthode de calcul décrite précédemment et des résultats expérimentaux à conditions identiques. Ces comparaisons sont effectuées sur le profil classique NACA 0012, sur un profil supercritique à charge arrière LC 90 DK 1.4 dont les cotes sont données figure 8 et sur un autre profil supercritique défini par l'Aérospatiale RA 16 SC1 et qui a été équipé d'un volet de bord de fuite à simple fente ayant une profondeur relative de 29 %. Pour ce profil double corps les cotes des 2 éléments ainsi que les lois du braquage du volet sont reportées figure 9.

Les essais du profil NACA 0012 et du profil double corps ont été effectués dans la soufflerie S1 Ca de l'ONERA et ceux du profil LC 90 DK 1.4 dans la soufflerie F1 du Fauga. Les conditions d'essais sont les suivantes :

	Profil NACA 0012	Profil LC 90 DK 1.4	Profil double corps
type de montage	entre panneaux b = 1 m	entre panneaux b = 1 m	entre panneaux b = 1 m
P_i	1 bar	1 bar	1 bar
V_o	40 m/s	40 m/s	40 m/s
corde de référence	0,75 m	0,75 m	0,50 m (volet rentré)
nombre de prises de pression sur le profil		65	50 (corps principal) 20 (volet)

Les essais ont été effectués en transition naturelle et les efforts C_z, C_m obtenus par intégration des pressions sur les profils. Le coefficient de trainée C_x est déduit d'un sondage du sillage effectué à 1/2 corde en aval du bord de fuite.

5.2. Profil monocorps NACA 0012 -

Les calculs réalisés sur le NACA 0012 ont été effectués avec la version initiale de la méthode de singularités, sans adjonction de densité tourbillonnaire supplémentaire. Dans le calcul de couche limite, la transition s'effectue de façon naturelle à l'extrados. A l'intrados, par contre, elle est imposée à 85 % de la corde lorsqu'elle n'est pas apparue naturellement plus tôt. Les résultats présentés font apparaître un très bon accord calcul-expérience sur la courbe $C_z - \alpha$, et ce jusqu'à des incidences élevées, de l'ordre de 15° (fig.10). La prédiction des C_x , toutefois n'atteint pas la même précision (fig. 11). Les courbes montrent un bon accord calcul-expérience, à 14° comme à 12° ou à 4° (fig.12 , 13, 14). Pour montrer l'importance des effets visqueux la courbe obtenue en fluide parfait à 14° est comparée aux résultats du calcul visqueux et à l'expérience, sur la figure 15. Enfin, sur la figure 16, obtenue à une incidence de 15°, on notera à l'extrados l'amorce d'un plateau de pression et l'extension de la zone décollée par rapport aux incidences précédentes.

5.3. Profil monocorps LC 90 DK 1.4

Le profil supercritique LC 90 DK 1.4, profil cambré dont la loi d'épaisseur est déduite par affinité du profil ONERA D, constitue un cas d'application plus difficile, compte tenu de l'importance des effets visqueux,

traduits notamment sur la courbe C_{ℓ}-α par l'écart notable entre les C_{ℓ} expérimentaux et ceux calculés en fluide parfait.

Dans la méthode de singularités, 10 termes tourbillonnaires supplémentaires ont été introduits, dans les 10 derniers pour cent de la corde. La ligne de sillage, rectiligne, a été orientée selon la direction de la vitesse au niveau de son premier point de contrôle déterminée lors d'un premier calcul.

Dans le calcul visqueux, la prévision correcte des phénomènes de bord de fuite suppose une grande précision dans l'évaluation des caractéristiques locales des couches visqueuses. Celle-ci ne peut être elle-même obtenue que par un calcul suffisamment précis dans la région de bord d'attaque. L'expérience indiquant la présence dans cette région d'un bulbe de décollement laminaire dont l'échelle réduite est incompatible avec celle des maillages présentement utilisés, les épaisseurs δ_1 et δ_2 ont été recalées sur l'expérience à l'extrados, à 22 % de la corde.

Sur la figure 17 sont comparées aux valeurs expérimentales et à celles calculées en fluide parfait, les courbes C_{ℓ}-α obtenues par la présente méthode d'une part et par une méthode de couplage "faible", plus conventionnelle, avec épaississement du profil en trois itérations successives, d'autre part. La méthode proposée ici, qui permet de retrouver plus de 80 % de l'écart entre les calculs de fluide parfait et l'expérience apporte une amélioration importante par rapport aux méthodes conventionnelles. Comme précédemment, la précision du calcul des C_{x} reste à améliorer (fig. 18). Les courbes $K_p(x)$ montrent un bon accord calcul-expérience (fig. 19, 20, 21, 22). La figure 23 où se trouve pour α = 13°, en plus des courbes de la figure 22, la courbe obtenue en fluide parfait, permet d'apprécier l'importance des effets visqueux. L'évolution calculée des épaisseurs de déplacement et de quantité de mouvement est en excellent accord jusqu'à l'incidence de 10° (fig. 24, 25 et 26) avec celle qui a été déterminée expérimentalement. Notons que l'accroissement de ces épaisseurs est soumis à un phénomène de grande dépendance par rapport aux valeurs initiales.

Pour α = 13° (fig. 27) une différence d'évolution est observée à l'extrados dans la région de bord de fuite entre le calcul et l'expérience; celle-ci fera l'objet d'une investigation ultérieure.

On notera d'une manière générale l'importance des effets visqueux sur ce profil, due à sa géométrie particulière près du bord de fuite, avec un dièdre important, et une forte courbure à l'extrados. Divers développements, notamment l'introduction d'un calcul de sillage dissymétrique, devraient apporter de nouveaux progrès.

5.4. Profil multicorps RA 16 SC1

Le profil RA 16 SC1, profil supercritique de 16 % d'épaisseur relative avec volet (fig. 9), constitue un cas d'application en multicorps, présentant un important décollement à l'intrados du corps principal à l'endroit du toit de volet.

Dans le calcul de couche limite, la transition a été déclenchée à l'intrados du corps principal, à 30 % de la corde 1 et sur le volet, à la fois à l'extrados et à l'intrados, respectivement à 0,005 l et 0,007 l du bord d'attaque. Dans la méthode de singularités, 25 termes tourbillonnaires supplémentaires ont été rajoutés sur le corps principal, dans les 24 derniers pour cent de la corde. Les sillages ont été alignés en deux itérations sur les valeurs issues du calcul. Les C_{ℓ} obtenus sont comparés dans le tableau suivant à ceux issus du calcul parfait et aux valeurs expérimentales, dans les deux cas de calcul traités, à une incidence de 8°, et pour des braquages de volet respectivement de 10° et de 20°.

C_{ℓ} ; α = 8°	δ = 10°	δ = 20°
fluide parfait	2,45	3,22
expérience	2,04	2,38
calcul couplé	2,21	2,79

Les courbes $K_p(x)$ obtenues dans ces deux cas présentent un très bon accord calcul-expérience dans la région du bord de fuite du corps principal (fig. 28 et 29), malheureusement il n'en est pas tout à fait de même à l'avant du profil et c'est pourquoi la portance calculée est supérieure à la portance mesurée de 5 à 7 %. Une bonne part de cet écart est probablement due à l'insuffisance du maillage dans la région de bord d'attaque.

6. CONCLUSION.

La présente méthode a fourni, sur le profil NACA 0012, des résultats très proches des valeurs expérimentales dans des cas présentant un décollement au bord de fuite, et ce jusqu'à des incidences élevées, voisines du décrochage.

Elle a permis, dans le cas difficile du LC 90 DK 1,4, caractérisé par une importante perte de portance due aux effets visqueux, de rendre compte de plus de 80 % de celle-ci, présentant ainsi des résultats nettement améliorés par rapport à ceux obtenus par une méthode de couplage faible plus conventionnelle.

Elle a donné également de bons résultats dans le cas du profil multicorps RA 16 SC1, qui présente notamment un décollement important à l'intrados du corps principal.

Ces résultats encourageants obtenus tant sur profil monocorps que multicorps, ainsi que l'introduction ultérieures de diverses améliorations, permettent d'espérer de nouveaux progrès de l'accord calcul-expérience dans le futur.

REFERENCES

[1] BRUNE G.W., RUBBERT P.E., NARK T.C. - A new approach to inviscid flow-boundary layer matching. AIAA paper n° 74601, Palo Alto (June 17-19, 1974).

[2] LE BALLEUR J.C. - Couplage visqueux-non visqueux : méthode numérique et application aux écoulements transsoniques et supersoniques. La Recherche Aérospatiale n° 1978-2, p. 67-76.

[3] LE BALLEUR J.C. - Calculs couplés visqueux - non visqueux incluant décollements et ondes de choc en écoulement bidimensionnel. VKI/AGARD LS-94 on Three-dimensional and unsteady separation at high Reynolds numbers (Febr. 1978).

[4] LE BALLEUR J.C., PEYRET R., VIVIAND H. - Numerical studies in high Reynolds number aerodynamics. Computers and Fluids, vol. 8, n° 1, pp. 1-30, (March 1980).

[5] BAUER F., KORN D. - Computer simulation of transonic flow past airfoils with boundary layer correction. 2n dAIAA Computational Fluid Dyn. Conf., Hartford (June 1975).

[6] BAVITZ P.C. - An analysis method for two-dimensional transonic viscous flow. NASA TN-D-7718 (January 75).

[7] COLLYER M.R., LOCK R.C. - Prediction of viscous effects in steady transonic flow past an aerofoil. Aeronautical Quarterly, vol. 30, p. 485 (August 1979).

[8] MELNIK R.E., CHOW R., MEAD H.R. - Theory of viscous transonic flow over airfoils at high Reynolds numbers. AIAA Paper 77-680 (1977).

[9] LE BALLEUR J.C., VIVIAND H. - Méthodes de calcul des écoulements décollés bidimensionnels aux grands nombres de Reynolds. 16e Colloque AAAF, Lille (Nov. 1979) ONERA TP n° 1979-145.

[10] HENDERSON M.L. - A solution to the 2-D separated wake modeling problem and its use to predict C_{Lmax} of arbitraty airfoil sections. AIAA Paper 78-156 (Jan. 1978).

[11] LE BALLEUR J.C. - Calcul des écoulements à forte interaction visqueuse au moyen de méthodes de couplage. AGARD CP on Computation of viscous inviscid interaction, Colorado-Springs (29 Sept. 1 Oct. 1980).

[12] LE BALLEUR J.C. - Couplage visqueux - non visqueux : analyse du problème incluant décollements et ondes de choc. La Recherche Aérospatiale n° 1977-6, pp. 349-358.

[13] ABOUT G. - Contribution à l'étude du décollement supersonique laminaire : mise en oeuvre et perfectionnement des méthodes de calcul intégrales. Thèse de Doctorat 3e Cycle - Note Technique ONERA n° 1980-1.

[14] COLES D.E. - The law of the wake in turbulent boundary layer. Journal of Fluid Mechanics, vol. 1, part 2 (1956).

[15] DELERY J. - Analyse du décollement résultant d'une interaction choc-couche limite turbulente en transsonique. La Recherche Aérospatiale n° 1978-6, pp. 305-320.

[16] COUSTEIX J., LE BALLEUR J.C., HOUDEVILLE R. - Calcul des couches limites turbulentes instationnaires en mode direct ou inverse, écoulements de retour inclus. Analyse des singularités. La Recherche Aérospatiale n° 1980-3, pp. 147-157.

[17] MICHEL R., QUEMARD C., COUSTEIX J. - Méthode pratique de prévision des couches limites turbulentes bi et tridimensionnelles. La Recherche Aérospatiale n° 1972-1.

[18] BRISTOW D.R. - A new surface singularity method for multi-element airfoil analysis and design, AIAA Paper n° 76-20.

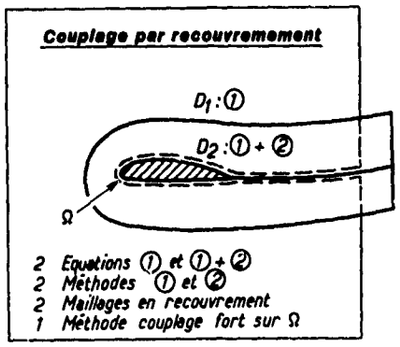


Fig. 1 – Couplage par recouvrement.

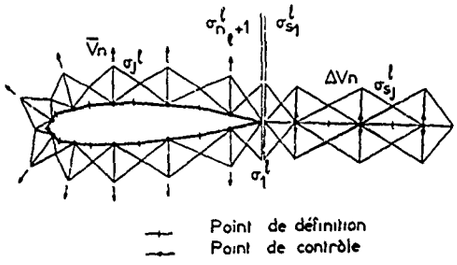


Fig. 3 – Discrétisation de chaque élément de profil.

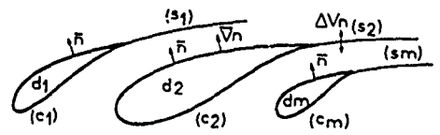
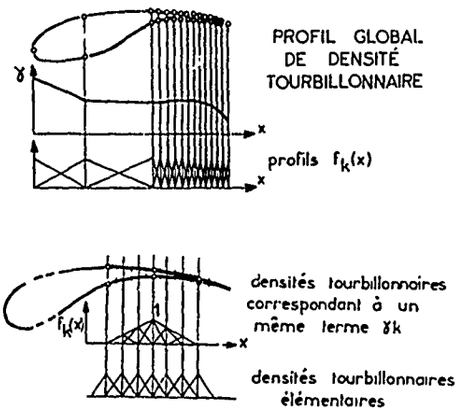


Fig. 2 – Modélisation du fluide parfait.



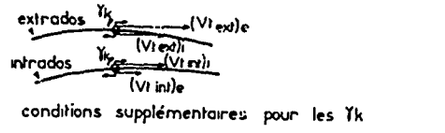


Fig. 4 – Densités tourbillonnaires supplémentaires et conditions associées.

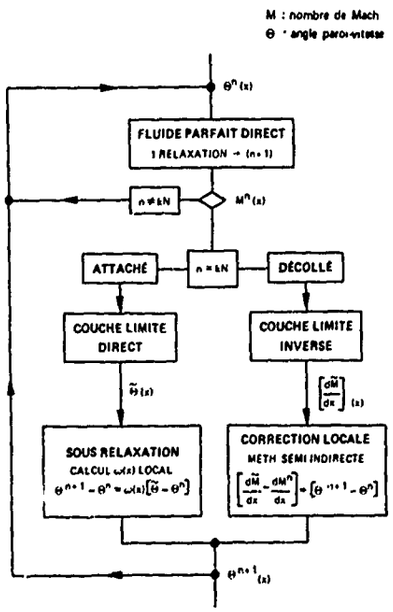


Fig. 5 – Organigramme de couplage.

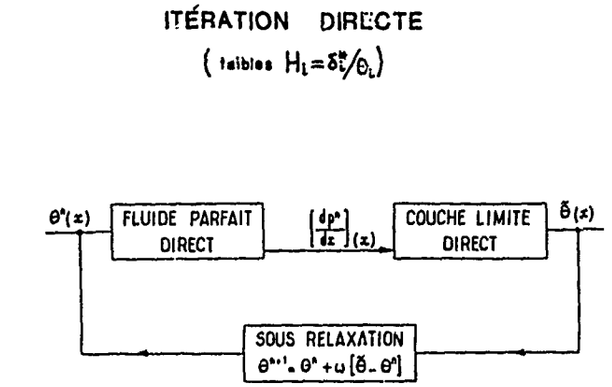
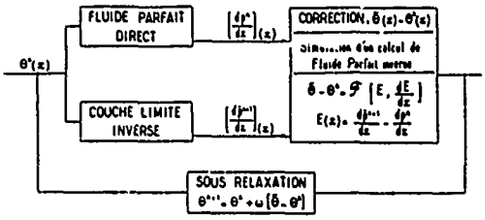


Fig. 6 – Itération directe.

ITERATION SEMI-INVERSE

(grande $H_L = \delta^*/\theta_L$)



► ETAPE DE CORRECTION :

Si $M < 1$:

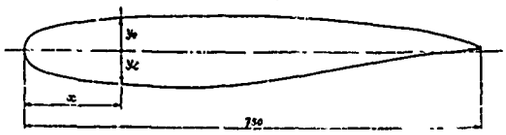
$$\Theta^{n+1} - \Theta^n = C_1(M, \delta^*, \bar{\delta}, \alpha)\left[\frac{d\bar{p}^{n+1}}{dx} - \frac{dp^n}{dx}\right]$$

Si $M > 1$:

$$\Theta^{n+1} - \Theta^n = C_2(M, \delta^*, \bar{\delta}, \alpha)\left[\frac{d^2\bar{p}^{n+1}}{dx^2} - \frac{d^2p^n}{dx^2}\right]$$

Fig. 7 – Itération semi-inverse.

Profil LC 90 D (K = 1.8)
Définition du profil



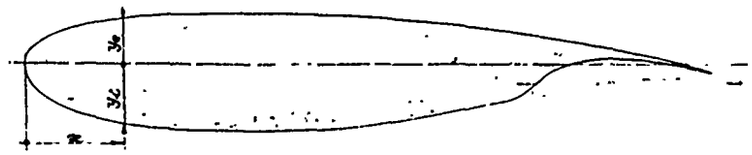
x	0	0,5	1	2,5	5	7,5	10	20	40	60	80	100	120	140	160
y_e	0	0,15	2,27	11,45	16,36	18,33	21,00	29,00	33,74	35,07	34,57	32,94	30,85	28,35	25,54
y_c	0	-2,15	-3,27	-5,45	-6,86	-6,89	-7,00	-7,00	-5,74	-4,93	-3,97	-2,95	-1,85	-0,75	0,34

180	200	220	240	260	280	300	320	340	360	380	400	420	440	460
31,98	33,00	33,56	34,11	34,19	33,36	33,00	32,79	32,30	31,66	30,90	30,13	29,33	28,51	27,66
-3,06	-3,83	-3,89	-3,84	-3,63	-3,43	-3,23	-2,79	-2,38	-1,98	-1,58	-1,18	-0,78	-0,39	0,00

480	500	520	540	560	580	600	620	640	660	680	700	720	740
26,80	25,93	25,03	24,10	23,14	22,16	21,14	20,10	19,03	17,93	16,80	15,64	14,45	13,23
0,39	0,77	1,14	1,50	1,85	2,19	2,52	2,84	3,15	3,45	3,74	4,01	4,27	4,52

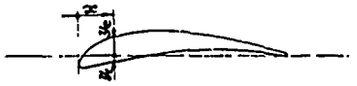
Fig. 8 – Profil LC 90DK1.4 – Cotes.

DÉFINITION DU PROFIL RA 16 SC1



$x_{\%c}$	0	0,25	0,5	1	1,5	2	2,5	3	4	5	7,5	10	15	20	30	40	50	60	80	100	120	140	160	180	200
y_e	0	2,4	3,4	4,74	5,85	6,70	7,43	8,15	8,36	10,07	12,76	14,66	17,67	19,96	23,87	27,07	27,81	28,66	30,77	32,27	33,30	33,91	34,09	33,91	33,84
y_c	0	-3,5	-4,85	-6,72	-8,07	-9,04	-10,23	-11,10	-12,61	-13,80	-16,62	-18,93	-22,86	-26,19	-30,79	-34,84	-36,54	-38,09	-41,06	-44,00	-46,57	-48,96	-50,58	-48,67	

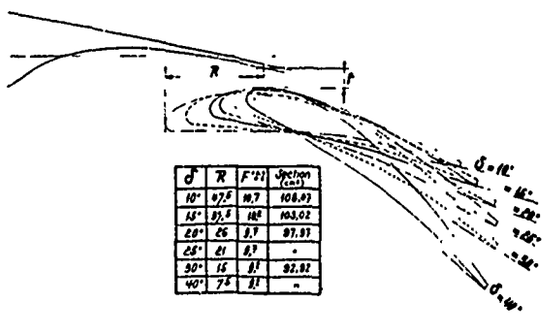
220	240	260	280	300	320	330	335	340	345	350	355	360	365	370	380	390	400	410	420	440	460	480	970	980
32,79	31,79	30,63	29,83	28,89	28,72			22,15				18,21			15,85		12,98		7,82		3,45	1,12	-1,15	-3,88	-5,65
-43,29	-41,34	-39,36	-36,68	-34,33	-29,65	-47,6	-28,6	-28,2	-29,7	-17,4	-14	-10,2	-6,88	-4,81	-1,9	1,32	4,22	6,5	10,8	12,8	10,8	7	2,8	-5,6	-7,63



$x_{\%c}$	0	0,5	1	2	3	4	6	8	11	15	25	35	45	55	65	75	85	95	105	115	125	135	145
y_e	-6,38	-2,70	-1,82	-0,80	0,60	1,56	3,09	4,60	6,46	8,60	12,24	14,86	16,76	18,32	19,26	19,64	19,56	19,16	18,29	17,16	15,82	14,28	12,65
y_c	-6,38	-6,50	-7,04	-7,76	-8,18	-8,22	-8,04	-7,72	-7,24	-6,68	-4,63	-2,78	-1,07	0,55	1,86	2,87	3,53	3,83	3,79	3,28	2,40	1,35	0

PROFIL RA 16 SC1 HYPERSUSTENTÉ

Loi de braquage du volet



δ	R	F°21	Section (cm²)
10°	97,5	10,7	108,03
15°	97,5	10,5	103,02
20°	96	9,7	97,93
25°	81	8,9	"
30°	15	8,1	92,92
40°	75	8,1	"

Fig. 9 – Profil RA 16 SC1 – Cotes - loi de braquage du volet.

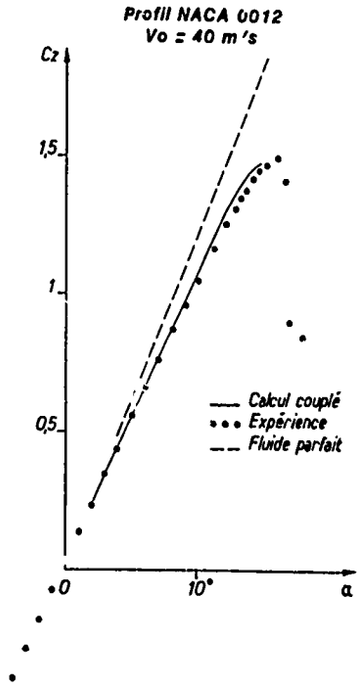


Fig. 10 – Profil NACA 0012 – Courbe Cz (α).

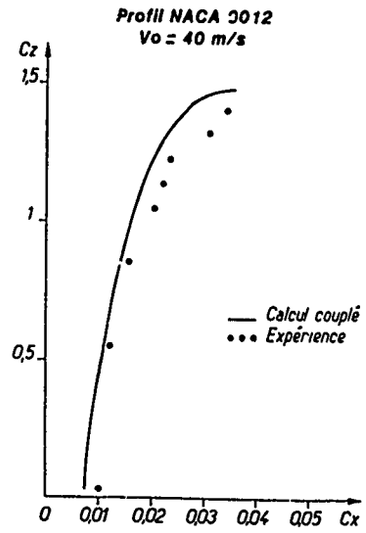


Fig. 11 – Profil NACA 0012 – Polaire.

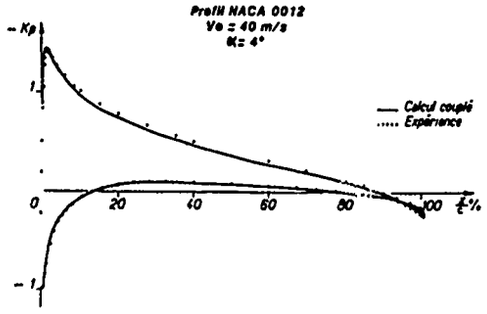


Fig. 12 – Profil NACA 0012 – Pressions – α = 4°.

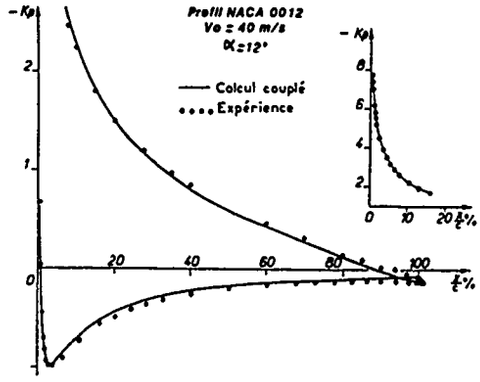


Fig. 13 – Profil NACA 0012 – Pressions – α = 12°.

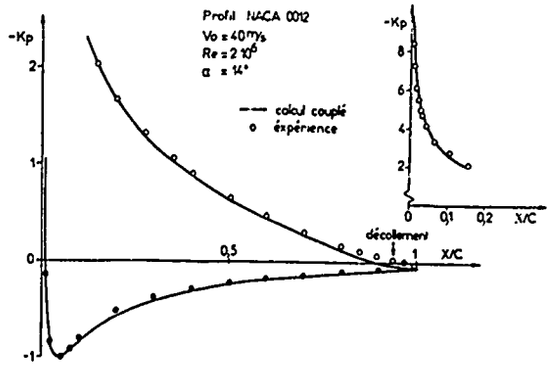


Fig. 14 – Profil NACA 0012 – Pressions – α = 14°.

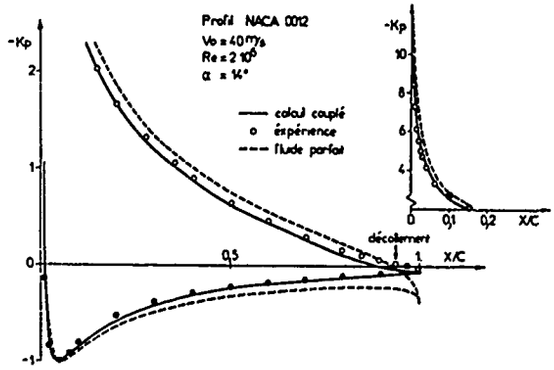


Fig. 15 – Profil NACA 0012 – Comparaison fluide parfait - fluide visqueux.

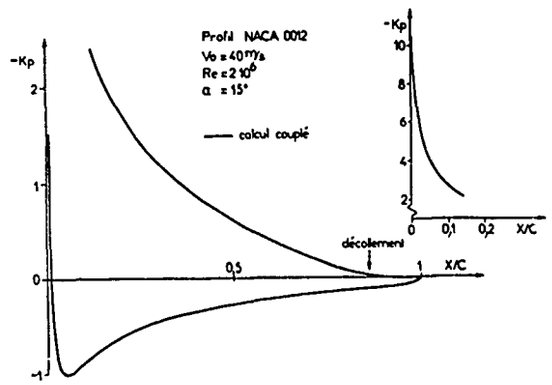


Fig. 16 – Profil NACA 0012 – Pressions – α = 15°.

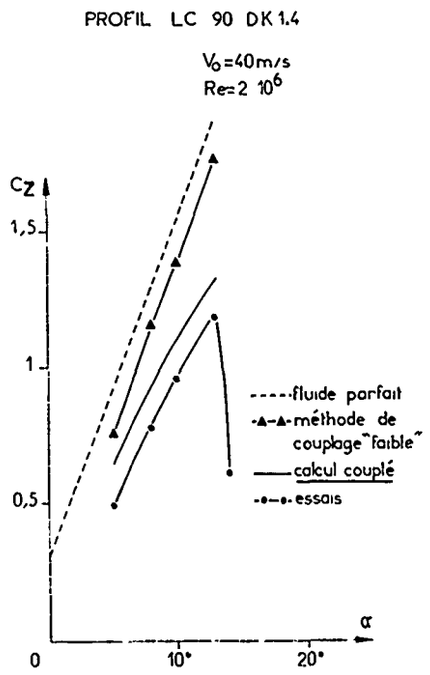


Fig. 17 – Profil LC 90DK1.4 – Courbe Cz (α).

PROFIL LC 90 DK 1.4

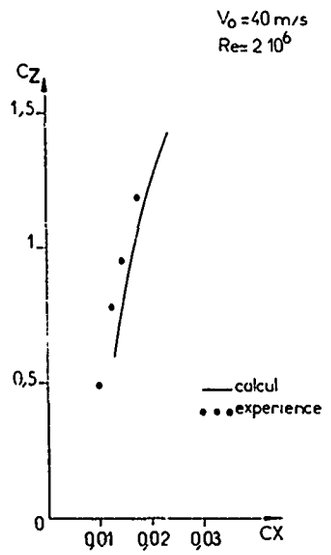


Fig. 18 – Profil LC 90DK1.4 – Polaire.

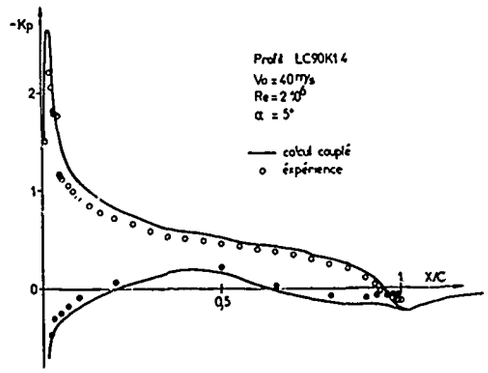


Fig. 19 – Profil LC 90DK1.4 – Pression – α = 5°.

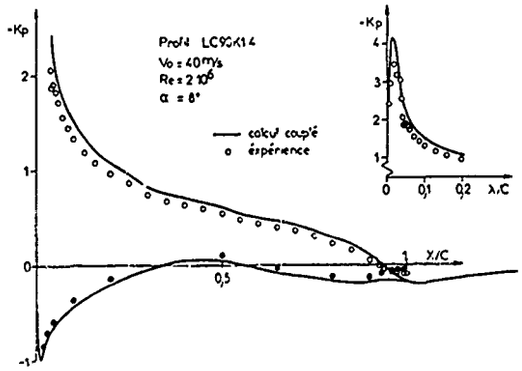


Fig. 20 – Profil LC 90DK1.4 – Pression – α = 8°.

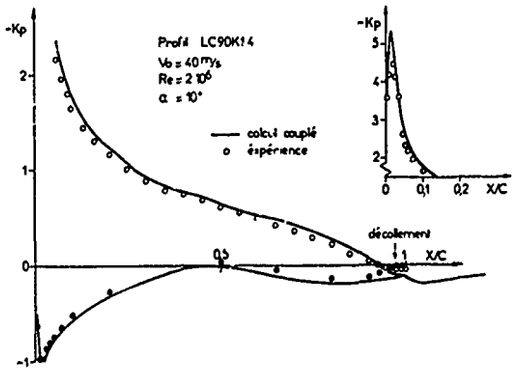


Fig. 21 – Profil LC 90DK1.4 – Pression – α = 10°.

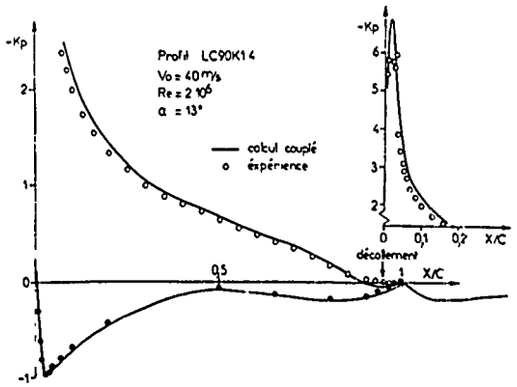


Fig. 22 – Profil LC 90DK1.4 – Pression – $\alpha = 13°$.

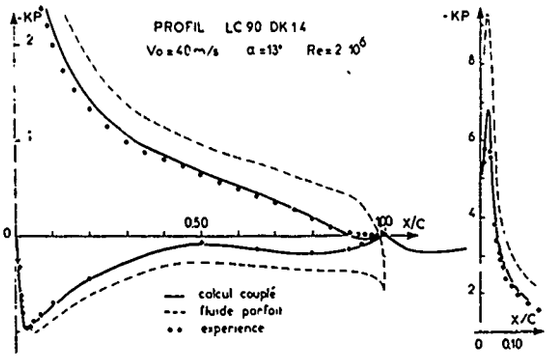


Fig. 23 – Profil LC 90DK1.4 – Comparaison fluide parfait - fluide visqueux.

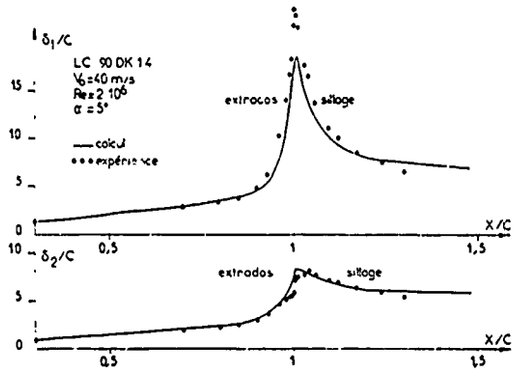


Fig. 24 – Profil LC 90DK1.4 – Épaisseurs δ_1, δ_2 – $\alpha = 5°$.

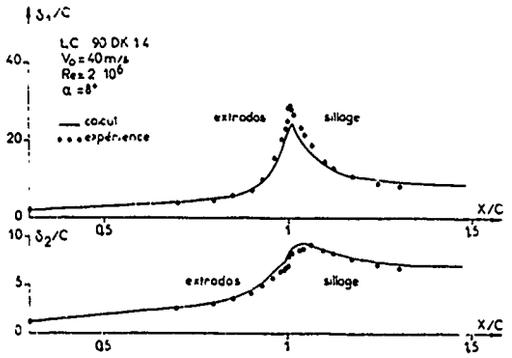


Fig. 25 – Profil LC 90DK1.4 – Épaisseurs δ_1, δ_2 – $\alpha = 8°$.

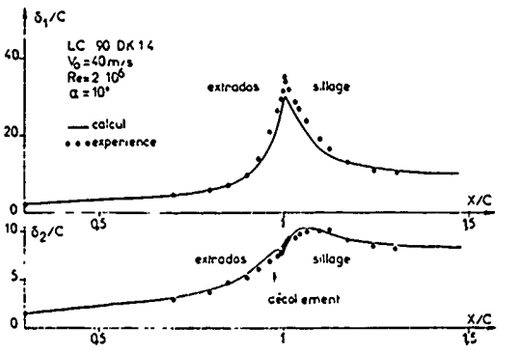


Fig. 26 – Profil LC 90DK1.4 – Épaisseurs δ_1, δ_2 – $\alpha = 10°$.

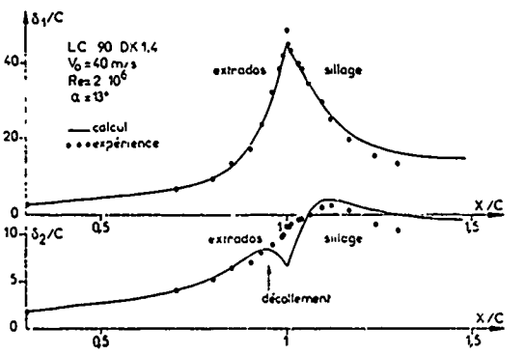


Fig. 27 – Profil LC 90DK1.4 – Épaisseurs δ_1, δ_2 – $\alpha = 13°$.

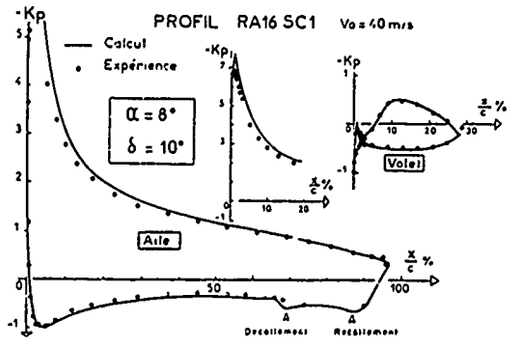


Fig. 28 – Profil RA 16 SC1 – Pression – $\alpha = 8° – \delta = 10°$.

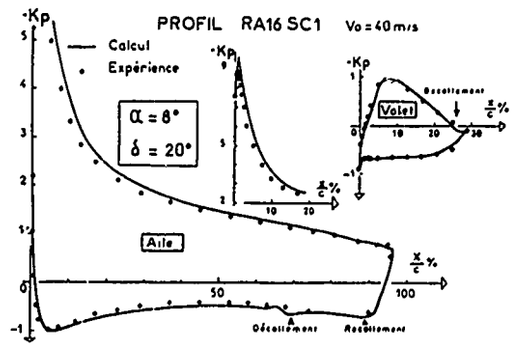


Fig. 29 – Profil RA 16 SC1 – Pression – $\alpha = 8° – \delta = 20°$.

THE CALCULATION OF INCOMPRESSIBLE BOUNDARY LAYERS WITH STRONG VISCOUS-INVISCID INTERACTION*

by
A.E.P. Veldman
National Aerospace Laboratory NLR
Anthony Fokkerweg 2
1059 CM Amsterdam
The Netherlands

SUMMARY

A quasi-simultaneous method is described to calculate laminar, incompressible boundary layers interacting with an inviscid external flow. The essence of the method is the numerical treatment of the interactive boundary condition which models the behaviour of the outer flow: it is regarded as a relation between the pressure and the displacement thickness where both quantities are simultaneously treated as unknowns. This way the method avoids difficulties incurred when either direct or inverse methods are used, resulting in fast convergence of the iterative procedure involved.

The numerical strategy can be regarded as a recognition of the lack of hierarchy of the "triple-deck" which asymptotically can describe interacting boundary layers. In such situations, without a definite hierarchy between the viscous and inviscid regions, we will speak of "strong interaction". In the paper the success of the quasi-simultaneous method will also be explained from a purely numerical point of view.

The feasibility of the quasi-simultaneous method is demonstrated by means of a variety of model problems, ranging from separation bubbles to asymmetric trailing edge flow. In the latter case the results of the present method can be compared with results of asymptotic triple-deck theory.

1. INTRODUCTION

The computation of viscous-inviscid interaction by the so-called direct iterative techniques is being hampered because methods for solving the boundary layer equations with prescribed pressure break down when flow separation is present. The breakdown is due to the fact that, apart from exceptional circumstances, the boundary layer solution will exhibit a Goldstein singularity at the point of separation when pressure is prescribed [1, 2]. Catherall and Mangler [3] were the first to show that relaxing the pressure but instead prescribing the displacement thickness regular solutions including separation can be obtained. This observation has subsequently led to other solutions of the boundary layer equations with either displacement thickness or wall shear prescribed [4-7].

A difficulty associated with the latter so-called inverse techniques is that the required displacement thickness (or wall shear) is not known a priori. The appropriate value has to be obtained, as part of the overall problem, from the interaction between the boundary layer and the inviscid flow. Calculations of viscous-inviscid interaction for subsonic and transonic flow which are essentially based on these inverse techniques have been presented in [8-11], e.g. A disadvantage of the latter methods is the slow convergence of the required iteration process between the viscous and inviscid parts of the flow field. In many cases severe underrelaxation has to be used to ensure convergence.

An improvement over the inverse method can be obtained by applying the semi-inverse technique introduced by Le Balleur [9]. Herein the boundary layer is calculated inversely, but the outer flow is calculated in the direct way. Thus both parts of the flow field yield updated pressure distributions which are combined into an updated displacement thickness by means of a relaxation formula. The method used by Carter [10] and Kwon and Pletcher [11] possesses the same type of organization but the relaxation formula is different. Whereas the choice for the relaxation formula of Le Balleur still requires underrelaxation, the choice of Carter [10], which has also been used in [11], is more satisfactory from a numerical point of view as it allows overrelaxation, leading to fast convergence. However, a straight-forward extension of the latter choice to more general situations is not yet available. Fig. 1 contains a sketch of the organization of the direct, inverse and semi-inverse methods.

In the methods mentioned above the numerical scheme provides only a weak, retarded coupling of the viscous and inviscid regions. However, near separation (and also near trailing edges) the interaction has a strong, simultaneous character, i.e. there does not exist a definite hierarchy between the boundary layer and the outer flow [12, 13]. As a consequence of this observation it may be expected that a numerical scheme which also possesses a simultaneous coupling between the viscous and inviscid parts of the flow field can have favourable properties. Designers of methods for calculating the interaction with a supersonic outer flow have recognized this point already many years ago [14], by applying a Prandtl-Meyer relation as a boundary condition for the boundary layer equations.

In the present paper a method is described that can be considered as a subsonic analogue of the latter methods. Herein the boundary layer equations are solved with a boundary condition which describes the interaction with the outer flow (interaction law). The boundary condition is considered to prescribe a linear combination of pressure and displacement thickness, in contrast with the methods reviewed above which prescribe either one or the other. The calculation method thus obtained appears to possess favourable convergence properties of the iteration process which is required due to the elliptic character of the interaction law; in many cases overrelaxation can be applied.

---

* Part of this investigation has been performed under contract with the Netherlands Agency for Aerospace Programs (NIVR, contractnumber 1865).

The behaviour of the calculation methods mentioned above can be understood from the asymptotic theory (for vanishing viscosity) of interacting boundary layers. More specifically, the structure of the boundary layer near a point of separation or a trailing edge can (in laminar flow) be described by triple-deck theory introduced by Stewartson [15] and Messiter [16]. In the author's view the most important property of the triple-deck is its lack of hierarchy. This property, which seems not to have been appreciated sufficiently in the literature, strongly suggests to use a calculation method in which pressure and displacement thickness are treated in an equivalent way. We will discuss this in more detail in section 2.

In section 3 the principle of the present calculation method will be formulated, with numerical details given in section 4. A numerical explanation of the performance of the method is presented in section 6. The feasability is demonstrated by means of a variety of model problems, ranging from separation bubbles to asymmetric trailing edge flow. These are described in sections 5 and 7.

2. ASYMPTOTIC THEORY OF INTERACTING BOUNDARY LAYERS

As mentioned above direct methods for solving the boundary layer equations break down in a point of separation where the solution becomes singular. This implies that Prandtl's boundary layer concept, which is one of the first applications of asymptotic theories, has to be revised, because an assumption behind asymptotic theory is that expansions (in the perturbation parameter) may not contain singular terms [17]. A description which can cover the latter situations in many cases is given by triple-deck theory [15, 16]. A comprehensive review of its applications has been presented by Stewartson [18]. We will confine ourselves here to a global description.

The triple-deck is a three-layered region which in incompressible flow has a streamwise extent $O(Re^{-3/8}L)$ around the singular point. In normal direction it consists of:

i) a viscous sublayer of thickness $O(Re^{-5/8}L)$ which is governed by the classical boundary layer equations;
ii) an inviscid middle layer of thickness $O(Re^{-1/2}L)$ where, effectively, the oncoming flow undergoes a downward displacement;
iii) an inviscid irrotational top layer of thickness $O(Re^{-3/8}L)$ which is described by thin airfoil theory.

In the author's opinion the following properties of the triple-deck are important:

P1: The boundary layer equations are sufficient to describe the lower two layers of the triple-deck, i.e. the viscous part of the flow.
P2: The interaction with the outer inviscid flow has a local character, as the triple-deck has only a small extent $O(Re^{-3/8}L)$. Furthermore the interaction can be described by thin airfoil theory.
P3: There is no definite hierarchy between the viscous region and the inviscid region; in fact in the triple-deck the hierarchy changes from direct to inverse [12, 13, 19]. This situation is defined <u>strong interaction</u>.

The above properties reveal much information on how to design a calculation method for interacting boundary layers: they indicate which set of equations is required (P1, P2), and they suggest how to choose the numerical method for solving the equations (P3). Moreover the scaling of the triple-deck is a guide for the distribution of gridpoints in the finite difference scheme to be used.

3. HIERARCHICAL AND NON-HIERARCHICAL DESCRIPTIONS

An approach in which the flow field is divided in a viscous boundary layer and an inviscid external region requires some sort of coupling mechanism between the two regions. Here we will perform the coupling in terms of the velocity at the edge of the boundary layer u_e, and the displacement thickness δ^*. The governing equations in the two parts of the flow field then each provide a relation between u_e and δ^*. In (quasi) operator notation we will write these relations as

(1) external flow region: $u_e = P\,\delta^*$,

(2) boundary layer : $u_e = B\,\delta^*$.

The above notation is to be considered purely formal. A possible choice for the operators P and B will be discussed in more detail next.

In this paper we confine ourselves to the calculation of laminar, incompressible flows, for which the boundary layer can be described satisfactorily by the boundary layer equations (consistent with property P1 of the triple-deck)

(3) $$u\,u_x - \tilde{\psi}_{\tilde{x}}\,u_{\tilde{y}} = u_e\,u_{e_x} + u_{\tilde{y}\tilde{y}}\,,\quad u = \tilde{\psi}_{\tilde{y}}\quad .$$

Here $\tilde{y} = Re^{\frac{1}{2}}\,y$ is a stretched coordinate normal to the surface given by $y = 0$, whereas $\tilde{\psi} = Re^{\frac{1}{2}}\,\psi$ is the scaled streamfunction. The displacement thickness follows from the behaviour at infinity

(4) $$\tilde{y} \to \infty\colon\ \tilde{\psi} \sim u_e(\tilde{y} - \delta),\ \delta^* = Re^{-\frac{1}{2}}\delta\quad .$$

The system formed by Eqs. (3) and (4), completed with initial conditions and the usual boundary conditions at $\tilde{y} = 0$, constitutes the boundary layer operator B. Note that a study by Briley and McDonald [20] confirms that the boundary layer equations can be sufficient to describe interacting boundary layers.

The P operator gives a precise description of the influence of the boundary layer on the outer flow. But in many cases an approximate description of this influence can be sufficiently accurate; this offers the possibility of a simpler numerical treatment. The approximate description will be called the <u>interaction</u>

law, symbolized by

(1') $u_e = I\,\delta^*$.

In supersonic flow the interaction law is often chosen to be a linearized Prandtl-Meyer relation, e.g. [14]. In subsonic flow a thin airfoil approximation may be used [20, 21] which is consistent with property P2 of the triple-deck. Also in our calculation thin airfoil approximations have been used as interaction law; an example hereof is

$$(5) \qquad u_e(x) = U_e(x) + \frac{1}{\pi} \oint_{x_b}^{x_e} \frac{d(U_e\delta^*)/d\xi}{x - \xi}\, d\xi \quad .$$

$[x_b, x_e]$ denotes the region in which the interaction is assumed to be important, and U_e denotes the value of u_e from a first order potential flow calculation.

The formulation (5) of the interaction law will be a good approximation when the displacement effect on the outer flow is small. In situations where this is not the case the physical point of view may require a different formulation: for instance one in which the edge velocity is linearized around a more accurate approximation than U_e. Also the source strength in the integrand may be replaced by $d(u_e\delta^*)/d\xi$. (Note that the combination $u_e\delta^*$ also appears in (4)). However, as will be clear from the considerations in section 6, from a mathematical point of view these different formulations behave the same. Therefore in this paper we will not concentrate on the specific choice of the interaction law which is made in the flow problems which are presented. Any other feasible choice will perform the same way, although the results obtained can be different.

The solution of (1), (2) - or alternatively (1'), (2) - requires iterative procedures for which various approaches can be followed. The hierarchical direct and inverse methods, discussed already in section 1, can be written as

$$(6) \qquad \text{direct method : } u_e^{(n)} = P\,\delta^{*(n-1)} \;,\; \delta^{*(n)} = B^{-1}\,u_e^{(n)} \;;$$

$$(7) \qquad \text{inverse method: } \delta^{*(n)} = P^{-1}\,u_e^{(n-1)} \;,\; u_e^{(n)} = B\,\delta^{*(n)} \;,$$

where the superscript n denotes the iteration count. P^{-1} and B^{-1} formally denote the inverse of P and B, respectively; existence is not guaranteed by this notation. In fact the singularities near a point of separation produced by the direct method occur because the range of B and hence the domain of definition of B^{-1} is limited.

In view of the drawbacks of the direct and inverse methods we have developed a different non-hierarchical approach for solving (1), (2). Property P3 suggests to use a method in which the coupling between the viscous and inviscid regions has a more simultaneous character. We remark that Brune, Rubbert and Nark [22] also advocate the use of a simultaneous approach. In the present method the equations (1') and (2) are regarded as two equations with two unknowns which we want to solve without iteration, hence

$$(8a,b) \qquad u_e - I\,\delta^* = 0,\; u_e - B\,\delta^* = 0 \quad .$$

In practice the situation is a bit more complicated than is suggested by this notation. After discretization u_e and δ^* are vectors consisting of values in the meshpoints in x-direction. At a given i-th boundary layer station the discrete versions of (8a, b) contain values of u_e and δ^* at this station and at other stations. We consider (8a) to be an implicit relation between the values of u_e and δ^* at the i-th station (hence $u_e(x_i)$ and $\delta^*(x_i)$ are simultaneously treated as unknowns), which then acts as a boundary condition to the boundary layer equation (8b). The presence of downstream values of δ^* in this relation is accounted for by means of an iterative procedure in which several boundary layer sweeps are made. Fig. 2 provides a sketch of this method, which is comparable to Fig. 1. The new method has been termed quasi-simultaneous since the most important part of the interaction with the outer flow (= interaction law) is treated simultaneously with the boundary layer. More details follow in section 4.

In summary, the interaction law is required to possess the following two (sometimes conflicting) properties:
i) it must be simple enough to allow the quasi-simultaneous numerical treatment;
ii) it must give a sufficiently accurate description of the interaction.
The first requirement allows the numerical algorithm to avoid singularities in the solution (at a point of separation or at a trailing edge) during the iteration process; whereas the second requirement controls the physical relevance of the solution obtained. In case the interaction law is not accurate enough the physical relevance of the solution can be increased by updating the outer flow calculation. Hereto we introduce an additional outer iteration process - indicated by the dashed line in Fig. 2 - which reads

$$u_e^{(k)} - I\,\delta^{*(k)} = P\,\delta^{*(k-1)} - I\,\delta^{*(k-1)} \quad ,$$

$$u_e^{(k)} - B\,\delta^{*(k)} = 0 \quad ,$$

such that upon convergence ($k \to \infty$) the solution satisfies the exact relations (1), (2).

4. THE NUMERICAL TREATMENT OF THE INTERACTION LAW

The essential feature of the present method is the way in which the interaction law is implemented in the numerical calculation. We have touched upon this point already in the previous section, and we will go into more detail now.

Discretization of the interaction law

In the calculations we have performed thusfar the following discretization of the thin airfoil integral in (5) appeared to be sufficiently accurate. Let the x-coordinates of the meshpoints be given by $x_i = x_b + ih$, $i = 0, \ldots, N$; $x_N = x_e$. Further let A_j be an abbreviation for $(U_e\delta)(x_j)$. The integral in (5), which has to be calculated for $x = x_i$, $i = 1, \ldots, N$, can be evaluated with the midpoint rule on intervals $[x_j, x_{j+1}]$, $j = 0, \ldots, N-1$. This results in

$$J_i \overset{df}{=} \int_{x_b}^{x_e} \frac{A'}{x_i - \xi}\, d\xi = h \sum_{j=0}^{N-1} A'_{j+\frac{1}{2}}/(x_i - x_j - \tfrac{1}{2}h) \quad .$$

The value of $A'_{j+\frac{1}{2}}$ has been discretized as $A'_{j+\frac{1}{2}} = (A_{j+1} - A_j)/h$, after which some algebraic manipulations result in

$$hJ_i = R_i^* + \sum_{j=1}^{N} c_{ij}A_j, \quad i = 1, \ldots, N, \tag{9}$$

where

$$R_i^* = \frac{-A_0}{i-\frac{1}{2}} \; ; \; c_{ij} = \frac{-1}{(i-j)^2-\frac{1}{4}} \; , \; j = 1, \ldots, N-1; \; c_{iN} = \frac{1}{i-N+\frac{1}{2}} \quad .$$

It can be deduced that

$$c_{ii} = \frac{1}{i-\frac{1}{2}} + \sum_{\substack{j=1 \\ j\neq i}}^{N} |c_{ij}|, \quad i = 1, \ldots, N \quad , \tag{10}$$

hence the matrix (c_{ij}) is diagonally dominant with positive diagonal entries. This property has an important influence on the overall convergence of the calculations as will be discussed in section 6.

Finally, substituting the discretization (9) into (5) we obtain a discrete interaction law

$$u_{e_i} = U_{e_i} + R_i + \sum_{j=1}^{N} \alpha_{ij}\, \delta_j \quad , \tag{11}$$

where

$$R_i = \beta R_i^*, \; \alpha_{ij} = \beta U_{e_i}\, c_{ij} \text{ and } \beta = (\pi\, h\, Re^{\frac{1}{2}})^{-1} \quad .$$

Implementation of the interaction law

The elliptic character of (11), which is expressed by the presence of downstream values of δ, requires that several sweeps through the boundary layer have to be made. In the n-th sweep the implementation of (11) is as follows

$$u_{e_i}^{(n)} - \alpha_{ii}\, \delta_i^{(n)} = U_{e_i} + R_i^{(n-1)} + \sum_{j=1}^{i-1} \alpha_{ij}\, \delta_j^{(n)} + \sum_{j=i+1}^{N} \alpha_{ij}\, \delta_j^{(n-1)} \quad . \tag{12}$$

Thus at the i-th boundary layer station (12) provides an implicit relation in which u_{e_i} and δ_i are simultaneously treated as unknowns. A discussion of the convergence properties of this method, and a comparison with the direct and inverse strategy is given in section 6.

The iterations are stopped when the following convergence criterion is satisfied

$$\max_i \, |\delta_i^{(n)} - \delta_i^{(n-1)}| < 10^{-4} \quad . \tag{13}$$

5. SEPARATION BUBBLES

The quasi-simultaneous method for calculating interacting boundary layers will be demonstrated first by applying it to separation bubbles. Use has been made of a configuration introduced by Carter and Wornom [8]: a dented plate given by

$$y_B = -t \operatorname{sech} 4(x-2.5), \quad 0 \leq x < \infty \quad ,$$

placed in an oncoming parallel flow with unit velocity (Fig. 3). The depth of the trough is controlled by the parameter t; we will present results for $t = 0.03$ (as in [8]) and $t = 0.1$. The Reynolds number $Re = 1/\nu$ has been taken $Re = 8 \times 10^4$ (as in [8]) or larger. The calculations have been restricted to $1 \leq x \leq 4$. Finally, the interaction law (1') is chosen as

$$(14) \qquad u_e(x) = I\,\delta^* \equiv 1 + \frac{1}{\pi} \int_1^4 \frac{d}{d\xi}\,(y_B + \delta^*)\,\frac{d\xi}{x-\xi} \quad .$$

This choice is more accurate for bubbles with a thickness of the order of the depth of the dent than the choice made in (5).

Small separation bubbles

A finite difference solution has been pursued of Eqs. (3), (4) and (14), with $x \in [x_b, x_e] = [1, 4]$, to calculate bubbles of which the thickness is comparable with the oncoming boundary layer thickness. In the finite difference calculation the outer edge of the boundary layer has been placed at $\tilde{y} = 7\,\delta(x)$, where δ is given the value from the previous boundary layer sweep. The bounded domain thus obtained has been covered by a (non-equidistant) mesh with gridpoints $(x_i, \tilde{y}_j)$, $i = 0, \ldots, N$; $j = 0, \ldots, M$. The x-derivatives in (3) have been replaced by the familiar three point backward formula. This scheme has also been used in regions of backflow, despite its destabilizing influence which, however, did not give rise to numerical difficulties. The $\tilde{y}$-derivatives in (3a) have been discretized with second order formulae centered around $\tilde{y}_j$, $j = 1, \ldots, M-1$; whereas in (3b) they have been centered around $\tilde{y}_{j+\frac{1}{2}}$, $j = 0, \ldots, M-1$. The resulting set of discrete equations at an x-station x_i has been combined with the boundary conditions at $\tilde{y} = 0$ and $\tilde{y} \to \infty$. The discretized form of the interaction law is given in (12). The complete set of non-linear equations is solved with Newton's method.

The present method typically required 10-20 iterations, using overrelaxation $\omega = 1.5$, to satisfy the convergence criterion (13). In all cases Blasius values were used as initial guess for the displacement thickness. The number of iterations was found not to depend critically on the relaxation factor.

The results of the present method agree excellently with those of Carter and Wornom. For the flow at $Re = 8 \times 10^4$ we will show here the pressure results, since from these the best impression of the influence of the interaction can be obtained (Fig. 4). Also shown is the pressure result of a calculation (for the same value of t) at a larger Reynolds number, $Re = 36 \times 10^4$. Here we observe a typical plateau region in the pressure. For the larger Reynolds number Fig. 5 depicts some velocity profiles in and near the separation bubble which show that the largest backflow velocities occur closely before the reattachment point. More results can be found in [23]. Further, a comparison with asymptotic triple-deck results for the same geometry is given in [24]

Recirculating eddies

Attempts to obtain solutions of the above equations for Reynolds numbers larger than about 4×10^5 failed, because at a boundary layer station with a thick backflow region the Newton process no longer converged. However, using an integral description for the boundary layer instead of the finite difference description, Oskam [25] is able to obtain results for arbitrarily large Reynolds numbers. This way flows can be calculated with reversed flow regions which are much larger than the oncoming boundary layer thickness. For the present geomtry the thickness of these recirculating eddies approaches the depth of the trough with increasing Reynolds number. Oskam [25] used the family of similar Falkner-Skan profiles to describe the boundary layer. It appeared that the calculation of those members of this family which possess a large backflow region required extreme numerical care. It is believed that these numerical difficulties have the same origin as the breakdown of the finite difference calculations referred to above.

One of the most interesting results obtained by Oskam is described next. He has calculated the flow over the trough for $t = 0.10$ at a Reynolds number of 10^6. The results for the pressure and the bubble shape are shown in Fig. 6 (conf. A). Hereafter he changed the geometry of the trough by removing the lower half, leading to conf. B in Fig. 6. It appeared that the position of the separation streamline and the interacted pressure distribution was the same for both configurations A and B, although the pressure distributions without interaction are completely different (Fig. 6).

6. INTERACTION FROM A NUMERICAL POINT OF VIEW

We are now in a position to make a numerical analysis of the performance of the various iterative procedures (6-8) for calculating interacting boundary layers. Here we will restrict this analysis to situations in which the interaction can be described by means of a Hilbert integral; hence the discrete version of the interaction law can be written

$$(15) \qquad \underline{u}_e - Re^{-\frac{1}{2}}\,\underline{H}\,\underline{\delta} = \underline{U}_e \quad ,$$

where $\underline{H}$, which denotes the discretized Hilbert integral as described in section 4, is a diagonally dominant matrix with positive diagonal entries. Further

$$\underline{u}_e = (u_e(x_1), \ldots, u_e(x_N))^t \text{ and } \underline{\delta} = (\delta(x_1), \ldots, \delta(x_N))^t$$

denote the vectors of unknowns $u_e(x_i)$ and $\delta(x_i)$.

The boundary layer operator B which describes the relation between u_e and δ^* via the viscous flow equations is essentially non-linear. The analysis in this section will be based on the discrete Jacobian of $Re^{-\frac{1}{2}}B$ which is denoted by $\underline{B}$ (the factor $Re^{-\frac{1}{2}}$ has been introduced to make $\underline{B}$ independent of Re). Thus the discrete boundary layer operator can be written in the form

$$(16) \qquad \underline{u}_e - \underline{B}\,\underline{\delta} = \underline{rhs}$$

Both $\underline{B}$ and $\underline{rhs}$ depend on $\underline{\delta}$, but in the present analysis this dependence will be ignored. $\underline{B}$ is a lower diagonal matrix (when a backward differencing of the x-derivatives is used throughout). Denoting the diagonal of $\underline{B}$ by $\underline{D}$, then $D_{ii} = \partial u_{e_i}/\partial \delta_i$. From the calculations of separation bubbles described in the previous section we have extracted the values of D_{ii}. It appears that these values are negative when the flow at x_i is attached, and D_{ii} is slightly positive when the flow at x_i is separated. Fig. 7 shows the values of D_{ii} for the calculation with $t = 0.03$ and $Re = 36 \times 10^4$ using a 60×40 grid. This figure suggests that the zeros of D_{ii} coincide with the points of separation and reattachment. For calculation methods employing an integral description this can be proved analytically [6, 25], but for finite difference calculations such a proof is still lacking.

The stability of the various iterative techniques for solving (15) and (16) can be studied from the homogeneous problem. The non-zero entries of $\underline{B}$ under the diagonal make such a study rather difficult; therefore we will introduce the following $\underline{\text{model problem}}$ which can be treated more easily

$$(17) \qquad \underline{u}_e - Re^{-\frac{1}{2}} \underline{H}\, \underline{\delta} = \underline{0}, \quad \underline{u}_e - \underline{D}\, \underline{\delta} = \underline{0} \quad .$$

The direct method to solve (17) can be written as

$$\underline{u}_e^{(n)} = Re^{-\frac{1}{2}} \underline{H}\, \underline{\delta}^{(n-1)} \quad , \quad \underline{\delta}^{(n)} = \underline{D}^{-1}\, \underline{u}_e^{(n)} \quad ,$$

or equivalently, eliminating $\underline{u}_e$,

$$\underline{\delta}^{(n)} = Re^{-\frac{1}{2}} \underline{H}\, \underline{D}^{-1}\, \underline{\delta}^{(n-1)} \quad .$$

A necessary and sufficient condition for the convergence of the direct method is [26]

$$(18) \qquad Re^{-\frac{1}{2}}\, \rho(\underline{D}^{-1}\underline{H}) < 1 \quad ,$$

where ρ denotes the spectral radius.

- For $\underline{\text{attached}}$ flow the eigenvalues of $\underline{D}^{-1}\underline{H}$ have negative real part, and hence the method converges for sufficiently large values of Re. For smaller values of Re underrelaxation of the type

$$(19) \qquad \underline{\delta}^{(n)} = \left[\omega\, Re^{-\frac{1}{2}} \underline{D}^{-1}\underline{H} + (1-\omega)\underline{I}\right] \underline{\delta}^{(n-1)}$$

  can make the direct method convergent. Further it follows that the convergence is oscillatory; this has also been observed for the full problem in [22].

- For $\underline{\text{separated}}$ flow the matrix $\underline{D}$ is singular or almost singular which makes it impossible in practice to satisfy (18); hence the direct method fails.

The inverse method, in which the role of u_e and δ is interchanged, can be written

$$\underline{\delta}^{(n)} = Re^{\frac{1}{2}}\, \underline{H}^{-1} \underline{D}\, \underline{\delta}^{(n-1)} \quad .$$

$\underline{H}$ is diagonally dominant and hence invertable. Therefore the iteration matrix exists for attached as well as for separated flows. Because $\rho(\underline{H}^{-1}\underline{D}) > 1/\rho(\underline{D}^{-1}\underline{H})$ the inverse method diverges when the direct method converges; but as long as

$$\text{Real part (eigenvalues of } Re^{\frac{1}{2}}\underline{H}^{-1}\underline{D}) < 1$$

is satisfied, the inverse method can be made convergent by applying sufficient underrelaxation of a type similar to (19). A satisfactory relaxation factor can in general be found only by trial and error. For large Re the relaxation factor is proportional to $Re^{-\frac{1}{2}}$.

The quasi-simultaneous method for finding the solution of (17) solves

$$\underline{Q}\, \underline{\delta} \equiv (Re^{-\frac{1}{2}}\underline{H} - \underline{D})\underline{\delta} = \underline{0}$$

by the Gauss-Seidel method. A sufficient although not necessary condition herefore to be convergent is diagonal dominance of the matrix $\underline{Q}$ [26].

- For $\underline{\text{attached}}$ flow $\underline{D}$ has negative entries. Since $\underline{H}$ is diagonally dominant with positive diagonal entries it follows that $\underline{Q}$ is diagonally dominant. Hence the quasi-simultaneous method is convergent.

- For $\underline{\text{separated}}$ flow $\underline{D}$ contains some nonnegative diagonal entries, however, of small magnitude. In view of (10) there will be many situations for which the matrix $\underline{Q}$ remains diagonally dominant, ensuring convergence. A fortiori, when the positive entries of $\underline{D}$ are too large for $\underline{Q}$ to be diagonally dominant the method still will be convergent in many cases because diagonal dominance is not a necessary condition for convergence; a more precise theoretical analysis for these situations is difficult to give and will not be presented here.

In the above analysis we have not yet studied the dependence of the stability on the mesh size. It is known from section 4 that $\underline{H}$ is inversely proportional to the mesh size, but the dependence of $\underline{D}$ on the mesh size is more complicated. We hope to report on this in more detail in future publications.

In the model problem studied above the non-linearity of the actual problem has been ignored, and, what may be more serious, the influence of the off-diagonal entries of $\underline{B}$ has been neglected. However, $\underline{B}$ should

represent the parabolic character of the boundary layer and hence in one boundary layer sweep no downstream error amplification will occur. This gives confidence that possible destabilizing effects on the iterative process with the outer flow probably will not be serious. By relating the properties of the full problem to those of the model problem we should keep these points in mind. However, practical experience with the full problem has confirmed the following properties of the iterative techniques, which above have been proved for the model problem:

1° The direct method breaks down in separation.

2° The inverse method requires severe underrelaxation.

3° The quasi-simultaneous method is convergent; although for some cases of separated flow convergence is not yet guaranteed theoretically.

7. TRAILING EDGE FLOW - A MODEL PROBLEM

As another demonstration of its feasibility the present method has been used to calculate the flow in the neighbourhood of the trailing edge of a (modified) flat plate at incidence. The plate occupies the interval [0, 1] of the x-axis, and is placed in an oncoming flow which makes an angle α with the x-axis. The theoretical pressure distribution according to potential flow is

$$p^{\pm} = \pm \alpha\left(\frac{1-x}{x}\right)^{\frac{1}{2}} \quad , \tag{20}$$

where the + and - sign refer to the upper and lower side of the plate, respectively.

In the present investigation we have restricted our interest to interaction effects of the flow in the vicinity of the trailing edge in cases where the oncoming boundary layer remains attached until (shortly before) the trailing edge. As the unfavourable pressure gradient of (20) is likely to provoke leading edge separation we have modified the plate such that the pressure becomes constant between the leading edge and the inflection point of (20) which lies at $x = 0.75$; the constant value is chosen such that the pressure remains continuous.

Thus we are going to solve a model problem in which the potential flow velocity distribution is given by

$$U_e^{\pm}(x) = U_s(x) \pm U_a(x) \quad ,$$

where

$$U_s(x) = 1 \quad , \quad U_a(x) = \begin{cases} \alpha(1/3)^{\frac{1}{2}}, & 0 \le x \le 0.75 \\ \alpha((1-x)/x)^{\frac{1}{2}}, & 0.75 \le x \le 1 \\ 0 \qquad\quad , & x \ge 1 \end{cases} \tag{21}$$

The interaction law, based on thin airfoil theory, has been chosen as

$$u_e^{\pm}(x) = u_s(x) \pm u_a(x) \quad , \tag{22}$$

where

$$u_s(x) = U_s(x) + \frac{1}{\pi} \oint_{x_b}^{x_e} \frac{d}{d\xi} \delta_s^* \frac{d\xi}{x-\xi} \qquad , x_b < x \le x_e \quad ; \tag{23}$$

$$u_a(x) = \begin{cases} U_a(x) + \frac{1}{\pi}\left(\frac{1-x}{x}\right)^{\frac{1}{2}} \oint_{x_b}^{1} \left(\frac{\xi}{1-\xi}\right)^{\frac{1}{2}} \frac{d}{d\xi} \delta_a^* \frac{d\xi}{x-\xi} & , x_b < x < 1 \quad , \\ \\ 0 & , 1 \le x \le x_e \quad . \end{cases} \tag{24}$$

Here δ_s^* and δ_a^* are the symmetric and antisymmetric parts of the displacement thickness. In the above description the Kutta condition at the trailing edge is implicitly satisfied.

With the above choice of the interaction law we have ignored the influence of the trailing edge region on the leading part of the "plate" $0 \le x \le x_b$. Herewith we do not intend to say that this influence is negligibly small; rather we want to focus our attention to the numerical feasability of the present method. Thus the physical description has been kept rather simple, allowing some loss of accuracy. But, as discussed already in section 3, the accuracy can be improved by introducing an outer iteration process which contains the exact outer flow operator P.

The interaction law (22) has been combined with the boundary layer equations (3). The latter have been solved in the same way as in section 5. In the wake use has been made of the translational invariance of the boundary layer equations by requiring that $\tilde{\psi} = 0$ at $\tilde{y} = 0$. The symmetric displacement thickness in the wake follows from

$$\delta_s^* = \tfrac{1}{2}\, Re^{-\frac{1}{2}}(\delta^+ - \delta^-) \text{ where } \tilde{\psi} \sim u_e^{\pm}(\tilde{y} - \delta^{\pm}) \text{ as } \tilde{y} \to \pm\infty \quad .$$

Note that the antisymmetric displacement thickness in the wake is not required in the present formulation. In these trailing edge calculations the thickness of the computational domain has been chosen as

$H(x) = 7\beta x^{\frac{1}{2}}$, where $\beta = 1.721$ is the Blasius displacement thickness. In both x- and $\tilde{y}$-directions use has been made of a non-equidistant mesh.

The discretization of the antisymmetric thin airfoil integral (24) requires some special care. The technique used in section 4 appears to be too crude near $x = 1$. Therefore a more accurate procedure was adopted. When evaluating (24) for $x = x_i$, δ_a^* was approximated by a piecewise linear function on intervals $[x_j, x_{j+1}]$, $j \neq i-1, i$. On the remaining interval $[x_{i-1}, x_{i+1}]$ δ_a^* was approximated by second order Lagrange interpolation. (Note that for a linear interpolation the Cauchy principal value would not exist). The resulting integrals have been calculated analytically, expressed in the values of δ_a^* in the nodal points x_j. Thus an expression of the form

$$u_a(x_i) = U_a(x_i) + \sum_{j=0}^{N_{te}} \beta_{ij}\, \delta_a^*(x_j) \; ; \; i = 1, \ldots, N_{te}$$

is obtained, where N_{te} is the index of the gridpoint coinciding with the trailing edge. For consistency the same approach has been used for the symmetric integral (23).

The matrix obtained in the discretization of the symmetric integral possesses the same properties as the one which is formed from the method in section 4, i.e. it is diagonally dominant with positive diagonal entries. However, the antisymmetric interaction matrix (β_{ij}) $(i, j = 1, \ldots, N_{te})$ is not diagonally dominant. This is due mainly to the entries in the $(N_{te}-1)$-st and N_{te}-th column which describe the influence of the immediate vicinity of the trailing edge. Because of the lack of diagonal dominance the convergence proof of the model problem given in section 6 cannot be generalized to the asymmetric case. But, as stated in section 6, diagonal dominance is only a sufficient condition, and convergence can be obtained under much weaker restrictions. We have found that for reasonable choices of the meshpoints in the x-direction, with not too small meshes near the trailing edge, the present calculation method will converge; sometimes a small amount of underrelaxation ($\omega = 0.8$) appeared necessary.

In the calculations performed the interaction interval $[x_b, x_e]$ and the distribution of meshpoints were chosen symmetrically around the trailing edge. The total number of gridpoints in x-direction is denoted by N (hence $N_{te} = \frac{1}{2} N$); the number of gridpoints in y-direction is M (where $\frac{1}{2}$ M points are situated on either side of $y = 0$). The choice of the mesh was dependent on the Reynolds number; the scaling of the triple-deck served hereby as a guide. In table 1 we give some numbers from which an impression can be obtained of the meshes employed. Also indicated is, for two values of the angle of incidence, the number of iterations that were required to satisfy the convergence criterion (13).

Table 1: Characteristic numbers of calculated trailing edge flow examples

Re	x_b	x_e	N x M	$x_{N_{te}-1}$	iterations	
					$\alpha = 0$	$\alpha = 0.7$
10^4	0.25	1.75	56 x 56	0.9772	18	32*
10^6	0.5	1.5	28 x 28	0.9892	12	17*
			56 x 56	0.9946	14	25*
			84 x 84	0.9964	18	34*
10^8	0.75	1.25	56 x 56	0.9987	11	25
10^{12}	0.99	1.01	56 x 56	0.999989	6	no sol.
10^{16}	0.999	1.001	56 x 84	0.9999995	9	no sol.

* with underrelaxation $\omega = 0.8$

Properties of the solution of Eqs. (3,22) for various combinations of α and Re are presented in Figs. 8 and 9. Shown are results for skin friction (upper and lower side), edge velocity and displacement thickness (symmetric and antisymmetric). The results plotted have been obtained with a 56 x 56 grid. For the larger values of the angle of attack α the solution shows a small separation bubble near the trailing edge. Further the figures for δ_a, δ_s and u_s show a rapid increase for increasing α and/or Re. This phenomenon has been pursued further in Fig. 10 where we have plotted, for fixed $Re = 10^6$, the values of some flow variables at the trailing edge as a function of the angle of attack. This figure suggests that there may be a critical value $\alpha^*(Re)$ such that as $\alpha \to \alpha^*$ (from below) the values of δ_a, δ_s and u_s at the trailing edge tend to infinity; hence for $\alpha > \alpha^*$ no solution will exist of (3, 22). From the calculation it follows that the value of α^* is slightly larger than the value of α for which trailing edge separation first occurs (for a discussion hereof see below).

These observations are consistent with the asymptotic theory for asymmetric trailing edge flow as formulated by Brown and Stewartson [27]. In this theory the triple-deck can describe the flow provided we let the angle of attack depend on the Reynolds number via

$$\alpha = Re^{-1/16}\, \tilde{\alpha} \quad , \tag{25}$$

where $\tilde{\alpha}$ is held fixed in the asymptotic limit process. The flow equations have been solved by Chow and Melnik [28]. From their solution the existence follows of a number $\tilde{\alpha}^* \approx 0.12$, called the asymptotic stall angle, such that for $\tilde{\alpha} > \tilde{\alpha}^*$ no solution of the triple-deck flow equations can be found. Further $\tilde{\alpha}^*$ corresponds exactly with the value for which trailing edge separation occurs. An analytical explanation of this correspondence can be given [29], which, however, also applies to our non-asymptotic equations. The difference in our results between α^* and the separation angle presumably can occur because our method is somewhat inaccurate near the trailing edge; it is not adapted to the singular behaviour of the flow variables (see e.g. u_s). A method like the one used in [13] would be more accurate.

It would be very interesting to investigate the nature of the singular behaviour of the solution when trailing edge separation occurs. Is it due to limitations of the triple-deck equations (interacting boundary

layer equations) and will it disappear when a larger set of equations is used? For example one might think of using the full Navier-Stokes equations in the boundary layer, or of an improved interaction law which is more accurate at larger angles of attack. Or is it a more fundamental phenomenon?

A further comparison between the present results and those of asymptotic theory is given in Figs. 11 and 12. Here we show the skin friction and the pressure $p = 1 - u_e$ at the trailing edge as a function of the angle of incidence for $Re = 10^6$, 10^{12} and 10^{16}. For the latter two values the velocity distribution without interaction is somewhat different from (21) as now we assume U_a to be constant up to x_b. For the comparison with asymptotic theory this is not relevant. In Figs. 11 and 12 triple-deck scaling has been applied to facilitate the comparison with the asymptotic results as obtained by Chow and Melnik [28]. The present results have a tendency to approach the asymptotic ones, although for $\alpha \neq 0$ the differences are rather large. However, (25) suggests that the asymptotic series may proceed in powers of $Re^{-1/16}$ which can account for the large differences.

8. CONCLUDING REMARKS

This paper describes a new technique for calculating interacting boundary layers. The essence of the method is the treatment of the interactive boundary condition: it is regarded as a relation between the edge velocity and the displacement thickness where both quantities are simultaneously treated as unknowns. This numerical strategy can be regarded as a strict recognition of the lack of hierarchy of the triple-deck which asymptotically can describe (certain types of) interacting boundary layers. Furthermore, as discussed in this paper, the success of the new quasi-simultaneous method can also be understood from a purely numerical point of view.

To demonstrate its possibilities the quasi-simultaneous method has been applied to a number of model problems, including separation bubbles and trailing edge flow. The method has also been used to solve the equations which describe the triple-deck [24]. In each of these applications the flow is considered laminar and incompressible. It is our belief that the philosophy behind the present method can also be used to design efficient calculation methods for turbulent, compressible flow. In these cases the design of the method can be guided by the asymptotic theory for turbulent trailing edge flow of Melnik, Chow and Mead [30], and by the theory for shock wave-boundary layer interaction of Adamson and coworkers (see [31]).

ACKNOWLEDGEMENTS

The author wishes to acknowledge many stimulating discussions with J.W. Slooff and with B. Oskam who kindly provided some of his preliminary results for recirculating eddies.

REFERENCES

[1] S.N. Brown and K. Stewartson: Laminar seperation, Ann. Rev. Fluid Mech. 1 (1969) 45-72.

[2] J.C. Williams: Incompressible boundary layer separation, Ann. Rev. Fluid Mech. 9 (1977) 113-144.

[3] D. Catherall and K.W. Mangler: The integration of the two-dimensional laminar boundary layer equations past the point of vanishing skin friction, J. Fluid Mech. 26 (1966) 163-182.

[4] J.M. Klineberg and J.L. Steger: On laminar boundary layer separation, AIAA paper 74-94 (1974).

[5] J.E. Carter: Solutions for laminar boundary layers with separation and reattachment, AIAA paper 74-583 (1974).

[6] H.P. Horton: Numerical investigation of regular laminar boundary-layer separation, in Flow Separation, AGARD-CP-168 (1975).

[7] T. Cebeci, H.B. Keller and P.G. Williams: Separating boundary-layer flow calculations, J. Comput. Phys. 31 (1979) 363-378.

[8] J.E. Carter and S.F. Wornom: Solutions for incompressible separated boundary layers including viscous inviscid interaction, NASA SP-347 (1975) 125-150.

[9] J.C. Le Balleur: Couplage visqueux-non visqueux: méthode numérique et applications aux écoulements bidimensionels transsoniques et supersoniques, La Recherche Aérospatiale 183 (1978) 65-76.

[10] J.E. Carter: A new boundary-layer inviscid iteration technique for separated flow, AIAA paper 79-1450 (1979).

[11] O.K. Kwon and R.H. Pletcher: Prediction of incompressible separated boundary layers including viscous-inviscid interaction, J. Fluids Eng. 101 (1979) 466-472.

[12] P.A. Lagerstrom: Solutions of the Navier-Stokes equation at large Reynolds number, SIAM J. Appl. Math. 28 (1975) 202-214.

[13] A.E.P. Veldman: Boundary layer flow past a finite flat plate, Ph. D. Thesis, Math. Inst. Univ. of Groningen (1976).

[14] L. Lees and B.L. Reeves: Supersonic separated and reattaching laminar flows: I. General theory and application to adiabatic boundary-layer/shock-wave interactions, AIAA J. 2 (1964) 1907-1920.

[15] K. Stewartson: On the flow near the trailing edge of a flat plate II, Mathematika 16 (1969) 106-121.

[16] A.F. Messiter: Boundary layer flow near the trailing edge of a flat plate, SIAM J. Appl. Math. 18 (1970) 241-257.

[17] M. Van Dyke: Perturbation methods in fluid mechanics, Academic Press, New York (1964).

[18] K. Stewartson: Multi-structured boundary layers on flat plates and related bodies, Adv. Appl. Mech. 14 (1974) 145-239.

[19] A.E.P. Veldman: Boundary layers with strong interaction: from asymptotic theory to calculation method, Proc. BAIL I Conference, Dublin (1980) 149-163.

[20] W.R. Briley and H. McDonald: Numerical prediction of incompressible separation bubbles, J. Fluid Mech. 69 (1975) 631-656.

[21] P. Crimi and B.L. Reeves: Analysis of leading-edge separation bubbles on airfoils, AIAA J. 14 (1976) 1548-1555.

[22] G.W. Brune, P.E. Rubbert and T.C. Nark: A new approach to inviscid flow/boundary layer matching, AIAA paper 74-601 (1974).

[23] A.E.P. Veldman: A numerical method for the calculation of laminar, incompressible boundary layers with strong viscous-inviscid interaction, Report NLR TR 79023 U (1979).

[24] A.E.P. Veldman and D. Dijkstra: A fast method to solve incompressible boundary-layer interaction problems, Proc. 7th int. conf. num. meth. fl. dyn., Stanford (1980).

[25] B. Oskam: On the interacting boundary layer model and large scale recirculating eddies, to be published (1980).

[26] R.S. Varga: Matrix iterative analysis, Prentice Hall, Englewood Cliffs (1962).

[27] S.N. Brown and K. Stewartson: Trailing edge stall, J. Fluid Mech. 42 (1970) 561-584.

[28] R. Chow and R.E. Melnik: Numerical solutions of the triple-deck equations for laminar trailing-edge stall, Proc. 5th int. conf. num. meth. fl. dyn., Enschede (1976) 135-144.

[29] K. Stewartson: High Reynolds-number flows, Proc. IUTAM conf. on Approximation Methods for Navier-Stokes problems, Paderborn (1979) 505-518.

[30] R.E. Melnik, R. Chow, and H.R. Mead: Theory of viscous transonic flow over airfoils at high Reynolds number, AIAA paper 77-680 (1977).

[31] T.C. Adamson, Jr. and A.F. Messiter: Analysis of two-dimensional interactions between shock waves and boundary layers, Ann. Rev. Fluid Mech. 12 (1980) 103-138.

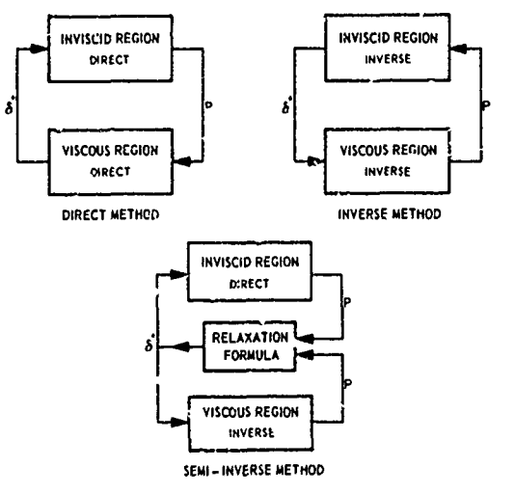


Fig. 1 Global organization of existing methods for calculating viscous-inviscid interaction

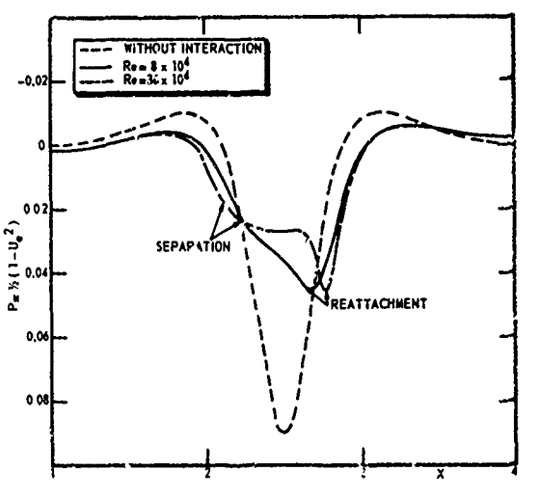


Fig. 4 Separation bubble : pressure distributions with and without interaction

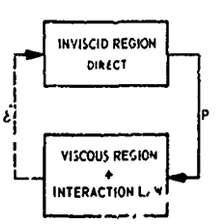


Fig. 2 Global organization of new, quasi-simultaneous method

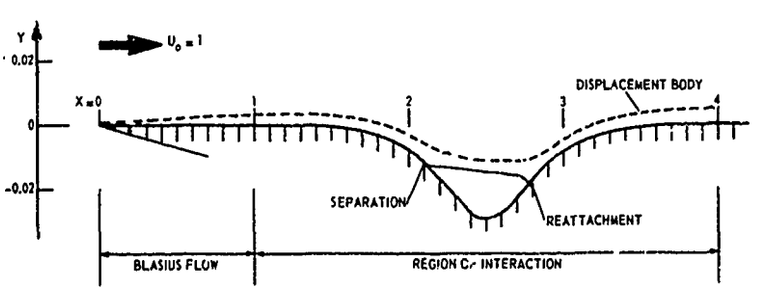


Fig. 3 The dented plate for the calculation of separation bubbles. Indicated is the solution for Re = 36 x 10⁶

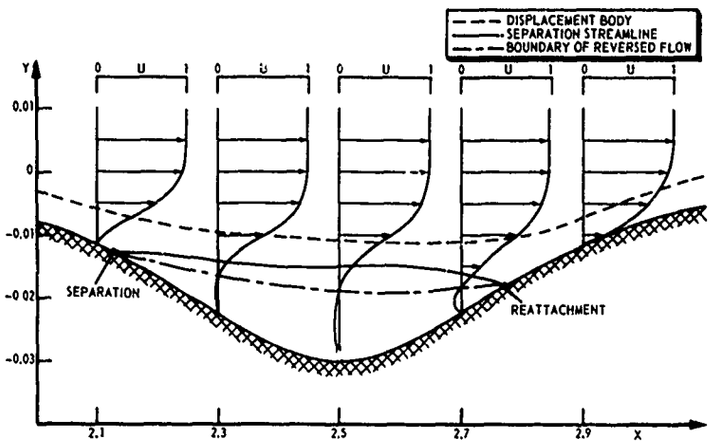


Fig. 5 Separation bubble : velocity profiles for a case with severe separation, Re = 36 x 10^4

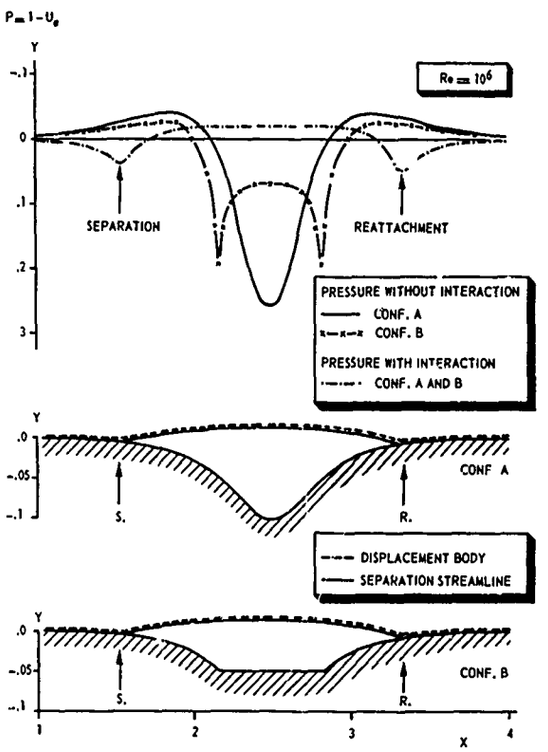
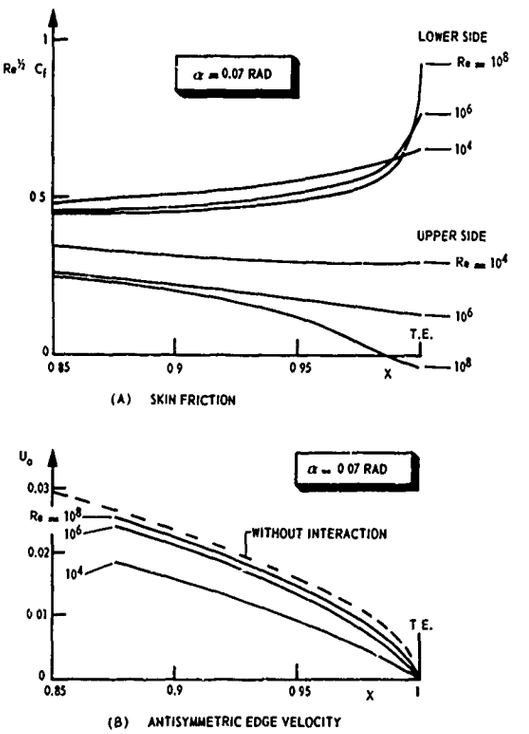


Fig. 6 Large separation bubbles and surface conditions



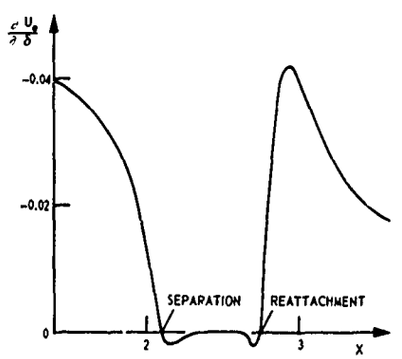


Fig. 7 Separation bubble : derivative of edge velocity with respect to displacement thickness at same boundary layer station (Re = 36 x 10^4, Δx = 1/20)

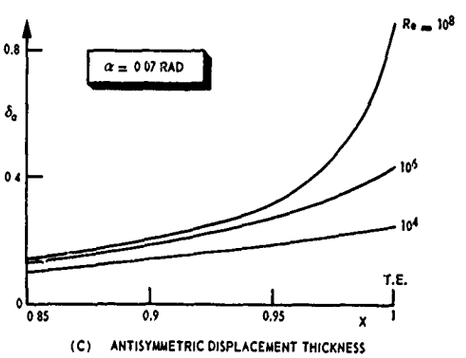
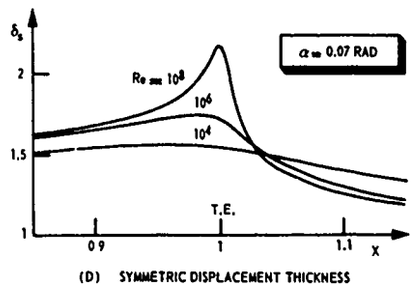
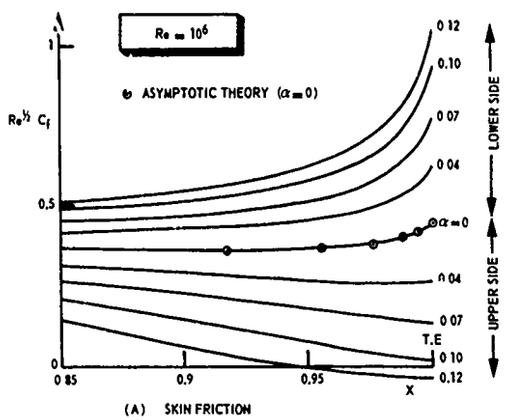


Fig. 8 Asymmetric trailing edge flow : Variation of flow variables with Reynolds number for fixed angle of attack α = 0.07

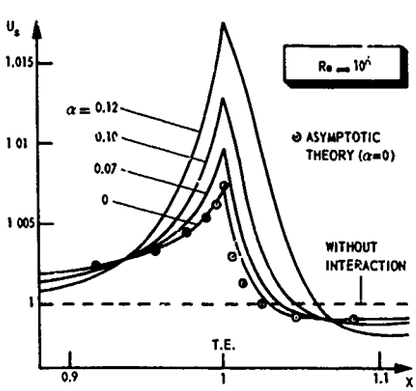


(D) SYMMETRIC DISPLACEMENT THICKNESS

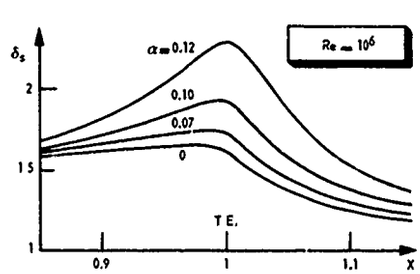
Fig. 8 (cont 'd)



(A) SKIN FRICTION



(B) SYMMETRIC EDGE VELOCITY



(C) SYMMETRIC DISPLACEMENT THICKNESS

Fig. 9 Asymmetric trailing edge flow : Variation of flow variables with angle of attack α for fixed Reynolds number $Re = 10^6$

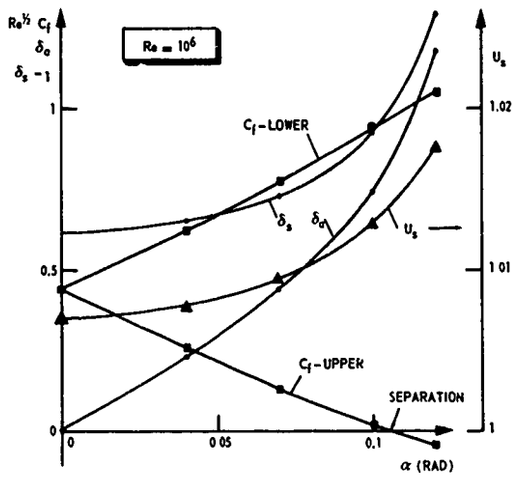


Fig. 10 Variation of value of flow variables at trailing edge with angle of attack α for fixed Reynolds number

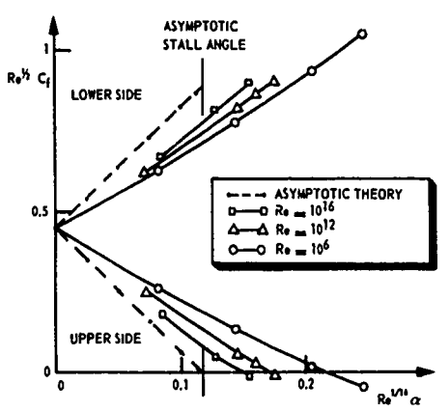


Fig. 11 Comparison of skin friction at trailing edge with results from asymptotic triple-deck theory

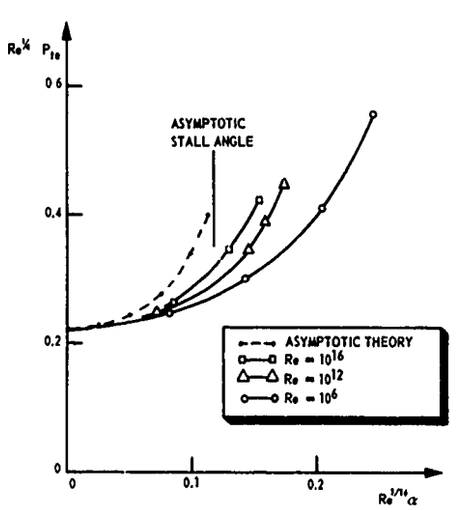


Fig. 12 Comparison of pressure at trailing edge with results from asymptotic tripledeck theory

A VISCOUS-INVISCID INTERACTION MODEL OF JET ENTRAINMENT

R. G. Wilmoth
Aerospace Engineer
NASA Langley Research Center
Hampton, Virginia 23665

and

S. M. Dash
Consultant
Aeronautical Research Associates of Princeton, Inc.
Princeton, New Jersey 08540

SUMMARY

A viscous-inviscid interaction model for predicting jet entrainment effects on axisymmetric, nozzle afterbodies at subsonic speeds is presented. The model is based on a displacement-thickness correction to the inviscid jet boundary that accounts for mixing-induced streamline deflections in the inviscid region. The displacement correction is shown to be related to the local mass entrainment rate and, for thin mixing layers, the model is shown to be analogous to displacement models used in conventional boundary-layer interaction theory. A method is presented for computing the entrainment rate by an overlaid mixing-layer model that accounts for the nonsimilar behavior and pressure gradients occurring in the near-field region. An iterative scheme for coupling the model to analyses for the external inviscid flow, the external boundary layer, and the inviscid jet exhaust is also given. Results are presented that illustrate the qualitative behavior of the entrainment interaction under various flow conditions and that demonstrate the validity of the model by comparisons with experiment.

SYMBOLS

A	viscous coefficient defined by Eq. (10)
$C_{D,\beta}$	boattail pressure drag coefficient
$C_{P,b}$	boattail base pressure coefficient
$C_{P,\beta}$	boattail pressure coefficient, $(p - p_\infty)/q_\infty$
C_1, C_2, C_μ	coefficients in $k\varepsilon 2$ turbulence model
d_b	boattail base diameter
D	boattail maximum diameter
f	solution vector in parabolic mixing equation, Eq. (9)
F_i	mass fraction of i^{th} species
g	source vector in parabolic mixing equation, Eq. (9)
H	total enthalpy of mixture
k	turbulent kinetic energy
ℓ	axial length of boattail
$\dot{m}$	mass-flow rate
M	Mach number
p	pressure
P	turbulence production term, Eq. (11)
Pr	turbulent Prandtl number
r	radial distance from axis
T	temperature
u	axial component of velocity
v	radial component of velocity
$\dot{w}$	chemical production term, Eq. (9)
W	molecular weight of mixture
x	axial distance
γ	ratio of specific heats of mixture
δ	thickness of viscous layer
δ^*	displacement thickness of viscous layer
Δ	incremental value
ε	turbulent dissipation rate
μ_t	turbulent viscosity coefficient, Eq. (12)
ρ	density of mixture
σ	coefficient vector in Eq. (9)
ψ	stream function, Eq. (13)

Subscripts

e	conditions at outer edge of viscous layer
eff	conditions at effective plume boundary
ent	entrainment
j	inviscid jet exhaust property at nozzle exit
∞	free-stream condition
1,2	inner, outer mixing-layer computational boundary

Superscript

I	equivalent inviscid property

INTRODUCTION

The viscous-inviscid interactions associated with near-field jet mixing are of fundamental interest in the prediction of nozzle afterbody-jet exhaust flow fields. In high Reynolds' number, turbulent flows over axisymmetric bodies, these mixing processes occur in a highly complex flow field characterized by relatively thick initial boundary layers and large pressure gradients caused by afterbody curvature and under/overexpanded jet exhausts (Fig. 1). Here, the mixing exhibits a highly non-similar behavior dominated by the transition from a boundary-layer-like mixing to a free-shear-layer-like mixing. The mixing away of the boundary-layer mass defect in this transition region perturbs the external flow significantly at subsonic and transonic speeds. The rate of mixing is strongly influenced by the pressure gradient which in turn is highly sensitive to the streamline deflections induced by the mixing.

A qualitative illustration of the role of the boundary layer in the viscous-inviscid interaction process is given in Fig. 2. Here, the interaction is modeled as a displacement of the inviscid streamlines due to the mass defect in the boundary layer, i.e., the inviscid flow is equivalent to that over the actual body augmented by the displacement thickness. If the inviscid jet plume boundary is treated as a solid, no-slip wall (no entrainment), the boundary-layer defect will persist indefinitely along the jet boundary. Although this model is physically invalid, it has been used in previous viscous-inviscid calculations of afterbody-jet interactions (Refs. 1 and 2) and does account for the inviscid plume blockage. However, if mixing effects are considered, the boundary-layer defect vanishes quickly (see Fig. 2), and the inviscid streamlines are deflected downward accordingly. The external flow is thus accelerated by the mixing process yielding a corresponding decrease in afterbody pressures as shown in Fig. 2. It is this acceleration process (which can also occur in the absence of initial boundary layers) that is termed the jet entrainment effect.

The importance of jet entrainment on measured afterbody drag (Ref. 3) is evident from the data shown in Fig. 3. These data were obtained by subtracting the boattail pressure drag for circular-arc boattail nozzles with solid-plume simulators from that for the same nozzles with a jet exhaust flow. The drag increment is due primarily to entrainment and increases as the ratio of jet to free-stream velocity increases accounting for as much as 50 to 60 percent of the boattail pressure drag. Such a large effect clearly cannot be neglected in the prediction of afterbody-jet interactions.

Previous viscous-inviscid calculations of afterbody-jet exhaust flows have attempted to model the entrainment interaction as a displacement-thickness correction to the inviscid plume boundary (Refs. 4-6). All of these models relate this correction, in some manner, to an estimate of the local mass entrainment rate computed by an integral analysis of the mixing layer. For example, Cosner (Ref. 4) applied an integral form of the boundary-layer equations to the inviscid plume boundary treated as a non-adiabatic moving wall. The mixing-layer displacement thickness was assumed to be just the resulting boundary-layer displacment thickness. This model does remove the no-slip condition along the plume boundary and therefore allows the boundary-layer defect to be accelerated; however, it does not account for mixing inside the jet and does not allow mass to cross the inviscid boundary. Yaros (Ref. 5) used the mixing layer analysis of Korst and Chow (Ref. 7) to account for the full mixing layer region and the initial internal nozzle boundary layer. However, the Korst and Chow analysis assumes the mixing to be isobaric which is not justifiable for this problem. Kuhn (Ref. 6) extended an integral boundary-layer analysis to the full mixing layer accounting for both axial inviscid pressure gradients and initial boundary-layer profiles characteristic of either attached or separated flows. An empirical model of the velocity profiles was used to describe the transition from a boundary-layer-like profile to the self-similar profile in the downstream shear layer. Kuhn's model appears to give qualitatively correct results for the predicted entrainment effect on afterbody drag; however, the sensitivity to initial conditions in his calculations appears to be attributable to the empiricism in the model. In view of the potentially large effects of entrainment shown earlier, a more complete assessment of these approximate models is clearly needed.

A computational jet entrainment model has been recently developed (Refs. 8 and 9) that provides a detailed and accurate analysis of near-field jet mixing, removing the need for many of the assumptions used in the more approximate models. This model employs a finite-difference procedure to integrate the parabolic turbulent mixing equations to determine the local mass entrainment rate. The computational grid for the mixing solution is overlaid onto a map of the inviscid flow field which is calculated a priori. By

this overlaid procedure, the local axial and radial pressure variations and variations in the mixing layer edge conditions are accounted for in the mixing calculation. The entrainment effect on the inviscid, external flow field is obtained by displacing the inviscid plume boundary such that the induced "inviscid" mass flow crossing the outer mixing-layer boundary is equivalent to that predicted by the turbulent mixing solution. The overall flow field solution, including the inviscid supersonic jet exhaust, inviscid subsonic external flow and external boundary layer, is obtained iteratively, as will be detailed in this paper.

Applications of this iterative model to the prediction of axisymmetric, nozzle afterbody flows with mildly underexpanded jet exhausts have shown very good agreement with experimental data (Refs. 9-11). The results of several numerical experiments have also been useful in providing an understanding of the basic mechanisms important to the viscous-inviscid interactive effects of mixing. The purpose of this paper is to fully describe the interactive jet entrainment model and to show how it has been incorporated into an iterative viscous-inviscid interaction scheme for predicting afterbody flow fields. Results are presented which illustrate the basic interactive effects under various flow conditions and which demonstrate the validity of the model by comparisons with experimental data.

JET ENTRAINMENT MODEL

Interactive Concept

The jet entrainment model developed is based on the concept of a weakly interacting mixing layer in which the mixing-induced streamline deflections are accounted for by a displacement-thickness type correction to the inviscid jet exhaust boundary. The magnitude of the interactive effect is proportional to the amount of local mixing-induced streamline deflection. The approach taken involves matching the streamline slopes predicted by a viscous mixing solution to those predicted by an equivalent inviscid solution (viz; if the local streamline slope, v/u, is known along the outer mixing-layer boundary, the flow field outside of the mixing layer may be solved by purely inviscid methods with the entrainment effect introduced by specifying the known $v/u = v_e/u_e$ as a boundary condition). This approach is completely analogous to that used in classical boundary-layer interaction theory.

Effective plume boundary.- Consider an axisymmetric jet exhausting into an external stream (Fig. 4(a)) where each stream may have an arbitrary velocity profile (e.g., representing an inviscid region plus a boundary-layer region). Applying the continuity equation to the control volume in Fig 4(a) and integrating from the axis to the outer edge of the mixing layer $(r = r_e)$ yields the relation

$$\int_0^{r_e} \frac{\partial \rho u}{\partial x}\, r\,dr = -\rho_e v_e r_e \tag{1}$$

where ρ and u are the actual (viscous) flow properties. Neglecting jet underexpansion effects for the moment, the term $-\rho_e v_e r_e \Delta x$ is defined as the mass entrained by the mixing layer between x and $x + \Delta x$, i.e.,

$$\frac{d\dot{m}_{ent}}{dx} = -\rho_e v_e r_e \tag{2}$$

An effective boundary $r_{eff}(x)$ is now sought such that an inviscid, external flow solution over this boundary produces the same mass flux across $r_e(x)$ as that given by the viscous solution. Applying continuity to the equivalent inviscid control volume shown in Fig. 4(b), it can readily be shown (see Ref. 11) that

$$\frac{d}{dx}\int_{r_{eff}}^{r_e} \rho^I u^I r\, dr = -\rho_e{}^I v_e{}^I r_e + \rho_e{}^I u_e{}^I r_e \frac{dr_e}{dx} \tag{3}$$

where the superscript I denotes inviscid flow quantities. In principle, Eq. (3) could be solved for r_{eff}. Such a solution requires an iterative procedure in which an initial guess is made for $r_{eff}(x)$, an inviscid outer solution is constructed subject to the

tangency condition $(v/u)_{r=r_{eff}} = dr_{eff}/dx$, and a viscous inner solution is obtained subject to the outer boundary conditions $\rho_e = \rho_e^I$ and $u_e = u_e^I$ at $r = r_e$. This iterative process would continue until the additional matching condition $v_e^I = v_e$ (or equivalently $d\dot{m}_{ent}^I/dx = d\dot{m}_{ent}/dx$) is met.

For thin mixing layers, Eq. (3) can be simplified considerably (in a manner consistent with the usual thin boundary-layer approximations) by assuming $\rho^I u^I$ to be approximately constant across the layer and equal to the local edge value, $\rho_e u_e$. After some rearrangement, Eq. (3) becomes

$$\frac{dr_{eff}^2}{dx} + (r_{eff}^2 - r_e^2)\frac{d\ell n \rho_e u_e}{dx} = 2\frac{v_e r_e}{u_e} \tag{4}$$

Neglecting axial variations in $\rho_e u_e$ for the moment, one can define a displacement thickness

$$\delta_{eff}^* \equiv r_{eff} - r_j \tag{5}$$

where $r_j(x)$ is the inviscid plume boundary. Assuming $\delta_{eff}^* << r_j$, Eq. (4) can be written as

$$\frac{dr_{eff}}{dx} \approx \frac{v_e r_e}{u_e r_j} \tag{6}$$

Thus, the viscous-inviscid interaction is essentially representable by a source distribution whose strength, given by Eq. (6), is proportional to the local mass entrainment rate. If the entrainment rate is known, the interaction may be accomplished either by integrating Eq. (4) to yield an effective boundary for the inviscid calculation or by simply specifying the source strength over the inviscid plume boundary. For thin mixing layers, the two methods should be nearly equivalent (Refs. 12-13). For the present work, the effective boundary method was used.

Displacement thickness for a mixing layer.- The effective displacement thickness defined by Eq. (5) is completely analogous to the usual definition given for boundary layers. To illustrate this analogy, we incorporate the definition into Eq. (3), eliminate the v_e-term with Eq. (1) and subtract $\int_o^{r_e} \frac{\partial \rho_e u_e}{\partial x} r dr$ from both sides. After some rearrangement, it can be shown (see Ref. 11) that

$$\delta_{eff}^* = \frac{1}{r_j}\int_o^{r_e}\left(1 - \frac{\rho u}{\rho_e u_e}\right) r dr + C \tag{7}$$

where C is the constant of integration. The analogy to a boundary-layer displacement thickness is evident with the main difference being that the integral in Eq. (7) must extend to the axis to account for the blockage of the jet exhaust flow. It can also be shown that the equivalence between source strength and displacement thickness is given by

$$v_e r_e = \frac{1}{\rho_e}\frac{d}{dx}(\rho_e u_e r_j \delta_{eff}^*) \tag{8}$$

again analogous to boundary-layer theory (Ref. 12). It is interesting to note that whereas the displacement thickness for a boundary layer always represents a mass defect (and is therefore always positive), δ_{eff}^* given by Eq. (7) can be either positive or negative depending on the mass flow parameter $\rho_j u_j/\rho_e u_e$.

Plume underexpansion effects.- The definition given for the effective plume boundary r_{eff} has so far been described only in terms of the mixing interaction. If the plume is underexpand there will be an additional interaction due to the geometry, $r_j(x)$, of the inviscid plume boundary. For mildly underexpanded plumes, r_j in Eq. (5) is assumed to be constant (equal to the nozzle exit radius). The underexpansion

effect can then be included in the effective boundary shape, with the displacement thickness, δ^*_{eff}, measured from the cylindrical surface $r = r_j$ as shown in Fig. 5. The effective boundary defined by Eq. (3) or (4) remains valid for the viscous-inviscid calculation with r_{eff} (and δ^*_{eff}) now containing this additional inviscid blockage contribution. In previous studies (Refs. 4-6), an attempt was made to separate these two effects; this distinction is not necessary here if the inflow term $(\rho_e v_e r_e)$ is computed in such a manner as to include both effects. For the overlaid mixing calculation (Ref. 8) to be described in the next section, this approach has been taken.

Overlaid Mixing Layer Model

In order to integrate Eq. (4), the local mass entrainment rate (or equivalently the entrainment velocity v_e) must be known. In the present work, v_e is obtained using the overlaid mixing analysis of Ref. 8 which solves the parabolic mixing equations in transformed (x,ψ) coordinates given by

$$\frac{\partial f}{\partial x} = \frac{1}{\psi} \frac{\partial}{\partial \psi} \left(\frac{A}{\sigma} \frac{\partial f}{\partial \psi}\right) + g \tag{9}$$

where

$$f = \begin{pmatrix} u \\ H \\ F_i \\ k \\ \varepsilon \end{pmatrix} \quad ; \quad \sigma^{-1} = \begin{pmatrix} 1 \\ Pr^{-1} \\ Pr^{-1} \\ 1 \\ .77 \end{pmatrix}$$

and

$$g = \begin{pmatrix} -\frac{1}{\rho u} \frac{\partial p}{\partial x} \\ \frac{1}{\psi} \frac{\partial}{\partial \psi} \left[A(1 - Pr^{-1}) u \frac{\partial u}{\partial \psi}\right] \\ \dot{w}/\rho u \\ (P - \varepsilon)/u \\ (C_1 P - C_2 \varepsilon)\varepsilon/uk \end{pmatrix}$$

The dependent variables are: u, the axial velocity; H, the total enthalpy; F_i, the mass fraction of the i^{th} species; k, the turbulent kinetic energy; and ε, the rate of turbulent dissipation. The term A is given by

$$A = \mu_t \frac{\rho u r^2}{\psi} \tag{10}$$

and the turbulence production term, P, by

$$P = \frac{Au}{\psi} \left(\frac{\partial u}{\partial \psi}\right)^2 \tag{11}$$

The turbulent viscosity, μ_t, in this formulation is given by

$$\mu_t = C_\mu \frac{\rho k^2}{\varepsilon} \tag{12}$$

where C_μ and the constants C_1 and C_2 employed in Eq. (9) are described in Ref. 8. The turbulent Lewis number has been assumed to be unity.

The system of equations, Eq. (9), is integrated along the streamlines by a one-step, explicit finite-difference procedure. The computational domain bounded by $\psi_1(x)$ and $\psi_2(x)$ (Fig. 6) is overlaid onto a previously computed inviscid flow field (also mapped into (x,ψ) coordinates). The physical location, $r(x,\psi_1)$ of the inner boundary is determined by interpolation from the inviscid flow map. Thus, the curvature of the inviscid jet exhaust streamlines is taken into account with the growth of the computational domain taking place about the inviscid plume boundary. The location of the outer boundary, $r(x,\psi_2)$, and the entrainment velocity, $v_e(x,\psi_2)$, are then determined by inversion of the stream function transformation given by

$$\psi \left.\frac{\partial \psi}{\partial r}\right|_x = \rho u r \tag{13a}$$

$$\psi \left.\frac{\partial \psi}{\partial x}\right|_r = -\rho v r \tag{13b}$$

Evaluating v_e along the computational boundary $\psi_2(x)$ yields

$$v_e = u_e \frac{dr_e}{dx} - \frac{1}{2\rho_e r_e} \frac{d\psi_2^2}{dx} \tag{14}$$

It should be noted that the $d\psi_2^2/dx$-term in Eq. (14) bears no direct relation to the mixing but arises simply due to the arbitrary growth rate of the computational boundary. The mixing effect is contained mainly in the dr_e/dx-term where $r_e(x)$ is evaluated by inversion of Eq. (13a).

At each integration step, the edge conditions and the pressure and pressure gradients at each grid point are determined by direct interpolation (in (x,ψ) coordinates) from the inviscid flow maps. Thus, a solution to the inviscid radial momentum equation is implied in the mixing solution by imposing $p(x,\psi)$ as a known quantity. The pressure field can therefore be treated by fully elliptic methods with coupling to the viscous effects accomplished through the interaction model. Of course, this approach is formally justified only when the mixing-induced perturbations on the pressure are small. For the cases studied herein, the weak-interaction hypothesis appears to be quite reasonable and the inclusion of inviscid pressure gradients in the mixing analysis will be seen to be quite important.

The overlaid model of Ref. 8 also allows for finite-rate chemical reactions in the mixing layer. To remove the stiffness associated with the chemical source term, $\dot{w}$, in Eq. (9), the species continuity equations are solved by a linearized, implicit finite-difference procedure.

COMPUTATIONAL APPROACH

The use of the jet entrainment model within the framework of a viscous-inviscid interaction technique requires, first, that the overall flow field be divided into distinct regions (Fig. 7). Each region is then treated by a computational approach that caters to the physical flow processes and length scales occurring within that region. For application to the problem of a supersonic jet interacting with a subsonic flow over a nozzle boattail, the following key assumptions are employed:

Region I: External Flow.- The external flow is assumed to be inviscid and irrotational, i.e., the velocity may be expressed as the gradient of a scalar potential function.

Region II: Boundary Layer.- The external boundary layer is assumed to be turbulent and to remain attached to the nozzle boattail surface. The internal nozzle boundary layer is assumed to be thin compared to the external boundary layer and its thickness at the nozzle exit is assumed to be constant.

Region III: Inviscid Jet Exhaust.- The inviscid jet exhaust flow is assumed to be supersonic at all computational boundaries, i.e., upstream inflow (at nozzle exit) boundary, outer plume boundary, and downstream outflow boundary, except at the jet center line where the flow may be subsonic downstream of the normal shock (Mach disc) which may develop when the jet is underexpanded $(p_j > p_\infty)$.

Region IV: Mixing Layer.- The mixing is assumed to be turbulent and only the radial shear stress term in the axial momentum equation is retained. The pressure field is imposed from the inviscid solution.

The final assumption needed is that the viscous-inviscid interaction is weak; i.e., the streamline deflections produced by the boundary-layer and mixing-layer displacement are small ($v_e/u_e \ll 1$).

Iterative Procedure

An iterative procedure for solving the complete flow field is now established consistent with the above assumptions. This procedure consists of the single iterative loop shown in Fig. 8.

The Region I solution is obtained by solving the full, nonlinear, potential flow equation by the relaxation technique of South and Jameson (Ref. 14). The computational boundary is the displacement body defined to match the viscous velocity component $v_e(x)$ along the outer edge of the viscous layer. The displaced body consists of the combined body plus boundary-layer displacement thickness from Region II and the inviscid plume plus mixing-layer displacement thickness from Region IV. In the iteration procedure, the displacement thickness is applied using a simple underrelaxation technique, i.e., $\delta^*(x) = \frac{1}{2}(\delta^*_{new} + \delta^*_{old})$, to enhance convergence.

Region II is solved next using a modified version of the integral boundary-layer method of Reshotko and Tucker (Ref. 15) with the edge conditions specified by Region I in the usual manner.

The inviscid jet exhaust (Region III) is computed by the shock-capturing, inviscid plume model of Dash and Thorpe (Ref. 16). This model uses an explicit, two-step marching procedure to solve the steady-state, inviscid flow equations in conservative, finite-difference form. The pressure along the inviscid plume boundary is prescribed by the Region I solution.

The mixing region is solved by the overlaid model described earlier with initial conditions from Region II and edge conditions and pressure from Regions I and III. Further details of the application of the individual computational models are given in Ref. 11.

The single iterative loop in Fig. 8 has been found to give excellent convergence for typical nozzle afterbody flows with mildly underexpanded plumes. A typical convergence history for the maximum pressure coefficient and displacement thickness (which occur at the end of the afterbody) is shown in Fig. 9. Most of the viscous-inviscid interaction is completed in the first three to four iterations with a convergence level of less than 0.1 percent being achieved in five to 10 iterations.

RESULTS

Basic Viscous-Inviscid Interaction for Parallel Mixing

The simplest case studied was the interaction of a uniform, subsonic stream with a simple axisymmetric shear layer (no external boundary layer). This case provides an illustrative example of the basic interactive effect since the inviscid flow is uniform and parallel everywhere and any perturbations are due solely to mixing.

The entrainment velocity for a velocity ratio, u_j/u_∞, of 5 is shown in Fig. 10. With the jet velocity larger than that of the external stream, the entrainment velocity is negative everywhere along the outer shear layer boundary and the resulting effective inviscid boundary has a negative slope. The matching of v_e/u_e between the viscous and inviscid calculations is very good, with a slight disagreement at the start of the shear layer caused by numerical smoothing of the slope discontinuity in the effective boundary in the inviscid calculation.

Since the mixing of parallel streams in the absence of boundary layers is essentially self-similar, the near-field entrainment velocity (and mass entrainment rate) is essentially constant. Therefore, the source strength, $v_e r_e$, can be used as a basic measure of the strength of the viscous-inviscid interaction. The computed variation in source strength with mass-flux ratio, $\rho_j u_j/\rho_\infty u_\infty$, is given in Fig. 11 for two different velocity ratios. These results suggest a qualitative behavior given by

$$\frac{v_e r_e}{u_e r_j} \propto \frac{u_j}{u_\infty}\left(1 - \frac{\rho_j u_j}{\rho_\infty u_\infty}\right) \tag{15}$$

That is, the magnitude of the source strength is proportional mainly to the velocity ratio while the sign (positive or negative displacement) depends on the mass-flux ratio. While the usual concept of entrainment effects is that of accelerating the external flow (negative displacement), these predictions show that, for $\rho_j u_j/\rho_\infty u_\infty < 1$, a decelerating effect (positive displacement) is possible. This effect will later be shown to be important in predicting nozzle afterbody drag.

Jet Entrainment Effects on Nozzle Afterbody Flows

The model was applied to the prediction of the subsonic flow over a circular-ar boattail nozzle ($\ell/D = 1.77$ and $d_b/D = 0.51$) with a sonic jet of exit radius $r_j/D = .50$.

Basic entrainment effect.- A comparison of results predicted with and without the entrainment correction are shown in Fig. 12. The displacement thickness without entrainment was obtained simply by continuing the boundary-layer calculation over the inviscid plume boundary treated as a no-slip, solid wall. The more negative source strength with entrainment results in a reduction in the effective "size" of the plume due to the removal of the boundary-layer defect. The predicted boattail pressures are thereby reduced and compare quite favorably with the experimental data of Ref. 3.

Boundary-layer effect.- To determine the importance of the boundary-layer defect, a calculation was performed in which the boundary-layer thickness was assumed to be zero over the entire body. The mixing calculation was still retained but was initialized with a self-similar profile characteristic of free shear-layer mixing (no defect). A comparison to the prediction with a boundary layer (Fig. 13) shows that the dominant contribution to the near-field interaction is due to the transition of the wakelike boundary-layer mixing to a simple shear-layer mixing.

Pressure gradient effect.- The influence of the inviscid pressure gradients on the mixing calculation is evident in the results of Fig. 14. The zero-pressure-gradient results were obtained by setting the pressure-gradient term in Eq. (9) equal to zero. As shown in Ref. 10, such a calculation gives essentially the same mixing-layer displacement as the isobaric mixing analysis of Korst and Chow. Significant differences in the near-field source strengths are evident which vanish downstream where the pressure gradient is small. However, the inviscid pressure distribution shows a strong sensitivity to the near-field interaction. Clearly, an isobaric mixing assumption is not justified in the near-field calculation.

Comparisons with Data

Comparisons of predicted boattail pressure distributions to the data of Ref. 3 are shown in Fig. 15 for various flow conditions. Figure 15(a) shows the effect of free-stream Mach number at a slightly underexpanded pressure ratio ($p_j/p_\infty = 1.1$). Since the jet velocity is essentially constant, these data also show the effect of shear-layer velocity ratio, u_j/u_∞. Figure 15(b) shows the effect of plume underexpansion at a constant Mach number. All predictions are in excellent agreement with the experimental data.

The correlation of the measured pressure at the rearward-most portion of the boattail, $C_{p,b}$, with u_j/u_∞ and p_j/p_∞ is shown in Fig. 16. Increasing the velocity ratio decreases $C_{p,b}$ due to the increased entrainment rate, while increasing the pressure ratio increases $C_{p,b}$ due to inviscid plume blockage. Both effects are predicted correctly by the theory, although the predicted magnitude of $C_{p,b}$ is slightly higher than the data. In view of the excellent overall agreement in Fig. 15, the jet entrainment model appears to provide a valid approach for predicting jet effects on nozzle afterbodies.

Predictions of Real Gas Effects

In addition to providing improved accuracy in near-field mixing calculations, the overlaid model of Ref. 8 also provides the capability to treat the mixing between streams of arbitrary gas compositions with or without chemical reactions. Since the entrainment interaction has been shown to depend on both the density and velocity ratios (both of which depend on composition, temperature, etc.), results are shown in this section to illustrate these effects. The calculations were all performed at a $M_\infty = 0.4$ and $p_j/p_\infty = 1.1$ for the same circular-arc nozzle used in the previous comparisons.

Composition effect.- Since the mass-flux ratio $\rho_j u_j/\rho_\infty u_\infty$ is proportional to $\sqrt{W_j/W_\infty}$, where W is the mixture molecular weight, the effect of composition can be seen by simply varying the molecular weight of the jet gas. A comparison of the entrainment interaction for a pure nitrogen and a pure hydrogen jet is shown in Fig. 17. Decreasing the jet density (molecular weight) increases the entrainment velocity resulting in an outward displacement of the effective plume boundary, an increase in boattail pressures and a decrease in boattail drag (Fig. 18). This density effect is in agreement with the qualitative model given by Eq. (15) and is verified by the experimental data of Peters (Ref. 17) for nitrogen and hydrogen jets. A similar effect can also be seen by increasing the jet temperature, since for a given composition, the mass-flux ratio varies as $\sqrt{T_\infty/T_j}$ (see Ref. 11).

Real jet exhaust effects.- To further demonstrate the capabilities of the overlaid mixing model, a test case was chosen with jet exhaust conditions where real gas and afterburning effects were likely to occur. Calculations were performed with and without chemical reactions. The exhaust gases were assumed to consist of 75 percent N_2, 5 percent O_2, 10 percent H_2O, and 10 percent CO where the CO represents the unburned "fuel." For the calculation with chemistry, trace quantities of CO_2, OH, H, O and H_2 were also assumed, and a standard set of chemical reactions for the combustion of CO and H_2

(Ref. 18) was used. A jet exhaust temperature of 1500 K and a nominal ratio of specific heats $\gamma = 1.27$ were used for the inviscid jet exhaust calculation.

Results for these two cases are compared to those for a cold-air jet in Fig. 19. The main effect is a simple increase in the entrainment "blockage" effect due to the increased temperature (and decreased density). The effect of CO afterburning is to increase the temperature in the mixing layer and to produce an additional outward shift in the effective boundary. However, the afterburning effect is not significant until several jet radii downstream, since the burning requires the entrainment of sufficient external air for the reactions to proceed. In both cases, the boattail pressures are increased with a corresponding decrease in the drag (Fig. 20).

CONCLUDING REMARKS

A viscous-inviscid interaction technique has been presented for computing the entrainment effects on nozzle afterbody-jet exhaust flow fields. The entrainment interaction is modeled as a displacement correction to the inviscid jet boundary which accounts for the mixing-induced streamline deflections. The displacement concept has been shown to be fully analogous to that used in standard boundary layer interaction theory, except that the mixing-layer displacement can have either positive or negative values depending on the density and velocity ratios between the jet and free-stream.

An iterative procedure for matching the viscous mixing region to an inviscid outer flow solution has been developed and its validity has been demonstrated by comparisons with experimental data. Applications of the procedure to the prediction of nozzle afterbody flows with underexpanded jet exhausts show clearly the need to account for both non-similar mixing and variable pressure gradients in the near-field mixing layer.

REFERENCES

1. Reubush, David E.; and Putnam, Lawrence E.: An Experimental and Analytical Investigation of the Effect on Isolated Boattail Drag of Varying Reynolds Number up to 130×10^6. NASA TN D-8210, 1976.

2. Putnam, Lawrence E.; and Abeyounis, William K.: Experimental and Theoretical Study of Flow Fields Surrounding Boattail Nozzles at Subsonic Speeds. AIAA Paper No. 76-675, July 1976.

3. Reubush, David E.: Experimental Study of the Effectiveness of Cylindrical Plume Simulators for Predicting Jet-On Boattail Drag at Mach Numbers up to 1.30. NASA TN D-7795, 1974.

4. Cosner, Raymond R.; and Bower, William W.: A Patched Solution of the Transonic Flowfield About an Axisymmetric Boattail. AIAA Paper No. 77-227, Jan. 1977.

5. Yaros, Steven F.: An Analysis of Transonic Viscous/Inviscid Interactions on Axisymmetric Bodies with Solid Stings or Real Plumes. AEDC-TR-77-106, U.S.Air Force, Feb. 1978.

6. Kuhn, Gary D.: Calculation of Separated Turbulent Flows on Axisymmetric Afterbodies Including Exhaust Plume Effects. AIAA J., vol. 18, no. 3, Mar. 1980, pp. 235-242.

7. Korst, H. H.; and Chow, W. L.: Non-Isoenergetic Turbulent ($Pr_t = 1$) Jet Mixing Between Two Compressible Streams at Constant Pressure. NASA CR-419, 1966.

8. Dash, Sanford M.; and Pergament, Harold S.: A Computational Model for the Prediction of Jet Entrainment in the Vicinity of Nozzle Boattails (The BOAT Code). NASA CR-3075, 1978.

9. Dash, S. M.; Wilmoth, R. G.; and Pergament, H. S.: Overlaid Viscous/Inviscid Model for the Prediction of Near Field Jet Entrainment. AIAA J., vol. 17, no. 9, Sept. 1979, pp. 950-958.

10. Wilmoth, R. G.; Dash, S. M.; and Pergament, H. S.: A Numerical Study of Jet Entrainment Effects on the Subsonic Flow Over Nozzle Afterbodies. AIAA Paper No. 79-0135, Jan. 1979.

11. Wilmoth, Richard G.: Viscous-Inviscid Calculations of Jet Entrainment Effects on the Subsonic Flow Over Nozzle Afterbodies. NASA TP-1626, 1980.

12. Lighthill, M. J.: On Displacement Thickness. J. Fluid Mech., vol. 4, pt. 4, Aug. 1958, pp. 383-392.

13. Burggraf, Odus R.: Choice of Boundary Conditions in Viscous Interaction Theory. AIAA J., vol. 4, no. 6, June 1966, pp. 1145-1146.

14. South, Jerry C., Jr.; and Jameson, Antony: Relaxation Solutions for Inviscid Axisymmetric Transonic Flow Over Blunt or Pointed Bodies. AIAA Computational Fluid Dynamics Conference, July 1973, pp. 8-17.

15. Reshotko, Eli; and Tucker, Maurice: Approximate Calculation of the Compressible Turbulent Boundary Layer With Heat Transfer and Arbitrary Pressure Gradient. NACA TN 4154, 1957.

16. Dash, S. M.; and Thorpe, R. D.: A New Shock-Capturing/Shock-Fitting Computational Model for Analyzing Supersonic Inviscid Flows (The SCIPPY Code). Rep. No. 366, Aeronaut. Res. Assoc. Princeton, Inc., Nov. 1978.

17. Peters, W. L.: Jet Simulation Techniques: Simulation of Temperature Effects By Altering Gas Composition. AEDC-TR-78-43, U.S. Air Force, Mar. 1979.

18. Jensen, D. E.; and Pergament, H. S.: Effects of Nonequilibrium Chemistry on Electrical Properties of Solid Propellant Rocket Exhaust Plumes, Combustion and Flame, vol. 12, no. 115, 1971.

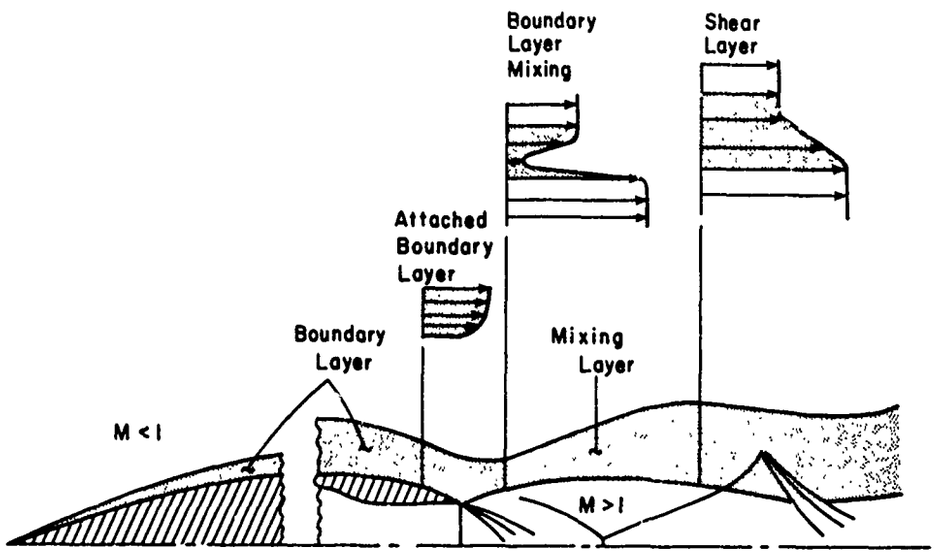


Figure 1.- Afterbody/exhaust flow field.

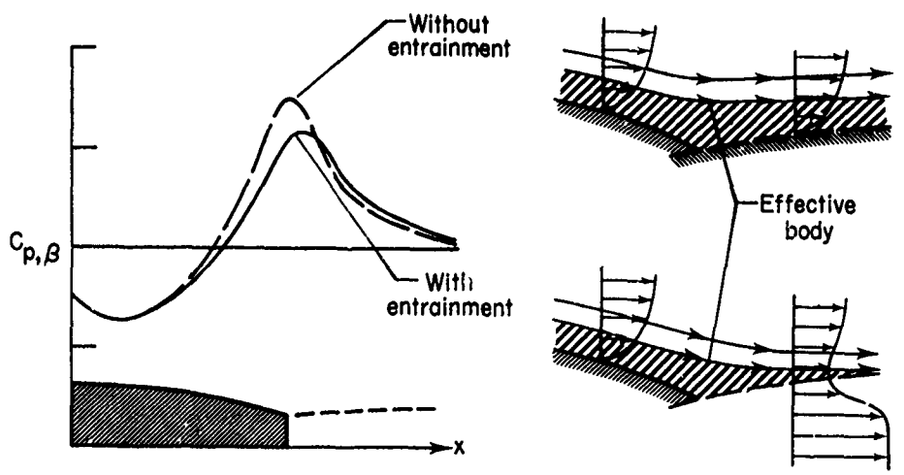


Figure 2.- Displacement models with and without entrainment.

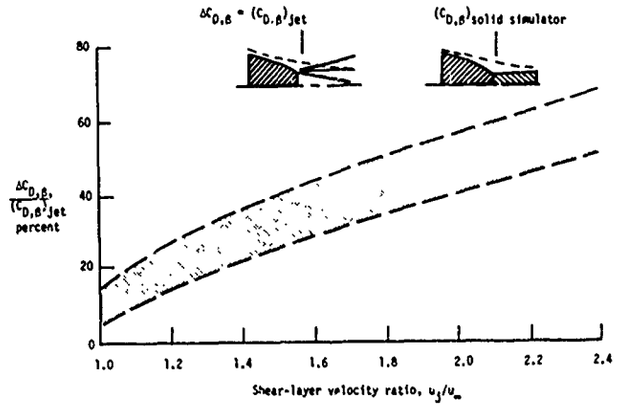
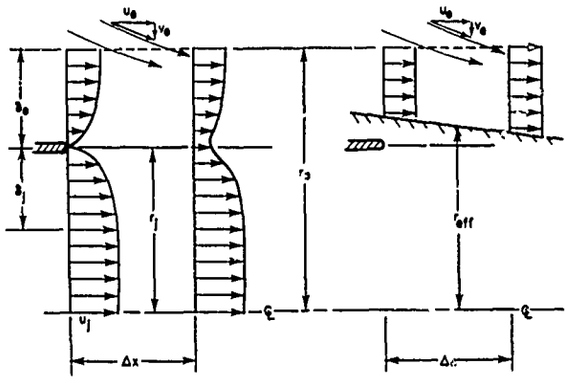


Figure 3.- Entrainment effect on measured boattail drag. $M_j = 1$. Data from Ref. 3.



(a) Viscous flow. (b) Equivalent inviscid flow.

Figure 4.- Control volumes for effective plume boundary definition.

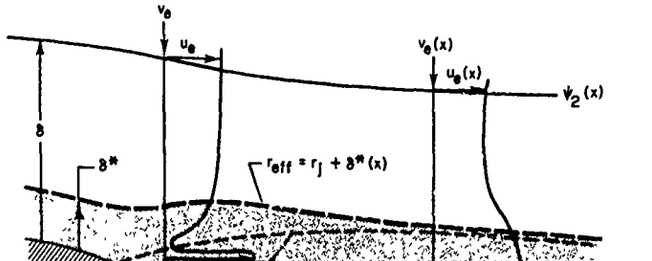


Figure 5.- Application of displacement correction for underexpanded plume.

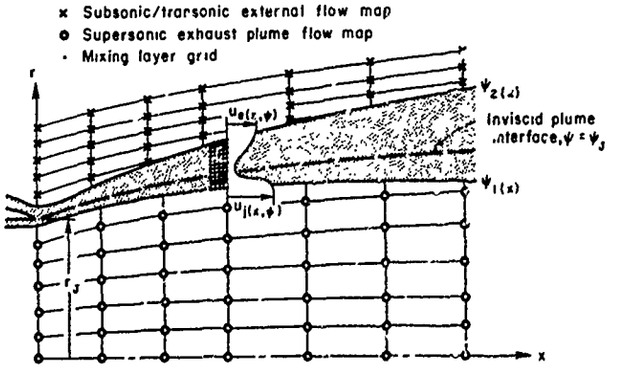


Figure 6.- Overlaid computational grids for mixing-layer analysis.

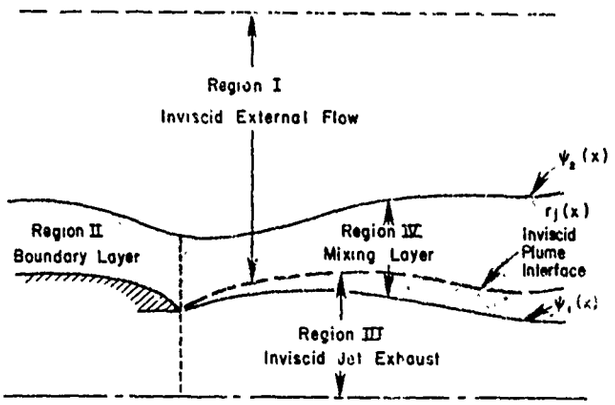


Figure 7.- Computational regions for viscous-inviscid analysis.

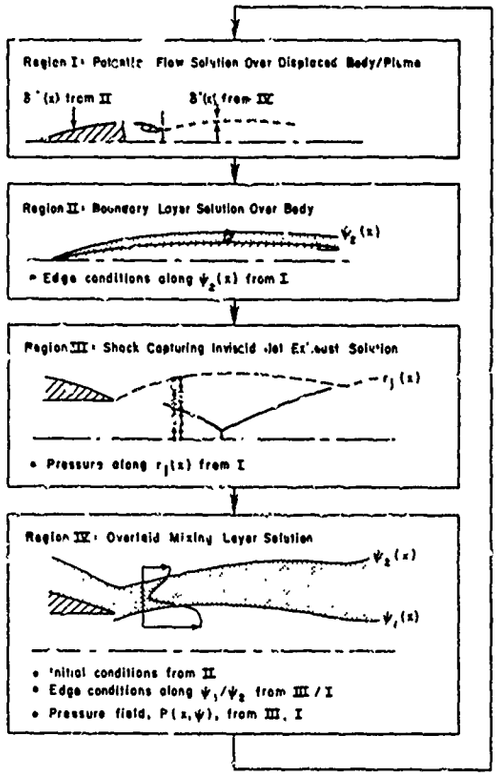


Figure 8.- Viscous-inviscid iteration procedure.

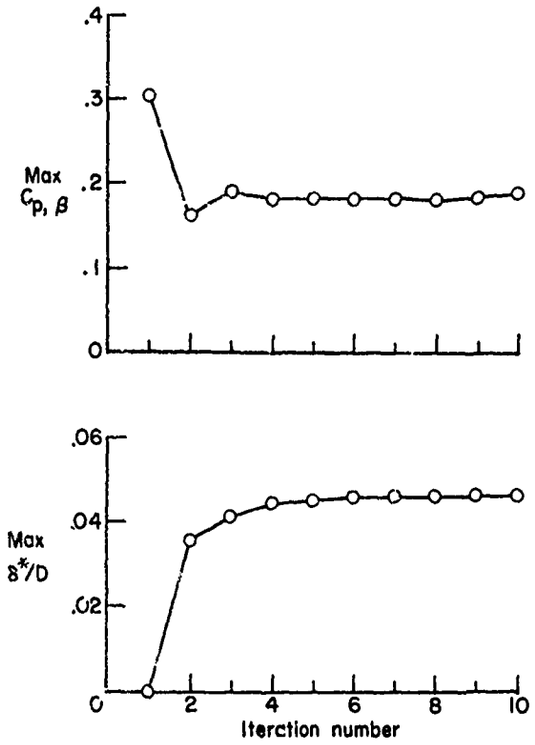


Figure 9.- Convergence characteristics of iterative scheme. $M_\infty = 0.4$, $p_j/p_\infty = 1.1$.

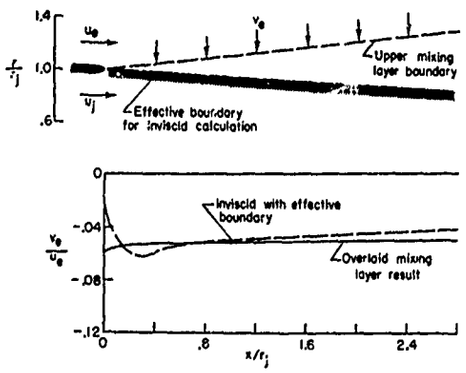


Figure 10.- Matching of entrainment velocity to equivalent inviscid flow for parallel mixing. $u_j/u_\infty = 5$, $p_j/p_\infty = 1$.

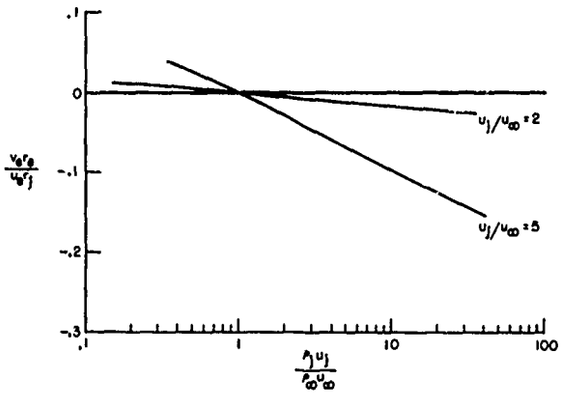
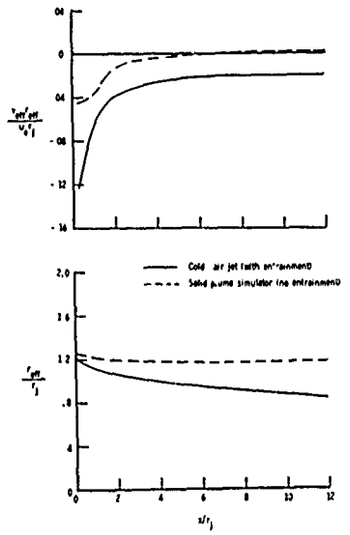
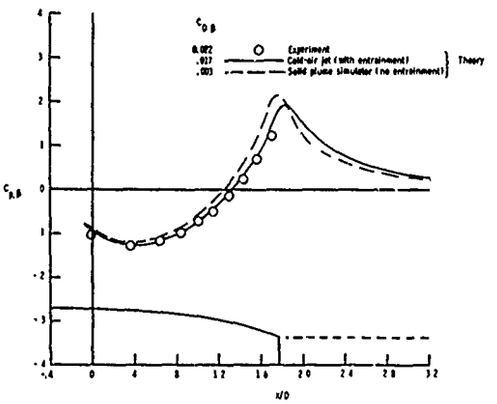


Figure 11.- Variation of mixing-induced source strength with mass-flux and velocity ratios. $p_j/p_\infty = 1$.

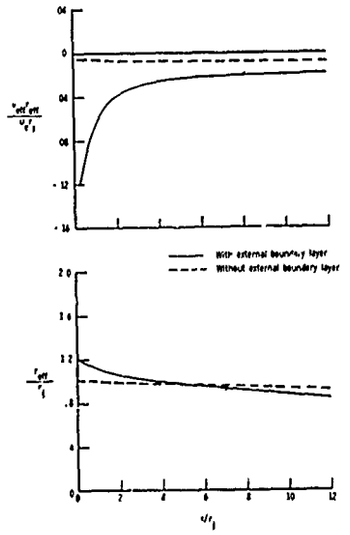


(a) Effective plume boundary and source strength distribution.

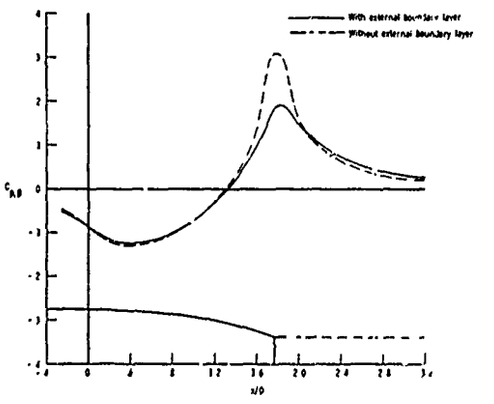


(b) Boattail pressure distribution. Data from Ref. 3.

Figure 12.- Basic entrainment effect on nozzle boattail/jet interaction. $M_\infty = 0.4$, $u_j/u_\infty = 2.3$, $p_j/p_\infty = 1.1$.

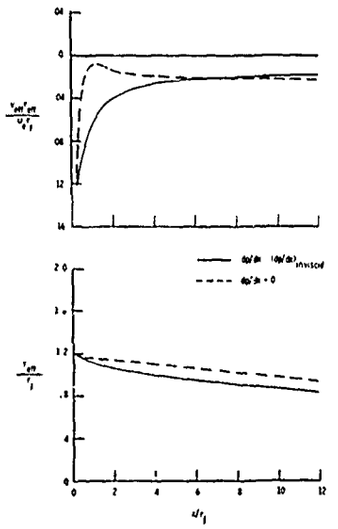


(a) Effective plume boundary and source strength distribution.

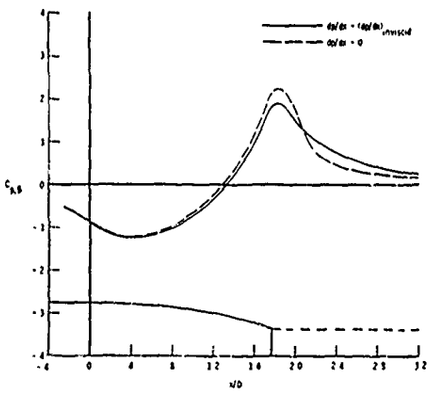


(b) Boattail pressure distribution.

Figure 13.- Effect of external boundary layer on boattail/jet interaction. $M_\infty = 0.4$, $u_j/u_\infty = 2.3$, $p_j/p_\infty = 1.1$.

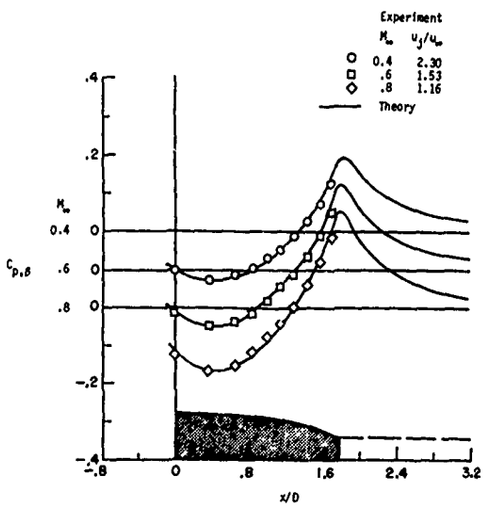


(a) Effective plume boundary and source strength distribution.

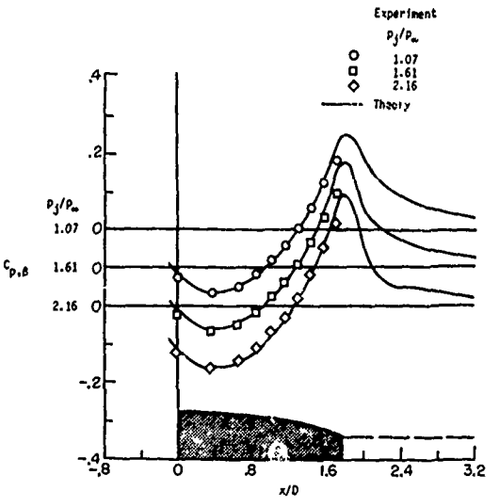


(b) Boattail pressure distribution.

Figure 14.- Effect of pressure gradient in near-field mixing layer on boattail/jet interaction. $M_\infty = 0.4$, $u_j/u_\infty = 2.3$, $p_j/p_\infty = 1.1$.



(a) Effect of velocity ratio. $p_j/p_\infty = 1.1$.



(b) Effect of pressure ratio. $u_j/u_\infty = 2.3$.

Figure 15.- Comparisons of predicted and measured boattail pressures. Data from Ref. 3.

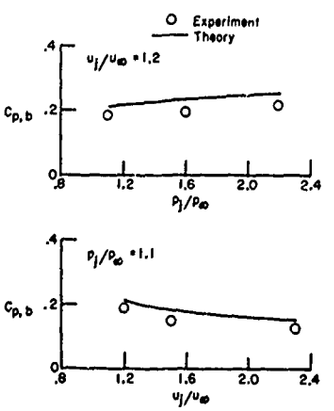


Figure 16.- Comparison of predicted and measured boattail base pressure variation with velocity and pressure ratios. Data from Ref. 3.

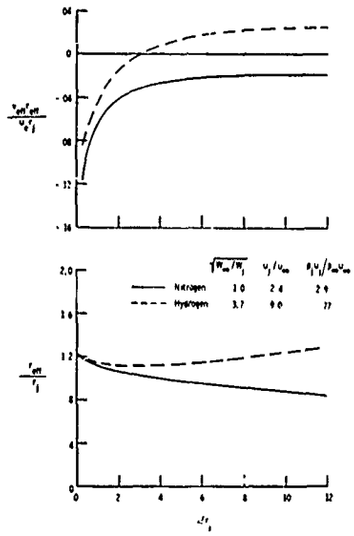


Figure 17.- Effect of jet exhaust molecular weight on boattail/jet interaction. $M_\infty = 0.4$, $M_j = 1.0$, $p_j/p_\infty = 1.1$.

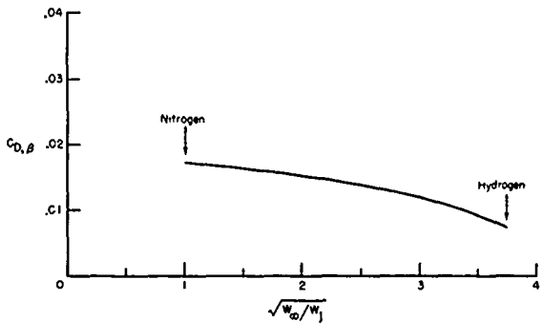


Figure 18.- Variation of predicted boattail drag with molecular weight ratio. $M_\infty = 0.4$, $M_j = 1.0$, $p_j/p_\infty = 1.1$.

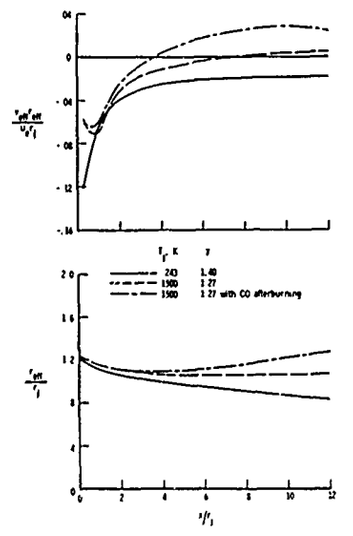


Figure 19.- Effect of jet temperature and afterburning on boattail/jet interaction. $M_\infty = 0.4$, $M_j = 1.0$, $p_j/p_\infty = 1.1$.

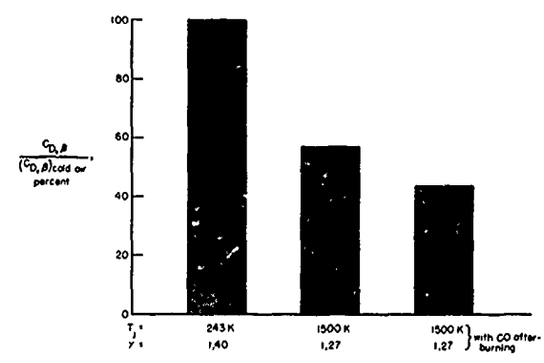


Figure 20.- Effect of jet temperature and afterburning on predicted boattail drag. $M_\infty = 0.4$, $M_j = 1.0$, $p_j/p_\infty = 1.1$.

ANALOGIE DES SINGULARITES DANS LES METHODES DIRECTES DE CALCUL DES COUCHES LIMITES TRIDIMENSIONNELLE STATIONNAIRE ET BIDIMENSIONNELLE INSTATIONNAIRE - ANALYSE DES MODES INVERSES

J. COUSTEIX & R. HOUDEVILLE

Département d'Aérothermodynamique
ONERA / CERT
31055 - TOULOUSE CEDEX, FRANCE

RESUME

Le problème de l'apparition de singularités dans les équations de couches limites instationnaire bidimensionnelle et tridimensionnelle stationnaire est étudié analytiquement à partir des équations globales de quantité de mouvement et d'entrainement.

En mode direct la vitesse est imposée. On montre que contrairement au cas bidimensionnel stationnaire, l'apparition d'écoulements de retour n'engendre pas, en général de singularité mais traduit une influence de l'aval sur l'amont. Dans les deux cas, l'étude analytique ou numérique montre que des lignes de discontinuité peuvent exister correspondant à des solutions faibles des équations mais ces lignes n'ont aucun sens physique. En particulier, dans le cas tridimensionnel elles ne doivent pas être interprétées comme des lignes de décollement.

Le calcul en mode inverse permet d'éviter toute singularité. La vitesse est alors une inconnue du problème de couche limite. Ces méthodes sont utiles pour traiter le couplage fluide parfait-couche limite mais sont aussi intéressantes pour valider des modèles de fermeture dans des régions décollées.

SUMMARY

The problem of occurrence of singularities in boundary layer equations, both in the unsteady two-dimensional and steady three-dimensional cases, is analytically studied by means of the global equations of momentum and entrainment.

In the direct mode the velocity is given. It is shown that in opposition to the steady two-dimensional case, the occurrence of reversed flows does not generally create singularities, but indicates a downstream influence. In both cases the analytical and numerical study shows that discontinuity lines can exist, corresponding to weak solutions of the equations, but these lines have no physical meaning. Particularly in the three-dimensional case they must not be confused with separation lines.

The calculations in the inverse mode avoid any singularity. The velocity is then an unknown of the boundary layer problem. Such methods are useful to solve the coupling problem between viscid-inviscid flow and are also interesting to verify closure relations of calculation models in separated regions.

NOTATIONS

x, z : coordonnées liées aux lignes de courant extérieures

y : direction normale à la paroi

h_1, h_2 : coefficients métriques pour x et z

∂, m : $\frac{\partial}{\partial \alpha} = \frac{1}{h_1}\frac{\partial}{\partial x}$; $\frac{\partial}{\partial m} = \frac{1}{h_2}\frac{\partial}{\partial z}$

ξ, ζ : coordonnées généralisées liées à la paroi

μ_1, μ_2 : éléments métriques suivant ξ et ζ

u, w, v : composantes de la vitesse suivant x, z, y

U, W, v : composantes de la vitesse suivant ξ, ζ et y

U_1, W_1 : composantes de la vitesse extérieure

K_1, K_2 : courbures géodésiques des lignes de courant extérieures

$$\delta_1 = \int_0^\delta \left(1 - \frac{u}{u_e}\right) dy \qquad \theta = \int_0^\delta \frac{u}{u_e}\left(1 - \frac{u}{u_e}\right) dy \quad (\theta_{11} \text{ en 3D})$$

$$H = \delta_1/\theta \qquad H^* = (\delta - \delta_1)/\theta$$

$$\delta_2 = \int_0^\delta -\frac{w}{u_e}\, dy \qquad \theta_{22} = \int_0^\delta -\frac{w^2}{u_e^2}\, dy \qquad \Delta_1 = \int_0^\delta \left(\frac{U_1}{u_e} - \frac{U}{u_e}\right) dy$$

$$\theta_{21} = \int_0^\delta -\frac{wu}{u_e^2}\, dy \qquad \theta_{12} = \int_0^\delta \frac{w}{u_e}\left(1 - \frac{u}{u_e}\right) dy \qquad \Delta_2 = \int_0^\delta \left(\frac{W_1}{u_e} - \frac{W}{u_e}\right) dy$$

C_{f_1}, C_{f_2} : coefficients de frottement suivant u_e et sa normale : $\frac{\tau_{e_1}}{\rho u_e^2}$ et $\frac{\tau_{e_2}}{\rho u_e^2}$

β_o : déviation limite de la ligne de courant pariétale par rapport à u_e :
$$tg\,\beta_o = \lim_{y\to o} \frac{w}{u} = \frac{C_{fn}}{C_{ft}}$$

C : pente du profil de vitesse en coordonnées polaires

G : paramètre de Clauser

$C_{\varepsilon s}$: coefficient d'entrainement en stationnaire

λ : direction réduite d'une ligne caractéristique

1. INTRODUCTION

Le calcul du champ de vitesse autour d'un obstacle peut théoriquement être effectué en résolvant les équations complètes de Navier-Stokes. Cependant, pour calculer pratiquement des écoulements à grand nombre de Reynolds, il peut être plus avantageux et plus commode de confiner les effets visqueux à des régions voisines des parois ou aux sillages, ce qui permet de ne traiter que les équations d'Euler dans presque toute l'étendue du domaine ; on doit alors résoudre le problème du couplage fluide visqueux-fluide réel et pour cela intégrer les équations de couche limite à partir de la connaissance de la vitesse extérieure (couplage faible). Cependant, même dans le cas le plus simple d'un écoulement bidimensionnel stationnaire une telle technique ne permet pas de traiter des régions décollées car il apparaît au point de frottement nul une singularité dépourvue de sens physique.

Les analyses effectuées par de nombreux auteurs en instationnaire bidimensionnel ou en tridimensionnel stationnaire tendent à montrer que des singularités peuvent également apparaître pour ces types d'écoulements, sans que la nature de celle-ci soit clairement mise en évidence /1,2,3/. De plus le caractère purement numérique de beaucoup d'études rend délicat l'interprétation des résultats ce qui conduit parfois à confondre les lignes de singularité avec de véritables lignes de décollement bien que celles-ci possèdent un caractère de régularité que n'ont pas les premières /4/.

Il se pose alors le problème de la validité des hypothèses de couche limite au voisinage du décollement. En fait, il est maintenant bien établi que dans le cas bidimensionnel stationnaire ces équations restent valables et que le recours aux méthodes dites inverses, dans lesquelles la vitesse extérieure est une inconnue du problème, permet d'éviter toute singularité /5,6/. On peut alors penser qu'il en est de même pour les cas instationnaire ou tridimensionnel.

Pour analyser le problème de l'apparition de singularités dans les équations de couche limite en mode direct, nous proposons une méthode analytique qui utilise les équations globales de quantité de mouvement et d'entrainement ainsi qu'un nombre restreint de relations de fermeture. Bien qu'une telle méthode ne s'identifie pas totalement à la résolution des équations de Prandtl, le bon accord toujours observé entre les deux méthodes, tant du point de vue de la précision des résultats que des comportements mathématiques, comme par exemple pour la singularité de GOLDSTEIN, permet d'accorder une certaine confiance quant à la généralité des conclusions que l'on peut en attendre. Une telle étude permet aussi de préciser la nature des conditions aux limites à imposer dans un calcul en mettant clairement en évidence les domaines de dépendance et d'influence. Ceci est particulièrement important en écoulement tridimensionnel.

Par une étude analogue des équations intégrales en mode inverse, nous montrerons ensuite que ces méthodes éliminent pratiquement le risque d'apparition de singularités, aussi bien en tridimensionnel qu'en instationnaire. Remarquons que le système d'équations à utiliser en mode inverse dépend de la position où se fait le raccordement avec le fluide parfait. Notre propos n'étant pas de traiter de façon générale le problème du couplage mais plus modestement de tester des modèles de calcul de la couche limite, nous nous intéressons plus particulièrement à une classe de méthodes pour lesquelles la donnée du problème est une ou deux épaisseurs de couche limite, suivant que l'on considère le cas instationnaire ou le cas tridimensionnel, et où l'une des inconnues principales est la vitesse extérieure. Pour ces deux cas, une comparaison à des résultats expérimentaux est présentée.

2. ETUDE DU MODE DIRECT

Les méthodes que nous considérons utilisent les équations intégrales de quantité de mouvement et d'entrainement ainsi qu'un petit nombre de relations de fermeture. Ces équations, écrites pour un fluide incompressible, sont regroupées sur la planche 1. Avant d'aborder les problèmes bidimensionnel instationnaire et tridimensionnel stationnaire nous rappelons brièvement les résultats fondamentaux relatifs au cas bidimensionnel stationnaire.

2.1. Cas bidimensionnel stationnaire

En mode direct la vitesse extérieure $u_e(x)$ est imposée, les inconnues du système d'équations (1a) sont donc les suivantes, au nombre de 5 : $C_{\varepsilon s}$, C_f , δ_1 , θ , S . Les relations supplémentaires de fermeture ont été obtenues à partir de solutions de similitude /8/. En-dehors des zones avec écoulement de retour elles peuvent s'écrire sous la forme suivante :

$$\text{(2)} \qquad \begin{aligned} &\delta_1/\delta = \gamma\, F_1(G) \qquad ; \gamma = \sqrt{C_f/2} \\ &1/\gamma = \frac{1}{\chi} \ln \frac{u_e \delta_1}{\nu} + D^*(G) \\ &C_{\varepsilon s} = \gamma\, P(G) \end{aligned}$$

F_1 , P et D^* sont des fonctions du paramètre de Clauser G lui-même relié au paramètre de forme H par :

$$G = \frac{H-1}{H\gamma}$$

	2 D STATIONNAIRE	2 D INSTATIONNAIRE	3 D STATIONNAIRE
EQUATIONS DE BASE	1a $\frac{d\delta}{dx} - \frac{v_e}{u_e} = \frac{1}{u_e}\frac{d}{dx}u_e$ *) $\frac{C_f}{2} = \frac{d\theta}{dx} + \theta\frac{H+2}{u_e}\frac{du_e}{dx}$	1b $\frac{\partial\delta}{\partial x} - \frac{v_e}{u_e} = \frac{1}{u_e}\frac{\partial}{\partial x}u_e(\delta-\delta_1)$ $\frac{C_f}{2} = \frac{\partial\theta}{\partial x} + \theta\frac{H+2}{u_e}\frac{\partial u_e}{\partial x} + \frac{1}{u_e^2}\frac{\partial}{\partial t}(u_e\delta_1)$	1c $\frac{\partial\delta}{\partial\Delta} - \frac{v_e}{u_e} = \frac{\partial}{\partial\Delta}(\delta-\delta_1) + (\delta-\delta_1)\left(\frac{1}{u_e}\frac{\partial u_e}{\partial\Delta} - K_1\right) - \frac{\partial\delta_2}{\partial n} - \delta_2\left(\frac{1}{u_e}\frac{\partial u_e}{\partial n} - K_2\right)$ $\frac{C_{f\Delta}}{2} = \frac{\partial\theta_{11}}{\partial\Delta} + \theta_{11}\left(\frac{H+2}{u_e}\frac{\partial u_e}{\partial\Delta} - K_1\right) + \frac{\partial\theta_{12}}{\partial n} + \theta_{12}\left(\frac{2}{u_e}\frac{\partial u_e}{\partial n} - 2K_2\right) + \delta_2\left(\frac{1}{u_e}\frac{\partial u_e}{\partial n} - K_2\right) + K_1\theta_{22}$ $\frac{C_{fn}}{2} = \frac{\partial\theta_{21}}{\partial\Delta} + \theta_{21}\left(\frac{2}{u_e}\frac{\partial u_e}{\partial\Delta} - 2K_1\right) + K_2\theta_{11}(H+1) + \frac{\partial\theta_{22}}{\partial n} + \theta_{21}\left(\frac{2}{u_e}\frac{\partial u_e}{\partial n} - K_2\right)$
ENTRAINEMENT	$\frac{\partial\delta}{\partial x} - \frac{v_e}{u_e} = C_{EQ}$	$\frac{\partial\delta}{\partial x} - \frac{v_e}{u_e} = C_{EQ} - \frac{1}{u_e}\frac{\partial\delta}{\partial t}$	$\frac{\partial\delta}{\partial\Delta} - \frac{v_e}{u_e} = C_{EQ}$
FERMETURE SIMPLIFIEE	3 $H^* = \frac{\alpha H^2 + H}{H-1}$; $\alpha = .631$	$H^* = \frac{\alpha H^2 + H}{H-1}$; $\alpha = .631$	$H^* = \frac{\alpha H^2 + 1}{H-1}$ + profil polaire de la forme $\frac{w}{u_e} = C\left(1 - \frac{u}{u_e}\right)$
SYSTEME DONNEE : u_e INCONNUES : δ_1, θ, C	4a $(H^* - HH^{*\prime})\frac{d\theta}{dx} + H^{*\prime}\frac{d\delta_1}{dx} = A_1$ $\frac{d\theta}{dx} = A_2$ $H^{*\prime} = \frac{dH^*}{dH}$ $A_1 = C_{EQ} - \frac{\delta-\delta_1}{u_e}\frac{du_e}{dx}$ $A_2 = \frac{C_f}{2} - \theta\frac{H+2}{u_e}\frac{du_e}{dx}$	4b $H^{*\prime}\frac{\partial\delta_2}{\partial x} + \frac{1+H^{*\prime}}{u_e}\frac{\partial\delta_2}{\partial t} + (H^* - HH^{*\prime})\frac{\partial\theta}{\partial x} + \frac{H^* - HH^{*\prime}}{u_e}\frac{\partial\theta}{\partial t} = A_1$ $\frac{1}{u_e}\frac{\partial\delta_1}{\partial t} + \frac{\partial\theta}{\partial x} = A_2$ $A_1 = C_{EQ} - \frac{\delta-\delta_1}{u_e}\frac{\partial u_e}{\partial x}$ $A_2 = \frac{C_f}{2} - \theta\frac{H+2}{u_e}\frac{\partial u_e}{\partial x} - \frac{\delta_1}{u_e^2}\frac{\partial u_e}{\partial t}$	4c $(H^* - HH^{*\prime})\frac{\partial\theta_{11}}{\partial\Delta} + H^{*\prime}\frac{\partial\delta_2}{\partial\Delta} + C\frac{\partial\delta_2}{\partial n} + \delta_2\frac{\partial C}{\partial n} = A_1$ $\frac{\partial\theta_{11}}{\partial\Delta} - C\frac{\partial\theta_{11}}{\partial n} + C\frac{\partial\delta_2}{\partial n} + (\delta_2 - \theta_{11})\frac{\partial C}{\partial n} = A_2$ $-C\frac{\partial\theta_{11}}{\partial\Delta} + C^2\frac{\partial\theta_{11}}{\partial n} - C^2\frac{\partial\delta_2}{\partial n} - \theta_{11}\frac{\partial C}{\partial\Delta} - 2C(\delta_2 - \theta_{11})\frac{\partial C}{\partial n} = A_3$ $A_1 = C_{EQ} - (\delta-\delta_1)\left(\frac{1}{u_e}\frac{\partial u_e}{\partial\Delta} - K_1\right)$ $A_2 = \frac{C_{f\Delta}}{2} - \theta_{11}\left(\frac{H+2}{u_e}\frac{\partial u_e}{\partial\Delta} - K_1\right) - K_1\theta_{22}$ $A_3 = \frac{C_{fn}}{2} - \theta_{21}\left(\frac{2}{u_e}\frac{\partial u_e}{\partial\Delta} - 2K_1\right) - K_2\theta_{11}(H+1) - \frac{\theta_{22}}{u_e}\frac{\partial u_e}{\partial n}$
EQUATION Caractéristique	Déterminant $\Delta = -H^{*\prime}$	6b $\lambda^2(H^* - HH^{*\prime}) + \lambda\left(1 - H^2 + H^{*\prime}(1+H)\right) - H^{*\prime} = 0$; $\lambda = \frac{dx}{u_e dt}$	6c $(H-1)C^3\lambda^3 - C^2\lambda^2\left[(H-1)(H^* - HH^{*\prime} + H^{*\prime} - 1) + 1\right] + C\lambda\left[H^* - 2HH^{*\prime} + 2H^{*\prime} - 1\right] + H^{*\prime} = 0$; $\lambda = \frac{dn}{d\Delta}$
RACINES	Singularité pour $H^{*\prime} = 0$ Point $C_f = 0$ Singulier	7b $\lambda_1 = \left[1 + (H-1)\sqrt{\alpha/(1+\alpha)}\right]/H$ $\lambda_2 = \left[1 - (H-1)\sqrt{\alpha/(1+\alpha)}\right]/H$ SYSTEME HYPERBOLIQUE $0 < \lambda_1 < 1$ $\lambda_2 > 0$ si $H < H_c$; $\lambda_2 < 0$ si $H > H_c \simeq 2,6$	7c $\lambda_1 = \frac{1 - \beta H}{C(H-1)}$ ⟶ LIGNE DE COURANT PARIETALE $\lambda_2 = \frac{1}{C(H-1)}$ $\beta = -\alpha + \sqrt{\alpha^2 + \alpha} = 0,382$ $\lambda_3 = \frac{(2\alpha+\beta)H + 1}{C(H-1)}$ SYSTEME HYPERBOLIQUE
FORME QUASI-CONSERVATIVE DES EQUATIONS		8b $\frac{\partial}{\partial x}u_e(\delta-\delta_1) + \frac{\partial\delta}{\partial t} = u_e C_{EQ}$ $\frac{\partial}{\partial x}u_e^2\theta + \frac{\partial u_e\delta_1}{\partial t} = u_e^2\frac{C_f}{2} - \delta_1 u_e\frac{\partial u_e}{\partial x}$	8c $\frac{\partial(\delta-\delta_1)}{\partial\Delta} - \frac{\partial\delta_2}{\partial n} = C_{EQ} - (\delta-\delta_1)\left(\frac{1}{u_e}\frac{\partial u_e}{\partial\Delta} - K_1\right)$ $\frac{\partial\theta_{11}}{\partial\Delta} + \frac{\partial\theta_{12}}{\partial n} = \frac{C_{f\Delta}}{2} - \theta_{11}\left(\frac{H+2}{u_e}\frac{\partial u_e}{\partial\Delta} - K_1\right) - K_1\theta_{11}$ $\frac{\partial\theta_{21}}{\partial\Delta} + \frac{\partial\theta_{22}}{\partial n} = \frac{C_{fn}}{2} - \theta_{21}\left(\frac{2}{u_e}\frac{\partial u_e}{\partial\Delta} - 2K_1\right) - K_2\theta_{11}(H+2) - \frac{\theta_{22}}{u_e}\frac{\partial u_e}{\partial n}$

L'analyse des solutions de similitude a permis de préciser numériquement les fonctions F_1, P et D^* et nous avons retenu les représentations analytiques suivantes :

$$F_1 = 0{,}613\,G - (36 + 76{,}86\,(1/G - 0{,}154)^2)/G$$
$$P = 0{,}074\,G - 1{,}0357/G$$
$$D^* = 2\,G - 4{,}25\sqrt{G} + 2{,}12$$

Les relations de fermeture (2) ne se prêtent pas à une étude analytique du système (1a) aussi devons nous les simplifier en introduisant une relation entre les paramètres $H^* = (\delta - \delta_1)\,\theta$ et H. D'après la définition de F_1 et G, on a :

$$\frac{\delta - \delta_1}{\theta} = H\left(\frac{G}{F_1}\frac{H}{H-1} - 1\right)$$

Lorsque G tend vers l'infini, ce qui est la cas au décollement, G/F_1 tend vers la valeur finie : 1,631 et l'on obtient :

$$H^* = \frac{\alpha H^2 + H}{H-1} \qquad \text{avec} \qquad \alpha = 0{,}631 \tag{3}$$

Cette formule reste en assez bon accord avec les solutions de similitude même loin du décollement, comme le montre la figure 1, pourvu que l'on considère des écoulements retardés ; la relation $H^*(H)$ ne dépend alors que très faiblement du nombre de Reynolds. De plus, lorsqu'il existe de faibles écoulements de retour cette relation reste en bon accord avec celles proposées par LE BALLEUR /9/ jusqu'à des valeurs du paramètre de forme voisines de 10.

Compte-tenu de la relation (3) le système (1a) se met sous la forme (4a). $u_e(x)$ étant donné, les inconnues principales sont θ et δ_1. Il est clair que le déterminant (5a) s'annule pour $H^{*\prime} = 0$. En général $d\delta_1/dx$ est alors infini. Cette singularité ne peut être évitée que si le système est indéterminé en ce point, ce qui se produit si l'on a :

$$\left(C_{f3} - \frac{\delta - \delta_1}{u_e}\frac{du_e}{dx}\right)\Big/ H^* = \frac{C_f}{2} - \theta\,\frac{H+2}{u_e}\frac{du_e}{dx} \tag{5}$$

En mode direct cette éventualité est très peu probable et l'on a donc au point $H^{*\prime} = 0$ une singularité. La relation (3) montre que ceci correspond à une valeur critique de paramètre de forme voisine de 2,6. De plus, la loi de frottement utilisée indique que cette valeur est très proche de celle qui annule le coefficient de frottement pariétal. Il suffirait d'ajuster très légèrement les relations de fermeture pour faire coïncider les deux valeurs. On retrouve donc bien avec la méthode intégrale l'équivalent de la singularité de Goldstein pour les équations locales /6/.

2.2. Cas bidimensionnel instationnaire

Considérons maintenant le système (1b) de la planche 1.

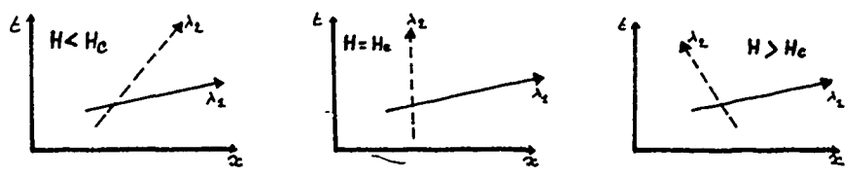
L'étude des solutions de similitude à nombre de Reynolds infini a montré que les relations de fermeture établies en stationnaire restaient valables /10/. Seul le coefficient d'entrainement est modifié par l'adjonction de la quantité $-\frac{\delta}{u_e}\frac{\partial \delta}{\partial t}$. En particulier la relation (3) reste valable, ce qui permet d'écrire les équations (1b) sous la forme (4b) qui est un système aux dérivées partielles du premier ordre en δ_1 et θ. La nature de ce système s'étudie à partir de son équation caractéristique (6b) où λ représente une direction caractéristique réduite :

$$\lambda = \frac{dx}{u_e\,dt}$$

Compte-tenu de la relation (3), les deux racines de l'équation caractéristique se calculent explicitement (7b) et l'on aboutit aux conclusions suivantes pour le domaine $H > 1$:

- Les deux racines sont réelles et distinctes, le système est hyperbolique,
- la première racine est toujours comprise entre 0 et 1,
- la seconde est positive pour $H < H_c \simeq 2{,}6$. Elle est négative pour $H > H_c$.

On constate donc que le point $H = H_c$, correspondant à $C_f = 0$, n'est pas en général un point singulier. Le changement de signe de la pente de la seconde caractéristique traduit simplement une influence de l'aval sur l'amont lorsque H devient supérieur à H_c, ce qui correspond à l'existence d'écoulement de retour. On doit alors imposer une condition limite à l'aval pour conserver un problème bien posé.



Bien que le point $H = H_c$ ne soit pas en général un point singulier, le fait que le système d'équations puisse se mettre sous la forme quasi-conservative (8b) permet de penser qu'il peut exister des solutions faibles discontinues.

Pour le montrer, supposons que σ soit la pente par rapport à l'axe x d'une telle ligne discontinue. Les indices a et b désignant les quantités de part et d'autre de cette ligne et le second membre de (8b) restant borné au travers de la discontinuité, les relations de conservation s'écrivent :

$$\left[u_e H^* \theta \sin\sigma - (H + H^*)\,\theta \cos\sigma\right]_a = \left[u_e H^* \theta \sin\sigma - (H + H^*)\,\theta \cos\sigma\right]_b$$
$$\left[u_e^2 \theta \sin\sigma - u_e H \theta \cos\sigma\right]_a = \left[u_e^2 \theta \sin\sigma - u_e H \theta \cos\sigma\right]_b$$

d'où en divisant membre à membre :

$$\left[\frac{u_e H^* \sin\sigma - (H + H^*)\cos\sigma}{u_e \sin\sigma - H \cos\sigma}\right]_a = \left[\frac{u_e H^* \sin\sigma - (H + H^*)\cos\sigma}{u_e \sin\sigma - H \cos\sigma}\right]_b$$

En adoptant la relation (3) pour exprimer H^*, l'équation ci-dessus est du second degré en H. Puisqu'elle admet une première racine évidente $H_b = H_a$, elle en admet une seconde non identique et l'on a bien une solution discontinue.

Pour illustrer notre propos, considérons l'exemple de calcul proposé par NASH et PATEL /11/. A l'instant $t=0$ la vitesse extérieure est constante et nous avons donc des conditions initiales de plaque plane. Pour $t>0$ la vitesse évolue comme indiqué sur la figure 2. Pour traiter un tel calcul, il est important d'utiliser une méthode numérique capable de prendre en compte l'existence de discontinuités. Pour cela un schéma de type prédicteur-correcteur (Mac-Cormack) a été utilisé et a donné des résultats identiques à ceux obtenus par une méthode de caractéristiques /10/. A l'instant $t = 0,03$ aucune singularité n'apparaît au point $H = H_c$. En ce point la tangente à la ligne λ_2 est simplement parallèle à l'axe des temps. Pour des temps supérieurs les lignes caractéristiques convergent et forment finalement une ligne de discontinuité sans signification physique à la traversée de laquelle l'épaisseur de déplacement a une dérivée infinie. Il ne faudrait cependant pas en déduire que les hypothèses de couche limite ne sont plus valables. En effet, une situation analogue se produit en stationnaire à l'approche du point $H=H_c$ où la dérivée de δ_1 augmente fortement jusqu'à devenir infinie. Or il est dans ce cas bien établi qu'il s'agit d'un problème lié à l'utilisation d'une méthode directe et que cette difficulté disparaît si l'on utilise un calcul inverse /5,6/.

2.3. Cas tridimensionnel stationnaire

2.3.1. Equations

La méthode intégrale proposée utilise les équations globales de quantité de mouvement et de continuité (1c) /12/. Pour faciliter les développements analytiques, ces équations sont écrites dans un système d'axes orthogonaux liés aux lignes de courant extérieures, l'axe des x étant confondu avec la direction de la vitesse. Dans les équations (1c) K_1 et K_2 sont les courbures géodésiques des lignes de courant extérieures et de leurs orthogonales. Elles sont reliées aux coefficients métriques par les relations :

$$K_1 = -\frac{1}{h_1 h_2}\frac{\partial h_2}{\partial x} \qquad K_2 = -\frac{1}{h_1 h_2}\frac{\partial h_1}{\partial z}$$

Pour un écoulement isoénergétique et sans choc, donc en particulier en incompressible, on a :

$$\vec{rot}\ \vec{V_e} \wedge \vec{V_e} = 0$$

Le vecteur tourbillon est soit nul, soit parallèle à $\vec{V_e}$ et donc sa composante suivant y est nulle ce qui entraîne :

$$-\frac{1}{h_1 h_2}\frac{\partial}{\partial z} h_1 u_e = 0$$

d'où :

$$K_2 = \frac{1}{u_e}\frac{\partial u_e}{\partial n}$$

Le champ de vitesse extérieur étant donné, le système (1c) contient 10 inconnues :

- Les épaisseurs : δ, δ_1, δ_2, θ_{11}, θ_{21}, θ_{12}, θ_{22}
- le frottement pariétal en module et direction : C_{f_1}, C_{f_n}
- le coefficient d'entrainement : $C_{e_1} = \frac{\partial \delta}{\partial x} - \frac{v_e}{u_e}$

On ne dispose que d'une relation déduite de la définition de δ_2, θ_{21} et θ_{12} :

$$\theta_{12} + \delta_2 = \theta_{21}$$

Les relations de fermeture supplémentaires ont été obtenues à partir de solutions de similitude /12/ comme dans le cas bidimensionnel. Elles dépendent des trois paramètres suivants :

$$G\ ,\ R_{\theta_{11}} \quad \text{et} \quad T = -\frac{\delta_2/\delta}{K_2\,\delta}$$

Les relations entre les grandeurs longitudinales de la couche limite sont identiques à celles du cas bidimensionnel, et l'on peut donc encore utiliser la formule (3) reliant $H^* = (\delta - \delta_1)/\theta_{11}$ à H.

Des relations simplifiées entre les épaisseurs transversales s'obtiennent en faisant l'hypothèse que dans le plan de l'hodographe le profil $w(u)$ est linéaire dans la région extérieure de la couche limite. En posant $\frac{w}{u_e} = C\left(1-\frac{u}{u_e}\right)$ on a :

$$(9) \qquad \frac{\delta_2}{\theta_{11}} = -CH \quad ; \quad \frac{\theta_{12}}{\theta_{11}} = C(H-1) \quad ; \quad \frac{\theta_{21}}{\theta_{11}} = -C \quad ; \quad \frac{\theta_{22}}{\theta_{11}} = -C^2(H-1)$$

L'hypothèse de linéarité tombe bien sûr en défaut près de la paroi à cause de la condition de non glissement. La région concernée est cependant trop mince pour que l'erreur introduite soit sensible, même si le maximum de w correspond à des valeurs de w/u_e de l'ordre de 0,5 à 0,6.

2.3.2. Nature du système

L'introduction des relations de fermeture simplifiées (3) et (9) ne laisse subsister que trois inconnues principales dans le système des équations globales (1c). En retenant les quantités δ_1, θ_{11} et C on obtient le système (4c) dont la nature est étudiée comme dans le cas précédent à partir de son équation caractéristique (6c). La relation (3) permet encore d'obtenir une forme explicite pour les racines de l'équation caractéristique.

On observe que les racines sont réelles et distinctes, le système est donc hyperbolique et l'on retrouve ainsi qualitativement un résultat déjà obtenu par MYRING /13/ qui a développé une analyse analogue à partir de relations de fermeture légèrement différentes.

Avant de préciser la disposition relative des trois directions caractéristiques, nous allons montrer que la ligne λ_1 peut être identifiée avec la ligne de courant pariétale. Pour cela nous devons préciser l'angle β_0 que fait cette ligne avec la vitesse extérieure. Parmi les relations déduites des solutions de similitude, considérons celle qui permet de calculer β_0 /12/. Pour des valeurs du paramètre de Clauser G suffisamment grandes cette relation se simplifie et s'écrit :

$$(10) \qquad \operatorname{tg}\beta_0 = \frac{C(H-1)}{1-\gamma H}$$

où γ est un coefficient pour lequel la valeur 0,438 a été retenue /12/.

La ligne caractéristique λ_1 et la ligne de courant pariétale doivent faire le même angle avec la direction de la vitesse extérieure pour être confondues, ce qui entraîne :

$$\operatorname{tg}\beta_0 = 1/\lambda_1$$

Comme $1/\lambda_1 = C(H-1)/(1-\beta H)$ pour que l'identification soit rigoureuse on devrait avoir $\beta = \gamma$. Il suffirait d'un léger ajustement de la loi de β_o proposée antérieurement ($\gamma = .382$ au lieu de $.438$) pour obtenir un accord rigoureux.

Les deux autres directions sont comprises entre la ligne de courant pariétale et la ligne de courant extérieure, ce qui intuitivement semble assez logique. En effet, il a été montré que le système des équations locales de la couche limite tridimensionnelle possède une infinité de directions caractéristiques qui sont les lignes de courant locales /14/. L'utilisation d'équations globales réduit le nombre de directions caractéristiques au nombre d'inconnues principales ; en introduisant des équations supplémentaires, comme par exemple pour les moments de quantité de mouvement, il serait possible d'augmenter le nombre des inconnues et donc celui des directions caractéristiques. Cependant, il semble que la mise en oeuvre de trois équations globales reflète déjà correctement les principaux traits de l'écoulement. En particulier, l'identification d'une famille de caractéristiques avec les lignes de courant pariétales est une bonne indication de la cohérence des relations de fermeture proposées.

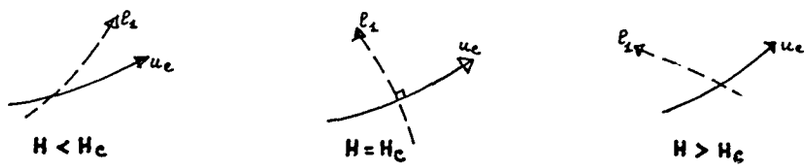
La mise en évidence de la nature hyperbolique du système d'équations globales a des conséquences pratiques importantes pour l'application de méthodes de calcul. En particulier il devient aisé de préciser exactement la nature des conditions aux limites à imposer aux frontières du domaine de calcul. On sait en effet que leur nombre doit être égal à celui des caractéristiques entrantes pour avoir un problème bien posé. Deux cas sont particulièrement simples à traiter ; il s'agit de ceux où les trois caractéristiques entrent ou sortent toutes suivant une portion de frontière. Dans le premier cas les trois épaisseurs δ_1, θ_{11} et δ_2 doivent être imposées, dans le second aucune condition n'est à préciser. Les cas intermédiaires sont à éviter dans la mesure du possible car leur traitement est beaucoup plus délicat.

La connaissance des directions caractéristiques est également importante au niveau de la discrétisation des équations. En effet, le schéma numérique doit respecter les domaines de dépendance et d'influence ce qui peut éventuellement nécessiter de décentrer les dérivées transversales ou entraîner des limitations des pas d'intégration dans le cas d'un schéma explicite.

2.3.3. Problème des singularités

L'étude des singularités se fait de la même façon qu'en bidimensionnel instationnaire et nous allons retrouver des résultats tout à fait analogues. En effet, le point $H^* = 0$ ($H = H_c$) n'a aucune raison, en général, d'être singulier puisqu'il existe toujours en ce point trois directions caractéristiques distinctes. On a simplement $\lambda_1 = 0$ ce qui signifie que la ligne de courant pariétale devient perpendiculaire à la ligne de courant extérieure.

Ceci traduit une influence de l'aval sur l'amont.



Les singularités en tridimensionnel n'apparaissent généralement pas de façon ponctuelle. On doit plutôt les rechercher, comme en instationnaire, dans des configurations pouvant conduire à une focalisation des lignes caractéristiques d'une même espèce ; en fait, ce sont les lignes de courant pariétales qui, en s'accumulant, définissent une ligne de singularité sans signification physique et qui ne doit pas être confondue avec une ligne de décollement.

Le fait que les équations globales puissent se mettre sous une forme quasi-conservative (8c) indique la possibilité de l'existence de solutions faibles avec des discontinuités. Voyons sur un exemple pratique de calcul comment une telle situation se présente. Pour cela, nous considérons une étude expérimentale réalisée au NLR reportée partiellement par LINDHOUT /15/. Il s'agit d'un raccord évolutif aile fuselage. Des mesures détaillées de la couche limite ainsi que de la vitesse extérieure ont été effectuées. Les données du calcul sont la distribution expérimentale de la vitesse extérieure en module et direction, ainsi que la couche limite sur une ligne de départ proche du bord d'attaque. Les relations de fermeture non simplifiées ont été utilisées pour effectuer le calcul afin d'améliorer la précision des résultats /16/.

La figure 3 représente le tracé des lignes de courant extérieures en traits continus et des lignes de courant pariétales calculées, en pointillés.

Le tracé des lignes de courant pariétales calculées est en bon accord avec les visualisations expérimentales, sauf près de la ligne de singularité. L'expérience indique bien la présence d'une ligne de décollement tridimensionnelle mais celle-ci n'est nullement singulière et il ne faut pas la confondre avec la ligne de singularité du calcul malgré la ressemblance de leurs configurations.

Nous avons vu dans le cas d'une couche limite instationnaire bidimensionnelle que la focalisation des lignes caractéristiques conduisait à la formation d'une ligne de discontinuité sans aucune signification physique. On peut penser qu'il en est de même en tridimensionnel et que l'accumulation des lignes de courant pariétales donne naissance à une telle discontinuité. Bien que nous ne disposions pas d'exemple numérique mettant en évidence une telle discontinuité, on peut montrer, à partir des équations globales, que cette éventualité est tout à fait plausible.

Pour cela considérons les équations intégrales écrites sous forme conservative (8c). En introduisant les relations de fermeture simplifiées (9) ce système s'écrit :

$$(11)\qquad \begin{aligned} &\frac{\partial \theta_{11}}{\partial \delta} + \frac{\partial}{\partial m}\left(C\,\theta_{11}(H-1)\right) = C_1 \\ &\frac{\partial}{\partial \delta}\left(-C\theta_{11}\right) + \frac{\partial}{\partial m}\left(-C^2\theta_{11}(H-1)\right) = C_2 \\ &\frac{\partial}{\partial \delta}\left(\theta_{11}H^*\right) + \frac{\partial}{\partial m}\left(C\,\theta_{11}H\right) = C_3 \end{aligned}$$

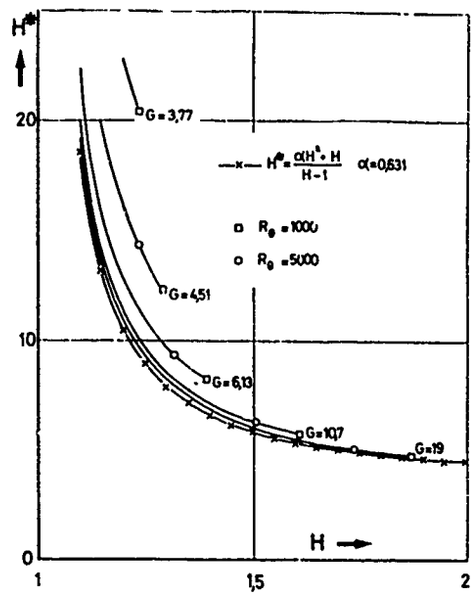


Fig. 1 : Relation H* (H)

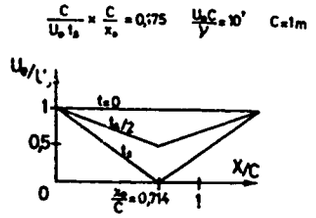
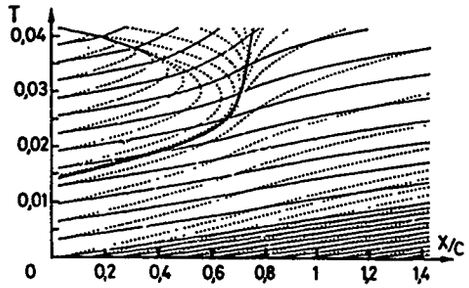


Fig. 2 : Exemple de calcul direct avec singularité d'une couche limite bidimensionnelle instationnaire. Trace des lignes caractéristiques /10/



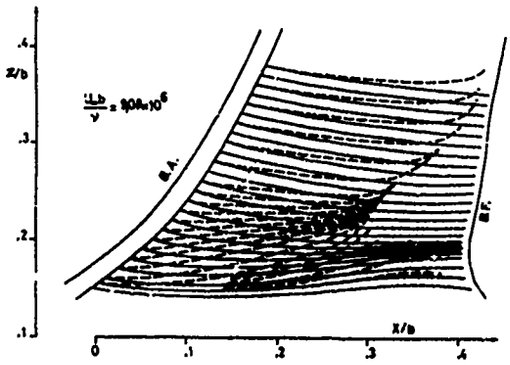


Fig. 3 : Exemple de calcul direct avec singularité d'une couche limite tridimensionnelle stationnaire. Trace des lignes de courant pariétales----et extérieures——

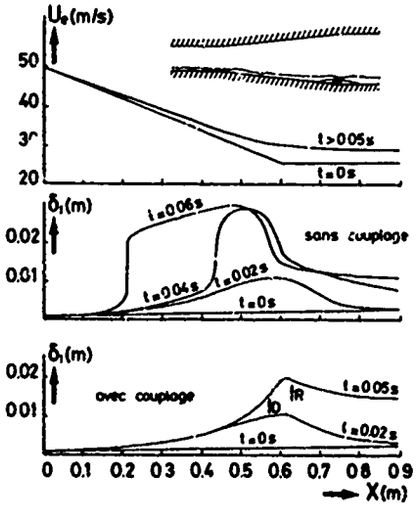


Fig. 4 : Exemple de couplage en mode direct /10/.

Soit σ l'angle que fait la ligne de discontinuité, si elle existe, avec la ligne de courant extérieure. Les équations (10) impliquent à la traversée de la discontinuité la conservation des grandeurs suivantes, les second membres restant bornés .

$$(12) \qquad [\theta_{11}\sin\sigma - C\theta_{11}(H-1)\cos\sigma]_a = [\theta_{11}\sin\sigma - C\theta_{11}(H-1)\cos\sigma]_b$$

$$(13) \qquad [C\theta_{11}\sin\sigma - C^2\theta_{11}(H-1)\cos\sigma]_a = [C\theta_{11}\sin\sigma - C^2\theta_{11}(H-1)\cos\sigma]_b$$

$$(14) \qquad [\theta_{11}H^*\sin\sigma - C\theta_{11}H\cos\sigma]_a = [\theta_{11}H^*\sin\sigma - C\theta_{11}H\cos\sigma]_b$$

Les indices a et b caractérisent les deux côtés de la discontinuité.

En divisant membre à membre les relations (12) et (13) puis (12) et (14), on obtient :

$$(15) \qquad C_a = C_b$$

$$(16) \qquad \left[\frac{H^*\sin\sigma - CH\cos\sigma}{\sin\sigma - C(H-1)\cos\sigma}\right]_a = \left[\frac{H^*\sin\sigma - CH\cos\sigma}{\sin\sigma - C(H-1)\cos\sigma}\right]_b$$

H_a, C_a et σ étant connus, l'équation (16) permet de calculer H_b, compte tenu de la relation (3) reliant H^* à H . Cette équation est du second degré en H et admet une première racine : $H_b = H_a$. Il existe donc une seconde racine distincte, d'où la possibilité d'une ligne de discontinuité. Si C est petit, l'équation (16) se réduit à $H_b^* = H_a^*$ ce qui montre clairement que la possibilité d'une discontinuité provient essentiellement du caractère non biunivoque de la relation $H^*(H)$.

2.4. Exemple de couplage en mode direct

Nous avons vu qu'une singularité existe au voisinage du point $C_f = 0$ dans les calculs de couches limites stationnaires bidimensionnelles. Aucune singularité n'existant a priori en ce point en instationnaire, on peut être tenté de calculer un décollement stationnaire comme la limite d'un état transitoire. Nous allons montrer sur un exemple numérique qu'il n'en est rien, car alors la condition de compatibilité (5) n'est pas vérifiée. Pour effectuer un tel calcul sans faire apparaître de singularité, on doit impérativement tenir compte du couplage avec le fluide parfait.

Considérons le cas schématique d'un diffuseur monodimensionnel /17/. Pour $t<0$, la vitesse extérieure est constante et la couche limite obéit à des lois de plaque plane. A $t=0$, la vitesse est modifiée impulsivement pour décroître linéairement comme indiqué sur la figure 4. Au cours du premier calcul, la vitesse u_e est conservée constante et l'on constate l'apparition d'une singularité dans l'évolution de δ_1 . De plus aucune solution stationnaire ne s'établit.

Dans le second calcul, un couplage très simple avec le fluide parfait est réalisé en s'imposant la conservation du débit par la formule :

$$\frac{\partial}{\partial t}\left(S - 2\delta_1\right) + \frac{\partial}{\partial x}\, u_e(S - 2\delta_1) = 0$$

où $S(x)$ représente la hauteur d'une section du diffuseur. A l'instant initial $S(x)$ est déterminée pour que la distribution de u_e déduite de $u_e(S-2\delta_1)=cste$ soit en accord avec celle du calcul précédent. Grâce à ce couplage très simple, il est possible d'obtenir une solution stationnaire continue incluant un bulbe de décollement. Dans ce cas, nous avons vérifié que la relation de compatibilité (5) était effectivement vérifiée au point $H = H_c$.

3. ETUDE DU MODE INVERSE

L'existence de singularités dans les équations de couche limite est essentiellement liée au fait qu'en méthode directe on s'impose la distribution de la vitesse extérieure. Pour éviter ces difficultés, l'un des remèdes possibles est de travailler en mode inverse. Il a en outre été montré que dans le cas bidimensionnel stationnaire ceci faciliterait la mise en oeuvre des méthodes de couplage /5,6/.

De plus, le recours au mode inverse permet de conserver un problème bien posé même si la frontière du domaine de calcul comporte des zones avec des écoulements de retour. Ceci autorise la comparaison à l'expérience des calculs de couches limites incluant des régions avec des vitesses négatives.

3.1. Cas bidimensionnel instationnaire

Une grande variété de méthodes inverses peut être envisagée suivant le choix des données que l'on s'impose ou la formulation du problème couplé que l'on considère. Le type de méthode de couplage est étroitement dépendant du modèle utilisé pour raccorder l'écoulement de couche limite à celui du fluide non visqueux. Ce raccord se fait généralement en imposant une direction commune aux deux écoulements sur une surface située dans la couche limite à une distance y_j de la paroi.

Nous examinerons deux cas uniquement : celui du prolongement jusqu'à la paroi ($y_j = 0$) et celui faisant intervenir une surface de déplacement ($y_j = \delta_1(x)$) .

Dans les deux cas la condition de couplage résulte de l'intégration selon y_j des équations de continuité appliquées aux fluides visqueux et non visqueux, ainsi que de l'adhérence du fluide visqueux à la paroi. L'équation de continuité ne comportant aucun terme instationnaire en écoulement incompressible, on peut appliquer directement les résultats stationnaires /18/. En posant α_{y_j} l'angle d'inclinaison du vecteur vitesse par rapport à la paroi dans le fluide parfait à l'altitude y_j , suivant que le couplage est effectué en $y_j = \delta_1$ ou en $y_j = 0$, on a :

$$(17) \qquad \alpha_{y_j=\delta_1} = \frac{\partial \delta_1}{\partial x}$$

$$(18) \qquad \alpha_{y_j=0} = \frac{\partial \delta_1}{\partial x} + \frac{\delta_1}{u_e}\frac{\partial u_e}{\partial x}$$

Pour l'étude qui va suivre nous supposerons que α_{y_j} est une donnée externe pour la couche limite.

3.1.1. Couplage en $y=\delta_1$ - Comparaison à l'expérience

Cette méthode revient à imposer la distribution de l'épaisseur de déplacement δ_1 . Elle est directement applicable pour comparer des modèles de calcul des couches limites à des résultats expérimentaux, la distribution de δ_1 étant alors fournie par les mesures.

La relation (3) liant H^* à H est toujours supposée valable et le système d'équation (1b) se met sous la forme :

$$(19)\qquad \begin{aligned} (H^*-H^{*\prime}H)\frac{\partial\theta}{\partial x}+\frac{H^*-H^{*\prime}H}{u_e}\frac{\partial\theta}{\partial t}+\frac{H^*\theta}{u_e}\frac{\partial u_e}{\partial x} &= A\\ \frac{\partial\theta}{\partial x}+\frac{\theta(H+2)}{u_e}\frac{\partial u_e}{\partial x}+\frac{\delta_1}{u_e^2}\frac{\partial u_e}{\partial t} &= B \end{aligned}$$

avec :

$$A = C_{es}-H^{*\prime}\frac{\partial\delta_1}{\partial x}-\frac{H^{*\prime}+1}{u_e}\frac{\partial\delta_1}{\partial t}$$

$$B = \frac{C_f}{2}-\frac{1}{u_e}\frac{\partial\delta_1}{\partial t}$$

L'analyse de ce système aux dérivées partielles du premier ordre pour θ et u_e se fait encore par l'intermédiaire de son équation caractéristique :

$$(20)\qquad H(H^*-HH^{*\prime})\lambda^2-2(H^*-HH^{*\prime})(H+1)\lambda+(H^*-HH^{*\prime})(H+2)-H^*=0$$

où λ est une direction caractéristique réduite : $\lambda=\frac{dx}{u_e\,dt}$

L'équation 20 possède toujours deux racines réelles et distinctes dans le domaine $H>1$. Le système est donc hyperbolique. De plus, compte tenu de la relation (3), on montre que les deux racines sont toujours positives, même dans les régions avec écoulement de retour, ce qui est intéressant pour les calculs pratiques : quelque soit l'état de la couche limite dans le domaine considéré, les seules conditions aux limites à imposer sont, en plus des conditions initiales, les distributions de $\theta(x_0,t)$ et $u_e(x_0,t)$ le long de la frontière amont.

L'analyse du problème direct a montré que la condition d'apparition d'une singularité analogue à celle de GOLDSTEIN dans les évolutions stationnaires était équivalente à l'existence d'une racine nulle de l'équation caractéristique. Pour $H>1$ les racines sont strictement positives et aucune singularité ne peut exister en stationnaire dans le mode inverse.

Bien qu'il ne semble pas possible de démontrer l'impossibilité d'apparition de singularités en instationnaire, la faible variation des pentes des lignes caractéristiques rend peu probable le développement de solutions discontinues. On ne peut cependant pas exclure que par le jeu des conditions initiales et aux limites on puisse arriver à une telle situation.

Pour illustrer l'intérêt des méthodes inverses au niveau des applications pratiques, nous considérons une comparaison de calcul à un cas expérimental. Il s'agit d'une couche limite pulsée soumise à un gradient de pression moyen positif suffisamment intense pour induire près de la paroi des vitesses négatives /19,20/.

Pour effectuer le calcul, les relations de fermeture non simplifiées (2) sont utilisées dans le domaine où la vitesse reste positive. Lorsque celle-ci est négative, le paramètre de Clauser G n'est plus adapté pour représenter les profils de vitesse et la relation simplifiée $H^*(H)$ est alors utilisée. En remplaçant dans le coefficient d'entrainement G par son expression en fonction de H et $\sqrt{C_f/2}$, on obtient :

$$C_{es} = 0{,}074\,(H-1)/H$$

Cette loi prolonge celle utilisée dans les régions à vitesse toujours positive et est en assez bon accord avec celle proposée par LE BALLEUR /5,6/ pour des écoulements décollés, jusqu'à des valeurs du paramètre de forme voisines de 10.

Les conditions aux limites nécessaires au calcul sont fournies par l'expérience. Il s'agit de la distribution de $\delta_1(x,t)$ présentée figure 5, et des conditions initiales $u_e(x_0,t)$ et $\theta(x_0,t)$. Toutes ces grandeurs sont introduites sous forme d'analyses harmoniques limitées à la fréquence fondamentale. Les distributions calculées de la vitesse extérieure et du paramètre de forme (Fig. 6 et 7) recoupent assez bien les résultats expérimentaux, y compris pour les régions avec écoulement de retour ($x>435$ mm).

On doit remarquer qu'il n'a pas été possible de commencer le calcul à la station $x = 50$ mm car à cette abscisse les conditions expérimentales imposent une forte accélération à la vitesse extérieure et l'absence de sondages assez resserrés dans cette région ne permet pas une prédiction correcte de u_e .

On peut signaler qu'un calcul effectué en mode direct a donné des résultats tout à fait analogues jusqu'à la station $x = 435$ mm située juste en amont de la zone avec écoulement de retour. En revanche, il n'a pas été possible de poursuivre ce calcul en mode direct vers l'aval à cause de l'apparition de fortes instabilités numériques.

3.2.2. Couplage à la paroi

Le système à considérer comporte, en plus des deux équations globales de couche limite, l'équation de couplage (18) et s'écrit :

$$(21)\qquad \begin{aligned} (H^*-HH^{*\prime})\frac{\partial\theta}{\partial x}+\frac{(H^*-HH^{*\prime})}{u_e}\frac{\partial\theta}{\partial t}+H^{*\prime}\frac{\partial\delta_1}{\partial x}+\frac{1+H^{*\prime}}{u_e}\frac{\partial\delta_1}{\partial t}+\frac{H^*\theta}{u_e}\frac{\partial u_e}{\partial x} &= C_{es}\\ \frac{\partial\theta}{\partial x}+\frac{1}{u_e}\frac{\partial\delta_1}{\partial t}+\theta\frac{H+2}{u_e}\frac{\partial u_e}{\partial x}-\frac{\delta_1}{u_e^2}\frac{\partial u_e}{\partial t} &= \frac{C_f}{2}\\ \frac{\partial\delta_1}{\partial x}+\frac{\delta_1}{u_e}\frac{\partial u_e}{\partial x} &= \alpha_{y=0} \end{aligned}$$

La déviation $\alpha_{y=0}$ de la vitesse par rapport à la paroi est supposée connue et donnée par le calcul du fluide parfait. Les trois directions caractéristiques de ce système sont solutions de l'équation :

$$dt^2\left[dx\left((H^*-HH^{*\prime})(H+2)+H(1+H^{*\prime})\right)-u_e\,d\left((H^*-HH^{*\prime})(H+1)\right)\right]=0$$

Deux de ces directions, parallèles à l'axe des x , sont confondues.

A partir de la relation (3), la troisième direction se met sous la forme : $\lambda_3=(H+1)/2H$.

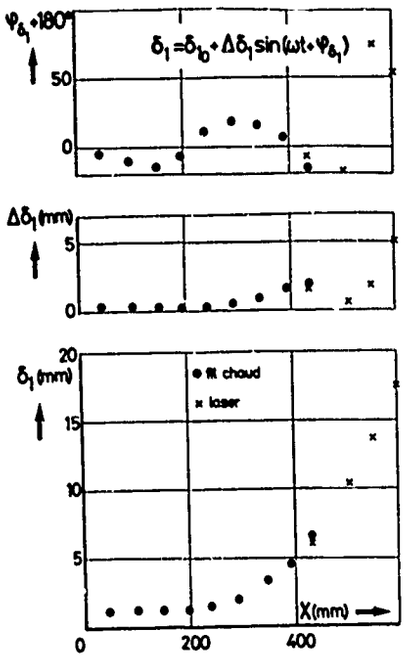


Fig. 5 : Données du calcul en mode inverse : évolution de δ_1 /19/.

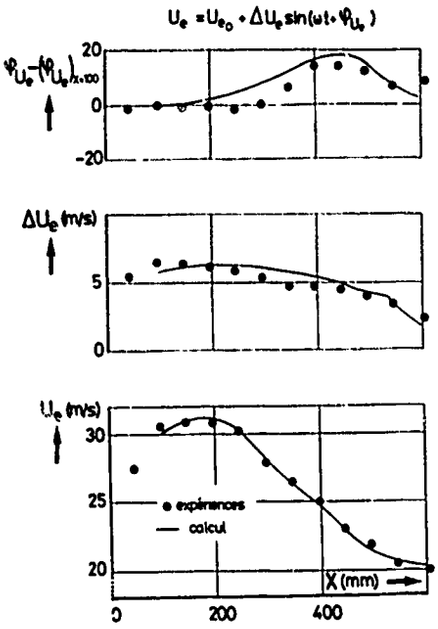


Fig. 6 : Comparaison calcul-expérience. Vitesse extérieure /19/.

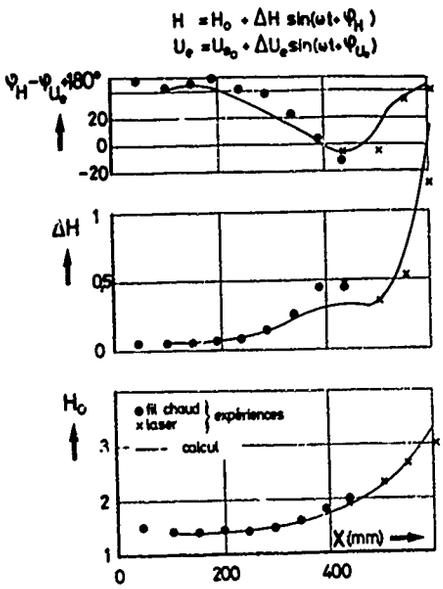


Fig. 7 : Comparaison calcul-expérience. Facteur de forme /19/.

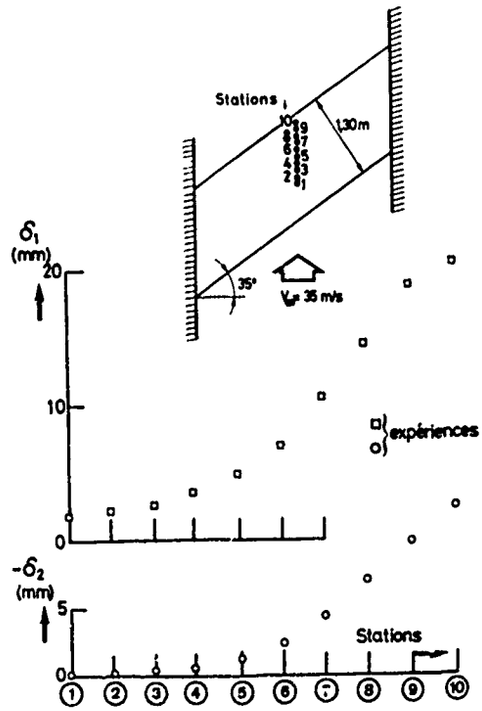


Fig. 8 : Application de la méthode inverse tridimensionnelle. Données du calcul /22/.

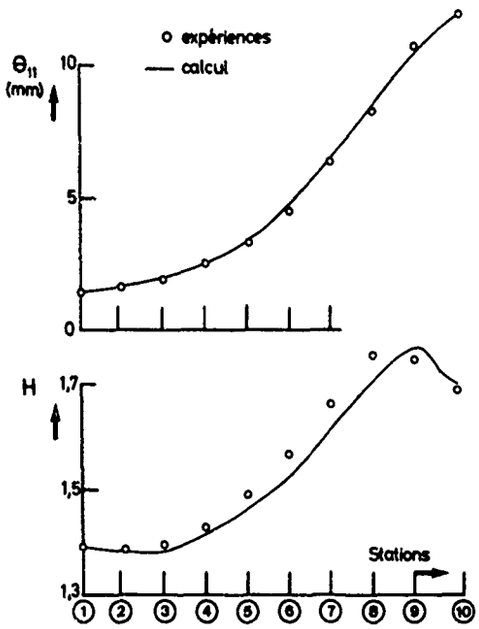


Fig. 9 : Application de la méthode inverse tridimensionnelle. Comparaison calcul-expérience /22/.

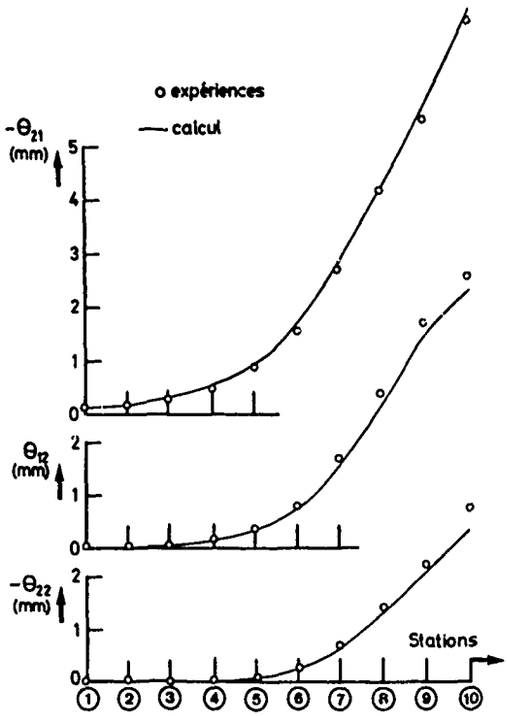


Fig. 10 : Application de la méthode inverse tridimensionnelle. Comparaison calcul-expérience.

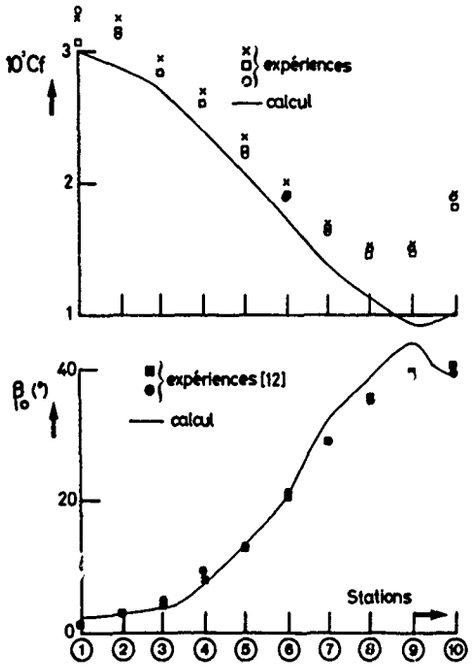


Fig. 11 : Application de la méthode inverse tridimensionnelle. Comparaison calcul-expérience /22/.

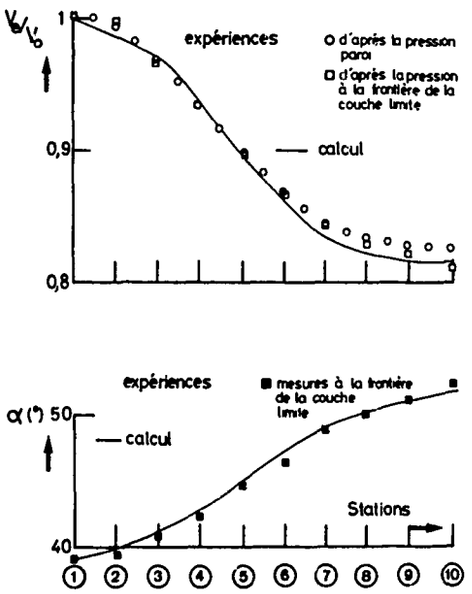


Fig. 12 : Application de la méthode inverse tridimensionnelle. Comparaison calcul-expérience /22/.

Cette racine étant toujours strictement positive, il n'existe pas d'influence possible de l'aval sur l'amont, à l'exception de celle contenue dans la donnée de la déviation à la paroi : $\alpha_{y=0}(x,t)$.

D'autre part aucune singularité n'existe en écoulement stationnaire, puisque celle-ci est liée à une racine nulle de l'équation caractéristique. On peut démontrer qu'il en est de même en instationnaire, bien que le système (21) puisse se mettre sous une forme quasi-conservative :

$$(22)\qquad \begin{aligned} &\frac{\partial}{\partial x} u_e \delta + \frac{\partial \delta}{\partial t} = u_e C_{\delta s} + u_e \alpha_{y=0} \\ &\frac{\partial}{\partial x}(\delta_1+\theta) u_e^2 + \frac{\partial}{\partial t} u_e \delta_1 = u_e^2 \frac{C_f}{2} + u_e^2 \alpha_{y=0} \\ &\frac{\partial}{\partial x} u_e \delta_1 = u_e \alpha_{y=0} \end{aligned}$$

Pour cela on admet qu'une ligne de discontinuité de pente $dx/V_o dt = \operatorname{cotg}\sigma$ existe. V_o est ici une vitesse arbitraire. Le second membre de (22) étant supposé borné et U et D caractérisant les grandeurs à l'amont et à l'aval de la discontinuité, les relations de conservation à la traversée de la ligne singulière s'écrivent :

$$(23)\qquad \left[u_e \delta \sin\sigma - \delta V_o \cos\sigma\right]_D = \left[u_e \delta \sin\sigma - \delta V_o \cos\sigma\right]_U$$

$$(24)\qquad \left[(\delta_1+\theta) u_e^2 \sin\sigma - \delta_1 u_e V_o \cos\sigma\right]_D = \left[(\delta_1+\theta) u_e^2 \sin\sigma - \delta_1 u_e V_o \cos\sigma\right]_U$$

$$(25)\qquad \left[\delta_1 u_e \sin\sigma\right]_D = \left[\delta_1 u_e \sin\sigma\right]_U$$

En divisant membre à membre respectivement les relations (23) et (24) par (25), on obtient :

$$(26)\qquad \left(\frac{\delta}{\delta_1}\right)_D \left[\sin\sigma - \frac{V_o}{u_e}\cos\sigma\right]_D = \left(\frac{\delta}{\delta_1}\right)_U \left[\sin\sigma - \frac{V_o}{u_e}\cos\sigma\right]_U$$

$$(27)\qquad \left[\left(1+\frac{1}{H}\right) u_e\right]_D = \left[\left(1+\frac{1}{H}\right) u_e\right]_U$$

d'où finalement :

$$(28)\qquad \left(\frac{\delta}{\delta_1}\right)_D \left(\sin\sigma - \frac{V_o \cos\sigma \left(\frac{H+1}{H}\right)_D}{\left[\left(1+\frac{1}{H}\right) u_e\right]_U}\right) = \left(\frac{\delta}{\delta_1}\right)_U \left[\sin\sigma - \frac{V_o}{u_e}\cos\sigma\right]_U$$

La relation (3) entraine :

$$\frac{\delta}{\delta_1} = \frac{(\alpha+1) H}{H-1}$$

et la relation (28) devient :

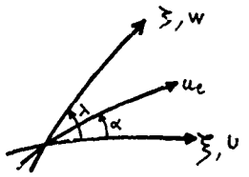
$$(29)\qquad \frac{H_D}{H_D-1}\left[\sin\sigma - \frac{V_o \cos\sigma \left(1+\frac{1}{H_D}\right)}{\left[\left(1+\frac{1}{H}\right) u_e\right]_U}\right] = \frac{H_U}{H_U-1}\left[\sin\sigma - \frac{V_o}{u_e}\cos\sigma\right]$$

C'est une équation pour H_D qui admet la solution unique $H_D = H_U$. Il ne peut donc exister de solution discontinue pour cette méthode, aussi bien en instationnaire que dans le cas cas stationnaire.

3.2. Cas tridimensionnel stationnaire

Nous ne nous intéresserons ici qu'aux méthodes de couplage analogues à celles étudiées dans le cas instationnaire, le raccord entre le fluide parfait et la couche limite se faisant par l'intermédiaire d'une déviation ε du vecteur vitesse par rapport à la paroi. Pour obtenir la relation définissant ε, on doit combiner l'équation globale de continuité écrite d'une part pour la couche limite et d'autre part pour le prolongement du fluide parfait jusqu'à la surface de raccordement.

Pour cela il est commode de considérer les équations dans un système d'axes quelconque liés à la paroi et de coordonnées ξ et ζ, l'axe y étant normal aux deux autres.



μ_1 et μ_2 sont les éléments métriques suivant ξ et ζ. Les hypothèses de couche limite permettent de prendre 1 comme élément métrique suivant y. Dans ce repère l'équation globale de continuité s'écrit :

$$(30)\qquad \frac{\partial}{\partial \xi}\left(\frac{q}{\mu_2}\rho U\right) + \frac{\partial}{\partial \zeta}\left(\frac{q}{\mu_1}\rho W\right) + q\frac{\partial}{\partial y}(\rho v) = 0$$

avec : $q = \mu_1 \mu_2 \sin\lambda$

Cette équation permet de prolonger l'écoulement de fluide parfait dans la couche limite à partir de $y=\delta$. Si les rayons de courbure de la paroi sont grands devant δ, on peut supposer que la masse volumique et la vitesse longitudinale de l'écoulement prolongé sont constantes et égales à leurs valeurs à l'extérieur, respectivement ρ_e et u_e. $\overline{v_y}$ étant la composante verticale de la vitesse de cet écoulement en y, un développement limité de $\overline{v}$ donne :

$$(31)\qquad \overline{v_y} = \overline{v_\delta} + (y-\delta)\left(\frac{\partial \overline{v}}{\partial y}\right)_{y=\delta}$$

L'équation (30) permet d'exprimer $\left(\frac{\partial \overline{v}}{\partial y}\right)_{y=\delta}$, d'où la nouvelle forme de (31) :

(32) $$\frac{\overline{v_y}}{u_e} = \frac{\overline{v_\zeta}}{u_e} - (y-\delta)\left[\frac{1}{\rho u_e q}\frac{\partial}{\partial \xi}\left(\frac{q \rho_e U_1}{\mu_1}\right) + \frac{1}{\rho u_e q}\frac{\partial}{\partial \zeta}\left(\frac{q \rho_e}{\mu_2}\ldots\right)\right]$$

U_1 et W_1 sont les composantes de U_e suivant ξ et ζ.

A la frontière δ, la vitesse $\overline{v_\zeta}$ est égale à celle donnée par l'équation globale de continuité écrite pour la couche limite :

(33) $$\frac{v_y}{u_e} = \frac{U_1}{u_e \mu_1}\frac{\partial \delta}{\partial \xi} + \frac{W_1}{u_e \mu_2}\frac{\partial \delta}{\partial \zeta} - \frac{1}{\rho u_e q}\left\{\frac{\partial}{\partial \xi}\left[\frac{\rho q}{\mu_1}\left(U_1 \delta - u_e \Delta_1\right)\right] + \frac{\partial}{\partial \zeta}\left[\frac{\rho q}{\mu_2}\left(W_1 \delta - u_e \Delta_2\right)\right]\right\}$$

La combinaison de (32) et (33) conduit à la relation cherchée. Il reste à préciser la surface sur laquelle s'effectue le couplage, c'est-à-dire y. Comme précédemment nous ne considérons que les deux cas les plus souvent utilisés :

1) $y = \delta^*$: épaisseur de déplacement
2) $y = o$: couplage à la paroi

Pour définir l'épaisseur de déplacement LIGHTHILL /21/ a proposé plusieurs interprétations aboutissant toutes à la même formulation qui, écrite dans un système d'axes quelconques, conduit à définir δ^* par l'équation suivante :

(34) $$\frac{\partial}{\partial \xi}\left[\frac{\rho q}{\mu_1}\left(\delta^* U_1 - \Delta_1 u_e\right)\right] + \frac{\partial}{\partial \zeta}\left[\frac{\rho q}{\mu_2}\left(\delta^* W_1 - \Delta_2 u_e\right)\right] = o$$

L'équation de couplage en $y = \delta^*$ est alors :

(35) $$\frac{\overline{v_{\delta^*}}}{u_e} = \frac{U_1}{u_e \mu_1}\frac{\partial \delta^*}{\partial \xi} + \frac{W_1}{u_e \mu_2}\frac{\partial \delta^*}{\partial \zeta}$$

Dans un repère lié aux lignes de courant extérieures, elle se simplifie pour devenir :

(36) $$\frac{\overline{v_{\delta^*}}}{u_e} = \frac{\partial \delta^*}{\beta_1 \partial x}$$

Remarquons que les épaisseurs Δ_1 et Δ_2 ne dépendent que de δ_1 et δ_2. La relation (34) fait donc intervenir ces deux quantités. On constate cependant que contrairement au cas bidimensionnel, le couplage en $y = \delta^*$ n'est pas équivalent à un calcul de couche limite pour lequel on se donne les épaisseurs δ_1 et δ_2.

Dans le cas du couplage à la paroi, il faut imposer la composante verticale de la vitesse. Compte tenu de la relation (33) qui donne $\overline{v_\zeta}$, $\overline{v}_{y=o}$ s'obtient à partir de la relation (32) écrite pour $y = o$:

(37) $$\frac{\overline{v}_{y=o}}{u_e} = \frac{1}{\rho u_e q}\left[\frac{\partial}{\partial \xi}\left(\frac{\rho_e u_e q \Delta_1}{\mu_1}\right) + \frac{\partial}{\partial \zeta}\left(\frac{\rho_e u_e q \Delta_2}{\mu_2}\right)\right]$$

Dans le système lié aux lignes de courant extérieures, cette relation devient :

(38) $$\frac{\overline{v}_{y=o}}{u_e} = \frac{1}{\rho_e u_e \beta_1 \beta_2}\left[\frac{\partial}{\partial \alpha}\rho_e u_e \beta_1 \delta_1 + \frac{\partial}{\partial \beta}\rho_e u_e \beta_1 \delta_2\right]$$

3.2.2. Méthode pratique de calcul - Comparaison à l'expérience

Sans négliger l'intérêt que représente la mise en oeuvre de méthodes couplées, le but de notre étude est d'abord de calculer des couches limites afin de vérifier la validité des modèles de fermeture dans des régions proches du décollement et au-delà. C'est pourquoi dans la méthode proposée, nous supposerons connues les distributions des épaisseurs δ_1 et $\delta_2(\alpha, \beta)$. Ceci facilite aussi grandement la mise en oeuvre pratique des calculs.

Les équations utilisées sont analogues à (1c) mais doivent être écrites dans un système d'axes quelconques non liés à la vitesse extérieure puisque celle-ci n'est pas connue. Les relations de fermeture non simplifiées déjà utilisées en mode direct et établies à partir de solutions de similitude restent valables, y compris dans des régions décollées pourvu que la vitesse longitudinale locale ne s'annule pas, ce qui est le cas pour certaines configurations tridimensionnelles. Le point $C_{f_\delta = o}$ définit pratiquement la limite de validité des relations de fermeture.

L'analyse du système ainsi obtenu peut être effectuée en suivant le même cheminement que pour le mode direct. Les distributions de δ_1 et δ_2 étant données, les inconnues principales sont θ_{11} et les deux composantes de la vitesse extérieure. On obtient ainsi une équation caractéristique du troisième degré. L'étude analytique n'ayant pu être menée à bien, nous ne donnerons aucune conclusion générale et nous nous limiterons à présenter un résultat pratique d'application.

L'étude expérimentale considérée concerne une aile en flèche infinie /22/. Les épaisseurs expérimentales δ_1 et $\delta_2(\alpha)$ sont utilisées comme données du calcul. On impose la nullité des dérivées suivant la direction parallèle au bord d'attaque uniquement au niveau des conditions aux limites.

Puisque la donnée des deux épaisseurs δ_1 et δ_2 ne suffit pas à caractériser une couche limite tridimensionnelle, on peut valablement juger des qualités de la méthode proposée en comparant aux valeurs expérimentales les évolutions calculées des autres paramètres. Les figures 9, 10 et 11 montrent un assez bon accord d'ensemble, même au voisinage de la ligne de décollement située entre les stations 8 et 9. Dans le cas considéré d'une aile en flèche infinie, la direction de la ligne de courant pariétale devient parallèle au bord d'attaque le long de la ligne de décollement ce qui correspond à $\alpha + \phi_o = 90°$, puisque α est l'angle entre la direction de la vitesse extérieure et la normale à la paroi. En mode direct il y a en ce point une singularité qui se traduit en particulier par une pente infinie pour ϕ_o. En mode inverse il n'en est rien et les lignes de courant pariétales tendent asymptotiquement vers la ligne de décollement.

La figure 12 montre l'évolution de la vitesse extérieure en module et direction par rapport à la normale au bord d'attaque. Le recoupement est assez satisfaisant, y compris après le décollement. De plus, on retrouve bien au niveau des résultats l'hypothèse d'aile en flèche infinie : la composante de la vitesse parallèle au bord d'attaque a une valeur sensiblement constante bien que cette condition ne soit pas imposée dans les équations mais uniquement pour les conditions aux limites.

4. CONCLUSIONS

L'existence de singularités dans les calculs en mode direct des couches limites bidimensionnelles instationnaires ou tridimensionnelles stationnaires peut être mise en évidence à partir de l'étude des propriétés des équations intégrales. Bien que ces équations ne soient pas équivalentes à celles de Prandtl, leur comportement tout à fait analogue au voisinage d'un décollement bidimensionnel stationnaire permet

d'accorder une certaine confiance quant à la généralité des conclusions obtenues. En particulier, on retrouve bien dans ce cas une singularité du type de celle de GOLDSTEIN.

Dans les cas bidimensionnel instationnaire ou tridimensionnel stationnaire le point $C_{f=0}$ n'est plus, en général, singulier mais indique simplement un changement d'orientation des domaines d'influence et de dépendance. La nature hyperbolique des systèmes d'équations permet de définir précisément ces domaines. On a montré que l'existence de solutions faibles pour ces équations pouvait conduire au développement de lignes de discontinuité correspondant à la focalisation des lignes caractéristiques d'une même espèce. Dans le cas tridimensionnel les lignes caractéristiques susceptibles de donner naissance à une discontinuité ne sont autre que les lignes de courant pariétales. Pour le montrer il a suffit d'ajuster légèrement un coefficient numérique dans les relations de fermeture. Malgré cette interprétation, la ligne de discontinuité ainsi formée n'a aucun sens physique et ne doit pas être confondue avec une ligne de décollement.

La présence de singularités en mode direct ne remet pas en cause les hypothèses de couche limite au voisinage du décollement car elle provient du fait que l'on s'impose la vitesse extérieure sans tenir compte des éventuelles relations de compatibilité, en particulier en écoulement stationnaire. Un moyen d'éviter de telles singularités est de faire appel à des méthodes inverses dans lesquelles la vitesse extérieure est l'une des inconnues du système. Ces méthodes facilitent la résolution des problèmes de couplage avec le fluide parfait. Dans le cas particulier du couplage à la paroi en bidimensionnel stationnaire, on a pu montrer l'impossibilité d'existence de solutions discontinues.

Ces méthodes sont également intéressantes du strict point de vue du calcul des couches limites. Elles permettent en particulier de vérifier des modèles de fermeture au voisinage du décollement et même au-delà. Pour cela, le plus simple est de s'imposer la distribution de l'épaisseur de déplacement en bidimensionnel ou des épaisseurs δ_1 et δ_2 en tridimensionnel. On conserve alors toujours un problème bien posé avec un calcul progressant de l'amont vers l'aval, l'influence de l'aval étant prise en compte par la distribution des épaisseurs que l'on s'impose. Les calculs ainsi effectués sont en bon accord avec les résultats expérimentaux, aussi bien en instationnaire qu'en tridimensionnel, ce qui justifie les relations de fermeture utilisées.

REFERENCES

/ 1 / TELIONIS D.P. — Unsteady boundary layer, separated and attached. AGARD CP n° 227 - Unsteady Aerodynamics - Ottawa, 26-28 sept. 1977.

/ 2 / CEBECI T., CARR L.W., BRADSHAW P. — Prediction of unsteady turbulent boundary layers with flow reversal. 2nd Symposium on turbulent shear flows, 2-4 Jan. 1979.

/ 3 / SHEN S.F., NENNI J.P. — Asymptotic solution of the unsteady two dimensional incompressible boundary layer and its implications on separation. Symposium on Unsteady Aerodynamics. R.B. Kinney Ed. Univ. Arizona, Tucson 1975, pp. 245-259.

/ 4 / LEGENDRE R. — Lignes de courant d'un écoulement permanent. Décollement et séparation. La Recherche Aérospatiale n° 1977-6.

/ 5 / LE BALLEUR J.C. — Couplage visqueux-non visqueux. Analyse du problème incluant décollements et ondes de choc. La Recherche Aérospatiale n° 1977-6.

/ 6 / LE BALLEUR J.C. — Couplage visqueux-non visqueux : méthode numérique et applications aux écoulements bidimensionnels transsoniques et supersoniques. La Recherche Aérospatiale n° 1978-2.

/ 7 / BRADSHAW P. — Singularities in unsteady boundary layers. AIAA Journal, Vol.17, n°7,pp.790-793.

/ 8 / MICHEL R., QUEMARD C., DURANT R. — Application d'un schéma de longueur de mélange à l'étude des couches limites turbulentes d'équilibre. Note Technique ONERA n° 154 (1969).

/ 9 / COUSTEIX J., LA BALLEUR J.C., HOUDEVILLE R. — Calcul des couches limites turbulentes instationnaires en mode direct ou inverse, écoulement de retour inclus. Analyse des singularités. La Recherche Aérospatiale n° 1980-3.

/ 10 / COUSTEIX J., HOUDEVILLE R. — Turbulent boundary layer calculations in unsteady flow. "Numerical method in Applied Fluid Dynamics". University of Reading, 4-5 Jan. 1978.

/ 11 / NASH J.F., PATEL V.C. — Calculations of unsteady turbulent boundary layers with flow reversal. NASA CR 2546-1974.

/ 12 / COUSTEIX J. — Analyse théorique et moyens de prévision de la couche limite turbulente tridimensionnelle. Publication ONERA n° 157 (1974). Traduction anglaise ESA TT-238.

/ 13 / MYRING D.F. — An integral prediction method for three-dimensional turbulent boundary layers in incompressible flow. RAE TR 70 147 (1970).

/ 14 / KRAUSE E. — Numerical treatment of boundary layer problems. AGARD Lecture Series n° 64 on Advances in Numerical Fluid Dynamics.

/ 15 / LINDHOUT J.P.F., MOEK G., DE BOER E., Van Den BERG B. — A method for the calculation of 3D boundary layers on practical wing configurations. The joint ASME-CSME Applied Mechanics, Fluids engineering and Bio-engineering. Niagara Falls, New-York (1979).

/ 16 / COUSTEIX J.
AUPOIX B.
Application of an integral prediction method to the test case of the Amsterdam Workshop on three-dimensional boundary layers calculations (1979).

/ 17 / COUSTEIX J.
HOUDEVILLE R.
DESOPPER A.
Résultats expérimentaux et méthodes de calcul relatifs aux couches limites turbulentes en instationnaire. AGARD Conférence on "Unsteady Aerodynamics", CP n° 227 (1977).

/ 18 / LE BALLEUR J.C.
Calculs couplés visqueux-non visqueux incluant décollements et ondes de choc en écoulement bidimensionnel. VKI/AGARD LS-94 on three-dimensional and Unsteady separation at high Reynolds numbers (1978). TP ONERA n° 1978-5.

/ 19 / HOUDEVILLE R.
COUSTEIX J.
Couches limites turbulentes en écoulement pulsé avec gradient de pression moyen défavorable. La Recherche Aérospatiale n° 1979-1.

/ 20 / COUSTEIX J.
HOUDEVILLE R.
RAYNAUD M.
Oscillating turbulent boundary layer with a strong mean pressure gradient. 2nd Symposium on turbulent shear flows, London 2-4 July 1979.

/ 21 / LIGHTHIL M.J.
On displacement thickness, J.F.M. n° 4, 1958.

/ 22 / Van Den Berg B.
ELSENAAR A.
Measurement in a three dimensional incompressible turbulent boundary layer in an adverse pressure gradient under infinite swept wing conditions. NLR TR 72 092 U (1972).

A PHENOMENOLOGICAL MODEL FOR DISPLACEMENT THICKNESS EFFECTS OF TRANSONIC SHOCK WAVE-BOUNDARY LAYER INTERACTIONS

Wen-Huei Jou, Senior Research Scientist
and
Earll M. Murman, Consultant
Flow Research Company
A Division of Flow Industries, Inc.
21414-68th Avenue South
Kent, Washington 98031
(206) 872-8500

SUMMARY

A simple algebraic model is developed to describe the shape of the viscous displacement thickness surface downstream of a weak "normal" shock wave ($M_1 < 1.3$) interacting with a turbulent boundary layer. Experimental and theoretical information is used to construct the shape of a "bump." The "bump" is then incorporated into inviscid transonic potential codes to model the strong interaction effects of the boundary layer in moving the shock wave forward and reducing its strength. Computed results compare favorably with two- and three-dimensional experiments.

I. INTRODUCTION

Inviscid potential flow calculations for transonic flows over airfoils and wings often predict the appearance of embedded shock waves which have subsonic downstream states. The predicted shock wave location is usually farther downstream and the shock is stronger than experimental measurements. This causes a significant error in predicting the surface pressures and forces. Physically, a turbulent boundary layer is present on the body surface and the resulting shock wave-boundary layer interaction is believed to be the main reason of the discrepancies.

To analyze the flow field under complete range of viscosity and compressibility parameters requires the use of the Navier-Stokes equation with proper turbulence modeling. At the present time, available computational facilities are not powerful enough for these computations to be used as practical engineering tools. However, for many design applications, the flow field around airfoils or wings can be well described by the potential flow with the viscous boundary layer confined to a thin region near the surface. In particular, for weak shocks with upstream Mach numbers less than about 1.3, the vorticity jump across the shock wave can be neglected and a potential flow is a suitable assumption. Also, for this range of Mach numbers the turbulent boundary layer near the shock foot is either attached or has only a small separation bubble behind the shock wave. This is the range of parameters considered in the present paper.

At the shock foot, simple consideration of the conservation of mass and momentum shows that the boundary layer displacement thickness and the momentum thickness increase across the shock wave. The amount of the increase depends on the strength of the shock and the boundary layer thickness ahead of the shock wave. This sudden jump in the boundary layer thickness violates the conventional boundary layer assumption and also fails to yield a consistent inviscid-viscous interaction in the sense of the conventional boundary layer theory.

In recent years several researchers have tried to analyze the flow field near the shock foot using matched asymptotic analysis.[1,2,3,4] Further results are being reported at this symposium. Both laminar and turbulent boundary layers have been considered with various assumptions made about the strength of the shock wave relative to the friction velocity. Once these flows are well understood, their outer limits should serve as boundary conditions for the outer inviscid computations. Due to the scale of the outer problem, the boundary condition is in the form of a source on the surface of the airfoil. The strength of the source depends on the shock strength and the boundary layer properties upstream of the shock wave. The existence of the source deflects the streamline and the shock wave becomes an oblique shock if the strength is below the critical value for maximum deflection. Indeed, if the strength of the source is beyond the critical value, a detached normal shock will create a new source at its new position and the shock location cannot be determined.

In typical numerical computations of the potential flow about bodies using a shock-capturing technique, the mesh spacing near the shock foot is of the order of magnitude of the interaction length. A suitable specification of the source distribution over the interaction region is desirable. Yet, the mesh is coarse enough that as long as the global properties of the interaction are properly determined, the inviscid solution should be insensitive, to some extent to the exact detail of the distribution of the source.

In many applications boundary layer methods are coupled to potential flow codes without any special considerations being made to treat the shock wave-boundary layer interaction.[5,6] It is generally reported that if the shock waves are smeared over several mesh points, the boundary layer equations may be integrated through the shock waves without difficulty. The boundary layer thickens and displaces the shock forward while weakening it. This method has little rational justification and probably will not be uniformly convergent as the mesh is refined near the shock.

A less justifiable approach which is often adopted is to use the incorrect nonconservative solution of the inviscid equations in place of the correct fully conservative methods. The nonconservative methods predict shock waves which are weaker and further forward than the conservative methods but generally are in better agreement with experiment. This effect, however, is due to an error in the numerical techniques[7] and is not a rational model for shock wave-boundary layer interaction.

The present work was motivated by the desire to develop a simple model for the strong interaction effects which the turbulent boundary layer has on the shock location and strength. A simple algebraic formula is developed for the above-mentioned source distribution. This "bump" is incorporated directly into the inviscid calculation in an iterative manner so that upon solution of the inviscid equations, the shock position and strength have already been modified to model the effects of the turbulent boundary layer. This provides a more rational model than the nonconservative method mentioned above but yet has its same advantages. It also may be used as a first step in a complete boundary layer-inviscid calculation, although generally this has not proven necessary. An early version of the method was reported by Murman[8] and recently used by Rizzetta and Yoshihara[9] for unsteady flows.

This report describes the refined and rationalized bump model based on information obtained from previous asymptotic theories and experiments for shock wave-turbulent boundary layer interaction. The model is incorporated into a small-disturbance code with wind tunnel effects, and the results of computations are compared to the experiments. It is also incorporated in a two-dimensional, full-potential, conservative, finite-volume code and a three-dimensional wing-fuselage code. Results of a three-dimensional test case for an A-7 aircraft are reported and compared to experiments and computations without the interaction model.

II. THE TWO-DIMENSIONAL BUMP MODEL

Yoshihara and Zonars[10] proposed that the thickening of the boundary layer behind the shock wave can be modeled as a "viscous wedge." The oblique shock wave is attached to the wedge apex. In the present model (Figure 1), the boundary layer displacement thickness "bump" starts as a wedge of angle θ and proceeds downstream as a convex curve which becomes parallel to the airfoil surface after a specified interaction length ξ. This results in a jump in displacement thickness $[\![\delta^*]\!]$ across the interaction region. In this section, we shall describe the parametric dependence of the bump model on the flow conditions ahead of the shock wave and the rationale behind them.

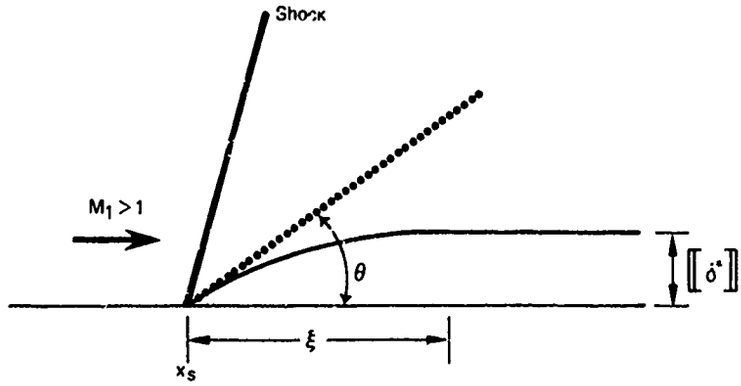


Figure 1. Bump Model.

Consider the velocity shock polar for a given upstream Mach number ($M_1 > 1$), as shown in Figure 2. The point P corresponds to the maximum deflection angle θ_{max} for which the shock wave can remain attached to the apex. P also separates the strong branch and the weak branch of the possible downstream states for a given deflection angle θ. For the assumption of an attached oblique shock wave, the deflection angle of the wedge must be $\theta \leq \theta_{max}$. Furthermore, the weak shock solution is preferred for the locally accelerating flow behind the shock wave over the convex bump. The point S on the shock polar separates the downstream solution for which the Mach number $M_2 < 1$ from that with $M_2 > 1$. If the flow at infinity is subsonic, the flow behind the shock wave must recover to the subsonic state. So, we assume that $M_2 \leq 1$, or $\theta_{max} \geq \theta \geq \theta_s$.

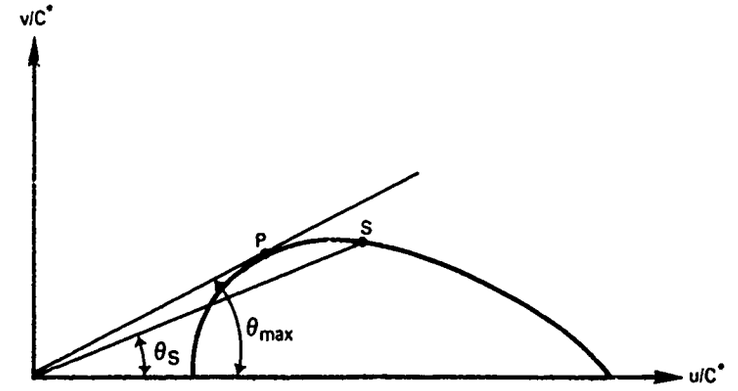


Figure 2. Velocity Shock Polar.

In Figure 3, the experimental data for pressure rise P_2/P_1 across shock waves on an airfoil are plotted versus the upstream Mach number M_1. The experimental results for P_2/P_1 are lower than the theoretical values for the normal shock waves, and indeed, the results seem to fall into the right range of θ if a viscous wedge is assumed. We shall select the wedge angle of the bump as the maximum turning angle θ_{max}. This choice produces the strongest attached oblique shock. For $M_1 > 1.3$, the boundary layer often separates, and the model discussed herein does not apply.

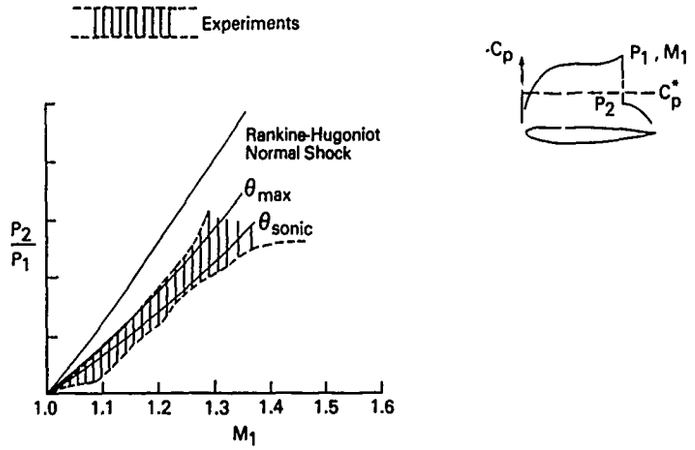


Figure 3. Pressure Rise Across Shocks.

As for the interaction length, the length scale $(M_1^2 - 1)^{1/2}\,\delta_o$ given by Melnik and Grossman[1] is used. Here δ_o is the thickness of the turbulent boundary layer upstream of the shock wave. Since $\delta_o = O(\delta_1^*/\sqrt{c_f})$, where c_f is the friction coefficient and δ_1^* is the upstream displacement thickness, the interaction length in the bump model is chosen as

$$\xi = C(M_1^2 - 1)^{1/2}\,\frac{\delta_1^*}{\sqrt{c_f}}\ , \tag{1}$$

where C is a constant of $O(1)$. For airfoil and wing geometries, we approximate δ_1^* by a linear growth law as

$$\delta_1^* = 3 \times 10^{-3}\, x_s\ , \tag{2}$$

where x_s is the location of the shock wave from the leading edge. The flat plate value for c_f is chosen to approximate that on the airfoil or wing, i.e.,

$$c_f = \frac{0.02666}{(Re_{x_s})^{0.139}}\ . \tag{3}$$

The constant C will be chosen by comparison with experimental results. In later sections, the sensitivity of the computed results to these parameters is explored.

The order of magnitude of the jump in displacement thickness can be estimated by the following:

$$\delta_2^* \sim \theta_{max} \cdot \xi + \delta_1^*$$

$$= \theta_{max} \cdot C(M_1^2 - 1)^{1/2}\,\frac{\delta_1^*}{\sqrt{c_f}} + \delta_1^*\ .$$

According to Melnik and Grossman,[1] for the problem under consideration, we have the following relation:

$$\frac{M_1^2 - 1}{M_1^2}\,\sqrt{\frac{2}{c_f}} = O(1)\ .$$

Also, noting that

$$\theta_{max} \sim 0 \left[(M_1^2 - 1)^{3/2} \right],$$

then

$$\left[\!\left[\delta^* \right]\!\right] \equiv \delta_2^* - \delta_1^* \sim 0 \left[(M_1^2 - 1)\, \delta_1^* \right] \quad . \tag{4}$$

This agrees in order of magnitude with the result given by Green[11]:

$$\left[\!\left[\delta^* \right]\!\right] = \frac{2(M_1^2 - 1)}{M_1^2}\, \delta_1^* \quad .$$

The shape of the bump needs to be specified. Trial and error led to a cubic-shaped function given by

$$\delta^* = \begin{cases} 0 & x \le x_s \\ \xi\, \theta_{max} \left(\eta - \eta^2 + \frac{1}{3}\eta^3 \right) & x_s \le x \le x_s + \xi \\ \frac{1}{3}\, \theta_{max}\, \xi & x \ge x_s + \xi \end{cases} \tag{5}$$

where

$$\eta = \frac{(x - x_s)}{\xi} \quad . \tag{6}$$

This has proven adequate for our studies, although Rizzetta and Yoshihara[9] selected a somewhat different model.

III. SMALL-DISTURBANCE CALCULATIONS

The model given in Section II has been incorporated in a two-dimensional, transonic, small-disturbance code (TSFOIL) which can also model wind tunnel wall interference.[12] Several calculations are reported to illustrate the utility of the model and the sensitivity of the results to values of the assumed parameters. For the transonic small-disturbance theory, the maximum turning angle is given by

$$\theta_{max} = \pm \frac{4}{\gamma + 1} \left[\frac{(\gamma + 1)\, \phi_{x_1} - K}{3} \right]^{3/2} \delta \ , \tag{7}$$

where γ is the specific heat ratio, ϕ_x is a perturbation velocity, K is the transonic similarity parameter, and δ is the airfoil thickness ratio.

An iterative line relaxation procedure is used to solve the small-disturbance equation. In this procedure, shock waves smeared over several mesh points appear automatically in the course of the solution. At the completion of each relaxation cycle, the airfoil surface is searched to detect the location of any shock waves. The point x_s is selected as the sonic velocity point using linear interpolation between the last supersonic and the first subsonic mesh point at the shock location. The parameters in Eqs. (1), (2), (3), and (7) are evaluated using conditions several mesh points ahead of x_s. Finally, the airfoil slope is modified using Eqs. (5) and (6), and the next relaxation cycle is started.

Two symmetrical airfoils at zero angle of attack have been selected for test cases. These nonlifting airfoils have pressure distributions which minimize the viscous effects at the trailing edge. Both airfoils were tested at chord Reynolds numbers of about 4×10^6 and had turbulent boundary layers. Also, the wind tunnel wall effects for these tests have previously been analyzed.[13] Thus the effects of wall interference may be separated from the viscous effects for the present study.

In Figure 4 results are presented for the 64A010 airfoil for a range of freestream Mach numbers. The results show the relative effects of wind tunnel wall interference and the shock wave-boundary layer interaction. At the lowest supercritical Mach number, the shock is weak and the effects are small but measurable. At the highest Mach number shown, the Mach number ahead of the shock is slightly above 1.3. This case reflects the upper limit of the validity of the present model. In general, the bump model gives good results compared to the experimental data.

For the results shown in Figure 4, the constant C in the interaction length formula, Eq. (1), was set to C = 4 . Figure 5 shows the sensitivity of the results to variations in C . The sensitivity of the results to the choice of θ was checked by using $\theta = \theta_{sonic} = 0.9186\ \theta_{max}$, and only slight differences were noted. It was also checked that the calculations have no hysteresis effect by approaching the solution from "above" and "below." It was found that by locating the apex of the wedge (x_s) at the sonic point determined from linear interpolation, the stability and the convergence rate of the calculating significantly improved. In the earlier version of the method,[8] x_s was assigned to a mesh point and the wedge location exhibited a flip-flop behavior on a coarse mesh. Lastly, it is interesting to note that the computing time required for the viscous wedge results shown in Figure 4 is actually less than that required without the viscous wedge.

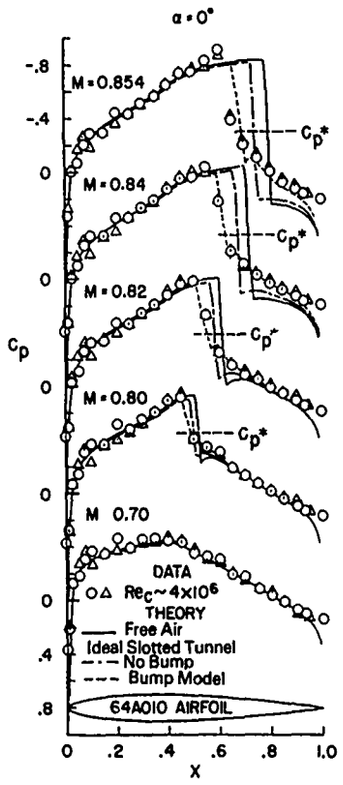


Figure 4. Surface Pressure Distributions.

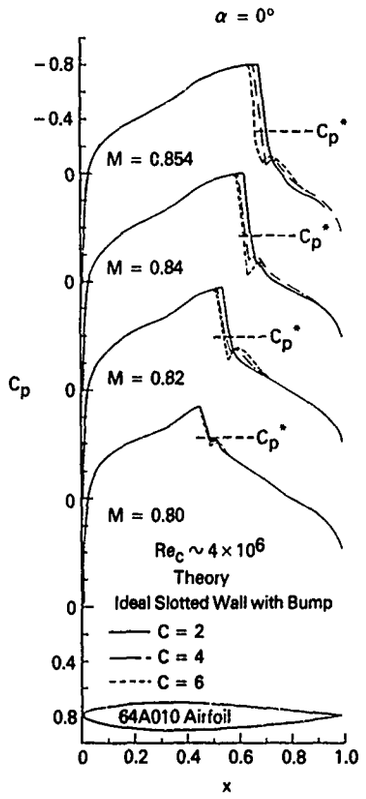


Figure 5. Sensitivity to Constant C.

In Figure 6 results are shown for a NACA 0012 airfoil wherein the above-determined value of C = 4 has been used. Based upon the above-computed examples, this appears to be the recommended value for this constant. We should note, however, that fine tuning of the bump model for other flow conditions and approximate formulae for δ_1^* and c_f might result in a slightly different value of C .

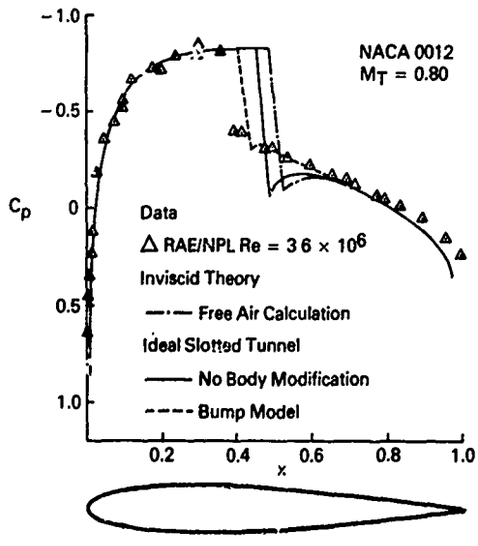


Figure 6. Small-Disturbance Theory.

IV. FINITE-VOLUME CALCULATIONS

The above model has been incorporated into the two-dimensional, conservative, full-potential, finite-volume code FLO 26 by Jameson. For better flexibility and control of mesh spacing, the original parabolic coordinate has been replaced by the mesh system shown in Figure 7. The mesh is generated by algebraic transformations using superellipses.

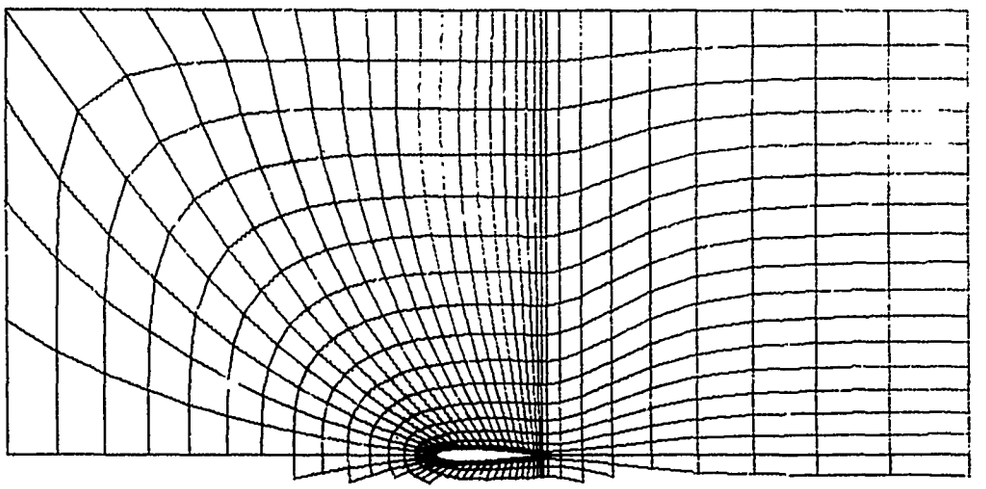


Figure 7. Mesh for Two-Dimensional Calculation.

To avoid generating a new mesh at each iteration to conform the coordinate line to the displaced airfoil surface, we enforce the boundary condition by the local mean surface approximation. The flow angle on the airfoil surface is

$$\frac{v}{u} = \left(f'(x) + \delta^{*'}(x) \right)_{y = f + \delta^*} \quad . \tag{8}$$

Instead of satistying the above condition on $y = f + \delta^*$, we enforce it on the airfoil surface $y = f(x)$ as an approximation. The variation of the velocity across δ^*,

$$\Delta\delta^* = \delta^* \cdot \frac{\partial}{\partial y} \left(\frac{v}{u} \right)\Big|_{y=f}$$

has been neglected. This assumption is justified a posteriori by performing test computations with and without $\Delta\delta^*$.

The boundary condition, Eq. (8), is transformed into the computational variables (X, Y) and the corresponding contravariant velocities (U, V) by the following relation:

$$\begin{pmatrix} u \\ v \end{pmatrix} = \begin{pmatrix} x_X & x_Y \\ y_X & y_Y \end{pmatrix} \begin{pmatrix} U \\ V \end{pmatrix} . \tag{9}$$

Noting that the surface of the airfoil is a coordinate line with

$$f'(x) = \left(\frac{y_X}{x_X} \right)_{Y=0} , \tag{10}$$

Eq. (8) is transformed to

$$\left\{\left[y_Y - X_Y\left(\frac{y_X}{x_X} + \delta^*{}'\right)\right] V\right\}_{Y=0} = \left\{\delta^*{}' x_X U\right\}_{Y=0} \quad . \tag{11}$$

Given the displacement thickness $\delta^*(x)$, the above equation is applied on the airfoil surface $Y = 0$ as an injection boundary condition.

At the end of each relaxation sweep through the field, the shock location x_s is searched. It is defined as the sonic point behind a supersonic region and located by linear interpolation. The shock Mach number M_1 is found, and the corresponding θ_{max} is computed by finding the maximum of the following function:

$$F(\beta) = \tan \theta = 2 \cot \beta \frac{M_1^2 \sin^2 \beta - 1}{M_1^2 (\gamma + \cos 2\beta) + 2} \quad , \tag{12}$$

where β is the shock angle. The displacement thickness variation $\delta^*(x)$ is given by Eq. (5). The value of the injection velocity V is computed and enforced as the boundary condition for the next iteration.

Three different locations of wedge apex have been tried. At first, the last supersonic mesh point upstream of a subsonic region was chosen as the location. Frequently, the computations showed flip-flopping of the wedge location between two mesh points. Then, the sonic point was chosen as the location of the wedge. It produced a converged solution with a peaky one-point re-expansion region behind the shock. Since there is always an upstream influence, we experimented with locating the wedge apex in the supersonic region. The results here are computed by locating the wedge at a distance $0.2\,\xi$ upstream of the sonic point. Figure 8 shows the result of computation for flow over a NACA 0012 airfoil at Mach number 0.8 and zero angle of attack. The potential flow computation obviously does not agree with the experimental pressure distribution. With the present interaction model, the agreement improves particularly downstream of the shock wave. The remaining discrepancy is attributed to the wind tunnel interference effect. This can be verified by comparison with the small-disturbance calculations reported in Section III.

Figure 9 shows the result of computation of a standard case for a lifting NACA 0012 airfoil at Mach number 0.75 and a 2° angle of attack. The lift coefficient is reduced by 10 percent. The shock Mach number is 1.32, which is beyond the applicability of the present model.

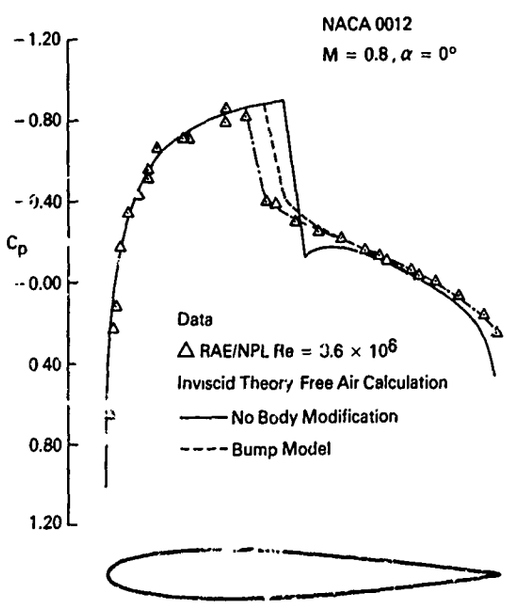


Figure 8. Full-Potential Theory.

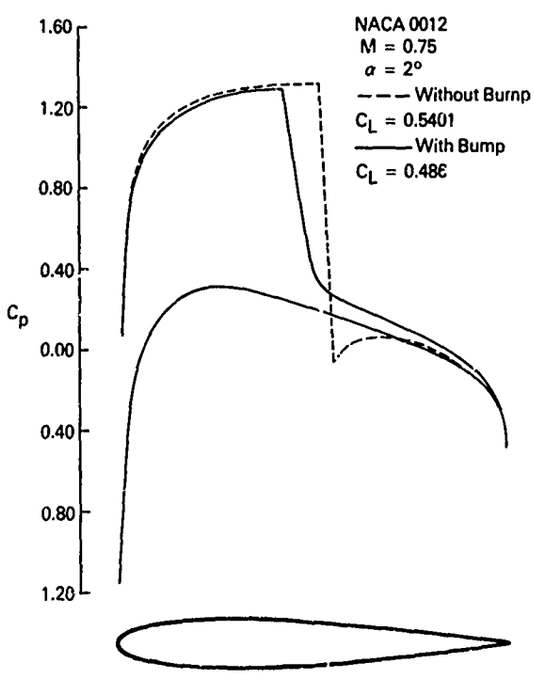


Figure 9. Lifting Airfoil.

V. THREE-DIMENSIONAL BUMP MODEL AND PRELIMINARY NUMERICAL RESULTS

The two-dimensional bump model discussed above has been extended to three dimensions. The spanwise length scale of the variations of the flow over an aircraft is the wing span. The length scale of the shock wave-turbulent boundary layer interaction is of the order of the boundary layer thickness. By comparing these length scales, it is obvious that the interaction is quasi-two-dimensional in nature. Through a three-dimensional shock wave, the velocity component parallel to the shock surface is conserved. Hence, the jump conditions across the shock wave are governed by the Mach number component normal to the shock foot.

For the above reason, the following quasi-two-dimensional model is used. Referring to Figure 10, for a given shock foot angle α_s and the flow direction α_q projected on the x-z plane, the normal shock Mach number is defined as

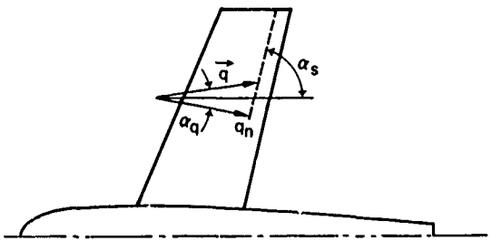


Figure 10. Three-Dimensional Bump Model.

$$M_n = M_1 \sin (\alpha_s - \alpha_q) \ . \tag{13}$$

The maximum turning angle θ_{max} corresponding to M_n is used. The physical injection velocity v_B on the bump surface is found by using

$$v_B = \left(u^2 + w^2\right)^{\frac{1}{2}} \delta_s^{*\prime}(x,z) \ , \tag{14}$$

where u and w are the velocity components in the x- and z-directions and $\delta_s^{*\prime}$ is the gradient of the bump surface in the direction of the flow. The physical injection velocity v_B together with u and w on the surface are then transformed to the contravarient velocity components (U, V_B, W) on the wing surface. V_B is applied as the boundary condition. This procedure assumes that the portion of the airfoil where the shock foot is located has small surface slope. The component of vertical velocity v_s due to the slope of the airfoil and v_B can be treated separately, and the resulting contravarient velocities can be superposed there.

For this preliminary study, we consider only the supersonic-subsonic shock wave. The shock foot is located by finding the sonic point along the chord and the bump applied as in the two-dimensiona calculation.

The model is incorporated into the transonic, full-potential, finite-volume, wing-body code FLO 30.[14,15] A modified, high-wing, A-7 aircraft calculation which showed good agreement with tunnel data except near the wing tip where a strong shock wave appeared was reported by Mercer and Murman.[15] Figure 11 shows a preliminary result of the computation repeated using the bump model. Comparison with the experimental results is considerably improved over the potential flow computation without the interaction model.

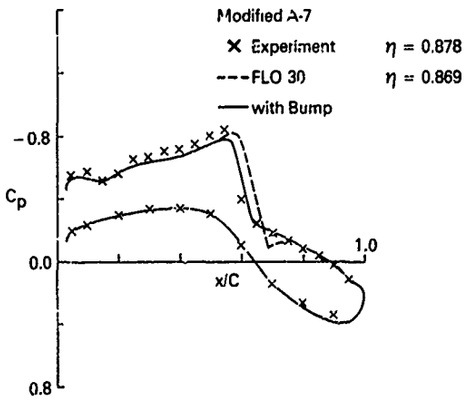


Figure 11. Three-Dimensional Calculation.

VI. CONCLUSIONS

In this work, the bump model previously proposed by Murman[8] and Rizzetta and Yoshihara[9] is rationalized and refined based on recent theoretical studies. The empirical interaction length has been replaced by one scaled according to the asymptotic theory of Melnik and Grossman.[1] The boundary layer parameters necessary in constructing the model are the displacement thickness δ_1^* and the friction coefficient c_f ahead of the shock wave. Simple approximate models of these parameters are used. For δ_1^*, a simple, linearly growing boundary layer is employed. The friction coefficient c_f is given by an expression for flow over a flat plate. For three-dimensional cases, a quasi-two-dimensional bump normal to the shock foot is proposed.

Both two- and three-dimensional models are incorporated into full-potential, conservative, finite-volume calculations after validation using a small-disturbance theory. Results of the computation agree well with experimental measurements. Even though the present bump model is not the exact outer limit of the inner interaction problem, it is scaled correctly according to the inner scale. The source strength is given by the phenomenologically determined condition $\theta = \theta_{max}$. In view of its simplicity in application to the full-potential calculation, it is a good practical means of obtaining a solution for unseparated shock wave-boundary layer interactions. It seems to model the essence of the physics in a rational way.

REFERENCES

1. Melnik, R. E., and Grossman, B., "Interactions of Normal Shock Waves with Turbulent Boundary Layers at Transonic Speeds," Transonic Flow Problems in Turbomachinery, Eds. T. C. Adamson and M. F. Platzer, Washington, D. C., Hemisphere Publishing, 1977, pp. 415-433.

2. Adamson, T. C., Jr., and Feo, A., "Interaction Between a Shock Wave and a Turbulent Boundary Layer in Transonic Flow," SIAM J. Appl. Math., 29, 1975.

3. Inger, G. R., and Mason, W. H., "Analytical Theory of Transonic Normal Shock Boundary Layer Interaction," Symposium Transsonicum II, Eds. K. Oswatitsch and D. Rues, Berlin, Springer-Verlag, 1976.

4. Bohning, R., and Zierep, J., "The Normal Shocks at a Curved Wall in the Viscous Case," Symposium Transsonicum II, Eds. K. Oswatitsch and D. Rues, Berlin, Springer-Verlag, 1976.

5. Melnik, R. E., Chow, R., and Mead, H. R., "Theory of Viscous Transonic Flow Over Airfoils at High Reynolds Number," AIAA Paper No. 77-680, 1977.

6. McClean, J. D., "Three Dimensional Turbulent Boundary Layer Calculations for Swept Wings," AIAA Paper No. 77-3, 1977.

7. Murman, E. M., "Analysis of Embedded Shock Waves Calculated by Relaxation Methods," AIAA J., Vol. 12, No. 5, 1974, pp. 626-634.

8. Murman, E. M., "A Rubber Wall Displacement Surface Model for Turbulent Boundary Layer-Shock Wave Interaction," Note prepared for Grumman Aerospace Corporation, 1975. (See Mason et al., AFFDL-TR-77-122, Vol. 1, p. 47, February 1978.)

9. Rizzetta, D. P., and Yoshihara, H., "Computations of the Pitching Oscillation of a NACA 64A-010 Airfoil in the Small Disturbance Limit," AIAA 18th Aerospace Sciences Meeting Paper No. 80-0128, 1980.

10. Yoshihara, H., and Zonars, D., "An Analysis of Pressure Distributions on Planar Supercritical Profiles with and without Jet Flaps at High Reynolds Numbers," GDCA-ERR-1684, December 1971.

11. Green, J. E., "Interactions Between Shock Waves and Turbulent Boundary Layer," Progress in Aerospace Sciences, Vol. 11, New York, Pergamon Press, 1970, pp. 235-340.

12. Murman, E. M., Bailey, F. P., and Johnson, M. J., "TSFOIL - A Computer Code for Two-Dimensional Transonic Calculations, Including Wind-Tunnel Wall Effects and Wave Drag Evaluation," NASA SP-347, 1975, pp. 769-788.

13. Murman, E. M., and Cole, J. D., "Inviscid Drag at Transonic Speeds," AIAA Paper No. 74-540, 1974.

14. Caughey, D. A., and Jameson, A., "Recent Progress in Finite Volume Calculations for Wing-Fuselage Combinations," AIAA Paper No. 79-1513, 1979.

15. Mercer, J. E., and Murman, E. M., "Application of Transonic Potential Calculations to Aircraft and Wind Tunnel Configurations," Paper No. 1, AGARD Conference Proceedings 285, May 1980 (in press).

SIMPLE APPROXIMATIONS FOR THE ASYMPTOTIC DESCRIPTION OF THE INTERACTION BETWEEN A NORMAL SHOCK WAVE AND A TURBULENT BOUNDARY LAYER AT TRANSONIC SPEEDS

T. C. Adamson, Jr. and A. F. Messiter
Department of Aerospace Engineering
The University of Michigan
Ann Arbor, Michigan 48109, USA

SUMMARY

The asymptotic description of the interaction between a normal shock wave and a turbulent boundary layer is reviewed briefly. The layers necessary in a rational analysis of the interaction are discussed with emphasis on the differences from an interaction with a laminar boundary layer, the uncoupling of solutions for the distribution of pressure and skin friction at the wall, and the role of the Reynolds shear stress in these solutions. The accuracy of asymptotic solutions in flows at Reynolds numbers of technical interest is discussed.

Solutions for the distribution of pressure and skin friction at the wall and the shape of the shock are considered for the case where the flow is near separation. For the pressure and skin friction, it is possible to write two simplified partial solutions, one valid at the beginning of the interaction and one valid somewhat downstream of the shock wave. A solution composed of these two parts and a linear interpolation between them appears to give good comparison with experiment; one unknown constant, independent of the parameters of the interaction, must be found from experiment. The simplified relations are presented. Comparison of numerical computations with experimental data indicates a possible value for the constant and shows quite satisfactory results.

1. INTRODUCTION

It is now well established that asymptotic methods can be used for the description of the interaction between a shock wave and a turbulent boundary layer in unseparated transonic flow at high Reynolds numbers. Specific solutions have been obtained for both oblique and normal shock waves over a range of flow conditions. The important parameters are the Mach number M_e of the incoming flow external to the boundary layer and the Reynolds number Re based on the external-flow variables and the distance $\bar{L}$ from the beginning of the boundary layer to the point of its intersection with the shock wave. Generally, however, small parameters $\epsilon = O(M_e - 1)$ and $u_\tau = O[(\ln \mathrm{Re})^{-1}]$ are introduced, where u_τ is the dimensionless (here with respect to the critical speed of sound in the external flow) friction velocity. Different flow problems are characterized by the relative orders of ϵ and u_τ. In references 1 to 7, solutions are presented for very weak oblique shock waves[1] ($\epsilon \ll u_\tau$), for somewhat stronger normal shock waves[2,3] ($\epsilon = O(u_\tau)$), and for normal[4,5,6] and oblique[7] waves which are still stronger ($\epsilon \gg u_\tau$), but which again occur at transonic speeds, since $\epsilon \ll 1$ in all cases. Most of the solutions are for flow over a flat plate, but in references 5 and 6 corrections for a curved wall are given; in addition, solutions for flow through an axisymmetric channel are shown in references 3 and 5. A more detailed discussion of the cases considered is given in a recent review paper.[8]

The present paper contains simplified versions of the wall pressure and skin-friction distributions derived in references 5 and 6. The result is a very simple set of equations which are easy to use and which give quite satisfactory results. There are many reasons why it is believed to be worthwhile to use asymptotic solutions as the basis for approximate descriptions of the interaction. First, because asymptotic solutions contain the correct essential physics at each stage of the calculation, the proper dependence of flow variables on parameters is exhibited. Moreover, even without the additional approximations described below, certain significant simplifications are achieved; in particular, it can be shown that calculation of the pressure distribution does not require knowledge of the changes in turbulent shear stresses. In addition, because a turbulence model, or closure condition, is used in the derivation for the skin friction, it is possible to introduce different models and thus compare effects, albeit with more work. Finally, and perhaps most importantly, because a rational method has been used, higher-order approximations can be found and one can estimate the errors involved in using a solution valid to a given order of approximation.

The numerical accuracy of the asymptotic solutions for this problem may be estimated since the error is of the same order as the first terms neglected. Such an estimate obviously requires an understanding of the orders of magnitude which appear in the expansions. In the absence of such information, no statement can be made in advance concerning the general usefulness, or more precisely the numerical accuracy, of an asymptotic solution for any given ranges of parameters. For example, the accuracy of laminar free-interaction ("triple-deck") theory is known to depend on the flow problem considered and, moreover, may be different for different flow quantities.[9] In the present case, it is desirable to obtain solutions for values of Re in the range 10^6 to 10^8, say, and for M_e between 1 and the value for incipient separation, roughly 1.3. For this range of parameters the corresponding ranges in ϵ and u_τ are

$0 < \epsilon < 0.23$ and $0.029 < u_\tau < 0.052$. Now, in the calculation of the wall pressure in reference 5, the first term neglected, and thus the error, is of order ϵu_τ^2, which is at most 0.00062. In reference 6, the first term neglected in the skin friction at the wall, and thus the error, is of order u_τ^2, which is at most 0.0027. Of course, these estimates may not be completely reliable, since it is certainly possible that the neglected terms might be multiplied by large numerical coefficients. Also, the solutions to be presented here are numerical approximations to the exact solutions. Nevertheless, it seems very clear that asymptotic solutions to this problem have the possibility of giving good accuracy in the range of parameters of technical importance, even in approximate numerical form.

In the following section, the structure of the interaction region and the governing equations are reviewed and discussed, with emphasis on the differences from the case when the boundary layer is laminar. Solutions for the shape of the shock wave and for the wall and pressure distributions when upstream influence is negligible are shown also. In section 3, approximate relations for the effects of upstream influence are derived. Then, in section 4, these solutions are joined to simplified expressions shown in section 2, to give approximate solutions for the wall pressure and skin-friction distributions which hold throughout the interaction region. Finally, section 5 contains a comparison of computations with available experimental data and a discussion of results.

A two-dimensional flow of a perfect gas is considered. For simplicity, an adiabatic wall is assumed and the total enthalpy is taken to be uniform. All lengths are made dimensionless with respect to $\bar{L}$ and velocities with respect to the critical speed of sound $\bar{a}_e^*$ in the flow external to the boundary layer (overbars indicate dimensional terms). Thermodynamic properties are referred to their critical values in the external flow. Rectangular coordinates X and Y and the corresponding velocity components, U and V, are measured parallel and perpendicular to the wall, respectively, with Y = 0 on the wall and X = 0 at the intersection of the shock wave with the edge of the boundary layer. The term $\overline{\rho' V'}/\rho$ has been included in V.

2. STRUCTURE OF THE INTERACTION REGION

The flow entering the interaction region external to the boundary layer has a velocity $U_e = 1 + \epsilon$. This relation defines ϵ; for transonic flow, $\epsilon \ll 1$. Near the wall, the incoming flow has the velocity profile of an undisturbed turbulent boundary layer. Thus, a two-layer structure is considered, consisting of the velocity-defect and wall layers. Following ideas introduced by Bush and Fendell,[10] Mellor,[11] and Yajnik,[12] this representation is considered to provide an asymptotic description of the turbulent boundary layer at large Reynolds numbers. Including effects of compressibility in essentially the manner of van Driest[13] and Maise and McDonald,[14] one can write the velocity distributions as follows:

$$U_u = U_e + u_\tau\, u_{01}(y) \qquad y = \frac{Y}{\delta} = O(1) \tag{1a}$$

$$\sim U_e + \frac{u_\tau}{\kappa}(\ln y - 2\Pi) \qquad y \to 0 \tag{1b}$$

$$U_u = u_\tau \left(\frac{T_w}{T_e}\right)^{1/2} \tilde{u}_{01}(\tilde{y}) \qquad \tilde{y} = Y/\tilde{\delta} = O(1) \tag{2a}$$

$$\sim \frac{u_\tau}{\kappa}\left(\frac{T_w}{T_e}\right)^{1/2} (\ln \tilde{y} + \kappa c) \qquad \tilde{y} \to \infty \tag{2b}$$

where

$$u_\tau = \left(\frac{\tau_{wu}}{\rho_e}\right)^{1/2} = U_e^2\, C_{fu} \tag{3a}$$

$$(1+\epsilon)^2 = \frac{\frac{1}{2}(\gamma+1)M_e^2}{1 + \frac{\gamma-1}{2}M_e^2} \tag{3b}$$

and where τ_{wu} and ρ_e are, respectively, the dimensionless shear stress at the wall at the point of intersection of the shock wave with the boundary layer and the dimensionless density in the external flow, both evaluated for undisturbed conditions. Subscripts e, w, and u refer to conditions in the external flow, at the wall, and in the undisturbed flow upstream of the interaction, respectively; c_f is the skin friction coefficient. The quantities $\delta = O(u_\tau)$ and $\tilde{\delta}$ refer to the dimensionless orders of the boundary-layer and wall-layer thicknesses, respectively, both evaluated at the point of intersection with the shock wave, and κ is the von Kármán constant. Equation (1a) is the (law of the wake) representation for U in the velocity-defect layer, the variable part of which, $u_{01}(y)$, is that of a corresponding incompressible boundary layer; in the present calculations, the form presented by Coles[15] is used. The effects of compressibility can be represented by a constant which has been absorbed into u_τ; u_τ is defined in terms of ρ_e in Eq. (3). As $y \to 0$, u_{01} has the logarithmic form shown by Eq. (1b). Here, Π is Coles' profile parameter;[15] $c \cong 5.0$ and for zero pressure gradient $\Pi \cong 0.5$. Eq. (2a) is the (law of the wall) representation for U in the wall layer, which as $\tilde{y} \to \infty$ behaves as shown in Eq. (2b). Because the density in the wall and velocity-defect layers has different limiting values, an equation valid for $\tilde{\delta} \ll Y \ll \delta$ must be used for matching purposes (see references 2 and 5 for details; this problem is also discussed in ref. 1). From matching it is shown that

$$u_\tau \kappa^{-1} \ln (\delta/\tilde{\delta}) = (T_e/T_w)^{1/2} U_i(\epsilon) - u_\tau (2\Pi\kappa^{-1} + c) \tag{4}$$

where

$$U_i(\epsilon) = \Gamma \sin^{-1} (\Gamma^{-1} U_e) \tag{5a}$$

$$\Gamma = [(\gamma+1)/(\gamma-1)]^{1/2} \tag{5b}$$

$$\tilde{\delta} = \frac{\mu_w}{\mu_e} \left(\frac{T_w}{T_e}\right)^{1/2} \frac{U_e}{u_\tau} \frac{1}{Re} \tag{5c}$$

Another relation between δ and u_τ for $\partial P/\partial X = 0$ is found using the von Kármán integral of the momentum equation:[5]

$$\frac{m_1}{8}\delta = \frac{u_\tau}{U_e} + \left\{\frac{2}{\kappa}\frac{U_e}{U_i}\left(\frac{T_w}{T_e}\right)^{1/2} + \frac{4}{m_1}\left(3\frac{T_w}{T_e} - 1\right)\int_0^\infty u_{01}^2\, dy\right\}\frac{u_\tau^2}{U_e^2} \tag{6a}$$

$$m_1 = -8\int_0^\infty u_{01}(y)\, dy \tag{6b}$$

As mentioned previously, Coles'[15] form will be used for u_{01}:

$$u_{01}(y) = \kappa^{-1} \ln y - \Pi\kappa^{-1}(1 + \cos \Pi y) \tag{7}$$

for $0 < y < 1$, with $u_{01}(y) = 0$ for $y > 1$. For future reference, it may be noted that the nondimensional distance, $Y = \delta_*$, from the wall to the sonic line in the undisturbed boundary layer, at the point of intersection with the shock wave, is found by setting $U_u = 1$ in Eq. (1b) and expanding for δ_*/δ small; thus

$$u_\tau \kappa^{-1} \ln \frac{\delta}{\delta_*} = \left(\frac{T_e}{T_w}\right)^{1/2} [U_i(\epsilon) - U_i(0)] - 2\Pi\kappa^{-1} u_\tau \tag{8}$$

In addition, the nondimensional displacement thickness δ^* and momentum thickness θ are, for the same conditions and for u_τ/U_e small,

$$\frac{\delta^*}{\delta} = \frac{(1+\Pi)}{\kappa}\left(2\frac{T_w}{T_e} - 1\right)\frac{u_\tau}{U_e} - \frac{2 + 3.18\Pi + 1.5\Pi^2}{\kappa^2}\left(\frac{T_w}{T_e} - 1\right)\left(3\frac{T_w}{T_e} - \frac{1}{2}\right)\frac{u_\tau^2}{U_e^2} \tag{9a}$$

$$\frac{\theta}{\delta} = \frac{(1+\Pi)}{\kappa}\frac{u_\tau}{U_e} - \frac{2 + 3.18\Pi + 1.5\Pi^2}{2\kappa^2}\left(3\frac{T_w}{T_e} - 1\right)\frac{u_\tau^2}{U_e^2} + \cdots \tag{9b}$$

Before consideration of the solutions in the interaction region, it is instructive to review the structure of this region when the boundary layer is turbulent and compare it with that found when the boundary layer is laminar. For laminar flow, there are three layers in the interaction region. In the outermost layer, which has a thickness large compared to that of the boundary layer, the flow is inviscid and irrotational. In the middle layer, which has a thickness of the order of the thickness of the boundary layer, the flow is inviscid and rotational, and finally, in the viscous sublayer which adjoins the wall, the flow is viscous and the boundary-layer equations hold. When the flow is turbulent, and the shock wave is weak, there are also two outer inviscid-flow layers which, although the scales of the layers and the velocity components are quite different, have the same essential fluid mechanisms; when the shock wave becomes stronger, these two outer layers merge to one in which the flow is still inviscid. As the wall is approached, however, fundamental differences arise, there being two layers in turbulent flow rather than one as in laminar flow. This can be explained physically by noting that in either case, the outer layers are governed by inviscid-flow equations; hence, a boundary layer must exist between the wall and the inviscid flow. The laminar boundary layer has a single-layer structure and so in the interaction with a laminar boundary layer, only a single viscous sublayer is necessary. On the other hand, the undisturbed turbulent boundary layer has a two-layer structure, as noted previously; hence, in the interaction region two inner layers are necessary. They are called here the Reynolds-stress sublayer and the wall layer. The Reynolds-stress sublayer, referred to as the blending layer in ref. 2, is the counterpart of the velocity-defect layer. In the equation of motion in the flow direction, inertia, pressure gradient, and Reynolds shear stress terms are most important. In the wall layer, even though there is a pressure gradient, only two terms remain in the governing equation, the Reynolds and viscous stress terms; that is, this equation is the same as that for the undisturbed wall layer.

The extent of the effects of the interaction upstream of the shock wave, i.e., the upstream influence, is of slightly smaller order than the thickness of the subsonic region in the boundary layer. For weak ($\epsilon \ll u_\tau$) or moderately strong ($\epsilon = O(u_\tau)$) shock waves, the sonic line lies at a distance of order δ from the wall. However, for stronger shock waves ($\epsilon \gg u_\tau$), the sonic line lies very close to the wall and so

the upstream influence is confined to a region which is exponentially small compared to the main part of the interaction region. In this event, in the main part of the boundary layer, the flow ahead of the shock wave is undisturbed.

A sketch illustrating the essential features of the interaction region as found from an asymptotic analysis for $\epsilon >> u_\tau$ is shown in figure 1. The small region of upstream influence has thickness of order δ_* and Δ_* in the y and x directions, respectively; δ_* is the dimensionless distance from the wall to the sonic line. The main part of the interaction region has corresponding characteristic thickness δ and Δ. The orders of the dimensionless thickness of the Reynolds-stress sublayer are $\hat{\delta}_*$ and $\hat{\delta}$ in the small region upstream of the shock wave and the main region, respectively; in both of these regions, the order of the thickness of the wall layer is $\tilde{\delta}$, the same as that found in the undisturbed boundary layer, defined in Eq. (5c). The relationships found for these various length scales are,[5,6,16] in terms of u_τ, δ, δ_*, and ϵ,

$$\Delta = b_0\,\delta = (\gamma+1)^{1/2}\,\epsilon^{1/2}\left\{1 - \frac{\epsilon}{4}\,(2\gamma+1) + \cdots\right\}\delta \tag{10a}$$

$$\Delta_* = \left(\frac{\gamma+1}{\kappa\, T_e}\right)^{1/2} u_\tau^{1/2}\,\delta_* \tag{10b}$$

$$\hat{\delta} = u_\tau\,\Delta \qquad\qquad \hat{\delta}_* = u_\tau\,\Delta_* \tag{10c,d}$$

A brief but representative illustration of the form of solution found and the manner in which these solutions are used may be given by showing the expansion for U and governing equation for the lowest order perturbation in each layer. To this end, only the main part of the interaction region will be considered.

Outer Inviscid Layer

In figure 2 is shown a sketch drawn to the scale of the outer inviscid region, for the case $u_\tau << \epsilon << 1$. Because the upstream influence is limited to the inner region which is negligibly small to this scale, the flow ahead of the shock wave is undisturbed. Again to this scale, the shock wave penetrates the boundary layer to the wall; it is normal to the lowest order, the equation for the shape of the shock being such that $x_s = O(u_\tau/\epsilon)$. In the flow downstream of the shock wave, the shock-polar equation suggests the proper form of expansion. It is convenient to separate the rotational part, which can be calculated from Crocco's Theorem, and the irrotational part, which must be derived, as follows:

$$U = (1+\epsilon)^{-1} + u_\tau\, u_1^{(r)}(x,y;\epsilon) + \cdots + u_\tau\,\phi_{1x}(x,y;\epsilon) + \cdots \tag{11a}$$

$$x = X/\Delta \qquad\qquad y = Y/\delta \tag{11b,c}$$

The differential equation for ϕ_1 is found to be Laplace's equation

$$\phi_{1xx} + \phi_{1yy} = 0 \tag{12}$$

which is solved by use of a distribution of sources along the y-axis, subject to the condition that $\phi_{1y}(x,0) = 0$, where $V = b_0\, u_\tau\, \phi_{1y} + \cdots$ and where b_0 is defined in Eq. (10a). The fact that V = 0 in lower orders at y = 0 is a very important point because it means that the solutions (to and including $O(u_\tau^2)$) in the outer inviscid-flow regions may be solved independently of the solutions in the inner layers. In this sense the interaction is a weak interaction when the boundary layer is turbulent, and therefore it is fundamentally different from the laminar-flow case. The reason is that the wall layer is so thin; that is, any lifting of the fluid in this layer, due to deceleration as a result of the unfavorable pressure gradient, is still so small in order of magnitude as to affect only terms of higher order than those considered here. This is easily checked by finding the lowest order approximation for V in the inner layers.[6]

The solution found for ϕ_1 is[5]

$$\phi_1(x,y) = -\frac{2}{\pi}\left\{1 + (\gamma-1)\epsilon + \cdots\right\}\int_{-\infty}^{\infty} u_{01}(\eta)\,\ln\left\{x^2 + (y-\eta)^2\right\}^{1/2} d\eta \tag{13}$$

and the corresponding shape of the shock is[5]

$$x_s(y) = \frac{u_\tau}{2\epsilon}\,(1 + \frac{\epsilon}{2} + \cdots)\left\{\phi_1(0,y;\epsilon) - \phi_1(0,1;\epsilon)\right\} + \cdots \tag{14a}$$

$$= x_s(0) + \frac{u_\tau}{2\epsilon}\left\{1 + (\gamma - \tfrac{1}{2})\,\epsilon + \cdots\right\}\left\{\frac{\pi}{\kappa}\,, + \cdots\right\}, \qquad y \to 0 \tag{14b}$$

$$= x_s(0) + \frac{u_\tau}{2\epsilon}\left\{1 + (\gamma - \tfrac{1}{2})\,\epsilon + \cdots\right\}\left\{\frac{m_1}{2\pi}\,\ln y + \frac{4}{\pi}\int_0^\infty u_{01}(\eta)\ln\eta\, d\eta\right\}, \qquad y \to \infty \tag{14c}$$

where $x_s(0)$ is the value of x_s at the wall. Now, because layers beneath the inviscid-flow layer are so thin, $\partial P/\partial Y = 0$ to the order desired, so the pressure at the wall is simply that calculated as $y \to 0$ in the inviscid layer. Since the entropy is nearly constant along a streamline, isentropic relations, the energy equation, and the equation of state may be used to relate the pressure to U. If higher-order terms are included and the result is written for $x \gg 1$, the result is as follows, for P_w, the pressure at the wall:[5]

$$\frac{P_w - P_f}{P_e} = -\gamma\left\{u_\tau\left[1 + (2\gamma - 1)\epsilon + \cdots\right] m_1 + u_\tau^2 (1 + \cdots) m_2 + \cdots\right\} \frac{1}{2\pi x} \tag{15a}$$

$$m_2 = 2(5\gamma + 9)\int_0^\infty u_{01}^2(y)\,dy - 2(\gamma + 1)\int_0^\infty \phi_{1y}^2(0,y)\,dy \tag{15b}$$

where m_1 is given in Eq. (6b) and where $P_f/P_e = 1 + \gamma\left\{2\epsilon + (2\gamma - 1)\epsilon^2 + \cdots\right\}$ is the pressure ratio across a normal shock wave when the upstream speed is $U_e = 1 + \epsilon$. Thus, the interaction has the effect of a source on the pressure distribution. The simplified form for P_w, i.e., the form valid for $x \gg 1$, is presented here because it has been found that it gives numerical results which agree very well with the exact solution for $x \geq 2$ and this is all that is necessary in the present application.

Reynolds-Stress Sublayer

The Reynolds-stress sublayer and the wall layer, as mentioned previously, may be thought of as being the two layers of another, thinner, turbulent boundary layer at the base of the interaction region. Across each layer $\partial P/\partial Y = 0$, and in each layer it is necessary to specify a closure condition. Here we use a mixing-length model, including the van Driest damping factor, to write an eddy viscosity;[17] evidently, this model gives satisfactory results when the flow is unseparated.[18]

In the Reynolds-stress sublayer, the important terms in the equation of motion in the flow direction are such that, with the above-mentioned eddy-viscosity model, the equation may be written as follows:

$$U\frac{\partial U}{\partial X} = -\frac{1}{\gamma}\frac{\partial P}{\partial X} + \frac{\partial}{\partial Y}\left[\rho\left(\kappa Y\frac{\partial U}{\partial Y}\right)^2\right] \tag{16}$$

Thus, in this layer, the damping factor is unity.[6] The expansion for U, P, and ρ are written in terms of perturbations from the incoming flow. For example,

$$U(x,\hat{y}) = (1+\epsilon)^{-1} + u_\tau\left[\frac{1}{\kappa}\left(\ln\frac{\hat{\delta}}{\delta} + \ln\hat{y} - 2\Pi\right) + \hat{u}_1(x,\hat{y})\right] + \epsilon u_\tau\frac{1}{\kappa}\ln\frac{\hat{\delta}}{\delta}\,\hat{u}_{1\ell}(x,\hat{y}) + \epsilon u_\tau u_{11}(x,\hat{y}) + \cdots \tag{17a}$$

$$x = X/\Delta \qquad \hat{y} = Y/\hat{\delta} \tag{17b,c}$$

Solutions for the various $\hat{u}_i$ indicate that $\hat{u}_1$ is a function of x alone, so that from matching $\hat{u}_1 = \phi_{1x}(x,0)$, and that $\hat{u}_{1\ell}$ and $\hat{u}_{11}$ satisfy a type of diffusion equation; e.g.,[6]

$$\frac{\partial u_{1\ell}}{\partial x} = \frac{\partial}{\partial\hat{y}}\left(2\kappa\hat{y}\frac{\partial\hat{u}_{1\ell}}{\partial\hat{y}}\right) \tag{18}$$

The resulting solutions for $\hat{u}_{1\ell}$ and $\hat{u}_{11}$ are such that their dependence upon $\hat{y}$ disappears exponentially as $\hat{y} \to \infty$ and they have a logarithmic dependence upon $\hat{y}$ as $\hat{y} \to 0$. The x dependence of U is found by matching Eq. (17a), written for $\hat{y} \to \infty$, with its counterpart from the inviscid-flow layer, found as $y \to 0$.

Wall Layer

As indicated previously, a simple ordering of the terms[6] in the equation of motion indicates that to the order desired, the only terms retained are the Reynolds and viscous shear stress terms. The equation is easily integrated once to give

$$\rho D(\tilde{y})\left(\kappa\tilde{y}\frac{\partial U}{\partial\tilde{y}}\right)^2 + \frac{\mu u_\tau}{A}\frac{\partial U}{\partial\tilde{y}} = u_\tau^2\rho_e\tau_w \tag{19a}$$

$$\tilde{y} = Y/\tilde{\delta} \tag{19b}$$

$$\tau_w(x) = \overline{\tau}_w/\overline{\tau}_{wu} \tag{19c}$$

$$A = \frac{\mu_w}{\mu_e}\left(\frac{T_w}{T_e}\right)^{1/2}\frac{1}{\rho_e} \tag{19d}$$

where μ is the nondimensional viscosity. Just as in the case of the undisturbed boundary layer, noted

previously, a solution for U based on a simple limit-process expansion will not match with the solution in the Reynolds-stress sublayer. Hence, instead of carrying out such an expansion, one notes that Eq. (19a) has a range of validity such that it holds for $\tilde{\delta} \ll Y \ll \hat{\delta}$. Thus, if one imagines $\tilde{y}$ continually increasing until solutions of U may be matched with those from the Reynolds stress sublayer, the same equation, (19a), holds throughout; no additional terms are necessary.[1,2] Moreover, as $\tilde{y} \to \infty$, the viscous term becomes small compared to the Reynolds-stress term, and $D(\tilde{y}) \to 1$, so that Eq. (19a) may be integrated easily to give, for $\tilde{y} \to \infty$,

$$U(x,\tilde{y}) = \Gamma \sin\left\{\frac{1}{\Gamma}\left(\frac{T_w}{T_e}\right)^{1/2}\left(\frac{\tau_w}{P_w/\Gamma_e}\right)^{1/2} u_\tau\left(\frac{1}{\kappa}\ln\tilde{y} + B(x)\right)\right\} \tag{20}$$

As pointed out by Melnik and Grossman,[2] it is not necessary, then, to calculate U in the wall layer to find τ_w; instead, τ_w can be found when Eq. (20) is matched with Eq. (17a) as $\hat{y} \to 0$ and $\tilde{y} \to \infty$. From this equation, it is seen that $\tau_w(x)$ is given in terms of $P_w(x)$. Thus, for $\epsilon \gg u_\tau$, results presented in references 5 and 6 can be used to show that, again for $x \gg 1$,

$$\tau_w - \tau_{wf} = u_\tau \frac{A}{x} + \epsilon u_\tau (-B + C\ln x) + \cdots \tag{21a}$$

$$A = -\frac{a_1}{4\pi} m_1 \left\{1 - \frac{\epsilon}{2}\left[1 - 3\gamma - \frac{3a_1}{2} + \frac{4\gamma}{a_1}(\gamma + \frac{1}{2})\right]\right\} \tag{21b}$$

$$B = -\kappa^{-1}\ln\frac{\hat{\delta}}{\delta}(2\gamma - a_1)(\gamma + \frac{1}{2} - \frac{a_1}{4}) + \kappa^{-1}\left[2\Pi(2\gamma - a_1)(\gamma + \frac{1}{2} - \frac{a_1}{4}) + (2\gamma + 1 - \frac{a_1}{2})(\gamma - \frac{a_1}{2})(\gamma_e - \ln 2\kappa)\right] \tag{21c}$$

$$C = \kappa^{-1}(2\gamma + 1 - \frac{a_1}{2})(\gamma - \frac{a_1}{2}) \tag{21d}$$

$$a_1 = -4\sqrt{\frac{\gamma - 1}{2}}\left(\sin^{-1}\frac{1}{\Gamma}\right)^{-1} + 2\gamma \tag{21e}$$

In Eq. (21c) $\gamma_e = 0.57721$ is Euler's constant and $\kappa = 0.41$ is the von Kármán constant. In Eq. (21a), τ_{wf} represents the wall shear stress calculated using the pressure downstream of the shock wave. For flow over a flat plate,[6]

$$\tau_{wf} = \left[\frac{1 + \left(\frac{\gamma+1}{2}\right)(U_e^2 - 1)}{1 - \left(\frac{\gamma-1}{2}\right)(U_e^2 - 1)}\right]\left[\frac{\sin^{-1}\left(\frac{1}{\Gamma U_e}\right)}{\sin^{-1}\left(\frac{U_e}{\Gamma}\right)}\right]^2 \tag{22a}$$

$$\sim 1 + a_1\epsilon + a_1(a_1 - 1)\frac{\epsilon^2}{2} + \cdots \qquad \epsilon \ll 1 \tag{22b}$$

Again, m_1 is defined in Eq. (6b).

The solutions for P_w (Eq. (15a)) and τ_w (21a) given here are valid for $x \gg 1$. Numerically, however, they give good results for $x \gtrsim 2$. They are written in terms of arbitrary velocity distributions, $u_{01}(y)$. If Coles' [15] form for u_{01} is used, then $m_1 = 8(1 + \Pi)/\kappa$. In order to calculate m_2, an approximation for the shock-wave shape is used to evaluate one of the integrals;[5] also, the function of Π appearing in this second-order source strength is approximated by a linear function for $0 \lesssim \Pi \lesssim 0.5$. When this is done, one finds that $m_2 = 120(1 + 6\Pi)$. The large magnitude of the ratio m_2/m_1 illustrates the possibility noted earlier that knowledge of orders of magnitude is not always sufficient for estimation of neglected terms. The above values of m_1 and m_2 will be used below; addition of the term proportional to $u_\tau^2 m_\tau$ can be seen to provide substantial improvement in the agreement between theory and experiment.

3. INITIAL PART OF THE INTERACTION

The solutions presented in section 2 were obtained for the main part of the interaction region, with simplifications derived for $x \gtrsim 2$. These solutions do not show the initial variations from undisturbed flow, i.e., the effects of upstream influence which, although small in the limit, may still be significant numerically. The equations which govern the flow in this small region where the shock wave forms are nonlinear. Hence, a numerical solution would be called for,[2] in general. However, analytical results can be derived for the form of P_w and τ_w at the beginning of the interaction.

Equation (14a) may be used to show that, if Eq. (7) is used for u_{01}, $x_s(0)$ becomes

$$x_s(0) = -\frac{2u_\tau b_0 \delta}{\pi\kappa\epsilon}\left[1 + (\gamma - \frac{1}{2})\epsilon + \cdots\right](2 + 1.59\,\Pi) \tag{23}$$

In the small upstream region, the proper scaling of the independent variables, and the expansions for U and V, are given by[4,5]

$$x^* = \frac{X - X_s(0)}{\Delta_*} \qquad y^* = \frac{Y}{\delta^*} \tag{24a,b}$$

$$U = 1 + \frac{u_\tau}{\kappa T_e^{1/2}} u^* + \cdots \qquad V = (\gamma+1)^{1/2} \frac{u_\tau^{3/2}}{(\kappa T_e^{1/2})^{3/2}} v^* + \cdots \tag{24c,d}$$

where the factors $\kappa T_e^{1/2}$ have been added for convenience. The governing equations are then the transonic small-disturbance equations with prescribed vorticity:

$$u^* u^*_{x^*} - v^*_{y^*} = 0 \tag{25a}$$

$$v^*_{x^*} - u^*_{y^*} = -\frac{1}{y^*} \tag{25b}$$

As $x^* \to -\infty$, $u^* \sim \ln y^*$, the undisturbed velocity; as $y^* \to 0$, $v^* \to 0$. Finally, as $x^* \to \infty$, $y^* \to \infty$, the solutions must match with those found in the main part of the interaction region.

As $x^* \to -\infty$, the solution has the form

$$u^* \sim \ln y^* + e^{kx^*} f(y^*) \qquad v^* \sim k^{-1} e^{kx^*} f'(y) \tag{26a,b}$$

where $f'' - (\ln y^*) k^2 f = 0$ subject to the conditions that $f'(0) = 0$ and that no incoming disturbances are present as $y^* \to \infty$; the latter implies $f' \sim -(\ln y^*)^{1/2} kf$ as $y^* \to \infty$. From numerical integration, $k = 0.59$. Since, from the equation of motion in the flow direction, $P^*_{x^*} = -\gamma u^*_{x^*}$, the solution for the wall pressure may be written as

$$P_w = P_e \left[1 + u_\tau \exp\ k(x^* - x_0^*) + \cdots\right] \tag{27}$$

where x_0^* is a constant, as yet unknown. The corresponding equation for τ_w can be found by calculations similar to those described above for the main interaction region.[16] In fact, the governing equations and hence the form of the solution are essentially the same in each region. In general, one finds that[16] to lowest order

$$\tau_w = \text{constant} + u_\tau \tau_1 + \cdots \tag{28}$$

In the main interaction region, the constant is τ_{w_f} and $\tau_1 = -a_1 u_1/2 = a_1 P_{w1}/2\gamma$; this is shown by comparison of Eqs. (15a) and (21a), the notation P_{w1} being self-explanatory. In the small upstream region under consideration here, the constant is 1, since perturbations are measured from the undisturbed values, and $\tau_1 = a_1 P_1^*/2\gamma$. Thus,

$$\tau_w = 1 + \frac{u_\tau a_1}{2\gamma} e^{k(x^* - x_0^*)} + \cdots \tag{29}$$

4. FORMULATION OF SIMPLIFIED SOLUTIONS

The solutions presented in sections 2 and 3 are valid in the main part of the interaction region and at the initial part of the interaction, respectively. A complete solution would require a numerical solution in the small region where upstream influence is important, which could be joined to the solution in the main part of the interaction to provide a composite solution. However, it appears that in the part of the interaction between the regions where the solutions are known, the variations both in P_w and τ_w are close to being linear. For greatly increased simplicity, without serious loss of accuracy, the solutions are completed in this section by means of linear interpolations. Before such equations can be used, it is necessary to have a value for x_0^*. However, since this is a constant in the dimensionless formulation of the equations and boundary conditions, it is independent of the parameters of the problem, so that only a single numerical value is needed. In the following section, this value is estimated from experimental data.

The descriptions given so far, in terms of P_e, P_f, τ_{w_d}, etc., would suffice for the idealized case of a flat plate in a uniform flow, where the pressure and skin friction approach constant values upstream and downstream of the interaction. For flow past an airfoil, these values may be replaced by the actual variable quantities. In the case of the wall pressure, for example, the boundary-layer effects can be expressed in terms of the difference from a potential-theory pressure which continues to vary as the distance from the shock increases. Thus, upstream of $X = X_u$, say, the exponential solution is added to a potential-flow solution $P_w = P_u(X)$. Downstream of $X = X_d$, say, the source solution is added to a

potential-flow solution $P_w = P_d(X)$. Close to the shock wave, for $X_u < X < X_d$, P_w is approximated by a straight line drawn tangent to these upstream and downstream representations. The tangency conditions are sufficient to determine the equation of the straight line and the values for X_u and X_d.

The functions $P_u(X)$ and $P_d(X)$ include the effects of nonuniform external flow associated with nonzero values of $\partial P/\partial X$ and $\partial P/\partial Y$ ahead of the shock wave. If $P_d(X)$ were known very accurately, the singular behavior due to the local surface curvature[5] would appear for $X \to 0$. However, if the potential-flow pressure distribution is found numerically, the shock wave may be spread over a few mesh points so that the singularity is obscured. The values of X_u and X_d are expected to lie outside the region of rapid pressure rise corresponding to the shock wave in the numerical computations; if this is not true, some simple extrapolation of $P_u(X)$ and/or $P_d(X)$ should be used so that the smearing of the shock wave resulting from the numerical calculations does not influence the pressures calculated here. A specific location must be estimated for the shock wave, so that the origin for x can be defined.

Three representations for the wall pressure are therefore proposed, one for each of three intervals, as follows:

$$X < X_u: \quad \frac{P_w}{P_t} = \frac{P_u(X)}{P_t} \left\{ 1 + u_\tau \, e^{k(x^* - x_0^*)} \right\} \tag{30a}$$

$$X_u < X < X_d: \quad \frac{P_w}{P_t} = \frac{P_d(X_d)}{P_t} + \alpha x + \beta \tag{30b}$$

$$X > X_d: \quad \frac{P_w}{P_t} = \frac{P_d(X)}{P_t} - \frac{1}{P_t} \frac{\gamma m u_\tau}{2\pi x} \tag{30c}$$

where $P_t = \{(\gamma+1)/2\}^{\gamma/(\gamma-1)} = 1.893$ for $\gamma = 1.4$, and where Eqs. (15) and (27) have been used in Eqs. (30c) and (30a), respectively. In Eq. (30c), m is the term in brackets in Eq. (15a) evaluated using the approximations mentioned previously:

$$m = 8 \frac{1 + \Pi}{\kappa} \{1 + (\gamma - 1)\epsilon + \cdots\} + 120 (1 + 6\Pi) u_\tau \tag{31}$$

The constants X_u, X_d, α, and β are determined from the requirements that P_w and $d P_w/dX$ be continuous. The equations from which they may be calculated are found to be[19]

$$\frac{P_d(X_d) - P_u(X_u)}{P_t} x_d = \frac{\gamma m u_\tau}{\pi P_t} \left(1 - \frac{x_u}{2x_d} \right) + x_d (x_d - x_u) \frac{P_d'(X_d)}{P_t} \Delta + \frac{P_u(X_u)}{P_t} x_d u_\tau \exp\{k(x_u^* - x_0^*)\} \tag{32a}$$

$$\left\{ \frac{P_u(X_u)}{P_t} k \frac{\Delta}{\Delta_*} + \frac{P_u'(X_u)}{P_t} \Delta \right\} u_\tau \exp\{k(x_u^* - x_0^*)\} = \frac{\gamma m u_\tau}{2\pi x_d^2 P_t} + \frac{P_d'(X_d) - P_u'(X_u)}{P_t} \Delta \tag{32b}$$

$$\alpha = \frac{\gamma m u_\tau}{2\pi x_d^2 P_t} + \frac{P_d'(X_d)\Delta}{P_t} \tag{32c}$$

$$\beta = -\frac{\gamma m u_\tau}{\pi x_d P_t} - \frac{x_d P_d'(X_d)\Delta}{P_t} \tag{32d}$$

where

$$x_u = \frac{X_u}{\Delta} = \frac{\Delta_* x_u^* + X_s(0)}{\Delta} \tag{32e}$$

Equations (32a) and (32b) are to be solved simultaneously for x_u and x_d. If $u_\tau \ll \epsilon$, then $\Delta_* \ll \Delta$, the exponential function is numerically small, and $|x_u| \ll x_d$. Also $P_u(X_u) \approx P_u(0)$ and $P_d(X_d) \approx P_d(0)$, the values found at $X = 0$ by extrapolation, and terms containing $P_u'(X_u)$ or $P_d'(X_d)$ are numerically small. These estimates can be used to give a first guess for x_d, and the equations can then be solved iteratively in essentially the form given. The constants found from Eqs. (32) are to be substituted into Eqs. (30) to give the wall pressure as a simple function of distance and a somewhat more complicated but known function of the parameters.

An analysis for the wall shear stress, similar to that carried out for the wall pressure, leads to the following set of equations, written here in terms of the skin friction, c_f, using the relation $\tau_w = c_f/c_{fu}$; thus $c_{fu}(X)$ and $c_{fd}(X)$ are considered to have been found using typical boundary-layer methods and so include the effects of wall curvature:

$$X < X_u: \quad c_f = c_{fu}(X)\left[1 + u_\tau \frac{a_1}{2\gamma} e^{k(x^* - x_0^*)} + \cdots\right] \tag{33a}$$

$$X_u < X < X_d: \quad c_f = c_{fd}(X_d) + \alpha_c x + \beta_c \tag{33b}$$

$$X > X_d: \quad c_f = c_{fd}(X) + c_{fu}(X_u)\left[u_\tau \frac{A}{x} + \epsilon u_\tau (-B + C \ln x)\right] \tag{33c}$$

where

$$x = \frac{X}{\Delta} = \frac{\Delta_* X^* + X_s(0)}{\Delta} \tag{34}$$

It may be noted that as x becomes very large, the term $-B + C \ln x$ does not approach zero. This term evidently indicates that relaxation to a final value of c_f takes place on a scale large compared to a boundary layer thickness. Because B is a large number $-B + C \ln x$ goes through zero for x large (e.g., $x \approx 200$). Moreover, since $\ln x$ does not vary rapidly with large x, the contribution of this term is not significant for a considerable range of values of x about the point at which it equals zero. Hence after the term $-B + C \ln x$ has gone to zero, it should be dropped from the expression for c_f.

The equations necessary to find X_u, X_d, α_c, and β_c are obtained by equating the relevant expressions for c_f and $d c_f/dX$ at X_u and X_d. They may be written as follows:

$$\begin{aligned} c_{fu}(X_u) - c_{fd}(X_d) = {} & \Delta x_u c'_{fd}(X_u) - \Delta x_d c'_{fd}(X_d) \\ & + u_\tau c_{fu}(X_u)\left[\frac{2A}{x_d} - \epsilon(B + C(1 - \ln x_d))\right] \\ & - u_\tau \left\{\Delta c'_{fu}(X_u) + \frac{k\Delta}{\Delta_*} c_{fu}(X_u)\right\}^{-1} \\ & \cdot \left\{\frac{\Delta}{u_\tau}(c'_{fu}(X_d) - c'_{fu}(X_u)) + c_{fu}(X_u)\left(-\frac{A}{x_d^2} + \frac{\epsilon C}{x_d}\right)\right\} \\ & \cdot \left\{c_{fu}(X_u)\left(1 - k x_u \frac{\Delta}{\Delta_*}\right) - x_u \Delta c'_{fu}(X)\right\} \end{aligned} \tag{34a}$$

$$\begin{aligned} e^{k(x_u^* - x_0^*)} = {} & \frac{2\gamma}{a_1}\left[\Delta c'_{fu}(X_u) + k \frac{\Delta}{\Delta_*} c_{fu}(X_u)\right]^{-1} \\ & \cdot \left\{\frac{\Delta}{u_\tau}[c'_{fu}(X_d) - c'_{fu}(X_u)] + c_{fu}(X_u)\left[-\frac{A}{x_d^2} + \frac{\epsilon C}{x_d}\right]\right\} \end{aligned} \tag{34b}$$

$$\alpha_c = \Delta c'_{fu}(X_d) + c_{fu}(X_u)\left\{-\frac{u_\tau A}{x_d^2} + \epsilon u_\tau \frac{C}{x_d}\right\} \tag{34c}$$

$$\beta_c = -\Delta x_d c'_{fu}(X_d) + u_\tau c_{fu}(X_u)\left\{\frac{2A}{x_d} - \epsilon(B + C(1 - \ln x_d))\right\} \tag{34d}$$

where $c'_f = d c_f/dX$. It should be noted that the values of X_u and X_d calculated for the skin friction are not the same as those calculated for the wall pressure.

5. COMPARISON WITH EXPERIMENTAL DATA

Relatively little data are available for interactions between shock waves and boundary layers in unseparated flow. Here, three comparisons are made with pressure distributions and one with skin friction. Because of the paucity of data it is not possible to give a definitive value for x_0^*. It may also be noted that accurate values of x_0^* imply an accurate value for the location of the shock wave; they are interdependent. As will be shown, values of x_0^* of -14 and -15 give quite good results when compared with available experimental data; more comparisons will no doubt lead to an improved value for x_0^*. As

already noted, $k \cong 0.59$. In each of the comparisons to be shown, the exponential and source solutions were drawn and then simply connected by a straight line tangent to each curve.

A comparison with an experimental wall pressure distribution from ref. 20 is shown in figure 3, with $x_0^* = -14$, for $M_e = 1.322$, ($\epsilon = 0.247$) $Re = 9.6 \times 10^5$, $\delta = 0.021$, $u_\tau = 0.051$, $\Pi = 0.28$, and $\delta_*/\delta = 0.26$. Effects of nonuniform external flow resulting from tunnel area change and longitudinal wall curvature have been estimated and included in the predicted pressure.[5] For a circular pipe, a comparison with experimental results from ref. 21 and a numerical solution from ref. 3 is shown in figure 4, again with $x_0^* = -14$, for $M_e = 1.12$, $Re = 6 \times 10^6$, $\delta = 0.02$, $u_\tau = 0.04$, $\Pi = 0.1$, and $\delta_*/\delta = 0.45$. Again, the effects of a nonuniform external flow, in this case resulting from a finite pipe radius and a small area change, are included. For these comparisons a value for $\delta*$ or δ_*/δ was regarded as given and the value of Π was calculated using the approximate form of Eq. (8) with δ_*/δ assumed to be small; use of the complete equation would change the theoretical curves slightly.

A third comparison of wall pressures is shown in figure 5, in this case for a transonic channel flow. The experimental points and the computations represented by the dashed curve are from ref. 22, 23. The computed points were found by using an asymptotic inviscid-flow solution with a wall shape given by the actual wall shape plus the displacement thickness due to a compressible turbulent boundary layer. The interaction is not accounted for and one can see the effects of the singularity induced by the wall curvature, immediately downstream of the shock wave. The solid line shows the pressure distribution found when the interaction between the shock wave and boundary layer is accounted for using the method presented in this paper,[23] with $x_0^* = -15$.

Finally, figure 6 shows a comparison of c_f with measured values from ref. 21, with $x_0^* = -14$, for $M_e = 1.15$, $Re = 7 \times 10^6$, wall temperature = 15°C, $\bar{P}_{te} = 137.9$ k Pa gauge, $\bar{\delta} = 0.305$ cm. Using these values, calculated parameters are[6] $\epsilon = 0.120$, $u_\tau = 0.0397$, $\delta = 0.016$, $\Pi = 0.312$. The origin in this figure, set to agree with that used in ref. 21, is at $P_w/P_{te} = 0.528$.

It is seen from the comparisons with experiment that quite good accuracy may be obtained with the equations presented here. The obvious simplicity of these results, when compared with numerical computations or even ad hoc models, coupled with this accuracy would seem to make them very appealing to use in practical airfoil calculations. In this regard, the equations presented for the skin friction appear to give adequate preductions of incipient separation.[6]

The present results, therefore, (a) are expressed by simple functions of distance with dependence on parameters shown explicitly; (b) are based on a systematic approximation to the equations of motion; and (c) for the cases shown, reproduce numerical and experimental results quite well. Furthermore, by use of results given in Ref. 5 the pressure distribution away from the wall can also be calculated. Several comments should be made, however, concerning values of constants and expected accuracy.

(1) The tentative value $x_0^* = -14$ is a rough estimate based on a comparison with two measured pressure distributions, and perhaps should be improved.

(2) Additional uncertainties appear in both theory and experiment. The shock-wave position is unsteady because of turbulent fluctuations in the boundary layer, and the largest measured dP_w/dX and $dc_f/d^{\vee}$ are therefore at least slightly reduced. If even a very thin separation bubble is present, the beginning of the pressure rise will be moved somewhat upstream. In the theory, some simplifying approximations have been introduced here in the expressions derived in ref. 5 for $X_s(0)$ and for the second term in m. Moreover, omitted terms of still higher order than retained in ref. 5 might be numerically important.

(3) The origin $x = 0$ has been placed at the intersection of the shock wave with the edge of the boundary layer; the position estimated from numerical potential-flow solutions alone is not sufficiently accurate. Perturbations in the external flow resulting from the local boundary-layer displacement effect must therefore be calculated, so that x can be measured from the perturbed shock wave position. For the simplest correction method, P_w obtained for the undisturbed shock wave can be used in the boundary-layer equations for calculation of the displacement thickness as a function of X in the interaction region. Calculation of the potential flow over the new equivalent body then gives the perturbed shock wave shape, and the origin for P_w can then simply be shifted appropriately. In this calculation, the neglect of P_Y is not justified; however, the error arises primarily for $X_u < X < X_d$, where the interpolation formula for P_w has been used. In a sense, then, this additional approximation can be regarded instead as a kind of interpolation for the displacement thickness, and probably introduces very little additional error.

(4) The theory was derived for unseparated flows with $u_\tau << \epsilon << 1$, but the approximate version, with the straight-line interpolation, is being proposed for use in a broader range. For figure 3, as noted in ref. 6, it is believed that a very thin separation bubble was present in the experiment. For figure 4, the Mach number is low enough that $u_\tau/\epsilon \approx 0.4$, which is certainly not very small. More comparisons with experimental data are needed to provide a better guide to the parameter ranges for which the approximation might remain reasonable.

This work was supported by NASA Langley Research Center, Grant NSG 1326

REFERENCES

1. Adamson, T.C., Jr., and Feo, A., Interaction between a Shock Wave and a Turbulent Boundary Layer in Transonic Flow, SIAM J. Appl. Math. 29 (1975), 121-145.

2. Melnik, R.E., and Grossman, B., Analysis of the Interaction of a Weak Normal Shock Wave with a Turbulent Boundary Layer, AIAA Paper No. 74-598 (1974).

3. Melnik, R.E., and Grossman, B., Further Developments in an Analysis of the Interaction of a Weak Normal Shock Wave with a Turbulent Boundary Layer, Symposium Transsonicum II, K. Oswatitsch and D. Rues, eds., Springer, Berlin (1976), pp. 262-272. See also Transonic Flow Problems in Turbomachinery, T.C. Adamson, Jr., and M.F. Platzer, eds., Hemisphere Publ. Co., Washington, D.C. (1977), pp. 415-433.

4. Adamson, T.C., Jr., and Messiter, A.F., Normal Shock Wave-Turbulent Boundary Layer Interactions in Transonic Flow near Separation, Transonic Flow Problems in Turbomachinery, T.C. Adamson, Jr., and M.J. Platzer, eds., Hemisphere Publ. Co., Washington, D.C. (1977), pp. 392-414.

5. Messiter, A.F., Interaction between a Normal Shock Wave and a Turbulent Boundary Layer at High Transonic Speeds. Part I: Pressure Distribution, ZAMP 31 (1980), 204-226.

6. Liou, M.S., and Adamson, T.C., Jr., Interaction between a Normal Shock Wave and a Turbulent Boundary Layer at High Transonic Speeds. Part II: Wall Shear Stress, ZAMP 31 (1980), 227-246.

7. Adamson, T.C., Jr., The Structure of Shock Wave-Boundary Layer Interactions in Transonic Flow, Symposium Transsonicum II, K. Oswatitsch and D. Rues, eds., Springer, Berlin (1976), pp. 244-251.

8. Adamson, T.C., Jr., and Messiter, A.F., Analysis of Two-Dimensional Interactions between Shock Waves and Boundary Layers, Ann. Rev. Fluid Mech. 12 (1980), 103-138.

9. Stewartson, K., Multistructured Boundary Layers on Flat Plates and Related Bodies, Advances in Applied Mechanics 14 (1974), 145-239.

10. Bush, W.B., and Fendell, F.E., Asymptotic Analysis of Turbulent Channel and Boundary-Layer Flow, J. Fluid Mech. 56 (1972), 657-681.

11. Mellor, G.L., The Large Reynolds Number Asymptotic Theory of Turbulent Boundary Layers, Int. J. Eng. Sci. 10 (1972), 851-873.

12. Yajnik, K.S., Asymptotic Theory of Turbulent Shear Flows, J. Fluid Mech. 42 (1970), 411-427.

13. van Driest, E.R., Turbulent Boundary Layer in Compressible Fluids, J. Aero. Sci. 18 (1951), 145-160.

14. Maise, G., and McDonald, H., Mixing Length and Kinematic Eddy Viscosity in a Compressible Boundary Layer, AIAA J. 6 (1968), 73-80.

15. Coles, D.E., The Law of the Wake in the Turbulent Boundary Layer, J. Fluid Mech. 1 (1956), 191-226.

16. Liou, M.S., Asymptotic Analysis of Interaction between a Normal Shock Wave and a Turbulent Boundary Layer in Transonic Flow, Ph.D. Thesis, The University of Michigan, Ann Arbor, Michigan (1977).

17. Cebeci, T., and Smith, A.M.O., Analysis of Turbulent Boundary Layers, Academic Press, New York (1974).

18. Viegas, J.R., and Coakley, T.J., Numerical Investigation of Turbulence Models for Shock-Separated Boundary Layer Flows, AIAA J. 16 (1978), 293-294.

19. Adamson, T.C., Jr., Liou, M.S., and Messiter, A.F., Interaction between a Normal Shock Wave and a Turbulent Boundary Layer at High Transonic Speeds, NASA CR 3194 (1980).

20. Ackeret, J., Feldmann, F., and Rott, N., Untersuchungen an Verdichtungsstössen und Grenzschichten in schnell bewegten Gasen, Mitteilungen aus dem Inst. für Aerodynamik, ETH Zürich, Nr. 10 (1946). Translated as NACA TM 1113 (1947).

21. Gadd, G.E., Interactions between Normal Shock Waves and Turbulent Boundary Layers, A.R.C. 22559, R & M 3262 (1961).

22. Sajben, M., and Kroutil, J.C., Unsteady Transonic Flows in a Two-Dimensional Diffuser, AFOSR-TR-78-1277 (1978).

23. Liou, M.S., McDonnell Douglas Research Labs, Box 516, St. Louis, MO 63166, Private Communication.

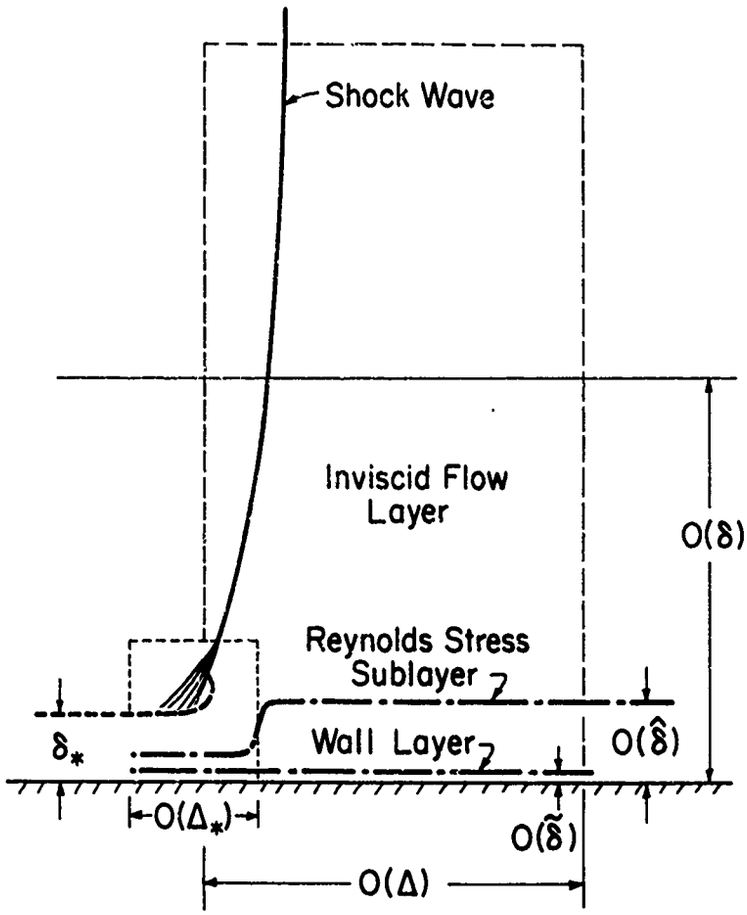


Figure 1. Sketch showing main part of interaction region ($x = O(\Delta)$, $y = O(\delta)$), thin upstream region containing upstream influence ($x = O(\Delta_*)$, $y = O(\delta_*)$) and Reynolds stress sublayer and wall layer in each region.

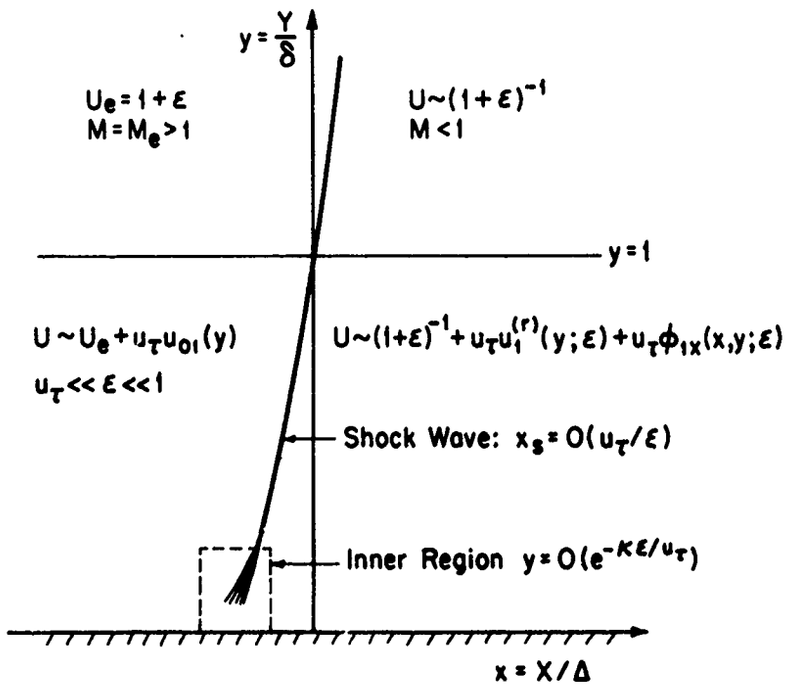


Figure 2. Asymptotic representation of flow in outer inviscid flow layer.

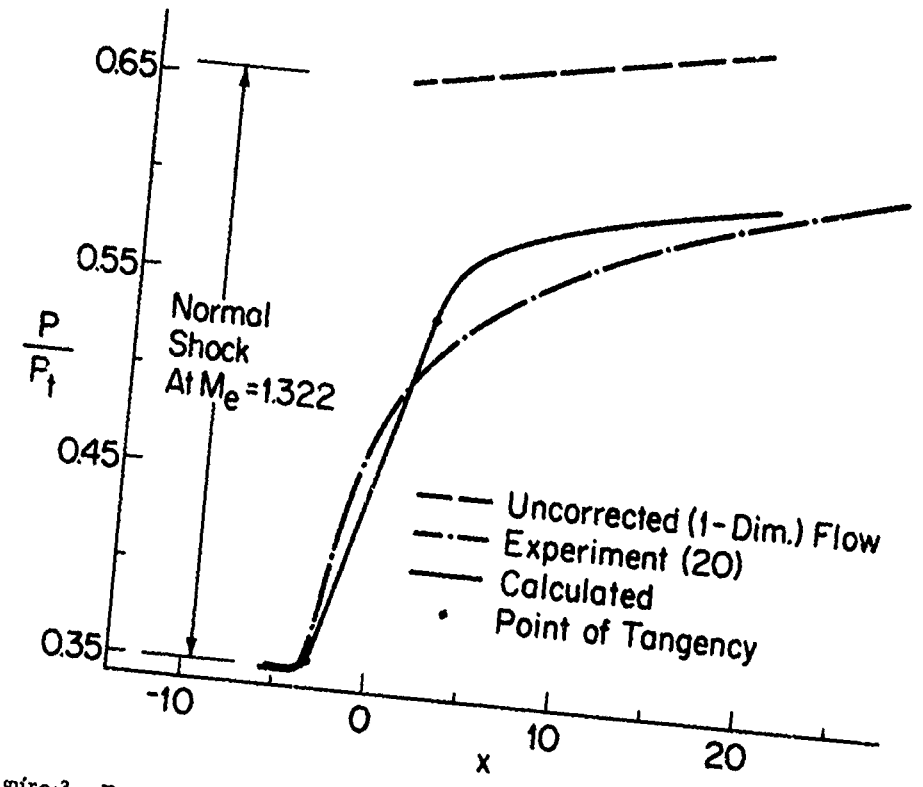


Figure 3. Pressure at wall with longitudinal curvature: $M_e = 1.322$, $Re = 9.6 \times 10^5$; $P_d(X)$ is calculated from solutions given in reference 5, with curvature effect included.

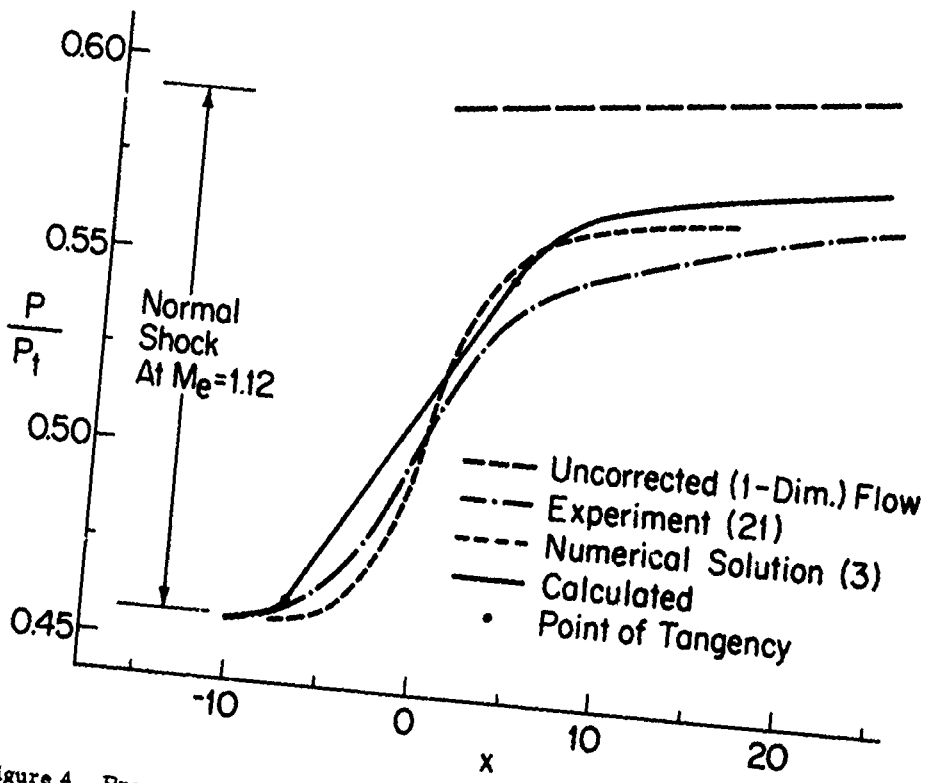


Figure 4. Pressure at wall of circular pipe: $M_e = 1.12$, $Re \approx 6 \times 10^6$; $P_d(X)$ is calculated from solutions given in reference 5, with effect of finite pipe radius ($\delta/R \approx 0.055$) included.

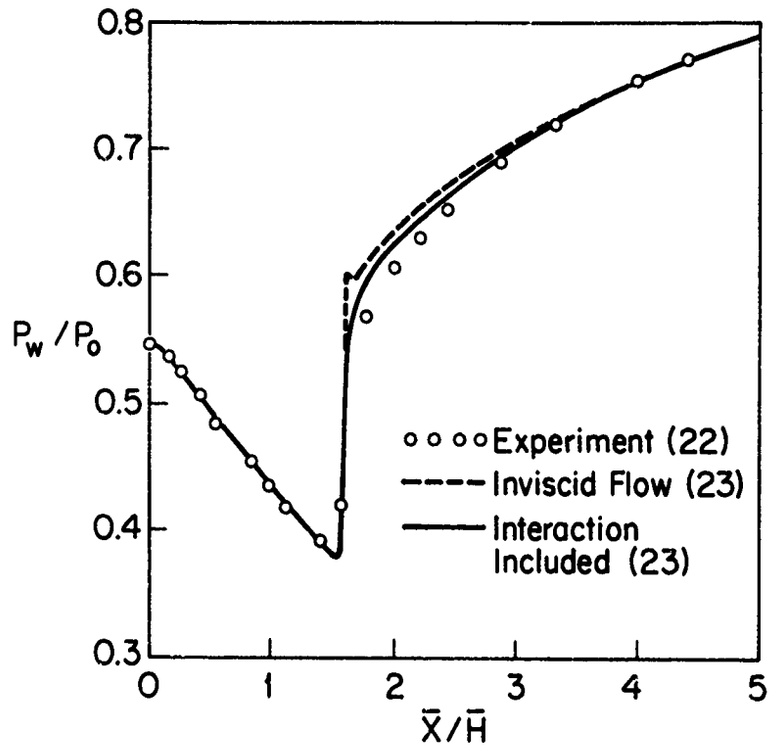


Figure 5. Pressure at upper wall in transonic channel flow. Ratio of static pressure at exit to stagnation pressure at inlet is 0.81. M_e is 1.25, $Re_\theta = 1.70 \times 10^4$ = Reynolds number based on momentum thickness. Effects of interaction calculated using present method. ($\bar{H}$ = throat height)

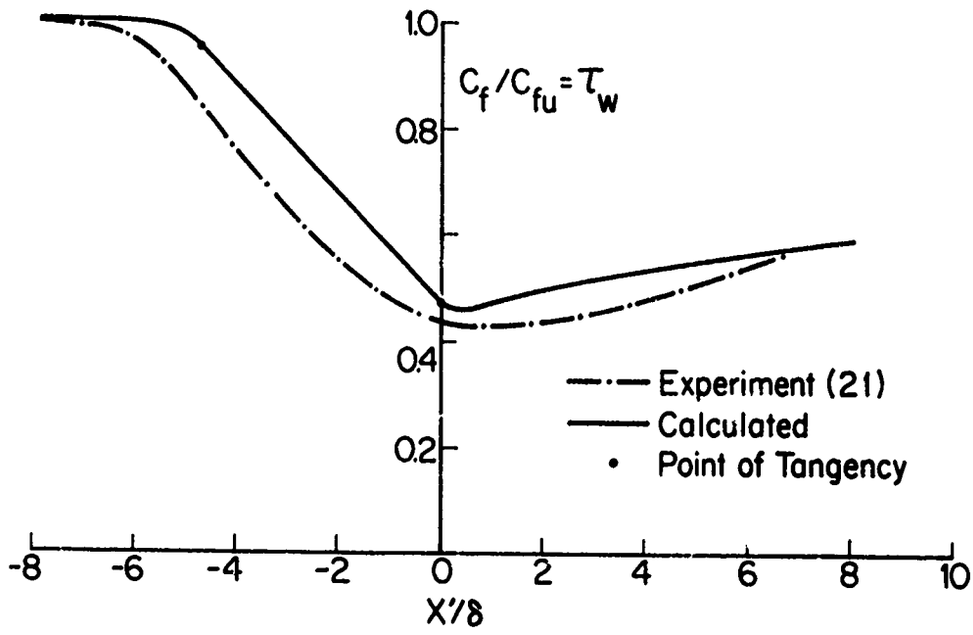


Figure 6. Skin friction on wall of circular pipe; $M_e = 1.15$, $Re = 7 \times 10^6$. Here, $X'/\delta = 0$ at $P_w/P_{te} = 0.528$.

NORMAL SHOCK-TURBULENT BOUNDARY LAYER INTERACTION AT A CURVED WALL

by
R. Bohning and J. Zierep
Institut für Strömungslehre und Strömungsmaschinen
Universität (TH) Karlsruhe
Kaiserstrasse 12, 7500 Karlsruhe

SUMMARY

A survey on our investigations of the interaction between a weak normal shock and a two-dimensional compressible turbulent boundary layer is presented. The theoretical results are compared with some measurements.

In our analytical model we devide the flow into three domains: a thin viscous sublayer (, which is different from the laminar sublayer,) adjacent to the wall, an inviscid shear layer and an inviscid transsonic potential flow. With regional solutions in closed form, which are coupled iteratively, we obtain the pressure and velocity distribution in the boundary layer. The thickness of the viscous sublayer is an essential parameter of the whole interaction problem. A characteristic behaviour of the gradient of the wall-shear-stress in flow direction is used to determine the thickness parameter. The result is confirmed by another independent analytical solution which we have derived recently using the method of matched asymptotic expansions. The theory includes the prediction of the incipient shock induced separation as a limiting case. With the condition of vanishing wall-shear-stress an analytical criterion follows from the explicit solution near the wall. We present a diagram which yields the combination of Mach number and Reynolds number which will result in separation for a given wall curvature and shape factor of the undisturbed velocity profile.

1. INTRODUCTION

The interaction between shock waves and boundary layers is of importance in many aerodynamic situations such as the transsonic flow around profiles. Often a shock causes flow separation and thereby produces global disturbances of the flow field. After the basic publications of Ackeret, Feldmann and Rott (1946) and Lighthill (1953) recently the problem of shock-boundary layer interaction has been treated in some experimental [e.g. 3,4,5] and theoretical investigations [e.g. 6,7] considering the flow along a plane wall as a rule. We include the wall curvature in the present survey on our investigations of the interaction between a weak normal shock and a compressible turbulent boundary layer. The analytical results are tested with a new independent solution and compared with measurements.

2. MODEL FOR FLUID FLOW, METHOD OF SOLUTION

Fig. 1 illustrates the model used. The turbulent, compressible boundary layer at a curved wall in transsonic slightly super-

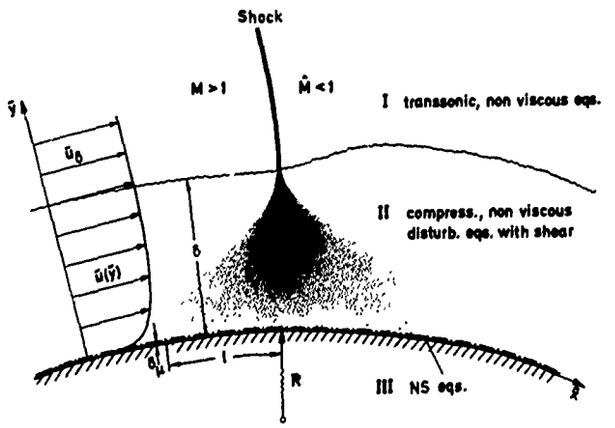


Fig. 1 Schematic flow model

sonic flow (Fig. 1 left) is disturbed by a weak normal shock (Fig. 1 middle). In the way as Lighthill [2] has done we divide the fluid field into three domains (Fig. 1 right). We distinguish between a frictionless, transsonic flow outside the boundary layer (I), an outer compressible boundary layer (II), in which the friction is considered to be due only to the prescribed velocity profile and a very thin compressible boundary layer (III) in the immediate neighbourhood of the wall where friction is fully efficient.

In the outer flow near the shock we use the solution for a shock at a curved wall of Oswatitsch and Zierep [8] in a generalized form. For larger distances from the shock this solution is given in form of a Fourier-expansion of the transsonic equation [9]. The flow in the outer boundary layer is given by a solution of a boundary value problem. For different classes of the undisturbed, turbulent velocity profile (velocity-distribution that can be approximated by power law functions in the outer boundary layer) we can give the solution in closed form by using confluent hypergeometric series [10]. The solution of the linearized Navier-Stokes-equations close to the wall gives on the one hand the thickness of the friction layer δ_μ and on the other hand - in combination with a suitable law of wall for the undisturbed profile - the wall shear stress.

The solutions of the outer flow and those in the outer boundary layer are iteratively coupled in the following way. First we state a pressure jump (pressure distribution 0th order) at the outer edge of the boundary layer and solve the boundary value problem. As a result we get the vertical component of the velocity v at the outer edge of the boundary layer. This value v is used in the solution of the frictionless outer flow. The resulting pressure distribution (1st order) at the edge of the boundary layer is quite different from the primary pressure jump. In particular behind the shock a pronounced deformation of the pressure curve appears, the well known post-shock expansion, which is due to the displacement of the boundary layer and the curvature of the wall; both effects are of comparable magnitude as a rule. This new pressure distribution is used again as a new boundary condition for the outer boundary layer. In this way we solve the boundary value problem again. In the boundary layer we get the pressure- and velocity distribution in closed form.

3. RESULTS

Fig. 2 shows a typical example of the pressure distribution for different wall distances; $y = 0$ means the wall, $y = 1$ the outer edge of the boundary layer. The Reynolds number is based on the critical speed of sound and the boundary layer thickness. The parameter α represents the exponent of the power law function of the undisturbed velocity profile. The wall curvature is given by the nondimensional radius R/δ. The influence of the shock reaches over 2-3 boundary layer thicknesses upstream. At the edge of the boundary layer both the curvature of the flow field and the displacing effect of the boundary layer causes a post-shock expansion. This behaviour was first observed experimentally in [1] and later found theoretically in the inviscous case by Oswatitsch and Zierep [8], too.

The structure of the flow field is given in Fig. 3 by the lines of constant Mach number. The isolines are lifted already upstream of the shock and even more strongly behind according to the impressed pressure distribution. Accordingly the boundary layer thickness increases and the wall shear stress decreases. Thus flow separation can occur if the Mach number ahead of the shock is too large.

The consideration of the lines of constant density in the fluid field allows a comparison with interferometric measurements (see chapter 7) and is therefore of special interest. Fig. 4a,b show two calculated isochoric fields, left for flow along a plane wall, right for a curved wall. Accordingly the density ratio ρ/ρ_0 outside the boundary layer is constant in y-direction (Fig. 4a left) or dependent on y (Fig. 4b left). Immediately behind the shock ($x \approx 0$) in both cases we register an after expansion. Comparing the numerical values we see that this expansion is considerably stronger in the case of a curved wall. This has an influence on the density distribution in the boundary layer. In Fig. 4b the isochoric lines run less steeply to the wall than in Fig. 4a and end there tangentially. Near the wall these lines may abruptly change their direction (Fig. 4a, $x > 0$). In this case we have separation of fluid flow.

4. CRITERION FOR INCIPIENT SEPARATION

With the condition of vanishing wall shear stress an analytical criterion [11] for the beginning shock induced separation follows from the explicit solution in the neighbourhood of the wall [10]. The result is shown in Fig. 5. The diagram yields the combination of Mach number and Reynolds number which will result in separation for a given wall radius R/δ and shape factor α of the undisturbed velocity profile. We get different curves with (---) and without (—) post-shock expansion. Below the solid curve we have no separation at all, above the dashed curves - belonging to different wall cur-

vatures - the flow must separate. The plane wall (limit $R/\delta \to \infty$) corresponds in good approximation to the curve $R/\delta = 1000$. The influence of the wall curvature is such that increasing curvature reduces the tendency to separation. The reason for this behaviour is that the post-shock expansion becomes stronger with increasing wall curvature. Down through the boundary layer the post-shock expansion influences the flow parameters at the wall and therefore counteracts a possible separation.

The solution depends on the kind of the incoming velocity profil, that means, the upstream history of the flow must be given as initial value in our theory. The diagram (Fig. 5) is valid only for a special combination of the Reynolds number, shape factor α and wall shear stress of the basic flow, which represents a fully developed turbulent flow. For other classes of the undisturbed velocity profil we get different diagrams. Before comparing the diagram (Fig. 5) with experimental results one has to make sure if the relation between the Reynolds number, shape factor and basic wall shear stress is really the same in the experiment.

5. DETERMINATION OF THE VISCOUS SUBLAYER THICKNESS

The solutions in the three layers contain the thickness δ_μ of the viscous sublayer as a parameter. Therefore the exact determination of δ_μ is of importance for the whole problem. An analytical relation between the dimensionless thickness $y_0 = \delta_\mu/\delta$ on the one hand and the Reynolds number Re_δ and the shape factor α of the undisturbed velocity profile on the other hand was derived as follows in [11]

(1)
$$y_0 = 1.14 \left(\frac{1}{Re_\delta} \right)^{\frac{1}{2+\alpha}} , \qquad 5 \cdot 10^3 \lesssim Re_\delta \lesssim 5 \cdot 10^5$$

This relation differs from the one for the laminar sublayer. The thickness parameter y_0 depends on the Reynolds number. Hence the turbulent character of the flow is included in the disturbance equations, too. In this way scaling effects due to the turbulent Reynolds stresses are taken into account approximately.

The determination of y_0 is based on the fact that the gradient of the wall-shear-stress in x-direction at a fixed position x_0 shows a characteristic behaviour when y_0 being varied. For a fixed y_0 a minimum occurs. At this position the influences of the viscous sublayer and of the outer shear-layer counterbalance evidently. The condition

(2)
$$\frac{\partial}{\partial y_0} \left[\frac{\partial \tau_w}{\partial x} \right]_{x = x_0} = 0$$

is regarded therefore as a defining equation for the parameter y_0.

6. MATCHED ASYMPTOTIC EXPANSIONS IN THE BOUNDARY LAYER

Using an independent way solutions in the outer and inner boundary layer were derived with matched asymptotic expansions in order to confirm the described theory. The solution from [10] for the limiting case $y \to 0$ is used as a first-order outer expansion. A suitable inner expansion, which can be matched for $Y = y/\bar{y}_0 \to \infty$ to the outer expansions, follows from the solution of the disturbance equations near the wall in terms of modified Bessel functions. The result for the velocity disturbance u_s parallel to the wall is compared with the theory of Bohning and Zierep in Fig. 6. It is seen that the dashed curve (---) calculated according to [10] and both first-order expansions (——) show good conformity in the asymptotic behaviour near the wall ($y \to 0$) as well as at the edge of the bourdary layer ($y \to 1$). This means that the parameter y_0 is determined correctly by the condition (2). The solution of Bohning and Zierep can be called a "composite expansion" in the sense of asymptotic series expansions. An estimation of the order of magnitude in the disturbance equation to the wall written in stretched coordinates ($X = x$; $Y = y/\bar{y}_0$) leads to a general analytic expression for the stretching factor $\bar{y}_0$ in the form

(3)
$$\bar{y}_0 \sim \left(Re_\delta \cdot \left. \frac{d M_0^*}{dy} \right|_{y=0} \right)^{-1/3}$$

where M_0^* is the distribution of the Mach number in the undisturbed boundary layer. This distribution is assumed to be a

linear function of $\bar{y}_0$ near the wall. Specially for the velocity profile used in [10,11] as given with

$$M_0^*(y) = \begin{cases} y^\alpha & ; \quad \bar{y}_0 \le y \le 1 \\ M_0^*(\bar{y}_0)\,\dfrac{y}{\bar{y}_0} & ; \quad 0 \le y < \bar{y}_0 \end{cases} \tag{4}$$

it sollows from (3)

$$\bar{y}_0 \sim \left(\frac{1}{Re_\delta}\right)^{\frac{1}{2+\alpha}} \tag{5}$$

This is in agreement with the relation (1) for the thickness of the viscous sublayer. The stretching factor $\bar{y}_0$ is therefore essentially identical with the relation for the thickness of the friction layer [11].
If we use instead of the linear assumption (4) a more accurate for M_0^*according to the logarithmic law for the velocity and compare the result with (5), we get only minor differences in the domain $Re_\delta < 1.5 \cdot 10^5$.

In order to get the thickness of the friction layer it is therefore sufficient to use (4); only small errors in the velocity disturbances will occur. Calculating the wall shear stress however we must proceed much more carefully. Here we use for the undisturbed flow a relation for

$$\left.\frac{d\,M^*}{dy}\right|_{y=0}$$

that results from the logarithmic law of the velocity.

7. COMPARISON WITH MEASUREMENTS

In the supersonic tunnels of our institute some measurements were done in order to proof our theoretical results. In a two-dimensional test section a steady shock wave was studied at different curved walls.

Fig. 7a shows a schlierenpicture of one of these flows. A nearly normal shock at the end of a supersonic region (left) runs in a turbulent boundary layer near the wall. The darkness behind the shock means an acceleration of the flow in horizontal direction. The structure of that field of acceleration agrees well with the theoretical result [9] (Fig. 7b) that is used as boundary condition behind the shock for outer boundary layer. The influence of wall curvature and of displacement of the boundary layer is of comparable magnitude according to experiments and theory.

Fig. 8 shows a typical example for the measured wall pressure distribution. Because of the wall curvature the pressure distributions for the plane wall and the curve wall differ considerably.

The same behaviour is found theoretically, too. In Fig. 9 we see the calculated wall pressure [10] for a plane wall (——) and for curved wall (-·-·-). The second curve may be compared with the experimental result given by Ackeret, Feldmann and Rott (---). The two curves agree basically. In the neighbourhood of the shock there is a small difference in the pressure gradient. At some distance downstream the theoretical pressure distribution lies some what above the measured result. This seems to be typical for those shock-boundary layer problems; we find them in other publications, too [e.g. 7, 12]. The reason for this is evidently the difference between theoretical assumptions and experimental realizations (e.g. nonsteady shock wave).

For quantitative studies we have made Mach-Zehnder-Differentialinterferograms of the flow field. The interferograms Fig. 10a and b are the experimental analogies to the theoretical results Fig. 4a and b. By comparison we see that the fluid fields agree very well even in details. Especially the bending of the isochoric lines in the neighbourhood of the wall is just the same (Fig. 10a and Fig. 4a) in the experiment. That means that we have separation at the plane wall while we have no separation at the curved wall at the same Mach number M_δ (Fig. 10b).

Due to this different behaviour of the isochoric lines near the wall (bending or tangential) we get upper and lower limits for the Mach number for starting of separation in other cases, too.

Some results are given in Fig. 11. The filled points (●) represent those measured values where separation was observed with confidence, the open points (○) indicate where no separation was observed at a given Reynolds number and wall curvature. The lines between the points show the theoretical values for beginning separation. Within the accuracy of the measurements the agreement between the experimental and the theoretical results is good. The triangles represent a new measurement published recently by Stanewsky [13]. At a Mach number of 1.24 no separation has been found at all. At the Mach number approximately 1.3 a very small separation bubble, visualized with colored oil, has been observed. The separation Mach number must have been therefore slightly under this value. This is in very good agreement with our theoretical prediction.

LITERATUR

[1] Ackeret J., Feldmann F., Rott N.: Untersuchungen an Verdichtungsstößen und Grenzschichten in schnell bewegten Gasen. Mitteilungen aus dem Institut für Aerodynamik, ETH Zürich, Nr. 10, 1946

[2] Lighthill M.J.: On Boundary Layers and Upstream Influence, II. Supersonic Flow Without Separation. Proc. Royal Soc., A 217 No. 1131, 1953, pp 479-507

[3] Gadd G.E.: Interactions between Normal Shock Waves and Turbulent Boundary Layers. R & M, 3262, 1961

[4] Kooi J.W.: Experiment on transsonic shock-wave boundary layer interaction. NLR MP 75002 U, 1975

[5] East L.F.: The application of a laser anemometer to the investigation of shock-wave boundary layer interactions. AGARD-CP-193, 1976

[6] Melnik R.E., Grossmann B.: Analysis of the Interaction of a Weak Normal Shock Wave with a Turbulent Layer. AIAA Paper 74-598, 1974

[7] Inger G.R., Mason W.H.: Analytical Theory of Transsonic Normal Shock-Turbulent Boundary-Layer Interaction. AIAA J. 14, 1266, 1976

[8] Oswatitsch K., Zierep J.: Das Problem des senkrechten Stoßes an einer gekrümmten Wand. ZAMM 40, 143-144, 1960, Tagungsheft

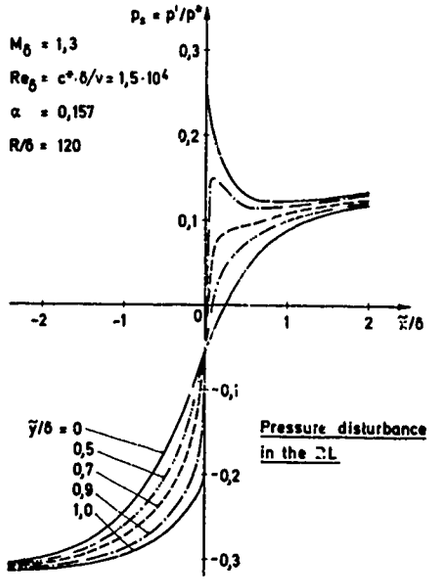
[9] Bohning R.: Untersuchung der Nachexpansion hinter einem senkrechten Verdichtungsstoß an der gekrümmten Wand. Recent Developments in Theoretical and Experimental Fluid Mechanics. Edited by: Müller U., Roesner K.G., Schmidt B., Springer Verlag, pp. 39-47 (1979)

[10] Bohning R., Zierep J.: Der senkrechte Verdichtungsstoß an der gekrümmten Wand unter Berücksichtigung der Reibung. ZAMP 27, 225-240, 1976

[11] Bohning R., Zierep J.: Bedingung für das Einsetzen der Ablösung der turbulenten Grenzschicht an der gekrümmten Wand mit senkrechtem Verdichtungsstoß. ZAMP 29, 130-198, 1978

[12] Messiter A.F.: Interaction between a Normal Shock Wave an a Turbulent Boundary Layer at High Transonic Speeds. Part I: Pressure Distribution. ZAMP 31, 1980, pp. 204-226

[13] Stanewsky E.: Transsonische Profile im Experiment. DFVLR-Nachrichten Heft 30, Juni 1980.



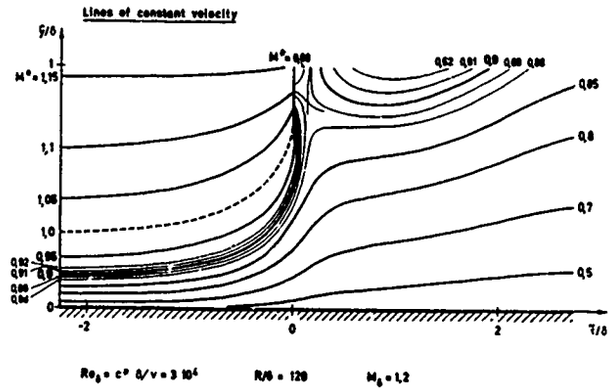


Fig. 3 Lines of constant velocity

◀ Fig. 2 Pressure distribution in the boundary layer

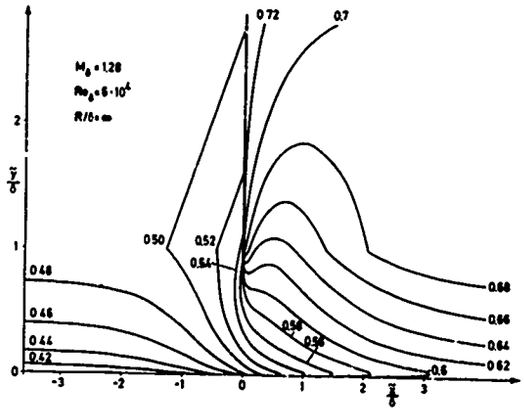


Fig. 4a Lines of constant density ρ/ρ_0

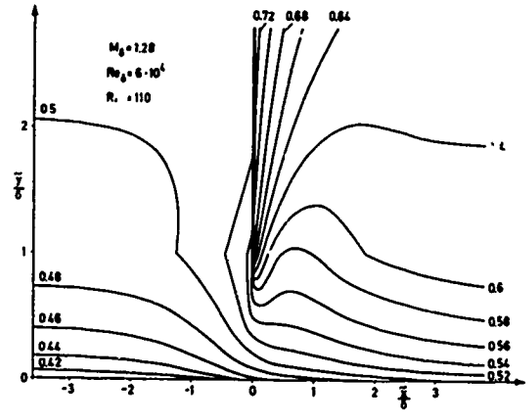


Fig. 4b Plane wall a, curved wall b

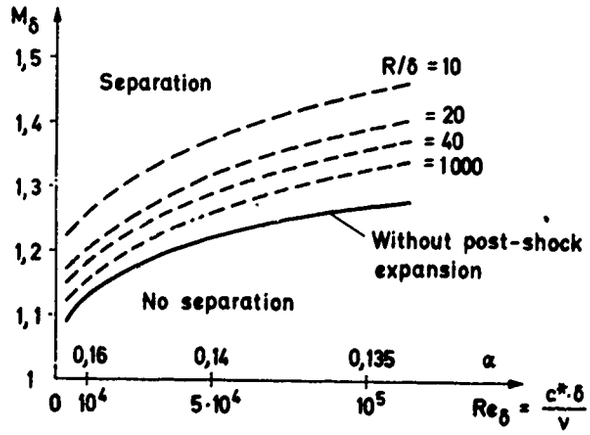


Fig. 5 Criterion for incipient separation

Fig. 6

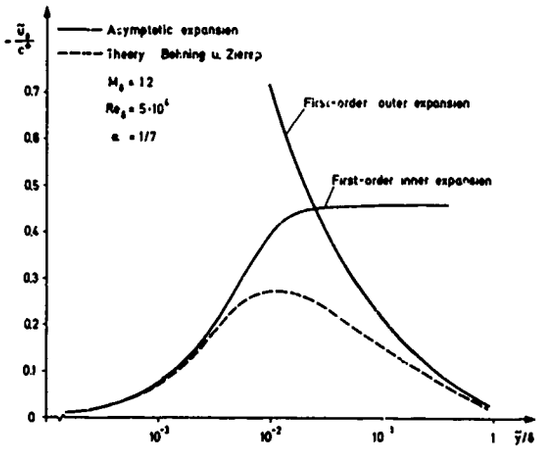
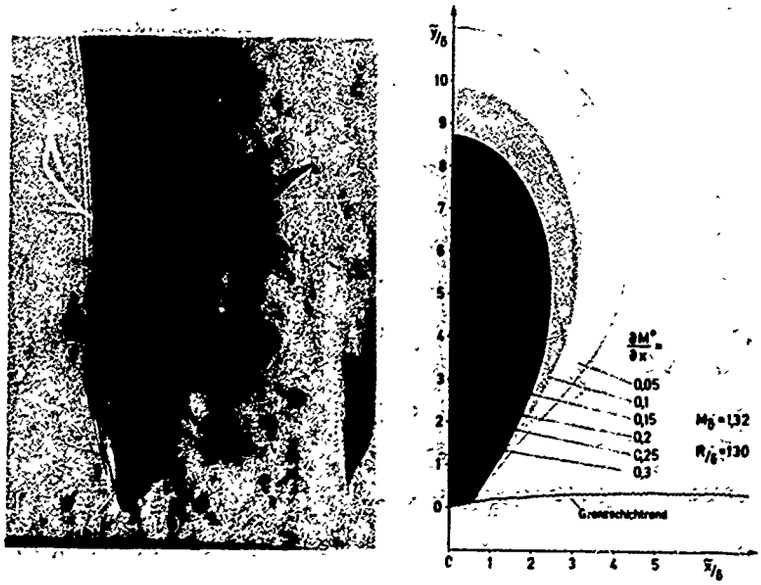


Fig. 7

a) Schlieren picture of normal shock-wave boundary-layer interaction

b) Structure of the acceleration field (theoretically)



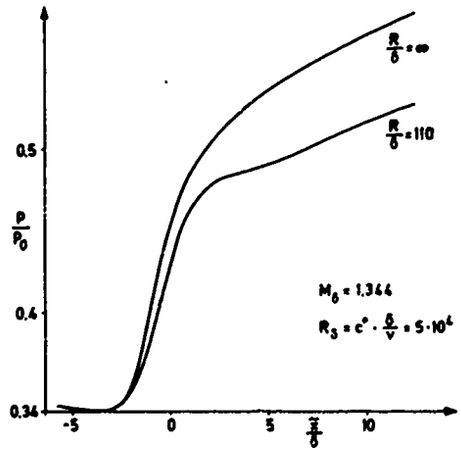
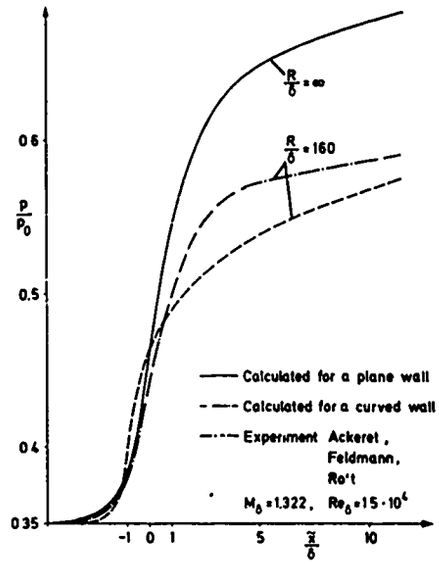


Fig. 8 Measured surface pressure distribution for a plane and a curved wall

Fig. 9 Calculated surface pressure distribution for a plane (——) and a curved (-·-·-) wall. Comparison with the measurement of Ackeret, Feldmann and Rott (---).



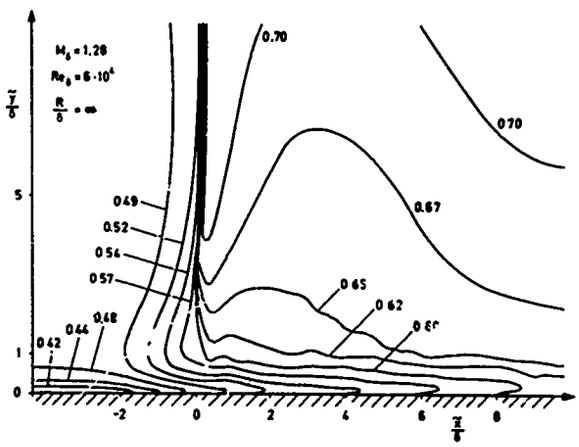


Fig. 10a Measured lines of constant density ρ/ρ_0 for a plane wall

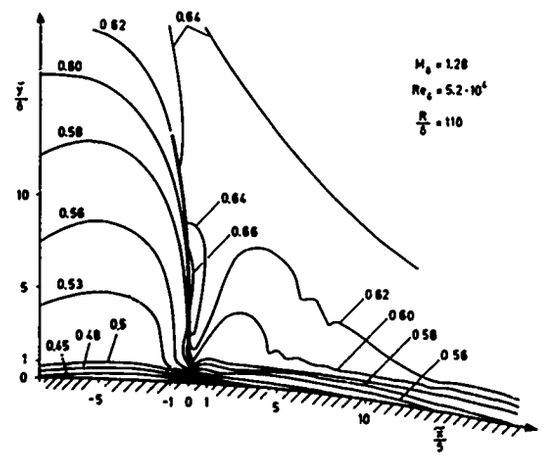


Fig. 10b Measured lines of constant density ρ/ρ_0 for a curved wall

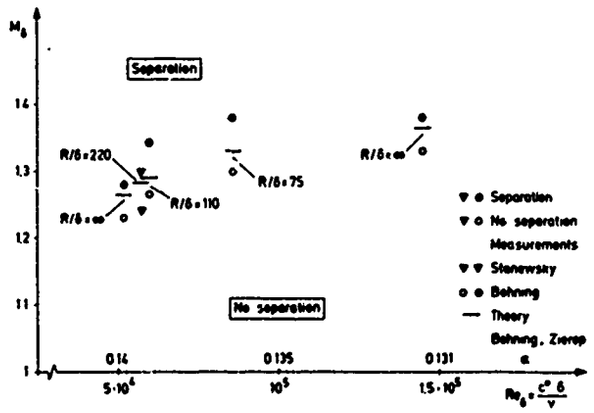


Fig. 11

"SOME FEATURES OF A SHOCK - TURBULENT BOUNDARY LAYER INTERACTION THEORY IN TRANSONIC FLOW FIELDS"

G. R. Inger†
Virginia Polytechnic Institute and State University
Blacksburg, Va. 24061

AGARD SYMPOSIUM ON "COMPUTATION OF VISCOUS - INVISCID INTERACTIONS"
(Colorado Springs, Sept. 1980)

Abstract

Shock-boundary layer interaction can significantly influence not only the local transonic flow on missiles, wings and turbine blades but its influence can also extend significantly downstream within the boundary layer and thereby alter the global aerodynamic properties of lift, drag and pitching moment. It is therefore important that shock-boundary layer interactions and their Reynolds and Mach number scaling be fundamentally understood and appropriate theoretical tools be developed for their prediction in engineering applications. This paper describes the features of an approximate non-asymptotic triple deck theory of shock-turbulent boundary layer interaction that accurately describes non-separating two dimensional flows over a wide range of practical Reynolds numbers and its application as an element in the overall viscous flow analysis of the body. Two main aspects of the problem are examined: (1) The local interactive thickening and skin friction drop in the shock foot region, including the effects of the incoming boundary layer shape factor, wall curvature, an improved "viscous ramp" model of the interaction and an approximate prediction of incipient separation behavior; (2) The significant influence of such interaction on the subsequent downstream turbulent boundary layer thickening, profile shape and skin friction behavior. Comparisons with experimental data are given and applications presented for both supercritical airfoils and transonic bodies of revolution.

Nomenclature

A	Van Driest-Cebeci wall turbulence damping parameter
C_f	skin friction coefficient, $2\tau_w/\rho_{e_0} U_{e_0}^2$
C_p	pressure coefficient, $2\ p'/\rho_{e_0} U_{e_0}^2$
H	boundary layer shape factor, δ^*/θ^*
H_i	incompressible shape factor
M	Mach number
p	static pressure
p'	interactive pressure perturbation, $p-p_1$
Δp	pressure jump across incident shock
Re_ℓ, $Re\delta$	Reynolds numbers based on length ℓ and boundary layer thickness, respectively
T	absolute temperature
$\bar{T}$	basic interactive wall-turbulence parameter (see Eq. 23)
u', v'	streamwise and normal interactive disturbance velocity components, respectively
U_0	undisturbed incoming boundary layer velocity in x-direction
x, y	streamwise and normal distance coordinates (origin at the inviscid shock intersection with the wall)
$y_{w_{eff}}$	effective wall shift seen by interactive inviscid flow (see Fig. 3)
ε	$\sqrt{M_1^2-1}$
γ	specific heat ratio
δ	boundary layer thickness
δ^*	boundary layer displacement thickness
δ_{SL}	inner deck sublayer thickness
ε_T	kinematic turbulent eddy viscosity
ε_T'	interactive perturbation of turbulent eddy viscosity
η	y/δ_0
μ	ordinary coefficient of viscosity
ν	μ/ρ

---

†Professor of Aerospace and Ocean Engineering

ω	viscosity-temperature dependence exponent, $\mu \sim T^{\omega}$
ρ	density
θ^{**}	boundary layer momentum thickness
τ	total shear stress
τ'	interactive perturbation of total shear stress

Supscripts

1	undisturbed inviscid values ahead of incident shock
e	conditions at the boundary layer edge
inc	incompressible value
inv	inviscid disturbance solution value
o	undisturbed incoming boundary layer properties

1. INTRODUCTION

Shock-boundary layer interaction can significantly influence the transonic flowfield and aerodynamics of missile wings and turbine blades. This influence is not only local but can also extend significantly downstream within the boundary layer and thereby alter the global properties of lift, drag and pitching moment. Some of the important effects that these interactions may exert even in the non-separating case are: (a) the interactive thickening slightly alters the large-scale local inviscid pressure and both the shock location and obliquity; (b) the interaction zone itself may not scale with the local boundary layer thickness, thereby introducing a kind of "unit Reynolds number" effect; (c) possible incipient local separation at the shock foot if the local shock strength is strong enough (and/or Reynolds number is low), which then drastically changes the entire nature and extent of the interaction to a larger scale one involving a bifurcated - shock interaction pattern; (d) an overall increase of the boundary layer displacement and momentum thicknesses downstream; (e) additional downstream distortion for some considerable distance of the more detailed boundary layer properties such as the shape factor and skin friction.

In view of these effects, it is important that shock-boundary layer interactions and their Reynolds and Mach number scaling be fundamentally understood and appropriate theoretical tools be developed for their prediction in engineering applications. This paper describes the features and applications of an approximate non-asymptotic triple-deck theory of transonic shock-turbulent boundary layer interaction which provides such a tool for non-separating two-dimensional flows over a wide range of practical Reynolds numbers. Section 2 contains a brief description of the foundation and essential features of the theoretical model including validating comparisons with experiment. It is shown how the theory is constructed to treat a wide range of practical Reynolds numbers and incoming turbulent boundary layer profile shapes, and how it may further be extended to treat moderately-curved as well as flat surfaces. Section 3 then describes the results of a comprehensive parametric study showing how the interactive pressure, displacement thickness and local skin friction distributions each depend on the shock strength, Reynolds number and shape factor. These results further provide an improved "viscous wedge" model of the local interaction which embodies proper scaling behavior as well as an approximate account of incipient separation that is in good agreement with experimental trends. In Section 4 we examine the application of this theory as an element in global viscous flow field analyses of both supercritical air-foils and transonic bodies of revolution. In such problems it will be shown that even in non-separating cases the changes across the interaction may significantly alter the subsequent turbulent boundary layer behavior for appreciable distances, especially when larger downstream adverse pressure gradients are present.

2. OUTLINE OF THE NON-ASYMPTOTIC SMALL DISTURBANCE INTERACTION THEORY

2.1) Rationale of Non-Asymptotic Triple Deck Approach

It is well-known[1] that when separation occurs, the disturbance flow pattern associated with a nearly-normal shock-boundary layer interaction is a very complicated one involving a bifurcated shock pattern, whereas the unseparated case pertaining to turbulent boundary layers up to roughly $M_1 \leq 1.3$ has instead a much simpler type of interaction pattern which is more amenable to analytical treatment (see Fig. 1). With some judicious simplifications, it is possible to construct a fundamentally-based approximate theory of the problem in the latter case, as documented in detail in Ref. 2-4. For purposes of orientation, a brief outline of this theory will be given here.

We consider small disturbances of an arbitrary incoming turbulent boundary layer due to a weak external shock (Fig. 2) and examine the detailed perturbation field within the layer. We purposely employ a non-asymptotic triple-deck flow model patterned in many ways after Lighthill's approach[5] because of its essential soundness[6] and adaptability to further improvement, because of its similarity to related types of multiple-deck approaches that have proven highly successful in treating turbulent boundary layer response to strong known adverse pressure gradients [7,8], because of the large body of turbulent boundary layer interaction data that supports the predicted results in a variety of specific problems, and finally because of our belief (confirmed strongly a posteriori) that asymptotic theory results for extremely high Reynolds numbers, although rigorous in this limit, do not extrapolate down to ordinary Reynolds numbers.

At high Reynolds numbers it has been established[2,9,10] that the local interaction disturbance field in the neighborhood of the impinging shock organizes itself into three basic layered-regions or "decks" (Fig. 2): 1) an outer region of potential inviscid flow above the boundary layer, which contains the incident shock and interactive wave systems; 2) an intermediate deck of frozen shear stress-rotational inviscid disturbance flow occupying the outer 90% or more of the incoming boundary layer thickness; 3) an inner shear-disturbance sublayer adjacent to the wall which accounts for the interactive skin friction perturbations (and hence any possible incipient separation) plus most of the upstream influence of the

interaction. The "forcing function" of the problem here is thus impressed by the outer deck upon the boundary layer; the middle deck couples this to the response of the inner deck but in so doing can itself modify the disturbance field to some extent, while the slow viscous flow in the thin inner deck reacts very strongly to the pressure gradient disturbances imposed by these overlying decks. This triple deck structure also has been employed in the theoretical studies of Gadd[11], Lighthill[5], Stratford[7], Honda[12] and others, and has been verified by a large body of experimental evidence and recent numerical studies with the full Navier-Stokes equations.[13] The essential correctness of this model is further supported by its success in related boundary layer perturbation problems involving viscous-inviscid interactions[14-17], turbulent boundary layer response to sudden changes in surface roughness or pressure gradient[18,19], and flow past various kinds of surface distortions[20-22] including skin friction measuring devices.[23-25]

While there is thus general agreement about the validity of the triple deck approach over a wide range of Reynolds numbers and the well-known qualitative differences in interactive response between laminar and turbulent flow (e.g., the much smaller upstream influence and larger separation-resistance of the latter), questions have been raised concerning (a) the relative interactive importance of the inner shear-disturbance deck and (b) the accuracy of deliberately using a non-asymptotic treatment of the details within the boundary layer. Regarding the first, we note that while asymptotic $Re_\ell \to \infty$ theory predicts an exponentially-small thickness and displacement effect contribution of the inner deck[9,10], this is not apparently true at ordinary Reynolds numbers, where many analytic and experimental studies[19,26-33] have firmly established that this deck, although indeed very thin, still contributes quite significantly to the overlying interaction and its displacement thickness growth. Bolstered by these facts, plus the unanimous conclusion reached in the detailed reviews by Green[33], Rose, Murphy and Watson[31] and Hankey and Holden[34] that the viscous sublayer is a very important component of turbulent interaction problems, we take the point of view here that the inner deck is in fact significant at the Reynolds numbers of practical interest. In this regard, we re-emphasize that this deck contains virtually all of the skin friction and incipient separation effects in any interaction, which alone are sufficient reasons to examine it in great detail. Regarding (b), it is pointed out that application of $Re_\ell \to \infty$ asymptotic theory results (no matter how rigorous in this limit) to ordinary Reynolds numbers is in itself an approximation which may in fact be inaccurate, indeed even more so than a physically well-constructed non-asymptotic theory. Direct extrapolated-asymptotic vs. non-asymptotic theory comparisons have definitely shown this to be the case for laminar flows (especially as regards the skin friction aspects[35]) and the situation may well be the same or worse in turbulent flow. For example, the asymptotic first order theory formally excludes both the streamwise interactive pressure gradient effect on the shear-disturbance deck and both the normal pressure gradient and so-called "streamline divergence" effects on the middle deck; however, physical considerations plus experimental observations and recent comparative numerical studies[36,37] suggest that these effects may in fact be significant at practical Reynolds numbers and should not be neglected. Of course, second order asymptotic corrections can be devised to redress this difficulty but, as Neyfeh and Regab[38] have shown, run the risk of breaking down even worse when extrapolated to ordinary Reynolds numbers. In the present work, we seek to avoid these problems by treating the triple deck using a deliberately non-asymptotic model appropriate to realistic Reynolds numbers that includes the inner deck pressure gradient terms plus the middle deck $\partial p/\partial y$ and streamline divergence effects, along with other simplifying approximations that render the resulting theory tractible from an engineering standpoint. With this veiwpoint in mind, we now examine in more detail the nature of the disturbance flow problem in each of the three basic decks.

2.2) Formulation of the Disturbance Problem in Each Deck

Outer Potential Flow Region

Assuming that the incident shock and its reflection system are weak with isentropic non-hypersonic flow, we have here a small disturbance potential inviscid motion imposed upon the undisturbed uniform flow U_{o_e} outside the boundary layer:

$$\left[M_{o_e}^2 - 1 + (\gamma + 1)\, u' \frac{M_{o_e}^2}{U_{o_e}}\right] \frac{\partial u'}{\partial x} \simeq \frac{\partial v'}{\partial y} \tag{1}$$

$$\partial v'/\partial x = \partial u'/\partial y \tag{2}$$

$$\frac{\partial^2 p'}{\partial y^2} + \left[1 - M_{o_e}^2 - 2\frac{u' M_{o_e}^2}{U_{o_e}}\right] \frac{\partial^2 p'}{\partial x^2} = 0 \tag{3}$$

where the third term within the square brackets of Eqs. (1) and (3) is significant in the transonic case $1 < M_{o_e} \lesssim 1.2 - 1.3$ and automatically includes the supersonic-subsonic jump conditions to this order of approximation[39]. Since a variety of efficient analytical or numerical methods are presently available to solve this system in either transonic flow or in purely supersonic flow (in which case Eqs. 1-3 further reduce to an Ackert-type problem), we assume that such a solution may be carried out for all x on the upper region $y \geq \delta_0$ subject to the usual far-field conditions as $y \to \infty$. The remaining disturbance boundary condition that must be supplied along $y = \delta_0$ then couples this solution to the underlying double-deck: it requires that the outer disturbance flow pertain to an effective streamline shape (relative to the wall) defined by the total interactive displacement effect of the inner decks. To insure physically-smooth matching along this outer-inner interface, then, we require both v'/U_{o_1} and p' to be continuous with their middle deck counterparts along $y = \delta_0$.

Middle Rotational-Disturbance Flow Deck

This layer contributes to and transmits the displacement effect, contains the boundary layer lateral pressure gradient due to the interaction and carries the significant influence of the incoming boundary layer profile shape. Our analysis of this layer rests on the key simplifying assumption that for non-separating interactions the turbulent Reynolds shear stress changes are small enough to have a negligible back effect on the mean flow properties along the interaction zone; hence this stress can be taken to be "frozen" along each streamline at its appropriate value in the undisturbed incoming boundary layer. This

approximation, likewise adopted by a number of earlier investigators with good results, is supported not only by asymptotic analysis[40] but especially by the results of Rose's several[32,41] detailed experimental studies of a non-separating shock-turbulent boundary layer interaction which showed that over the short-ranged interaction length straddling the shock the interactive pressure gradient and inertial forces outside a thin layer near the wall are at least an order of magnitude larger than the corresponding changes in Reynolds stress. Furthermore, there is a substantial body of related experimental results on turbulent boundary layer response to various kinds of sudden perturbations and rapid pressure gradients which also strongly support this view [18-21, 42-46]; these studies unanimously confirm that, at least for non-separating flows, significant local Reynolds shear stress disturbances are essentially confined to a thin sublayer within the Law of the Wall region (see below) where the turbulence rapidly adjusts to the local pressure gradient, while outside in the Law of the Wake region the turbulent stresses respond very slowly and remain nearly frozen at their initial values far out of local equilibrium with the wall stress.

Confining attention, then, to the short range local shock interaction zone where the aforementioned "frozen turbulence" approximation is applicable, the disturbance field caused by a weak shock is one of small rotational inviscid perturbation of the incoming non-uniform turbulent boundary layer profile $M_o(y)$, governed by the equations

$$\frac{\partial}{\partial y}\left[\frac{v'(x,y)}{U_o(y)}\right] = \frac{1-M_o^2(y)}{\gamma M_o^2(y)} \cdot \frac{\partial(p'/p_o)}{\partial x} \tag{4}$$

$$\frac{\partial u'}{\partial x} = -\frac{\partial p'/\partial x}{\rho_o(y)\, U_o(y)} - \frac{dU_o}{dy} \cdot \frac{v'}{U_o} \tag{5}$$

$$\frac{\partial^2 p'}{\partial y^2} - \frac{2}{M_o}\frac{dM_o}{dy}\frac{\partial p'}{\partial y} + \left(1-M_o^2 - \frac{2\,u'M_o^2}{U_o}\right)\frac{\partial^2 p'}{\partial x^2} = 0 \tag{6}$$

where Eq. (4) is a result of the combined particle-isentropic continuity, x-momentum and energy equations. It is noted here that, consistant with the assumed short range character of the interaction, the streamwise variation of the undisturbed turbulent boundary layer properties that would occur over this range are neglected, taking $U_o(y)$, $\rho_o(y)$ and $M_o(y)$ to be arbitrary functions of y only with δ_o, δ_o^* and τ_{w_o} as constants. Now Eq. (6) is a slight generalization of Lighthill's well-known pressure perturbation equation for non-uniform flows[5] which includes a non-linear correction term that accounts for possible transonic effects within the boundary layer including the diffracted impinging shock above the sonic level of the incoming boundary layer profile. Excluding the hypersonic regime, Eqs. (4)-(6) therefore apply to a wide range of initially supersonic external flow conditions and the complete speed range across the boundary layer except at the singular point $M_o \to 0$ (which we avoid by consideration of the inner deck as shown below). In particular, use of Eq. (6) provides an account of any lateral pressure gradient that developes across the interacting boundary layer.

As is the case with the outer deck, a variety of analytical or numerical methods may be used to solve this middle deck disturbance problem (see, e.g., Refs. 2, 5, 31). Whatever the method chosen, we imagine that it provides at each streamwise station x an evaluation of the disturbance pressure distribution $p'(x,y)$; then y-integration of Eq. (4) gives as

$$\frac{v'(x,y)}{U_o(y)} = \underbrace{\left[\frac{v'}{U_o}\right](x,y_{w_{eff}})}_{=0} + \frac{\partial}{\partial x}\left\{\int_{y_{w_{eff}}}^{y} \frac{p'}{\gamma p_{e_1}}\left[\frac{1-M_o^2(\bar{y})}{M_o^2(\bar{y})}\right]d\bar{y}\right\} \tag{7}$$

where $y_{w_{eff}} > 0$ is the effective wall shift or displacement height associated with the inner deck defined such that the inviscid $v'(x,y_{w_{eff}})$ and hence $\partial p'/\partial y(x,y_{w_{eff}})$ both vanish (see below).

Equation (7) thus provides the disturbance streamline slope distribution streamline slope distribution across the boundary layer at any streamwise station, and its value at $y = \delta_o$ yields the total streamline displacement effect of the two inner decks (the lower limit on the integral being the inner deck contribution). We then may obtain the corresponding total displacement thickness growth along the interaction by streamwise-quadrature of the perturbation boundary layer continuity equation integral; this yields to first perturbation

$$\Delta\delta^*(x) \simeq \int_{-\infty}^{x} \frac{v_e'(x)}{U_{o_e}}\,dx + (\delta_o-\delta_o^*)\left[\frac{M_{e_1}^2-1}{\gamma M_{e_1}^2 p_{e_1}}\right]p_w'(x)$$

$$\simeq \int_{y_{w_{eff}(x)}}^{\delta_o} \frac{p'}{p_{e_1}}\left[\frac{1-M_o^2(\bar{y})}{M_o^2}\right]d\bar{y} + (\delta_o-\delta_o^*)\left[\frac{M_{e_1}^2-1}{M_{e_1}^2 p_{e_1}}\right]p_w'(x) \tag{8}$$

The Inner Shear-Disturbance Layer

This very thin inner deck contains the significant viscous and turbulent shear stress disturbances due to the interaction, plus the small upstream influence and an important contribution to the viscous displacement effect. In fact it lies well within the Law of the Wall region of the incoming turbulent boundary layer profile and hence also (for the high Reynolds numbers of interest here) below the sonic level of the profile[47]; our resulting theory indeed confirms this aposteriori. The original work of Lighthill[5] and others treated the problem by further neglecting the turbulent stresses altogether and considering only the laminar sublayer effect; while this greatly simplifies the problem and yields an elegant analytical solution, the results can be significantly in error at high Reynolds numbers and cannot explain (and indeed conflicts with) the ultimate asymptotic behavior that must pertain in the $Re_\ell \to \infty$ limit. The present theory remedies this by extending Lighthill's approach to include the entire Law of the Wall region turbulent stress-effects; the resulting general shear-disturbance sublayer theory provides a non-asymptotic treatment which encompasses the complete range of Reynolds numbers. It is noted in this connection that our consideration of the entire Law of the Wall combined with the use of effective inviscid wall concept to treat the inner deck displacement effect eliminates the need for the "blending layer"[9] that is otherwise required to match the disturbance field in the laminar sublayer region with the middle inviscid deck; except for higher order derivative aspects of asymptotic matching, our inner solution for all practical purposes automatically includes this blending function since it imposes a boundary condition of vanishing total shear disturbance at the outer edge of the deck. In addition, our retention of the explicit disturbance pressure gradient term for the inner deck not only provides the correct physics at practical Reynolds numbers but also (not-withstanding the question of the turbulence model) correctly models the situation near separation ($\tau_w \to 0$) where this term becomes of dominant importance.

To facilitate a tractible theory, we retain only the main physical effects by introducing the following simplifying assumptions. (a) The incoming boundary layer is free from any post-transitional memory or low Reynolds number effects and its Law of the Wall region is characterized by a constant total (laminar plus turbulent eddy) shear stress and a Van Driest-Cebeci type of damped eddy viscosity model[48]. This model is known to be a good one for a wide range of upstream non-separating boundary layer flow histories. (b) For the weak incident shock strengths of present interest, the sublayer disturbance flow is assumed to be a small perturbation upon the incoming boundary layer; in the resulting linearized disturbance equations, however, all the physically-important effects of streamwise pressure gradient, both streamwise and vertical acceleration, and both laminar and turbulent disturbance stresses are retained. Although the resulting theory necessarily becomes inaccurate near separation, it provides a valuable physical insight to the interactive physics close to the wall for non-separating flow and a firm basis for subsequent improvement. Moreover, it can be shown that the form of the particular set of linear equations used here is in fact unaltered by non-linear effects; hence even the quantitative accuracy of the present theory is expected to be good until rather close to separation. (c) For adiabatic flows at low-to-moderate external Mach numbers, the undisturbed and perturbation flow Mach numbers are both quite small within the shear disturbance sublayer; consequently the treatment of compressibility effects therein can be greatly simplified without any significant error. Thus, the influence of the density perturbations on the sublayer disturbance flow may be neglected altogether[49], while the corresponding modest compressibility effect on the Law of the Wall portion of the undisturbed profile is quite adqequately treated by the Eckert reference temperature method[50-52] wherein incompressible relations are used based on wall recovery temperature properties*. (d) The turbulent fluctuations and the small interactive disturbances are assumed uncorrelated in both the lower and middle decks. (e) The thinness of the inner deck allows the boundary layer-type approximation of neglecting its lateral pressure gradient; the wall pressure distribution $p_w'(x)$ is taken equal to the overlaying pressure perturbation field along the bottom of the middle deck.

Under these assumptions, the disturbance field is governed by the following continuity and momentum equations:

$$\frac{\partial u'}{\partial x} + \frac{\partial v'}{\partial y} = 0 \tag{9}$$

$$U_o \frac{\partial u'}{\partial x} + v' \frac{dU_o}{dy} + (\rho_{w_o}^{-1}) \frac{\partial p_w'}{\partial x} = \frac{\partial}{\partial y} \left(\nu_{w_o} \frac{\partial u'}{\partial y} + \varepsilon_{T_o} \frac{\partial u'}{\partial y} + \varepsilon_T \frac{dU_o}{dy} \right) \tag{10}$$

$$\partial p'/\partial y = 0 \; ; \; p' = p'(x) = p_w'(x) \tag{11}$$

where ρ_{w_o} and ν_{w_o} are evaluated at the adiabatic wall recovery temperature and where it is noted that the kinematic eddy viscosity perturbation ε_T' is being taken into account. The corresponding undisturbed turbulent boundary layer Law of the Wall profile $U_o(y)$ is governed be

$$\tau_o(y) = \text{const.} = \tau_{w_o} = [\mu_{w_o} + \rho_{w_o} \varepsilon_{T_o}(y)] \frac{dU_o}{dy} \tag{12}$$

where according to the Van Driest-Cebeci eddy viscosity model with $y^* = y \sqrt{\tau_{w_o}/\rho_{w_o}}/\nu_{w_o}$

$$\varepsilon_T = [.41y(1-e^{-y+/A})]^2 \frac{\partial u}{\partial y} \tag{13a}$$

*Excluding hypersonic flow, this is equivalent in accuracy to (but easier than) the use of Van Driest's compressible Law of the Wall profile.[54]

which yields for non-separating flow disturbances that

$$\varepsilon_{T_o} = [.41y(1-e^{-y^+/A})]^2 \frac{dU_o}{dy} \tag{13b}$$

$$\varepsilon_T' = (\frac{\partial u'/\partial y}{dU_o/dy})\varepsilon_{T_o} \tag{13c}$$

Here, A is the so-called Van Driest damping "constant"; we used the commonly-accepted value A = 26 although it is understood that a larger value may improve the experimental agreement in regions of shock-boundary layer interaction.[52] Substituting (13c) into (10) we thus have the disturbance momentum equation

$$U_o \frac{\partial u'}{\partial x} + v' \frac{dU_o}{dy} (\rho_{w_o}^{-1}) \frac{\partial p_w'}{\partial x} = \frac{\partial}{\partial y} [(\nu_{w_o} + 2\cdot\varepsilon_{T_o}) \frac{\partial u'}{\partial y}] \tag{14}$$

from which we see that inclusion of the eddy viscosity perturbation has exactly doubled the turbulent shear stress disturbance term.

We seek to solve Eqs. (9) and (14) within the incoming flow $U_o(y)$ governed by Eqs. (12) and (13b) subject to the impermeable wall no slip conditions $U_o(0) = u'(x,o) = v'(x,o) = 0$ plus an initial condition $u'(-\infty,y) = 0$ that requires all interactive disturbances to vanish far upstream of the impinging shock. Furthermore, at some distance δ_{SL} sufficiently far from the wall, u' must pass over to the inviscid solution u'_{inv} along the bottom of the middle deck, this latter being governed by Eq. (9) plus

$$U_o \frac{\partial u_{inv}}{\partial x} + v'_{inv} \frac{dU_o}{dy} + (\rho_{w_o})^{-1} \frac{\partial p_w}{\partial x} = 0 \tag{15}$$

with δ_{SL} defined as the height where the total shear disturbance $(-\partial u'/\partial y)$ of the inner solution vanishes to a desired accuracy.

Following Lighthill[5], it now proves convenient to convert the foregoing problem into one involving the normal disturbance velocity field v'(x,y). Thus, by differentiating Eq. 14 w.r.t. x, substituting Eq. 9 so as to eliminate u' and then differentiating the result w.r.t. y so as to eliminate p_w' by virtue of Eq. 11, one obtains the following fourth-order equation for v':

$$\frac{\partial}{\partial x}\left(U_o \frac{\partial^2 v'}{\partial y^2} - \frac{d^2U_o}{dy^2} v'\right) = \frac{\partial^2}{\partial y^2}[(\nu_{o_w} + 2\cdot\varepsilon_{T_o}) \frac{\partial^2 v'}{\partial y^2}] \tag{16}$$

This differential equation, which resembles a "turbulent" Orr-Sommerfeld equation without critical layer terms, contains a three-fold influence of the turbulent flow: the profile $U_o(y)$, its curvature d^2U_o/dy^2 (non-zero outside the laminar sublayer) and, what is new here, an eddy disturbance stress term $2\cdot\varepsilon_{T_o}$.

Equation (16) is to be solved together with (11) and (13b) subject to the wall boundary conditions $v'(x,o) = \partial v'/\partial y(x,o) = 0$. A third condition involving v' is obtained by satisfying the x-momentum equation (14) right at the wall; when this is differentiated w.r.t. x and Eq. (9) used together with the fact that $\varepsilon_T \to 0$ at $y = 0$ we obtain the non-homogeneous condition

$$\frac{\partial^3 v'}{\partial y^3}(x,o) = -(2\,\nu_{o_w})^{-1} \frac{d^2 p_w'}{dx^2} \tag{17}$$

The fourth boundary condition is the v' equivalent of the outer inviscid matching requirement (15), which yields $v'(x,\delta_{SL}) = v'_{inv}(x,\delta_{SL})$ with the inviscid solution governed by

$$\frac{\partial}{\partial x}\left(U_o \frac{\partial^2 v'_{inv}}{\partial y^2} - v'_{inv} \frac{d^2U_o}{dy^2}\right) = 0 \tag{18}$$

and δ_{SL} pertaining to $\partial^2 v'/\partial y^2 = 0$ (i.e., vanishing total disturbance shear) somewhere within the Law of the Wall region.[12]

Once this v'(x,y) field is obtained, the attendant streamwise velocity and disturbance shear stress fields may be found from

$$u' = \int_{-\infty}^{x} \frac{\partial u'}{\partial x}\,dx = -\int_{-\infty}^{x} \frac{\partial v'}{\partial y}\,dx \tag{19}$$

$$\frac{\tau'}{\mu_{w_o}} = (1+2\frac{\varepsilon_{T_o}}{\nu_{o_w}}) \frac{\partial u'}{\partial y} = -(1+\frac{2\varepsilon_{T_o}}{\nu_{w_o}}) \int_{-\infty}^{x} \frac{\partial^2 v'}{\partial y^2}\,dx \tag{20}$$

An important and useful feature of this approach is the definition of an "effective inviscid wall" position (or displacement thickness) that emerges from the asymptotic behavior of v' far from the wall[5]: see Fig. 3. As schematically illustrated in Fig. 3a, this is defined by the value y_{weff} where the "back projection" of the v_{inv} solution* vanishes; physically, y_{weff} thus represents the total mass defect height due to the shear stress perturbation field and hence the effective wall position seen by the overlying inviscid middle deck disturbance flow. As indicated in Fig. 3b, this concept serves to couple the inner and middle deck solutions in a direct physically-obvious way by providing the non-singular inner equivalent slip-flow boundary conditions $\partial p'/\partial y\,(y_{eff}) = v_{inv}(y_{weff}) = 0$ at $U_0(y_{weff}) > 0$ for the middle deck solution of Eq. (6). In practice, this approach has proven quite useful for creating a variety of interaction problems [2,20,55]; a more detailed discussion of its application to the present problem is given in the following section

2.3) Approximate Solution by Operational Methods

An analytical solution is further achieved by assuming small linearized disturbances ahead of, behind and below the nonlinear shock jump plus an approximate treatment of the detailed shock structure within the boundary layer†, which gives reasonably accurate predictions for all the properties of engineering interest when $M_1 \geq 1.05$. As described in detail in Refs. 2 and 4, the resulting equations can be solved by Fourier transform methods yielding the interactive pressure rise and displacement thickness growth inputs to the above extended theory of the inner-disturbance sublayer. The resulting solution contains all the essential physics of the mixed transonic viscous interaction field for non-separating flows including the upstream influence, the lateral pressure gradient near the shock and the onset of incipient separation; numerous detailed comparisons with experiment[56] have shown that it thus gives a good account of all the important engineering features of the interaction over a wide range of Mach-Reynolds number conditions.

The matching of the outer two decks with the inner shear-disturbance deck in connection with the Fourier inversion process yields the determination of the upstream influence distance; typical numerical results for it showing the important typical parametric effects of Reynolds number and shape factor are presented in Fig. 4. The solution procedure (see Ref. 4 for details) further yields the inner deck displacement thickness

$$\frac{y_{eff_w}}{\delta_0} = .677\left[\frac{C_{f_0}}{2}\,Re_{\delta_0}^2/(T_w/T_{e_0})^{1+2\omega}\right]^{-1/3}(\kappa_{min}\cdot\delta_0)^{1/3}\cdot H(\mathcal{T})\cdot\left[\frac{3\,\kappa_{min}\int_{-\infty}^{x} p_w'^{3/2}dx}{2\,p_w'^{3/2}}\right]^{1/3} \tag{21}$$

and the interactive skin friction relationship

$$\frac{\tau_w'(x)}{\tau_{w_0}} = -\left(\frac{\kappa_{min}}{\lambda}\right)^{2/3}\cdot S(\mathcal{T})\cdot\sqrt{\frac{\beta}{C_{f_0}}}\cdot C_{p_w}'\left[\frac{2\,C_{p_w}'^{3/2}}{3\,\kappa_{min}\int_{-\infty}^{x}(C_{p_w}')^{3/2}dx}\right]^{2/3} \tag{22}$$

with

$$\mathcal{T} = (.41)^2\left[\frac{C_{f_0}}{2}\,Re_{\delta_0}/(T_w/T_e)^{1+2\omega}\right]^{1/3}/(\kappa_{min}\cdot\delta_0)^{2/3} \tag{23a}$$

$$\lambda\delta_0 = .744\,\beta^3(C_{f_0}/2)^{5/4}\,Re_{\delta_0}/(T_{w_0}/T_{e_0})^{\omega+1/2} \tag{23b}$$

where $\kappa_{min} = \ell_\mu^{-1}$ is given in Fig. 4 while the functions $H(\mathcal{T})$ and $S(\mathcal{T})$ are given in Fig. 5 and represent the wall turbulence effect on the interactive displacement effect and skin friction, respectively, of the inner deck. Fig. 5, in fact, is a central result of the general non-asymptotic theory, providing a unified account of the entire Reynolds number range in terms of the single new turbulent interaction parameter $\mathcal{T}$ (Eq. 23a): it ranges from the limiting behavior of negligible wall turbulence effect pertaining to Lighthill's theory at $\mathcal{T} \to 0$ (lower Reynolds numbers) to the opposite extreme of wall turbulence-dominated behavior at $\mathcal{T} >> 1$ pertaining to an asymptotic-type of theory at very large Reynolds numbers where the inner deck thickness and its disturbance field become vanishingly small. The relationship between these two heretofore-disparate theories has thus been explained and established: they belong at opposite extremes of a general non-asymptotic theory that describes the transition between them. Another important result emerging from Fig. 5 is that the asymptotic trends occurring at very large Re_ℓ cannot be extrapolated down to ordinary Re_ℓ values; doing so can yield appreciable error in the inner deck properties of practical interaction problems. This would appear to explain the success of the Lighthill theory in correlating lower Reynolds number turbulent interactions in spite of the mathematical rigor of asymptotic theory: the former is simply much closer to the actual physics and correctly predicts more significant interaction effects and scaling under the decidedly non-asymptotic conditions involved. By the same token, the extreme approximation involved in the $\mathcal{T} = 0$ limit significantly breaks down at larger Re_ℓ's pertaining to $\mathcal{T} >> 1$, clearly warranting the use of the present theory to account for the increasing role of the wall turbulence effect on the interaction.

---

*i.e., the (generally non-linear) solution curve obtained by inwardly-integrating (18) and (12) in the negative y direction starting at δ_{SL}.

†As far as the overall interaction properties are concerned, this non-linear shock jump provision plus the various non-uniform viscous flow effects within the boundary layer reduce the lower Mach number limit otherwise pertaining to the linearized supersonic theory in purely inviscid potential uniform flow.

An important and useful final consequence of the foregoing analysis is that it yields an explicit analytical criterion for the onset of incipient separation due to an interactive pressure field; thus setting $\tau_w = \tau_{w_o} + \tau_w = 0$, Eq. (22) predicts this to occur when

$$C'_{p_w}\left[\frac{2\ C'^{\,3/2}_{p_w}/\kappa_{min}}{3\cdot\int_{-\infty}^{x}(C'_{p_w})^{3/2}dx}\right]^{2/3} \geq \frac{\sqrt{C_{f_o}/\beta}}{S(\bar{T})}\left(\frac{\lambda}{\kappa_{min}}\right)^{2/3} \qquad (24)$$

where it is re-emphasized that C_{p_w} here is the local interactive distribution. Equation (56) bears a general resemblance to a Stratford-type[7] of incipient separation relation for turbulent flow, except that the present formula contains the integrated history effect along the interaction whereas Stratford's result involves purely local properties of C_f and dC_{p_w}/dx. It is understood, of course, that the present theory actually breaks down approaching separation owing to the combination of its linearization assumptions and the Van Driest/Cebeci wall turbulence model used; nevertheless, Eq. (24) does give at least a roughly-correct indication of where this will occur, and indeed does so without containing any adjustable empirical constants.

A computer program which is the outgrowth of Mason[2] and Panaras[57] earlier work has been constructed to carry out the foregoing solution method; it involves the middle-deck disturbance pressure solution coupled to the inner deck by means of the effective wall shift (Eq. 21) combined with an upstream influence solution subroutine. The corresponding local total interactive displacement thickness growth and skin friction are obtained from Eqs. (8) and (22), respectively. If desired the attendant boundary layer shape factor change along the interaction may then also be calculated as $H = [\delta^*_o + \Delta\delta^*(x)]/\theta^*(x)$ with θ^* given by an x-wise integration of the overall momentum integral equation for the total local boundary layer since $p(x)$, δ^* and C_f are known. The incoming turbulent boundary layer is treated by the compressible version of a universal composite Law of the Wall - Law of the Wake model due to Walz[58] that not only has a convenient analytical form (see Appendix) but also provides a very general fundamental description of this boundary layer in terms of three arbitrary parameters: preshock Mach number, boundary layer displacement thickness Reynolds number, and the incompressible shape factor H_{1_i}. This enables us to assess the important but heretofore - neglected influence of the upstream flow history (pressure gradient, suction, etc.) on the interaction.

2.4) Comparisons of the Theory with Experiment

Numerous verification comparisons of the present theory with experimental data from both wind tunnel and free flight experiments have already been documented; a sample is presented in Fig. 6 to illustrate the predicted behavior and good agreement for the interactive pressure, displacement thickness and skin friction distributions in a typical non-separating case. Note especially in Fig. 6b the important lateral pressure gradient effect that occurs in the vicinity of the shock. Regarding the skin friction comparison shown in Fig. 6d, we note that the "experimental" values were actually inferred from measured velocity profiles along the interaction (hence θ^* and δ^*) by means of the 2-D momentum integral equation; considering the well-known uncertainties involved in their experimental set up and this method, combined with the present theory's own limitations, the agreement is considered good as regards both the magnitude and shape of the C_f curve.

Fig. 7 shows a comparison of the predicted local shape factor change along an interaction with some ONERA measurements; it is seen that the theory nicely captures the characteristic local peaking of H near the shock foot as well as the overall behavior.

A particularly interesting comparison with some very recent DFVLR-AVA (Gö) experiments[59] is shown in Fig. 8, where we compare with measurements along the non-separating interaction zones on two supercritical airfoils. The experimental C_f values were inferred from various streamwise station boundary layer profile surveys by means of the Ludwig-Tillman relationship

$$C_f = .246(T^*/Te)^{.796}\ Re_{\theta^*}^{-.268}\ e^{-1.561\ H_i} \qquad (25)$$

where H_i is given by Eq. 28 and $T^*/Te \approx 1 + .14\ M_e^2$ for $\gamma = 1.40$ as $P_r \approx .7$ on an adiabatic wall. Theoretical predictions of the entire airfoil flow field were also made with a composite inviscid transconic - turbulent boundary layer - shock interaction numerical scheme in which the present theory was used as a local interactive module astride the inviscid shock location (see Ref. 59 for details). It is seen that the present theory yields an excellent prediction of the local skin friction values upstream and slightly downstream of the shock (including the minimum value) and a good qualitative account of the overall shape of the streamwise distribution. Well downstream of the shock, the theory clearly over estimates the post-shock C_f recovery inferred by the Ludwig-Tillman relationship. Nevertheless, in view of the combined limitations of the experimental Ludwig-Tillman method and the present small disturbance theory, the overall agreement with the data here is regarded as quite good.

2.5) The Effects of Wall Curvature

The influence of local surface curvature is of particular interest since interactions often occur on curved surfaces (especially in cascade/turbine-blade applications) and since a singularity is associated with a normal shock in the purely inviscid limit of curved wall flow.[60] The present theory has been extended to enable treatment of the viscous interaction problem for such flows: the results show that the inviscid singularity disappears (the external flow being now quite regular) when the boundary layer displacement effect is taken into account. Because of its importance in the interpretation and understanding of theory and experiment, we present here a short overview of this analysis (see Ref. 61 for more details).

Inviscid Outer Region

Oswatitsch and Zierep[60] have shown that normal shock impingement on a curved wall in a purely inviscid flow introduces a logarithmic singularity in the wall pressure in the form of a sharp post-shock expansion (Fig. 9a) and this phenomenon has indeed been observed in inviscid numerical solutions.[62] However, in real flows even at high Reynolds numbers, viscous smearing and upstream influence effects arise due to the thin boundary layer along the surface which are known to profoundly influence the physics of the local interactive flow. In particular, whether the wall is flat or curved, the local outer inviscid flow "sees" the overall viscous effects in the interaction as an effective thickening of the geometrical surface by the interactive displacement thickness growth. In the vicinity of the shock, this is seen to involve both a rapid growth in the effective body slope at the shock foot and an overall downstream increase of the effective body thickness; at the very least, these two features must be included in any realistic mathematical model of the local outer inviscid flow in such interactions.

A detailed analysis of the local mixed transonic small perturbation field in the vicinity of the shock has been made by Sobieczky[61] in hodograph variables (Fig. 9b) in the case where this flow pertains to an effective body consisting of the bare wall $h_w = h_1 = C_1 \cdot x^2$ plus a slope jump C_2 at the shock foot followed by a further interactive displacement thickness growth, giving $h_2 = h_{w,eff} = C_2 x + D_2 x^2$ (Fig. 9c). The results yield two basically different types of physical behavior (one regular, the other singular) depending on whether the interactive deflection effect is included ($C_2 > 0$, $D_2 \neq C_1$) or neglected a priori ($C_2 = 0$, $D_2 = C_1$), as follows:

$C_2 > 0$, $D_2 \neq C_1$: REGULAR SOLUTION with δ^*

$$\text{Shock Shape } Xs = y + y^2 \qquad (26a)$$

$$M_2 - 1 = K + Lx$$

$C_2 = 0$, $D_2 = C_1$: SINGULAR SOLUTION without δ^*

$$\text{Shock Shape } Xs = y^2 (Q + R\ell\, y) \qquad (26b)$$

$$M_2 - 1 = -K (1 - Lx - Fx\ell\, x)$$

where K, L, ..., Q, P, R are constants. Now solution (26b) is in fact the aforementioned singular solution for a "bare" curved wall. The result (26a) shows, at least for non-separating interactions, that the viscous displacement effect does indeed eliminate the singularity (giving in fact a well-behaved external inviscid disturbance flow). To be sure, wall curvature does have some influence, as shown below, but this is quite regular and does not derive from any singular behavior in the inviscid part of the flow.

Inner Boundary Layer Region

Here wall curvature influences the solution in two ways: (1) it alters the incoming undisturbed turbulent boundary layer profile upon which the perturbation solution depends; (2) it introduces new explicit terms in the small disturbance equations. For the typical radii of curvature encountered in practice ($\delta_0/R_B < .01 - .02$), detailed examination[61] has shown that (2) are all of order δ_0/R_B and hence completely negligible*. Regarding (1), while the explicit new curvature terms again have a negligible effect, there is a significant influence on the eddy viscosity relation[63] which in turn manifests itself as a slight skin friction reduction and shape factor increase, respectively, approximately described by

$$C_{f_0} \simeq \left(1 - 10\,\frac{\delta_0}{R_B}\right) \cdot \left(C_{f_0}\right)_{flat} \qquad (27a)$$

$$H_{i_1} \simeq \left(1 + 5\,\frac{\delta_0}{R_B}\right) \cdot \left(H_{i_1}\right)_{flat} \qquad (27b)$$

where to this first order accuracy the corresponding effect on δ_0 is much smaller and therefore neglected. Note that the typical value $\delta_0/R_B \approx .01$ yields a reduction and increase in C_{f_0} and H_{i_1} of 10% and 5%, respectively, which are an order of magnitude larger than the explicit new curvature terms in either the mean or perturbation flow equations (including the outer inviscid disturbances). The use of Eqs. (27) with δ_0/R_B as an additional input parameter in the foregoing viscous interaction theory enables a straightforward appraisal of the first order curvature effects on the non-separating normal shock-turbulent boundary layer interaction problem.

A systematic study of the wall curvature effect has been made based on the foregoing extended interaction theory. Typical results are presented in Fig. 10, where it is seen that the effect generally is a small one and derives primarily from the curvature effect on the boundary layer shape factor. Since the curvature tends to slightly spread out the interaction and thus reduce the pressure gradient, it slightly increases $C_{f_{min}}$ and hence delays incipient separation. The results for the interactive pressure distribution along the boundary layer edge bring out the farther fundamental point that a small subsonic expansion region occurs behind the disturbance shock regardless of the wall curvature: since this expansion was shown to be an inherent feature of the mixed transonic viscous interaction flow along a flat surface by Inger and Mason[2] and is further confirmed by detailed numerical solutions[9], we may conclude (contrary to what is sometimes alleged), that wall curvature per se is not the cause of such expansion regions in non-separating turbulent interactions.

---

* As regards the (regular) influence of curvature on the inviscid outer boundary conditions via the displacement effect, the foregoing analysis shows that this is also of order δ_0^*/R_B and hence very small in the leading approximation.

3. PARAMETRIC STUDY OF LOCAL INTERACTION EFFECTS

The foregoing theory provides a fundamental analytical tool for examining the influence of the basic physical parameters on the local interactive properties of engineering interest. Such a study has been carried out and its results will be described in this section.

3.1) Influence of Mach Number (Shock Strength)

The effects of increasing Mach number on the pressure, displacement thickness, skin friction and shape factor distributions are shown in Figs. 11a-d for fixed Reynolds number and shape factor values typical of a practical flight condition for an aerodynamic body. As expected on the basis of earlier studies[2], the theory predicts that the interactive pressure gradient, displacement thickening, skin friction drop and local shape factor peak all increase with increasing pre-shock Mach number while the overall streamwise scale contracts. In particular, owing to the increased interactive pressure gradient with increasing M_1, we see the tendency of incipient separation to occur (i.e., $C_{f_{min}} \to 0$) as $M_1 \gtrsim 1.30$ —see below.

3.2) Influence of Incoming Boundary Layer Profile Shape

The predicted effects of the incoming boundary layer incompressible shape factor H_i, related to the adiabatic compressible value to a good approximation by the expression [57]

$$H_i = (H - .273\ M^2) / (1.0 + .1145\ M^2) \quad , \tag{28}$$

is shown for a typical Reynolds number case in Fig. 12. In general this effect is seen to be quite significant: increasing H_{1_i} (which corresponds to reduced profile fullness typical of an adverse upstream pressure gradient history and/or blowing history[64]) causes the interaction pressure field to spread out with a resulting large increase in its upstream influence distance (Fig. 12a) and displacement thickness growth, especially downstream (Fig. 12b). This displacement thickness sensitivity to H_{1_i} is of significant practical importance since δ^* can have a significant back-effect on the inviscid flow and shock position on airfoils or in channel flows.

The shape factor influence on the interactive skin friction (Fig. 12c) is also significant but not monotone in the vicinity of the shock foot; whereas increasing H_{1_i} yields a continual reduction of the downstream C_f level, its effect on $C_{f_{min}}$ is much less and in fact reverses at larger H_{1_i} values > 1.5 (such that further H_{1_i} increase slightly increases $C_{f_{min}}$) owing to the influence of the reduced interactive pressure gradient that also occurs (Fig. 12a). These results are quite similar to the shape factor-effects observed by Squire et al[64] in purely-supersonic shock-boundary layer interactions.

3.3 Reynolds Number (Scale) Effect

The predicted Reynolds number effect on the interaction field along a typical $M_1 = 1.20$ shock-boundary layer interaction is shown in Fig. 13, where it is noted that the abscissa of these curves has been normalized with respect to the undisturbed boundary layer thickness δ_0 (which itself contains a Reynolds number effect). We observe from Fig. 13a that there is little influence of Reynolds number (other than that absorbed in δ_0) on the upstream pressure distribution; the upstream influence distance has the expected small value (~1.0 to 1.5 δ_0) that scales essentially with δ_0 itself. In contrast, the downstream interaction region shows a Reynolds number effect involving a contraction of the non-dimensional streamwise scale with increasing Re_{δ^*}. These trends, including the tendency toward a very short range nearly step-like pressure rise at very high Reynolds numbers, are in agreement with experimental observation and the results of Navier-Stokes numerical simulation of turbulent boundary layer-shock wave interaction.[65]

The corresponding displacement thickness predictions in Fig. 13b shows a similar behavior; only the downstream thickening exhibits a significant Reynolds number effect when plotted as $\Delta\delta^*/\delta_0^*$ vs. x/δ_0^*. Moreover, this effect evidently vanishes at higher Reynolds numbers for a given boundary layer shape factor, implying that $\Delta\delta^*$ becomes proportional to δ_0^*. The local shape factor distribution shown in Fig. 13c also exhibits this Re-independent limiting behavior at sufficiently layer Re_{δ^*}.

The predicted influence of Reynolds number on the interactive skin friction is shown in Fig. 13d, where it may be seen that both $C_{f_{min}}$ (located slightly downstream of the shock foot) and the value well downstream of the shock (which recovers quite slowly) decrease significantly with increasing Re_{δ^*} at the larger Reynolds numbers pertaining to full-scale flight vehicles. However, this trend does not persist at low Reynolds numbers but in fact appears to reverse owing to the spreading out of the interaction and attendant reduction of the interaction pressure gradient which ultimately causes the $C_{f_{min}}$ to increase with reducing Re_ℓ at the lower Reynolds numbers. At sufficiently low Reynolds number and large shock strength, the present theory in fact predicts vanishing or slightly negative $C_{f_{min}}$ values and hence incipient separation with a very small separation bubble slightly behind the shock foot. Of course the present theory ceases to be valid for separated flow; nevertheless it does give a useful indication as to trends toward this situation and an approximate idea of when incipient separation occurs — see below for a more systematic examination of this behavior.

In conjunction with the foregoing results, we have also made some comparisons with predictions given by the Ludwig-Tillman ("LT") skin friction formula[25] when applied along the interaction using the H and $\theta^* = \delta^*/H$ values given by the present theory; this is of interest since Eq. 25 is frequently used to empirically find C_f values from velocity profile sourveys along such interaction (see Fig. 8 and Ref. 59). The typical results are shown in Fig. 14, where it is seen that while the preshock and minimum L-T values agree fairly well with the present theory for $Re_{\delta^*} \sim 10^5$, the overall L-T prediction trends are at variance with the present interaction theory. In particular, the L-T predictions differ in three important respects: (a) in contract to the noticeable $C_{f_{min}}/C_{f_0}$ increase with Re_δ predicted by the present theory, the L-T relationship for the same pressure field predicts no such increase, hence indicating a higher $C_{f_{min}}/C_{f_0}$ ratio at the lower Reynolds numbers; (b) compared with the present prediction of a gradual but significant C_f rise well downstream, L-T predicts virtually no such recovery and hence notably lower downstream C_f values;

(c) the L-T predicts rather weak Reynolds number effect trends on the downstream C_f behavior that are opposite in sense to the much stronger Re-effect implied by the present theory. These interesting differences must be borne in mind when interpreting theoretical comparisons with experimental C_f values that have been inferred from the L-T formulae applied along an interaction zone.[57]

Apropos the foregoing comparison, we also evaluated the accuracy of using a localized version of the well-known Stratford analysis of turbulent boundary layer behavior in strong adverse pressure gradients.[73] As typically illustrated in Fig. 14, when based on the correct interactive pressure distribution, this approach is unsatisfactory, drastically over-predicting the skin friction reduction and consequently the appearance of incipient separation (indeed, it predicted incipient separation at $M_1 \sim 1.10 - 1.15$ at the lower Reynolds numbers).

3.4) Viscous Ramp Modeling of the Interaction

In certain engineering applications to global flow field analysis computer programs for wings or turbine blades, it has proven expedient to model the interaction as a simple local inviscid δ^* - "bump" or "ramp". A serious deficiency of this approach is that it does not account for the dependence of the bump shape and size on Reynolds number, shock strength and boundary layer shape factor, while the additional interaction effects on the downstream boundary layer (such as C_f reduction) are ignored altogether. With the aforementioned parametric study results in hand, however, the present theory can provide (if desired) a much improved "viscous ramp" representation of the interaction whose key physical features have the correct dependence on M_1, Re_{δ^*} and H_{ij}.

Results for these viscous wedge properties[66] are presented in Figs. 15, where the upstream and downstream influence distances, the slope and overall height of the δ^* - bump are plotted along with the downstream C_f/C_{f_0} values that may be needed along with δ^* to re-initialize a subsequent turbulent boundary layer calculation downstream. We note in general that the overall scale of the interaction (which can be a sensitive effect in both steady and unsteady applications where such viscous wedge models are employed) does not scale according to the undisturbed boundary layer thickness even in the non-separating case. It is further noted that the viscous wedge slopes are in rough agreement with the maximum attached shock deflection value observed empirically[59], although here of course there is a dependence on Re_δ and H_{ij} as well as Mach number. Finally, in all of these curves we see a significant dependence on the incoming boundary layer shape factor that would appear to be an important consideration in practical applications.

3.5) Incipient Separation

As mentioned above the present theory, although it breaks down at separation, does yield a useful indication of incipient separation where $C_{f_{min}} \to 0$, i.e., where Eq. 24 is satisfied. Since this occurence is of great practical interest, a parametric study of incipient separation conditions inherent in the present theory was carried out[66]; the results for a normal shock are presented in Fig. 16, where the shock Mach number $M_{1_{inc.\,sep.}}$ above which incipient separation occurs is plotted as a function of the Reynolds number with the shape factor as a parameter; also shown in the Figure is the approximate experimental boundary determined by a careful examination[66] of a large number of transonic interaction tests, besides Nussdorfers[67] famous $M \sim 1.30$ criterion for turbulent flow. It is seen that the theoretical prediction of a gradual increase in the $M_{1_{incip.sep.}}$ value with Reynolds number is in agreement with the trend of the data; moreover, the theoretical prediction of only a small influence of shape factor on the incipient separation conditions is also bourne out by the lack of any consistent H-effect for the same Re discernable in the data (Squire has observed a similar insensitivity to H_{ij} in purely supersonic flow interactions[64]). The absolute values of $M_{1_{incip.sep.}}$ predicted by the present interaction theory are seen to be consistently slightly lower than the average experimental value; this is attributable to the combined effects of the linearized inner deck theory (which overpredicts the pressure gradient effect on C_f and hence too small on incipient separation shock strength) and the assumption of a normal shock when in fact most of the experiments likely entail some shock obliquity (which also delays separation to somewhat higher shock-strengths). As shown above, wall curvature effects are expected to play a neglibible role since they lie well within the data scatter.

In conjunction with Fig. 16, it is interesting to note that Nussdorfers original incipient separation criterion, based as it was on a very limited base, does roughly go through the average of the data although it does not account for the proper Reynolds number effect.

4. GLOBAL INTERACTION EFFECTS

4.1) Downstream Effects of Interactions on Supercritical Wings

In addition to the increased displacement thickness, the foregoing discussion shows that the skin friction level following the interaction is significantly reduced; combined with the attendant sensitivity to the profile shape, this suggests that the subsequent downstream boundary layer development may retain a memory of the interaction effects for a considerable distance (over and above a simple thickening), particularly as regards possible incipient separation in any adverse pressure gradients downstream. As indicated in Fig. 17, this downstream "interaction after effect" in the boundary layer influences the sensitive trailing edge region and thus may be important in the design and analysis of rear-loaded airfoils, especially at higher lift coefficients with increasingly-aft shock locations; it likewise may be important on three dimensional wing configurations where the shock interaction zones are well aft.

The aforementioned "after-effect" question was therefore subjected to detailed study using the two-layer turbulent boundary layer program of Moses[68] as a model of the downstream viscous flow; the program is coupled to the present interaction theory by initializing it with the post-interactive flow properties so as to account either fully (both C_f and δ^*), partially (δ^* only) or not at all for the changes across the interaction. Calculations were then made of the subsequent downstream turbulent boundary layer behavior (H, C_f, θ^*, δ^*) in various constant post-shock adverse pressure gradients typical of airfoils for different assumed local interactive shock strengths and positions or Reynolds numbers. The results serve

as a paradigm of the downstream sensitivity question in real flows.

A variety of cases were studied[69], typcial results of which are presented in Fig. 18 where we show the predicted behavior of the boundary layer shape factor and skin friction in three increasingly-strong adverse pressure gradients downstream of an interaction occurring at a typically rearward position; the consequences of either fully, partially or negligently-treating the boundary layer changes across the interaction are indicated. Generally, it is seen that the downstream behavior of the boundary layer is indeed sensitive to detailed modeling of the interactive effects and that this sensitivity increases with the strength of the downstream adverse pressure gradient. The adverse pressure gradient magnifies the subsequent influence of the skin friction (as well as the δ^* rise) across the interaction so that downstream separation tends to occur earlier than would be predicted by either neglecting or treating only the δ^* effect of the upstream interaction. As shown in Fig. 19, these predictions are supported by a comparison with boundary layer measurements downstream of a non-separating shock interaction zone on a supercritical air-foil; both the skin friction and shape factor data are poorly predicted when the interaction is neglected but are reasonably well predicted when the complete interaction effects are taken into account.

Examination of results for a wide variety of cases[69] leads to the further conclusion that such interactive after-effects extend at least 20-30% chord distances downstream on a typical air-foil or wing, and increases (as expected) with either larger shock strength or decreasing Reynolds number. If the trailing edge region lies within this range of the shock, it is thus seen that a simple thickening effect alone is not sufficient to account for the interaction and may result in an inaccurate prediction of the rearward boundary layer shape factor, skin friction and incipient separation properties including their scaling.* This is of practical importance for two major reasons: (1) in regions of sustained adverse pressure gradient that often follow the short-scale interaction zone, the shape of the velocity profile and streamwise shear stress distribution (as well as thickness) are of considerable importance to the aerodynamic design of an airfoil or wing[33]; (2) the altered boundary layer properties (especially possible incipient separation) near the trailing edge and into the wake can further exert a powerful effect on the overall aerodynamics via their influence of the Kutta condition[70] and on possible buffet onset. Consequently, Nandanan et al have carried out an even more detailed study of interactions (using the present theory as the local interactive module) on actual supercritical airfoils including experimental comparisons; the results are reported in a companion paper (Ref. 59).

4.2) Multiple Interaction Effects on Transonic Bodies of Revolution

Another important application of interaction theory has been to the analysis of the flow field around axi-symmetric bodies at supercritical transonic speeds. An interesting aspect of this problem for the boat-tailed bodies found in practice is the occurrence of two interaction regions in sequence, as illustrated in Fig. 20A. The problem has been treated by a composite inviscid-boundary layer-shock interaction flow field analysis utilizing the present non-asymptotic interaction theory.

Briefly, the approach consists of a global numerical inviscid flow region calculation based on the transonic small disturbance method of Reklis et al[71] coupled to the compressible turbulent boundary layer code of Dwyer et al[71] (which includes the influence of body spin, if present); the local transonic shock-turbulent boundary layer interaction effects are treated by interposing astride the inviscid shock location the axi-symmetric body extension of the above non-asymptotic theory, the required inputs being the inviscid shock location (about which the interactive solution is "centered"), the corresponding streamwise component of the inviscid flow Mach number and the streamwise thickness Reynolds number plus the shape factor from the turbulent boundary layer code. The interactive solution is thus inserted as a local "module" at each shock location to produce a general combined inviscid-boundary layer-interaction solution code that is fully operational. In addition to the resultant rapid displacement thickness growth, the interactive distortion of the boundary layer profile shape and skin friction are also thereby accounted for. Furthermore, the influence of these changes on the subsequent turbulent boundary layer development downstream is included by appropriate post-interaction reinitialization using a composite Law of the Wall - Law of Wake profile model.[58]

Typical results for a transonic boat-tailed body of revolution at a flight member of $M_\infty = .940$ and zero angle of attack are illustrated in Figs. 20 (b)-(d), where the predicted pressure, displacement and skin friction distributions are shown along with some supporting experimental data obtained by Danberg[71]. Even though no separation occurs, the significant local interaction regions and their after-effect are clearly evident in these distributions. Another interescing set of results is presented in Fig. 21 for a slightly lower flight Mach case (.908), where the predictions of the composite theory are not only compared favorably with data due to Danberg[72] but also to predictions obtained by Nietubicz[72] using a Navier-Stokes numerical code. The ability of the composite approach to resolve the physical behavior in the smaller scale interaction zones is clearly evident.

5. CONCLUDING REMARKS

The results of this study have shown that it is now possible to incorporate as an interactive module within a global flow field analysis the correctly - modelled (and scaled) local shock-boundary layer interaction affects for the non-separating case. The non-asymptotic triple-deck interaction theory involved covers a wide range of practical Reynolds numbers and turbulent boundary layer profile shape factors including the effect of wall curvature; moreover, it gives an approximate indication of when incipient separation occurs. It was further shown that such theory is generally desireable when accurate predictions are desired in the important trailing edge region of rear-loaded supercritical air-foils (or approaching the base of axi-symmetric projectile bodies), because the detailed changes across an upstream interaction can significantly alter the subsequent turbulent boundary layer behavior for appreciable distances downstream.

---

* In such cases, of course, it might be desirable to employ a more sophisticated finite-difference turbulent boundary layer code with a relaxation-type eddy viscosity model.

Three areas of future application warranting further study appear to be of practical interest. (1) Extension of the present interaction theory to the unsteady case (examining first the validity of the quasi-steady approximation) in order to study unsteady air loads due to flutter at transonic speeds. (2) Adaptation to three dimensional flow fields of finite-span wings, at least outside wing/fuselage juncture or tip - influence regions. (3) More detailed study of the effects of shock-boundary layer interactions on transonic internal flows within engine inlets and ducts and turbomachinery blade passages and cascades. The influence of these interactions on the resulting losses and downstream effects, especially with incipient separation, is important to understand and predict in practice.

REFERENCES

1. Ackeret, J., F. Feldman and N. Rott, "Investigations of Compression Shocks and Boundary Layers in Gases Moving at High Speed," NACA TM-1113, Jan 1947.

2. Inger, G. R. and W. H. Mason, "Analytical Theory of Transonic Normal Shock-Boundary Layer Interaction," AIAA Paper 75-831, June 1975 (abbreviated version published in AIAA Jour. 14, pp. 1266-72, Sept. 1976)

3. Inger, G. R., "Shock Wave Penetration and Lateral Pressure Gradient Effects on Transonic Normal Shock-Turbulent Boundary Layer Interactions," AIAA J. 15, Aug. 1977, pp. 1179-1200, plus 16, May 1978, p. 541.

4. Inger, G. R., "Upstream Influence and Skin Friction in Non-Separating Shock Turbulent Boundary Layer Interactions," AIAA Paper 80-1411, Snowmass, Colorado, July 1980.

5. Lighthill, M. J., "On Boundary Layers and Upstream Influence; II. Supersonic Flow Without Separation," Proc. Royal Soc. A 217, 1953, pp. 478-507

6. Stewartson, K. and P. G. Williams, "Self-Induced Separation," Proc. Royal Soc. A312, 1969, pp. 181-206.

7. Stratford, B. S., "The Prediction of Separation of the Turbulent Boundary Layer," Jour. Fluid Mech. 5, pp. 1-16, 1959.

8. Townsend, A. A., "The Behavior of a Turbulent Boundary Layer Near Separation," Jour. Fluid Mech. 12, 1962, pp. 536.

9. Melnik, R. E., and B. Grossman, "Analysis of the Interaction of a Weak Normal Shock Wave with a Turbulent Boundary Layer," AIAA Paper 74-598, June 1974.

10. Adamson, T. C. and A. Feo, "Interaction Between a Shock Wave and a Turbulent Layer in Transonic Flow," SIAM Jour. Appl. Math 29, July 1975, pp. 121-144.

11. Gadd, G. E., "Interactions Between Wholly Laminar or Wholly Turbulent Boundary Layers and Shock Wave Strong Enough to Cause Separation," Jour. of the Aeronaut. Sci. 20, Nov. 1953, p. 729.

12. Honda, M., "A Theoretical Investigation of the Interaction Between Shock Waves and Boundary Layers," Jour. Aero/Space Sci. 25, Nov. 1958, pp. 667-677.

13. Hankey, W. and J. Shang, "Numerical Solution of the Navier-Stokes Equations for Supersonic Turbulent Flow over a Compression Ramp," AIAA Paper 75-3, Pasadena, Jan. 1975.

14. Reeves, B. L., "Two-Layer Model of Turbulent Boundary Layer," AIAA Jour. 12, July 1974, pp. 932-39.

15. Bogdonoff, S. M. and C. Kepler, "Separation of a Supersonic Turbulent Boundary Layer," Jour. Aero. Sci. 22, June 1955, pp. 414.

16. McDonald, H., "A Study of the Turbulent Separated Flow Region Occuring at a Compression Corner in Supersonic Flow," Jour. Fluid Mech. 22, pt. 3, 1965, pp. 481-505.

17. Ray, A. K., "Correlation of Shock-Boundary Layer Interactions," Zeit. Flugwiss. 10, Heft 6, 1962.

18. Tani, I., "Review of Some Experimental Results on the Response of a Turbulent Boundary Layer to Sudden Perturbations," Proc. of AFOSR-IFP Stanford Conference on Computation of Turbulent Boundary Layers - 1968, Vol. 1, pp. 483-494.

19. Narasimha, R. and K. R. Screenivasan, "Relaminarization in Highly-Accelerated Turbulent Boundary Layers," JFM 61, 1973, pp. 417-447.

20. Inger, G. R. and E. P. Williams, "Subsonic and Supersonic Boundary-Layer Flow Past a Wavy Wall," AIAA Jour., Vol. 10, pp. 636-642, May 1972.

21. Zilker, D. P., G. W. Cook and T. J. Hanratty, "Influence of the Amplitude of a Solid Wavy Wall on a Turbulent Flow. Part 1: Non-Separated Flow," Jour. Fluid Mech. 82, Pt. 1, 1977, pp. 29-51.

22. Lekoudis, S. G., A. H. Nayfeh and W. S. Saric, "Compressible Boundary Layers Over Wavy Walls," Physics of Fluids 19, 4, April 1976, pp. 514-519.

23. Trilling, L. and R. J. Hakkinen, "The Calibration of the Stanton Tube as a Skin Friction Meter," M.I.T. Dept. of Aeronautics Report, Cambridge, 1958 (NASA Memo 2-17-59W, 1959.)

24. Ludwig, H. and W. Tillman, "Investigation of the Wall Shearing Stress in Turbulent Boundary Layers," NACA TM-1285, 1950.

25. Brown, G., "Theory and Application of Heated Films for Skin Friction Measurement," in Proc. 1967 Heat Transfer and Fluid Mechanics Institute, Stanford Univ. Press, pp. 361-383.

26. Tyler, R. D. and A. Shapiro, "Pressure Rise Required for Separation in Interaction Between Turbulent Boundary Layers and Shock Waves," Jour. Aero. Sci. 20, Dec. 1953, pp. 858-860.

27. Stalker, R. J., "Sweepback Effects on Turbulent Boundary Layer-Shock Wave Interaction," Jour. Aero Sci. 27, May 1960, pp. 348-356.

28. Gai, S. L., "On the Upstream Influence Associated with the Critical Pressure Rise in Shock-Boundary Layer Interactions," Zeit. FlugWiss. 18, Heft 1, 1970, pp. 8-11.

29. Horstmann, C. C., G. Settles, I. Vas, S. Bogdonoff and C. Hung, "Reynolds Number Effects on Shock-Wave-Turbulent Boundary Layer Interactions," AIAA Jour. 15, Aug. 1977, pp. 1152-58.

30. Rose, W. C. and D. A. Johnson, "Turbulence in Shock Wave-Boundary layer Interactions," AIAA Jour. 13, pp. 884-89, July 1975.

31. Rose, W. C., J. D. Murphy and E. C. Watson, "Interaction of an Oblique Shock Wave with a Turbulent Boundary Layer," AIAA Jour. 7, Dec. 1969, pp. 2211-2221.

32. Rose, W. C., "A Method for Analyzing the Interaction of an Oblique Shock Wave with a Turbulent Boundary Layer," NASA SP-228, pp. 541-568.

33. Green, J. E., "Interactions Bewteen Shock Waves and Boundary Layers," in Progress of Aero. Sci., Vol. 11, Pergamon, N.Y., 1965, pp. 319.

34. Hankey, W. L. and M. S. Holden, "Two-Dimensional Shock Wave-Boundary Layer Interactions in High Speed Flow," AGARDograph 203, June 1974.

35. Burggraf, O. R., "Asymptotic Theory of Separation and Attachment of a Laminar Boundary Layer on a Compression Ramp," in AGARD CP-168 - Flow Separation, 1975.

36. Werle, M. and S. D. Bertke, "Application of an Interacting Boundary Layer MOdel to the Supersonic Turbulent Separation Problem," Univ. of Cincinnati Report AFL 76-4-21, Aug. 1976.

37. Le Balleur, J. C., R. Peyret and H. Vivand, "Numerical Studies in High Reynolds Number Aerodynamics," in Computers and Fluids, Vol. 8, Pergamon, 1980, pp. 1-30.

38. Ragab, S. A. and A. H. Neyfeh, "A Second Order Asymptotic Solution for Laminar Separation of Supersonic Flows Past Compression Ramps," AIAA 78-1132, 1978.

39. Murman, E. M. and J. D. Cole, "Calculation of Plane Steady Transonic Flow," AIAA Jour. 9, Jan. 1971, pp. 114-121.

40. Yajnik, A., "Asymptotic Theory of Turbulent Wall Boundary Layer Flows," JFM 42, 1970, pp. 411-427.

41. Rose, W. C. and M. E. Childs, "Reynolds Shear Stress Measurements in a Compressible Boundary Layer within a Shock Wave-Induced Adverse Pressure Gradient," JFM 65, 1, 1974, pp. 177-138.

42. Davis, R. E., "Perturbed Turbulent Flow, Eddy Viscosity and the Generation of Turbulent Stresses," JFM 63, pt. 4, 1974, pp. 673-693.

43. Deissler, R. G., "Evolution of a Moderately-Short Turbulent Boundary Layer in a Severe Pressure Gradient," JFM 64, 1974, pp. 763-774.

44. Rotta, J. C., "Turbulent Boundary Layers in Incompressible Flow," in Progress of Aero. Sci 2, Pergamon, NY., 1962, pp. 1-220.

45. Anatonia, R. A. and R. E. Luxton, "The Response of a Turbulent Boundary Layer to a Step Change in Surface Roughness," Jour. of Basic Eng. 93, 1, March 1971, pp. 22-34.

46. Schofield, W. H., "Measurements in Adverse Pressure Gradient Turbulent Boundary Layers with a Step Change in Surface Roughness," JFM 10, 1975, pp. 575-593.

47. Settles, G. S., "An experimental Study of Compressible Turbulent Boundary Layer Separation at High Reynolds Numbers," Ph.D. Thesis, Aerospace & Mechanical Sciences Dept., Princeton University, Sept. 1975.

48. Cebeci, T. and P. Bradshaw, Momentum Transfer in Boundary Layers, McGraw-Hill/Hemisphere, Wash., D.C., 1977, p. 365.

49. Lew, H. G. and H. Li, "The Role of the Turbulent Viscous Sublayer in the Formation of Surface Patterns," General Electric Missile and Space Systems Report R685D12, King of Prussia, Pa., June 1968.

50. Spence, D. A., "Velocity and Enthalpy Distributions in the Compressible Turbulent Boundary Layer," JFM 8, 1960, pp. 368-387.

51. Burggraf, O. R., "The Compressibility Transformation and the Turbulent Boundary Layer Equation," Jour. of the Aerospace Sci. 29, 1962, pp. 434-439.

52. Fiore, A., "Law of the Wall Correlations of Hypersonic Turbulent Boundary Layer Experiments," AFFDL Report, Wright-Patterson AFB, Sept. 1979 (AFFDL-TR-77-80)

53. Jobe, C. E. and W. L. Hankey, "Turbulent Boundary Layer Calculations in Adverse Pressure Gradient Flows," AIAA Paper 80-0136, Pasadena, Jan. 1980.

54. Van Driest, E. R., "Turbulent Boundary Layers in Compressible Fluids," Jour. of the Aeronaut. Sci. 18, March 1951, pp. 145-160.

55. Inger, G. R., "Three-Dimensional Heat Transfer and Ablation Disturbances in High Speed Flows," AIAA Jour. 10, Dec. 1972, pp. 1641-46.

56. Inger, G. R., "Transonic Shock-Turbulent Boundary Layer Interaction with Suction or Blowing," AIAA Paper 76-0005, New Orleans, Jan. 1979. (also see Jour. of Aircraft 15, Nov. 1978, pp. 750-54.

57. Panaras, A. G. and G. R. Inger, "Normal Shock-Boundary Layer Interaction in Transonic Speed in the Presence of Streamwise Pressure Gradient," ASME Paper 77-GT-34, Phila., Pa., April 1977.

58. Walz, A., "Boundary Layers of Flow and Temperature," M.I.T. Press, Cambridge, Mass., 1969, pp. 113.

59. Nandanan, M., E. Stanewsky and G. R. Inger, "A Computational Procedure for Transonic Airfoil Flow Including a Special Solution for Shock-Boundary Layer Interaction," AIAA Paper 80-1389, Snowmass, July 1980.

60. Oswaitisch, K. and J. Zierep, "Das Problem des Senkrechten Stosses an Einer Gerkrumpten Wand," ZAMM 40, 1960, p. 143.

61. Inger, G. R. and H. Sobieczky, "Normal Shock Interaction with a Turbulent Boundary Layer on a Curved Wall," VPI&SU Report Aero-088, Blacksburg, Oct. 1978.

62. Jameson, A., "Iteractive Solution of Transonic Flows Over Airfoils and Wings," Comm. Pure & App. Math 27, 1974, pp. 253-309.

63. Bradshaw, P., "Effects of Streamline Curvature on Turbulent Flow," AGARDograph 169, Aug. 1973.

64. Squire, L. C. and M. J. Smith, "Interaction of a Shock Wave with a Turbulent Boundary Layer Disturbed by Suction," Aeronautical Quarterly (to be published).

65. Deiwert, G. S., "Numerical Simulation of High Reynolds Number Transonic Flows," AIAA J. 13, pp. 1354-1359, Oct. 1975.

66. Deane, A., M. S. Thesis, VPI&SU (In preparation)

67. Nussdorfer, T. J., "Some Observations of Shock-Induced Turbulent Separation on Supersonic Diffusors," NACA RM E51L26, May 1956.

68. Moses, H. L., "A Strip-Integral Method for Predicting the Behavior of Turbulent Boundary Layers," Proc. Computation of Turbulent Boundary Layers - 1968 AFOSR-IFP-Stanford Conf., Vol. 1, (S. Kline et. al., Ed.) Stanford U. Press, Aug. 1968, pp. 76-82.

69. Inger, G. R. and J. C. Cantrell, "Application of Shock-Turbulent Boundary Layer Interaction Theory to Transonic Aerodynamics," Proc. 1979 U.S.A.F.-Fed. Republic of Germany D.E.A. Meeting, April 1979 (also see J. C. Cantrell, M.S. Thesis in Aero Eng., VPI&SU, Blacksburg, June 1979).

70. Melnik, R. E., R. Chow and H. R. Mead, "Theory of Viscous Transonic Flow Over Airfoils at High Reynolds number", AIAA Paper 77-680, June, 1977.

71. Rekiis, R. P., J. E. Danberg and G. R. Inger, "Boundary Layer Flows on Transonic Projectiles," AIAA Paper 79-1551, Williamsburg, July 1979.

72. Nietubicz, C. J., J. E. Danberg and G. R. Inger, "A Theoretical and Experimental Investigation of a Transonic Projectile Flow Field," in Proc. 1980 U. S. - F.R.G.D.E.A. Meeting, Annapolis, MD., April 1980.

73. Liu, C. Y., "Turbulent Skin Friction Coefficient and Momentum Thickness in Adverse Pressure Gradient," Jour. of Aircraft 6, Jan. 1969, pp. 78.

ACKNOWLEDGEMENT

This work was partially supported by the Office of Naval Research under Contract N00014-80-C-0470.

APPENDIX

COMPOSITE LAW OF THE WALL - LAW OF THE WAKE TURBULENT VELOCITY PROFILE RELATIONSHIPS

Because of its convenient analytical form, accurate blended representation of the combined Law of the Wall - Law of the Wake behavior and generality, we have adopted Walz's model for the incoming turbulent boundary layer upstream of the interaction.[22] For the low Mach number adiabatic wall conditions appropriate to transonic interactions, it may be satisfactorily corrected for compressibility effects by the Eckert Reference Temperature method which under these conditions is, in fact, comparable in accuracy to, but far simpler to implement than, the Van Driest compressibility transformation approach.

Let π be Coles' (incompressible) Wake Function, $\eta \equiv y/\delta$ and denote for convenience $R \equiv .41\, Re_{\delta_0}^*/[(1+\eta)(T_w/T_e)^{\omega+w}]$, $T_w/T_e = 1 + .18\, M_e^2$ with $w = .76$ for a perfect gas; then the compressible form of Walz's composite profile may be written

$$\frac{U_o}{U_e} = 1 + \frac{1}{.41}\sqrt{\frac{C_{f_o}}{2}\left(\frac{T_w}{T_e}\right)}\left\{\left(\frac{R}{1+R}\right)\eta^2(1-\eta) - 2\pi + 2\pi\cdot\eta^2(3-2\eta) + \ln\left(\frac{1+R\eta}{1+R}\right) - (.215 + .655\,R\eta)e^{-.3R\eta}\right\} \tag{A-1}$$

subject to the following condition linking π to C_{f_o} and $Re_{\delta_0^*}$:

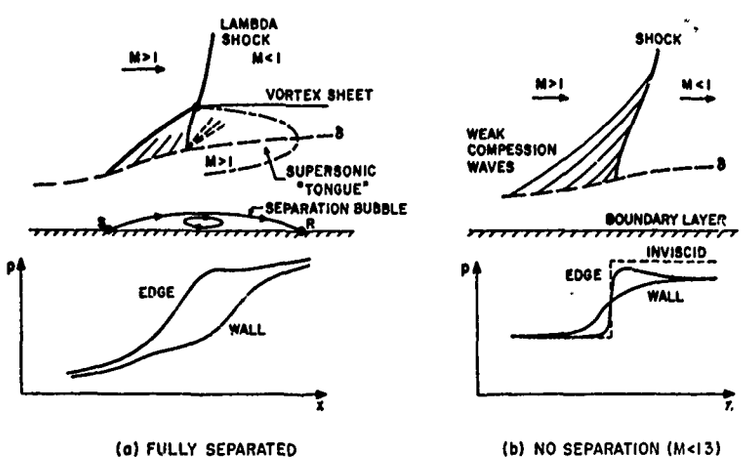
$$2\pi + .215 + \ln(1+R) = \frac{.41}{\sqrt{\frac{C_{f_o}}{2}\left(\frac{T_w}{T_e}\right)}} \tag{A-2}$$

Eqs. (A-1) and (A-2) have the following desirable properties: (a) For $\eta \geq .10$ or so, $\frac{U_o}{U_e}$ is dominated by a Law of the Wake behavior which correctly satisfies both the outer limit conditions $U_o/U_e \to 1$ and $dU_o/dy \to 0$ as $\eta \to 1$; (b) on the otherhand, for very small η values, U_o assumes a Law of the Wall - type behavior consisting of a logarithmic term that is exponentially damped out extremely close to the wall into a linear laminar sublayer profile $U/U_e = R\eta$ as $\eta \to 0$; (c) Eq. (A-1) may be differentiated W.R.T. η to yield an analytical expression for dU_o/dy also, which proves advantageous in solving the middle and inner deck interaction problems (see text) where dU_o/dy must be known and vanish at the boundary layer edge.

The use of the incompressible form of (A-1) in the defining integral relations for δ_i^* and θ_i^* yields the following relationship that links the wake parameter to the resulting incompressible shape factor $H_{1_i} = (\delta_i^*/\theta_i^*)_o$:

$$\frac{H_{1_i} - 1}{H_{1_i}} = \frac{2}{.41}\sqrt{\left(\frac{T_w}{T_e}\right)\frac{C_{f_o}}{2}}\left(\frac{1 + 1.59\pi + .75\,\pi^2}{1+\pi}\right) \tag{A-3}$$

Equations (A-2) and (A-3 together with the defining relation for R enable a rather general and convenient parameterization of the profile (and hence the interaction that depends on it) in terms of three important physical quantities: the shock strength (M_e), the displacement thickness Reynolds number Re_{δ^*} and the shape factor H_{1_i} that reflects the prior upstream history of the incoming boundary layer including possible pressure gradient and surface mass transfer effects. With these parameters prescribed, the aforementioned three equations may be solved simultaneously for the attendant skin friction value C_{f_o}, the value of R and, if desired, the π value appropriate to these flow conditions.



(a) FULLY SEPARATED (b) NO SEPARATION (M<13)

Fig. 1 Separation Effect on Transonic Shock-Turbulent Boundary Layer Interaction.

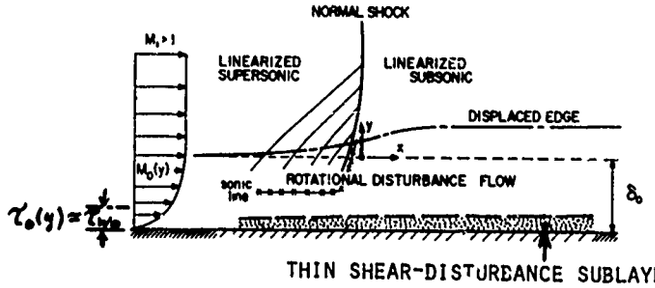


Fig. 2

Triple-Deck Structure of the Local Disturbance Field in a Transonic Interaction.

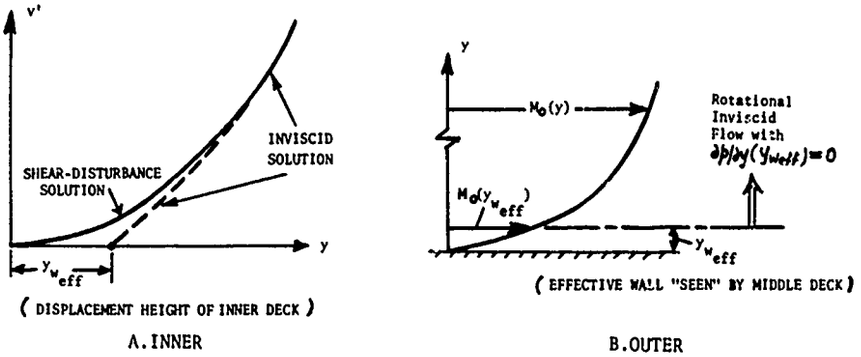


Fig. 3 Middle-Inner Deck Matching by the Effective Wall Concept.

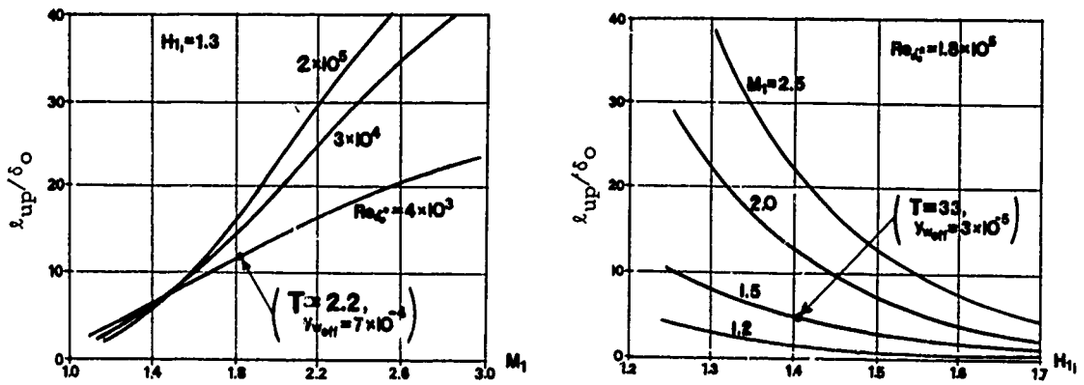


Fig. 4 Upstream Influence Distance for Turbulent Interactions Based on Law of Wall/ Wake Profile.

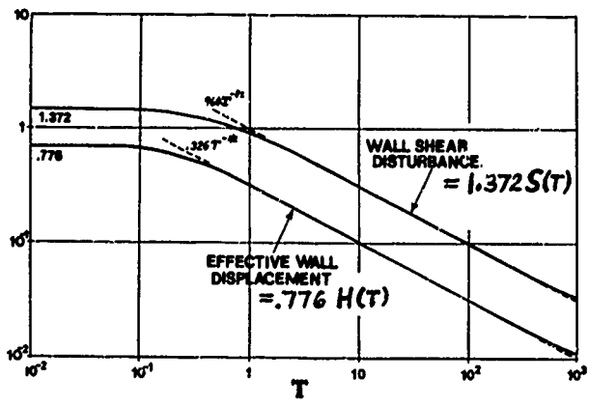
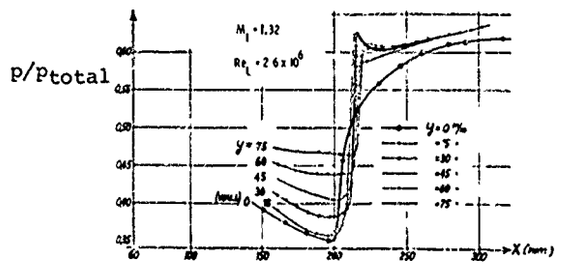


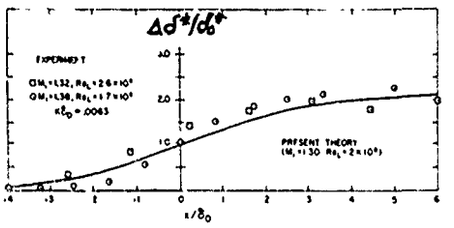
Fig. 5

Wall Turbulence Effect on Inner Deck Displacement Thickness and Disturbance Skin Friction.

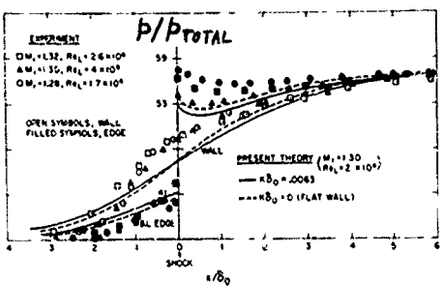
$M_1 = 1.32 \quad Re_L = 2.6 \times 10^6$



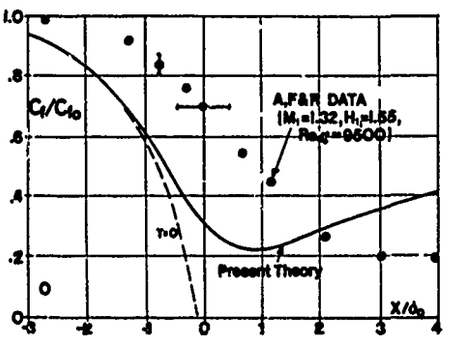
a) Typical Pressure Data



c) Displacement Thickness



b) Wall and B.L. Edge Pressures



d) Skin Friction

Fig. 6 Comparisons of Present Interaction Theory Results with Experimental Data of Ackeret, Feldman and Rott

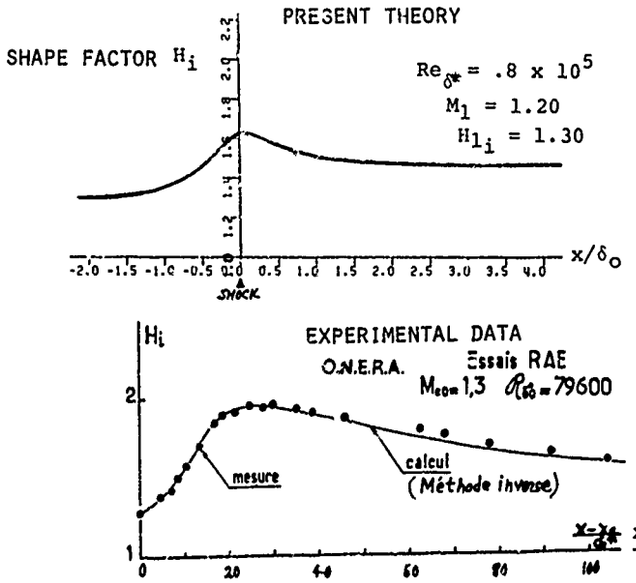


Fig. 7 Comparison of Theoretical and Experimental Shape Factor Distributions Along the Interaction.

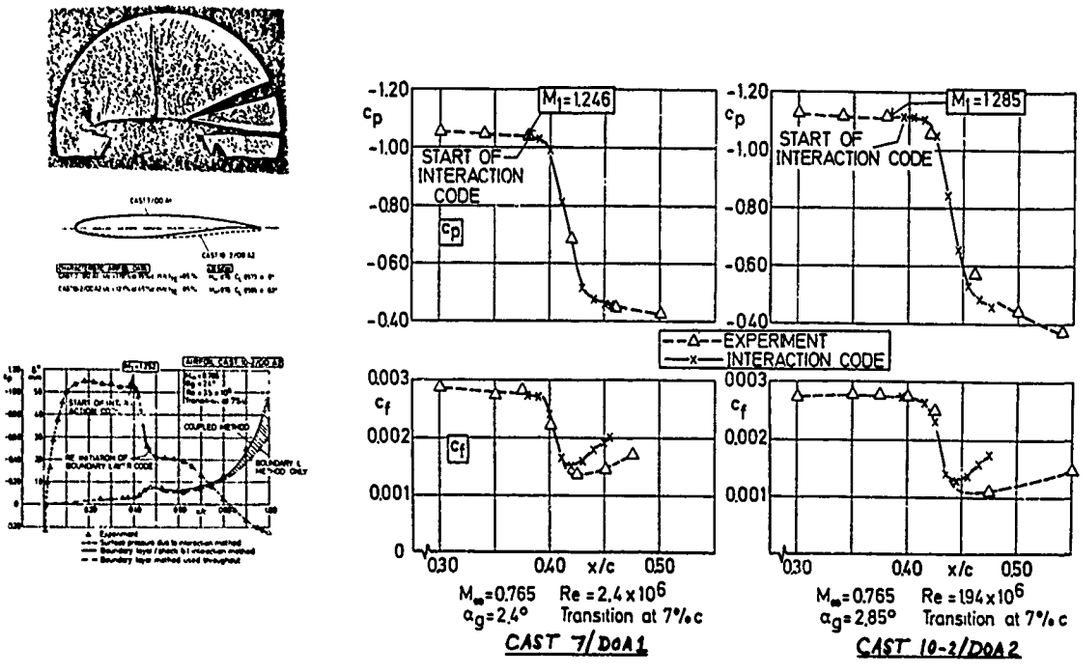
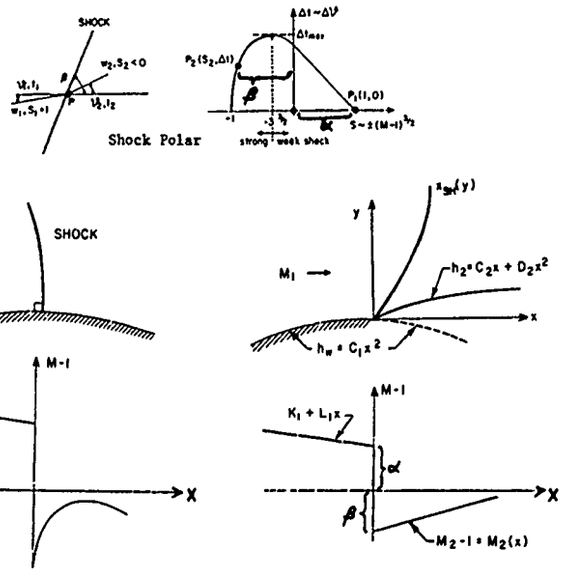


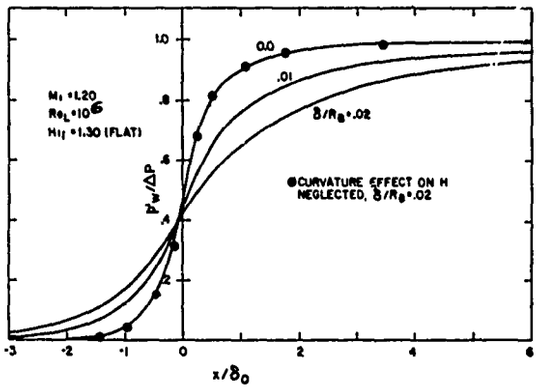
Fig. 8 Comparison of Present Interaction Theory with Experimental Data of Stanewsky (DFVLR-GÖ)



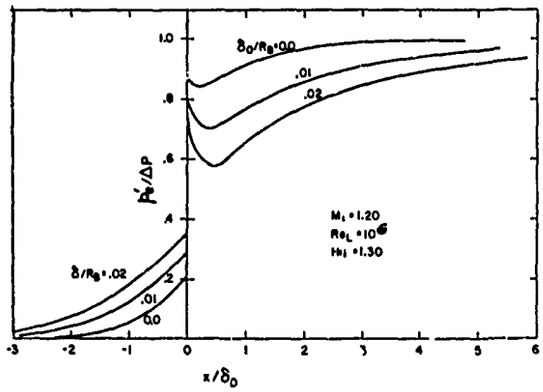
A. Singular: Viscous Displacement Effect Neglected.

B. Regular: Viscous Displacement Effect Included.

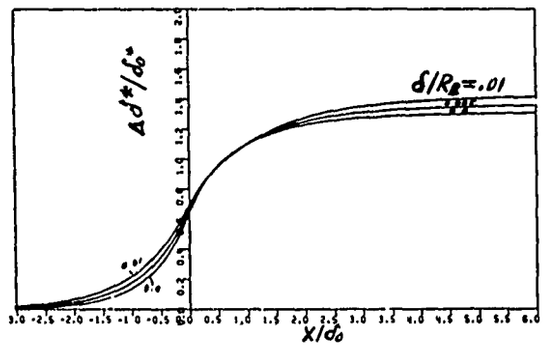
Fig. 9 Singular and Regular Inviscid External Flow Models for Curved Wall Interactions



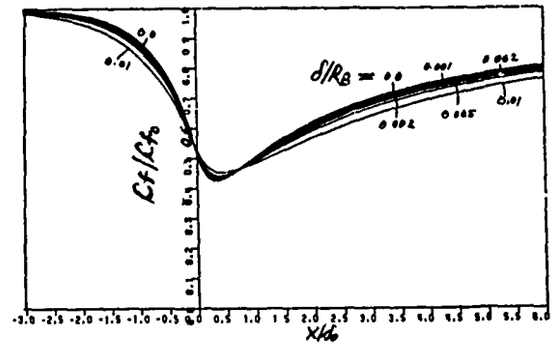
a) Wall Pressure



b) B.L. Edge Pressure

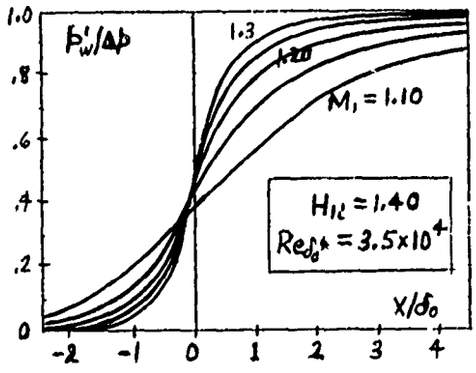


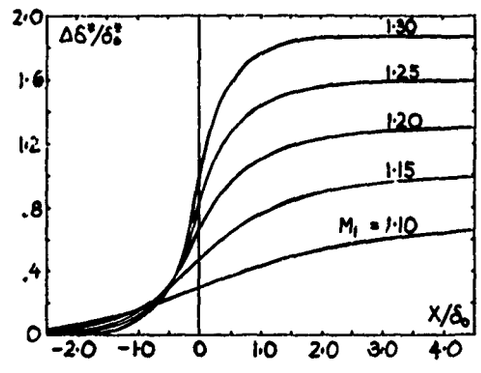
c) Displacement Thickness

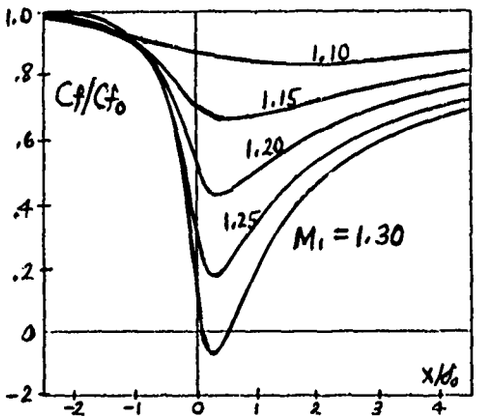


d) Skin Friction

Fig. 10 Parametric Study of Wall Curvature Effect







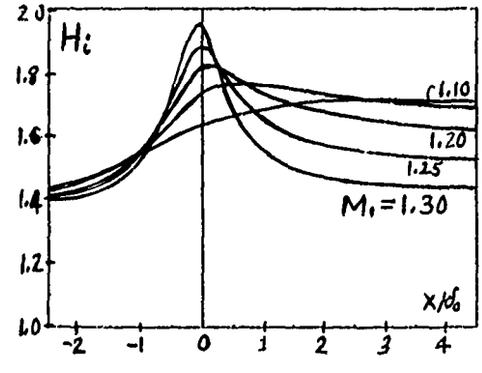


Fig. 11 Parametric Study of the Interaction Solution: Effect of Shock Strength.

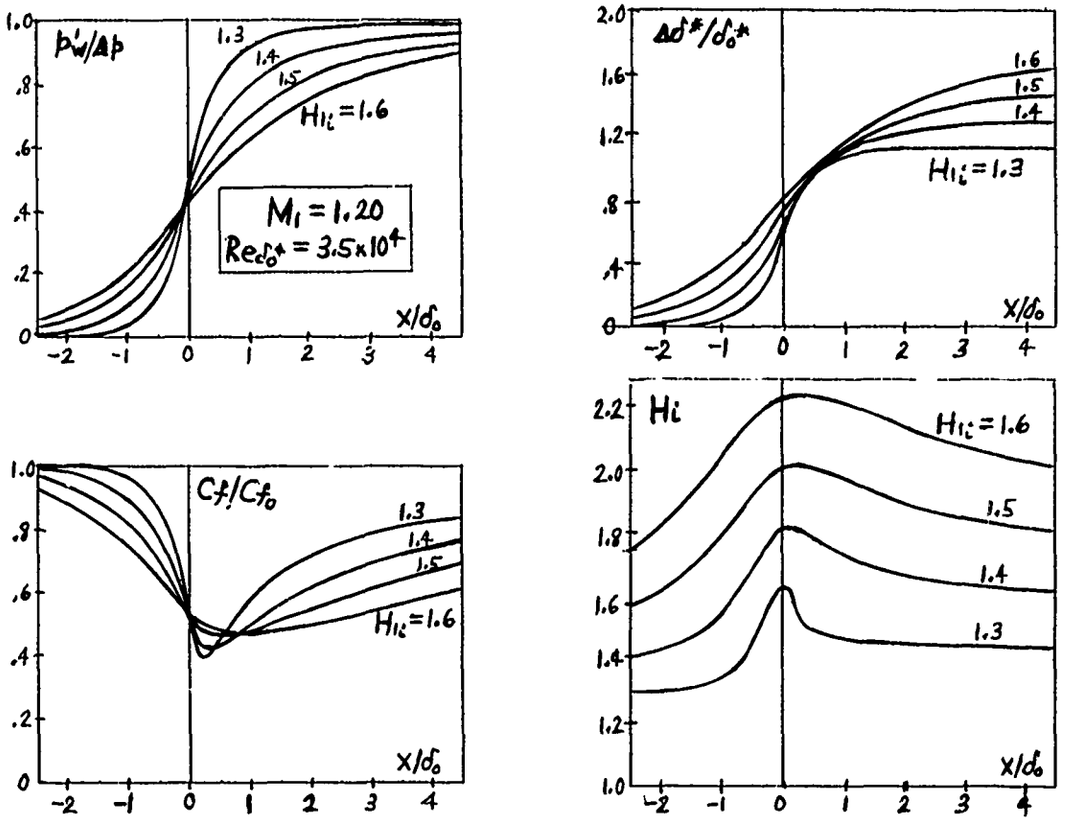


Fig. 12 Parametric Study of the Interaction Solution: Effect of Shape Factor.

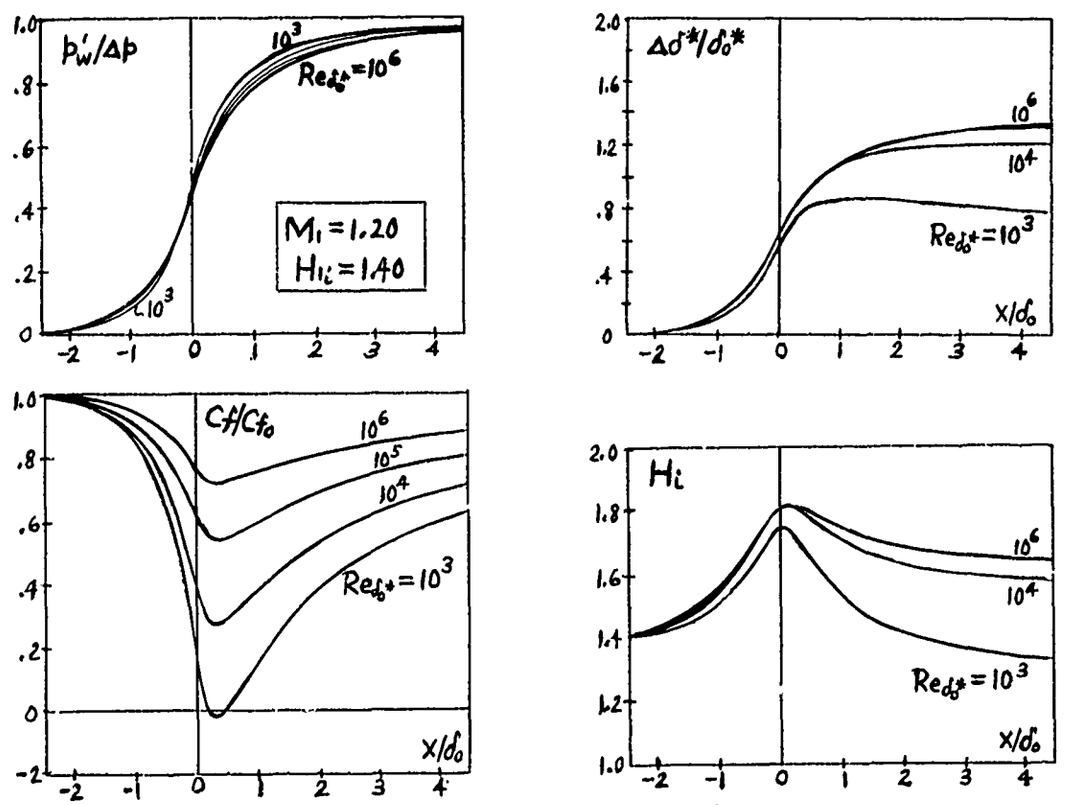


Fig. 13 Parametric Study of the Interaction Solution: Reynolds Number (Scale) Effect

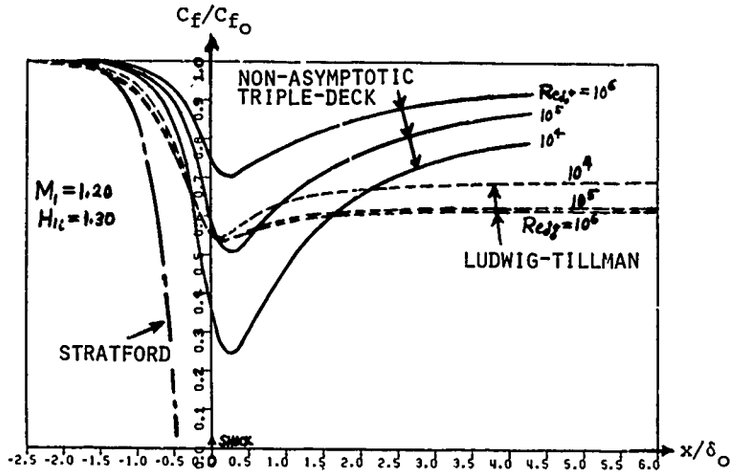


Fig. 14

Ludwig-Tillman Predictions in Interaction Region.

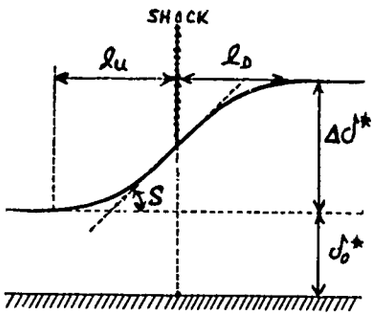
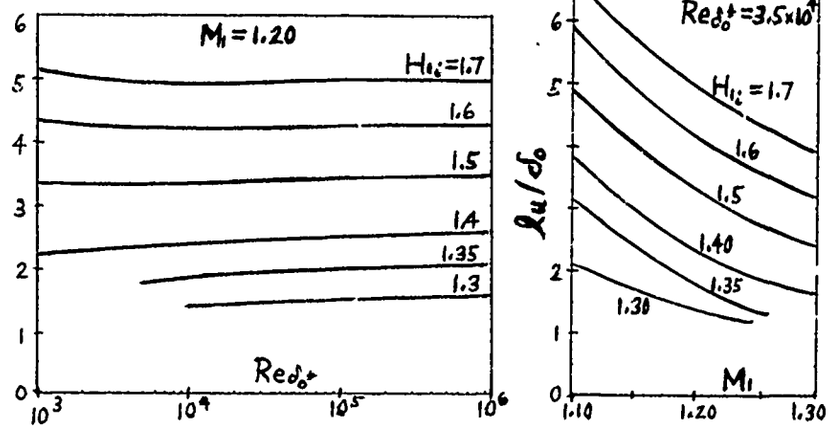
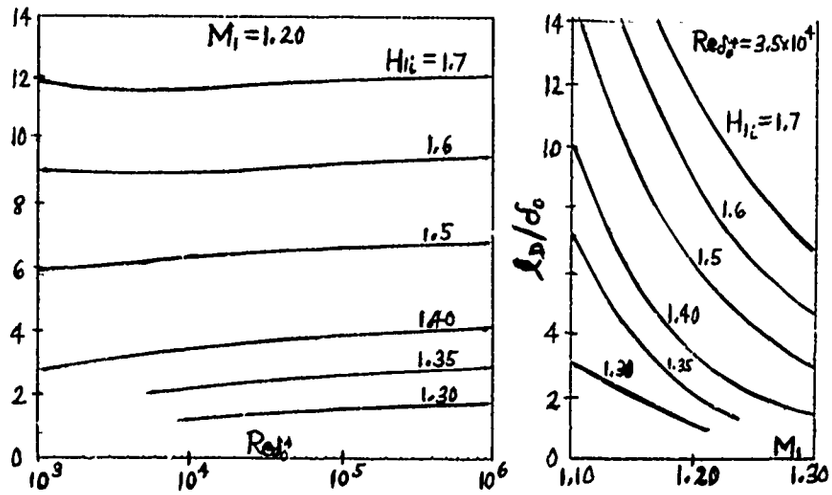


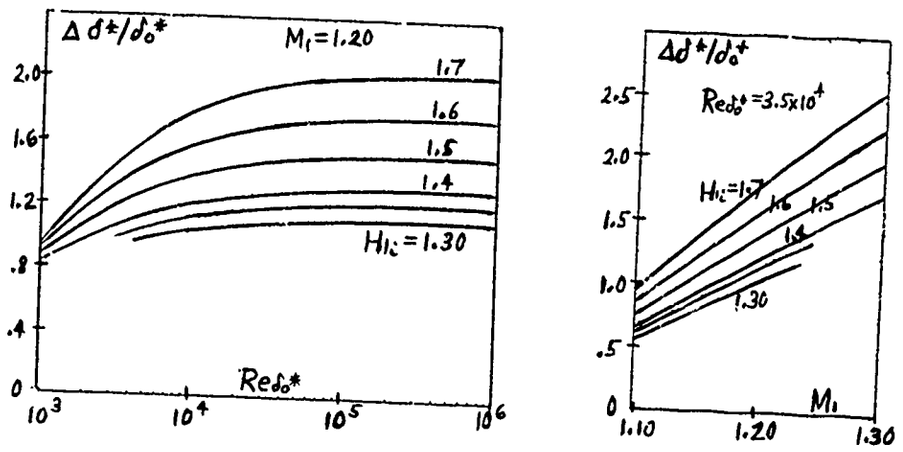
Fig. 15 Parametric Study of Viscous Wedge Interaction Model

a. Upstream Influence Distance

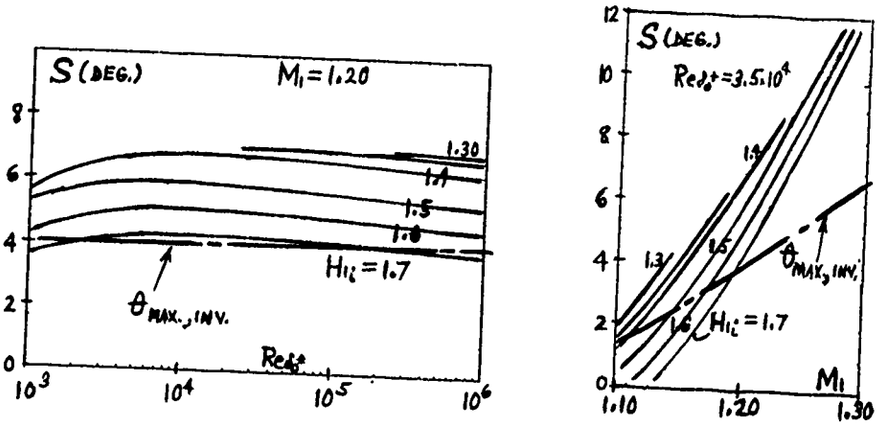


b. Downstream Influence Distance

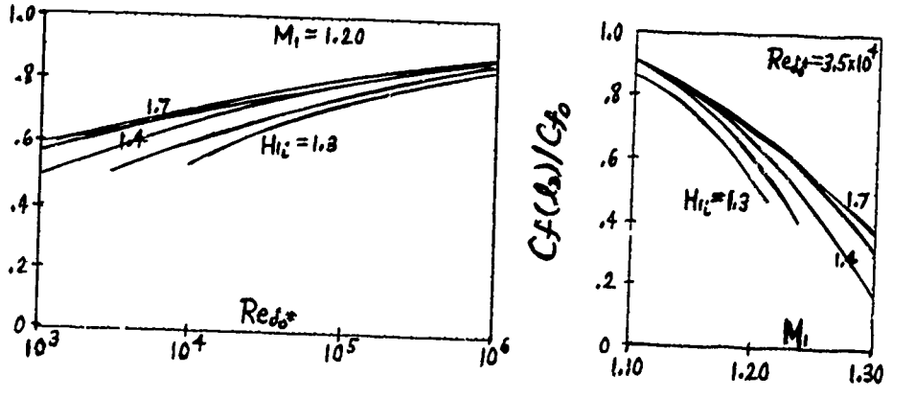




c. Overall Displacement Thickening



d. Viscous Wedge Slope



e. Post-Interactive Skin Friction Level

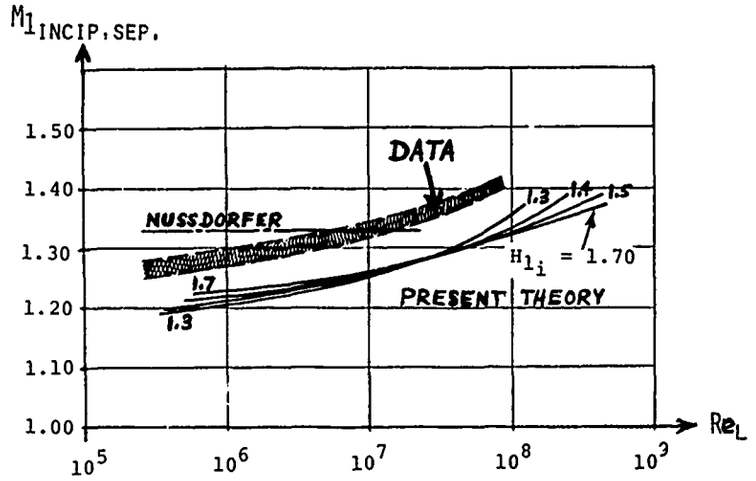
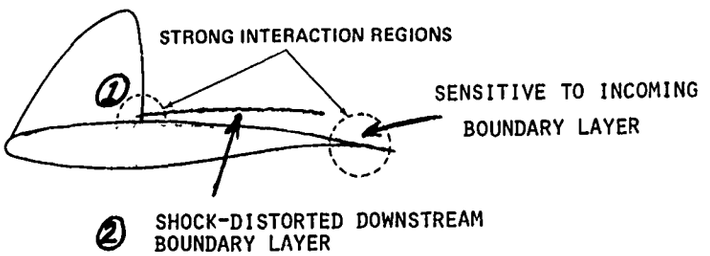


Fig. 16

Incipient Separation Conditions

Fig. 17

The Global Viscous-Inviscid Interaction Problem for Supercritical Airfoils (Schematic)



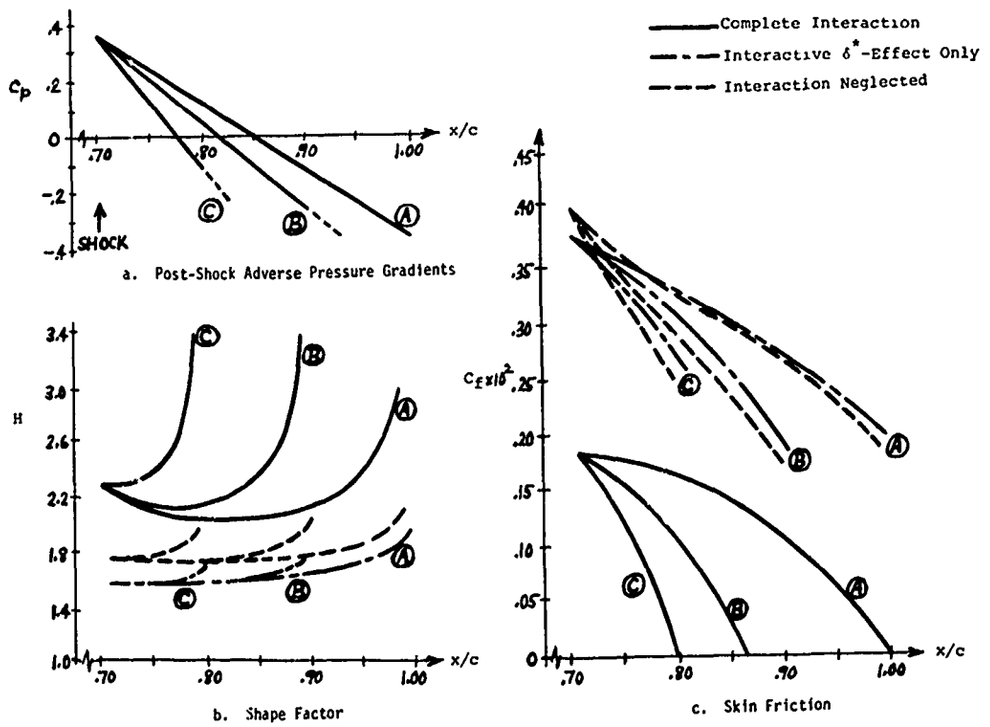
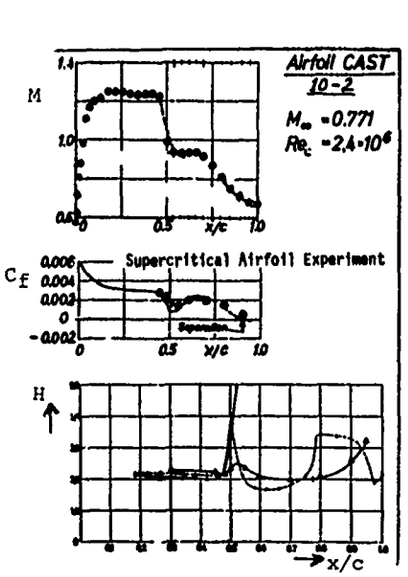


Fig. 18

Sensitivity Study of Interaction Effects on Downstream Turbulent Boundary Layer Behavior



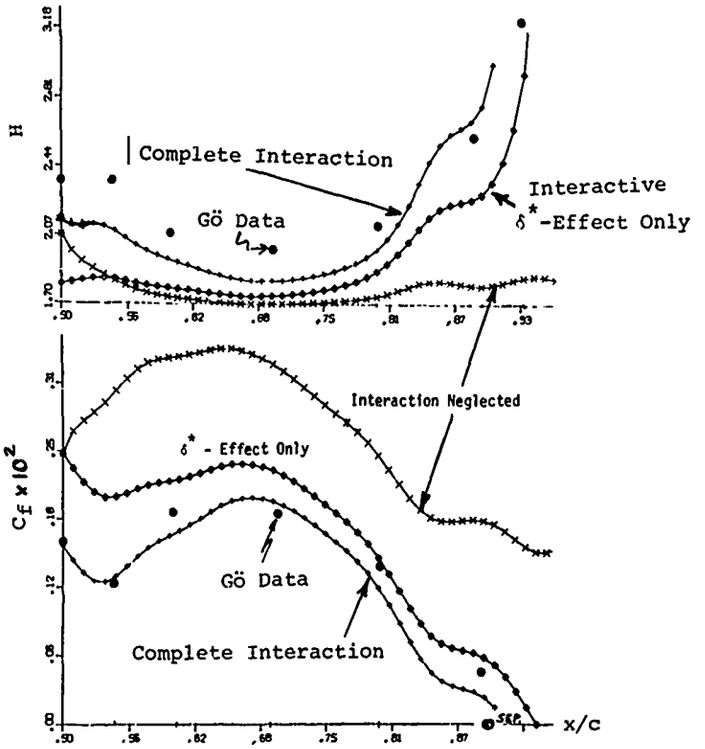
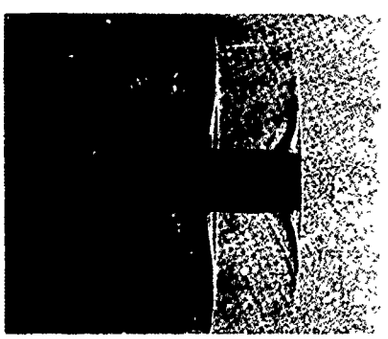
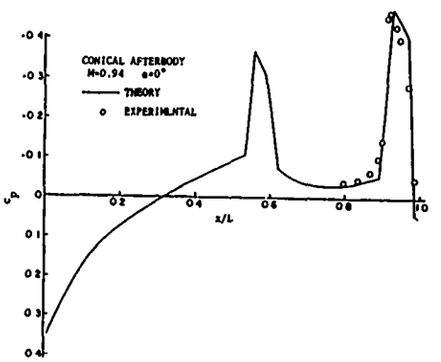


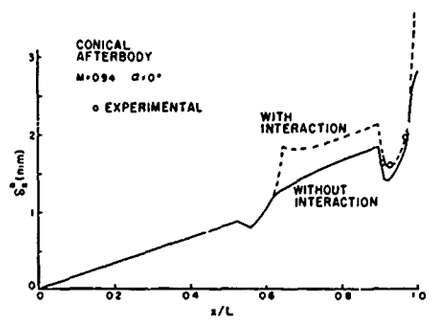
Fig. 19
Comparison of Post-Interaction Turbulent Boundary Layer Predictions with Experiment on a Supercritical Airfoil



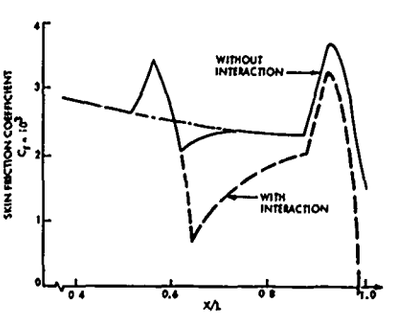
Typical Multiple-Shock Pattern



Pressure Distribution

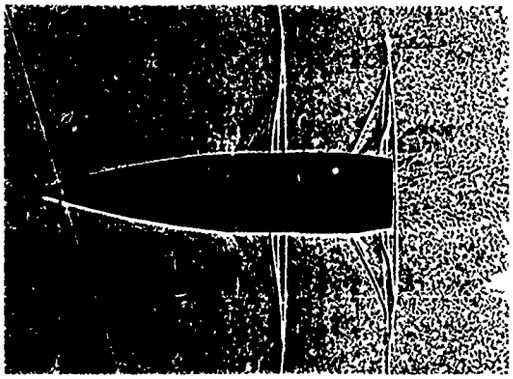


Displacement Thickness



Skin Friction

Fig. 20 Composite Inviscid-Boundary Layer-Interaction Theory Predictions for a Boattailed Body of Revolution at M_∞ = .940



SECANT OGIVE-CYL-BOATTAIL
M_∞ = .908 , α = 0

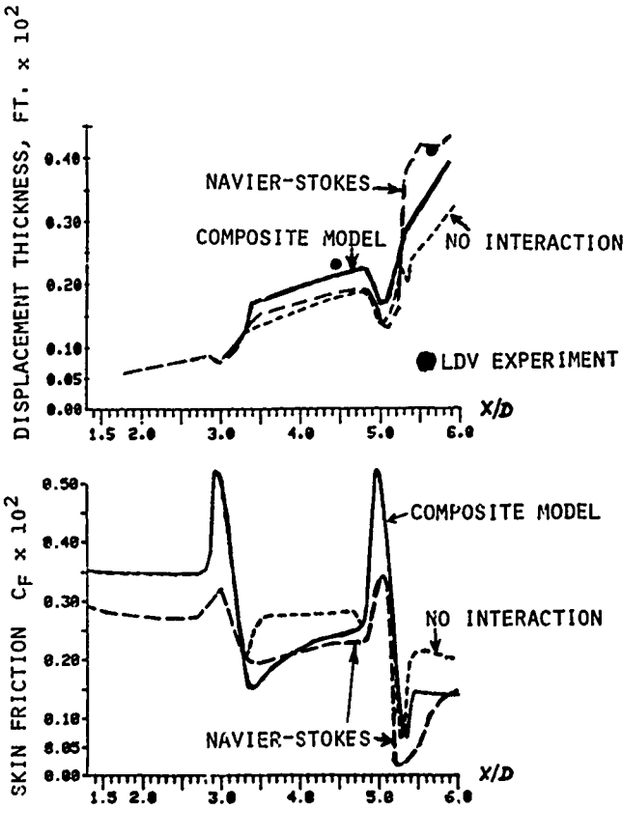


Fig. 21 Comparison of Composite Interaction Solution with Navier-Stokes Code Results and Experiment for a Transonic Body of Revolution.

COMPUTATIONAL ASPECTS AND RESULTS OF LOW SPEED VISCOUS FLOW ABOUT MULTICOMPONENT AIRFOILS*

by
B. Oskam
National Aerospace Laboratory NLR
Anthony Fokkerweg 2
1059 CM AMSTERDAM
The Netherlands

SUMMARY

The viscous flow about multicomponent airfoils has been calculated solving incompressible potential flow and boundary layer problems iteratively. The presence of the shear layers is modeled in the potential flow by an outflow boundary condition on the airfoil surface and the wake centerline. Example solutions show that high accuracy of the potential flow solution is required to justify the correction for viscous effects, especially near the wing trailing edge of a slotted configuration. A second element of the present study is the phenomenon of leading edge stall. Turbulent boundary layer separation at 3 per cent chord, downstream of a laminar separation bubble, is found on the nose of a NACA 63-009 airfoil at high Reynolds number indicating the occurence of turbulent leading edge stall. This phenomenon, being difficult to distinguish from laminar leading edge (short bubble) stall, occurs at such a small scale that it is observed only if one obtains high resolution results. A third point being made concerns the importance of the wing wake of a slotted configuration. The experimental and computational results agree reasonably well at moderate angles of attack. At higher angles of attack it is found that the wing wake streaming along the upper surface of the flap is subjected to a large adverse pressure gradient. The associated extreme growth of the displacement thickness of the wing wake is found to be the major item determining the loss of lift due to viscous effects.

1 INTRODUCTION

Traditionally, the design of high-lift systems has been accomplished mainly by wind tunnel testing The actual steps taken in such a design process are heavily based on experimental data obtained previously. At the same time Smith (Ref. 1) has pointed towards a more scientific approach to the aerodynamic design of high-lift devices. One aspect of such an approach is the unification of theoretical models of various physical flow phenomena, providing a computational tool to analyse for example the viscous flow about multicomponent airfoils. The program of Stevens et al. (Ref. 2) represents one of the first attempts along these lines. Since this initial effort continued usage of the program has resulted in improved versions, see for example Morgan (Ref. 3) and Brune et al. (Ref. 4).

At NLR this line of work towards the use of computers and wind tunnels as complementary aids to design (Ref. 5) is also being pursued. The present research is a continuation of earlier work by Labrujère et al. (Ref. 6) studying the feasibility of using potential flow calculations in the development of high-lift systems. More generally speaking there have been quite a number of studies concerning the viscous flow around multicomponent airfoils. For examples Seebohm et al. (Refs 7 and 8) and Olsen et al. (Ref. 9) have presented experimental data as well as numerical methods.

One of the problems of high-lift aerodynamics is the calculation of maximum lift. Since flows with partial separation are encountered at angles of attack well below the maximum lift condition, one is essentially facing the problem of modeling separated flow, e.g. see Maskew et al. (Ref. 10). Although separated flow models are also being studied at NLR, in the present paper we will only consider viscous flows which remain attached to the surface except possibly for some short laminar separation bubbles. These viscous flows are calculated solving potential flow and boundary layer problems iteratively. The main ingredients, such as the 2D panel method (Ref. 6) and a 2D turbulent boundary layer calculation method (Ref. 11), were developed previously. Evaluation of these theoretical methods has exposed certain defects, requiring both major and minor modifications, which is a similar situation as referred to above (Refs 3 and 4).

In the present method the presence of the boundary layer and wake is modeled in the inviscid flow by an outflow boundary condition which has also been employed by Piers et al. (Ref. 12). The selection of a "Kutta condition" to render this flow unique is not obvious. Melnik et al. (Ref. 13) have indicated that one cannot obtain an asymptotically correct approximation to the lift in viscous flow from the classical (weak) interaction theory. To be consistent one should take normal pressure gradients into account in case of turbulent trailing edge flow, in contrast with laminar flow where normal pressure gradients result in a higher order effect only, see Brown et al. (Ref. 14). At NLR these asymptotically correct formulations are being studied by Veldman (Ref. 15). However, this line of work has not been extended to turbulent flow as yet. The present method, being formulated in 1977, incorporates the Kutta condition of equal pressure at the edge of upper and lower trailing edge boundary layer. Asymptotically speaking it is not a consistent approximation, although it appears to yield a rather good prediction of the viscous correction to lift, see reference 8. Giesing (Ref. 16), following the earlier work presented in the book by Thwaites (Ref. 17), also employed this Kutta condition.

This paper starts with a brief description of the potential flow and boundary layer methods, sections 2 and 3. The viscous-inviscid matching conditions and associated iterative technique to satisfy these conditions are discussed in section 4. Viscous flow solutions, including comparisons between experimental and computational data, are given in the last section. A detailed description of the method of analysis can be found in reference 18.

* Part of this investigation has been performed under contract with the Netherlands Agency for Aerospace Programs (NIVR; contract number 1738).

2 POTENTIAL FLOW METHOD

2.1 Preview

The potential flow panel method utilizes surface source distributions and internal doublet distributions. In the original version of this panel method (Ref. 6) the chordwise variation of the internal doublet strength is prescribed. For thin geometries it has been found that the accuracy of the solution depends critically on the particular form of the assumed doublet shape. Following a study of Rubbert et al. (Ref. 19), and unpublished work by Piers at NLR, this disadvantage is overcome by applying boundary conditions on the mean line and solving for the internal, continuous doublet distributions and surface source distributions simultaneously.

A second point concerns the effects of compressibility. Although even in low speed flow compressibility effects can be quite important, the present study deals with the potential flow of an incompressible fluid only. A field panel method, see Piers et al. (Ref. 20), to solve the full potential equation is being studied at present. This approach may be particularly attractive for low speed flows involving small pockets of high subsonic or transonic speeds.

2.2 Mathematical formulation

We shall consider boundaries as sketched in figure 1. The inviscid, irrotational and incompressible fluid flow in the external domain is given by a total velocity potential Φ satisfying Laplace's equation and the following boundary conditions:

$$\bar{\nabla}\Phi \to \bar{\nabla}\Phi_\infty \qquad \text{at infinity, wake excluded} \tag{1}$$

$$\bar{n}_p \cdot \bar{\nabla}\Phi^+ = v_n^+(P) \qquad P \in TBT^i, \text{ position known} \tag{2}$$

$$\left.\begin{aligned} &\bar{n}_p \cdot \bar{\nabla}\Phi^+ = \tfrac{1}{2} v_n(P) \\ &\bar{n}_p \cdot \bar{\nabla}\Phi^- = -\tfrac{1}{2} v_n(P) \\ &\Phi^+(P) - \Phi^-(P) = \text{constant} \end{aligned}\right| \quad P \in TC^i, \text{ position unknown} \tag{3}$$

$$\text{Kutta condition component } i \tag{4}$$

The outflow distribution v_n is either zero or known from a preceding shear layer calculation. The implementation of the Kutta condition, i.e. equal pressure at the edge of upper and lower boundary at the trailing edge, will be described in section 4.3.

To complete the boundary value problem we formulate the boundary conditions which are applied to the nonphysical flow interior to each component i:

$$\bar{n}_p \cdot \bar{\nabla}\Phi^+ = \bar{n}_p \cdot \bar{\nabla}\Phi^- = v_n(P) \qquad P \in AT^i, \text{ mean line} \tag{5}$$

$$\Phi^- = \Phi^+(P) \qquad P \in TBT^i, \text{ contour} \tag{6}$$

These boundary conditions depend on the solution of the external problem. The normal velocity on the line AT is defined as the difference of the normal velocity on the lower and upper surface divided by two, constituting a mean surface approximation of the external lift problem.

It may be shown, using Green's third identity and part of the boundary conditions, that the solution of the coupled, internal plus external, boundary value problems may be represented by the perturbation potential induced by a distribution of sources σ and doublets μ on the appropriate boundaries, while the undisturbed velocity potential is given by

$$\Phi_\infty(P) = U_\infty \left[\cos\alpha\, x(P) + \sin\alpha\, y(P)\right] . \tag{7}$$

Perturbation potential due to sources of component i:

$$\varphi_s^i(P) = \int_{TBT^i} \frac{\sigma(Q)}{2\pi} \ln|\bar{s}_{PQ}|\, d\ell_Q + \int_{TC^i} \frac{\sigma_w(Q)}{2\pi} \ln|\bar{s}_{PQ}|\, d\ell_Q \tag{8}$$

Perturbation potential due to doublets of component i:

$$\varphi_d^i(P) = \int_{AT^i} \frac{\mu(Q)}{2\pi} \frac{\partial}{\partial n_Q} \ln|\bar{s}_{PQ}|\, d\ell_Q + \int_{TC^i} \frac{\mu_w}{2\pi} \frac{\partial}{\partial n_Q} \ln|\bar{s}_{PQ}|\, d\ell_Q \tag{9}$$

Total potential:

$$\Phi(P) = \Phi_\infty(P) + \sum_{i=1}^{i_c} \left[\varphi_s^i(P) + \varphi_d^i(P)\right] \tag{10}$$

where $\sigma_w(Q) = \bar{n}_Q \cdot \bar{\nabla}\varphi^+ - \bar{n}_Q \cdot \bar{\nabla}\varphi^- = v_n(Q) \qquad Q \in TC^i$

$-\mu_w = \varphi^+(Q) - \varphi^-(Q) = \text{constant} \qquad Q \in TC^i$

i_c : total number of components

$\bar{s}_{PQ} = \bar{x}_Q - \bar{x}_p$, $\bar{x}$ position vector.

Before differentiating the integral representations we will integrate equation (9) by parts. The integration yields:

$$\varphi_d^i(P) = -\int_{AT^i} \frac{\gamma(Q)}{2\pi}\,\theta_{PQ}\,d\ell_Q + \frac{\mu(A^i)}{2\pi}\,\theta_{PA} \qquad (11)$$

where $\theta_{PQ} = \text{atan}\left[\frac{y(Q) - y(p)}{x(Q) - x(p)}\right]$ and $-\frac{\partial \mu}{\partial t_Q}(Q) = \gamma(Q)$ the vorticity.

To satisfy the velocity boundary conditions we differentiate equation (10) to obtain a linear integral representation of the velocity in terms of the distribution of singularities. If the source distribution in the wake vanishes, the boundary conditions reduce to a set of linear integral equations for the unknown singularity distributions σ and γ. Once the linear problem is solved the wake position may be determined by tracing the streamline from each trailing edge. The nonlinear problem, $\sigma_w \neq 0$, may be solved by iteration. A first approximation to the wake position is already known from the solution of the linear problem, $\sigma_w = 0$. An improved approximation may be found by solving a linear problem with $\sigma_w \neq 0$, but a known wake position. The velocity components at the wake centerline may be found subsequently and be used to update its position.

2.3 Panel method

The numerical solution of the linear boundary value problem is accomplished by applying a panel discretization to the set of integral equations. The geometry is approximated by flat panels. The source distribution on the contour and wake is taken to be constant on each panel. The vorticity distribution on the mean line is continuous and varies linearly on each panel. Panel midpoints are selected as control points at which normal velocity boundary conditions are required to be satisfied. Upon integration one obtains a system of m linear algebraic equations, where m is equal to the total of all contour and mean line panels. The total number of unknown singularity parameters equals m+p, however, where p is the number of components. To close the system of algebraic equations we have to add the Kutta conditions, which are generally nonlinear, to the system of m linear algebraic equations. Linearization of the Kutta conditions results in a n by n system of linear algebraic equations, where n equals m+p. The matrix of coefficients cannot be factorized once and for all for a given geometry since the coefficients of the linear equations relating to the Kutta conditions do change. The first m equations remain fixed, however, during the iteration process and during changes in Reynolds number or angle of attack.

This computational effort may be formulated as a large number of linear systems of identical order n which have the first m equations in common. After initial factorization of the first linear system every subsequent solution of another linear system takes only a R/T fraction of the operational counts of the initial solution. It may be shown (Ref. 13) that, if $n \gg 1$ and $p/n \ll 1$, the asymptotic behaviour of R/T is given by

$$\frac{R}{T} = \frac{3}{2}\frac{p}{n} + \frac{3}{n}\,, \qquad (12)$$

where p denotes the number of components. This result is plotted in figure 2 for a range of p and n. The theoretical fraction of operational counts is compared to the corresponding ratio of the Central Processor time on a CDC Cyber 72 computer, showing agreement. It is found that in the present range of application every subsequent solution of a linear system only consumes 2 or 3 per cent of the Central Processor time needed for the initial factorization.

Before starting the discussion of the example solutions we note that the classical Kutta-Joukowski condition of finite velocity at the trailing edge, pertaining to the first inviscid flow solution, cannot be applied in a numerical procedure as it stands. The general approach in numerical procedures is to deduce a flow property, close to the trailing edge, from exact solutions and implement this related property numerically, serving as a Kutta condition, see Hess (Ref. 21). One of the simplest related properties requires the bisector of the trailing edge to be a streamline of the local flow. Example solutions presented in section 2.4 are based on this particular Kutta condition.

2.4 Example solutions

The first example, figure 3, illustrates the solution for an 0.2 per cent thick airfoil at an angle of attack of 3 degrees using 64 contour panels, i.e. $N_c = 64$. The computational results and the corresponding exact solution of a flat plate at 3 degrees incidence are indiscernible. The results of the method of reference 6, the original panel method, clearly show that this method is not applicable to extremely thin geometries. It demonstrates the extended capability of the revised panel method.

The second example involves the application of the present panel method to a two-element airfoil for which an exact solution by Williams (Ref. 22) is available for comparison. This exact solution is compared with the computed pressure distribution in figure 4, where the last 20 per cent of the main element is displayed on an enlarged scale. The agreement with the exact solution is good. The lift and drag coefficients at zero and ten degrees incidence, including the exact values, are given in table 1. The differences between computed and exact coefficients are found to be of the order of 10^{-2}, which compares favourably with other first order panel methods.

The final example is the NLR 7301 airfoil with single slotted flap. Special attention is being paid to the slot area displayed in figure 5. Two potential flow pressure distributions, one obtained with the original panel method (Ref. 6) and the other with the present method, are plotted. It is observed that the original method overpredicts the adverse pressure gradient on the wing upper surface, which in viscous-inviscid computation invariably led to the prediction of early turbulent boundary layer separation. This separation is not found experimentally, however, the false prediction being the result of errors in the original panel method solution.

Reducing the number of panels on the configuration, by a factor of 4, does not change the pressure level on the wing, although the resolution becomes questionable. The corresponding pressure distribution

on the flap near the slot is shown in figure 6 as panel distribution A. Panel distribution B has the same number of panels but distributed differently. The paneling of distribution B is more dense near wing and flap leading edges and sparse near the trailing edges. The results using distribution A have less resolution, but show a more accurate pressure level. The errors in the pressure distribution on the flap using paneling B with 48 source panels may be attributed to the coarse paneling near the trailing edge of the main wing. This exercise shows that fine paneling is required to generate accurate potential flow solutions. In the present study care was taken to generate such accurate potential flow pressure distributions for use in detailed boundary layer analyses.

3 VISCOUS FLOW ANALYSIS

3.1 Boundary layer methods

The various viscous flow calculation procedures have been chosen with the aim of balancing the computational effort required against the overall accuracy obtained. For the present purposes it suffices to mention the shear layer methods used in the calculations.

- Laminar boundary layer is calculated by Thwaites' integral method (e.g. Ref. 23).
- Natural transition in the attached boundary layer is predicted by the Granville method (Ref. 24), making use of correlations for the instability Reynolds number and for the Reynolds number increment from the point of instability to the actual transition location.
- The treatment of laminar separation bubbles is based on a method proposed by Van Ingen (Ref. 25). The laminar part of the bubble is calculated by an inverse boundary layer method of the integral type in which the position of the separation streamline is prescribed by an empirical relation. The interaction of the reattaching transitional shear layer with the inviscid flow is approximated by the Stratford zero skin friction pressure distribution for turbulent boundary layers, which may be interpreted as the result of an inverse boundary layer method with prescribed skin friction.
- The turbulent shear layer analysis is based on the model shear stress equation of Bradshaw et al. (Ref. 26).

To start the turbulent shear layer calculation method we employ the Coles' wall-wake formula as a two parameter family of velocity profiles. One parameter follows from the requirement of continuity of the momentum defect thickness, which is known from the laminar boundary layer or laminar separation bubble calculation. The second parameter is obtained by assuming that the turbulent boundary layer is in equilibrium. The initial stress profile is assumed to follow from the mixing length formula. The effect of these assumptions, concerning the initial data, on the results will be discussed in section 5.

As a last point it needs to be recalled that the existing boundary layer method (Ref. 11) does not cover turbulent wakes. To demonstrate the importance of a turbulent wake analysis method we have extended the basic boundary layer method, on a tentative basis, to treat symmetric half wakes (Ref. 18).

3.2 Drag

The most promising method for predicting the drag is to continue the boundary layer calculation beyond the trailing edge as a turbulent wake analysis up to some point far downstream and then apply the Squire and Young formula or Jones method (Ref. 27). The most important parameter of these two drag evaluation methods is the level of the pressure coefficient at the last station where the turbulent shear layer is calculated. If this pressure coefficient is positive, the wake downstream will only experience favourable pressure gradients. In this case the drag coefficients obtained by the Squire and Young formula show negligible differences with those obtained by the method of Jones. This particular equivalence was also found in a comparative numerical study by Zwaaneveld (Ref. 28). This observation applies directly to the evaluation of the drag of single component airfoils with attached flow up to the trailing edge. Adding an intermediate turbulent wake calculation to the classical Squire and Young formula will change the drag coefficient only slightly in these cases, which means that the viscous losses in wake are not significent as long as the pressure gradient remains favourable.

In case of multicomponent airfoils the situation is quite different, however. The turbulent wake from a slat, or the main component of a slotted configuration, follows the components downstream and is subjected to a considerable adverse pressure gradient. The viscous losses incurred by the wake are no longer negligible, such that the wake flow cannot be treated as if it were inviscid as in the Jones method. The Squire and Young formula is not useful either, also under predicting the viscous losses. The present strategy in case of multicomponent airfoils is to calculate the turbulent wake flow, subjected to a known pressure distribution, far enough downstream such that the pressure level at the last station of the turbulent shear layer calculation is fairly close to the pressure at infinity.

4 VISCOUS-INVISCID COUPLING

4.1 Matching conditions

Viscous-inviscid interaction for two-dimensional flows, including rational asymptotic methods as well as numerical matching, has been discussed by Le Balleur (Ref. 29) recently. Let us consider the (s, z) boundary layer coordinate system where (u, v) is the solution of the viscous flow and Φ the solution of the inviscid flow. Matching the two solutions along their common boundary requires

$$u\,(s,\ z = \delta) = \frac{\partial \Phi}{\partial s}\,(s,\ z = \delta) \tag{13a}$$

$$v\,(s,\ z = \delta) = \frac{\partial \Phi}{\partial z}\,(s,\ z = \delta) \quad . \tag{13b}$$

These matching conditions (13) may be approximated by continuing the inviscid flow solution Φ into the viscous flow domain. If this continuation is represented by a Taylor series expansion around the edge of the inviscid flow domain, i.e. $z = \delta$, we may approximate the normal velocity component this way and

rewrite the matching conditions (13) as

$$U_e(s) = \frac{\partial \Phi}{\partial s}(s, z = \delta) \tag{14a}$$

$$\frac{\partial \Phi}{\partial z}(s, z = 0) = \frac{d}{ds}(U_e \delta^*) + O(\delta^2) \tag{14b}$$

where $U_e(s) = u(s, z = \delta)$ and $\delta^*(s) = \int_0^{\delta(s)} \left(1 - \frac{u}{U_e}\right) dz$.

Further approximation by also replacing condition (13a) introduces an lower order truncation error in the matching condition for the tangential velocity component,

$$U_e(s) = u(s, z = \delta) = \frac{\partial \Phi}{\partial s}(s, z = 0) + O(\delta) \tag{15a}$$

$$\frac{\partial \Phi}{\partial z}(s, z = 0) = \frac{d}{ds}(\delta^* U_e) + O(\delta^2) \tag{15b}$$

where $U_e(s)$ is the boundary condition for the viscous flow and $\frac{\partial \Phi}{\partial z}(s, z = 0)$ the outflow boundary condition modeling the viscous effects in a inviscid flow problem. Smallness of the truncation errors in the approximate conditions (15), if applied to the trailing edge region, is not obvious, see section 4.3.

4.2 Outflow boundary condition

The outflow boundary condition involves differentiation of the computed displacement flux $U_e \delta^*$. This displacement distribution is known from applying the viscous flow calculation procedures outlined in section 3. These discrete results are differentiated using an algorithm based on spline functions. A detailed description and implementation of the algorithm used is given in reference 18.

At present the algorithm is applied successively to the upper surface boundary layer, lower surface boundary layer and total wake of each component individually. For completeness it is recalled that the strong interaction of the laminar separation bubble is treated heuristically. It is assumed that the relatively short laminar separation bubbles have only a negligibly small effect upon the pressure distribution except in the bubble itself where the pressure is assumed to follow from inverse boundary-layer methods. For this reason the full displacement flux of this local phenomenon is not represented in the potential flow. Instead we have taken the displacement flux of the separation bubble to be represented by a linear variation between separation and reattachment.

4.3 Trailing edge region

To obtain an impression of the inviscid flow in the trailing edge region it is opportune to look at a realistic example. The NLR 7301 plus flap configuration, already discussed at some length in section 2.4, is chosen. The detailed pressure distribution in the trailing edge region is displayed in figure 7. The boundary conditions applied to obtain these numerical results conform with the first inviscid solution, i.e. zero outflow plus classical Kutta-Joukowski condition implemented by requiring the bisector to be a streamline (see section 2.3). Figure 7 clearly shows the singular behaviour of the first potential flow solution near the trailing edge, leading to substantial differences between the inviscid flow solution at the surface ($z = 0$) and at some distance off the surface. To preclude the occurrence of this type of singular behaviour in the boundary condition $U_e(s)$ of the viscous flow we use the matching conditions (14) at and just upstream of the trailing edge. The boundary condition $U_e(s)$ immediately downstream of the trailing edge is taken as a linear variation between its trailing edge value and the calculated wake centerline value at a boundary layer thickness downstream.

It should be emphasized here that for the sake of computational efficiency one should rather use matching conditions (15) than the conditions (14). The favourable aspect of conditions (15) is that they apply at the surface which is fixed during the iteration between inviscid and viscous flow solutions, the matrix of influence coefficients remaining unchanged as a result. At present the following compromise has been made, i) apply conditions (15) outside the trailing edge region for computational efficiency, ii) apply conditions (14) at the trailing edge to preclude the occurrence of singularities in U_e, iii) construct a smooth blending of (14a) and (15a) in the trailing edge region.

Subsequent potential flow solutions are obtained by applying the Kutta condition of equal pressure at two points just outside the boundary layer. These points are located at a local boundary layer thickness from the trailing edge measured along the normal to the bisector of the trailing edge angle. These boundary conditions are effectively the same as those used by Seebohm et al. (Ref. 8). Their results show a rather good agreement between the predicted overall lift on a slotted airfoil and experimental data. This agreement is rather surprising in view of a more recent study by Melnik et al. (Ref. 13) and asks for further examination.

Figure 8 shows the details of the pressure distribution in the trailing edge region of the NLR 7301 airfoil. These computational results pertain to a potential flow in which the viscous effects have been modeled by the outflow boundary condition and the Kutta condition of equal pressure outside the boundary layers at the trailing edge, as set out previously. The important observation to be made is the variation of the pressure over a boundary layer thickness in the trailing edge region. It is found that the present Kutta condition leads to a pressure jump at the trailing edge when the solution is continued analytically to the surface.

To compare the results of Melnik et al. (Ref. 13) to the present we observe that in case of incompressible potential flow "the homogeneous solution" of reference 1. is a solution to Laplace's equation applying boundary conditions at the airfoil surface and wake centerline. Thus the "homogeneous solution" of reference 13 is to some extent comparable with the present solution displayed in figure 8. Qualitative

agreement is found in the sense that both solutions have a pressure jump at the trailing edge and give a rather good prediction of overall lift. However, the mechanism causing the pressure jump is widely different. Further conclusions cannot be drawn because the normal static pressure gradients across the viscous shear layers have not be resolved in any detail as yet (Ref. 29).

5 RESULTS AND DISCUSSION

This section summarizes some viscous flow results obtained by applying the method outlined in the previous sections. These results are compared with experimental data. For completeness it needs to be remarked that these comparisons are based on experimental data limited to Reynolds numbers above approximately 2 million, more or less excluding the occurrence of large laminar separation bubbles and/or tripped boundary layers

5.1 NACA 63-009

Figure 9 presents a comparison between predicted and measured characteristics (Ref. 30) of the NACA 63-009 airfoil at a Reynolds number of 5.8×10^6. The pressure distributions show reasonable agreement. Similar agreement has been found for lift and drag values. The theory does not predict a bubble bursting, however. Although the independent experimental studies of references 31 and 32 clearly show a maximum lift coefficient of 1.1 and 1.06 respectively, the present results show no tendency towards bubble bursting at 12° incidence with a 1.26 lift coefficient. This failure of the theory to predict bubble bursting for the NACA 63-009 airfoil has also been found by Van Ingen (Ref. 33).

A practical aspect of the problem is the characteristic short length of the laminar separation bubble, typically 0.4 per cent chord in the present case. Therefore a large number of surface panels have been employed to obtain high resolution potential flow pressure distributions near the airfoil nose, as displayed in figure 10. The length of the bubble decreases as the angle of attack increases while the Reynolds number is fixed. This decrease of the bubble length is predicted mainly by the transition criterium and is consistent with the detailed experimental observations by Gault (Ref. 32). At the same time Gault concluded that abrupt stall resulted when the transitional shear layer near the leading edge was unable to reattach to the surface, which is at variance with the present predictions as noted before. Compressibility has been considered in this context, but its inclusion does not resolve the discrepancy.

From a more detailed experimental study of the leading edge flow on a semi-ellipse nose section Ridder (Ref. 34) concluded that at higher Reynolds numbers the reattachment process of the transitional shear layer in the bubble need not be critical. Above a certain Reynolds number the pressure load on the bubble does not increase when the peak of minimum pressure increases, but levels off at a value well below the critical level instead. For these conditions the main influence of the bubble is said to be on the initial conditions of the downstream turbulent boundary layer flow. The mechanism that causes the abrupt stall is regarded to be turbulent boundary layer separation downstream. Closer examination of the turbulent boundary layer predictions reveals the development of a critical condition at approx. 2 per cent downstream of the reattachment point, see figure 11. However, quite a margin with respect to separation remains at 12° incidence. We may demonstrate the feasibility of the occurrence of <u>turbulent leading edge stall</u> by lowering the Reynolds number from 5.8 to 5.0×10^6 to predict turbulent flow separation between 11° and 12° incidence at a location of 3 per cent airfoil chord. This type of flow mechanism is considered to be the most likely candidate that causes the abrupt stall observed experimentally (Refs 31 and 32). It is noted that this conclusion is at variance with the notion that the abrupt stall of NACA 63-009 at a Reynolds number of about 6 million is caused by bubble bursting.

Before starting to discuss the results for other airfoils we will pay some attention to the convergence history of the iterative cycle between inviscid and viscous flow solutions for single component airfoils. Experience with the method indicates that the numerical solutions converge after three inviscid flow solutions, provided no turbulent flow separation occurs during the iterative process. In case of turbulent flow separation during the initial cycle of the iterative process, as found for the NACA 63-009 airfoil at 11° incidence and $Re = 5 \times 10^6$, convergence is slowed down considerably. As much as 5 to 6 iterations may be needed to obtain satisfactory numerical convergence, as may be observed from the results plotted in figure 12.

5.2 NLR 7301 airfoil

The calculation results pertaining to the viscous flow around the NLR 7301 airfoil are presented in figures 13 and 14 and compared with experimental data obtained in the NLR-LST facility at a Reynolds number of 2.6×10^6 and a Mach number of 0.2 (Ref. 35). This airfoil designed for transonic speeds, incurs extensive turbulent flow separation at higher angles of attack occurring in low speed flow operations. Since separated turbulent boundary layers are outside the scope of the present study, the calculation results are only expected to be accurate up to the incipient separation angle of about 6° incidence. The predicted lift and drag at angles of attack above approx. 9° incidence are indicative of the failure to account for the turbulent separated flow near the trailing edge. Inviscid modeling employing free streamline separation is possibly one way to remedy the situation, as has been investigated concurrently at NLR.

One aspect of the comparisons of figure 14 which needs clarification is the apparent spread in the experimental drag data. This spreading is observed as a spanwise variation of the viscous drag as measured downstream of a two-dimensional wind tunnel model by a total pressure rake. The calculation results agree with the minima of the continuous spanwise surveys measured at one chord distance downstream of the trailing edge.

Another aspect of the experimental data shown in figure 14 is the sudden loss of lift from approx. 1.6 to 1.2 at 16 degrees incidence. On account of the initial revelation of the possibility of turbulent leading edge stall for NACA 63-009 (Ref. 18) more detailed measurements (Ref. 36) were made for NLR 7301 to check whether the sudden loss of lift (Fig. 14) is possibly associated with turbulent boundary layer

separation just downstream of the laminar separation bubble. These recent measurements suggest that turbulent leading edge stall does occur, but in the presence of a large turbulent separation in the rear leading to a mix of turbulent leading-edge and trailing-edge stall for the NLR 7301 airfoil.

5.3 NLR 7301/flap

The NLR 7301 with a single 32 per cent chord trailing edge flap, already mentioned in section 2.4, was designed such that no turbulent flow separations occur, serving as a test case for the evaluation of the present method of analysis. Experimental data as well as calculation results have been presented in reference 37. From the comparisons it was concluded that the calculation results showed satisfactory agreement with the boundary layer data in many respects. In the light of these findings (Ref. 37) we shall mainly be interested in the viscous-inviscid interaction and the wing wake calculations. In addition we shall pay some attention to the effect of the assumptions concerning the initial data of the turbulent boundary layer analysis as mentioned in section 3.1.

Figure 15 shows calculation results pertaining to the inviscid/viscous flow solution for the wing plus flap configuration at 6 degrees incidence and a Reynolds number of 2.5 million. The predicted pressure distribution agrees with the experimental data, except for a slight deviation at the suction peak, which presumably is due to the fact that compressibility effects have not been accounted for as mentioned in section 2.1. The iterative process to obtain the solution given in figure 15 is found to converge in about three iterations between the inviscid and viscous flow.

As already mentioned in section 5.1 the separation bubble determines the initial conditions of the turbulent boundary layer downstream of it. A question associated with this statement is how sensitive the results of the turbulent boundary layer calculation are with respect to these initial conditions. To study this question in some detail we have determined the sensitivity of the results to initial conditions for a fixed pressure distribution by independently changing:
a) the shape of the velocity profile, i.e. $H = \delta^*/\theta$,
b) the magnitude of the shear stress profile, τ ,
c) the momentum thickness.
For the wing upper surface turbulent boundary layer, with $\alpha = 6$ degrees and $Re = 2.5 \times 10^6$, it is found that the effect of the initial velocity profile and τ-profile on the skin friction distribution vanishes after some 10 per cent chord downstream of the laminar separation bubble, as may be seen in figure 16. These changes a) and b) have no effect on the development of the momentum thickness, i.e. the drag of the configuration. Changing the initial momentum thickness, however, does effect the entire turbulent boundary layer at the wing upper surface significantly, as is well-known. Thus the main influence of the short laminar separation bubble for these conditions is its effect on the initial momentum thickness of the turbulent boundary layer behind the bubble. Thus it is important that the laminar separation bubble calculation predicts the viscous losses in the bubble correctly as in the case in the present example, see reference 37.

Omitting the bubble calculation, by assuming turbulent flow at the laminar separation location, is certainly no alternative because one may not be able to calculate turbulent boundary layers at such low Reynolds numbers reliably. If one does omit the bubble the experience learns that the momentum defect of the downstream turbulent boundary layer is underestimated as shown by Ridder (Ref. 34) and also by Gleyzes et al. (Ref. 38).

Results of the turbulent wake analysis are shown in figure 17 and compared with the experimental data showing reasonable agreement at 6 degrees incidence. At higher angles of attack, $\alpha = 10.1^\circ$ and 13.1°, the extreme growth of the displacement thickness inherent to the occurrence of flow reversal is detrimental to the convergence of the present iteration procedure, such that no converged solutions would be obtained. In order to assist the iteration scheme in arriving at a converged solution for the $\alpha = 10.1^\circ$ and 13.1° incidence configurations the shape factor H in the turbulent wake analysis method is artificially limited to a maximum value $H_{max} = 3$.

The experimental and theoretical lift and drag characteristics at 6, 10.1 and 13.1 degree incidence are shown in figure 18. The results indicate good agreement with experimental data at 6 degrees incidence. This figure also presents results obtained with only the near wake of the wing taken into account, i.e. leaving out the increase in displacement thickness due to the far wake of the wing. It is seen that the wing wake alongside the flap upper surface is the major item in determining the loss of lift due to viscous effects above say 6 degrees incidence. At 13.1 degrees incidence the predicted loss of lift depends critically upon the displacement of the wing wake. The development of the wing wake is also important for the drag. With the present tentative wake analysis the drag coefficient is underestimated by 100 counts at $\alpha = 13.1^\circ$. These findings directly lead to the conclusion that the present tentative wake analysis method is inadequate. A turbulent wake analysis method handling asymmetric wakes in adverse pressure gradient is needed to predict the drag characteristics of the NLR 7301 + flap configuration at higher angles of attack.

6 CONCLUSIONS

(i) A method for making routine and economical computations of the viscous flow about multicomponent airfoils has been developed. The method solves incompressible potential flow and boundary layer problems, accounting for viscous-inviscid interaction through an iterative scheme.

(ii) The present potential flow method has been formulated such that good accuracy is obtained in such critical areas as the shroud of slotted flap configurations. Also a high computational efficiency of the present panel method is realized by using a special factorization algorithm.

(iii) Matching the viscous and inviscid flow solutions near the trailing edge at the edge of the boundary layer is found to be a workable concept. However, there clearly is a need for continued investigation, both theoretically as well as experimentally, in order to resolve the static pressure gradients across the turbulent shear layers at the trailing edge.

(iv) The computational solutions for the viscous flow show satisfactory agreement with the experimental data in may respects.

(v) Detailed analysis of the viscous flow near the leading edge of the NACA 63-009 airfoil at high Reynolds number suggests the occurrence of turbulent leading edge stall; this observation is at variance with the notion that the abrupt stall is caused by bubble bursting. There are indications that turbulent leading edge stall may occur frequently at high Reynolds numbers.

(vi) Further applications have indicated that future work to extend the range of applicability of the underlying aerodynamic models should concentrate on
- the analysis of turbulent wakes, particularly asymmetric wakes in adverse pressure gradient,
- the modeling of extensive turbulent separation and
- the effect of compressibility in the potential flow.

ACKNOWLEDGMENT

The author gratefully acknowledges helpful discussions with J.W. Slooff and A.E.P. Veldman, throughout the course of this project.

REFERENCES

1. Smith A.M.O.: High-Lift Aerodynamics. Journal of Aircraft, Vol. 12, No. 6, June 1975.
2. Stevens, W.A., Goradia, S.H. and Braden, J.A.: Mathematical Model for Two-Dimensional Multi-Component Airfoils in Viscous Flow. NASA CR-1843, July 1971.
3. Morgan, H.L.: A Computer Program for the Analysis of Multi-Element Airfoils in Two-Dimensional Subsonic, Viscous Flow. NASA SP-347, March 1975.
4. Brune, G.W. and Manke, J.W.: An Improved Version of the NASA/Lockheed Multi-Element Airfoil Analysis Computer Program. NASA CR-145323, March 1978.
5. Slooff, J.W.: Wind Tunnel Tests and Aerodynamic Computation; Thoughts on Their Use in Aerodynamic Design. NLR MP 76013 U, June 1976.
6. Labrujère, Th.E., Schipholt, G.J. and De Vries, O.: Potential Flow Calculations to Support Two-Dimensional Wind Tunnel Tests on High Lift Devices. NLR MP 72016 U, Paper at 8th ICAS Congress, Amsterdam, September 1972.
7. Seebohm, T.: Boundary Layer, Transition and Wake Measurements at Low Mach Number for an Aerofoil with Single-Slotted Flap. McGill University Report 69-1, June 1969.
8. Seebohm, T. and Newmann, B.G.: A Numerical Method for Calculating Viscous Flow Round Multiple-Section Aerofoils. Aeronautical Quarterly, August 1975.
9. Olsen, L.E., James, W.D. and McGowan, P.R.: Theoretical and Experimental Study of the Drag of Multi-Element Airfoils. AIAA Paper 78-1223, July 1978.
10. Maskew, B. and Dvorak, F.A.: The Prediction of $C_{\ell_{max}}$ Using a Separated Flow Model. Journal of the American Helicopter Society, April 1978.
11. Lindhout, J.P.F. and Boer, E. de: A program for the computation of a compressible turbulent boundary layer under infinite swept wing conditions. NLR TR 75090 U, July 1975.
12. Piers, W.J. and Slooff, J.W.: Calculation of Displacement Effect in Two-Dimensional Subsonic Attached Flow around Airfoils; Examples of Calculations using Measured Displacement Thickness. NLR TR 72116 U, May 1972.
13. Melnik, R.E., Chow, R. and Mead, H.R.: Theory of Viscous Transonic Flow Over Airfoils at High Reynolds Number. AIAA Paper 77-680, June 1977.
14. Brown, S.N. and Stewartson, K.: Wake Curvature and the Kutta Condition in Laminar Flow. Aeronautical Quarterly, November 1975.
15. Veldman, A.E.P.: The Calculation of Incompressible Boundary Layers with Strong Viscous-Inviscind Interaction. Paper to be presented at AGARD Symp., Colorado Springs, September 1980.
16. Giesing, J.P.: Potential Flow about Two-Dimensional Airfoils, Part I and II. Douglas Aircraft Div. Report No. LB31946, December 1965.
17. Thwaites, B.: Incompressible Aerodynamics. Clarendon Press, 1960.
18. Oskam, B.: A Calculation Method for the Viscous Flow Around Multicomponent Airfoils. NLR TR 79097, 1979.
19. Rubbert, P.E. and Saaris, G.R.: Review and Evaluation of Three-Dimensional Lifting Potential Flow Analysis Method for Arbitrary Configurations. AIAA Paper No. 72-188, January 1972.
20. Piers, W.J. and Slooff, J.W.: Calculation of Transonic Flow by Means of a Shock-Capturing Field Panel Method. NLR MP 79022 U, May 1979.
21. Hess, J.L.: The Problem of Three-Dimensional Lifting Potential Flow and its Solution by Means of Surface Singularity Distributions. Computer Methods in Applied Mechanics and Engineering 4, pp. 283-319, North-Holland Publishing Company, 1974.
22. Williams, B.R.: An Exact Test Case for the Plane Potential Flow about Two Adjacent Lifting Airfoils. RAE TR 71197, 1971.
23. Cebeci, T. and Bradshaw, P.: Momentum Transfer in Boundary Layers. Hemisphere Publishing Corporation, 1977.
24. Cebeci, T. and Smith, A.M.O.: Analysis of Turbulent Boundary Layers. Academic Press, 1974.
25. Van Ingen, J.L.: On the Calculation of Laminar Separation Bubbles in Two-Dimensional Incompressible Flow. AGARD-CP-168, Paper 11, May 1975.
26. Bradshaw, P., Ferriss, D.H. and Atwell, N.P.: Calculation of Turbulent Boundary Layers using the Turbulent Energy Equation. JFM 28, 1967.
27. Schlichting, H.: Boundary Layer Theory. McGraw-Hill, 1968.
28. Zwaaneveld, J.: Comparison of Various Methods for Calculating Profile Drag from Pressure Measurements in the Near Wake at Subcritical Speeds. AGARD CP-124, 1973.
29. Le Balleur, J.C.: Calculs Couplés Visqueux - Non Visqueux Incluant Décollements et Ondes de Choc en Ecoulement Bidimensionnel. AGARD-IS-94, February 1978.
30. McCullough, G.B. and Gault, D.E.: Examples of Three Representative Types of Airfoil-Section Stall at Low Speed. NACA TN 2502, September 1951.
31. Loftin, L.K. and Bursnall, W.J.: The Effects of Variations in Reynolds Number Between 3×10^6 and 25×10^6 upon the Aerodynamic Characteristics of NACA 6-Series Airfoil Sections. NACA Report 964, 1950.

32. Gault, D.E.: Boundary Layer and Stalling Characteristics of the NACA 63-009 Airfoil Section. NACA TN 1894, June 1949.
33. Van Ingen, J.L.: Transition, Pressure Gradient, Suction, Separation and Stability Theory. Paper 20, AGARD-CP-224, 1977.
34. Ridder, S.O.: Experimental Studies of the Leading Edge Suction Force, Including the Maximum Attainable Suction Force versus Reynolds Number and the Induced Distributions on various Wing Planforms and Air Intakes. ICAS Proceedings, Volume 1, August 1974.
35. Joosen, C.J.J. and Kho, C.G.: Two Dimensional Low-Speed Wind Tunnel Investigation on a NLR 73-108-10 Airfoil with Fowler Type Flap, Part 1: Text, Tables and Figures. NLR TR 74058 C, September 1975.
36. Van den Berg, B.: On The Role of Laminar Separation Bubbles in Airfoil Leading Edge Stalls. NLR MP 80010, 1980.
37. Van den Berg, B. and Oskam, B.: Boundary Layer Measurements on a Two-Dimensional Wing with Flap and a Comparison with Calculations. Paper 18, AGARD-CP-271, 1979.
38. Gleyzes, C., Cousteix, J. and Bonnet, J.L.: Bulbe de Décollement Laminaire avec Transition (Théorie et Expérience), L'Aéronautique et L'Astronautique, No. 80, 1980-1.

TABLE 1

Comparison of aerodynamic coefficients of Williams' two-element airfoil, Configuration A (number of countour panels: $N_C = 70 + 82 = 152$)

Component index →	i	Exact solution	Present panel method	Difference	Exact solution	Present panel method	Difference
		$\alpha = 0^o$			$\alpha = 10^o$		
C_ℓ	1	2.906	2.918	+.012	4.376	4.393	+.017
C_ℓ	2	0.830	.829	-.001	.762	.761	-.001
C_ℓ	1+2	3.736	3.748	+.012 (.3 %)	5.138	5.154	+.016 (.3 %)
C_d	1	-.3839	-.3817	+.0022	-.5104	-.4981	+.0123
C_d	2	+.3838	+.3848	+.0010	+.5103	+.5113	+.0010
C_d	1+2	.0	+.0031	+.0031	.0	.0132	+.0133

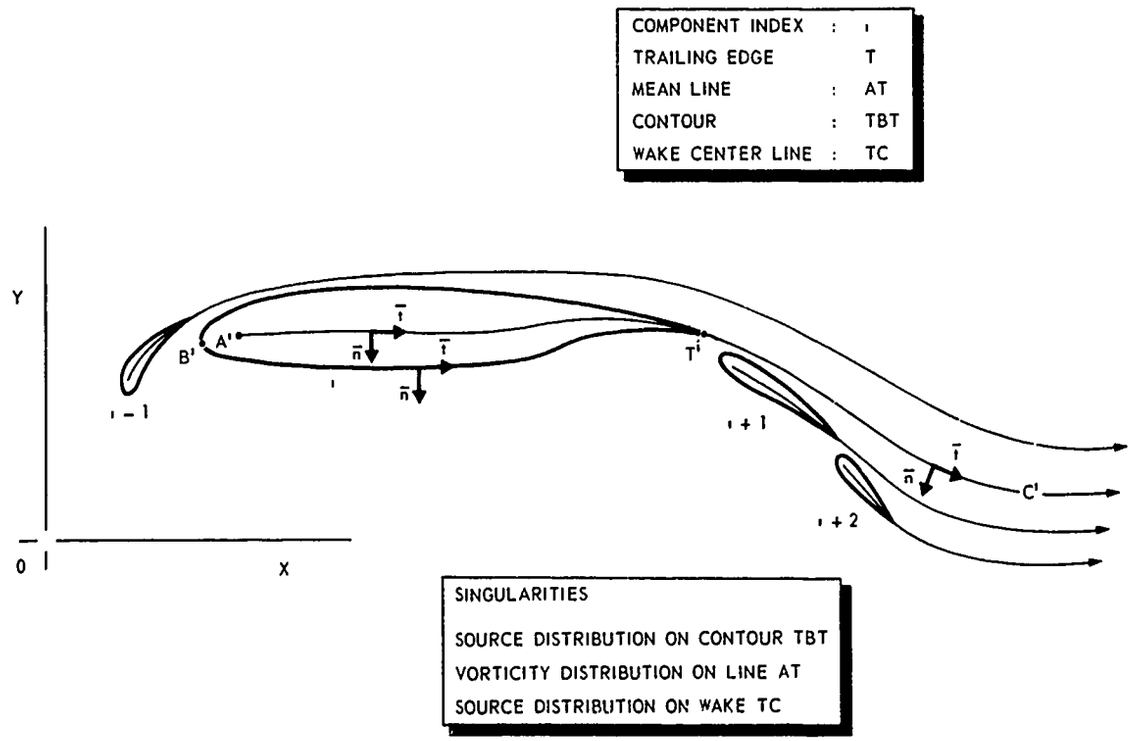


Fig. 1 Sketch of potential flow boundaries

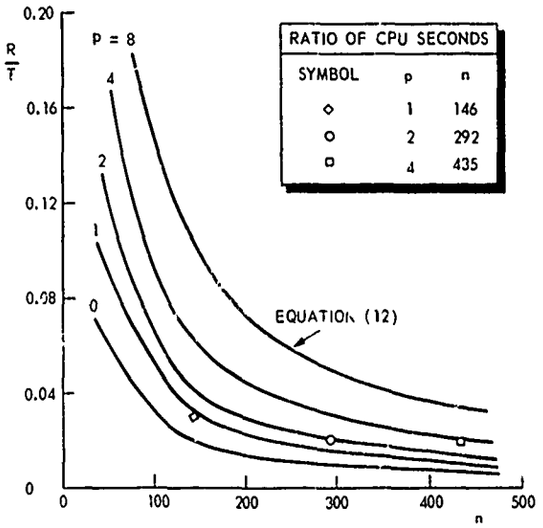


Fig. 2 Comparison between asymptotic operation counts and CPU seconds

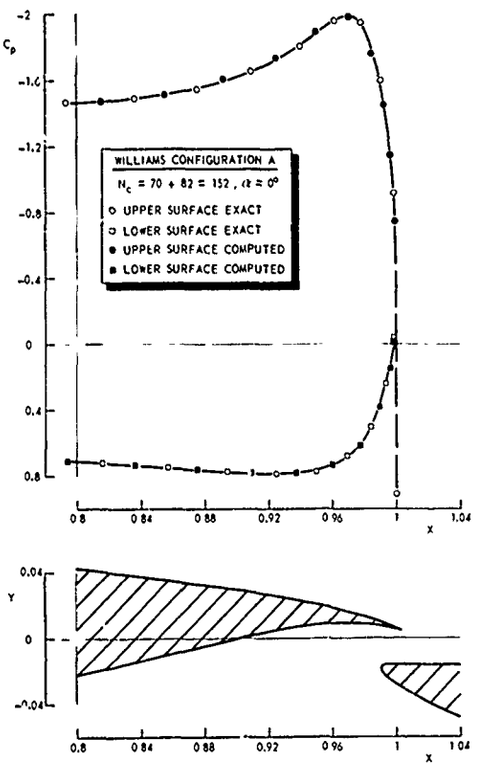


Fig. 4 Slot area of Williams' configuration A; comparison between present panel method and exact solution

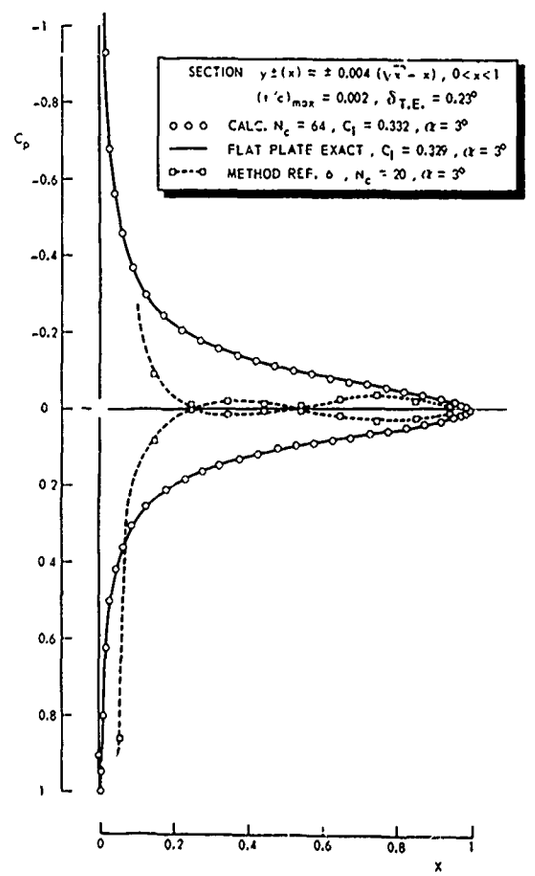


Fig. 3 Extremely thin airfoil section; comparison between present panel method and exact solution of a flat plate

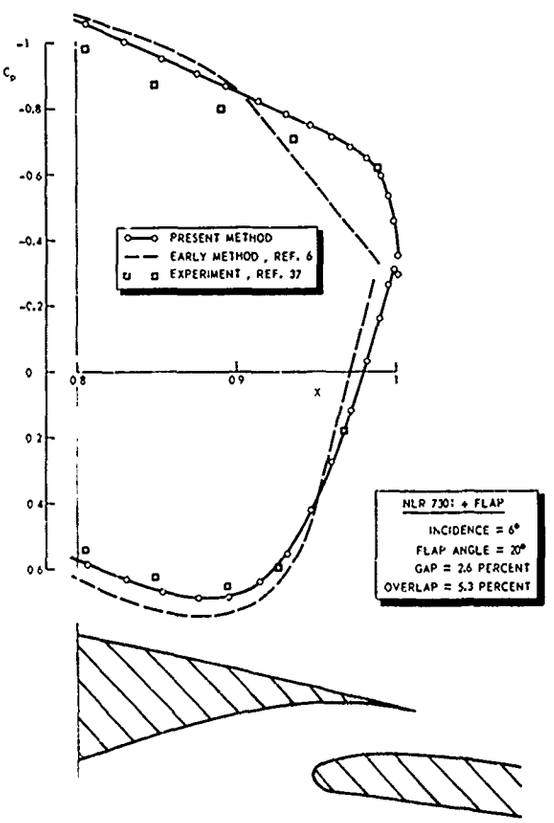


Fig. 5 Slot area of NLR 7301 + flap; comparison of early panel method (Ref. 6) and present panel method

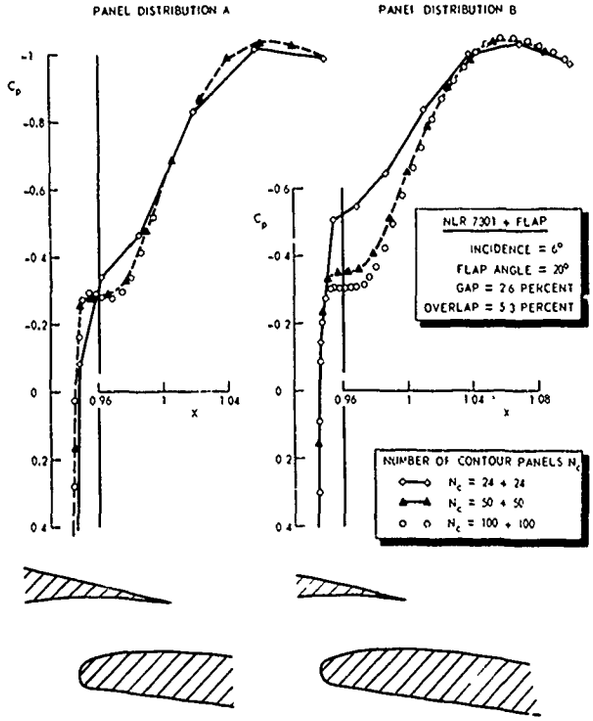


Fig. 6 Slot area of NLR 7301 + flap; effect of variation of panel distribution

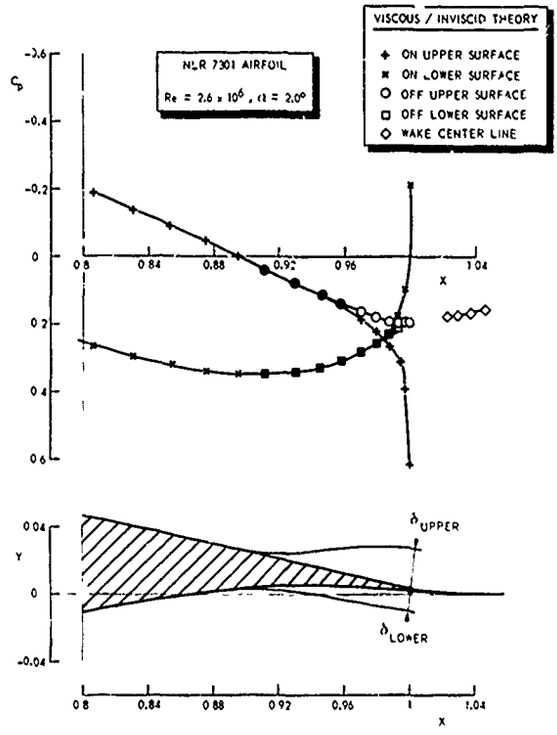


Fig. 8 Trailing edge of NLR 7301 at $\alpha = 2^{\circ}$; static pressure distribution

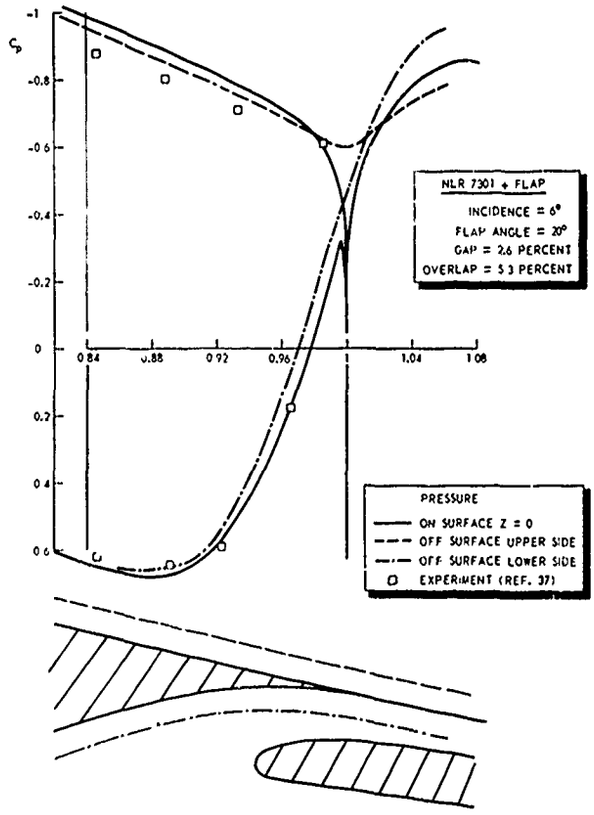


Fig. 7 Wing trailing edge region · NLR 7301 + flap; static pressure o · first potential flow solution

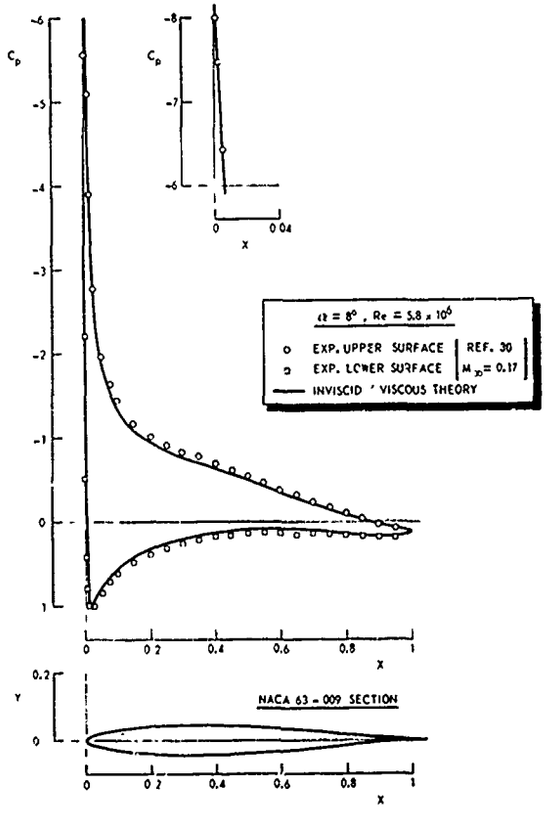


Fig. 9 NACA 63-009 airfoil section; comparison of pressure distribution

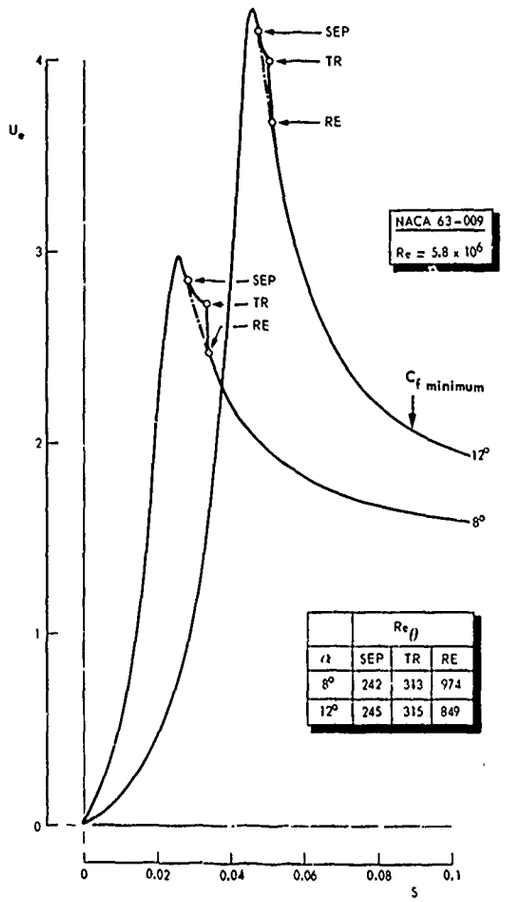


Fig. 10 Computed velocity distribution at nose of NACA 63-009

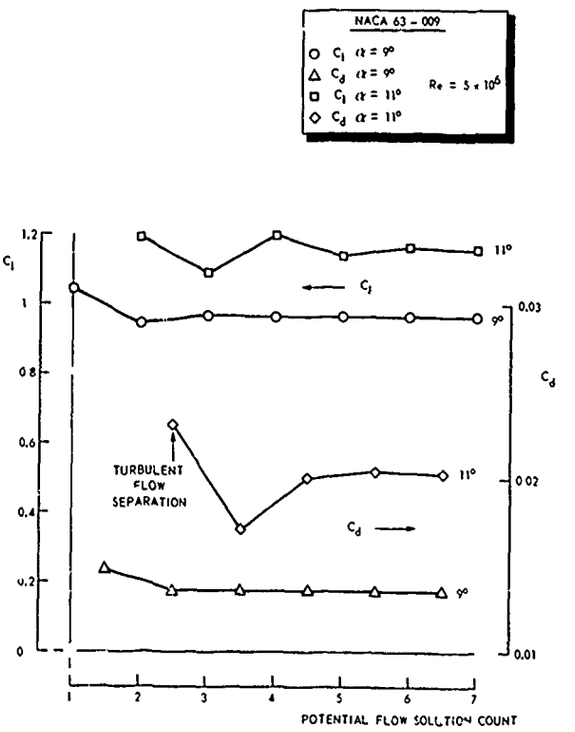


Fig. 12 Iteration history of NACA 63-009

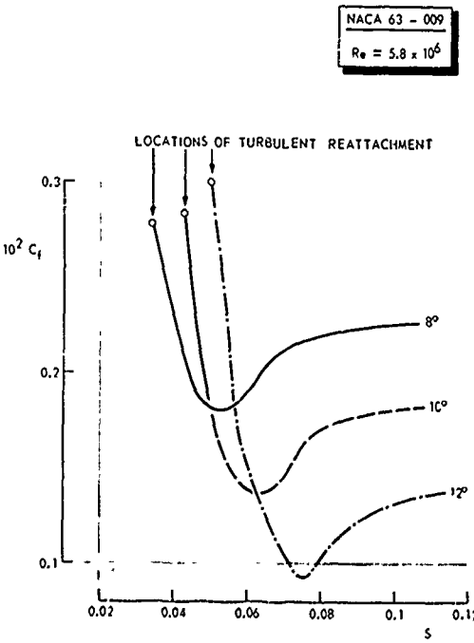


Fig. 11 Turbulent boundary layer flow downstream of bubble (NACA 63-009)

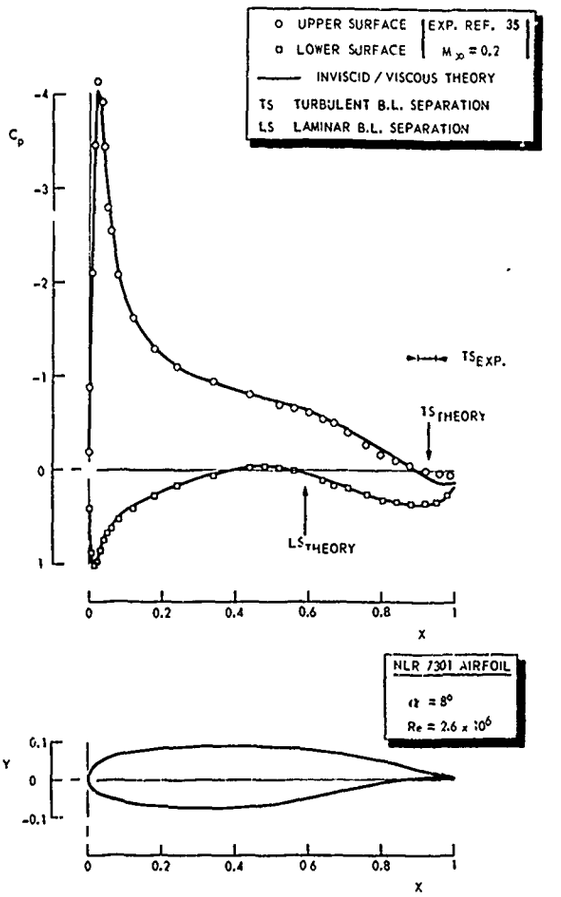


Fig. 13 Pressure distribution NLR 7301, $\alpha = 8^\circ$

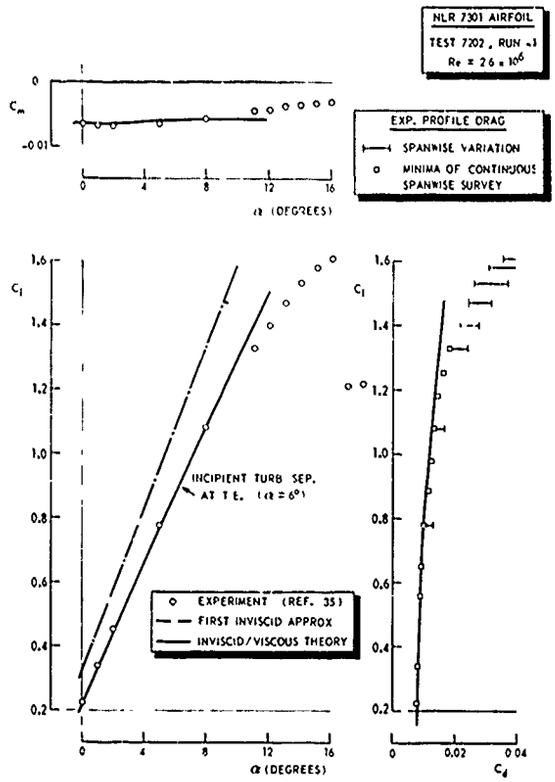


Fig. 14 Lift and drag characteristics of NLR 7301

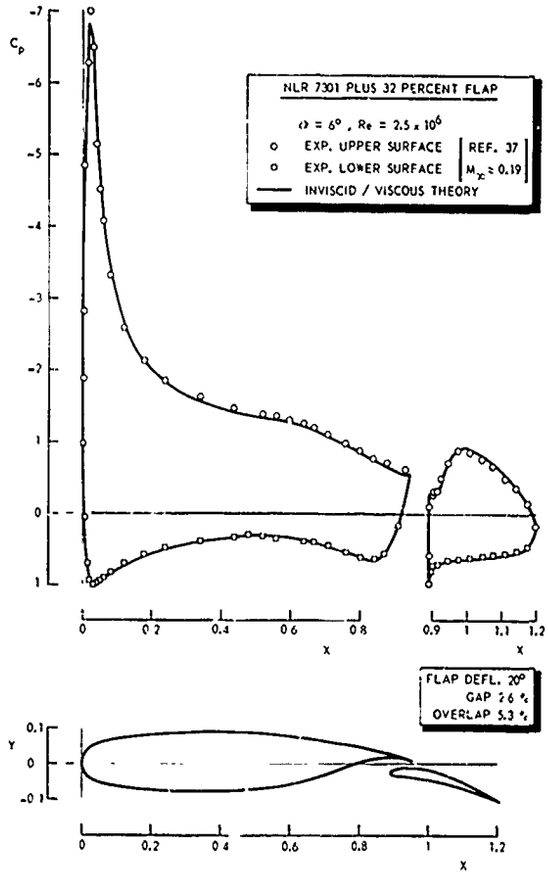


Fig. 15 NLR 7301 + flap configuration; comparison of pressure distribution

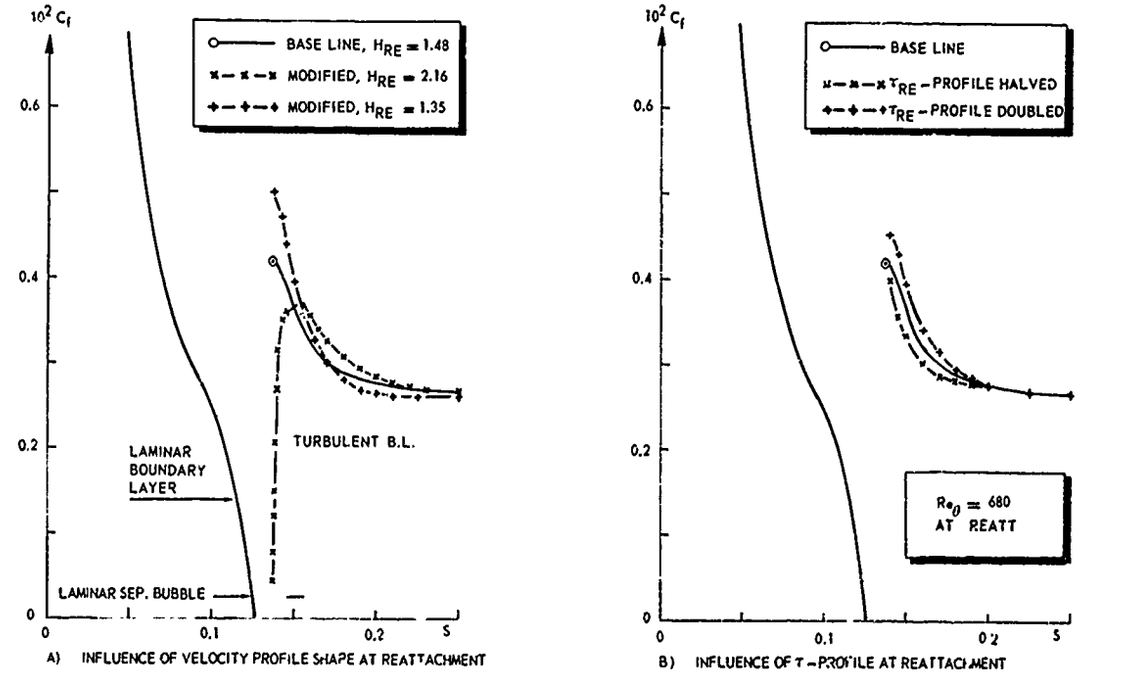


Fig. 16 Effect of different initial conditions on the computed local skin friction of turbulent boundary layer of wing upper surface (Fig. 15)

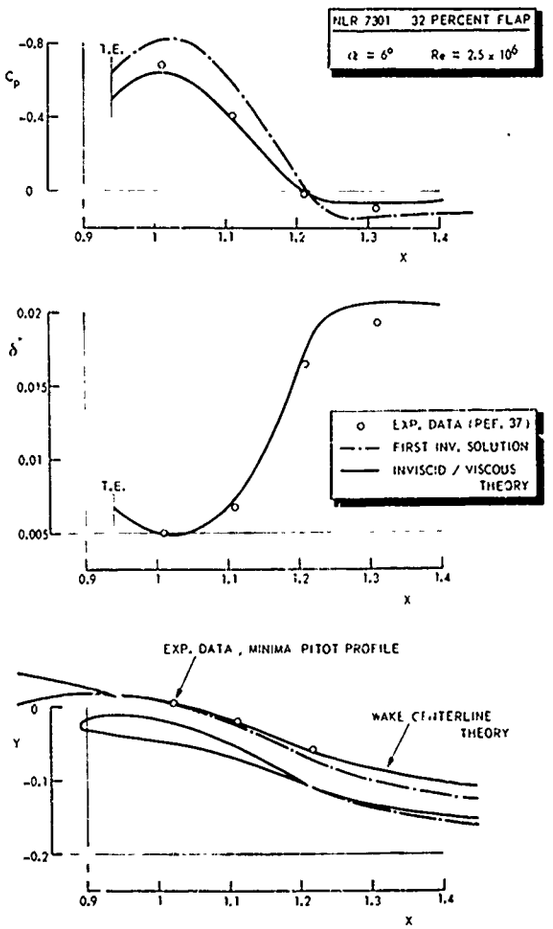


Fig. 17 Wing wake characteristics of NLR 7301 + flap configuration

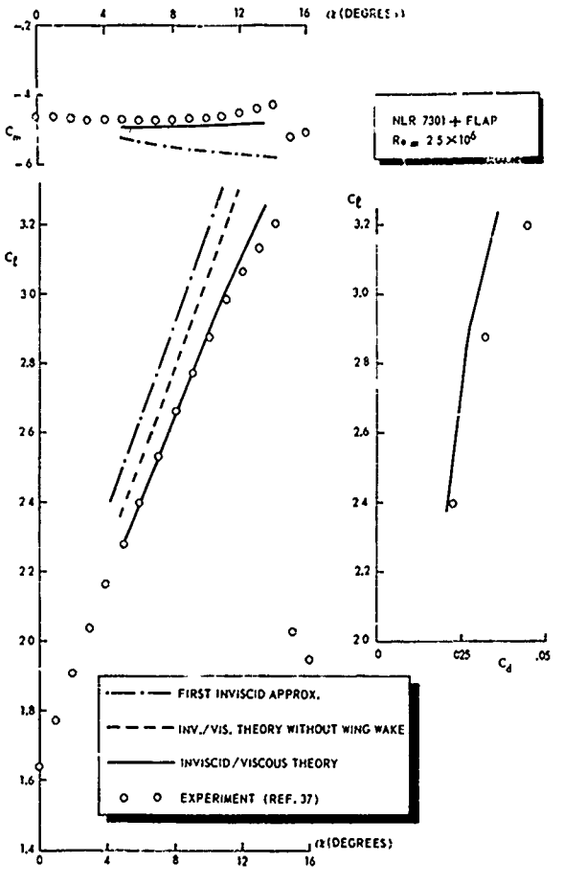


Fig. 18 Lift and drag characteristics of NLR 7301 + flap

SEPARATION AND REATTACHMENT NEAR THE LEADING EDGE OF A THIN AIRFOIL AT INCIDENCE

by
Tuncer Cebeci
Aerodynamics Research
Douglas Aircraft Company
Long Beach, California 90846, U.S.A.
and
Mechanical Engineering Department
California State University at Long Beach
Long Beach, California 90840, U.S.A.

and

Keith Stewartson and P. G. Williams
Department of Mathematics
University College
London WC1E, England

SUMMARY

The paper is concerned with the calculation of the leading-edge separation which occurs on thin airfoils with increasing angle of attack. To develop a general method and provide a basis for its evaluation, the simplified problem of a parabola at incidence is considered. The boundary-layer equations are solved, in finite-difference form, with the Mechul method to allow the determination of the external velocity distribution and a Hilbert integral to allow the modification of the external velocity distribution by the displacement thickness. The results show that, if the separation is laminar, reattachment occurs in a very limited range of the reduced angle of attack. With prescribed transition, and an algebraic eddy-viscosity formulation, the trend of the results are in line with experiment and help to confirm that the solution method is appropriate for application to real airfoil geometries.

1. INTRODUCTION

Local regions of separated flow are common on thin airfoils at an angle of attack and they are important because of their association with the phenomenon of stall. For thin airfoils the laminar boundary layer grows from the stagnation point and is subjected to an adverse pressure gradient when still near the leading edge, causing separation and subsequent transition to turbulent flow. Reattachment occurs and a turbulent boundary layer extends to the trailing edge. As the angle of attack is increased, the separation region moves towards the leading edge, and eventually the bubble of the separated flow bursts. Reattachment does not occur and stall sets in.

Here we examine a simple leading-edge separation problem as an initial step towards the development of a method for calculating the properties of the flows described in the previous paragraph. A parabola at incidence has been chosen because it requires only two parameters in the formulation of the problem, namely the reduced angle of attack ξ_0 and the interactive parameter ε and provides a pressure distribution which resembles that found in practice. The numerical approach of reference 1, which involves the Mechul method, is used to solve the boundary-layer equations and to determine the variation of the freestream velocity. In addition, the displacement thickness is allowed to modify the freestream velocity through a Hilbert integral and is determined by the procedure of Veldman (ref. 2), with some modifications. The results for laminar flow show that reattachment occurs for a very limited range of ξ_0. The prescription of transition and the use of the algebraic eddy-viscosity formulation of Cebeci and Smith (ref. 3) to remove the closure problem leads to results which show trends in qualitative agreement with experiment.

Early investigations of separation bubbles have been reviewed by Tani (ref. 4) who showed that the sequence of events from the first appearance of upper-surface separation to the bursting of the bubble depends on many factors but of particular importance are the geometric properties of the airfoil and on the chord Reynolds number. More recent experiments have been reported by Arena and Mueller (ref. 5) and computational investigations by Briley and McDonald (ref. 6), Kwon and Pletcher (ref. 7), Van Ingen (ref. 8) and Crimi and Reeves (ref. 9). The last two investigations made use of integral methods and the first combined solutions of the boundary-layer elsewhere. Kwon and Pletcher, like the present contribution, combined use of the boundary-layer equations with a Hilbert integral. Their calculations were confined to mid-chord separation situations where curvature effects are less important and the iteration procedure was carried out in a different way.

These studies have the disadvantage that a number of approximations of uncertain validity are made in deriving the basic equations used and it is desirable that where possible a more rational approach be used. For this purpose we can take advantage of

the significant advances in the theory of laminar flows at high Reynolds number that have taken place in recent years using the concept of the triple-deck (see Stewartson (ref. 10) for a recent review). Previously the existence of the Goldstein singularity at separation when the pressure gradient is prescribed had effectively brought such studies to an end at this point and prevented the development of a rational theory of separated flows. The triple-deck enables the pressure gradient to be related to the displacement thickness and now the singularity must disappear. Indeed Dijkstra (ref. 11) and Smith (ref. 12) were able to carry out extensive integrations into the reversed-flow region. In particular Smith (ref. 13) was able to analyze the laminar flow around a circular cylinder at large values of the Reynolds number R using the Kirchhoff-Sychev theory and obtained good agreement with observation when $R \sim 100$.

In this paper the procedure we have adopted is in general only quasi-rational i.e. as in the earlier studies we make a number of approximations that cannot be fully justified. There is, however, one set of circumstances in which the theory can be completely justified. This is when the angle of attack of the parabola is very close to that needed to provide separation and the Reynolds number based on the later section of parabola is large. Then an application of the triple-deck theory leads to an interactive problem of the type we shall discuss in the present paper. Thus by taking ε and $\xi_0 - \xi_{0c}$ to be very small, where ξ_{0c} is the reduced angle of attack which just provokes separation, we should obtain results close to those of this rational theory.

2. GOVERNING EQUATIONS

For two-dimensional steady incompressible flows, the boundary-layer equations are well known and can be written in the following form:

$$\frac{\partial u}{\partial s} + \frac{\partial v}{\partial n} = 0 \tag{1}$$

$$u \frac{\partial u}{\partial s} + v \frac{\partial u}{\partial n} = u_e \frac{du_e}{ds} + \frac{1}{\rho} \frac{\partial \tau}{\partial n} \tag{2}$$

where

$$\tau = \mu \frac{\partial u}{\partial n} - \rho \overline{u'v'} \tag{3}$$

Usually the boundary-layer calculations for the above equations, with a model for $-\rho\overline{u'v'}$, are performed for prescribed boundary conditions given by

$$u(s,0) = 0, \qquad v(s,0) = 0, \qquad u(s,n_e) = u_e(s) \tag{4}$$

For convenience we shall refer to this as the standard problem. In Eq. (4), the external velocity distribution $u_e(s)$ is given either from experiment or from inviscid flow theory. In the latter case, it is often necessary to consider the effect of the boundary-layer on the calculated external velocity distribution. This can be done in several ways. One procedure is to write the edge boundary condition, with u_e^o denoting the inviscid velocity distribution, as

$$u(s,n_e) = u_e(s) = u_e^o(s) + u_c(s) \tag{5}$$

and compute u_c from the so-called Hilbert integral,

$$u_c(s) = \frac{1}{\pi} \int_{-\infty}^{\infty} \frac{d}{d\sigma} (u_e \delta^*) \frac{d\sigma}{s - \sigma} \tag{6}$$

where $d/d\sigma\,(u_e\delta^*)$ is the blowing velocity induced by the boundary layer. Equation (6) is valid only for straight walls. The effect of the boundary layer is accounted for by solving the governing equations subject to the wall boundary conditions in Eq. (4) and the edge boundary condition given by Eq. (5). Several sweeps over the flow field are made until the solutions converge. There are several difficulties or questions which arise in this procedure and require further study.

One question concerns the Hilbert integral. When computing its contribution to u_e, we must bear in mind that generally the blowing velocity is small and has little effect. This is not, however, the case in the interaction region especially when the flow has separated, but the iteration process will be laborious and slow if at each stage we have to compute anew the effect of the blowing velocity over the entire airfoil. It would be convenient and indeed in some practical problems necessary to assume that the interaction region is limited to a finite range $s_a \leq s \leq s_b$ of s. As a result, numerical problems arise in evaluating Eq. (6) when s is near the limit of integration but they may be reduced if a smooth function is subtracted from the blowing velocity. In other words we may rewrite Eq. (6) as

$$u_e(s) = \frac{1}{\pi}\left[\int_{s_a}^{s_b} \frac{(u_e\delta^*)' - K(\sigma)}{s-\sigma}\,d\sigma + A\right] \tag{7}$$

where $K(\sigma)$ is a suitable function of σ and A denotes the residue of the Hilbert integral, namely

$$A = \int_{-\infty}^{s_a} \frac{(u_e\delta^*)' - K(\sigma)}{s-\sigma}\,d\sigma + \int_{s_b}^{\infty} \frac{(u_e\delta^*)' - K(\sigma)}{s-\sigma}\,d\sigma + \int_{-\infty}^{\infty} \frac{K(\sigma)}{s-\sigma}\,d\sigma \tag{8}$$

Clearly the limits s_a, s_b of σ must be chosen so that $(u_e\delta^*)'$ varies slowly outside the range of integration and in addition we would like to choose K so that the effect of A on $u_e(s)$ is negligible.

A second difficulty is that, as already pointed out, Eq. (6) is only valid for straight walls. Modifications should be introduced when curvature effects are taken into account and, once we have chosen appropriate values of s_a, s_b, we must consider whether these effects can be reduced to a simple multiplicative factor in Eq. (7) or are more fundamental.

A third difficulty arises if the boundary-layer solutions contain regions of flow reversal across the layer. Appropriate modifications must be made in the numerical method to compute such flows. There are several inverse boundary-layer procedures that can be used to cope with this difficulty (ref. 1, 7, 14-16) but all are limited to small regions of separation of size which remains to be explored.

The turbulence model required to describe the Reynolds shear stress, $\rho\overline{u'v'}$, in terms of known properties, presents a fourth difficulty. As shown in (ref. 17), the CS model is adequate for attached boundary-layer flows but greater uncertainty exists in regions of separation, where the transport of tubulence properties may be important. Even with existing "nigher turbulence models" the problem of wall functions remains. In particular, existing wall functions are based on the law of the wall which, itelf, does not allow severe pressure gradients and is deduced from the properties of attached boundary layers. In addition, and with the exception of the earlier attempt of Jones (ref. 18), only the CS model has been tested in such comparatively low Reynolds number flows as those found near the leading edge of airfoils.

Transition from laminar to turbulent flow introduces a further difficulty. Although methods such as e^9 have been used (ref. 8), and offer some promise, they must be regarded as untested and need further exploration. Since the transitional region is large at low Reynolds number flows, and is important, it is necessary to calculate the onset of transition and modify the turbulence model for $-\rho\overline{u'v'}$ to represent the flow through and downstream of the transition region.

3. MODEL PROBLEM

The study reported here is one phase of a larger effort on interactive flows. In this paper we investigate the computational problems arising in leading-edge separation and use the CS model to represent the Reynolds shear stress term.

We consider a thin ellipse of major axis $2a$ and minor axis $2at$ at an angle of attack, α, in a uniform stream of speed u_∞. We take (x,y) axes to be at the center of the ellipse and with θ denoting a polar angle (see fig. 1), we represent the ellipse by

$$x = -a\cos\theta, \qquad y = at\sin\theta \tag{9}$$

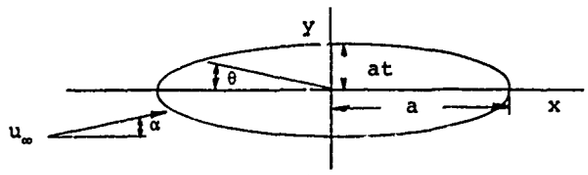


Figure 1. Flow Configuration for the Model Problem.

In the classical inviscid flow theory of attached flow, the circulation is adjusted so that the rear stagnation point occurs at $\theta = \pi$, and the velocity distribution can be calculated from the expression given by Lamb (ref. 19),

$$u_e^o = u_\infty\left(\frac{1+t}{t}\right)\frac{\sin(\theta+\alpha) + \sin\alpha}{\left|1 + (1/t^2 - 1)\sin^2\theta\right|^{\frac{1}{2}}} \tag{10}$$

We now assume that the interaction region is confined to a region near the nose in which

$\theta = 0(t)$. In this region Eq. (9) becomes

$$x = -a[1 - 1/2\ \theta^2(1 + 0(t^2))], \quad y = at\theta[1 + 0(t^2)] \tag{11}$$

so that both x and y are $0(at^2)$. Thus neglecting terms where the relative error is $0(t^2)$, we can approximate the ellipse locally by the "nose-fitting" parabola

$$x = -a(1 - 1/2\ \theta^2), \qquad y = at\theta \tag{12}$$

If we let

$$\xi = \theta/t \tag{13}$$

then the relations given by Eq. (12) can also be written as

$$x = -a(1 - 1/2\ \xi^2t^2), \quad y = at^2\xi \tag{14}$$

Expanding Eq. (10), we have to leading order

$$\frac{u_e^c}{u_\infty} = (1 + t)\ \frac{\xi + \xi_o}{(1 + \xi^2)^{1/2}} \tag{15}$$

where $\xi_o = \alpha/t$.

To find the surface distance s needed for the boundary-layer equations, we use the relations given by Eq. (14) and write

$$s = at^2 \int_0^\xi (1 + \xi^2)^{1/2} d\xi + \text{const} \tag{16}$$

With $R_a = 2au_\infty/\nu$, we now introduce a dimensionless normal distance, y, defined by

$$y = \left[\frac{R_a(1 + t)}{2t^2(1 + \xi^2)}\right]^{1/2} \frac{n}{a} \tag{17}$$

a dimensionless stream function, $f(\xi,y)$, defined by

$$\psi = [(1 + t)2u_\infty a\nu t^2]^{1/2}\ f(\xi,y) \tag{18}$$

and the of eddy viscosity, defined by

$$-\rho\overline{u'v'} = \rho\varepsilon_m \frac{\partial u}{\partial n} \tag{19}$$

By means of Eqs. (16) to (19), the boundary-layer equations given by Eqs. (1) and (2) can be written as

$$(bf'')' + \frac{\xi}{1 + \xi^2}(f')^2 + (1 + \xi^2)\bar{u}_e \frac{d\bar{u}_e}{d\xi} = f' \frac{\partial f'}{\partial \xi} - f'' \frac{\partial f}{\partial \xi} \tag{20}$$

where primes denote differentiation with respect to y. The boundary conditions corresponding to Eq. (20) follow from Eq. (4),

$$f = f' = 0 \quad \text{at} \quad y = 0, \qquad f' \to (1 + \xi^2)^{1/2}\ \bar{u}_e(\xi) \quad \text{as} \quad y \to \infty \tag{21}$$

Here

$$\bar{u}_e(\xi) = \frac{u_e(\xi)}{u_\infty(1 + t)} \approx \frac{\xi + \xi_o}{(1 + \xi^2)^{1/2}} + \frac{u_c}{u_\infty} \tag{22}$$

We now use parabolic coordinates (ξ,η) chosen so that the nose fitting parabola is $\eta = 1$ and the fluid region is defined by $\eta > 1$. Then as is shown in reference 20,

$$\frac{u_c}{u_\infty} = \frac{2^{1/2}}{tR_a^{1/2}\pi(1 + \xi)^{1/2}} \frac{1}{(1 + \xi^2)^{1/2}} \int_{-\infty}^{\infty} \frac{\Delta'(\bar{\xi}) - \Delta_\infty}{\xi - \bar{\xi}}\, d\bar{\xi} \tag{23}$$

Here the prime denotes differentiation with respect to $\bar{\xi}$, $\Delta_\infty = 1.2168$ and the parameter $\Delta(\xi)$ is defined by

$$\Delta(\xi) = \lim_{y \to \infty} \left[y\bar{u}_e(\xi)(1 + \xi^2)^{1/2} - f(\xi,y)\right] \tag{24}$$

Thus the "edge" boundary condition in Eq. (21) can be written as

$$f' + \xi + \xi_o + \varepsilon \int_{\infty}^{\infty} \frac{\Delta'(\bar{\xi}) - \Delta_\infty}{\xi - \bar{\xi}} d\bar{\xi} \tag{25}$$

where

$$\varepsilon = \frac{2^{\frac{1}{2}}}{tR_a^{\frac{1}{2}}\pi(1+t)^{\frac{1}{2}}} \tag{26}$$

The eddy-viscosity (ε_m) formulation used here is the algebraic CS model described in reference 3 and is given by two separate formulas. In the so-called inner region of the boundary layer ε_m is defined as

$$(\varepsilon_m)_i = L^2 \left|\frac{\partial u}{\partial n}\right| \gamma_{tr} \tag{27}$$

where

$$\begin{aligned} L &= 0.4n\left|1 - \exp(-n/A)\right|, \qquad A = 26\nu\left(\frac{\rho}{\tau}\right)^{\frac{1}{2}}_{max} \\ \gamma_{tr} &= 1 - \exp\left[-G(s - s_{tr}) \int_{s_{tr}}^{s} \frac{ds}{u_e}\right], \quad G = \frac{u_e^3}{\nu^2} R_{s_{tr}}^{-1.34} \frac{1}{1200} \end{aligned} \tag{28}$$

In the outer region, ε_m is defined by

$$(\varepsilon_m)_o = \alpha_1 \int_0^{\infty} (u_e - u)dn \tag{29}$$

where, with $z_1 = R_\theta/425 - 1$,

$$\alpha_1 = 0.0168 \frac{1.55}{1 + \Pi}, \qquad \Pi = 0.55\left[1 - \exp(z_1^{\frac{1}{2}} - 0.298z_1)\right] \tag{30}$$

The inner and outer regions are established by the continuity of the eddy-viscosity formulas.

In terms of dimensionless parameters defined by Eqs. (17) and (18), Eqs. (27) to (30) can be written as

$$(\varepsilon_m^+)_i = 0.16y^2 \sqrt{\tfrac{1}{2}R_a}\, t\sqrt{1+t}\, \left[1 - \exp(-n/A)\right]^2 |f''|\gamma_{tr} \tag{31}$$

$$(\varepsilon_m^+)_o = \alpha_1 \sqrt{\tfrac{1}{2}R_a}\, t\sqrt{1+t}\, (f'_e y_e - f_e)\gamma_{tr} \tag{32}$$

where $\varepsilon_m^+ = \varepsilon_m/\nu$ and

$$\frac{n}{A} = \frac{y}{26}\left[\sqrt{\tfrac{1}{2}R_a}\, t\sqrt{1+t}\, |f''_{max}|\right]^{\frac{1}{2}} \tag{33}$$

The relation between s and ξ needed for the s-term appearing in Eq. (20) is given by Eq. (16).

4. ASYMPTOTIC STRUCTURE

In section 2 we discussed some of the difficulties associated with the use of the Hilbert Integral in interaction boundary-layer studies. For one of these, namely the estimate of A, Eq. (8), the laminar studies are especially useful in giving us firm information about the behavior of the displacement thickness when ξ is large. We may set up a consistent asymptotic expansion of the solution in the form

$$u_e \sim 1 + \frac{\xi_o}{\xi} + \frac{\alpha_2}{\xi^2} + \ldots \tag{34}$$

with a corresponding form

$$f = \xi f_B(y) + f_1(y) + \frac{\mu \log\xi}{\xi}(yf'_B - f_B) + \xi^{-1}f_2(y) + \ldots \tag{35}$$

for f where μ is a constant to be found. Here f_B is the Blasius function satisfying $f'''_B + f_B f''_B = 0$ with the usual boundary conditions while f_1, satisfy linear equations of which the second can only be solved if

$$\mu = -0.499 - 4.329\xi_o^2 - 1.204\alpha_2 \tag{36}$$

The corresponding form for Δ is

$$\Delta = \xi\Delta_\infty + \Delta_1 + \mu\Delta_\infty\bar{\xi}' \log\xi + \bar{\xi}'\Delta_2 + \ldots \tag{37}$$

where $\Delta_1 = 3.796\xi_o$. We now see that the integral Eq. (23) converges for all ξ and the error, by truncating at a large value of ξ, $\approx\Delta_1/\xi$. It also follows from Eq. (23) that

$$\alpha_2 = -1/2 \tag{38}$$

and it may be shown that further terms in Eq. (34) are different according as $\xi \lesseqgtr 0$.

5. NUMERICAL METHOD

We use the Box method coupled with the Mechul function approach to solve the boundary-layer equations given by Eqs. (20), (21) and (25). The application of this method to the solution of inverse boundary-layer flows with prescribed displacement thickness has been described in several references, see for example references 1 and 14, so the present description is brief.

According to the Mechul function method, we treat the pressure or, as in this case, the "edge" velocity as a function of y as well as ξ and, by defining

$$f' = u \tag{39a}$$

$$u' = G \tag{39b}$$

$$w' = 0 \tag{39c}$$

we write Eq. (20) as

$$(bG)' + \frac{\xi}{1+\xi^2}(u^2 - w^2) = u\frac{\partial u}{\partial \xi} - G\frac{\partial f}{\partial \xi} - w\frac{\partial w}{\partial \xi} \tag{39d}$$

Here

$$w = u_e(1+\xi^2)^{1/2} \tag{40}$$

The wall boundary conditions in Eq. (21) become

$$f = u = 0 \tag{41a}$$

Similarly the "edge" boundary conditions, with f' at edge now denoted by f'_e, are

$$f'_e = w_e \tag{41b}$$

$$w_e = \xi + \xi_o + \varepsilon\int_{-\infty}^{\infty}\frac{D'(\bar{\xi})d\bar{\xi}}{\xi - \bar{\xi}} \tag{41c}$$

where $D(\xi) = \Delta(\xi) - \Delta_\infty\xi$. Except for the evaluation of the integral in Eq. (41c), the system of equations given by Eqs. (39) and (41) are tailor-made for the Mechul function method. We assume that the initial conditions which, in this case, correspond to the stagnation point solutions and are known at $\xi = \xi_o$ and then, on $\xi_1 \le \xi \le \xi_N$, $0 \le y \le y_e$, we choose a possibly nonuniform net

$$\begin{aligned} &\xi_1 = -\lambda_1 \quad \xi_n = \xi_{n-1} + k_n \qquad 2 \le n \le N \\ &y_o = 0 \qquad y_j = y_{j-1} + h_j \qquad 1 \le j \le J \qquad y_J = y_e \end{aligned} \tag{42}$$

Here λ_1 is a large number, which in our calculations was varied up to as much as 50. More will be said of the net selection in Section 6.

If we temporarily postpone the evaluation of the integral in Eq. (41c), we can proceed to write difference approximations to Eqs. (39) as described in reference 14. The resulting nonlinear difference equations are then linearized by Newton's method. For each fixed n in $2 \le n \le N$ the system with $1 \le j \le J$ contains $4J$ equations and with the four equations resulting from the boundary conditions, this yields $4J + 4$ equations for as many unknowns δf_j, δu_j, δv_j and δw_j and are solved by the block-elimination method described in reference 21. The solution algorithm can be arranged so that the solutions are obtained for standard (specified external velocity distribution) and inverse problems. For flows with separation, where regions of negative velocity occur, it is necessary to overcome the stability problem in order to continue the calculations past the separation point. In our scheme we use the approximation first suggested by Reyhner and Flügge-Lotz (ref. 22). This approximation neglects the $u\partial u/\partial x$ term in the region of negative u-velocity. If the separated region is not extensive, this approximation is satisfaccory and there is no need to improve the calculations by the DUIT procedure described in reference 23. All separated flow calculations reported here were performed without the DUIT procedure.

In order to write Eq. (41c) in a form which relates to our boundary-layer method, we use a procedure due to Veldman (ref. 2) with some changes in detail.

As a first step the tails of the Hilbert integral, i.e. the contributions from the ranges $(-\infty,\xi_1)$ and (ξ_N,∞) were neglected. Some tests were carried out to check the validity of this approximation and it was concluded that errors in u_e from this source would be typically of order 10^{-4}, and negligible.

To evaluate the integral at $\xi = \xi_n$ over (ξ_1,ξ_N) we split it up as follows:

$$I_n = \int_{\xi_1}^{\xi_n} \frac{D'd\bar{\xi}}{\xi_n - \bar{\xi}} = \sum_{k=2}^{n-1} \int_{\xi_{k-1}}^{\xi_k} \frac{D'd\bar{\xi}}{\xi - \bar{\xi}} + \int_{\xi_{n-1}}^{\xi_{n+1}} \frac{D'd\bar{\xi}}{\xi - \bar{\xi}} + \sum_{k=n+2}^{N} \int_{\xi_{k-1}}^{\xi_k} \frac{D'd\bar{\xi}}{\xi - \bar{\xi}} \qquad (43)$$

For the integrals in the two sums, i.e. over intervals outside the two enclosing ξ_n, we take D' to be approximated in each interval by the constant value

$$D' = \frac{D_k - D_{k-1}}{\xi_k - \xi_{k-1}} \qquad (44)$$

Thus

$$\int_{\xi_{k-1}}^{\xi_k} \frac{D'd\bar{\xi}}{\xi_n - \bar{\xi}} = \frac{D_k - D_{k-1}}{\xi_k - \xi_{k-1}} \ln\left|\frac{\xi_n - \xi_{k-1}}{\xi_n - \xi_k}\right| = E_k^n(D_k - D_{k-1})$$

where

$$E_k^n = (\xi_k - \xi_{k-1})^{-1} \ln\left|\frac{\xi_n - \xi_{k-1}}{\xi_n - \xi_k}\right| \qquad (k \neq n \text{ or } n+1)$$

For the double interval containing ξ_n, because of the cancellation in the constant term, we take account of the linear variation in D' and obtain

$$\int_{\xi_{n-1}}^{\xi_{n+1}} \frac{D'd\bar{\xi}}{\xi_n - \bar{\xi}} = E_n^n(D_n - D_{n-1}) + E_{n+1}^n(D_{n+1} - D_n) \qquad (45)$$

where

$$E_n^n = \frac{L_n(\xi_{n+1} - \xi_n) + 2}{\xi_n - \xi_{n-1}}, \qquad E_{n+1}^n = \frac{L_n(\xi_n - \xi_{n-1}) - 2}{\xi_{n+1} - \xi_n}$$

if

$$L_n = (\xi_{n+1} - \xi_{n-1})^{-1} \ln\left|\frac{\xi_n - \xi_{n-1}}{\xi_n - \xi_{n+1}}\right|$$

When $n = 1$ or N we need values for D at neighboring stations outside the range (ξ_1, ξ_N). These are obtained by quadratic extrapolation, which is consistent with the assumption of linear behavior for D'.

Using these results the integral in (41c) may be expressed in the form

$$\sum_{k=1}^{N} c_{k,n} D_k \qquad (46)$$

where the $c_{k,n}$ are coefficients which need calculating only once if the mesh is fixed. They have the property that

$$c_{n,n} = 0\left(\frac{\varepsilon}{\xi_{n+1} - \xi_{n-1}}\right), \qquad c_{k,n} = 0\left(\frac{\varepsilon}{\xi_k - \xi_n}\right)$$

We now set up a global iteration for coupling the "elliptic" boundary condition, Eq. (41c) with the system given by Eqs. (39) and (41a,b). After the i^{th} iteration has been completed we may suppose that we have estimates $D_n^{(i)}$ for the D_n and an estimate $\xi_0^{(i)}$ for the stagnation point where the current u_e distribution is zero. We assume that $f = 0$ for all y at this point and integrate away from it, first along the upper surface $[\xi > \xi_0^{(i)}]_m$ and then along the lower $[\xi < \xi_0^{(i)}]$. Since the stagnation point moves as the iterations proceed and also there is no profile to store, we do not use it as a regular ξ-station; we essentially use its position to determine a profile at the first ξ-station to the right of $\xi_0^{(i)}$, say where $n = n_1$, then continue the integration for $n = n_1 + 1, \ldots, N-1$. Similarly on the lower surface we start by determining a profile at $n = n_1 - 1$, then continue the integration for $n = n_1 - 2, \ldots, 2$.

At each ξ-station we take advantage of the key feature of Veldman's method, which is to use an inverse boundary condition, derived from (41c), which prescribes neither

$(u_e)_n$ nor D_n, but a linear combination of them. This is obtained by writing (41c) as

$$(w_e)_n^{(i+1)} - c_{n,n}\bar{D}_n = \xi_n + \xi_o + \sum_1 c_{k,n}\bar{D}_k + \sum_2 c_{k,n}D_k^{(i)} \tag{47}$$

where the overbar denotes values that are computed during the current double sweep. $\sum_1$ denotes a sum over those ξ-stations that have already been updated and $\sum_2$ denotes a sum over those ξ-stations that remain to be dealt with. Since

$$\bar{\Delta}_n = y_e w_{n,J}^{(i+1)} - f_{n,J}^{(i+1)} \tag{48}$$

we can write Eq. (47) in the form

$$c_{n,n}f_{n,J}^{(i+1)} + (1 - c_{n,n}y_e)w_{n,J}^{(i+1)} = g_n \tag{49}$$

where g_n is the right-hand side of Eq. (47) and can be computed before the start of the current Newton iterations.

Since we avoid computing

$$\int_{\xi_1}^{\xi_N} \frac{D'd\bar{\xi}}{\xi_n - \bar{\xi}}$$

for $n = 1$ and N by stopping the above calculations short of ξ_1 and ξ_N, we determine D_1 and D_N by quadratic extrapolation for interior values. The $(i+1)^{th}$ iteration is then completed by using overrelaxation to update the $D^{(i)}$:

$$D_n^{(i+1)} = \bar{D}_n + \omega[\bar{D}_n - D_n^{(i)}] \tag{50}$$

Thus our experience is similar to Veldman's in that we find overrelaxation to be possible. Also we find that Veldman's preferred value of $\omega = 1.5$ is close to optimum for the cases we have tested. However, since slightly higher values prevented convergence and near optimum convergence could be obtained with values nearer unity, we tended to use smaller values, mostly 1.1. As ξ_o approached a critical value (for given ε), this global iteration did ultimately fail to converge and no new choice of ω or the limits ξ_1, ξ_N appeared to be of any avail.

6. RESULTS AND DISCUSSION

Laminar Flows

Using the numerical method discussed above we performed calculations for laminar flows taking $R_a = 2 \times 10^6$ and $t = 0.1$ i.e. $\varepsilon = \varepsilon_1$ (= 0.003035) which are presented in Figures 2 to 7. In addition some data was obtained for $\varepsilon = 0.03183$ for checking purposes. In these calculations the spacing in the ξ-grid was uniform and equal to 0.2 while that in the y-grid was either uniform and equal to 0.1 or nonuniform, varying from 0.01 at the wall with a geometrical ratio of 1.14. The smoothness of the approach to the limit $u \to w_e$ as $y \to y_e$ was monitored at each ξ-station and the boundary-layer edge y_e adjusted accordingly. The number of points used in the y-grid for these calculations varied from 30 to 40.

It was pointed out in Cebeci, Khattab and Stewartson, reference 24, that if $\varepsilon = 0$ and $\xi_o < 1.155 = \xi_{oc}$ the boundary layer does not separate and we may then expect Δ to take on moderate values. Hence with the small values of ε chosen here the converged values of u_e, should be little different from those with $\varepsilon = 0$. This proved to be the case and so we shall concentrate on the flow properties when $\xi_o > \xi_{oc}$.

The variation of f_w'' with ξ for various ξ_o is shown in fig. 2. Separation first occurs when $\xi_o = 1.205$ the difference from ξ_{oc} being accounted for partly by the mollifying effect of Δ on the pressure gradient but also by a slight loss of accuracy due to the omission of an extrapolation procedure to the limit of zero step size. There is no reason to believe that the addition of such a procedure would materially alter our conclusions. Once separation occurs the Hilbert integral is of central importance to the prevention of the Goldstein singularity and the skin friction passes smoothly into negative values. Further, provided $\xi_o - 1.205$ is small, reattachment is achieved. Outside the range of ξ in the graphs we note that the skin friction is almost linear, the boundary layer taking on a Blasius form and showing little dependence on ξ_o or ε. The variation of displacement thickness with ξ is displayed in fig. 3 and is seen to be more marked once separation has occurred. However, the convergence of the iteration procedure now becomes much slower, fails marginally at $\xi_o = 1.219$ and altogether when $\xi_o = 1.220$. Various tests were then carried out to test the validity of this procedure but they made little impact on these conclusions. In figures 4 and 5 we show the strong contrast between convergence of the iterations when $\xi_o = 1.218$ and their divergence when $\xi_o = 1.220$.

This phenomenon, which we believe to be genuine, is associated with a nonexistence of solution and is preceded by a rapid downstream motion of the reattachment point. We can see from fig. 3 that Δ achieves a maximum near reattachment and so its effect on u_e reverses from that near separation. Instead of reducing the pressure gradient increases it, inhibiting and ultimately preventing reattachment.

The value $\xi_{oc} = 1.155$ of ξ_o is critical in the theory of laminar flows at high Reynolds number as it marks the largest possible value of ξ_o for which attached flow is possible according to classical rules, i.e. inviscid attached flow together with an associated boundary layer as the leading term in the asymptotic expansion in descending powers of R for the flow past a properly designed body with a parabolic nose whose thickness ratio is proportional to the angle of attack and small. For $\xi_o > \xi_{oc}$ the boundary-layer separated with a singularity. The only alternative which stands up sufficiently well to study for it to be plausible is now the Kirchhoff-Sychev free-streamline flow. However, in this theory the free streamline must spring off the body at the pressure minimum. According to attached theory this occurs at $\xi = \xi_o^{-1}$ whereas separation takes place at $\xi = 3.26 = \xi_{os}$ and so an abrupt discontinuity must occur in the limit flow as ξ_o passes through ξ_{oc}. There are still some queries to be answered about the free-streamline theory and the present study is useful in throwing new light on its plausibility.

For when $\varepsilon \to 0$ and $\xi_o \to \xi_{oc}$ our formulation is equivalent to that of a triple-deck theory (Stewartson and Cebeci, ref. 20) which in turn may be interpreted as part of the leading term in the asymptotic expansion of the solution of the Navier-Stokes equations in descending powers of R. According to this theory solutions can exist if $\xi_o - \xi_{oc}$ is negative or sufficiently small in comparison with ε, but not for larger positive values of $\xi_o - \xi_{oc}$. This conclusion is entirely in accord with our present numerical results and reinforces previously held views (Stewartson, ref. 10) that the onset of separation heralds an abrupt change from one class of flows to another. It should be emphasized that in the present instance this change is not strictly due to difficulties at separation - the displacement thickness effectively presents them - but to the failure of the flow to reattach. In this connection Kraemer (ref. 25) reports that at $R = 42{,}000$ laminar separation was not followed by reattachment whereas at $R = 75{,}000$, reattachment did occur. It is possible that transition occurred in the separated flow at the higher Reynolds number.

Besides these studies at $R = 2 \times 10^6$ some additional studies were carried out at the higher values of ε. They confirmed that solutions can only be found for a limited range (~ 0.02) of values of ξ_o greater than that (1.210) at which separation occurred and, reasonably enough, the mollifying effect of ε is greater.

A number of tests designed to help choose the most convenient values of s_b, s_a, K in Eq. (7) were also carried out. Figures 6 and 7 show the effect of limits of integration on wall shear parameter, f_w'' and displacement thickness δ^*, respectively for $\xi_o = 1.215$. In the calculations Δ_∞ was not set equal to zero and the interaction region was confined to a small region of the upper surface. It was found that varying the lower limit of integration in the Hilbert integral somewhere between the stagnation point and the separation point did not have much effect, so it was set at $\xi = 0$. It is clear that the results in the interaction region are converging satisfactorily as the upper limit increases, and that an upper limit of $\xi = 10$ would be adequate for most purposes. Possibly smaller limits could be used if some smoothing procedure could be used to avoid the effects of the small jump at the end of the interaction region.

We have also investigated, to some extent, the effects of ignoring the curvature at the leading edge. Using the usual boundary-layer variables, arc length and scaled normal distance, and with the Hilbert integral expressed directly in terms of arc length, we found, for example, that for $\xi_o = 1.18$ the effect on the skin friction amounted to less than 2% over most of the region and rose to about 8% in the center of the interaction.

Turbulent Flows

We have also performed calculations for turbulent flows with the CS turbulence model discussed previously. It should be noted that these calculations are of an exploratory nature and are performed to test the numerical method for turbulent flows with separation. Additional calculations are needed and will be performed to test the turbulence model by comparing numerical calculations with available experimental data. It is likely that the CS model will have to be modified or even replaced since, for example: (1) the wall function in this formulation may not be satisfactory for flows with separation, (2) the intermittency factor used for the transitional region is based on flows where it occurs in entirely attached flows and, (3) in turbulent flows preceded by laminar separation, the Reynolds number is rather low.

The calculations in figures 8 and 9 are for $\xi_o = 1.22$ and were obtained by assuming laminar flow from the stagnation point up to $\xi = 4.4$ at which point the turbulent flow calculations were started. For comparison purposes, we also show the distributions of the wall shear parameter f_w'' and the displacement thickness for a laminar flow with $\xi_o = 1.21$. As can be seen, there is a drastic change in the variation of these parameters with slight increase in angle of attack. Laminar flow results could not be obtained with $\xi_o = 1.22$ but were readily obtained with turbulent-flow assumptions. The solutions, however, and in common with those for laminar flow with $\xi_o = 1.22$, break down as ξ_o increases beyond 1.22.

The results shown in figures 10 and 11 are similar in nature to those in figures 8 and 9 except that the transition location has been moved forward to $\xi = 3.2$. This enabled the calculations to be performed for larger angles of attack; with this transition assumption, the solutions break down for $\xi_o = 1.32$.

The numerical calculations for turbulent flow, as is evidenced by these results, indicate the strong influence which the transition location plays in the solutions. This may, however, be less important in practice since transition usually occurs very soon after laminar separation. It is probably much more important to correctly model the transition region in low Reynolds number turbulent flows. It is clear, however, that the numerical procedure is satisfactory for the calculation of these flows and that future investigations, with new turbulence assumptions, can proceed without further numerical development.

REFERENCES

1. Cebeci, T., Separated Flows and their Representation by Boundary-Layer Equations, California State University at Long Beach, Mech. Eng. Rept. ONR-CR215-234-2, 1976.

2. Veldman, A.E.P., A Numerical Method for the Calculation of Laminar Incompressible Boundary Layers with Strong-Inviscid Interaction, NLR TR 79023L, 1979.

3. Cebeci, T. and Smith, A.M.O., Analysis of Turbulent Boundary Layers, Academic Press, New York, 1974.

4. Tani, I., Low-Speed Flows Involving Bubble Separations, Progress in Aeronautical Science, Vol. 5, Pergamon Press, New York, 1964, pp. 70-103.

5. Arena, A.V. and Mueller, T.J., On the Laminar Separation, Transition, and Turbulent Reattachment of Low Reynolds Number Flows Near the Leading Edge of Airfoils, AIAA J., Vol. 18, No. 8, Aug. 1980, pp. 883-891.

6. Briley, W.R. and McDonald, H., Numerical Prediction of Incompressible Separation Bubbles, J. Fluid Mech., Vol. 69, Pt. 4, June 1975, pp. 631-656.

7. Kwon, O.K. and Pletcher, R.H., Prediction of Incompressible Separated Boundary Layers Including Viscous-Inviscid Interaction, J. Fluids Eng., Vol. 101, Dec. 1979, pp. 466-472.

8. van Ingen, J.L., On the Calculation of Laminar Separation Bubbles in Two-Dimensional Incompressible Flow, AGARD-CP-168, Flow Separation, paper 17, 1975.

9. Crimi, P. and Reeves, B.L., Analysis of Leading-Edge Separation Bubbles on Airfoils, AIAA J., Vol. 14, Nov. 1976, pp. 1548-1555.

10. Stewartson, K., D'Alembert's Paradox, to be published in SIAM Review, 1981.

11. Dijkstra, D., Separating Incompressible Laminar Boundary-Layer Flow Over a Smooth Step of Small Height, Proc. 6th Inter. Conf. Numerical Methods in Fluid Dynamics, Tbilisi, USSR, 1978, pp. 45-52.

12. Smith, F.T., The Laminar Separation of an Incompressible Fluid Streaming Past a Smooth Surface, Proc. Roy. Soc., London, Vol. A356, 1977, pp. 433-463.

13. Smith, F.T., Laminar Flow of an Incompressible Fluid Past a Bluff Body; the Separation, Reattachment, Eddy Properties and Drag, J. Fluid Mech., Vol. 92, 1979, pp. 171-205.

14. Cebeci, T., Keller, H.B. and Williams, P.G., Separating Boundary-Layer Flow Calculations, J. Comp. Physics, Vol. 31, No. 3, 1979, pp. 363-378.

15. Carter, J.E. and Wornom, S.F., A Forward Marching Procedure for Separated Boundary-Layer Flows, AIAA J., Vol. 13, 1975, pp. 1101-1103.

16. Arieli, R. and Murphy, J.D., Pseudo-Direct Solutions to the Boundary-Layer Equations for Separated Flow, AIAA J., Vol. 18, No. 8, 1980, pp. 883-891.

17. Cebeci, T. and Meier, H.U., Modelling Requirements for the Calculation of the Turbulent Flow Around Airfoils, Wings and Bodies of Revolution. AGARD Conf. Proceedings No. 271, Turbulent Boundary Layers: Experiments, Theory and Modelling, Paper No. 16, 1980.

18. Jones, W.P., Laminarization in Strongly Accelerated Boundary Layers, University of London Ph.D. Thesis, 1971.

19. Lamb, H., Hydrodynamics, Cambridge University Press, 6th Ed., 1932.

20. Stewartson, K. and Cebeci, T., Marginal Separation, paper in preparation.

21. Cebeci, T. and Bradshaw, P., Momentum Transfer in Boundary Layers, Hemisphere-McGraw Hill, Washington, D.C. 1977.

22. Reyhner, T.A. and Flügge-Lotz, I., The Interaction of a Shock Wave with a Laminar Boundary Layer. Int. J. Nonlinear Mech., Vol. 3, No. 2, 1968, pp. 173-199.

23. Williams, P.G., A Reverse Flow Computation in the Theory of Self-Induced Separation, in R.D. Richtmyer (ed.), Lecture Notes in Physics, Vol. 35, Proc. of the Fourth Intern. Conf. on Numerical Methods in Fluid Dynamics, Springer-Verlag, Berlin, 1975, pp. 445-451.

24. Cebeci, T., Khattab, A.A. and Stewartson, K., On Nose Separation, J. Fluid Mech., Vol. 97, 1980, pp. 435-454.

25. Kraemer, K., Flügelprofile im Kritischen Reynoldszahl-bereich, Forsch. a.d. Geb. d. Ing., Vol. 27, 1961, pp. 33-46.

ACKNOWLEDGMENT

It is a pleasure to acknowledge the support of the Office of Naval Research for this work done under contract N00014-77-0156.

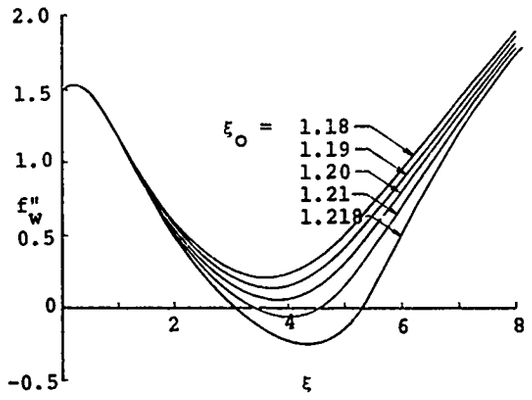


Figure 2. Variation of Laminar Wall Shear Parameter f''_w with ξ for Various Reduced Angles of Attack, ξ_o.

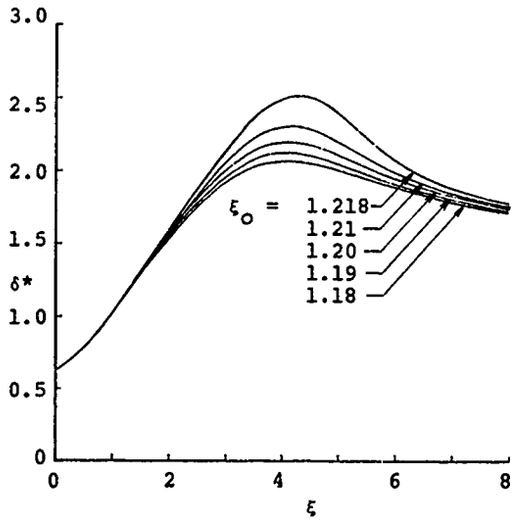


Figure 3. Variation of Laminar Displacement Thickness δ^* with ξ for Various Reduced Angles of Attack, ξ_o.

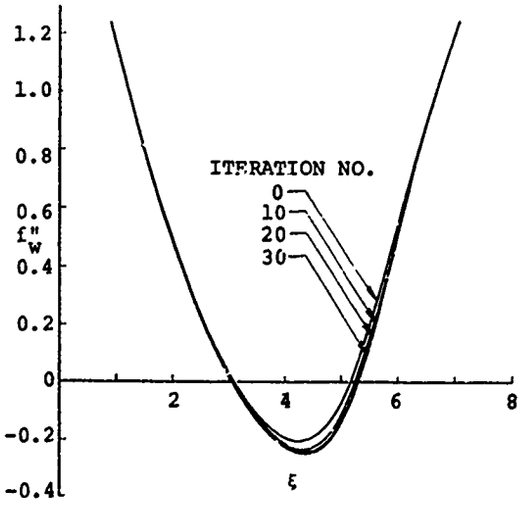


Figure 4. Variation of Laminar Wall Shear Parameter in Various Iterations for ξ_o = 1.218.

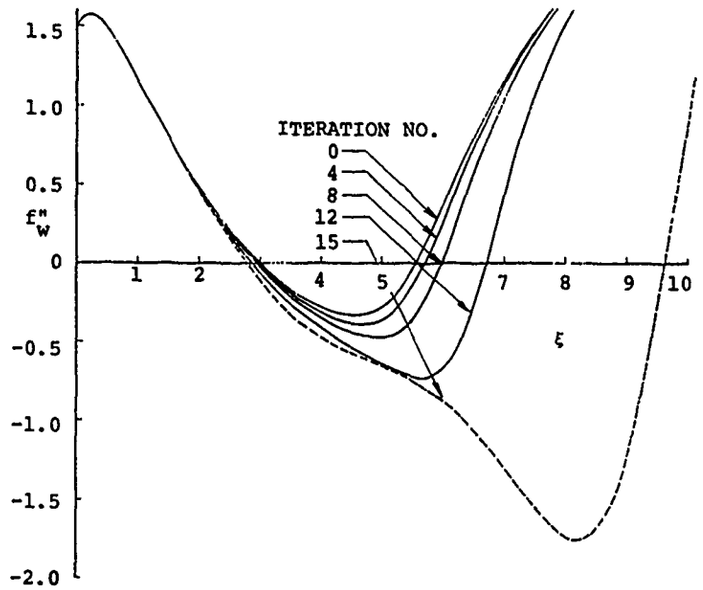


Figure 5. Variation of Laminar Wall Shear Parameter in Various Iterations for $\xi_o = 1.220$. In the Dashed Curve, the Interaction Region Extended Downstream Beyond the Range of Integration of Eq. (23).

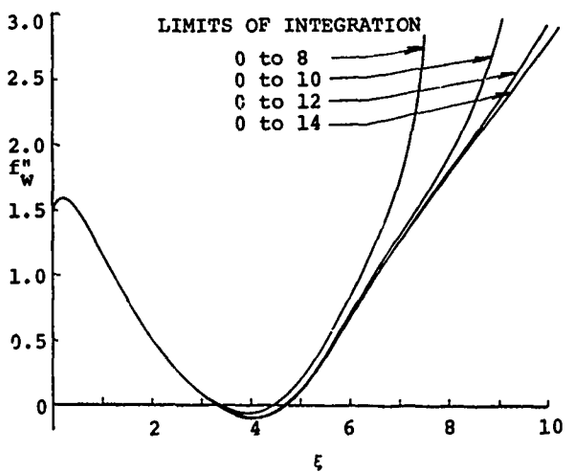


Figure 6. The Effect of Limits of Integration on Laminar Wall Shear Parameter f''_w for $\xi_o = 1.215$.

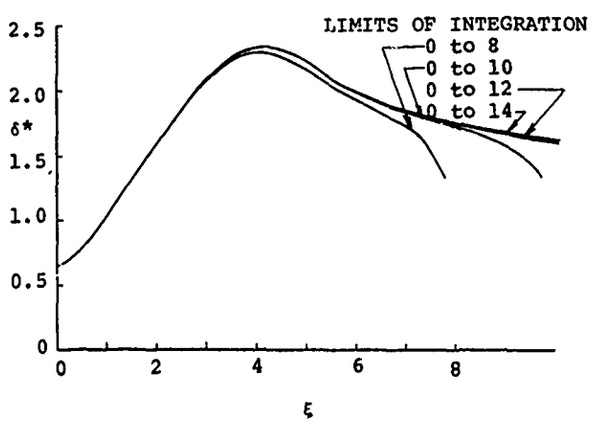


Figure 7. The Effect of Limits of Integration on the Laminar Displacement Thickness δ* for $\xi_o = 1.215$.

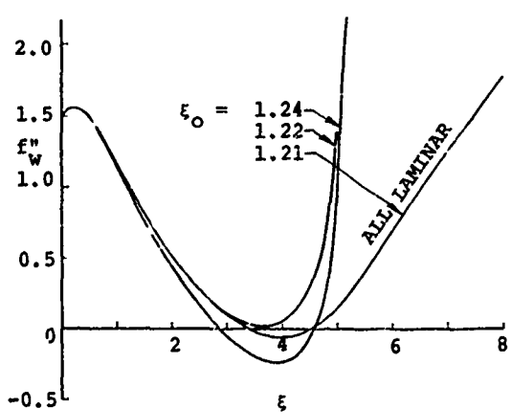


Figure 8. Variation of the Wall Shear Parameter f''_w when Transition is Set at $\xi = 4.40$.

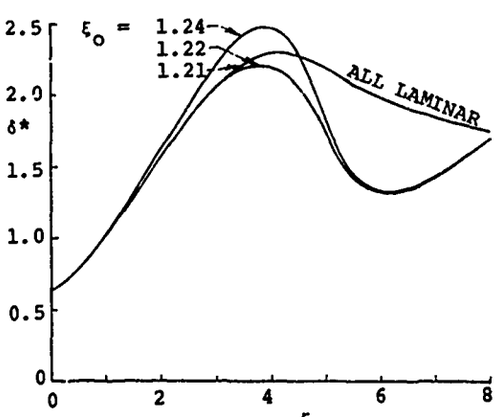


Figure 9. Variation of the Displacement Thickness δ* with ξ when Transition is Set at $\xi = 4.40$.

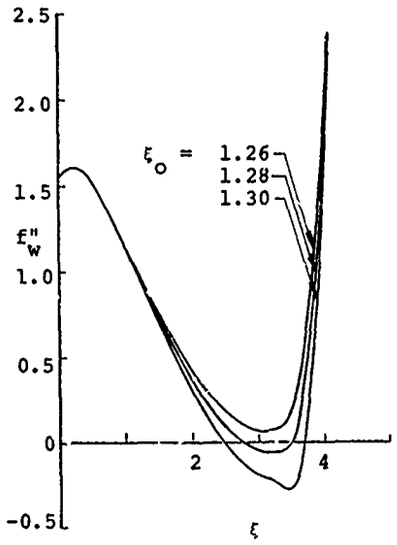


Figure 10. Variation of the Wall Shear Parameter f''_w with ξ when Transition is Set at ξ = 3.2.

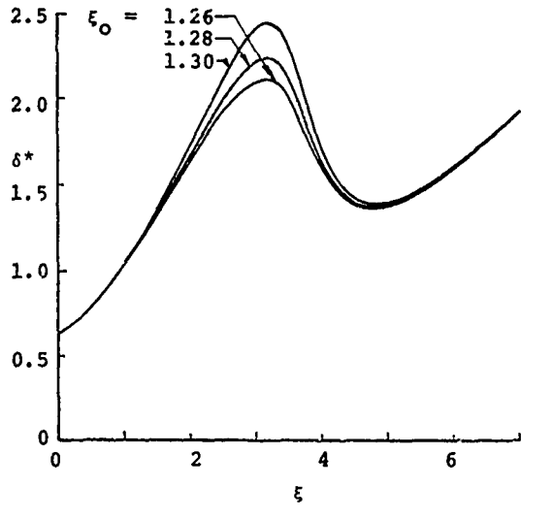


Figure 11. Variation of the Displacement Thickness δ^* with ξ when Transition is Set at ξ = 3.2.

BULBE DE DECOLLEMENT LAMINAIRE AVEC TRANSITION
- Essai de prévision avec couplage local -

C. GLEYZES, J. COUSTEIX, J.L. BONNET

Département d'Aérothermodynamique
ONERA/CERT
31055 - TOULOUSE CEDEX, FRANCE

RESUME

On décrit les résultats expérimentaux obtenus dans l'étude du bulbe de décollement de bord d'attaque sur un profil de type peaky. Des mesures de couche limite, vitesse moyenne et intensité longitudinale de turbulence, ont été effectuées pour plusieurs valeurs du nombre de Reynolds ($10^5 < R_c < 10^6$).

On présente également une étude du processus de transition dans un bulbe long. Deux méthodes de calcul applicables aux bulbes courts sont proposées. Elles font toutes deux appel à un schéma simple de couplage local. Leurs résultats sont comparés à ceux de nos expériences.

SUMMARY

The experimental results of a study of a leading edge separation bubble on a peaky airfoil are presented. Boundary layer measurements, mean velocity and longitudinal turbulence intensity, were carried out for several values of Reynolds number ($10^5 < R_c < 10^6$). We also present a study of the transition process in a long bubble.

Two calculation methods for short bubble are proposed. They both use a simple local viscid-inviscid interaction scheme. These results are compared to our experimental ones.

NOTATIONS

c	corde du profil
C_f	coefficient de frottement local $\frac{C_f}{2} = \frac{\tau_p}{(1/2\,\rho_e u_e^2)}$
C_E	coefficient d'entrainement $C_E = \frac{d\delta}{dx} - \frac{v_e}{u_e}$
H	paramètre de forme $H = \frac{\delta_1}{\theta}$
H^*	paramètre de forme $H^* = \frac{\delta - \delta_1}{\theta}$
R_c	nombre de Reynolds global formé avec la corde du profil $R_c = \frac{U_\infty c}{\nu}$
R_x	nombre de Reynolds formé avec l'abscisse x $R_x = \frac{U_\infty x}{\nu}$
$R\theta_s$	nombre de Reynolds local formé avec l'épaisseur de quantité de mouvement au point de décollement $R\theta_s = \frac{U_s \theta_s}{\nu}$
s	abscisse curviligne sur le profil comptée à partir du bord d'attaque géométrique
x	abscisse d'un point du profil comptée selon la corde à partir du bord d'attaque géométrique
y	normale au profil
U, V	vitesses moyennes dans les directions x, y
u', v'	fluctuations autour des vitesses moyennes U et V
U_∞	vitesse à l'infini amont
$U_{ref.}$	vitesse de référence pour les calculs
U_p	vitesse potentielle
δ	épaisseur de la couche limite
δ_1	épaisseur de déplacement $\delta_1 = \int_0^\delta \left(1 - \frac{U}{U_p}\right) dy$
θ	épaisseur de quantité de mouvement $\theta = \int_0^\delta \frac{U}{U_p}\left(1 - \frac{U}{U_p}\right) dy$

Indices

S	décollement
T	fin de transition
R	recollement
D	début de transition
p	potentiel

1. INTRODUCTION

L'extrapolation des résultats obtenus en soufflerie aux conditions réelles de vol s'avère très délicate quand le nombre de Reynolds est assez faible pour modifier la configuration générale de l'écoulement. Ainsi, par exemple, dans l'étude des profils de type peaky en subsonique, l'existence d'une pointe de survitesse importante, même à faible incidence, donne naissance à un décollement laminaire et un bulbe transitionnel si le nombre de Reynolds est trop faible ; en revanche, à grand nombre de Reynolds, la couche limite rapidement turbulente ne subit pas de décollement. Des études antérieures ont déjà montré que l'effet du bulbe sur le développement de la couche limite est très important, et qu'il faut en tenir compte de manière très précise pour être capable, par exemple, de prévoir le décollement éventuel de la couche limite sur l'arrière du profil.

Le problème du bulbe de bord d'attaque n'est pas cependant lié uniquement aux essais en soufflerie. En effet, il peut se rencontrer également en vol, par exemple au voisinage du bord d'attaque d'entrées d'air ou dans l'aérodynamique des turbomachines.

Il s'agit donc là d'une question d'un grand intérêt qui avait déjà justifié plusieurs études antérieures. Nous nous sommes proposés en fait, de reprendre ce travail en essayant de préciser certaines données expérimentales manquantes ou difficilement disponibles et de les rendre systématiques.

Une étude détaillée de la transition dans un bulbe de décollement du type "long" nous a permis, au moyen de visualisations alliées à une ananlyse spectrale du signal fluctuant, de caractériser ce processus de transition et d'étudier son influence sur la couche limite turbulente aval. Une étude systématique en fonction du nombre de Reynolds nous a donné les informations nécessaires pour la confrontation des méthodes que nous proposons pour le calcul des bulbes de type "court".

La première méthode fait appel à la résolution en mode direct des équations locales instationnaires de la couche limite, l'élimination de la singularité au point de décollement étant réalisée à l'aide d'un schéma de couplage local.

La deuxième méthode reprend les mêmes hypothèses de couplage, mais associées à la résolution en mode inverse des équations globales de la couche limite. Dans les deux cas, la répartition de vitesse en fluide parfait est une donnée du problème.

2. ETUDE EXPERIMENTALE

2.1. Dispositif expérimental.

Nous avons choisi pour cette étude un profil ONERA LC 100 D de 200 mm de corde. Ce profil est monté entre les parois de la veine de 300 x 400 mm^2 de section, d'une soufflerie subsonique de type Eiffel. Des essais préliminaires nous avaient conduit à retenir une incidence de 7.5° de façon à pouvoir étudier les différentes configurations de bulbe par simple variation de la vitesse amont (entre 3 et 80 m/s). Suivant le type de mesures réalisées, un nombre plus ou moins important de vitesses d'essai a été retenu ; nous préciserons les valeurs lors de la description des résultats.

Le taux de turbulence de l'écoulement est porté , figure 1, en fonction de la vitesse à l'infini amont. On constate qu'il diminue quand la vitesse augmente. Il est certain que ce paramètre peut agir sur le processus de transition et effectivement certains critères (dont nous reparlerons au chapitre des méthodes de calcul) le font intervenir. Cependant, on peut penser que dans le processus général de transition le paramètre gradient de pression est dominant. Néanmoins, l'étude expérimentale de l'influence du taux de turbulence est à envisager.

Globalement, l'écoulement a été caractérisé par la distribution de pression à la paroi ; pour celà, on disposait d'un profil équipé de prises de pression.

En fait, la partie essentielle de l'étude expérimentale a consisté en une analyse détaillée du développement de la couche limite et notamment du processus de transition et de son influence sur la turbulence. Les mesures réalisées à ce jour sont la détermination du champ de vitesse moyenne et d'intensité longitudinale de turbulence à l'aide d'un anémomètre à fil chaud. De cette façon, on peut déjà avoir une vue générale des phénomènes. Une étude plus approfondie permettant de préciser la nature de la transition a été effectuée par le biais de l'analyse spectrale du signal fil chaud, conjointement à une visualisation de l'écoulement par la technique du plan de lumière.

2.2. Mesures de pression

La variation systématique de la vitesse amont fait apparaître sur la figure 2 différents types de répartition de vitesse dans la région du bord d'attaque du profil :

. Pour U_∞ = 80 m/s (soit $R_c \simeq 10^6$) les visualisations par bouillies ne semblent pas indiquer la présence d'un décollement. Cela veut probablement dire que la transition a lieu avant le décollement, ou bien que le bulbe est trop petit pour être détecté. Dans nos calculs, nous utiliserons cette distribution comme approximation de celle du fluide parfait.

. Pour les mesures à 39.8 et 34.6 m/s ($R_c > 0.45\ 10^6$) apparaît une petite zone perturbée de l'ordre de 10 à 15 mm (soit 5 à 7.5 % de la corde). On ne dispose malheureusement que de deux à trois prises de pression dans cette région, mais au vu des travaux antérieurs (GASTER /9/), on peut penser que ces distributions devraient faire apparaître un plateau de pression constante. Une diminution de la pointe de survitesse est également visible.

. Entre 34.6 et 33.2 m/s ($R_c \simeq 0.45\ 10^6$), un changement assez brusque de configuration de ces distributions apparaît. Certains auteurs (OWEN et KANFER /15/ , GASTER /9/) ont présenté ce phénomène comme l'éclatement du bulbe court en un bulbe long ("Short bubble Bursting"). Nous dirons que la zone de perturbation s'est brutalement étendue et que la maximum par rapport à la répartition du fluide parfait marque également une brusque diminution.

. Au dessous de 33.2 m/s ($R_c < 0.45\ 10^6$), cette zone continue son extension vers l'aval. A la perturbation locale due au décollement, doit probablement se superposer une modification globale de la circulation autour du profil associée au rapide déplacement du point d'arrêt enregistré au moment de l'éclatement du bulbe.

Le qualificatif de "bulbe court" sera réservé aux zones de perturbation du premier type, celui du "bulbe long" à l'autre type.

2.3. Mesures de couche limite

Des mesures de vitesse moyenne et d'intensité longitudinale de turbulence ont été réalisées pour cinq valeurs de la vitesse amont :

13, 19.8 et 26.9 m/s pour les bulbes longs

38.7 et 53 m/s pour les bulbes courts

Il faut d'abord remarquer que les profils sont représentés sous la forme U/U_p et $\sqrt{\overline{u^2}}/U_p$. Du fait de la courbure de paroi on a en effet un gradient normal de la vitesse potentielle, et il est alors préférable d'utiliser la quantité $U_p(y)$, extrapolation à l'intérieur de la couche limite de la vitesse potentielle mesurée à l'extérieur. L'extrapolation jusqu'à la paroi donne la vitesse potentielle à la paroi U_{P_e} qui est en bon accord avec les résultats des mesures de pression. D'autre part, lorsque la vitesse instantanée $u(t)$ devient négative, les valeurs que donnent l'anémomètre à fil chaud sont erronées. Nous les avons donc pas reportées.

Nous avons donc, compte-tenu de toutes ces remarques, reporté les résultats obtenus dans le cas d'un bulbe long à 13 m/s sur les figures 3 et 4.

Aux stations x/c = 3.5, 5 et 8%, existent des vitesses négatives près de la paroi. Au dessus de cette zone de retour se développe une couche de cisaillement très fort. Celle-ci correspond à un pic très marqué de l'intensité de turbulence, de niveau très élevé (jusqu'à 25 % en x/c = 11 %) pour des profils de vitesse apparemment laminaires. La forme de ces profils d'intensité de turbulence n'est en effet pas celle que l'on trouverait en couche limite turbulente ; il faut la rapprocher de celle obtenue dans les études de transition avec gradients de pression assez intenses (AKNAL, JUILLEN /1/ - COUSTEIX, PAILHAS /8/). Les modifications dans la forme des profils de vitesse notées près de la paroi (x/c = 8, 11 et 15%) s'étendent ensuite progressivement à la partie supérieure de la couche limite, et l'on tend ainsi assez lentement vers un profil turbulent. Des observations analogues sont à faire quant aux profils d'intensité de turbulence. L'écoulement n'atteint un caractère turbulent que vers x/c = 65 %.

Dans le cas de bulbes courts, le phénomène observé est analogue, quoi que plus rapide. Le bulbe est en effet de petite dimension, et l'écoulement de retour est très difficile à caractériser. On retrouve cependant la même évolution au niveau des profils de turbulence (le maximum est cependant un peu plus faible de l'ordre de 15 %) ainsi que des profils de vitesse moyenne. L'écoulement atteint là un caractère turbulent dès 15 % de la corde.

A partir des profils de vitesse moyenne, on a pu également déterminer les différentes grandeurs intégrales caractéristiques de la couche limite. Sur la planche 5 est reportée l'évolution du paramètre de forme H pour les différentes valeurs de U_∞. On retrouve en amont les valeurs élevées de H correspondant à la zone décollée, en aval les valeurs de H correspondant à une couche limite turbulente classique. Entre les deux, l'évolution de ce paramètre est d'autant plus lente que la vitesse est faible. Notons cependant que si pour les bulbes courts les évolutions de H sont pratiquement indépendantes de la vitesse il n'en est plus de même pour les bulbes longs ; en particulier, on ne retrouve plus la discontinuité qui apparaît sur les répartitions de vitesse extérieure, les résultats à 26,9 m/s présentant une évolution intermédiaire.

Cette remarque est confirmée par la figure 6 où est reportée en fonction de U_∞ l'épaisseur de quantité de mouvement θ mesurée au point x/c = 75 % du profil. On a reporté également le résultat d'un calcul effectué en supposant une transition brutale au point de décollement, l'écart entre les deux courbes correspondant à l'accroissement de θ provoqué par le bulbe. Celui-ci est faible et assez peu dépendant de la vitesse pour les bulbes courts (U_∞ > 34 m/s), beaucoup plus élevé pour les bulbes longs en dessous de 20 m/s, mais ne présente pas de discontinuité au niveau de l'éclatement ; la courbe évolue assez rapidement, mais régulièrement, lorsque la vitesse diminue de 35 à 20 m/s.

Une autre façon de mettre en évidence le sur-épaississement dû au bulbe est présentée sur la figure 7 où on a représenté pour les différentes vitesses choisies, l'évolution du paramètre $(\theta/x)\ R_x^{1/6}$ le long du profil. Cette quantité est pratiquement indépendante de la vitesse amont lorsque l'écoulement est supposé turbulent depuis le point de décollement laminaire. L'écart qui apparaît sur les courbes expérimentales est donc significatif du seul sur-épaississement dû au bulbe, et on peut faire les mêmes remarques que précédemment.

2.4. Analyse spectrale et visualisations.

A ce niveau nous avons essayé d'examiner plus en détail le processus de transition, et ceci au moyen, d'une part d'une analyse spectrale du signal fluctuant, et d'autre part de visualisations par plan de lumière. Nous n'avons malheureusement pas pu, sur ce montage expérimental, nous pencher sur le problème du bulbe court. Du fait de la petite taille de ces bulbes, les sondages au fil chaud n'étaient possibles qu'à partir d'un point situé au voisinage du recollement, et ne pouvaient donc nous donner aucune information sur la transition elle-même ; d'autre part, du fait des limites de la caméra que nous utilisions, nous n'avons pu obtenir de visualisations exploitables que pour des vitesses faibles.

La suite de ce paragraphe ne concerne donc que le processus de transition dans un bulbe long, l'étude de la configuration bulbe court étant actuellement en cours sur un nord d'attaque agrandi.

Le principe d'obtention du plan vertical de lumière dans l'axe de la soufflerie, à partir d'un faisceau laser de 18 W, est expliqué sur le schéma de la figure 8. Une injection de fumée d'encens réalisée en aval du point d'arrêt, tangentiellement à la paroi permet l'ensemencement de la couche limite en amont du décollement. Une caméra rapide (maximum 5000 images/s) nous a permis d'obtenir un ralenti suffisant pour appréhender le phénomène.

Les photographies de la figure 8, bien que correspondant à des vitesses de l'ordre de 3 m/s donnent une image qualitativement en très bon accord avec les résultats de l'anémométrie fil chaud reportés sur la figure 9.

Examinons ces résultats en parallèle :

Sur les lignes iso - U/U_ρ tout comme sur les photographies, on retrouve sur la gauche la couche de cisaillement et l'écoulement de retour. Cette couche de cisaillement évolue vers l'aval en se déstabilisant et en donnant naissance à des tourbillons régulièrement espacés, ceci expliquera la présence d'une fréquence privilégiée aux stations 1 et 2 de la figure 9.

Si on suit le tourbillon repéré par une flèche sur les deux images, on voit qu'il s'enroule sur le tourbillon émis juste avant pour donner une structure plus importante (apparition du sous-harmonique aux stations 3 et 4) ; cette structure va persister un certain temps (stations 5 et 6) puis finit par se désagréger. Sur le spectre, on voit les fréquences privilégiées disparaître par une augmentation générale du niveau de l'ensemble du spectre. Remarquons que si dès la station 8 ($x/c \simeq 15\%$) le spectre du signal a une allure turbulente, les profils de vitesse moyenne ne seront turbulents qu'à partir de $x/c = 65\ \%$.

Il est à noter que l'ensemble de ces constatations est à rapprocher de celles effectuées à propos du processus de transition dans les gradients de pression (ARNAL, JUILLEN /1/ , COUSTEIX, PAILHAS /8/). En particulier, on n'observe à aucun moment la formation de spots bien définis comme dans le cas de transition avec gradient de pression nul.

3. ETUDE THEORIQUE

3.1. Essais d'application de méthodes simples

Nous avons tout d'abord essayé d'appliquer à nos expériences deux méthodes simples de calcul des bulbes courts.

Ces deux méthodes (HORTON /11/ et VINCENT DE PAUL /18/) supposent connues à l'avance la répartition de vitesse en fluide parfait, la position du point de décollement et la valeur de $R\theta_s$ en ce point.

On définit alors le point T dit de "fin de transition" par la relation :

$$x_T - x_s = k\ (\theta_s / R\theta_s)$$

où k est une constante égale à 4.10^4 pour HORTON, une fonction de $R\theta_s$ comprise entre 3 et 5.10^4 pour VINCENT DE PAUL. L'indice s correspond au point de décollement, l'indice t au point de fin de transition.

Dans la zone ST, la vitesse est supposée constante et égale à Ut ($U_t = U_s$ pour HORTON, $U_t = U_s/1.03$ pour VINCENT DE PAUL), on détermine alors les quantités nécessaires au calcul en T.

On suppose alors que le recollement a lieu au point R que l'on cherche à déterminer. Pour cela, on utilise entre T et R des équations intégrales (quantité de mouvement et énergie cinétique pour HORTON, entrainement et énergie cinétique pour VINCENT DE PAUL) et moyennant certaines hypothèses simplificatrices (vitesse décroissant linéairement entre T et R en particulier), on obtient une équation du lieu ($\mathcal{L}$) des points possibles de recollement dans le plan (U, x). L'intersection de ($\mathcal{L}$) et de la courbe de répartition de vitesse en fluide parfait donne le point de recollement R. "L'éclatement" du "bulbe court" en "bulbe long" correspond à la position limite où la courbe ($\mathcal{L}$) est tangente à la courbe u(x).

Si on applique ces deux méthodes à nos résultats expérimentaux, la position du point de décollement et les valeurs des paramètres nécessaires en ce point étant déterminés au préalable au moyen d'une méthode intégrale laminaire / 5 /, on obtient les résultats présentés sur la planche (10). La méthode de HORTON prévoit que l'on ne peut avoir de bulbe court que pour des vitesses U_∞ supérieures à 120 m/s. En revanche, la méthode VINCENT DE PAUL prévoit un éclatement du bulbe pour une vitesse voisine de 27 m/s, la valeur expérimentale étant comprise entre 32 et 33 m/s. De plus, la valeur de θ au point R obtenue dans le cas ou $U_\infty = 40$ m/s est assez voisine de la valeur expérimentale.

Cependant, cette méthode présente quelques inconvénients ; en particulier le schéma proposé pour la répartition de vitesse en présence du bulbe est assez simpliste puisqu'il suppose des variations linéaires de la vitesse entre les différents points caractéristiques ; de plus, elle est incapable de prévoir l'évolution du bulbe au delà du point d'éclatement du bulbe court ; enfin, l'intégration des équations intégrales fait appel à un certain nombre d'hypothèses simplificatrices.

Il nous a donc semblé nécessaire de mettre au point des méthodes de calcul qui soient capables de déterminer avec plus de rigueur et de précision l'évolution des différents paramètres de la couche limite dans le bulbe court, et que l'on puisse étendre au calcul des zones décollées de plus grande dimension moyennant l'utilisation de schémas plus élaborés.

3.2. Position du problème.

Le but des méthodes que nous avons développées est de permettre le calcul de l'évolution d'une couche limite au passage d'une zone décollée de faibles dimensions.

Il est bien connu que la présence d'un bulbe de décollement, même mince, amène une modification de la répartition de pression que l'on aurait sur un profil en l'absence de bulbe ; en fait, si l'on introduit comme conditions aux limites d'un calcul de couche limite la répartition de vitesse extérieure obtenue par un calcul de fluide parfait par exemple, on se heurte au niveau du point Cf = 0 à une singularité de type GOLDSTEIN / 10 /. Il n'est donc pas possible de calculer une couche limite en aval du point de décollement au moyen d'une méthode directe classique où l'on impose la répartition de vitesse extérieure. Il est donc nécessaire de faire intervenir un couplage entre la couche limite et l'écoulement extérieur.

D'autre part, un autre problème posé par les écoulements de retour, est lié au changement de direction de la vitesse longitudinale dans la zone décollée. Bien que les équations de couche limite demeurent paraboliques en x, nous ne nous trouvons plus devant un problème de conditions initiales, mais il faut, après le point de décollement, faire intervenir les conditions aval. Si de plus on fait intervenir le couplage, l'interaction a nécessairement un caractère elliptique.

Pour résoudre ces problèmes, certains auteurs (CATHERAIL et MANGLER / 4 /, KLINEBERG et STEGER /12/, CARTER / 3 /, LE BALLEUR /13/) ont développé des méthodes de calcul dans lesquelles une distribution de $C_f/_2$ ou δ_1 est spécifiée, la vitesse extérieure étant solution du problème de couche limite. La singularité au point de décollement se manifestant dans les méthodes directes par des valeurs infinies des dérivées suivant x de l'épaisseur de déplacement et du coefficient de frottement, ces méthodes dites "inverses" permettent de l'éliminer. Ces méthodes peuvent être associées par exemple à une technique de calcul inverse du fluide non visqueux. On obtient alors une méthode complète permettant de traverser des zones avec recirculation.

D'autres auteurs ont préféré utiliser l'approche instationnaire du problème . COUSTEIX et HOUDEVILLE / 6/, par exemple, ont utilisé une méthode intégrale instationnaire pour le calcul des couches limites stationnaires turbulentes avec décollement, et ont montré qu'une loi de couplage simple (loi de section pour un diffuseur mono-dimensionnel) permettait d'éliminer la singularité. Mac DONALD et BRILEY / 2 /, se sont intéressés au problème du bulbe de décollement laminaire et résolvent les équations locales instationnaires de la couche limite en termes de fonction de courant et de vorticité. Un couplage local leur permet de franchir le point de décollement.

Nous avons utlisé les deux approches pour déterminer l'évolution de la couche limite dans un bulbe transitionnel. La première a été mise en oeuvre en faisant appel à une méthode de résolution des équations globales de la couche limite. La seconde a été développée en résolvant les équations locales de la couche limite. Nous décrirons d'abord cette technique.

3.3. Calcul avec les équations locales de la couche limite.

La méthode employée s'inspire de celle développée par BRILEY et MAC DONALD / 2/. La couche limite est calculée par une méthode instationnaire et à chaque pas en temps, la distribution de la vitesse extérieure est modifiée suivant un schéma stationnaire.

3.3.1. Interaction fluide parfait-fluide visqueux.

La prise en compte du couplage entre la couche limite et le fluide non visqueux repose sur les hypothèses suivantes de faible interaction locale :

- La répartition de vitesse extérieure ne diffère de la répartition de fluide parfait que dans une région limitée au voisinage du bulbe.
- Cette perturbation par rapport à la vitesse potentielle est uniquement due à la distribution de l' épaisseur de déplacement.

On peut alors écrire : $U_e(x) = U_{fp}(x) + U_i(x)$ où U_{fp} est la vitesse que l'on obtient par un calcul de fluide parfait (c'est une donnée du problème) et U_i est la vitesse induite par le couplage.

La résolution de ce problème au moyen d'une fonction de GREEN nous donne alors :

$$U_I(x) = \frac{1}{\pi}\int_{-\infty}^{+\infty} \frac{\vartheta_e(\chi)}{(\chi - x)}\, d\chi$$

qui moyennant les hypothèses faites, permet d'écrire en tout point M d'abscisse curviligne x_M

$$U_I(x_M) = \frac{1}{\pi}\int_{x_0}^{x_F} \frac{\partial}{\partial x}(\delta_1 u_e)\ \frac{dx}{x_M - x}$$

où U_e : vitesse que l'on a au point d'abscisse x, et au temps t.

δ_1 : épaisseur de déplacement au point d'abscisse x, et au temps t,

x_0 : abscisse du point d'arrêt,

x_F : abscisse d'un point en aval du bulbe situé à une distance suffisante pour que son influence en tout point du domaine soit négligeable.

Si x_1 et x_2 sont les bornes du domaine de calcul, on peut alors écrire :

$$\pi U_I = \underbrace{\int_{x_0}^{x_1} \frac{\partial}{\partial x}(\delta_1 u_e)\ \frac{dx}{x_M - x}}_{(1)} + \underbrace{\int_{x_1}^{x_2} \frac{\partial}{\partial x}(\delta_1 u_e)\ \frac{dx}{x_M - x}}_{(2)} + \underbrace{\int_{x_2}^{x_F} \frac{\partial}{\partial x}(\delta_1 u_e)\ \frac{dx}{x_M - x}}_{(3)}$$

Le premier terme de l'intégrale est une fonction de M qui ne dépend que de l'évolution de la couche limite laminaire en amont du domaine de calcul. Il est donc indépendant de l'évolution du calcul et est déterminé lors de l'initialisation. Le troisième terme est calculé en supposant à l'aval du domaine une couche limite turbulente de plaque plane ayant pour épaisseur de déplacement initiale celle calculée en x_2, et ceci à chaque pas en temps.

Enfin le deuxième terme qui est le terme prépondérant, peut s'écrire :

$$\pi . U_{I(2)} = \int_{x_1}^{x_M-\varepsilon} \frac{\partial}{\partial x}(\delta_1 u_e)\ \frac{dx}{x_M - x} + \int_{x_M-\varepsilon}^{x_M+\varepsilon} \frac{\partial}{\partial x}(\delta_1 u_e)\ \frac{dx}{x_M - x} + \int_{x_M+\varepsilon}^{x_2} \frac{\partial}{\partial x}(\delta_1 u_e)\ \frac{dx}{x_M - x}$$

Les deux termes extrêmes sont définis et s'intègrent numériquement sans aucune difficulté. Le terme central, moyennant un développement au premier ordre de la fonction $\partial(\delta_1 u_e)/\partial x$, peut s'écrire sous la forme :

$$\int_{x_M-\varepsilon}^{x_M+\varepsilon} \left[\frac{\partial}{\partial x}(\delta_1 u_e)_M + (x - x_M)\frac{\partial^2}{\partial x^2}(\delta_1 u_e)_M\right]\frac{dx}{x_M - x}$$

ce qui en définitive se réduit à : $-2\varepsilon \frac{\partial^2}{\partial x^2}(\delta_1 u_e)$

3.3.2. Equations de couche limite.

Les équations que nous avons à résoudre dans le cas d'un écoulement instationnaire incompressible sont les suivantes :

(E.1.) Continuité : $\frac{\partial}{\partial x_i}\left(U_i + u'_i\right) = 0$ (E.2.) Navier-Stokes : $\frac{D}{Dt}\left(U_i + u'_i\right) = -\frac{1}{\rho}\frac{\partial\left(P + p'\right)}{\partial x_i} + \nu\nabla^2\left(U_i + u'_i\right)$

où U_i est la moyenne d'ensemble de la vitesse dans la direction i, u'i étant la fluctuation turbulente autour de cette moyenne.

Les hypothèses que nous adoptons (couche limite bidimensionnelle) permettent de simplifier ces équations. En prenant la moyenne d'ensemble, on en déduit alors :

(E.3.) $\frac{\partial U}{\partial x} + \frac{\partial V}{\partial y} = \frac{\partial u'}{\partial x} + \frac{\partial v'}{\partial y} = 0$ (E.4.) $\frac{\partial U}{\partial t} + U\frac{\partial U}{\partial x} + V\frac{\partial U}{\partial y} + \frac{\partial}{\partial x}\left(\langle u'^2\rangle - \langle u'v'\rangle\right) = -\frac{1}{\rho}\frac{\partial P}{\partial x} + \nu\frac{\partial^2 U}{\partial y^2}$

(E.5.) $\frac{\partial V}{\partial t} + \frac{\partial}{\partial x}\left(\langle u'v'\rangle\right) + \frac{\partial}{\partial y}\left(\langle v'^2\rangle\right) = -\frac{1}{\rho}\frac{\partial P}{\partial y}$

De plus, si l'on suppose que les corrélations $\langle u'v'\rangle$ et $\langle v'^2\rangle$ sont du même ordre de grandeur, l'équation (E.5.) devient : $\frac{P}{\rho} = \frac{P_e}{\rho_e} - \langle v'^2\rangle + \int_y^\delta \frac{\partial V}{\partial t}\,dy$

En reportant dans (E.4.) en en négligeant le terme : $\frac{\partial}{\partial x}\left[\langle u'^2\rangle - \langle v'^2\rangle + \int_y^\delta \frac{\partial V}{\partial t}\,dy\right]$, on obtient alors pour le mouvement moyen les equations :

(E.6.) $\frac{\partial U}{\partial x} + \frac{\partial V}{\partial y} = 0$ (E.7.) $\frac{\partial U}{\partial t} + U\frac{\partial U}{\partial x} + V\frac{\partial U}{\partial y} = -\frac{1}{\rho}\frac{dP_e}{dx} + \frac{\partial}{\partial y}\left(\nu\frac{\partial U}{\partial y} - \langle u'v'\rangle\right)$

Ce système d'équations ne diffère de celui d'un écoulement stationnaire, que par le terme $\partial U/\partial t$ Nous avons donc un système de deux équations pour les trois inconnues U, V et $-\langle u'v'\rangle$. Il est donc nécessaire de définir un schéma de turbulence pour déterminer le frottement turbulent $-\langle u'v'\rangle$.

3.3.3. Critère de transition. Modèle de turbulence.

Lorsque la couche limite n'est pas décollée, l'appel à la théorie de l'instabilité laminaire peut permettre de déterminer le début de la région de transition. Dans ce cas, on peut supposer que l'interaction avec l'écoulement non visqueux est négligeable et la distribution de vitesse extérieure est donc fixée. Grâce à cette distribution, on calcule la couche limite laminaire comme s'il n'y avait pas de transition. Les profils de vitesse de couche limite ainsi obtenus sont utilisés comme profils de base moyens dans la théorie de l'instabilité laminaire. Suivant cette théorie, on calcule l'amplification d'une perturbation superposée à ces profils de base, et en utilisant un critère empirique formulé à partir d'un taux d'amplification de ces pertubations, on est en mesure de prévoir le début de la région de transition. Cette technique devrait s'appliquer aisément quand la transition commence avant le point de décollement.

Lorsque le début de transition se situe après le point de décollement, le problème est beaucoup plus délicat. En effet, on doit alors s'attendre à une interaction non négligeable avec l'écoulement non visqueux. En particulier, la détermination des profils laminaires de base nécessite le recours à un calcul couplé avec l'écoulement extérieur. Mais le résultat de ce calcul dépend de ce qui se passe à l'aval, c'est à dire de la position de la région de transition. Il faudrait donc imaginer un processus itératif dans lequel on vérifierait à chaque étape si le point de début de transition fixé pour le calcul de la couche limite et de l'écoulement extérieur est en accord avec la théorie de l'instabilité. Un tel calcul, très lourd a priori est tout à fait concevable, mais il n'a pas encore été entrepris. Pour l'instant, on se limite à utiliser un critère beaucoup moins élaboré pour fixer la région de transition.

Nous avons donc utilisé un schéma simple de longueur de mélange dont la formulation est très directement déduite de celle établie en stationnaire. Le frottement tutbulent est donné par la relation :

$-\langle u'v'\rangle = \gamma F^2 \ell^2 \left|\frac{\partial U}{\partial y}\right| \frac{\partial U}{\partial y} = \nu_t \frac{\partial U}{\partial y}$ où ℓ/δ est supposé fonction universelle de y/δ :

$\frac{\ell}{\delta} = 0.085\ th\left[\frac{0.41}{0.085} \times \frac{y}{\delta}\right]$ et F est une fonction qui tient compte des effets de viscosité :

$F = 1 - \exp\left[\frac{-\ell\sqrt{\tau\rho}}{26 \times 0.41 \times \nu}\right]$ et γ est une fonction de la position du point de transition.

La méthode employée pour déterminer γ suppose que la distance entre le point de décollement et le point de fin de transition T est une fonction de $R\theta_3$. Le point de début de transition D est alors déterminé de telle sorte que le rapport $R\theta_T / R\theta_D$ ait une valeur donnée. La fonction γ passe alors de 0 à 1 entre D et T.

3.3.4. Méthode numérique

Afin de rendre les équations adimensionnelles, on utilisera les variables réduites suivantes :

$X = x/L$; $\eta = y/h$; $\bar{t} = t/T$; $\bar{U} = U/U_e$; $\bar{V} = V/U_e$; $\bar{\nu} = \nu/\nu_e$; $\bar{\nu}_t = \nu_t/\nu_e$

où T et L sont les constantes, h une fonction de x seulement, U_e et ν_e des fonctions de x et t.

Les équations s'écrivent alors,

. Continuite : $\frac{\partial}{\partial\eta}\left(\bar{V} - \bar{U}.\eta.\frac{dh}{dx}\right) = \frac{h}{L}\frac{\partial\bar{U}}{\partial X} + \bar{U}\left(\frac{dh}{dx} + \frac{h}{L.U_e}\frac{\partial U_e}{\partial X}\right)$

. Quantité de mouvement suivant X :

$$\bar{U}\left[\frac{\bar{U}h}{L}.\frac{1}{U_e}\frac{\partial U_e}{\partial X} + \frac{h}{T.U_e}.\frac{1}{U_e}.\frac{\partial U_e}{\partial\bar{t}}\right] + \frac{\partial\bar{U}}{\partial\bar{t}}\frac{h}{T.U_e} + \frac{\partial\bar{U}}{\partial X}\frac{h\bar{U}}{L} + \frac{\partial^2\bar{U}}{\partial\eta^2}\left[-\frac{\nu_e}{h.U_e}.\left(\bar{\nu}+\bar{\nu}_t\right)\right]$$
$$+ \frac{\partial\bar{U}}{\partial\eta}\left[\left(\bar{V} - \bar{U}\eta\frac{dh}{dx}\right) - \frac{\partial}{\partial\eta}\left(\bar{\nu}+\bar{\nu}_t\right).\frac{\nu_e}{h.U_e}\right] = \frac{h}{U_e^2}\left(\frac{U_e}{L}.\frac{\partial U_e}{\partial X} + \frac{1}{T}.\frac{\partial U_e}{\partial\bar{t}}\right)$$

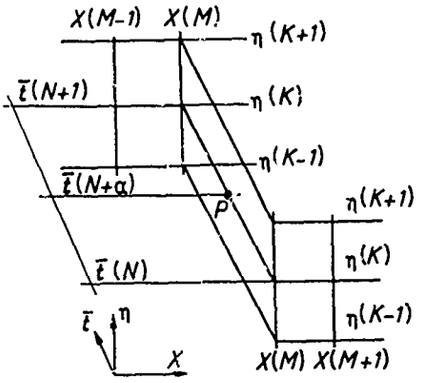
L'équation de quantité de mouvement peut s'écrire sous la forme :

$$A\frac{\partial \bar{U}}{\partial \bar{t}} + B\frac{\partial^2 \bar{U}}{\partial \eta^2} + C\frac{\partial \bar{U}}{\partial \eta} + D\frac{\partial \bar{U}}{\partial X} + E.\bar{U} = F \qquad \text{où A, B, C, D, E et F sont des fonctions de } \bar{u},\ X,\ \eta \text{ et } \bar{t}.$$

On discrétise alors cette équation en utilisant un schéma de différences centrées du premier ordre.

Les dérivées et les quantités A, B, C, D, E, et F sont alors écrites au point P représenté sur le schéma ci- contre et défini par :

$$X(P) = X(H)\ ;\ \eta(P) = \eta(K)\ ;\ \bar{t}(P) = \bar{t}(N+\alpha) \qquad 0 < \alpha < 1$$



Pour simplifier les notations, nous écrirons la variable quelconque $Z(X(H), \eta(K), \bar{t}(N+\alpha))$ sous la forme $Z_{H,K,\alpha}$.

Les dérivées partielles suivant $\bar{t}$ et η s'écrivent alors :

$$\left(\frac{\partial \bar{U}}{\partial \bar{t}}\right) = \left(\bar{U}_{H,K,1} - \bar{U}_{H,K,0}\right)/\left(\bar{t}_1 - \bar{t}_0\right)$$

$$\left(\frac{\partial \bar{U}}{\partial \eta}\right)_{H,K,\alpha} = \alpha\left(\frac{\partial \bar{U}}{\partial \eta}\right)_{H,K,1} + (1-\alpha).\left(\frac{\partial \bar{U}}{\partial \eta}\right)_{H,K,0}$$

avec :

$$\left(\frac{\partial \bar{U}}{\partial \eta}\right)_{H,K,N} = \left(\bar{U}_{H,K+1,N} - \bar{U}_{H,K-1,N}\right)/\left(\eta_{K+1} - \eta_{K-1}\right)$$

De même pour les dérivées seconder en η

Le problème de l'écoulement de retour pour lequel le calcul doit être fait en tenant compte des conditions à l'aval a amené de nombreux auteurs à utiliser deux expressions différentes pour les dérivées suivant x selon le sens de la vitesse locale u (BRILEY, Mc DONALD / 2/). Nous avons préféré utiliser ici un schéma un peu différent et qui permet de conserver la même discrétisation quelque soit le sens de u :

$$\left(\frac{\partial \bar{U}}{\partial X}\right)_{H,K,\alpha} = \left(\bar{U}_{H+1,K,0} - \bar{U}_{H,K,0}\right)/\left(X_{H+1} - X_H\right) + \left(\bar{U}_{H,K,1} - \bar{U}_{H-1,K,1}\right)/\left(X_H - X_{H-1}\right)$$

Ce schéma permet alors, connaissant des conditions initiales dans le plan t = 0 et les conditions aux limites dans le plan X = 0, de calculer la solution au point X_M et au temps N + 1 à partir de la solution en X_{M+1} au temps N et en X_{M-1} au temps N + 1.

Pour chaque point en X on est donc en présence d'un système tridiagonal de la forme :

$$A_0\,\bar{U}_{H,K+1,1} + B_0\,\bar{U}_{H,K,1} + C_0\,\bar{U}_{H,K-1,1} = D_0 \qquad \text{que l'on résout par une méthode de chasse.}$$

3.4. Calcul avec les équations globales de la couche limite.

3.4.1. Principe. Couplage.

La résolution des équations globales de la couche limite, effectuée en mode inverse permet, en considérant l'évolution suivant x de l'épaisseur de déplacement comme une donnée, de déterminer l'évolution suivant x de la vitesse U_e. Les mêmes hypothèses qu'au paragraphe 3.3.1. permettent alors de définir une vitesse induite $U_i = U_e - U_{fp}$ où la répartition de vitesse en fluide parfait $U_{fp}(x)$ est une donnée du problème.

Les hypothèses de couplage étant toujours les mêmes qu'au paragraphe 3.3.1, on se retrouve devant le même type de problème mais ici, sous forme de résolution inverse, à savoir, déterminer l'évolution de δ_1 connaissant la vitesse induite U_i.

On résout là aussi le problème à l'aide d'une nouvelle fonction de GREEN qui nous donne la vitesse verticale $V_p(x)$ sous la forme :

$$v_p(x) = \frac{1}{\pi}\int_{-\infty}^{+\infty} \frac{U_s(\chi)}{(\chi - x)}\,d\chi$$

Moyennant nos hypothèses et en gardant les mêmes notations qu'au paragraphe 3.3.1., on peut réduire cette intégrale à :

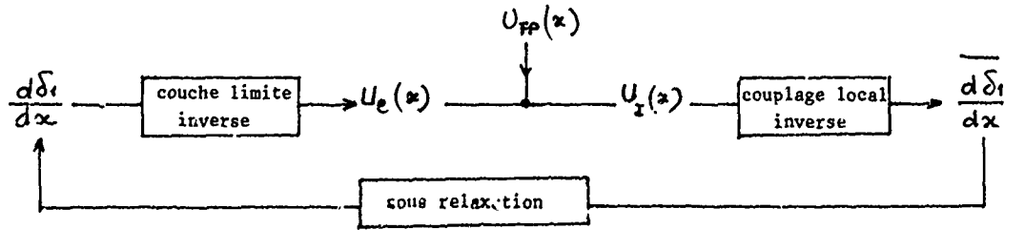
$$v_p(x) = \frac{1}{\pi}\int_{x_0}^{x_f} \frac{U_s(\chi)}{\chi - x}\,d\chi$$

L'intégration à chaque itération est alors réalisée suivant le même principe qu'au paragraphe 3.3.1.. Enfin la relation de couplage écrite à la paroi nous donne :

$$\frac{d\delta_1}{dx} = \frac{v_p}{u_e} - \frac{\delta_1}{u_e}\cdot\frac{du_e}{dx}$$

qui permet d'obtenir une nouvelle répartition de l'épaisseur de déplacement. Celle-ci est alors réintroduite comme donnée du calcul de couche limite, moyennant une sous relaxation importante nécessaire à la stabilité des itérations (LE BALLEUR /13/).

Le schéma du calcul peut donc être présenté sous la forme suivante :



3.4.2. Equations de couche limite

Le système de deux équations globales que nous avons choisi se compose de l'équation globale de quantité de mouvement et de l'équation d'entrainement :

$$\frac{C_f}{2} = \frac{d\theta}{dx} + \theta (H+2) \cdot \frac{1}{u_e} \frac{du_e}{dx}$$

$$C_E = \frac{1}{u_e} \frac{d}{dx} \left(u_e (\delta - \delta_1) \right)$$

C'est un système de deux équations pour les six inconnues suivantes :
$C_f/2$, C_E, θ, H (ou δ_1), H^* et u_e

Le couplage fournissant une équation supplémentaire, il est donc nécessaire d'obtenir trois relations complémentaires entre ces différentes inconnues. C'est l'exploitation de solutions de similitude, tant en laminaire qu'en turbulent qui les fournit.

a) Domaine laminaire

Pour le régime laminaire, nous avons utilisé des solutions calculées à partir de l'hypothèse de FALKNER-SKAN. Pour les valeurs négatives du paramètre de gradient de pression, on sait que la solution de l'équation de similitude est double : l'une correspond à la solution non décollée, l'autre à la solution décollée. La prise en compte de cette seconde solution nous permet donc d'inclure des profils de vitesse avec écoulement de retour nécessaires pour le calcul d'un bulbe.

Les résultats de cette solution sont constitués par une famille de profils U/U_e de $y/x \cdot \sqrt{Rx}$ dépendant d'un paramètre. Pour l'utilisation pratique de ces résultats, nous avons utilisé le paramètre de forme H. L'analyse des propriétés de ces profils permet alors d'exprimer les trois relations de fermeture manquantes sous la forme : $\frac{C_{f_L}}{2} R_\theta = \frac{C_f}{2}_L R_\theta (H_L)$, $C_{E_L} R_\theta = C_{E_L} R_\theta (H_L)$ et $H^*_L = H^*_L (H_L)$

où l'indice L correspond au régime laminaire.

Il est à remarquer que ce type de relations faisant intervenir le coefficient d'entrainement est assez peu utilisé dans le cas de méthodes intégrales laminaires, et qu'en général l'équation que l'on résout en plus de l'équation de KARMAN est l'équation globale d'énergie cinétique. Nous avons en fait préféré utiliser l'équation d'entrainement pour conserver le même système en laminaire et en turbulent.

b) Domaine turbulent

Nous avons utilisé les solutions de similitude proposées par MICHEL, QUEMARD, DURANT /14/ et étendues aux écoulements de retour ($H_T < 10$) (COUSTEIX, LE BALLEUR, HOUDEVILLE / 7/).

De la même manière, nous disposons d'une famille à deux paramètres (gradient de pression et nombre de Reynolds) qui nous permet d'établir là aussi les relations :

$$\frac{C_f}{2}_T = \frac{C_f}{2}_T (H_T, R_\theta), \quad C_{E_T} = C_{E_T} (H_T, R_\theta) \text{ et } H^*_T = H^*_T (H_T, R_\theta)$$

où l'indice T correspond au régime turbulent.

C) Calcul de la région de transition

A ce niveau se pose un certain nombre de problèmes, et en particulier la détermination de la région de transition. Nous verrons plus loin les tentatives que nous envisageons de faire pour résoudre ces problèmes.

On suppose donc connue une certaine fonction $\gamma(x)$ appelée "fonction de transition", dont la valeur passe de 0 à 1 dans la région de transition. Nous verrons au paragraphe suivant la détermination de cette fonction.

En tout point d'abscisse X_M on connait donc, en plus des inconnues du problème, la valeur $\gamma(X_M)$. On connait donc en particulier le rapport δ_1/δ. On fait alors l'hypothèse qu'en ce point M on a deux couches limites fictives, laminaire et turbulente, correspondant au même paramètre δ_1/δ.

On peut donc déterminer tous les paramètres laminaires et turbulents nécessaires à la fermeture du système. On écrit alors que dans la région de transition, les grandeurs intégrales définissant la couche limite transitionnelle peuvent se déduire de la manière suivante à partir des deux couches limites fictives :

$$H = (1-\gamma) H_L + \gamma H_T \; ; \; C_f = (1-\gamma) C_{f_L} + \gamma C_{f_T} \; ; \; C_E = (1-\gamma) C_{E_L} + \gamma C_{E_T}$$

Cette hypothèse a été vérifiée de façon très satisfaisante au DERAT pour le calcul de la transition dans des écoulements non décollés.

3.4.3. Détermination de la région de transition.

Les problèmes demeurent les mêmes que ceux exposés au paragraphe 3.3.3. Nous avons donc pour le moment utilisé le même type de détermination de la région de transition : nous avons ici fait appel à un critère un peu moins empirique, proposé par VAN INGEN / 17/ et partiellement déduit de la théorie de l'instabilité laminaire (il suppose en particulier que l'amplification des perturbations ne devient significative qu'après le point de décollement). On définit alors une constante σ_F fonction d'un taux de turbulence effectif qui permet de déterminer un point de fin de transition à partir du point de décollement par la relation

$$\frac{X_F - X_S}{\theta_S} = \frac{R_{\theta_S}}{550} \cdot \left(\frac{10^4}{R_{\theta_S}} \cdot \sigma_F - 70 \right)$$

où X_F est le point de fin de transition. X_S est le point de décollement.
θ_S est l'épaisseur de quantité de mouvement au point de décollement.
R_{θ_S} est le nombre de Reynolds formé avec θ_S.
$\sigma_F = 5 - 6.8 \log_{10} (Tu)$
Tu est un taux de turbulence effectif

La fonction γ passe de 0 à 1 entre X_S et X_F.

3.5. Comparaison avec l'expérience

Du fait des hypothèses utilisées concernant la méthode de couplage, nous nous sommes pour le moment limités à des essais de calcul de couche limite en présence de bulbes courts. Le déplacement du point d'arrêt dans le cas des bulbes longs impose probablement l'utilisation d'un calcul du fluide parfait plus complet.

Nous avons donc effectué une série de calculs à différentes valeurs de la vitesse U_∞. Dans les deux méthodes, le domaine de calcul a été choisi de telle sorte qu'il comprenne une région où le gradient de vitesse est constant ; ceci permet l'introduction de conditions aux limites plus précises : on s'impose en $x = x_0$ de partir d'une solution de point d'arrêt (donnée par exemple par les solutions de similitude). Nous présentons ici deux exemples de calcul effectués avec nos méthodes.

3.5.1. Méthode locale.

Sur la planche 11 est présentée une série de résultats caractéristiques obtenus pour une vitesse $U_\infty = 40$ m/s.

Dans la région du bulbe, quelques écarts sont à noter : la correction de vitesse est en effet assez faible et ne semble pas correspondre aux résultats expérimentaux déduits des mesures de pression. Ceci est probablement dû à la représentation de la région de transition, qui a une grande influence sur l'évolution de δ_1 et θ dans la région du bulbe, et donc, qui influe de manière importante sur la vitesse induite. Ces écarts sont également visibles sur l'évolution de H et θ mais peuvent là être en partie imputables aux mesures, étant donnée la très faible épaisseur de la couche limite dans cette région.

3.5.2. Méthode globale.

Le critère de transition que nous avons employé fait appel à un taux de turbulence effectif ; nos expériences nous fournissent un taux de fluctuation longitudinale de la vitesse $\sqrt{\overline{u'^2}}/U_\infty$, nous avons donc introduit dans les calculs un taux de turbulence Tu déduit de $\sqrt{\overline{u'^2}}/U_\infty$ en supposant une turbulence isotrope, et nous avons adapté la loi de γ pour que nos calculs recoupent une série de résultats expérimentaux (pour une valeur fixée $U_\infty = 40$ m/s). Les calculs aux autres valeurs du nombre de Reynolds ont été alors effectués en prenant un taux effectif de turbulence, et en conservant la même loi de γ.

La planche 12 montre un exemple de calcul pour $U_\infty = 53$ m/s. Les résultats concernant l'épaisseur de quantité de mouvement sont en très bon accord avec nos valeurs expérimentales ; de même, pour la vitesse extérieure, pour laquelle on peut vérifier a posteriori la validité des hypothèses de couplage local. Le paramètre de forme H présente par contre des évolutions moins rapides que dans nos expériences dans la région de décollement. Ceci provient probablement de la difficulté que nous avons eue à déterminer une loi de transition, du fait des nombreux paramètres entrant en jeu (début et fin de transition, forme de la fonction γ) ; ce calcul y est en effet extrêmement sensible et de petites variations de cette loi ont des conséquences importantes au niveau de l'évolution des différents paramètres.

Si on prolonge ce calcul avec une méthode intégrale turbulente classique ;en prenant les conditions initiales à la fin du domaine de calcul du bulbe, et en introduisant comme conditions extérieures la vitesse en fluide parfait, les résultats reportés sur la planche 13 montrent que la prise en compte du bulbe de décollement laminaire permet une représentation très correcte de la couche limite à l'aval ; on voit très nettement le progrès par rapport à un calcul supposant une couche limite turbulente depuis le point de décollement.

4. CONCLUSIONS

Nous avons présenté ici une première série d'expériences concernant un profil de 200 mm de corde. Nous avons pu, dans les différentes configurations étudiées, préciser l'évolution de la couche limite en aval d'un bulbe de décollement laminaire avec transition, mais nous n'avons pas pu, du fait de la taille du profil, obtenir de résultats détaillés sur le bulbe court lui-même.

Une deuxième série d'expériences est actuellement en cours afin d'étudier en détail le processus de transition dans un bulbe court. Le montage utilisé est un bord d'attaque agrandi correspondant à un profil de 2500 mm de corde. L'épaisseur de la couche limite laminaire avant le décollement ainsi que la taille du bulbe nous permettront d'une part, d'obtenir par vélocimétrie laser des résultats détaillés sur la couche limite dans le bulbe, et d'autre part, de réaliser des visualisations par plan de lumière.

Ces résultats détaillés nous permettront d'une part, d'obtenir des données expérimentales dans le bulbe lui-même, afin de mieux valider nos méthodes de calcul ; et d'autre part, les informations détaillées sur la transition que nous comptons obtenir nous permettront d'améliorer la représentation de cette région dans nos méthodes de calcul. Des améliorations devraient également être apportées à ce niveau par l'étude que nous avons entreprise concernant la stabilité des profils de vitesse avec écoulement de retour. Elle porte sur les profils de similitude des solutions de FALKNER SKAN que nous avons présentées précédemment, et est destinée à l'élaboration d'un critère de transition dans les zones décollées. Nos résultats de calcul nous ont en effet montré que l'évolution de la couche limite au passage du bulbe était très fortement dépendante de la manière dont était définie la fonction de transition.

D'une façon générale, on peut conclure que l'emploi d'une hypothèse simple de couplage local peut permettre un calcul peu coûteux d'une région décollée de faible dimension, les hypothèses de faible perturbation dans une région limitée au voisinage du bulbe étant bien vérifiées tant au niveau expérimental qu'a posteriori au niveau des résultats de calcul.

REFERENCES

/1/ ARNAL. D, JUILLEN J.C.
Résultats expérimentaux relatifs à l'influence des processus de transition sur la structure initiale d'une couche limite turbulente.
AGARD CP 271, La Haye, Sept. 1979

/2/ BRILEY W.R., Mc DONALD H.
Numerical prediction of incompressible separation bubble.
J.F.M. n° 69, Part. 4, 1975.

/3/ CARTER J.
Solution for laminar boundary layers with separation and reattachment.
AIAA Paper n° 74-583

/4/ CATHERALL D., MANGLER K.W.,
The integration of two dimensional laminar boundary layer equations past the point of vanishing skin friction.
J.F.M. n° 26, Part. 1, 1966.

/5/ COUSTEIX J., GLEYZES C.,
Couches limites laminaires bidimensionnelles avec flux de chaleur. Etablissement et analyse des solutions de similitude. Méthode intégrale de calcul et comparaison avec une méthode de résolution des équations locales exactes.
1974 (Rapport interne).

/6/ COUSTEIX J., HOUDEVILLE R.,
Turbulent boundary layer calculations in unsteady flows.
Conférence sur les méthodes numériques en dynamique des fluides appliquées, Université de Reading, 4-6 Janvier 1978. T.P. ONERA n° 1978-2.

/7/ COUSTEIX J., LE BALLEUR J.C., HOUDEVILLE R.
Calcul des couches limites turbulentes instationnaires en mode direct ou inverse, écoulements de retour inclus. Analyse des singularités.
La Recherche Aerospatiale n° 1980-3.

/8/ COUSTEIX J., PAILHAS G.,
Etude exploratoire d'un processus de transition laminaire turbulent au voisinage du décollement d'une couche limite laminaire.
La Recherche Aerospatiale n° 1979-3.

/9/ GASTER M.,
The structure and behaviour of laminar separation bubbles.
AGARD CP-4, Separated Flows, Part. 2.

/10/ GOLDSTEIN S.,
On laminar boundary layer flow near a position of separation.
Quart. J. of Mech. and Appl. Math, 1-43, 1948.

/11/ HORTON H.P.,
A semi empirical theory for the growth and bursting of laminar separation bubbles.
ARC, CP n° 1073, 1969.

/12/ KLINEBERG J.M., STEGER J.L.,
On laminar boundary layer separation.
AIAA Paper n° 74-94.

/13/ LE BALLEUR J.C.,
Couplage visqueux, non visqueux : méthode numérique et application aux écoulements bidimensionnels transsoniques et supersoniques.
La Recherche Aerospatiale n° 1978-2.

/14/ MICHEL R., QUEMARD C., DURANT C.,
Application d'un schéma de longueur de mélange à l'étude des couches limites d'équilibre.
Note Technique ONERA n° 154 (1969).

/15/ OWEN P.R., KLANFER L.,
On the laminar boundary layer separation from the leading edge of a thin airfoil.
Aero. Rep. 2508, RAE, October 1953.

/16/ RUSSEL J.M.,
Length and bursting of separation bubbles : a physical interpretation.
AIAA Aerospace Science Meeting, Paper n° 17, New Orleans (LA) 17-17 Jan. 1979.

/17/ VAN INGEN J.L.,
Transition, pressure gradient, suction, separation and stability theory.
AGARD CP 224, Laminar Turbulent Transition (1977).

/18/ VINCENT DE PAUL M.,
Prévision du décrochage d'un profil d'aile en écoulement incompressible.
AGARD CP 102 (1972).

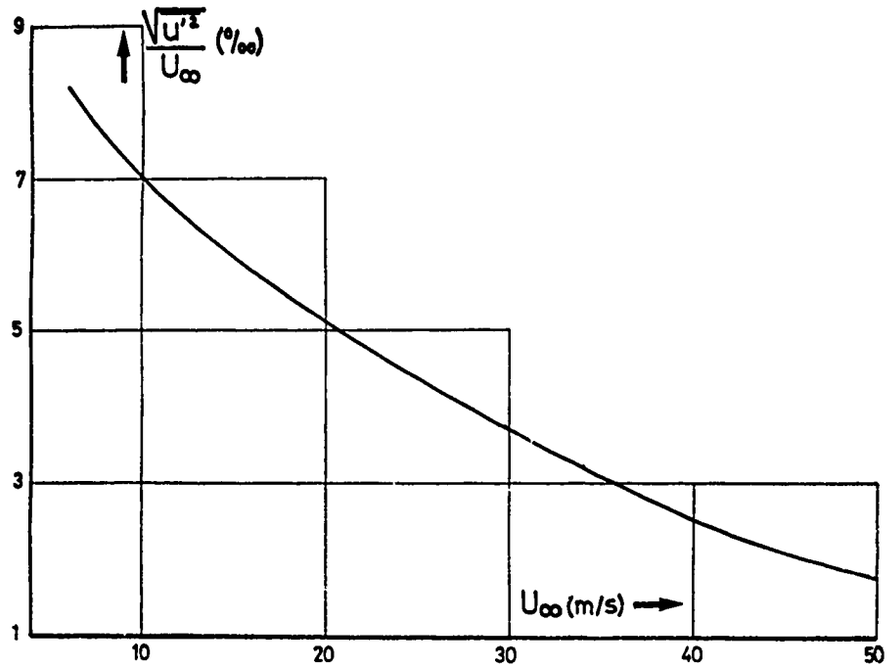


Fig. 1 – Evolution du taux de turbulence de l'écoulement infini amont.

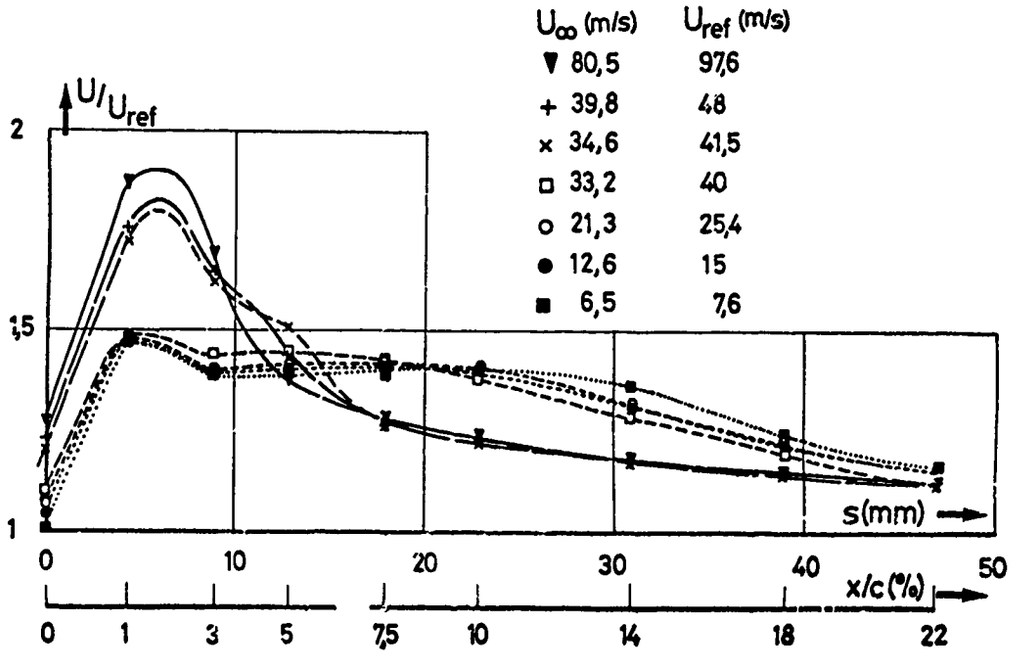


Fig. 2 – Répartition de vitesse extérieure sur le profil.

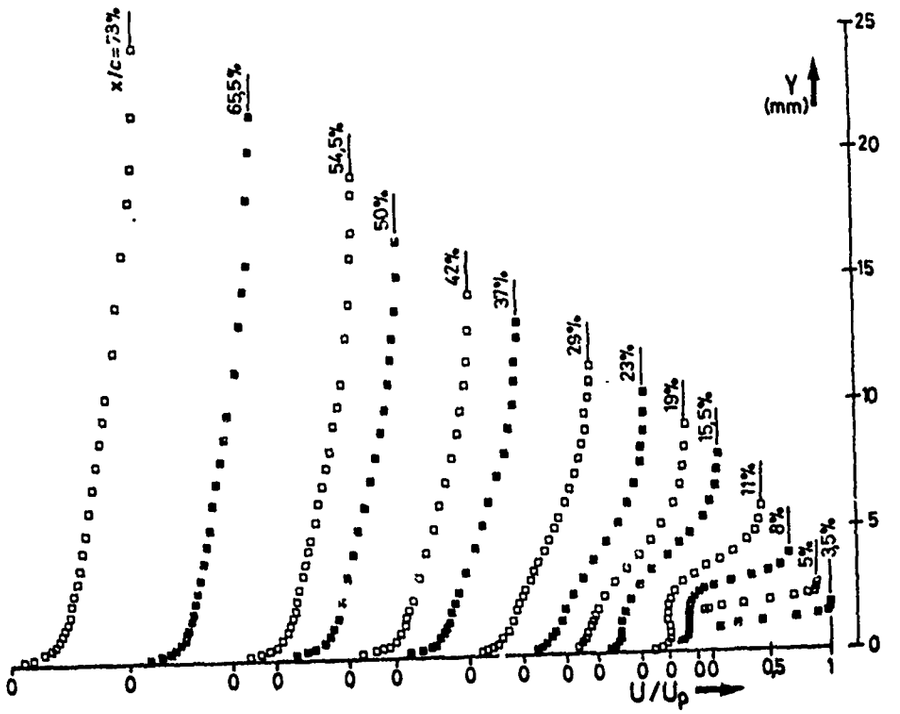


Fig. 4 – Profil d'intensité longitudinale de turbulence pour U_∞ = 13 m/s.

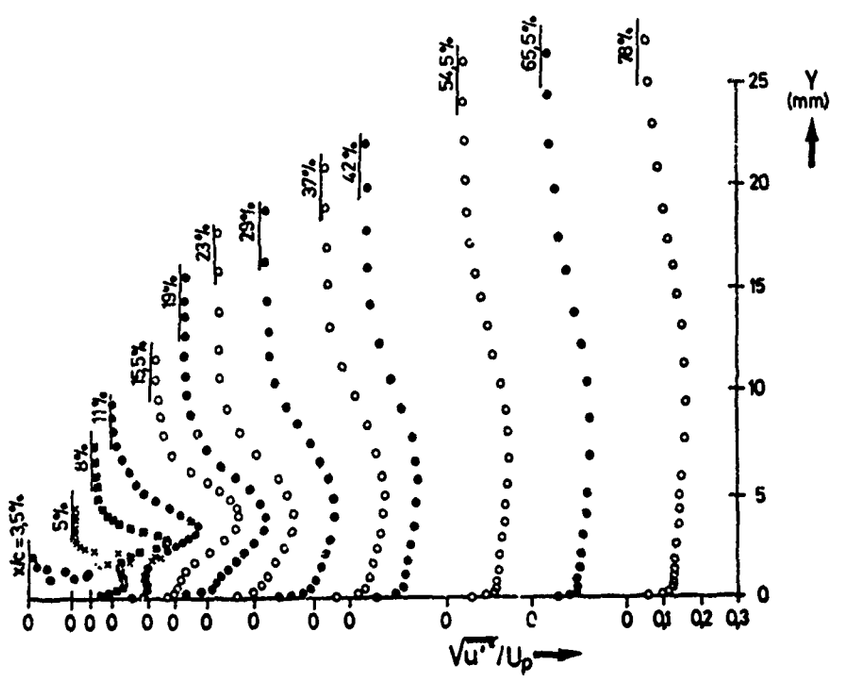


Fig. 3 -- Profil de vitesse moyenne pour U_∞ = 13 m/s.

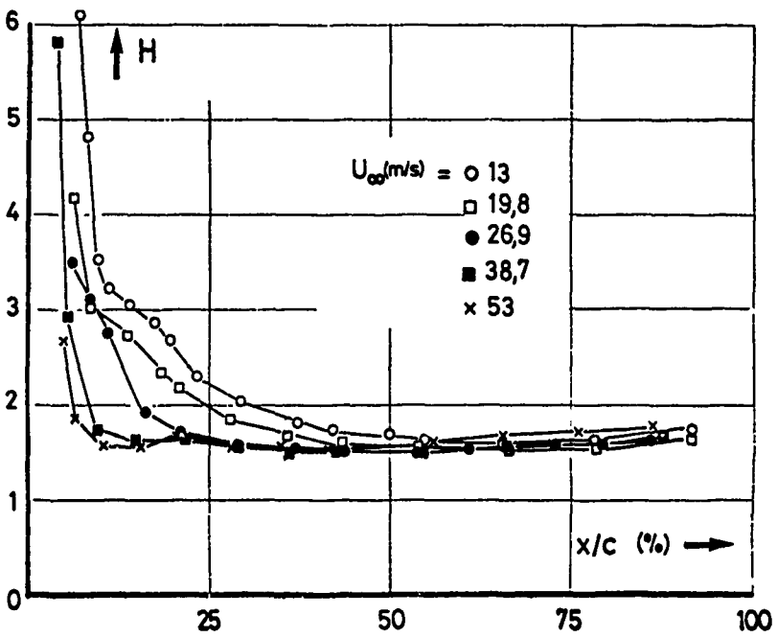


Fig. 5 – Evolution du paramètre de forme H.

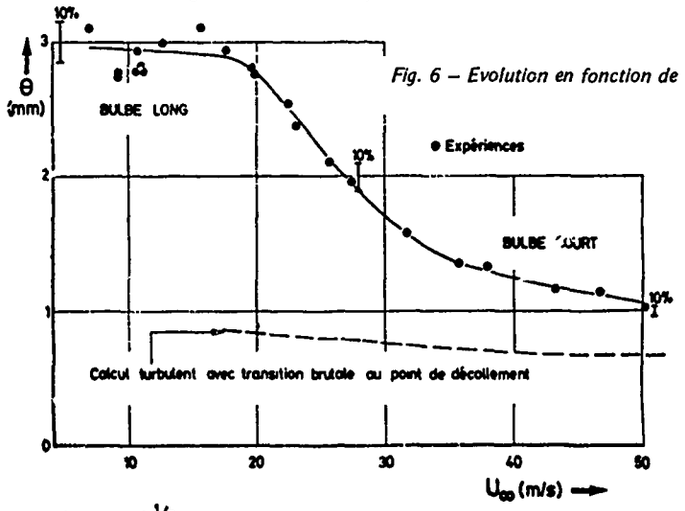


Fig. 6 – Evolution en fonction de U_∞ de θ à x/c = 75%.

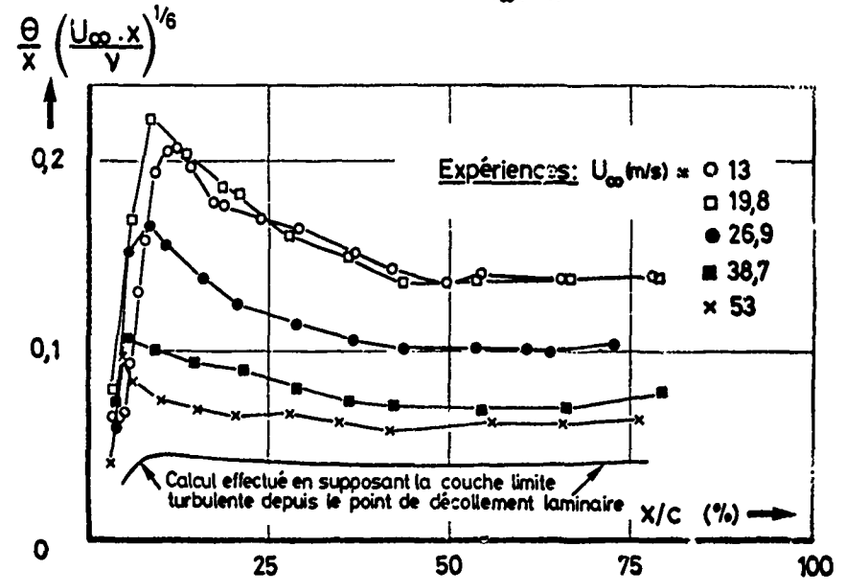
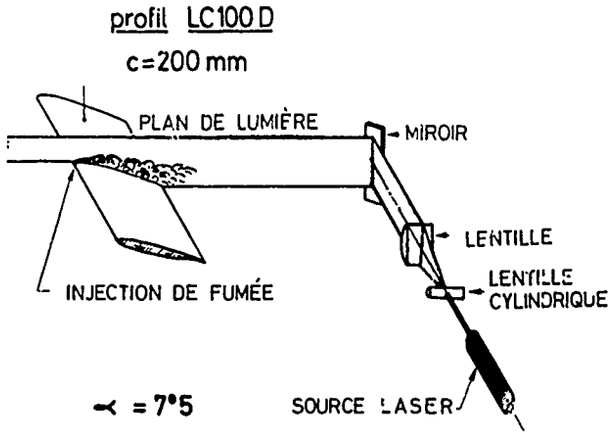


Fig. 7 – Evolution de la quantité réduite $(\theta/x)\,(Rx)^{1/6}$.





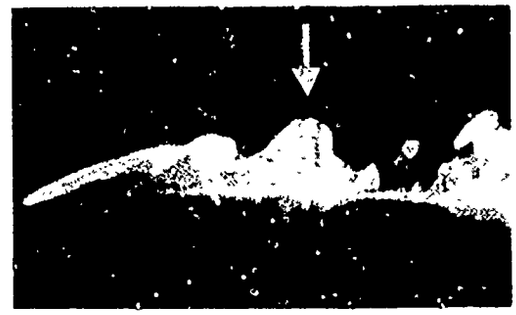


Fig. 8 – Visualisations, schéma de principe, résultats.

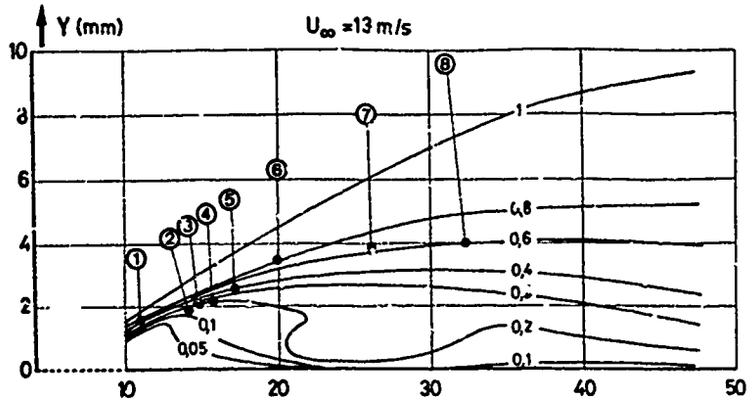
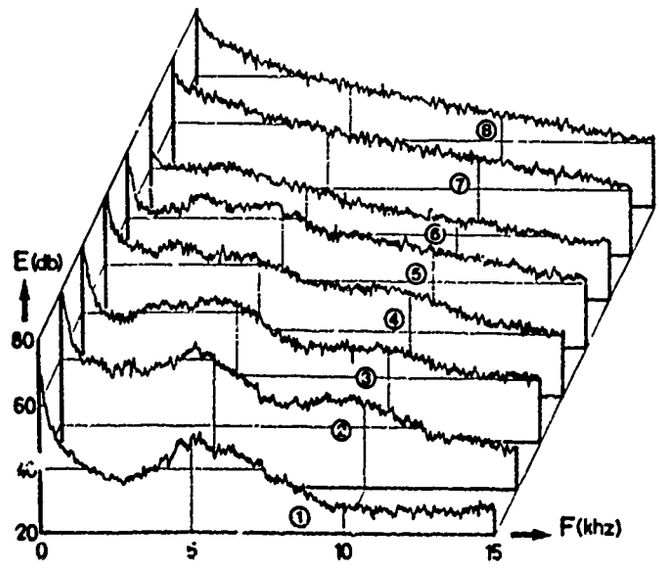


Fig. 9 – Analyse spectrale. Résultats le long de la ligne $\frac{\sqrt{\overline{u'^2}}}{U_p}$ MAX.



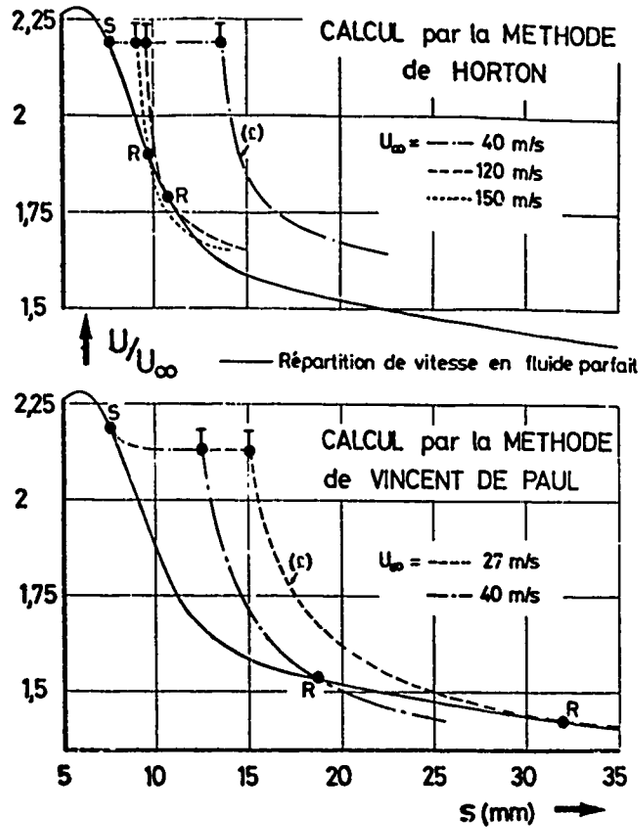


Fig. 10 – Calculs suivant les méthodes de Horton et Vincent de Paul.

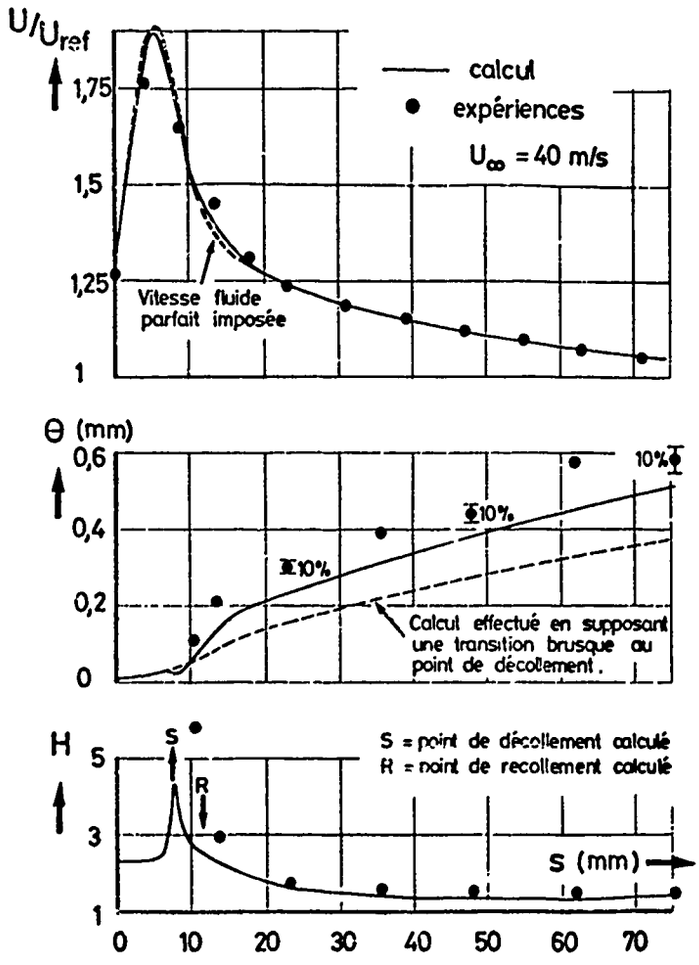


Fig. 11 – Comparaison avec l'expérience : méthode locale.

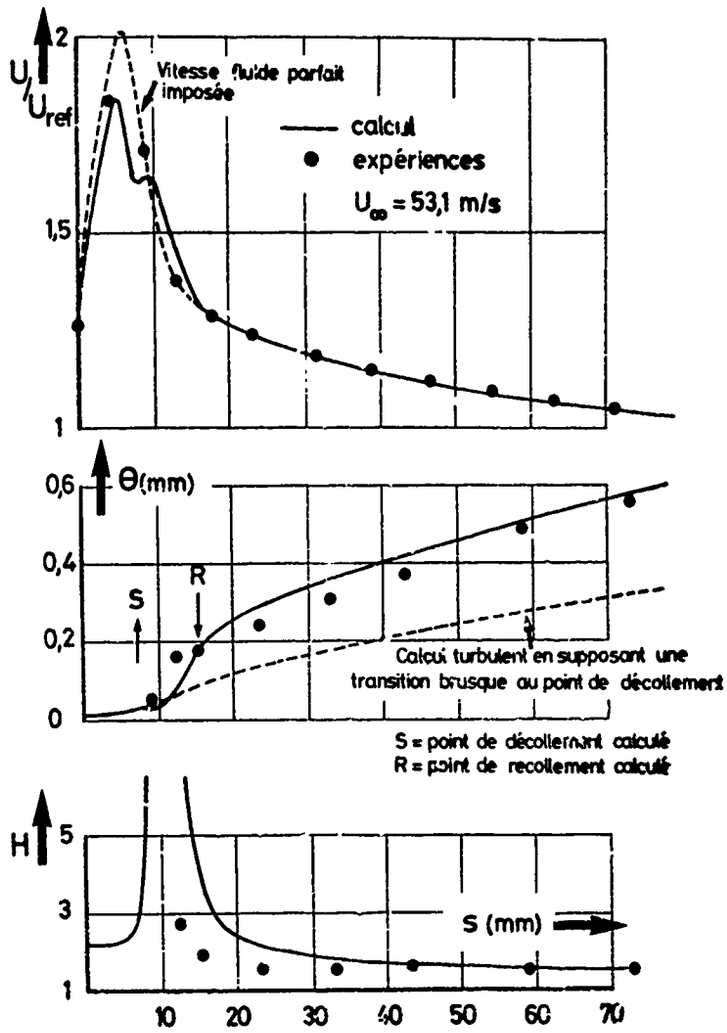


Fig. 12 – Comparaison avec l'expérience. Méthode globale.

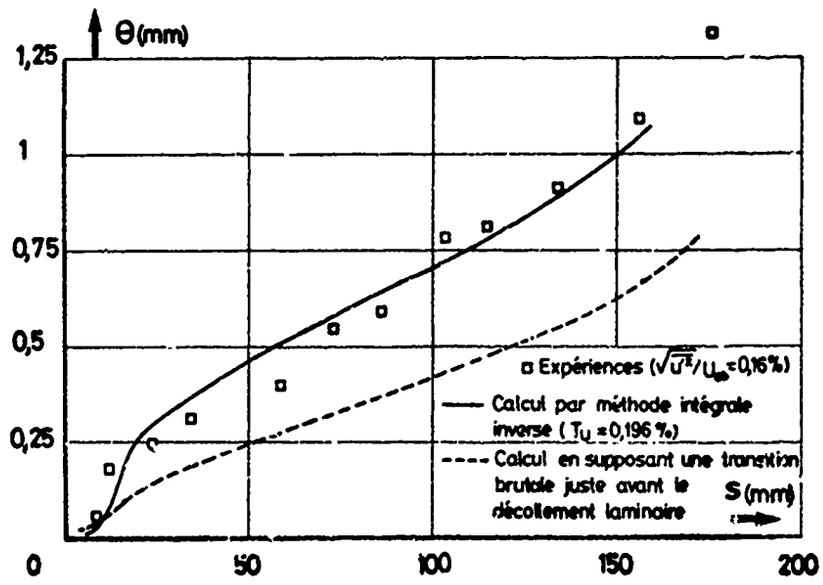


Fig. 13 – Calcul complet en prolongeant la méthode inverse par une méthode intégrale turbulente directe.

1980–81 AFOSR-HTTM-STANFORD CONFERENCE ON COMPLEX TURBULENT FLOWS: COMPARISON OF COMPUTATION AND EXPERIMENT*

by

S.J.Kline
Department of Mechanical Engineering
Stanford University
Stanford
California 94305

1. GOALS OF THE CONFERENCE

The Conference has three related goals:

(1) To reach consensus in the research community on trustworthy data sets that can be used as input for modeling of turbulence in complex flows and as the basis for standard "trials" for checking output of computations.

(2) The creation of a "data library" on magnetic tape. This library will hold the data selected as trustworthy in standard normalized form. The data will be computer-readable and widely accessible at a moderate fee.

(3) Comparison of the output of current methods of computation for turbulent flows for a set of "basic test cases" covering a broad range of flows.

The first objective is the result of the effort of nearly 200 workers during 1979–80 culminating in the 1980 meeting of the Conference. The second objective is an ongoing project that is intended to continue for at least some years. The third objective will be the focus of the 1981 meeting of the Conference.

The word "conference" is somewhat misleading for this project, albeit no better term seems to be available. It is more accurate to think of the project as a several-year-research effort by a considerable fraction of the research community aimed at establishing a more solid data base and clarifying both the situation in the data and the state-of-the-art in computation. Such a clarification should be of assistance to both users of computational methods and to the research community in perceiving more clearly what can now be done, and profitable roads to further advances.

It has been my privilege to coordinate these efforts as Chairman of the Organizing Committee. The experience has been educational. The purpose of this introduction is to share some of that education with the readers of this and subsequent volumes dealing with the Conference and the Data Library. It will perhaps be most useful to begin with a brief history. This is followed by a discussion of some current difficulties in turbulence research and fluids engineering. The third and final topic is a description of the Conference and how it plans to ameliorate some of the difficulties described.

2. A BRIEF HISTORY

From the early years of this century until the late 1960s the problem of computation of turbulent shear layers was considered a classic unsolved problem. With the advent of wide accessibility to digital computers a number of individuals began to construct codes for solution of shear-layer problems. By the late 1960s, 25 methods had been generated, but there was no consensus that any of them were trustworthy. This lack of consensus was evidenced by the continued efforts to construct new methods, and by the funding of such efforts by governments in several countries.

In order to clarify this situation, a number of individuals, including D.E.Coles, M.V.Morkovin, W.C.Reynolds, G.Sovran and the writer, conceived of the idea of holding a meeting at which as many methods as possible would be tested against carefully standardized and trustworthy data. D.E.Coles, with E.Hirst assumed the task of standardizing the data. The remainder of the group with assistance from D.J.Cockrell and many others, organized the meeting and coordinated efforts among the research groups. The results are recorded in the two-volume Proceedings of the 1968

* The sponsorship of the US Air Force Office of Scientific Research under Contract F49620-80-C-0027 and the Industrial Affiliates of the Stanford Thermosciences Division is gratefully acknowledged. Suggestions by Gino Sovran, Brian Launder, Peter Bradshaw, Jim Johnston, Brian Cantwell, Geoffrey Lilley, and John Eaton on an earlier draft led to significant improvements and are also gratefully acknowledged

AFOSR-IFP Stanford Conference on Computation of Turbulent Boundary Layers.* The conference was highly structured and involved some unique organizational features that are described by Kline, et al. (1969).

The most significant result of the 1968 conference, from the perspective of this volume, is that the result radically altered the common wisdom concerning the ability to compute turbulent shear layers. Before the 1968 Conference, the general belief was that no satisfactory method existed. The excellent report of the Evaluation Committee† in the 1968 Conference showed that seven methods were quite satisfactory, within well-defined limits, and that nine more had useful properties for some applications. Another nine were deemed inadequate, and have been for the most part abandoned. As a direct result of the 1968 Conference, the bulk of work on developing programs for attached, incompressible, turbulent boundary layers ceased, and the research community moved on to more complex problems.

Within a few years following 1968, NASA (1969, 1972) organized similar conferences for compressible boundary layers and for free-shear layers. These conferences demonstrated reasonable simulation for compressible boundary layers and the far zones of free-shear layers, but indicated a lack of both data and simulation for the near zone of wakes, jets and mixing layers.

The 1968 Conference had also shown that available methods were successful for attached zones, but generally failed or required ad hoc "fixes" in regions of detachment. All the methods presented in 1968 failed, qualitatively, in the prediction of a reattached free-shear-layer. Subsequent experiments, particularly that of Kim et al. (1979), have shown that such a reattached layer does not follow the type of correlation used by most methods in 1968. Moreover, all the successful methods in the 1968 "trials" employed the "law" of the wall, indicating a heavy dependence on data correlation and hence a lack of fundamental input in turbulence-closure modeling.

During the 1970s a considerable effort at improving numerical methods and turbulence-closure modeling has been carried out in many research centers around the world. The resulting computational methods have moved beyond the "postdiction" of thin shear layers to the computation of entire flow fields, in some cases involving unsteadiness, appreciable zones of separated flow, and other complexities. By the late 1970s, we again find ourselves in a situation where many methods exist, but there is no consensus on what problems they will succeed or which methods have advantages for what flows. Since about 1976, in the words of the old cliché, we have been literally "confused on a higher level". As a result, a number of workers** who had been involved in the 1968 Conference again began to discuss what needed to be done. The 1980–81 Conference grew from those discussions.

Because the 1980–81 Conference concerns "Complex Turbulent Flows", that is, complete flow fields with such complications as shock/boundary-layer interactions, detachment, reattachment of shear layers, large zones of separation, blowing/suction, strong wall-curvature and other phenomena, the task is at once far more complex and far larger than in 1968. In order to understand these tasks, and hence the motivations for the structure of the Conference, it will be useful to give a brief overview of some current difficulties in turbulent flow research, both technical and institutional. One other historical remark is in order before discussion of these difficulties.

Preparatory work for the 1980–81 Conference during 1979 and 1980, has already shown that an important element of the common wisdom does not stand up to detailed examination. At the beginning of the work, every member of the Organizing Committee was concerned with the question, 'Are there enough trustworthy data sets of the needed type to form a basis for a conference of the 1968 type on complex turbulent flows?" The Committee believed that if as many as 10 or 15 such sets of data could be identified, a meeting would be well worthwhile. As data evaluations have accumulated, more than 50 cases†† have been identified, and something like that many more exist but have not been fully evaluated. Moreover, as the work progressed and evaluation reports were circulated for review, workers in various parts of the world volunteered still further data sets; that process is still continuing.

This disclosure of data has obvious benefits, but has also overloaded the finite manpower available for entering the data onto magnetic tape checking, and providing the needed descriptions for each magnetic tape file. As a result, it is the intention of the writer, and Prof. B.J.Cantwell who is supervising the data library work, to continue inputs into the library for at least a few years after 1980 until the backlog of existing data is substantially "caught up". In this work priority has gone to recording the "basic test cases" for the 1981 meeting (see below). After September 1980 priorities will be assigned primarily so that the data collection is balanced and rounded out, and secondarily on a first-come, first-served basis. Further details appear in the section on Organization of the Conference below.

---

* Available for purchase from the Thermosciences Division of the Department of Mechanical Engineering, Stanford University, CA 94305, USA. Price for both volumes, including mailing, $17.50.

† Chaired by H.W.Emmons; see 1968 Proceedings for detail.

** Particularly, M.V.Morkovin, P.Bradshaw, H.W Emmons, W.C.Reynolds, and the writer.

†† In this volume a "flow" denotes a class of situations usually related to geometries. A "case" is one experimental realization of a flow, or a synthesis of realizations, amalgamated into a single "trial" for computations.

3. SOME DIFFICULTIES IN TURBULENT FLOW RESEARCH

A. Technical Difficulties

1. The Complexity and Variety of Flows

Thin shear layers form a relatively cohesive class of flows. Even when one restricts consideration to one-phase flow of a single, pure Newtonian substance, the totality of complex turbulent flow fields known to exist is quite diverse and far from cohesive. In early research, turbulence was implicitly considered as a single state or condition (hopefully) describable by a few simple models. As data from hot wires became widely available, largely after WW II, it became clear that turbulence is not a single state, but a complex of behaviors that is affected by many parameters. This complexity is well demonstrated by a list of the things that can, and sometimes do, affect the behavior of turbulence. Such a list, collected over some time by the author, is given in Table 1. All the effects of Table 1 are known to be appreciable in some instances; however, there is no guarantee the list is complete. (Every time the author has read the list at a technical meeting someone has commented on still another item – at least thus far.)

The complexity of turbulent flow fields is also exhibited by the variety of problems or classes of flows that have been considered by the Organizing Committee for the 1980–81 Conference. This list is exhibited as Table 2, which shows the categorization of flow problems for the Conference. These categories are neither unique nor entirely complete. They have been reorganized several times and updated as more information appeared. The version shown in Table 2 is the status as of July 1980. Very probably further updating will occur as a result of the meeting on data for which this volume will form the Proceedings.

Still a third indication of the complexity of turbulent flow fields is given by the variety of levels of modeling that are currently employed for simulation of turbulent flows in computer models. One taxonomy by Kline et al (1978) is given in Table 3. Most current modeling is at level three in this taxonomy. Level 3 contains a number of subcategories of models from simple mean strain to "many-equation" models. Since both the mean flow and the turbulence can be modeled locally (zone by zone) or globally (uniformly), four combinations of global and local modeling exist. An excellent taxonomy of level 3 models is given by Reynolds (1968). However, the totality of modeling is not confined to level 3; appreciable current efforts exist at all five levels for some problems.

A fourth taxonomy of turbulent flows has been suggested in several papers by Bradshaw (1975). This taxonomy arranges flows according to the type of strains the flow undergoes; it is a very fruitful idea for organizing model assumptions for tubulence closure and suggesting experiments that will give needed model information. A number of such experiments have been provided by Prof. Bradshaw's group, and some are included in Table 2. However, examination of Table 1 shows that categorization via strain type does not include all the effects that we shall ultimately have to be able to model if we are to say that we have adequate models for the computer simulation of all kinds of complex turbulent flows. Table 1 provides a warning for those who would claim too much too early and thereby do disservice to the insightful and continuing efforts of the turbulence research community as a whole.

In 1980, we still lack a viable method for relating the several taxonomies just discussed. We do not know what methods are best applied to a given flow configuration of Table 2, nor do we know what level of computation will ultimately be needed to model various kinds of strains and effects accurately. As long as that remains the case, we shall not have what is needed for engineering work in complex turbulent flow fields. It is hoped that the 1981 meeting of the Conference will begin to clarify the situation. More discussion on this point appears in the final section.

2. The Measurement Problem – Accuracy Control

Measurement of turbulence is inherently difficult. We have lacked instruments to measure some important quantities, for example vorticity, pressure fluctuations, pressure-strain correlation, local temporary flow reversals,* and some components of the Reynolds stress tensor. Fixed hot-wire data taken at $X/D \leq 5$ behind bluff bodies and in the edges of wakes and jets are far more uncertain than has been generally recognized owing to very large fluctuations (see for example: evaluation by B.J.Cantwell, Flow 0410; Tutu and Chevray, 1975; Coles et al., 1978). Even where we have instruments, the uncertainty in many quantities is high, for example: the rate of dissipation of turbulent energy, Reynolds stresses and higher order correlations. We have lacked adequate means for calibration of hot-wires for fluctuations (see Young et al., 1976). As a result, what is called the N^{th}-order uncertainty in the paper that follows has remained relatively high for turbulence data of nearly every kind. It is salutary in this connection to read the remarks of J.B.Jones concerning comparisons of turbulence data in the inlet zone of smooth, round pipe in turbulent Flow 0130, and of J.H.Ferziger on strained homogeneous fields, Flow 0370.

The neophyte worker, moreover, is faced with a lack of unified literature describing instrument techniques. The last attempt at complete coverage of fluid instrumentation seems to be that of R.C.Dean, Jr (1952). Dean's work was excellent for its time, but is badly in need of updating. Publishers have been unwilling to underwrite or even undertake this task, and no institution seems to assume the responsibility for seeing that such needful technical tasks are carried out.

---

* This problem is coming under control via laser anemometry and recent instrument innovations by Westphal et al. (1980) and Owen and Johnston (1980), but there are as yet few data.

Many engineering schools have never had, or have abandoned, advanced courses in thermal and flow measurements that would provide the student with solid preparation for careful data-taking and reduction.* The result is that all too often our data sets are generated by an untrained research-internee supervised solely by a single overworked and overcommitted faculty person.

The only known method for reliable control of accuracy is via uncertainty analysis of experients.† However, the results of the data evaluations show that uncertainty analysis is still not used by many workers The experienced worker, in a known situation, can perhaps produce trustworthy data without formal uncertainty analysis. For a neophyte or a person designing an experiment of a really new type, however, it would seem critical to the production of trustworthy data. For this reason, a separate position paper on experimental uncertainty has been prepared by R.J.Moffat. Looking to the future, we are fortunate that this paper is a major contribution to several long-standing conceptual problems and also provides a means by which the formal details of uncertainty analysis are made trivial for any experiment employing data reduction in a computer. This paper is strongly recommended to any individual intending to produce data for possible future "trials" of computation or input to turbulence modeling.

B. Institutional Difficulties

No one in the turbulence research community needs to be told that the number of papers has grown in recent years and that with growth has come a compression of both presentation times in meetings and the length of papers acceptable to many journals. This compression of presentation times and paper lengths has direct impact on the data base available for "trials" of computations.

The length requirement of papers in most journals usually prevents discussion of experimental difficulties in adequate detail and in most cases suppresses full publication of data. This means that data must often be read from too-small graphs, and details are sometimes omitted. As a result, data evaluators for the Conference have often had to refer to the originators of data to complete the necessary files. Such a task is not insuperable for a person focusing on evaluation of a single class of flows, but is normally not feasible for computors** who might want to test models against a variety of flows. This need to resort to the originators of data is one reason why a collective effort of the research community has been needed in order to bring the data base into usable form. Moreover, without such a system as the data library now being established, the personal knowledge and files of the individual researchers would have been lost to accurate recapture, over time.

The now-common ten-minute presentation time effectively prevents fully carrying through discussion on points of disagreement in technical meetings. Individual workers may carry out such discussions, but they are no longer part of the publicly accessible record. As Ziman (1968) told us at book length some time ago, what one of us believes is not "science". Information and hypotheses become "science" only when they are subjected to full public discussion and become accepted by the large majority of workers in the relevant field.

Still another institutional difficulty has arisen from what one might characterize as the "ten-thousand-card program". Such large programs have not been accessible to review in the older sense of "review" for publication. The typical reviewer can devote a matter of hours, or perhaps days, to a given review. This is grossly insufficient to unravel a large program, even if a printout of the code is provided. This problem compounds with the difficulties of the data base already cited. The usual test for the output of computation has of necessity been comparison with one or more sets of data. Even this is sometimes foregone, but let us assume for this discussion that comparison with a few sets of data is given in a paper that is sent to a reviewer. What is the position of this reviewer? About all he (or she) can do in "reviewing" is to examine the general statements provided about the code and see whether agreement with the data is obtained. It is nearly impossible for the reviewer to penetrate to the implications of the inevitable assumptions made in the turbulence closure and numerics. He (or she) cannot take the time to unravel the code. Moreover, the 1968 experience showed clearly that comparison with as few as three data sets has little meaning in verifying the utility of codes.†† Even for the restricted class of flows studied in the 1968 meeting, it became clear that the 16 mandatory flows constituted something like a "minimum" test of viability. Moreover, since the computer rarely has the time to assess data sets, it is altogether possible that untrustworthy data will be employed; see remarks of Owen and Johnson (1980).

This combination of difficulties was known to the Organizing Committee for the Conference in principle when the planning began in 1978. Experience gained since that time has tended in nearly every instance to reinforce the significance of these problems. Data that evaluations showed were wrong by half an order of magnitude have been used as

---

* The writer is aware of only two sequences of such courses at the graduate level – both at Stanford. He would welcome knowledge of others, and has several times so stated in public meetings.

† The writer is a biased observer on this topic, having written a base paper in the field. However, any other approach leaves significant questions unanswered and fails to provide numerical criteria by which comparisons between data sets or between data and computations can be made quantitative. Similar remarks have been made independently by D.A.Humphreys and B.van den Berg in the evaluation of data for three-dimensional turbulent boundary layers, Flow 0250.

** The word "computor" denotes a person doing numerical fluid dynamics, as opposed to a "computer", which denotes hardware for doing numerical calculations.

†† This difficulty is also revealed and emphasized by the questions of managing engineers responsible for utilizing computational codes. In a number of instances, such managers have expressed to the writer perplexity concerning how to judge codes offered to them by consulting firms which create numerical codes.

input to models in some cases. Questions and requests for further information have had to be referred by data evaluators to the originators of the data in many instances where the published record was not sufficient. Many deficiencies in both planning and detailed execution of experiments have come to light that could have been avoided had the experience available in the research community on provision for accuracy and on the difficulties of laboratory control of fluid flow been brought to bear in a timely manner.

The Conference was designed to ameliorate some of these difficulties, and thus hopefully to improve matters in the future. The steps taken are described in the next section.

4. ORGANIZATION OF THE CONFERENCE

Some, but not all, of the difficulties recited in the previous section could be significantly reduced by three accomplishments:

(1) Provision of a trustworthy data base backed by consensus of the research community on its reliability and on its possible difficulties. To be fully effective, this data base needs to be computer-readable and widely accessible.

(2) Clarification of data needs for constructing and checking computer models including: types of new or improved data required; data standards; the methodology for quantitative comparison of data and computation accounting for residual uncertainty in the data. To be fully effective, this knowledge needs to be implemented via thorough review processes.

(3) The public comparison of the standard "trials" with at least a large number of different kinds of computer simulations in order to test several questions:

   (a) Does an adequate "closure" model exist that can be utilized in feasible running times, or, on the contrary, will it be necessary for engineering computation to utilize distinct "fine-tuned" models that are "tailored" to specific problems or to classes of problems in order to obtain reliable results of engineering accuracy?

   (b) What kinds of turbulence-closure models and numerics are more/less successful, and in what classes of flows?

   (c) What are the limits, if any, for successful computer simulation of complex turbulent flows in one-phase Newtonian substances in 1981?

Initially, the Organizing Committee, reasoning from the 1968 experience, thought that it might be possible to establish the data base in a suitable closed form. As work progressed, it became clear that both improved data and data of new kinds are still needed. As a result, the concept of a data library as a separate, ongoing function evolved. Agreements have been made with two organizations in Europe and one in the United States to hold the tapes produced for the data library to sell them for a fee not to exceed approximately $100. The addresses of these organizations are given in Appendix I. Similar arrangements in other parts of the world will be considered.

Procedures were instituted to insure against the inclusion of data on review by only one worker, that is, to create consensus on the data base. Each data evaluation was reviewed by a committee of three to five other workers,* and in most instances this resulted in significant revisions and improvements. In addition, as each final evaluation report and its summary, plus a "specification for computations", was received at Stanford, it was sent to at least two other attendants of the 1980 meeting for review and possible comment. As in the 1968 Conference, the attendants were asked in advance to agree to assist with the work as a condition for attendance, and almost without exception that agreement has been honored to the extent requested by the Organizing Committee. Also, as in 1968, procedures to drive discussion to full completion will be employed; such completion need not imply agreement, disagreements will also be focused and recorded as the basis for further investigations. These meeting procedures have been recorded in an advice to Session Chairmen and are bound into this volume as Appendix II to this paper.

In addition to the procedures of the preceding paragraph, one member of the Organizing Committee acted as a liaison person for each flow evaluation in order to coordinate information and assist in formation of standards. Initially, the Organizing Committee was not able to provide detailed standards for the data evaluators, since the character of the various flows is so diverse. Only general guidance was given the data evaluators. The most critical task, that of formulating a data base, is thus the result of the efforts of the data evaluators. Their task was made even more difficult by the fact that the shape of the work process was evolved as information accumulated, and the evaluators were only later asked to formulate summaries (for publication) and specifications (for trial computations). The field owes a considerable debt to the arduous and insightful work of these experts on the various flow classes.

These procedures do not guarantee infallibility; science as a process is not infallible. When it comes to establishing matters of truth, however, the full public discussion of science is much better than any other known method. The *public* discussion of science is the best we have, and it is at least an order of magnitude better than the assessment by individual data takers with respect to their own output. Even a cursory review of the full data evaluations for this Conference and the comments on them shows this clearly. For this reason and also to make them available to future "data takers", the

* A few evaluations were received too late for prior review, and were instead discussed in the 1980 meeting.

full evaluation reports are being held in file at Stanford and can be obtained without charge by writing to the Thermosciences Division, Department of Mechanical Engineering, Stanford, CA, USA 94305. Some will be published in serials accepting long articles or condensed for journals; one already has been (Eaton & Johnston, 1980); another (Launder & Rodi) has been accepted for publication.

A different lesson also emerged from study of the data evaluations as they were formulated over time. Initially, the common wisdom suggested that tests of computations should be concerned with detailed comparison with single flow fields of high complexity, for example the data of Cantwell and Coles (Flow 0410). However, it became clear from discussions with computors and the results of the data evaluators that at least two other types of comparisons are important. The first is limits on physical behavior, for example: the cessation of turbulence production when a flow passes through a lower critical Reynolds number (Flow 0280); or the reduction to similarity solutions for asymptotic flows, as in a mixing layer or tube flow (Flows 0110, 0170, 0260). Finally, the use of composites of data on first-order results over a wide range of parameters is an important check, for two reasons. First, testing over a range verifies turbulence models independently from "tuning" processes involved in setting up particular flows. Second, the use of composite data insures estimates of n^{th}-order uncertainty in the sense defined in the paper in this volume by R.J.Moffat, and thus avoids the difficulties of "one-lab" experiments. These three kinds of checks are all in addition to checks on mathematical consistency as emphasized by a number of workers, for example Coleman Donaldson and John Lumley

As in 1968, the Evaluation Committee for study of the comparison of the data with the computations will be chaired by Prof. H.W.Emmons of Harvard University. After input from the 1980 meeting and the Organizing Committee, the methods of assessment are the responsibility of Prof. Emmons and his committee. They are left so in order to provide assessment independent from the organizers, data takers, and computors, and because they cannot be properly realized until the results are themselves in hand.

A problem that was foreseen but not initially understood was the question of how to review codes. In 1968 every program utilized was checked by graduate students at Stanford to insure completeness and repeatability. Given the size of current codes and the time required to adapt them to specific problems, such a procedure is not feasible. Moreover, the basic problem of how to "review" codes needed some form of answer. The Organizing Committee dealt with this problem by designing a questionnaire that we hope will assist in this problem. The questionnaire will appear in the Proceedings for the 1981 meeting. It is worth noting that it took six revisions to create this questionnaire. It was only after it was found that new language had to be invented to properly describe the hierarchical structure often used in computations that an apparently usable questionnaire was achieved. The Organizing Committee hopes that the questionnaire will assist in reviews of codes by journals and industrial personnel, and will accordingly furnish copies on request.

These steps will hopefully relieve some of the problems that currently exist in computational fluid dynamics. However, several problems mentioned in the prior section lie outside the scope of work on the Conference and remain unanswered. In particular, the lack of adequate description of experimental uncertainty and the lack of experimental control it implies remain continuing problems. They are well evidenced by the data scatter in the evaluations.

Another problem that lies beyond the scope of the Conference is the need for an adequate treatise on experimental methods that will assist the data-taker in avoiding known pitfalls in mensuration.

Still another remaining problem is the matter of oversight in what are intended to be record experiments as the basis for possible future "trials" of computer output. The nature of data needed for this use is significantly different from the needs for past uses of data. These new needs have been little discussed and hence are the subject of a spearate paper in this volume. These new needs, the lack of an up-to-date treatise and the paucity of formal courses in aerodynamic measurements, all speak to the need for increased oversight in planning experiments beyond faculty persons working alone (or with untrained assistants) who are contractually obligated to produce results on a short time-table. How this may be accomplished is not clear at this time. A start in this direction has recently been made by two sets of monitors for government bureaus,* and these examples may serve as at least a partial model.

Finally, the 1980–81 Conference will differ from the 1968 Conference in an important regard that needs to be clearly stated. In 1968 the timing was fortunate. The state of the art was such that the 1968 Conference essentially finished one stage of work and led to another by showing that the problem was essentially solved. No such outcome can be expected from the 1980–81 Conference. The data will not be complete. More flows will need to be added to the library. Data are needed on additional classes of flows; improved data are needed in many. Nor is it reasonable to expect that computational methods will be finished. Computational fluid dynamics is a young and rapidly improving field. The most that can be expected is the beginning of a broad, trustworthy data base and a snapshot of the state of the art that will aid assessments of utility for industrial "consumers" of programs and provide us with a better guide to profitable avenues for further researches. Finally, it needs to be remembered that the class of flows covered in the current data library, and hence the basic test cases for the 1981 meeting, are not yet universal, as a comparison of Tables 1 and 2 shows. It must follow that even a successful model for a large number of basic test cases will not yet be verified as "universal". Moreover, an almost unblemished record of past failures in extrapolation of turbulence models to new classes of flows should warn us against easy assumptions concerning generality.

* M.Rubesin and I.Marvin of NASA-Ames and J.McCroskey and L.W.Carr of Air Mobility Command, Moffett Field, CA.

Editorial Note: Figures use in presentation on this conference are included as Appendix III.

TABEL 1

Some Effects that can Influence Characteristics of Turbulence

A. Nature of Fluid
   1. Viscosity (i.e., Re)
   2. Constitutive (e.g., polymers)
   3. Energy release (e.g., chemical reactions)
   4. Surface tension (e.g., oil-slick calming)
   5. Cryogenic effects
   6. Multiphase fluid (several subcases)

B. Nature of Outer Flow
   7. $\partial p/\partial x$, $\partial p/\partial z$
   8. Free-stream fluctuations (noise, turbulence)
   9. High Mach number (hypersonic)

C. Wall Effects
   10. Blowing/suction
   11. Roughness
   12. Compliant walls
   13. Moving wall

D. Body Forces
   14. Coriolis
   15. Centrifugal
   16. Density gradients
   17. EHD, MHD
   18. Wall curvature: convex, concave (could be placed in type E)
   19. Curvature in free-shear layers (could be placed in type E)

E. Strain and Interaction Effects
   20. Shear rate and type
   21. Dilatation; transverse stretching/compression
   22. Turbulence-turbulence interactions
   23. Downstream effects of transitions

TABLE 2

Flow Cases

The 1980–81 AFOSR-HTTM-Stanford Conference on Complex Turbulent Flows: Comparison of Computation and Experiment

Group I – Basic Test Cases (see comments at end)

Group a. *Numerical Checks*
1. Potential flow in 90° corner
2. Howarth flow (solution by Briley)
3. Axisymmetric jet flow (solution in Rosenhead)
4. Flow in square cavity with a moving lid

Group b. *Simple Test Cases* –

	Flow Number*	*Evaluator*
5. Sheared homogeneous turbulence	0370	J.H.Ferziger
6. Attached boundary layer – Wieghardt from '68 Conf.	0620	D.E.Coles (68)
7. Attached boundary layer – Bradshaw Case C from '68 Conf.	0630	D.E.Coles (68)
8. Planar mixing layer (including SABIN-ABRAMOVITZ relation for mixing parameter versus velocity ratio)	0310	S.Birch
9. Subsonic axisymmetric wake	0360	V.C.Patel

(Continued)

* "Flow" denotes a geometry or class of related geometries; "case" denotes a recommended realization of a given geometry.

	Flow Number*	*Evaluator*
Group c. *Entry Test Cases – Incompressible*		
10. Boundary layer with blowing/suction	0240	L.Squire
11. Free shear layer with streamwise curvature	0330	P.Bradshaw
12. Boundary layer with streamwise wall curvature	0230	T.Simon/S.Honami
13. Wall jet – tangential blowing (plane case and curved cases including rate of growth of layer width)	0260	B.Launder/W.Rodi
14. Pressure-driven (skewed) secondary flow (fully established flow in duct)	0510	R.B.Dean
15. Entry into rectangular duct – up to fully established flow	0110	F.Gessner
16. Predictive case α (fully established duct flow enters region with added "internal" walls)		Org. Committee
17. Backward-facing step (includes reattached boundary layer)	0420	J.Eaton/J.Johnston
18. Predictive case β (systematic variations in downstream geometry of a backward-facing step)		Org. Committee
19. Separating diffuser: two-dimensional planar (may include overall recovery as function of divergence angle for one non-dimensional length: potential core flow)	0430	R.Simpson
20. Predictive case γ (separated) planar diffuser with inviscid rotational inlet flow		Org. Committee
21. Axisymmetric boundary layer with strong streamwise and transverse curvature	0390	V.C.Patel
Group d. *Simple Test Cases – Compressible*		
22. Flat plate:		
Variation in C_f/C_{fo} versus Mach number (insulated plate)	0810	M.Rubesin/C.Horstman
23. Variation in C_f/C_{fo} versus T_w/T_o (fixed M)	0820	MR/CH
24. Variation in C_f/C_{fo} with blowing (fixed M, $T_w = T_r$)	0830	L.Squire
25. Boundary layers in adverse pressure gradient: Considering two or three cases from the following Fernholz-Finley Collection (AGARD-AG-223):		
Peake, Brakman, Romeskie (axisym.), Cat. 710-2	0840	MR/CH
Lewis, Gran, Kubota (axisym.), Cat. 720-1	0841	MR/CH
Zwarts, F.J. (planar), Cat. 700-7	0842	MR/CH
Horstman and Kussoy (new data)	0843	MR/CH
26. Spreading parameter σ as a function of M for mixing layer	0850	P.Bradshaw
Group e. *Entry Test Cases – Compressible*		
27. Impinged normal shock wave, boundary layer interaction at transonic speeds	0860	MR/CH
28 Transonic flow over "bump", induced shock wave boundary layer interaction	0861	MR/CH
29. Transonic airfoils	0862	R.Melnik
30. Two-dimensional compression corner (supersonic)	0863	MR/CH
31. Reattaching planar free shear layer (supersonic)	0864	MR/CH
32. Axisymmetric shock impingement (high supersonic)	0865	MR/CH
33. Three-dimensional shock impingement (supersonic)	0866	MR/CH
34. Pointed axisymmetric bodies at angle of attack (supersonic)	0867	D.Peake
35. Axisymmetric, supersonic near-wake	0868	Favre
36. Non-lifting transonic airfoil, shock-separated	0869	MR/CH

Comments on Basic Test Cases

(1) The general form will be as shown and will include: (i) numerical checks; (ii) shear layers and other "simple" cases; (iii) incompressible entry flows; (iv) predictive cases; and (v) compressible entry cases. The details may be altered depending on results of data evaluations under way and other comments received.

(2) Most flow types will involve one specific flow; a few will involve two or more flows. For example, a "slow" and "fast" shear rate for homogeneous flows may be called for; several wall jet flows will be included and four blowing/suction cases will be recommended to cover various aspects of modeling.

(3) Each flow case in Section c will have an associated numerical test case from flows 1–4 *requested*.

(4) Details of format; starting and ending sections; output variables requested, and specific stations for output will be presented to the 1980 meeting and modified just after that meeting.

(Continued)

* "Flow" denotes a geometry or class of related geometries; "case" denotes a recommended realization of a given geometry.

(5) ENTRY REQUIREMENTS: See also Appendix A, Part 3.c.
  (a) Incompressible flows: one case from among flows 10–21, inclusive.
  (b) Compressible flows: one case from among flows 27–36, inclusive.

	Flow Number*	*Evaluator*
Group II – Other Cases under Evaluation		
1. Two-dimensional, planar channel with wave perturbation	0150	M.Acharya
2. Effect of free-stream turbulence on boundary layer	0210	P.Bradshaw
3. Circular cylinder and related bluff bodies	0410	B.Cantwell
4. Flow over the trailing edge of blades and airfoils	0470	P.Drescher
5. Three-dimesional boundary layers	0250	D.Humphreys/ B. van den Berg
6. Complex wakes (inadequate data found)	0350	V.C.Patel
7. Laminar-turbulent transition (inadequate data)	0290	E.Reshotko
8. Unseparated diffuser flows	0140	R.Simpson
9. Stalled airfoil	0440	A.Wadcock
10. Relaminarization, laminarescent and retransitional boundary layers	0280	K.R.Sreenivasan
11. Flows with buoyancy forces	0900	J.C.Wyngaard
12. Entry zone of round tube	0130	J.B.Jones
13. Tillman ledge flow from '68 Cont.	0610	D.E.Coles

Group III – Some Cases Warranting Further Study

1. Full details of several blunt bodies including wakes: (ships, buildings, bumps, . . .)
2. Radial wall jet flows
3. Wall jets impinging at angles to surface
4. Unsteady mean flows (detailed report to be presented by L.Landarr at 1980 meeting)
5. "Momentum-less" wakes
6. Jets in cross and counter flow
7. Two-dimensional separated flows (airfoil flaps)
8. "Low" Reynolds number boundary layers
9. Rough wall cases
10. Laminar-turbulent transition
11. Airfoil cases other than transonic
12. Two-dimensional wakes
13. Flows with swirl

Comments on Group III Cases

(1) Data on several flows in this group were called to the attention of the Organizing Committee too late to provide evaluation or a suitable "Evaluator" has not been found. Hence they remain for future possible "evaluation" and inclusion in the data library.

(2) Comments to the Organizing Committee will be appreciated on other cases, where data exist and need study, or where important need for the data exists. Such cases will be included where appropriate in "Comments" in the Proceedings of the 1980 Meeting.

* "Flow" denotes a geometry or class of related geometries; "case" denotes a recommended realization of a given geometry.

TABLE 3

(from JFE, 100, 1978)

Level	*Example*	*Comments*
1. Nondimensional correlation of data.	f versus Re for pipe flow; C_p* as a function of geometry for straight-walled diffusers; C_D versus Re for flow normal to cylinders, over spheres, etc.	Slow, expensive, accretive; high reliability within carefully defined class of flow situation.
2. Zonal models.	(a) Conventional boundary layer theory for attached flows, matched to external flow via δ*.	The major class of engineering solutions currently.
	(b) Hyper-boundary layer viscid-inviscid zonal models, for strong interactions such as detaching flows.	Advancing rapidly, good promise for many more classes of practical solutions and design tools by 1988. Computing costs well within engineering feasibility. A number of research groups currently active.
3. Numerical solutions for Reynolds equations (time-averaged Navier-Stokes equations).	A number of codes now exist. Can be used for part of flow and matched to external flow like 2b or over entire field.	Also advancing rapidly. To date methods don't appear to extrapolate well; as in Class 2 need to be fitted to specific classes of flows.
4. Large eddy simulation with subgrid closure.	Current research – few solutions yet available.	Computing costs still relatively high. Outcome highly dependent on further advances in large computers.
5. Complete solutions to Navier-Stokes equations	(a) Analytic. A dozen or so closed solutions (for very simple cases) exist as the results of 150 years' work.	New solutions likely to be scarce, slow; restricted to laminar flows.
	(b) Numerical. Only the very simplest cases, which have few applications, so far accessible via numerical methods.	All but these simplest cases at very modest Reynolds numbers still too large for existing computers; progress dependent on rate of growth of computers and decrease in computing costs.

REFERENCES

Bradshaw, P. — *Complex Turbulent Flows*, JFE, 97, p.146, 1975.

Coles, D.E.; Cantwell, B.J.; Wadcock, A.J. — *The Flying Hot Wire and Related Instrumentation*, NASA-CR 3066, 1978.

Eaton, J.K.; Johnston, J.P. — *A Review of Research on Subsonic Turbulent Flow Reattachment*, AIAA Meeting, Snowmass Colorado, July 1980.

Dean, R.C., Jr, (Ed.) — *Aerodynamics Measurement*, MIT Press, (out of print), 1952.

Kline, S.J.; Ferziger, J.H.; Johnston, J.P. — Opinion: *The Calculation of Turbulent Shear Flows: Status and Ten-Year Outlook*, TASME, JFE 100, 1, pp.3-5, March 1978.

Kim, J.; Kline, S.J.; Johnston, J.P. — *Investigation of a Reattaching Turbulent Shear Layer. Flow over a Backward-Facing Step*, ASME Symposium on Flow in Primary Non-Rotating Passages in Turbomachines, 1979.

NASA — *Compressible Turbulent Boundary Layers*, NASA-SP-216, 1969.

NASA — *Free Turbulent Shear Flows*, Vol.5. Conference Proceedings, NASA SP-321, 1972.

Owen, F.K.
Johnson, D.A. — *Separated Skin Friction Measurement – Source of Error, an Assessment and Elimination*, AIAA-80-1409, 1980.

Reynolds, W.C. — *A Morphology of Prediction Methods*, Proceedings of the 1968 AFOSR-IFP-Stanford Conference on Computation of Turbulent Boundary Layers, Vol.I, pp.1-15, 1968.

Tutu, N.
Chevray, R. — *Cross-Wire Anemometry in High Intensity Turbulence*, JME, 71, pp.785-800, 1975.

Westphal, R.V.
Eaton, J.K.
Johnston, J.P. — *A New Probe for Measurement of Velocity and Wall Shear Stress in Unsteady, Reversing Flow*, to be presented at 1980 Winter Annual Meeting, ASME (available temporarily from the Thermosciences Division, Department of Mechanical Engineering, Stanford University, Stanford, CA 94305), 1980.

Young, M.F.
Kline, S.J. — *Calibration of Hot Wires and Hot Films for Velocity Fluctuatio.* port TMC-3, Dept of Mechanical Engineering, Stanford University, 1976.

Zimen, J. — *Public Knowledge: The Social Dimensions of Science*, Cambridge University Press, 1968.

Appendix I

SOURCES FOR DATA LIBRARY ON TAPE

1. Harold G.Hale, Jr
   COSMIC
   112 Barrow Hall
   University of Georgia
   Athens, GA 30602

2. DFVLR Bunsenstrasse 10, 340 Göttingen, Germany
   Forschungsbereich Strömungsmechanik Institut für Experimentelle Strömungsmechanik
   c/o H.U.Meier
   Telefon (05 51) 70 91; Telex 096 839 (avagoe d)

3. Netherlands National Aerospace Laboratory
   c/o Mr F.J.Heerema
   P.O. Box 153
   8300 AD Emmeloord
   The Netherlands
   Tel. 05274-2828

Appendix II

THE OPERATION OF SESSIONS – THE ROLE OF EVALUATORS, SESSION CHAIRMEN AND TECHNICAL RECORDERS: 1980 Meeting on Data

Goals of Sessions:

(1) Reach consensus on flows within the Basic Test Cases and as many other flows as time and available evaluations allow.

(2) Complete discussions by the end of the Meeting.

Each flow case will be presented by the Data Evaluator. The Evaluator will be asked to cover the following points:

(i) Selection criteria
(ii) Flows selected
(iii) Specific computations (zones and output) for each selected flow
(iv) Advices for future data takers; Data needs, cautions, checks, etc.

A number of attendees, in addition to the review committee, will have been asked to study each evaluation and prepare comments. These comments when offered will take priority in discussions. (Review Committee comments will have already been taken into account by the Data Evaluators.)

Each session will be about 90 minutes in length and will typically cover three flows. All sessions will be recorded on tape. Each session will have two "Technical Recorders" to assist the Chairman.

In the evening following a given session, a committee on that session will convene to complete the discussion and clarify points under question. Normally this committee will include the Session Chairman, Evaluator, Review Committee Chairman, Technical Recorders, and a few others. The task of this committee will be to produce a succinct, clear record of the significant points of the session – in general, this will not be a verbatim transcript.

The tapes will not be transcribed; this is an enormous but seldom valuable task. Rather, the operators of the tape machines will be instructed to create a footage log showing where various persons speak in order to provide access for checking remarks where needed.

Given these resources, the Chairman's task will be to moderate the discussion and be sure that points are completed and accurately reduced to writing by the Recorders. It is nearly always important in this process to keep asking questions of the persons expressing position until full clarity is reached, and then have the recorder read back the statement for concurrence by the worker concerned; the process should be iterated to closure. As noted above in this packet, consensus as used herein implies not only agreements, but also sharply focused disagreements with the name(s) of each individual holding a given position stated. The iterative process just mentioned is particularly important in registering and focusing disagreements about specific ideas or matters of fact.

The Conference will provide sufficient secretarial assistance so that the typed version of the output from the committee on each session can be produced and posted by the end of lunch on the following day. Individuals will be asked to approve (by initialling) or alternatively comment in writing to the Session Chairman by the evening of that day.

Appendix III

FIGURES USED IN PRESENTATION OF "AN OVERVIEW OF 1980–81 AFOSR-HTTM-STANFORD CONFERENCE ON COMPLEX TURBULENT FLOW: COMPARISON OF COMPUTATION AND EXPERIMENT"

AN OVERVIEW OF THE
1980-81 AFOSR-HTTM-STANFORD CONFERENCE ON COMPLEX TURBULENT FLOWS: COMPARISON OF COMPUTATION AND EXPERIMENT

I. GOALS OF THE CONFERENCE

1. TO REACH CONSENSUS IN THE RESEARCH COMMUNITY ON TRUSTWORTHY DATA SETS THAT CAN BE USED AS INPUT FOR MODELING OF TURBULENCE IN COMPLEX FLOWS AND AS THE BASIS FOR STANDARD "TRIALS" FOR CHECKING OUTPUT OF COMPUTATIONS.

2. TO CREATE A "DATA LIBRARY" ON MAGNETIC TAPE. THIS LIBRARY WILL HOLD THE DATA SELECTED AS TRUSTWORTHY IN STANDARD, NORMALIZED FORM. THE DATA WILL BE COMPUTER-READABLE AND WIDELY ACCESSIBLE AT A MODERATE FEE.

3. TO COMPARE THE OUTPUT OF CURRENT METHODS OF COMPUTATION FOR TURBULENT FLOWS FOR A SET OF "BASIC TEST CASES" COVERING A BROAD RANGE OF FLOWS.

Figure 1

ORGANIZING COMMITTEE

STEPHEN KLINE, STANFORD UNIVERSITY, CHAIRMAN

PETER BRADSHAW, IMPERIAL COLLEGE, LONDON
BRIAN CANTWELL, STANFORD UNIVERSITY
BRIAN LAUNDER, UNIVERSITY OF MANCHESTER
ELI RESHOTKO, CASE-WESTERN RESERVE UNIVERSITY
MORRIS RUBESIN, NASA-AMES RESEARCH CENTER
GINO SOVRAN, GENERAL MOTORS RESEARCH LABORATORIES

EVALUATION COMMITTEE, 1981 MEETING

H. W. EMMONS, HARVARD UNIVERSITY, CHAIRMAN

D. R. CHAPMAN, NASA-AMES RESEARCH CENTER
P. G. HILL, UNIVERSITY OF BRITISH COLUMBIA
G. M. LILLEY, UNIVERSITY OF SOUTHAMPTON
MARVIN LUBERT, GENERAL ELECTRIC, KAPL
M. V. MORKOVIN, ILLINOIS INSTITUTE OF TECHNOLOGY
W. C. REYNOLDS, STANFORD UNIVERSITY
J. STEGER, STANFORD UNIVERSITY
P. J. ROACHE, CONSULTANT

Figure 2

HISTORY IN BRIEF

BELIEF BEFORE 1968. TURBULENT BOUNDARY LAYER AN UNSOLVED PROBLEM

AFTER 1968 (1969, 1972): SHEAR LAYERS COMPUTABLE
(WITH SOME EXCEPTIONS: DETACHMENT, REATTACHED LAYERS, NEAR-ZONE FREE-SHEAR LAYERS)

1972-1980: GREAT ADVANCES, NEW CONFUSIONS

Figure 3

SOURCES OF CONFUSION, DIFFICULTIES IN TURBULENCE RESEARCH
(LATE 1970's)

TECHNICAL:

- DIVERSITY, COMPLEXITY OF FLOWS
  (DATA EVALUATION OF ~ 40 CLASSES)

- TURBULENCE NOT A SINGLE "STATE"
  23 KNOWN PHYSICAL EFFECTS MODIFY TURBULENCE
  (TYPE OF STRAIN ONLY ONE)

- MEASUREMENT DIFFICULTIES
  - (LACK MEANS TO MEASURE $\overline{u^2}$, $\overline{pu}$, FLOW REVERSALS)
  - UNCERTAINTY ANALYSIS, CALIBRATION CHAINS, CLOSURE CHECKS -- TOO SELDOM USED
  - NO COMPLETE, UP-TO-DATE TEXT MATERIALS ON EXPERIMENTAL METHODS.

RESULTS: NO TRUSTWORTHY DATA BASE

Figure 4

MORE SOURCES OF CONFUSION, DIFFICULTIES

INSTITUTIONAL

- TEN-MINUTE PRESENTATIONS
- TEN-PAGE PAPERS
- 10,000 CARD PROGRAMS
  - LACK OF MEANS FOR REVIEW

RESULTS: INADEQUATE EVALUATIONS, NO MEANS TO FORM UNIFIED PICTURE OF FIELD.

CONCLUSION: TOTAL PROBLEMS TOO LARGE FOR INDIVIDUAL RESEARCH GROUP.

Figure 5

A RESPONSE:

1980-81 AFOSR-HTTM-STANFORD CONFERENCE ON COMPLEX TURBULENT FLOWS: COMPARISON OF COMPUTATION AND EXPERIMENT

ATTITUDE:

A COOPERATIVE LEARNING PROCESS INVOLVING A LARGE FRACTION OF RESEARCH COMMUNITY

Figure 6

CONTENTS OF PROCEEDINGS, VOL. I

COMPLEX TURBULENT FLOWS: COMPARISON OF COMPUTATION AND EXPERIMENT--THE 1980-81 AFOSR-HTTM-STANFORD CONFERENCE

VOLUME I: DATA	AUTHORS
A. INTRODUCTION	S. J. KLINE
B. TABLE OF FLOWS, INCLUDING ORGANIZATION, RANGE OF PARAMETERS, ETC.	S. HONAMI/S. KLINE
C. EXPERIMENTAL DATA NEEDS FOR COMPUTATIONAL FLUID DYNAMICS	P. BRADSHAW/B.CANTWELL/ J. FERZIGER/S. KLINE
D. CONTRIBUTIONS TO THEORY OF UNCERTAINTY ANALYSIS FOR SINGLE-SAMPLE EXPERIMENTS	R. J. MOFFAT
E. THE DATA LIBRARY	B. CANTWELL
F. A 1-3 PAGE SUMMARY OF EACH FLOW, INCLUDING: 1. VARIABLES AND THEIR RANGES, 2. LOCATIONS ON TAPE OF DATA, 3. MIN/MAX DATA, 4. PROVISOS ABOUT DATA SET, 5. CAUTIONS FOR FUTURE DATA TAKERS, AND QUESTIONS NEEDING RESOLUTION.	DATA EVALUATORS (AND COMMITTEES), B. CANTWELL
G. COMMENTS FROM 1980 MEETING	
H. REPORTS OF COMMITTEES	
I. CONCLUSIONS	S. J. KLINE

Figure 7

CONTENTS OF PROCEEDINGS, VOL. II

COMPLEX TURBULENT FLOWS: COMPARISON OF COMPUTATION AND EXPERIMENT--THE 1980-81 AFOSR-HTTM-STANFORD CONFERENCE

VOLUME II: COMPUTATION	AUTHORS
A. INTRODUCTION	S. J. KLINE
B. LEVELS OF COMPUTATION AND MORPHOLOGY OF TURBULENCE MODELS	J. H. FERZIGER AND W. C. REYNOLDS
C. COMPLEX STRAIN FIELDS	P. BRADSHAW
D. A USER'S VIEW	G. SOVRAN, A.D. WELLIVER
E. TABULATION OF RESULTS OF COMPUTATION; EACH COMPUTOR'S RESULTS WILL INCLUDE A COMPLETED SET OF EXTENSIVE QUESTIONS DESCRIBING ASSUMPTIONS, MODELS, NUMERICS, ETC.	
F. REPORT OF EVALUATION COMMITTEE	H. W. EMMONS/COMMITTEE
G. COMMENTS FROM MEETING	
H. REPORTS FROM AD HOC COMMITTEES	

Figure 8

ORGANIZATION
MEETING ON DATA BASE--SEPTEMBER 3-6, 1980

PROCEDURES

- EVALUATIONS (INPUT FROM DATA TAKERS SOLICITED)
  (THREE TYPES OF EXPERIMENTS: ENGINEERING RESULTS; MODEL BUILDING/TESTING COMPUTATIONS; NEW KNOWLEDGE)
- REVIEW, REVISE EVALUATIONS
- PREPARE:
  - SUMMARY
    CHARACTER OF FLOW
    CRITERIA OF SELECTION
    ADVICES TO FUTURE DATA TAKERS
  - SPECIFICATIONS
  - PREPARE MAGNETIC TAPE: DESCRIPTION AND DATA
- MEETING:
  - PRESENTATION
  - DISCUSSION
  - CLOSURE VIA EVENING COMMITTEES
  - AD HOC COMMITTEES

Figure 9

SPECIFIC DECISIONS FROM 1980 MEETING

TEST CASES FOR 1981
- ~ 30 INCOMPRESSIBLE
- ~ 20 COMPRESSIBLE
  USE STANDARD MIN/MAX CHARTS
  (THREE TYPES OF CASES: DETAILED, PARAMETRIC, LIMITS)

PLUS

PREDICTIVE CASES
8 UNDER WAY
3-4 PROBABLY USABLE

RESPONSE
- ~ 45 COMPUTOR GROUPS
- ~ 16 INTEND TO DO 10 OR MORE FLOWS
  RESPONSE RELATIVELY FLAT

CENTRAL CASES -- REQUEST: IF POSSIBLE DO

- INCOMPRESSIBLE
  - BACK-STEP + PREDICTIVE CASE
  - CURVED FREE-SHEAR LAYER

OR

- COMPRESSIBLE
  - TRANSONIC AIRFOIL
  - COMPRESSION CORNER

Figure 10

1980 DECISIONS (CONT.)

NUMERICAL CHECKS:
- ONE MESH-REFINEMENT, IF POSSIBLE ON CENTRAL CASE
- LAUNDER/RODI GROUP
- FERZIGER/STEGER/REYNOLDS GROUP

STUDIES AND TAXONOMY
- RESULTS TO BE SENT IN AS FINISHED
- QUESTIONNAIRES: THE DISCLOSURE PROBLEM
- COMPILATIONS/STUDIES ⟶ TAXONOMY
- PRESENT BY METHOD (IN GROUPS) AND BY FLOWS (IN GROUPS)

SCHEDULING
30 NOVEMBER 1980 ~ 30 CASES
31 JANUARY 1981 ~ 20 CASES

RESULTS ON STANDARD PLOTS
≤ 15 JULY 1981 -- ALLOWS STUDY, PREPARATION

Figure 11

SOME MAJOR CONCLUSIONS FROM THE PREPARATORY WORK AND 1980 MEETING

I. FAR MORE USABLE CASES EXIST THAN WAS INITIALLY BELIEVED
   ~ 50 FOR 1981
   20 MORE FOR LIBRARY
   (PLUS OTHERS NOT YET EVALUATED)

II. IN MANY CLASSES OF FLOW, TWO KINDS OF ADVICES TO FUTURE DATA TAKERS HAVE ARISEN FROM SYSTEMATIC REVIEW
   - IMPROVED EXPERIMENTS AND EXPERIMENTAL CONTROL
   - DATA NEEDS FOR CFD

III. SOME PROBLEMS CONCERNING APPROPRIATE SPECIFICATION OF TEST CASES HAVE BEEN CLARIFIED:
   WALL FUNCTIONS, BLOCKAGE INTERACTIONS, DOWNSTREAM B.C.'S IN ELLIPTIC FLOWS, ∗ ON C.S. -- SEE DATA-NEEDS PAPER

Figure 12

IV. MORE REGULAR AND COMPLETE USE OF UNCERTAINTY ANALYSIS, CALIBRATION CHAINS, CLOSURE CHECKS, AND MULTIPLE EXPERIMENTS NEEDED TO:

- CLARIFY EXISTING UNCERTAINTY INTERVALS
- REDUCE MAGNITUDE OF UNCERTAINTY (PARTICULARLY IN COMPRESSIBLE CASES)
- GUARANTEE EXPERIMENTAL CONTROL

V. INADEQUATE MEANS CURRENTLY EXIST FOR SEPARATING NUMERICAL ERRORS FROM TURBULENCE MODELING ERRORS

VI. A NEED EXISTS FOR INCREASED INTERACTION BETWEEN COMPUTORS AND EXPERIMENTS TO:

- CLOSE LOOP ITERATIVELY BETWEEN COMPUTATION AND EXPERIMENT, AND THEREBY TO
- CREATE IMPROVED DATA FOR COMPARISON WITH COMPUTATION;
- DECREASE USE OF REPRESENTATIONS (MODELS) LACKING BASES IN MEASURABLE QUANTITIES.

Figure 13

VII. SOME FLOWS WITH NO (OR INSUFFICIENT) TEST CASES INCLUDE:

- THREE-DIMENSIONAL CASES (OTHER THAN BOUNDARY LAYERS)
- COMPLEX WAKES
- TURBULENCE-TURBULENCE INTERACTIONS
- STRONGLY NON EQUILIBRIUM FLOWS
- LAMINAR-TURBULENT TRANSITION
- RELAMINARIZING AND RETRANSITIONAL FLOWS
- FLOWS WITH DISTRIBUTED BUOYANCY EFFECTS

Figure 14

CONCLUSIONS

THE 1980-81 MEETING

WILL:

- PROVIDE USABLE DATA BASE CLARIFYING STATE OF THE ART
- IMPROVE COMMUNICATIONS BETWEEN EXPERIMENTALISTS AND COMPUTORS
- FOCUS REMAINING EXPERIMENTAL, COMPUTATIONAL PROBLEMS
- SUGGEST IMPROVED EXPERIMENTS, METHODOLOGY

WILL NOT:

- FINISH THE DATA BASE

OR

- THE COMPUTATION METHODS
- MANY NEEDFUL EXTENSIONS WILL REMAIN

Figure 15

THEORETICAL AND EXPERIMENTAL INVESTIGATIONS OF TWO-DIMENSIONAL FLOWS WITH SEPARATED REGIONS OF FINITE LENGTH

K. Gersten, H. Herwig, P. Wauschkuhn

Institut für Thermo- und Fluiddynamik
Universität Bochum
4630 Bochum, Federal Republic of Germany

SUMMARY

Theoretical and experimental investigations of two-dimensional incompressible flows containing separated regions of finite length have been carried out. Separation of both laminar and turbulent boundary layers have been considered. However, in the case of laminar separation it was assumed that the separated free shear layer remains laminar. The separation bubbles were originated by backward facing steps with sharp or rounded edges or by dents in a flat plate. The flow along a flat plate having a backward facing step with sharp or rounded edges has been generalized to flows in channels with sudden enlargements or to flows in diffusors, respectively.

In all cases considered the theoretical modelling of the flow fields has taken into account the strong mutual viscous-inviscid interaction between outer flow and separated flow region.

All flow problems considered depend essentially on two or more independent Reynolds numbers. These Reynolds numbers are assumed very large (asymptotic theory). However, the way the Reynolds numbers tend to infinity may be different and can be characterized by the ratio of the thickness of the oncoming boundary layer and the step height (dent depth). The two limiting cases when this ratio is very small or very large have been treated theoretically.

1. INTRODUCTION

Flows are considered where a boundary layer separates followed by a separated region of finite length. Examples of flows with those characteristics are shown in Fig. 1. They can be found in many technical applications. In the following, two-dimensional incompressible and stationary flow will be assumed. The oncoming boundary layer leading to separation can be laminar or turbulent. However, in the case of laminar separation it is assumed that the flow will remain laminar even beyond the reattachment point. So-called transitional separation bubbles are explicitly excluded.

Fig. 2 shows the basic geometries which will be considered in detail. In the laminar case the separation bubble is originated by a dent in a flat plate at zero incidence (Fig. 2a), whereas in the turbulent case backward facing steps with sharp edges (Fig. 2b) or round edges (Fig. 2d) induce the separation. The latter cases could be generalized to flows in channels with sudden enlargement (Fig. 2c) and to flows in diffusors (Fig. 2e). Cases 2b and 2c can be considered as limiting cases $l \to 0$ of cases 2d and 2e respectively.

When the form of the contoured walls in cases 2a, 2d and 2e are prescribed the flow characteristics depend on certain independent dimensionless parameters, for instance Reynolds numbers based on the reference velocity (U_∞ or U_1) and the various lengths given in Fig. 2. Hence, case 2b depends on two, cases 2a, 2c and 2d on three and case 2e on four Reynolds numbers. It is assumed that all Reynolds numbers involved are very large, in other words, the asymptotic behaviour of the flows in the limits $Re \to \infty$ will be considered.

However, the way the Reynolds numbers tend to infinity may be different and can be characterized by the ratio of the thickness of the oncoming boundary layer and the step height (dent depth).

For the two limiting cases when this ratio is very small or very large, theoretical investigations have been carried out, the results of which will be compared with experiments where possible.

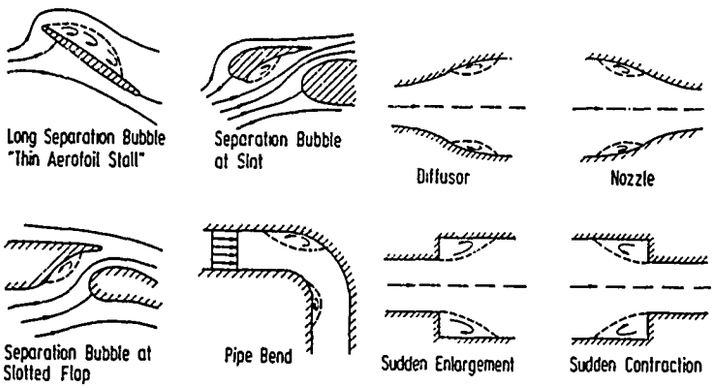


Figure 1. Flows with Closed Separated Regions

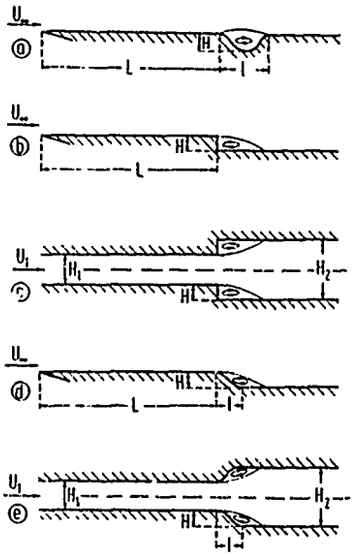


Figure 2. Basic Geometries

2. LAMINAR SEPARATION BUBBLES

2.1. Classification

To produce separation bubbles of finite length a dent in a plane wall was chosen for the model geometry. Its general shape is:

$$y = -\frac{H}{4}\left\{\cos 2\pi\left(\frac{x}{l} - \frac{1}{2}\right) - 1\right\}^2 \qquad (1)$$

There are three geometric parameters as shown in Fig. 3a: l (length of the dent), H (depth of the dent) and L (distance to the leading edge). Together with the Reynolds number of the problem three dimensionless parameters appear:

$$\text{(i)}\ \frac{H}{l}\ ; \qquad \text{(ii)}\ \frac{L}{l}\ ; \qquad \text{(iii)}\ Re_L = \frac{U_\infty L}{\nu}$$

Asymptotic theory is applied ($Re_L \to \infty$) but nevertheless the Reynolds number is still an essential parameter of the whole problem when viscous-inviscid interaction occurs.

To clarify this point Fig. 3b shows the plane H/l = 0,003 of the three-dimensional parameter field. There are two limits which must be treated in quite a different manner:

(I) The oncoming boundary layer is large compared to H (depth of the dent); in Fig. 3a beneath surface ① .

(II) The oncoming boundary layer is small compared to H; in Fig. 3a above surface ② .

These two regions also appear in Fig. 3b, each of them divided into attached and separated areas.

Knowledge of the two limiting cases serves as a guide to understand the general case.

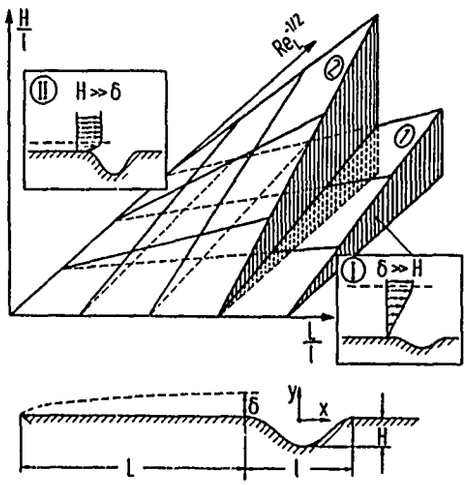


Figure 3a. Three-Parameter Field of Flow Past a Dent in a Plane Wall

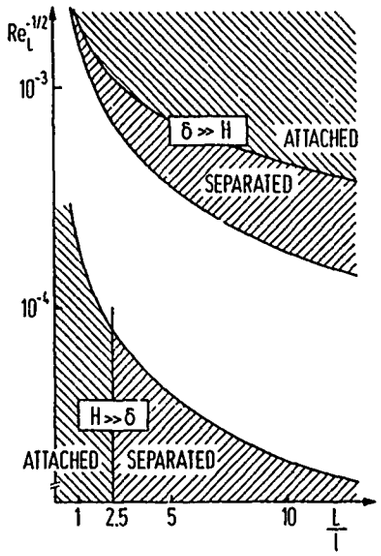


Figure 3b. Plane H/l=0,003 of Fig. 3a

2.2. Boundary Layer Thickness Large Compared to H; Case (I)

In this case the deformation of the wall and (if separation occurs) also the separation bubble are imbedded in the lower region of the oncoming boundary layer. Conventional boundary layer theory fails for two reasons:

1) When separation occurs the boundary layer exhibits a singularity at the separation point, the well known "Goldstein singularity". This can be avoided by use of an inverse boundary layer method: The displacement thickness is prescribed as a regular function which leads to a non-singular behaviour of the boundary layer as a whole even through the point of separation.

2) The perturbation of the potential outer flow by the dent is much stronger than second order effects of the boundary layer and this must be taken into account.

Therefore the usual hierarchy of inviscid outer flow and boundary layer calculation does not work: both must be solved simultaneously by an iteration process.
In doing this, the Reynolds number is kept as an interaction parameter. In a more rigorous asymptotic theory, the so-called triple deck theory (Stewartson, ref. 1), Re_L drops out of the problem thus reducing the three independent parameters by one. The scaling parameter of the triple deck is $\varepsilon = Re_L^{-1/8}$, the substructure of the flow field is the following, (ref. 1):

		dimensions		independent variables	
		stream-wise	across		
UPPER DECK	region outside the boundary layer	$O(\varepsilon^3)$	$O(\varepsilon^3)$	$\tilde{X} = \frac{x}{L\varepsilon^3}$	$\tilde{Y} = \frac{y}{L\varepsilon^3}$
MAIN DECK	continuation of the oncoming boundary layer	$O(\varepsilon^3)$	$O(\varepsilon^4)$	$X = \frac{x}{L\varepsilon^3}$	$Y = \frac{y}{L\varepsilon^4}$
LOWER DECK	region near the wall viscous, rotational	$O(\varepsilon^3)$	$O(\varepsilon^5)$	$\bar{X} = \frac{x}{L\varepsilon^3}\lambda^{5/4}$	$\bar{Y} = \frac{y}{L\varepsilon^5}\lambda^{3/4}$

λ = 0,332 in this case

Dependent variables are correspondingly scaled. The boundary layer equations are solved in the lower deck with an inverse method to avoid the Goldstein singularity; the boundary conditions come from the upper deck as a consequence of the interaction process. The outer potential flow in the upper deck can be treated by linearized theory (thin airfoil theory). It should be pointed out that each triple deck solution covers an infinite number of solutions in the three-parameter field of Fig. 3a. As a consequence of the triple deck scaling the two parameters

$$\text{(i)}\quad \frac{H}{l}\,Re_L^{1/4} \quad ; \quad \text{(ii)}\quad \frac{L}{l}\,Re_L^{-3/8}$$

cover the whole field of solutions of region (I) in Fig. 3a.

In Fig. 4a the areas of attached and separated flow are marked. Fig. 4b shows the details of one attached flow example (point A in Fig. 4a); Fig. 4c shows the example of separated flow (point B in Fig. 4a). The broken lines in Fig. 4b apply to the same flow treated with a conventional direct boundary layer method (pressure prescribed from potential flow) without taking interaction into account. Separation occurs and the Goldstein singularity marks the end of the calculation.

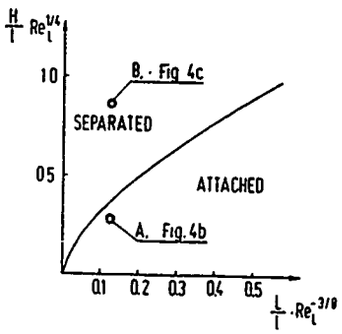
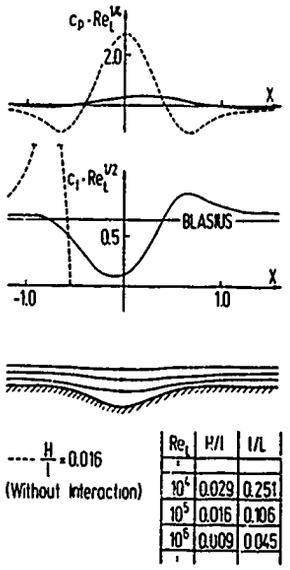
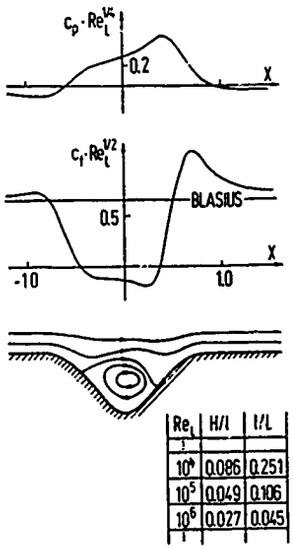


Figure 4a. Boundary Between Attached and Separated Laminar Flow Past a Dent



Re_l	H/l	l/L
10^4	0.029	0.251
10^5	0.016	0.106
10^6	0.009	0.045

Fig. 4b. Attached Flow Point A in Fig.4a



Re_l	H/l	l/L
10^4	0.086	0.251
10^5	0.049	0.106
10^6	0.027	0.045

Fig. 4c. Separated Flow Point B in Fig.4a

2.3. Boundary Layer Thickness Small Compared to H; Case (II)

In this case the small oncoming boundary layer will separate as a whole and will be continued as a free shear layer still small compared to H. Two main problems arise:

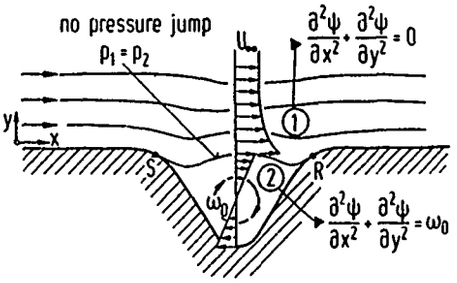
1) How to describe the flow near the point of separation?
2) What kind of interaction occurs between the separation bubble and the potential outer flow?

The shear layer leaving the wall is thin in an asymptotic sense. Thus, as the Reynolds-number goes to infinity, this free layer becomes a singular surface with a finite jump of velocity across it. The shape of this singular surface which separates the bubble from the outer potential flow must be known before the inviscid outer flow can be calculated. To start a boundary layer calculation at some point upstream of the dent the inviscid solution for the potential outer flow must be known. As soon as separation occurs this solution is no longer unique as it is with attached flow because the shape of the dividing

streamline is not known a priori.

It is obvious that information about the dividing streamline must come from modelling the flow inside the separation bubble.

As a first term of an asymptotic expansion of the flow field the approach of G.K. Batchelor (ref. 2) seems quite promising. He suggests constant vorticity inside the closed bubble. This model is physically reasonable and when adapted to the dent problem gives the flow picture in Fig. 5.



free parameters

1) vorticity ω_0
2) location of point S

Figure 5. Inviscid Flow Structure After G.K. Batchelor

There are two inviscid flow regimes: One regime outside the separation bubble with zero vorticity governd by the Laplace equation, and the separation bubble itself governed by the Poisson equation with a constant but nonzero right hand side. A velocity distribution is sketched with the jump across the dividing streamline. Across this line the pressure condition holds; that is the pressure is the same on both sides though it varies of course along this zero-streamline.

Free parameters in the model are:
(1) the constant vorticity ω_o , (2) the location of the separation point S.

A detailed study of the flow in the region around the separation point S fixes one parameter. As suggested by V.V. Sychev (ref. 3) and worked out by F.T. Smith (ref. 4) triple deck theory describes separation as a non-singular process of strong viscous-inviscid interaction. There is no adverse pressure gradient upstream of the separation point except in a region of $O(Re_L^{-1/16})$. According to this the free streamline leaves the surface with definite powers of x: $x^{3/2}$ for $Re_L^{-1} \to 0$; $x^{5/2}$ for $Re_L^{-1} = 0$. As a consequence of this, the pressure gradient ahead of separation (for $x \to S^-$) is $\sim(-x)^{-1/2}$ and is $\sim(-x)^{1/2}$ respectively as Fig. 6 shows. From this a condition for the validity of the Batchelor model as a first term of an asymptotic expansion arises: the pressure gradient at S^- must be zero; that is the free streamline must leave the surface with $x^{5/2}$. Unfortunately no combination of the two parameters, ω_o and location of S, can be found that gives $dc_p/dx = 0$ at S^-. Fig. 7 shows variations of both parameters.

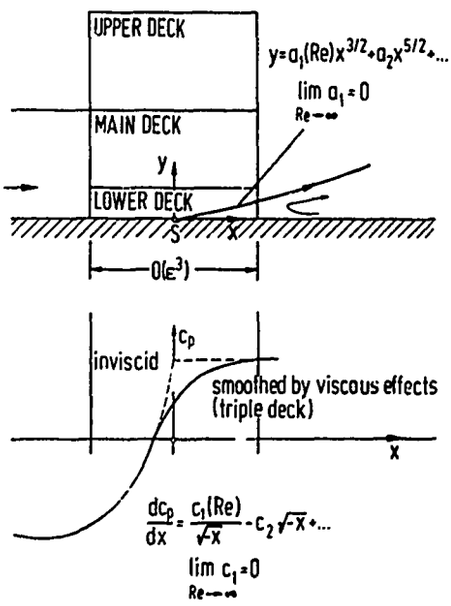


Figure 6. Triple Deck Structure Around the Separation Point S

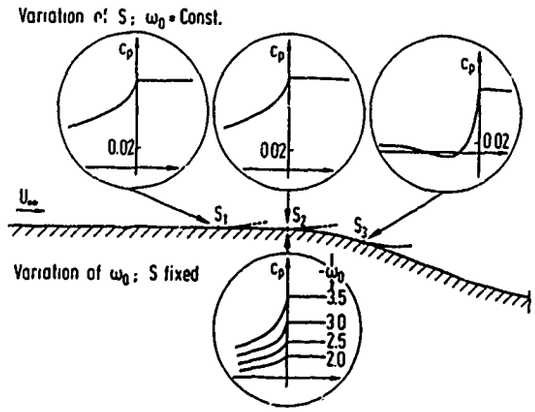


Figure 7. Pressure Distribution Around the Separation Point

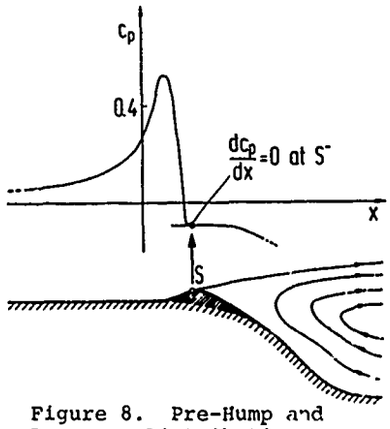


Figure 8. Pre-Hump and Pressure Distribution

A more detailed study shows that the zero-pressure gradient condition can only be fulfilled if the pressure at some point upstream of separation is at a higher level than c_p at S^-. In this sense the Batchelor model fails for the simple dent in the plane wall.

To form an example that works in this sense, a "pre-hump" has been added to the simple dent as shown in Fig. 8. The effect of this is to retard the oncoming flow. This pressure comes down from a higher level with $dc_p/dx = 0$ at S^- for a proper choice of ω_o and location of S. Within the separation bubble a vortex core with constant vorticity ω_o creates an internal circulating boundary layer which in the lower part follows the wall and above the vortex core is part of the free shear layer. This circulating boundary layer must be periodic, a condition which fixes the second parameter, ω_o for example. Here a contradiction arises:

(i) The Batchelor model leads to a finite vorticity within the separation bubble in the limit $Re_L^{-1} = 0$ from physical arguments.

(ii) Finite vorticity inside the separation bubble always leads to secondary separations of the internal circulating boundary layer. As a consequence of the two inner stagnation points (at S and R in Fig. 5) fluid in the inner boundary layer is brought to rest which inevitably leads to (secondary) separation. This exempts the circulating boundary layer from a periodic behaviour. The constant vorticity ω_o therefore should either be $O(Re_L^{-\alpha})$, $\alpha > 0$ or $\omega_o = 0$ either of which contradicts (1).

Thus we conclude that the Batchelor model with $\omega_o \neq 0$ at the limit $Re_L^{-1} = 0$ is inadequate as a first term of an asymptotic expansion of the flow field. The way out of this dilemma is to set $\omega_o = 0$ for $Re_L^{-1} = 0$ and that is what we suggest: the first term of an asymptotic expansion should be the deadwater separation area with a streamline leaving the surface with a power of x larger than 3/2, i.e. $x^{5/2}$ for the dent with a pre-hump. Fig. 9 shows the deadwater region with constant pressure, the value of which is simply $c_p = 0$ for the dent alone, or the constant non-zero value comes out of the calculation for the dent with a pre-hump. Nonzero flow velocities inside the separation bubble are effects of higher order in the asymptotic expansion.

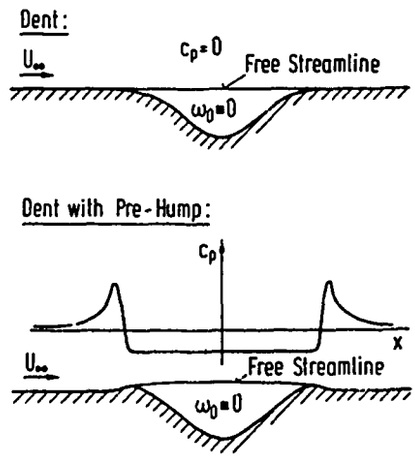


Figure 9. Deadwater Regions

3. TURBULENT SEPARATION BUBBLES WITH FIXED SEPARATION POINT (SHARP EDGE)

3.1. Backward Facing Step

As a typical example for a turbulent separated region of finite length the incompressible turbulent flow past a backward facing step is considered. It is assumed that the thickness δ_2 of the oncoming boundary layer is small compared to the step height($\delta_2/H<1$). For one particular example ($\delta_2(0)/H = 0{,}11$) the distributions of wall pressure and boundary layer characteristics are shown in Fig. 10. Due to the step and the separation bubble the pressure is not constant along the wall, but shows a decrease in front of the step and beyond reattachment. The upstream effect of the separation region is not included in the

classical boundary layer theory and hence follows from a strong mutual interaction between the separation bubble geometry and the outer flow. Deviations from flat plate occur in the region forty step heights in front of the step to about fifty step heights beyond the step. The additional drag of the step compared to the flat plate friction drag is not a constant but dependent on the length of the plate beyond the step. Only the pressure drag characterized by the dimensionless base pressure coefficient c_{pB} is a constant. It should be noted that the displacement thickness far downstream of the step is larger than the displacement thickness of the undisturbed flat plate by a constant value $\Delta\delta_1$, which can be interpreted as an effective reduction of the step height. As a consequence, the pressure distribution will be determined by the effective step height

$$H_e = H - \Delta\delta_1 \qquad (2)$$

which again shows the strong mutual interaction between the shear layers and the outer flow.

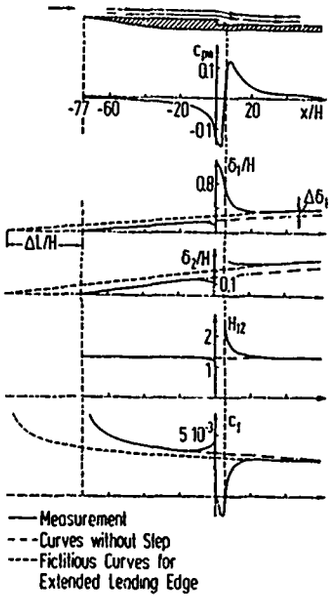


Figure 10. Wall Pressure and Boundary Layer Characteristics at a Backward Facing Step ($Re_L = 2{,}0\cdot10^6$; $Re_H = 2{,}6\cdot10^4$)

A prediction method for flows past backward facing steps has been developed by using the following assumptions:

a) From the available experiments it could be concluded that there exists one universal displacement line for all backward facing step flows when the x-coordinate is bases on the reattachment length x_R and the height based on the effective step height H_e .

b) There are universal displacement line contours on which the corresponding pressure distribution can be calculated by means of potential theory methods. In particular, the pressure coefficients at separation c_{pB} and at reattachment c_{pR} can be determined. In Fig. 11 these values are shown as functions of H_e/x_R and H_{2e}/H_{1e} , where the latter parameter is the effective aspect ratio of an equivalent two-dimensional channel with a sudden enlargement of ratio H_2/H_1 . The single backward facing step correspondends to the limiting case $H_{2e}/H_{1e} \to 1$.

c) Following a concept of J.F. Nash (ref. 5) it was assumed that the free shear layer between separation and reattachment behaves like a free shear layer in constant pressure where the velocity jumps from U_B (outer flow velocity at station x = 0) to zero (separated region). At the separation point the boundary-layer velocity profile was replaced by a free shear-layer profile having the same displacement and momentum thickness. The further assumption was made that the pressure at the reattachment point is equal to the total pressure of the dividing streamline at that point. Due to

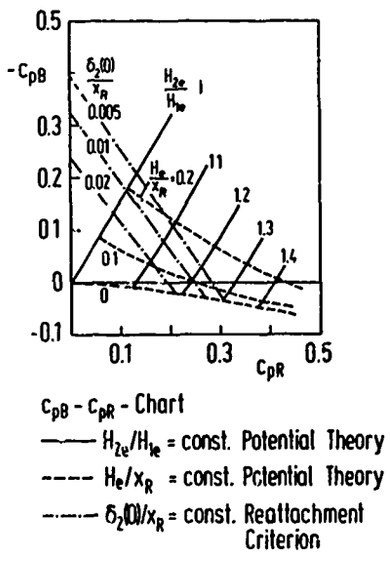


Figure 11. $c_{pB} - c_{pR}$ Chart for Enlargement and Step

these assumptions the momentum thickness $\delta_2(0)$ of the oncoming boundary layer at the step is given by

$$\frac{\delta_2(0)}{x_R} = 0{,}027 \quad \frac{0{,}334 - c_{pR} + 0{,}666\ c_{pB}}{c_{pR} - c_{pB}} \tag{3}$$

In the $c_{pB} - c_{pR}$ - chart (Fig. 11) the curves $\delta_2(0)/x_R = \text{const}$ are straight lines as shown in Fig. 11.

d) According to the characteristics of the free shear layer the increase of displacement thickness is proportional to the separation bubble length:

$$\Delta\delta_1 = 0{,}013\ x_R \tag{4}$$

where the numerical factor was found from experiments.
Combining Eqns.(2) and (4) leads to

$$H = H_e\ (1 + 0{,}013\ \frac{x_R}{H_e}) \tag{5}$$

i.e. the ratio H/H_e can be determined in Fig. 11.

e) The ratio $\delta_2(0)/\delta_{2s}$ can be found by comparing two simple boundary layer calculations one with constant pressure and one with the given pressure distribution. Using a power law formula for the momentum thickness leads in a first approximation to

$$\frac{\delta_2(0)}{\delta_{2s}} = 1 + 1{,}5\ c_{pB} \tag{6}$$

where δ_{2s} is the momentum thickness of the oncoming boundary layer, which would exist at the location of the step in the absence of the step.

The results of the prediction method described have been compared with experiments as shown in Fig. 12. The absolute value of the base pressure is reduced whereas the reattachment length is increased due to boundary layer thickness. Comparison with experiments of different authors shows reasonable agreement.

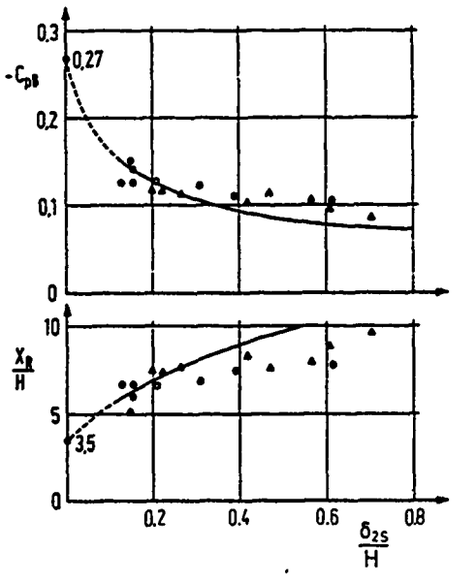


Figure 12. Base Pressure and Reattachment Length for Backward Facing Step

3.2. Effect of Suction at the Step

The preceding analysis can be easily extended to cases where there is a suction slot in the corner of the step, Fig. 13. A certain layer of height h of the free stream will finally be sucked into the slot. As a consequence the separation line and the dividing streamline are different. Results of a modified analysis, where these facts are taken into account, are shown in Fig. 13 for a particular value δ_{2s}/H. Comparison with experiments by Arnold (ref. 6) are also made in Fig. 13.

3.3. Sudden Enlargements

The analysis can also be extended to sudden enlargements of two-dimensional channels. When $H_{12} = \delta_1/\delta_2$ is the shape parameter of the oncoming boundary layer the area ratio of the sudden enlargement is given by

$$\frac{H_2}{H_1} = \frac{H_{2e}}{H_{1e}} + \left(\frac{H_{2e}}{H_{1e}} - 1\right)\left(0{,}013\,\frac{x_R}{H_e} - 2\,\frac{H_{12}\,\delta_{2s}}{H_1}\right) \qquad (7)$$

From Fig. 11 it can be seen that the analysis leads to results only for area ratios up to about $H_2/H_1 = 1{,}3$. For higher area ratios the flow might become unsymmetrical (ref. 7), whereas in the analysis presented symmetrical flow was assumed. The results of the analysis for $\delta_{2s}/H = 0{,}1$ are shown in Fig. 14.

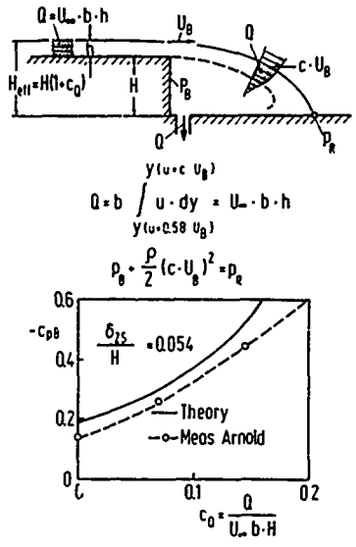


Figure 13. Backward Facing Step with Suction

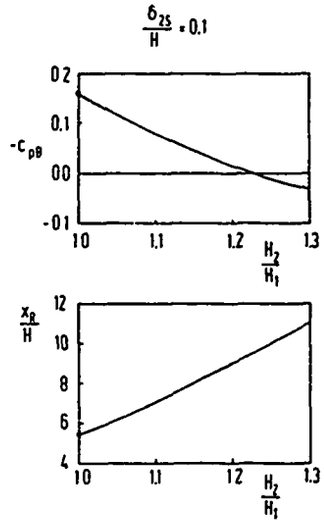


Figure 14. Base Pressure and Reattachment Length for Sudden Enlargement

Although no experimental data are available for direct comparison (the available experiments show much higher ratios $\delta_{2s}/H > 0{,}2$) the following tendencies can be found in agreement with experiments. Increasing the area ratio leads to longer separation bubbles (see ref. 8) and to decreasing absolute values of the base pressure. The loss coefficient (dimensionless dissipation) as a function of area ratio is shown in Fig. 15 and compared with the classical Carnot formula for sudden enlargements. It can be seen that the Carnot formula fails for $H_1/H_2 \to 0$ (single backward facing step) and that prediction could be improved considerably by the present analysis.

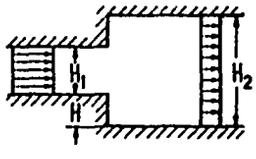
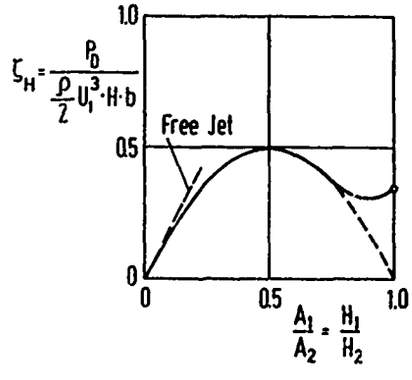


Figure 15. Friction Coefficient for Sudden Enlargement



4. TURBULENT FLOW ON CONTINUOUS WALLS WITHOUT AND WITH SEPARATION

4.1 Rounded Backward Facing Step

Many flows exist where turbulent boundary layers are exposed to strong adverse pressure gradients and in which the flow remains attached only if the strong viscous-inviscid interaction is taken into account. Typical examples are the flows past rounded backward facing steps as shown in Fig. 16. The geometry is a flat plate of length L followed by a rounded backward facing step of height H and length l. The contour is a polynomial of fifth degree such that the curvature of the wall contour is continuous everywhere. Potential flow theory would lead to a pressure distribution shown by the dotted curve. The turbulent boundary layer under such a pressure distribution would separate, as can be seen from the dotted shear stress curve. The measurements show a pressure distribution quite different from the one found by potential theory. In particular, the measured pressure gradients are so much smaller that the turbulent boundary does not separate. The experimental pressure distribution can be determined theoretically when the displacement effect of the boundary layer is taken into account. In this particular example, the fictitious contour (contour plus displacement thickness) is quite different from the geometrical contour, and so are the corresponding pressure distributions. The consequence is that one pressure distribution leads to boundary layer separation whereas the other one does not. In order to get the correct results the displacement effect has to be taker into account by an iteration procedure. A boundary layer separation during the iteration does not mean necessarily that the final result will show separation. The strategy of the iteration procedure has to be chosen such that in every iteration step separation is avoided if possible. On the boundary between separation and no separation (incipient separation), the wall shear stress curve just touches the abscissa.

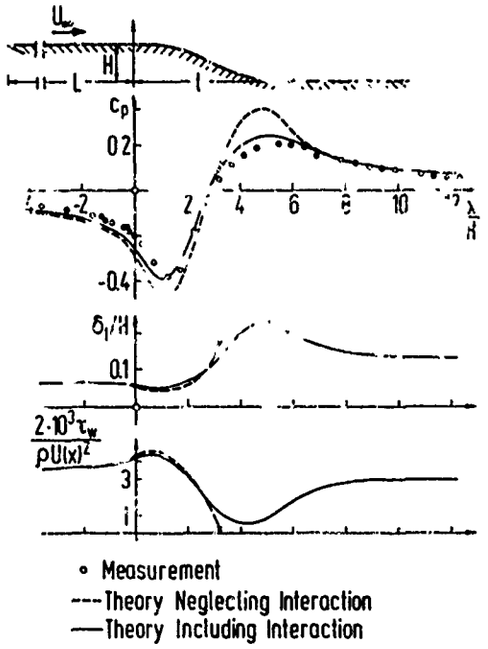


Figure 16. Viscous-Inviscid Interaction of the Turbulent Flow Past a Rounded Backward Facing Step
$L/l = 5{,}3$; $H/l = 0{,}17$; $Re_l = 1{,}6\cdot10^6$; $Re_H = 5\cdot10^4$

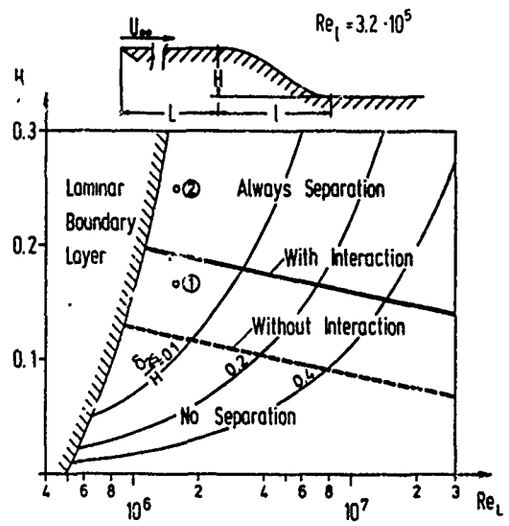


Figure 17. Boundary Between Attached and Separated Turbulent Flow Past a Backward Facing Step

In Fig. 17 this boundary of incipient separation is shown for flows past rounded backward facing steps. As can be seen the boundary of incipient separation is shifted drastically to larger step heights if viscous-inviscid interaction is taken into account. By neglecting the interaction, separation would be

predicted for almost half the step height to critical step height ratios. There is obviously good agreement of the theoretical result with experiment, because measurements of configuration ② showed separation, whereas in configuration ① , which corresponds to the example shown in Fig. 16, no separation occurs. According to Fig. 17 separation may appear when the step height and/or the thickness of the oncoming boundary layer are increased. The smaller the thickness of the oncoming boundary layer, the larger the critical step height of incipient separation.

4.2. Diffusors

The procedure described was applied to predict incipient separation in subsonic diffusors. That is the flow regime was divided into boundary layer and rotational or irrotational outer flow depending on whether the inlet velocity profile of the diffusor was rotational or not. For $l/H_1 \gg 1$, see Fig. 2e, a simple formula was adapted to calculate the pressure distribution of irrotational outer flow along the wall contour:

$$c_{pK} = \frac{p_K^* - \bar{p}_{-\infty}^*}{\frac{\rho}{2}\bar{w}_{-\infty}^{*2}} = 1 - \left(\frac{H_1/2}{y_K}\right)^2 \left[1 + \frac{2}{3} y_K y_K'' - \frac{1}{3} y_K'^2 + \frac{4}{9} y_K^2 y_K' y_K'''\right] \qquad (8)$$

$\bar{p}_{-\infty}^*$, $\bar{w}_{-\infty}^*$ are pressure and velocity values a distance H_1 upstream of the diffusor entrance, $y_K(x)$ is the fictitious diffusor geometry where dashes refer to differentiation with respect to x. Eq.(8) is based on a quadratic Ansatz for the pressure profile perpendicular to the diffusor axis.

Interaction was taken into account as described in Section 4.1. By means of this procedure critical values of H_2/H_1 could be calculated in very good agreement with experiment (ref. 9). Line a-a in Fig. 18 marks the onset of incipient separation. In the theoretical prediction of this line necessarily interaction has to be taken into account. Calculations of this line without interaction gives noticeable deviations from line a-a, as Fig. 18 shows.

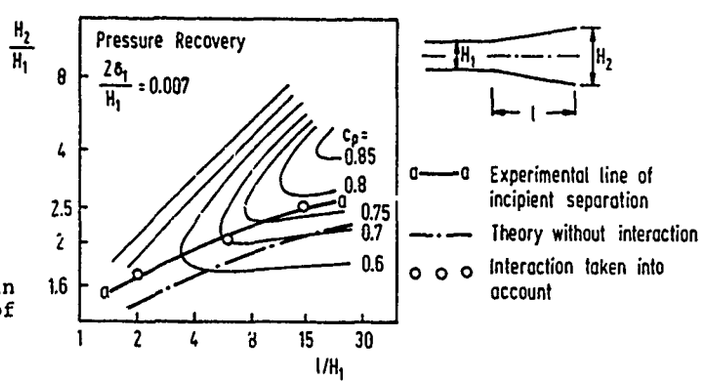


Figure 18. Pressure Recovery in Diffusors; Effect of Viscous-Inviscid Interaction

Further important results of these calculations are:

- Viscous-inviscid interaction obviously decreases the effect of expansion in diffusors with free discharge. The diffusor can be continued in a pipe or channel which numerically is much easier to handle than the case of free discharge.
- If interaction is not taken into account, wall curvature in the entrance region of the diffusor has a strong influence, extremely small radii produce pressure peakes which lead to early separation. Viscous-inviscid interaction smooths the effective wall contour and thus effectively eliminates the influence of a change in the local wall contour.
- In accordance with experimental observations the influence of the Reynolds number on

the critical value of H_2/H_1 for example is small.

It is intended to extend the theoretical approach including:

- inhomogeneous inlet velocity profiles
- small areas of separated flow

4.3. Turbulent Separation Bubbles of Finite Length

In principle, a prediction method for turbulent flows including separated regions would work the same way as the method described in Section 4.1. The main additional difficulty arises in the modelling of the separated region. One connection between the displacement line and the pressure distribution is given, as before, by the inviscid potential theory. The other connection is supplied by the "boundary layer" calculation of the viscous part of the flow. In case of flows with separated regions this "boundary-layer calculation" is divided into three parts, see Fig. 19, namely the region in front of the separation bubble, the region of the separation bubble, and the region beyond the separation bubble. The 1st and 3rd region can be covered by ordinary prediction methods for attached turbulent boundary layers. The main problem left is a prediction method for calculating the displacement distribution within the bubble region and the bubble length. Analogous to the separation bubbles in Section 3 the following assumptions are made that:

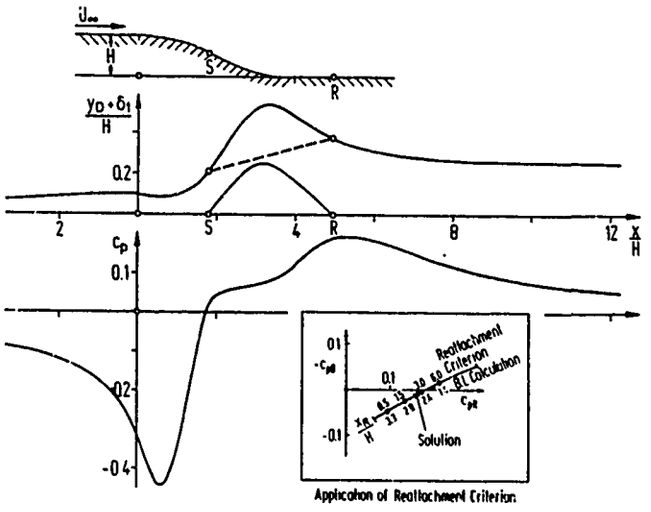


Figure 19. Viscous-Inviscid Interaction for Turbulent Flows with Separated Regions of Finite Length (H/l = 0,25)

a) The geometry of the bubble (dividing streamline) is universal if properly scaled. This geometry is shown in Fig. 19, taken from experiment. The ratio of height to length of the bubble is assumed to be a constant, namely 0,08. This is in agreement with the results in ref. 10 .

b) The free shear layer between the separated region and the inviscid outer flow is approximated by the simple shear layer solution of a free jet boundary where the displacement thickness increases proportional to the coordinate, the gradient being approximately $d\delta_1/dx = 0{,}05$.

c) The location of the reattachment point and, hence, the bubble length are determined by using the same reattachment criterion as in Eq.(3), in which it is assumed that the total pressure on the dividing streamline is constant near reattachment.

The final result of the iteration process is reached when the distributions of pressure and displacement thickness generate each other, by inviscid theory as well as by "boundary layer" calculation including modelling of the separated region. Application of the reattachment criterion Eq.(3) gives the correct solution of the problem, which is shown in the insert of Fig. 19 (example ② in Fig. 17).

More sophisticated models of the separated region are now under consideration. This procedure is being applied to diffusors in order to calculate optimal diffusors which have optimum efficiency for a given ratio of length to inlet width or for a given area ratio.

5. REFERENCES

1. Stewartson, K.: Multistructured boundary layers on flat plates and related bodies. Adv. Appl. Mech. 14 (1974), 145-239

2. Batchelor, G.V.: On steady laminar flow with closed streamlines at large Reynolds number. JFM 1 (1956), 177-190

3. Sychev, V.V.: Concerning laminar separation. Jzv. Akad. SSSR, Mekh, Zhidk Gaza 3, 47-59 (1972)

4. Smith, F.T.: The laminar separation of an incompressible fluid streaming past a smooth surface. Proc. R. Soc. Lond. A, 356, 443-463 (1977)

5. Nash, J.F.: An analysis of two-dimensional turbulent base flow, including the effect of the approaching boundary layer. ARC R&M 3344, July 1962

6. Arncld, K.O.: Untersuchungen über die Auftriebserhöhung eines Klappenflügels durch Schlitzabsaugung. Z.Flugwiss. 15 (1967), 37-56

7. Abbott, D.E., Kline, S.J.: Experimental investigation of subsonic turbulent flow over single and double backward facing steps. Transactions of the ASME, J. Basic Engg. Vol. 84, 317

8. Kuehn, E.M.: Effects of adverse pressure gradient on the incompressible reattaching flow over a rearward-facing step. AIAA Journal, Vol. 18 (1980), 343-344

9. Reneau, L.R., Johnston, J.P., Kline, S.J.: Performance and design of straight, two-dimensional diffusors. Journal of Basic Engg., Ser. D 89 (1967), 141-150

10. Briley, W.R., McDonald, H.: Numerical Prediction of Inkompressible Separation Bubbles. J. Fluid Mech. 69 (1975), 4, 631-656

TWO-DIMENSIONAL SEPARATED FLOW: EXPERIMENT AND DISCRETE VORTEX DYNAMICS SIMULATION

W. T. Ashurst
Sandia National Laboratories
Livermore, CA 94550, U.S.A.

F. Durst
C. Tropea
SFB80, University of Karlsruhe
D-7500 Karlsruhe, FRG

Summary

This paper describes an experimental and theoretical investigation of turbulent flow over a two-dimensional backward-facing step. A Laser Doppler Anemometer (LDA) was used to measure the time-averaged flow properties and their fluctuations in an open-water channel test section. Experimental results include the flow and normal-direction velocities (mean and root mean square), Reynolds shear stress, and separated-flow length. The variation of the reattachment location was also obtained as a function of Reynolds number and flow expansion ratio. Flow visualization was employed to gain further understanding of the flow structure. The paper also describes numerical results obtained with a method known as discrete vortex dynamics. This method provides a Lagrangian description of fluid flow in which the distribution of vorticity is discretized and its time-dependent motion is calculated. Thus, unsteady flow phenomena can be included within this time-dependent computational method. From comparison of the experimental and numerical results we conclude that, while qualitative agreement has been obtained, for close quantitative agreement with separated-flow data, a purely two-dimensional calculation requires a dissipation model. This model must provide the dissipation caused by small-scale three-dimensional vorticity.

Nomenclature

- h = upstream water height
- H = step height (=40 mm)
- L = numerical reference length
- Re_H = Reynolds number ($= U_o H/\nu$)
- U_o = freestream reference velocity
- $\sqrt{u^2}$ = root-mean-square velocity in longitudinal direction
- U = mean velocity in longitudinal direction
- $\sqrt{v^2}$ = root-mean-square velocity in normal direction
- $-\overline{uv}$ = Reynolds shear stress
- V = mean velocity in normal direction
- X_R = mean reattachment location
- x = longitudinal coordinate
- y = normal coordinate
- z = spanwise coordinate
- $\hat{z}$ = spanwise coordinate normalized to channel half-width
- ν = kinematic viscosity
- ρ = density
- σ = standard deviation of random walk
- ω = vorticity

Introduction

Turbulent separated flows occur in nature and in many engineering flow situations. They are generally caused by adverse pressure gradients generated by changes in the geometry of the flow boundaries. Such changes result in highly turbulent, recirculating flows with high pressure losses and augmented heat and mass-transfer rates. Many of these properties of separated flows are extensively utilized in engineering equipment irrespective of the fact that little is known about the details of the flow inside the separation zone. The acquisition of such knowledge has so far been hampered by the lack

of suitable measuring techniques, and it is only recently that advances in laser-Doppler anemometry have resulted in instruments suitable to study highly turbulent, recirculating flows.

The first part of this paper describes an experimental investigation of the flow over a backward-facing step in the flow regime designated as fully turbulent. The step was located in a two-dimensional open-channel flow. Laser-Doppler measurements and flow visualization studies were carried out to obtain insight into the physics of backward-facing step flows. Accurate measurements of the mean and root-mean-square velocity components, the Reynolds shear stress, and the reattachment location were obtained. Considerable effort was spent to create a flow with nominally two-dimensional time-averaged properties in the mid-plane of the test section, and to insure that this two-dimensional flow extended beyond the separated flow region. Two-dimensional behavior was also maintained at the upstream and downstream flow boundaries. Despite all this experimental care, the region directly behind the backward-facing step exhibited three-dimensional flow, as observed in the dye injection experiments. However, the extensive measurements that have been obtained will be valuable in developing and testing prediction methods for two-dimensional, separated, turbulent flow.

The second part of this paper concerns the numerical simulation of the backward-facing step flow using the method of discrete vortex dynamics. This method is a Lagrangian description of fluid flow in which the governing equation of motion is obtained from the vector curl of the Navier-Stokes equation. These calculations are purely two-dimensional, and the lack of fluctuations in the third dimension appears to cause disagreement between the calculations and experimental results. A previous simulation of the planar mixing layer did show the ability of the vortex method to reproduce the coherent flow structure experimentally found in turbulent mixing layers [1]. It was also found that the measured Reynolds shear stress could be predicted if the vortex short-range behavior includes diffusion due to molecular viscosity. Computations have now been extended to the experimentally studied backward-facing step flow. The numerical results are compared with the experimental data. Existing discrepancies are pointed out and reasons for them are given. Conclusions are given with respect to the modification required of the two-dimensional discrete vortex dynamics method for predicting turbulent separated flows.

Experimental Investigation

The two-dimensional backward-facing step is a simple geometry which can produce a complex turbulent flow. Therefore, a careful experimental investigation will provide a basis for developing flow prediction methods. Such experiments have been done at the University of Karlsruhe, and this section describes the experimental apparatus and measuring technique. The experimental results and observations are also given.

The experiments were carried out in a 600-mm-wide open-water channel with major dimensions given in Figure 1. The test section was situated near the downstream end of the channel and consisted of a second floor with a leading edge for initiating a new floor boundary layer. A raised backward-facing step 40 mm high was placed at a downstream position from the leading edge such that the boundary layer at separation would be fully turbulent for all Reynolds numbers investigated. Considerable effort was expended in placing flow straighteners and screens upstream from the test section so that a nominally two-dimensional approach flow in the mean properties was insured. The success of the flow-straightening devices is shown in Figure 2, which presents spanwise profile of the mean longitudinal velocity component and its root-mean-square at five locations in the test section. These data show that the freestream turbulence is approximately three percent.

The wall boundary layer before the step edge also has spanwise uniformity and obeys the law of the wall over at least the center half of the channel. Figure 3 shows the boundary layer profile in normalized coordinates at three spanwise locations, all 2 mm upstream from the step.

Velocity was measured with a one-component forward-scatter laser-Doppler anemometer (LDA) equipped with frequency shifting. Several features of the LDA system make it one of the few devices suitable for velocity measurement in recirculating flow: 1) nonintrusiveness, 2) instantaneous velocity direction resolution, 3) single velocity component measurement without contamination from other components, 4) high spatial and temporal resolution, 5) accurate measurement in regions with very high turbulent levels, and 6) no calibration necessary (especially advantageous in the presence of temperature fluctuations.) The LDA was mounted, in the present experiment, on a cradle-type traversing carriage which straddled the water channel on rails and thus permitted three-dimensional movement of the measuring volume to almost any desired position within the flow. The measuring volume is approximately 0.25 mm in diameter and 1.5 mm long. Further details are given in reference [2].

Signals were processed with a digital processor based on a transient recorder that was developed at the University of Karlsruhe and is described in detail in reference [3]. This processing system can accurately determine the frequencies of individual Doppler bursts. Sampling procedures, as outlined by Tropea and Durst [4], ensured nonbiased estimates of the velocity. Measurement times at each point varied from one region of the flow to another, but were generally 15-20 minutes inside the recirculating zone and about 5 minutes in the potential flow region.

For a determination of the velocity component normal to the flow direction, it is necessary to measure, at each measuring point, the mean Doppler frequency and root-mean-square (RMS) values of the Doppler frequency fluctuations using three different orientation angles with respect to the flow direction (beam plane at ±30° and 0° to the channel floor). The normal direction mean and fluctuating velocities and the correlation of fluctuating velocities and the correlation of fluctuations of the two velocity components, i.e. the Reynolds shear stress, were calculated in a manner similar to that used for the decomposition of time-averaged inclined hotwire signals. The laser beams were not parallel to the channel floor, and thus it was not possible to traverse all the way to the floor for all the turbulence quantities of interest.

Detailed measurements of the mean and fluctuations of the two velocity components are given in reference [2]. Examples are presented in Figure 4 for flow conditions of Reynolds number $Re_H = 12{,}000$ ($Re_H = U_0 H/\nu$) and an expansion ratio $(H + h)/h$ equal to 1.14, where U_0 is the mean free stream velocity, H the step height, and h is the upstream water height. In the figures, velocities have been normalized by U_0 and lengths by step-height H. Figure 4a shows the distribution of the mean longitudinal velocity component at several equally spaced stations downstream of the step. From the mean velocity data one can deduce that the recirculation region extends over a distance of six step heights. From the mean velocity component normal to the channel floor (Figure 4b) one can see that the mean flow at the step edge is upward, indicating an upstream influence of the separating flow.

The RMS profiles of the two velocity components (Figures 4c and 4d) have similar distributions throughout the entire flow field, both in shape and magnitude. The maximum values reached in these normal stress terms compare favorably with similar data taken by independent workers [5] and [6].

The Reynolds shear stress, Figure 4e, reaches a maximum value about midway between the step and mean reattachment location. Note that the locations of maximum Reynolds shear stress and maximum mean velocity gradient do not coincide.

Data were also taken at several stations far downstream from the reattachment location, and the mean velocity for the reattached boundary layer is presented in Figure 5 in "log-law" coordinates. Near the y^+ of 100 there is a small dip away from the log law evident in all these profiles and indicates that the boundary layer has not yet recovered to its unperturbed state, even after 35 step heights downstream of the step. This result is in good agreement with the findings of Bradshaw and Wong [7]. The Reynolds shear stress also shows a tendency to remain at high levels in this downstream region. The boundary layer departure from the log law is thought to be caused by remnants of vortex structures which were created upstream in the free shear layer. Evidence for this interpretation comes from flow visualization studies.

Flow visualization was achieved by injecting small amounts of dye into the boundary layer one step height upstream of the step edge. Photographs were taken from above and from the side of the step to record the shear layer development after separation. Typical results of these dye studies are shown in Figure 6 in which traces of the photographs are given for several different Reynolds numbers. The size of the individual vortices at first increases with Reynolds number and then decreases until, at the highest Reynolds number, no particular large structure in the flow is recognizable. The changes in the sizes of the vortex structures are strongly coupled to changes in the measured separation length. Figure 7 presents the measured variation of separation length with Reynolds number and expansion ratio.

The Reynolds number at which the minimum reattachment length occurs corresponds closely to the largest observed vortex structure in the shear layer. As the structures decrease in scale, the reattachment length approaches a fully turbulent value which, from previous studies, is known to be Reynolds-number independent [8]. Because of the apparent influence of large scale structures on this flow, the vortex dynamics method of computation, which can generate structures very similar to those observed, appears to be an appropriate numerical technique for simulating this flow.

Finally, there were observations from the flow visualization study which suggested that there was augmented three-dimensional activity in the flow region immediately downstream of the step. Viewed from above the step, a portion of the dye injected into the shear layer was seen to enter the region of the secondary vortex next to the step face and then spread symmetrically away from the centerline towards the wall boundaries. This spreading, however, was confined to a zone within about one step height downstream of the step, and the dye remained there, apparently mixing little with the primary separation zone. It was also found that only in this region did the velocity vector, as calculated from the mean velocity components, deviate from the streamline tangent formed by integrating the U velocity profile from the floor. It appears, therefore, that within the first downstream step height assuming two-dimensional behavior may not be appropriate.

Vortex Dynamics Method

For a discrete-vortex calculation, several numerical parameters must be selected: discrete time-step size, maximum vortex strength, vortex short-range behavior, and method of vortex creation at flow boundaries. Some of these have been chosen by comparing numerical simulation of a planar mixing layer with experimental results [1]. This study showed that the vortex method can reproduce the coherent flow structure found experimentally in turbulent mixing layers. Also, the measured Reynolds shear stress can be predicted if

the vortex short-range behavior includes diffusion due to molecular viscosity. Since the application of the discrete vortex dynamics method is somewhat new, its computer implementation will be briefly described.

The discrete vortex dynamics method is a Lagrangian description of fluid flow. Vorticity is kinematically defined as the vector curl of velocity, $\bar{\omega} = \bar{\nabla} \times \bar{u}$. In the vortex dynamics method the distribution of vorticity is discretized and the trajectory of each discrete vortex is calculated. The governing equation of motion is obtained by taking the vector curl of the Navier-Stokes equation, yielding

$$\frac{D}{Dt}\left(\frac{\bar{\omega}}{\rho}\right) = \frac{\bar{\omega}}{\rho} \cdot \nabla \bar{u} + \nu \nabla^2 \bar{\omega}$$

for constant density ρ. The symbol D/Dt is the material, or Lagrangian, derivative. The change in vorticity per unit mass is given by two terms: (a) vortex stretching and rotation, $(\bar{\omega}/\rho) \cdot \nabla \bar{u}$, and (b) vorticity diffusion by molecular viscosity, $\nu \nabla^2 \bar{\omega}$. For two-dimensional flow the vorticity vector is normal to the velocity vector and thus $\bar{\omega} \cdot \nabla \bar{u}$ is always zero. For large-Reynolds-number flows (small ν) Chorin [9] has suggested that the diffusion effect be approximated by a random walk. Each discrete vortex is given a random component of motion (at each time step) which is taken from a Gaussian distribution of random numbers. The standard deviation of the random numbers is specified by the numerical time step Δt and the kinematic viscosity ν (or Reynolds number):

$$\sigma = \sqrt{2\ \Delta t\ \nu} = L\sqrt{2\left(\frac{U\Delta t}{L}\right)\left(\frac{\nu}{UL}\right)}\ .$$

To advance the vorticity to the next time step one requires the velocity of each discrete vortex. There are two ways to determine the vortex velocity: direct vortex interaction or solution of the Poisson equation for the streamfunction. The direct interaction method is given by the Biot-Savart law, which determines the velocity at a point from a volume integral over all regions that have nonzero vorticity. Because only the discrete vortices have nonzero vorticity, each vortex velocity is given by direct interaction of all the other vortices. The calculational cost will be proportional to the number of vortex interactions, which is $(N - 1) \cdot N/2$, or $\sim N^2$, for N discrete vortices. Only the vortex locations and strengths are needed to determine the velocity field. Thus spatial resolution of the flow field is automatically treated. There is no loss of resolution due to finite mesh spacing. Of course, the core size of the discrete vortex is the lower limit of spatial resolution and the finite time step is the upper limit to resolvable frequencies.

The second way to calculate the velocity field requires a solution of a Poisson equation. Since any vector field may be described in terms of a scalar potential $\emptyset$ and a vector potential $\bar{A}$, the velocity field is written as $\bar{u} = \nabla \emptyset + \nabla \times \bar{A}$. From the kinematic relation of vorticity and velocity ($\bar{\omega} = \nabla \times \bar{u}$) the vector potential Poisson equation is obtained: $\nabla^2 \bar{A} = -\omega$; and, in 2 dimensions, $\nabla^2 A_z = -\omega_z$. Thus the velocity is given as $\bar{u} = \nabla \times A_z$ where A_z is the stream function. Calculational cost of the Poisson solution is proportional to M log M, where M is the number of mesh points. The cost of putting the discrete vorticity onto the mesh and finding the velocity from the streamfunction will be proportional to N, the number of vortices. The cost of this method is M log M + N; and for large N, this method will be faster than the direct method which cost N^2.

However, the discrete numerical approximation of ∇^2 does not produce the point vortex velocity field. Instead of an infinite velocity at the vortex location with a r^{-1} decay (where r is the distance from the vortex) the velocity is zero at the vortex location, increases with r until a maximum is reached, and then decays. The r^{-1} behavior is achieved only when r is large compared with the mesh spacing. The short-range velocity is also nonisotropic. These nonphysical, numerical effects are removed by artificially expanding the vorticity to cover many mesh cells when the vorticity distribution is determined for the Poisson equation [10]. This spreading of vorticity results in an isotropic velocity field which approaches the r^{-1} behavior within a few mesh cells (three cells in this work). The incorrect velocity behavior can be replaced with the desired behavior for all interactions that occur within the short-range region. During the creation of the vorticity distribution a linked list is made so that only those vortices that are near each other must be examined for the velocity correction. If all the pairs were examined, the cost would become the same as for the direct method, i.e., proportional to N^2.

The choice of which method to use for the velocity determination also depends on the flow problem being considered. For exterior flows (e.g., a bluff body shedding vorticity into a wake) the direct method allows easy treatment of the outer boundary conditions. For interior flows (e.g., a channel with flow separation) the outer boundary conditions can be included in the Poisson solution. In addition, the solid wall boundaries act as sources and sinks of vorticity when the condition of zero relative velocity is enforced. Thus for some exterior flows the direct method might be selected where as for interior flows the Poisson method is faster.

A previous study treated both symmetric and asymmetric planar sudden expansion flows [11]. The numerical simulation reproduced the asymmetric flow which can occur within the symmetric sudden-expansion geometry. The calculated time-average unequal separated flow lengths also agreed well with experimental data. This study concentrates upon the single backward-facing step flow and presents detailed comparisions with the velocity profiles already presented in Figure 4. The geometry is a channel with a step increase in flow

cross-sectional area, which ensures that flow separation occurs at a fixed location. The boundary layer before the step is used as the calculation entrance boundary condition. The boundary layer vorticity is discretized, and this flux of vorticity is added at each time step. New discrete vorticity is also introduced along the channel side walls at each time step so that a no-slip velocity boundary condition is maintained [12]. In a calculation of flow over a backward facing step by Clements and Maull [13] the freestream vorticity was removed when the vortices reached a certain distance from the wall. They found that this artificial viscous wall had the most realistic comparison with experiment when the removal distance was 0.125 step heights. However, their wall model does not entrain the wall boundary layer into the recirculating flow region.

For convenience at this time, the confined channel flow program has been used to calculate the open water channel flow. The free-surface boundary condition has been approximated as an inviscid rigid wall instead of the correct condition of constant pressure with variable height. In an open channel, as the velocity decreases because of the expanding flow area, the surface rises in order to conserve energy at constant pressure. An estimate of the surface height change can be obtained by analysis of an inviscid flow over a smooth step. Assume a smooth bottom shape with slope $\frac{db}{dx}$ such that over a long distance the change in bottom elevation equals the step height. In order to conserve energy at constant pressure and flow rate (q), the free surface slope must be

$$\frac{dh}{dx} = -\frac{db}{dx}\Big/\left(\frac{gq}{u^3(x)} - 1\right)$$

where u(x) is the local average velocity and g is the acceleration of gravity. For the expansion ratios of interest the free surface will rise about 3 to 6 percent of the step height. Thus, with a constant height, the calculated flow will have a freestream velocity that will be a few percent greater than the experimental results downstream of the separated region. It is possible to incorporate a free surface with the vortex method, and preliminary work has been done by Zaroodny and Greenberg [14] for the time-dependent motion of a water wave.

Discussion of Vortex Dynamics Results

This discussion focus on how the numerical results depend upon the modelling of different sections of the flow field. It will be shown that, in a pure two-dimensional calculation, the inlet model affects the separated flow length and the Reynolds shear stress while the longitudinal normal stress is sensitive to the magnitude of the vorticity created at the viscous wall boundary. To illustrate these effects, results from many different calculations are described and some typical examples presented. The first numerical result was a computer-generated flow visualization of the vorticity motion. These movies, having qualitative agreement with experiment, showed that Lagrangian tracking of the upstream wall boundary layer vorticity combined with a vortex viscous-wall model did produce a separated recirculating flow behind the step. Observation of these movies does not reveal a precise reattachment location but indicates its inherent unsteady nature. This unsteady flow is caused by creation of large vortex structures formed in the separated free shear layer.

For quantitative comparison with experimental data, velocity mean and fluctuation values were calculated at various locations in the flow region. Figure 8 presents the calculated mean and fluctuation velocity profiles for a flow with expansion ratio of 1.33 and a Reynolds number of 12,500 ($= U_0 H/\nu$). For comparision, the experimental data at the same Reynolds number are also shown (dotted lines). The computational averaging time corresponds to about one minute of real time in the water channel and used 80 minutes of CDC 6600 time. The time-average profiles of the longitudinal velocity component, Figure 8a, show the recirculation region to be about nine step-heights long. A calculation at a small expansion ratio of 1.14 did not indicate any significant change in reattachment location. Thus, the experimental variation with expansion ratio, as shown in Figure 7, is not obtained numerically.

Both of these calculations were done with the inlet vorticity distributed over the experimental boundary layer thickness, which is 1.5 step heights. Previous calculations [11] with a single inlet vortex, corresponding to a very thin boundary layer, produced a reattachment length of approximately 7 step heights (expansion ratio of 1.33) and a reverse flow behind the step comparable to experimental values ($u \sim -0.2$). In this calculation the formation of vortex structures was enhanced and the flow structure was similar to the experimental results at an Re_H of 4,000 (Figure 6). In this situation the reattachment location appears to be determined by the two or three large vortex structures which form down stream of separation. Another possible cause for the reattachment disagreement with experiment is the lack of spanwise velocity fluctuations in these purely two-dimensional calculations. It is known that spanwise fluctuations are produced in wall boundary layers by the bending of the transverse vorticity into the streamwise vorticity component. Therefore, the separated shear layer contains a streamwise vorticity component from the upstream wall boundary layer which is not included in the two-dimensional vortex dynamics method. In order to assess the effects of streamwise vorticity an earlier calculation [11] was done which included dissipation of the transverse vorticity. The dissipation was incorporated in a uniform manner (i.e. non-physical) by reducing the circulation of each vortex by five percent per unit time. This dissipation changed the reattachment location from ten to 7 step heights downstream of the step. Hence the vortex dynamics results can produce a variation in reattachment location comparable to the experimental shift; but, as expected, the calculated results are sensitive to the inlet vorticity distribution and might require a modeling of the effect of streamwise vorticity.

The normal velocity profiles (Figure 8b) in the first 6 step heights downstream of the step do not agree with the experimental data. After 6 step heights the profile shape and magnitude do have reasonable agreement. Previous calculations at larger expansion ratios did produce a secondary vortex directly behind the step face. It is possible that at this low expansion ratio, the secondary vortex depends upon the three-dimensional motion that is experimentally observed near the step face.

The root-mean-square (RMS) flow direction velocity component (Figure 8c) follows the trend of the experimental data, with the exception of the near-wall region. The experimental data indicate a slight decrease in value as the wall is approached while the discrete vortex dynamics result show an increase in RMS value. The peak wall value depends upon the maximum allowed discrete vortex strength that is created at the wall. In this calculation the maximum strength is $0.1\ U_0H$ and the peak RMS value is 0.2. A previous calculation with twice the maximum strength produced near-wall RMS peaks that are twice the current results. The RMS normal-direction velocity component (Figure 8d) has reasonable agreement with the experimental data. Since the normal velocity goes to zero at the wall, the fluctuations are also zero at the wall and the increase of RMS values seen in the flow direction component is not found in the normal component.

The calculated Reynolds shear stress (Figure 8e) is generally smaller than the experimental results. The previous numerical calculation of the free mixing layer showed that the Reynolds shear stress depended upon the discrete vortex core shape. With all the vortices having the same core shape and size, the shear stress was approximately twice the experimental value. Changing the calculational procedure, so that the core size would grow with time and approximate the viscous diffusion of vorticity, produced results in agreement with experiment. A choice can also be made as to the exact short-range velocity behavior that is to be used. For a single isolated line vortex, the exact result has an exponential behavior. A reasonable approximation to this shape is achieved by adding a small, but growing, distance to the interaction distance r. Thus instead of $(u,v) \propto \frac{(-y,x)}{r^2}$, one should use $(u,v) \propto \frac{(-y,x)}{r^2+r_{core}^2}$, where $r_{core}^2 = 5t\nu$. This model produced a free mixing layer shear stress which was 70% of the experimental value and has been used in these back-step calculations.

In the sudden-expansion work [11] it was found that the calculated shear stress depended upon the distribution of inlet discrete vortices. Figure 9 presents results of calculated Reynolds shear stress with the inlet shear layer one-fourth of the previous thickness. Six step heights down stream of the step the calculated shear stress matches or exceeds the experimental values. Near the step edge the calculated shear stress still does not agree well with the real three-dimensional wall boundary layer that has become separated and which contains streamwise vorticity.

Conclusions

This paper has shown that is possible to simulate unsteady separated flow with the discrete vortex dynamics method. Like experimental flow visualization, the computer-generated time-dependent vorticity motion provides further understanding of this inherently unsteady-flow problem. The qualitative features of separated flow are predicted by this numerical method, but close quantitative agreement with experiment will require extension of the method. To improve the vortex dynamics results, a model of dissipation caused by small-scale three-dimensional vorticity should be added to the two-dimensional calculation or a full three-dimensional discrete vortex dynamics calculation should be done. An example of the latter approach has been provided by Leonard's simulation of a turbulent spot in a laminar boundary layer [15]. The experimental investigation of this paper has shown that the laser Doppler anemometer can be used in highly turbulent recirculating flow. The comprehensive data set that has been obtained will be useful in the development of any numerical technique that is applied to separated flows.

References

1. Ashurst, W. T., "Numerical Simulation of Turbulent Mixing Layers via Vortex Dynamics," Turbulent Shear Flows I, ed. by F. Durst, et al, Springer-Verlag, Berlin, 1979, pp. 402-413.

2. Durst, F., Popp, M., and Tropea, C. D., "Turbulence Measurements Over a Backward-Facing Step," SFB 80 Report (1980), University of Karlsruhe.

3. Tropea, C. D., "Frequency Determination in an LDA Digital Processor," SFB 80 Report ME 152 (March 1980), University of Karlsruhe.

4. Durst, F., and Tropea, C. D., "Digital Processing of LDA-Signals by Means of a Transient Recorder and a Computer," presented at Symposium on Long and Short Range LDA, Institute Saint Louis, France, Sept. 13-17, 1980.

5. Eaton, J. K. and Johnston, J. P., "Turbulent Flow Reattachment: An Experimental Study of the Flow and Structure Behind a Backward-Facing Step," Stanford Report MD-39 (June 1980), Stanford University.

6. Kim, J., Kline, S. J., and Johnston, J. P., "Investigation of Separation and Reattachment of a Turbulent Shear Layer: Flow Over a Backward-Facing Step," Stanford Report MD-37 (1978), Stanford University.

7. Bradshaw, P. and Wong, F. Y. F., "The Reattachment and Relaxation of a Turbulent Shear Layer," J. Fluid Mech. 52 (1972), p. 113-135.

8. Abbot, D. E. and Kline, S. J., "Experimental Investigation of Subsonic Turbulent Flow Over Single and Double Backward Facing Steps," Trans. ASME, J. Basic Engineering, Vol. 84D, Series D, (1962) pp. 317-325.

9. Chorin, A. J., "Numerical Study of Slightly Viscous Flow," J. Fluid Mech., 57 (1973) pp. 785-796.

10. Eastwood, J. W. and Hockney, R. W., "Shaping the Force Law in Two-Dimensional Particle-Mesh Models," J. Computational Physics 16 (1974), pp. 342-359.

11. Ashurst, W. T., "Calculation of Plane Sudden Expansion Flow via Vortex Dynamics," presented at 2nd Symposium on Turbulent Shear Flows, July 2-4, 1979, Imperial College, London.

12. Chorin, A. J., "Vortex Sheet Approximation of Boundary Layers," J. Computational Physics, 27 (1978), pp. 428-442.

13. Clements, R. R. and Maull, D. J., "The Representation of Sheets of Vorticity by Discrete Vortices," Prog. Aerospace Sci. 16 (1975), pp. 129-146.

14. Zaroodny, S. J. and Greenberg, M. D., "On a Vortex Sheet Approach to the Numerical Calculation of Water Waves," J. Computational Physics, 11 (1973), pp. 440-446.

15. Leonard, A., "Vortex Methods for Flow Simulation," J. Computational Physics, to appear.

Acknowledgements

The present work was carried out under partial financial support from the United States Department of Energy and the Deutsche forschungsgemeinschaft. The third author gratefully acknowledges support from the Thomas Hogg Scholarship administered by the University of Toronto.

Thanks are also due to June Winter and Sheryl Johnson for assistance in finalizing this paper.

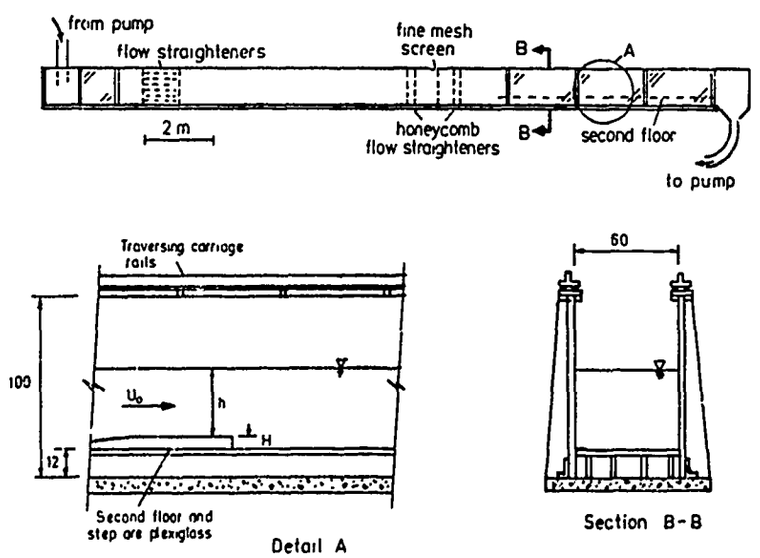


Figure 1. Water channel and details of the test section (dimensions in centimeters unless otherwise noted).

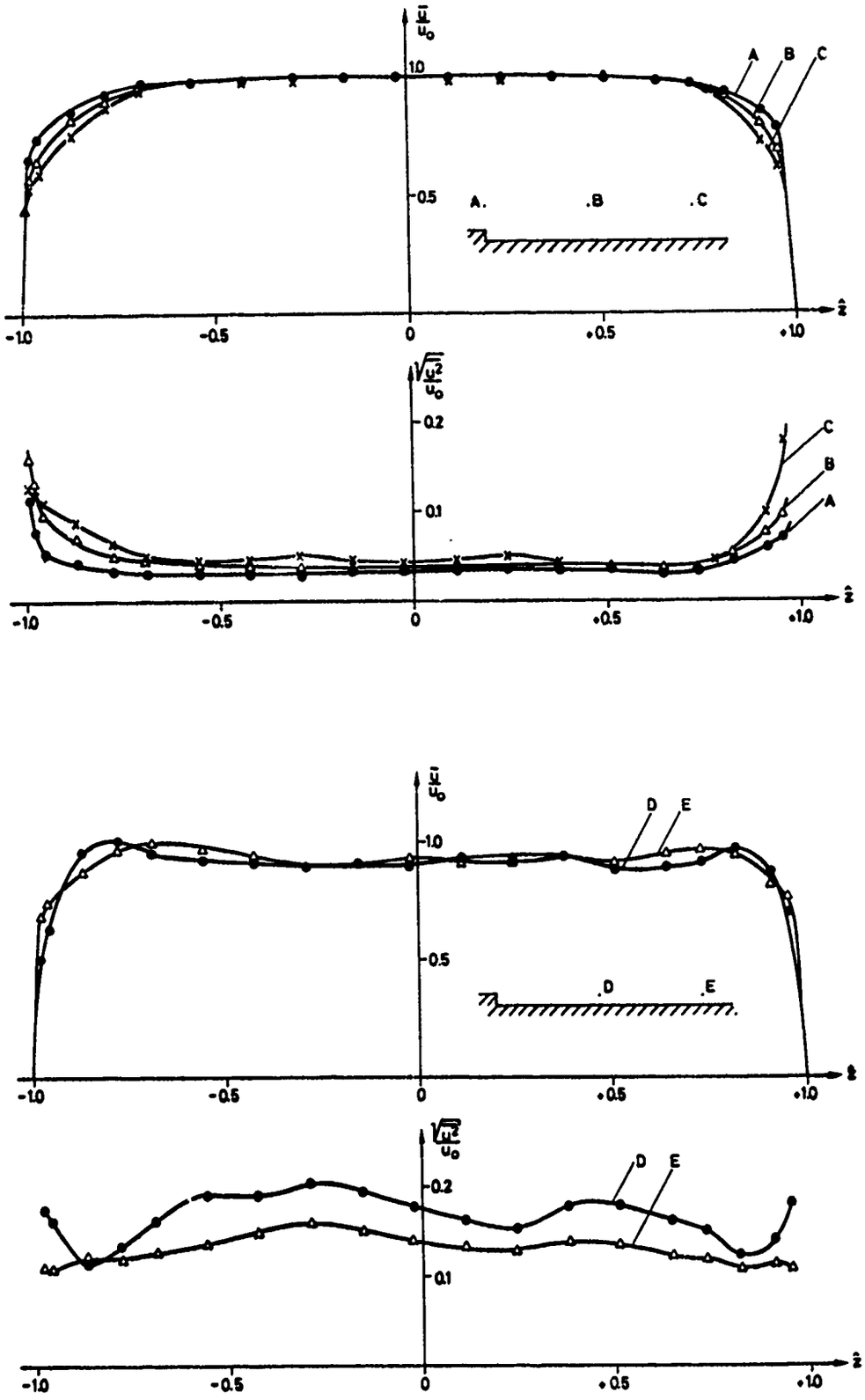


Figure 2. The spanwise uniformity of the mean and root-mean-square longitudinal velocity shown at five locations [the x,y coordinates, in mm, with respect to the step edge are: A(0,80), B(200,80), C(400,80), D(200,0) and E(400,0); and the step height is 40 mm].

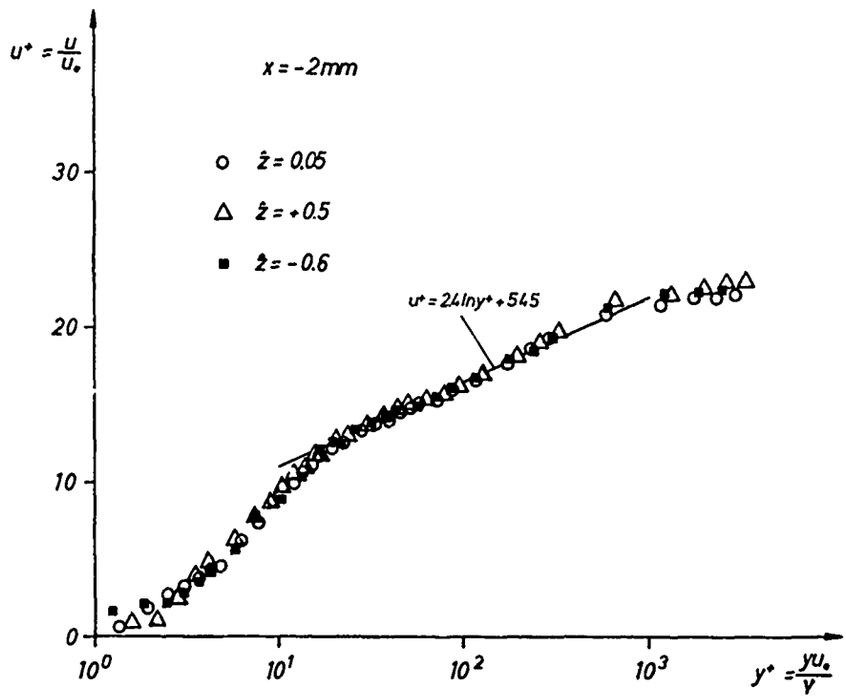


Figure 3. Profile of the wall boundary layer 2 mm upstream of the step, showing full turbulence and good spanwise uniformity (the spanwise coordinate $\hat{z}$ is normalized by the channel half-width,300 mm, and the origin is at the channel mid-plane).

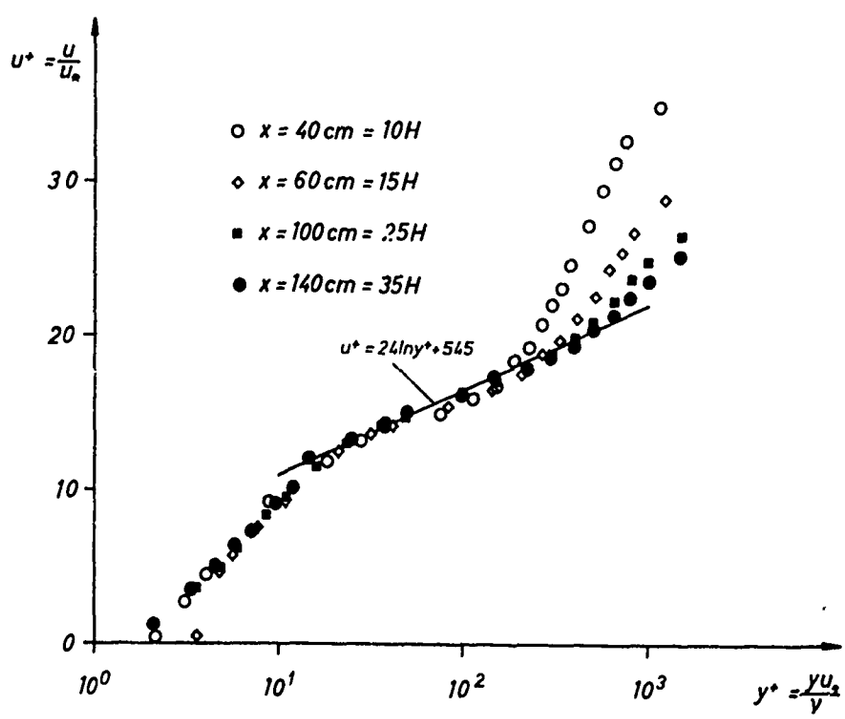
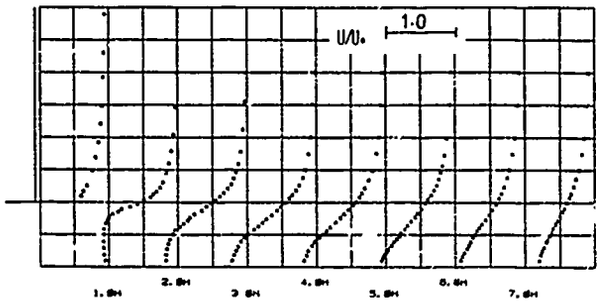
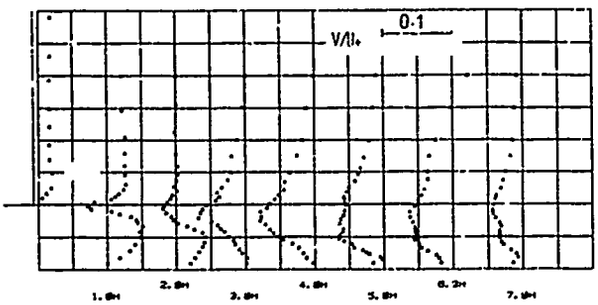


Figure 5. Profile of the reattached wall boundary layer far downstream of the separated flow showing continued deviation from an unperturbed turbulent boundary layer profile.

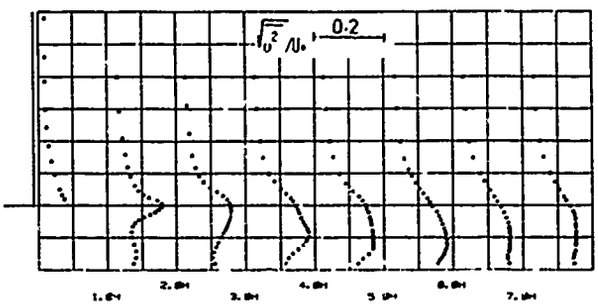
4a



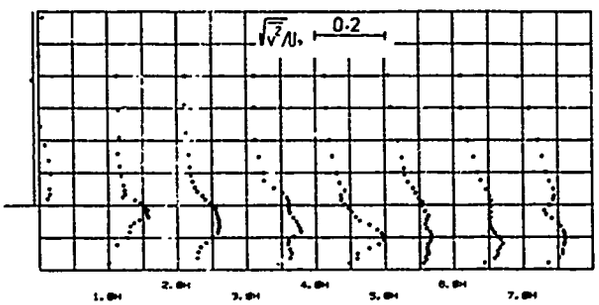
4b



4c



4d



4e

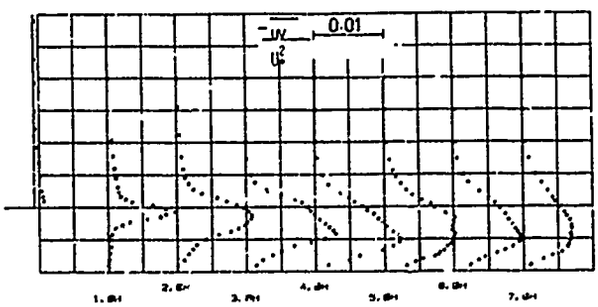


Figure 4a thru e. Mean and fluctuating velocity components in the backward-facing step flow at Reynolds number of 12,000 (= U_0 H/ν), where U_0 is the freestream velocity ahead of the step and H is the step height. The expansion ratio is 1.14. The origin of the left profile is at 0.075 H before the step edge and the remaining profiles have their origins at each step-height interval.

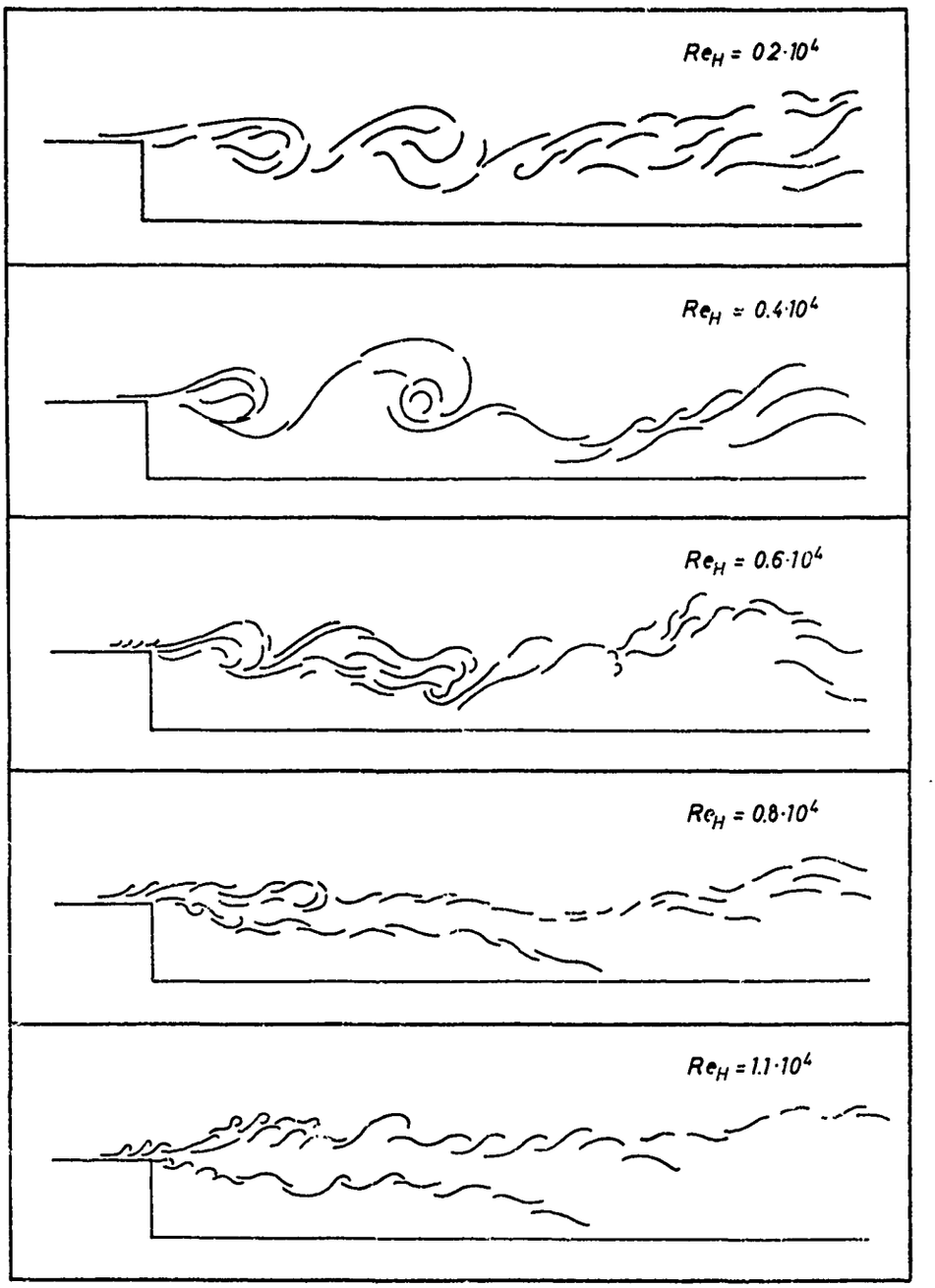


Figure 6. Variation of separated shear layer structure with Reynolds number. The largest structure (Re ~ 4,000) corresponds to the minimum separation length (see Figure 7).

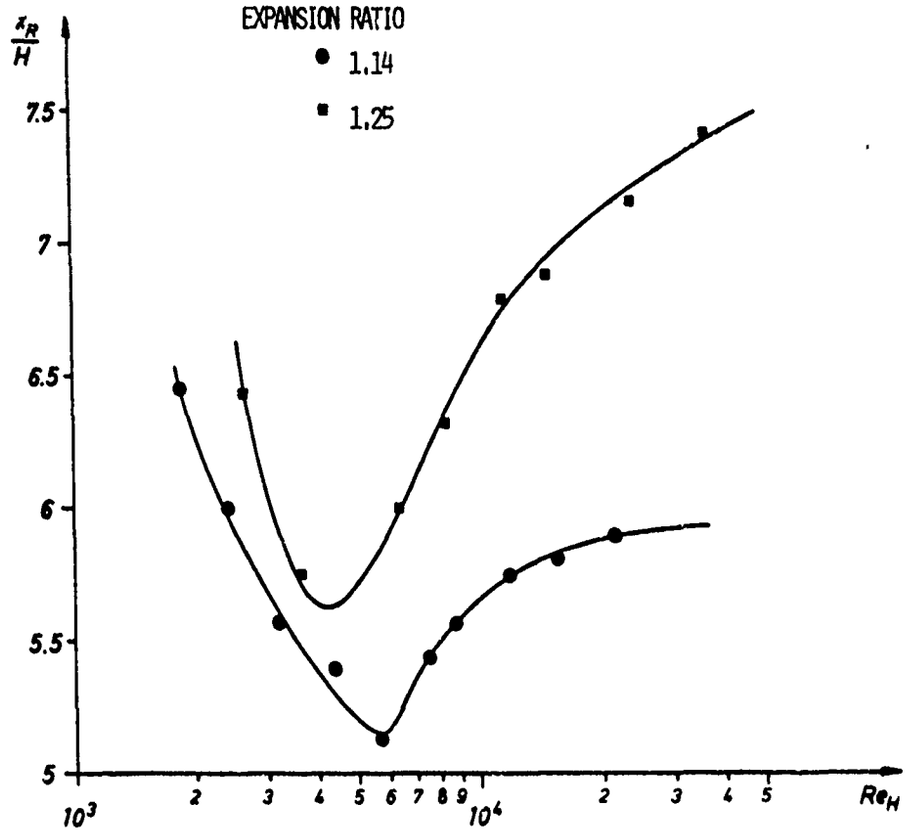


Figure 7. Experimental separation length variation with Reynolds number and expansion ratio (H is the step height).

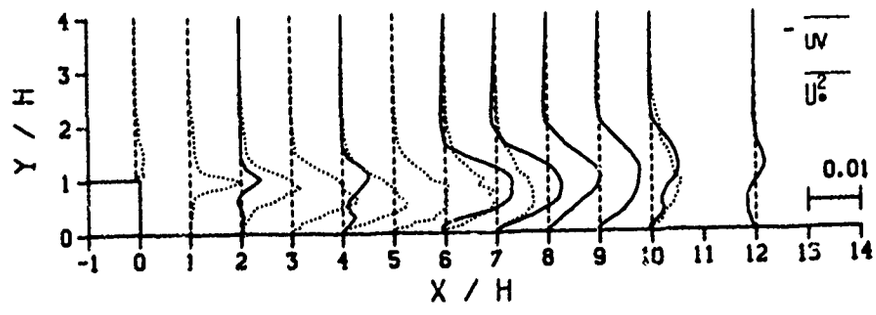
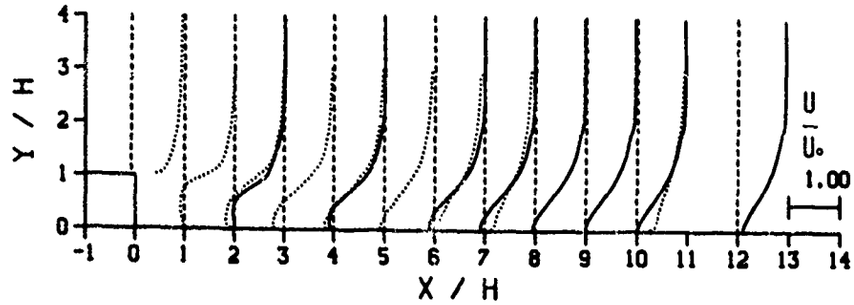
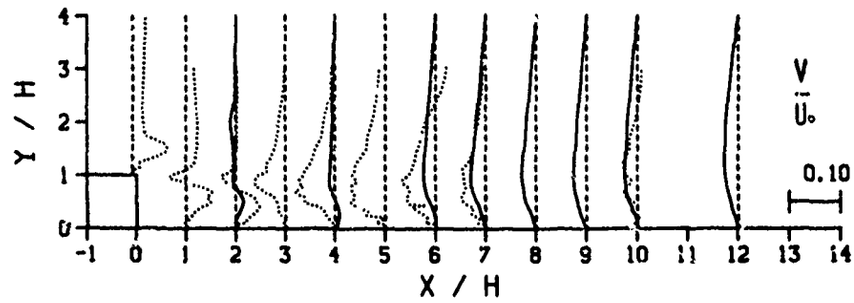


Figure 9. Calculated (solid line) and measured (dotted line) Reynolds shear stress. In this calculation the inlet shear layer was 0.4 step heights and produced larger results than the thick inlet shear layer shown in Figure 8e.

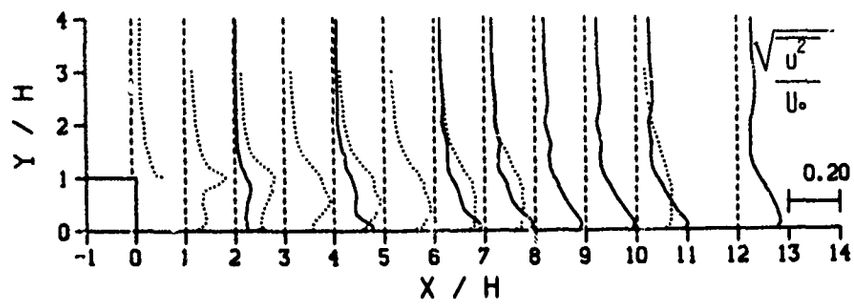
8a



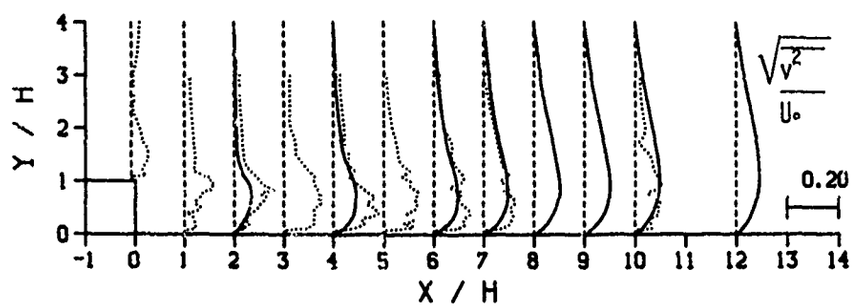
8b



8c



8d



8e

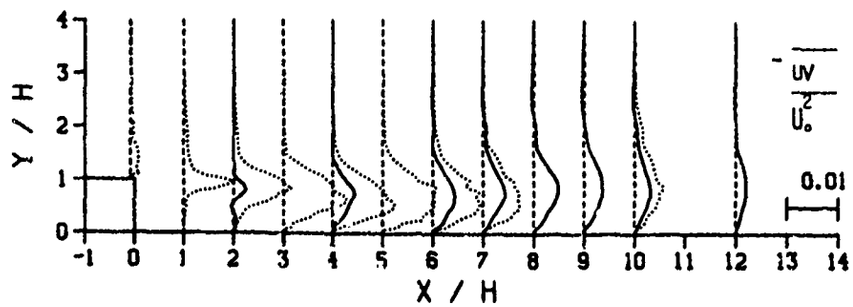


Figure 8a thru e. Calculated (solid line) and measured (dotted line) mean and fluctuating velocity components in a backward-facing step flow at Reynolds number of 12,000. The vertical dashed lines denote the velocity origin.

THE DEVELOPMENT AND APPLICATION OF A METHOD FOR CALCULATING THE VISCOUS FLOW ABOUT HIGH-LIFT AEROFOILS

by

D. J. Butter
British Aerospace
Manchester Division
Stockport
Cheshire SK7 1QR

and

B. R. Williams
Royal Aircraft Establishment
Farnborough
Hampshire GU14 6TD

SUMMARY

The preliminary stages in the design of a high-lift wing usually involves the extensive testing of simplified models in wind tunnels; this is both time-consuming and expensive. Development of a Multiple Aerofoil Viscous Iterative System (MAVIS), a method for calculating the flow about two-dimensional high-lift sections, will give great economies at the initial design stage provided that the design method can predict not only the maximum lift coefficient and the profile drag but is also very fast and easy to use. However, this appears difficult as the nature of the flow is complex; the flow region is multiply-connected; wakes from upstream elements interact with the boundary layers on downstream elements; there are regions of separated flow on the lower surfaces of the slat and wing and the possibility of separated flow on the upper surface of the flap throughout the incidence range.

In the UK we have developed methods for calculating each region of the flow and the methods are combined by an iterative procedure. This modular approach means that improved approximations in a particular region can be easily inserted into the system. The method has been programmed so that the calculations can be made in a wind tunnel and predictions compare well with the measurement of two-dimensional flow on high-lift wings.

Applications of this method can permit the effective design of the leading edge slat, slat/wing cut profiles, wing upper surface shrouds and trailing edge flaps. It can be further used in the design of a flap system to optimise the gap and overlap of the various elements and also their deflection angles.

NOTATION

C_D	drag coefficient	y_m	position of maximum velocity
C_f	skin friction	α	angle of incidence
C_L	lift coefficient	β	$(1-M_{\infty}^2 \cos^2\alpha)^{1/2}$
C_p	pressure coefficient	δ	boundary layer thickness
c	aerofoil chord	δ^*	boundary layer displacement thickness
H	shape parameter, $= \delta/\theta$	$\bar{\delta}$	boundary layer thickness parameter (see Eq. (3))
M	Mach number	θ	boundary layer momentum thickness
p	mean static pressure	$\bar{\theta}$	boundary layer thickness parameter (see Eq. (5))
R_s	Reynolds number	k	curvature
U	x-component of mean velocity	ρ	fluid density
u	x-component of fluctuating velocity	ϕ	velocity potential
V	y-component of mean velocity	w	relaxation factor
v	y-component of fluctuating velocity		
V_n	component of velocity normal to surface		

Subscripts

i	solution of the inviscid equations for the equivalent inviscid flow
s	conditions at the body surface
t	conditions at the trailing edge
w	conditions on the wake centre line

1. THE NATURE OF THE FLOW

The flow about a multi-component aerofoil at high lift is one of the most complex flows to be modelled by theoretical methods. It contains many features, such as supercritical flow on the slat, separated flow on the flap and a complex interaction of shear layers, all of which would be difficult to compute in isolation; the combination of these features compounds the difficulty of modelling the flow. This complexity also means that it is difficult to perform simple and useful wind-tunnel tests. For example, individual elements of the high-lift aerofoil can be quite small and are consequently very susceptible to scale effects. The difficulty of providing the correct scale for the experiment is compounded by the existence of the supercritical flow on the slat. Useful wind-tunnel tests can however be performed in pressurised low-speed tunnels (e.g. RAE 5m. tunnel), which allow the Mach and Reynolds numbers to be varied independently thus providing a firm basis for extending the results to full scale. The nature of the problem is indicated in Figure 1, which shows the variation in maximum lift with independently varying Reynolds and Mach number obtained from some tests on a high-lift wing in the RAE 5m. tunnel. As the Reynolds number decreases there is a marked decrease in the maximum lift, which is probably a result of low Reynolds numbers on the slat. At higher free stream Mach numbers the maximum lift again decreases as a result of the appearance of supercritical flow on the slat and a possible interaction between a shock wave and the slat boundary layer.

Flow about a high-lift aerofoil is indicated schematically in Figure 2 and some of the features of the flow are:-

a) the region of flow is multiply-connected with the wakes from upstream elements interacting with the boundary layers of downstream elements.

b) the shear layers over the flap are very thick and the curvature of the flow gives rise to a static pressure variation across the shear layer.

c) the slat and the flap must fit snugly back to form the cruise aerofoil with the result that there are cavities beneath the slat and shroud in which separation bubbles are formed.

d) if the angle of deflection of the flap is sufficiently large then the flow will separate from the flap. Although the drag is markedly increased the complete aerofoil will not necessarily stall and, in fact, the separated flow on the flap can exist throughout the incidence range.

e) at the leading edge of the aerofoil the suctions on the slat can be high enough to indicate that the supercritical flow has developed even though the freestream Mach number is only about 0.2.

The fluid mechanics underlying the efficient operation of high-lift aerofoils can be explained by examining, in Figure 3, the pressure distributions at two angles of incidence for a four element high-lift aerofoil. Here the load is shared between the elements so that the peak suctions on each element are greatly reduced. The flap and vane are almost totally protected by the rest of the aerofoil from the effects of changing incidence and the interaction between the elements raises the suction at the trailing edge of the slat, wing and vane, which also has the effect of reducing the pressure rise on each element.

As the slat is moved closer to the wing, the load on the slat is increased whilst the load on the wing is reduced. It follows that the pressure rise on the wing is reduced and the flow is less likely to separate from the wing. If the slat is brought too close to the wing then either the increased pressure rise on the slat will cause the flow to separate from the slat or the interaction of the slat wake with the wing boundary layer will provoke a flow separation on the wing. Foster et al., Reference 1, found that the maximum lift on a slatted wing with a flap initially increased with decreasing gap until, as shown in Figure 4, there was a marked decrease in maximum lift below a slat gap of 1.5% chord. In Figure 5 it can be seen that the slat wake interacts strongly with the wing boundary layer for slat gaps larger than the optimum and the stall is provoked by the interaction of these viscous layers. Although this mechanism may not always define the optimum slat gap, it is important to represent it in the theoretical method.

We have indicated the aspects of the flow which ought to be included in a satisfactory treatment of the problem and these suggest that the theoretical model should be as comprehensive as possible.

However, the method should also be fast and easy to use, so that an aircraft designer will be able to replace the costly and time consuming tests of simplified wind-tunnel models, which currently form the initial stage in the design of a high-lift wing. The designer will require that the method predicts the maximum lift coefficient of the aerofoil, the profile drag and should also be sufficiently sensitive to provide a sensible optimisation of the devices. A reasonably fast method is provided by matching a solution of the external flow with a solution for the shear layers around the aerofoil. However, it must be borne in mind that the thickness of the shear layers, especially above the flap, may invalidate the basic assumptions of the matching procedure.

Sections 2, 3 and 4 of the paper describe the methods of calculating the inner and outer flows and the process used to match the inner and outer solutions. We also consider the representation of separated flows the prediction of profile drag, the constraint of the flow due to a wind tunnel and the allowance for the effects of compressibility. Finally the method is compared with wind-tunnel data for single and multi-aerofoils and applied to the design of a flexible shroud.

2. INVISCID SOLUTION

For the external flow we have seen that we need solutions of the potential equations of compressible flow. But at take-off and landing it is very unlikely that the shock wave on the slat will be strong enough to require a solution of the Euler equations and a solution of the compressible potential equations will be sufficient. However, the solution of the compressible potential equations is complicated by the multiply connected nature of the flow region. Grossman and Melnik, Reference 2, have transformed the region external to two aerofoils to the annulus between two circles, each of which represents one of the original aerofoils. This annulus provides a suitable computing plane for a field method. However, this approach appears to be practically limited to considering two aerofoils. An alternative approach is to consider the unmodified external flow field or its transformation to a region of finite extent. Either an aligned grid, numerically generated by the method of Thompson et al., Reference 3, or a non aligned grid system could be used.

But none of these methods has been sufficiently developed for use in a routine calculation, so we have solved the incompressible potential equations by a panel method and used a compressibility correction: obviously we are unable to represent shock waves by this method. However, even for a panel method, the geometry of the high-lift aerofoil can still present difficulties and, for some methods, poor accuracy is obtained over the shroud and other thin regions of the aerofoil. We use a method which is particularly suited to calculating the potential flow over high-lift aerofoils.

This method was developed by Newling at BAe Manchester in 1976, Reference 4, and solves Laplace's equation by using the external Neumann boundary conditions with a mix of source and vortex singularities placed on the surface of the aerofoil. However, instead of arbitrarily chosing either the source or vortex distribution, the method solves for both as unknowns. Obviously, if an unknown source strength and an unknown vortex strength are associated with each panel then there will be twice the number of unknowns as equations for the normal velocity. To reduce the number of unknowns to be the same as that of the equations, the source and vortex density on opposite panels on the upper and lower surface are prescribed to be equal.

Normally in panel methods it is argued that the order of the singularity distributions should be chosen to be the same for both the source and the vorticity. However, it is well known that when solving the analysis problem with normal velocity boundary conditions at the panel mid-points then, unless some extra constraints are introduced, the source distribution will be stable only if it is of an even order, such as piecewise constant, piecewise quadratic etc., and the vorticity distribution will only be stable if it is of an odd order, such as discrete vortices, piecewise linear etc. For reasonable accuracy at reasonable computing costs, this leads us to a model with a piecewise constant source distribution, defined at the panel mid-points, and a piecewise linear vorticity distribution, defined at the panel edges.

Fortunately, the equal upper and lower formulation for the two dimensional flows tends to minimise the source gradients and consequently reduce the leakage errors of the constant source panels. Also the resulting large gradients in vorticity, particularly at the leading edge, are adequately treated with the continuous linear distribution. Hence, using the notation of Figure 6, the velocity at the j^{th} point for a body with N panels is given by:-

$$V_{nj} = \sum_{i=1}^{N/2} (A_{i_{upper}j} + A_{i_{lower}j}) \sigma_i + \sum_{i=1}^{N/2+1} (B_{i_{upper}j} + B_{i_{lower}j}) \gamma_i \qquad (1)$$

which gives N+1 unknowns and N equations. The additional condition is provided by the Kutta condition, which requires smooth flow at the trailing edge. In this method, this can be implicitly satisfied precisely at the trailing edge by equating the vortex strength on the upper and lower trailing edges to zero.

Now we have a system of N equations and N unknowns which can be solved by normal matrix algebra. For multi-aerofoils, to reduce the computer storage and time requirements, the equations are solved with a block iterative technique. Here each individual body's self influence matrix is inverted using a direct algorithm, (and stored for future use in the viscous iterations) and a solution to the equations is iterated, block by block, with the standard Jacobi technique.

This method is inherently more accurate than that of Hess and Smith because of its lower leakage, reduced vorticity in the trailing edge region and the implicit Kutta condition. Figure 7 illustrates the improved accuracy by a comparison between the two methods and an exact solution for a cambered Karman aerofoil. The figure also demonstrates that the accuracy of the method does not depend on the opposite panels on both surfaces being of equal length. Comparisons for other configurations by ourselves and other workers have shown similar agreement for other configurations, particularly for the exact solution of the two element aerofoil of Williams, Reference 5.

Figure 8 shows a comparison between this method and that of Hess and Smith for a three element aerofoil. This comparison clearly shows the differences between the two methods and the improvements offered by our method. It can also be seen how an erroneous boundary layer development and slot flow would be predicted with the Hess and Smith method.

3. CALCULATION OF SHEAR LAYERS

In this method the development of all the shear layers is calculated by integral methods rather than finite difference methods: we are prepared to accept a small loss in accuracy in order to obtain a method which is sufficiently fast for the aircraft designer. The laminar portion of the boundary layer is calculated by the method due to Thwaites, Reference 6, with allowance for compressibility by the Stewartson-Illingworth transformation, Reference 7. Transition from laminar to turbulent flow in the boundary layer is predicted by the empirical correlation of Granville, Reference 8. If laminar separation occurs upstream of natural transition then the development of the laminar separation bubble is predicted by the semi-empirical method of Horton, Reference 9. Williams, Reference 10, has shown that Horton's method, with a slight modification, can predict the growth and bursting of a laminar separation bubble on the slat of a high-lift aerofoil. We can also specify transition at a fixed position corresponding to the artificial fixing of transition in a wind-tunnel experiment.

Over portions of the aerofoil, where the turbulent boundary layer is unaffected by the wake of the preceding element, the development is calculated by the lag entrainment method of Green, Reference 11. Downstream of the trailing edge of the slat, wing and vane, the pressure changes are much greater than those associated with a single aerofoil. In these regions the lag-entrainment method is also used to calculate the development of the wake. The interaction between the wake and boundary layer is calculated by the integral method due to Irwin, Reference 12, in which a reasonably simple algebraic expression, containing six unknown quantities, is used to describe the velocity profile of the boundary layer and a single wake. An integration of the boundary layer equations across the combined layer yields six ordinary differential equations, which are integrated in the streamwise direction. The performance of the method is illustrated in Figure 9 by a comparison with experimental measurements, taken from tests of Foster et al., Reference 1, for an aerofoil at an angle of incidence of 15° with the slat deflected 25° and the flap deflected 10°. This method can only model a single wake, but it is a reasonable approximation to add the slat wake and the wing wake to form a single wake to interact with the flap boundary layer.

4. MATCHING OF THE INNER AND OUTER SOLUTIONS

The effect of the shear layers about the aerofoil is represented by defining an equivalent inviscid flow which is identical to the real flow outside the shear layers. There are at least two methods of defining the equivalent inviscid flow: the displacement surface method and the surface transpiration method. In the first method the surface of the aerofoil is replaced by the displacement surface, which is extended into the wake, and the mass flow between the displacement body and the edge of the shear layer in the equivalent inviscid flow is equal to the mass flow in the boundary layer. In the second method the inviscid flow is continued analytically through the shear layer on to the surface of the aerofoil or the centre line of the wake and identity of the flows outside the shear layers is obtained by applying an appropriate transpiration velocity at the surface of the aerofoil or discontinuity in normal velocity along the centre line of the wake in the equivalent inviscid flow. The required transpiration velocity, V_{is}, is obtained by applying the continuity equation to the shear layer and the equivalent inviscid flow and integrating the difference across the shear layer; then

$$V_{is} = \frac{1}{\rho_{is}} \frac{d}{dx} \int_o^{\delta} (\rho_i U_i - \rho U) \, dy \qquad (2)$$

where the suffix i refers to the inviscid quantities and s to quantities evaluated either at the aerofoil surface or on the wake streamline. This can be written as

$$V_{is} = \frac{1}{\rho_{is}} \frac{d}{dx} (\rho_{is} U_{is} \bar{\delta}) \qquad (3)$$

where

$$\bar{\delta} = \frac{1}{\rho_{is} U_{is}} \int_o^{\delta} (\rho_i U_i - \rho U) \, dy$$

and $\bar{\delta}$ is the quantity that naturally arises in a general formulation of the momentum integral equation over a curved surface. It can be easily demonstrated that $\bar{\delta}$ is not equal to the displacement thickness δ^* for flows in which the component of velocity U_i parallel to the surface, cannot be regarded as constant out from surface. However, Dr. Lock has indicated in an earlier paper at this conference that for single aerofoils the difference between $\bar{\delta}$ and δ^* is generally small.

East, Reference 13, has obtained the momentum integral equation for a general flow over a curved surface by taking differences of the appropriate equations for the equivalent inviscid and the viscous flows and integrating the difference across the shear layer. This gives the X-momentum equation as

$$\frac{d\bar{\theta}}{dx} + (H + 2 - M_{is}^2)\frac{\bar{\theta}}{U_{is}}\frac{dU_{is}}{dx} - \frac{C_f}{2}$$

$$= -\frac{1}{\rho_{is}U_{is}^2}\frac{d}{dx}\int_o^\delta (p_i - p)\,dy - \frac{k_s}{\rho_{is}U_{is}^2}\int_o^\delta (\rho_i U_i V_i - \rho UV)\,dy$$

$$+ \frac{1}{\rho_{is}U_{is}^2}\frac{d}{dx}\int_o^\delta \rho u^2\,dy + \frac{k_s}{\rho_{is}U_{is}^2}\int_o^\delta \rho\overline{uv}\,dy \qquad (4)$$

$$\text{where } \bar{\theta} = \frac{1}{\rho_{is}U_{is}^2}\int_o^\delta ((\rho_i U_i^2 - \rho U^2) - U_{is}(\rho_i U_i - \rho U))\,dy \qquad (5)$$

and k_s is the curvature of the surface.

The terms on the right hand side of Equation (4) represent the effects due to flow curvature and normal stresses. These terms are generally of second order and in the present analysis have not been included in the integration of the shear layer equations. It should be noted that in this formulation the equivalent inviscid pressure distribution, rather than the viscous pressure distribution, is used in the calculation of the development of the shear layer: this will only have a noticeable effect when the curvature of the flow is sufficiently large and the surface pressures in the two flows are not equal.

For the representation of the wake, Lock, Reference 14, has argued that the curvature of the wake close to the trailing edge is sufficiently large to warrant the use of a higher order approximation to take account of the pressure change across the wake in the equivalent inviscid flow, a vortex sheet is introduced along the dividing streamline from the trailing edge, such that there is a jump in tangential velocity given by

$$-k\,U_w\,(\bar{\delta}_w + \bar{\theta}_w)$$

where k is the mean curvature of the wake, and the suffix w refers to the quantities in the wake.

To this order of approximation the pressure changes across the boundary layer in the real flow and the equivalent inviscid flow are different and a small correction $k\rho_{is}u_{is}(\bar{\theta}+\bar{\delta})$ must be subtracted from the calculated inviscid pressures. As noted earlier, this correction should only be applied in comparisons with experimental pressure distributions and for the development of the shear layer the equivalent inviscid velocity is used.

To represent the effect of the shear layers on the flow about a high-lift aerofoil, we have adopted the transpiration model for the following reasons:-

a) the boundary condition is applied on the surface of the aerofoil in the panel method is inverted only once on the first iteration. For the displacement surface model the body geometry changes on each iteration so that the influence matrix must be recomputed and re-inverted at each iteration.

b) the wakes from the slat and wing are more easily represented by the transpiration method, although the derivation of the transpiration velocity needs more careful consideration. First we look at the case in which the wake and boundary layer have not merged, Figure 10a. The differences between the continuity equation applied to each of the flows could be integrated across the whole shear layer giving an expression for the transpiration velocity on the surface in the equivalent inviscid flow. However, it is preferable to integrate the difference across the boundary layer and then across each half of the wake to give a transpiration velocity at the surface and a distribution of sinks placed along the dividing streamline of the wake in the viscous flow. In practice, we place the sinks on the dividing streamline in the inviscid flow.

In the second case, Figure 10b, the wake and boundary layer have merged forming a single shear layer and it is not possible to evaluate the transpiration velocity for a portion of the shear layer corresponding to the boundary layer. If the difference is integrated from the surface to the first velocity maximum in the viscous flow at y_m we obtain

$$\rho_{is} V_{is} = \frac{d}{dx} \int_o^{y_m} (\rho_i U_i - \rho U)\, dy + (1 + k y_m)(\rho_{i y_m} V_{i y_m} - \rho_{y_m} V_{y_m}) \qquad (6)$$

Now in contrast to the non-merged case, we no longer have equality of the normal velocities in the two flows and the second term on the right hand side is not zero. It follows that, for the merged case, the transpiration velocity should be applied at the surface and derived by integration across the whole shear layer. However in practice it is found that the displacement effect of the portion of the flow predominantly derived from the wakes is quite small.

c) if there are significant variations of pressure across the shear layer, the displacement surface does not represent the true displacement of the external layer. However, if the term $\bar{\delta}$ is calculated from the boundary layer equation, Equation (3), including terms of the appropriate order, then the normal velocity given by Equation (3) will give a true representation of the equivalent inviscid flow.

The effect of the shear layers are represented in the panel method either by adding discrete singularities to the flow or by altering the boundary conditions; both these only change the right hand side of the influence matrix equations so that the first inversion of the matrix can always be used. The transpiration velocities on the aerofoil are modelled by modifying the Neumann boundary condition from zero to

$$V_n = \frac{1}{\rho_{is}} \frac{d}{dx} (\rho_{is} U_{is} \bar{\delta}) \qquad (7)$$

whilst a piecewise constant distribution of sinks along the wake centre line up to the point of merging of the wake and boundary layers is used to approximate the jump in normal velocity. The vortex sheet along the wake is approximated by a piecewise linear distribution of vorticity on the centre line; the mean curvature of the displacement surfaces on either side of the wake, calculated by numerical differentiation, is used as an approximation to the curvature of the flow. The curvature of the displacement surface is also used to calculate the pressure correction on the aerofoil.

We have only been able to obtain convergent solutions for the viscous flow if under-relaxation is used in calculating the correction terms. In calculating the transpiration velocity the under-relaxation is applied to the quantity $\bar{\delta}$ so that for the n th iteration, we take

$$\bar{\delta}_n = (1 - w)\, \bar{\delta}_{n-1} + w\, \bar{\delta}_n \qquad (8)$$

where the value $w = 0.25$ has been found to produce convergent results. For the vortex sheet in the wake, the relaxation has been applied to the vorticity and the singularity distributions are repositioned along the streamline from the trailing edge at every fifth iteration.

5. SEPARATED FLOW

There can be two distinct areas of separated flow on the upper surface of a multi-aerofoil. At large flap deflection angles, the flow can be separated over a significant part of the flap without causing the complete aerofoil to stall and still giving an increase in the overall lift with increasing flap angle or incidence. To calculate the flow over an aerofoil in this condition the method is being extended to include the separated flow model of Maskew and Dvorak, Reference 15, where the separated wake is modelled as a free shear layer. When completed it will permit sensible calculations to be made with larger flap deflection angles and for the optimum flap angle to be computed.

The second problem of separated flow is to compute the maximum lift coefficient of the complete configuration. Here the major flow breakdown is usually a separation from the upper surface of the shroud of the main element ahead of the flap and in some cases there will be distinct separated flows on the main element and the flap. It is not obvious whether the model of Maskew and Dvorak is directly applicable to this case or whether some more complicated model is required. However, the results of Henderson, Reference 16, would indicate that the concept of a free shear layer emanating from each body is valid for the multiple separations.

6. PREDICTION OF PROFILE DRAG

The profile drag on a single aerofoil can be calculated from the momentum thickness at the trailing edge by the Squire and Young formula.

$$C_D = 2 \left(\frac{\theta_t}{c}\right) \left(\frac{U_t}{U_\infty}\right)^{1/2(H_t + 5)} \qquad (9)$$

where U_t is the inviscid velocity and H_t is the shape parameter at the trailing edge. The Squire and Young formula can be derived by integrating the momentum equation along the length of the wake with the assumption that the shape parameter takes the constant value $1/2(H_t + H_\infty)$. There appears to be nothing in the derivation of the formula which would prevent it being applied to multi-aerofoils with the same degree of success as for single aerofoils. We have used the momentum thickness calculated at the trailing edge of the last element, but the pressure distribution through which the total wake develops is more closely represented by a value of U_t at the centre of the total wake rather than from a value calculated at the trailing edge of the last element.

Williams, Reference 17, has compared measured values of the profile drag, measured by the wake traverse technique, for a range of high-lift devices with predictions by the modified Squire and Young formula using values of the momentum thickness measured at the trailing edge of the aerofoil. The results are given in Table 1 and demonstrate that the profile drag can be predicted with an accuracy of 7% provided reliable values for the momentum thickness are used.

7. WIND TUNNEL EFFECTS

Because of the difficulty of predicting the effects of a wind tunnel for a high-lift wing, whose effective chord can be very large compared with the tunnel height, the program has been written to allow the tunnel to be modelled. We have chosen to model the tunnel by representing the walls as a solid boundary with piecewise constant source panels. Checks are made to ensure that the tunnel is sufficiently well panelled and that the leakage through the walls is minimised by computing the velocities upstream and downstream of the aerofoil. This approach, rather than the popular transformation technique, has been adopted so that at a later date the effect of the tunnel wall boundary layer can be included and also because it can be extended to three dimensions.

Unfortunately, largely because of the shortage of suitable data, it has not been possible to conduct an exhaustive comparison with experimental results. Those which are available tend to be for large values of tunnel height to chord ratio for which the corrections would be expected to be small, and in these cases the method agrees well with the simpler traditional methods.

However, the increase in computing time for modelling the tunnel is small and it allows comparisons with experiment to be routinely computed with tunnel effects, thus removing one area of uncertainty.

8. COMPRESSIBILITY EFFECTS

A suitable method of solution of the fully compressible potential flow equations for multiple bodies is not yet available and consequently the panel method has been extended to predict subcritical flows by using the Prandtl-Glauert transformation in the Gothert Rule 2 form of Reference 18. In this form the flow equations are solved about the affine body but satisfying the boundary conditions along the real normal. This ensures that the real velocities, when transformed from the affine plane are normal to the real body. The method is further advanced by a semi-empirical higher order correction developed at BAe Warton. Here the longitudinal perturbation velocity is modified retrospectively after the Prandtl-Glauert solution has been achieved. The correction is developed from the second order accurate field equation.

$$\beta^2 \phi_{xx} + \phi_{yy} = M_\infty \cos\alpha \frac{\partial}{\partial x} \left(\left(1 + \frac{\gamma-1}{2} M_\infty^2 \cos^2\alpha \right) \phi_x^2 + \phi_y^2 + 2 \sin\alpha \phi_y \right) \qquad (10)$$

by using the previously calculated flow quantities to yield a new value of ϕ_x. This has been shown to work well for single aerofoils at high free stream Mach numbers with the local velocities close to their critical value.

Although this method cannot handle shock waves, it does nevertheless predict the subcritical effects of compressibility and show where the boundaries of supercritical flow are likely to occur. Figure 11 shows the pressure distribution on a three body aerofoil at 0.30 Mach number compared with the incompressible result.

9. COMPARISON WITH EXPERIMENT

We have compared the theoretical method with the experimental results for a single aerofoil and a three element aerofoil. For the single aerofoil we have taken the tests on a 12.2% thick RAE 100 section reported by Woodward in Reference 19. The experimental results have been corrected for tunnel constraint and the pressure distribution at an angle of incidence of 5.86° is compared with the theoretical prediction in Figure 12. Agreement between experiment and theory is good except at the trailing edge where the theoretical method does not predict sufficient load. In Figure 13 the rate of convergence of the lift coefficient for two angles of incidence is illustrated and the method can be seen to have effectively converged after 15 iterations. Unfortunately the profile drag was not measured in the experiment, but we would expect the Squire and Young formula to give a reasonably accurate result. Figure 14 shows the results of a calculation which does not include the effect of wake curvature. In this case the predicted lift coefficient is slightly higher than the experimental value and in particular the method under predicts the suction on the lower surface of the aerofoil.

A three element aerofoil with the flap deflected to a typical take-off setting of 20°, with optimum lap and gap settings, represents an interesting test case. Here the actual pressure gradients on the flap upper surface are high and the flow is close to separation. As can be seen from Figure 15 the agreement of the pressure distributions reveals that the agreement in C_L is somewhat fortuitous. On the flap, MAVIS predicts a separation about three quarters of the chord back from the leading edge and this persists throughout the iterative procedure. The empirical fixes to estimate the boundary layer parameters after separation are not good enough to reduce the calculated pressure gradients and to allow the separation to move rearwards.

This difficulty also explains the discrepancy in predicted C_D, particularly at high lift coefficients, because the fixes used to produce a converged solution do not allow the correct development of the boundary layer and wakes over the flap and consequently the trailing edge parameters are in error.

10. FLEXIBLE SHROUD DESIGN

Most multi-aerofoils stall from the wing shroud and by increasing the curvature in this region, over what would normally be expected from the clean aerofoil profile, the boundary layer growth is suppressed and the maximum lift increased by both the increased camber and by being able to achieve higher incidences, However, the likely optimum shape of the shroud for maximum lift at low speed would almost certainly compromise the high speed clean aerofoil design. So, in order to optimise the maximum lift at take-off and still retain good high speed characteristics, a study was made of a flexible shroud which deflected as the flap was deployed.

This optimisation is obviously highly dependent on the effects of viscosity, not only on the boundary layer development on the shroud but also on the effects of the slat wake and flow through the slots. Therefore to avoid a protracted experimental design study and to be able to complete the process theoretically, it is essential that a method is used which models all the required features. In our study we used the current MAVIS method and by predicting the maximum lift by examining the boundary layer development on the main element, it was possible to achieve an increase in C_{Lmax} of 0.25 as shown in Figure 16.

REFERENCES

1. Foster D. N., Irwin H.P.A.H., Williams B.R. — The two dimensional flow around a slotted flap. ARC R & M 3681 (1971)

2. Grossman B, Melnik R.E. — The numerical computation of the transonic flow over two element airfoil systems. 5th International Conference on Numerical Methods in Fluid Dynamics Springer-Verlag (1976)

3. Thompson J. F. et al — Numerical solution for viscous and potential flow about arbitrary two dimensional bodies using body fitted coordinate systems. J. Comp. Phys. Vol 24 (1977)

4. Newling J.C. — An improved two dimensional multi-aerofoil program. HSA-MAE-R-FDM-0007 (1977)

5. Williams B.R. — An exact test case for the plane potential flow about two adjacent lifting aerofoils. ARC R & M 3717 (1973)

6. Thwaites B. — Incompressible aerodynamics: Fluid Motion Memoirs. Clarendon Press (1960)

7. Curle N. — The laminar boundary layer equations. Oxford Mathematical Monograph (1962)

8. Granville P.S. — The calculation of viscous drag of bodies of revolution. DTMB Report 849 (1953)

9. Horton H.P. — A semi-empirical theory for the growth and bursting of laminar separation bubbles ARC CP 1073 (1967)

10. Williams B.R. — RAE unpublished report

11. Green J.E. et al — Prediction of turbulent boundary layers and wakes in compressible flows by a lag entrainment method. RAE TR 72231 (1973) Unpublished

12. Irwin H.P.A.H. — A calculation method for the two dimensional turbulent flow over a slotted flap. ARC CP 1267 (1974)

13. East L.F. — The influence of normal pressure gradients and normal shear stresses on two dimensional momentum integral equation. RAE Report to be published

14. Lock R.C. — RAE unpublished report

15. Maskew B. Dvorak F. — The prediction of C_{Lmax} using a separated flow model. J. American Helicopter Soc. April 1978

16. Henderson M. — A solution to the 2-D separated wake modelling problem and its use to predict C_{Lmax} of arbitrary airfoil sections. A.I.A.A. 78-156 1978

17. Williams B.R. — The measurement and prediction of profile drag for high lift aerofoils. RAE report to be published

18. Shapiro A.H. — The dynamics and Thermodynamics of compressible fluid flow. Ronald Press Company New York (1953)

19. Woodward D.S. — The two dimensional characteristics of a 12.2% thick RAE 100 aerofoil section. ARC R & M 3648 (1968)

TABLE 1

PREDICTION OF PROFILE DRAG BY SQUIRE AND YOUNG FORMULA

No. of elements	Angle of incidence	Profile drag Wake traverse	Profile drag Squire and Young
2	0	0.0135	0.0145
2	4	0.0178	0.0189
2	9	0.0310	0.0299
4	17	0.0747	0.0761
4	17	0.0747	0.0725
4	18.5	0.0812	0.0798
5	15	0.0849	0.0810
5	17	0.0922	0.0991

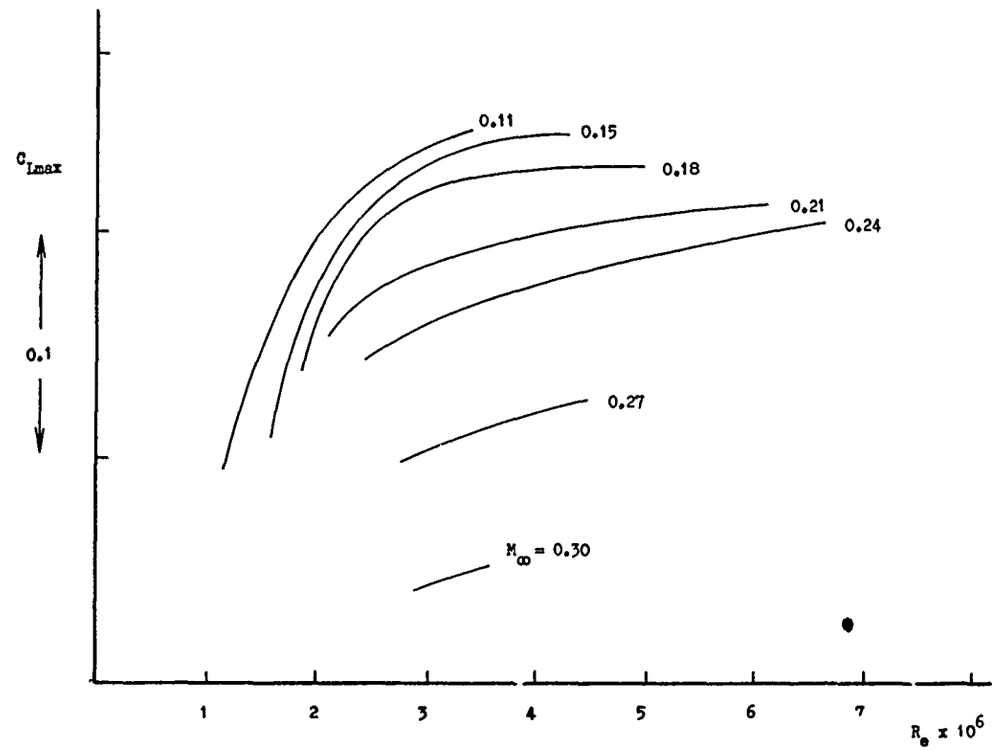


FIGURE 1 Maximum lift coefficient at various Mach and Reynolds numbers.

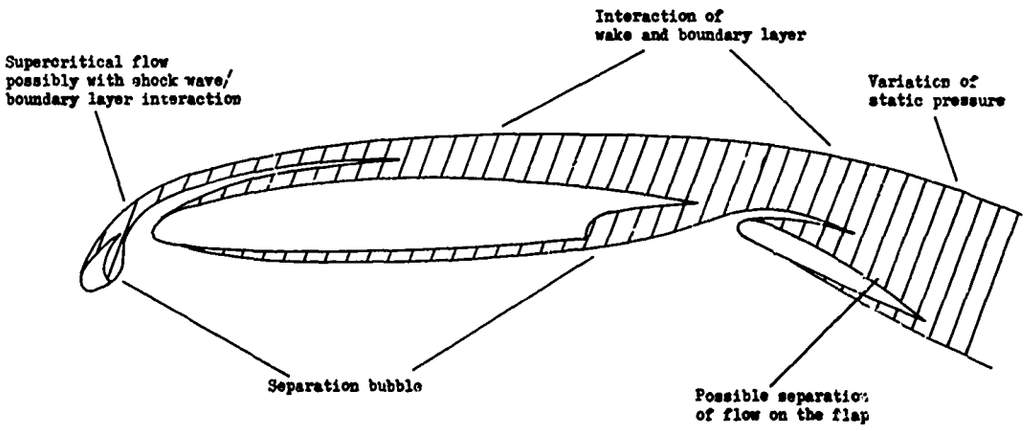


FIGURE 2 Nature of the flow about a high lift wing

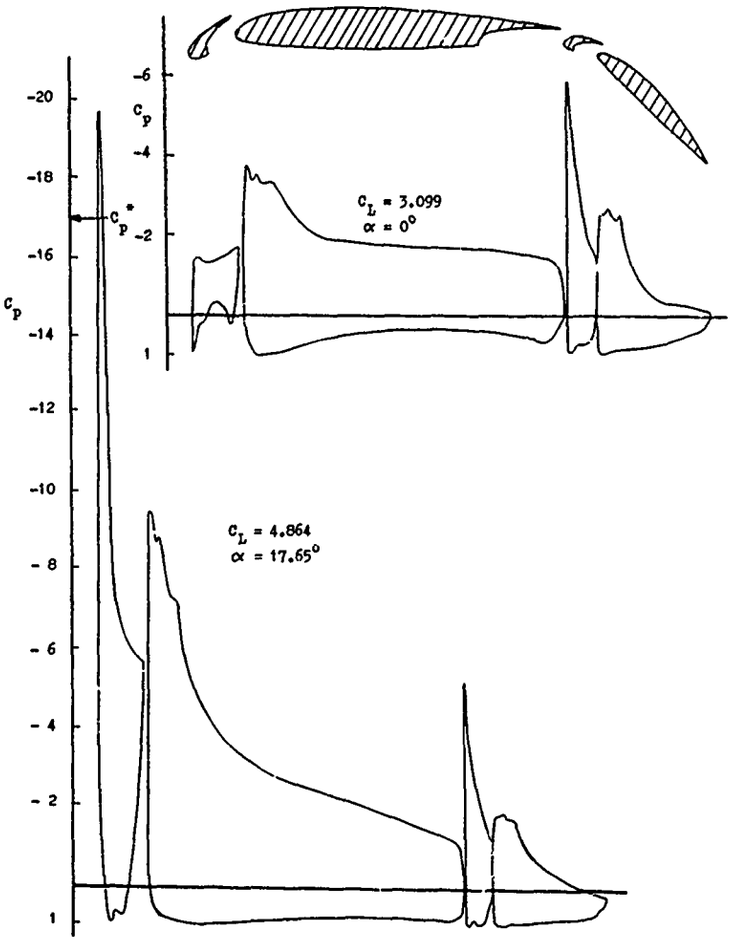


FIGURE 3 Typical pressure distributions at two incidences: $R_e = 3.1 \times 10^6$ M = 0.2

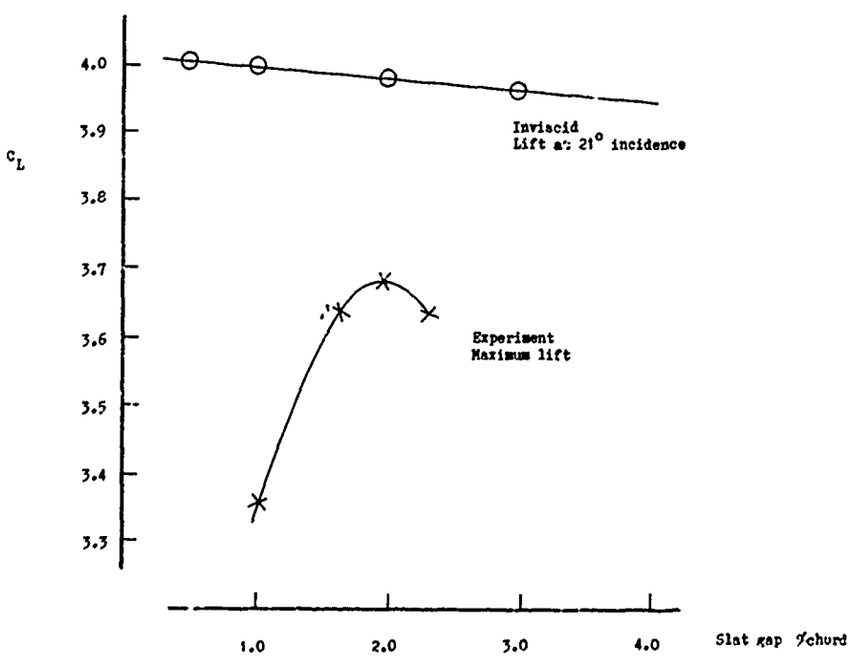
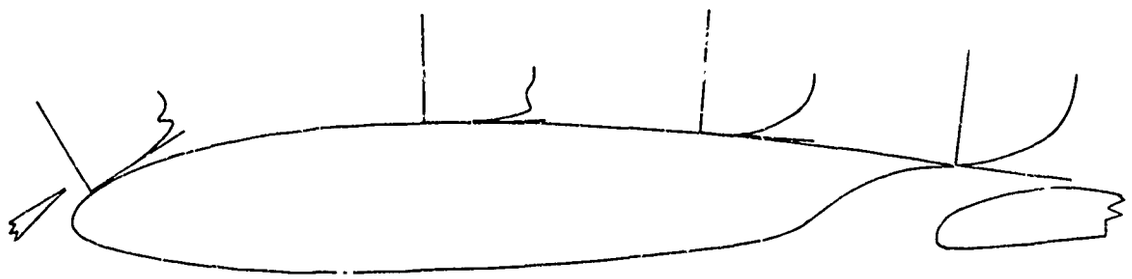
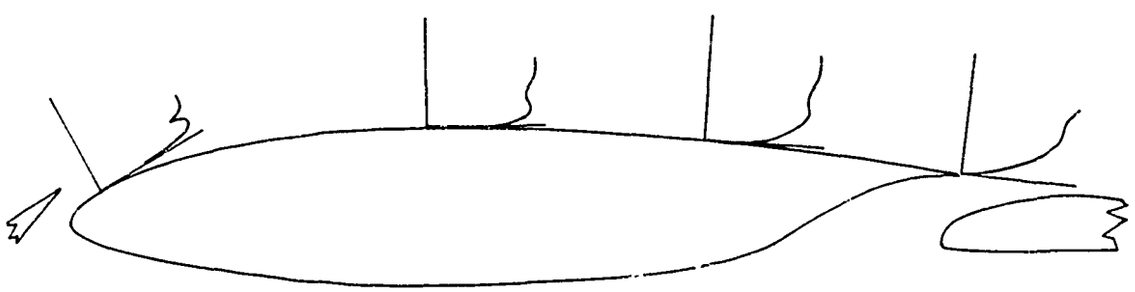


FIGURE 4 Variation of lift with slat gap

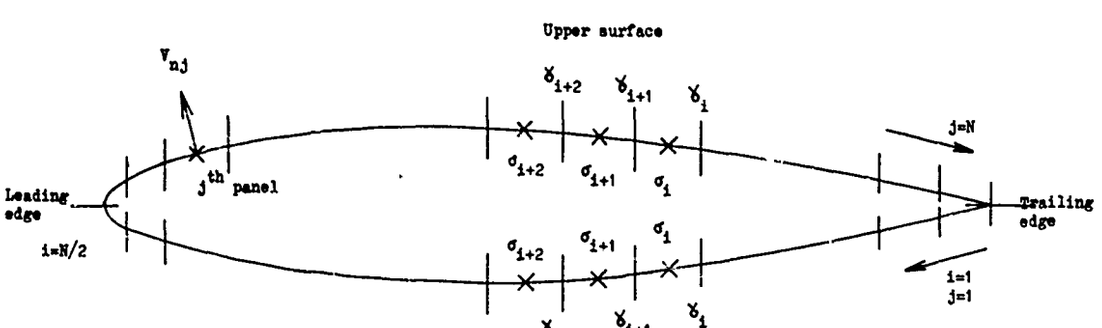


1.75 % slat gap



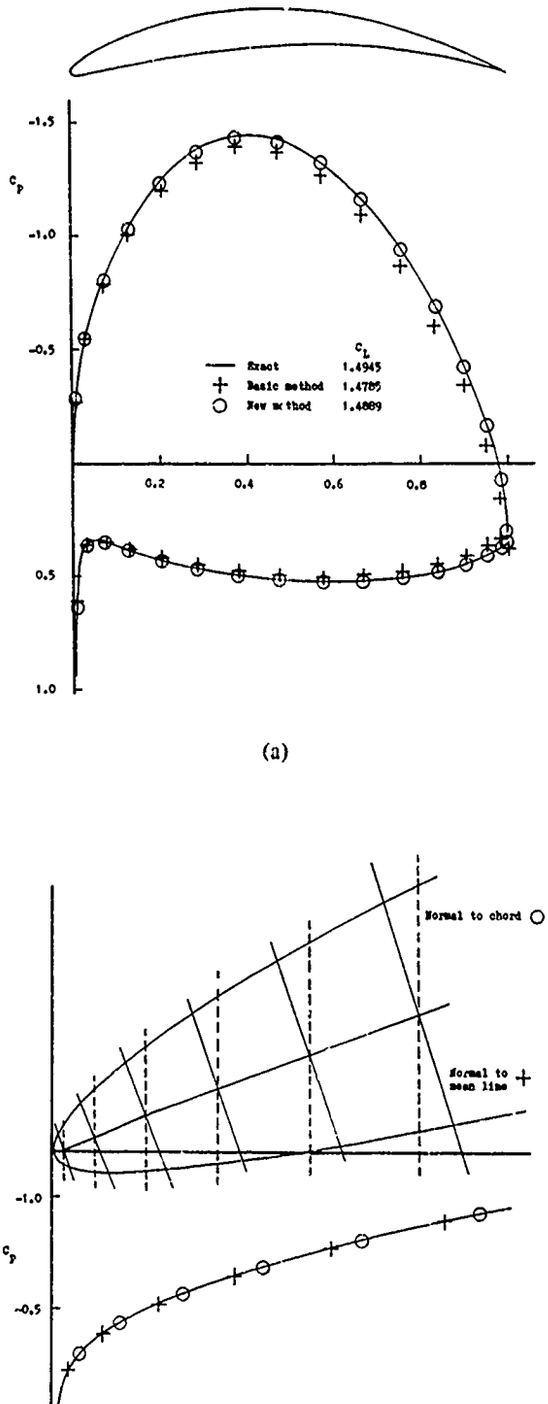
2.15 % slat gap

FIGURE 5 Viscous layer development over the main aerofoil of a slatted wing



$$(V_{nj})_i = A_{ij}\sigma_i + (B_{ij}\gamma_i + B'_{ij}(\gamma_i - \gamma_{i+1}))$$

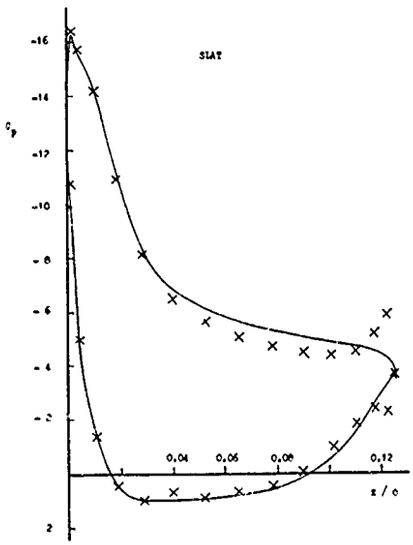
FIGURE 6 Notation used for panel method modelling



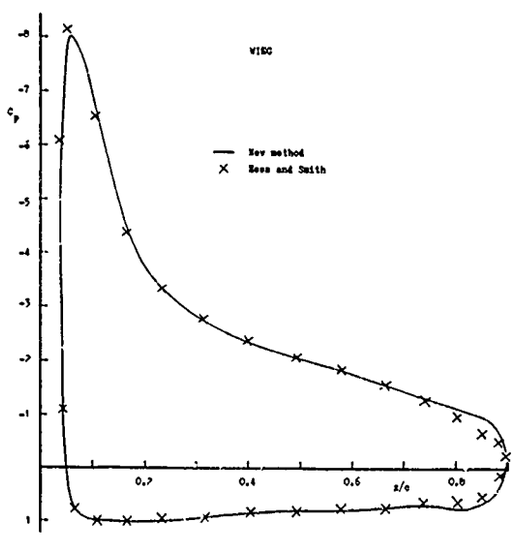
(a)

(b)

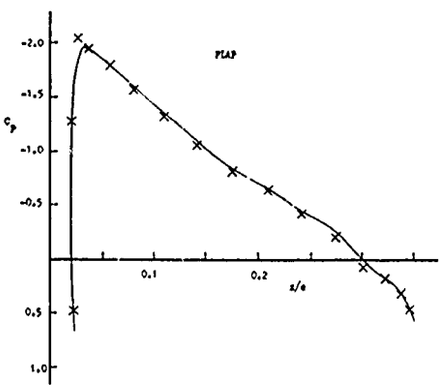
FIGURE 7 ... ...ion with an exact solution for a cambered aerofoil



(a)



(b)



(c)

FIGURE 8 Comparison with the Hess and Smith method for a three element aerofoil

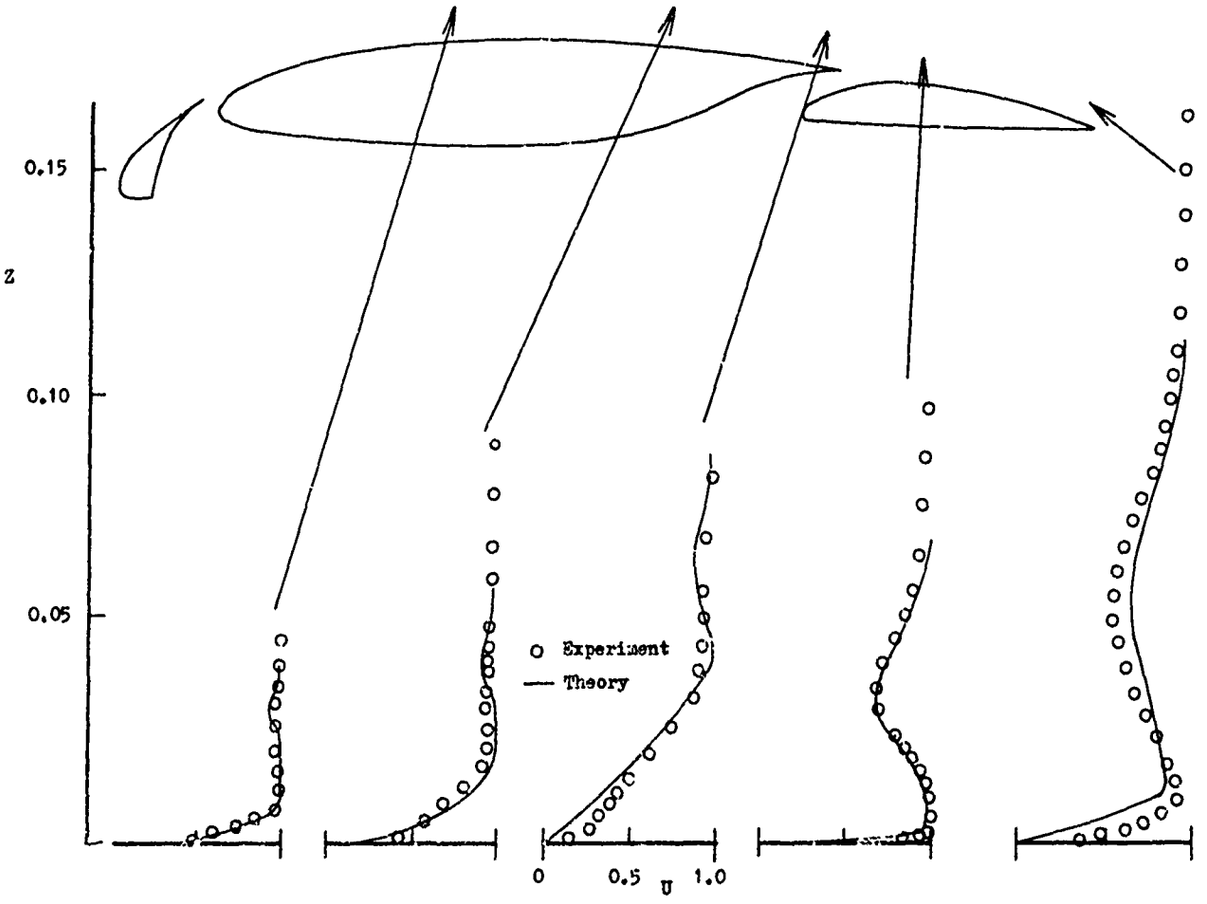
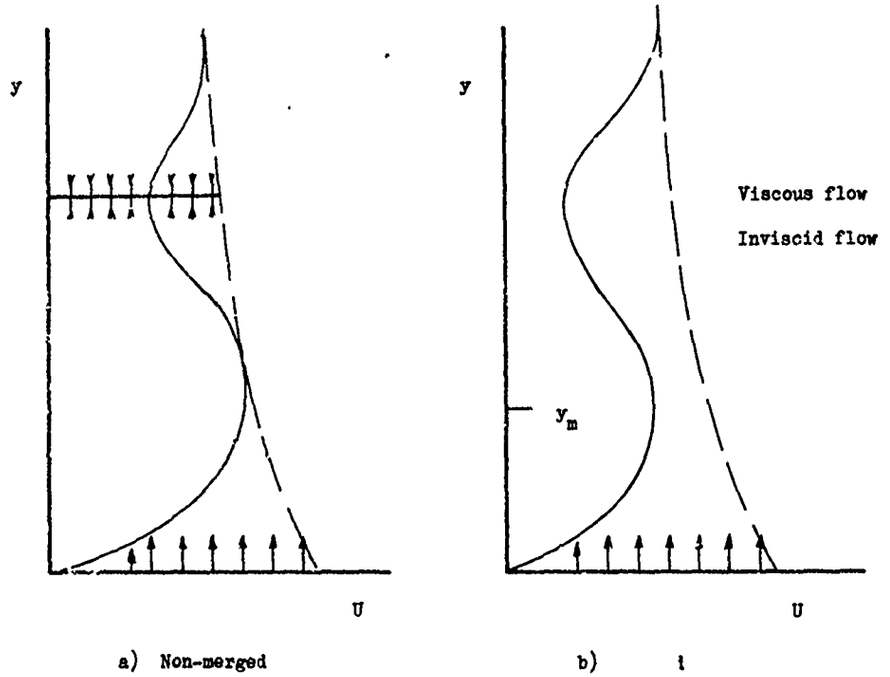
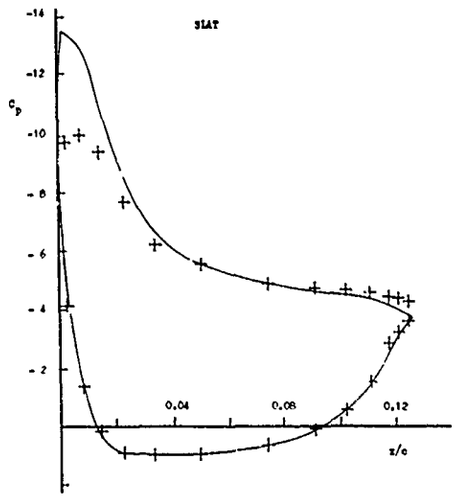


FIGURE 9 Prediction of the shear layer development over a multi-aerofoil

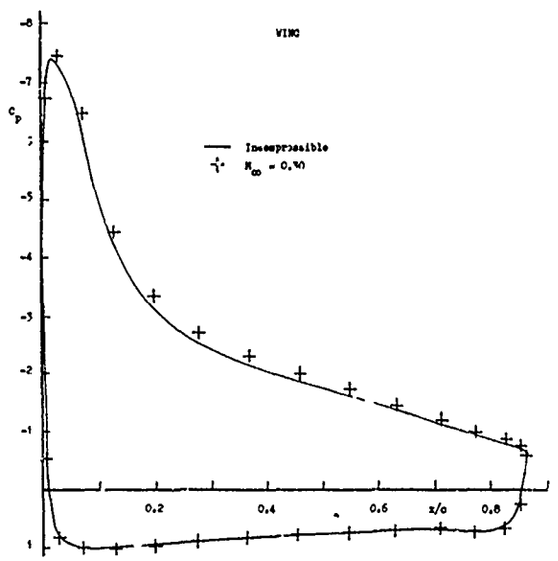


a) Non-merged b) i

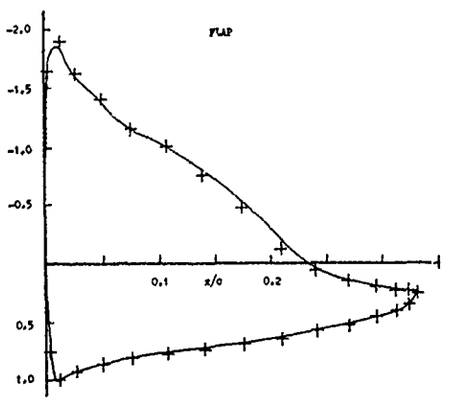
FIGURE 10 Determination of the equivalent inviscid flow for complex shear layers



(a)



(b)



(c)

FIGURE 11 Effect of compressibility on a three element aerofoil at 18° incidence

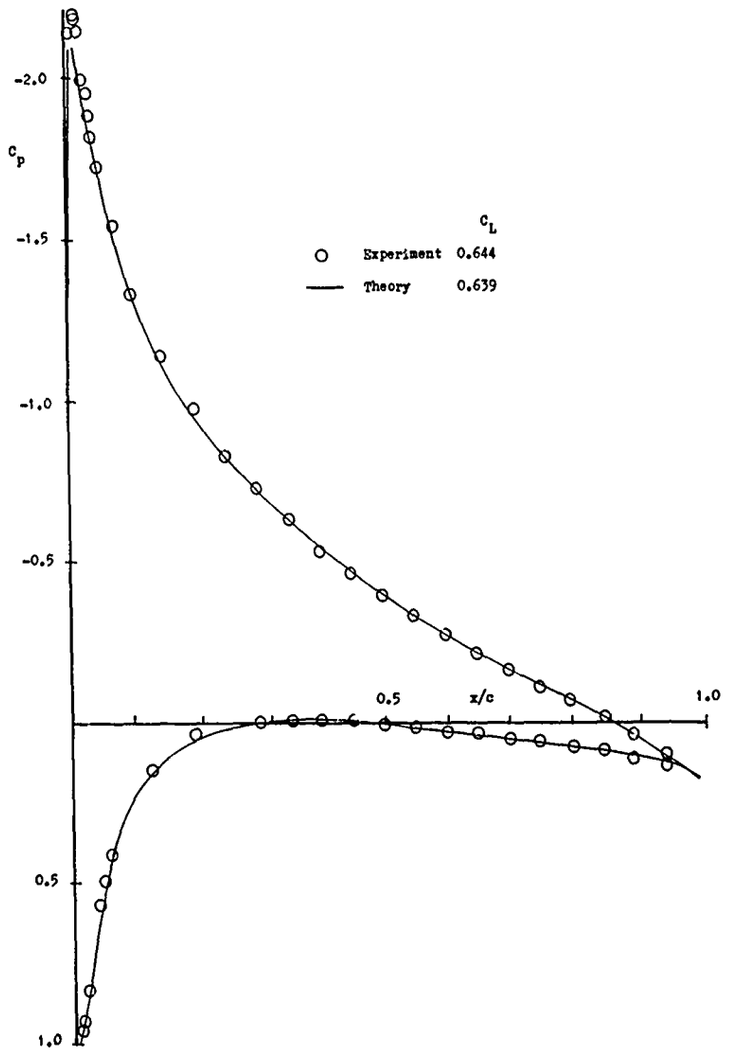


FIGURE 12 Comparison with experiment for a 12.2% RAE 100 aerofoil at 5.86° incidence

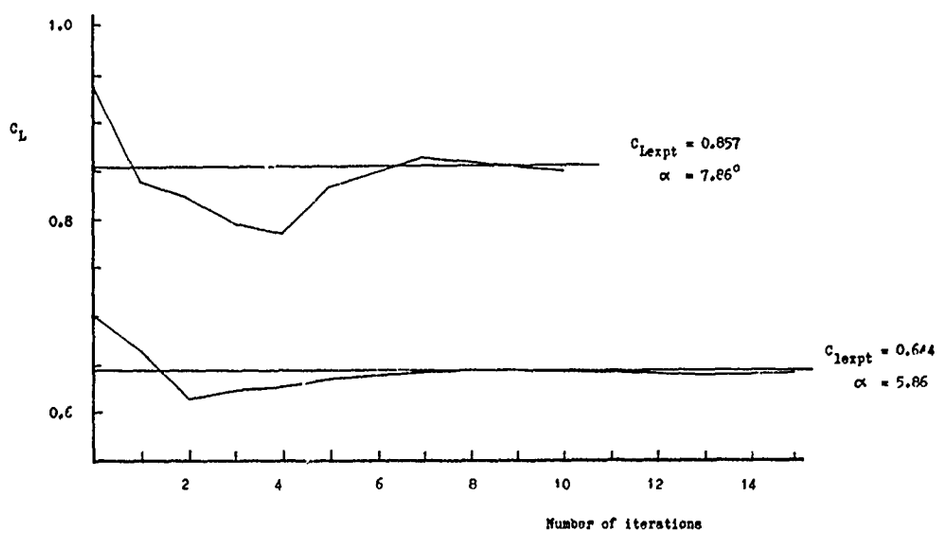


FIGURE 13 Convergence history for the RAE 100 aerofoil

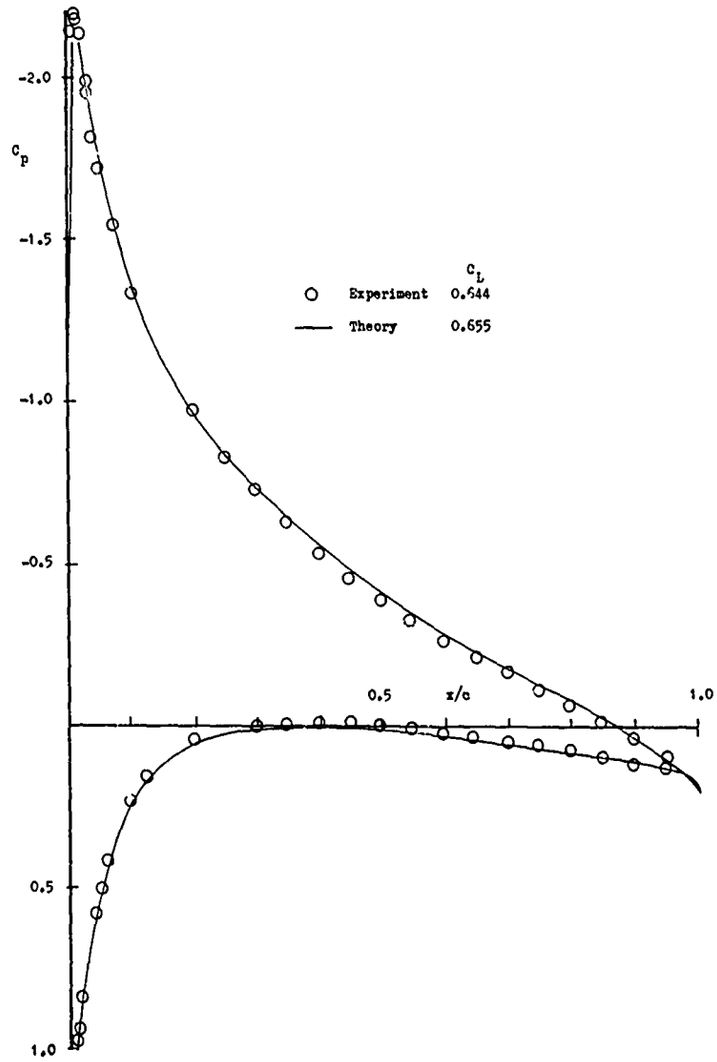


FIGURE 14 Comparison with experiment for a 12.2% RAE 100 aerofoil at 5.86° incidence without allowance for wake curvature

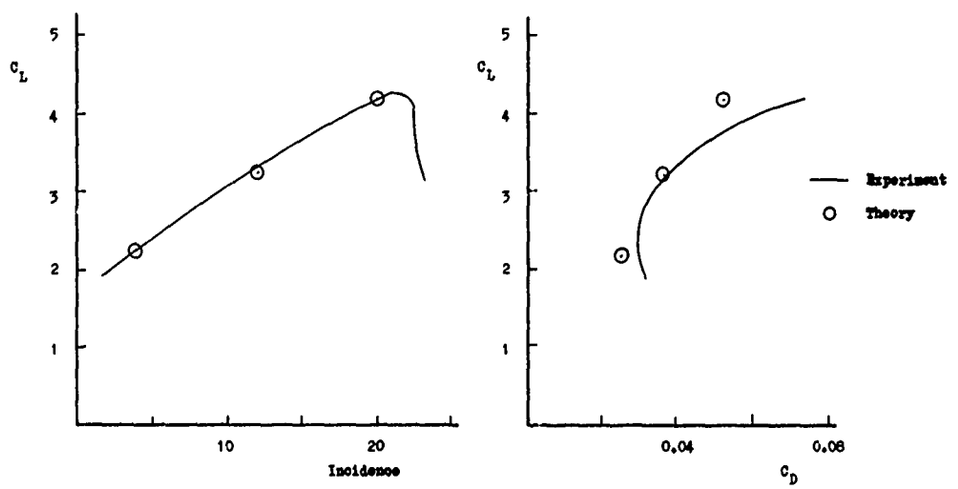
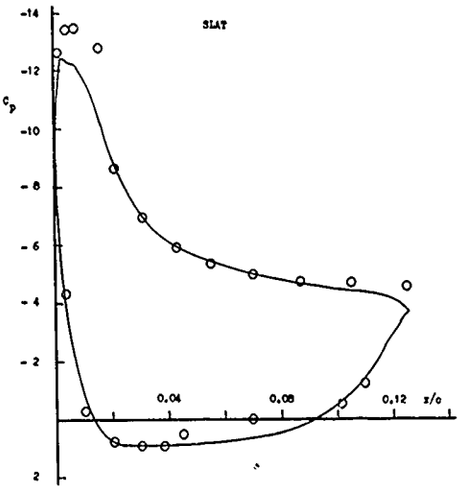
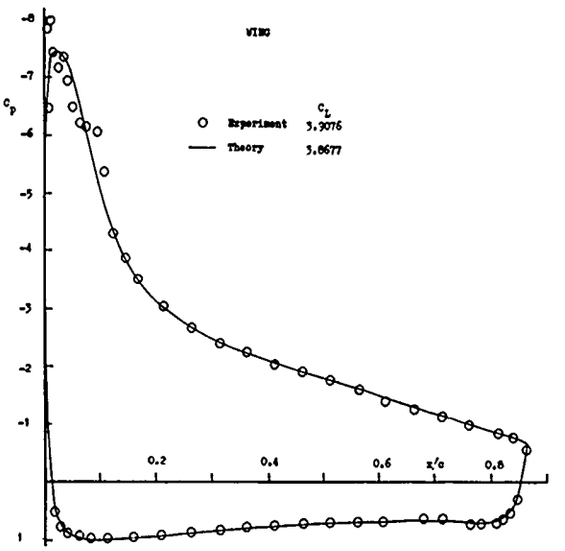


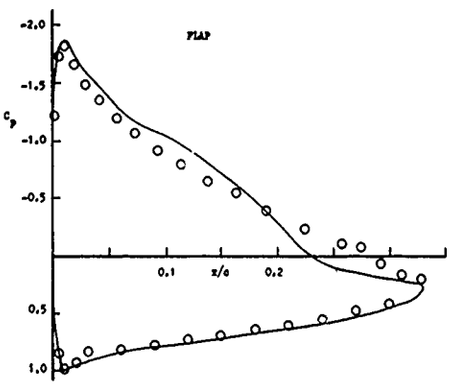
FIGURE 15 Comparison with experiment for a three element aerofoil at 18° incidence



(b)



(c)



(d)

FIGURE 15 (cont) Comparison with experiment for a three element aerofoil at 18° incidence

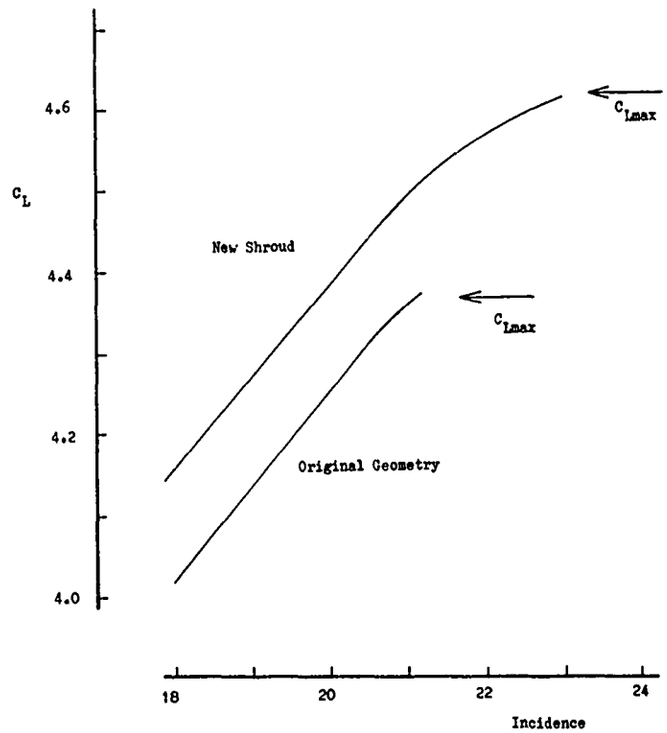


FIGURE 16 Flexible shroud design for a three element aerofoil

A DIRECT-INVERSE TECHNIQUE FOR LOW SPEED HIGH LIFT AIRFOIL FLOWFIELD ANALYSIS

Leland A. Carlson
Professor, Aerospace Engineering Department
Texas A&M University
College Station, Texas 77843

SUMMARY

A direct-inverse method is presented for computing the flow about low speed airfoils under high lift massive separation conditions. On the lower surface the flowfield is determined using an iterative inviscid relaxation technique coupled to a laminar-turbulent momentum integral boundary layer scheme using direct (airfoil specified) boundary conditions. On the upper surface, the flowfield is also computed directly with viscous interaction up to the separation point, with the separation point and separated pressure level determined as part of the solution. Downstream of separation, inverse boundary conditions (pressure specified) are utilized; and the flowfield and displacement surface are calculated. Typical results and comparisons with experimental data for GA(W)-2 and NACA 4412 airfoils are presented, including pressure distributions, lift, and drag coefficients versus angle of attack. It is believed that the method can yield accurate engineering estimates of aerodynamic properties at moderate Reynolds numbers and that, thus, it is applicable to general aviation and helicopter aerodynamics.

INTRODUCTION

Over the past several years, the finite-difference direct-inverse approach has been successfully used for the design and analysis of subsonic and transonic airfoils (Ref. 1). This method can be used in either the direct (analysis) mode in which the airfoil shape is prescribed and the flowfield, surface pressures, and aerodynamic coefficients are determined, or in the direct-inverse (design) mode in which an initial nose shape is given along with the pressure distribution on the remainder of the airfoil. In the latter case, the flowfield and actual airfoil shape are computed. This method and others (Ref. 2) have been found to yield accurate predictions of transonic airfoil behavior at design and near design conditions.

However, in the analysis of high performance airfoils, aerodynamicists would also like to be able to predict airfoil pressure distributions at high lift, high angle of attack conditions. Since such situations are characterized by large regions of separated flow and are dominated by strong viscous interaction effects, inviscid methods are definitely not applicable. Furthermore, subsonic-transonic analysis and design methods (Refs. 1-2) typically only include the effects of weak viscous interaction and fail to give acceptable answers whenever the length of the separated zone exceeds a few percent of the airfoil chord.

Fortunately, Barnwell (Ref. 3) demonstrated a few years ago that the direct-inverse technique could be successfully applied to the low speed high lift case. By specifying the separation point, he was able to obtain excellent agreement with experimental data by solving the small perturbation inviscid flow equation with direct boundary conditions (airfoil ordinates specified) upstream of separation and inverse boundary conditions (pressure specified) downstream of separation. Since Barnwell did not include a boundary layer calculation or coupling, the questions arose--Could similar results be obtained using the full potential equation coupled with viscous interaction and letting the separation point and pressure level be determined as part of the solution?

The purpose of this paper is to describe a model which can be used to determine the flowfield about a low speed single element airfoil at high angle of attack high lift conditions and to present typical results obtained with the model. This model has been incorporated into a computer program (Ref. 4), called TRANSEP, which is a modification of the basic TRANDES code (Ref. 1). Thus, it can also be used for subsonic-transonic airfoil analysis and design, including the effects of weak viscous interaction.

FLOW MODEL AND SOLUTION METHOD

As indicated above, the present technique is based upon the previously developed transonic direct-inverse method and its ability to use either the displacement surface (airfoil ordinate plus displacement thickness) or pressure as the airfoil boundary condition. For the low speed high angle of attack case, the airfoil lower surface only experiences weak viscous interaction (i.e., no extensive separation). The lower surface boundary layer, however, frequently has a long laminar run before transitioning to fully turbulent flow. Thus, the model needs to include an initial laminar boundary layer in its viscous interaction section. On the upper surface the boundary layer is also initially laminar, but it quickly becomes turbulent in character followed by boundary layer separation and a separatic zone sometimes extending over as much as three-fourths of the airfoil upper surface. Fortunately, the separated region at low freestream velocities is characterized by an approximately constant pressure level.

Consequently, the low speed massive separation problem has been modeled as shown on Figure 1. To obtain the inviscid portion of the flowfield, the complete second order partial differential perturbation potential equation is represented by a system of second order accurate finite difference equations. These difference equations are then solved iteratively by column relaxation, which in order to obtain rapid convergence is usually done on several grids. Normally, these equations are first solved on a very coarse grid which is then interpolated and used as an initial condition for a coarse grid (typically 25 x 13). This procedure is normally repeated twice more to obtain a solution on a medium grid (49 x 25) and, if desired, on a fine grid (97 x 49). The latter has 130 points on the airfoil; however, acceptable results are usually obtained on the medium grid, particularly considering the computer time involved.

To include viscous effects the basic approach is to calculate for weak interaction regions a boundary layer displacement thickness and to use it to correct the location of the displacement surface (i.e., airfoil ordinate plus displacement thickness, δ^*). For the strongly interacting separated zone, the pressure is specified and the location of the displacement surface is computed by integrating the surface tangency conditions, with the initial conditions specified by the displacement surface slope and ordinate at the interface between the two regions. Normally, the displacement surface of the entire airfoil is updated every ten relaxation cycles.

Thus, on the lower surface the flow is computed using direct boundary conditions (airfoil specified) including the effects of weak viscous interaction. On the upper surface, the flowfield is also computed directly with viscous interaction up to the separation point, which is determined as part of the solution. Downstream of separation, inverse boundary conditions are utilized, and the pressure is assumed to be constant in the separated zone. Studies with this model have shown that the separated zone pressure, which has to be computed as part of the solution, must be determined by conditions at both the separation point and at the trailing edge and not just on conditions in the vicinity of separation. This result is in agreement with the conclusion of Gross (Ref. 5) that conditions at the downstream end of the separation bubble determine bubble pressure.

Hence, in the present formulation, the pressure coefficient for the constant pressure separated zone is computed by:

$$C_{P_{sep}} = \frac{-2\left(\phi_{ITE} - \phi_{sep}\right)}{X_{ITE} - X_{sep}} \qquad (1)$$

Here, as shown on Figure 2, ϕ_{ITE} and ϕ_{sep} are the nondimensional perturbation potentials at the displacement surface "trailing edge" and the turbulent boundary layer separation point. Note that Eq. (1) is a small perturbation approximation for $C_{P_{sep}}$; and while this form introduces some error into the problem, its usage has been found to be simple, accurate, and reliable.

In principle, the separated region and wake should be accurately modeled with respect to physical phenomena and details, and this approach has been taken by other investigators (Refs. 5-7). In the present model, however, the wake region contains very few computational points since the coordinate system rapidly stretches to infinity. Thus, the wake is assumed to be inviscid with a constant pressure trailing edge formed by the upper and lower displacement surfaces. Fortunately, extensive numerical experiments with the present model indicate that the results for the pressure distribution and aerodynamic coefficients are primarily dependent upon obtaining accurate predictions for the location of the separation point and the magnitude of the separated pressure. Apparently, the details of the wake region are of secondary importance.

In the present method, the laminar portion of the boundary layer is computed using a compressible Thwaites method and the turbulent boundary layer is computed using the Nash-Macdonald (Ref. 9) method. These integral methods are efficient and reliable and yield excellent predictions for displacement thicknesses (Ref. 10). Internally, the transition point is determined from a Granville type correlation (Ref. 11) based upon the difference between the local momentum thickness Reynolds number and the value at the laminar instability point combined with the pressure gradient history. Sometimes, particularly on the upper surface at high angles of attack, laminar separation is predicted upstream of the transition point. In these cases, the local momentum thickness Reynolds number is compared to an empirical correlation in order to determine if the laminar bubble is long or short. If the bubble is short, its length is assumed to be one horizontal ΔX grid width and the turbulent flow computation is initiated at the next downstream grid point. No attempt is made to handle long bubbles.

As indicated, the theoretical results are primarily dependent upon accurate prediction of the upper surface separation point location. In the Nash-Macdonald integral method, separation is assumed to occur when the value of $(-\theta/q)dq/ds$ exceeds a specific value, SP. Here θ is the local momentum thickness and q is the local boundary layer edge velocity. Obviously, accurate predictions require an appropriate selection of the value of SP in order to obtain the correct separation point. Extensive studies with the present method indicate that accurate results can only be obtained at high angles of attack by making SP a function of angle of attack, Reynolds number, and the low angle of attack lift curve slope; and an empirical correlation has been developed for this purpose.

Now the solution scheme for the present method is iterative with respect to not only the flowfield but also the separation point and separated pressure level. A convergence history for a typical case is shown on Figure 3. Initially, some oscillation occurs on each grid, but, as can be seen, the values quickly converge. Normally 400 iterative cycles are performed on both medium and fine grids. Also, the location of the separation point on the fine grid (97 x 49, 130 airfoil points) is held fixed at the chordwise location computed on the medium grid (49 x 25). Typical run times for a medium grid result on an Amdahl 470/V6 are about one minute.

TYPICAL RESULTS

In the development of the present model, the NACA 4412 and GA(W)-2 airfoils were primarily used as test cases due to the excellent experimental pressure distributions available for these airfoils (Refs. 12-13). The importance of including strong interaction for such airfoils even at relatively low angles of attack is shown on Figure 4, which compares the strong interaction model (IMASS=1) with a calculation using only weak viscous interaction (IMASS=0). Notice that the present model predicts a significantly different upper surface pressure distribution, and a separated zone on the last ten percent of the airfoil. As a result of the latter, the lower surface and trailing edge pressures are also different. While the results (i.e., C_L = 1.0768) shown on Figure 4 were obtained with an early version of the model, the present version predicts for this case a C_L of 1.15, which is very close to the experimentally measured value of 1.18 and significantly lower than the weak interaction result.

A typical result for the GA(W)-2 airfoil is portrayed on Figure 5, which compares the predicted pressure distribution with results obtained from experimental measurements (Ref. 12). This case, which is near C_{Lmax}, has an extensive upper surface separated region from about 60% chord to the trailing edge. On the lower surface the boundary layer remained entirely laminar, although results with an all turbulent lower surface showed no significant difference. On the upper surface, transition with a short separation bubble occurred near the leading edge. As can be seen, the agreement with experiment, particularly for the C_p distribution, is excellent. Other results for the GA(W)-2 have been previously reported in Reference 14.

The flow about a NACA 4412 airfoil, which is a typical conventional airfoil, has also been investigated for Reynolds numbers from 10^5 to 6.3 x 10^6 and angles of attack from -0.54 degrees up to about 20 degrees. Some typical results are shown on Figures 6-8, and additional results are presented in Reference 15. As can be seen, the lower surface pressure distributions are in excellent agreement with the experimental data (Ref. 13); and the upper surface results and lift coefficients are sufficiently accurate for engineering usage. The only obvious discrepancy is near the turbulent separation point where the predicted pressures appear to be usually slightly high. However, the average separated pressure level is quite representative of the measured data.

Figures 9 and 10 present a comparison of the theoretical and experimental aerodynamic coefficients at the higher angles of attack. Here the drag coefficients have been computed using an empirically modified form (Ref. 14) of the classical Squire-Young formulation (Ref. 16). Also, it should be noted that the present results above C_{Lmax} are sensitive to the method of determining upper surface separation. This sensitivity indicates that the present method could probably be improved by using a more accurate turbulent boundary layer calculation scheme. In addition, experimental data (Refs. 13, 17-18) in the vicinity of C_{Lmax} disagrees by as much as 0.3 in lift coefficient and three degrees in angle of attack, even at the same Reynolds numbers. Nevertheless, the present method should lead to reasonable results for the flow about low speed airfoils up to C_{Lmax}, and sometimes even beyond C_{Lmax}.

Finally, some comment should be made concerning the accuracy and applicability of the present method. Based upon experimental comparisons, it should yield accurate pressure distributions and aerodynamic coefficients for airfoils at low speeds at Reynolds numbers above 1 x 10^6 and for angles of attack above six degrees. For lower angles, the non-massive separation model (IMASS=0) is recommended. Such results can be obtained on either the medium or the fine grid. However, due to the finite mesh size used in the finite difference formulation, the separation point may only be accurate to three percent chord. Consequently, at very high lift coefficients the overall accuracy of the method will be somewhat less. Currently, the method is being extended into the medium and low transonic Mach number range.

REFERENCES

1. Carlson, L. A., NASA, "TRANDES: A Fortran Program for Transonic Airfoil Analysis or Design," June 1977, NASA CR-2821.

2. Bauer, F., Garabedian, P., Korn, D., and Jameson, A., Supercritical Wing Sections II, New York, Springer-Verlag, 1975.

3. Barnwell, R., AIAA, "Two Inviscid Computational Simulations of Separated Flow about Airfoils," July 1976, Paper No. 76-379.

4. Carlson, L. A., Texas A&M Research Foundation, "TRANSEP: A Program for High Lift Separated Flow about Airfoils," February 1980, Report 3224-80-2.

5. Gross, L. A., AIAA, "The Prediction of Two-Dimensional Airfoil Stall Progression," January 1978, Paper No. 78-155.

6. Maskew, B. and Dvorak, F. A., American Helicopter Society, "Investigation of Separation Models for the Prediction of C_{Lmax}," May 1977, Paper 77-33-01.

7. Zumwalt, G. W. and Nark, S. N., Wichita State University, "An Analytical Model for Highly Separated Flow on Airfoils at Low Speeds," May 1977, Report AR-77-2.

8. Henderson, M. L., AIAA, "A Solution to the 2-D Separated Wake Modeling Problem and its Use to Predict C_{Lmax} of Arbitrary Airfoil Sections," January 1978, Paper No. 78-156.

9. Nash, J. F. and Macdonald, A. G. J., Aerospace Research Council, "The Calculation of Momentum Thickness in a Turbulent Boundary Layer at Mach Numbers up to Unity," 1967, C. P. No. 963.

10. Carlson, L. A., NASA, "Inverse Transonic Airfoil Design Including Viscous Interaction," November 1976, Conference Proceedings 2001, pp. 1387-1395.

11. Schlichting, H., Boundary Layer Theory, 6th ed., New York, McGraw-Hill, 1968, p. 479.

12. McGhee, R. J., Beasley, W. D., and Somers, D. M., NASA, "Low Speed Aerodynamics Characteristics of a 13-Percent Thick Airfoil Section Designed for General Aviation Applications," May 1977, TMX-72697.

13. Pinkerton, R. M., NACA, "The Variation with Reynolds Number of Pressure Distribution Over an Airfoil Section," 1938, Report 613.

14. Carlson, L. A. and Rocholl, B. M., NASA, "Application of Direct-Inverse Techniques to Airfoil Analysis and Design," March 1978, Conference Publication 2045, Part I, pp. 55-72.

15. Carlson, L. A., Texas A&M Research Foundation, "Inverse Transonic Airfoil Design Methods Including Boundary Layer and Viscous Interaction Effects," July 1979, Report No. 3224-79-03.

16. Schlichting, H., Boundary Layer Theory, 6th ed., New York, McGraw-Hill, 1968, pp. 714-717.

17. Pinkerton, R. M., NACA, "Calculated and Measured Pressure Distributions over the Midspan Section of the NACA 4412 Airfoil," 1936, Report. No. 563.

18. Loftin, L. K. Jr. and Smith, H. A., NACA, "Aerodynamic Characteristics of 15 NACA Airfoil Sections at Seven Reynolds Numbers from 0.7×10^6 to 9×10^6," 1949, TN 1945.

ACKNOWLEDGEMENTS

The work reported in this paper was primarily sponsored by NASA Grant NSG 1174 and partially supported by the Texas Engineering Experiment Station through its Data Processing Center. The author also acknowledges the assistance of Michael Watts and Robert Simmons, students in the Aerospace Engineering Department, who worked on this project.

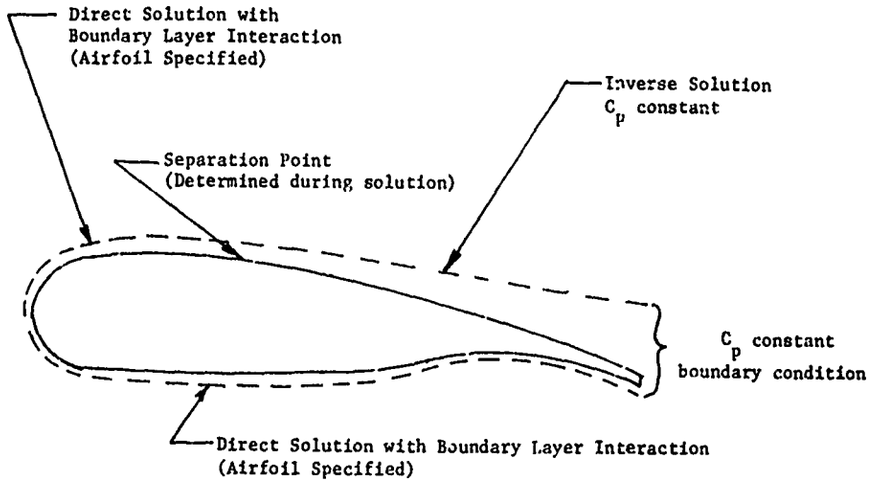


Figure 1 -- Problem Formulation

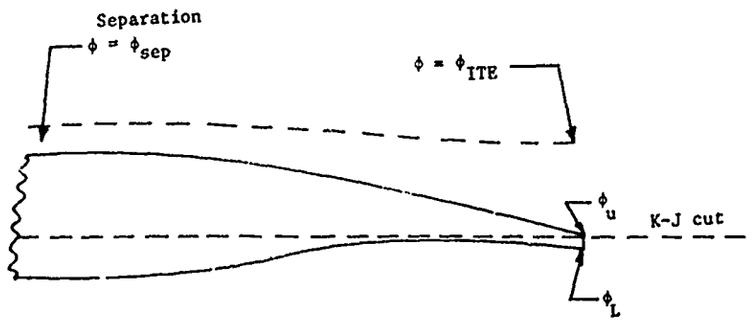


Figure 2 -- Separated Region Treatment

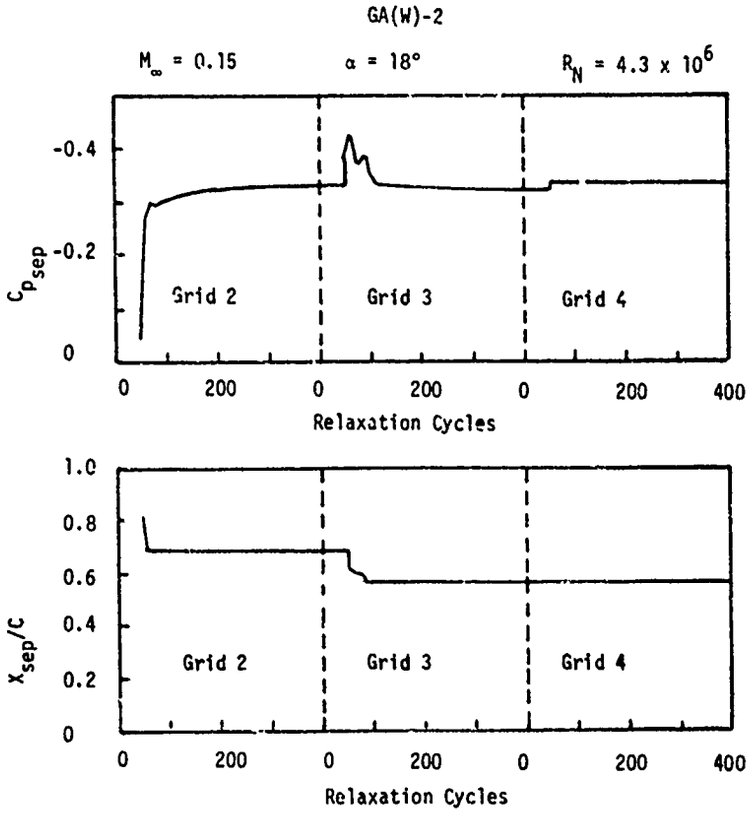


Figure 3 -- Separation Point and Pressure Behavior During the Relaxation Process

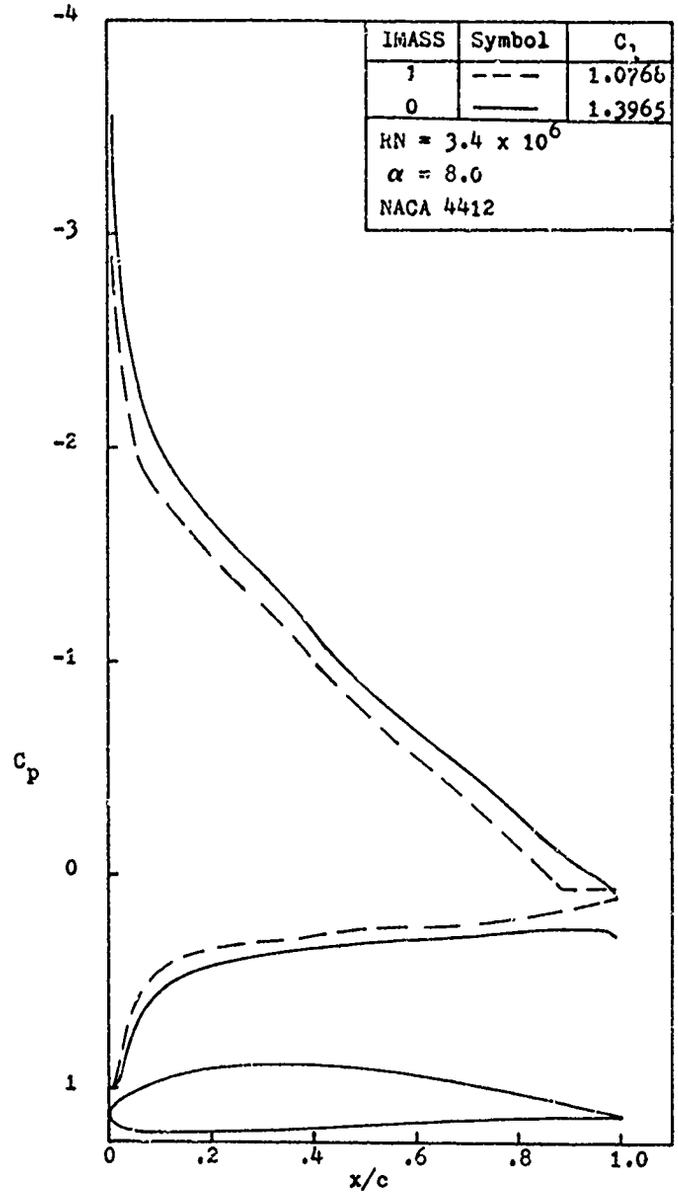


Figure 4 -- The Effect of Including Massive Separation on the C_p Distribution

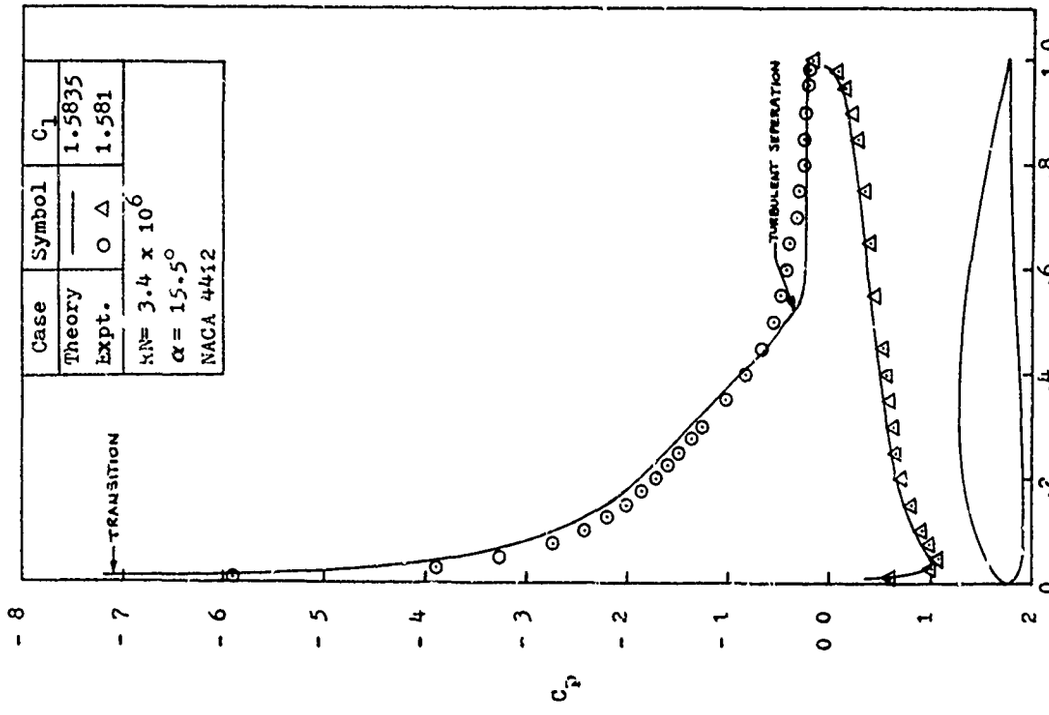


Figure 6 -- Results for NACA 4412 Near $C_{L_{max}}$ - Case I

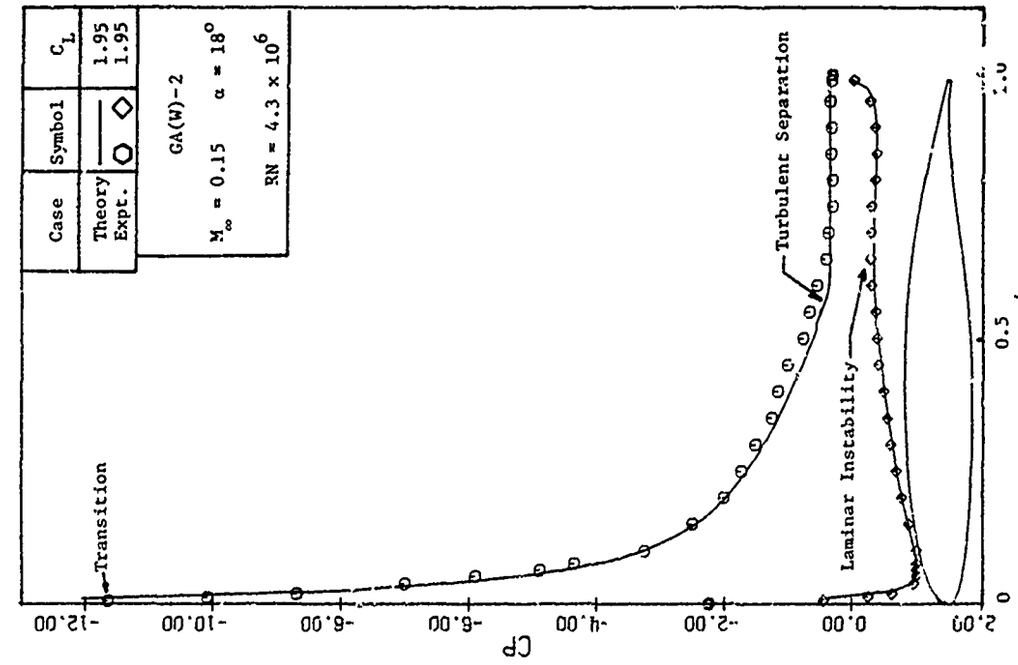


Figure 5 -- Theoretical and Experimental Pressure Distribution Comparisons for the GA(W)-2 Airfoil

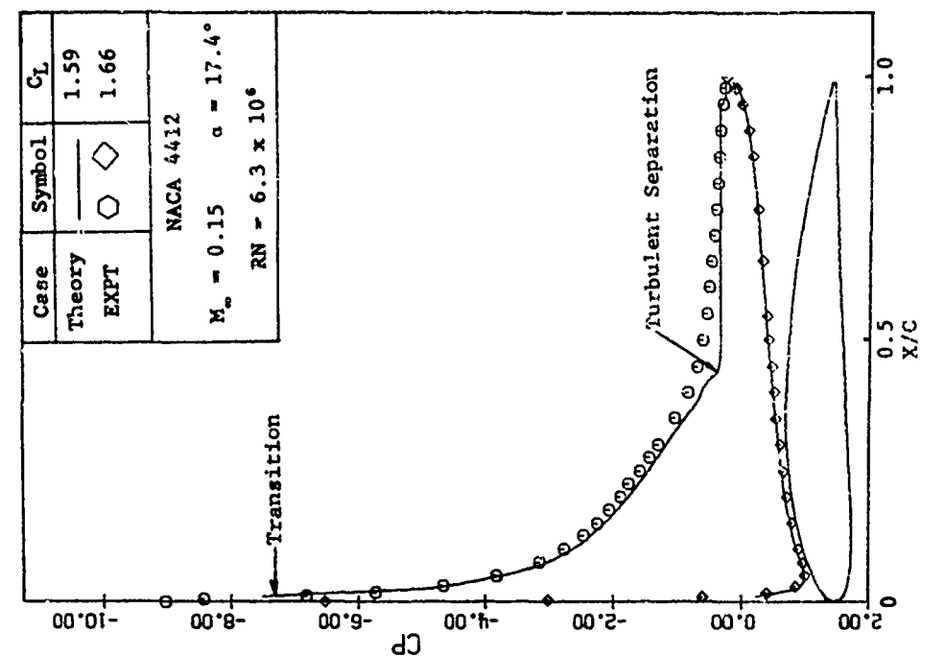


Figure 8 -- Results for NACA 4412 Above $C_{L_{max}}$

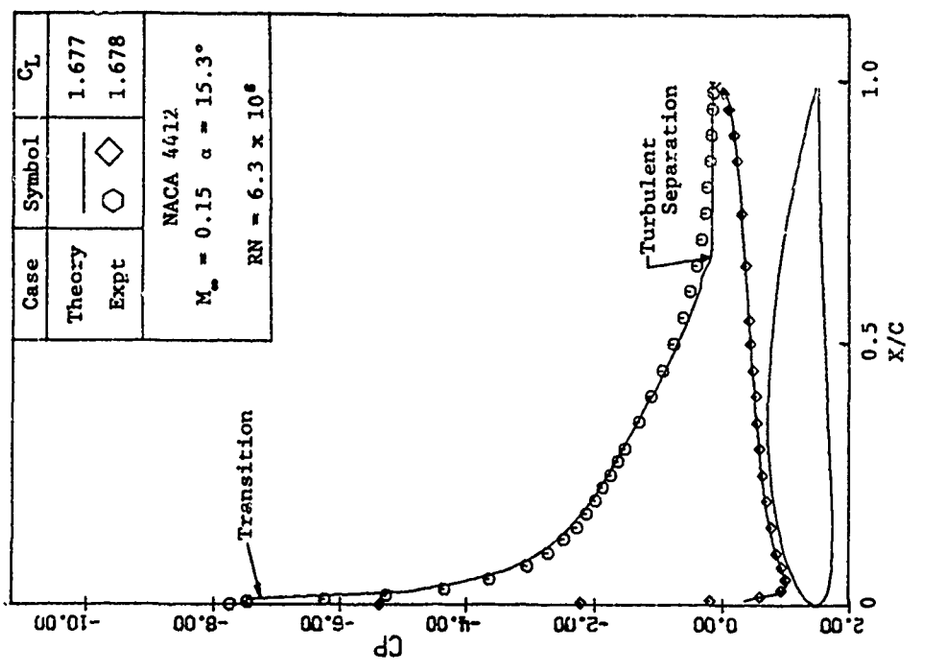


Figure 7 -- Results for NACA 4412 - Case II

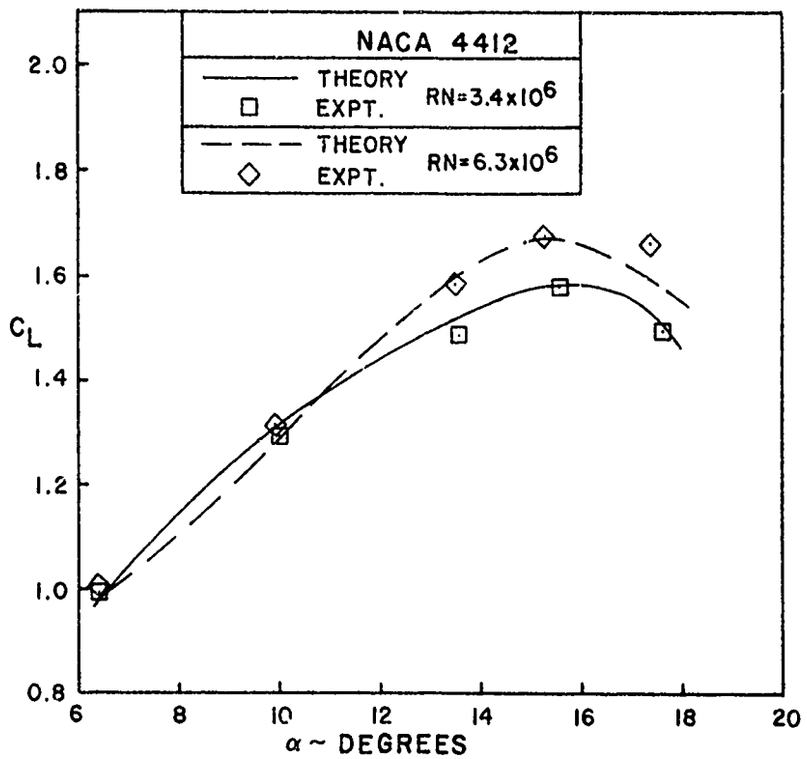


Figure 9 -- Experimental and Theoretical Comparisons of Lift with Angle of Attack

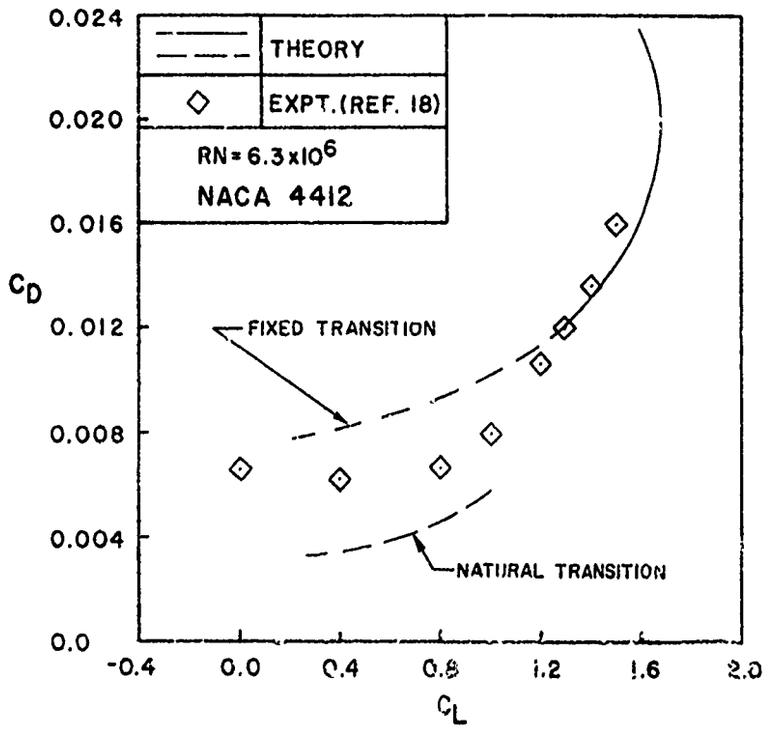


Figure 10 -- Theoretical and Experimental Drag Polars

A SECOND ORDER ACCURATE NUMERICAL METHOD FOR SUPERSONIC INTERACTING BOUNDARY LAYER FLOW PAST A COMPRESSION CORNER.

by

Bernardo Fortunato
Istituto di Macchine
Università di Bari
Via Re David 200
70125 Bari
Italy

SUMMARY

The supersonic interacting boundary layer equations are solved for laminar flow past a configuration with an interior (concave) compression corner region. The approach employs conformal coordinates to map the body geometry into stagnation point flow and uses the boundary layer scale laws to identify the principal terms of the compressible counterpart of the Navier-Stokes equations. A Levy-Lees type transformation is used in these coordinates to simplify the governing equations. The viscous-inviscid interaction law is given by evaluating the small perturbation theory inviscid flow past the displacement body obtained as the sum of the body surface plus the viscous displacement thickness. A fictitious time dependent term is introduced in the governing equations, that are then relaxed using an alternating direction implicit (A.D.I.) technique. The numerical scheme is second order accurate in both the longitudinal and normal directions.

LIST OF SYMBOLS

A	inviscid parameter
B	geometry flow variable
CR	Crank- Nicolson parameter
c_p	specific heat at constant pressure
F	nondimensional boundary layer longitudinal velocity
g	nondimensional total enthalpy
h, h_1, h_2	scale factors
K_c	conductivity of the gas
ℓ	viscosity function
$\tilde{\ell}$	characteristic length of the flat plate preceding the compression corner
M	Mach number
N	stretched normal coordinate
Pr	Prandtl number
p	nondimensional pressure
R	universal constant of gas
Re	Reynolds number
s	nondimensional longitudinal surface distance
t	time
T	nondimensional temperature
U_∞	undisturbed reference velocity
u	nondimensional longitudinal velocity in the boundary layer
V	nondimensional boundary layer normal volocity
$\bar{V}$	nondimensional velocity vector
v	nondimensional normal velocity in the boundary layer
$\bar{v}$	stretched normal velocity
x	nondimensional Cartesian coord.
y	nondimensional Cartesian coord.
α	Levy-Lees variable
β_{∞_w}	pressure gradient parameter
β, β_1	compressible pressure gradient parameters
γ	specific heat ratio
δ	displacement thickness
$\tilde{\delta}$	semiangle of the wedge trailing the compression corner
Δ	step size
∇	nondimensional "del" operator
ζ	Levy-Lees variable
η	nondimensional normal conformal coordinate
$\bar{\eta}$	shifted normal conformal coord.
θ	nondimensional boundary layer temperature
$\bar{\theta}$	inviscid flow deflection angle
$\bar{\theta}_s$	local inclination angle of surface
μ	nondimensional viscosity
μ_R	physical viscosity evaluated at the reference temperature
ξ	nondimensional longitudinal conformal coordinate
ρ	nondimensional density
τ	shear stress

Subscripts

b	body surface
c	center location between two longitudinal stations
e	upper edge of the boundary layer
$i-1, i, i+1, j$	grid point location
η, ξ, α, ζ	partial derivative with respect to the indicated variable
w	wall
∞	upstream undisturbed location
R	reference

Superscripts

$\dddot{\ }$	dimensional quantity
$\ddot{\ }$	time level $t^{\ddot{\ }}$
n	time level t^n
$n+1$	time level t^{n+1}

I INTRODUCTION

The design of high performance turbomachineries requires a good knowledge of the cascade flow field; reliable algorithms must therefore be developed for solving complex flow fields including separation effects.

The aim of present work is the development of a second order accurate numerical scheme for the solution of the interacting boundary layer equations applied to supersonic flow past a family of flat plate/wedge type configurations. The interacting boundary layer equations are particularly suitable for studying flow problems where strong inviscid-viscous flow interaction occurs, due to rapid boundary layer growth and to the failure of the classical boundary layer theory whenever flow separation is present. The approach here used first employs conformal coordinates to map the body geometry to a flat wall and uses boundary layer scale laws to identify the principal terms of the compressible counterpart of the Navier-Stokes equations in primary variable form. Levy-Lees type variables are used for capturing self-similar solution, wherever it might occur and a coordinate transformation is made to reduce the infinity flow region to a unit square. The inviscid flow is supposed to be an isentropic one over the displacement body, that is, over the surface obtained adding to the original geometry the displacement thickness, with the local properties obtained from linear theory. The nature of the problem is no more an initial value one /1/, as for the classical boundary layer equations, because the momentum equations assumes the form /2/

$$\int_0^{\infty} F_{xx}\, dy + F_{yy} = G(x, y)$$

These equations, very similar to the classical elliptic partial differential equation, require, therefore, also a downstream boundary condition. In order to solve the governing equations a fictitious time derivative of the displacement thickness is introduced in the momentum equation. The relaxation technique used to solve this equation is very similar to the alternating direction implicit method (A.D.I.) proposed by Werle and Vatsa /2/. Results of non separating flow over the compression corner family represented in figure 1, are presented for $M_\infty = 3$, for adiabatic and cold wall conditions and compared with those obtained with classical boundary layer equations.

All the calculations have been performed by an I.B.M. 370/158 computer.

II GOVERNING EQUATIONS

II.1 Geometry

The flow past a compression corner is transformed into a stagnation point flow using the following conformal transformation /3,4,5/:

$$z = (\tilde{\zeta} / B + 1)^{(1 - \beta_\infty / 2)} \qquad (1)$$

where $z = y + ix$ (physical plane) (1a)

$$\tilde{\zeta} = \eta + i\xi \quad \text{(conformal plane)} \qquad (1b)$$

where x, y and z have been nondimensionalized by the characteristic length $\tilde{\ell}$ of the flat plate preceding the compression corner (see figure 1), β_∞ is the incompressible Falkner Skan pressure gradient parameter /6/, related to the semivertex angle of the compression wedge $\tilde{\delta}$ trough the relation

$$\beta_\infty = 2\tilde{\delta} / \pi \qquad (2)$$

The parameter B is defined as:

$$B = (2 - \beta_\infty)^{2/(2-\beta_\infty)} \tag{3}$$

The scale factors for trasformation (1) are the same for both the ξ and η coordinates and are given /4,5/ as:

$$h = h_1 = h_2 = \frac{\sqrt{\xi^2 + \eta^2}}{\sqrt{\{(\xi^2+\eta^2)^2+2B(\eta^2-\xi^2)+B^2\}^{\beta_\infty/2}}} \tag{4}$$

The use of ξ and η variables allows the study of flow past any of the family of bodies formed by any line of constant η, denoted as η_b (see figure 1).

II.2 Conservation laws: the Navier-Stokes equations.

The nondimensional governing steady flow equations of a viscous, compressible, heat conducting fluid are /7/:

Continuity:

$$\nabla\cdot(\rho\,\bar{V}) = 0 \tag{5}$$

Momentum:

$$(\bar{V}\cdot\nabla)\bar{V} = -\frac{1}{\rho}\nabla p + \frac{1}{Re}\frac{\nabla\cdot\tau}{\rho} \tag{6}$$

Energy:

$$\rho(\bar{V}\cdot\nabla)T - (\bar{V}\cdot\nabla)p = -\frac{1}{Re}\nabla\left(\frac{\mu}{Pr}\nabla T\right) + \frac{1}{Re}(\tau:\nabla\bar{V}) \tag{7}$$

In these equations the velocities have been nondimensionalised by $U_R^{***} = U_\infty^{***}$, the lengths by $L_R^{***} = \tilde{\ell}$, the pressure by $p_R^{***} = \rho_\infty^{***} U_\infty^{***2}$, the density by $\rho_R^{***} = \rho_\infty^{***}$, the temperature by $T_R^{***} = U_\infty^{***2}/c_p$, the viscosity by μ_R^{***}, which is the viscosity evaluated at the reference temperature T_R^{***} and finally the stress tensor components by $\tau_R^{***} = \mu_R^{***} U_\infty^{***}/\tilde{\ell}$. The Reynolds number Re and the Prandtl number Pr are defined as:

$$Re = \rho_\infty^{***}\tilde{\ell}\,U_\infty^{***}/\mu_R^{***} \qquad Pr = \mu_R^{***} c_p / K_c^{***}$$

The gas is assumed to be air with constant specific heats and constant Prandtl number, with the perfect gas law:

State equation:

$$p = \rho\,R\,T \tag{8}$$

The last equation is the viscosity law:

Viscosity law:

$$\mu = \mu(T) \tag{9}$$

II.3 The boundary layer approximation.

Boundary layer like equations similar to the classical ones of Prandtl and Van Dyke /8/ are still valid in case of separated supersonic flow, as shown by Stewartson and Williams /9/; no new viscous terms over those included in the classical boundary layer equations are therefore contained in the interacting ones. To obain these equations the followings boundary layer scaling laws are introduced in the conformal plane

/10/:

$$\varepsilon = 1/Re^{1/2} \quad ; \quad \eta = \eta_b + \varepsilon\bar{\eta} \quad ; \quad v = \varepsilon\bar{v} \tag{10a,b,c}$$

The scale factor h becomes:

$$h = h_b \{1+\varepsilon[\frac{\eta_b \bar{\eta}}{\xi^2+\eta_b^2} - \frac{B(\eta_b^3\bar{\eta} + B\eta_b\bar{\eta} + \xi^2\eta_b\bar{\eta})}{\xi^4+\eta_b^4+2\xi^2\eta_b^2+2B\eta_b^2-2B\xi^2+B^2}] + O(\varepsilon^2)\} \tag{11}$$

where h_b is the scale factor at the surface ($\eta = \eta_b$). The application of the scaling laws to the governing equations gives:

Continuity:

$$\frac{\partial}{\partial\xi}(h_b\rho u) + \frac{\partial}{\partial\bar{\eta}}(h_b\rho\bar{v}) = 0 \tag{12}$$

Longitudinal Momentum:

$$uu_\xi + \bar{v}u_{\bar{\eta}} = -\frac{p_\xi}{\rho} + \frac{1}{\rho h_b}\frac{\partial}{\partial\bar{\eta}}(\mu u_{\bar{\eta}}) \tag{13}$$

Normal Momentum:

$$p_{\bar{\eta}} = 0 \tag{14}$$

Energy:

$$\rho u T_\xi + \rho\bar{v}T_{\bar{\eta}} - up_\xi = \frac{1}{Pr\, h_b}\{\frac{\partial}{\partial\bar{\eta}}(\mu T_{\bar{\eta}})\} + \frac{\mu}{h_b}u_{\bar{\eta}}^2 \tag{15}$$

Equation (14) shows that the pressure p is only function of ξ, and therefore equal to the inviscid pressure p_e, evaluated along the surface of the displacement body /2,11/. The expression of p_ξ is obtained from the inviscid nondimensional longitudinal momentum equation:

$$p_\xi = p_{e_\xi} = -\rho_e u_e u_{e_\xi} \tag{16}$$

Boundary conditions

At $\bar{\eta} = \eta_b$ the classical no slip and zero injection conditions are used:

$$u = 0 \quad ; \quad \bar{v} = 0 \tag{17a,b}$$

and the wall temperature is imposed:

$$T = T_w(\xi) \tag{17c}$$

The asymptotic boundary condition for $\bar{\eta} \to \infty$ are:

$$u \to u_e \quad ; \quad T \to T_e \tag{17d,e}$$

II.4 Boundary layer equations in transformed variables.

The boundary layer equations given before are here recast using the Levy-Lees variables /12/. Thus defining:

$$F = u/u_e \quad ; \quad \theta = T/T_e \quad ; \quad g = (2\theta + A F^2)/(2 + A) \tag{18a,b,c}$$

$$\zeta = \int_0^\xi \rho_e u_e \mu_e h_b\, d\xi \quad ; \quad \alpha = u_e h_b \int_0^{\bar{\eta}} \rho\, d\bar{\eta}/\sqrt{2\zeta} \tag{18d,e}$$

$$\bar{v} = \frac{1}{\rho h_b}\left(\frac{1}{\sqrt{2\zeta}}\frac{\partial\zeta}{\partial\xi}V - \sqrt{2\zeta}\frac{\partial\alpha}{\partial\xi}F\right) \tag{18f}$$

the governing equations (12) through (15) become:

Continuity

$$F + V_\alpha + 2\zeta F_\zeta = 0 \tag{19}$$

Longitudinal momentum

$$\frac{\partial}{\partial\alpha}(\ell F_\alpha) - VF_\alpha + \tilde{\beta}(\theta - F^2) - 2\zeta FF_\zeta = 0 \tag{20a}$$

or

$$\frac{\partial}{\partial\alpha}(\ell F_\alpha) + \tilde{\beta}_1(g - F^2) - VF_\alpha - 2\zeta FF_\zeta = 0 \tag{20b}$$

Static temperature energy equation

$$\frac{\partial}{\partial\alpha}\left(\frac{\ell}{Pr}\theta_\alpha\right) - V\theta_\alpha + \frac{u_e^2}{T_e}\ell F^2 - 2\zeta F\theta_\zeta = 0 \tag{21a}$$

or

Total temperature energy equation

$$\frac{\partial}{\partial\alpha}\left(\frac{\ell}{Pr}g_\alpha\right) - \frac{2A}{2+A}\frac{\partial}{\partial\alpha}\left\{\ell\left(\frac{1}{Pr} - 1\right)FF_\alpha\right\} - Vg_\alpha - 2\zeta Fg_\zeta = 0 \tag{21b}$$

where A, $\tilde{\beta}$ and $\tilde{\beta}_1$ are obtained from the local inviscid flow as:

$$A = \frac{u_e^2}{T_e} \quad ; \quad \tilde{\beta} = \frac{2\zeta}{u_e}\frac{du_e}{d\zeta} \quad ; \quad \tilde{\beta}_1 = \frac{(2+A)}{2}\tilde{\beta} \tag{22a,b,c}$$

The viscosity parameter ℓ is defined by:

$$\ell = \frac{\mu\rho}{\mu_e \rho_e} \tag{23a}$$

If μ is expressed by the Sutherland law /13/, ℓ becomes:

$$\ell = \frac{1+c}{\theta+c}\theta^{1/2} \quad \text{where } c = 198.6/T_e''' \tag{23b,c}$$

T_e''' beeing the dimensional inviscid temperature.

The assumption of linear theory for $\mu=\mu(T)$ gives:

$$\ell = 1 \tag{23d}$$

Boundary conditions

At $\alpha = 0$ $\quad F = 0 \quad ; \quad V = 0 \quad ; \quad \theta_w = \frac{T_w}{T_e}$ or $g = g_w$ or $g = \frac{2\theta_w}{2+A}$ (24a,b,c,d,e)

As $\alpha \to \infty$ $\quad F \to 1 \quad ; \quad \theta \to 1$ or $g \to 1$ (24f,g)

The introduction of the total energy g in the governing equations is convenient because, for the particular case with Pr=1, ℓ=1 and g_w=1, g is identically unity everywhere (adiabatic flow) and the governing equations are reduced to the simpler incompressible ones.

II.5 Inviscid-viscous interaction model

For present purposes the inviscid properties u_e, T_e, μ_e, ρ_e are obtained using the linearized theory applied to the displacement body. According to this theory the inviscid velocity parallel to the body is given by /5/:

$$u_e = 1 - \frac{\bar{\theta}}{\sqrt{M^2-1}} \quad \text{where} \quad \bar{\theta} = \bar{\theta}_s + \varepsilon\frac{d\delta}{ds} \tag{25a,b}$$

The expression of the slope of the body $\bar{\theta}_s$ is given in Reference 5.

The displacement thickness appearing in equation (25b) has the following expression:

$$\delta = \int_0^\infty \left(1 - \frac{\rho u}{\rho_e u_e}\right) dN \tag{26}$$

which using the Levy-Lees variables becomes:

$$\delta = \frac{\sqrt{2\zeta}}{2u_e h_b \rho_e}\int_0^\infty \{(2+A)g - AF^2 - 2F\}\, h\, d\alpha \tag{27}$$

Using equations (25a,b) the driving function becomes:

$$\tilde{\beta}_1 = -K_p \{ \frac{d\bar{\theta}_s}{d\xi} + \varepsilon \frac{d}{d\xi} (\frac{1}{h_b} \frac{d\delta}{d\xi}) \} \quad \text{where} \quad K_p = \frac{(2+A)\zeta}{\rho_e u_e^2 \mu_e h_L} \frac{1}{\sqrt{M_\infty^2 - 1}} \tag{28a,b}$$

The interaction law introduces in the governing equations, through the driving function $\tilde{\beta}_1$, a term proportional to $\frac{d^2\delta}{d\xi^2}$ (proportional to $\int_0^\infty \frac{\partial^2 F}{\partial \xi^2} d\alpha$) that changes the parabolic nature of the boundary layer equations in elliptic. Besides the upstream condition at the leading edge is therefore required also a downstream boundary condition.

III NUMERICAL METHOD

III.1 General statement

The numerical technique used to solve the governing equations is very similar to the alternating direction implicit (A.D.I.) /14/ proposed by Werle and Watsa /2,4/. According to them a fictitious time dependent derivative for the dislacement thickness $\frac{\partial \delta}{\partial t}$ is added to the momentum equation, which is relaxed in time until a steady state solution is obtained. The numerical technique used consists of two time steps (:: and n+1 sweeps).

III.2 Solution of the :: sweep equations

a) Governing equations

The governing equations written at time $t^{::}=t^n+\Delta t/2$ are:

Continuity

$$F^{::} + V_\alpha^{::} + 2\,\zeta F_\xi^{::} \xi_\zeta = 0 \tag{29}$$

Longitudinal momentum

$$\frac{\partial}{\partial \alpha} (\ell^{::} F_\alpha^{::}) - V^{::} F_\alpha^{::} + (F^{::2} - g^{::}) \{ K_p^n \frac{\partial \bar{\theta}_s}{\partial \xi} + \varepsilon \frac{K_p^n}{h_b} \frac{\partial^2 \delta^n}{\partial \xi^2} + \varepsilon K_p^n \frac{\partial \delta^n}{\partial \xi} \frac{d}{d\xi} (\frac{1}{h_b}) - \frac{\partial \delta^*}{\partial t} \} - 2\zeta F^{::} F_\xi^{::} \xi_\zeta = 0 \tag{30}$$

Energy equation

$$\frac{\partial}{\partial \alpha} (\frac{\ell^{::}}{Pr} g_\alpha^{::}) - \frac{2A^n}{2+A^n} \frac{\partial}{\partial \alpha} \{ \ell^{::} (\frac{1}{Pr} - 1)\, F^{::} F_\alpha^{::} \} - V^{::} g_\alpha^{::} - 2\zeta\, F^{::} g_\xi^{::} \xi_\zeta = 0 \tag{31}$$

The second order accuracy in the ξ direction is achieved by writing the equations at the central longitudinal station /5/ (see figure 2), according to the Crank Nicolson technique. Finite difference representation of the governing equations are obtained as follows:

Longitudinal momentum

The equation is written at point $P_{c,j}$ (see figure 2). Central differences are used to represent α derivatives. The non linear terms are quasilinearized according to the scheme:

$$A_c B_c = A_{i-1} B_c + A_c B_{i-1} - A_{i-1} B_{i-1} + O(\Delta\xi^2) \tag{32a}$$

where A_c and B_c at the center of the interval are expressed as the average of the two extreme values. The non linear terms of the momentum equation become therefore:

$$(V^{::} F_\alpha^{::})_{c,j} = CR\, (V_{i,j}^{::} F_{\alpha_{i-1,j}}^{::} + V_{i-1,j}^{::} F_{\alpha_{i,j}}^{::}) - (2CR-1)\, V_{i-1,j}^{::} F_{\alpha_{i-1,j}}^{::} \tag{32b}$$

$$F_{c,j}^{::2} = 2\,CR\, F_{i,j}^{::} F_{i-1,j}^{::} - (2CR-1)\, F_{i-1,j}^{::2} \tag{32c}$$

$$F^{::} F_\xi^{::} = (F_{i-1,j}^{::} + \frac{\Delta\xi}{2} F_{\xi_{i-1,j}}^{::}) (\frac{F_{i,j}^{::} - F_{i-1,j}^{::}}{\Delta\xi}) \tag{32d}$$

having expressed the longitudinal derivative $F_{\xi_{c,j}}^{::}$ with a central difference about point $P_{c,j}$. For the self similar solution (solution at the starting longitudinal station) the Crank Nicolson parameter CR is set to 1 and the the term $F^{::} F_\xi^{::}$ is dropped; for all the other stations on the surface CR =1/2 . The terms $\partial^2\delta^n/\partial\xi^2$, $\partial\delta^n/\partial\xi$ and K_p^n (that contains ξ derivatives) can be expressed as central differences with the known values of the old time t^n. Backward difference is used to represent $\partial\delta^{::}/\partial t$. The final finite difference form of the momentum equation is:

$$\omega_{1_j} F_{i,j-1}^{::} + \omega_{2_j} F_{i,j}^{::} + \omega_{3_j} F_{i,j+1}^{::} + \omega_{4_j} V_{i,j}^{::} = \omega_{5_j} \tag{33}$$

where $\omega_{2_j} = \omega_{2_j}(\delta_i^{\ddot{}})$ and $\omega_{5_j} = \omega_{5_j}(g_{i,j}^{\ddot{}}, \delta_i^{\ddot{}})$ (33a,b)

Continuity equation

The continuity equation is written at point $Q_{c,j-\frac{1}{2}}$ (see figure 2) as:

$$V_{i,j}^{\ddot{}} = V_{i,j-1}^{\ddot{}} + \omega_{6_j}(F_{i,j}^{\ddot{}} + F_{i,j-1}^{\ddot{}}) + \omega_{7_j} \quad (34)$$

In this way it is possible to couple directly this equation to the momentum one and solve directly the set of equations by the Davis coupled scheme /12,5/, i.e.:

$$F_{i,j}^{\ddot{}} = R_j F_{i,j-1}^{\ddot{}} + T_j + S_j V_{i,j-1}^{\ddot{}} \quad (35)$$

with the following boundary conditions:

$$F^{\ddot{}}(\xi,0) = 0 \quad ; \quad F^{\ddot{}}(\xi,\infty) = 1 \quad ; \quad V^{\ddot{}}(\xi,0) = 0 \quad (35a,b,c)$$

Energy equation

This equation, written at point $P_{c,j}$ is considered already linearized because it is solved using the most currently estimated values of $F_{i,j}^{\ddot{}}$, $V_{i,j}^{\ddot{}}$ and $\ell_{i,j}^{\ddot{}}$. By expressing each variable at the center of two longitudinal stations as seen before for the momentum equation, the energy equation assumes the form:

$$\omega_{8_j} g_{i,j-1}^{\ddot{}} + \omega_{9_j} g_{i,j}^{\ddot{}} + \omega_{10_j} g_{i,j+1}^{\ddot{}} = \omega_{11_j} \quad (36)$$

with the boundary conditions

$$g^{\ddot{}}(\xi,0) = \frac{2\theta_w}{2+A} \quad ; \quad g^{\ddot{}}(\xi,\infty) = 1 \quad (37a,b)$$

This is again a set of tridiagonal equations which are then solved by means of the Thomas algorithm:

$$g_{i,j}^{\ddot{}} = R_{1_j} g_{i,j-1}^{\ddot{}} + T_{1_j} \quad (38)$$

b) Solution technique

The complete solution algorithm in each longitudinal station at the $\ddot{}$ sweep is iterative and follows this scheme:

b1 - $\delta_i^{\ddot{}}$ is guessed.

b2 - $V_{i,j}^{\ddot{}}$, $F_{i,j}^{\ddot{}}$ and $\ell_{i,j}^{\ddot{}}$ are guessed.

b3 - The energy equation is solved.

b4 - The continuity and momentum equations are solved together.
The steps b3 and b4 are repeated until the required convergence is achieved.

b5 - $\delta_i^{\ddot{}}$ is calculated and compared with the value guessed at step b1; if the convergence has not been reached all the algorithm is repeated using the Regula Falsi method /14/ for guessing the new value of $\delta_i^{\ddot{}}$.

III.3 Solution of the n+1 sweep equations

In order to proceed with the solution technique from $t^{\ddot{}}$ to $t^{n+1}=t^{\ddot{}}+\Delta t/2$ the momentum equation is written at the wall by expressing the term $\partial\delta^{n+1}/\partial t$ as backward derivative, in the following way:

$$\frac{\partial}{\partial\alpha}(\ell^{\ddot{}}F_\alpha^{\ddot{}}) - g_w^{\ddot{}} K_p^n \frac{d\bar{\theta}_s}{d\xi} - \varepsilon K_p^n g_w^{\ddot{}}\{\frac{1}{h_b}\frac{\partial^2\delta^{n+1}}{\partial\xi^2} + \frac{\partial\delta^{n+1}}{\partial\xi}\frac{d}{d\xi}(\frac{1}{h_b})\} + g_w^{\ddot{}}\frac{\delta^{n+1}-\delta^{\ddot{}}}{\frac{\Delta t}{2}} = 0 \quad (39)$$

Rearranging:

$$\frac{1}{h_b}\frac{\partial^2\delta^{n+1}}{\partial\xi^2} + \frac{\partial\delta^{n+1}}{\partial\xi}\frac{d}{d\xi}(\frac{1}{h_b}) + \omega_{12}\,\delta^{n+1} = \omega_{13} \quad (39a)$$

where

$$\omega_{12} = -\frac{2}{\Delta t\,\varepsilon\,K_p^n} \quad (39b)$$

$$\omega_{13} = \frac{\frac{\partial}{\partial\alpha}(\ell^{\ddot{}}F_\alpha^{\ddot{}})}{\varepsilon K_p^n g_w^{\ddot{}}} - \frac{K_p^n \frac{d\bar{\theta}_s}{d\xi}}{\varepsilon K_p^n} - \frac{2}{\Delta t}\frac{\delta^{\ddot{}}}{\varepsilon K_p^n} \quad (39c)$$

In equation (39) the coefficient K_p is evalueted at time n instead of :: /2/ in order to obtain a simpler expression for the coefficient ω_{13}. In fact from equation (30) evaluated at the wall it is possible to obtain:

$$\omega_{13} = \frac{1}{h_b}\frac{\partial^2\delta^n}{\partial\xi^2} + \frac{d}{d\xi}\left(\frac{1}{h_b}\right)\frac{\partial\delta^n}{\partial\xi} + \frac{2}{\Delta t}\frac{(\delta^n - 2\,\delta^{::})}{\varepsilon\, K_p^n} \tag{40}$$

Note that at convergence $K_p^n = K_p^{::}$ and the results will obviously concide.
Central differences approximations are used for $\partial^2\delta^{n+1}/\partial\xi^2$ and for $\partial\delta^{n+1}/\partial\xi$ in equation (39a) . The final difference equation has the following tridiagonal form:

$$\omega_{14_i}\,\delta_{i-1}^{n+1} + \omega_{15_i}\,\delta_i^{n+1} + \omega_{16_i}\,\delta_{i+1}^{n+1} = \omega_{17_i} \tag{41}$$

that can be solved with the Thomas algorithm seen before.
An upstream and a downstream boundary condition must be applied to equation (41). At the first station of integration the self similar solution must be imposed and therefore the upstream boundary condition is the value of the displacement thickness corresponding to the self similar solution. Downstream the boundary layer should asymptotically approach the constant pressure gradient self similar state, analytically expressed by setting:

$$\frac{\partial\delta^{n+1}}{\partial\xi} = 0 \quad \text{at } \xi = \xi_{max} \tag{42}$$

IV RESULTS

The compression corner of figure 1 characterized by different wedge angles(from 0 to 6) , by η_b=0.02 and η_b=0.06, has been considered in the present numerical study for supersonic flow at M_∞=3. The coordinate transformations in the α and ξ directions are taken as $\alpha = 10\bar{\alpha}$ for $\bar{\alpha}$ from 0 to 1 and $\xi = \xi_{start} + \bar{\xi}(\xi_{max} - \xi_{start})$ for $\bar{\xi}$ from 0 to 1, ξ_{start} beeing the conformal coordinate of the first station and ξ_{max} that of the last one. ξ_{start} cannot be taken at the leading edge of the compression corner because the small perturbation theory is not valid near the stagnation point. ξ_{start} has been taken in a quasi-flat plate region so that the local similarity concept could be used to obtain a reliable and accurate starting solution. The corrisponding value of the driving function has been taken from the pressure gradient distribution calculated along the displacement body, that is along the body obtained as the sum of the physical surface and the displacement thickness(computed with the classical boundary layer equations). This distribution, as already shown by Fortunato and Werle /5/ for the non interacting case, has a localized region of rapid drop near the leading edge and then a quasi-flat region around ξ=0.7, that has been taken therefore as starting longitudinal coordinate value. ξ_{max} has been taken equal to 2.7.

Figures 3,4 and 5 refer to the adiabatic wall compression corner, characterized by η_b=0.02 and $\tilde{\delta}$=0. Figure 3 shows the influence of the initial guessed profile of the displacement thickness δ: the broken line refers to an initial non interacting boundary layer profile, while the solid line to the δ distribution proportional to the longitudinal conformal coordinate ξ. It is evident in figure 3 that both the displacements converge to the final interacting solution in a few iterations, thus indicating that the initial solution does not influence sensibly the number of iterations. Figure 4 shows the time behaviour of $\delta^{::}$ and δ^{n+1}; it is clear that only 5 or 6 iterations are necessary for the convergence of both the displacement thicknesses and that this number is practically indipendent of the longitudinal station. In figure 5 the displacement thickness values for different time steps are plotted versus the iterations number; the figure shows that, at least in the time step range analyzed here, the time step does not influence the number of iterations necessary to reach the convergence; in fact the results are practically identical already after 4 iterations. The influence of the downstream boundary position has been assessed changing the last station coordinate from 2.7 to 3.7; no difference has been noted in the solution and in the number of time iterations necessary to reach the

convergence.

Figures 6,7 and 8 show the inviscid pressure and pressure gradient and the wall shear stress distributions for the non interacting boundary layer case respectively, for adiabatic wall with η_b=0.06 and various semivertex angles. Figures 9,10 and 11 show the same parameters calculated with the interacting boundary layer equations for the same geometries. It is interesting to note that for the cases in which the classical boundary layer equations do not encounter the separation singularity the results are very close to those found by solving the interacting equations. For greater angles the classical boundary layer equations encounter the separation singularity near the wedge of the compression corner (ξ≈1.4), whilst the interacting boundary layer equations indicate that interaction smoothes the pressure gradient so that the flow is still attached.

All the adiabatic cases considered so far require less computation time than the corresponding cold wall cases; in fact for adiabatic flow conditions, with ℓ=1 and Pr=1, the energy equation can be totally eliminated. The computer time required for solving the adiabatic interacting boundary layer equations with 81x26 grid points(13 iterations in time) is about 4 C.P.U. minuts of an I.B.M. 370/158 computer.

The last case studied here is the cold wall ($T_w/T_{o\infty}$=0.5) compression corner with the same geometry as before. Only two inner iterations in the iterative solution of the system of continuity, momentum and energy equations are necessary to achieve the second order accuracy in space, as shown by Fortunato and Werle /5/. Therefore the present results have been given in figures 12 ,13 ,14 . It is possible to note that the cold wall condition allows greater angles without the occurrence of separation. The computer time required for solving one cold wall case (9 iterations in time) with 41x26 grid points is about 10 C.P.U. minuts.

V Conclusion and recomandations

A second order accurate numerical method for solving the interacting boundary layer equations has been presented and results for non separating cases (adiabatic and cold wall) have been obtained.

Interaction effects have been shown to eliminate separation for cases in which classical boundary layer theory fails.

A logical extension of the present work is the study of separation; the solution algorithm is the same with some small modifications, as the upwind derivative concept.

A refinement of the algorithm could finally be sought in order to improve the efficiency and reduce computer time.

VI References

1. Garvine,R.W. — Upstream influence in viscous interaction problems. The Physics of Fluids, Vol.II,pp.1413-1423,July 1968.

2. Werle,M.J. Vatsa,V.N. — Numerical solution of interacting supersonic boundary layer flows including separation effects. University of Cincinnaty ,ARL 73-0162, December 1973.

3. Napolitano,M. Werle,M.J. Davis,R.T. — Numerical solution for high Reynolds number laminar separation at interior corners. University of Cincinnaty,AFL 76-12-28, December 1976.

4. Napolitano,M. Werle,M.J. Davis,R.T. — Numerical solutions for high Reynolds number separeted flow. 16th Aerospace Sciences Meeting,Huntsville,Alabama,January 1978. Computer and Fluids,Vol.7,pp.165-175,1979.

5. Fortunato,B. Werle,M.J. — A second order numerical method for supersonic boundary layer flow past a compression corner. University of Cincinnaty, AFFDL-TR-79-3061,June 1979.

6. Rosenhead,L.(editor) — Laminar boundary layers Oxford at the Carendon Press,1966, Great Britain.

7. Back,L.H. — Conservation equations of a viscous heat conducting fluid in curvilinear orthogonal coordinates. NASA Technical Report 32-1332,September 1968.

8. Van Dyke,M.D. — Higher approximations in boundary layer theory.Part I:General analysis. Journal of Fluid Mechanics , Vol.14, pp. 161-177, 1963.

9. Stewartson,K. Williams,P.G. — Self-induced separation. Proceedings of the Royal Society of London, Ser.A, Vol.312, pp.181-206, September 1969.

10. Werle,M.J. Bernstein,J.M. — A comparative numerical study of models of the Navier-Stokes equations for incompressible separated flows. Paper 75-8 presented at the A.I.A.A. 13th Aerospace Sciences Meeting, Pasadena, California, January 1975.

11. Werle,M.J. Vatsa,V.N. — A new method for supersonic boundary layer separations. A.I.A.A. Journal pp. 1491-1497, November 1974.

12. Blottner,F.g. — Computation technique for boundary layers. AGARD Lecture Series n. 73, pp.3-9, February 1975.

13. Schlichting,H. — Boundary layer theory. Mc Graw Hill Book Company.

14. Carnahan,B. Luther,H.A. Wilkes,J.A. — Applied numerical methods. John Wiley and Sons, Inc., 1969.

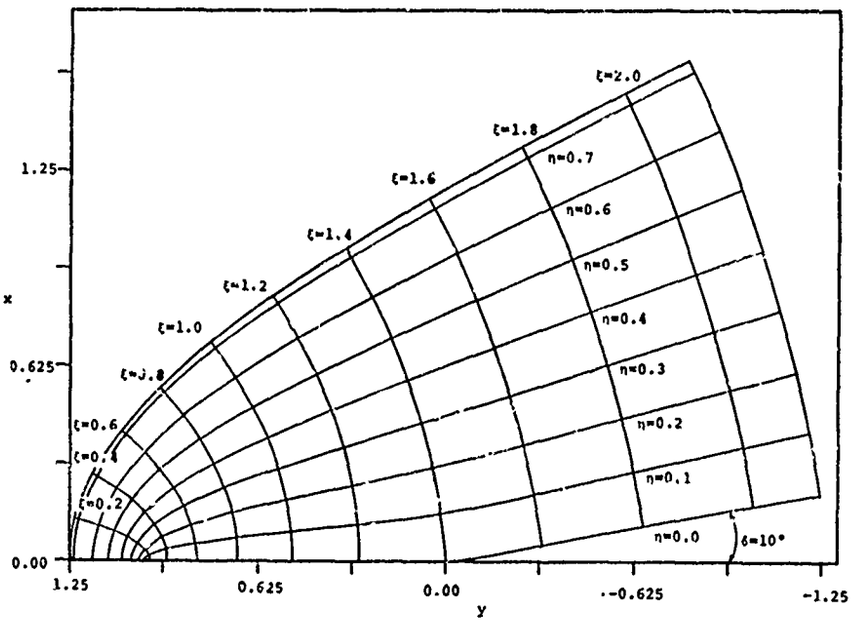


Figure 1. Body surface geometry

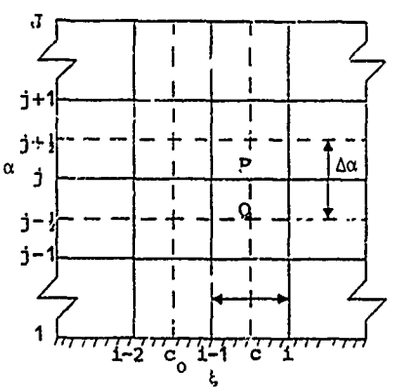


Figure 2. Grid configuration

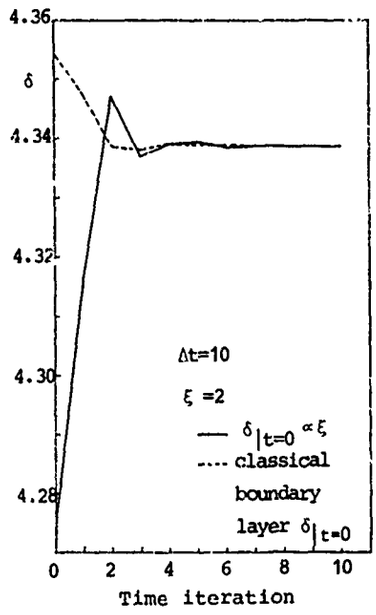


Figure 3. Influence of initial guess on convergence rate of A.D.I. method

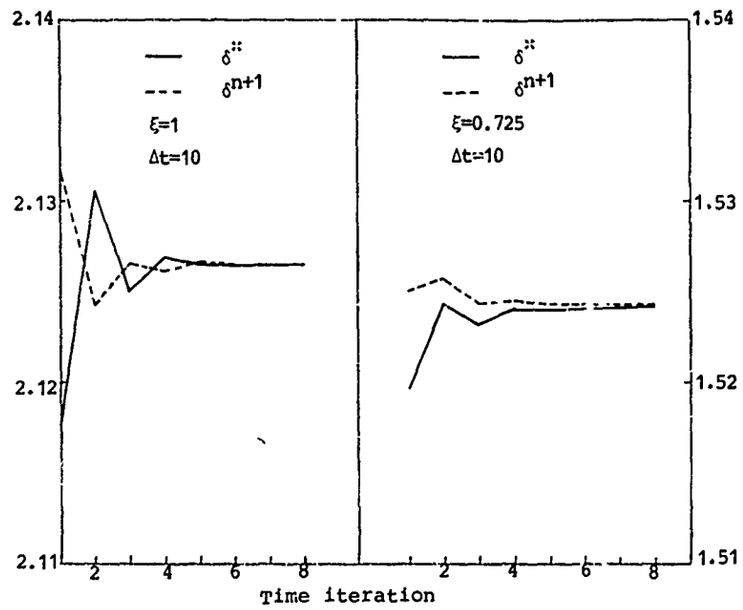


Figure 4. A.D.I. method convergence rate

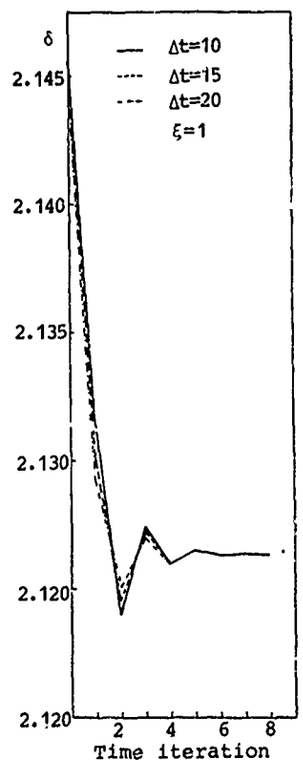


Figure 5. Time increment influence on A.D.I. convergence

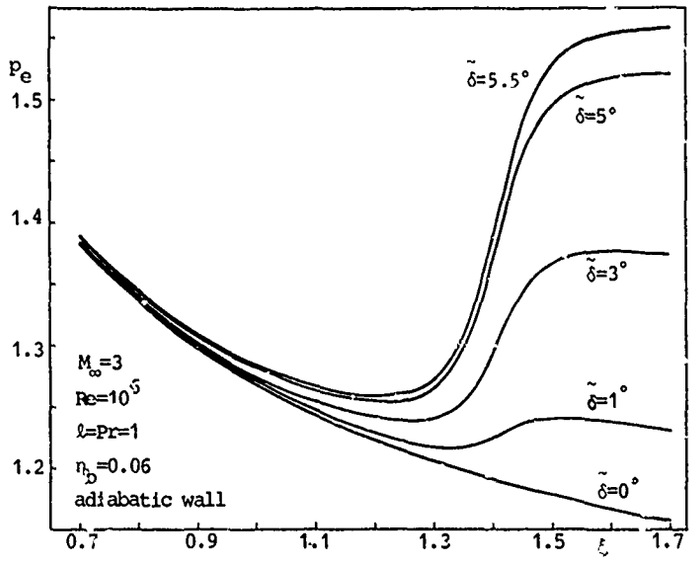


Figure 6. Classical boundary layer inviscid pressure distribution

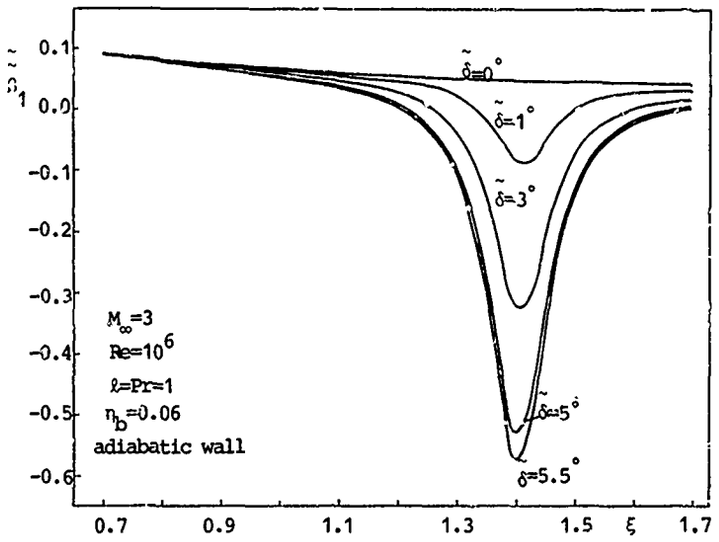


Figure 7. Classical boundary layer pressure gradient distribution

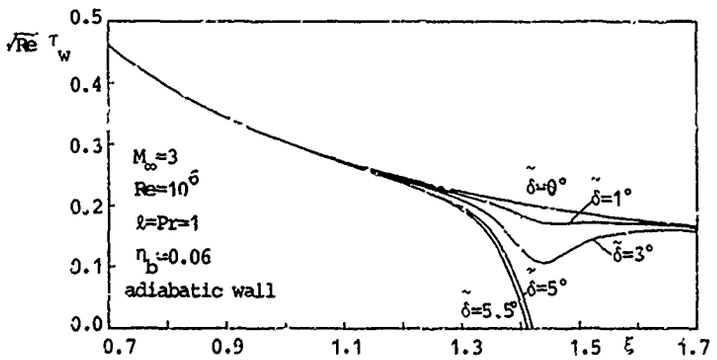


Figure 8. Classical boundary layer wall shear stress

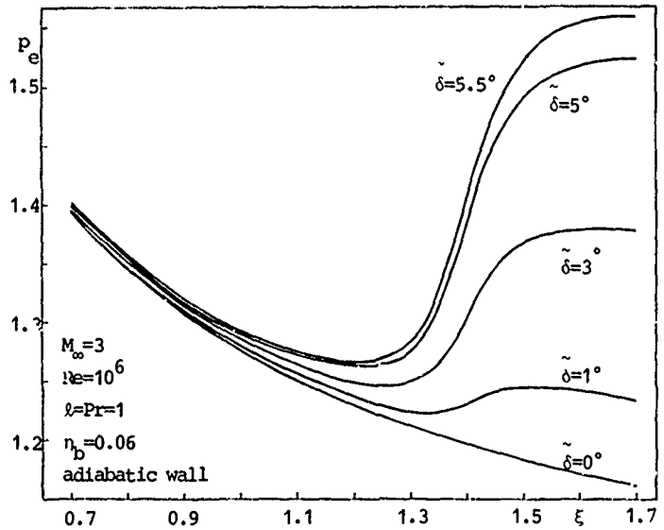


Figure 9. Interacting pressure distribution

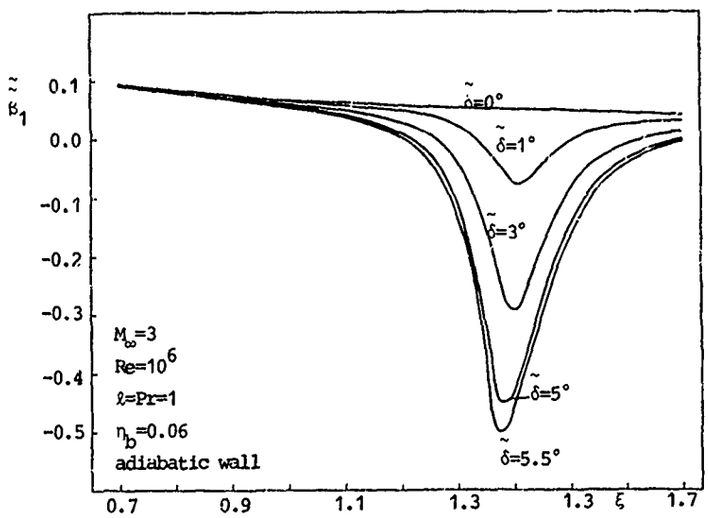


Figure 10. Interacting pressure gradient distribution

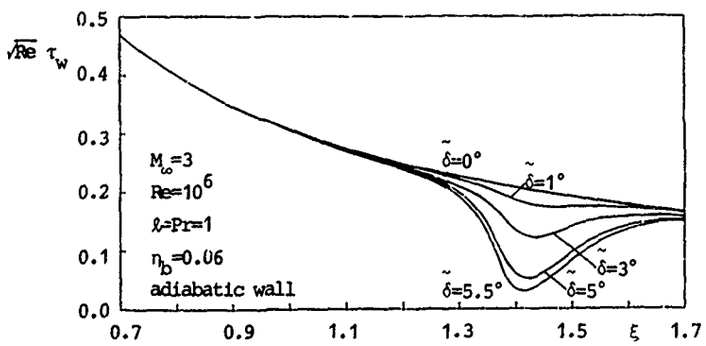


Figure 11. Interacting wall shear stress

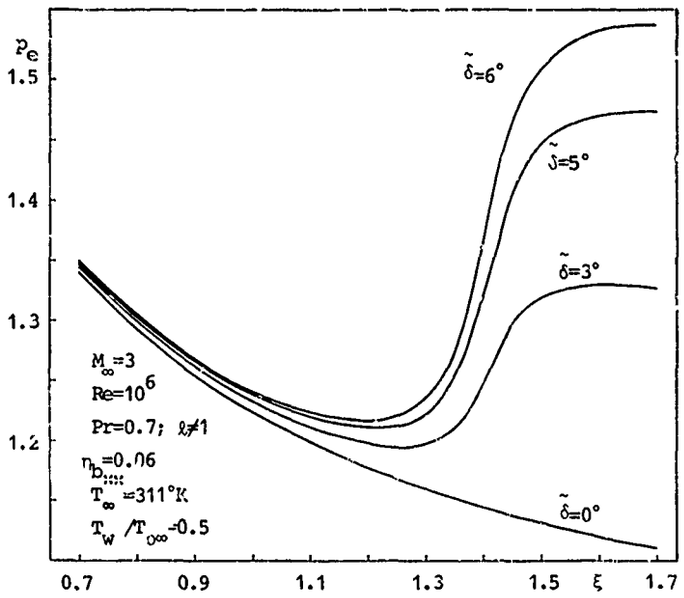


Figure 12. Interacting pressure distribution

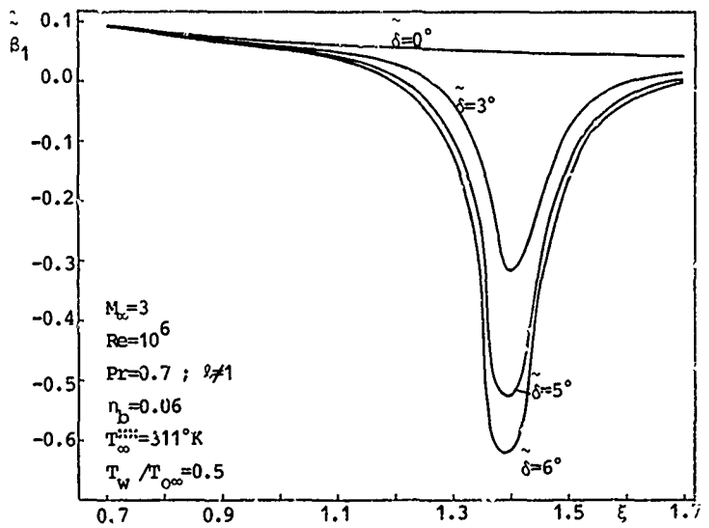


Figure 13. Interacting pressure gradient distribution

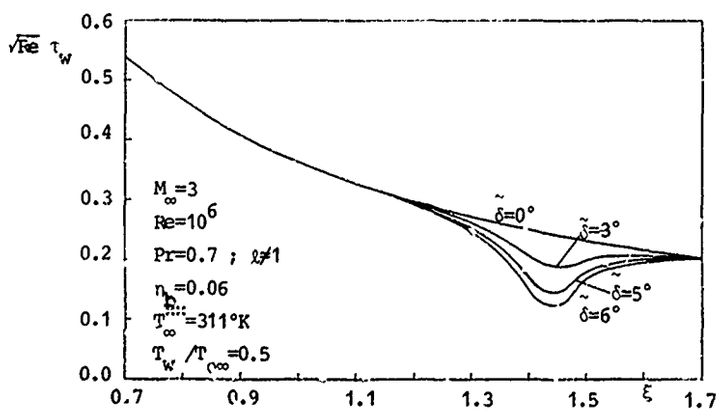


Figure 14. Interacting wall shear stress

CALCUL DE L'INTERACTION ONDE DE CHOC/COUCHE LIMITE AVEC DECOLLEMENT

COMPUTATION OF THE SHOCK-WAVE BOUNDARY LAYER INTERACTION WITH FLOW SEPARATION

Ardonceau P.*, Alziary Th.**, Aymer D.**

Centre d'Etudes Aérodynamiques et Thermiques
43 Rue de l'Aérodrome
86000 Poitiers, France

RESUME

Une nouvelle méthode de calcul de l'interaction onde de choc-couche limite est présentée. Le concept de couche limite est utilisé pour décrire l'écoulement à la paroi, l'écoulement externe est approximé par une relation pression-déviation (dièdre tangent en supersonique linéarisé).

Les équations de couche limite sont résolues en différences finies et la question de l'existence et de l'unicité de la solution est envisagée pour le problème direct (pression imposée) ou inverse (épaisseur de déplacement, coefficient de frottement imposés). De cette analyse ainsi que des considérations relatives au couplage visqueux-non visqueux, la quantité $\rho_e u_e \delta^*$ est choisie comme variable de raccordement.

L'algorithme de couplage présenté traite implicitement la condition limite aval nécessaire pour fermer correctement le problème de la couche limite en interaction. L'algorithme utilise une technique de linéarisation de Newton qui permet une convergence rapide. Un exemple d'application est donné.

Abstract

A new method to compute the shock wave-boundary layer interaction is presented. The boundary layer concept is used to describe the viscous flow near the wall and the outer inviscid flow is calculated by a pressure-turning relation (tangent wedge or linearized supersonic) for simplicity.

The boundary layer equations are solved in finite difference form and the question of the existence and unicity of the solution is examined for the direct (pressure imposed) or inverse (displacement thickness, friction coefficient... imposed) problem. From the aforementioned analysis together with viscous-inviscid matching considerations a particular choice is made for the matching variable ($\rho_e u_e \delta^*$).

An algorithm is presented to converge the matched solution which implicitely includes the downstream condition necessary to close the interacting boundary layer problem. The algorithm makes use of a Newton linearization technique which is shown to provide a fast convergence. A typical example is presented.

NOTATIONS

$C_f = \dfrac{\tau_p}{\frac{1}{2}\rho_\infty U_\infty}$ coefficient de frottement

D	fonction d'amortissement
F	fonction de mélange amont/aval
K	coefficient d'expansion du maillage
P	pression externe
P_r	nombre de Prandtl = $\mu C_p/\lambda$
P_{rT}	nombre de Prandtl turbulent
R	densité externe
R_e	nombre de Reynolds = $\rho_\infty U_\infty X_c/\mu_\infty$
S	fonction de sensibilité (couplage)
U	vitesse longitudinale externe ou discrétisée
V	vitesse verticale externe ou discrétisée
X	coordonnée discrétisée
Y	coordonnée transformée y/ε ou discrétisée

---

* Attaché de Recherches, Centre National de la Recherche Scientifique
** Professeur, Université de Poitiers
*** Attaché de Recherches, Direction des Recherches Etudes et Techniques

h enthalpie statique

ℓ longueur de mélange

p pression interne

u vitesse longitudinale interne

v vitesse verticale interne

x, y coordonnées

$\gamma = C_p/C_v$ ou fonction d'intermittence

δ épaisseur de couche limite

δ^* épaisseur de déplacement

$\varepsilon = R_e^{-1/2}$ ou viscosité turbulente

$\bar{\varepsilon}$ $(1 + \frac{\varepsilon}{\mu})$

$\hat{\varepsilon}$ $(1 + \frac{\varepsilon}{\mu} \frac{P_r}{P_{rT}})$

τ coefficient de frottement $\mu \frac{\partial u}{\partial y}$

θ angle des lignes de courant

μ viscosité dynamique

ω coefficient de relaxation

$ABCDE$
$\alpha\gamma\delta\varepsilon$ coefficients matriciels

Indices

I numérotation verticale du maillage
J numérotation longitudinale du maillage
T totale
c charnière
e variable externe
i variable interne ou incompressible
k indice d'itération
o valeur externe
w valeur à la paroi
∞ valeur à l'infini

1. INTRODUCTION

Diverses méthodes ont été proposées pour le calcul de l'interaction onde de choc/couche limite. Les plus anciennes basées sur la résolution des équations intégrales de couche limite sont encore couramment utilisées, malgré leur caractère approximatif, du fait de leur rapidité {1, 2, 3}. Plus récemment sont apparues des méthodes toujours basées sur la notion de couche limite mais résolues cette fois en différences finies {4, 5}, puis une solution des équations de Navier Stokes complète est devenue possible grace à l'utilisation de moyens de calculs puissants et d'algorithmes efficaces {6, 7}.

La méthode de calcul présentée dans cet article a pour objectif principal d'étudier l'influence des modèles de turbulence sur la qualité des prévisions. Son application à des écoulements tridimensionnels est aussi envisagée. Ces deux objectifs paraissent pour l'instant difficilement compatibles avec une résolution directe des équations de Navier-Stokes qui semble à la limite des moyens actuels de calcul, au moins pour des maillages assez serrés. D'autre part, les méthodes intégrales, dont l'efficacité est bien démontrée, nécessitent un apport semi-empirique en plus de la modélisation de la turbulence et par conséquent il est difficile de tirer des conclusions sur la modélisation de la turbulence elle-même. La méthode choisie est de type couche limite mais résolue par différences finies, le caractère approché résidant alors seulement dans l'approximation de couche limite elle-même.

L'étude de la modélisation de la turbulence dans l'interaction onde de choc/couche limite a fait l'objet d'un travail expérimental {8} mais le calcul présenté est pour l'instant limité à un modèle de turbulence algébrique classique, un effort important ayant été accordé à l'optimisation du calcul de couche limite et de l'algorithme de couplage.

Dans le premier paragraphe on rappelle brièvement le principe de l'approche couche limite qui découle du comportement des équations de Navier-Stokes aux grands nombres de Reynolds. Les divers modes de raccordement entre la couche limite et l'écoulement externe sont envisagés (à la paroi, en δ^*, en δ).

Le second paragraphe est consacré au calcul de la couche limite et en premier lieu au choix du mode de calcul, "direct" ou "inverse", et donc de la condition limite imposée à la couche limite. Cette étude, purement numérique, montre l'importance du choix de cette condition sur l'existence et l'unicité de la solution locale des équations de couche limite, en particulier au décollement.

L'analyse numérique du programme de calcul de couche limite est présentée dans le paragraphe suivant. La méthode d'intégration de la région décollée est également décrite ainsi que le modèle de turbulence algébrique utilisé.

Le quatrième paragraphe est entièrement consacré à l'algorithme de couplage entre la couche limite et l'écoulement extérieur. Une méthode originale a été développée. Il a été démontré [9] que pour être "bien posé" le problème de couche limite en intéraction forte nécessite une condition limite aval. L'algorithme développé traite implicitement cette condition aval et optimise en même temps le processus itératif de couplage.

L'application de la méthode décrite à un cas d'interaction onde de choc/couche limite en écoulement supersonique est présentée en comparaison avec les résultats expérimentaux de LAW [10] et de divers calculs publiés à ce jour [5, 6, 7]. La prévision des distributions de pression pariétale et de C_f présente des divergences sensibles avec des résultats obtenus par méthode de Navier-Stokes, en particulier au niveau de la pression "plateau". Il ne semble pas encore possible d'attribuer ces divergences au modèle de turbulence utilisé, à l'amélioration du maillage par rapport aux méthodes de Navier-Stokes, ou à l'approximation de couche limite.

II. CONDITIONS DE RACCORDEMENT ENTRE LA COUCHE LIMITE ET L'ECOULEMENT EXTERNE

II.1. Généralités

La méthode de calcul présentée dans cet article est de type couche limite, c'est-à-dire que l'on admet implicitement que les effets visqueux contenus dans les équations de Navier-Stokes sont confinés dans une petite région proche de la paroi à l'extérieur de laquelle le fluide peut être correctement décrit par les équations d'Euler. Cette structure des couches visqueuses à des nombres de Reynolds élevés est observée expérimentalement depuis très longtemps mais une formulation mathématique rationnelle du comportement des équations de Navier-Stokes lorsque $R_e \to \infty$ n'a été publiée que beaucoup plus tardivement [11, 12].

La méthode des développements asymptotiques raccordés consiste à chercher une solution régulière au voisinage de $\varepsilon = 0$, $\varepsilon = R_e^{-1/2}$ caractérisant les effets visqueux. On recherche donc une solution interne valide au voisinage de la paroi et une solution externe valide partout ailleurs. Les développements asymptotiques externes :

$$\begin{aligned} U(x,y,\varepsilon) &= U_1(x,y) + \varepsilon U_2(x,y) + O(\varepsilon^2) \\ V(x,y,\varepsilon) &= V_1(x,y) + \varepsilon V_2(x,y) + O(\varepsilon^2) \\ R(x,y,\varepsilon) &= R_1(x,y) + \varepsilon R_2(x,y) + O(\varepsilon^2) \\ P(x,y,\varepsilon) &= P_1(x,y) + \varepsilon P_2(x,y) + O(\varepsilon^2) \end{aligned} \qquad (1)$$

sont introduits dans les équations de Navier-Stokes et fournissent au premier ordre les équations d'Euler, et au deuxième ordre une forme de petites perturbations des équations d'Euler.

Les développements limités valides au voisinage de $y = 0$ sont introduits de la même manière après une transformation de la variable normale à la paroi définie par :

$$Y = y/\varepsilon \qquad (2)$$

$$\begin{aligned} u(x,y,\varepsilon) &= u_1(x,Y) + \varepsilon u_2(x,Y) + O(\varepsilon^2) \\ v(x,y,\varepsilon) &= \varepsilon v_1(x,Y) + \varepsilon^2 v_2(x,Y) + O(\varepsilon^3) \\ \rho(x,y,\varepsilon) &= \rho_1(x,Y) + \varepsilon \rho_2(x,Y) + O(\varepsilon^2) \\ p(x,y,\varepsilon) &= p_1(x,Y) + \varepsilon p_2(x,Y) + O(\varepsilon^2) \end{aligned} \qquad (3)$$

(la forme particulière du développement de v est imposée par l'équation de continuité).

L'injection de ces développements dans les équations de Navier-Stokes fait apparaître au premier ordre les équations de couche limite de Prandtl qui apparaissent donc comme une approximation à l'ordre 1 des équations de Navier-Stokes et au deuxième ordre une forme de petite perturbation des équations de Prandtl (en l'absence de courbure).

II.2. Relations de couplage

Les conditions de raccordement entre la solution interne et la solution externe fournissent les relations de couplage aux divers ordres d'approximation [12, 13]. Lorsqu'il s'agit d'une interaction "faible" la solution externe d'ordre 1 peut être calculée en utilisant la condition de glissement à la paroi ($V(x,0) = 0$). La solution interne est ensuite calculée puis la solution externe d'ordre 2 et ainsi de suite suivant le principe de la hiérarchie de la solution externe (fig. 1).

Ce processus tombe en défaut lorsque des chocs apparaissent dans la solution externe d'ordre 1 ($dP/dx \to \infty$) ou un décollement dans la couche limite d'ordre 1 ($d^2\delta^*/dx^2 \to \infty$). Ce type de singularité peut être évité en considérant simultanément les effets d'ordre 1 et 2 à l'extérieur avec la couche limite d'ordre 1 (fig. 2). Cette méthode de couplage relative aux interactions "fortes" fournit la relation de raccordement sur V :

$$V^*(x,0) = \lim_{Y \to \infty} \varepsilon \left(v_1(x,Y) - Y \frac{\partial V^*}{\partial y}(x,0) \right) + O(\varepsilon^2) \qquad (4)$$

où V^* désigne la solution externe d'ordre 1 et 2 définie par : $V^* = V_1 + \varepsilon V_2$.

En utilisant l'équation de continuité la relation (3) peut être écrite sous la forme bien connue :

$$RV(x,0) = \frac{d}{dx}\left(RU(x,0) * \delta^*\right) \qquad R = \text{densité dans l'écoulement externe} \qquad (5)$$

Si l'on cherche à écrire cette relation à $y = \delta^*$ par un développement limite au voisinage de $y = 0$:

$$RV(x,\delta^*) = RV(x,0) + \delta^* \frac{\partial RV}{\partial y}(x,0) + \ldots$$

et en appliquant l'équation de continuité la relation de couplage s'écrit :

$$RV(x,\delta^*) = RU(x,0) * \frac{d\delta^*}{dx}$$

soit en approximant $RU(x,\delta^*)$ par $RU(x,0)$

$$RV(x,\delta^*) = RU(x,\delta^*) * \frac{d\delta^*}{dx}$$

ou

$$\left(\frac{V}{U}\right)_{y=\delta^*} = \frac{d\delta^*}{dx} \qquad (6)$$

On peut de la même manière obtenir une relation de couplage en $y = \delta$ {14}.

L'avantage évident du couplage en δ^* est que la surface de déplacement apparaît comme une ligne de courant pour l'écoulement extérieur. Par contre dans le couplage en paroi, la couche limite joue le rôle d'une distribution de sources placées à la surface {12} et il y a par conséquent échange de fluide entre la couche limite et l'écoulement extérieur (fig. 3). Cette perméabilité de la couche limite pose un problème de raccordement lorsque le fluide externe ne vérifie pas la condition isentropique valable à l'extérieur de la couche limite. Cette incohérence ne semble pas cependant remettre en cause la procédure puisque des conditions de raccordement supplémentaires peuvent être fournies par l'étude du raccordement de la couche limite du second ordre {26}.

Une difficulté associée à la notion de surface de déplacement et donc au couplage en δ^* est le comportement supersonique de la couche limite au-delà d'un nombre de Mach de l'ordre de 1.4 pour une couche limite turbulente {15}. La couche limite raccordée à l'écoulement externe en δ^* ne permet pas alors la naissance du phénomène d'auto-induction et les solutions de branchement correspondant à l'interaction forte n'apparaissent pas. La technique couramment utilisée consiste à appliquer à la couche limite une discontinuité (jump supercritique-subcritique) pour développer des solutions d'interaction forte. Le caractère empirique de cette méthode peut être évité en prolongeant l'écoulement externe à la paroi. LE BALLEUR {16} a montré que le couplage en paroi, qui découle directement de la méthode des développements asymptotiques raccordés, garantit, au moins dans une plage étendue de nombres de Mach, le comportement subcritique de la couche limite en interaction. Malgré les difficultés liées à la perméabilité de la couche limite, ce type de couplage a été préféré pour éviter le recours à la technique du "jump".

III. CALCUL DE LA COUCHE LIMITE

III.1. Introduction

Parmi les problèmes liés au calcul de la couche limite soumise à de forts gradients, on peut citer celui de la modélisation de la turbulence d'une part et d'autre part le calcul du décollement qui implique une modification du mode d'intégration, la couche limite n'ayant plus dans ce cas le caractère purement parabolique d'une couche limite attachée.

Par opposition aux méthodes de calcul dites "directes" dans lesquelles le gradient de pression est imposé à la couche limite {17} sont apparues des méthodes "inverses" {18, 19} le gradient de pression étant alors le résultat de l'intégration des équations avec une condition limite externe telle que l'épaisseur de déplacement δ^* ou le coefficient de frottement pariétal Cf. Le choix de la condition externe à prescrire est important et la question de l'existence et de l'unicité de la solution du problème de couche limite doit être envisagée pour les différents modes d'intégration.

III.2. Choix de la condition limite

Lors des itérations de couplage entre la couche limite, on est amené à imposer des conditions "non physiques" à la couche limite et le problème se pose de savoir si à une abscisse donnée X_{J+1} le problème de la couche limite a une et une seule solution pour toute valeur de la condition imposée. Afin de répondre à cette question la procédure suivante a été mise en oeuvre : la couche limite est calculée jusqu'à l'abscisse X_J et au point X_{J+1} on fait varier la condition imposée {10}. L'état de la couche limite au point J conditionne en partie le résultat et le calcul a été reproduit pour différentes situations (couche limite accélérée, ralentie ou à gradient de pression nul jusqu'à X_J). Pour connaître le comportement de la solution, décollement inclus, le calcul est effectué soit en méthode inverse (δ^* prescrit) lorsque l'écoulement est décollé soit en méthode directe lorsque l'écoulement est attaché.

Les termes de convection $\rho u\, du/\partial x$ et $\rho u\, \partial h/\partial x$ sont négligés lorsque la couche limite est décollée afin de préserver la stabilité du calcul. (Approximation suggérée par Flugge Lotz et Reyhner {21}). Le résultat présenté fig. 4 est relatif à une couche limite turbulente "supercritique" ($M = 2.96$). La procédure de calcul est la même que celle décrite au paragraphe III.3.

En abscisse est porté le rapport $p(X_{J+1})/p(X_J)$ et en fonction de cette variable est représentée la variation du C_f, de δ^* et $\rho_e u_e \delta^*$, et de $\rho_e v_e$ c'est à dire le flux de masse qui entre ou sort de la couche limite.

La première constatation est l'existence d'un rapport de pression maximal entre les points J et J+1, le maximum correspondant grossièrement au décollement de la couche limite. Une fois le décollement naissant dépassé, la pression diminue légèrement lorsque la couche limite est plus décollée. Ce résultat est observé quel que soit l'état initial de la couche limite, qualitativement du moins, et montre que :

1°/ le problème direct (grad p imposé) n'a pas toujours de solution
2°/ au voisinage du décollement il existe une solution double

Ainsi le problème de la singularité au décollement peut être facilement relié à un problème d'existence et d'unicité de la solution et l'utilisation de méthodes directes pour calculer des couches limites décollées paraît assez dangereuse.

Si l'on considère maintenant le C_f comme variable imposée à la couche limite on observe que le C_f décroît de manière monotone jusqu'au décollement et qu'en ce point la dérivée $dCf(J+1)/dp(J+1)$ est infinie. Dans le domaine décollé le C_f présente une décroissance monotone jusqu'à une valeur limite inférieure et ensuite augmente légèrement. Notons que rechercher une solution par méthode inverse consiste à rechercher l'intersection de la courbe avec une droite horizontale. On peut en conclure que le décollement est facilement franchissable à C_f prescrit mais que là encore un problème d'existence et d'unicité se pose pour de forts décollements.

La variable $\rho_e v_e$ est indiquée mais vu l'allure de la courbe $\rho_e v_e(J+1) = f(p(J+1))$ qui présente presque un point de rebroussement, l'emploi de $\rho_e v_e$ comme variable est à proscrire absolument.

Restent les deux variables basées sur l'épaisseur de déplacement δ^* et le produit $\rho_e u_e \delta^*$. (Fig. 4). La pente négative de la courbe $\delta^*(J+1) = f(p(J+1))$ est symptomatique d'un écoulement supercritique.

En effet, une couche limite supercritique est caractérisée par son inaptitude à générer son propre gradient de pression {22}. Si une perturbation externe entraîne une augmentation de l'épaisseur de déplacement soit $d\delta^*/dx > 0$, le gradient de pression correspondant est négatif (grad p<0). Ceci conduit à un amortissement de la pression initiale et la solution couplée ne se branche pas sur des solutions de forte interaction {22}.

Notons néanmoins qu'au-delà d'une certaine compression la dérivée $d\delta^*(J+1)/dp(J+1)$ redevient positive et les techniques de "jump" consistent à passer artificiellement de la branche supercritique à la branche subcritique (II.2).

En ce qui concerne le calcul de couche limite proprement dit il n'a pas été possible de calculer la couche limite à δ^* prescrit dans la branche subcritique et de plus un tel calcul serait sujet à caution étant donné l'existence d'une solution double. Par contre dans la branche plus verticale (décollement naissant et décollement franc) le calcul à δ^* prescrit ne pose pas de problème, la solution existe et est unique même pour de très forts décollements.

L'utilisation de $\rho_e u_e \delta^*$ comme variable est plus avantageuse car la branche supercritique n'existe pas $d\rho_e u_e \delta^*(J+1)/dp(J+1)$ est toujours positif et dans le décollement la solution est bien définie, comme pour δ^*.

Le couplage en paroi faisant intervenir $(\rho_e u_e \delta^*)$ et non δ^* seul, ainsi que l'absence de branche supercritique dans la solution locale du problème de couche limite, conduisent donc naturellement à utiliser $\rho_e u_e \delta^*$ comme quantité à imposer à la couche limite.

III.3. Intégration numérique des équations de couche limite

Le système d'équations à résoudre est le suivant :

$$\text{a/}\quad \frac{\partial \rho u}{\partial x} + \frac{\partial \rho \tilde{v}}{\partial y} = 0 \qquad \left(\tilde{v} = v + \frac{\overline{\rho' v'}}{\bar{\rho}}\right)$$

$$\text{b/}\quad \rho u \frac{\partial u}{\partial x} + \rho \tilde{v} \frac{\partial u}{\partial y} = \rho_e u_e \frac{\partial u_e}{\partial x} + \frac{\partial}{\partial y}\left(\frac{\mu}{R_e} \bar{\varepsilon} \frac{\partial u}{\partial y}\right)$$

$$\text{c/}\quad \rho u \frac{\partial h}{\partial x} + \rho \tilde{v} \frac{\partial h}{\partial y} = -u\rho_e u_e \frac{\partial u_e}{\partial x} + \frac{\partial}{\partial y}\left(\frac{\mu}{R_e P_r} \hat{\varepsilon} \frac{\partial h}{\partial y}\right) + \frac{\mu}{R_e} \bar{\varepsilon} \left(\frac{\partial u}{\partial y}\right)^2$$

$$\text{d/}\quad \frac{\partial p}{\partial y} = 0 \qquad (7)$$

$$\text{e/}\quad \int_0^\infty (\rho_e u_e - \rho u) dy = \rho_e u_e \delta^* = f(x) \text{ donné}$$

$$\text{f/}\quad \frac{p}{\rho} = \frac{h}{\gamma - 1}$$

avec les conditions aux limites suivantes :
$u(x,0) = v(x,0) = 0$ adhérence

$$\text{g/}\quad \frac{\partial h}{\partial y}(x,0) = 0 \quad \text{paroi adiabatique}$$

$$h_e + \frac{u_e^2}{2} = h_T \quad \text{enthalpie totale constante à l'extérieur}$$

Le modèle de turbulence $\bar{\varepsilon}$, $\hat{\varepsilon}$ est du type algébrique et sera discuté ultérieurement (III.5).

Les équations sont écrites sous forme adimensionnelle mais en variables non transformées afin de se prêter facilement à l'emploi de modèles de turbulence plus complexes que les modèles algébriques. Les variables principales choisies sont u et h et les termes contenant soit ρ soit p sont exprimés en fonction de h et h_e (enthalpie à l'extérieur de la couche limite). Les équations sont ensuite complètement linéarisées et écrites sous forme de différences finies du second ordre en x et y. Une formulation implicite est évidemment adoptée pour sa stabilité.

La condition intégrale $\int(\rho_e u_e - \rho u)dy = f(x)$ est traitée simultanément avec les équations de quantité de mouvement selon x et d'énergie. Contrairement aux méthodes directes la pression et par conséquent u_e sont traitées comme des inconnues. L'intégration simultanée des équations de quantité de mouvement et d'énergie est imposée par la présence de ρ et u dans l'expression $\rho_e u_e \delta^*$.

Une intégration successive de l'équation de quantité de mouvement et d'énergie imposerait une solution itérative de l'équation

$$\text{a/} \quad \int(\rho_e u_e - \rho u)dy = f(x) \quad \text{du type}$$

$$\text{b/} \quad \int(\rho_e^{k-1} u_e^{k} - {}^{k-1}u^{k})dy = f(x) \quad \text{où k désigne l'indice d'itération sur les termes non linéaires} \tag{8}$$

Cette procédure qui consiste à intégrer l'équation de quantité de mouvement avec la relation intégrale 8b/ ne permet pas le calcul de régions décollées à des nombres de Mach élevés car le signe de $df(x)/d\rho(x,y)$ dépend du nombre de Mach local M(x,y) alors que $df(x)/du(x,y)$ est toujours négatif.

La relation (8.a) est donc résolue avec les termes faisant intervenir u et ρ (donc h et h_e) sous forme explicite et linéarisée complètement suivant le principe $((AB)^+ = AB+(A^+-A)B+A(B^+-B))$.

La structure générale de la matrice pour un profil donné est représentée fig.5. Chaque terme représente une matrice 2*2. Le vecteur représentant la solution est écrit sous la forme :

$$\vec{X} = \begin{pmatrix} U(1) \\ H(1) \\ U(2) \\ H(2) \\ \cdot \\ \cdot \\ \cdot \\ U(NDIM) \\ H(NDIM) \end{pmatrix} \tag{9}$$

La matrice est de type tridiagonale avec en plus une ligne et une colonne. La dernière ligne est utilisée pour écrire la relation intégrale 7e/ alors que la colonne représente l'inconnue $U(NDIM) = u_e$ et $H(NDIM) = h_e$.

Chaque ligne est donc de la forme :

$$|A(I)|*\begin{pmatrix}U(I-1)\\H(I-1)\end{pmatrix}+|B(I)|*\begin{pmatrix}U(I)\\H(I)\end{pmatrix}+|C(I)|*\begin{pmatrix}U(I+1)\\U(I+1)\end{pmatrix}+|G(I)|*\begin{pmatrix}U(NDIM)\\H(NDIM)\end{pmatrix} = (D(I)) \tag{10}$$

la dernière ligne s'écrivant :

$$\sum_{I=1}^{NDIM} |E(I)|\times\begin{pmatrix}U(I)\\H(I)\end{pmatrix} = (D(NDIM)) \tag{11}$$

La résolution est effectuée par un algorithme de substitution dérivé de l'algorithme de THOMAS {23}. Dans un premier temps, la matrice est mise sous la forme présentée fig.6, où $|1|$ est la matrice unité $\begin{vmatrix}1&0\\0&1\end{vmatrix}$ et les coefficients $|\alpha|$ $|\gamma|$ et (δ) sont donnés par les relations de substitution :

$$\begin{aligned}
|\alpha(I)| &= |G(I)|*(|B(I)|-|A(I)|*|\alpha(I-1)|)^{-1} \\
|\gamma(I)| &= (|G(I)|-|A(I)|*|\gamma(I-1)|)*(|B(I)|-|A(I)|*|\alpha(I-1)|)^{-1} \\
(\delta(I)) &= ((D(I))-|A(I)|*(\delta(I-1)))*(|B(I)|-(A(I))*|\alpha(I-1)|)^{-1}
\end{aligned} \tag{12}$$

La dernière ligne est elle-même réduite par une relation de substitution.

$$\begin{aligned}
|\varepsilon(I)| &= |E(I)|-|\varepsilon(I-1)|*|\alpha(I-1)| \\
|\varepsilon(NDIM)| &= |E(NDIM)| - \sum_{I=1}^{NDIM} |\varepsilon(I)|*(\delta(I)) \\
(\delta(NDIM)) &= (D(NDIM)) - \sum_{I=1}^{NDIM} |\varepsilon(I)|*(\delta(I))
\end{aligned} \tag{13}$$

Dans un second temps le vecteur $\vec{X}$ est calculé par résolution de la matrice en commençant par la dernière ligne et en remontant. Les termes non linéaires sont résolus pour chaque profil avant de calculer le suivant en itérant jusqu'à convergence. Une sous-relaxation est nécessaire au moins pour les profils décollés et la valeur relaxée du vecteur X à l'itération k est donnée par :

$$\vec{X} = \vec{X}^k + (1-\omega)\vec{X}^{k-1}$$

Le coefficient de relaxation est choisi égal à 0.5 ce qui correspond à une optimisation pour l'intégration d'une couche limite comportant des profils décollés. La valeur de ω peut être prise égale à 0.8 ou 0.9 si la couche limite est complètement attachée. Le test de convergence est effectué sur les U(1)...U(NDIM) et l'itération arrêtée lorsque :

$$\frac{U^k(I)-U^{k-1}(I)}{U^k(NDIM)} < .0001 \quad \text{pour tous les I.}$$

Le nombre moyen d'itérations par profil est de l'ordre de 25 pour le cas de calcul présenté. Ce nombre doit pouvoir être nettement réduit par l'utilisation de modèles de turbulence ne comportant pas de termes du genre $|\partial u/\partial y|$ ou basés sur τ_w ce qui n'est pas sans poser des problèmes lorsque $\tau_w \to 0$ (Cf. III.5).

III.4. Intégration dans la région décollée

En l'absence de décollement l'intégration de la couche limite dont les équations sont de type parabolique s'effectue dans le sens de x croissant, le résultat étant entièrement fonction des valeurs initiales et des conditions aux limites. Le caractère parabolique en +x est perdu dans le décollement car les termes $\rho u\, \partial u/\partial x$ et $\rho u\, \partial h/\partial x$ changent de signe ce qui autorise une influence de l'aval vers l'amont. Les équations sont encore de type parabolique dans les régions décollées mais dans le sens des x décroissants.

Trois solutions sont possibles pour traiter cette influence de l'aval vers l'amont :

1/ l'approximation proposée par Flugge Lotz et Reyhner
2/ le changement du sens d'intégration dans la région décollée
3/ les balayages successifs de toute la couche limite en modifiant les molécules de différences finies dans les régions décollées

a) Approximation de Flugge Lotz et Reyhner {21}

Cette approximation consiste simplement à négliger les termes convectifs en x lorsque la vitesse longitudinale devient négative. Ceci permet de préserver le caractère parabolique en +x et d'intégrer la couche limite en un seul balayage en x. Les termes

$$\rho u \frac{\partial u}{\partial x} \text{ et } \rho u \frac{\partial h}{\partial x} \quad \text{sont transformés en}$$

$$\rho\left(\frac{u+|u|}{2}\right) \frac{du}{dx} \qquad (14)$$

$$\rho\left(\frac{u+|u|}{2}\right) \frac{dh}{x}$$

qui s'annulent donc lorsque $u<0$. Cette méthode, très utile pour initialiser une distribution de vitesse dans la couche limite ou pour calculer de faibles décollements, pose néanmoins des problèmes de convergence pour de forts décollements. Elle n'a de plus qu'un caractère approximatif, assez raisonnable en écoulement laminaire où les vitesses de retour sont faibles, beaucoup plus contestable en turbulent où des vitesses de retour de $\sim 0.2\, u_e$ sont rencontrées.

b) Changement du sens d'intégration dans la région décollée

La solution adoptée par CEBECI {24} d'intégrer l'extérieur du bulbe de l'amont vers l'aval et le bulbe de l'aval vers l'amont et d'itérer jusqu'à convergence du champ global est certainement la plus efficace sur le plan du temps de calcul. Cependant l'algorithme est relativement complexe. De plus, dans un calcul couplé couche limite/fluide parfait, des itérations de couplage sont imposées et cette propriété peut être utilisée pour converger à la fois le bulbe de décollement et la solution couplée.

c) Balayages successifs amont-aval

L'unfluence de l'aval vers l'amont est dans ce cas rendue possible par la modification du type de différenciation ("backward" si $u(x,y)>0$, "forward" si $u(x,y)<0$) des dérivées partielles $\partial u/\partial x$ et $\partial h/\partial x$. Pour stabiliser la frontière $u(x,y) = 0$ une différenciation centrée est appliquée lorsque $|u(x,y)|<u_m$. La remontée des perturbations de l'aval vers l'amont n'excède pas alors 2 mailles par iteration pour un schéma du second ordre et un nombre d'itérations important doit être effectué (l'ordre de grandeur est donné par le nombre de profils décollés). Cet inconvénient par rapport à la deuxième méthode n'est pas critique lorsque des itérations de couplage sont à envisager. Le mode de différenciation adopté est le suivant :

$$\frac{\partial u}{\partial x} = \frac{F+1}{2} \frac{\partial u}{\partial x}\bigg|_b + \frac{F-1}{2} \frac{\partial u}{\partial x}\bigg|_f \qquad (15)$$

avec

$$\frac{\partial u}{\partial x}\bigg|_b = \frac{3U(J,I)-4U(J-1,I)+U(J-2,I)}{2\Delta x}$$

$$\frac{\partial u}{\partial x}\bigg|_f = \frac{-3U(K,I)+4U(J+1,I)-U(J+2,I)}{2\Delta x}$$

La fonction F assurant le mélange amont aval étant définie par :

$$F(J,I) = \frac{U(J,I)}{|U(J,I)|} * \left(1-\exp\left(\frac{|U(J,I)|}{u_m}\right)\right) \qquad (16)$$

La vitesse de référence u_m est égale à :

$$u_m = .02\ u_e$$

Une transition "douce" entre les deux modes de différenciation évite une oscillation de la ligne u(x,y) = 0 au cours des itérations de convergence des termes non linéaires. La vitesse de référence est choisie suffisamment petite pour éviter de prendre en compte des dérivées aval pour des profils bien attachés.

III.5. Modèle de turbulence

Le modèle algébrique de turbulence est un modèle à deux couches classiques. Les termes $\bar{\varepsilon}$ et $\hat{\varepsilon}$ apparaissant dans 7b et c sont donnés par :

$$\bar{\varepsilon} = 1 + \frac{\varepsilon}{\mu}$$
$$\hat{\varepsilon} = 1 + \frac{\varepsilon}{\mu} * \frac{Pr}{Pr_t} \qquad (17)$$

où ε désigne la viscosité turbulente, le nombre de Prandtl est pris égal à 0.725 et le rapport au nombre de Prandtl turbulent est de $Pr/Pr_t = 0.80$.

Le modèle externe ε_o est donné par :

$$\varepsilon_o = .0168\ u_e\ \delta_i^* \qquad (18)$$

δ_i^* est l'épaisseur de déplacement incompressible comptée à partir de l'ordonnée y où la vitesse s'annule dans le cas d'un profil décollé

$$\delta^* = \int_{y(u=0)}^{y_e} \left(1 - \frac{u}{u_e}\right) dy \qquad (19)$$

La fonction d'intermittence γ est représentée par $\gamma = (1+5.5(y/\delta)^6)^{-1}$ δ étant l'épaisseur de couche limite à 0.99 u_e. Contrairement aux calculs effectués avec les équations de Navier-Stokes complètes où la vitesse varie à l'extérieur de la couche limite {7} et où des chocs prennent naissance au voisinage de $y = \delta$, la frontière δ est bien définie.

Le modèle interne est de type longueur de mélange

$$\varepsilon_i = \ell^2 \left|\frac{du}{dy}\right|$$

avec $\ell = 0.4\ y\ D$

où D est le facteur d'amortissement de Van Driest donné par l'expression

$D = 1-e^{-y/y_s}$ y_s = épaisseur de la sous couche "laminaire"

$$y_s = \frac{26\mu}{\sqrt{\rho \times |\tau_\omega|}}$$

Le modèle de turbulence ainsi défini n'a pas fait l'objet de tentative d'optimisation. Il est qualifié de modèle "d'équilibre" suivant la terminologie de SHANG et HANKEY et de MAC CORMACK {6, 7}.

IV. ALGORITHME DE COUPLAGE

IV.1. Calcul de l'écoulement externe

Bien que le mode de calcul de couche limite soit de type inverse, la relation de couplage permet d'utiliser indifféremment une méthode directe ou inverse pour le calcul de l'écoulement externe. Il est prévu de coupler le présent calcul de couche limite à un calcul externe en méthode des caractéristiques. On utilise actuellement une relation pression déviation donnée par :

$$P = P_\infty(1+A\theta+B\theta^2+C\theta^2) \qquad (22)$$

où θ est l'angle de l'écoulement externe prolongé en paroi et déduit de la relation de couplage (17) :

$$\theta = \frac{RV}{RU}(x,0) = \frac{d\delta^*}{dx} \cdot \frac{\delta^*}{RU(x,0)} \frac{d}{dx} RU(x,0)$$

soit

$$\theta = \frac{d\delta^*}{dx} + \frac{\delta^*}{\rho_e u_e} \frac{d\rho_e u_e}{dx} \qquad (23)$$

Ces coefficients dans le développement limite (22) sont respectivement égaux à :

$$A = \frac{\gamma M_\infty^2}{\sqrt{M_\infty^2-1}}$$

$$B = \frac{M_\infty^2}{\gamma+1} \qquad (24)$$

$$C = \frac{1}{2}\gamma\left(\frac{\gamma+1}{4}\right)^2 M_\infty^2 \sqrt{M_\infty^2-1}$$

IV.2. Méthode de couplage

L'algorithme de couplage a pour fonction de permettre de calculer la distribution de pression qui satisfait simultanément les équations de la couche limite et celles de l'écoulement externe, les deux écoulements étant reliés par la relation de couplage (17).

De nombreuses procédures existent mais les méthodes paraissent assez laborieuses. Bien que la couche limite soit de nature parabolique et que dans le cas d'un écoulement externe supersonique les équations d'Euler soient hyperboliques, le problème couplé nécessite une condition à la limite aval pour être correctement posé {9, 13}. Cette constatation rappelle le caractère initialement elliptique des équations de Navier-Stokes. Le couplage entre les deux régions externe et interne autorise en effet la remontée de l'information ce qui implique l'existence d'une condition à la limite aval pour fermer complètement le problème.

L'algorithme proposé par VERLE et VATSA {4} qui prend automatiquement en compte cette condition aval par l'intermédiaire de l'équation de quantité de mouvement écrite à la paroi constitue une amélioration sensible par rapport aux méthodes de "tir" précédemment utilisées. La méthode paraît mal adaptée au calcul de couches limites décollées (calcul direct de la couche limite) et son application à une couche limite supercritique avec couplage en δ^* a jeté un doute sur la validité des méthodes de couche limite en interaction {5}.

La présente méthode comme celle de WERLE et VATSA traite implicitement la condition à la limite aval et optimise le nombre d'itérations de couplage. Elle est applicable aux calculs directs ou inverses, et est présentée ici sous la formulation "mixte" (CL inverse, ext direct).

Soit k l'indice d'itération de couplage. Une estimation du gradient de pression en un point dans la couche limite à l'itération k+1 en fonction de l'angle θ de couplage peut être fournie par la relation :

$$\text{grad } p^{k+1} = \text{grad } p^k + \frac{\partial \text{ grad } p^k}{\partial \theta^k}(\theta^{k+1}-\theta^k) \qquad (25)$$

De la même manière on peut relier la pression externe P^{k+1} à l'angle θ^{k+1} en linéarisant la relation pression/déviation (22).

$$p^{k+1} = p^k + AP_\infty(\theta^{k+1}-\theta^k) \qquad (26)$$

Les angles θ ainsi que les gradients de pression dans la couche limite étant calculés entre les mailles (dérivation en deux points) la pression externe p doit elle-même être définie à la demi-maille soit :

$$p^{k+1}(J+\tfrac{1}{2}) = \frac{p^{k+1}(J)+p^{k+1}(J+1)}{2} \quad \text{etc.....}$$

Les distributions de pression externes et internes devant être identiques à l'itération k+1, on doit donc vérifier $p^{k+1}(J) = p^{k+1}(J)$.

Les relations (25) et (26) peuvent être combinées en éliminant θ ce qui donne sous forme discrétisée :

$$\frac{p^{k+1}(J)-p^{k+1}(J-1)-\left(p^k(J)-p^{k+1}(J-1)\right)}{\Delta x * \left.\frac{\partial \text{ grad } p}{\partial \theta}\right|_k} = \frac{p^{k+1}(J)+p^{k+1}(J-1)-p^k(J)+p^k(J-1)}{2\,AP_\infty}$$

ou en notant S le rapport

$$S = \frac{\Delta x * \left.\frac{\partial \text{ grad } p}{\partial \theta}\right|_k}{2\,AP_\infty} \qquad (27)$$

la précédente relation s'écrit :

$$p^{k+1}(J-1) = \frac{p^k(J)*(1-S)-\left(p^k(J)-p^k(J-1)\right)+2\,S*\left(P^k(J)+P^k(J-1)\right)}{S+1} \qquad (28)$$

Cette relation permet d'estimer à la maille J-1 la pression p^{k+1} qui doit satisfaire les équations de couche limite et de l'écoulement extérieur. Sachant que de plus on impose que la pression aval soit égale

à une certaine valeur P_{e+} la relation (28) intégrée de l'aval vers l'amont fournit une nouvelle distribution de pression $p^{k+1}(J=1...JMAX)$.

Dans le présent calcul, la couche limite est calculée en méthode inverse et donc, connaissant $p^{k+1}(J)$ il est facile de recalculer θ^{k+1} à partir d'une des relations (25) ou (26). La nouvelle distribution de $\rho_e u_e \delta^*$ est redéfinie par l'intégration de l'amont vers l'aval de la distribution θ^{k+1}

$$(\rho_e u_e \delta^*)^{k+1}(x) = \rho_e u_e \delta^*(x_o) + \int_{x_o}^{x} \theta^{k+1}(x)dx \qquad (29)$$

Le profil initial est perturbé , sa pression devant être égale à $p^{k+1}(1)$ mais le produit $\rho_e u_e \delta^*$ est maintenu constant. On retrouve ainsi la solution de faible intéraction, dans la mesure où la forme du profil initial est compatible avec cette solution. En tout état de cause, un profil de type plaque plane fournit une bonne approximation.

La présente méthode se révèle extrêmement rapide pour les interactions ne conduisant pas au décollement de la couche limite (15 à 20 itérations) (fig.7). Une sous relaxation est nécessaire pour des calculs incluant des décollements du fait d'une part de la non linéarité des courbes $\rho_e u_e \delta^*/p$ au voisinage du décollement (fig.4) et d'autre part parce que le bulbe de décollement est intégré par des balayages successifs et que donc les distributions de $\rho_e u_e \delta^*$ ne doivent pas varier trop d'une itération à l'autre. Le nombre d'itération nécessaire est alors de 30 à 40.

IV.3. Calcul de la dérivée $S = \dfrac{d\ \text{grad}\ p}{d\theta}$

La linéarisation de la relaxation du comportement local de la couche limite utilisée pour l'accélération de la convergence de la méthode de couplage nécessite la connaissance du terme $S(x) = d\ \text{grad}\ p/d\theta$ (Cf relation (28)).

Notons que pour une couche limite de caractère strictement parabolique (attachée) la solution en un point donné $x = X_J$ dépend, outre des conditions initiales, de la distribution en x de la condition à la limite, soit en méthode inverse de $\rho_e u_e \delta^*$ de $x = X_1$ à $x = X_J$:

$$p(X_J) = (\rho_e u_e \delta^*(X_L),\ L = 1, \ldots, J) \qquad (30)$$

L'optimisation idéale du processus itératif de couplage imposerait la connaissance des dérivées (Jacobien)

$$\frac{dp_J}{d(\rho_e u_e \delta^*)_L} \quad \text{pour } L = 1, \ldots, J \qquad (31)$$

ce qui conduirait au calcul de J^2 termes. La linéarisation de la relation $\text{grad}\ p(J)/\theta(J)$ revient donc à ne considérer que les deux diagonales principales de la relation (31). Si k est l'indice de l'itération de couplage la pression en J à l'itération k+1 est estimée par :

$$p^{k+1}(J) = p^{k+1}(J-1) + S^k(J)(\theta^{k+1}(J) - \theta^k(J)) \qquad (32)$$

On observe pratiquement que la convergence est assurée sans relaxation sur la distribution de $\theta(J)$ donc de $\rho_e u_e \delta^*(J)$ lorsque la couche limite est attachée. Par contre lorsque le décollement se produit la dérivée S(J) change de signe dans les régions décollées et une sous relaxation paraît alors nécessaire. On doit en plus considérer que l'influence de l'aval sur l'amont remet, au moins en théorie, la validité de la relation (31) en cause puisque la pression en J dépend alors aussi de la distribution de $\rho_e u_e \delta^*(X_L)$ pour L>J.

Cependant, pour le cas du calcul présenté en (V) les dérivées $\text{grad}\ p\ (X_J)$ ont été évaluées en négligeant les points en aval, soit :

$$\text{grad}\ p_{J-1/2} = \frac{p(X_J) - p(X_{J-1})}{\Delta x}$$

$$\theta_{J-1/2} = f(\rho_e u_e \delta^*(X_J) - \rho_e u_e \delta^*(X_{J-1}))$$

La méthode la plus directe pour obtenir la dérivée $d\ \text{grad}\ p/d\theta$ consiste à faire deux calculs successifs au point X_J en perturbant la valeur de $\rho_e u_e \delta^*$ au point J. Cette méthode nécessite alors deux calculs de couche limite par itération de couplage.

L'étude de la relation de comportement (III.2) a montré que le terme de sensibilité S (pente de la normale à la courbe $\rho_e u_e \delta^*/p$) changeait de signe lors du décollement. Il est alors intéressant de relier S au C_f pour éviter le double calcul de couche limite :

$$S(J) \propto C_f^k(J) \qquad (33)$$

Le coefficient de proportionnalité est calculé en divers points du champ par un double calcul de la couche limite comme indiqué précédemment et la relation (33) fournit une bonne approximation pour les autres points.

V. RESULTATS ET DISCUSSIONS

V.1. Résultats

Le calcul présenté est relatif au cas expérimental étudié par LAW (10) et qui a servi de standard pour divers calculs d'interaction soit en méthode de couche limite (5, 22) soit par résolution des équations de Navier-Stokes (6, 7). Le maillage utilisé est de 60×60, le pas en x est constant, le pas en y variable avec un coefficient d'expansion de K = 1.120 :

$$\Delta Y(I+1) = K\ \Delta Y(I)$$

La question du maillage au voisinage de la charnière n'a pas été abordée. Le calcul est effectué sur paroi plane, la déviation intervient simplement au niveau de l'écoulement externe, c'est-à-dire que le cas de calcul est relatif à l'interaction par choc incident et non pas par déviation de la paroi. L'équivalence entre les deux modes de comparaison est bien établie en laminaire car l'interaction s'étend sur un domaine relativement grand par rapport à l'épaisseur de couche limite et donc par rapport à la maille en X. Dans le cas présent l'équivalence n'est pas assurée, comme en témoigne le calcul de SHANG et HANKEY (27) effectué pour les deux modes de compression.

Les données du calcul sont $M_\infty = 2.96$, le nombre de Reynolds à la charnière de $R_e = 10^7$, le nombre de Prandtl $P_r = 0{,}725$. Le domaine de calcul s'étend de $X_o/X_c = 0{,}88$ à $X_{max}/X_c = 1{,}124$ et $Y_{max}/X_c = 0{,}07$.

La viscosité dynamique est approximée par une loi en puissance :

$$\frac{\mu}{\mu_\infty} = \left(\frac{T}{T_\infty}\right)^{0.76} \qquad (34)$$

Les deux profils initiaux sont donnés par un calcul de couche limite direct (25). Le calcul d'interaction est initialisé par une première itération effectuée en méthode directe à gradient de pression nul. La pression imposée dans les itérations de couplage est imposée en $X=X_{max}$ et égale à la pression à l'infini aval fournie par la relation (22). Compte tenu de la sous relaxation appliquée dans la relation de couplage la pression infini aval n'est atteinte qu'au bout de 7 itérations. La valeur imposée est ensuite dépassée puis converge lentement (fig.8). L'évolution de p et du C_f avec le nombre d'itérations est présentée sur la figure suivante (fig.9). La pression pariétale finale est présentée sur la figure 10 en comparaison avec les résultats expérimentaux et ceux obtenus par divers auteurs (5, 6, 7). Le C_f final est présenté figure 11.

Le temps de calcul nécessaire pour obtenir une convergence de 0,5% sur la pression finale est de 12 minutes sur IBM 370/168 ce qui correspond à 40 itérations de couplage.

V.2. Discussion

L'observation des résultats que ce soit la pression pariétale ou le C_f (fig. 10, 11) montre des écarts importants entre les divers résultats obtenus. L'approximation de couche limite, dont la validité semblait douteuse à la suite des travaux de WERLE et BERTKE, ne semble pas devoir être remise en cause. Il semble que dans le cas cité l'algorithme de couplage (méthode directe/couplage en δ^*) soit plus vraisemblablement à l'origine du résultat très décevant.

Le modèle de turbulence employé dans le présent calcul se rapproche très nettement de celui de HUNG et MAC CORMACK, la différence se situant au niveau du modèle interne :

$$\rho \ell^2 \left|\frac{\partial u}{\partial y}\right| \qquad \text{présent calcul}$$

$$\rho \ell^2 \left(\left(\frac{\partial u}{\partial y}\right)^2 + \left(\frac{\partial v}{\partial x}\right)^2\right)^{1/2} \qquad \text{HUNG et MAC CORMACK (7)}$$

Cette différence semble assez mineure et les différences entre les calculs de HUNG et MAC CORMACK et le présent calcul peuvent avoir plusieurs origines :

1/ la cause la plus probable est liée à la résolution numérique faite sur paroi plane, c'est-à-dire que le cas traité est celui de l'interaction par choc incident. Le calcul comparatif d'une interaction par choc incident et par déviation de la paroi (27) montre que dans le premier cas la distribution de pression pariétale est décalée vers l'amont, ce qui correspond bien au résultat, et que le minimum du C_f avant le recollement est lui moins prononcé ce qui est également observé.

On peut aussi citer :

2/ des questions relatives au maillage (60 pas en y dans le présent calcul, 31 seulement dans le calcul de HUNG et MAC CORMACK pour la couche dissipative et une part de l'écoulement non visqueux).

3/ la définition des grandeurs telle que u_e , la valeur à la frontière de la couche limite, en méthode de Navier-Stokes, (SHANG et HANKEY utilisent u_{max} qui semble se situer en dehors de la couche limite).

4/ l'approximation $dp/dy = 0$ de couche limite.

L'obtention des résultats présentés est assez récente et il n'a pas encore été effectué de tests comparatifs, en particulier l'évaluation des termes négligés dans l'équation de quantité de mouvement normale à la paroi. Ces contrôles ainsi qu'un effort sur la modélisation des termes turbulents seront entrepris ultérieurement. La rapidité du calcul autorise en effet une étude plus systématique des modèles de turbulence dont l'importance est évidente pour le traitement des écoulements décollés.

VI. CONCLUSION

Une méthode de calcul de l'interaction onde de choc/couche limite a été développée. Elle utilise le concept de couche limite formulée en méthode inverse, la condition à la limite imposée est le produit $\rho_e u_e \delta^*$. Cette condition limite semble constituer le meilleur choix, malgré la relative complexité qu'elle entraîne au niveau de l'intégration de la couche limite, car d'une part le couplage conserve un caractère subcritique à des nombres de Mach élevés en écoulement turbulent, et d'autre part l'existence et l'unicité de la relation paraît assurée dans les régions de forts gradients, décollement inclus.

L'algorithme de couplage basé sur le comportement local de la couche limite prend implicitement en compte une condition imposée à l'aval pour le problème couplé. Les durées de calcul sont extrêmement compétitives, par rapport à une résolution des équations de Navier-Stokes complètes ce qui autorise l'emploi d'un maillage serré (60×60) sur un mini-calculateur.

Des divergences apparaissent par rapport aux méthodes exactes (NS) mais il n'est pas possible d'en tirer de conclusion définitive, le mode de production de l'intéraction OC/CL n'étant pas le même (choc incident/déviation de la paroi).

Plusieurs applications sont prévues ou en cours actuellement. En premier lieu, le raccordement à une méthode exacte de l'écoulement externe (caractéristiques). Une extension à des écoulements tridimensionnels est également prévue. Enfin un gros effort doit être consenti envers la modélisation de la turbulence dont l'importance paraît primordiale pour une prévision "raisonnable" de l'écoulement.

- REFERENCES -

{1} - LEES L., REEVES B.L.
"Supersonic separated and reattaching laminar flows"
AIAA Journal Vol.2, n°10, 1964

{2} - KLINEBERG J.M., LEES L.
"Theory of laminar viscous-inviscid interactions in supersonic flow"
AIAA Journal Vol.7, n°2, 1965

{3} - AYMER de la CHEVALERIE D.
"Application d'une méthode intégrale au calcul d'interactions onde de choc-couche limite turbulente en écoulements faiblement supersoniques"
Thèse de 3ème Cycle, Université de Poitiers, 1976

{4} - WERLE M.J., VATSA V.N.
"New method for supersonic laminar boundary layer separations"
AIAA Journal Vol.12, n°11, 1974

{5} - WERLE M.J., BERTKE S.
"Application of an interacting boundary layer model to the supersonic turbulent separation model"
Report AFL n°76.4.21, University of Cincinatti, 1976

{6} - SHANG J.S., HANKEY W.L.
"Numerical solution of the Navier-Stokes equations for supersonic turbulent flow over a compression ramp"
AIAA Paper n°75-3, 1975

{7} - HUNG C.M., MAC CORMACK R.W.
"Numerical simulation of supersonic and hypersonic turbulent compression corner flows"
AIAA Journal Vol.15, n°3, 1977

{8} - ARDONCEAU P., LEE D.H., ALZIARY T., GOETHALS R.
"Turbulence behaviour in a shock wave/boundary layer interaction"
AGARD CP 271, 1979

{9} - CARVINE R.
"Upstream influence in viscous interaction problems"
Physics of Fluid Vol.11, n°7, 1968

{10} - LAW C.H.
"Supersonic turbulent boundary layer separation"
AIAA Journal Vol.12, n°6, 1974

{11} - VAN DYKE M.
"Perturbation methods in fluid mechanics"
Applied Mathematics and Mechanics Vol.8, 1964

{12} - VAN DYKE M.
"Higher order approximations in boundary layer theory"
Journal of Fluid Mech., Vol.14, P.2, 1962

{13} - ALZIARY de ROQUEFORT T.
"Couplage fort et couplage faible entre couche limite et écoulement extérieur"
13e Colloque Association Aéronautique et Astronautique de France, 1976

{14} - LE BALLEUR J.C.
"Calculs couplés visqueux-non visqueux incluant décollement et onde de choc en écoulement bidimensionnel"
AGARD LS 94, 1978

{15} - WEINBAUM S., GARVINE R.W.
"On the two dimensional viscous counterpart of the one dimensionai sonic throat"
Journal of Fluid Mechanics Vol.39, P.1, 1969

{16} - LE BALLEUR J.C.
"Détermination des effets de couplage entre écoulement de fluide parfait transsonique et couche limite"
Rapport ONERA N2/3073 AY, 1977

{17} - CEBECI T., SMITH A.M.O., MOSINSKIS G.
"Calculation of compressible adiabatic turbulent boundary layers"
AIAA Journal Vol.8, n°11, 1974

{18} - KLINEBERG J.M., STEGEK J.L.
"On laminar boundary layer separation"
AIAA Paper n°74-94, 1974

{19} - CARTER J.E.
"Solutions for laminar boundary layers with separation and reattachment"
AIAA Paper n°74-583, 1974

{20} - ARDONCEAU P.L., ALZIARY de ROQUEFORT T.
"Direct and inverse calculation of the laminar boundary layer solution"
AIAA Journal (to be published Nov. 1980), 1980

{21} - REYNER T.A., FLUGGE LOTZ I.
"The interaction of a shock wave with a laminar boundary layer"
Int. Journal of Non Linear Mech. Vol.13, 1968

{22} - LE BALLEUR J.C., PEYRET R., VIVIAND H.
"Numerical studies on high Reynolds number aerodynamics"
Computers and Fluids Vol.8, 1980

{23} - BLOTTNER F.G.
"Computational techniques for boundary layers"
AGARD LS 73, 1975

{24} - CEBECI T., KELLER H.B., WILLIAMS P.G.
"Separating boundary layer flow calculations"
Journal of Comp. Physics, n°31, 1979

{25} - HARRIS J.E.
"Numerical solution of the equations for compressible laminar, transitional and turbulent boundary layers and comparison with experimental data"
NASA TR-R-368, 1961

{26} - DAVIS R.T., WERLE M.J., WORNOM S.F.
"A consistent formulation of the compressible boundary layer theory with second order curvature and displacement effects"
AIAA Journal Vol.8, n°9, 1970

{27} - SHANG J.S., HANKEY W.L.
"Supersonic turbulent separated flows utilizing the Navier-Stokes equations"
AGARD CP 168, 1975

Ce travail a été soutenu par la Direction des Recherches, Etudes Techniques sous le contrat n°78/240.

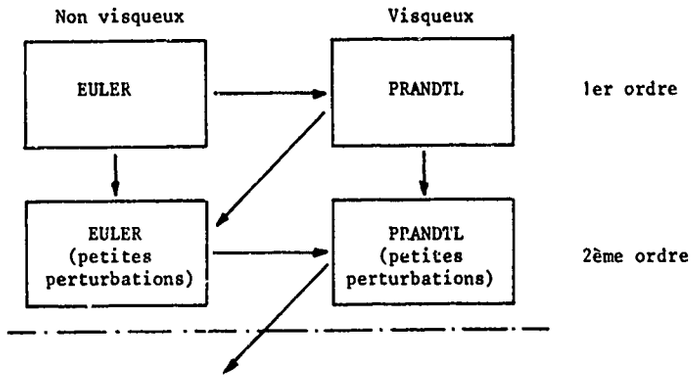


FIG.1 - Couplage régulier (hiérarchique) entre la couche limite et l'écoulement externe -

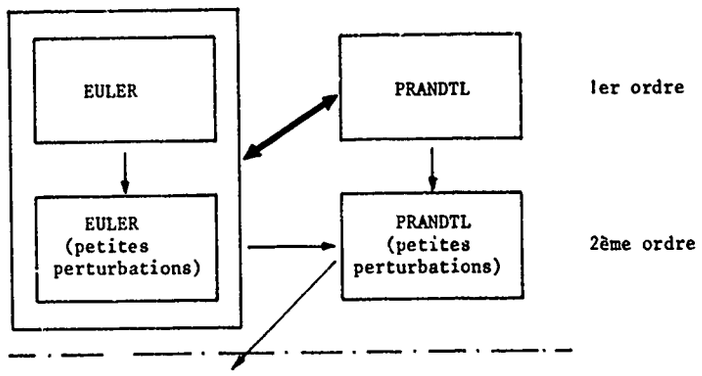
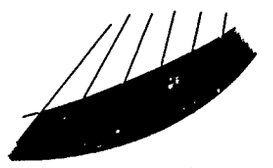
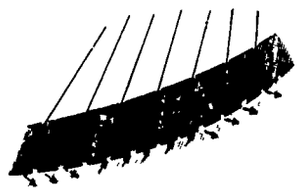


FIG.2 - Couplage singulier (simultané) entre la couche limite et l'écoulement externe -



a/ couplage en δ^*



b/ couplage à la paroi

FIG.3 - Interprétation physique du couplage en δ^* et à la paroi

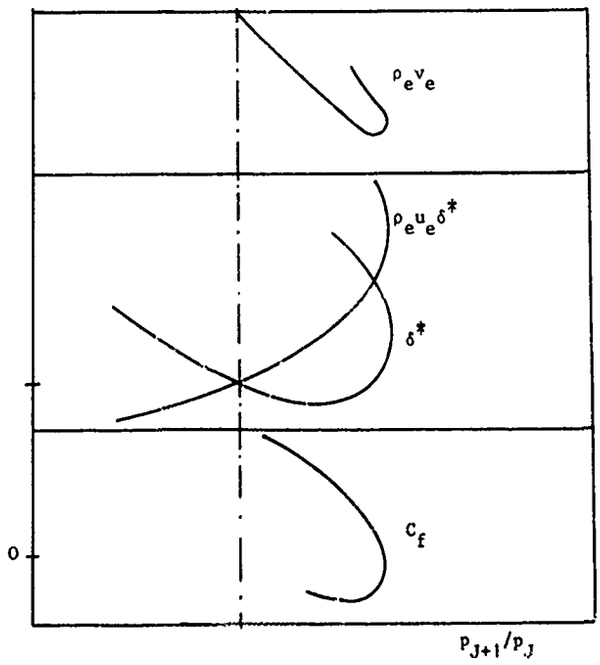


FIG.4 - Relation locale de comportement entre $\rho_e v_e$, δ^*, $\rho_e u_e \delta^*$, le C_f et la pression -

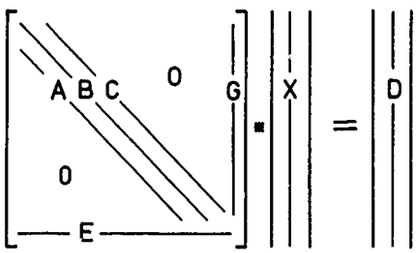


FIG.5 - Structure de la matrice en méthode inverse (δ^* ou $\rho_e u_e \delta^*$ imposé) -

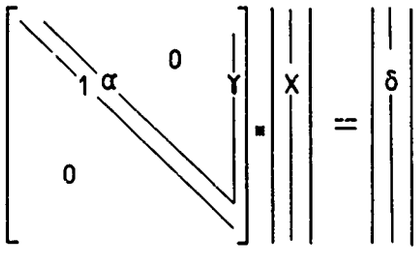


FIG.6 - Structure de la matrice après réduction

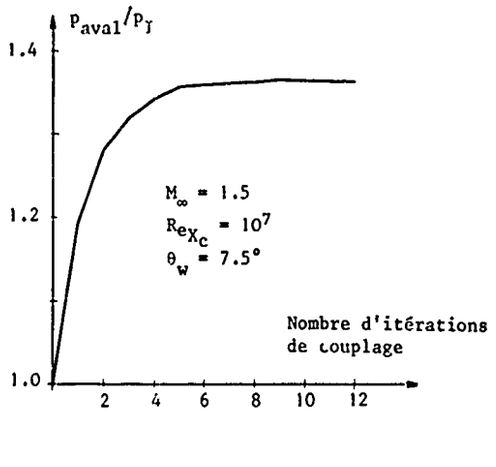


FIG.7 - Convergence de la pression finale (couche limite attachée)

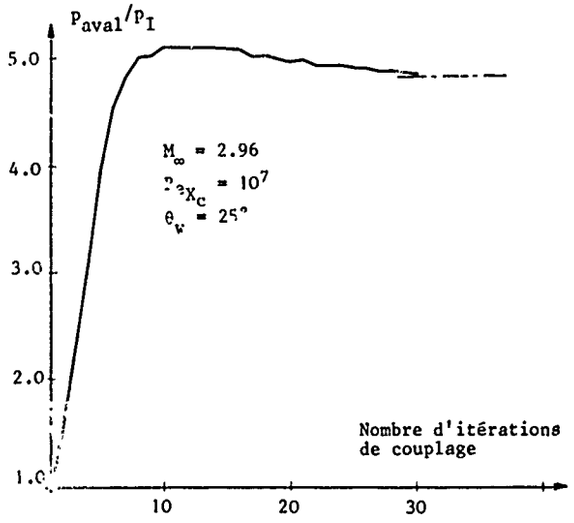


FIG.8 - Convergence de la pression finale (couche limite décollée)

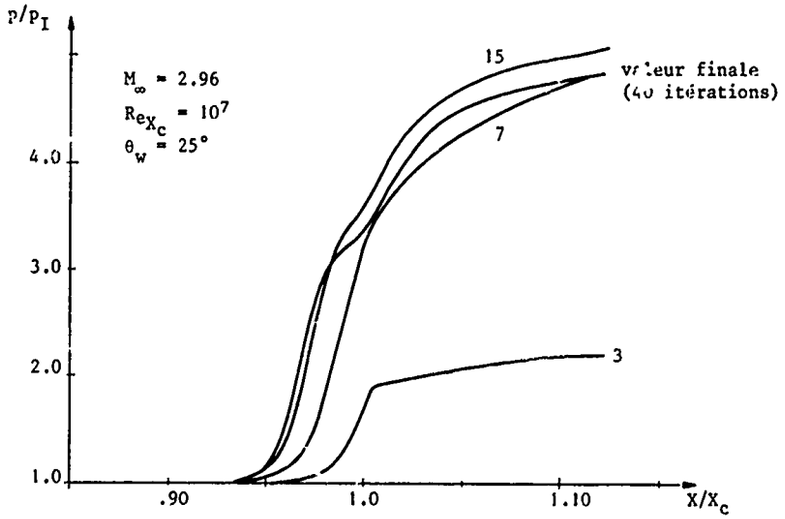


FIG.9a - Convergence de la distribution de pression pariétale -

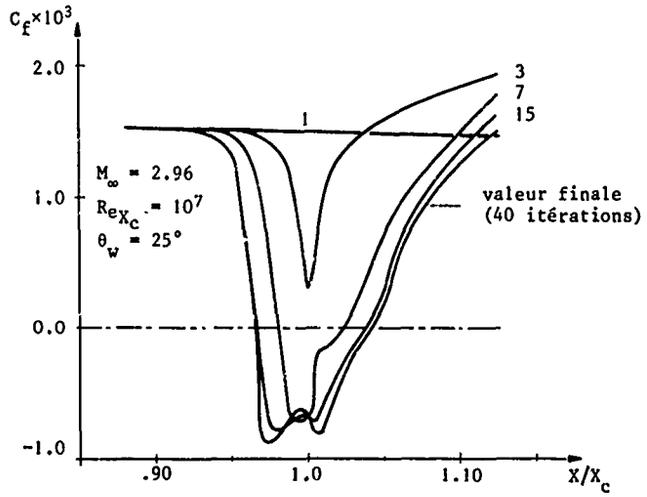


FIG.9b - Convergence de la distribution de C_f -

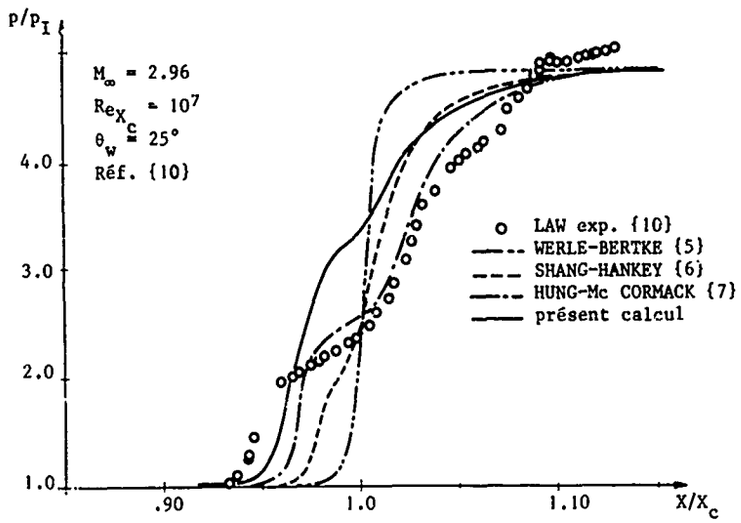


FIG.10 - Comparaison entre les distributions de pression pariétale (Modèle de turbulence en "équilibre") -

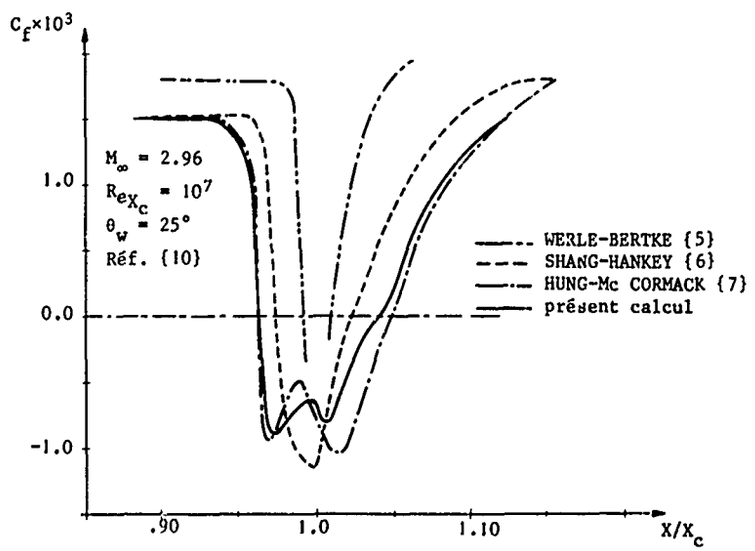


FIG.11 - Comparaison entre les distributions de Cf
(Modèle de turbulence en "équilibre")

TOWARD A SPLINE TECHNIQUE FOR THE HIGH REYNOLDS NUMBER INTERACTION (TRIPLE DECK) PROBLEM

BY

M. Napolitano and G. Vacca
ISTITUTO DI MACCHINE, VIA RE DAVID 200,
70125 BARI ITALY

SUMMARY

The present paper is concerned with the high Reynolds number viscous-inviscid interaction problem. The numerical solution of the asymptotic triple deck equations for supersonic as well as subsonic flow conditions is considered. The experience gained by the 1st author on the continuous development of an efficient triple deck solver is briefly outlined and some results worthy of attention are presented. The need for higher order numerical accuracy is pointed out and the fundamental steps necessary for developing a high-order numerical method for the triple deck equations are followed thru. A fourth-order-accurate spline Cauchy integral solver is presented and an interesting matrix singularity problem connected with such a problem is analyzed in some detail. The intrinsic instability of spline techniques, as applied to the time-like variable for the case of parabolic partial differential equations, is removed and a stable procedure, particularly suitable for the triple deck (or interacting boundary layer) equations, is presented and verified for a simple model problem. The logical steps, necessary for combining all the above into a fourth-order-accurate spline triple deck solver, are finally indicated.

1. INTRODUCTION

The problem of high Reynolds number viscous-inviscid interaction, including flow separation, has attracted the attention of many engineers and scientists for quite a long time. Whereas, due to Prandtl boundary layer theory (see, e.g., Ref. 1), high Reynolds number attached flows have been thoroughly understood for more than half a century and the skin friction and heat transfer coefficients at the surface of a body can be routinely evaluated by solving the compressible flow boundary layer equations, the phenomena of viscous-inviscid interaction and laminar separation have challenged for a long time the theoreticians and the experimentalists as well. In particular, for the classical problem of the shock-induced separation of a laminar (or turbulent) boundary layer, it has been quite a challenge to understand how the interaction of an inviscid supersonic flow (for which the governing equations are hyperbolic) with a boundary layer (for which the governing equations are parabolic) produces upstream propagation insofar as the boundary layer separates before the shock inpingement point. Without neglecting the contribution of many other researchers to the understanding of this phenomenon, see for example Crocco (Ref.2), Goldstein (Ref. 3), Lees and Reeves (Ref. 4), a complete and rational explanation of the laminar separation phenomenon has been obtained only with the triple deck theory of Stewartson and Williams (Ref. 5), Stewartson (Ref. 6), Sychev (Ref. 7), Neiland (Ref. 8) and Messister (Ref. 9). For the case of high Reynolds number laminar separation the asymptotic triple deck theory shows that, around the separation point, the flow field is made up of three regions, the inner, middle and outer deck, characterized by viscous, inviscid rotational and inviscid irrotational flows, respectively. These three regions have characteristic nondimensional length of order $Re^{-3/8}$, and height of order $Re^{-5/8}$, $Re^{-1/2}$ and $Re^{-3/8}$, respectively, Re being the Reynolds number of the flow.

To first order in the perturbation parameter ε ($\varepsilon = Re^{-1/8}$) the inviscid flow in the outer deck is described by the thin airfoil theory, where the thin airfoil profile is the

total displacement function, sum of the body surface profile and of the viscous displacement thickness, the flow in the inner deck is governed by boundary-layer-like equations with the pressure gradient and the total displacement thickness related by the inviscid thin airfoil interaction law and the middle deck is a displaced Blasius boundary layer flow,which has the passive role of transmitting the pressure interaction between the outer inviscid and the inner viscous flows.

The theoretical significance of the triple deck equations goes beyond its numerous practical applications, see for example Stewartson (Ref. 6), insofar as this rational asymptotic theory has finally explained the mechanism of upstream propagation in high Reynolds number interacting fl 's. Moreover, they provide a theoretical basis for most of the approximations to the Navier-Stokes equations commonly known as interacting boundary layer or parabolized Navier-Stokes equations and clearly indicate the scale laws which all numerical techniques have to honor in order to accurately resolve high Reynolds number separated flows, see Davis and Werle (Ref. 10) and Davis and Rubin (Ref. 11) for a more detailed discussion of this point. Recent comparisons between interacting boundary layer and triple deck equations for the problem of supersonic flow past a compression corner, see Burggraf et al. (Ref. 12), and for the problem of laminar separation by strong slot injection, see Napolitano (Ref. 13), have indicated that the triple deck equations become realistic only for extremely high values of the Reynolds number.

This would apparently reduce the practical interest of this set of equations. However, all efficient numerical techniques, developed for the triple deck equations, can be easily extended to the interacting boundary layer equations and used for the solution of practical problems.

In addition, for the case of subsonic flow it has been shown, by Jobe and Burggraf (Ref. 14), and by Chow and Melnik (Ref. 15) independently, that higher order triple deck theory predicts the drag of a finite flat plate quite accurately even at moderate values of the Reynolds number.

Furthermore, it has been postulated by Sychev (Ref. 7), and recently verified by Smith (Ref. 16), that also for the case of catastrophic separation, e.g. for flow past a circular cylinder, the flow field takes on a triple deck structure around the separation point. In conclusion,it is now generally aknowledged that for properly modeling the high Reynolds number viscous-inviscid interaction phenomenon, including separation effects, the full set of Navier-Stokes equations is not necessary and it is sufficient to combine a set of boundary-layer-like equations with a thin airfoil inviscid interaction law,which provides a connection between the inviscid pressure gradient and the viscous displacement thickness.

In spite of the great theoretical and practical significance of the interacting boundary layer and triple deck equations, the number of numerical methods available for their solution is by no means comparable with that of the Navier-Stokes solvers, and plenty can still be done with respect to their efficiency and accuracy as well. For example, some numerical techniques (see Ref. 5 and 17) are not capable of properly assessing separated flows, due to ineffective imposition of the required downstream boundary condition. Other techniques (e.g., Ref. 14, 15 and 18) use a true unsteady time dependent approach which converges very slowly and, especially for the subsonic flow case (Ref. 14 and 15), requires a lengthy iteration procedure for satisfying the interaction law at every time step.

Werle and Vatsa (Ref. 19) have developed an ADI (Alternating Direction Implicit) numerical procedure for the supersonic flow interacting boundary layer equations, which effectively accounts for the boundary value nature of the interaction phenomenon. Napolitano, Werle and Davis (Ref. 20) have then generalized such a numerical technique to the supersonic and subsonic triple deck equations. Napolitano (Ref. 13) and Napolitano and Messick (Ref. 21) have further improved that approach for the case of supersonic and subsonic flows, respectively. However, numerical accuracy, particularly in the streamwise direction,is still an issue. In this respect,the use of splines interpolating polynomials or high order compact (Hermitian) finite difference schemes (see, e.g., Ref. 22 and 23) could produce a significant improvement of the ADI approach. Unfortunately, most Hermitian

and spline procedures (see, e.g., Ref. 22 and 23) have been applied successfully for the case of boundary-layer-like equations only in the direction normal to the flow. This is probably due to the fact that a direct application of a cubic spline to the solution of a parabolic partial differential equation, leads to an unconditionally unstable algorithm.

Aim of the present work is to remove such a difficulty and develop a high order numerical procedure for the triple deck (or interacting boundary layer) equations which successfully introduces interpolating spline polynomials in both streamwise and normal directions.

In section 2, the ADI technique of Napolitano et al. (Ref. 20) will be briefly outlined together with its improvements, necessary for solving the difficult problems of supersonic (Ref. 13) and subsonic (Ref. 21) strong slot injection within a reasonable computer time. In section 3, the development of a spline numerical procedure for the viscous-inviscid (pressure-displacement thickness) interaction law is considered. For the supersonic flow case, such an interaction law is a two-point boundary value problem with the additional difficulty of having the first and second derivatives possibly discontinuous at one or more points (see, e.g., Ref. 13,20 and 21), and the method developed by Napolitano and Vacca (Ref. 24) is directly applicable. For the subsonic flow case, the interaction law contains a Cauchy integral, for which Napolitano et al. have developed a fourth-order-accurate spline numerical procedure (Ref. 25). However, such a technique is somewhat awkward to use, coupled to a triple deck equations solver, insofar as it requires the integrand and the integral (in the Cauchy integral relation) to be evaluated at the gridpoints and at the midpoints of the computational grid, respectively. Therefore, its formulation capable of evaluating both the integral and the integrand at the nodal points is derived and a very interesting matrix singularity problem is explained in detail.

In section 4, a stable spline procedure for a parabolic partial differential equation, particularly suitable for the boundary-layer-like interacting boundary layer and triple deck equations, is developed and verified for a model problem.

Finally, the logical steps for combining the two techniques of sections 3 and 4 into a high order accurate spline supersonic and subsonic triple deck (or interacting boundary layer) equations solver are briefly outlined. The authors are presently completing the development of the supersonic flow code and hope to present at least preliminary results at the meeting.

2. THE TRIPLE DECK EQUATIONS AND THE ADI NUMERICAL TECHNIQUE

The problem of interest is that of high Reynolds number laminar (supersonic or subsonic) flow of a Newtonian fluid past a flat plate (Ref. 6). (It is noteworthy to specify that the theory is valid also for more complex geometries, e.g., a circular cylinder (Ref. 16).). At a distance L from the leading edge of the flat plate a disturbance region is produced by any of several causes (see Ref. 6). In order to accurately describe the flow field around the disturbance region, according to the triple deck theory, independent and dependent variables are nondimensionalized according to the following scalings:

$$x^* = L + L\,\frac{C^{3/8}(T_w^*/T_\infty^*)^{3/2}}{\lambda^{5/4}(M_\infty^2-1)^{3/8}}\,\varepsilon^3 x\ , \tag{1}$$

$$y^* = L\,\frac{C^{5/8}(T_w^*/T_\infty^*)^{3/2}}{\lambda^{3/4}(M_\infty^2-1)^{1/8}}\,\varepsilon^5 y\ , \tag{2}$$

$$u^* = U_\infty^*\,\frac{\lambda^{1/4}C^{1/8}(T_w^*/T_\infty^*)^{1/2}}{(M_\infty^2-1)^{1/8}}\,\varepsilon u\ , \tag{3}$$

$$v^* = U_\infty^*\,\lambda^{3/4}(M_\infty^2-1)^{1/8}C^{3/8}(T_w^*/T_\infty^*)\,\varepsilon^3 v\ , \tag{4}$$

and

$$p^* = p^*_\infty + \rho^*_\infty U^{*2}_\infty \lambda^{1/2}(M^2_\infty - 1)^{-1/4} C^{1/4} \varepsilon^2 p \ . \qquad (5)$$

In equations (1) - (5), x, y, u and v are the longitudinal and normal coordinates and velocity components respectively; p is the pressure, ρ the density, M the Mach number, T the temperature, μ the viscosity coefficient, $C = \mu^*_w T^*_\infty / \mu^*_\infty T_w$ is the Chapman constant, and $\lambda = 0.332$ is the Blasius skin friction coefficient. Subscripts ∞ and w indicate free stream and wall conditions respectively. Equations (1) through (5) are then substituted into the Navier-Stokes equations and to first order in the perturbation parameter ε the following triple deck equations are obtained:

$$u_x + v_y = 0 \qquad (6a)$$

and

$$uu_x + vu_y = - \frac{dp}{dx} + u_{yy} \qquad (6b)$$

with boundary conditions

$$u(x,F) = 0 \ , \qquad (7)$$

$$v(x,F) = V_w \ , \qquad (8)$$

$$u(x,y\to\infty) \to y - \delta - F \ , \qquad (9)$$

and the initial condition

$$u(x\to-\infty,y) \to y \ , \qquad (10)$$

where F(F=F(x)) is the profile of a physical disturbance on the plate (i.e., a hump, a compression corner, etc.), V_w is the value of the velocity with which a secondary fluid is eventually injected into the boundary layer, and δ is the perturbation viscous displacement thickness.

In the momentum equation (6b) the pressure gradient dp/dx is related to the total displacement thickness, D (D = δ + F), by the following interaction law:

$$\frac{dp}{dx} \quad \frac{d^2D}{dx^2} \ , \qquad (11)$$

or

$$\frac{d^2D}{dx^2} = \frac{1}{\pi} \oint_\infty^\infty \frac{dp/d\xi}{x-\xi} \, d\xi \ , \qquad (12)$$

where the integral is a Cauchy principal value one, for supersonic and subsonic flow, respectively.

Because of equation (11), or (12), the triple deck fundamental problem is of the boundary value tipe and a boundary condition is required for p (or D equivalently) at upstream as well as downstream infinity. The key of the success of any numerical technique for this problem is the correct imposition of such a downstream boundary condition.

This has been accomplished by Werle and Vatsa for the supersonic interacting boundary layer equations (Ref. 19) and by Napolitano, Werle and Davis (Ref. 20) for both the supersonic and subsonic triple deck equations. Their idea is quite simple: a relaxation-like time derivative for the total displacement, D, is added to the right hand side of the momentum equation (6b), to give:

$$uu_x + vu_y = - \frac{dp}{dx} + u_{yy} + \frac{\partial D}{\partial t} \ ; \qquad (13)$$

then, a two sweep Alternating Direction Implicit (ADI) procedure is used to relax the equations in time until convergence is achieved. In the two sweeps, the solution is advanced from time t^n to time $t^* = t^n + \Delta t/2$ and then from t^* to $t^{n+1} = t^* + \Delta t/2$ by writing the momentum equation as:

$$(uu_x + vu_y - u_{yy})^* = - \left(\frac{dp}{dx}\right)^n + \lambda(D^* - D^n) \qquad (14a)$$

and

$$(uu_x + vu_y - u_{yy})^* = -\left(\frac{dp}{dx}\right)^{n+1} + \lambda(D^{n+1} - D^*) \quad , \qquad (14b)$$

respectively; ($\lambda = 2/\Delta t$). In practice, the numerical algorithm proceeds as follows. In the first sweep, the pressure gradient $(dp/dx)^n$ is a known function and equation (14a) is solved numerically, coupled to continuity equation (6a), to provide u^*, v^*, D^*. In the second sweep, the right hand sides of equations (14a) and (14b) are combined to give:

$$\left(\frac{dp}{dx}\right)^{n+1} = \left(\frac{dp}{dx}\right)^n + \lambda(D^{n+1} - 2D^* + D^n) \qquad (15)$$

The expression of $\left(\frac{dp}{dx}\right)^{n+1}$, given by equation (15), is then introduced in the supersonic or subsonic interaction law, respectively, to give

$$\left(\frac{d^2D}{dx^2}\right)^{n+1} - \lambda D^{n+1} = \left(\frac{dp}{dx}\right)^n - \lambda(2D^* - D^n) \qquad (16)$$

and

$$\left(\frac{d^2D}{dx^2}\right)^{n+1} = \frac{1}{\pi} \int_{\infty}^{\infty} \frac{\left(\frac{dp}{d\xi}\right)^n + \lambda(D^{n+1} - 2D^* + D^n)}{x - \xi} d\xi \quad . \qquad (17)$$

After evaluating the D^{n+1} distribution by means of equation (16) or (17), equation (15) allows to evaluate the n+1 time level pressure gradient and the whole process is repeated until a satisfactory convergence criterion is met. Equations (6a) and (6b) are solved by standard finite difference methods (see, e.g., Ref. 19, 20 and 13). In order to evaluate D^*, Werle and Vatsa iterate at every location x (Ref. 19), whereas Napolitano, Werle and Davis use a more efficient linear superposition technique (Ref. 20 and 13). The nonlinear terms in the momentum equation (6b) were first linearized in space (Ref. 20) and later in time, in order to allow for a simpler accomodation of windward differencing (for reverse flow regions) and of local discontinuities (Ref. 13 and 21). Variable grid in the x direction has been successfully used by Napolitano (Ref. 13) and Napolitano and Messick (Ref. 21), in order to properly resolve flow properties (e.g., pressure and wall shear), which change very rapidly near the separation point and decay very slowly far upstream and downstream. Some interesting results have been obtained by Napolitano (Ref. 13) for the problem of strong slot injection into a supersonic laminar boundary layer. The wall shear, pressure and displacement thickness profiles, for various values of the injection velocity V_w, are presented in figures 1, 2 and 3. The major points of interest are that the discontinuous pressure gradients at the two slot edges are properly captured (see Ref. 13 for details) and that separation first occurrs ahead of the slot (see figure 1), as expected by Smith and Stewartson (Ref. 17) on the base of linear theory and already verified by Werle for a finite value of the Reynolds number (Ref. 29). A step size study for the pressure at the leading edge of the slot is also presented in figure 4, which clearly indicates that accuracy in the streamwise direction is quite a problem. It is true that three different finite difference representations of the pressure at the slot leading edge, indicated as I, II and III, produce the same extrapolated (to zero step size) value. However, for finite values of the step size Δx, the truncation errors are seen to be quite significant (all results in figures 1 to 3 are extrapolated to zero step size for the sake of accuracy).

The technique of Napolitano, Werle and Davis (Ref. 20) used originally a Crank Nicolson approach for the star (*) sweep finite difference equations and was second-order-accurate also in the streamwise direction, x. With such an approach Werle has obtained second-order-accurate results for supersonic flow past a compression corner. In figure 5 the shear and pressure profile obtained with a rather coarse step size, $\Delta x = 0.6$, are presented for the case of a normalized ramp angle, α, equal to 2.5 and are favorably compared with the extrapolated results of References 19 and 26. However, such an approach presented the typical oscillations of the Crank Nicolson scheme for small values of the step sizes ratio $\Delta x/\Delta y$, and it was therefore ill suited for solving the triple deck problem for flow past a small parabolic hump (see Ref. 20). For this reason, the first-order-accurate

scheme was preferred and the results of figure 5 have never been published before.

Another point worthy of attention is the solution of the second sweep equation (17), for the case of subsonic flow. The Cauchy integral is evaluated with second order accuracy, by integrating the term $\frac{d\xi}{x-\xi}$ analytically over every mesh of the integration domain after extracting the node point values of the remaining regular terms of the integrand (see Ref. 20, 27 and 28 for more details). In this way, equation (17) is reduced to a system of linear algebraic equations of the type

$$A_{ij} D_j^{n+1} = b_i \tag{18}$$

whose solution provides the sought D_i^{n+1} vector. In the original approach (Ref. 20), an iterative procedure was used to solve the system (18). This was first written as

$$[T_{ij} + (A_{ij} - T_{ij})]\ D_j^{n+1} = b_i \tag{19}$$

where T_{ij} is the tridiagonal matrix whose main, upper and lower diagonals, coincide with the corresponding ones of A_{ij}. The system was then solved as

$$T_{ij}\ D_j^{n+1} = b_i - (A_{ij} - T_{ij})\ D_{pj}^{n+1} \tag{20}$$

by Gaussian tridiagonal reduction until the new and the previous iteration values D_j^{n+1} and D_{pj}^{n+1} converged.

In order to obtain convergence, underrelaxation was found necessary as in previous studies (Ref. 14 and 15) and the overall convergence rate for the subsonic flow code was about an order of magnitude slower than that of the supersonic flow code. Later (Ref. 21), since the matrix A_{ij} is the same at every new n+1 time level, the inverse A_{ij}^{-1} was calculated once and for all and the solution to the second sweep equation was obtained directly as:

$$D_i^{n+1} = A_{ij}^{-1}\ b_j\ . \tag{21}$$

With such a technique, also employing the variable grid spacing of Ref. 13, Napolitano and Messick (Ref. 21) were able to solve the very difficult problem of strong slot injection into a subsonic laminar boundary layer, with a computational effort comparable to that required for the corresponding supersonic flow problem. The wall shear profiles, for various values of the slot injection velocity V_w, are presented in figure 6, where it is seen that, for the case of subsonic mainstream, separation first occurrs after the slot.

Again, it is important to realize that accuracy in the x direction is the major difficulty of the ADI technique discussed in this section. A spline approach, fourth-order-accurate in the y direction has been derived by the present authors. However, they have decided that it was much more important to improve the accuracy in the streamwise direction. This required a much longer effort, whose results, todate, are presented in the next two sections.

3. A SPLINE CAUCHY INTEGRAL SOLVER

It has been seen that, for the case of subsonic flow, an integral equation of the Fredholm type has to be solved at each second sweep of the ADI solution procedure. In order to obtain a spline numerical technique for the triple deck equations, it is then necessary to be able to apply a spline technique to the numerical solution of such an integral equation. Napolitano et al. (Ref. 25) have developed a cubic spline procedure for the numerical solution of a Cauchy integral of the type:

$$I(x) = \oint_a^b \frac{f(\xi)\,d\xi}{x-\xi}\ ,\quad a < x < b\ . \tag{22}$$

They have considered both the direct and inverse problem, i.e. either the numerical evaluation of I(x), for a given $f(\xi)$, or that of $f(\xi)$, for a known I(x). The integration domain (a,b) is divided into an arbitrary number of meshes of constant length h and a computational grid is formed with x_j (j=1,2,...,N; x_1=a; x_n=b) being its gridpoints and $\tilde{x}_i$ ($\tilde{x}_i = x_i + \frac{h}{2}$, i=1,2,...,N-1) being its midpoints.

In equation (22) the integrand is replaced by its cubic spline interpolating polynomial $S(\xi)$ on each mesh, to give

$$I(\tilde{x}_i) = \sum_{j=1}^{N-1} \oint_{x_j}^{x_{j+1}} \frac{S(\xi)\,d\xi}{\tilde{x}_i - \xi} \quad , \tag{23}$$

where

$$S(\xi) = k_j \frac{(x_{j+1}-\xi)^3}{6h} + k_{j+1} \frac{(\xi - x_j)^3}{6h} + (f_j - k_j h^2/6) \frac{x_{j+1}-\xi}{h}$$

$$+ (f_{j+1} - k_{j+1} h^2/6) \frac{\xi - x_j}{h} \quad , \tag{24}$$

(see, e.g., Ref. 22) and f_j and k_j are the spline approximations of $f(\xi)$ and its second derivative $d^2f(\xi)/d\xi^2$ at the nodal point x_j. All these f_j and k_j values, which are constant over each mesh, are then brought out of the integrals, see equation (23), and all the terms containing ξ are integrated analytically. After some lengthy algebra, the following final equation is obtained

$$I(\tilde{x}_i) = \sum_{j=1}^{N-1} \left[k_j \left\{ \frac{(\tilde{x}_i - x_j)^3 - (\tilde{x}_i - x_{j+1})^3}{18h} - \frac{(\tilde{x}_i - x_{j+1})^3}{12h} \mathrm{Ln} + \frac{\tilde{x}_i - x_{j+1}}{4h} \right.\right.$$

$$\left[(\tilde{x}_i - x_{j+1})^2 - (\tilde{x}_i - x_j)^2 \right] + \left. \frac{(\tilde{x}_i - x_{j+1})^2}{2} \right\} + (f_j - k_j \frac{h^2}{6}) \times$$

$$(+1 - \frac{\tilde{x}_i - x_{j+1}}{2h} \mathrm{Ln}) \Big] + \sum_{j=1}^{N-1} \left[k_{j+1} \left\{ \frac{(\tilde{x}_i - x_{j+1})^3 - (\tilde{x}_i - x_j)^3}{18h} \right.\right.$$

$$+ \frac{(\tilde{x}_i - x_j)^3}{12h} \mathrm{Ln} - \frac{\tilde{x}_i - x_j}{4h} \left[(\tilde{x}_i - x_{j+1})^2 - (\tilde{x}_i - x_j)^2 \right] - \left. \frac{(\tilde{x}_i - x_j)^2}{} \right\}$$

$$+ (f_{j+1} - k_{j+1} \frac{h^2}{6}) \times (-1 + \frac{\tilde{x}_i - x_j}{2h} \mathrm{Ln}) \Big] \quad , \tag{25}$$

with

$$\mathrm{Ln} = \ln \left(\frac{\tilde{x}_i - x_j}{\tilde{x}_i - x_{j+1}} \right)^2$$

Equation (25), after that all the k_j have been determined by the known values of f_j, allows to evaluate $I(\tilde{x}_i)$ at all midpoints with fourth order numerical accuracy (see Ref. 25). For the case of the inverse (Cauchy integral) problem, after eliminating all the k_j unknowns in terms of the f_j unknowns, equation (25) provides a system of N-1 linear equations, which, together with a closure equation, is solved to provide all the f_j (j=1,2,...,N) unknowns. Such a closure equation was needed because the Cauchy integral was evaluated at the midpoints of the integration domain , in order to avoid the singularity at the two extremes, a and b, where I(x) diverges if $f(\xi)$ does not vanish. It is clear that in the triple deck problem, where the integration domain is infinite and the integrand vanishes as $x \to \pm\infty$, such a problem does not arise. Moreover, it is extremely important to be able to evaluate the integral $I(x_i)$ and the integrand $f(x_j)$ at the same nodal points. Therefore, the method of Ref. 25 has been generalized to the case in which $\tilde{x}_i = x_i$. A straightforward application of equation (25), with $\tilde{x}_i = x_i$, is seen to produce 4 singular logarithmic terms, due to the integration over the two meshes immediately adjacent to the point $x_j = x_i$, where the argument of the integral diverges. However, such a difficulty can be easily removed and the Cauchy integral can be properly evaluated at the nodal points, as follows. Equation (23) is rewritten as:

$$I(x_i) = \sum_{j=1}^{i-2} \oint_{x_j}^{x_{j+1}} \frac{S(\xi)\,d\xi}{x_i - \xi} + \oint_{x_{i-1}}^{x_{i+1}} \frac{S(\xi)\,d\xi}{x_i - \xi} + \sum_{j=i+1}^{N-1} \oint_{x_j}^{x_{j+1}} \frac{S(\xi)\,d\xi}{x_i - \xi} \tag{26}$$

The first and last terms in the right hand side of equation (26) lead to two equa-

tions formally identical to equation (25), without any singular term. Moreover, a correct evaluation of the middle term gives

$$\oint_{x_{i-1}}^{x_{i+1}} \frac{S(\xi)d\xi}{x_i-\xi} = k_{i-1}\frac{h^2}{18} + (f_{i-1}-k_{i-1}\frac{h^2}{6}) - k_{i+1}\frac{h^2}{18} - (f_{i+1}-k_{i+1}\frac{h^2}{6}). \qquad (27)$$

It is noteworthy that the same correct value for $I(x_i)$ is obtained by using equation (25) and setting all the logarithmic terms equal to zero, if either the numerator or the denominator of the argument of the logarithm is zero. A final difficulty arises when the Cauchy integral is evaluated at either extreme of the integration domain (where f must be zero in order for I to exist). For this case, e.g., for I(a), it is convenient to write

$$I(a) = \oint_{a}^{a+h} \frac{S(\xi)d\xi}{a-\xi} + \oint_{a+h}^{b} \frac{S(\xi)d\xi}{a-\xi} \qquad (28)$$

The second term of the right hand side of equation (28) is evaluated by means of equation (25) by replacing 1 with 2 as the lower index of the summation signs and the first term can be easily shown to provide

$$\oint_{a}^{a+h} \frac{S(\xi)d\xi}{x-\xi} = -f_2 + k_1\frac{h^2}{4} + \frac{(k_2-k_1)h^2}{9} \qquad (29)$$

Again, the same result is obtained by using equation (25) and setting to zero the singular logarithmic terms.

It is noteworthy that, for the case of the subsonic interaction law, the integration domain is infinite and the far upstream and downstream contributions are accounted for, analytically. For this case, f_1 does not need to be zero and I(a) is evaluated by combining the contributions from a-h to a and from a to a+h, as in equation (27). Also, the present approach provides the nodal points extension of the second-order-accurate Cauchy integral solver of Napolitano (Ref. 27) by simply replacing the cubic spline $S(\xi)$ of equation (24) with its linear counterpart, obtained by dropping all k_j terms.

In order to verify the present procedure, the following two model problems, for which the analytical solution is available (Ref. 30), have been considered

$$I_1(x) = \oint_{-1}^{1} \frac{(1+\xi)(1-\xi)}{x-\xi}\,d\xi = (1-x^2)(x \ln\frac{1+x}{1-x} - 2) + \frac{2}{3} \qquad (30)$$

$$I_2(x) = \oint_{-1}^{1} \frac{(1+\xi)(1-\xi)\xi^2}{x-\xi}\,d\xi = x(1-x^2)(x \ln\frac{1+x}{1-x} - 2) + \frac{2}{3}x\,, \qquad (31)$$

for which f(a) = f(b) = 0, so that I(a) and I(b) are finite. $I_1(x)$ has been chosen because the present fourth-order-accurate cubic spline method should provide the exact solution for any step size, h; $I_2(x)$, as a general model problem. Equation (25), with the previously outlined special treatments for the otherwise singular logarithmic terms, has been used to evaluate $I_1(x_i)$ and $I_2(x_i)$. The exact values of f_j have been used and, according to Ref. 25, the k_j values have been evaluated as

$$k_j = \frac{f_{j-1}-2f_j+f_{j+1}}{h^2} \qquad (32)$$

at all the internal gridpoints and as their linear extrapolation from the two neighboring points at the two extremes of the integration domain, i.e.,

$$k_1 = 2k_2 - k_3\,, \quad k_N = 2k_{N-1} - k_{N-2} \qquad (33a,b)$$

The same computer program has been used to evaluate $I_1(x)$ and $I_2(x)$ according to both the fourth-order-accurate and the second-order-accurate methods (by setting all k_j values identically to zero in the second case). The results for $I_2(0.2)$ are plotted in figure 7 as the truncation errors, ε (difference between analytical and numerical values) versus the step size, h and are seen to verify the expected order of accuracy of the present nodal points Cauchy integral evaluation technique. Moreover, the fourth-order-accurate cubic spline procedure has evaluated $I_1(x)$ exactly, as expected.

In the subsonic flow interaction law, the unknown displacement thickness appears also inside the Cauchy integral. It is therefore extremely important to be able to solve for the unknowns f_j, given the values of $I(x_i)$. For this Cauchy integral inverse problem, the

use of equation (25), after that all the k_j have been eliminated in favor of the f_j unknowns, by means of equations (32) and (33a,b), provides a system of N linear algebraic equations for the N unknowns, f_j.

For simplicity, since f_1 and f_N must be zero in order for $I(x_1)$ and $I(x_N)$ to be finite, equation (25) is written only at all internal gridpoints and provides a system of N-2 linear algebraic equations,

$$A_{ij} f_j = I_i \qquad (i = 2,\ldots,N-1;\ j = 2,\ldots,N-1) \ . \qquad (34)$$

It is noteworthy that, by evaluating both I_i and f_j at the same nodal points, the closure equation required in Ref. 25 becomes unnecessary. However, the present approach has produced a new difficulty, due to a particular symmetry property of the matrix A_{ij}. For both the cubic and linear spline methods, the elements a_{ij} of matrix A_{ij} are such that

$$a_{i,j} = - a_{(N-1-i),(N-1-j)} \qquad (35)$$

and, therefore, A_{ij} is singular for all odd values of N, whereas it is invertible for all even values of N. This result is extremely important insofar as it indicates that the system (34) has a unique solution vector f_j, only for values of the step size h associated with even values of the order of the matrix A_{ij}. This is obviously a numerical difficulty, due to the discretization of the Cauchy integral problem, and requires a full explanation. It can be seen that the singularity of the matrix A_{ij} is due to the row corresponding to $x_i = 0$. This row is clearly antisymmetric (see equation (35)) as it can be easily understood by noting that every function $f(\xi)$, which is even with respect to the midpoint of the integration domain (a,b), produces a Cauchy integral $I(x)$ which vanishes at such a point. Therefore, it is the coincidence of a gridpoint with the center of the numerical integration domain, which causes the matrix A_{ij} to be singular and allows for ∞^1 spurious solution vectors, f_j. Each of these vectors is symmetric and its elements f_j change sign at every successive gridpoint. It is therefore clear that they are a nonphysical solution, since, for $N \to \infty$, the only regular function which changes its sign infinite times is the null function. At this point, it is also clear why, when the Cauchy integral values are given at the midpoints of each mesh (Ref. 25), no singularity is encountered. For this case, in fact, if the integral $I(\tilde{x}_i)$ happens to be evaluated exactly at the middle of the integration domain the spurious solution vectors should have two successive elements (adjacent to $\tilde{x}_i$) equal and with opposite sign.

The function $f(\xi)$, corresponding to the model problem of equation (31), has been evaluated for several <u>even</u> values of N, using both the cubic and the linear spline approximations. The numerical results, presented in figure 8, again as the truncation errors versus the step size h, clearly demonstrate the correctness of the approach.

The relevance of the present study to the solution of the interacting boundary layer and triple deck equations is quite evident. Every numerical technique, for evaluating the argument of the Cauchy integral in the subsonic interaction law, is liable to produce a matrix A_{ij} which is singular for odd values of N. Since most of these numerical techniques are iterative in nature (see, e.g., Ref. 14, 15 and 20), such a singularity (of A_{ij}) would invariably produce a divergent solution. It is probably due to this reason that, before Napolitano et al. (Ref. 20) have successfully used an inverse technique for the subsonic interaction law, only direct methods were considered feasible.

4. A SPLINE TECHNIQUE FOR A PARABOLIC PARTIAL DIFFERENTIAL EQUATION

In section 2, it has been seen that for the ADI technique, as applied to the triple deck equations, the accuracy in the direction normal to the body surface is much higher than the accuracy in the streamwise direction. Therefore, it would be extremely beneficial to introduce a high-order-accurate method, based on spline polynomials, at least in the x direction. However, most numerical procedures, applied to parabolic partial differential equations (PDE) use high order spline and Hermitian concepts only for the nonmarching

direction (see, e.g., Ref. 22 and 23), whereas first-order-accurate backward or second-order-accurate central (Crank Nicolson) finite difference approximations are used in the marching (time-like) variable.

In the present section a high-order-accurate spline technique (in both directions) for a parabolic PDE is developed and verified for the following linear model problem:

$$f_{yy} = f_x \qquad (0 \le x \le 1;\ 0 \le y \le 1) \tag{36}$$

with initial and boundary conditions such that the exact solution is:

$$f(x,y) = e^{-\pi^2 x} \sin \pi y \tag{37}$$

For the problem given in equation (36), a fourth-order-accurate (in y) spline procedure using a fifth order interpolation polynomial is given by Rubin and Khosla (Ref. 22). A block tridiagonal system of equations is solved at every location x_i to provide the spline approximations to f and f_{yy}, i.e., f_{ij} and L_{ij} $(i=1,2,\ldots,I;\ j=1,2,\ldots,J)$. In order for the f_{ij} values to be fourth-order-accurate also in the time-like x variable, it is sufficient to introduce a cubic spline, S(x), formally identical to $S(\xi)$, given in equation (24), with f_{ij} and k_{ij} being the cubic spline approximations to the function $f(x_i,y_i)$ and its second (partial) derivative $f_{xx}(x_i,y_i)$. For such a cubic spline S(x), fourth-order-accurate forward and backward approximations to the first order derivative, f_x, are given in terms of the f_{ij} and k_{ij} values (Ref. 22) as

$$f_x(x_{i-1},y_j) = -\frac{\Delta x}{3}\,(k_{i-1,j} + 0.5k_i) + \frac{f_{i,j}-f_{i-1,j}}{\Delta x} \tag{38}$$

$$f_x(x_i,y_j) = \frac{\Delta x}{3}\,(k_{i,j} + 0.5k_{i-1,j}) + \frac{f_{i,j}-f_{i-1,j}}{\Delta x}\ . \tag{39}$$

These, together with the fourth-order-accurate spline approximations of f_{yy}, given by Rubin and Khosla (Ref. 22), provide the following fourth-order-accurate approximations to the governing equation (36)

$$-\frac{\Delta x}{3}\,(k_{i-1,j} + 0.5k_i) + \frac{f_{i,j}-f_{i-1,j}}{\Delta x} = M_{i-1,j} \tag{40}$$

$$\frac{\Delta x}{3}\,(k_{i,j} + 0.5k_{i-1}) + \frac{f_{i,j}-f_{i-1,j}}{\Delta x} = M_{i,j} \tag{41}$$

with

$$M_{i,j} = (L_{i,j+1} + 10L_{i,j} + L_{i,j-1})/12\ . \tag{42}$$

If the initial conditions $f_{1,j}$, $k_{1,j}$ and $L_{1,j}$ are known for all j values, equation (41) written at all $x_{2,j}$ nodal points provides a set of two by two block tridiagonal equations in the unknowns $f_{2,j}$, $L_{2,j}$, $k_{2,j}$ $(j=1,2,\ldots,J)$.

Moreover, equation (40), written at all $x_{2,j}$ locations, allows to eliminate all $k_{2,j}$ in favor of the $f_{2,j}$ and $L_{2,j}$ unknowns which can then be straightforwardly solved by block tridiagonal Gaussian reduction (Ref. 31). The solution is then advanced to the next stations $x_{3,j}$ by writing equations (40) and (41) at the $x_{3,j}$ locations and so on. Unfortunately, this very simple high-order-accurate numerical procedure is unconditionally unstable, as a rather complex Von Neumann stability analysis clearly indicates (Ref. 32) and numerical experiments inevitably verify. This instability is basically due to the intrinsic stiffness of spline interpolating polynomials, which are extremely sensitive to branching phenomena, whenever the boundary conditions are given on the same side of the integration domain. It is therefore clear that such an instability would certainly be eliminated if one could provide a downstream boundary condition, e.g., $f_{I,j}$ or $k_{I,j}$. However, the problem given in equation (36) is parabolic in nature and does not require any downstream (in the x direction) boundary condition. At this point, it is necessary to recall that the triple deck (or interacting boundary layer) equations are of the boundary value nature because of the interaction law. Therefore, for this case of extreme practical interest, $k_{I,j}$ can be either taken to be zero or evaluated by an asymptotic theory and an iterative stable procedure can be easily constructed: equations (40) and (41) are solved by considering an old iteration value of $k_{i,j}$ and evaluating the new iteration values of $k_{i-1,j}$, $f_{i,j}$ and $L_{i,j}$ for all gridpoints x_i, y_j. The final $k_{I,j}$ values are fixed boundary condi-

tions, whereas all the other $k_{i,j}$ values are updated at every iteration. A fictitious time derivative f_t can be eventually added to equation (37) in order to optimize the convergence of the algorithm.

It is obvious that this high-order-accurate method is expected to be very efficient for the triple deck problem,where an iteration procedure is already required because of the interaction law. For the case of a simple parabolic equation, the gain in accuracy is offset by the increased computational effort and by the lack of the required downstream boundary condition. However, this last difficulty is easily removed by using a simple backward finite difference representation for f_x in the first sweep of the solution procedure. In this way a first order accurate initial solution for $f_{i,j}$ is obtained together with the following boundary conditions for $k_{I,j}$:

$$k_{I,j} = (2f_{I,j} - 5f_{I-1,j} + 4f_{I-2,j} - f_{I-3,j}) / \Delta x^2 \qquad (43)$$

Two points are of particular interest: first, the use of a first-order-accurate solution as the initial guess for the iterative procedure accelerates its convergence (the method is unconditionally stable); second, the local first order accuracy of $k_{I,j}$ does not reduce the overall order of accuracy of the method (see, e.g., Ref. 24). The algorithm, as described above, has been applied to the model problem of equation (36). The results for $f_{i,j}$, $M_{i,j}$ and $k_{i,j}$, at the center of the integration domain ($x_i = y_i = 0.5$), are provided as the logarithms of the truncation errors versus the logarithms of the step size h ($\Delta x = \Delta y = h$), in figure 9, where the fourth order accuracy of $f_{i,j}$ and $M_{i,j}$ and the second order accuracy of $k_{i,j}$ are clearly verified.

For the sake of completeness, it is pointed out that an improvement in the convergence rate of the present algorithm can be obtained by updating all the $k_{i,j}$ values after each iteration by enforcing the continuity of the spline first derivative on each mesh of the integration domain, i.e., by evaluating all $k_{i,j}$ from the following tridiagonal system of equations

$$\frac{6}{\Delta x^2} (f_{i-1,j} - 2f_{i,j} + f_{i+1,j}) = k_{i-1,j} + 4k_{i,j} + k_{i+1,j} \cdot \qquad (44)$$

CONCLUSIONS

The numerical procedures developed in sections 3 and 4 can be combined together, to provide a fourth-order-accurate spline ADI procedure for the triple deck (or interacting boundary layer) equations, on the lines of References 20, 13 and 21. The authors are presently working at this problem and hope to present preliminary results at the conference. However, sections 3 and 4 present two novel approaches,which are of considerable interest per se, for their relevance to computational fluid dynamics.

AKNOWLEDGEMENTS

The authors are grateful to dr. M.J. Werle for providing the results of figure 5. Section 3 was developed by the first author while working as a visiting scientist at the Air Force Wright Aeronautical Laboratory, Dayton, Ohio. He his grateful to Prof. R.T. Davis for his encouragement to investigate this problem. Mr. Lippolis has cooperated to section 4. Finally, Mr. G. Marin has typed the manuscript with patience and skill.

REFERENCES

1. SCHLICHTING, H., "Boundary-Layer Theory", Mc Graw-Hill, 1968.
2. CROCCO, L., "Considerations on the shock-boundary layer interaction", Proc. Conf. on High Speed Aero., Brooklyn Cent., 75-112 (1955).
3. GOLDSTEIN, S., "On laminar boundary layer flow near a point of separation", Q.J. Mech. App. Math., Vol. 1, 43-69 (1948).

4. LEES, L. and REEVES, B.L., "Supersonic separated and reattaching laminar flows", AIAA J., Vol. 2, 1907-20 (1964).
5. STEWARTSON, K. and WILLIAMS, P.G., "Self-induced separation", Proc. Roy. Soc., London, A 312, 181-206 (1969).
6. STEWARTSON, K., "Multistructured Boundary Layers on Flat Plates and Related Bodies", Advances in Applied Mechanics, Vol. 14, 146-239 (1974).
7. SYCHEV, V. YA., "Concerning Laminar Separation", Izv. Akad. Nauk. SSSR, Mekh, Zhidk. Gaza, n. 3, 47-59 (1972).
8. NEILAND, V. YA., "Towards a Theory of Separation of the Laminar Boundary Layer in a Supersonic Stream", Izv. Akad. Nauk. SSSR, Mekh, Zhidk. Gaza, n. 4 (1969).
9. MESSITER, A.F., "Boundary Layer Flow Near the Trailing Edge of a Flat Plate", S.I.A.M. J. Appl. Math., 18, 241-247 (1970).
10. DAVIS, R.T. and WERLE, M.J., "Numerical Methods for Interacting Boundary Layers", Proc. of the 1976 Heat Transfer and Fluid Mechanics Institute, Stanford University Press, 317-339 (1976).
11. DAVIS, R.T. and RUBIN, S.G., "Non-Navier Stokes Viscous Flow Computations", Computers and Fluids, Vol. 8, n. 1, 101-131 (1980).
12. BURGGRAF, O.R., RIZZETTA, D., WERLE, M.J. and VATSA, V.N., "Effect of Reynolds Number on Laminar Separation of a Supersonic Stream", AIAA J., Vol. 17, n. 4, 336-343 (1979).
13. NAPOLITANO, M., "A Numerical Study for Strong Slot Injection into a Supersonic Laminar Boundary Layer", AIAA J., Vol. 18, n. 1, 72-77 (1980).
14. JOBE, C.E. and BURGGRAF, O.R., "The Numerical Solution of the Asymptotic Equations of Trailing Edge Flow", Proc. Roy. Soc., London, A 340, 91-111 (1974).
15. CHOW, R. and MELNIK, R.E., "Numerical Solutions of the Triple-Deck Equations for Laminar Trailing Edge Stall", Proc. 5th Int. Conf. Num. Meths. in Fluid Dyn., Lecture Notes in Physics, Vol. 59, Springer Verlag (1976).
16. SMITH, F.T., " The Laminar Separation of an Incompressible Fluid Streaming Past a Smooth Surface", Proc. Roy. Soc., London, Series A, Vol. 356, 443-463 (1977).
17. SMITH, F.T. and STEWARTSON, K., "On Slot Injection into a Supersonic Laminar Boundary Layer", Proc. Roy. Soc., London, Series A, Vol. 332, 1-22 (1973).
18. JENSON, R., BURGGRAF, O.R., RIZZETTA, D., "Asymptotic Solution for Supersonic Viscous Flow Past a Compression Corner", Proc. 4th Int. Conf. Num. Meths. in Fluid Dyn., Lecture Notes in Physics, Vol. 35, Springer Verlag (1975).
19. WERLE, M.J. and VATSA, V.N., "A New Method for Supersonic Boundary Layer Separation", AIAA J., Vol. 12, n. 11, 1491-1497 (1974).
20. NAPOLITANO, M., WERLE, M.J. and DAVIS, R.T., "A Numerical Technique for the Triple-Deck Problem", AIAA J., Vol. 17, n. 7, 699-705 (1979).
21. NAPOLITANO, M. and MESSICK, R.E., "On strong slot injection into a subsonic laminar boundary layer", Computers and Fluids, Vol. 8, n. 2, 199-212 (1980).
22. RUBIN, S.G. and KHOSLA, P.K., "Polynomial Interpolation Methods for Viscous Flow Calculations", J. Computational Phys., Vol. 24, 217-244 (1977).
23. CIMENT, M., LEVENTHAL, S.H. and WEINBERG, B.C., "The Operator Compact Implicit Method for Parabolic Equations", J. Computational Phys., Vol. 28, 135-166 (1978).
24. NAPOLITANO, M. and VACCA, G., "A Spline Technique for Boundary Value Problems with Discontinuous Derivatives", Atti dell'Istituto di Macchine dell'Università di Bari (1979), submitted to Meccanica.
25. NAPOLITANO, M., RUBINI, F. and VACCA, G., "A fourth-order-accurate direct and inverse Cauchy integral solver", Computers and Fluids, to appear (1980).
26. RIZZETTA, D., "Asymptotic Solution for Two-Dimensional Viscous Supersonic and Hypersonic Flows Past Compression and Expansion Corners", Ph. D. Dissertation, The Ohio State University (1976).
27. NAPOLITANO, M., "On the computation of Cauchy integrals", Annali della Facoltà di Ingegneria, Università di Bari, Nuova Serie, Vol. III, 87-95 (1978).
28. NAPOLITANO, M., WERLE, M.J. and DAVIS, R.T., "Numerical Solutions of the Triple-Deck Equations for Supersonic and Subsonic Flow Past a Hump", University of Cincinnati, Dept. of Aerospace Engineering, AFL Report n. 78-6-42 (1978).
29. WERLE, M.J., "Supersonic Laminar Boundary Layer Separation by Slot Injection", AIAA J., Vol. 17, n. 2, 160-167 (1979).
30. VAN DYKE, M.D., "Second Order Subsonic Airfoil Theory", NACA Report n. 1274 (1959).
31. ISAACSON, E. and KELLER, H.B., "Analysis of Numerical Methods", Wiley, New York (1966).
32. LIPPOLIS, A., "Private Communication".

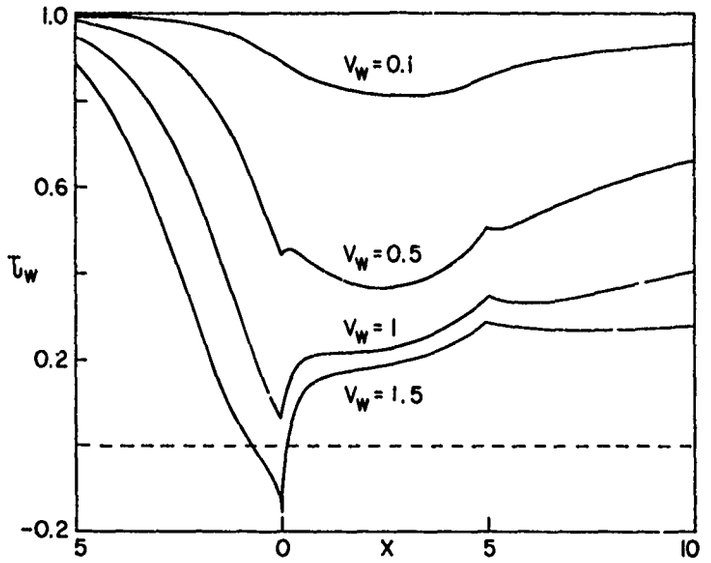


Fig.1 Wall shear profiles for the supersonic strong slot injection problem (Ref. 13)

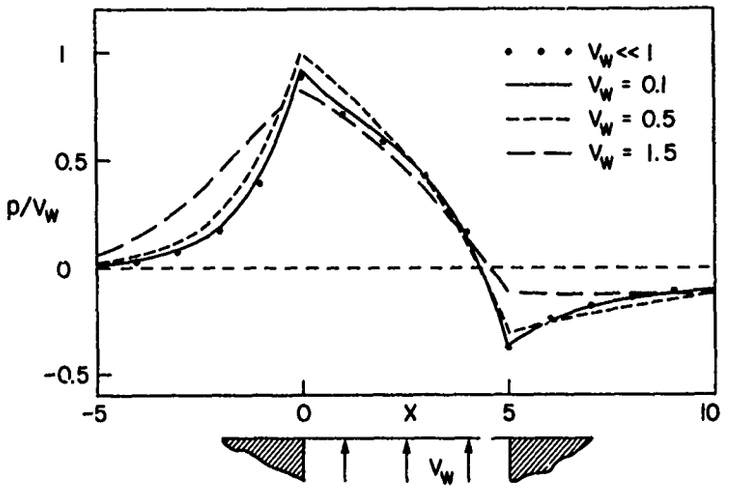


Fig.2 Pressure profiles for the supersonic strong slot injection problem (Ref. 13)

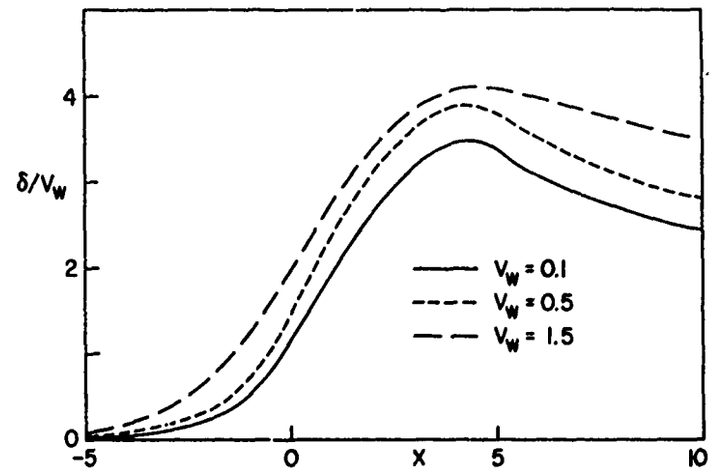
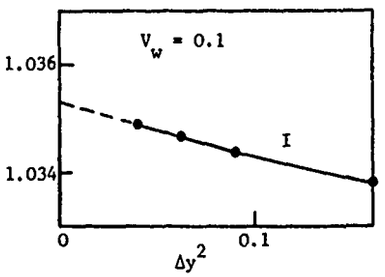


Fig.3 Displacement thickness profiles for the supersonic strong slot injection problem (Ref. 13)



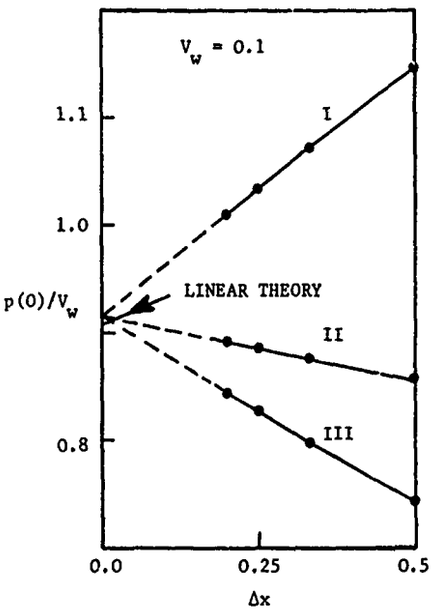


Fig.4 Step size study for the supersonic strong slot injection problem (13)

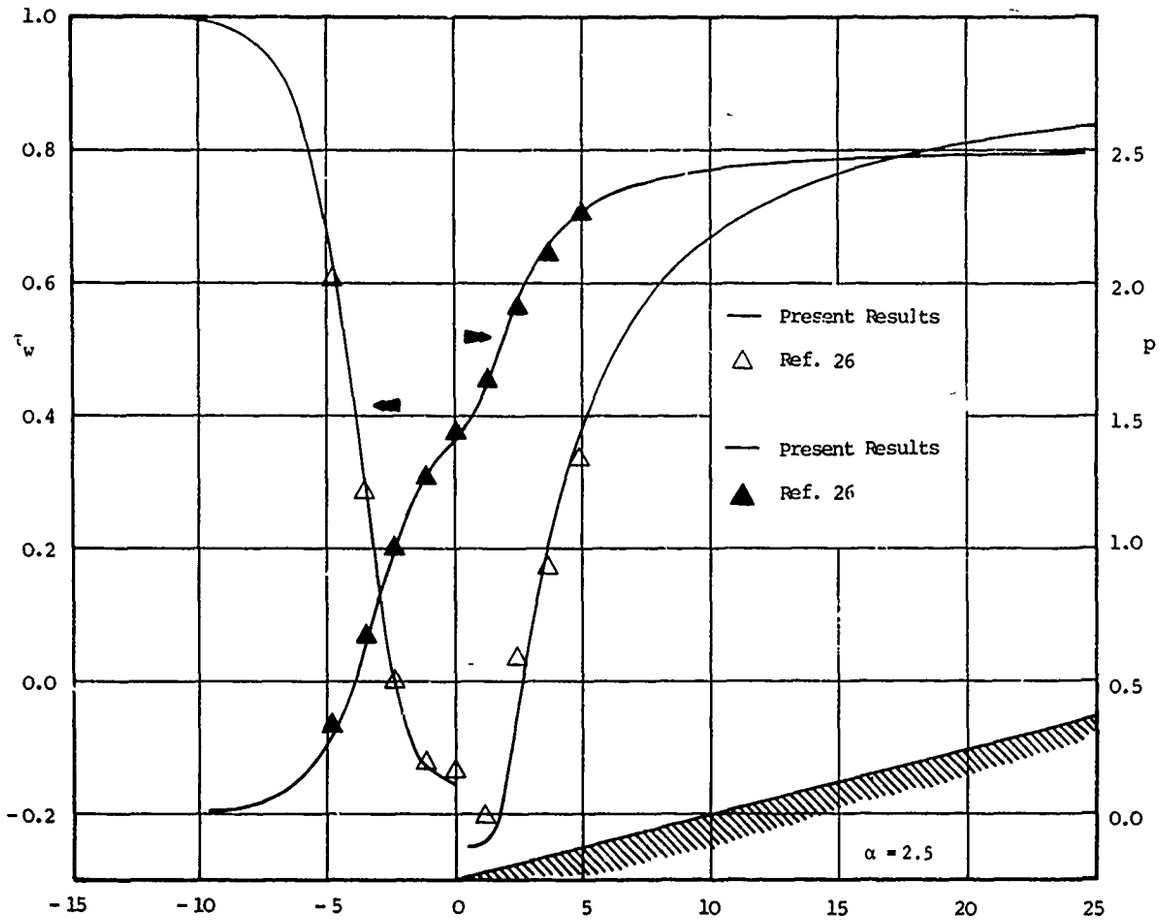


Fig. 5 Wall shear and pressure profiles for supersonic flow past a compression corner

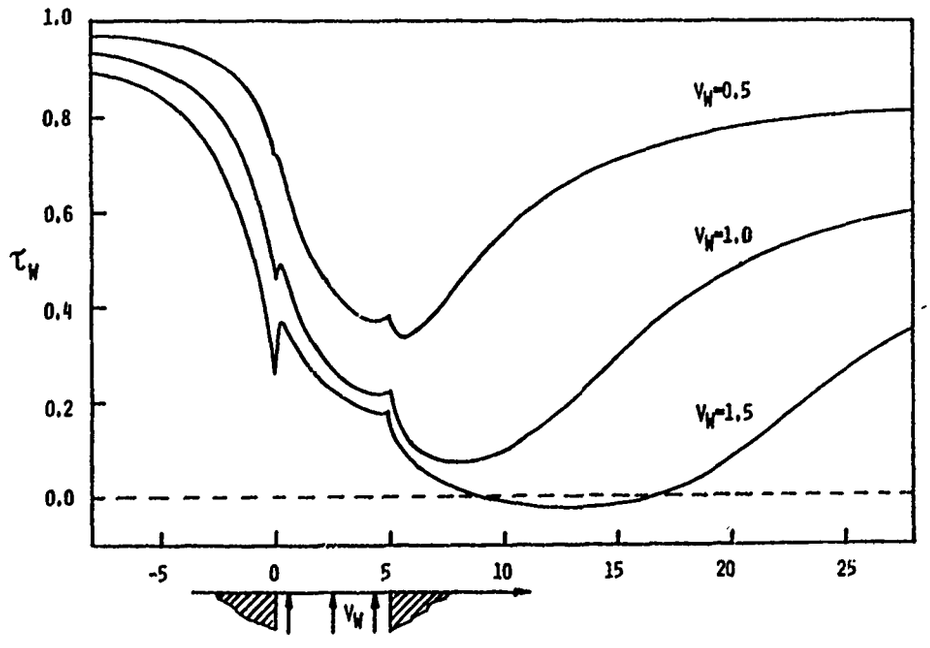


Fig. 6 Wall shear profiles for the subsonic strong slot injection problem (Ref. 21)

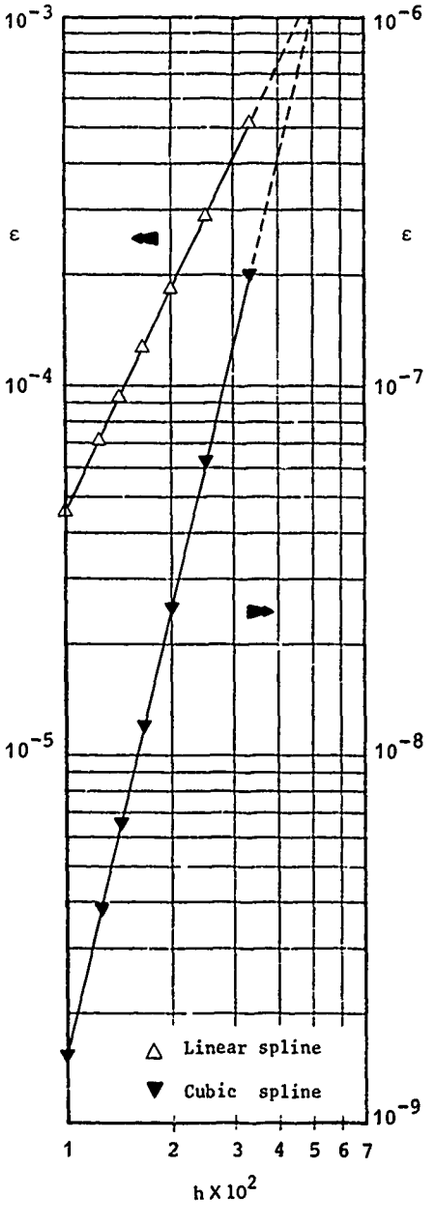


Fig. 7 Cauchy integral direct problem - step size study for $I_2(0.2)$

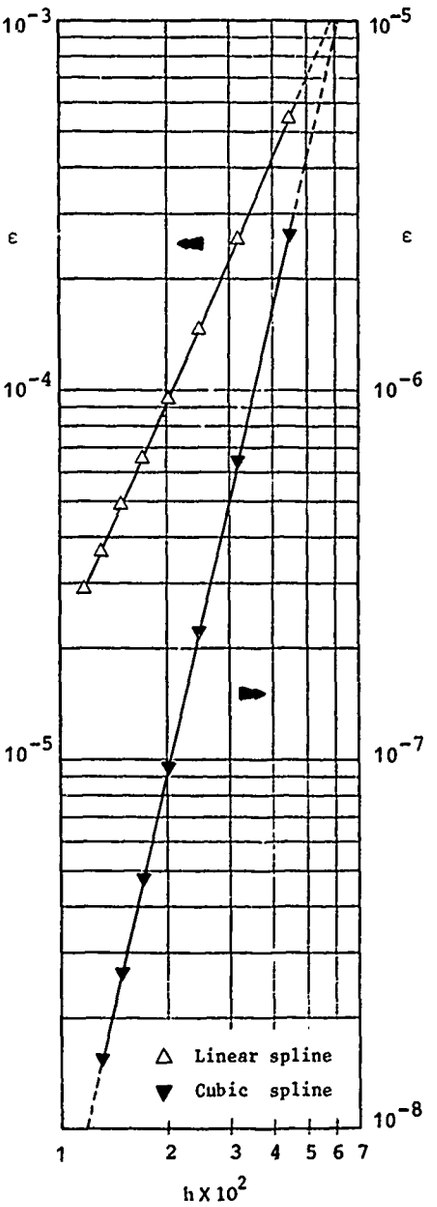


Fig. 8 Cauchy integral inverse problem - step size study for $f_2(1/9)$

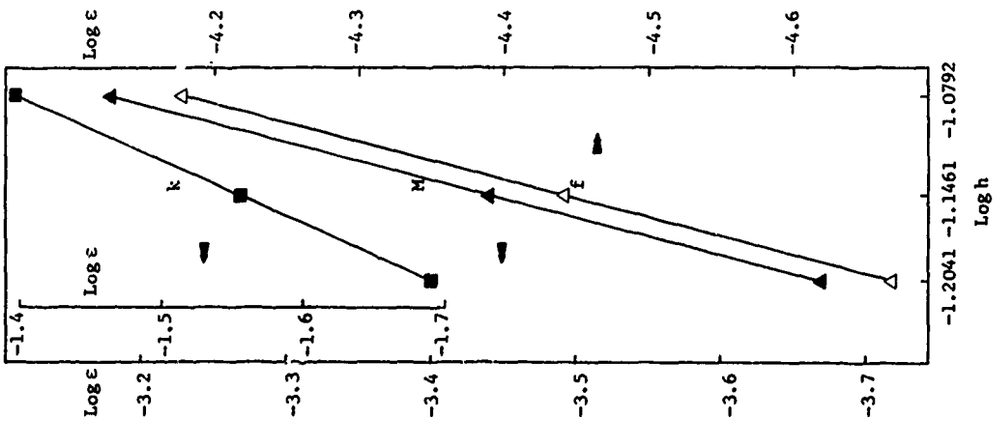


Fig. 9 Model parabolic Partial Differential Equation - step size study at x = y = 0.5

A THEORY OF THE SEPARATED FLOW PAST A SLENDER ELLIPTIC CONE AT INCIDENCE

S. P. Fiddes
Aerodynamics Department
Royal Aircraft Establishment
Farnborough, Hampshire, UK

SUMMARY

A method has been developed for calculating the laterally symmetric separated flow past a slender elliptic cone at incidence, including the calculation of the position of the separation line when the boundary layer is laminar. The method falls into two parts; a vortex sheet model for the outer, inviscid separated flow, and a triple-deck model of the viscous-inviscid interaction of this external flow with a laminar boundary layer on the cone.

A uniformly valid representation of the vortex sheet is adopted, which represents a considerable advance on previous techniques for calculating vortex sheets using slender body theory. The method is capable of calculating the shape of the vortex sheet, its vorticity distribution, the pressure distribution over the cone, etc, for an elliptic cone of arbitrary cross-sectional eccentricity at incidence with specified, symmetric, separation positions.

These pressure distributions have been used to 'drive' a conventional laminar boundary-layer calculation in an attempt to predict the separation position in an iterative manner. It is shown that this approach is unsatisfactory and that a triple-deck is needed to describe the interaction. Results are presented for the predicted separation positions, which show good agreement with experiment.

LIST OF SYMBOLS

a	length of semi-major axis
A	coefficient in equation for sheet shape (Fig 1)
A_1	coefficient in equation for sheet shape (Fig 16)
A'	coefficient in equation for pressure gradient (Fig 14)
b	length of semi-minor axis
c	numerical constant (Eq.(6))
C_p	pressure coefficient
g	vortex sheet strength (Eq.(4))
h	height above cone surface
i	$\sqrt{-1}$
j	integer index
k	slenderness parameter
p	static pressure
q	dynamic pressure
r	radius
Re_x	Reynolds number
t	cone thickness ratio (b/a)
x, y, z	Cartesian body axis coordinates
$\tilde{y}, \tilde{z}$	local axis system near separation (Fig 1)
W	complex potential
Z	complex coordinate
α	incidence
Γ	circulation of isolated vortex
θ	angular coordinate
σ	arc length along vortex sheet
τ	skin friction
Φ	velocity potential
ϕ	perturbation velocity potential
ϑ	vortex sheet angle
Ψ	vortex sheet tangent angle
subscript s	separation
subscript e	external (to boundary layer)

1 INTRODUCTION

Aircraft aerodynamicists have been predominantly concerned with the flow over wings for many years. This is hardly surprising, as the function of a wing is to generate a large aerodynamic force which makes up nearly all of the lift and a large part of the drag acting upon an aircraft in flight. However, within the last thirty years it has been realised that various body-like shapes can produce appreciable forces that must be considered in the design of an aerospace vehicle. In particular, attention has recently been focussed on the problem of forebody separation from the noses of aircraft and missiles being flown at high incidences. These separations produce lifting and side forces that are important when considering the stability and control of flight under such extreme conditions.

The cone may be regarded as the simplest forebody shape that exhibits the important features of such flows, *ie* the separations, and study of the flow about a cone at incidence will help in the understanding of the fundamental fluid mechanics involved in such flows. As such, the cone holds a position with respect to flows about the wider class of slender bodies similar to that held by the plane delta wing with respect to flows about slender wings. In either case, the main feature of the flow at moderate to high incidences is the presence of separations in the form of rolled-up spiral shear layers lying above the wing or body. In the case of the wing, these separations spring from the (usually sharp) leading edges, as the boundary layers from the upper and lower surfaces flow off the wing and merge to form a free shear layer. The vorticity contained in the shear layer causes it to roll up and ultimately convect into a vortex core which lies in a predominantly streamwise direction. Because of the geometric simplicity of the plane delta wing, and because the separation position is fixed by the sharp leading edges, it has attracted many attempts to model this flow, leading, notably, to the development of the vortex sheet model[1].

When a slender body of smooth cross section, such as a cone, is placed at a large incidence in a flow, separations that are of a fundamentally similar nature to those seen on the delta wing are observed (Fig 1). However, there are now no sharp (salient) edges to fix the separation position, which appears as a line running along the body. This separation is the result of a rather more subtle interaction between the boundary layer and the external flow than is the case with the wing. Since it is hoped to model this interaction mathematically, great care must be taken in the representation of the vortex sheet in the vicinity of the separation line, as this local behaviour is found to dominate the interaction. An analysis of the inviscid flow in the vicinity of the separation line on a smooth, slender body has been carried out by Smith[2], who, using the vortex sheet model within the framework of slender body theory, obtained two important results:

(i) if vorticity is being shed from the body and convected into the vortex sheet, the sheet leaves the surface of the body tangentially;

(ii) the curvature of the sheet, measured in the plane normal to the separation line, is generally infinite at its base ('singular' separation) or has a curvature locally equal to that of the body ('smooth' separation).

These results are of particular importance when considering the development of a vortex sheet model to describe flows over slender bodies, and an important part of the work reported here is the incorporation of this local behaviour of the sheet into a global model of the flow.

Having obtained a model of the inviscid flow that properly represents the vortex sheets, the boundary layer must be considered, so that the separation position may be found and thus complete the theory. Cooke[3] calculated the development of a laminar boundary layer on a cone at incidence, without representing the vortex sheets in the inviscid flow, *ie* he considered only attached flow. It is a straightforward extension of his work to replace the attached flow pressure distributions used by him with pressure distributions from the vortex sheet model This suggests an iterative procedure for matching viscous and inviscid separation positions, as first outlined by Smith[4], but results presented here show that this is an unsatisfactory approach, as the viscous-inviscid interaction cannot be described by conventional laminar boundary layer theory alone.

A closer examination of the problem in the vicinity of the separation reveals that a triple-deck is required to describe the interaction. An analysis of this problem has been carried out by F.T. Smith[5] as an extension of his earlier two-dimensional work based on the ideas of Sychev[6]. The results of this analysis show that the triple-deck introduces a Reynolds number effect on the position of the separation line, which, when included, gives separation line positions that agree well with experimental values.

2 MATHEMATICAL MODEL OF THE FLOW

The complete problem is of course one of solution of the full Navier-Stokes equations, but various simplifying assumptions can be made to bring the problem closer to the classical aerodynamic one of matching viscous and inviscid flows, but in a rational[7] rather than an empirical way. These assumptions are summarised below.

(i) The flow is steady and laminar. Disturbances of large time scale (sheet motion, sheet tearing and unsteady shedding) are not described.

(ii) The Reynolds number of the flow is high. A consequence of this is that the effects of viscosity are confined to thin shear layers on the body and in the flow. Vorticity is generated in the boundary layers and convected into free shear layers. In the limit of infinite Reynolds number, when the flow is inviscid, these layers become infinitesimally thin, and the free shear layers are represented by surfaces of discontinuity in the velocity field, or vortex sheets, and there is no viscous diffusion of vorticity.

(iii) The body is slender. The cross-sectional extent of the body is small compared with its length. It is also assumed that the meridional slope of the body is sufficiently smooth in some sense (see Ward[8] for details, and Lighthill[9]). An immediate consequence of this assumption is that at moderate Mach numbers, any shocks present (*eg* bow shocks) will be weak. This, combined with the high Reynolds number assumption from above, means that any vorticity not contained in the shear layers will be weak, and the flow outside the layers may be approximated by an irrotational one. As such, the flow velocity may be written as:

$$\underline{U} = \nabla\Phi$$

ie a velocity potential exists. The governing equation for Φ is the so-called full potential equation, which is a nonlinear partial differential equation. However, the assumption of slenderness yields a further simplification. Because of the difference in longitudinal and transverse length scales, variation in flow quantities, including the potential, are greater in the transverse 'cross-flow' planes than along the length of the body. Consequently, terms like $\frac{\partial\Phi}{\partial x}$ are regarded as small in comparison with $\frac{\partial\Phi}{\partial y}$ and $\frac{\partial\Phi}{\partial z}$, and dropped from the full potential equation. This is an incomplete argument, as far from the body the longitudinal perturbations are as great as the cross-flow perturbations, which have decayed, and the near-field or 'inner' approximation of slenderness is no longer valid in this outer region. The inner problem, to leading order, is when the body is approached so closely that only the cross-sectional extent of the body is 'seen' by the flow, the body appearing to be of infinite length. In the outer region, the finite extent of the body is realised. A more detailed analysis may be found in Ref 10. It emerges that the outer solution is only needed to determine an overall pressure level at each cross-flow station and is not considered further.

The inner problem is the main concern of this paper, and may be expressed in general terms as follows. Within a region close to the body, where y and z are $O(k)$, where k is some slenderness parameter (see Fig 2), we assume that if $F(x,y,z)$ is some function, then $\frac{\partial F}{\partial x} = O\left(k\frac{\partial F}{\partial y}, k\frac{\partial F}{\partial z}\right)$, and write the potential as:

$$\Phi = Ux + k^2\phi$$

where ϕ is $O(1)$. Inserting these into the full potential equation yields:

$$\frac{\partial^2\phi}{\partial y^2} + \frac{\partial^2\phi}{\partial z^2} + k^2(1 - M_\infty^2)\frac{\partial^2\phi}{\partial x^2} = o(k^2) .$$

Or, to $O(k^2)$:

$$\frac{\partial^2\phi}{\partial y^2} + \frac{\partial^2\phi}{\partial z^2} = 0 . \qquad (1)$$

So, a consequence of the slenderness assumptions is that the flow appears two-dimensional, at least in terms of its governing equation. However, careful study will show that the ghost of three-dimensionality still haunts the boundary conditions. For example, consider the body boundary condition of flow tangency at the body surface. If the equation of the body surface is $S(x,y,z) = 0$, then this condition is:

$$\nabla S \cdot \nabla\Phi = 0 . \qquad (2)$$

On introducing the slenderness assumptions, this becomes:

$$U\frac{\partial S}{\partial x} + \frac{\partial\Phi}{\partial y}\frac{\partial S}{\partial y} + \frac{\partial\Phi}{\partial z}\frac{\partial S}{\partial z} = 0 .$$

The last two terms will be recognised as a velocity component normal to the body surface in the cross-flow plane, so the body cross-section is not a streamline of the two-dimensional cross flow.

The outer boundary condition is, in terms of the body axes used here:

$$\phi \sim \alpha z + O\left(\log(z^2 + y^2)\right) . \qquad (3)$$

We note that, strictly, we require $\alpha = O(k)$.

Along with the body surface, the vortex sheets are also boundaries of the potential flow region, and boundary conditions must be specified on them. These boundary conditions reflect the requirements that the vortex sheets are stream surfaces of the three-dimensional flow, and that they sustain no pressure difference. The slender body versions of these two conditions are well known[1,11]. In principle, the vortex sheets are each of infinite extent, but for computational convenience only a finite part of the sheet is represented, the many turns representing the core being replaced by a concentrated vortex, joined to the free end of the finite part of the sheet by a cut. This cut renders the potential single-valued, and represents the vestiges of the sheet feeding the core. The isolated line vortex will not in general be aligned with the flow, and so will experience a force. This force is balanced by an equal and opposite force on the cut, so the fluid is globally force free. The two components (in the cross-flow plane) of this vector force condition are sufficient to determine the position of the isolated vortex, but a further condition is required to determine its circulation. For separation from a sharp edged wing, the Kutta condition of smooth flow off the leading edge is invoked[1] to remove the singularity that is present in attached flow. For flow past a body, there is no singularity in the attached flow that is 'relieved' by separation and so the Kutta condition has to be redefined. At the separation line we have already enforced that the sheet be tangential to the body, but this is not sufficient to prevent flow from crossing the sheet there, as it may effectively 'slide' between the sheet and the body. To prevent this, we constrain the velocity vector on the inside of the sheet, between it and the body, to lie along the separation line at the base of the sheet[2].

A limiting case of the vortex sheet model is when the finite part of the vortex sheet is omitted, and the entire separation represented by an isolated vortex and cut. A model of this type has been used by Bryson[12] for the flow past cones. It emerges from his study that solutions could not be obtained for all combinations of incidence and separation line location.

The greatest failing of slender body theory is that it does not allow for upstream and downstream influence (except via convected vorticity) between one cross-flow plane and another. Apart from the case of supersonic flow (which has *not* been excluded from the inviscid model), there will always be an upstream influence of the base of the body which has a marked effect on pressures, etc. This is in general due to some Kutta condition at the trailing edge. For a real, finite body in subsonic flow, slender body theory is only relevant some way upstream of the base. In supersonic flow no information can be transmitted upstream, and slender body theory is a uniformly valid approximation. However, as we are concerned with forebodies, there are no trailing edges.

To complete the assumptions used in deriving the inviscid model, we note:

(iv) the flow is assumed to be conical with separation in the form of symmetrical vortex sheets. Secondary separations are ignored. The assumption of conical flow simplifies the specification of the boundary conditions, as terms like $\frac{\partial \Gamma}{\partial x}$ may be replaced by $\frac{\Gamma}{x}$. Conical flow is a similarity solution in which the configuration of the vortex sheets, etc, need only be found in one cross-flow plane, the solution in other planes following by simple scaling of the appropriate quantities.

The conical form of the vortex sheet boundary conditions, and conditions on the isolated vortex, are shown in Fig 3. Here, and in all subsequent sections, the variables have been non-dimensionalised; lengths with respect to the local length, a, of the semi-major axis of the cone cross section, and velocities with respect to kU, where k, the slenderness parameter, is chosen to be the tangent of the cone semi-apex angle as measured in the horizontal plane ($= a/x$), and U is the velocity of the free stream.

The inviscid problem has now been reduced to finding the solution of Eq.(1) subject to boundary conditions (2) and (3), and boundary conditions on the sheet and isolated vortex summarised in Fig 3, along with the Kutta condition at the base of the sheet.

3 SOLUTION OF THE BOUNDARY VALUE PROBLEM

Writing ϕ as the real part of a complex analytic function $W(Z)$, where $Z = y + iz$, then ϕ automatically satisfies Eq.(1), and the problem is now to construct a complex potential (or more usually, its derivative $\frac{dW}{dZ} = v - iw$, the conjugate complex velocity) that satisfies the appropriate boundary conditions. In particular, $W(Z)$ can be written as a sum of terms representing various components of the flow, *ie* body thickness, incidence, vortex sheets, etc and, by using appropriate singularities, the boundary condition (3) can be readily satisfied. As we are dealing with the two-dimensional Laplace equation, the use of conformal mapping techniques is possible, and this greatly simplifies the construction of the complex potential. The use of image systems also ensures that boundary condition (2) is satisfied. A series of conformal transformations is used, as it is simpler to specify different terms of the potential in different complex planes, and a special transformation is used to regularise the behaviour of the sheet shape near its base. The sequence of transformations is shown in Fig 4. The first transformation maps the elliptic cross section of the cone onto a circular contour. In this plane, it is a simple matter to write the terms that represent the incidence of the cone, its downstream growth (the tangential flow condition on the cone surface), and the terms representing the isolated line vortices (the cores). For the vortex sheet, we have the usual integral representation[1], so we write:

$$\frac{dW}{dz_1} = \frac{dz_2}{dz_1}\left[-\frac{i\alpha}{k}\left(1+\frac{r^2}{z_2^2}\right) + \frac{t}{z_2} + \frac{\Gamma}{2\pi i}\left(\frac{1}{z_2 - z_{2v}} - \frac{1}{z_2 - \frac{r^2}{\bar{z}_{2v}}} - \frac{1}{z_2 + \bar{z}_{2v}} + \frac{1}{z_2 + \frac{r^2}{\bar{z}_{2v}}}\right)\right.$$

$$\left. + \frac{1}{2\pi i}\int_0^{\sigma_{max}} g(\sigma)\left(\frac{1}{z_2 - z_{2s}(\sigma)} - \frac{1}{z_2 - \frac{r^2}{\bar{z}_{2s}(\sigma)}} - \frac{1}{z_2 + \bar{z}_{2s}(\sigma)} + \frac{1}{z_2 + \frac{r^2}{\bar{z}_{2s}(\sigma)}}\right)d\sigma\right] \quad \ldots\ldots(4)$$

where α is the incidence of the cone,

t is the cross-sectional thickness ratio of the cone $\left(\frac{b}{a}\right)$,

r is equal to $\frac{a+b}{2}$ and results from the mapping (transformed cone radius),

z_{2v} is the transformed complex position of the isolated line vortex,

Γ is the circulation of the isolated line vortex,

$g(\sigma)$ is the strength of the vortex sheet,

$z_2(\sigma)$ is the transformed sheet position,

σ is the arc length along the sheet,

σ_{max} is the length of the finite part of the sheet.

An overbar denotes complex conjugate. Note that this expression is non-dimensionalised according to the convention mentioned earlier.

A numerical approximation to the integral in Eq.(4) must be made, but this approximation is fraught with difficulties peculiar to the separation from a smooth surface. Conventional integration formulae as used in previous vortex sheet studies (*eg* Simpson's or trapezoidal rule) have errors which are unbounded as the vortex sheet is approached closely. This is because these integration formulae effectively replace the continuous distribution of vorticity over the sheet by point-vortex like terms, whose position and strength depend upon the particular integration rule used. As the sheet is approached, this 'lumped', discrete nature of the vorticity is apparent, and the sheet is not represented satisfactorily. An image of the vortex sheet lies on the other side of the cone surface, and is put there to satisfy the flow tangency condition on the body surface. At the base of the sheet, this image runs into tangential (cusped) contact with the sheet. As boundary conditions are to be applied on the sheet, and details of the solution in the region of the sheet base are required for modelling the interaction, a different integration process has to be used, as the tangential contact of sheet and image makes the problem one of close approach there. In contrast, for the case of the wing, the image is effectively a continuation of the main sheet with continuous tangent, and this close approach problem does not arise.

What is needed is a representation of the integral that preserves the continuously distributed vorticity on the sheet, and this is achieved by use of a 'panel' method. The finite part of the sheet is discretised into a series of contiguous segments of specified arc lengths. Values of the sheet strength and sheet tangent angle, g and ψ, at the panel junctions are produced during the course of the iteration process to be described later, but the variation of these quantities over the length of the segment is left to be chosen (freely). So, the integral is written as:

$$\int_0^{\sigma_{max}} \frac{g(\sigma)d\sigma}{Z - Z(\sigma)} = \sum_{j=1}^{j_{max}} \int_{\sigma_{j-1}}^{\sigma_j} \frac{g(\sigma)d\sigma}{Z - Z(\sigma)} \quad . \qquad (5)$$

The choice of assumed variation of panel shape and vorticity over the panel is guided by the wish that each part of the sum (5) be expressed in closed form. This is not possible directly, as again the requirement for a good representation of the vortex sheet near its base means we should be prepared to deal with infinite curvature there. So, before the sheet integral is evaluated, some further transformations are applied. The circular contour representing the cone cross section is first collapsed onto a vertical slit, then the origin is translated to the transformed separation position. The vertical axis is then folded into the lines bounding the upper right-hand quadrant of the final transformed plane. It may readily be shown that as a result of this last folding transformation, the curvature at the sheet base of the form shown in Fig 1 is made finite. In fact, the image of the sheet in the final transformed plane has everywhere finite curvature, and its shape may be approximated by a set of contiguous circular arcs having common tangents at their junctions. This may be seen if we consider the intrinsic equation of the transform of the vortex sheet (Fig 5). The slope of this curve is the curvature of the sheet, and a circular arc appears as a straight line. By patching together circular arcs, we obtain a 'trapezoidal' approximation to the variation of ψ

with σ. An assumed variation of sheet strength over the panel is adopted that matches at the end points, so the sheet strength is continuous. The choice of distribution of sheet strength is governed by the desire to express the components of the sum (5) in closed form. Following Mangler and Smith[13], we select a distribution of the form $g(\theta) = g_1 \cos\theta + g_2 \sin\theta$ over the arc, where θ is an intrinsic angle for the segment (see Fig 6). The integral representing the velocity induced by a circular arc having this distribution of vorticity is evaluated in closed form. Because of the continuity of sheet tangent and strength, this velocity is continuous along the entire length of the sheet, except at the free end, and consequently we may specify boundary conditions at the panel junctions. If we have n panels, then we have $2n$ unknowns, namely the sheet tangent angle and strength at one end of each panel. The sheet strength and tangent angle at the other end are identical with the values for the abutting panel. The base segment end, at the separation position, has its sheet angle fixed by the requirement of tangency to the body, and its strength set to zero, so as to obtain a finite value in the physical plane, through the singularity in the mapping derivative there. To solve for these $2n$ unknowns, the pressure condition and normal velocity condition are applied at the panel junctions and midway along the length of the last panel, which has a free end, so we obtain $2n$ equations. The distribution of panel lengths is arbitrary, but it may be chosen to give fine detail near the separation position. Here, the folding transformation helps, as it tends to concentrate points in the vicinity of the separation line when they are mapped back to the physical plane. It is useful to reduce panel size in the core, where the radius of curvature of the sheet again becomes small.

With this construction of the complex potential, we can take a guessed configuration of the vortex sheets, separating from a specified position on a cone of elliptic cross section at given incidence, automatically satisfying the boundary conditions on the body and at infinity, and evaluate the errors in the boundary conditions on the sheets and at the isolated vortices. It remains to obtain a configuration for the vortex sheets and isolated vortices that will satisfy the boundary conditions to within an acceptably small tolerance of error. This is done in an iterative fashion.

4 ITERATIVE SOLUTION PROCEDURE

The technique used is a scheme similar to that developed by Barsby[14]. In this method, an initial approximation to the solution (a guessed sheet shape, etc) is successively improved by a multi-dimensional Newton iteration scheme. The solution is regarded as having converged when the sum of the squares of the difference between the velocities required to satisfy the boundary conditions and those actually achieved is typically less than 10^{-6} to 10^{-8}. This scheme requires a 'good' starting approximation to the solution, and so a thin, wing-like cone was first taken, with one of Smith's[1] wing solutions as the starting guess for the sheet shape, etc. When convergence had been attained for this thin ellipse, the thickness of the cone cross section was increased, and that solution used as a starting guess. In this way, the thickness of the cone was successively increased between iterations, until a right circular cone solution was obtained. It was also possible to vary the incidence and separation position in a similar way between iterations.

5 INVISCID RESULTS

An example of the type of solution found by the inviscid model is shown in Fig 7. This is for a circular cone at an incidence equal to three times its semi-apex angle, (*ie* a relative incidence of 3), with separation occurring 113° around from the windward generator. This separation position was taken from the experimental results of Rainbird *et al*[15]. Their experiments were carried out in a water tunnel, and the boundary layers were laminar. The observed core position is marked by a cross on the figure, and the location of the computed core corresponds to a shift outboard of the order of 10% of the cone radius. A similar discrepancy has been found with vortex sheet solutions for wings when the secondary separation is laminar. It may partly be accounted for in this case by the presence of a large secondary separation that was visible in the experiments, but not accounted for in the calculation. This was seen to lie under the main core, and could displace this core inboard. It is of note that for the cone incidence and separation position found in this experiment, no solution exists using Bryson's[12] model. Another set of experiments were carried out by Rainbird[16], for a cone in a supersonic flow at high Reynolds number, with turbulent boundary layers. One of the effects of a turbulent boundary layer, indeed the only one from the point of view of the inviscid model, is to move the separation position further around the cone from the windward generator. One of Rainbird's[16] cases has been computed, corresponding to a circular cone at a relative incidence of 2.52, with separation occurring 132° from the windward generator, and the result for the sheet shape shown in Fig 8. Again, a small error in core location is evident. Rainbird[16] also carried out a total-head survey for this case, and the results of this, with the calculated vortex sheet overlaid, is shown in Fig 9. The discrepancy in the apparent location of the early part of the sheet as indicated by this survey is attributed to the displacement effect of the boundary layer.

In Ref 17, Zacharov presents results for the calculation of the separated flow past a slender, circular cone using a time evolution method based upon the equivalence of three-dimensional conical steady flow and two-dimensional unsteady flow. His result for the sheet shape for this case is also shown in Fig 9. It is seen that his solution gives a rather more flattened core than has been obtained by the present method. The total-head survey would tend to indicate that his sheet intrudes into the secondary separation, the main core appearing to be more circular. The position of the isolated vortex in the two methods is very close, having almost the same error in location with respect to the observed core location.

One of the solutions for a 10% thick ellipse is shown in Fig 10. This is for an elliptic cone at an incidence equal to three times the semi-apex angle of the cone as measured in the horizontal plane. This is close to a wing-like solution, with a large core. The core position is practically indistinguishable from that for a wing of the same semi-apex angle at the same incidence.

The effect of cone thickness on nonlinear lift is illustrated in Fig 11. This shows the variation of the nonlinear component of the normal force with separation position for different cone thicknesses, all at a relative incidence of 3. The separation angle is a parametric one, so that the coordinates of the separation position in the cross-flow plane are given by

$$y_s = \cos \theta_s$$

$$z_s = t \sin \theta_s$$

where t is the thickness ratio of the cone and θ_s is the parametric angle.

A lower limit to the separation angle was found during the course of the calculations, corresponding to the sheet just making regular contact with the cone surface at separation (*ie* smooth separation). A lower value for θ_s would have the sheet turning into the cone after separation. Thus, smooth separation marks one end of the plots shown in Fig 11, the other end of the plot being arbitrarily truncated at the 90^o separation position, *ie* the end of the semi-major axis. The effect of thickness is to reduce the amount of nonlinear lift, the maximum value being found for the case of the wing. For a given thickness, the maximum nonlinear lift occurs at smooth separation. It should be noted that the amount of linear lift is independent of separation position and cone thickness.

The circumferential pressure distribution corresponding to the first solution shown (Fig 7) is shown in Fig 12. Also shown for comparison are the pressure distributions for attached flow (no vortex sheets), and the pressures as measured in Ref 14. The suction peak due to the vortex core is well marked. The attached flow pressure distribution was used by Cooke[3] to calculate the development of a laminar boundary layer on the cone, and a natural extension of his work is to repeat his calculations using the pressures from the vortex sheet model. This is discussed below.

6 BOUNDARY-LAYER CALCULATION

The pressure in conical flow is constant along rays passing downstream from the apex of the cone. As the elliptic cone has a developable surface, it may be 'unwrapped' into a plane circular sector, where these rays form a radial ordinate. The normal to the cone surface, and the circumferential direction, complete a cylindrical polar coordinate system. If the laminar boundary layer equations are written down in this coordinate system, and the result that pressure is constant along rays is used, then a similarity solution for the radial development of the boundary layer is possible, and the calculation of the three-dimensional boundary layer reduces to solving for the radial and circumferential velocity profiles at one cross-flow station (constant radial position), the solutions at other stations following from a simple scaling. Unlike the inviscid flow, this scaling is not a linear one but a parabolic one for such quantities as the boundary-layer thickness. A computer program based on a Keller box technique for solving the laminar boundary-layer equations in a plane circular sector has been written by Boyd[18] and used here in conjunction with the circumferential pressure distribution found by the vortex sheet model.

7 PREDICTION OF SEPARATION POSITION

Cooke[3] calculated the development of the boundary layer up to separation (defined for this conical flow, as the vanishing of the circumferential component of skin friction), subject to the external inviscid flow being attached. This is inconsistent, because as soon as separation occurs the external flow is modified by that separation. Smith[4] suggested improving upon this by using the vortex sheet model to provide a consistent pressure distribution and obtaining the separation position in an iterative way. First, for a cone at given incidence, a separation position is guessed, and the vortex sheet solution is found. The pressure distribution from this solution is used in the boundary-layer calculation, which will predict a (generally) different separation position to that assumed. The inviscid calculation is repeated, with the assumed separation position moved nearer to that given by the boundary-layer calculation, and the process repeated. The inviscid separation position thus 'chases' the viscous separation until the two agree. The results of the first cycle of such an iteration are shown on Fig 12, where 'A' marks the inviscid separation position, and 'B' the position of the laminar separation with this pressure distribution, which is well before the assumed position. Moving the inviscid separation position nearer to the windward generator eventually leads to a converged result as shown in Fig 13, with viscous and inviscid separation positions agreeing. This occurred with separation some 76^o from the windward generator, a position well removed from any experimental results. Of note is that this position corresponds to smooth separation, *ie* $A = 0$ in Fig 1.

These results are in fact predicted by Smith's[2] local analysis of the vortex sheet in the vicinity of the separation line. He was able to obtain the behaviour of the

circumferential pressure gradient just upstream of the separation (Fig 14). In the figure, $A' > 0$, so there is an infinite adverse pressure gradient at separation, unless A' vanishes, when the pressure gradient is finite, but not locally determined. Now A' is related to A in Fig 1, such that both vanish simultaneously, that is when the curvature of the vortex sheet at separation becomes finite (smooth separation) so does the pressure gradient. It seems unlikely that a laminar boundary layer could withstand approaching an infinite adverse pressure gradient, and indeed no solutions have been found for boundary layers separating *at* such a point, they always separate upstream of it. (See also Ref 19.) So the converged viscous-inviscid match using conventional laminar boundary-layer theory gives a separation position for which the curvature of the vortex sheet is finite, *ie* smooth separation - a position which can be found by a purely inviscid calculation.

Further analysis of the viscous problem in the vicinity of the separation line by Riley[19] and F.T. Smith[5], along lines proposed by Sychev[6], has shown that conventional laminar boundary-layer theory is insufficient when attempting to describe the viscous-inviscid interaction and a triple-deck is needed in the neighbourhood of the separation line to describe the interaction (Fig 15). The triple-deck effectively 'smears out' the infinite pressure gradient over a finite length, which is Reynolds number dependent. An immediate result of the analysis is that the converged solution described above, smooth separation, is the infinite Reynolds number limit, and at finite Reynolds number a correction is applied to it. This correction is found by matching the pressure rise across the triple-deck to that given by the inviscid flow, this resulting in an expression that relates the 'strength' of the singularity in the pressure gradient, A', to the Reynolds number. A quantity called A_1 is shown in Fig 16, which is a simple multiple of A', and is calculated by the vortex sheet program. When this quantity vanishes, we have smooth separation - the infinite Reynolds number limit. As the Reynolds number decreases, the triple-deck can 'smear out' a larger amount of singularity and the separation position moves further around the cone. Finding this correction requires that the scale of the triple-deck be determined. The Reynolds number dependence of this scaling is readily found (Fig 15), but the explicit term for the scale of the triple-deck involves the skin friction of the boundary layer as it enters the triple-deck. This is found by performing a laminar boundary calculation with the pressure distribution corresponding to smooth separation. The results of such a boundary-layer calculation are shown in Fig 17.

The calculation is terminated at the dotted line, where the sheet leaves the body. The procedure for calculating the separation position using the triple-deck results is as follows. Having decided on the parameters of the problem, *ie* the relative incidence of the cone and its thickness ratio, a series of inviscid calculations is performed with varying separation position, θ_s, giving the variation of the coefficient A_1. This leads to a plot like Fig 16. The position of smooth separation is identified, ($A_1 = 0$) and a pressure distribution obtained for this case, which is then used in the boundary-layer program. The circumferential component of skin friction at smooth separation (τ) is then used to determine the position of the separation line at finite Reynolds number via[5]:

$$A_1 = 2c\left(\frac{U_e}{V_e}\right)^{\frac{7}{4}} \tau^{\frac{9}{8}} \left(k^2 Re_x\right)^{-\frac{1}{16}} \qquad (6)$$

where $c = 0.44$;

Re_x = the Reynolds number based on cone length;

U_e = component of external velocity tangential to the smooth separation line;

V_e = the external velocity normal to the smooth separation line;

k = the tangent of the semi-apex angle of the cone planform;

$\tau = \left(\frac{V_e}{kU_e}\right)\left(\frac{\partial}{\partial z}\frac{V}{V_e}\right)\Big|_{z=0}$ where V is the circumferential velocity in the boundary layer;

z = the scaled normal coordinate in the boundary layer.

The value of θ_s corresponding to this value of A_1 is the separation position corresponding to that Reynolds number Re_x. So, we may write:

$$\theta_s = \theta_{smooth} + f\left(\frac{\alpha}{k}, t\right)\left(k^2 Re_x\right)^{-\frac{1}{16}} .$$

This result for the case of a circular cone at a relative incidence of 3 is shown in Fig 18, which is a plot of predicted separation position against what is effectively a cross-flow Reynolds number $k^2 Re_x$. Also shown are the position of smooth separation, and the results for the separation position using attached external flow, *ie* no sheets, as obtained by Cooke[3]. The three crosses show experimental results reported in Ref 14. Note that the result with attached external flow is independent of Reynolds number, but the triple-deck gives a separation position moving nearer to the windward generator with increasing Reynolds number. This trend is confirmed by the experimental points. An interesting feature of this result is that the Reynolds number used is strictly a local

one, which increases with distance along the cone. Consequently, the theory predicts that the separation line on a given cone is slightly curved, moving closer to the windward generator as we go downstream. However, because of the very small exponent in the Reynolds number dependence shown in Eq.(6) the curve is only a very slight departure from a straight line over most of the cone. The theory predicts a separation position about 10^{o} too far around the cone, and possible causes for this are:

(i) the Reynolds number may not be high enough for the triple-deck perturbation parameter to be regarded as small. In principle this would mean taking more terms in the expansion that gives the triple-deck correction, and not just the first term as used here;

(ii) no account is taken of the secondary separation in these calculations;

(iii) the coefficient c in Eq.(6) has been determined numerically, and may have a small error.

8 DISCUSSION

As the method has successfully produced solutions for the title problem, it is useful to consider its development for application to less restricted cases. The assumption of conical flow may easily be relaxed for the inviscid model, the only change being in the boundary conditions on the vortex sheet, where derivatives are reintroduced. The problem of inviscid flow past a non-conical slender body could then be solved by a downstream marching integration/iteration technique, similar to that developed by Clark[20]. However, this would have to be used in conjunction with a full three-dimensional boundary-layer calculation to predict the separation position. Another problem with non-conical bodies is how to start the downstream marching. Unless the nose is pointed, and separation starts from there, the starting solution is currently not known. Indeed, for some cases, such as an ogive-cylinder combination, it appears that the upstream origin of separation may be non-slender, and the removal of the slenderness requirement would then be necessary.

The restriction to lateral symmetry may be removed from the inviscid model by using a different set of conformal mappings to regularise the sheet shape, the assumption of symmetry being implicit in the mappings used here. The flow past yawed cones could then be calculated, although there is some doubt over how to start the boundary-layer calculation at the attachment line for this case.

The restriction to laminar boundary layers is, at present, the one that seems most difficult to overcome. Although some asymptotic analyses of the behaviour of turbulent boundary layers are available for cases such as shock-wave boundary-layer interaction, no work has yet been done on the interaction of a turbulent boundary layer with a large scale separation such as a vortex sheet. Indeed, only incipient separation has so far been tackled as far as the author is aware. So, results akin to a separating 'turbulent triple-deck' are not yet available, but appear to be necessary before further progress is made with this case.

9 CONCLUSION

A method has been developed that successfully represents the separated flow about a slender elliptic cone and its interaction with a laminar boundary layer via a triple-deck, demonstrating a rational approach to the prediction of separated flows on pointed noses.

Comparisons with the limited experimental data available tend to confirm the applicability of the vortex sheet model to open separation from smooth surfaces and the relevance of the triple-deck model of viscous-inviscid separation to three-dimensional laminar separation.

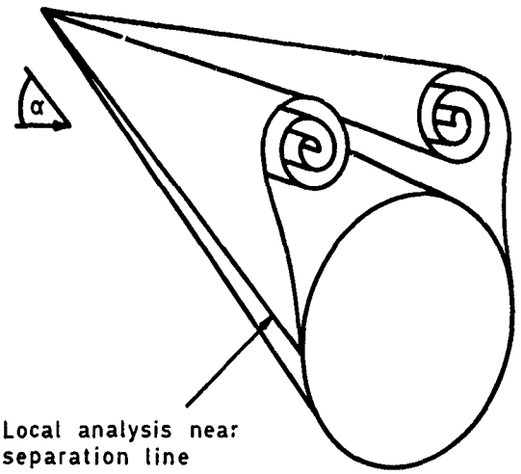
REFERENCES

No.	Author	Title, etc
1	J.H.B. Smith	Improved calculations of leading-edge separation from slender delta wings. RAE Technical Report 66070 (1966)
2	J.H.B. Smith	Behaviour of a vortex sheet separating from a smooth surface. RAE Technical Report 77058 (1977)
3	J.C. Cooke	The laminar boundary layer on an inclined cone. RAE Technical Report 65178 (1965)
4	J.H.B. Smith	A review of separation in steady three-dimensional flow. AGARD CP 168, Paper 31 (1975)
5	F.T. Smith	Three-dimensional viscous and inviscid separation of a vortex sheet from a smooth non-slender body. RAE Technical Report 78095 (1978)

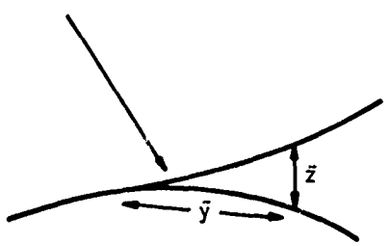
REFERENCES (concluded)

No.	Author	Title, etc
6	V.V. Sychev	On laminar separation. *Izv. Akad. Nauk., Mekh. Zhid. i Gaza*, 3, pp 47-59 (1972) Translated in Fluid Mechanics, Plenum Pub. Corp., pp 407-417, March-April 1974
7	K. Stewartson	On the asymptotic theory of separated and unseparated fluid motions. *SIAM J. Appl. Math.*, 28, pp 501-518 (1975)
8	G.N. Ward	The linearised theory of steady high speed flow. Cambridge University Press (1955)
9	M.J. Lighthill	Supersonic flow past slender bodies of revolution the slope of whose meridian section is discontinuous. *Quart. J. Mech. Appl. Math.*, 1, pp 90-102 (1948)
10	H. Ashley M.T. Landahl	Aerodynamics of wings and bodies. Addison-Wesley (1965)
11	J.H.B. Smith	Inviscid fluid models, based on rolled-up vortex sheets for three-dimensional separation at high Reynolds number. Presented at AGARD Lecture Series 94 (1978)
12	A.E. Bryson	Symmetric vortex separation on circular cylinders and cones. *J. Appl. Mech.* (ASME Trans) 26, pp 643-646 (1959)
13	K.W. Mangler J.H.B. Smith	A theory of the flow past a slender delta wing with leading-edge separation. *Proc. Roy. Soc. Lond.*, A251, pp 200-217 (1959)
14	J.E. Barsby	Calculation of the effect of blowing from the leading edges of a cambered delta wing. ARC (GB) R & M No.3790 (1975)
15	W.J. Rainbird R.S. Crabbe L.S. Jurewicz	A water tunnel investigation of flow separation about circular cones at incidence. NRC (Canada) Aeronautical Report LR 385 (1963)
16	W.J. Rainbird	The external flow field about yawed circular cones. AGARD CP 30, Paper 19 (1968)
17	S.B. Zacharov	The calculation of inviscid separated flow about a slender cone for large angles of attack. *Uchenye Zapiski TsAGI VII*, 6 (1976) Translation available as RAE Library Translation 2009 (1979)
18	C.F.M. Boyd	Private communication
19	N. Riley	Separation from a smooth surface in slender conical flow. *J. Eng. Math.*, 13, pp 75-91 (1979)
20	R.W. Clark	Non-conical flow past wings with leading-edge vortex sheets. ARC (GB) R & M No.3814 (1973)

Copyright ©, Controller HMSO London, 1980

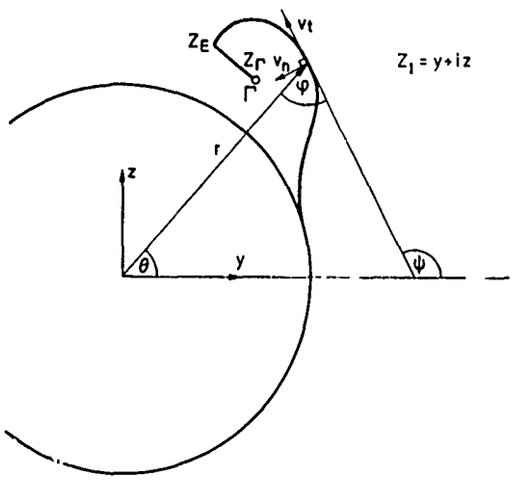


Local analysis near separation line



$$\bar{z} = A\bar{y}^{\frac{3}{2}} + B\bar{y}^{\frac{5}{2}} + \ldots$$

Fig 1 Results of local analysis of vortex separation from a smooth surface (Smith[2])



$$\frac{v_n}{U} = -\frac{r}{x}\sin\varphi$$

$$\frac{\Delta\bar{z}}{x} = \Delta v_t\left[\frac{U_\Gamma}{x}\cos\varphi - v_{tm}\right]$$

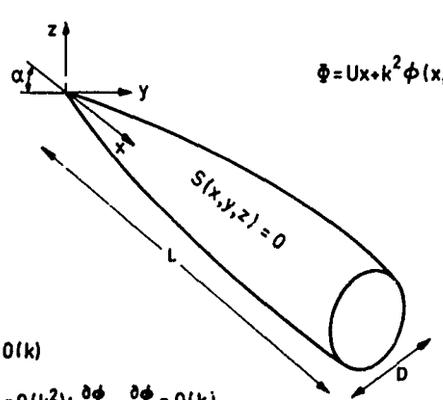
$$U(Z_\Gamma - Z_E)\frac{\Gamma}{x} + U\Gamma\frac{Z_\Gamma}{x} = U\Gamma \lim_{Z\to Z_\Gamma}\frac{d}{dZ}\left(W - \frac{\Gamma}{2\pi i}\ln(Z - Z_\Gamma)\right)$$

Δ = difference operator (across sheet)

v_{tm} = mean convective velocity of sheet

W = complex potential

Fig 3 Boundary conditions on a conical vortex sheet



$$\Phi = Ux + k^2\phi(x,y,z)$$

$$\frac{D}{L} = O(k)$$

$$\frac{\partial\phi}{\partial x} = O(k^2);\ \frac{\partial\phi}{\partial y},\ \frac{\partial\phi}{\partial z} = O(k)$$

$$\longrightarrow \frac{\partial^2\phi}{\partial y^2} + \frac{\partial^2\phi}{\partial z^2} = O(k^2)$$

Boundary conditions

$\nabla\Phi \cdot \nabla S = 0$ on S

$$\Phi \to Ux + U\alpha z + O\left(\log(y^2+z^2)\right) \text{ as } (y^2+z^2)\to\infty$$

Fig 2 Slender body theory

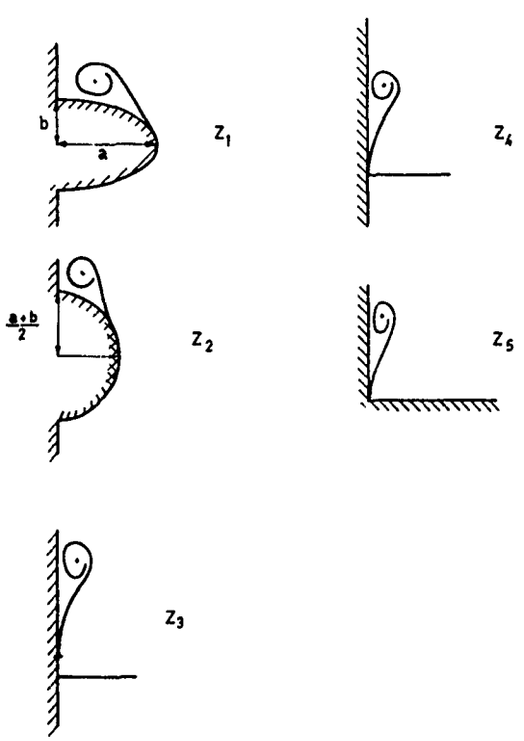


Fig 4 Transformation sequence

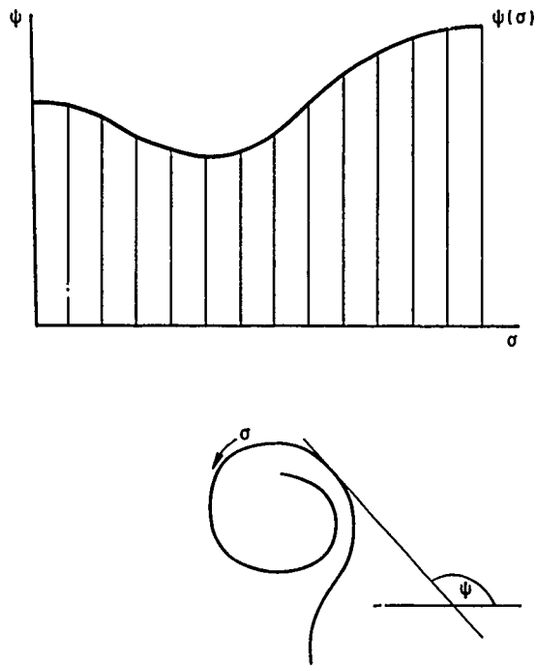


Fig 5 Approximation of intrinsic equation for sheet shape

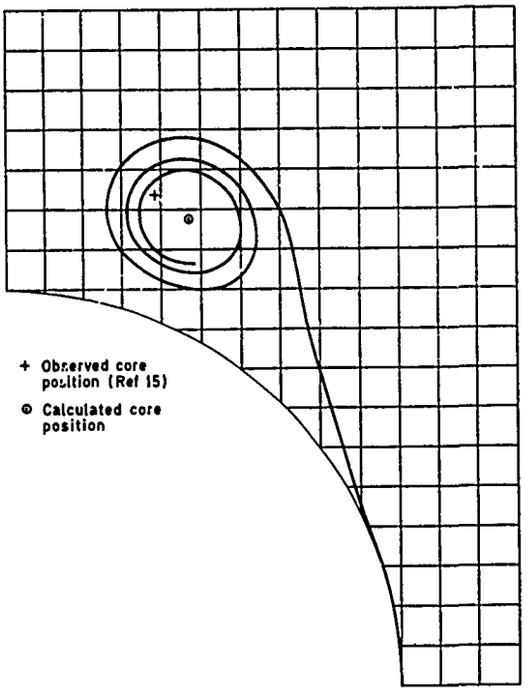
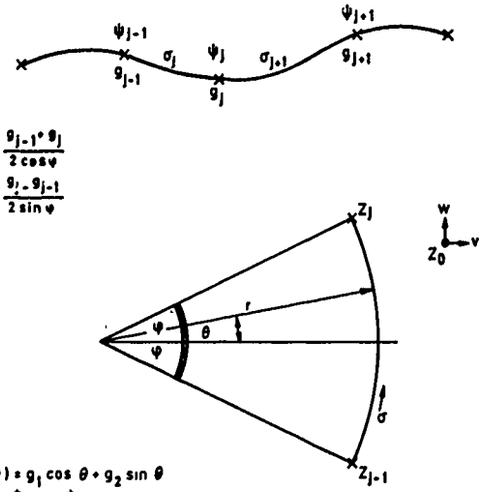


Fig 7 Sheet shape for circular cone at an incidence equal to 3 times its semi-apex angle, with separation position 113° from windward generator



$$g_1 = \frac{g_{j-1} + g_j}{2\cos\psi}$$

$$g_2 = \frac{g_j - g_{j-1}}{2\sin\psi}$$

$$g(\theta) = g_1\cos\theta + g_2\sin\theta$$

$$\psi = \frac{\psi_{j+1} - \psi_j}{2}$$

$$r = \frac{g}{\psi}$$

$$G = g_1 + ig_2$$

$$v - iw\big|_{Z_0} = \frac{-r}{4\pi}\left[\left(\frac{\bar{G}}{r} + \frac{Gr}{Z_0^2}\right)\log_e\left(\underbrace{\frac{Z_0 - Z_{j-1}}{Z_0 - Z_j}}\right) + \frac{2iG}{Z_0}\left(\frac{r\psi}{Z_0} + \sin\psi\right)\right]$$

If Z_0 is on the sheet, this becomes $Z_j - Z_0$

Fig 6 Circular arc vortex sheet segment

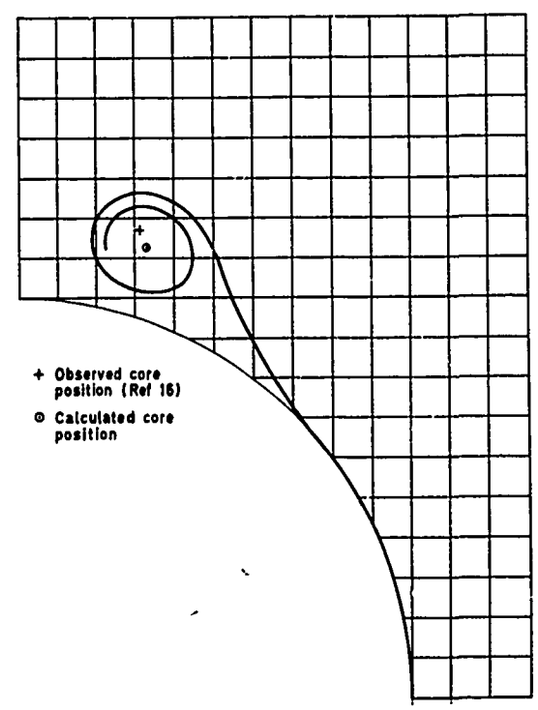


Fig 8 Sheet shape for circular cone at an incidence equal to 2.52 times its semi-apex angle, with separation position 132° from windward generator

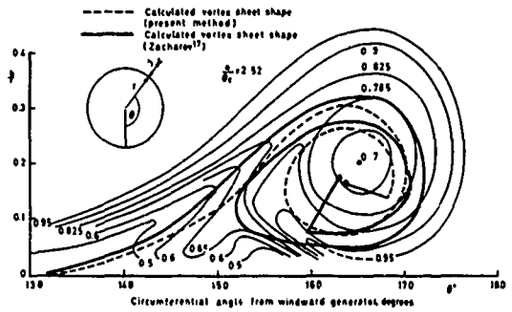


Fig 9 Pitot pressure contours in flow field above yawed 5^0 cone, $M_\infty = 1.80$ (Ref 16)

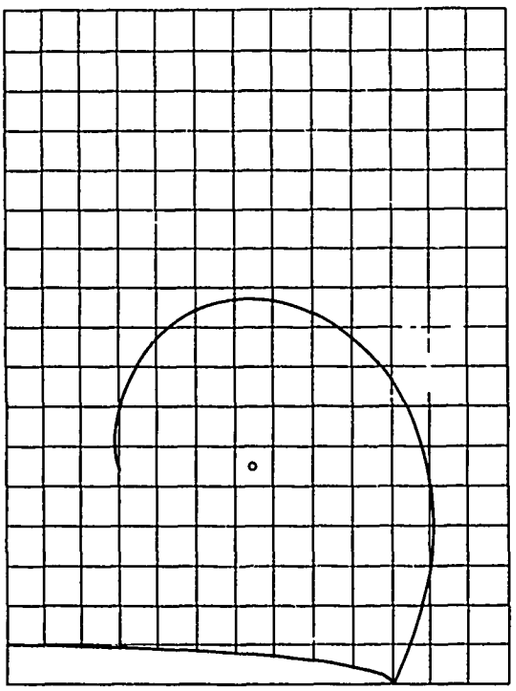


Fig 10 Sheet shape for 10% thick cone at an incidence equal to three times its apex angle and separation from the end of the major axis

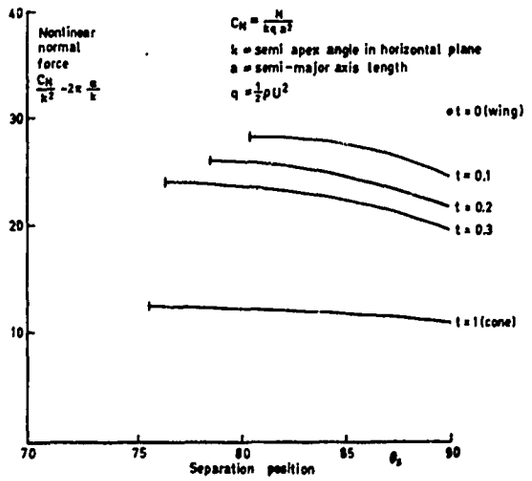


Fig 11 Variation of nonlinear component of normal force with separation position for cones of various thicknesses, all at a relative incidence of 3.

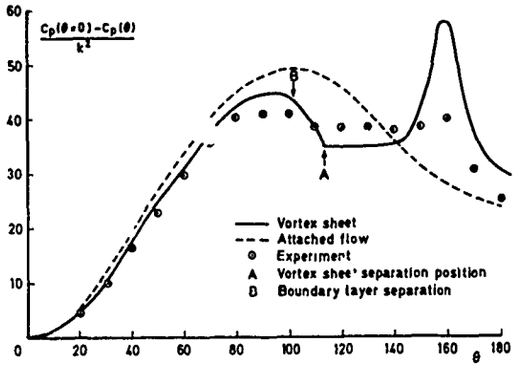


Fig 12 Pressure distribution; $\frac{a}{k} = 3.0$, $\theta_{sep} = 113^0$

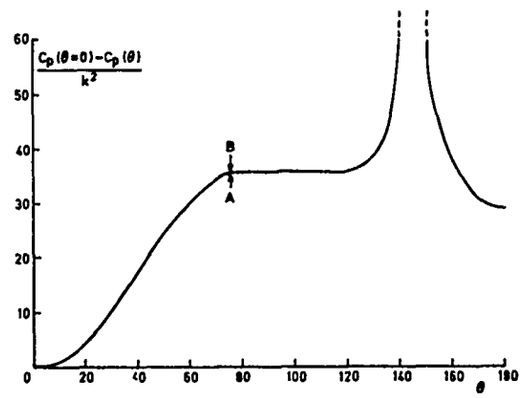
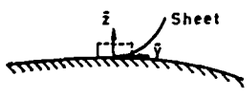
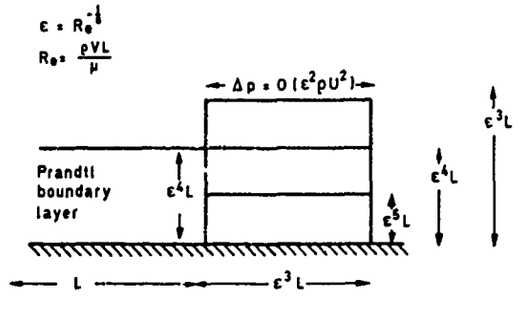


Fig 13 Pressure distribution; $\frac{a}{k} = 3.0$, $\theta_{sep} = 76^0$



$$\frac{\partial p}{\partial \tilde{y}} = \frac{A'}{(-\tilde{y})^{\frac{1}{2}}} + B' + C'(-\tilde{y})^{\frac{1}{2}} + O(\tilde{y}) \quad [\tilde{y} \lesssim 0]$$

Fig 14 Inviscid pressure distribution near separation (Ref 2)



$\frac{\Delta p}{\Delta y} = O(\varepsilon^{-1} \rho V^2 / L)$ Matches inviscid pressure if $A' = O(\varepsilon^{-\frac{1}{2}})$

Fig 15 Triple-deck structure (Ref 5)

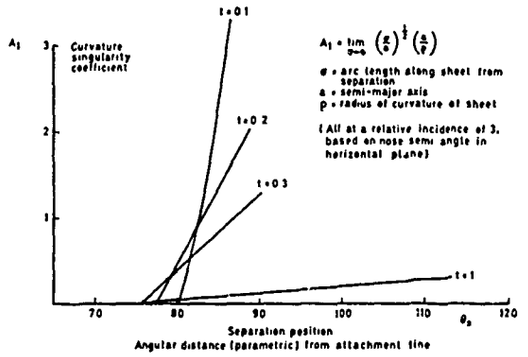


Fig 16 Variation of curvature singularity with separation position

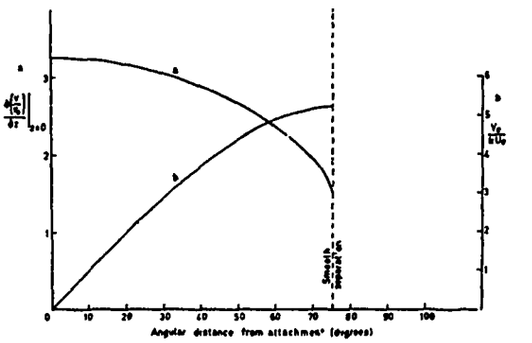


Fig 17 Results from laminar boundary-layer calculation

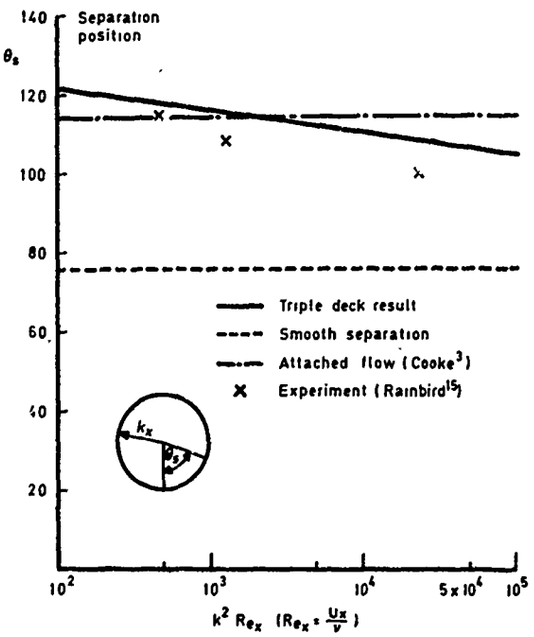


Fig 18 Predicted variation of separation position with Reynolds number for a circular cone at $\alpha = 3k$

PREDICTION OF AERODYNAMIC CHARACTERISTICS FOR WINGS WITH EXTENSIVE SEPARATIONS

B. Maskew, B.M. Rao and F.A. Dvorak
Analytical Methods, Inc.
100 - 116th Avenue S.E.
Bellevue, Washington 98004
U.S.A.

SUMMARY

The development of a simple yet effective technique for modelling the effects of trailing-edge separation is discussed. The model encloses the low energy region with free vortex sheets coupled with a potential flow panel method. The technique includes an iteration cycle between viscous and potential flow routines, and its development from the two-dimensional case to the three-dimensional case is discussed. A description of the potential flow panel method, which is based on an internal Dirichlet boundary condition, is included.

LIST OF SYMBOLS

A,B,W,O	Regions of the idealized model, Figure 8
C_p	Pressure coefficient
C_L	Lift coefficient
$\underline{i},\underline{j},\underline{k}$	Orthogonal unit vector system defining the axes of the Cartesian coordinate system,
$\underline{n}$	Unit normal vector to a surface
S	Surface
s	Distance
$\underline{V}$,V	Velocity vector, modulus
x,y,z	Cartesian coordinates, Figure 9
α	Incidence
δ^*	Boundary layer displacement thickness
∇	Gradient operator
Φ	Total velocity potential
ϕ	Perturbation velocity potential

Subscripts

A,B,W,O	Pertaining to regions A, B, W, and O, respectively
OA, etc.	Pertaining to the common boundary between regions O and A, etc., and facing region O
e	Outer edge of boundary layer
p	Conditions at a point, P
U,L	Upper, lower surface, respectively
SEP	Conditions at separation
∞	Conditions in the undisturbed onset flow

1.0 INTRODUCTION

The loss of flight path control that often follows the condition of extensive separation on wings is a serious problem influencing the safety of all aircraft operations and the combat effectiveness of fighter aircraft. Recent investigations of a "controlled separation" concept (see, for example, (1) and (2)) have demonstrated the possibility of maintaining control through the condition of maximum lift. If such a concept is to be fully exploited, it needs to be considered early in the design process of new aircraft. Theoretical methods capable of predicting the aerodynamic characteristics under the

conditions of extensive separation are, therefore, needed.

Considerable effort has been applied to calculation of flow characteristics for well defined vortex separation (2). The present paper is concerned with the modelling of viscous separation starting from the wing trailing edge. The work is part of a multi-phase program aimed at predicting aerodynamic characteristics of combat aircraft at high angle of attack with leading-edge and side-edge vortex separations modelled as well as trailing-edge separations.

2.0 BACKGROUND

The pressure distribution in a trailing-edge separation region is usually characterized by a constant pressure region extending back to the trailing edge followed by a short recompression region (e.g., (3)). A simplification of this characteristic is modelled in the two-dimensional CLMAX program (4), (5) using a pair of constant strength vortex sheets to enclose the separated region, Figure 1. The length of the sheets required a semi-empirical approach and the condition that the sheets be force free is satisfied in an iterative cycle in which segments of the sheet are aligned with local flow directions. The method combines boundary layer and potential flow codes in an outer iteration cycle. The potential flow pressure distribution--which includes the influence of the free vortex sheets--is passed to the boundary layer routine which then supplies the separation points and the boundary layer displacement thickness distribution for the next iteration. The boundary layer displacement effect in the attached flow region is modelled by transpiration (i.e., source distribution) rather than by a displacement surface. The main advantage of the transpiration approach is that the matrix of influence coefficients in the panel method remains essentially the same from one iteration to the next; only the wake condition changes.

The thin vortex sheet model of the upper separated shear layer was demonstrated by Young and Hoad (6) to be a reasonable representation of the flow as far back as the trailing edge. For example, a comparison from (6) of a laser-velocimeter flow survey, and a CLMAX program calculation is shown here in Figure 2. Downstream of the trailing edge the vortex sheet model becomes less representative of the flow; however, a later evaluation of a graded vorticity model over the recompression zone had little effect on the airfoil solution. Closer modelling of the recompression zone (such as, for example, the approaches used by Gross (7) or Zumwalt (8)) would be desirable in cases where the wake interacts closely with a downstream component.

A particular feature of the vortex sheet model enclosing the region of low energy is that pressures can be calculated directly in the separated zone (4). This is an additional advantage over the displacement surface approach of Henderson (9) and over the source outflow model of Jacob (10). The CLMAX method generally gives very close agreement with experimental pressure distributions. For example, Figure 3 shows the post-stall pressure distribution for a GA(W)-1 airfoil at 20° incidence. Calculations have been performed over a wide range of conditions, and the variations of lift coefficient on a NACA 0012 section over a range of incidence from 0° to 90° is shown in Figure 4. Experimental values are taken from Hoerner (11). The CLMAX model has been extended to the case of transonic (12) and also unsteady (5) flows in two dimensions.

An early extension of the CLMAX method to the three-dimensional non-lifting case of bluff-body separation was formulated with a surface source panel method (13). Although the procedure gave reasonable correlation with experimental base pressure when the experimental separation line was used, the model gave an "overshoot" in the calculated pressure just ahead of separation, see Figure 5. This caused the boundary layer calculation to predict an earlier separation at every iteration.

An improvement of the three-dimensional model was developed using distributed vorticity (14) on the surface panels rather than source singularities. On each panel, the vorticity was constant spanwise and varied linearly chordwise, and the Neumann boundary condition was satisfied at a control point on each panel. The basic method was the VIP3D code (15) which already had a viscous/potential iteration procedure. Again, the boundary layer displacement effect was modelled by the transpiration technique. A typical example of its application at low angle of attack is shown in Figure 6 for the Kolbe and Boltz (16) wing. This spanwise lift distribution (previously presented in (15)) was recalculated recently after correcting a program error uncovered in VIP3D during the extension to separated flow. The separated flow model was first assembled in a stripwise manner, Figure 7(a), to expedite development of the procedure. A calculated pressure distribution for a rectangular wing at 19° is shown in Figure 7(b), compared with experimental measurements (17). The calculations were performed with and without a simple model of tip-edge separation.

Although the model illustrated in Figure 7(a) is a reasonable one for rectangular wings, it is not suitable for more general planforms. In developing the method further, the complete model was reviewed and reformulated.

3.0 BASIC FORMULATION

In Figure 8, we have taken a streamwise cut through the wing and its wake and, based on the earlier work, (4) and (14), have formed an idealized model using four closed regions; airfoil (A), bubble (B), wake (W) and outer flow (O). The latter region is closed by an outer boundary, S_∞, at a large distance from the wing and its wake where the disturbances to a uniform onset flow, V_∞, have essentially disappeared.

We assume the existence of velocity potential fields, Φ_A, Φ_B, Φ_W, Φ_O, that satisfy Laplace's equation throughout the regions A, B, W and O, respectively. By applying Green's theorem to each of these regions and combining the resulting contributions, the velocity potential at a point, P, situated within any of these regions can be written:

$$\Phi_P = \frac{1}{4\pi} \iint_{S_{OA}} \left\{ (\Phi_O - \Phi_A)\, \underline{n}_O \cdot \nabla\left(\frac{1}{r}\right) - \frac{1}{r}\, \underline{n}_O \cdot (\nabla\Phi_O - \nabla\Phi_A) \right\} dS_{OA}$$

$$+ \frac{1}{4\pi} \iint_{S_{BA}} \left\{ (\Phi_B - \Phi_A)\, \underline{n}_B \cdot \nabla\left(\frac{1}{r}\right) - \frac{1}{r}\, \underline{n}_B \cdot (\nabla\Phi_B - \nabla\Phi_A) \right\} dS_{BA}$$

$$+ \frac{1}{4\pi} \iint_{S_{OW}} \left\{ (\Phi_O - \Phi_W)\, \underline{n}_O \cdot \nabla\left(\frac{1}{r}\right) - \frac{1}{r}\, \underline{n}_O \cdot (\nabla\Phi_O - \nabla\Phi_W) \right\} dS_{OW}$$

$$+ \frac{1}{4\pi} \iint_{S_{OB}} \left\{ (\Phi_O - \Phi_B)\, \underline{n}_O \cdot \nabla\left(\frac{1}{r}\right) - \frac{1}{r}\, \underline{n}_O \cdot (\nabla\Phi_O - \nabla\Phi_B) \right\} dS_{OB}$$

$$+ \frac{1}{4\pi} \iint_{S_{BW}} \left\{ (\Phi_B - \Phi_W)\, \underline{n}_B \cdot \nabla\left(\frac{1}{r}\right) - \frac{1}{r}\, \underline{n}_B \cdot (\nabla\Phi_B - \nabla\Phi_W) \right\} dS_{BW}$$

$$+ \Phi_\infty \qquad (1)$$

where S_{OA}, S_{OB}, etc., are the common boundaries, respectively, between regions O and A, and between O and B, etc. Vectors $\underline{n}_O$, $\underline{n}_B$ are unit normals to the surface directed into the regions O and B, respectively. The quantity, r, is the distance between an element of surface and the point, P.

Equation (1) is an extension of the two-region case given by Lamb (18), ART 58. The present equation includes an additional term, Φ_∞, which is the contribution from the boundary S_∞ due to a uniform onset flow, whereas Lamb assumed the flow at infinity to be at rest.

If the point, P, lies on one of the surfaces, say the S_{OA} facing region O, then the local contribution to Φ_P is obtained by a limiting process using a small hemispherical distortion of the surface centered on P. The local contribution (from the first term in the integral) is

$$\Delta\Phi_P = \left(\frac{\Phi_O - \Phi_A}{2} \right)_P \qquad (2)$$

This is half the jump in potential across the surface at point P. The surface integral over S_{OA} in Eqn. (1) would exclude point P in this case. A similar treatment is performed if P lies on any of the surfaces. Note that the first potential appearing in the expression for $\Delta\Phi_P$ is the one in the region that point P is "facing".

Each of the integral expressions in Eqn. (1) represents the perturbation potential due to distributions of doublets and sources over the respective boundaries. For example, the first integral is the perturbation potential for a doublet distribution of strength

$(\Phi_O - \Phi_A)$ on the boundary, S_{OA}, and with axes $\underline{n}_O$, plus the perturbation potential for a source distribution of strength $-\underline{n}_O \cdot (\nabla\Phi_O - \nabla\Phi_A)$.

4.0 BOUNDARY CONDITIONS

For a given region there exists an infinite number of combined doublet and source distributions over the boundary of that region giving the same velocity potential field within the region but producing different solutions in other regions. Thus a unique solution for the idealized model in Figure 8 exists only if appropriate boundary conditions are imposed on both sides of each boundary surface. (Some of these conditions can be implied by suitable choice of model.) In the present case a set of boundary conditions has been assembled based on the earlier work (4), (14), but with an improved basic model for the three-dimensional potential flow. Summarizing the main boundary condition:

(i) Inside the wing we specify an internal Dirichlet boundary condition:

$$\Phi_A = \Phi_\infty$$

(ii) On the exterior surface of the wing we specify the Neumann boundary condition:

(a) in the attached flow region on boundary S_{OA}, we set

$$\underline{n}_O \cdot \nabla\Phi_O = -\frac{\partial}{\partial s}(Ve\delta^*)$$

i.e., the transpiration model of the boundary layer displacement effect;

(b) in the separated zone on boundary S_{BA}, we set

$$\underline{n}_B \cdot \nabla\Phi_B = 0$$

(iii) On boundary S_{OB} (free-shear layers), we apply the condition of zero entrainment. (Later this condition could be changed in order to model the recompression zone.) With zero entrainment, the source terms disappear on this boundary in Eqn. (1). In addition, we satisfy the condition that the shear layer be a streamline of the flow, but this is not applied directly: the shear layer geometry is first prescribed then the streamline condition is satisfied in a wake shape iteration cycle.

The shear layer model used earlier (4), (14), is represented here by a doublet distribution with a linear variation along streamlines in S_{OB}:

$$\Phi_O(s) = \Phi_{SEP} + s\left.\frac{\partial\Phi_O}{\partial s}\right|_{SEP}$$

where s is measured along each streamline starting at a point on the separation line. The potential gradient is taken from the wing surface immediately upstream of the separation point. Note that at each spanwise station, S_{OB} has both an upper and a lower part corresponding to two separation points, Figure 8. The two resulting potential gradients must be related as follows.

(iv) Kutta Condition.

At each spanwise station the velocity potential surface gradients, $\left.\frac{\partial\Phi_O}{\partial s}\right|_{SEP}$, at the upper and lower separation points are set equal. This is equivalent to the Kutta condition used in the earlier work (4), (14).

(v) The downstream wake region, W, is reduced to zero thickness with zero entrainment for the time being. (This is an adequate model for wing-alone cases; however, a thick downstream wake model with appropriate conditions in region W is being considered for the case of multiple components.) With the assumption of small thickness, the contribution from corresponding upper and lower parts of boundary S_{OW} in Eqn. (1) can be combined, leaving a constant doublet value with strength equal to the jump in potential at the downstram end of region B.

Finally, with the appropriate boundary conditions applied in the idealized model, Eqn. (1) is applied at points P on the inside surface of the wing:

$$0 = \frac{1}{4\pi} \iint_{S_{OA}} \left\{ \phi_O \, \underline{n}_O \cdot \nabla\left(\frac{1}{r}\right) - \frac{1}{r}\left(- \frac{\partial}{\partial s}\left(V_e \delta^*\right) + \underline{n}_O \cdot \underline{V}_\infty \right) \right\} dS_{OA}$$

$$+ \frac{1}{4\pi} \iint_{S_{BA}} \left\{ \phi_B \, \underline{n}_B \cdot \nabla\left(\frac{1}{r}\right) - \frac{1}{r} \, \underline{n}_B \cdot \underline{V}_\infty \right\} dS_{BA} - \frac{\phi_P}{2}$$

$$+ \frac{1}{4\pi} \iint_{S_{OBU}} \left\{ \phi_{SEPU} + s \left.\frac{\partial \phi_O}{\partial s}\right|_{SEP} \right\} \underline{n}_O \cdot \nabla\left(\frac{1}{r}\right) \, dS_{OBU}$$

$$+ \frac{1}{4\pi} \iint_{S_{OBL}} \left\{ \phi_{SEPL} + s \left.\frac{\partial \phi_O}{\partial s}\right|_{SEP} \right\} \underline{n}_O \cdot \nabla\left(\frac{1}{r}\right) \, dS_{OBL}$$

$$+ \frac{1}{4\pi} \iint_{S_{OWU}} \left\{ \phi_{SEPU} - \phi_{SEPL} + \left(S_U - S_L\right) \left.\frac{\partial \phi_O}{\partial s}\right|_{SEP} \right\} dS_{OWU} \qquad (4)$$

where $\phi_O = \Phi_O - \phi_\infty$ is the perturbation potential. The integral over S_{OA} and S_{OB} excludes the point, P, when it lies on that part of the boundary. The quantities, ϕ_{SEPU} and ϕ_{SEPL}, SU, SL and $\left.\frac{\partial \phi_O}{\partial s}\right|_{SEP}$ are all functions of spanwise location. S_U, S_L are the streamline lengths from the separation line to the downstream end of the upper and lower parts, S_{OBU} and S_{OBL}, respectively, of the boundary, S_{OB}.

5.0 NUMERICAL PROCEDURE

The general arrangement of the configuration is shown in Figure 9 relative to the coordinate axes. The x-axis is normally taken downstream with z upwards and y spanwise. The z-x plane is regarded as a plane of symmetry in unyawed flight.

The complete surface of the wing, including the tip-edge surface is represented by a number of flat quadrilateral panel over each of which the doublet and source distribution are assumed constant. The surfaces, S_{OB} and S_{OW}, also are represented by flat quadrilateral panels but with constant doublet distributions only; i.e., for the zero entrainment case. Over S_{OB}, the linear doublet variation is therefore represented in a stepwise manner at this time. (This appears to be a satisfactory model but a linear streamwise doublet variation over each panel would be a straightforward extension.)

Using this model the boundary condition equation, Eqn. (4), is satisfied simultaneously at a control point underneath each surface panel on the wing. If there are N panels on the wing, then we have N simultaneous equations in N unknown doublet (or perturbation velocity potential) values. On each chordwise set of panels involving a separation zone, one Dirichlet boundary condition equation is replaced by the explicit Kutta condition. This treatment is not necessary where a regular wake is shed from the trailing edge.

Following the solution of the surface doublet distribution, the surface velocity vectors are obtained from the gradient of the potential using a second-order distribution through the panel control point values. Forces and moments are obtained by pressure integration. Pressures in the separated zone are obtained as in (4):

$$C_p = 1 - \left(\frac{V}{V_\infty}\right)^2 + \frac{\Delta H}{q_\infty}$$

where q_∞ is the free-stream dynamic head and ΔH is the change in total pressure in the separated zone relative to the value in the undisturbed onset flow. In the present case

$$\Delta H = \rho \bar{V} \left.\frac{\partial \Phi_O}{\partial s}\right|_{SEP}$$

and is calculated for each spanwise station. $\bar{V}$ is the average velocity in the shear layer.

For the initial solution the wake geometry is prescribed starting at the separation line geometry. Iterative routines are installed in the code to relax the wake geometry and, hence, satisfy the force-free condition. So far this has only been applied to the tip-edge separation (e.g., (19)), and has not been tried for the bubble region. Also, at this time the complete viscous/potential iteration cycle has not been activated with the modified code.

It should be pointed out that without the separation model, the basic equation used here is the same as that given by Morino (20), who applied Green's theorem directly to the exterior flow field. The attached flow formulation is also similar to that used by Johnson and Rubbert (21) and also Bristow (22), except that they used higher-order singularity distributions. Earlier evaluation of higher-order distributions in the work leading to the present program had indicated a severe cost penalty when running the three-dimensional code because of data storage and retrieval of the interpolation coefficients for each panel. Also, the conditions at an arbitrary separation line become very cumbersome with the higher-order distributions. The piecewise constant model, on the other hand, offers a much simpler formulation and has proven to be very cost effective. In fact, comparisons against higher-order methods have shown essentially the same accuracy for a given density of control points. For example, Figure 10 shows the chordwise distribution of Vy at stations on either side of the planform kink on a wing with strake at $\alpha = 5°$. The wing, which has a NACA 0002 section, is one of the test cases in (23). The Vy calculation is particularly difficult in this region and several methods gave several different solutions. The present solution is very close to the second-order Panair method (21). The present computation involving 946 panels took ten minutes of CDC Cyber 175 CPU time (approximately 2½ minutes of CDC 7600). Most of the panels were concentrated in the leading-edge region because of the high curvature there and the tip surface was closed by a half body of revolution. With more regular thickness/chord ratios, adequate results are obtained using considerably lower panel densities.

6.0 DISCUSSION OF RESULTS

The separated flow model was tested on a 10° swept wing at 21° incidence. The constant chord wing had an aspect ratio of 6. The number of panels representing the wing was 260, arranged in a 40 (chordwise) by 5 (spanwise) array on the main surface and a 3 x 20 array on the tip surface. The latter was a half body of revolution based on the NACA 0012 profile of the wing. Calculations were performed using a prescribed separation line corresponding to experimental measurements (17); the x location of this line was approximately .06 of the chord back from the leading edge. For these calculations, region B of the wake (Figure 8) extended about 5 chord lengths beyond the T.E. (Preliminary calculations had confirmed earlier findings (13) that unlike the two-dimensional case (4), the solution in three dimensions is relatively insensitive to the length of the vortex sheet modelling the shear layer.) In the present calculations 18 panels were used to represent the linear doublet distribution on each streamwise strip of wake panels. The wake geometry was prescribed, leaving the surface at approximately $\alpha/2$, based on earlier experience (4), (5). The wake was shed continuously along the upper surface separation line to the tip, down the tip edge to the trailing edge and back along the lower side of the trailing edge.

Figure 11 shows calculated pressure distributions compared with experimental measurements (17) at two spanwise stations, $\eta = .6$ and .9 of the semispan approximately. The calculations include the case of fully attached as well as separated flows and indicate the large influence of the separated flow model. (Note that the attached flow pressures at the $\eta = .9$ station are perhaps shifted too much in the negative direction over the downstream half of the chord. This is because this station is at the last column of panels before the tip edge and so the spanwise acceleration of the flow as it passes round the tip surface (19) is calculated prematurely. This problem is less severe for the separated flow case because of the influence of the tip-edge separation model. In any event, more columns of panels would normally be used in the tip region.)

The results from the separated flow model compare very favorably with the experimental data. In particular, the pressure in the separated region is in very good agreement and should lead to a good prediction of the drag force. Differences in the peak suction area may be caused by incorrect location of the separation line; i.e., a small forward movement at the inboard station and a small rearward movement at the outboard station would improve the predictions.

It is clear from the experimental results in Figure 11 that the separation was unsteady and it is interesting to observe that some of the apparently "bad" values are, in fact, very close to the attached flow calculation. This is particularly so at the $\eta = .6$ station.

The computation time for the separated flow case was 96 seconds of CDC Cyber 175 time, which is approximately equivalent to 24 seconds on the CDC 7600. It should be emphasized, however, that this calculation represents just the first pass through a complete solution. Even so, such a computation time is a good basis for practical computing costs for a complete iterative procedure. Before the iteration loops for wake

relaxation and boundary layer calculations are switched on, sensitivity studies will be conducted to examine the effect of panel density, wake location and separation line path through the panels. This will lead to a better understanding of the calculation model and will help to ensure good convergence characteristics of the overall procedure.

7.0 CONCLUSIONS

Initial results from a three-dimensional potential flow code with simple separated wake modelling and internal Dirichlet boundary conditions are in very favorable agreement with experimental measurements for the case of extensive upper-surface separation on a wing. The simple basic panel method using piecewise constant source and doublet distributions is justified not only from the favorable comparisons of its performance against higher-order methods and experimental results, but also on its low computing costs. The latter is especially important as a basis for a practical iterative procedure for separated flow predictions.

8.0 REFERENCES

1. Feistel, T.W. and Anderson, S.B., "A Method for Localizing Wing Flow Separation at Stall to Alleviate Spin Entry Tendencies", AIAA Paper No. 78-1476, August 1978.

2. High Angle of Attack Aerodynamics, AGARD-CP-247, October 1978.

3. Seetharam, H.C., "Experimental Investigation of Separated Flow Fields on an Airfoil at Subsonic Speeds", Ph.D. Dissertation, Wichita State University, March 1975.

4. Maskew, B. and Dvorak, F.A., "The Prediction of C_{LMAX} Using a Separated Flow Model", J. Amer. Hel. Soc., April 1978.

5. Dvorak, F.A., Maskew, B. and Rao, B.M., "An Investigation of Separation Models for the Prediction of C_{LMAX}", Final Technical Report Prepared for U.S. Army Research Office, Research Triangle Park, N.C. 27709, 1976-1979.

6. Young, W.J., Jr., and Hoad, D.R., "Comparison of Flow surveys above Stalled Wings", AIAA Paper 79-0147, January 1979.

7. Gross, L.W., "The Prediction of Two-Dimensional Airfoil Stall Progression", AIAA Paper No. 78-155, January 1978.

8. Zumwalt, G.W. and Naik, S.N., "An Analytical Method for Highly Separated Flow on Airfoils at Low Speeds", Wichita State University Aeronautical Report 77-2, May 1977.

9. Henderson, M.L., "A Solution to the Two-Dimensional Separated Wake Modelling Problem and Its Use to Predict $C_{L_{max}}$ of Arbitrary Airfoil Sections", AIAA Paper 78-156, January 1978.

10. Jacob, K., "Advancement of a Method for Calculating Separated Flows Around Airfoils with Special Consideration of Profile Drag", DLR-FB-76-36, Translated as ESA-TT-373, April 1977.

11. Hoerner, S.F., Fluid Dynamic Drag, Hoerner Fluid Dynamics, Brick Town, N.Y., 1965.

12. Dvorak, F.A. and Maskew, B., "The Modelling of Airfoil Separation in Subsonic and Transonic Flow", To be published in an AFFDL Technical Proceedings Report.

13. Dvorak, F.A., Maskew, B. and Woodward, F.A., "Investigation of Three-Dimensional Flow Separation on Fuselage Configurations", U.S. Army USAAMRDL Report TR-77-4, March 1977.

14. Rao, B.M., Maskew, B. and Dvorak, F.A., "Prediction of Aerodynamic Characteristics of Fighter Wings at High Lift", ONR Report CR-215-258-1, July 1979.

15. Dvorak, F.A., Woodward, F.A. and Maskew, B., "A Three-Dimensional Viscous/Potential Flow Interaction Analysis Method for Multi-Element Wings", NASA CR-152012, July 1977.

16. Kolbe, C.D. and Boltz, F.W., "The Forces and Pressure Distribution at Subsonic Speeds on a Plane Wing Having 45° Sweepback, an Aspect Ratio of 3, and a Taper Ratio of 0.5", NACA RM-A51G31, 1951.

17. Yip, L.P. and Shubert, G.L., "Pressure Distributions on a 1- by 3-Meter Semispan Wing at Sweep Angles from 0° to 40° in Subsonic Flow", NASA TM-72755, December 1976.

18. Lamb, Sir H., Hydrodynamics, 6th Ed., Dover Publications, New York, N.Y., 1945.

19. Maskew, B., "Influence of Rotor Blade Tip Shape on Tip Vortex Shedding--An Unsteady Inviscid Analysis", Paper 80-6 in Proceedings of the 36th Annual Forum of the American Helicopter Society, May 1980.

20. Morino, L., Chen, L.-T. and Suci, E.O., "Steady and Oscillatory Subsonic and Supersonic Aerodynamics around Complex Configurations", AIAA J., Vol. 13, No. 3, March 1975.

21. Johnson, F.T. and Rubbert, P.E., " Advanced Panel-Type Influence Coefficient Methods Applied to Subsonic Flows", AIAA Paper No. 75-50, January 1975.

22. Bristow, D.R. and Grose, G.G., "Modification of the Douglas Neumann Program to Improve the Efficiency of Predicting Component Interference and High Lift Characteristics", NASA CR-3020, 1978.

23. Sytsma, H.S., Hewitt, B.L. and Rubbert, P.E., "A Comparison of Panel Methods for Subsonic Flow Computation", AGARD-AG-241, 1979.

Acknowledgements

The present work is part of a multiphase program funded by the Office of Naval Research under Contract N00014-78-C-0128. It is an extension of earlier two-dimensional separated flow modelling, which was funded by the U.S. Army Research Office, Research Triangle Park, N.C., under Contract DAAG29-76-C-0019; and three-dimensional non-lifting separated flow modelling which was funded through the Eustis Directorate of the U.S. Army Air Mobility Research and Development Laboratory under Contract DAAJ02-75-C-0036. The basic method for the present work is taken from a viscous/potential flow iterative method, the development of which was funded by NASA Ames Research Center under Contract NAS2-8788.

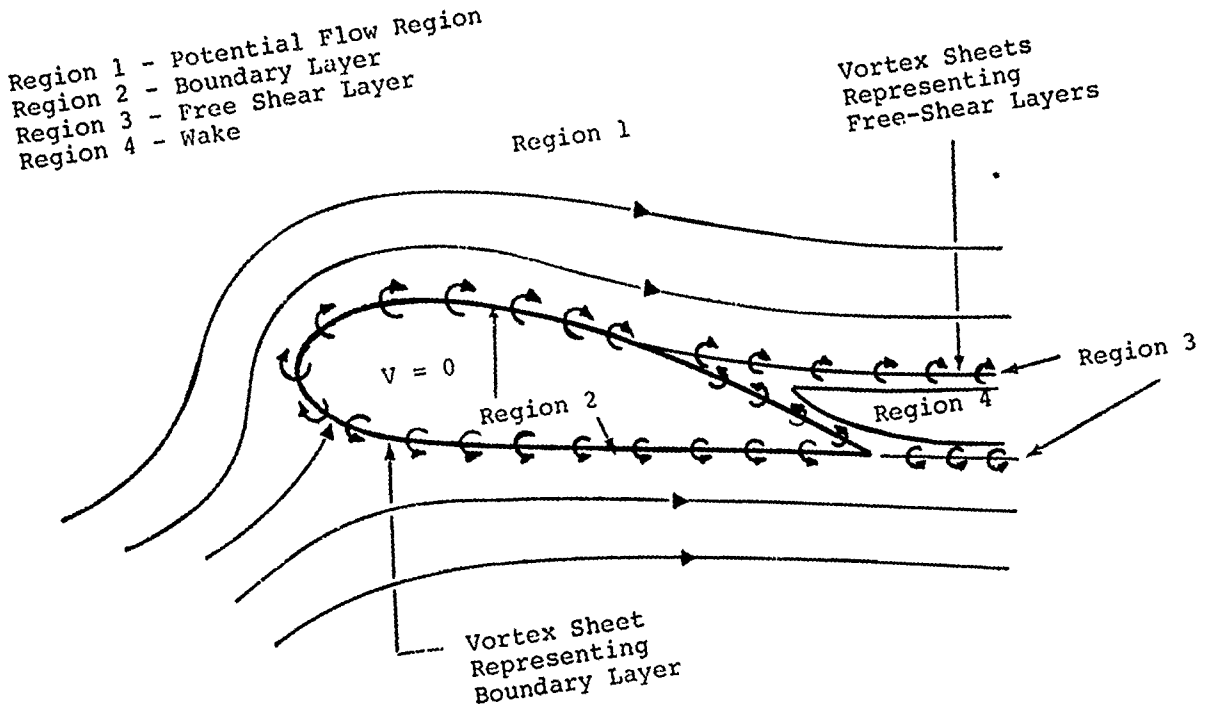


Fig. 1. Mathematical Flow Model.

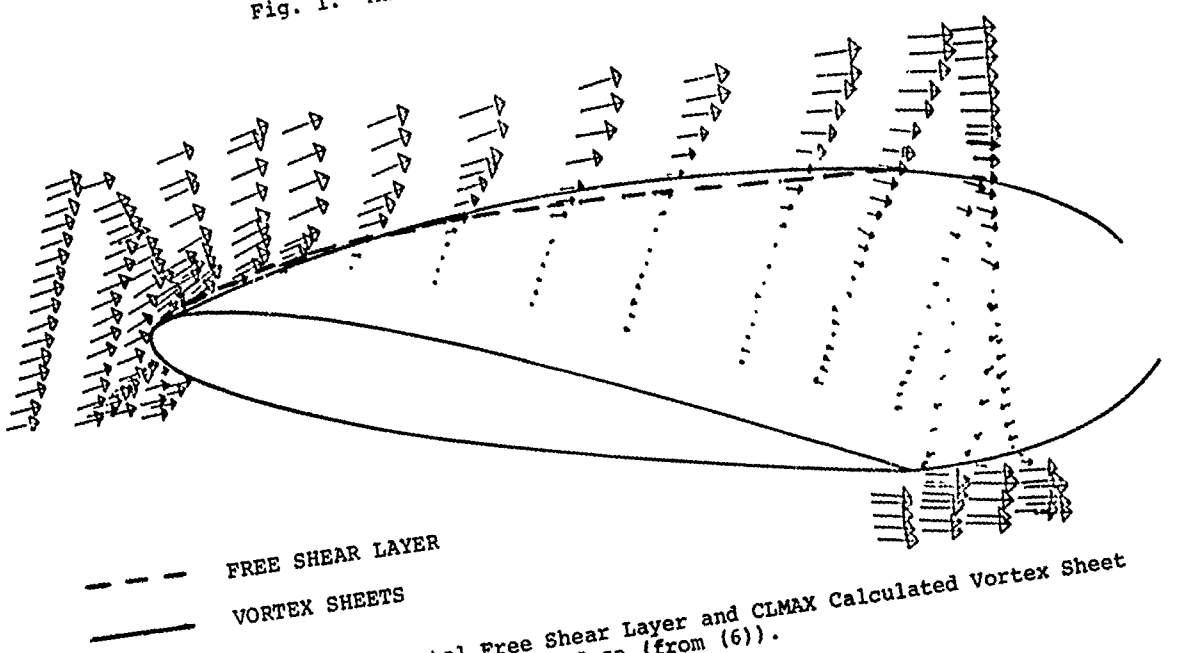


Fig. 2. Location of Experimental Free Shear Layer and CLMAX Calculated Vortex Sheet Centerlines for Low Mach Number Case (from (6)).

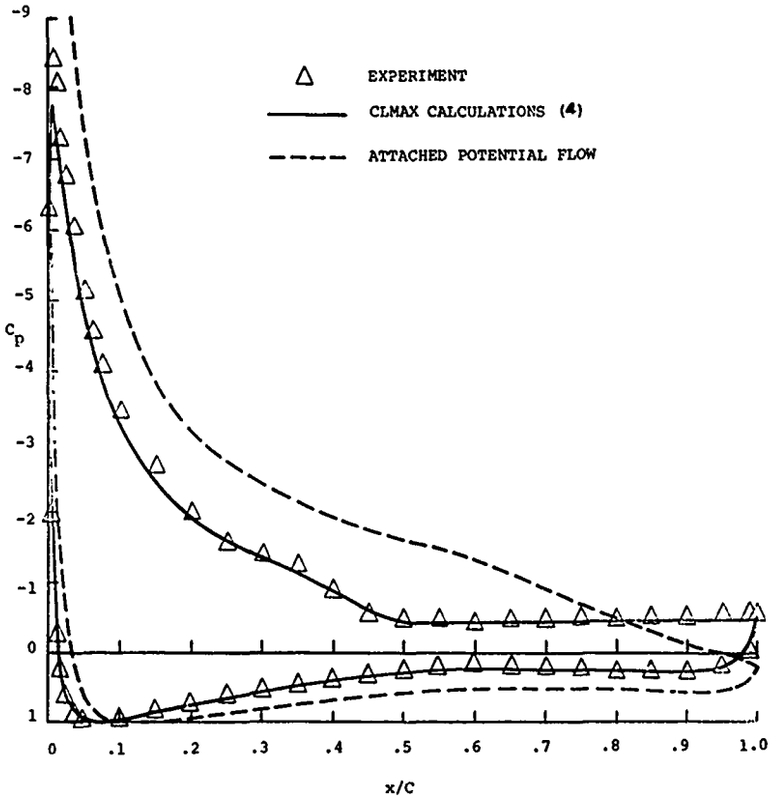


Fig. 3. Comparison of Calculated and Experimental Pressure Distributions on a GA(W)-1 Airfoil (Re = 6.3 x 10^6; α = 20.05°).

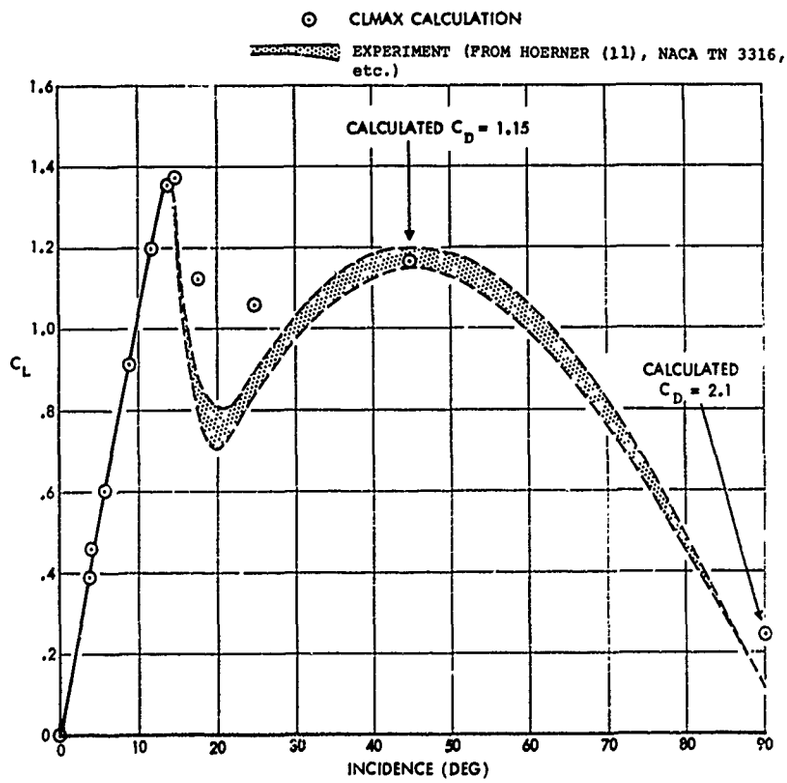


Fig. 4. Comparison of Calculated and Experimental Lift Characteristics for a NACA 0012 Airfoil (Re = 6.0 x 10^6; M = 0.2).

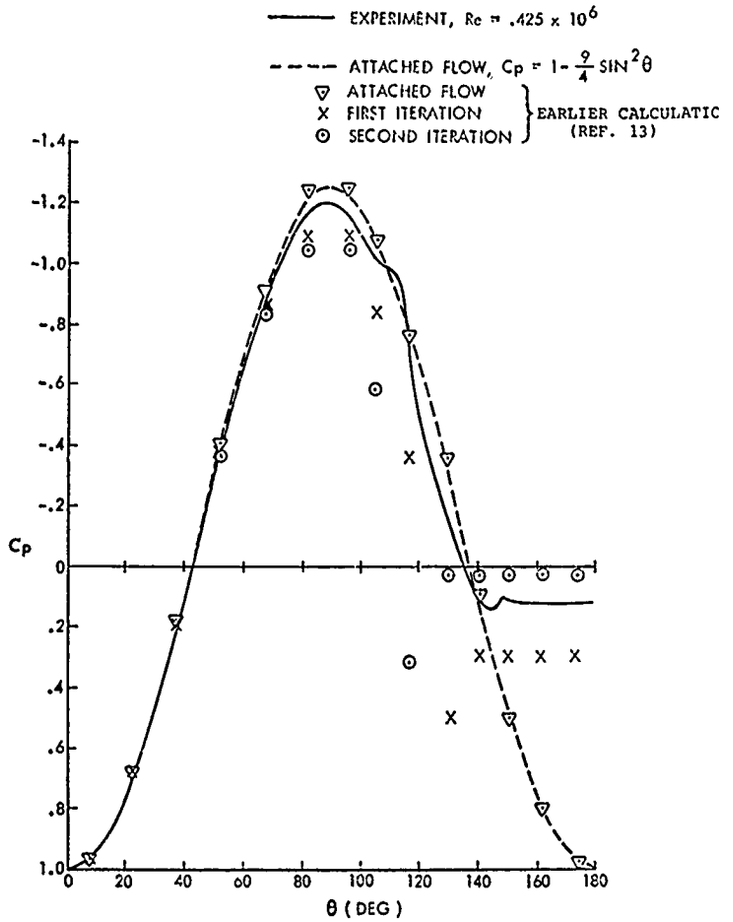


Fig. 5. Comparisons of Pressure Distributions on a Sphere.

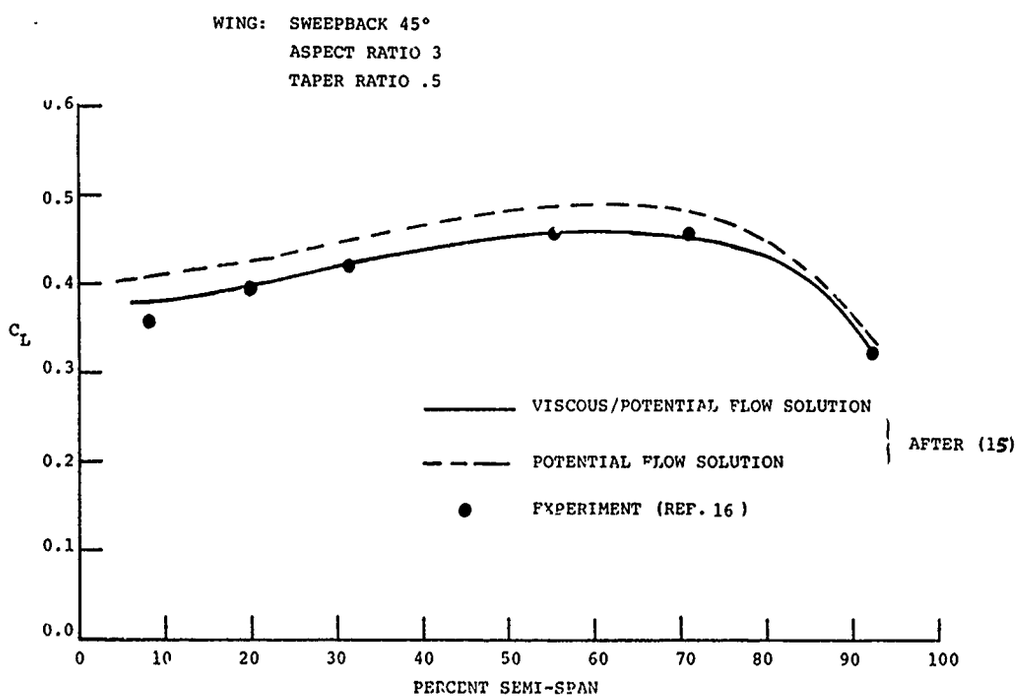


Fig. 6. Comparison of Lift Distribution on the Kolbe and Boltz Wing (Re = 4 x 10^6; α = 8°; M = 0.25).

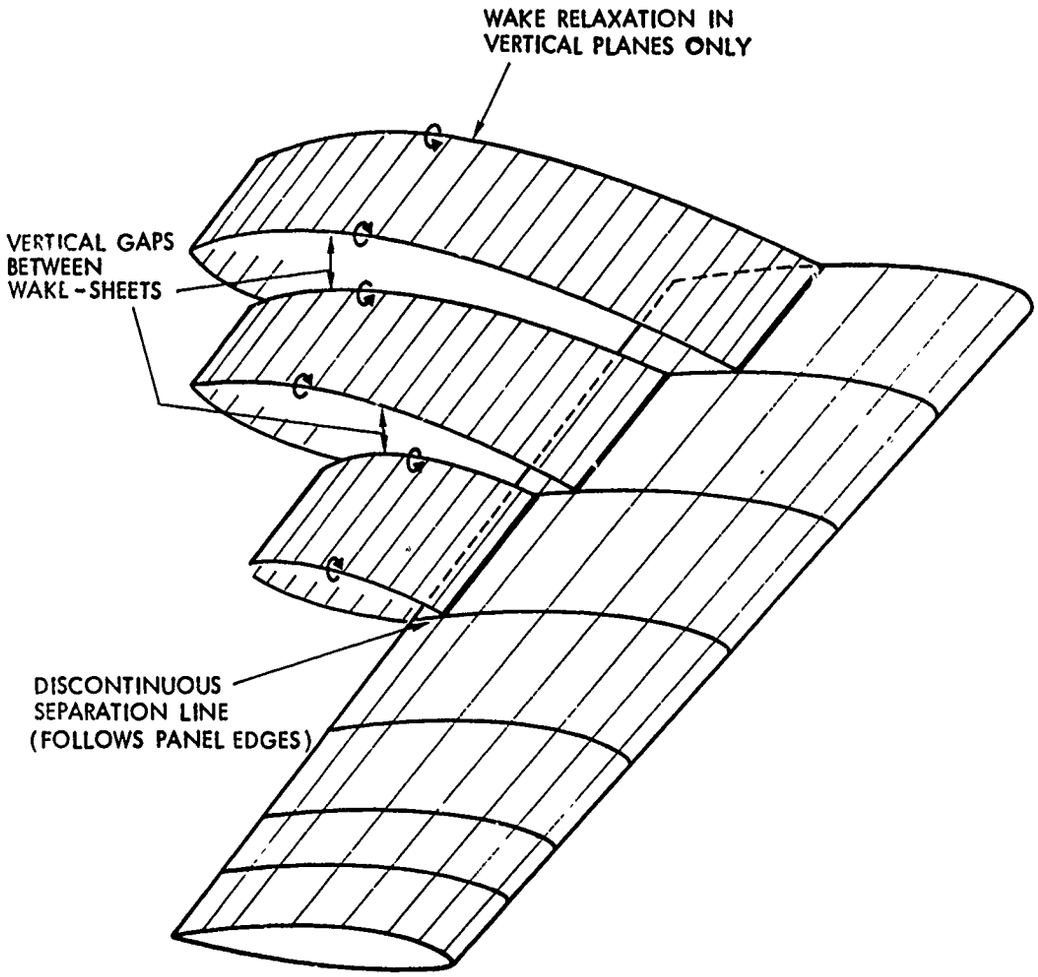


Fig. 7(a). Earlier Separated Flow Model (14).

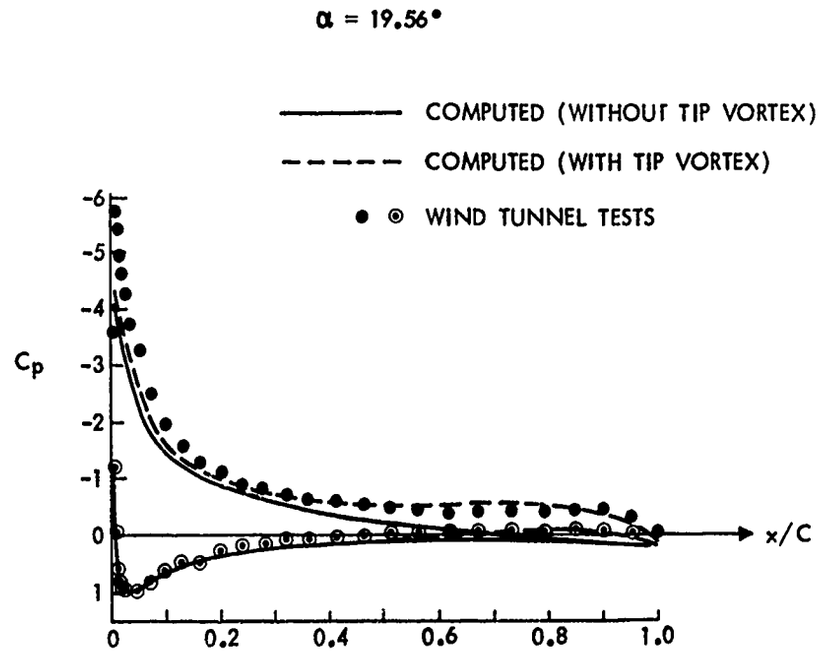


Fig. 7(b). Chordwise Pressure Distribution on a Rectangular Wing Near the Tip Section; (y/b = 0.95).

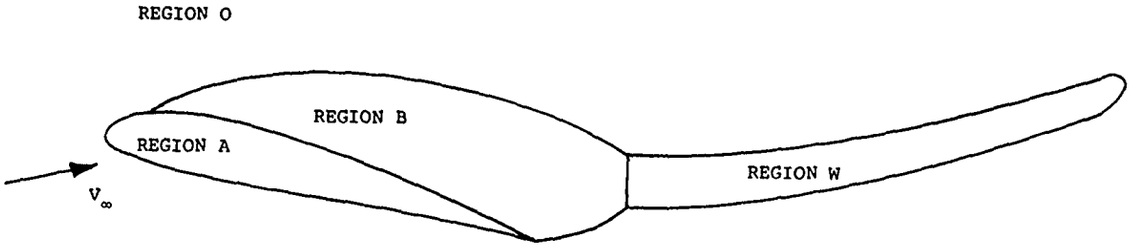


Fig. 8. Idealized Flow Model--Section through the Wing and Its Wake.

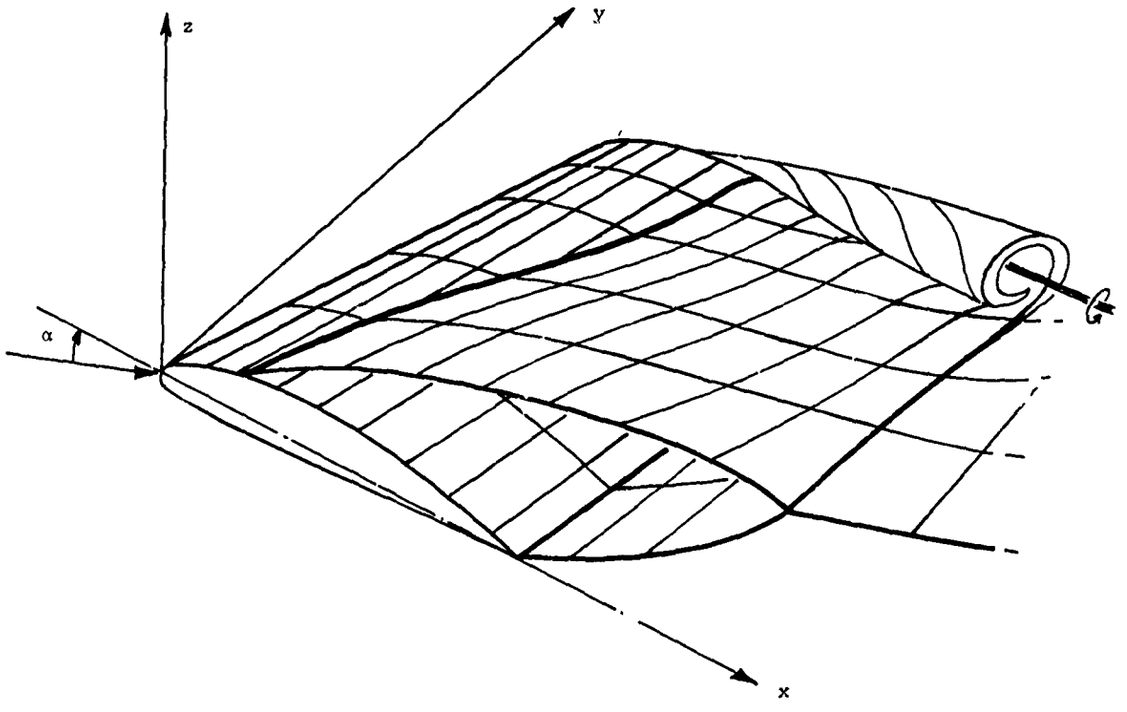


Fig. 9. General Arrangement of the Configuration with a Schematic of the Separation Model.

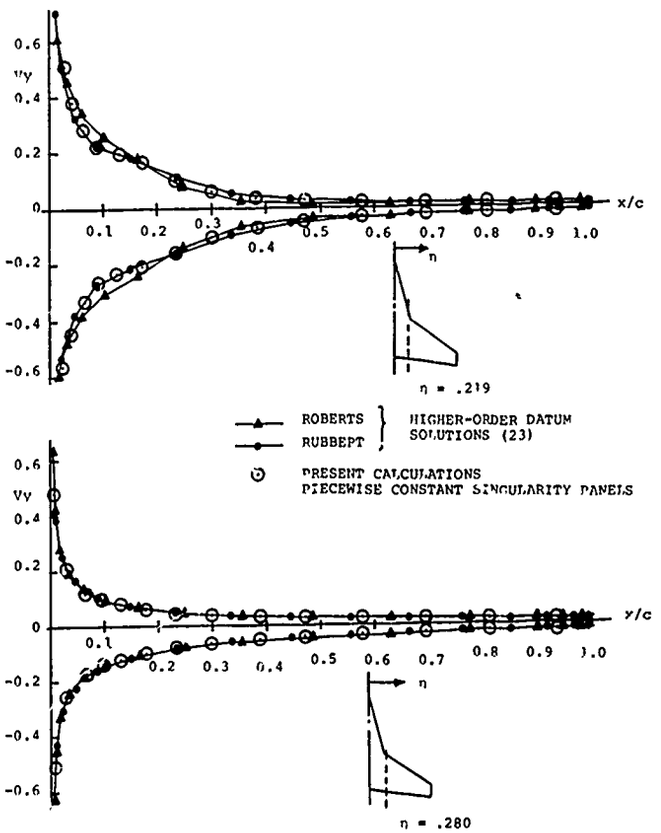


Fig. 10. Comparison of Calculated y-Component of Velocity at Two Stations on a Straked Wing (Attached Flow); t/c = .02, α = 5°.

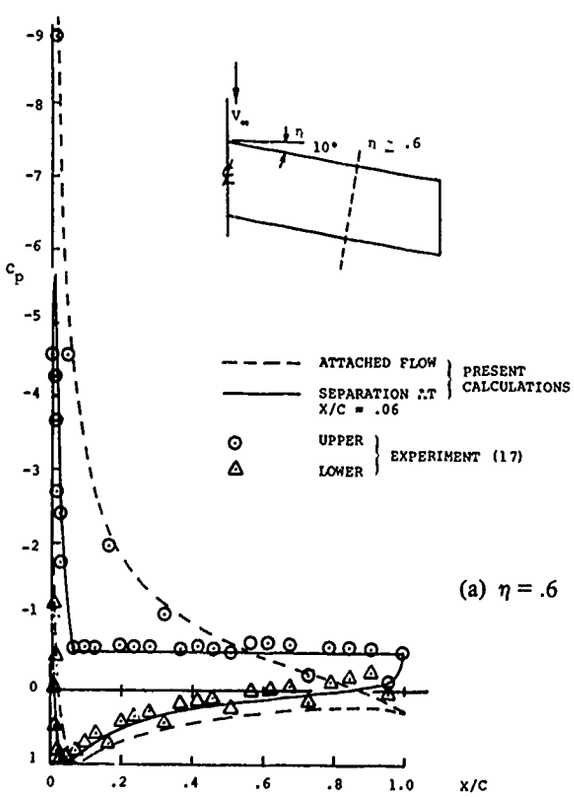
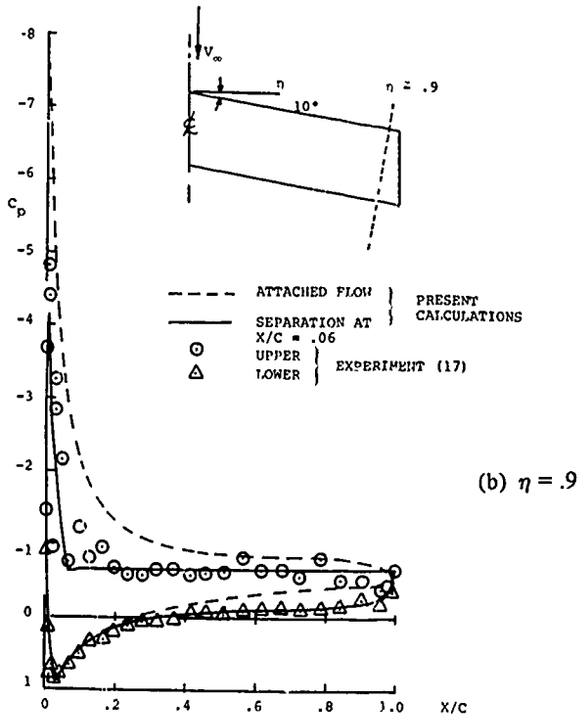


Fig. 11. Comparison of Calculated and Experimental Pressure Distribution at Two Stations on a Wing with Extensive Separation; α = 21.38°.



(b) $\eta = .9$

Fig.11 concluded

AN EXPERIMENTAL STUDY OF THE FLOW ON A SWEPT WING IN FLIGHT

A.Bertelrud
F.F.A., The Aeronautical Research Institute of Sweden
Box 11021, S-161 11 Bromma, Sweden

A short resumé will be given concerning a series of flight tests presently being performed in Sweden on a swept wing aircraft. A large amount of wind tunnel data on the wing of the aircraft has been obtained earlier[1,2], making the complete data set a promising case for correlation of wind tunnel and free flight tests. Preliminary tests in flight have also been reported earlier[3].

Figure 1 shows the aircraft, a SAAB 32 A Lansen, and the main region of experimental investigation. The coordinates given refer to the system used in one of the wind tunnel tests. The aircraft is equipped with accelerometers, rate gyros, indicators for control surface deflection angles and other reference information. Time averages of all reference information as well as the aerodynamic probes are scanned with a frequency of 40 Hz. This enables an extensive description of aircraft rigid body motion, wing flexibility and flight reference data together with the corresponding aerodynamic flow conditions.

The aerodynamic flow is investigated using surface static pressure taps, modified Preston tubes and boundary layer rakes as well as different types of heated films for the measurement of local skin friction and boundary layer turbulence. The time average values are recorded via a digital system whereas the turbulence data is also recorded directly on six analog channels.

Figure 2 exemplifies the stationary flight conditions investigated, ranging from $M = 0.27$ to 0.9. In addition a rather varied program of manoeuvres is flown to investigate flow properties during instationary conditions. In the flight envelope examples are found of laminar and turbulent attachment line flow, natural and bubble transition, shock-free flow as well as flow with shocks and even in some cases shock induced separation. Extensive flow visualization is performed.

Figure 3 exemplifies some static pressure distribution results at $y/b = 0.6$ for a Mach number of 0.8. The open symbols are from the flight tests ($\alpha = 2.45^0$), in this case at $Re_c = 20 \cdot 10^6$, the closed symbols from the wind tunnel tests[2], at $Re_c = 16 \cdot 10^6$ and an angle of attack of 2.9 degrees. The line indicates results obtained with the Jameson-Caughey FLOW 22 code[4], which is used as a production code to obtain rapid comparisons.

Figure 4 shows a detail of the pressure distributions at $M = 0.5$ obtainable in the leading edge region. Flights performed at various altitudes yield a variation in angle of attack, and in the figure three different angles of attack are shown. At 3.2^0 there is natural transition, at 4.7^0 there are indications of a closed separation bubble occurring roughly between 22 and 32 mm from the leading edge. At 5.9^0 there are indications of either a shock, a bubble or both in combination. Note that a total of 10 pressure taps are located within 1% of the chord on the suction side, which is better than the detail obtainable on most wind tunnel models. Also indicated in the figure is computations with a three-dimensional panel method[5] developed at the FFA.

At present 25 flight hours have been flown in a program of approximately 50 hours. The static pressure and skin friction distributions on the wing have been determined and presently the test is focussed at completing the boundary layer measurements as well as improving the determination of for example shock position and shock unsteadiness on the wing.

CONCLUSIONS

The results from the present flight test program may be of value in the areas of
- wind tunnel/flight correlation of viscous flow on swept wings
- inviscid and viscous code development
- transition prediction
- shock/boundary layer interaction
- testing techniques

REFERENCES

1. Bertelrud, A. — An Experimental and Computational Investigation of a Swept Wing Flow at Subsonic Speeds. AIAA Paper 78-1200

2. Sörensén, H. — Effects of Reynolds Number on Swept-Wing-Body Configurations with Leading Edge Flaps in Transonic Flow. FFA Test Data Report AU-1065 (1979)

3. Bertelrud, A. — Local Skin Friction and Static Pressure on a Swept Wing in Flight. AIAA Paper 80-0423 CP

4. Jameson, A. and Caughey, D.A. — Numerical Calculation of the Transonic Flow Past a Swept Wing. New York University, Mathematics and Computers, C00-3077-140, June 1977

5. Eriksson, L.-E. — Development of a Computer Program for a Higher-Order Panel Method for Three-Dimensional Subsonic Flow. FFA AU-1558 (to be published)

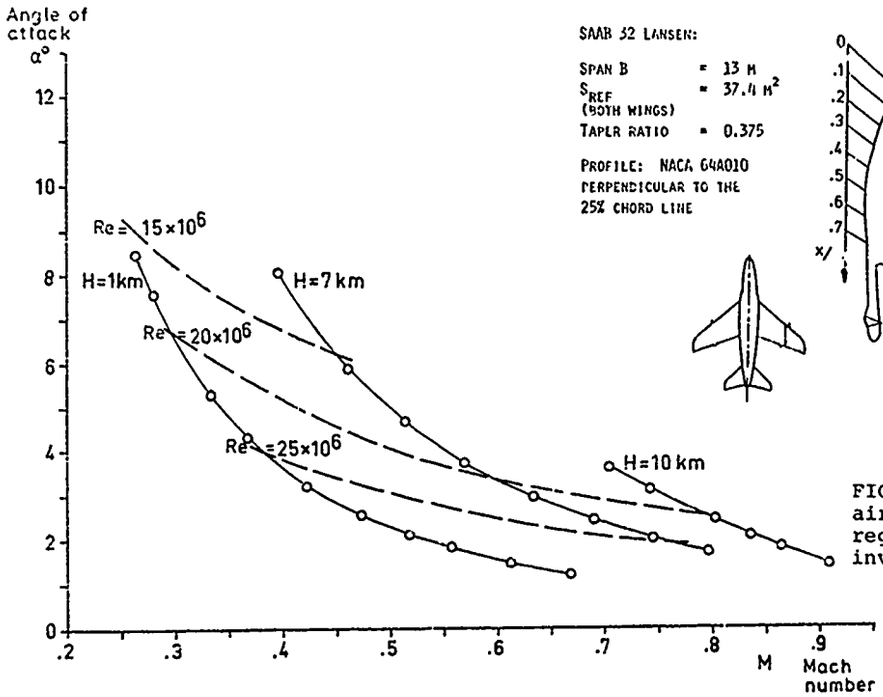


FIG. 1. Flight test aircraft and the main region of experimental investigation.

FIG. 2. Flight envelope.

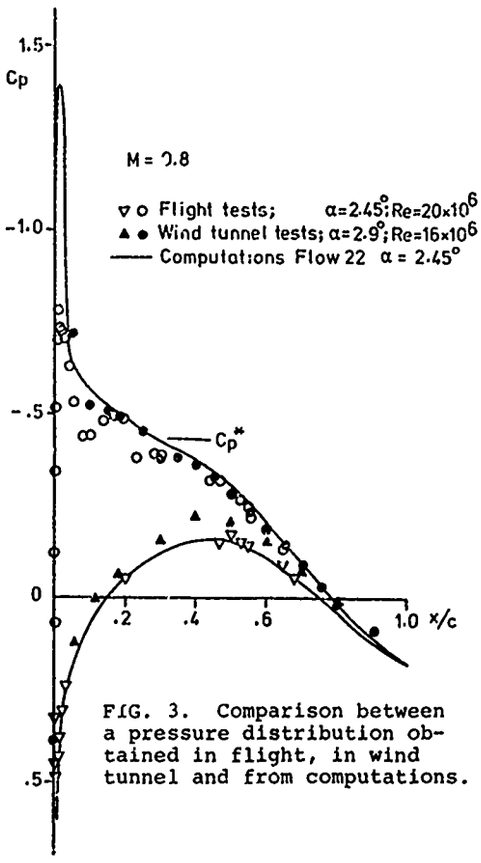


FIG. 3. Comparison between a pressure distribution obtained in flight, in wind tunnel and from computations.

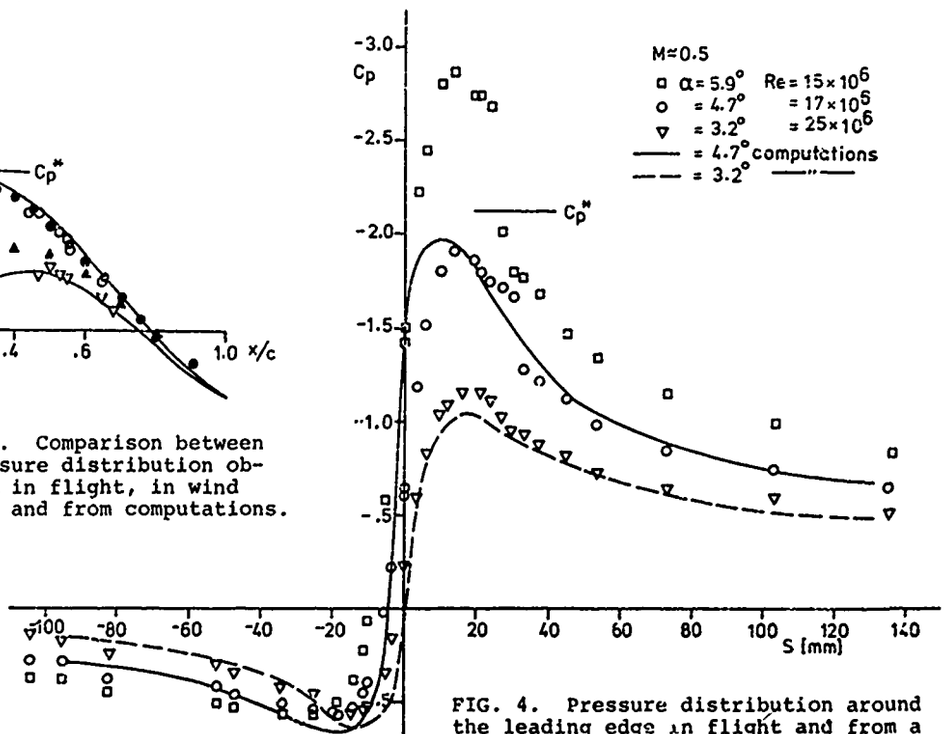


FIG. 4. Pressure distribution around the leading edge in flight and from a 3-D panel method.

FLUID DYNAMICS PANEL SYMPOSIUM
"COMPUTATION OF VISCOUS-INVISCID INTERACTIONS"
ROUND TABLE DISCUSSION

Dr. Quinn

The idea behind the last three days has been to share with each other the different ideas and concepts that are being used to design surfaces over which there are flows with strong viscous and inviscid interactions. We have heard a number of them. All have agreed with some experimental data, and that itself, might be an issue we would care to discuss. I presume that everybody is to some extent content with what he has seen with respect to the different techniques used to calculate such flows. Maybe you would care to discuss some of the shortcomings, whether or not you are, in fact, content with them; what are the limitations in the different procedures?

To jog our memories on the different calculation techniques that have been presented over the last three days, I have asked M. Le Balleur, Dr. Kline, and Dr. Melnik to take no more than about 5 minutes each in reviewing or giving their impressions of the three sessions in which each of them presented remarks. We will start with the first, M. Le Balleur, Session 1.

M. Le Balleur

If we look back at the beginning of our session, the theme was that of unseparated flows, using the thin-layer concept, and all of the presentations dealt essentially with wing profiles or airfoils. You will recall that we heard Dr. Lock's paper, presented by Dr. Green, on a review of methods for predicting viscous effects on airfoils and wings at transonic speeds. We then had a paper by Messrs Nebeck, Sobieczky and Seebass which defined methods taking into account the viscous effects for the generation of shock-free airfoils. Then we had a paper by Messrs Stanewsky, Nandanan and Inger that showed the importance of the problems of the boundary layer and shock wave interaction. Then we had a paper by Messrs Desopper and Grenon which showed the possibility of carrying out coupled computations for viscous unsteady flows. Then we had a paper by Dr. Leicher on high-lift airfoils, one by Messrs Rosch and Klevenhusan on multi-element airfoils in transonic flow. Then Dr. Firmin talked to us about the difficult three-dimensional problem of wings with a coupling where you have a transonic small disturbance inviscid calculation and a wake calculation. Finally, Dr. Wai and Dr. Yoshihara spoke of the problem of two-dimensional airfoils and this particularly included the separation problems, as well as a specific treatment for the shockwaves interactions, using the viscous ramp model.

So my comments in regard to that particular session are that we heard about a number of different methods concentrating to some extent on the two-dimensional problems, or the problems of multi-element airfoils, both on the three-dimensional and two-dimensional unsteady problems, and concluding with the calculation of separation by a method which goes beyond the stage of a separation modelling limited to isobars, as is often the case in multi-element airfoils. The characteristic of all of these computations is that they used integral methods for calculating the viscous effects, and I think that this is an important point. A second point is that, except for the techniques that include the separation problems, they used a simple successive iteration coupling technique, with possibly an under-relaxation to ensure convergence. It would appear, offhand, that there is now a great deal of precision in computing the two-dimensional profiles, and I think that it would be interesting for us to evaluate and discuss this point.

The major elements that are common to all of these computations are the necessity to take into account the displacement effects, and particularly the thickness effects (or displacement) of the wake. Reference was also made to the need, in order to take good estimates of the wake, to take the curvature effects into account. It seems to me worthwhile to stress one particular point, mentioned by Dr. Green, which was the possibility of choosing for the wake curvature either its mean curvature, or the curvature induced in the inviscid flow which was indicated as K* curvature or displacement surface curvature. One last point is that of taking into account the wake geometry. This therefore represents the points of agreement among all of the papers.

However, it would appear that a certain number of controversies in the different techniques have emerged. First of all, although all of the computations used potential programs, you will note that some of these use non-conservative versions, some that are fully conservative, and others that are partially-conservative. It appears to me therefore that a first question that would be very worthwhile to look at would be to see whether there is a weighting in the two types of the schemes that might produce with universality an approximate solution for the Euler equations, or are these Euler equations indeed necessary to be solved. Another point that wasn't brought up very much, but one that we ought to discuss, is that of the question of the wall corrections in the transonic range. All of the comparisons were given with such corrections. It would seem very important to me to see whether we can make comparisons with experiment that might be derived from this limitation. If we leave aside the three-dimensional problems, for which the first results indicate the importance of the leading edge area, the problem that gave rise to the greatest controversy is the question of the interaction between the shock wave and the boundary layer and the problem of the trailing edge; I noted it was said in Dr. Lock's presentation that the treatment of the shock-boundary layer interaction as well as the trailing edge treatment in terms of a strong local interaction were not essential, but I think that Dr. Melnik will comment on that point. During the second day, Dr. Melnik said that on the contrary the problem of the trailing edge was essential, particularly for drag problems. For the shock-boundary layer interaction, it seems to me that there are two major directions that emerge from this, if you don't adopt the position that consists of saying that one shouldn't be concerned with this. The first concern will be connected to the problem of the inviscid flow and tied to the intensity of recompression under shock. The viscous techniques essentially are intended to offset the over-recompression at the wall due to a fully conservative code. The second point involves the calculation of the viscous flow and was brought out by Dr. Stanewsky's paper, which shows that, beyond the intensity of the after-shock recompression, you have the problem of whether one can predict with accuracy the thicknesses of the boundary layer downstream of the shock, in order that the trailing edge area can be properly predicted.

This raises the problem of the validity of the boundary layer equations, and particularly of their resolution with a distribution of pressure which results from a numerical spreading of the shock wave. In some cases, there is then a question of inaccurate prediction or the downstream boundary layer, which may depend on the numerical thickening of the shock wave.

Dr. Melnik

There was a great deal of overlap between the second session and the first and third sessions. In this session there were a number of papers involving flows that were not separated including my review paper and a couple of papers that did address flows with separation. The separation zones in these papers looked to be reasonably extensive and so overlapped somewhat with the third session. Most of Le Balleur's comments on the papers in the first session apply equally well to the second session. Rather than trying to summarize each paper, I will try to identify the areas where there is general agreement and the areas where there is still some contention on how these problems should be approached.

I think, in agreement with Dr. Le Balleur, it now seems clear now that the effects of the wake can be important. Techniques have been developed to include them in airfoil calculations and also in wing calculations so there seems to be little reason not to include them in the theoretical model. There is a related point in the paper dealing with mixing of jets with external flows. In this paper the authors used a set of matching conditions to couple a mixing layer with a set that seems not to be related to previous analyses of matching and I think that there is some question in my mind, and perhaps in others, concerning the correctness of these matching conditions. The results presented look good, and the conditions are probably correct, but I think that some further work should be done to better justify the matching conditions employed and to relate them to the standard matching conditions for this problem previously derived by, say, Viviand.

On the question of shock wave boundary layer interactions there were a variety of methods developed to treat the local solution near a shock wave when the shock waves are weak. However, this is an area of contention between two groups, myself, Adamson and Messiter, on the basis of rational asymptotic analysis, feel that the sublayer is not important; on the other side, Inger and his students feel that the interacting sublayer is an important element in the determination of the pressure. I think that this is a topic worthy of discussion in this roundtable discussion.

As far as the trailing edge interaction goes, I think that there is a minor area of contention between us and the British. I have computed cases with and without the trailing edge correction, and generally, the effects are not large. However, there are cases, which I did show in my talk, where you can underpredict the drag by about 20 - 25% if you don't include trailing edge interaction effects. That theory applies just to cusped trailing edge, and there is a need to extend it to more general airfoils with non-zero trailing edge angles. Results in the written version of my paper, that I did not have a chance to discuss, showed significant discrepancies in drag when the trailing edge angle was larger than 15°. This indicates a need to do more work on these types of airfoils, and maybe we can talk about that in the roundtable discussion.

What came out loud and clear in the meeting was that integral entrainment methods seem to work very well for airfoil flows. I think we are very lucky since viscid-inviscid interactions would take a great deal of computer time, if we had to do finite difference methods. I think the availability of integral entrainment methods makes the prospects of doing efficient numerical calculations with these methods very likely in 3D.

The papers on separated flows demonstrated that we have at least two or three workable iterative methods for iterating between the inviscid and viscid flows when separation is present, provided the separation zone is not too large. The main remaining issue, which has been with us for a long time, is the physics of separated flows for which not much progress was demonstrated at this meeting. The turbulence models that are being used are not adequate. It is not clear whether entrainment methods or integral type methods will be adequate, although there have been some promising results obtained with integral methods shown in this meeting. I think, all in all, our understanding of how to model turbulence and how to close turbulence, particulary for small separation bubbles with substantial pressure gradients across the bubble, is still rather poor. This should also provide an interesting subject for discussion.

One of the issues addressed in the Symposium was the question of normal pressure gradients in two-dimensional flows. Dr. Le Balleur (and Prof. Bradshaw) have been developing procedures based on a generalized set of shear layer equations that include an approximation to the normal momentum equation, while I and others have concentrated on the use of local asymptotic solutions in regions where normal pressure gradients are important. Although calculations have not yet been presented with Le Balleur's method, his approach could prove to be a flexible and accurate method for including normal pressure gradient effects in strong viscid/inviscid interactions. Perhaps the relative merits of these two approaches could be discussed later in this session.

Finally, as an introduction to what I am sure Prof. Kline is going to talk about, I heard in the conversations during the coffee breaks that this audience seems to appreciate the fact that we really don't know how well these CFD codes are performing. We compare them to experiment, and every originator of a code shows extremely good agreement, even in situations where I feel the agreement should not be good. For airfoil flows, the problem seems to be that the experimentalist generating wind tunnel data have not been able to adequately pin down the free stream Mach number and angle of attack, due mainly to wind tunnel wall interference and, perhaps, also to side wall boundary layer effects. Consequently, theoreticians have felt free to adjust both angle of attack and Mach number in their calculations to minimize disagreements with data. I think that we are now at the point where, if we are to make progress, we must have good wind tunnel data with accurate estimates of the experimental values of M and α. In the future we must strive to eliminate this source of uncertainty in correlations of theory and experiment. I feel the question of code validation is also an important subject for discussion in this session.

Dr. Kline

Dr. Quinn has suggested that we summarize, add on, or clarify. M. Le Balleur and Bob Melnik have done an excellent job of summarizing. I would like to clarify some earlier semantic problems concerning flow detachment of a turbulent boundary layer from a faired surface, add on a bit about the physics of that phenomenon, and discuss what this physics implies concerning appropriate modeling of detachment in viscid-inviscid interactions.

Regarding clarification, a question was asked me earlier in the meeting concerning what I meant by "detachment" (or separation). Upon reflection, it became clear that we were using the term from three different viewpoints. These three might be called: (i) computational/parametric; (ii) analytical; (iii) correlative/physical/computational.

In viewpoint (i), Bob Melnik, R.E. Green, and others were considering detachment as a function of parameters, particularly shock incidence, Mach number, and Reynolds number, for a given computational procedure. In viewpoint (ii), several authors, particularly Houdeville, Ardonceau, and Veldman, were analyzing where computations become "stiff" owing to the approach to singular points and discussing means for avoiding these difficulties. In viewpoint (iii), I was discussing an improved physical correlation for detachment in what might be called "shape-factor space", the relation of that correlation to flow structure, and the implications of both the correlation and the flow physics for viscid-inviscid interaction models in computations. I would now like to add to viewpoints (ii) and (iii). Let me begin by saying a little about the improved correlation.

In research at Stanford, for about two years we have been using an improved correlatin plane hv vs.Λ; where: h = (H-1)/H and$\Lambda = \delta^*/\delta$. This plane has several useful properties. The range of both h and Λ is 0-1. One can show from the "wall-wake" correlation, say in the form given by D.. Coles (1956), that the function h = h(Λ) is at most only weakly dependent on Re, and, more important, in a zone of either detachment or reattachment h = h(Λ) is linear and independent of Re.

Figure 1 is an h-Λ plane with the Coles wall-wake function (curve W-W) and the Sanborn-Kline correlation for incipient detachment (curve I-D) shown. All known points for detachment recorded in the literature are also shown. When we eliminate flows with boundary layers far from equilibrium, we see that all the data center on the intersection of curve W-W and curve I-D, but considerable scatter exists. To understand the scatter, we need to understand something about the physics, i.e., the flow structure.

The important thing for our present purpose is to remember that the detachment of a turbulent boundary layer from a faired surface is a zone -- not a line. Detachment occurs as the result of an increasing number of small bits of unsteady, three-dimensional backflow. $C_f = 0$ occurs at, or extremely close to, the point where, on average, the flow goes forward 50% of the time and backward 50% of the time. Turbulent detachment is thus essentially unsteady and three-dimensional, unlike the textbook pictures that describe the laminar case.

For about two years, we have also been using a new instrument called a "thermal tuft". The thermal tuft is comprised of three wires very close to the wall. The center wire is heated, and the outer wires are used as thermometers. (See Eaton, et. al. 1979.) With this instrument, we can obtain quite accurate measurements of the time-average fraction of forward flow (denoted γ_p). Thus we can delineate where $C_f = 0$ with good accuracy. We also obtain a "metric" of boundary layer state (or"stall margin"). We call the location where $\gamma_p = 50\%$ and $C_f = 0$ full detachment.

One point from a thermal tuft with 5% average backflow (95% forward flow) owing to Ashjaee (1980) is shown in Fig. 1 as ☼ . Ashjaee's point lies essentially at the intersection of the curves W-W and I-D in Fig. 1; it thus verifies the location of incipient separation using the new, more accurate technique.

In many early computing methods, full detachment was taken to be somewhere in the range $1.8 \leq H \leq 2.6$. However, Fig. 1 shows that full detachment occurs when H = 4. This was shown explicitly by Coles (1956) in his seminal paper on the "Law of the Wake". Coles demonstrated that at detachment $C_f = 0$, $\delta^*/\delta = \Lambda = 0.5$, and this leads immediately to H = 4, as shown in Fig. 1. Hence both the early computation methods and the data center on incipient detachment, although it is taken to be full detachment by nearly all researchers. It is not difficult to explain why this is so.

In visual techniques, markers will move upstream until there is some small fraction of backflow; the exact location of farthest upstream movement will depend on the type of marker used. Since a variety of uncalibrated visual methods were employed, we must expect considerable scatter centering on incipient detachment -- just what is observed in Fig. 1.

The reason why some theories have also mistaken incipient for full detachment leads directly to the connection between the physics and computation. If one thinks of the boundary layer blockage δ^*/δ, it becomes clear that only a relatively small value of the time-average fraction of backflow will cause δ^* to increase rapidly, thus strongly increasing the interaction between the viscid and inviscid zones. This increased interaction implies the need for improved matching procedures, and this often is displayed mathematically by "stiff" matrices in a given solution algorithm. To put this differently, the first appearance of singularities in the solution matrix is usually associated with incipient detachment -- rather than full detachment. This can clearly be seen in the results of the 1968 AFOSR-IFP-Stanford Conference on Computation of Turbulent Boundary Layers. All 28 methods either stopped or were continued by some ad hoc modification of the interaction procedure, up to full detachment.

Since the appearance of singularities is highly "equation-dependent", the degree of difficulty will depend on the precise form of the governing equations for the solution matrix, including the variable chosen. the governing equations used, and the differencing scheme employed. This conclusion is common

mathematical knowledge, and is evident in the presentations of this meeting, particularly those of Ardonceau, of Houdeville, and of Veldman. The 1968 experience suggests in addition, that any procedure following the standard boundary layer algorithm of Prandtl is not likely to carry all the way to full detachment, since the 28 methods in the '68 Conference embody a wide variety of equations and numerical procedures.

Recognition that singularities can arise well ahead of full detachment is important, even though the physical distance from incipient to full detachment is quite short in many flows. The knowledge advises us when to be careful concerning possible singular behavior. It also advises when we need to shift our modeling to account for effects of detachment and the presence of free shear layers.

In modeling passage flows at Stanford in the last few years, we have had considerable success with very simple programs when we have followed these twin ideas of modifying matching and flow models at incipient detachment. Bardina et al. (1981) summarize the results for two-dimensional, incompressible, planar diffusers. They show success in computing three flow regimes (unstalled flow, transitory stall, and full stall) with a single program running less than a second in a medium-sized computer. We use a boundary layer program with conventional matching until we reach $\Lambda = 0.42$. At this point the models are shifted to fit free shear layers and conditions derived from the physics of separated flows introduced.

Initially, the method was found from physical reasoning. More recently, we have been routinely studying the Jacobean of the coefficients of the solution matrix. When singularities occur, we then seek means for removing the singularities from the domain of computation. This has led to a number of further advances for internal flow cases. We expect to report in relatively short times (measured on research-project time-constants) advances covering inverse procedures, other geometries, compressible flows up to M = 0.9, and flows with forced unsteady mean streams. All these methods run in times one or two orders of magnitude less than required for grid computations using the time-average Navier-Stokes equations (even with simple closure models). Thus, we have several methods of considerable utility for many engineering computations.

We have not yet seen methods of this sort applied to external flows, but we believe they may have something to offer not only in rapid computation but also possibly in improving the modeling of some cases of shock/boundary-layer interaction where one suspects the flow physics near the wall will be similar to that described above.

References

Ashjaee, J., Dissertation Mech. Engr. Stanford University, June 1980.
Bardina, J., A. Lyrio, S.J. Kline, J.H. Ferziger, J.P. Johnston (1981), "A Prediction Method for Planar Diffusers", to be published in Journal of Fluids Engineering, ASME.
Coles, D.E. (1956), "The Law of the Wake", Journal of Fluid Mechanics, 1, pp. 191-226.
Eaton, J.K., J.P. Johnston, A.H. Jeans, and J. Ashjaee (1979), "A Wall Flow Direction Probe for Use in Separating and Reattaching Flows", Trans. ASME, Journal of Fluids Engineering, 101, pp. 326-330.

Dr. Quinn

Thank you gentlemen. Dr. Melnik brought up the question of wind tunnel data. Mr. Rosch has some comments appropriate to that topic.

Mr. Rosch

Dr. Melnik and I were talking about this special problem during lunch. I want to make it very clear. Everyone dealing with inviscid and viscous numerical schemes compared their results with measurements. But, as it turns out, everyone has their own airfoil section together with some experiments from wind tunnels to which they have access. I find that it is very difficult to compare one method with another one. On the other hand, a computer code has to be compared with some sort of measurement. If you want to compare your numerical experiment with measurements, you have to know at least the free stream Mach number and the angle of attack. It turns out that the Mach number and the angle of attack you should use in a numerical calculation are depending on the wind tunnel and the wind tunnel wall corrections, so no one really knows which effect of misagreement depends on the Mach number and which one on the mismatch of the angle of attack. The aim of this remark is only to make it very clear and to suggest that in future work for wind tunnels some details should be laid on wind tunnel wall corrections and they should be stated in the papers when they are published.

Dr. Quinn

Thank you Mr. Rosch. Let's keep on with this point, I would like to get some discussion. Is there anyone in the wind tunnel community who would like to address this point?

Mr. King

I wanted to mention that rather than trying to make wind tunnel wall corrections, we have used a pressure survey tube to measure the pressure distribution both above and below the airfoil inside the wind tunnel. We have then used these measured pressures as boundary conditions on our numerical calculations. These results we presented at the AIAA Snowmass meeting and the effects of the pressure boundary condition on the calculated results were quite significant.

Dr. Quinn

Quite significant - how much, 10%, 15%?

Mr. King

We could get a movement of the shock on the airfoil in an essentially weak interaction case, in which the boundary layer had little effect on shock position. The shock position on the airfoil would move by 15 to 20%.

Dr. Quinn

That is a lot. Who else would like to comment?

Mr. Firmin

I wish to agree with what has been said by Mr. King and support the view that the boundary conditions near the wind tunnel walls must be known and taken into account in calculatins. I would like to remind the audience that a recent AGARD report exists, AGARD-AR-138, where Winter and Ohman make recommendations about wind tunnel testing, both for two dimensional and three dimensional flows. They recommend, in addition to the boundary layer and wake measurements that have normally been made, that for aerofoil tests:

1. The boundary conditions for the inviscid flow in the vicinity of the roof and floor be measured, and
2. The side wall boundary layer thicknesses are determined, and if possible, the sensitivity to end walls conditions be determined by using suction to change the thicknesses. If these measurements are made, then doubts about the effects of tunnel walls can largely be overcome.

Dr. Quinn

Any further comments?

Mr. Ohman

As a matter of course we now measure the wall boundary conditions on all two-dimensional tests done in our wind tunnel. We use a method similar to the one developed by M. Capellier and Chevallier at ONERA to compute the wall corrections. That, in our case, seems to work quite well. Concerning the side-wall boundary layer effect, that is still a very tricky problem, and I don't think that we have a final solution to that one. We find that the application of side wall suction in the vicinity of the model seems to work quite well in our case. I know that there are other situations where it apparently doesn't work.

We have seen in most cases very good agreement between calculations and measurements in supercritical flow. Nowhere has mention been made of the geometric accuracy of the model. I suspect that in most cases the authors have used the theoretical coordinates of the airfoil section, rather than the measured ones. If the model is accurately made, there may be no cause for concern. However, the sensitivity of supercritical flow to model geometry is extremely high, so for a not-so-well made model, you can easily get calculated results that are quite different according to whether you use actual measured model coordinates or theoretical design coordinates. Some of us, who have presented comparisons of theoretical and experimental results, should look into this point.

Mr. Rosch

Mr. Ohman, I disagree with some of your statements and I won't put the blame on the mismatch between the design airfoil coordinate and the coordinate that actually is manufactured. In our firm we make various checks, and we see that we get different results between different wind tunnels. So it isn't really the model construction problem.

Mr. Ohman

Just a very quick response. We have done comparisons of wind tunnels, in our case with NLR. NLR used a slotted wall, we used a perforated wall wall tunnel, and we got the same results in supercritical flows.

Dr. Green

I would like to raise the importance of knowing the geometry in 3-D model testing. In this case aeroelastic distortion comes in and the effects can be appreciable, though they can in principle be incorporated in viscous interaction codes. This brings up a question that I wanted to ask Dr. Drougge, had time permitted, at the end of his presentation - are any aeroelastic measurements going to be made to define the shape of the aircraft in the FFA flight experiments?

Dr. Drougge

Yes.

Dr. Tydeman

I would like to make a remark on the application of shock-wave - boundary layer interaction models in numerical schemes. There are a number of flow patterns in which the straight-forward application is doubtful. I am thinking, for instance, on the double shock configuration of Mr. Stanewsky (Paper 4, Fig. 13). The critical value of C_p is not indicated, but probably remains below the first pressure jump in his figure. It is questionable whether the first shock indeed ' the airfoil surface. This implies that it is also questionable whether the shock-wave - boundary model should be applied.

Some other flow patterns which may give rise to problems have been sket ' in Figure 2. These patterns were observed during experiments on an airfoil with flap.

Dr. Quinn

Thank you Dr. Tydeman. This seems to be a point that we could continue discussing and perhaps even have a symposium. I am going to halt discussion on this particular aspect, and if there is time later on, we will come back to it. In closing the discussion, I want to try to give the flavor of what has been said: If wall conditions or small errors in local incidence reposition a shock by as much as 10 or 15%, the error in pressure may be considerably more. Consequently, when we see agreement between calculations and not-very-well-discussed experimental data, we should keep in mind the liklihood of errors in the experimental facility, in the model geometry, and in the analysis.

Dr. Tydeman

I would like to comment on the wall corrections and the displacement of the shock wave. You must be aware that it depends very much on the type of pressure distribution. For instance, when you have a flat pressure distribution ahead of the shock wave, you need only a few tenths of a degree to change the shock position quite a lot. On the other hand, when there is a steep gradient ahead of the shock wave, the shock is hardly willing to move. In other words, it is very dangerous to make a common statement.

Dr. Quinn

Let's end the discussion for the moment on shock waves and boundary layer interactions in wind tunnels and move on to a point that received a lot of discussion on the first and second days. You recall that authors provided calculations and contrasted them with experiments to show they were in reasonable agreement. Dr. Melnik and others then asked if they had included wake effects; and the response would provoke considerble discussion. I want to touch on the wake effects now. Mr. Slooff had some questions on the trailing edge conditions, and I think that might relate to the wake problem.

Mr. Slooff

I would like to dwell briefly on a subject that was barely touched at this conference; Bob Melnik mentioned it briefly. It is a subject I have a problem with and it has been a problem for several years. I would like to share it with the community here. Maybe there is somebody here that has solved it or perhaps it will trigger somebody to solve it in the future. It is in fact an inviscid problem already. We may think of solutions of the Euler equations and in particular of solutions of the flow over an airfoil with a finite trailing edge angle and with a shock on the upper surface, across which we have a jump in total pressure and no shock on the lower surface (Fig. 3). Then it is quite easy to show that the only possible type of flow at the trailing edge which will satisfy zero pressure jump across the wake is one in which the flow leaves the trailing edge tangential to the lower surface. If there is a shock only on the lower surface, the situation is just the other way around and in general one might say that the flow will have to leave the surface in the direction towards the strongest shock, if there are shocks on both surfaces. We can play the game in mind that the shock strength reduces to zero, and what we end up with then is a potential flow. However, there is no reason to believe that something sudden happens with that trailing edge flow at the moment that the total pressure jump goes to zero. On the other hand the classical picture of potential flow, as obtained for instance, from the theory of conformal mapping, is that the flow leaves a trailing edge along the bisector. It seems that we have a conflict here.

Another way to look at the problem is from the point of view of three-dimensional wing flow. It was shown sometime in the late 60's, I think, by Mangler and Smith that, on a 3-d wing with a vortex sheet leaving the trailing edge, depending on the sign of the shed vorticity and the angle between the vorticity vector and the trailing edge, flow also has to leave the trailing edge parallel to either the upper or the lower surface. Again we may play a game of limits and say that the 2-d case is obtained when we let the aspect ratio go to infinity. Again we end up with a flow at the trailing edge which is either parallel to the upper or the lower surface. The question now is, what is the relevant inviscid trailing edge flow solution? I think that we might also put the question in this way: what is the limit of trailing edge flow when the Reynolds number goes to infinity?

I also have a comment, which is that a good viscous-inviscid interaction method should contain the proper limit for delta star going to zero at the trailing edge. It seems to me that we are not sure what that limit is in the 2-d case, but in the 3-d case it seems inevitable that it should be according to the Mangler and Smith criterion. I would like to draw your attention to a formulation of viscous 3-d trailing edge flow which was given by Piers and some colleagues in 1975*, which is a formulation which satisfies the criteria that if the delta star goes to zero then we satisfy the Mangler-Smith criterion. I don't think any method discussed at this symposium satisfied this.

* NLR Report TR75076 U

Dr. Quinn

Dr. Green is anxious to speak to this point.

Dr. Green

Could we have the slide again please. I would like to have an argument with Mr. Slooff over this. The upper picture which he draws, I would support wholeheartedly. You don't need a shock wave in there, what you need to draw in is the boundary layer and then argue that its behavior near the trailing edge region is quasi inviscid - the important part of the boundary layer behaves inviscidly. The boundary layer looks like a flow with slip velocity at the wall and, if the airfoil is generating much lift, the boundary layer on the upper surface will have a higher value of shape factor because of the adverse pressure gradients and will therefore have a lower slip velocity and a lower total head at the wall.

The only solution in that case, for the trailing edge region modelled as a rotational inviscid region of strong interaction, is as Mr. Slooff has drawn it on the top. I made this point in 1971 in the paper I gave in the AGARD meeting in Gottingen on high Reynolds number flow. In fact, the argument came from Mangler and Smith; it is the argument that you can't have two contiguous corner flows separated by a free stream line if the stagnation pressure on the dividing streamline differs in the two flows. So when we come to the question of what is the relevant inviscid trailing edge flow solution in the limit of Reynolds number going to infinity, I would say that the limit Reynolds number going to infinity is not relevant. When we are looking for the equivalent inviscid flow that is part of our interactive solution, what is said in Lock's paper is that we are seeking an inviscid flow which is identical to the real flow outside the viscous region. This equivalent inviscid flow has in it at the trailing edge a discontinuity in the axial distribution of the velocity components normal to the boundary. The sum of the discontinuities in the upper and lower parts of the flow must match the trailing edge angle. The solution for the inviscid flow must be such that, when it is matched with a model of the strong interaction behavior in the trailing edge region, in the combined solution the boundary streamline on the under surface is continuous through the trailing edge region whilst that on the upper surface is turned sharply through the trailing edge angle. It seems to me that, on the basis of what Lock has said, one can put together an entirely self-consistent model for the inviscid flow which matches the picture that Mr. Slooff has suggested for us here. The arguments carry over quite logicaliy to three dimensions, although in three dimensions there is the possibility of the vortex sheet changing direction as it comes off the trailing edge in some strange lifting cases. I believe that the principles set down in Lock's paper meet the point that has been raised here.

Mr. Slooff

I know and accept the heuristic argument based on the different total head in the mean part of the boundary layers approaching the trailing edge. It already follows immediately from Dr. Küchemann's inviscid shear flow trailing edge model. I think, if I understood you correctly, that you agree with me that the proper picture of inviscid flow at the trailing edge might be the one in which the flow leaves the trailing edge parallel to whatever surface is appropriate for the particular case. Not the bisector. I think that we agree basically on that.

Dr. Melnik

I would like to comment on the points raised by Drs. Slooff and Green. I thought that I wasn't going to find anything to disagree with John Green about, but at the last minute he came through with something that I think I disagree with. First let's get to the problem raised by Slooff. He did raise a good point, and it is interesting that Jerry South raised it in a telephone conversation to me a couple of months ago. It is the kind of question that people who do singular perturbation theory love to get. It is a singular perturbation problem, and it is a question of non-uniform limits. If there is a total pressure difference on the upper and lower sides of the airfoil, the argument is correct that the streamline must come off tangent to the lower surface, (i.e., tangent to the surface that has the higher total pressure). If the total pressure difference is exactly zero, it is also true that the streamline must go along the bisector. Both statements are true. So, the question to ask is, how does this difference in behavior get resolved in the limnt as the difference in total pressure vanishes? What happens is that if, for example, you have an infinitesmally weak shock on the upper surface, the streamline will come off tangent to the lower surface and soon turn in a direction to approach the bisector. As the shock strength gets weaker and weaker, the region of turning, where you go from tangent to the lower surface to tangent to the bisector, shrinks. This question gets resolved in the non-uniform approach to the limit as the total pressure difference goes to zero. As the total pressure loss across the shock wave goes to zero, the streamline at the limit is exactly along the bisector, but for any small but non-zero total pressure loss there is an infinitesmal region that shrinks to zero where the streamline direction transitions from the direction of the lower surfasce to the direction of the bisector. Now, with regard to what John Green said about Robin Lock's statement about the displacement thickness forming a corner that just cancels the geometric corner, so that you have a smooth equivalent displacement surface and no stagnation point. That is true, and it is a situation where interacting boundary layer theory can eliminate a singularity to get a smooth solution. The problem is that although the solution is now regular, it is incorrect. The streamwise length scale over which the displacement thickness exactly conceals the geometric corner turns out to be the order of the displacement thickness, which is very narrow. In the terms that I use, that would be $O(\varepsilon^2)$ (where ε is the dimensionless friction velocity). Bernie Grossman and I nave extended my cusped trailing edge theory to precisely this problem, that is, an airfoil with finite trailing edge angle. From the resulting theory you find that if you take into account normal pressure gradients through the boundary layer, the interaction spreads over the order of the boundary layer thickness which is $O(\varepsilon)$ and much larger than the displacement thickness. With the theory you treat the flow as inviscid and rotational over most of the boundary layer. Of course, in that theory, there is then no requirement that the streamline comes along the bisector. You solve the rotational flow and the streamline at the bottom of the boundary layer, the one with the higher total pressure, will leave tangent to the lower surface. As the Reynolds number goes to infinity, and the non-uniformity in the boundary layer goes to zero, that region where it transitions to the direction of the bisector will again shrink to zero as the boundary layer thickness goes to zero, and you will be left with the streamline along the bisector in the limit. So, to summarize, Lock is right, in that solution of the interacting boundary layer equations without normal pressure gradients will eliminate the singularity, but it is an improper solution. If you take into account normal pressure gradients, you get a self-consistent solution and a different, but theoretically correct, resolution of what happens in the limit.

Dr. Green

With regard to interest in the flow at infinite Reynolds number, I would repeat that the inviscid solution that we are concerned with in our computation of real flows is always one to which we have applied the appropriate boundary conditions so as to match it to a viscous flow. Therefore, it is an inviscid flow which has to match the conditions at the trailing edge that are enforced by there being a region of strong viscous interaction at the trailing edge. With reference to Lock's analysis, I should

like to make it clear that this can embrace normal pressure gradients. It is a misconception to think that it depends on the assumption of constant pressure across the boundary layer. It is a question of how you define your boundary layer quantities. This point is dealt with in Lock's paper, and I believe Dr. Melnik will find the analysis to be self-consistent.

Mr. Melmuth

I was concerned about this finite trailing edge. We studied this to some extent on our upper-surface blowing paper presented in January at AIAA and we were concerned with similar kinds of questions regarding the orientation of the stagnation streamline. I think that what has been said here is correct regarding total heads, and the impact of that with respect to the tangency of the dividing streamline. One concern that I have on the finite trailing edge angle is that you just can't use Prandtl-Glauert theory in the vicinity of the trailing edge. You have to include the non-linear effects associated with the stagnation.

Dr. Quinn

I am afraid our time has run out. I would like to be able to say that the Round Table Discussion summarized our present ability to compute flows with meaningful viscous and inviscid interactions, and to some extent it has. But equally important, through your discussion, you have all brought attention to situations that were discussed either incompletely or not at all. Perhaps this symposium should be followed up by another to treat the unresolved issues. M. Monnerie and I have each heard favorable remarks concerning the technical content of this symposium. We hope you all share those sentiments and we take this opportunity to thank the authors for their excellent presentations of new research. We particularly thank M. Le Balleur, Dr. Lock by way of Dr. Green, Dr. Melnik and Prof. Kline for sharing their perspectives of specific areas. We also thank all of you for your participation and your interesting comments. Good conferences just don't happen, they are the result of hard work and in this regard, M. Monnerie and I express our very special gratitude to our colleagues who served on the program committee; Dr. Green, Prof. Hindelang, Prof. Gersten, Prof. von Ingen, Prof. Mattioli, Dr. Panaras, and seeking expertise beyond that which we have on the panel, we co-opted two members: Prof. Kline and M. Serieix. At this time I take great pleasure in introducing the Chairman of the Fluid Dynamics Panel Dr. Orlik-Rückemann.

Dr. Orlik-Rückemann

We have come to the end of this long, but very informative, sometimes controversial and on the whole very thought-provoking meeting. I am sure that we have all greatly enjoyed the last three days. We are very much in debt to the Air Force Academy and to the U.S. Air Force for providing these fine facilities. I hope that we now will all go home feeling a little bit richer, not only by virtue of having acquired additional pieces of knowledge, but also in the sense of having established personal contacts of lasting value, or maybe just having cultivated and strengthened some of the old ones.

I have heard several positive comments about this symposium. Of course, the fact that we all have enjoyed it so much is due to the combined efforts of a whole team of dedicated people. Some of those were already mentioned. It is now my very pleasant duty to recognize these people, so that we can all express our appreciation and our sincere thanks for their efforts and for a job very well done.

Firstly, Mr. Monnerie and Dr. Quinn and the members of their committee for putting together such a fine technical program, chairing the various sessions, and leading and stimulating the discussion. Then the U.S. panel coordinator, Dr. Keith Richey, for selecting such a beautiful site, making the necessary arrangements, and performing an outstanding job in personally supervising the administrative and logistic functions during this meeting. In this effort, Dr. Richey was ably and tirelessly assisted by our most efficient Panel staff from Paris, Mr. Bob Rollins, the Panel Executive and Mademoiselle Anne-Marie Rivault. On behalf of the Academy, the local arrangements were graciously handled by Mrs. Janet Shea. The audio and visual equipment, respectively, was expertly operated by Mr. Art Young of the State Department and Staff Sargent Cary Harpley of the Academy. Their performance certainly equalled the very best I have ever seen.

Last, but not least, the translation. We have been very fortunate indeed in having with us a truly efficient team of interpreters, who in most cases performed smoothly and seemingly without effort, despite the usual difficulties associated with speakers who talk too fast or with a foreign accent such as mine. Our interpreters were Mrs. Sophia Porson, Mrs. Margaret Mark, and Miss Doris Kirsch.

Now a few words about our future plans. Next year there will be two Symposia. The first in Toulouse, France, on the 11-14 of May, on the "Aerodynamics of Powerplant Installation" and the second in Lisbon, Portugal, on the 2-5 of November on the "Fluid Dynamics of Jets with Applications to V/STOL". The Panel will also sponsor a Lecture Series on "Dynamic Stability Parameters" to be given on the 2-5 of March at NASA Ames, USA, and on the 16-19 of March at VKI, Belgium. We hope to see as many of you as possible on those occasions. If you cannot participate yourself, please pass the word on to your colleagues. With that, I would like to thank you all for your participation and to wish you a pleasant trip home. This meeting is now adjourned.

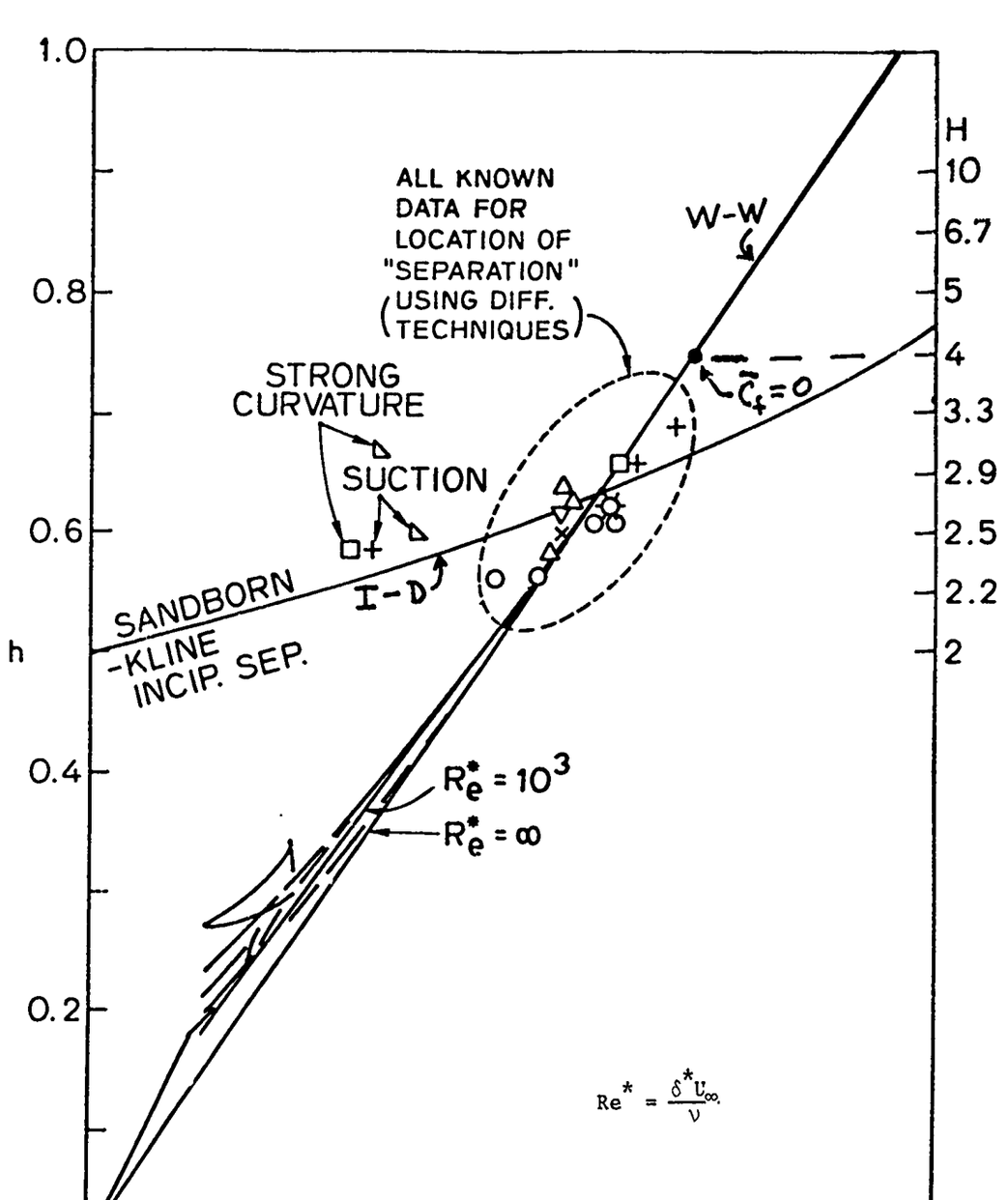
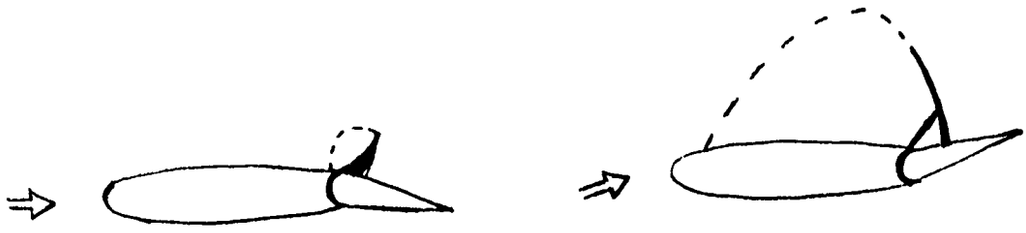


Figure 1. Correlation of all known data for Flow Detachment in h-Λ plane.

$h = \frac{H-1}{H}$, $H = \delta^*/\theta$, $\Lambda = \delta^*/\delta$



Expansion around convex corner between wing and aileron

λ-shock in concave corner between wing and aileron

Figure 2

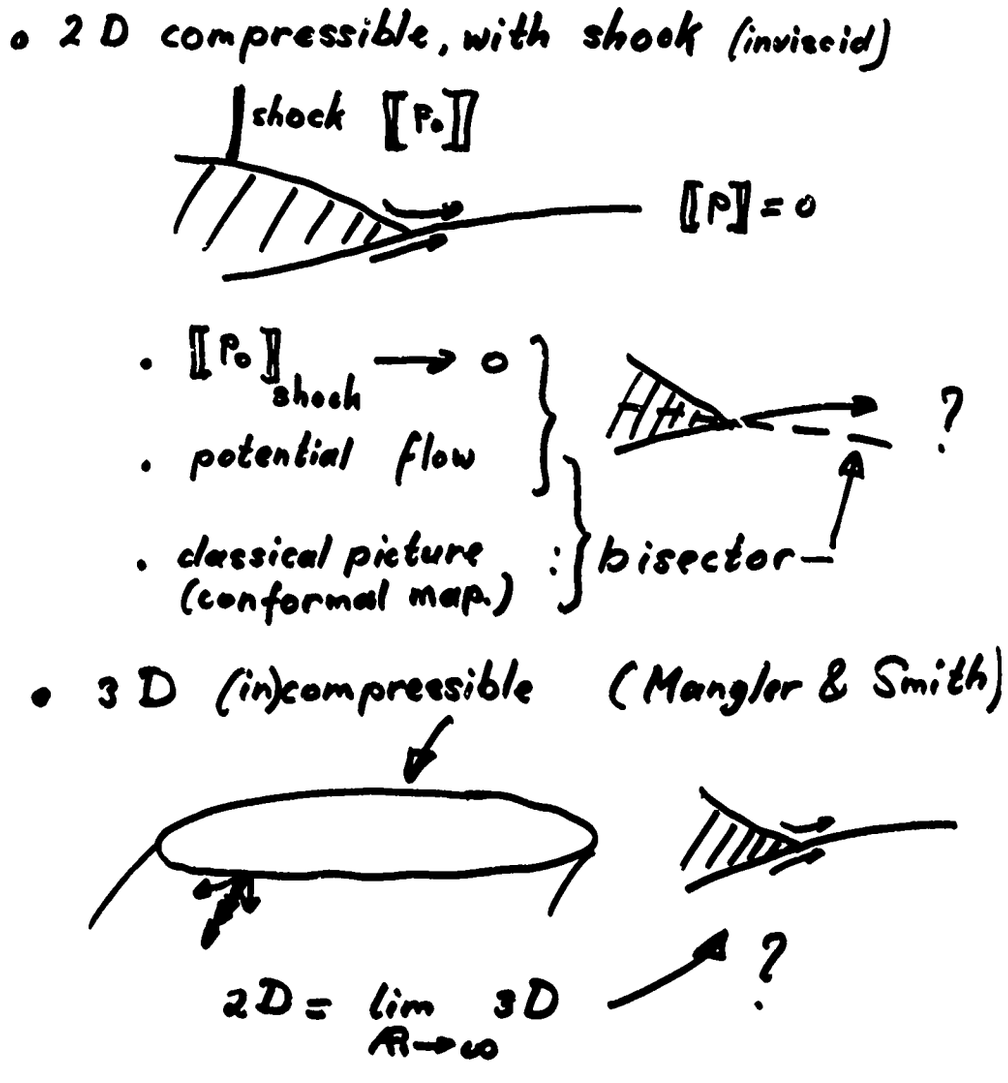


Fig.3 Finite T.E. angle problem

REPORT DOCUMENTATION PAGE			
1. Recipient's Reference	2. Originator's Reference	3. Further Reference	4. Security Classification of Document
	AGARD-CP-291	ISBN 92-835-0286-8	UNCLASSIFIED

5. Originator	Advisory Group for Aerospace Research and Development North Atlantic Treaty Organization 7 rue Ancelle, 92200 Neuilly sur Seine, France
6. Title	COMPUTATION OF VISCOUS-INVISCID INTERACTIONS
7. Presented at	the Fluid Dynamics Panel Symposium held at the United States Air Force Academy, Colorado Springs, Colorado, USA – 29 September–1 October 1980.

8. Author(s)/Editor(s)	9. Date
Various	February 1981
10. Author's/Editor's Address	**11. Pages**
Various	538

12. Distribution Statement This document is distributed in accordance with AGARD policies and regulations, which are outlined on the Outside Back Covers of all AGARD publications.

13. Keywords/Descriptors

Fluid dynamics	Computation
Inviscid flow	Applications of mathematics
Viscous flow	
Boundary layer separation	

14. Abstract

The Symposium was organized by the AGARD Fluid Dynamics Panel to review work on procedures for coupling the knowledge of viscous flow in the boundary and shear layers with the perfect fluid assumptions made for the remainder of the flow; to determine methods and algorithms to link the viscous and inviscid parts of the flows.

Thirty-one papers comprised the meeting; four of these papers were invited reviews. A general introduction was followed by sessions on: (1) Unseparated flows, thin-layer concept, (2) Turbulent strong interaction without extensive separated flow, and (3) Separated flows. One additional paper was presented and the meeting was closed with a Round Table Discussion which was transcribed for the Proceedings. A Technical Evaluation Report will be published at a later date.

Papers presented and discussions held at the Fluid Dynamics Panel Symposium held at the United States Air Force Academy, Colorado Springs, Colorado, USA – 29 September – 1 October 1980.

AGARD Conference Proceedings No.291 Advisory Group for Aerospace Research and Development, NATO COMPUTATION OF VISCOUS-INVISCID INTERACTIONS Published February 1981 538 pages The Symposium was organized by the AGARD Fluid Dynamics Panel to review work on procedures for coupling the knowledge of viscous flow in the boundary and shear layers with the perfect fluid assumptions made for the remainder of the flow; to determine methods and algorithms to link the viscous and inviscid parts of the flows. P.T.O.	AGARD-CP-291 Fluid dynamics Inviscid flow Viscous flow Boundary layer separation Computation Applications of mathematics	AGARD Conference Proceedings No.291 Advisory Group for Aerospace Research and Development, NATO COMPUTATION OF VISCOUS-INVISCID INTERACTIONS Published February 1981 538 pages The Symposium was organized by the AGARD Fluid Dynamics Panel to review work on procedures for coupling the knowledge of viscous flow in the boundary and shear layers with the perfect fluid assumptions made for the remainder of the flow; to determine methods and algorithms to link the viscous and inviscid parts of the flows. P.T.O.	AGARD-CP-291 Fluid dynamics Inviscid flow Viscous flow Boundary layer separation Computatien Applications of mathematics
AGARD Conference Proceedings No.291 Advisory Group for Aerospace Research and Development, NATO COMPUTATION OF VISCOUS-INVISCID INTERACTIONS Published February 1981 538 pages The Symposium was organized by the AGARD Fluid Dynamics Panel to review work on procedures for coupling the knowledge of viscous flow in the boundary and shear layers with the perfect fluid assumptions made for the remainder of the flow; to determine methods and algorithms to link the viscous and inviscid parts of the flows. P.T.O.	AGARD-CP-291 Fluid dynamics inviscid flow Viscous flow Boundary layer separation Computation Applications of mathematics	AGARD Conference Proceedings No.291 Advisory Group for Aerospace Research and Development, NATO COMPUTATION OF VISCOUS-INVISCID INTERACTIONS Published February 1981 538 pages The Symposium was organized by the AGARD Fluid Dynamics Panel to review work on procedures for coupling the knowledge of viscous flow in the boundary and shear layers with the perfect fluid assumptions made for the remainder of the flow; to determine methods and algorithms to link the viscous and inviscid parts of the flows. P.T.O.	AGARD-CP-291 Fluid dynamics Inviscid flow Viscous flow Boundary layer separation Computation Applications of mathematics

Thirty-one papers comprised the meeting; four of these papers were invited reviews. A general introduction was followed by sessions on: (1) Unseparated flows, thin-layer concept, (2) Turbulent strong interaction without extensive separated flow, and (3) Separated flows. One additional paper was presented and the meeting was closed with a Round Table Discussion which was transcribed for the Proceedings. A Technical Evaluation Report will be published at a later date.

Papers presented and discussions held at the Fluid Dynamics Panel Symposium held at the United States Air Force Academy, Colorado Springs, Colorado, USA – 29 September – 1 October 1980.

ISBN 92-835-0286-8

Thirty-one papers comprised the meeting; four of these papers were invited reviews. A general introduction was followed by sessions on: (1) Unseparated flows, thin-layer concept, (2) Turbulent strong interaction without extensive separated flow, and (3) Separated flows. One additional paper was presented and the meeting was closed with a Round Table Discussion which was transcribed for the Proceedings. A Technical Evaluation Report will be published at a later date.

Papers presented and discussions held at the Fluid Dynamics Panel Symposium held at the United States Air Force Academy, Colorado Springs, Colorado, USA – 29 September – 1 October 1980.

ISBN 92-835-0286-8

Thirty-one papers comprised the meeting; four of these papers were invited reviews. A general introduction was followed by sessions on: (1) Unseparated flows, thin-layer concept, (2) Turbulent strong interaction without extensive separated flow, and (3) Separated flows. One additional paper was presented and the meeting was closed with a Round Table Discussion which was transcribed for the Proceedings. A Technical Evaluation Report will be published at a later date.

Papers presented and discussions held at the Fluid Dynamics Panel Symposium held at the United States Air Force Academy, Colorado Springs, Colorado, USA – 29 September – 1 October 1980.

ISBN 92-835-0286-8

Thirty-one papers comprised the meeting; four of these papers were invited reviews. A general introduction was followed by sessions on: (1) Unseparated flows, thin-layer concept, (2) Turbulent strong interaction without extensive separated flow, and (3) Separated flows. One additional paper was presented and the meeting was closed with a Round Table Discussion which was transcribed for the Proceedings. A Technical Evaluation Report will be published at a later date.

Papers presented and discussions held at the Fluid Dynamics Panel Symposium held at the United States Air Force Academy, Colorado Springs, Colorado, USA – 29 September – 1 October 1980.

ISBN 92-835-0286-8

B.III/4

AGARD

NATO OTAN

7 RUE ANCELLE · 92200 NEUILLY-SUR-SEINE

FRANCE

Telephone 745.08.10 · Telex 610176

DISTRIBUTION OF UNCLASSIFIED AGARD PUBLICATIONS

AGARD does NOT hold stocks of AGARD publications at the above address for general distribution. Initial distribution of AGARD publications is made to AGARD Member Nations through the following National Distribution Centres. Further copies are sometimes available from these Centres, but if not may be purchased in Microfiche or Photocopy form from the Purchase Agencies listed below.

NATIONAL DISTRIBUTION CENTRES

BELGIUM
Coordonnateur AGARD – VSL
Etat-Major de la Force Aérienne
Quartier Reine Elisabeth
Rue d'Evere, 1140 Bruxelles

CANADA
Defence Science Information Services
Department of National Defence
Ottawa, Ontario K1A OK2

DENMARK
Danish Defence Research Board
Østerbrogades Kaserne
Copenhagen Ø

FRANCE
O.N.E.R.A. (Direction)
29 Avenue de la Division Leclerc
92320 Châtillon sous Bagneux

GERMANY
Fachinformationszentrum Energie,
Physik, Mathematik GmbH
Kernforschungszentrum
D-7514 Eggenstein-Leopoldshafen 2

GREECE
Hellenic Air Force General Staff
Research and Development Directorate
Holargos, Athens

ICELAND
Director of Aviation
c/o Flugrad
Reykjavik

ITALY
Aeronautica Militare
Ufficio del Delegato Nazionale all'AGARD
3, Piazzale Adenauer
Roma/EUR

LUXEMBOURG
See Belgium

NETHERLANDS
Netherlands Delegation to AGARD
National Aerospace Laboratory, NLR
P.O. Box 126
2600 A.C. Delft

NORWAY
Norwegian Defence Research Establishment
Main Library
P.O. Box 25
N-2007 Kjeller

PORTUGAL
Direcção do Serviço de Material
da Forca Aerea
Rua da Escola Politécnica 42
Lisboa
Attn: AGARD National Delegate

TURKEY
Department of Research and Development (ARGE)
Ministry of National Defence, Ankara

UNITED KINGDOM
Defence Research Information Centre
Station Square House
St. Mary Cray
Orpington, Kent BR5 3RE

UNITED STATES
National Aeronautics and Space Administration (NASA)
Langley Field, Virginia 23365
Attn: Report Distribution and Storage Unit

THE UNITED STATES NATIONAL DISTRIBUTION CENTRE (NASA) DOES NOT HOLD STOCKS OF AGARD PUBLICATIONS, AND APPLICATIONS FOR COPIES SHOULD BE MADE DIRECT TO THE NATIONAL TECHNICAL INFORMATION SERVICE (NTIS) AT THE ADDRESS BELOW.

PURCHASE AGENCIES

Microfiche or Photocopy
National Technical
Information Service (NTIS)
5285 Port Royal Road
Springfield
Virginia 22161, USA

Microfiche
Space Documentation Service
European Space Agency
10, rue Mário Nikis
75015 Paris, France

Microfiche
Technology Reports
Centre (DTI)
Station Square House
St. Mary Cray
Orpington, Kent BR5 3RF
England

Requests for microfiche or photocopies of AGARD documents should include the AGARD serial number, title, author or editor, and publication date. Requests to NTIS should include the NASA accession report number. Full bibliographical references and abstracts of AGARD publications are given in the following journals:

Scientific and Technical Aerospace Reports (STAR)
published by NASA Scientific and Technical
Information Facility
Post Office Box 8757
Baltimore/Washington International Airport
Maryland 21240, USA

Government Reports Announcements (GRA)
published by the National Technical
Information Services, Springfield
Virginia 22161, USA

Printed by Technical Editing and Reproduction Ltd
Harford House, 7–9 Charlotte St, London W1P 1HD

ISBN 92-835-0286-8